

R&D 6418-MS-02

DATA 45-90-M-0117.

AD-A246 363



This document has been approved
for public release and sale; its
distribution is unlimited.

DTIC
SELECTE
JAN 31 1992
S D

Science and Technology of Nanostructured Magnetic Materials

Edited by
George C. Hadjipanayis and
Gary A. Prinz

NATO ASI Series

Series B: Physics Vol. 259

92 1 28 098

92-02317



Science and Technology of Nanostructured Magnetic Materials

NATO ASI Series

Advanced Science Institutes Series

A series presenting the results of activities sponsored by the NATO Science Committee, which aims at the dissemination of advanced scientific and technological knowledge, with a view to strengthening links between scientific communities.

The series is published by an international board of publishers in conjunction with the NATO Scientific Affairs Division

| | |
|---|--|
| A Life Sciences | Plenum Publishing Corporation |
| B Physics | New York and London |
| C Mathematical and Physical Sciences | Kluwer Academic Publishers |
| D Behavioral and Social Sciences | Dordrecht, Boston, and London |
| E Applied Sciences | |
| F Computer and Systems Sciences | Springer-Verlag |
| G Ecological Sciences | Berlin, Heidelberg, New York, London, |
| H Cell Biology | Paris, Tokyo, Hong Kong, and Barcelona |
| I Global Environmental Change | |

Recent Volumes in this Series

Volume 255—Vacuum Structure in Intense Fields
edited by H. M. Fried and Berndt Müller

Volume 256—Information Dynamics
edited by Harald Atmanspacher and Herbert Scheingraber

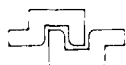
Volume 257—Excitations in Two-Dimensional and Three-Dimensional Quantum Fluids
edited by A. F. G. Wyatt and H. J. Lauter

Volume 258—Large-Scale Molecular Systems: Quantum and Stochastic Aspects—
Beyond the Simple Molecular Picture
edited by Werner Gans, Alexander Blumen, and Anton Amann

Volume 259—Science and Technology of Nanostructured Magnetic Materials
edited by George C. Hadjipanayis and Gary A. Prinz

Volume 260—Self-Organization, Emerging Properties, and Learning
edited by Agnès Babloyantz

Volume 261—Z⁰ Physics: Cargèse 1990
edited by Maurice Lévy, Jean-Louis Basdevant, Maurice Jacob,
David Speiser, Jacques Weyers, and Raymond Gastmans



Series B: Physics

Science and Technology of Nanostructured Magnetic Materials

Edited by

George C. Hadjipanayis

University of Delaware
Newark, Delaware

and

Gary A. Prinz

Naval Research Laboratory
Washington, D.C.

| | |
|--------------------|-------------------------------------|
| Accession For | |
| NTIS CRA&I | <input checked="" type="checkbox"/> |
| DTIC TAB | <input type="checkbox"/> |
| Unannounced | <input type="checkbox"/> |
| Justification | |
| By 149.50 | |
| Distribution | |
| Availability Codes | |
| Dist | Avail and/or Special |
| A-1 | 21 |



Plenum Press
233 Spring Street
New York, NY 10013
NW 1-29-92 \$149.50

DAJ A45-90-M-0117

Plenum Press
New York and London
Published in cooperation with NATO Scientific Affairs Division

Proceedings of a NATO Advanced Study Institute on the
Science and Technology of Nanostructured Magnetic Materials,
held June 24-July 6, 1990,
in Aghia Pelaghia, Crete, Greece

Library of Congress Cataloging-in-Publication Data

NATO Advanced Study Institute on the Science and Technology of
Nanostructured Magnetic Materials (1990 : Aghia Pelaghia, Greece)
Science and technology of nanostructured magnetic materials /
edited by George C. Hadjipanayis and Gary A. Prinz.
p. cm. -- (NATO ASI series. Series B, Physics ; v. 259)
"Proceedings of a NATO Advanced Study Institute on the Science and
Technology of Nanostructured Magnetic Materials, held June 24-July
6, 1990, in Aghia Pelaghia, Crete, Greece.
"Published in cooperation with NATO Scientific Affairs Division.
Includes bibliographical references and index.
ISBN 0-306-43924-7
1. Magnetic materials--Congresses. 2. Solids--Magnetic
properties--Congresses. I. Hadjipanayis, George C. II. Prinz,
Gary A. III. North Atlantic Treaty Organization. Scientific Affairs
Division. IV. Title. V. Series.
QL764.5.N37 1990
538'.4--dc20

91-20197
CIP

ISBN 0-306-43924-7

© 1991 Plenum Press, New York
A Division of Plenum Publishing Corporation
233 Spring Street, New York, N.Y. 10013

All rights reserved

No part of this book may be reproduced, stored in a retrieval system, or transmitted
in any form or by any means, electronic, mechanical, photocopying, microfilming,
recording, or otherwise, without written permission from the Publisher

Printed in the United States of America

PREFACE

In the last twenty years a great amount of progress has been made in the development of new magnetic materials. Permanent magnets have progressed from the AlNiCo's (with $(BH)_m \sim 8$ MGOe) to the strong rare-earth magnets of SmCo_5 ($(BH)_m \sim 20$ MGOe), $\text{Sm}_2(\text{Co,Fe,Cu,Zr})_{17}$ ($(BH)_m \sim 30$ MGOe) and the recently discovered Nd-Fe-B super-magnets with $(BH)_m \sim 50$ MGOe. For years the magnetic storage industry has employed Fe_2O_3 and CrO_2 for storage media and permalloys and ferrites for recording heads. The recent development of thin film heads, the demand of higher density of information storage and the emergence of completely new technologies, like magneto-optics, call for entirely new types of magnetic materials. Another area in which new techniques of materials preparation have made a dramatic impact is the epitaxial growth of magnetic films. Recent work has shown that this process can be controlled on the scale of atomic monolayers permitting the growth of totally artificial structures, such as artificial superlattices with a resolution on this scale. Epitaxial growth has also permitted the stabilization of metastable phases in thin film form. These new phases often possess striking properties, such as strong perpendicular anisotropies, which may prove useful for technological applications such as recording. Research on magnetic multilayers and superlattices is increasing at an accelerating pace. Complex couplings between different magnetic layers lead to new properties not seen in bulk materials. Magnetic surfaces and interfaces show large magnetic anisotropy (surface anisotropy), coercivity, galvano-magnetic and magneto-optic effects that can lead to future storage technologies. Ultrafine particles also show interesting and unique properties ranging from superparamagnetism to strong magnetic hysteresis in particles with a size close to that of single domain particle. The investigation of these new materials is shedding new light on magnetism in general, and yields unusual materials in powder form which have potential use in magnetic tapes as well as in many other technological areas.

The remarkable progress made in magnetic materials has been aided by an interplay between experimental measurements and theoretical models. The Stoner and Wohlfarth model of single domain particles helped significantly in understanding the origin of magnetic hysteresis in permanent magnets. However, this oversimplified theory is often used incorrectly to describe the hysteresis behavior of complex magnetic materials where a "domain wall pinning" or a "nucleation of reversed domains" process is rather more appropriate. The origin of surface anisotropy in thin films and ultrafine particles is not yet clear, and the effects of film thickness and interfaces on the intrinsic and extrinsic magnetic properties are not well understood. In superlattices, it is now found that strong coupling between two ferromagnetic layers can be carried through an intervening layer which is not ferromagnetic. Transport measurements in these structures show giant magneto-resistance effects. The progress in band theory of magnetic materials has also been remarkable. Using novel statistical techniques of Monte Carlo calculation the Curie temperature of Fe has been calculated accurately. This progress has now paved the way for addressing the important "secondary" phenomena such as magnetic anisotropy, galvano-magnetism and magneto-optic rotations which are due to "spin-orbit coupling." All of these properties have been poorly understood in the past and are decisive for many applications.

The NATO Advanced Study Institute (ASI) on the Science and Technology of Nano-structured Magnetic Materials which was held June 24 - July 6, 1990 in Aghia Pelaghia, Crete, Greece, reviewed the remarkable progress made in magnetic materials over the last few years and addressed the current state-of-the-art research and its impact on technological applications. The subject matter fell into a number of broad areas including thin films, multilayers, disordered systems, ultrafine particles, intermetallic compounds, permanent magnets and magnetic imaging techniques. The present volume contains the invited lectures as well as a number of contributed papers. The book is divided into seven chapters representing the various topics discussed at the meeting. We hope that this book will serve as a reference to all researchers in magnetic materials and other related fields.

The workshop was made possible due to the generous support by NATO Scientific Affairs Division, Brussels, Belgium. The directors wish also to express their gratitude for the additional support by the Office of Naval Research, European U. S. Army, IBM, General Electric, Philips Hamburg and Du Pont. We are grateful to Dr. Luigi Pareti for his many helpful suggestions and his assistance in coordinating financial support for the workshop. We also thank Mrs. Helen Long for her efficient assistance with many aspects of the workshop and Mrs. Voula Hadjipanayis for her enthusiastic support during the time of the meeting.

George C. Hadjipanayis
Gary Prinz

CONTENTS

THIN FILMS, SURFACES AND INTERFACES

| | |
|---|----|
| Electronic Structure and Magnetism of Metal Surfaces, Overlayers and Interfaces | 1 |
| A.J. Freeman, C. Li and R.Q. Wu | |
| Growth and Magnetic Properties of Metastable Structures | 15 |
| B. Heinrich, A.S. Arrott, J.F. Cochran, Z. Celinski, and K. Myrtle | |
| Spin-Resolved Photoemission | 25 |
| J. Kirschner | |
| Correlation of Crystalline and Electronic Structure in Epitaxial FCC-Cobalt Monolayers on Cu(100) | 37 |
| C.M. Schneider, J.J. deMiguel, P. Schuster, R. Miranda, B. Heinrich, and J. Kirschner | |
| Hybrid Ferromagnetic/Semiconductor Structures | 41 |
| G.A. Prinz | |
| Mössbauer Studies of Ultrathin Magnetic Films of Fe/Ag(100) | 55 |
| N.C. Koon | |
| Spin-Dependence of Absorbed and Reflected Current on Fe(110) | 61 |
| M.S. Hammond, G. Fahsold, and J. Kirschner | |
| MBE Growth of Metal/Semiconductor Interfaces | 67 |
| J.M. Slaughter, B.N. Engel, M. H. Wiedman, P.A. Kearny, and C.M. Falco | |
| Surface and Interface Magnetism | 71 |
| F. Meier, M. Stamparoni, and A. Vaterlaus | |
| Ferromagnetic Resonance Studies of BCC Epitaxial Ultrathin Fe(001)/Cu(001) Bilayers and Fe(001)/Cu(001)/Fe(001) Trilayers | 77 |
| Z. Celinski, B. Heinrich, J.F. Cochran, K. Myrtle, and A.S. Arrott | |
| Laser Ablation Deposition of Metallic Thin Films | 81 |
| J.P. Gavigan | |
| Exchange Coupled Films for Magneto-Optic Applications | 91 |
| R.J. Gambino | |

| | |
|---|-----|
| Temperature Dependence of Micromagnetic Domain Structure in Cobalt Films | 99 |
| I.R. McFadyen and P.S. Alexopoulos | |
| Hyperfine Interaction Techniques Applied to the Study of Surfaces and Interfaces | 103 |
| M. Rots | |
| Surface Magnetostriction | 109 |
| R.C. O'Handley and S.W. Sun | |

MULTILAYERS

| | |
|---|-----|
| Magnetic Rare Earth Artificial Metallic Superlattices | 117 |
| J.J. Rhyne, R.W. Erwin, J.A. Borchers, M.B. Salamon, F. Tsui, R. Du, and C.P. Flynn | |
| X-Ray Characterization of Magnetic Multilayers and Superlattices | 137 |
| C.M. Falco, J.M. Slaughter, and B.N. Engel | |
| The Characterization of Interface Roughness and Other Defects in Multilayers by X-Ray Scattering | 145 |
| S.K. Sinha, M.K. Sanyal, A. Gibaud, S.K. Satija, C.F. Majkrzak, and H. Homma | |
| Magnetism of Nanostructured Rare Earth Multilayers | 151 |
| D.J. Sellmyer and Z.S. Shan | |
| FMR Studies of Metallic Magnetic Thin Films in Layered Structures | 171 |
| H. Hurdequint | |
| Compositionally Modulated Magnetic Multilayers: Temperature- and Modulation-Dependent Properties | 177 |
| N.K. Flevaris, P. Pouloupoulos, R. Krishnan, and M. Porte | |
| Structural and Magnetic Properties of Epitaxial Co/Pd Superlattices | 181 |
| B.N. Engel, C.D. England, M. Nakada, R. Van Leeuwen, and C.M. Falco | |
| First-Principles Calculation of the Magnetocrystalline Anisotropy Energy of Co_nPd_m Multilayers | 185 |
| G.H.O. Daalderop, P.J. Kelly, and M.F.H. Schuurmans | |
| Structural and Magnetic Studies in Co-Pt Multilayers | 191 |
| R. Krishnan, M. Porte, M. Tessier, and N.K. Flevaris | |
| Magnetic Properties of Hexagonal Fe/Ru Superlattices With Short Periodicity | 195 |
| M. Piecuch, M. Maurer, M.F. Ravet, J.C. Ousset, J.M. Broto, and B. Dieny | |
| Magnetic Studies of Fe-Si Compositionally Modulated Thin Films | 201 |
| J. Tejada, B. Martinez, F. Badia, and R. Ribas | |
| Mössbauer Spectroscopy of the Fe/Ni Interface | 209 |
| E. Colombo, O. Donzelli, G.B. Fratucello, and F. Ronconi | |
| Analysis of Amorphous Dysprosium-Transition Metal Nanoscale Magnetic Multilayers | 215 |
| Z.S. Shan and D.J. Sellmyer | |

| | |
|---|-----|
| Transport Properties of Thin Metallic Films and Multilayers | 221 |
| A. Fert | |

DOMAIN WALLS, MAGNETIC DOMAINS AND TECHNIQUES FOR THEIR OBSERVATION

| | |
|--|-----|
| Micromagnetics of Longitudinal Recording Media | 239 |
| P.S. Alexopoulos, I.R. McFadyen, I.A. Beardsley, T.A. Nguyen, and R.H. Geiss | |
| MO-Recording: The Switching Process and Its Relation to the Magnetic Properties of Thin Films | 249 |
| D. Mergel, R. Hansen, S. Klahn, and D. Raasch | |
| Micromagnetic Computations of Magnetization Configurations | 255 |
| J.P. Jakubovics | |
| Domain Walls and Wall Structure | 269 |
| F.B. Humphrey | |
| Domain Wall Multiplication in Amorphous Ferromagnetic Alloys | 275 |
| C. Beatrice, P. Mazzetti, and F. Vinai | |
| Electron Microscope Methods for Imaging Internal Magnetic Fields at High Spatial Resolution | 279 |
| J.C.H. Spence and Z.L. Wang | |
| Scanning Tunneling Microscopy and Force Microscopy Applied to Magnetic Materials | 301 |
| N. García | |
| Special Session on Spin-Polarized Vacuum Tunneling | 331 |
| Notes by K. Hathaway | |
| Magnetic Imaging Via Scanning Electron Microscopy with Polarization Analysis | 335 |
| R.J. Celotta, M. Scheinfein, J. Unguris, and D.T. Pierce | |
| Atomic Scale Probe into High-Tc Superconductors Using Scanning Tunnelling Microscopy | 339 |
| J. Nogues and K.V. Rao | |

MAGNETIC ANISOTROPY AND RANDOM MAGNETS

| | |
|---|-----|
| Magnetic Anisotropy | 349 |
| H.J.F. Jansen | |
| Random Anisotropy in Magnetic Materials | 367 |
| J.R. Cullen | |
| Perpendicular and In-Plane Anisotropy in Amorphous Tb-Fe | 377 |
| M.J. O'Shea | |
| Magnetostriction in Amorphous Ferromagnets | 387 |
| A. Hernando, M. Vázquez, J. Barandiarán, and G. Rivero | |
| Anderson Localization in 3-Dimensional Amorphous Alloys: Evolution with the Content of Magnetic Ions | 393 |
| J. Filippi, B. Barbara, V.S. Amaral, J.B. Sousa, J.M. Moreira, and A.G.M. Jansen | |

| | |
|--|-----|
| On the Law of Approach to Saturation in the Series of Amorphous Alloys a-Dy _x Gd _{1-x} Ni | 399 |
| V.S. Amaral, J. Filippi, and B. Barbara | |
| Magnetoresistance of Amorphous U _{1-x} Sb _x Films | 405 |
| P.P. Freitas and T.S. Plaskett | |
| Absence of Temperature-Driven First-Order Phase Transitions in Systems with Random Bonds | 411 |
| A.N. Berker and K. Hui | |

MAGNETIC SEMICONDUCTORS AND INTERMETALLIC COMPOUNDS

| | |
|--|-----|
| Magnetic Behavior of Diluted Magnetic Semiconductors | 419 |
| W.J.M. de Jonge and H.J.M. Swagten | |
| Intermetallic Compounds and Crystal Field Interactions | 439 |
| J.M.D. Coey | |
| Crystal-Field and Exchange Interactions in Hard Magnetic Materials | 459 |
| J.J.M. Franse and R.J. Radwanski | |
| First Order Magnetization Processes | 465 |
| G. Asti | |
| Structure and Properties of Novel Ternary Fe-Rich Rare-Earth Carbides | 471 |
| T.H. Jacobs and K.H.J. Buschow | |

FINE PARTICLES

| | |
|---|-----|
| Granular Solids | 477 |
| C.L. Chien | |
| Ultrafine Magnetic Particles | 497 |
| G.C. Hadjipanayis, S. Gangopadhyay, L. Yiping, C.M. Sorensen, and K.J. Klabunde | |
| Magnetic Nanometer Systems and Mössbauer Spectroscopy | 511 |
| A.H. Morrish and X.Z. Zhou | |
| Some Topics in Fine Particle Magnetism | 533 |
| A.E. Berkowitz | |
| Mössbauer Studies of Fine Fe-Based Particles | 545 |
| S. Morup | |
| Mössbauer Studies of Fine Particles of Fe-Cr-B | 551 |
| A. Kostikas, V. Papaefthymiou, A. Simopoulos, Y.P. Li, and G.C. Hadjipanayis | |
| Chemical Preparation of Amorphous Fe-Cr-B Particles | 559 |
| C.B. Koch, S. Linderorth, and S. Morup | |
| Composition and Structure of Fe-Ni-B Alloy Particles Prepared by Chemical Reduction with NaBH ₄ | 563 |
| S. Linderorth, S. Morup, and S.A. Sethi | |
| Quantum Effects in Ultrafine Nd-Fe-B Particles | 567 |
| M.A. López Quintela, J. Rivas, L. Liz, and I. Winter | |

| | |
|---|-----|
| Magnetization Reversal in Clusters of Magnetic Particles | 573 |
| P.V. Hendriksen, S. Morup, G. Christiansen, and K.W. Jacobsen | |
| Electric and Magnetic Properties of Small Systems | 577 |
| S. Aarj | |
| Existence of Frequency Cut-Off in the Spin Wave Spectrum of Small Magnetic Particles | 581 |
| N. Garcia | |

MAGNETIC HYSTERESIS AND PERMANENT MAGNETS

| | |
|--|-----|
| Mechanically Alloyed Permanent Magnets | 583 |
| L. Schultz | |
| Melt-Spun Magnets | 591 |
| F.E. Pinkerton | |
| Solid NdFeB Magnets Made by Gas Atomization and Extrusion | 599 |
| E.J. Dulis and V.K. Chandhok | |
| The Role of Microstructure in Permanent Magnets | 607 |
| G.C. Hadjipanayis | |
| Lorentz Microscopy Studies in Permanent Magnets | 627 |
| J. Fidler | |
| Coercivity in Hard Magnetic Materials | 635 |
| D. Givord, Q. Lu, and M.F. Rossignol | |
| Micromagnetism and Magnetization Processes in Modern Magnetic Materials | 657 |
| H. Kronmüller | |
| Micromagnetic Approach to Magnetic Hysteresis | 677 |
| R.H. Victora | |
| Magnetic Hysteresis in Disordered Magnets | 683 |
| C.M. Soukoulis | |
| Coercivity of Nanostructured Materials | 695 |
| Y. Otani | |
| Magnetic Hysteresis of CoPt Films | 701 |
| A. Tsoukatos, G.C. Hadjipanayis, C.P. Swann, S. Ismat Shah | |
| Technology and Applications of Permanent Magnets | 707 |
| K.S.V.L. Narasimhan | |
| Author Index | 717 |
| Subject Index | 719 |

ELECTRONIC STRUCTURE AND MAGNETISM OF METAL SURFACES, OVERLAYERS AND INTERFACES

A.J. Freeman, Chun Li and R.Q. Wu

Department of Physics and Materials Research Center
Northwestern University, Evanston, IL 60208-3112

INTRODUCTION AND BACKGROUND PERSPECTIVE

As is clear from the subject of this NATO Institute, the importance of low-dimensional systems (including surfaces, interfaces and thin films) in determining the physical properties of technologically important materials has stimulated theoretical efforts to determine from first principles a detailed understanding of their chemical, electronic and mechanical properties. Fortunately, this has now become possible as a result of the dramatic advances in condensed matter theory made in the last decade, driven in large part by new and sophisticated experiments on high purity materials which have been well and carefully characterized. Particularly in electronic structure, these advances may be attributable directly to the close collaboration of theoretical and experimental researchers. Indeed, the new-found ability to apply fundamental theoretical concepts to real materials (rather than to simple model systems) made possible by utilizing the continued rapid development of computer power, has served to fill the increasingly urgent demand of experimentalists for theoretical interpretation of their data. Also, in some cases, these computational efforts can be used to provide data which would be currently impossible or impractical to obtain experimentally. This development has been an essential element in the phenomenal growth seen in this area of materials science.

More specifically, the advent of accurate self-consistent (local) spin density functional (LSDF) calculations for surfaces, interfaces and multilayers means that theory is no longer limited to simple parameter-dependent models. These complex systems are of growing interest because the reduced symmetry, lower coordination number, and availability and role of highly localized surface and interface states offers the possibility of inducing new and exotic phenomena and so holds out the promise of new device applications.

The range and variety of materials under investigation is enormous. One of the recent important developing trends lies in the preparation of synthetic structures on the submicron level, which will permit, in the near future, new scientific phenomena to be investigated, and novel device applications to be made on artificially made materials not found in nature. In addition to the technological reasons for focusing attention on submicron problems, there are interesting phenomena to study which are of fundamental and physical interest in themselves. Indeed, our own scientific attention has spread from consideration of bulk properties to obtaining a better fundamental understanding of reduced-dimensionality-phenomena at surfaces and interfaces.

In the following, we limit ourselves to discuss only a few selected examples taken from the several different systems we have been studying recently. Our aim is to provide a general overview of the complexity of the different issues involved and, at the same time to illustrate the kind of answers that our theoretical-computational approach can offer to the understanding of these issues by yielding well-defined results and making precise predictions. Various examples have demonstrated that it is possible not only to make quantitative predictions for real systems, but more importantly, to gain insights into the underlying physics of these materials which are essential not only for the pure science but also for potential device applications.

METHODOLOGY AND APPROACH

Since many of the phenomena are directly related to the electronic structure at surfaces and interfaces, attention has been focused on extending well-known theoretical methods for calculating bulk properties to treat these low dimensional systems. This timely and successful pursuit resulted from the fact that considerable activity has been focused in recent years on quantum mechanical theories which describe the dynamics of many-interacting electrons in an external potential, e.g., due to the atomic nuclei. An important breakthrough was the development of density-functional theory. In its local approximation, density-functional theory leads to Schrödinger-like one-particle equations (Kohn-Sham equations) containing an effective potential energy operator which is determined by the self-consistent charge distribution. Thus, the local density-functional one-particle equations have to be solved iteratively.

One of the most accurate and powerful schemes to solve the local spin density functional (LSDF) one-particle equations is our all-electron full-potential linearized-augmented-plane-wave [1] (FLAPW) method which can be applied for bulk and superlattice calculations as well as for film calculations. The basic idea in this variational method is the partition of real space into three different regions, namely, spheres around the nuclei, vacuum regions on both sides of the slab in the case of film calculations, and the remaining interstitial region. No shape approximations are made to the charge density and the potential. Both the charge density and the effective one-electron potential are represented by the same analytical expansions, i.e., a Fourier representation in the interstitial region, an expansion in spherical harmonics inside the spheres, and (for films) a 2-dimensional Fourier series in each vacuum plane parallel to the surface.

Thus, the FLAPW method allows a fully self-consistent solution of the LSDF one-particle equations and yields charge densities and spin densities close to the LSDF limit. Besides the total charge density, the key quantity in density-functional theory is the total energy corresponding to the ground state charge density. The capability of total energy calculations for various geometrical arrangements provides a powerful theoretical tool to study the energetics and, at least in principle, the dynamics of bulk solids and surfaces.

MAGNETISM OF METAL SURFACES AND OVERLAYERS

3d Ferromagnetic Metal Surfaces and Overlayers

As is clear from other contributions to this volume, the magnetism of the 3d ferromagnetic transition metals at surfaces and interfaces is of special interest because of their possible use in high-technology information storage devices. Because of the breakdown of the three dimensional crystal symmetry, the electronic and magnetic properties are expected to be significantly different from that seen in the bulk solids. The interface features strongly control the magnetism of the material at least a few Å's deep into the bulk. This interface influence on magnetism depends on the atomic structure and the nature of the materials on both sides of the interface.

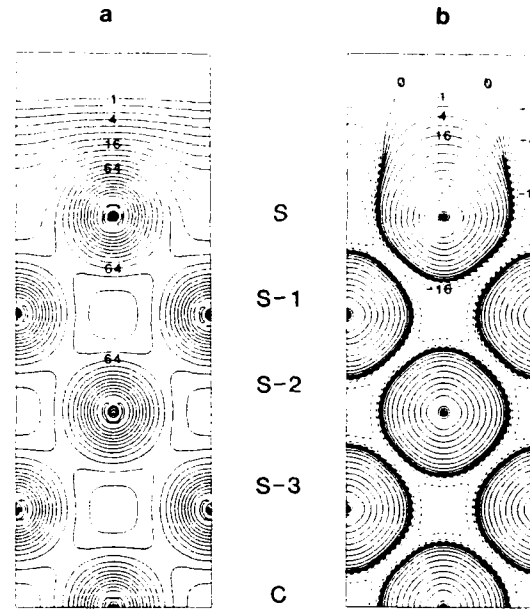


Figure 1 (a) Charge and (b) spin density contour plots for a nine-layer fcc-Co(001) slab in the (100) plane. For (a), the numbers indicated are in units of 10^{-3} e/a.u.; subsequent contour lines differ by a factor of $\sqrt{2}$. For (b), the numbers indicated are in units of 10^{-4} e/a.u.; subsequent contour lines differ by a factor of 2.

Unusual properties of surface magnetism (viewed as an interface between solid and vacuum) have been obtained from theoretical studies of various ferromagnetic transition metal surfaces; these include surface magnetic moments enhanced over the bulk values, narrowed $3d$ band-widths for the states in the surface layer and largely reduced surface magnetic hyperfine fields (except for bcc Cr, for which the hyperfine field is enhanced). Listed in Table 1 are the calculated magnetic moments of $3d$ -transition metal surfaces using the FLAPW method. As a general phenomenon, enhanced magnetic moments at the surface layer (with respect to bulk moments) are predicted. The magnetic moments calculated are comparable with experimental findings. Table 2 contains the FLAPW results for magnetic overlayers on Cu, Ag, and Au substrates. Giant magnetic moments for monolayer Fe overlayers on Cu, Ag and Au(001) substrates are predicted. The effect of the magnetic properties of the substrate on the magnetic films is also carefully studied.

Table 1 Calculated magnetic moments (M , in μ_B) of $3d$ -transition metal bulk and surfaces

| | | | M_{surf} | M_{bulk} | ref. |
|----|-----|--------|------------|---------------------------|------|
| Ni | fcc | (100) | 0.68 | 0.56 | [3] |
| | | (110) | 0.63 | | [4] |
| Cr | bcc | (100) | 2.49 (FM) | 0.89 (AFM) 0.59 (Exp.) | [5] |
| | | (110) | 2.65 | | [7] |
| Fe | fcc | (100) | 2.85 | 1.99 | [8] |
| | | (110) | 2.65 | | [7] |
| Co | fcc | (100) | 1.86 | 1.65 | [9] |
| Co | hcp | (0001) | 1.76 | 1.65 | [10] |
| Co | bcc | (100) | 1.95 | 1.76 | [11] |
| Co | bcc | (110) | 1.84 | 1.76 | [4] |

Table 2 Calculated magnetic moments (M , in μ_B) of 3d-transition metal thin film overlayers on noble metals. S denotes surface and S-1 subsurface layers.

| thin films | M | ref. | thin films | M | ref. |
|----------------|--------------|------|-----------------|-------------|------|
| 1V/Au(001) | 1.75 | [12] | AFM 2Fe/Cu(001) | 2.38 (S) | [13] |
| 1V/Ag(001) | 1.98 | [12] | | -2.22 (S-1) | [13] |
| 2V/Ag(001) | 1.15 (S) | [12] | 1Fe/Ag(001) | 2.96 | [12] |
| | < 0.05 (S-1) | [12] | 2Fe/Ag(001) | 2.94 (S) | [12] |
| Cr monolayer | 4.12 | [12] | | 2.63 (S-1) | [12] |
| 1Cr/Au(001) | 3.70 | [12] | 1Fe/Au(001) | 2.97 | [31] |
| 2Cr/Au(001) | 2.90 (S) | [12] | 1Fe/W(110) | 2.18 | [14] |
| | -2.30 (S-1) | [12] | 1Co/Cu(001) | 1.79 | [15] |
| Fe monolayer | 3.20 | [12] | 1Ni/Ag(001) | 0.57 | [16] |
| FM 2Fe/Cu(001) | 2.85 (S) | [13] | Cr/Fe/Au(001) | 3.10 (Cr) | [12] |
| | 2.60 (S-1) | [13] | | -1.96 (Fe) | [12] |
| | | | Fe/Cr/Ag(001) | 2.30 (Fe) | [12] |
| | | | | -2.40 (Cr) | [12] |

To illustrate the electronic and magnetic properties of transition metal surfaces and interfaces, we present briefly the FLAPW computational studies of the fcc Co(001) surface and of a Co overlayer on a Cu(001) substrate. The charge and spin densities in the (100) plane of a nine layer fcc Co(001) slab is shown in Fig.1 (a) and (b), respectively. Features similar to those of the other ferromagnetic transition metal surfaces are seen in that the effect of the surface on the charge density is mostly localized to the surface layer. The other layers, including even the sub-surface layer, appear to be very much bulk-like. This is also confirmed by examining the detailed charge population (not shown) within each muffin-tin (MT) sphere of the atom; the charge distribution of the non-surface layer atoms is found to be very much the same.

Unlike the charge density distribution, which has a larger spherical-like component for each atom, the spin density shows strong anisotropic features around the atoms. Similar features have also been found in ferromagnetic metal surfaces of Fe, Ni and Co.

The charge and spin densities in the (100) plane of a Co overlayer on an fcc Cu(001) substrate are shown in Fig.2 (a) and (b), respectively. The charge density at the overlayer Co

Table 3 The contact hyperfine field (in kGauss) and the ratio of core electron contribution and effective magnetic moments of bcc Co(001), fcc Co(001) and hcp Co(001) surfaces and Co overlayer on a Cu(001) substrate.

| | atom | core | conduction | total | core/M | moment (μ_B) |
|--|------|------|------------|-------|--------|-----------------------|
| bcc Co(001) surface (9 layer slab model) | S | -285 | +104 | -181 | -147 | 1.94 |
| | S-1 | -255 | -12.1 | -268 | -144 | 1.78 |
| | S-2 | -252 | +13.6 | -238 | -144 | 1.76 |
| | S-3 | -253 | +6.3 | -247 | -144 | 1.76 |
| | C | -257 | +18.3 | -238 | -146 | 1.76 |
| fcc Co(001) surface (9 layer slab model) | S | -266 | +55.5 | -211 | -144 | 1.86 |
| | S-1 | -236 | -75.1 | -311 | -144 | 1.64 |
| | S-2 | -237 | -70.5 | -307 | -144 | 1.65 |
| | S-3 | -236 | -69.1 | -305 | -144 | 1.64 |
| | C | -237 | -69.5 | -306 | -144 | 1.65 |
| hcp Co(0001) surface (7 layer slab model) | S | -257 | -31.5 | -287 | -146 | 1.76 |
| | S-1 | -244 | -84.7 | -297 | -144 | 1.68 |
| | S-2 | -237 | -76.1 | -314 | -145 | 1.65 |
| | C | -239 | -75.5 | -314 | -145 | 1.64 |
| Co/Cu(001) interface | | -257 | +161 | -96 | -144 | 1.79 |

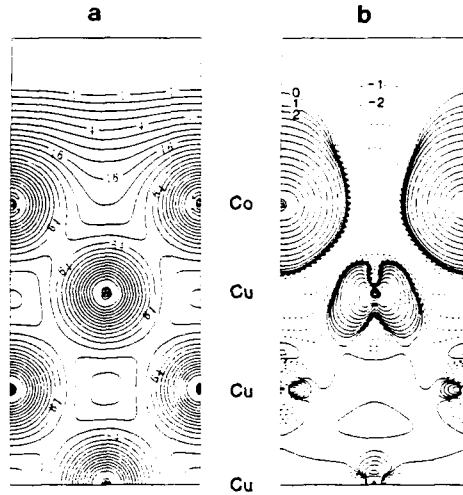


Figure 2 (a) Charge and (b) spin density contour plots for Co overlayer on a Cu(001) substrate in the (100) plane — as in Fig. 1.

atoms shows few anisotropic features in the contour shapes. The interface Cu atom charge density contours are slightly different compared with those of the other Cu atoms. The sub-interface ($S - 2$) and center layer (C) Cu atoms have primarily the same charge distribution, and are thus quite bulk-like. The spin density contours for the overlayer magnetic atoms shows stronger anisotropic features than do the charge density contours. The interface Cu atom also has a region of positive spin density distribution around the center of the atom. The spin density on the non-interface Cu atoms is relatively much smaller. These features have also been seen in other interfaces between ferromagnetic and noble metals.

The hyperfine magnetic field — an important property of magnetic transition metals which can be directly measured by Mössbauer effect and NMR experiments — provides information related to the magnetism which is sensitive to the environment of the atom. The contact part of the hyperfine field (listed in Table 3 are those of bcc Co(001), fcc Co(001) and hcp Co(001) surfaces, and the Co overlayer on Cu(001) substrate) is determined by the spin density at the nucleus [2]: this is mostly enhanced by the magnetism of the valence d -electrons and so is strongly dependent on the total magnetic moment. The contribution to the hyperfine field by core electrons is found to be rather precisely proportional to the magnetic moment, whereas the total hyperfine field varies from ~ -96 kGauss for the overlayer Co atom in Co/Cu(001) to -314 kGauss for the bulk-like (center layer) atoms in fcc Co. The almost identical constant value ($-144 \pm 2\%$ kGauss/ μ_B) of the ratio of the core hyperfine field and the magnetic moment is evidence that the core polarization coupling constant is not sensitive to the atomic environment.

Magnetic Anisotropy of Fe Thin Films

The magnetic anisotropy properties of ferromagnetic thin-films (Fe, Co, Ni, etc.) on various substrates have been studied via surface magneto-optic Kerr effect [17] (SMOKE), ferromagnetic resonance (FMR), spin-polarized photoemission, etc. In ultra-thin Fe(001) films on Ag(001) (less than 2.5 monolayers), the magnetization is found to lie along the surface normal [18, 19]. Both in-plane [20] and perpendicular anisotropy [21] are observed for

monolayer range Fe(001) on Au(001). Liu et al. [21] reported a universal behavior of perpendicular spin orientation below a critical thickness of 6 monolayers or less in fcc Fe(100) on Cu(100), fcc Fe(111) on Ru(0001), bct Fe(100) on Pd(100) and bcc Fe(100) on Au(100).

The origin of magnetic anisotropy of 3d ferromagnetic materials [22] was proposed by van Vleck [23] more than 50 years ago to be the spin-orbit interaction. Still today, the theoretical understanding of the magnetic anisotropy in realistic systems remains a great challenge, because it is necessary to know in precise detail both the electronic structure and the total energy (the latter to $\pm 10^{-5}$ eV).

To study the magnetic anisotropy of metal surfaces and thin-films, [25] we developed a so-called "second variation" method based on our highly-precise total energy FLAPW approach, i.e., to solve the relativistic Dirac equation of the electronic system with a charge density obtained from a previous semi-relativistic self-consistent calculation. As the first test of this method for calculating magnetic anisotropy, the free standing Fe monolayer with a square lattice structure and with lattice constants matching either fcc Ag(001) ($a_{Ag} = 4.086$ Å) or fcc Au(001) ($a_{Au} = 4.078$ Å) was studied [25]. The charge density of monolayer Fe is determined with the semi-relativistic FLAPW method. The magnetic anisotropy energy is estimated by the second variation procedure. In both systems, a small in-plane preference of the spin orientation of order $\sim 3 \times 10^{-5}$ eV/atom (or an equivalent anisotropy magnetic field of ~ 1.7 kGauss along the in-plane direction) is obtained from the calculations [25]. This result is in contrast with the result of Gay and Richter [24] who obtained a perpendicular spin orientation in an unsupported Fe monolayer. We also calculated the anisotropy between the two in-plane directions, namely, $(\theta = \frac{\pi}{2}, \phi = 0)$ and $(\theta = \frac{\pi}{2}, \phi = \frac{\pi}{4})$. This anisotropy energy is found to be about two orders of magnitude smaller than the perpendicular/in-plane anisotropy, i.e., $\sim 1\%$ of the anisotropy energy between the $(\theta = 0, \phi = 0)$ and $(\theta = \frac{\pi}{2}, \phi = 0)$ directions.

Similar calculations were then carried out for Fe monolayers on Au, Ag and Pd(001) substrates. For these theoretical studies, the Fe/metal systems were modeled by a single-slab geometry with one layer of $p(1 \times 1)$ Fe coupled with one layer of Ag (or Au or Pd) atoms, and with the Fe atoms located at the four-fold hollow site of the Ag (or Au or Pd) square lattice. The experimental Ag, Au and Pd lattice constants were assumed. The computational results can be summarized as: (1) in all three systems, i.e., 1Fe/1Au, 1Fe/1Ag and 1Fe/1Pd, the easy direction of the spin-orientation is perpendicular to the surface of the film, in contrast with the results for the free standing Fe(001) monolayer; (2) the values of the magnetic anisotropy energy for these systems are considerably larger than the results for the free standing Fe monolayer, i.e., 0.5 meV/atom for 1Fe/1Au, 0.1 meV/atom for 1Fe/1Ag and 0.4 meV/atom for 1Fe/1Pd. In this case, the result for 1Fe/1Ag is in agreement with the preliminary result reported by Gay and Richter [24] for an Fe/Ag(001) slab with 5 Ag layers sandwiched by a monolayer of Fe on either side. Surface and interface magnetism continue to attract considerable attention, largely because novel electronic and magnetic features are expected to arise from the breakdown of three dimensional crystal symmetry.

Rare-Earth Metal Surface Magnetism: Gd(0001)

The structural, electronic and magnetic properties of rare-earth metal surfaces and thin-films have attracted considerable attention in recent years. Among them, hcp Gd(0001) is of special interest because of its novel magnetic properties, including surface-enhanced magnetic ordering (SEMO) at a temperature well above the bulk Curie point [26, 27].

The first experimental evidence for SEMO was provided by Rau and Eichner [26], using electron-capture-spectroscopy measurements. A SEMO up to $T = 310$ K was extrapolated

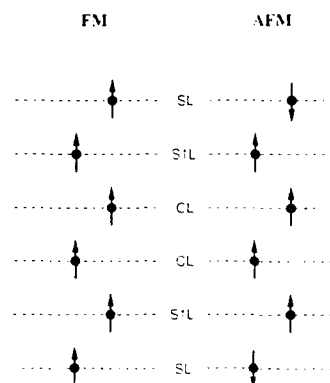


Figure 3 Schematic ferromagnetic and antiferromagnetic configurations for a 6 layer Gd(0001) slab.

from the measurements on polycrystalline thin films. Similar conclusions were drawn by Weller et al. [27] for epitaxial hcp Gd(0001) thin films grown on a single crystal W(110) substrate, employing spin-polarized low-energy-electron diffraction (SPLEED) and magneto-optic Kerr effect (MOKE) techniques. Again, the SMO critical temperature is found to be ~ 22 K above the bulk T_c . Very interestingly, the top-most surface atomic layer magnetic moments were inferred *not* to be ferromagnetically coupled to the underlying bulk layers.

Despite these developments in experimental knowledge of the surface magnetism of Gd, no detailed theoretical research has been reported previously. In this lecture, we provide first results of FLAPW studies of the structural, electronic and magnetic properties of the hcp Gd(0001) surface.

The Gd(0001) surface --- with the top-most atomic layer ferromagnetically (FM) or antiferromagnetically (AFM) coupled to the underlying bulk-like layers as shown in Fig. 3 --- is simulated primarily by an hcp slab geometry with 6 Gd atomic layers. This thickness is reasonable since test calculations carried out on an 8 layer AFM slab confirm most of the results. The 2D lattice constant and the distances between adjacent bulk layers were chosen in accordance with the experimental data ($a = 6.8446$ a.u., $c = 10.8622$ a.u., $c/a = 1.587$), while the distance between the surface layer and the underlying bulk layer is determined by minimizing the total energy. The minimum of the fitting curve gives an equilibrium distance between the surface layer and the adjacent underlying layer = 5.53 a.u., i.e., $\sim 2\%$ expansion in comparison with the bulk-like spacing. With this assumed equilibrium atomic structure, the total energy for AFM coupling is about 3 mRy lower than the minimum for FM coupling. Thus we find that the surface AFM coupling is more stable than the FM one, in support of the experimental observation by Weller et al. [27].

The total valence charge densities, which are fundamentally important quantities in LDA and usually give clear insights for understanding the surface interactions, are presented in Figs. 4 (a) and (b) for the AFM and FM hcp Gd(0001) surfaces, respectively. It is seen that the electrons in the surface atoms spill out into the vacuum region to lower their kinetic energy. The density corrugation along the horizontal direction is very small even not far above the surface atoms, indicating the smoothness of the Gd(0001) surface. Dramatically, the spatial charge distribution just below the surface layer shows a typical metallic interaction between the Gd atoms whereas no noticeable special bond-orientation exists.

Figure 5 presents the calculated valence spin densities on the (1010) plane for the FM

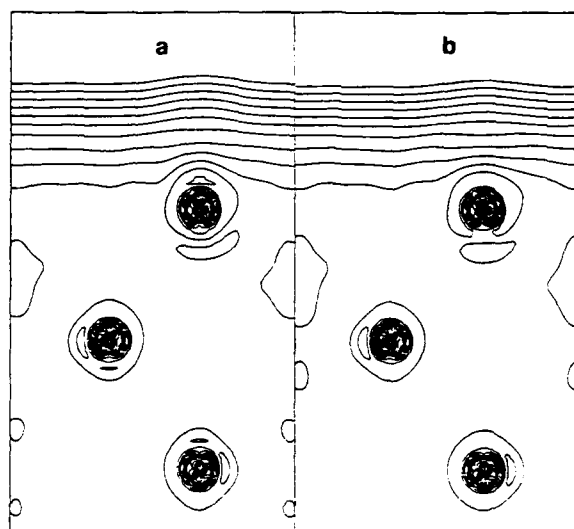


Figure 4 The total valence charge density of the Gd(0001) surface on the $(10\bar{1}0)$ plane for (a) FM surface coupling; and (b) AFM surface coupling. Contours start from $5 \times 10^{-4} e/(\text{a.u.})^3$ and increase successively by a factor of $\sqrt{2}$.

and AFM hcp Gd(0001) surfaces. Because the valence spin-polarization is induced by the $4f$ shell, the majority spin exceeds the minority spin in the whole space for the FM surface — different from that usually obtained for the transition metal surfaces. For the AFM case, since the $4f$ spin polarization in the surface layer is antiparallel to that of the underlying layers, the valence spin-density in surface region becomes negative in order to follow this change. As listed in Table 4, the FM Gd bulk, the total calculated valence magnetic moment is $0.59 \mu_B$ per atom. This value agrees well with the experimental result [28] ($0.63 \mu_B$) — suggesting the validity of present day theoretical treatments. For the FM and AFM Gd(0001) surface, the moments inside the center MT spheres are very close to the calculated result for bulk FM Gd. For the FM state, the valence magnetic moment at the surface is enhanced (by $\sim 20\%$). Because the surface $4f$ spin polarization is antiparallel to the underlying layer for the AFM state, the induced valence spin density decreases markedly (with a node) in the in-between region. As a result, the AFM magnetic moments in the topmost two layers become smaller than those for the FM coupling. Nevertheless, the surface magnetic enhancement is sizable because the negative surface magnetic moment is still larger than the corresponding value in the center layer MT sphere.

Table 4 Calculated magnetic moments for bulk Gd and the Gd(0001) surface.

| | | FM | AFM |
|----------|-----------|------|-------|
| Gd bulk | MT | 0.47 | — |
| | Int./atom | 0.12 | -- |
| | total | 0.59 | — |
| | expt. | 0.63 | -- |
| Gd(0001) | S | 0.58 | -0.49 |
| | S-1 | 0.44 | 0.39 |
| | C | 0.46 | 0.45 |
| | Int./atom | 0.14 | -- |

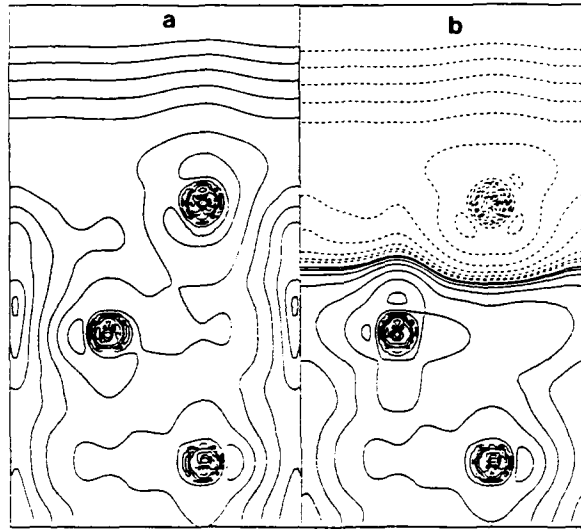


Figure 5 Spin densities on the $(10\bar{1}0)$ plane of (a) FM Gd(0001); (b) AFM Gd(0001). Contours start from $\pm 1.0 \times 10^{-4} e/(\text{a.u.})^3$ and increase by a factor of 2.

To conclude, (1) unlike the usual results for transition metal surfaces, the FM Gd(0001) surface layer expands outwardly (by 2%); (2) the surface Gd layer couples antiferromagnetically with the underlying bulk, and the stability of the AFM coupling originates mainly from the enhancement of the second-neighbor interaction between the surface layer and the third layer; and (3) the surface magnetic moment is enhanced from the bulk value.

METAL-CERAMIC INTERFACES

Our basic physical understanding of the simplest metal-ceramic interfaces falls far short of their obvious importance. As an illustration of the first steps taken to study the metal-ceramic interfaces from first principles, we cite some recent work [29] on Fe on MgO(001). Some remarkable results have been obtained which show that MgO is an extremely non-interactive substrate for metal overlayers and, hence, that it might be an ideal two-dimensional substrate for studying magnetization, magnetic anisotropy, phase transitions and critical behavior.

To determine the interface structure between Fe metal and MgO(001), two different positions for monolayer Fe on MgO(001) were studied, i.e., Fe above the O site and above the Mg site. The total energy study determined that the position of Fe atoms above the O atom site is preferred, similar to the results of our previous Ag/MgO(001) calculations. This result is consistent with experimental findings by Urano et al. [30]. The interlayer spacing between monolayer Fe and the MgO(001) substrate was determined to be, 2.30 Å. In the following, we discuss the properties of the Fe/MgO (001) system for the case of the Fe above O site with this optimized interlayer spacing. The same interface structure between Fe and MgO (i.e., the interface Fe atoms sitting at 2.30 Å above O sites) was then assumed in our model calculations of 2Fe/MgO(001).

The charge density contour plot of the ferromagnetic 1Fe/MgO(001) is shown in Fig. 6(a). As expected, the charge density of the MgO substrate remains basically unchanged in

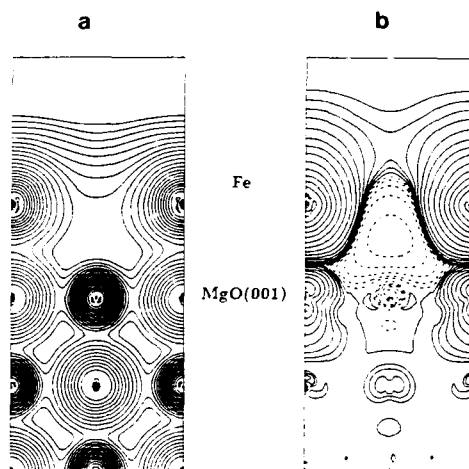


Figure 6 (a) Charge and (b) spin density distributions for Fe/MgO(001) (Fe above O site) plotted for the upper half of a single slab unit cell in the (100) plane. — as in Fig. 1.

comparison with clean MgO. A small interface effect is seen at the interface O atoms. The Fe atom shows a surface-like charge distribution, i.e., with the charge smoothly extended into the vacuum region. The overlayer Fe atom has a total charge of 6.31, which is equal to that of the free standing monolayer Fe, despite the presence of the MgO(001) substrate. Also interestingly, the MgO electron population in 1Fe/MgO(001) differs from that of the clean MgO(001) surface by only ~ 0.02 electron at the interface O atom, while the population of the other atoms remains almost unchanged. Thus, any strong direct reaction between Fe and MgO can be ruled out.

Shown in Fig. 6(b) is the spin density contour plot of ferromagnetic 1Fe/MgO(001) in the (100) plane. Large positive spin density is seen at the overlayer Fe atom, showing a *d*-like shape. Some negative spin density appears in the interstitial region between the overlayer Fe atoms (i.e., the region above the interface Mg atom). At the interface O atom, the positive net spin density has a *p*-like shape, indicating the slight influence of the magnetic Fe overlayer on the 2*p* electronic states of the interface O. The other atoms, i.e., all Mg atoms and the non-interface O atoms in the MgO(001) substrate, show almost no net spin density. The calculated magnetic moment of Fe, $3.07 \mu_B$, is close in value (1%) to that of a free standing Fe monolayer ($3.10 \mu_B$), and hence larger than that of the bcc Fe free surface value [6] ($2.98 \mu_B$) or Fe monolayers on noble metal (Au and Ag(001)) surfaces [31].

The charge density shape of the MgO substrate in 2Fe/MgO (not shown) is close to that seen in both 1Fe/MgO and clean MgO, a result of the lack of interaction between Fe metal and the MgO substrate. The charge density of the surface Fe atom shows surface-like features typical of metal surfaces, while that of the interface Fe(S-1) atom shows some influence from the substrate. The layer-projected charge and spin populations of 2Fe/MgO(001) show that the surface Fe atom has a total muffin-tin (M.T.) charge of 6.40 electrons or about ~ 0.1 electrons more than that of Fe in 1Fe/MgO. The interface Fe (S-1) atom has a total M.T. charge of 6.43 electrons, a value very close to that of the surface Fe. Again, the charge population of the MgO substrate atoms is almost unchanged from that of clean MgO or 1Fe/MgO.

The calculated spin density in the (100) plane of the 2Fe/MgO(001) slab (not shown for lack of space) shows large positive spin densities at the two Fe atoms, with a strongly anisotropic shape. Positive spin density appears also at the interface O atom, similar to the 1Fe/MgO(001) results. Negative spin density is found in the interstitial regions between the Fe atoms. The total magnetic moment of the surface Fe in 2Fe/MgO is $2.96 \mu_B$, which is close in value to that of the free bcc Fe(001) surface atom, $2.98 \mu_B$. Very interestingly, the interface Fe atom has a magnetic moment, $2.85 \mu_B$, which is smaller than that of the surface Fe by only $\sim 0.1 \mu_B$. Compared with the calculated magnetic moment of the bulk-like bcc Fe atom, $2.25 \mu_B$, both the surface and interface Fe atoms have largely enhanced moments (by 32% and 27%, respectively).

In conclusion: (i) MgO(001) forms an extremely non-interactive substrate for Fe thin films, and the scale of charge difference induced by the Fe/MgO interface effect is limited to less than 0.02 electrons/atom. Thus, Fe/MgO(001) might be an ideal two-dimensional electronic/magnetic system. It is also anticipated that other similar systems, i.e., transition metals interfaced with stable ionic insulator substrates, will yield interesting features of an ideal two-dimensional system. (ii) Monolayer Fe adsorbed on an Mg(001) substrate shows a giant magnetic moment ($\sim 3.07 \mu_B$) which is close to that of a free standing Fe(001) monolayer ($\sim 3.10 \mu_B$). This moment is even larger than the previously calculated monolayer Fe moments in Fe/Ag, Fe/Au and Fe/Cu, etc. (iii) In 2Fe/MgO(001), the surface Fe atom has a magnetic moment of $2.96 \mu_B$, which is close to that of the fcc Fe(001) surface ($2.98 \mu_B$). Interestingly, the interface Fe atom (S-1) also shows a large magnetic moment, $2.85 \mu_B$, as well as a density of states extremely close to that of the surface Fe atom -- again indicating the extremely weak interface effect on Fe from the MgO(001) substrate.

CONCLUSIONS

We have presented results of state of the art local spin density (LSD) calculations using the highly precise FLAPW total energy method on some novel systems. The work described here gives a good indication of the power and applicability of the LSD approach to treating what are complex materials with an all-electron approach that can simultaneously determine the structural, electronic and magnetic properties. Specific predictions have been made and comparisons with experiment -- when available -- have been given. Clearly, the theoretical and experimental efforts are still only in their infancy. Much more of both are needed in order to elucidate the complex properties inherent in these fascinating artificial materials.

ACKNOWLEDGMENTS

We thank our various colleagues for collaboration on the work cited. Work supported by the ONR (Grant No. N00014-89-J-1290), the DOE (Grant No.88-ER45372) and the NSF (Grant No. DMR88-16126).

References

- [1] E. Wimmer, H. Krakauer, M. Weinert and A.J. Freeman, *Full-potential self-consistent linearized-augmented-plane-wave method for calculating the electronic structure of molecules and surfaces: O₂ molecule*, Phys. Rev. B24, 864 (1981).
- [2] C.L. Fu, A.J. Freeman and E. Wimmer, *Hyperfine fields at surfaces and interfaces*, Hyperfine Interactions 33, 53 (1987).

- [3] E. Wimmer, H. Krakauer, M. Weinert and A.J. Freeman, *Total-energy all-electron density functional method for bulk solids and surfaces*, Phys. Rev. **B26**, 4571 (1982) and references therein.
- [4] J.I. Lee, A.J. Freeman and C.L. Fu, *Electronic structure and surface magnetism of bcc Co(110)*, J. of Magn. Magn. Mats., to be published.
- [5] C.L. Fu and A.J. Freeman, *Surface ferromagnetism of Cr(001)*, Phys. Rev. **B33**, 1755 (1986).
- [6] S. Ohnishi, A.J. Freeman and M. Weinert, *Surface magnetism of Fe(001)*, Phys. Rev. **B28**, 6741 (1983).
- [7] C.L. Fu and A.J. Freeman, *Magnetism and the electric and magnetic hyperfine interaction at transition metal surfaces: Fe(110)*, J. Mag. Magn. Mats. **69**, L1 (1987).
- [8] C.L. Fu and A.J. Freeman, *Electronic and magnetic properties of the fcc Fe(001) thin films: Fe/Cu(001) and Cu/Fe/Cu(001)*, Phys. Rev. **B35**, 925 (1987).
- [9] C. Li, A.J. Freeman and C.L. Fu, *Electronic structure and surface magnetism of fcc Co(001)*, J. of Magn. Magn. Mats. **75**, 53 (1988).
- [10] C. Li, A.J. Freeman and C.L. Fu, *Electronic structure and surface magnetism of hcp Co(0001)*, J. of Magn. Magn. Mats., to be published.
- [11] J.I. Lee, C.L. Fu and A.J. Freeman, *Electronic structure and magnetism of metastable bcc Cr(001)*, J. of Magn. Magn. Mats. **62**, 93 (1986).
- [12] C.L. Fu, A.J. Freeman and T. Oguchi, *Prediction of strongly enhanced two-dimensional ferromagnetic moments on metallic overlayers, interfaces and superlattices*, Phys. Rev. Lett. **54**, 2700 (1987).
- [13] C.L. Fu and A.J. Freeman, *Structural, electronic and magnetic properties of Au/Cr/Au(001) sandwiches: theoretical total-energy studies*, Phys. Rev. **B33**, 1611 (1986).
- [14] S.C. Hong, A.J. Freeman and C.L. Fu, *Structural, electronic and magnetic properties of clean and Ag-covered Fe monolayers on W(110)*, Phys. Rev. **B38**, 12156 (1988).
- [15] C.Li, A.J. Freeman and C.L. Fu, *Electronic structure and magnetism of surfaces and interfaces: selected examples*, J. Magn. Magn. Mats. **83**, 51 (1990).
- [16] S.C. Hong, A.J. Freeman and C.L. Fu, *Structural, electronic and magnetic properties of a Ni monolayer on Ag(001): Ni adsorption versus Ag surface segregation*, Phys. Rev. **B39**, 5719 (1989).
- [17] S.D. Bader, E.R. Moog and P. Grünberg, *Magnetic hysteresis of epitaxially-deposited iron in the monolayer range: a Kerr effect experiment in surface magnetism*, J. Magn. Magn. Mat., **53**, L295 (1986).
- [18] B. Heinrich, K.B. Urquhart, A.S. Arrott, J.F. Cochran, K. Myrtle and S.T. Purcell, *Ferromagnetic-resonance study of ultrathin bcc Fe(100) films grown epitaxially on fcc Ag(100) substrates*, Phys. Rev. Lett. **59**, 1756 (1987).
- [19] N.C. Koon et al., *Direct evidence for perpendicular spin orientations and enhanced hyperfine fields in ultrathin Fe(100) films on Ag(100)*, Phys. Rev. Lett **59**, 2463 (1987).
- [20] W. Dürr et al., *Magnetic phase transition in two-dimensional ultrathin Fe films on Au(100)*, Phys. Rev. Lett. **62**, 206 (1989).

- [21] C. Liu and S.D. Bader, *Perpendicular surface magnetic anisotropy in ultrathin epitaxial Fe films*, submitted to J. of Vac. Sci. and Tech. A.
- [22] H. J. F. Jansen, *Magnetic Anisotropy*, this book.
- [23] J.H. Van Vleck, *On the anisotropy of cubic ferromagnetic crystals*, Phys. Rev. **52**, 1178 (1937).
- [24] J.G. Gay and R. Richter, *Spin anisotropy of ferromagnetic films*, Phys. Rev. Lett. **56**, 2728, (1986).
- [25] C.Li, A. J. Freeman, H. J. F. Jansen and C. L. Fu, *Magnetic Anisotropy in low-dimensional ferromagnetic systems: Fe monolayers on Ag, Au and Pd(001) substrates*, in press, Phys. Rev. B. (1990).
- [26] C. Rau, *Magnetic order at surface and electron capture spectroscopy (ECS)*, J.Magn. Magn. Mat. **31-34** (1983) 874 .
- [27] D. Weller, S. F. Alvarado, W. Gudat, K. Schröder and M. Campagna, *Observation of surface-enhanced magnetic order and magnetic surface reconstruction on Gd(0001)*, Phys. Rev. Lett. **54** (1985) 1555.
- [28] L.W. Roeland, G.J. Cock, F.A. Muller, A.C. Moleman, R.G. Jordan and K.A. McFwen, *Conduction electron polarization of gadolinium metal*, J. Phys. **F5** (1975) L233.
- [29] C. Li and A.J. Freeman, *Giant monolayer magnetization of Fe on MgO: a nearly ideal 2D magnetic system*, in press, Phys. Rev. B. (1990).
- [30] T. Urano and T. Kanaji, *Atomic and electronic structure of ultrathin iron film on MgO(001) surface*, J. Phys. Soc. Jpn. **57**, 403 (1988).
- [31] C. Li, A.J. Freeman and C.L. Fu, *Monolayer magnetism : electronic and magnetic properties of Fe/Au(001)*, J. Magn. Magn. Mats. **75**, 201 (1988).

GROWTH AND MAGNETIC PROPERTIES OF METASTABLE STRUCTURES

B.Heinrich, A.S.Arrott, J.F.Cochran, Z.Celinski, and K.Myrtle

Physics Department, Simon Fraser University
BURNABY, BC, Canada, V5A 1S6

Ultrathin magnetic metallic structures have become a major field in material science. The main motivation stems from the ability to grow epitaxially a variety of interesting systems: Well defined interfaces have been prepared exhibiting unusual anisotropic properties^{1, 2}; new metastable structures were grown which do not exist in nature^{3, 4, 5}; and multilayered and superlattice structures were formed exhibiting unexpected exchange and electron transport properties^{6, 7, 8}. Experimentalists have benefited greatly by a close cooperation with theoretists. First principal band calculations have played an immense role and active feedback between theories and experiments have helped and speeded up the whole field of metallic epitaxy. The applied aspects of metallic epitaxies have been pursued in parallel and provided needed inspiration and excitement.

It should be pointed out that all these advances and future progress in atomic engineering would not be possible without Molecular Beam Epitaxy (MBE) techniques such as controlled atomic beams in ultra high vacuum (low 10^{-10} torr range) and using state of the art surface science tools such as Reflection High Energy Electron Diffraction (RHEED) and Auger and XPS spectroscopies whose power has been further augmented by adding to them the spin polarized and angular resolved options.

In this paper we summarize our recent studies of metastable multilayer structures composed of bcc Fe, bcc Ni, bcc Cu and lattice expanded Pd. Besides presenting their interesting physical properties we would like to highlight two experimental techniques: RHEED and Ferromagnetic Resonance (FMR). We found these techniques to be extremely effective and useful in the MBE studies of ferromagnetic metallic structures.

The expression "ultrathin" will be used throughout the whole paper, therefore a word of explanation is needed. Ultrathin films (layers, overlayers, bilayers, trilayers) are epitaxial structures thinner than the exchange length: $(A/2\pi M_s^2)^{1/2}$ ($\approx 3.3\text{nm}$ in Fe), where A is the exchange stiffness constant. Magnetic moments separated by a distance smaller than the exchange length are locked together by the exchange interaction. A system having a spatial scale smaller than the exchange length responds as a single unit to the total torque acting on the system.

GROWTH STUDIES

Epitaxial growth of our ultrathin structures was carried out in a Physical Electronics MBE system-PHI-MBE 400. This MBE system is equipped with RHEED, allowing one to monitor the growth and a double pass CMA analyzer which permits the Auger (AES) and X-ray photo-electron spectroscopy (XPS) studies. The RHEED screen was equipped with a magnifying lens which focussed a small area of the RHEED screen onto a photomultiplier tube

in order to measure either the intensity of the RHEED specular spot as a function of the film thickness or to scan a diffracted beam to obtain a measure of the atom-atom correlation function of the surface.

All our growths were carried out on bulk singular Ag(001) ($\Theta < .25^\circ$) substrates 15 mm in diameter and 3.5mm thick. They were prepared by standard metallographic techniques¹¹. Ag(001) substrates were ion etched using a 2 keV Ar⁺ gun in UHV in a typical thermal cycle: starting at 550° C the substrate was annealed for 1 hour and then sputtered for 10min, the substrate temperature was then decreased by 50° C and sputtered and annealed for 30 min. The substrate temperature was reduced by 50° C steps with 30 min. of sputter-annealing at each temperature. This process was repeated until 350° C was reached. At 350° C the substrate was not sputtered anymore, but annealed for 10 min. and then cooled down to room temperature. The substrates prepared in this way exhibited sharp RHEED patterns with short RHEED streaks and an easily identifiable specular spot. No visible impurities were present in the Auger spectra. During the deposition the vacuum in the growth chamber was held in low 10⁻¹⁰ torr. The substrate was held at room temperature to avoid atomic intermixing between the substrate and overlayers.

The quality of growth was monitored by RHEED intensity oscillations. RHEED oscillations were observed by monitoring the intensity of the specular spot with the primary electron beam directed close to the first anti-Bragg condition. Computer simulations were carried out¹⁰ to determine the role of surface roughness on the amplitude of RHEED intensity oscillations. We found that a growth having 3 or more unfilled atomic layers does not show any RHEED oscillations. In our view the presence of RHEED oscillations indicates a good epitaxial growth having the surface roughness confined mostly to the top two atomic layers. The film formation evolving in this manner will be termed "layer by layer growth". The overall homogeneity of a deposited film was determined by monitoring the intensity of the dominant substrate AES peaks as a function of the film thickness.

Epitaxial growth is expected when the square lattice mesh of the deposited film is closely matched to the substrate mesh. Fe(001) grown on a Ag(001) substrate is a typical example. It turns out that this rule can be extended in some cases to metastable structures. The strongly attractive potential of the interface traps add-atoms in its square mesh and often results in lattice structures corresponding to that of the substrate.

Ni, Cu and Pd grow well on Fe(001) substrates. Large RHEED oscillations show that their growth proceeds in a layer by layer mode, Fig 1. We found that Fe(001) layers can also be grown well on Cu(001) and Pd(001) templates. In this way a variety of ultrathin epitaxial structures were formed such as Fe/Ni, Fe/Cu, Fe/Pd bilayers and Fe/Cu/Fe, Fe/Pd/Fe trilayers. The growth and structural details are presented in our papers^{2,5,11}. Here we present only a brief summary pertinent to a discussion of the magnetic properties.

(a) **Fe(001)**: It is well known that the square lattice of the Fe(001) matches well that of Ag(001) if the cubic unit cells are rotated by 45°. However it is less well known that an

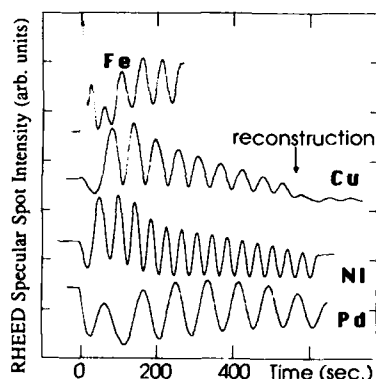


Fig. 1. RHEED intensity oscillations measured at the specular spot during growth. The 5 ML Fe film was grown on a Ag(001) substrate and the Cu, Ni and Pd films were grown on 5, 6 and 5 ML films of Fe on Ag(001) substrates. Note that the reconstruction of the Cu film produces a clearly visible change in the RHEED intensity oscillations. The angle of the beam was $\approx 1^\circ$ with respect to the sample surface. The sample was rotated azimuthally so that the beam was directed 5° from the [110] in plane axis to avoid the Kikuchi lines.

appreciable vertical mismatch remains due to the large tetragonal distortion between the fcc and bcc lattices. Therefore the presence of atomic steps affects the growth, and consequently the magnetic properties of Fe grown on singular Ag(001) substrates. The Fe(001) films showed regular RHEED oscillations only after 2ML were grown, see Fig 1. This is a healing distance for covering atomic steps. The Fe(001) RHEED streaks are not common. The Fe(001) RHEED streaks very quickly develop (after ~ 2 ML) a narrow split which is azimuthally symmetric¹³, see Fig 2a. Once the split is created it remains throughout the whole growth. It was shown by Henzler's group in their work on W(110)¹⁴ that such behavior is consistent with a simple nucleation and growth mechanism in which a new atomic layer starts to form around nucleation sites. The nucleation sites are randomly distributed but they maintain an approximately equidistant separation (the inverse value of the streak splitting, ~ 3.0 nm). The growth proceeds by attaching deposited add atoms to the edges of atomic islands which have been already formed, see Fig 2b. The continuing presence of RHEED spot splitting shows that a new set of atomic islands is nucleated (on the top of an already existing set) before the expanding atomic islands coalesce to form a complete atomic layer. Clearly the Fe growth proceeds with at least two unfinished atomic layers. Large RHEED oscillations and our computer simulations suggest that only two partly covered atomic layers exist at any moment during the growth.

(b) Ni(001): The first 3 ML follow the bcc stacking with the same lateral spacing and the same vertical relaxation as observed for Fe(001)¹⁵. After reaching a critical thickness, 3ML, the Ni overlayers transform gradually to a more complicated structure². The transformed "bcc Ni" shows that the main features of the RHEED patterns along the {001} and {110} principal azimuths remain, but the RHEED patterns along {110} azimuths show in addition weak diffraction streaks positioned 2/5 of the way between the bcc streaks. The additional superlattice streaks are also visible for azimuths away from {100} and {110} directions. Their complicated dependence indicate that the Ni transformation is a rather severe distortion of the basic bcc lattice. Structural modifications occurring after the bcc overlayers reach a critical thickness suggests that the minimum energy atomic spacing of the bcc Ni metastable structure does not match the bcc Fe substrate spacing. The elastic energy stored in the initial strained homeomorphic bcc Ni structure is eventually released and the lattice transforms and develops a network of crystallographic defects which in the simplest description can be represented by a network of misfit dislocations. Much as we might like to know an exact distribution of atoms in the transformed "bcc Ni" or whether the local order is bcc or fcc, it is more important to realize that "bcc Ni" overlayers in Fe/Ni bilayers form a unique structure accompanied by magnetic properties which are truly different from those observed for fcc Ni and bcc Fe. Even though we do not yet know the atomic structure of "bcc Ni", we can use in-situ RHEED to identify this structure from its characteristic diffraction features.

(c) Cu(001): The growth of Cu(001) overlayers maintains the in-plane symmetry of the Fe(001) substrate for the first 10-11 ML compared with Ni(001) overlayers which could be grown that way only for the first 3 ML. The RHEED streak separation for Cu(001) overlayers is approximately 1.2% smaller than those for the Fe(001) layers indicating a corresponding increase in the Cu(001) lattice spacing⁵. It would require a 12.5% distortion to match fcc Cu to bcc Fe(001) square mesh. The angular resolved XPS (ARXPS) studies by Egelhoff et al¹⁶ of

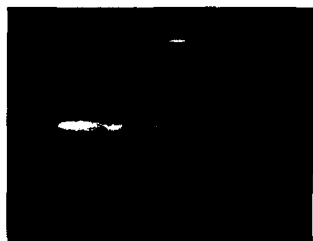


Fig. 2a RHEED pattern along the {11} azimuth for 5 ML Fe on Ag (001) substrate.

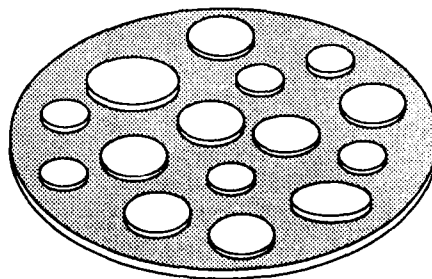


Fig. 2b Pattern of islands during Fe growth.

epitaxial Cu on Ag(001) (note that the Ag(001) and Fe(001) templates are very similar) showed that a vertical contraction occurs which yields a lattice quite close to the bcc structure. One can therefore conclude that the Cu(001) overlayers grow on Fe(001) in a nearly perfect bcc structure. The RHEED patterns are significantly altered when the Cu(001) overlayers reach a critical thickness. The {100} azimuths develop two additional symmetrically spaced streaks, suggesting that the Cu(001) superlattice repeats along the {100} azimuths every three unit cells. Superlattice streaks along the {110} azimuths do not seem to be commensurate with the lattice and this is similar to our observations on the transformed "bcc Ni".

(d) **Pd(001)**: RHEED patterns show that the growth follows the Fe(001) square mesh very closely, no visible reconstruction are visible for films thinner than 12 ML¹². An excellent coverage of the Fe substrate layer is also evidenced by a well defined exponential decay of the Fe L₃VV Auger intensity with an increasing Pd thickness. The electron mean free path in Pd is even 20% (5.6 ML) smaller than the value calculated from the universal Seah-Dench's formula (7ML). The lateral spacing in Pd(001) is identical to that of the Fe(001) substrate. Since its lateral spacing is 5% larger than in the regular fcc Pd one can say that this structure is metastable and very likely fcc; however the last point must be left to future LEED and ARXPS studies to decide.

MAGNETIC STUDIES USING FMR

FMR is an extremely sensitive tool. One ML of Fe can be easily detected; and it is a relatively simple technique which is not expensive to implement.

The Landau-Lifshitz equation of motion for the magnetization, \vec{M} , is

$$-\frac{1}{\gamma} \frac{\partial \vec{M}}{\partial t} = \vec{M} \times \vec{H}_{\text{eff}}$$

where \vec{M} and \vec{H}_{eff} have contribution from both static and dynamic components, that is $\vec{M} = \vec{M}_s + \vec{m}$ and $\vec{H}_{\text{eff}} = \vec{H}_0 + \vec{h} + \vec{h}_d + \vec{H}_k + \vec{h}_G + \vec{h}_{\text{ex}}$, \vec{M}_s is the equilibrium saturation magnetization and \vec{m} is the rf component of \vec{M} . \vec{H}_0 is the static internal field usually applied in the plane of the specimen (parallel configuration). \vec{h} is the parallel component of the applied rf field.

$\vec{h}_d = -4\pi D \vec{m}_\perp$ is the demagnetizing field perpendicular to the sample surface. The demagnetizing field in ultrathin layers depends on the number of atomic layers². The anisotropy field \vec{H}_k depends on the direction of the magnetization \vec{M} with respect to crystallographic axes. The intrinsic damping will be described by the Gilbert damping $\vec{h}_G = -i(\omega/\gamma) \vec{m} / M_s^2$, where G is the Gilbert damping, ω is the microwave angular frequency and γ is the spectroscopic splitting factor. \vec{h}_{ex} is the exchange field².

Ultrathin films of cubic materials grown along [001] crystallographic direction exhibit tetragonal symmetry. In ultrathin films the magnetic moments across the sample are nearly parallel. The system responds as a rigid unit. The total torque is shared equally by all moments. Consequently the surface anisotropies divided by the film thickness, d , appear as effective bulk-like anisotropies¹⁷. The magnetocrystalline anisotropy energy can therefore be written as:

$$E = -\frac{1}{2} K_{1\parallel}^{\text{eff}} [\alpha_x^4 + \alpha_y^4] - \frac{1}{2} K_{1\perp}^{\text{eff}} \alpha_z^4 - \frac{K_u^s}{d} \alpha_z^2 \quad \text{where} \quad K_{1\parallel}^{\text{eff}} = K_{1\parallel} + \frac{1}{d} K_{1\parallel}^s$$

$$K_{1\perp}^{\text{eff}} = K_{1\perp} + \frac{1}{d} K_{1\perp}^s \quad (1)$$

where $\alpha_x, \alpha_y, \alpha_z$ are directional cosines with respect to [100], [010] and [001] crystallographic axis; and $K_{1\parallel}, K_{1\perp}, K_{1\perp}^s, K_{1\parallel}^s$ are the bulk and the surface 4th order anisotropies respectively. K_u^s is the uniaxial surface anisotropy perpendicular to the sample surface. When the saturation magnetization, \vec{M}_s , is oriented in the plane of the film (parallel configuration) the 4th order perpendicular uniaxial anisotropy plays no role in FMR. On the other hand when the saturation magnetization is perpendicular to the film (perpendicular configuration) the in-plane 4th order plays no role. Note that the perpendicular uniaxial anisotropy acts like the perpendicular demagnetizing field resulting in the effective demagnetizing field,

$4\pi DM_{\text{eff}} = 4\pi M_s - 2K_u^s/(M_s d)$. Positive K_u^s creates an effective field which tries to orient the M_s along the normal.

The linearized L-L equations of motion lead to resonance conditions:

$$\left(\frac{\omega}{\gamma}\right)^2 = \left[H_0 + 4\pi DM_{\text{eff}} + \frac{K_{1\parallel}^{\text{eff}}}{2M_s} (3 + \cos 4\phi) \right] \left[H_0 + \frac{2K_{1\parallel}^{\text{eff}}}{M_s} \cos 4\phi \right] \quad (\text{parallel FMR}) \quad (2a)$$

$$\frac{\omega}{\gamma} = H_0 - 4\pi DM_{\text{eff}} + \frac{2K_{1\perp}^{\text{eff}}}{M_s} \quad (\text{perpendicular FMR}) \quad (2b)$$

where ϕ is the angle between the saturation magnetization, M_s , and the in-plane [100] direction. Equations (2a) and (2b) summarize algebraically the power of FMR. The in-plane angular dependence of the resonance fields determines $K_{1\parallel}^{\text{eff}}$. The variation of the resonance fields with applied microwave frequencies (at least two microwave frequencies are required) determines the effective demagnetizing field $4\pi DM_{\text{eff}} = 4\pi M_s - 2K_u^s/M_s$ and the spectroscopic splitting factor γ (or g-factor). The 4th order perpendicular anisotropy, $K_{1\perp}^{\text{eff}}$, can be determined by perpendicular FMR measurements.

The frequency dependence of the FMR linewidth in ultrathin films can be described by

$$\Delta H = \Delta H(0) + 1.16 \frac{\omega}{\gamma} \frac{G}{\gamma} \frac{1}{M_s} \quad (3)$$

where the frequency dependent part is caused by the intrinsic Gilbert damping arising from the spin-orbit contributions to the electron valence band energies. The frequency independent part $\Delta H(0)$ is caused by magnetic inhomogeneities¹⁸. In ultrathin structures the magnetic inhomogeneities contributing to FMR linewidth are caused by crystallographic defects which are on a scale comparable to or bigger than the exchange length.

Note that FMR condition can not be used to determine the saturation magnetization M_s . However the total integrated intensity of the FMR signal is directly proportional to the total magnetic moment of the specimen:

$$I \propto M_s d \frac{[H_{\text{FMR}} + (4\pi M_s)_{\text{eff}}]}{[2H_{\text{FMR}} + (4\pi M_s)_{\text{eff}}]}$$

Therefore FMR can be used to measure the relative magnetic moments. In our measurements the reference samples 5Fe/Au(001) and 10Fe/Au(001) are commonly used (5 and 10 represents the number of ML).

Exchange coupled ferromagnetic layers

Magnetic ultrathin bilayers and superlattices separated by non magnetic interlayers are increasingly gaining prominence. We have presented a detailed model of exchange coupled ultrathin structures². In this limit the static magnetic moments are parallel throughout the structure and rf magnetic moments are parallel in each constituent ferromagnetic layer. There are two resonance modes: The low frequency acoustic mode in which all moments are parallel and the high frequency optical mode in which the magnetic moments of two adjacent ferromagnetic layers are out of phase. The character of the interlayer coupling can be easily identified from the relative position of the acoustic and optical modes. In FMR the optical mode is located at a higher field than the acoustic mode for antiferromagnetic coupling and the optical peak is located at a lower magnetic field for ferromagnetic coupling. The optical modes are easy to identify since their intensities decrease rapidly with an increasing exchange coupling. In our theoretical treatment the exchange interface energy, E^{AB} is given² by

$$E^{AB} = -4 (A^{AB}/a) (M^A/M^A) (M^B/M^B),$$

where A^{AB} (in the ferromagnetic bulk $A^{AB} \sim 10^{-6}$ ergs \cdot cm⁻¹) is the exchange coupling coefficient between layers, M^A , M^B are the saturation magnetizations of adjacent layers A and B, and a is the lattice constant. The positions and intensities of both modes depend in a complicated way on the strength of the exchange coupling. Simple behavior occurs for either

the trivial case of fully decoupled layers or for strongly coupled layers. In strong coupling only the acoustic mode is observed. Its position is determined by the overall bilayer properties given by a simple scaling law involving the effective fields of the individual layers². One should point out that in FMR (homogeneous driving) the optical mode is visible only if the Fe layers have different resonance frequencies in the absence of exchange coupling. In our case that was achieved by using Fe films having different thicknesses (5 and 10 ML) which resulted in different contributions to the perpendicular uniaxial field, see eq. 1.

RESULTS OF MAGNETIC STUDIES

Bcc Ni, bcc Cu and lattice expanded Pd epitaxial structures are magnetically unique systems. The Cu 3d band is filled and therefore non magnetic. The ground states of bcc Ni were studied theoretically by Marcus and Moruzzi²². They showed that the ground state of bcc Ni is non-ferromagnetic, but that lattice expanded bcc Ni can result in magnetic moments comparable to that of fcc Ni. Pd closes the 4d transition group of elements. The Pd 4d bands are not entirely filled. The strong intra-atomic Coulomb interaction between 4d electrons is responsible for an anomalously large Pauli susceptibility. The repulsive intra-atomic Coulomb interaction is so strong that the 4d band is near the threshold of becoming ferromagnetic. Numerous experiments were carried out to test the tendency for Pd to become ferromagnetic. Those include the giant magnetic moments of magnetic impurities in host Pd¹⁹, the giant Pauli susceptibility enhancement in [Ag/Pd] superlattices²⁰, and the induced magnetic moment in bulk Pd by submonolayer Fe overlayers²¹. However none of these experiments observed a long range magnetic order in metallic Pd. Recent first principles band calculations²³ suggested that a long range ferromagnetic order could be established in a 5% expanded Pd lattice. **Ni(001)**: Two Ni(001) structures the pure bcc and transformed "bcc Ni" showed very different properties. The magnetic moment in Fe/Ni bilayers was enhanced by both the pure bcc Ni and lattice transformed "bcc Ni". The saturation magnetizations of both forms of bcc Ni, ~5 kG, are nearly as large as in fcc Ni. This is in agreement with the calculations by Moruzzi and Marcus²².

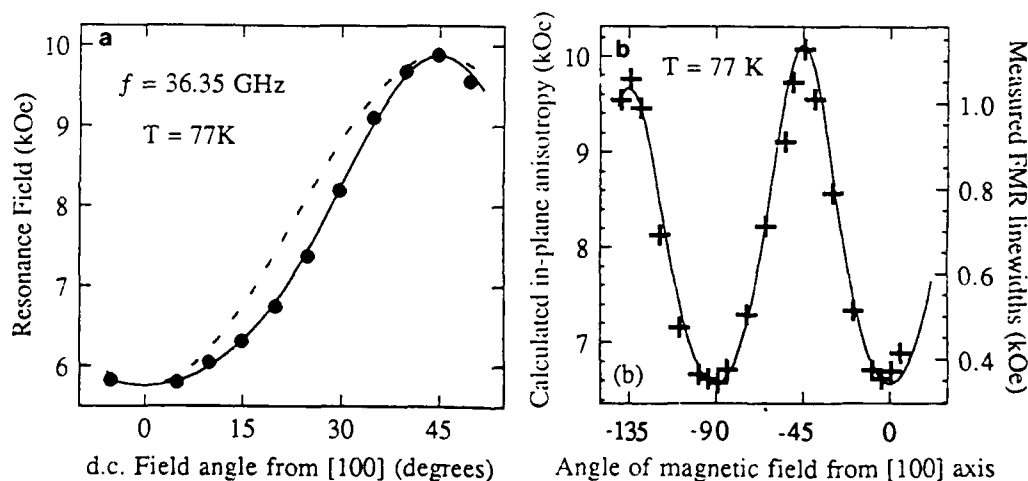


Fig.3a The angular dependence of the FMR fields for a 9Fe/15Ni sample. The dashed and solid lines are the calculated angular variation; the dots are resonance experimental values. The solid line corresponds to the case where the magnetization is allowed to drag behind the applied d.c. field. The dashed line corresponds to the case where the magnetization is assumed to be parallel to the applied field. Fig.3b. The in-plane angular dependence of FMR linewidth for a 6Fe/10Ni sample at 36.6 GHz. The superimposed solid curve is a fit to the observed angular variation in the FMR resonance field values.

However it was the lattice transformed "bcc Ni" which showed truly remarkable magnetic properties². The in-plane 4th order anisotropies were significantly enhanced in bilayers with "bcc Ni", no enhancement was observed in bilayers having bcc Ni. The 4th order anisotropies in Fe/Ni bilayers far exceeded those observed in regular 3d transition metals and their alloys. Effective fields, $2K_1/M_s$, at room temperature are easily controlled by an appropriate choice of the Fe and Ni layer thicknesses. The angular dependences of the FMR linewidth and the FMR field in transformed bilayers show a very similar behavior, see Fig 3b Obviously both anisotropies have a common origin. The microwave frequency dependence of ΔH showed a typical linear dependence with a zero frequency offset $\Delta H(0)$, see eq. 3. The linear slope corresponding to the intrinsic Gilbert damping is isotropic as it is in all 3d transition metals; it is the $\Delta H(0)$ which is strongly angular dependent. As we pointed out, $\Delta H(0)$ is caused by sample magnetic inhomogeneities and therefore the origin of the in-plane 4th order anisotropy must lie in crystallographic faults generated during the Ni overlayer transformation. The strong angular dependence of the FMR linewidth could indicate that the measured 4th order anisotropies were of dynamic origin. However, the angular dependence of the FMR field exhibited clear features of a lag of the direction of the saturation magnetization behind the in-plane applied dc magnetic field, see Fig. 3a. A lag of the saturation magnetization is a clear indication that the measured anisotropies are truly a direct consequence of a static 4th order term. It is remarkable that crystallographic defects triggered by the lattice mismatch can create well defined 4th order anisotropies. To our knowledge these Fe/Ni bilayers represent the first system in which controllable 4th order anisotropies were engineered by a lattice relaxation.

The crystallographic defects have to satisfy the fourfold in-plane symmetry. If we were to assume that these defects are described by a simple network of misfit dislocations then they would have to be equally distributed between the {110} directions. Large anisotropy due to dislocation arrays might be attributed to the enhancement of the spin orbit contribution to the 3d band energies which appears with broken symmetry around crystallographic defects.

Bcc Cu(001): Fe/Cu bilayers with lattice transformed Cu(001) overlayers ($d > 12$ ML) did not show any enhancement of the in-plane 4th order anisotropy. Therefore the magnetic state of the lattice transformed "bccNi" is a crucial factor in the development of large in-plane anisotropies.

Fe/Cu/Fe trilayers showed very interesting behavior in magnetic coupling. Since the exchange coupling through bcc Cu(001) will be described in a separate paper presented at this School²⁴ only the main results will be briefly listed: We found that bcc Cu(001) interlayers 9. - 12.6 ML thick couple the Fe layers antiferromagnetically. The maximum antiferromagnetic coupling occurred at ~ 11 ML ($A^{AB} = -1.6 \cdot 10^{-9}$ ergs \cdot cm⁻¹). The crossover to ferromagnetic coupling appeared when the Cu(001) interlayer thickness reached ~ 8 ML.

Lattice expanded Pd(001): The magnetic parameters of constituent Fe layers and their exchange coupling in Fe/Pd/Fe trilayers were determined by using the full theory of exchange coupled Fe bilayers starting from the magnetic properties of the individual Fe layers (5Fe/8Pd, 8Pd/10Fe). The final adjustment of the magnetic parameters was carried out by using a "Minuit" least squares fitting routine. It turns out that the exchange coupling is the only variable which is strongly dependent on the Pd(001) interlayer thickness. All other parameters, especially $4\pi DM_{eff}$, are very close to their single Fe layer counterparts. However a noticeable difference was found for some in-plane 4th order anisotropies. Results are summarized in Table I.

FMR measurements of exchange coupled trilayers show the power of resonance techniques. The positions of acoustic and optical peaks identify quickly the type of coupling and their exact positions determine quantitatively the strength of the exchange coupling. In all our Fe/Pd/Fe trilayers the optical mode occurred at a smaller field than the acoustic peak showing that the exchange coupling is always ferromagnetic. This result is expected since Pd should be very inclined to become ferromagnetic. The truly surprising result is that this coupling is very weak even for Pd interlayers less than 10 ML thick. 7ML thick Pd is significantly less coupled than an equivalent bcc Cu(001) interlayer. In fact only the 4ML thick Pd layer results in strong coupling, no optical mode was observed, and we believe that this layer is ferromagnetic throughout the whole Pd layer. Ferromagnetic 4ML Pd interlayer has to be ferromagnetic since the spin polarized calculations²⁵ indicate that each Fe interface should carry two

Table I. Magnetic parameters of the Fe/Pd and Pd/Fe bilayers and Fe/Pd/Fe trilayers. For the trilayers the upper and lower values apply to the 5 and 10 ML Fe films

| Sample | $(4\pi M_s)_{\text{eff}}$ (kG) | | $2 K_1/M_s$ (kOe) | | $10^9 A^{\text{AB}}$ (ergs/cm) | |
|----------------|-----------------------------------|-------|----------------------|------|-----------------------------------|------|
| | 295K | 77K | 295K | 77K | 295K | 77K |
| 5Fe/8Pd/20Au | 9.40 | 10.71 | .116 | .238 | - | - |
| 8Pd/10Fe/20Au | 16.94 | 18.56 | .171 | .303 | - | - |
| | 9.44 | 10.93 | .108 | .232 | | |
| 5Fe/11Pd/10Fe | | | | | 0.19 | 0.13 |
| | 16.73 | 18.30 | .209 | .339 | | |
| | 9.30 | 10.67 | .111 | .235 | | |
| 5Fe/10Pd/10Fe | | | | | 0.08 | 0.04 |
| | 16.85 | 18.63 | .219 | .358 | | |
| | 9.38 | 10.51 | .119 | .238 | | |
| 5Fe/6Pd/10Fe | | | | | 0.31 | 1.35 |
| | 16.93 | 18.52 | .192 | .363 | | |
| | 9.90 | 10.14 | .149 | .186 | | |
| 5Fe/5.5Pd/10Fe | | | | | 0.51 | 1.56 |
| | 16.87 | 18.18 | .193 | .329 | | |
| | 9.97 | 10.92 | .110 | .192 | | |
| 5Fe/5Pd/10Fe | | | | | 0.86 | 2.16 |
| | 16.49 | 18.47 | .243 | .307 | | |

ferromagnetically ordered Pd atomic layers. One extra Pd atomic layer leads to a weak coupling, see Fig. 4a which implies that the long range ferromagnetic order in Pd is destroyed. However the samples having interlayer thicknesses between 5 and 6 ML exhibit very strong temperature dependent coupling, see Fig 4b. The exchange coupling in the sample 5Fe/5Pd/10Fe shows a Curie-Weiss dependence, $1/(T+T_0)$. A net magnetic moment in the Pd layer would certainly increase the magnetic coupling between Fe layers since the exchange torque increases with the moment. Therefore a Curie-Weiss like behavior of the exchange coupling suggests very strongly that these Pd layers possess a fluctuating moment which is partly polarized by the adjacent Fe layers.

The temperature dependence of the exchange coupling in thick Pd interlayers is weak and even reverses its behavior. The 5Fe/11Pd/10Fe trilayer shows a decreased value of the exchange coupling at LN₂ temperatures compared with that at room temperature. Therefore thick Pd layers ($d > 8\text{ML}$) do not exhibit fluctuating moments and their temperature dependence suggests that the exchange coupling is caused by small parts of the Fermi surface which are sensitive to changing temperature.

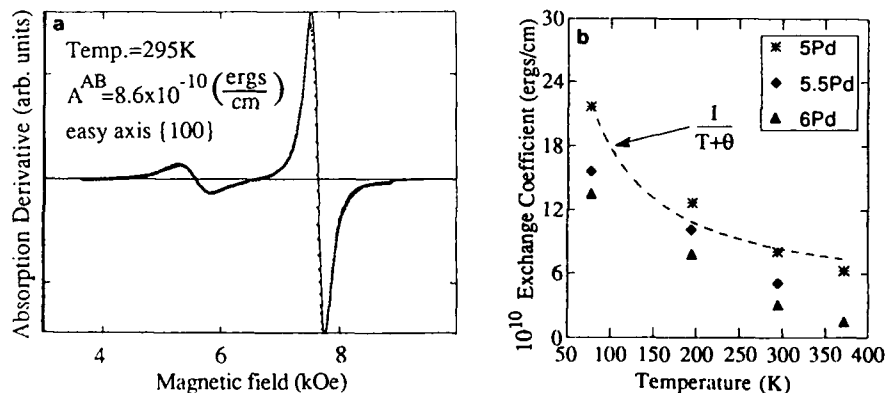


Fig.4a The absorption derivative vs. applied field for a 5Fe/5Pd/10Fe sample at 36.3 GHz. The solid line represents the theory using the parameters in Table I.

Fig.4b Exchange coefficient vs temperature for 5Fe/xPd/10Fe films ($x = 5, 5.5, 6$).

CONCLUSIONS

We have demonstrated that a variety of interesting and well defined epitaxial structures can be grown by MBE. The RHEED and Auger intensity studies allow one to determine structures with an accuracy better than 1ML and at the same time to identify various growth modes and lattice transformations. FMR is a very useful tool to determine quantitatively all magnetic parameters in ultrathin structures. FMR identified the origin of enhanced 4th order anisotropies in Fe/Ni bilayers. We can engineer samples having variable 4th order anisotropies corresponding to room temperature effective fields in the range 0. - 2.5 kOe. FMR also served very well to study the exchange coupling between Fe layers separated by non-magnetic interlayers. We have shown that laterally expanded Pd very reluctantly participates in the long range order. Despite the filled 3d band of bcc Cu the coupling in Fe/Cu/Fe interlayers was found to be antiferromagnetic. The spatial range of the antiferromagnetic coupling in bcc Cu is even larger than that observed in bcc Cr.

ACKNOWLEDGEMENTS

The authors would like to thank the National Sciences and Engineering Research Council of Canada for grants which provided support for this work.

REFERENCES

1. B.Heinrich, K.B.Urquhart, J.R.Dutcher, S.T.Purcell, J.F.Cochran, A.S.Arrott, W.F.Egelhoff, J.Appl.Phys.63:3863 (1988)
2. B.Heinrich, S.T.Purcell, J.R.Dutcher, K.B.Urquhart, J.F.Cochran, A.S.Arrott, Phys.Rev. B 38:12879 (1988)
3. W.F.Egelhoff, I.Jacob, Phys.Rev.Lett. 62:921 (1988)
4. C.M.Schneider, J.J.deMiguel, P.Bressler, J.Garbe, S.Ferrer, R.Miranda, J.Kirschner, J.Phys.Colloq. 49:C8-1657 (1988)
5. B.Heinrich, Z.Celinski, J.F.Cochran, W.B.Muir, J.Rudd, Q.M.Zhong, A.S.Arrott, K.Myrtle, J.Kirschner, Phys.Rev.Lett, 64:673 (1990)
6. F.Saurenbach, V.Waltz, L.Hinchey, P.Grunberg, W.Zinn, J.Appl.Phys. 63:3473 (1988)
7. M.N.Baibich, J.M.Broto, A.Fert, F.Nguyen VanDan, E.Petroff, P.Etienne, G.Creuzet, A.Friedrich, J.Chazalas, Phys.Rev.Lett. 61:2472 (1988)
8. J.J.Krebs, P.Lubitz, A.Chaiken, G.A.Prinz, Phys.Rev.Lett. 3:1645 (1989)
9. F.J.A.M.Greidanus, W.B.Zeper, F.J.A.denBroeder, W.F.Gotlieb, P.F.Garcia, Appl.Phys.Lett 54:2481 (1989)
10. S.T.Purcell, A.S.Arrott, B.Heinrich, J.Vac.Sci.Techn. 6:794 (1988)
11. B.Heinrich, K.B.Urquhart, A.S.Arrott, J.F.Cochran, K.Myrtle, S.T.Purcell, Phys.Rev.Lett.59:1756 (1987)
12. Z.Celinski, B.Heinrich, J.F.Cochran, W.B.Muir, A.S.Arrott, J.Kirschner submitted to Phys.Rev.Lett.
13. A.S.Arrott, B.Heinrich, S.T.Purcell in "Kinetics Of Ordering and Growth at Surfaces", edited by M.G.Lagally, Plenum, New York, to be published
14. P.Hahn, J.Clabes, M.Henzler, J.Appl.Phys. 51:2079 (1980)
15. Z.Q.Wang, Y.S.Li, F.Jona, P.M.Marcus, SolidStateComm. 61:623 (1987)
16. W.F.Egelhoff, I.Jacob, J.M.Rudd, J.F.Cochran, B.Heinrich, J.Vac.Sci.Tech, to be published
17. B.Heinrich, J.F.Cochran, A.S.Arrott, S.T.Purcell, K.B.Urquhart, J.R.Dutcher, W.F.Egelhoff, Appl.Phys. A 49:473 (1989)
18. B.Heinrich, J.F.Cochran, R.Hasegawa, J.Appl.Phys. 57:3690 (1985); J.F.Cochran, R.W.Qiao, B.Heinrich, Phys.Rev. B 39:4399 (1989)
19. A.Oswald, R.Zeller, P.H.Dederichs, Phys.Rev.Lett. 56:1419 (1986)
20. M.B.Brodsky, J.Appl.Phys. 52:1665 (1981)
21. C.Liu, S.D.Bader, Physica B 161:253 (1989)
22. V.L.Moruzzi, P.M.Marcus, K.Swartz, P.Mohn, Phys.Rev.B 34:1748 (1986)

23. V.L.Moruzzi, P.M.Marcus, Phys.Rev.B 39:471 (1989)
24. Z.Celinski, B.Heinrich, J.F.Cochran, K.Myrtle, A.S.Arrott this issue
25. S.Blugel, B.Drittler, R.Zeller, P.H.Dederichs, Appl.Phys A 49:547 (1989)

SPIN-RESOLVED PHOTOEMISSION

J. Kirschner

Inst. f. Experimentalphysik
Freie Universität Berlin
1000 Berlin 33 Germany

1. INTRODUCTION

Momentum-resolved photoemission has over the past decade developed into a mature tool for the study of two- and three-dimensional electronic states at surfaces and in thin films. Though not all complexities of the emission process have yet been fully incorporated into the analysis of photoemission spectra (one such problem is temperature), and though samples with complicated unit cells still pose severe problems for theory and experiment, a number of excellent review articles¹ impressively demonstrate the present state of the art. However, the electron is mostly treated as a charged mass only, disregarding its spin. The rich information contained in the components of the spin polarization vector is just starting to be fully exploited. Though a number of pioneering spin-polarized photoemission experiments, both with magnetic² and non-magnetic³ samples, had been carried out quite early, the full potential of the technique became available with the advent of spin- and momentum-resolved photoemission⁴ in 1981. Since then, progress has been steady but relatively slow, due to the still unsatisfactory performance of spin polarization analyzers. Even the best analyzers today suffer from an intensity loss by roughly three orders of magnitude. This required specialized equipment, mostly not commercially available, and long measurement times. No wonder, therefore, that the progress in this field went parallel to the development of dedicated synchrotron radiation light sources, which provide sufficient photon flux to (partly) compensate for the count rate losses in the detector. For a review see ref. 5. A new chapter was opened when the circular polarization of the photons emitted above and below the plane of the electron orbit in a storage ring was exploited. Non-magnetic materials and, since very recently⁶, magnetic samples have been studied in this way. There is now considerable promise to circumvent the complexities of a direct spin analysis by harnessing the spin-orbit interaction in magnetic samples.

The purpose of the present paper is to discuss the origin of spin-polarized photoelectrons both from magnetic and non-magnetic samples and the information that can be obtained from them. According to the general topic of this book we concentrate on magnetic samples. For non-magnetic samples and adsorbates we refer to a recent review⁷. In sect. 2 we discuss in general terms the origin of polarized photoelectrons, while sect. 3 is devoted to a case study: exchange split valence bands in Co. The combined action of both, exchange interaction and spin-orbit interaction, is discussed in sect. 4, where the novel effect of Magnetic X-ray Dichroism in Photoemission is presented.

2. THE ORIGIN OF SPIN-POLARIZED PHOTOELECTRONS

There are two main spin-dependent interactions in a solid: exchange interaction and spin-orbit interaction. Both are always present in any material, but are most easily observable in different regions of the electronic structure. Exchange interaction is most clearly seen in the valence band of ferromagnets or antiferromagnets, while spin-orbit interaction is most clearly seen in the splitting of core level energies of the heavy elements. We will see, however, that spin-orbit interaction may also be observed in the valence band, and exchange interaction in core levels.

The conceptually simplest case leading to emission of spin-polarized electrons is photoemission from the valence band of an itinerant ferromagnet. This is shown schematically in Fig. 1.

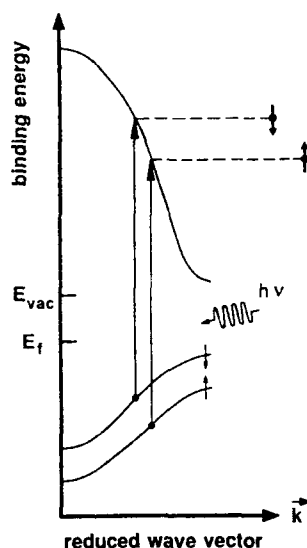


Fig.1 Schematic representation of the emission of polarized photoelectrons from an itinerant ferromagnet. Electrons from minority and majority states may be analyzed outside the crystal and yield information on the dispersion of the initial bands.

In a reduced zone scheme the absorption of a photon leads to the transition of an electron from an occupied state below the Fermi energy E_f to an empty state above E_f , which looks like a vertical transition because of the smallness of the photon momentum (which, of course, is conserved in the transition). If the electron energy in the final state is above the vacuum level E_v , the electron may eventually be observed in vacuum and analyzed with respect to its spin orientation (strictly speaking its projection onto the magnetization quantization axis). It is important to note that the electron spin is conserved during the transition, if small photon energies ($\ll 100$ keV) are used. Electric dipole transitions dominate magnetic dipole transitions by a factor $(h\omega/mc^2)^2$ where $h\omega$ is the photon energy. The point in the Brillouin zone where the transition occurs is, in principle, different for majority and minority electrons since the bands are shifted by the exchange energy Δ . Very often, in particular when slowly dispersing d-bands are studied, the difference is

small. The upper states are, in principle, also split in energy. The exchange splitting of the empty states plays a role for the absorption and reflection of polarized electrons and for the polarization fine structure in secondary electron emission, as is demonstrated at another place in this book⁸. The exchange splitting is considerably smaller than in the d-bands, though, and its effects are relatively weak, so that we neglect it here. The transport of the electrons towards the surface and their escape into vacuum are, in principle, not independent of the spin of the electrons. As is known from the analysis of Stoner excitations by polarized electron scattering⁹, the probability of inelastic exchange scattering is larger for minority electrons than for majority electrons. Therefore, the number of majority electrons arriving at the surface is somewhat enhanced, at the expense of the minority electrons. The transmission through the surface is slightly spin-dependent since the surface potential as seen by majority electrons is somewhat different from that seen by minority electrons. These effects are known from spin-polarized LEED and are of order of a few percent difference. These secondary effects modify the spin polarization as measured outside the crystal, but at the present level of sophistication of theory and experiment they may be disregarded here. The essential information, i.e. the spin character of the initial bands, is preserved. Using the established techniques of photoemission analysis the dispersion of the initial bands then may be mapped out for majority and minority bands separately. From this, essential features like the k-dependent exchange splitting or the crossing of bands with the Fermi surface may be obtained. Also, since the spin polarization is a vector quantity which is directly related to the magnetization vector, the magnetization direction in a thin film or at the surface of a bulk material may be read directly from the spin orientation of the electrons in vacuum.

A few words, on the character of the photons to be used are in order. The spin of the emitted electrons does, to first order, not depend on the polarization state of the light. Therefore, the process works with unpolarized light. Using linearly polarized light is advantageous since by parity conservation (i.e. in the absence of spin-orbit coupling) the space group symmetry of the initial (or final) bands may be found out. The intensity of particular transitions then depends on whether certain (non relativistic) dipole selection rules are fulfilled or not. The spin polarization of the electrons remains unchanged, however. The same holds for circularly polarized light, to the extent that spin-orbit coupling in the electron states can be neglected. If this is not so, to second order the intensities and the spin polarization depend on the helicity of the light. This will be discussed below and is demonstrated in sect. 5.

Within the three-step-model which we have adopted, unpolarized or linearly polarized light does not give rise to spin polarization as far as the dipole operator term is concerned. However, the transmission step T may in this case also lead to polarized electrons in vacuum. In fact, in the first momentum- and spin-resolved photoemission experiment⁴ unpolarized light and a W crystal were used. The photoelectron polarization in this case is due to spin-dependent matching of the electron wavefunctions at the W surface. These effects obey certain spatial and time reversal symmetries^{4,10,11} and can be suppressed by a suitable selection of the experimental parameters. We are interested here only in the 'matrix element' part of the photocurrent expression and we show that circularly polarized light leads to polarized electron emission:

$$j(E_f, \mathbf{k}, \mathbf{q}) = |\langle f | \mathbf{O}_p | i \rangle|^2 \cdot D(E_f, \mathbf{k}, \mathbf{q}) \cdot T(E_f, \mathbf{k}, \mathbf{q})$$

We assume two spin-orbit split initial bands Γ_7 and Γ_8 at the Γ point, a free-electron-like final band Γ_6 , and circularly polarized light (see Fig. 2). The initial states are all occupied by at least two electrons, in contrast to a ferromagnet where in general each band is occupied by one electron only. In spite of this, we observe experimentally polarized

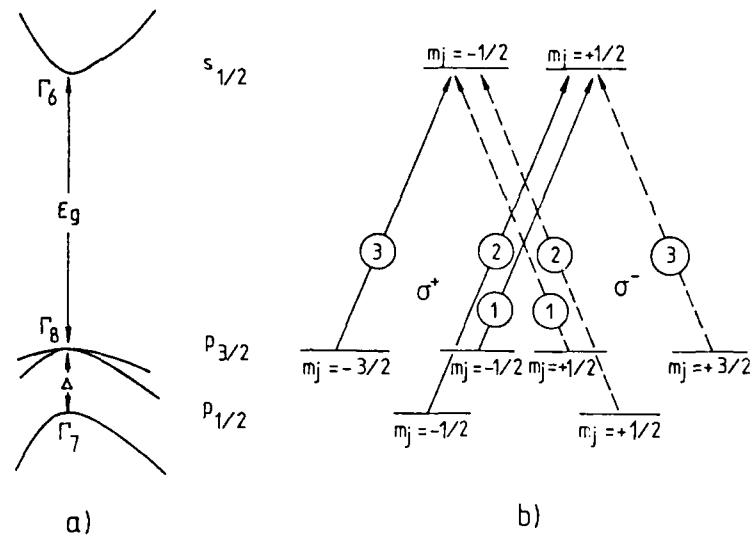


Fig.2 A section of a diamond-type bandstructure around the Γ point with spin-orbit split Γ_8 and Γ_7 bands (which is that of GaAs with a band gap of 1.52eV). The Γ_8 level is 4 fold, the Γ_7 level two-fold spin degenerate. The right hand side indicates the transition with right hand circularly polarized light (σ^+) corresponding to the dipole selection rules $\Delta l = -1$, $\Delta m_j = -1$ in full lines, those for σ^- light in dashed lines. The numbers in circles give the relative strengths of the corresponding matrix elements.

photoelectrons. In the case shown, we observe 'up' electrons from the lower band Γ_7 and 'down' electrons from the upper band Γ_8 for σ^+ light. If we reserve the light helicity, the spins also reverse. This means, that by circularly polarized light from the two spin states in each band one particular state is preferentially excited. The spin orientation is related to the photon spin orientation-therefrom the name 'optical orientation'^{3,12}. The intensities for both light helicities are exactly the same, but the analysis of the spin states provides a clue to the symmetry of the wavefunctions involved. This effect is of fundamental interest in itself, but also has important applications. For example, the well-known source of spin-polarized electrons using GaAs or its ternary compounds uses this effect. In fact, our diagram refers precisely to this case. As may be seen from the right hand side of Fig. 2, transitions from Γ_7 lead to completely positively polarized electrons, while those from Γ_8 only to -50% polarization since two transitions with $\Delta m_j = -1$ compete. Since the transition matrix elements are different with the ratio 3:1 the transition $m_j = -3/2 \rightarrow m_j = -1/2$ dominates. In the case of GaAs no momentum analysis of the photoelectrons is necessary if the photon energy matches exactly the band gap of 1.52eV. In general, different transitions in the Brillouin zone with different final state spin polarizations tend to null the total yield polarization. Using momentum analysis, on the other hand, some very detailed results on the double group symmetry properties, i.e. the spin-orbit coupling in valence bands have been obtained¹³⁻¹⁵. We mention, that photoemission from GaAs also allowed to observe clearly the action of the transport term D on the electron spin. Due to spin-dependent elastic transport properties along certain directions an orientation of the spin polarization vector along certain crystallographic directions was observed¹⁶.

We will resume this discussion in sect. 4 in the context of Magnetic X-ray Dichroism in photoemission, where we will encounter a similar level diagram at energies higher by about two orders of magnitude and for a ferromagnetic material.

3. SPIN-RESOLVED ELECTRONIC STRUCTURE OF ULTRATHIN LAYERS: fct Co ON Cu(100)

In this section we present a case study of spin-polarized photoemission applied to a ferromagnetic thin film system. The system Co/Cu(100) has been extensively studied and is one of the best known systems to date^{15,17}. Its growth has been characterized by thermal atom scattering and by medium energy electron diffraction (MEED) and Auger spectroscopy simultaneously during growth. The Cu(100) substrate had been characterized by Scanning Tunneling Microscopy. Large, atomically flat terraces of several hundred nm extension have been found, separated by coalesced step bands of 10 to 20 atomic layers. On these terraces Co grows in the Frank-v.d.Merwe mode, i.e. layer-by-layer at room temperature up to about 450K (above 500K interdiffusion sets in). The Co layer structure is tetragonally distorted face-centred-cubic (fct). The in-plane lattice constant is expanded by 2% relative to fcc Co, while the layer distances perpendicular to the surface are reduced. For a 5 monolayer thick film the average tetragonal compression is about 5%. This has been determined from comparing LEED I-V curves for clean Cu to those from Cu with Co overlayers. Magnetically these films should behave like a two-dimensional system since they are much thinner than the characteristic exchange length. In fact, the ordering temperature T_C was found to depend strongly on the film thickness and to be much smaller than in the bulk. The critical exponent β was found to be substantially smaller than in bulk Co. Therefore, it is of interest to see whether the electronic structure is essentially two-dimensional also, and from what thickness on three-dimensional dispersion may be observed. This system is also of general interest, since the spin-resolved electronic bandstructure of fcc Co was experimentally not known. The reason is that the fcc modification does not exist under ambient conditions but only above about 700K. Photoemission studies with fcc single crystals are therefore hardly possible.

A sample of the experimental photoemission spectra is shown in Fig. 3 for 5ML at three photon energies. The photon incidence is perpendicular to the surface and the electron take-off is along the surface normal. The full lines on the left hand side of Fig. 3 denote the conventional, spin-averaged, intensity spectra. There are essentially two peaks, one close to the Fermi energy, the other at about -3eV binding energy. The former is due to the emission from the Co d-bands, while the latter stems partly from the d-bands of the Cu substrate and partly also from the Co layer. The distinction between these contributions has been made by utilizing circularly polarized light and analysing the components of the spin polarization vector. The electrons from the substrate have their polarization parallel or antiparallel to the surface normal, due to the optical orientation process. They are distinguished from the electrons from the Co layer by the polarization of the latter being along the surface plane. This proves that the Co layer is magnetized in the plane and also demonstrates how the two contributions can be distinguished in an elegant way by exploiting spin-orbit effects in the Cu bandstructure.

The Co-derived peak near E_F seems to be independent of the photon energy, while the broadening at 24eV must to a good part attributed to a decreased resolution of the monochromator. Photoemission peaks near the Fermi energy which do not disperse with photon energy are often attributed to surface states. Since a surface state, being a two-dimensional state, is characterized by a wave vector $k_{||}$ parallel to the sur-

face, its energy is independent of the wave vector component k_{\perp} along the surface normal. Since this component only is changed in normal emission when changing the photon energy, a surface state emits electrons at all photon energies at the same energetic position relative to E_F . At first glance the experimental results therefore seem to indicate a two-dimensional electronic structure of the Co film, apparently in line with its two-dimensional magnetic behaviour.

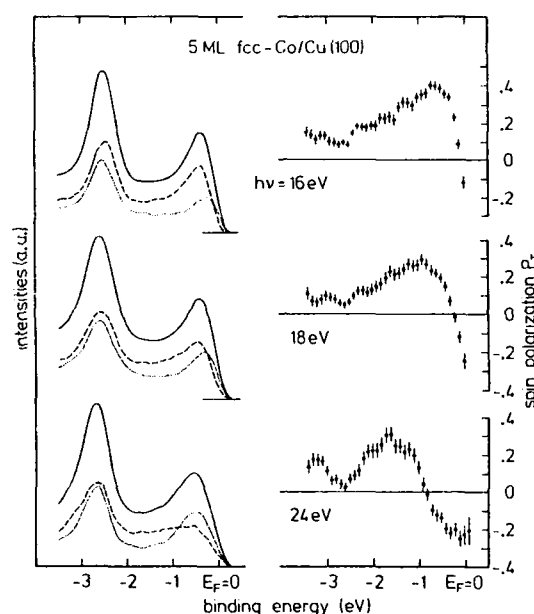


Fig.3 Total intensity spectra (full lines, left hand side) and polarization distribution curves (right hand side) from the system 5ML Co/Cu(100) as a function of binding energy with the photon energy as a parameter. The partial intensities (i.e. the total intensity decomposed into contributions from majority electrons (dashed) and minority electrons (dotted)) are shown on the left hand side. They indicate the contributions from Co (near E_F) and from Cu (around -3eV).

This picture changes drastically, however, if the spin polarization is taken into account. The right hand side of Fig. 3 shows the polarization distributions as a function of binding energy for the polarization component parallel to the surface plane. Here one sees clearly that the polarization features disperse with the photon energy. The majority peak moves to higher binding energies while a minority peak moves towards and below the Fermi energy. This result shows definitely that the spin-split electronic states disperse with k_{\perp} , i.e. that there is three-dimensional dispersion in a film with only 5 Monolayers. The intensity spectra can now be explained by decomposing them into two components, the one due to electrons of majority character (dashed), the other one due to minority electrons (dotted). This is strictly allowed only in the Co-region where there are no electrons with other spin orientations. In the Cu-region this decomposition is incorrect, but the non-equality of dashed and dotted curves shows that there are Co states also in this region (e.g. at -2.4eV for $h\nu = 16\text{eV}$). The total polarization vector is oblique in this energy range. The partial intensities in the Co region show that the apparent intensitivity of the spin-averaged intensity with respect

to the photon energy is accidental and does not indicate the presence of a surface state. The peak changes its spin character from predominantly majority-type at $h\nu = 16\text{eV}$ to predominantly minority type at $h\nu = 24\text{eV}$. This result could not have been obtained by conventional means and it demonstrates nicely the large amount of additional information contained in the spin polarization vector.

Since we know now that there is three-dimensional dispersion in a 5ML film, the question arises over what thickness range the transition from 2D to 3D states of Co occurs. We found the following: even 2ML show already some 3D dispersion; for 3ML the dispersion is already close to that for 5ML, and at 5ML it is practically indistinguishable from that of 8 or 10ML which is considered bulk material. Therefore we compare our dispersion data for 5ML to a band structure calculation¹⁸ for fcc Co at its bulk lattice constant in Fig. 4. The minority and majority bands (dotted and dashed, respectively) may change from one into the other at hybridization points due to spin-orbit coupling which is fully taken into account in this calculation. The experimental data points are given

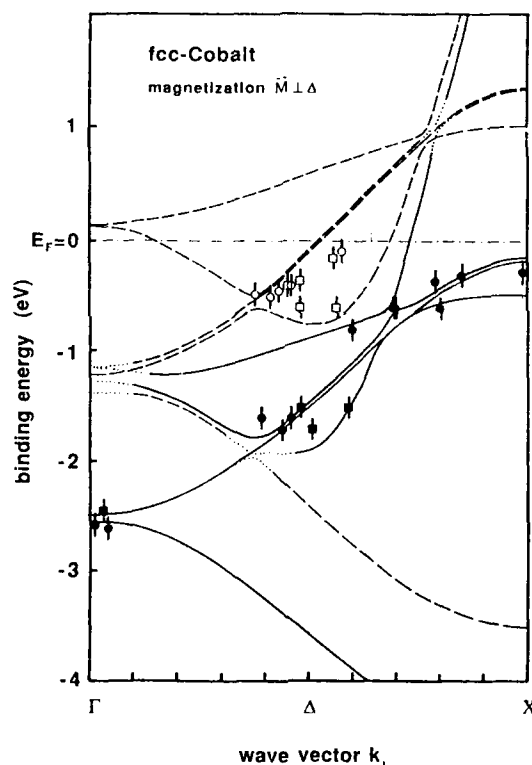


Fig.4 Comparison of experimental spin-resolved dispersion of bands from a 5ML thick film of fcc Co on Cu(100) with a fully relativistic bandstructure calculation for fcc Co.

in full (majority) or open (minority) symbols. The circles have been obtained at normal incidence of the light, the squares at oblique incidence, both at normal electron emission. This serves to distinguish different (single group) symmetries of the initial bands. The final states have been assumed to be represented by free-electron-like parabolae

fitted to the calculated empty band states. We note quite good agreement of experiment and theory with respect to the spin character, the single group symmetries, and the energy eigenvalues. The exchange splitting is somewhat smaller in the experiment, and we find a systematic deviation in the topmost minority bands just below E_F . The experimental dispersion is seen to be somewhat weaker than in theory and the crossing with the Fermi surface occurs somewhat closer to the X point. At this point we recall that the experiments have been carried out on tetragonally distorted fcc Co, while the theory assumed a strictly cubic crystal. It was checked¹⁸, that the slight expansion in the plane by 2% does not bring about such changes. We speculate that the stronger compression along [100] might move the topmost bands somewhat below E_F . This will have to be studied by band structure calculations allowing for non-cubic unit cells.

We close this section with the remark, that this direct comparison of spin-resolved experimental bands with spin-polarized fully relativistic band structure calculations is the first of its kind. We found it quite surprising that even in ultrathin films, only a few monolayers thick, a three-dimensional dispersion of the electronic states develops which is very close to that of the bulk. While this observation has also been made on a few paramagnetic systems by now, we find it remarkable that a ferromagnetic layer with an exchange-split bandstructure shows the same behaviour, in spite of its magnetic properties being largely characteristic of a 2D system.

4. MAGNETIC X-RAY DICHOISM IN PHOTOEMISSION

In the preceeding section we made use of circularly polarized light to distinguish contributions from the paramagnetic substrate, leading to polarized electron emission via spin-orbit coupling in the valence band, and a ferromagnetic overlayer with spin-split states due to exchange interaction. In this section we will discuss an effect of the combined action of exchange and spin-orbit interaction. It will be shown that spin-dependent effects may give rise to characteristic intensity changes in photoemission if the relative alignment of photon spin and electron spin in the sample is changed.

Consider the following experiment¹⁹: An Fe(110) crystal is irradiated by circularly polarized photons from the BESSY storage ring in the energy range 800 to 900eV at oblique incidence ($\sim 10^\circ$ with respect to the sample surface). The sample is in a single domain state, magnetized in the surface plane, parallel or antiparallel to the photon spin, i.e. along the direction of the light beam. Photoelectrons are collected by an analyzer with a transport lens at an angle of 55° relative to the surface normal, with an estimated collection angle of 7° . The resulting photoelectron spectrum averaged over the magnetization directions is shown in Fig. 5a, upper curve. It shows the well-known spin-orbit split $2p_{1/2}$ and $2p_{3/2}$ lines of Fe. The new observation is that the intensity depends on whether photon spin and electron spin are parallel or antiparallel. The resulting asymmetry function is shown in Fig. 5b, showing a large plus/minus feature and a smaller minus/plus structure. Translating this back into the partial intensities according to the two electron spin orientations yields the insert curves in Fig. 5a. These show clearly that each line is split into two lines with a separation of $0.3\text{eV} \pm 0.2\text{eV}$ and $0.5\text{eV} \pm 0.2\text{eV}$ for $2p_{1/2}$ and $2p_{3/2}$, respectively. It was confirmed that the sign of the asymmetry function reverses, if the photon helicity is reversed, which also proves that the effect is not due to magnetic stray fields related to the sample magnetization reversal. This effect is not to be confused with dichroism in X-ray absorption²⁰,

which is interpreted as being due to the spin-dependence of the empty density of states above the Fermi level. In our case the photon energy is about 100eV higher than the electron binding energy. The excited photoelectrons can therefore safely be assumed to be in free-electron like final states. The spin-dependent excitation probability must be due to exchange splitting of the core level states, since it evidently depends on the orientation of the majority-type d-electrons in the filled part of the valence band. For better understanding we refer to the level diagram of Fig. 3, there used for explaining the origin of polarized electrons from GaAs. Since we now consider atomic levels the notations $p_{1/2}$, $p_{3/2}$ are valid. The same physical processes as there now occur at photon energies of roughly 800eV and a spin-orbit splitting of ~13eV. If we shine in positive helicity photons (σ^+) we will excite selectively up spin electrons from the $p_{1/2}$ level and predominantly down spin electrons (50% polarization) from the $p_{3/2}$ level. As stated above, the intensities are exactly the same for the opposite light helicity, i.e. no asymmetry will be found. If the valence band of the material contains aligned electron spins, such as in ferromagnetic iron, the core levels may also become split in energy by exchange interaction with the d-electrons. Since we experimentally observe the excited state of the atom only, one may assume that the photohole couples to the valence band. However, be-

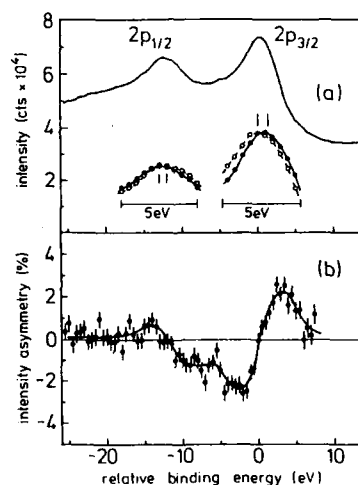


Fig.5 The Effect of Magnetic X-ray Dichroism in Photoemission

- a) top curve: photoemission intensity distribution in the vicinity of the spin-orbit split 2p core levels of Fe, averaged over the two magnetization states of the sample, parallel or antiparallel to the circularly polarized photon beam. The insert shows on an enlarged scale with zero suppression the partial intensities for the two magnetization states separately. Note the splitting of the peaks, indicating the exchange splitting of the core levels.
- b) Asymmetry function of the difference of the partial intensities divided by their sum. Note the opposite behaviour of plus/minus features for $2p_{1/2}$ and $2p_{3/2}$.

cause of the existence of hyperfine fields which are due to an inhomogeneous spin density of the core electrons, one may assume an exchange splitting in the ground state already. This case has been treated by Ebert²¹ recently, who calculated hyperfine fields and core level splittings in Fe. This modifies the level diagram of Fig. 3 in the following way: the degeneracy of the m_j sublevels of the $p_{1/2}$ level is lifted: $m_j = -1/2$ is shifted up (minority state) while $m_j = +1/2$ is shifted down. The degeneracy of the four $p_{3/2}$ sublevels is also lifted - each sublevel now has its own energy. Only the $m_j = -3/2$ and the $m_j = +3/2$ states are pure spin states, while the two $|m_j| = 1/2$ states are of mixed spin character (≈ 0). If we now apply positive helicity photons and align them with the majority spins of the sample, we again excite selectively 'up' (= majority) - electrons from $p_{1/2}$, but since their binding energy is now somewhat greater, they appear at a smaller kinetic energy. Likewise, we excite preferentially 'down' (= minority) - electrons from the $p_{3/2}$ level which appear at a somewhat higher kinetic energy. Conversely, when using negative helicity light (or equivalently, if we reverse the sample magnetization) electrons from the other corresponding exchange-split levels will be excited. Therefore, when forming the asymmetry function now, it will not be zero but rather show qualitatively what we observe experimentally. From our arguments on the degree of spin polarization in the $p_{1/2}$ level being higher than in the $p_{3/2}$ level we should expect a larger asymmetry on the $2p_{1/2}$ line. One has to take into account that this line is of weaker intensity and, in addition, rides on a larger background than the $2p_{3/2}$ line. These two effects reverse the relative magnitudes of the two asymmetry features.

We note that for the first time the existence of an exchange splitting and its magnitude in the 2p core levels of iron has been demonstrated. It will be interesting to extend these observations to the 3s and 3p levels, to see whether the magnitude of the exchange splitting, and with it that of the coupling to the valence band changes. Also, it remains to be studied, whether the excited state or the ground state is predominantly observed. This will also contribute to a better understanding of dichroitic effects in photon absorption.

We wish to emphasize that this effect of magnetic dichroism, i.e. emission intensities which depend on the magnetization orientation of the sample, is due to the combined action of spin-orbit and exchange interaction. Each of them separately leads to emission of polarized electrons, but only their combination leads to intensity asymmetries. From the experimental point of view this is of great advantage, since the technique promises to make an explicit spin analysis obsolete in many cases. This would represent a gain of about two orders of magnitude in count rate, since one gains three orders by not using a spin analyzer, but loses roughly one order of magnitude by going off-plane of the storage ring. This loss could even be compensated by multichannel detection at the electron spectrometer exit. Thus, one may envisage magnetic analyses to be carried out with about the same ease as in present day standard XPS work.

The technique is element specific and provides information about the local magnetic order. For example one may in a ferrimagnet analyse two magnetic sublattices separately. The technique is also surface sensitive, which makes it ideally suited for studies of magnetism at surfaces, interfaces and in thin films. For example one may study induced magnetic moments in nonmagnetic materials in intimate contact with a ferromagnet. One may even envisage to study the sublattice magnetizations in binary antiferromagnets. What is needed is to produce a one-domain region of the size of the illuminating photon beam aligned with respect to the photon spin. This can e.g. be accomplished by heating the sample above the Néel temperature and cool it in a magnetic field. It seems that the full potential of Magnetic Dichroism in Photoemission has yet to be explored.

Acknowledgements

The author gratefully acknowledges the organizers invitation to serve as a lecturer at the NATO Advanced Study Institute.

References

- /1/ E.W. Plummer and W. Eberhardt, "Adv. Chem. Phys.", Vol. 49
ed. I. Prigogine and S.A. Rice (Wiley, New York, 1982) p. 533
F.J. Himpsel, Adv. Phys. 32:1 (1983)
R. Courths and S. Hüfner, Phys. Reports 112:53 (1984)
N.V. Smith, Reports Progress Phys. 51:1227 (1988)
- /2/ G. Busch, M. Campagna, P. Cotti, and H. Siegmann, Phys. Rev. Lett.
22:597 (1969)
K. Sattler and H.C. Siegmann, Phys. Rev. Lett. 29:1565 (1972)
- /3/ D.T. Pierce and F. Meier, Phys. Rev. B 13:5484 (1976)
see also chap. 10 in ref. 5 below
- /4/ J. Kirschner, R. Feder, and J.F. Wendelken, Phys. Rev. Lett.
47:614 (1981)
- /5/ R. Feder (ed.) "Polarized electrons in surface physics" (World
Scientific, Singapore, 1985) chap. 12 by E. Kisker
- /6/ C.M. Schneider, Thesis, Freie Universität Berlin, 1990
(unpublished)
- /7/ U. Heinzmann and G. Schönhense, chap. 11 in ref. 5
- /8/ M.S. Hammond, G. Fahsold and J. Kirschner, this book
- /9/ J. Kirschner, chap. 8 in ref. 5
- /10/ E. Tamura, W. Piepke, and R. Feder, Phys. Rev. Lett. 59:934 (1987)
- /11/ B. Schmiedeskamp, B. Vogt, and U. Heinzmann, Phys. Rev. Lett.
60:651 (1988)
- /12/ F. Meier and B. Zakharchenya (eds.) "Optical Orientation" (North
Holland, 1984)
- /13/ D. Venus, J. Garbe, S. Suga, C.M. Schneider, and J. Kirschner,
Phys. Rev. B 34:8435 (1986)
- /14/ J. Garbe and J. Kirschner, Phys. Rev. B 39:6115 (1989) and
B 39:1530 (1989)
- /15/ C.M. Schneider, J.J. deMiguel, P. Bressler, P. Schuster, R.
Miranda, and J. Kirschner, J. Electron Spectr. Rel. Phen. 51:263
(1990)
- /16/ S.F. Alvarado, H. Riechert, and N.E. Christensen, Phys. Rev. Lett.
55:2716 (1985)
- /17/ C.M. Schneider, J.J. deMiguel, P. Schuster, R. Miranda,
B. Heinrich, and J. Kirschner, this book
- /18/ C.M. Schneider, P. Schuster, M. Hammond, H. Ebert, J. Noffke, and
J. Kirschner (submitted to Phys. Rev.)
- /19/ L. Baumgarten, C.M. Schneider, H. Petersen, F. Schäfers, and
J. Kirschner (submitted to Phys. Rev. Lett.)
- /20/ G. Schütz, W. Wagner, W. Wilhelm, P. Kienle, R. Zeller, R. Frahm,
and G. Materlik, Phys. Rev. Lett. 58:737 (1987)
- /21/ H. Ebert, J. Phys. Condens. Matter 1:9111 (1989)

CORRELATION OF CRYSTALLINE AND ELECTRONIC STRUCTURE IN EPITAXIAL
FCC-COBALT MONOLAYERS ON Cu(100)

C.M. Schneider¹, J.J. de Miguel², P. Schuster¹, R. Miranda²,
B. Heinrich³ and J. Kirschner¹

¹Institut für Experimentalphysik, Freie Universität Berlin
D-1000 Berlin 33, West Germany

²Dept. de Física de la Materia Condensada, Universidad
Autónoma de Madrid, E-28049 Madrid, Spain

³Surface Physics Laboratory, Simon Fraser University
Burnaby, British Columbia, Canada

Initiated by the need for improved magnetic recording media, recently the ferromagnetism of low-dimensional systems has received wide interest. A layered system may be realized by epitaxially growing films of a ferromagnetic material on top of a suitable non-magnetic substrate. The magnetism of these systems, however, is strongly determined by the electronic structure of the films which in turn depends on their crystalline structure. The knowledge of this correlation is of major importance in the understanding of the magnetic properties of ultrathin films (being a necessary basis for successful technological application). The task to characterize the crystalline and electronic structure may be accomplished by a combination of in situ LEED and angle-resolved photoemission (ARUPS) experiments. Ambiguities in the classification of majority and minority spin states in a ferromagnet (being immanent to the conventional spin-integrated ARUPS method) can only be avoided by including a spin-polarization analysis of the photoelectrons. The present contribution outlines exemplarily the interplay of crystalline and electronic structure in the model system fcc-Cobalt on Cu(100) by means of the approach sketched above.

RESULTS AND CONCLUSIONS

The structure of cobalt single crystals under ambient conditions is hcp. A fcc phase occurs only at temperatures in excess of 750 K. Therefore, despite the structural studies having been performed almost no results about the electronic states of the fcc modification are available up to now. Gonzalez et al¹ have shown, however, that fcc-Co thin films may be stabilized on top of a Cu(100) lattice. This provides a way to investigate the properties of the fcc phase at or even below room temperature. Our cobalt films have been epitaxially grown on top of atomically flat and well-ordered Cu(100) surfaces (see ref. 2 for details of sample preparation). To ensure a reliable calibration of the film thickness and a thorough characterization of the growth process, each overlayer has been prepared under

control of medium energy electron diffraction (MEED)². The sample cleanliness has been checked by Auger Electron Spectroscopy (AES). A simultaneous MEED/AES approach² confirmed the growth to proceed in a layer-by-layer fashion as already reported earlier¹.

The intensity vs. kinetic energy ($I(E)$) curves have been obtained by means of rear-view LEED optics, the diffraction pattern being imaged with a TV camera system. An image processing unit is employed to record the intensity within defined screen areas covering the various diffraction spots ("windows"). The position of each window is continuously readjusted to trace the individual diffraction spots during a scan of the primary electron energy E . After the in situ LEED investigations the sample may be placed in front of the electron spectrometer to analyze its electronic structure. The spin- and angle-resolved photoemission experiments referred to below have been performed in normal emission and normal incidence geometry using circularly polarized synchrotron radiation at the storage ring BESSY. The experimental set-up and the photoelectron spectrometer have been described in considerable detail elsewhere³. Subsequent to the energy analysis the photoelectrons are analyzed with respect to their spin-polarization vector by means of a LEED spin detector⁴.

Fcc-Co films as prepared above are found to be ferromagnetic with an in-plane remanent magnetization. A surprising feature of this system is the striking thickness dependence of the Curie temperature, causing films of less than 2ML to be paramagnetic at room temperature². Earlier investigations revealed a three-dimensional initial state band dispersion already in films as thin as 5ML³. The spin-resolved electronic structure of these films agrees well with recent calculations for bulk fcc cobalt⁵.

RESULTS AND CONCLUSIONS

The LEED patterns obtained from the Co overlayers (up to 10ML thickness) appear essentially identical to those from the clean Cu(100) surface with respect to the geometrical arrangement of the diffraction spots. In particular, no indication of any superstructure (e.g. a $c(2 \times 2)$ reported on earlier¹) could be found in the absence of carbon contamination. This indicates that Co adapts the lateral lattice parameter of the Cu substrate ($a=3.61\text{\AA}$), a situation which causes a slight biaxial expansion compared to the equilibrium lattice constant of bulk fcc-Co ($a=3.55\text{\AA}$). To account for this lateral expansion one would expect the Co lattice to be vertically compressed (assuming a constant volume of the unit cell). This effect may be indeed concluded from Fig. 1, comparing the $I(E)$ curves of the (00) specular beam for clean copper (the sample has been rotated off the normal incidence condition by $\sim 2^\circ$ in order to reflect the (00) beam on the fluorescent screen). Obviously the prominent diffraction peaks shift to higher kinetic energies with increased cobalt coverage. Measurements of the (10) and (11) beams show a behaviour essentially alike. This shift is predominantly caused by a change of the vertical lattice constant and can be translated into an average contraction of about 5%. A similar value may be extracted from a recent LEED study on thicker films ($\sim 8\text{ML}$)⁶. These experimental results suggest the unit cell of the fcc-Co films to be tetragonally compressed.

One may raise the question whether the tetragonal distortion will influence the electronic structure to be observed in the photoemission experiment. Some deviations of the above mentioned band mapping results⁶ from the band structure calculations for fcc-Co (i.e. the energetic position of

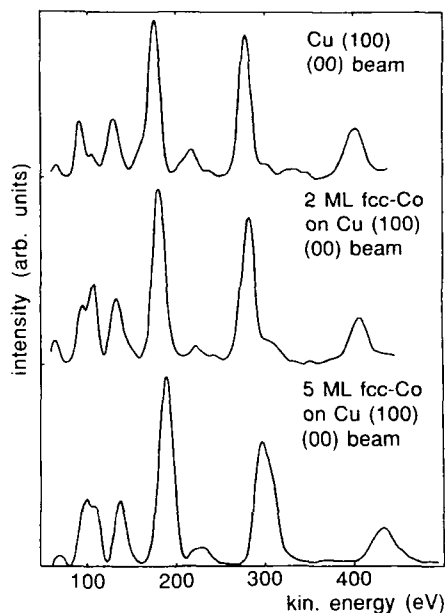


Fig.1. Intensity vs. kinetic energy curves of the LEED (00) specular beam obtained for clean Cu(100) and two fcc-Co films of different thicknesses (2 and 5 monolayers, respectively).

the Δ_5 band) might indeed be interpreted that way. To clarify this point, we recorded thickness dependent spin-resolved normal emission spectra at fixed photon energy, the coverage varying between 2 and 8 ML. The results obtained for the two extreme coverages are shown in Fig. 2. The experimental geometry (normally incident light) selects only band symmetries of the types Δ_5 . The maximum spin-polarization at about -0.5eV binding energy is attributed to transitions from the Δ_5 band, whereas the small minority contribution at the Fermi level originates from an initial state of Δ_5 symmetry. The direct comparison of the spectra reveals a distinct shift of the minority contribution towards higher binding energies in the 2 ML film, with the majority feature remaining essentially unaffected. This behaviour is found to be compatible with a recent model calculation for simple tetragonal iron⁷. There, upon expanding the c-axis along Δ a d-like band moves upwards across the Fermi level. Conversely, if we assume a similar behaviour for a fct-lattice, we would expect the d-band (in this case the Δ_5 band) to move downwards upon compression. A very similar mechanism has been predicted in photocurrent calculations for fct-copper just recently⁸.

The above results from LEED and spin-polarized ARUPS clearly indicate the impact of the crystalline structure on the electronic states in these ultrathin films. This correlation may have important consequences for the magnetism, in particular magnetic anisotropies. It should be recalled that anisotropies depend very sensitively on details of the electronic structure. Small shifts in the energetic position of the spin-split bands in the vicinity of the Fermi level could thus lead to strong changes in the aniso-

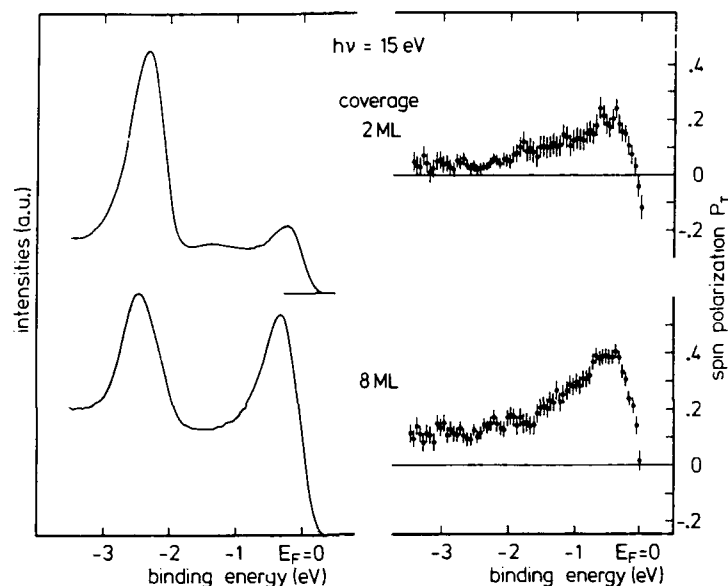


Fig.2. Spin- and angle-resolved photoemission from fcc-Co films on Cu(100) at $h\nu=15\text{ eV}$ photon energy. Energy distribution curve (left column) and corresponding spin-polarization along the remanent sample magnetization (right column). Positive (negative) values of the spin-polarization correspond to majority (minority) spin states.

tropy. This effect might explain findings like the flip in the easy axis of magnetization as a function of coverage in Fe/Ag(100)⁹. The characterization of the correlations between crystalline and electronic structure certainly represents a step towards a deeper understanding of the mechanisms which determine the magnetic behaviour observed in ultrathin layered systems.

REFERENCES

1. L. Gonzalez, R. Miranda, M. Salmeron, J.A. Verges and F. Yndurain, *Phys. Rev. B* 24: 3245 (1981)
2. C.M. Schneider, P. Bressler, P. Schuster, J. Kirschner, J.J. de Miguel and R. Miranda, *Phys. Rev. Lett.* 64: 1059 (1990)
3. C.M. Schneider, J.J. de Miguel, P. Bressler, P. Schuster, R. Miranda and J. Kirschner, *J. Electron Spectr. Rel. Phen.* 51: 263 (1990)
4. J. Kirschner, in: *Polarized Electrons in Surface Physics*, R. Feder, ed., World Scientific, Singapore (1985)
5. C.M. Schneider, P. Schuster, M. Hammond, H. Ebert, J. Noffke and J. Kirschner, to be published
6. A. Clarke, G. Jennings, R.F. Willis, P.J. Rous and J.B. Pendry, *Surface Sci.* 187: 327 (1987)
7. P. Strange, J.B. Staunton and H. Ebert, *Europhys. Lett.* 9: 169 (1989)
8. F. Maca and M. Scheffler, Spring Meeting of the Deutsche Physikalische Gesellschaft, Regensburg (1990) and private communication
9. J. Araya-Pochet, C.A. Ballentine and J.L. Erskine, *Phys. Rev. B* 38: 7846 (1988)

Hybrid Ferromagnetic/Semiconductor Structures§

Gary A. Prinz

Naval Research Laboratory
Washington, DC

Abstract

Ultrahigh vacuum growth techniques are now being employed to grow single crystal films of magnetic materials. This growth, carried out in the same molecular beam epitaxy systems commonly used for the growth of semiconductor films, has yielded a variety of new materials and structures which may prove useful for integrated electronics and integrated optical device applications. Examples are given for growth on GaAs and ZnSe, including magnetic sandwiches and patterned structures.

The past three decades have witnessed the rapid advance of solid state electronics, first in replacing discrete elements and finally in integrating many circuit elements onto one semiconductor chip. Schottky barrier diodes replaced rectifier tubes, and various manifestations of the three-terminal transistor replaced the vacuum triode used for signal modulation or amplification. Resistive and capacitive circuit elements were also readily transferred to the new integrated circuit technology. The only fundamental discrete circuit elements which have been left behind in this revolution are elements involving magnetic materials. In fact, in all of the dramatic advances made in electronic materials processing over the past decade, very little work has been devoted to magnetic materials in order to incorporate them into planar integrated electronic (or photonic) circuitry. This is unfortunate, because there are several tasks for which magnetic materials are irreplaceable and these remain unaddressed in modern integrated electronics. In addition, there are potential applications which have no analog in vacuum electronics, but which remain unrealized awaiting the development of appropriate materials and processing procedures. In this article it will be shown that ferromagnetic metals can now be prepared in thin-film

form compatible with semiconductor device fabrication and that their properties can be exploited for various applications.

Growth of Epitaxial Films

The ferromagnetic metal/semiconductor system which has been the most thoroughly studied is iron/gallium arsenide, although iron/zinc selenide now also has a large body of data. Both compound semiconductors have the zincblende structure, which is composed of two nested face-centered-cubic structures, one for each of the constituents. The (unreconstructed) (001) face of the zincblende structure is illustrated in Figure 1a as viewed in the [001] direction. The projection of the unit cell face is illustrated by the dashed line, with the cubic lattice constant, a_0 , given for both compounds. The sizes of the atoms reflect their ionic radii given on the drawing. Also indicated are the high symmetry axes in the plane. The reason that these zincblende surfaces support the epitaxial growth of single crystal iron films is that the unit cell is almost exactly twice that of body centered cubic α -Fe, the low temperature ferromagnetic phase, as shown in Figure 1b. In fact, if one pictures an As or Se terminated (001) surface, the Fe atoms will occupy the vacant cation sites as well as sites of similar symmetry half-way between any two anion sites along a $\langle 100 \rangle$ direction in the (001) plane. A pseudomorphic epilayer of Fe arranged like this is under 1.3% compression on GaAs and 1.0% compression on ZnSe. Because of the factor of two relationship between the two unit cells, oriented parallel epitaxy is obtained, as follows,

$$(001)_{\text{Fe}} \parallel (001)_{\text{zb}} : [100]_{\text{Fe}} \parallel [100]_{\text{zb}} \quad (1)$$

$$(110)_{\text{Fe}} \parallel (110)_{\text{zb}} : [001]_{\text{Fe}} \parallel [001]_{\text{zb}}$$

and so on, for all faces in spite of the fact that the substrate is fcc and the overlayer is bcc. The strain is ultimately relieved by misfit dislocations, however these are not necessarily generated in the overlayer. bcc-Fe is such a stiff structure and so tightly bonded to GaAs, it has been observed in cross-sectional TEM photographs that dislocations are actually generated at the interface and penetrate into the GaAs substrate (1). The tight bonding is readily observed if one cleaves a GaAs substrate covered with a thick ($\approx 1 \mu\text{m}$) Fe film. The film maintains its integrity and any attempt to tear it apart at the cleave results in its being peeled off the substrate, tearing small crystallites of GaAs out of the substrate in the process. This bonding is understood from photoemission studies which show the formation of FeAs at the interface, which has a greater heat of formation than GaAs itself. In fact, on the (110) surface of GaAs, which is stoichiometrically balanced, an Fe overlayer actually displaces the surface Ga layers to form FeAs, leaving free Ga metal (2). It is interesting to compare the growth of Fe on the III-V GaAs with that on II-VI ZnSe. Although both substrates

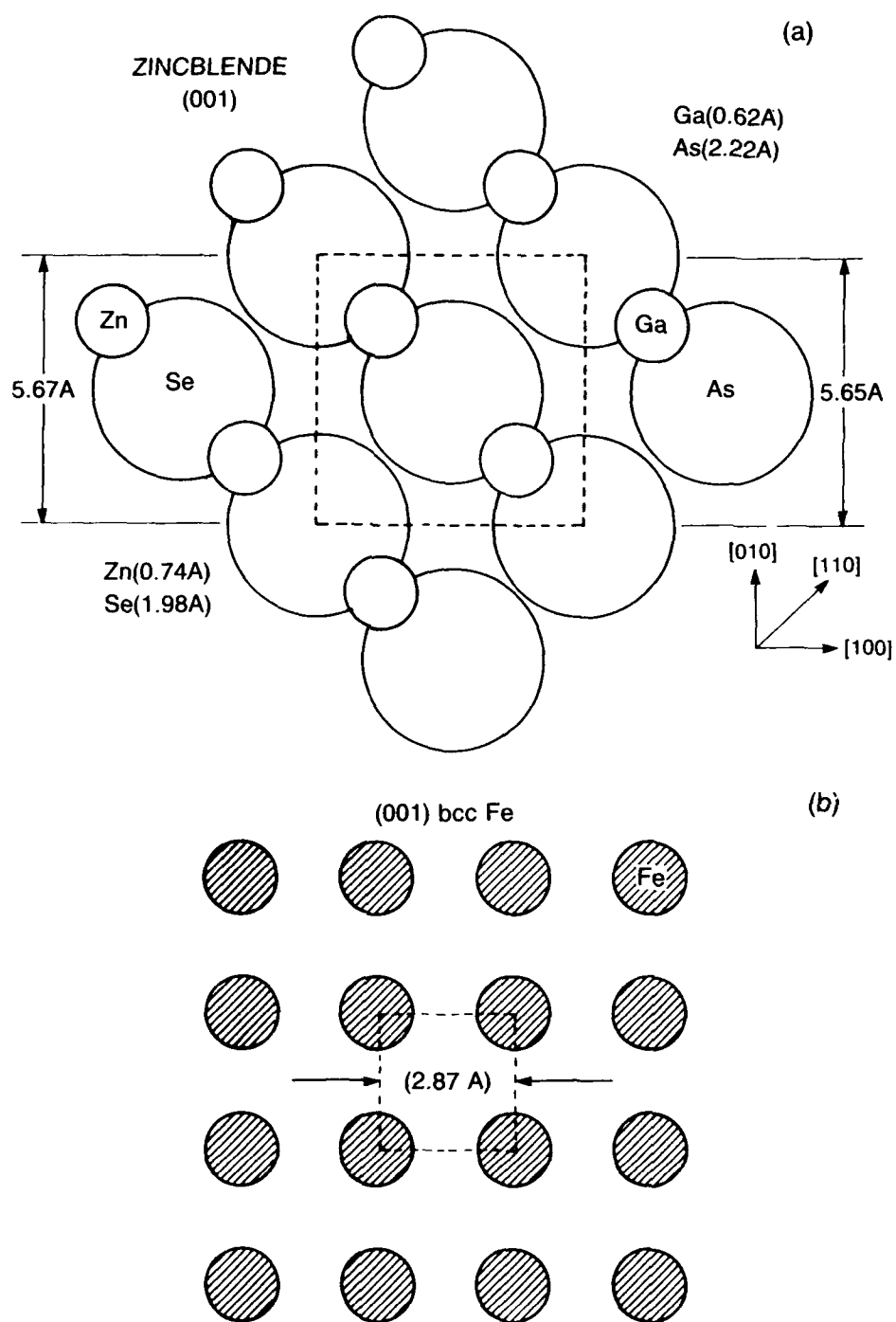


Fig. 1. (a) Unreconstructed (001) surface of zincblende structure terminated in cation layer. (b) Unreconstructed (001) surface of bcc α -Fe.

have zincblende structures and are closely latticed matched to α -Fe, II-VI compounds are much more ionic and less reactive with Fe. Consequently, photoemission studies show no evidence of Zn-Fe interchange at the interface. Recent Auger diffraction studies also show that while Fe exhibits island-like three dimensional growth at 175°C for low coverages on GaAs, the initial growth on ZnSe at this temperature proceeds as layer-by-layer two-dimensional growth (3). This growth temperature was found to be optimum for Fe/GaAs in terms of the narrowest electron diffraction linewidth. It also correlated well with the optimum magnetic properties such as narrow ferromagnetic resonance linewidth (see discussion below). At lower growth temperatures there is insufficient energy to anneal the metal surface during growth resulting in increased step density. Higher temperatures encourage interdiffusion at the Fe/GaAs interface. There is evidence of As leaving the interfacial region and penetrating into the Fe lattice 10 Å to 20 Å from the Fe/GaAs boundary (1), while there is no such evidence for Se near the Fe/ZnSe boundary (2). These details of the structure, composition and chemistry near the interface significantly affect the magnetic properties of films several hundred angstroms thick. For certain high frequency resonance modes they also dramatically alter the electromagnetic boundary conditions at the interface and change the coercive fields (the applied magnetic field necessary to reverse the magnetization). These issues affect various applications of the ferromagnetic films as discussed below.

Magnetostatic Fields

It is well known that magnetic fields applied to semiconducting materials can produce significant changes in the electrical and optical properties. Indeed this is one of the most powerful techniques to probe the electronic structure of semiconductors. These properties change either because the field shifts the energy of electronic levels or acts directly on the carriers in the material. However, even though magnetic fields are widely used for studying semiconductors, they are seldom employed in applications because of the difficulty of generating large magnetic fields in device configurations. For example, consider the field one can generate by simply providing a current carrying conductor lithographically overlaid in close proximity to some device element. A simple calculation shows that a one dimensional conductor carrying 1 milliampere will generate approximately 2 Oe at a point 1 μ m away from the conductor axis. This field is too small to be useful, and the significantly higher power levels for larger current would be prohibitive.

However, consider the situation illustrated in Fig. 2. Here we have a ferromagnetic film in which a small gap has been cut. If the magnetization in the film is uniform as indicated, the magnetic poles at the interface will give rise to a magneto-static field $H = \alpha(4\pi M)$ where $\alpha \leq 1$. Two locations are considered: A in the gap; B in the fringing field

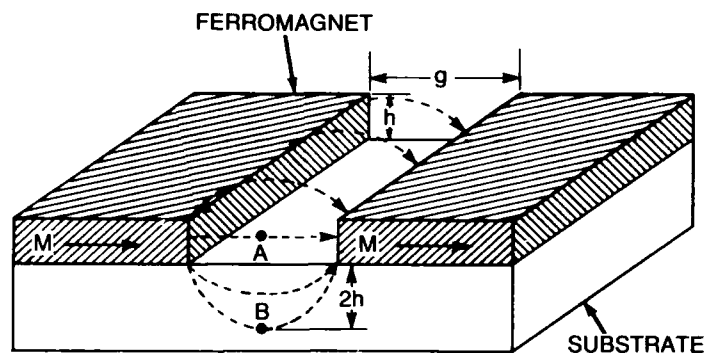


Fig. 2. Magnetic flux generated at gap in ferromagnetic film.

region. If we assume the gap width equals the film thickness ($g=h$), then at A, $\alpha \approx 0.1$. At B (a distance $2h$ below the film's bottom surface) $\alpha \approx 0.02$. For Fe, $4\pi M = 21,500$ Oe, which gives $H \approx 2$ kOe at A and $H \approx 400$ Oe at B. These are now fields which may be useful for some purposes and they are obtained without any dissipative power input into the system. Furthermore, they are fields which are easily manipulated. Fig. 3 shows a hysteresis loop (M vs H) for an epitaxial Fe film grown on ZnSe. As one can see, the coercive field (H_c) is less than 4 Oe. Fields this size are readily obtainable from a current carrying overlay line, so one is in a position to rotate or reverse a field of, say, 2kOe from a $1 \mu\text{m}$ thick film, in a $1 \mu\text{m}$ gap by the application of 4 Oe.

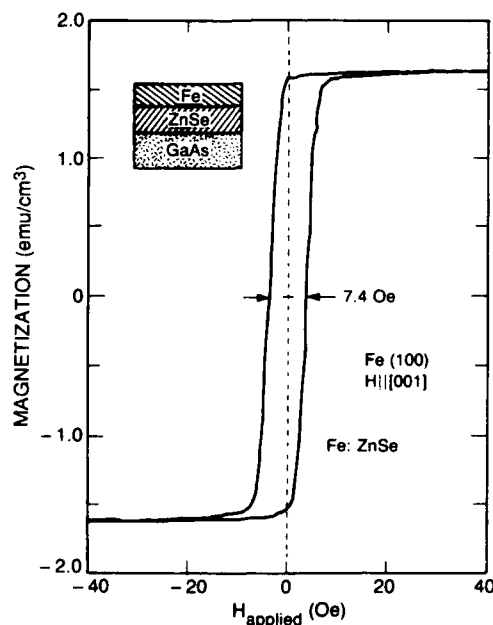


Fig. 3. M vs. H hysteresis curve for 200 Å Fe film on ZnSe (100)(8)

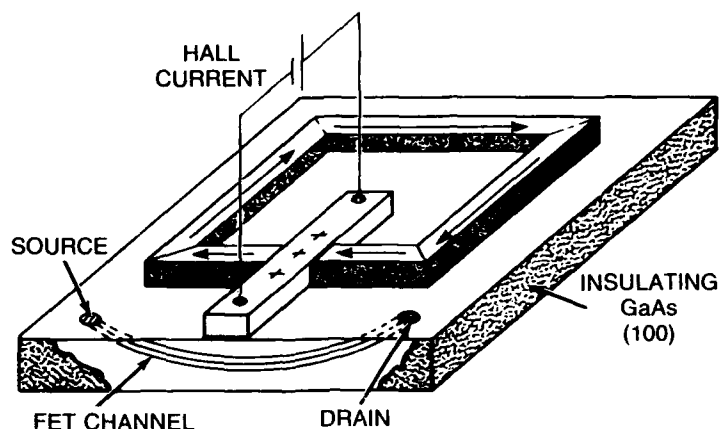


Fig. 4. Thin-film magnetic picture-frame memory element with integrated read-out.

It is this multiplication of 10^2 to 10^3 which encourages one to consider device structures which include magnetic fields to affect performance.

An example of such a proposed device is shown in Fig. 4. It is a magnetic memory element which is a thin-film analog of a ferrite core. The element is formed by first depositing an epitaxial magnetic film on a semiconductor substrate, such as Fe on GaAs. Most of the film is lithographically removed except for the square "picture frame" structure shown, which is oriented to have its legs parallel to the $[100]$ axes. These are the magnetically "easy" axes. This structure has only two stable magnetic orientations: It may be magnetized either clockwise (as shown) or counter-clockwise. These two states represent either a '0' or '1' bit, respectively. In order to read which bit is set, a small gap is opened in the magnetic circuit as shown and a material is deposited within the gap which exhibits a large Hall effect. By maintaining a current through the Hall bar, a voltage is generated between its upper and lower surface, whose polarity reveals the magnetic state of the magnetic circuit. Finally, if the GaAs substrate was prepared, before the deposition of the magnetic and Hall elements, with a source, drain, and channel which lie beneath the Hall bar, then the charge generated on the lower face of the Hall bar can be utilized to bias the FET channel beneath it. Thus in a single compact unit, one has a non-volatile memory element with semiconductor readout. Since the magnetic properties are independent of size down to elements of $\approx 10^2 \text{ \AA}$ in dimension, the limits of scaling are set by the semiconductor components. Furthermore, since one feature of the picture frame design is that it generates no external magnetic fringing fields, elements can be packed very densely without fear of cross-talk between them. Of course, to complete the device, one must provide overlayer current lines which can carry current pulses of appropriate polarity to reverse the stored bit, but these have not been shown on the figure.

A second device configuration which exploits magneto-static fields is illustrated in Fig. 5. This is also a closed magnetic circuit concept, however it achieves this, not through lithography, but by forming a sandwich structure. This structure may actually possess four stable magnetic states if it is properly constructed. Two of them are shown in

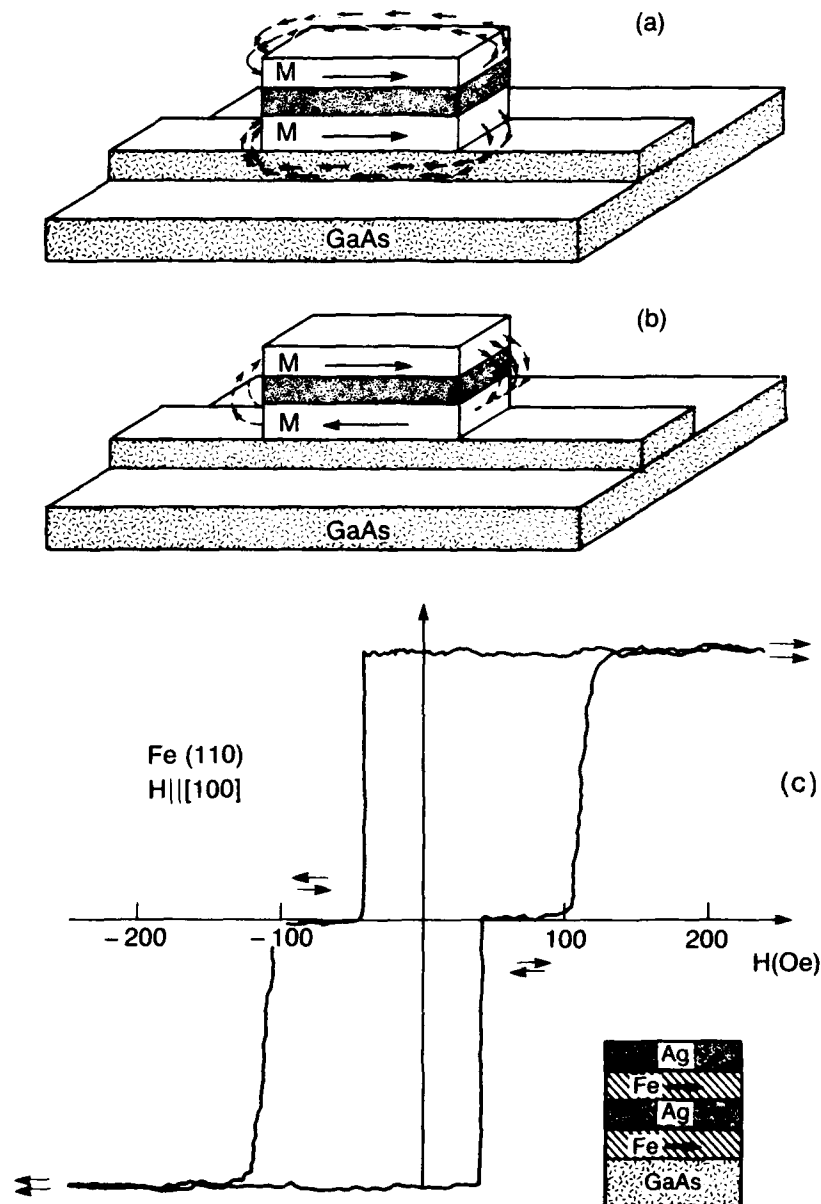


Fig. 5. Magnetic sandwich structure in (a) aligned configuration, and (b) anti-aligned configuration. (c) M vs. H hysteresis curve for magnetic sandwich structure.(4)

Fig. 5a and 5b. In the former, the two layers are aligned so that the structure possesses a net magnetic moment while in the latter they are antialigned, forming a closed circuit with no external moment. The other two states are obtained simply by reversing all of the moments in both figures. This structure has actually been fabricated and the hysteresis loop is shown in Fig. 5c (4). Note that there are four stable states in zero applied field, not simply the two saturated states shown. The $M=0$ states are also stable. If one reaches an $M=0$ condition on the loop and then reduces $H \rightarrow 0$, the system will remain at $M=0$ in a remnant state. One might expect from just considering the energy arising from the magneto-static poles at the edges of the films, that only the two $M=0$ states would be stable. In the absence of magnetic anisotropy that would be true. However the two films possess different anisotropies because they do not have identical interfaces. One Fe film is grown on GaAs, the other is grown on Ag. This can give rise to different strain or structural anisotropies, which in turn can cause the films to have different coercive fields H_c . The observed behavior in the hysteresis loop simply arises from the fact that the films reverse at different applied fields and this effect overwhelms the magneto-static energy contribution. The value of these coercive fields at which switching occurs may be altered by changing the film thickness and growth conditions. In the absence of anisotropy, the only remaining energy would be the magneto-static contribution (assuming that there is no coupling through the intervening Ag film). In that case, there would be only two stable states, as with the picture frame, with $M=0$. Such a structure is in fact utilized in a thin film magnetic memory element recently reported (5). The bits are set by current pulses, but the readout is via the magneto-resistance of the films themselves. The magnetic material in this memory device is permalloy and the power requirements are sufficiently low to permit packing densities of 10^8 elements/cm² driven by standard CMOS (complementary metal oxide semiconductor) circuitry. Finally, it should be pointed out that while ferromagnetic coupling through the intervening layer could prevent the $M=0$ state from being formed, an antiferromagnetic coupling would stabilize it. This has also been recently observed for a very thin Cr layer replacing the Ag intervening layer (6).

Coupling to Radiation Field

One of the most useful properties of magnetic materials is the fact that they can couple to a radiation field. In the microwave region of the spectrum this coupling occurs when the magnetization vector \vec{M}_0 is driven by the h component of the radiation. In the most common case with a thin film, the magnetization \vec{M}_0 lies in the plane of the film. Plane-polarized radiation propagating normal to the plane of the film as illustrated in Figure 6a, exerts a torque on the magnetization vector when $h \perp \vec{M}_0$ which causes it to exhibit gyroscopic rotation. This system is driven into resonance when

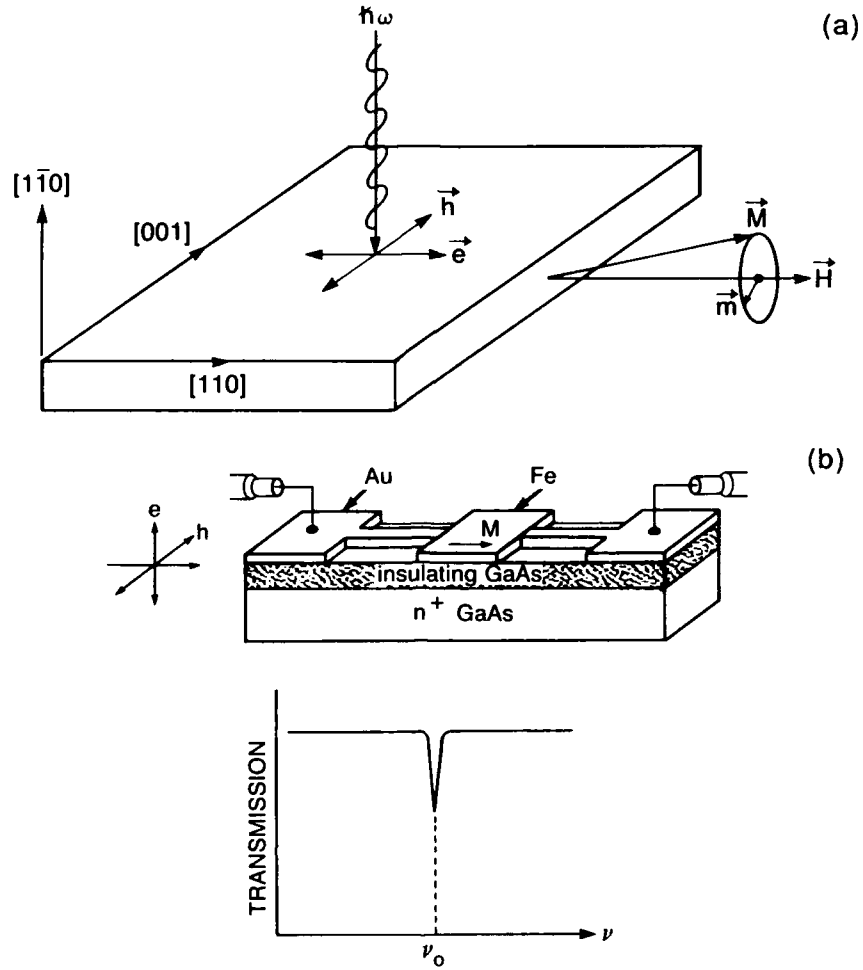


Fig. 6. (a) Illustrating plane-polarized radiation of energy $\hbar\omega$ at normal incidence to film magnetized in the plane. (b) Stripline microwave "notch filter", where ν_0 is defined by Eq. (2).

$$2\pi\nu_0 = \gamma \sqrt{H_{\text{eff}}(H_{\text{eff}} + 4\pi M_0)} \quad (2)$$

where ν_0 is the frequency of the radiation, γ is the gyromagnetic ratio, and H_{eff} is the externally applied magnetic field plus any internal anisotropy field.

For Fe films, where $4\pi M_0 = 21,500$ Oe, this resonance occurs near 10 GHz when $H_{\text{app}} = 0$. Here $H_{\text{eff}} = H_{\text{an}} + H_{\text{app}}$ and $H_{\text{an}} = 500$ Oe. This is a very useful frequency regime for many microwave devices. An example is shown in Fig. 6b, which is a schematic drawing of a microwave stripline device concept. Striplines are an effective way to carry microwave signals in planar circuits. They are guided wave devices into which, in this illustration, a microwave signal is injected on

the left from a coaxial cable. The n^+ -GaAs layer acts as a ground plane and the structure sustains an electric field between the ground plane and the conducting strip located above the insulating layer of GaAs. The radiation field is thus plane polarized with its electric vector \vec{e} vertical and corresponding \vec{h} vector horizontal and it propagates down the device structure from left to right, emerging on the other end where it is again picked up by another coaxial cable. If a ferromagnetic metal section replaces the conducting strip, as shown, then in that region the radiation field can transfer energy into the ferromagnetic metal if the magnetization vector \vec{M} is parallel to the direction of propagation. In this orientation, the ferromagnetic resonance condition can be satisfied that is $(\vec{M} \perp \vec{h})$, and the radiation field can couple to the magnetization. It will, however, couple effectively only at the ferromagnetic resonance frequency $\omega_0 = 2\pi\nu_0$ given above, so that a display of power transmitted versus frequency will show a sharp decrease in transmission at ν_0 . This device is called a "notch" filter. It should be noted that the location of the "notch" can be moved by applying an external magnetic field, as indicated by Eq. 2, parallel to the magnetization direction \vec{M} . Furthermore, if an external magnetic field is applied perpendicular to the direction \vec{M} as shown in Fig. 6b and has sufficient size to reorient the direction of \vec{M} perpendicular to the direction of signal propagation, the radiation field can then no longer couple to \vec{M} , since now $\vec{h} \parallel \vec{M}$. This will effectively turn the filter off. As discussed earlier, this requires an applied field of <10 Oe, easily achieved in a device configuration. The device described here is not intended to be a prototype design, but rather a pedagogical example to illustrate the concepts involved. Real devices are currently under study and have been reported upon.⁽⁷⁾

The width of the "notch" in the filter device described is just the line width of the ferromagnetic resonance observed in the film. This line width is a measure of the quality of the films, insofar as there are variations in \vec{M} or in the internal anisotropy field caused by variations in strain, thickness or composition. In this regard, the epitaxial Fe films grown on ZnSe have shown the narrowest linewidths ever observed for a ferromagnetic metal (45 Oe at 35 GHz) (8) which become comparable to those observed in ferrimagnetic insulators (ferrites). Ferromagnetic metals were abandoned years ago for high frequency device applications because their observed linewidths were too large, compared to ferrites. These recent results for epitaxial metal films suggest that those conclusions should be reconsidered. This is especially true for higher frequency applications where the low $4\pi M$ of ferrites ($\approx 2\text{kOe}$) keeps their zero field resonance frequency low, well below the range of interest for most high frequency planar device applications.

Spin Injection Devices

One of the most interesting uses of ferromagnetic metal films is as a source of spin polarized carriers. If one considers the simple Stoner

picture of an ideal rigid-band ferromagnetic metal, the majority-spin d states lie below the Fermi level and are all filled, but the minority states are filled only up to the Fermi level. Assuming the s- and p-state electrons to be unpolarized, one might expect that some fraction of the carriers will be polarized to the extent that the minority d states contribute to the conductivity. One could exploit this condition to obtain polarized carriers by using a ferromagnetic metal film as an electrical contact on a non-magnetic metal or semiconductor.

The pioneering work on this concept was reported in 1970 by Meservey, et al (9) in which they carried out tunneling experiments from a ferromagnetic metal film through an Al_2O_3 barrier into a superconducting metal film (Al). The superconducting film, with its sharply peaked density of states at the superconducting gap, acted as a spin-polarized electron detector in the presence of an applied magnetic biasing field. The tunneling current, originating from the ferromagnetic film, proved to be highly polarized (+44% for Fe, +34% for Co and +11% for Ni) (10) where the polarization is defined as $P = (n_+ - n_-) / (n_+ + n_-)$, n_{\pm} being the number of carriers of each spin character.

This was a surprisingly high degree of polarization, but even more surprising was that the polarization direction was that for the majority spins. For the simple band structure assumed, carriers would only be available from the minority spin-states near the Fermi level. After several years, an explanation was finally provided by Stearns (11), who pointed out that while most of the d electrons occupy energy bands as described by a Stoner model, a small number of d electrons possess an itinerant character. These itinerant d states are the main component of the tunneling current. The relative number of majority and minority spins in these itinerant d bands is proportional to the magnetic moment of the material and thus accounts for the observed sign and magnitude of the polarization of the tunneling current.

A more recent achievement in this field was the injection of spin-polarized carriers into a paramagnetic metal by Silsbee and Johnson in 1985 (12). This is illustrated in Fig. 7 where the paramagnetic metal (Al) is shown as a long bar with two pads of ferromagnetic metal deposited upon it to act as a source and drain of carriers. These carriers will be polarized, since they originate in a magnetized material as shown in the figure. The injected carriers travel through the bar and are picked up at the second ferromagnetic pad. The physics is illustrated, again in a simple Stoner picture, as minority electrons entering the paramagnet, going into unoccupied minority states at the Fermi level; traveling through the metal, under the influence of the applied electric field; finally, leaving the metal by entering unoccupied minority states in the second ferromagnetic pad. The pads may thus be thought of as polarizing filters acting on the current passing through the circuit. If this picture is correct, the polarized current in the paramagnet should act to unbalance the equally populated up- and

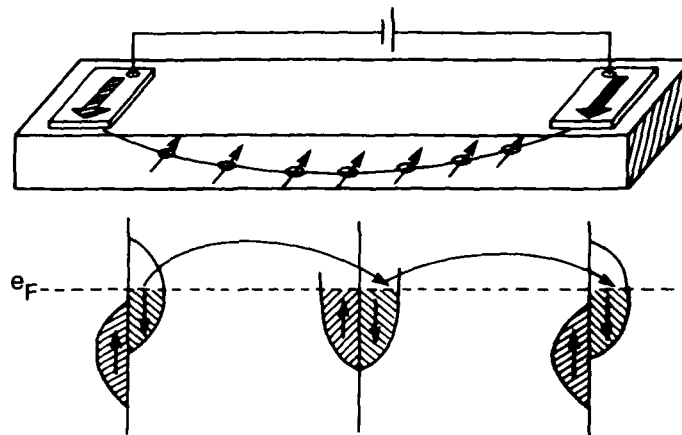


Fig. 7. Injection of spin polarized current into paramagnetic bar from ferromagnetic pads (13)

down-spin bands, inducing a net magnetization. Because there will be spin-flip scattering events during the transit through the paramagnet, the magnitude of the induced magnetization should decrease along the path. Its measurement would thus yield a determination of the spin-flip scattering length. This measurement was carried out by putting thin-film SQUID pick-up loops down on the surface of the bar, in a regular array between the two pads, and measuring the induced magnetic moment. It was found that the polarization relaxed with a decay length of $100\text{ }\mu\text{m}$ at 40K (13). It should be noted that, since the two pads act as polarizing filters for the current, by reversing one of them the polarized current can be blocked, much in the same way that crossed optical polarizers can block light passing through them.

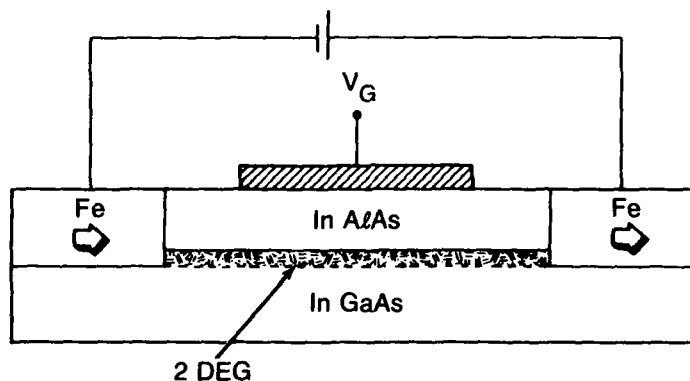


Fig. 8. Proposed spin-polarized field effect transistor. (14)

This analogy was recently invoked for a proposed device which would apply the spin injection concept to ferromagnetic metal films on semiconductors. Datta and Das (14) have suggested the construction of a spin-polarized field effect transistor (Spin-FET) as illustrated in Fig. 8. The current carrying medium would be an inversion layer formed at the heterojunction between InAlAs and InGaAs. The two-dimensional electron gas in that layer would provide a very high mobility, free of spin-flip scattering events. The spin-polarized carriers are injected and collected by ferromagnetic metal pads as discussed above. However, one can expect that the strong internal electric field present in the inversion layer heterostructure interface region, oriented perpendicular to the layer, will cause the spins of the carriers to precess, due to spin-orbit coupling. This precession will rotate them out of alignment with the magnetization of the second ferromagnetic pad, decreasing the transmitted current of the device. Finally, if a gate electrode is deposited on top of the device, one can apply a gate voltage V_g to increase or decrease the effective electric field causing the spin precession. This will serve to control the alignment of the carriers' spin with respect to the magnetization vector in the second pad, thus permitting modulation of the current passing through the device. Although this proposed device demands carefully controlled material growth and lithography, its fabrication is well within the reach of current technology. Devices such as these, which distinguish between spin-up and spin-down carriers essentially possess an added dimension of device parameter space which, up until now, has not been exploited.

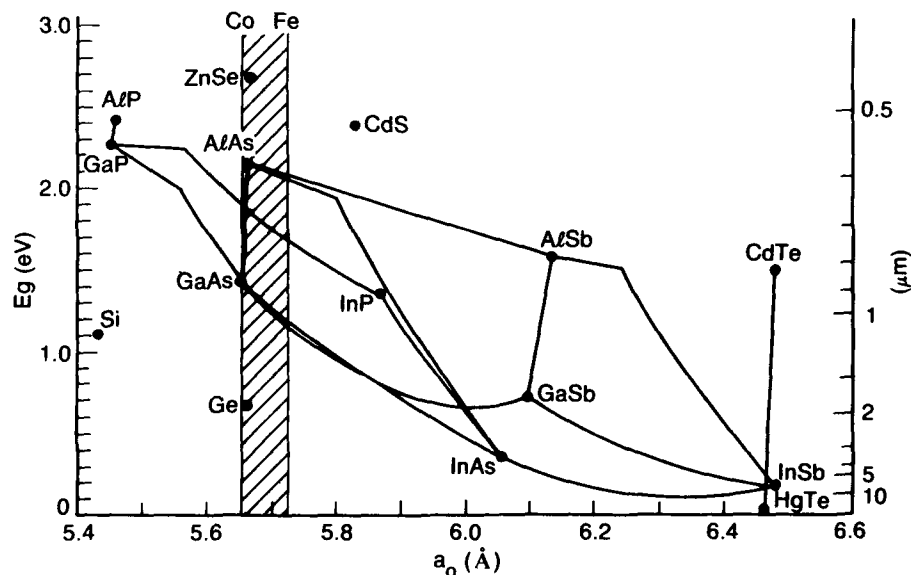


Fig. 9. Lattice constants a_0 of cubic semiconductors with region of epitaxial lattice match to the bcc Fe-Co alloy system indicated by cross hatch. Bandgap is plotted in eV on the left and photon wavelength on the right.

Conclusion

This short review provides some examples of the current status of the preparation of hybrid ferromagnetic/semiconductor materials by modern thin film techniques. The regions of metal/semiconductor epitaxial match are indicated in Fig. 9, with growths already demonstrated for Fe/Ge; Fe/GaAs; Fe/ZnSe and Co/GaAs. Many of the applications discussed here might be suitable for non-epitaxial magnetic films as well, which opens the way for a host of new possibilities, including alloys of both rare-earth and transition metal ferromagnets, as well as ferromagnetic and ferrimagnetic insulators. Work on these possibilities is underway at a number of laboratories, and it can be anticipated that new hybrid magnetic/semiconducting materials will provide not only technological opportunities but additional opportunities for scientifically probing condensed matter behavior.

REFERENCES AND NOTES

1. R. F. C. Farrow, et. al. in *Epitaxy of Semiconductor Layered Structures*, edited by R. T. Tung, L. R. Dawson, and R. L. Gunshor, Eds. (Mater. Res. Soc. Symp. Proc. 102, Pittsburgh, PA, 1988) p. 483.
2. M. W. Ruckman, J. J. Joyce, J. J. Weaver, Phys. Rev. B33, 1756 (1986).
3. B. T. Jonker and G. A. Prinz, Bull. Amer. Phys. Soc. 35, 579 (1990).
4. J. J. Krebs, C. Vittoria, B. T. Jonker, G. A. Prinz, J. Mag., Mag. Mat. 54-57, 811 (1986).
5. A. V. Pohm, J. S. T. Huang, J. M. Daughton, D. R. Krahn, V. Mehra, IEEE Trans. Magn., MAG-24, 3117 (1988).
6. P. Grunberg, R. Schreiber, Y. Pang, M. B. Brodsky, H. Sowers, Phys. Rev. Lett. 57, 2442 (1986).
7. E. Schloemann, F. Tustison, J. Weissman, H. J. Van Hook, T. Varitimos, J. Appl. Phys. 63, 3140 (1988).
8. G. A. Prinz, B. T. Jonker, J. J. Krebs, J. M. Ferrari, F. Kovanic Appl. Phys. Lett. 48, 1756 (1986).
9. R. Meservey, P. M. Tedrow, P. Fulde, Phys. Rev. Lett. 25, 1270 (1970).
10. P. M. Tedrow and R. Meservey, Phys. Rev. B7, 318 (1973).
11. M. B. Stearns, J. Mag., Mag. Mat., 5 167 (1977).
12. M. Johnson and R. H. Silsbee, Phys. Rev. Lett. 55, 1790 (1985).
13. M. Johnson and R. H. Silsbee, Phys. Rev. B37, 5326 (1988).
14. S. Datta and B. Das, Appl. Phys. Lett. 56, 665 (1990).
15. Financial support from the Office of Naval Research is gratefully acknowledged, as are numerous discussions with many collaborators, in particular J.J. Krebs and K.B. Hathaway.

§This article first appeared in Science, by the same title and author, in Vol. 250, page 1092, 23 November 1990. It is © by AAAS and reprinted here by permission.

MOSSBAUER STUDIES OF ULTRATHIN MAGNETIC FILMS OF Fe/Ag(100)

Norman C. Koon

Naval Research Laboratory
Washington, DC 20375-5000
United States of America

INTRODUCTION

Magnetic studies of very thin magnetic films, where only small amounts of material are present and where surface and interface effects may be almost completely dominant, represent a difficult challenge to the experimentalist. The Mossbauer effect utilizing Fe^{57} has proved to be very useful tool in such investigations, since under favorable circumstances it can provide important information about both the physical and electronic structure of the film as well as the magnetization, spin orientations, and dynamic processes. In contrast to some techniques, the Mossbauer effect generally probes all the Fe^{57} spins which are present in the film, even those which are not magnetically ordered, and thus makes it possible to determine if some spins are decoupled from the main part of the film. The isomer shift and the quadrupole splitting (in the case of cubic materials) can sometimes be used to infer the location of the atoms being probed (interior, exterior, or at the interface of a film); the magnetic hyperfine field can be related both to the degree of magnetic order as well as to the electronic structure, and the line intensities can be used to determine the orientation of the spins. Broadening of the spectra may also be used to study the nature of the spin dynamics in the film. Ultrathin (< 10 monolayer) Fe/Ag(100) films are particularly interesting for such studies because all of these phenomena prove to be useful in developing our understanding of these near 2-d systems.^{1,2} For further details concerning applications of the Mossbauer effect see the article by A. Morrish in these proceedings.

Because an isotropic 2-d Heisenberg ferromagnet has no magnetic order at non-zero temperatures in absence of magnetic anisotropy³, the properties of very thin magnetic films are dominated by their anisotropies - both intrinsic and from dipolar (demagnetizing) fields. In cases where the crystalline surface anisotropy favors the direction perpendicular to the plane, as has been shown to occur often in very thin transition metal films, this intrinsic anisotropy opposes the dipolar fields which favor alignment in the plane. To produce a very thin film which can be compared with a 2-d Heisenberg model therefore requires that the perpendicular crystalline anisotropy approximately cancel the demagnetizing energy. Perpendicular crystalline anisotropy was first suggested for Fe/Ag(100) films by Jonker, et al⁴ from spin polarized photoemission studies, which showed that for films of less than 3 monolayers (ML), there was no in-plane moment. It was suggested that this resulted from a perpendicular anisotropy strong enough to overcome the demagnetizing fields and orient the spins along the normal to the surface. From renormalization group calculations by Bander and Mills⁵ it can be expected that such a perpendicular anisotropy would induce an Ising type of behavior in certain temperature regimes.

The Mossbauer work which we have done on Fe/Ag(100) multilayer films was undertaken primarily in order to demonstrate conclusively whether or not the films were magnetically ordered perpendicular to the film plane. In addition to establishing the predominant spin orientations,¹ we determined from the thickness dependence of the hyperfine interactions that the magnetic hyperfine field increases in going from the center of the thin films (< 5-6 ML) to the surface, as predicted by Ohnishi, Weinert, and Freeman⁶ from band structure calculations. In addition, we observed broadening of the spectra² which we propose is due to slow, Ising type fluctuations of large blocks of spins in the manner suggested by the renormalization group calculations.⁵ This paper is a summary of that work.

EXPERIMENTAL

The Fe/Ag(100) system is particularly favorable for epitaxial growth because there is only a 0.8% mismatch between the Fe(100) and Ag(100) surface nets, with the Fe slightly expanded for pseudomorphic growth. Several studies have shown that the growth of Fe on Ag(100) proceeds layer by layer for the first three layers and then exhibits island growth for thicker films. RHEED patterns and a more detailed description of the growth procedure are given elsewhere.¹ Samples having thicknesses of 0.9, 2.4, and 5.5 ML were studied.

The conversion electron Mossbauer spectrometer used is of the cylindrical mirror analyzer type, with an energy resolution of approximately 4 %. The samples were mounted on a Cu block connected via a Cu braid to a closed cycle refrigerator. The transducer and source were inside the vacuum chamber. The Mossbauer gamma-rays were incident perpendicular to the plane of the sample.

RESULTS

Clear evidence for almost complete perpendicular alignment of spins in the 2.4 ML sample is given in Fig. 1, where we compare its Mossbauer spectrum at 15 K with that of a thick film (~500 Å), which is known to have its moment in-plane. Information about the orientation of the spins is contained in the ratios of line intensities, which for pure magnetic hyperfine splitting is given by $3 : x : 1 : 1 : x : 3$, where $x = 4\sin^2\theta/(1+\cos^2\theta)$ and θ is the angle between the incident γ -ray direction and the direction of the magnetic hyperfine field. For the thick film the ratios are $3 : 4 : 1$; exactly what should be observed if the Fe moments lie in the plane ($\theta = 90^\circ$). It is clear in the 2.4 ML spectrum, however, that the second and fifth major lines (the $\Delta m = 0$ forbidden ones) are very weak compared to those of the thick film, indicating close alignment of the spins to the perpendicular direction ($\theta = 0$).

The structure in the spectrum of the 2.4 ML film indicates the presence of more than one crystallographically inequivalent site (as one would expect for 2.4 ML). To quantitatively estimate the hyperfine fields and the integrated intensities we fit the spectra assuming only two types of Fe sites. This yielded average integrated intensity ratios of $3 : 0.5 : 1$ and hyperfine fields of 358 kG and 344 kG (compared to 340 kG for bulk Fe). The corresponding values of the quadrupole splitting (indicative of deviation from cubic symmetry), isomer shifts (a measure of the conduction electron spin density at the nuclei), and the weighting factors are given in Table 1. From the integrated intensity ratios we calculate a uniform spin deviation from perpendicular of 28° or, equivalently, that approximately 22 % of the spins lie in the plane and 78 % are perpendicular to it. Because of domain formation and imperfections in the films the correct physical picture probably lies in between these two extremes.

Spectra for the 5.5 ML sample at room temperature and 15 K are shown in Figure 3. The line intensity ratios at room temperature are $3 : 4 : 1$, indicating that the magnetization is in the plane of the film. At 15 K the intensity ratios are $3 : 1.6 : 1$, which corresponds to a uniform angle from perpendicular of 49° or to 57 % of the spins oriented in the plane and 43 % perpendicular.

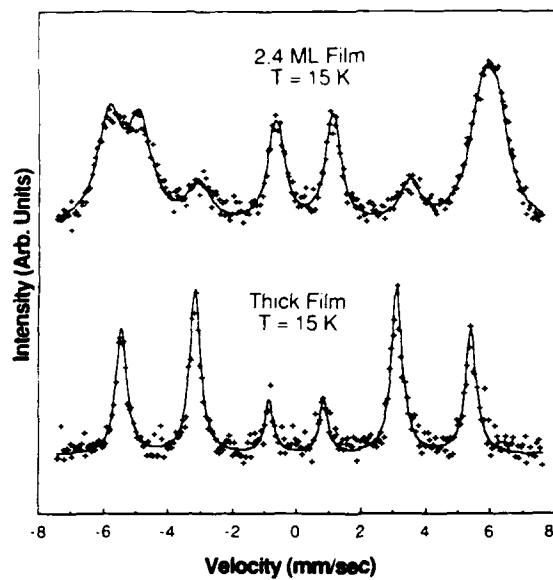


Fig. 1 Conversion-electron Mossbauer spectra taken at 15 K for a thick film of Fe^{57} compared to that of a 2.4 ML multilayer film of Fe^{57} on $\text{Ag}(100)$.

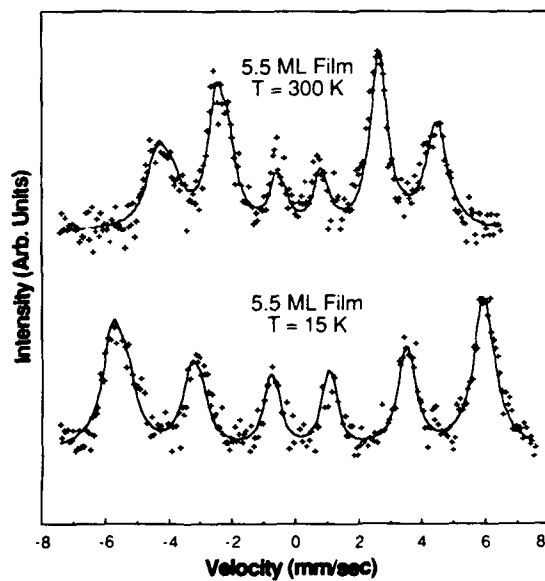


Fig. 2 Conversion-electron Mossbauer spectra taken at 15 and 300 K on a 5.5 ML film of Fe^{57} on $\text{Ag}(100)$.

This suggests that at low temperatures the perpendicular anisotropy of the 5.5 ML film is comparable to the demagnetization field, whereas at room temperature the demagnetization field dominates. The perpendicular anisotropy energy therefore seems to increase faster than the demagnetization energy as the temperature is lowered.

The 5.5 ML spectra were also fit using the 2-site model with the parameters given in Table I. The best fits to the 15 K data were generally obtained using zero quadrupole splitting and slightly larger hyperfine fields than for the 2.5 ML film. The fit at room temperature was calculated by allowing only the hyperfine magnetic fields to vary from the 15 K values. The decrease in H_{hf} from 15 K to 300 K is much greater than for bulk Fe, suggesting a lower Curie temperature for the film. It is also interesting to note that the 0.65 to 0.35 weighting factors are in almost exactly the ratio of interior to interface atoms one would expect for a 5.5 ML film, which suggests that the higher field component (363 kG) of the spectrum is due to interior atoms, while the lower field (352 kG) is due to interface atoms. This is also consistent with the respective values of the isomer shift, which should be small for interior atoms.

A similar identification can be made for the 2.4 ML film, although the weighting factors yielded by the fitting process for the two sites are nearly equal instead of being in favor of interface atoms. However, both the isomer shift and the quadrupole interactions are larger for the smaller hyperfine field than for the larger one, which is again consistent with the smaller hyperfine magnetic field being associated with interface atoms.

Table I. Hyperfine field parameters for bulk Fe and for the 2.4 and 5.5 ML films. The parameters were determined using a two site fit as described in the text.

| 15 K (300 K) | Weighting Factor | H_{hf} (kG) | QS (mm/sec) | IS (mm/sec) |
|--------------|---------------------|------------------|----------------|----------------|
| Bulk Fe | 1.0 | 340(330) | 0.0 | 0.0 |
| 2.4 ML | 0.52 | 358 | -0.11 | 0.06 |
| 5.5 ML | 0.48 | 344 | 0.16 | 0.49 |

The hyperfine field calculations which appear to most closely match the conditions realized in this experiment are those of Ohnishi, Freeman, and Weinert⁶, who treated the problem of a Fe/Ag(100) 7-layer slab where the outer two layers were Ag. For the center Fe layer they calculated $H_{hf} = 359$ kG, with a decrease to 339 kG for the next-to-interface layer and 335 kG for the interface Fe layer. With a simple two site fit we obtain 363 kG (65 %) and 352 kG (35 %), which is in good qualitative agreement if one identifies the larger hyperfine field with interior atoms as described above. For the 2.4 ML sample there is at present no model calculation whose assumptions permit reasonable comparison with our data.

The temperature dependence of Mossbauer spectra for the 2.4 ML sample are shown in Fig. 3, along with fits to the data using the same hyperfine field parameters as in Table I with the addition of a simple relaxation theory^{7,8} applicable to a spin 1/2 Ising model to describe the broadening observed at temperatures above about 50 K. There are several important points to be noted. First is that even in the regime where there is broadening, the $\Delta m = 0$ lines are weak, indicating that the spins are still ordered perpendicular to the plane of the film. Second is the distinct splitting of the innermost lines (3 and 4), which indicates clearly that there is a non-zero order parameter. Third is that there is no evidence for a significant central peak at low to intermediate temperatures, indicating that almost all of the iron spins are strongly coupled to the films as a whole.

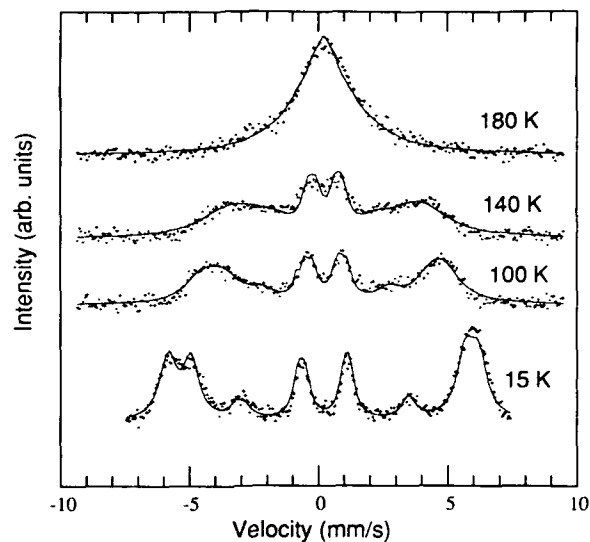


Fig. 3. Mossbauer spectra as a function of temperature for the 2.4 ML superlattice film. Solid lines represent fits to the model described in the text.

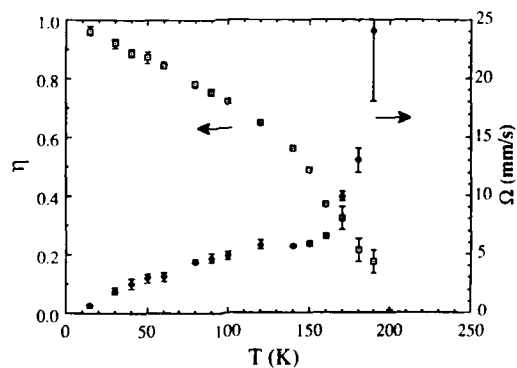


Fig. 4. Temperature dependence of the order parameter η and the relaxation frequency Ω for the 2.5 ML superlattice film (one mm/s = $7.3 \times 10^7 \text{ s}^{-1}$).

The theoretical fit which was used to describe the broadening is based on simple stochastic relaxation between spin up and spin down states as treated by van der Woude and Dekker⁷ and Blume and Tjon.⁸ It only contains two parameters, the relaxation rate Ω , and the order parameter η , and is independent of the mechanism responsible for the relaxation. The only differences in the calculated spectra of Fig 3 are in η and Ω , whose temperature dependence is given in Fig. 4.

CONCLUSIONS

The line intensity data shown in Fig. 1 conclusively establish the perpendicular orientation of the iron magnetic moments at low temperatures in very thin (less than about 4-5 ML) films of Fe/Ag(100). From the temperature dependent data on the 5.5 ML film we conclude that the perpendicular magnetic anisotropy increases faster than the demagnetizing energy as the temperature is lowered. From the thickness dependence of the hyperfine fields we conclude that the hyperfine magnetic field varies with position through the film in a manner very close to the predictions of band theory.⁶ The type of broadening which we see is similar to that observed in superparamagnetic relaxation, however, fits to the theory utilizing a zero order parameter could not reproduce the relatively sharp and distinctly split inner peaks shown in Fig. 3. In order to fit that feature it was necessary to make the order parameter non-zero, which is inconsistent with normal superparamagnetism. It could be consistent with a film consisting of interacting clusters which all have the same order parameter or with the renormalization group picture of an Ising model where the order parameter describes the fluctuations of large blocks of spins. Because we see in the fits only a single nonzero order parameter and relaxation frequency for each temperature, with no evidence for a distribution, we suggest that the latter explanation is more likely.

REFERENCES

1. N. C. Koon, B. T. Jonker, F. A. Volkening, J. J. Krebs, and G. A. Prinz, Phys. Rev. Letters, **59**, 2463 (1987)
2. F. A. Volkening, B. T. Jonker, J. J. Krebs, G. A. Prinz and N. C. Koon, J. de Phys. Colloq. C8, Suppl. 12, 1699 (1988)
3. N. D. Mermin and H. Wagner, Phys. Rev. Lett. **17**, 1133 (1966)
4. B. T. Jonker, K.-H. Walker, E. Kisker, G. A. Prinz, and C. Carbone, Phys. Rev. Lett. **57**, 142 (1986)
5. M. Bander and D. L. Mills, Phys. Rev. B **38**, 12015 (1988)
6. S. Ohnishi, M. Weinert, and A. J. Freeman Phys. Rev. **B30**, 36 (1984)
7. F. van der Woude and A. J. Dekker, Phys. Stat. Sol. **9**, 775 (1965)
8. M. Blume and J. A. Tjon, Phys. Rev. **165**, 446 (1968)

SPIN-DEPENDENCE OF ABSORBED AND REFLECTED CURRENT ON FE(110)

M.S. Hammond, G. Fahsold, and J. Kirschner

Institut für Experimentalphysik
Freie Universität Berlin
D-1000 Berlin 33, West Germany

New electron microscopies such as SEMPA and LEEM increasingly require a more thorough knowledge of the low-energy electron scattering processes at and near surfaces. Electron reflection¹ and absorption^{2,3,4,5} measurements have proven useful in identifying major features in the unoccupied electronic band structure of solids and their surfaces, as well as determining the effect of such band structures on electron scattering processes. The elastic reflected current spin asymmetry has been calculated⁵, demonstrating the usefulness of such measurements for studying the unoccupied band structure of ferromagnetic single crystals. Earlier measurements on absorbed current spin asymmetries from a metallic glass⁶ were concerned mainly with the asymmetry near the zero crossing in the absorbed current rather than the low-energy asymmetries; therefore further work on the angular and energy dependence of the absorbed and reflected current, and its spin dependence, is desirable. In particular, we wish to demonstrate the important connection between secondary electron polarization fine structure⁷ and absorbed (or reflected) current spin asymmetry⁵, as they both relate to band structure.

The spin-dependent absorption and reflection results reported here are expressed in terms of a normalized asymmetry, $A(E_0)$, for a primary electron beam energy E_0 of 0 to 50 eV:

$$A(E_0) = \frac{1}{P_0} \cdot \frac{I^{\uparrow} - I^{\downarrow}}{I^{\uparrow} + I^{\downarrow}} \quad (1)$$

where P_0 is the incident beam polarization magnitude and I^{\uparrow} (I^{\downarrow}) is the absorbed or reflected current for incident beam polarization parallel (anti-parallel) to the sample majority spin direction. The absorbed and (energy-integrated) reflected current asymmetries (A_a and A_r , respectively) are found to be reciprocal to one another, being opposite in sign and possessing the same general structure, while their magnitudes are simply related by:

$$\frac{A_a}{A_r} = - \frac{\rho}{\alpha} \quad (2)$$

where ρ/α is the ratio of reflection to absorption coefficients ($\rho+\alpha=1$). The apparatus used to measure absorbed and reflected current asymmetries, described in detail elsewhere^{8,9} is shown schematically in Figure 1. Briefly, a spin-polarized primary electron beam ($P_0=20-30\%$) is focussed through the center of a 3-grid hemispherical LEED analyzer, which is used to collect all the reflected current. The primary electrons impinge on the

(110) face of an iron single crystal remanently magnetized along the $\langle 100 \rangle$ direction (incident angle, $\theta = 0^\circ$ to 60°). The electron spin-polarization vector and the sample magnetization vector are both perpendicular to the scattering plane. The polarization of the incident beam is reversed at a frequency of 1 kHz, enabling the use of a lock-in technique to detect the resulting difference in the (absorbed or reflected) current upon polarization reversal.

Figures 2(a) and (b) show the reflected current spin asymmetry A_r and the reflected current (normalized by the incident beam current), respectively, as a function of primary electron kinetic energy for a range of incident angles. Figure 3 shows similarly the absorbed current spin asymmetry A_a and the absorbed current. The reciprocity exhibited by the absorbed and reflected asymmetries is obvious; i.e. they are opposite in sign and maxima in the absorbed current asymmetries correspond to minima in the reflected current asymmetries (except at very low energies and large incident angles due to finite collection angles, as discussed in more detail elsewhere^{8,9}). This reciprocity explicitly demonstrates that the information contained in the two asymmetries is basically the same, which is to be expected from simple charge conservation considerations. The spin-averaged reflected and absorbed currents (Figures 2(b) and 3(b), respectively) also contain information about the bulk band structure of the Fe(110) crystal. At normal incidence there is a peak in the reflected current at approximately 20 eV incident energy (marked by an arrow) that corresponds to a local minimum in the absorbed current (also marked by an arrow). This is clear evidence of a gap in the band structure and it occurs close to the position of the band gap along the [110] direction calculated for a nearly free-electron dispersion relation with an inner potential of 12 eV. A band gap results if a decrease in the absorbed current, and a concomitant increase in the reflected current, due to the lack of states into which incident electrons can couple. The band gap at 20 eV results in a strong feature in the asymmetries due to the spin-splitting of the bulk band structure. Because the minority spin electron states are shifted upward in energy with respect to the majority spin states, there will exist relatively more empty minority states at the low energy end of a band gap and majority states at the high energy end. This situation results in the sharp features seen in both asymmetries at approximately 20 eV. The arrows in Figures 2(a) and 3(a) mark the energetic position of the minimum (maximum) in the spin-averaged absorbed (reflected) current. Note that the inflection points in the asymmetries occur at a lower energy than in the currents.

The spin-polarization, as a function of emission energy and angle, of secondary electrons excited by high energy (2 keV) primary electrons from the same Fe(110) sample in an earlier experiment¹⁰ is shown in Figure 4. The polarization is along the majority spin direction. The polarization

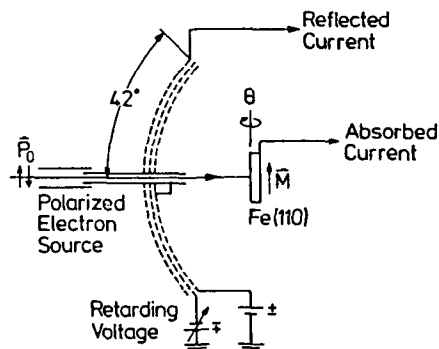


Fig. 1. Schematic of apparatus for measuring absorbed and reflected current and current spin asymmetries.

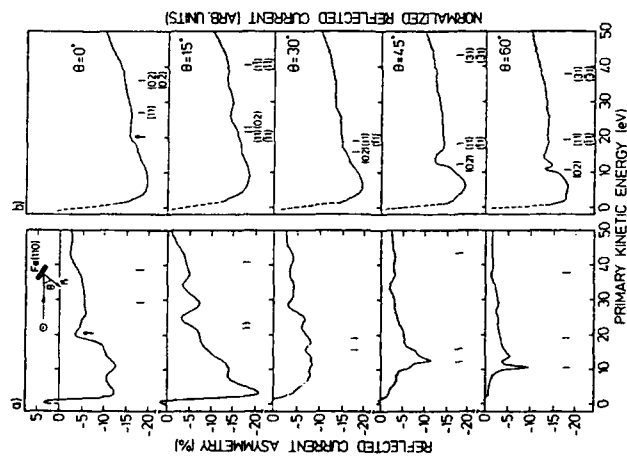


Fig. 2. Reflected current asymmetry Ar (a) and normalized reflected current (b) from Fe(110). Dashed lines are shown where normalization to small incident currents yields unreliable data. Tic marks indicate LEED beam emergence energies.

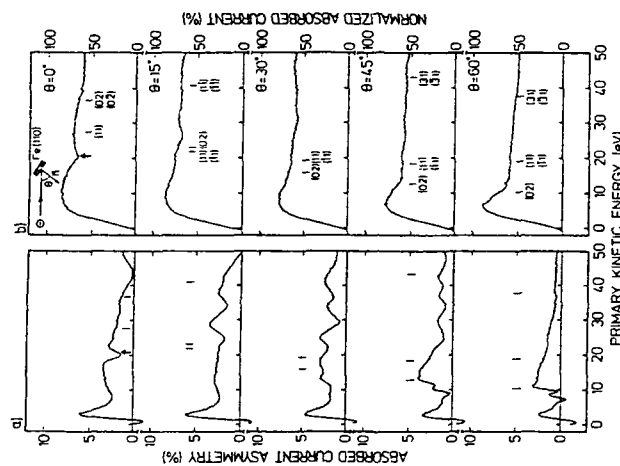


Fig. 3. As Fig. 2., but for absorbed current asymmetry Aa (a) and absolute normalized absorbed current.

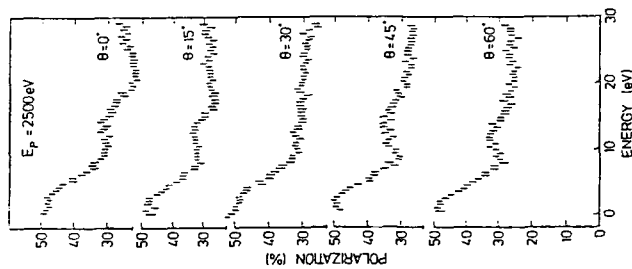


Fig. 4. Spin-polarization distributions for secondary electrons emitted at angles of 0° to 60° from normal for Fe(110).

exhibits a low-energy enhancement and an angle dependent fine structure. This fine structure in the polarization, which has been identified with the spin-split bulk band structure⁷, concerns us here. If the structure in the asymmetries in Figures 2(a) and 3(a) are in fact a result of the bulk band structure, then there should be a correspondence between these structures and the secondary electron polarization fine structure. In general, the absorbed current asymmetry is observed to be positive and the reflected current asymmetry negative. That is, majority spin incident electrons result in a larger absorbed current while minority spin electrons result in more reflected current. This may, at first sight, appear in contradiction to the majority spin polarization of secondary electrons ejected at similar energies; however, it is important to realize that measuring the absorption of low-energy electrons incident on the crystal is essentially the time-reversal of measuring the emission of low-energy electrons originating inside the crystal. Consideration of time-reversal symmetry requires that the absorbed current asymmetry be related to the secondary electron polarization fine structure¹¹. Comparison of the spin-polarized secondary electron emission measurements shown in Figure 4, with the absorbed current spin asymmetries more clearly demonstrates the complementary nature of these two measurements. In keeping with the requirements of time-reversal symmetry, the secondary electron emission angles are compared to the incident angles in the absorbed current. It can be seen that maxima and minima in the absorbed current asymmetry roughly correspond to the maxima and minima in the secondary polarization fine structure. A positive feature at 3-4 eV, a valley just below 10eV that increases in sharpness as the angle (of incidence or emission) increases, and a dip at 20 eV that is present only for normal incidence or emission are the more prominent structures in the two sets of data. The similarities between secondary electron polarization fine structure and absorbed current asymmetry suggests that the latter is also determined by the spin-dependent bulk band structure.

The present spin asymmetry measurements from a single crystal ferromagnetic sample have demonstrated the reciprocity of the total reflected and absorbed current asymmetries. This reciprocity allows one to monitor the experimentally more accessible target current to obtain band structure information. The reflected current measurements, however, allow the separation of elastic and inelastic contributions to the total asymmetry⁹. The spin-polarization of secondary electrons emitted from the same Fe(110) sample exhibit fine structure that corresponds to the structure in the absorbed and reflected asymmetries. The structures in both the polarization fine structure and the asymmetries are identified as spin-split band structure effects and demonstrate the time-reversal symmetry between absorption and emission of low-energy electrons.

Acknowledgments - This work was supported by the Deutsche Forschungsgemeinschaft through Sonderforschungsbereich 6.

REFERENCES

- ¹ E.N. Sickafus, Phys. Rev. B16 (1977) 1436, 1448.
- ² R.C. Jaklevic and L.C. Davis, Phys. Rev. B26 (1982) 5391.
- ³ S.A. Lindgren, L. Wallden, J. Rundgren and P. Westrin, Phys. Rev. B29 (1984) 576.
- ⁴ S.A. Komolov and L.T. Chadderton, Surf. Sci. 90 (1979) 359.
- ⁵ E. Tamura, R. Feder, J. Krewer, R.E. Kirby, E. Kisker, E.L. Garwin and F.K. King, Sol.State Commun. 55 (1985) 543.
- ⁶ H.C. Siegmann, D.T. Pierce and R.J. Celotta, Phys. Rev. Lett. 46 (1981) 452.

- ⁷ E. Tamura and R. Feder, Phys. Rev. Lett. **57** (1986) 759.
- ⁸ M.S. Hammond, G. Fahsold, K. Koike and J. Kirschner, Vacuum (accepted for publication).
- ⁹ G. Fahsold, M.S. Hammond and J. Kirschner (to be published).
- ¹⁰ J. Kirschner and K. Koike (to be published).
- ¹¹ R. Feder and J.B. Pendry, Sol.State Commun. **26** (1978) 519.

MBE GROWTH OF METAL/SEMICONDUCTOR INTERFACES

J. M. Slaughter, Brad N. Engel, M. H. Wiedmann, Patrick A. Kearney, and Charles M. Falco

Optical Sciences Center and Department of Physics
The University of Arizona, Tucson, AZ 85721

INTRODUCTION

Metal/semiconductor structures are of interest in several fields including thin-film magnetism, electronics, and x-ray optics. Well controlled and characterized interfaces are crucial for the understanding of the properties of nanostructured materials. We describe techniques used to grow and characterize three such material systems: Co/Pd on GaAs(110) (using a bcc-Co seed layer), Co on Si(111), and Mo on Si(111).

The Co/Pd system is of interest for its magnetic and magneto-optic properties. In particular, several workers have observed polarization of the Pd in Co/Pd multilayers¹ as well as a strong perpendicular magnetic anisotropy.² We have grown epitaxial Co/Pd superlattices on GaAs(110) substrates by first depositing a suitable buffer layer of Pd. The growth of the Pd buffer layer and the behavior of Co deposited upon it are discussed in the present paper. Structural and magnetic properties of the superlattices are discussed elsewhere in these proceedings.³

Heteroepitaxy of a variety of pure metals on GaAs has been achieved by various workers. In many cases, structures with sharp interfaces as well as good atomic order have been obtained. However, in contrast to the case with GaAs, Si reacts with most metals to form silicides, making it impossible to produce epitaxial pure-metal/Si structures similar to those made on GaAs. In fact, many metals react with Si even at room temperature. Although the problems associated with pure metals are severe, Co and several other metals (e.g. Ni and Mo) form epitaxial silicides with proper treatment. MBE techniques can then be used to form high quality epitaxial silicide/silicon multilayer structures. In the second half of this paper we discuss such techniques and their application to the growth of Co and Mo on Si(111).

GROWTH OF Co/Pd ON GaAs

The evaporations were performed in a Perkin-Elmer 433-S MBE system⁴ which was specifically designed for growth of Si and refractory metals. The Pd was evaporated from a high-temperature Knudsen cell and the Co was electron-beam evaporated. Deposition rates were 0.25 Å/s and 0.15 Å/s for Co and Pd respectively. The base pressure was 5×10^{-11} torr, and the pressure during deposition was typically 1×10^{-9} torr, with H₂ making up 70% of that total. The Co deposition rate was held constant by active feedback from an Inficon Sentinel III deposition controller⁵ which uses an electron impact emission spectroscopy

monitor to measure the flux. The substrate temperature is controlled with a feedback stabilized graphite heater, enabling temperatures as high as 1100 C to be reached when desired. Reflection high energy diffraction (RHEED) and low energy electron diffraction (LEED) are available in the growth chamber. The sample is in the growth position for RHEED but must be moved for LEED. Figure 1 shows a series of RHEED patterns taken at different stages during the depositions.

The GaAs(110) substrates were first heated to ~625 C for ~30 min to desorb the oxide from the surface. The RHEED pattern after this heating procedure is shown in Figure 1. A seed layer of Co (6 Å) was then deposited at room temperature to begin the growth. The one attempt made to grow the Pd directly on the GaAs yielded a Pd layer which was rough and disordered compared to those grown on top of a Co seed layer. The seed layer is epitaxial bcc-Co in agreement with previous work.⁶ The RHEED and LEED patterns both indicate that, although 6 Å of Co was deposited, it is rough and may not form a continuous layer.

A high quality Pd(111) layer was formed by deposition onto the 6 Å Co seed layer at room temperature. Depositing additional Pd with the sample heated to 200 C produced a surface which was better still. Interestingly, the RHEED pattern degrades at the beginning of the Pd deposition. However, after deposition of ~20 Å of Pd, the pattern begins to recover, indicating healing of the surface roughness. In addition, there is a "rotation" of the Pd with respect to the substrate. The bottom left photo in Figure 1 shows the RHEED pattern for the Pd surface formed by the deposition of 300 Å of Pd at room temperature. The "rotation" of the Pd [211] axis with respect to the GaAs [111] axis is apparent in this figure. Continuing the deposition at 200 C produced a sharper RHEED pattern as shown. However, depositing the entire Pd layer at 200 C resulted in a poor quality (three-dimensional) surface. The final photo of Figure 1 shows the same Pd RHEED with the sample rotated slightly to center the pattern.

The angle of the Pd [211] with respect to the GaAs [111] axis was measured by comparing LEED patterns from before and after the Pd deposition. Unfortunately there is a significant amount of mechanical backlash in our present substrate rotation apparatus, which made it difficult to position the sample with exactly the same orientation for each measurement. We can only say that the rotation is on the order of 5°. Future work will include improving the rotation apparatus to allow more reproducible positioning of the sample.

Finally, the growth of thin Co layers on the Pd buffer was studied. RHEED was monitored continuously during the Co deposition, and LEED was performed after the deposition of 2 Å and 4 Å of Co. A series of LEED patterns taken at different energies clearly shows an enlargement of the spot distances during the Co depositions. The Pd lattice constant was determined to be that of the bulk material (3.890 Å) within the experimental uncertainty of ~1%. The Co lattice constant was determined to be 3.80 ± 0.04 Å after the deposition of 2 Å of Co and 3.63 ± 0.07 Å after 4 Å. In comparison, the bulk lattice constant of fcc Co is 3.544 Å. From these measurements, we infer that the thin fcc-Co layer is initially strained to match the Pd buffer layer, but rapidly relaxes toward its bulk lattice constant. It should be noted that after only ~1 monolayer (ML) of Co the surface has become significantly more disordered, and becomes worse with increasing Co coverage. One could argue that the Co may be growing as small bulk-like islands, giving rise to a LEED pattern which has contributions from both the bulk Pd and bulk Co to form broad shifted spots. However, there is some evidence against this Co island interpretation from our x-ray diffraction data of Co/Pd multilayers. Since multilayers with 1 ML thick Co layers show high-angle satellite peaks and a low-angle Bragg peak, it is unlikely that the Co is forming islands.

Plans for future work includes a study of the behavior of the magnetic anisotropy in thin Co films as a function of the Co strain.

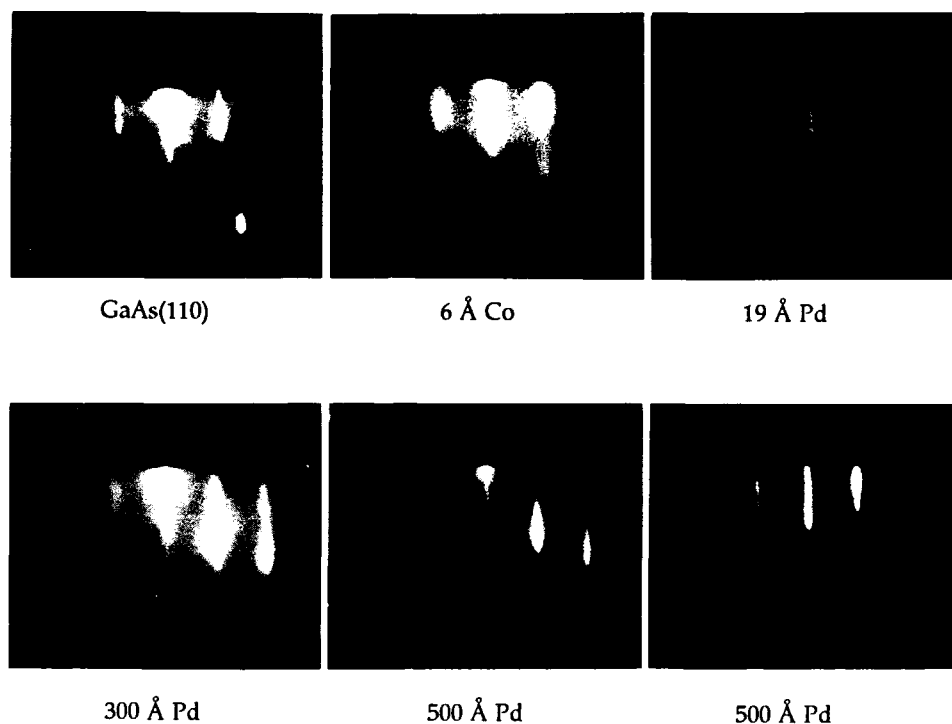


Figure 1. RHEED patterns for various stages during the growth of Pd/Co on GaAs(110). The electron beam energy was 10 Kev.

Co AND Mo ON Si(111)

Both Co and Mo form metallic disilicides which have a small lattice mismatch with Si (1.2% and 4.1% mismatch for CoSi_2 and MoSi_2 respectively).⁷ Epitaxy of CoSi_2 and MoSi_2 on Si have been studied extensively, revealing some common problems. In either case, deposition of the metal directly onto a hot Si substrate results in epitaxial films with, at best, pinholes or, at worst, large islands. Recent studies have shown that high quality CoSi_2/Si interfaces can be formed by depositing a thin ($<10 \text{ \AA}$) metal layer at $T < 100 \text{ C}$ followed by an anneal to $\sim 500 \text{ C}$.⁸ In the present work, we have studied the formation of thin epitaxial CoSi_2 and MoSi_2 layers.

A high-temperature substrate heater was used to heat the Si(111) substrates to 900 C to desorb the native oxide. A buffer layer of pure Si was then deposited at 800 C . RHEED indicates that the resulting surface exhibits the well known 7×7 reconstruction, and the Auger spectra show no surface contamination. A thin layer of metal (Co or Mo) was then deposited at $T < 100 \text{ C}$, following which the temperature was raised at 15 C/min. to T_{high} , where $400 \text{ C} \leq T_{\text{high}} \leq 600 \text{ C}$. Analyzing the evolution of the RHEED and LEED patterns during heating of $\sim 1 \text{ ML}$ of Co on Si(111) reveals the following sequence of events. The Co reacts at the low temperature to form a disordered layer, as indicated by the high background intensity in RHEED and LEED. The diffraction patterns are dim but consistent with those expected for CoSi_2 . For $T \approx 140 - 300 \text{ C}$ two different phases of CoSi_2 are present, for $T \approx 300 - 350$ only one phase is present, and for $T > 350$ there is a dominant phase with a slight trace of a second.

Mo forms an amorphous silicide layer (diffuse RHEED and LEED patterns) at the low temperature. Peak shifts in the Si-2p and Mo-3d x-ray photoelectron spectroscopy

(XPS) spectra indicate silicide formation at the Mo/Si interface for growth temperatures as low as 50 C (the lowest temperature studied). The energy shift observed here is in the opposite direction from that which we have observed in well-annealed films which formed crystalline MoSi₂. This is a strong indication that the amorphous silicide which forms at 50 C and 200 C is not MoSi₂. Annealing to T_{high} = 500 - 600 C produces an epitaxial single-crystal MoSi₂ film. However, for layers with more than ~6 Å of Mo, the diffraction patterns quickly disappear. Even for the thinner layers, the MoSi₂ films are more disordered than the equivalent CoSi₂. In addition, a series of growth studies involving continuous growth of multiple Mo coverages on the silicon have been performed. The data analysis and experimental details of these growth studies are beyond the scope of the present paper, and will be published elsewhere. Here we have discussed only that part which is interesting for comparison to the case of Co on Si.

SUMMARY

High quality Pd(111) layers were formed by deposition, at room temperature, of a Co buffer layer on GaAs(110) followed by the Pd. This surface was improved by depositing additional Pd with the sample heated to 200 C. The RHEED pattern degrades at the beginning of the Pd deposition and then recovers after depositing > ~20 Å of Pd. The Pd lattice constant, after depositing 300 Å, was determined to be that of the bulk material. The thin fcc-Co layer is initially strained to match the Pd buffer layer, but rapidly relaxes toward its bulk lattice constant.

Thin Co layers were shown to react with Si(111)(7X7) at room temperature and form a single-phase CoSi₂ epilayer when annealed to ~400 C. Thin Mo layers react to form an amorphous silicide layer at temperatures as low as 50 C. The MoSi₂ films are more disordered than the equivalent CoSi₂ films.

ACKNOWLEDGEMENTS

The authors thank Craig England for useful discussions. This work is supported by the Air Force Office of Scientific Research under contract AFOSR-90-0140 and the Joint Services Optics Program under contract F-49620-88-C-0009.

REFERENCES

1. F.J.A. den Broeder, H.J.G. Draaisma, H.C. Donkersloot and W.J.M. de Jonge, J. Appl. Phys. **61**, 4317 (1987).
2. P.F. Carcia, A. Suna, D.G. Onn and R. van Antwerp, Superlattices and Microstructures **1**, 101 (1985).
3. Brad N. Engel, Craig D. England, Masafumi Nakada, Robert van Leeuwen, and Charles M. Falco, these proceedings.
4. Perkin-Elmer Physical Electronics, Eden Prairie, MN, USA.
5. Inficon Leybold-Heraeus, Inc., East Syracuse, NY, USA.
6. G. A. Prinz, Phys. Rev. Lett. **54**, 1051 (1985).
7. See for example K.L. Wang and Y.C. Kao in Heteroepitaxy on Silicon, eds. J.C.C. Fan and J.M. Poate, MRS Symp. Proc. **67**, 235 (1986).
8. See for example: Raymond T. Tung in Silicon-Molecular Beam Epitaxy, vol. II, eds. Erich Kasper and John C. Bean, CRC Press, Boca Raton, FL (1988), or J. Derrien and F. Arnaud d'Avitaya, J. Vac. Sci. Technol. **A5**, 2111 (1987).

SURFACE AND INTERFACE MAGNETISM

F. Meier, M. Stampanoni, and A. Vaterlaus

Laboratorium für Festkörperphysik
ETH Hönggerberg
CH-8093 Zurich
Switzerland

Thin ferromagnetic epitaxial films display the most remarkable magnetic phenomena known in surface and interface magnetism. Some characteristic properties of these systems are described with emphasis on face-centered cubic Fe grown on a Cu(100) substrate.

Strong, characteristic effects in thin film magnetism have been discovered and are firmly established [1]. At the root of this development is the fact that very thin single-crystalline films consisting of 1 or a few monolayers (ML) can be grown on suitable substrates. Although the films are single-crystalline and have reproducible magnetic properties even rudimentary knowledge of the atomic arrangement in the interface - intermixing, layer-by-layer growth, surface roughness - is often missing or based on indirect evidence. The relation between film morphology and magnetism constitutes the most controversial issue in the field.

Ultimately, the solution to this problem requires a nanoscale local probe able to assess simultaneously the nature of the atomic environment in the interface and its magnetic properties. At present, this probe does not exist. Therefore a pragmatic point of view seems most reasonable: To study the magnetic phenomena occurring in monolayer systems even if there is not yet a complete atom-by-atom knowledge of the interface.

The fascination stirred by epitaxial thin film magnetism will be exemplified primarily by discussing one particular system: face-centered cubic (fcc) Fe grown on Cu(100). The structural controversy about this system is documented in the literature [2]. It concerns the intermixing of Fe and Cu within the first 2 - 3 monolayers. In many respects fcc Fe/Cu(100) is prototypical for epitaxial monolayer films: in spite that it is not a structural equilibrium phase it grows

epitaxially up to 15 ML before decaying into a polycrystalline film of bcc structure opening the possibility of creating a completely new magnetic system. Under normal conditions fcc Fe exists only in the paramagnetic phase ($T > 1180 \text{ K}$) but forcing the overlayer atoms to fit into the crystalline registry of the substrate it can be stabilized to low temperatures. In case of Fe/Cu(100) the lattice mismatch between Cu(100) [3.59 \AA at $T = 20 \text{ }^{\circ}\text{C}$] and the $T = 20 \text{ }^{\circ}\text{C}$ extrapolation of the equilibrium fcc structure of Fe [3.615 \AA] is less than 1 % [3].

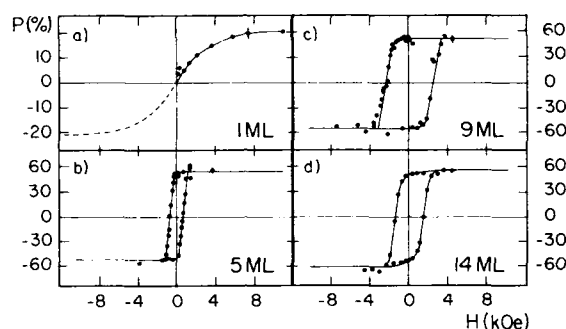


Fig.1. Magnetic field dependence of the spin-polarization of the photoelectrons emitted from fcc Fe/Cu(100) films consisting of 1, 5, 9 and 14 monolayers. The measuring temperature was 30 K.

Of basic interest is the question whether ferromagnetism persists in these thin films down to the monolayer range. This problem was recognized already in the early days of solid state physics [4]. It arises due to the circumstance that in 2 dimensions the number of spin waves excited diverges at $T > 0 \text{ K}$, assuming a magnon dispersion $E \sim k^2$ with the states $|k\rangle$ being occupied according to the Bose distribution $n(k) = (e^{E(k)/kT} + 1)^{-1}$. Experimentally, ferromagnetism in ultrathin films has been demonstrated in the pioneering work of Neugebauer [5] and, in particular, Gradmann [6].

For fcc Fe/Cu(100) ferromagnetic order has been unambiguously verified using various techniques [1]. The measurements shown in Fig. 1 have been obtained with spin-polarized photoemission [7]. In this experiment the spin-polarization of the electrons photoemitted from fcc Fe/Cu(100) films of various thicknesses t has been measured and plotted as function of the perpendicularly applied external magnetic

field H . The spin-polarization is defined as $P = (N\uparrow - N\downarrow) / (N\uparrow + N\downarrow)$ where $N\uparrow$ ($N\downarrow$) is the number of photoelectrons with spin magnetic moment parallel (antiparallel) to the direction of the surface normal. As light source the full spectrum of a Hg-Xe-lamp was used with a cut-off energy of 5.4 eV. The photothreshold of the samples was 4.7 ± 0.1 eV.

From measurements as shown in Fig. 1 several remarkable properties of thin fcc Fe/Cu(100) films emerge:

1) The fcc Fe/Cu(100) films are ferromagnetic above 1 ML.

2) At remanence the films are magnetized along the surface normal for $t > 2$ ML.

3) At remanence the films are magnetically saturated, i.e., in a single domain state for $t > 2$ ML. Whether this also applies to the in-plane magnetized 1 ML film cannot be decided from Fig. 1a.

To allow for ferromagnetism in very thin films a mechanism is needed which reduces the number of long wavelength magnon excitations. This is achieved by opening a gap in the spin wave spectrum at $k = 0$. Such a gap is produced by a magnetocrystalline anisotropy [8] defining an easy axis of the magnetization: then, the destruction of an elementary quantum of angular momentum by turning the spins unison ($k = 0$) away from the preferred axis requires a minimum amount of energy. This qualitative picture is valuable because it immediately shows the importance of anisotropy for establishing magnetic order. However, far from trivial is the observation that the magnetic ordering temperature is only very weakly dependent on the magnitude of the anisotropy [9]. A very small anisotropy - accompanied by a correspondingly small energy gap - is in fact sufficient to bring about a Curie temperature determined essentially by the mean field like expression $kT_c \sim zJ$ where J is the exchange constant and z the coordination number of the atoms [10]. Thus, not only the existence of magnetic order at $T > 0$ K but even the high transition temperatures observed in ferromagnetic monolayer films like fcc Fe/Cu(100) become understandable. - Another mechanism which removes the divergence of the long wave length spin wave excitations in 2 dimensions is the dipolar interaction: it gives rise to a term linear in k of the spin wave spectrum [10].

A most extraordinary feature of the magnetization curves of fcc Fe/Cu(100) for $t > 2$ ML is the occurrence of a perpendicular remanent magnetization: For a perpendicularly magnetized thin film the shape anisotropy energy reaches the maximum possible value $E_{\text{shape}} = 2\pi M^2$, M = magnetization. For a fcc Fe/Cu(100) film the energy to be gained by turning the spins into the film plane amounts to 3×10^{-5} eV/atom [11]. This is a very large energy compared e.g. to the bulk magnetocrystalline anisotropies of cubic transition metals which are of the order 10^{-6} eV/atom. Evidently, another much stronger anisotropy must be active which gives rise to the perpendicular easy axis observed in Fig. 1.

The possibility of a perpendicular extra anisotropy has been pointed out by Néel [12]. In cubic materials, the direction cosines of the bulk anisotropy enter for symmetry reasons only in 4th or higher order. However, at the surface

the symmetry is broken and an anisotropy term appears which contains the second power of the angle between the spin magnetic moment and the surface normal of the film. Considering nearest neighbour interactions only with constant material parameters throughout the film the resulting anisotropy is confined entirely to the surface. It gives rise to an anisotropy energy per atom which has been shown by Néel to be of a magnitude comparable to or even larger than the dipolar energy. Depending on the sign of the surface anisotropy constant a magnetization direction perpendicular to the plane of the film is favoured.

Although the possibility of a strong perpendicular surface anisotropy had been predicted almost 40 years ago it proved very elusive to direct experimental verification. It became possible only with the development of techniques providing the sensitivity required for measuring ferromagnetism of samples consisting of as little material as a 1 atomic layer [1].

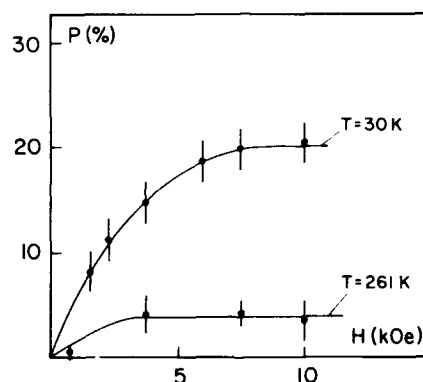


Fig.2. Spin-polarization of the photoelectrons emitted from a 1 ML fcc Fe/Cu(100) film versus applied magnetic field at $T = 30$ K and $T = 261$ K.

The shape anisotropy - or demagnetizing - energy of the film grows proportional to its thickness whereas the surface area and therefore the surface anisotropy energy remain constant. For a film exceeding a critical thickness the demagnetizing energy will therefore always overwhelm the surface anisotropy putting the magnetization in-plane. In case of the fcc Fe/Cu(100) films this phenomenon is not observed: For films thicker than 1 ML the easy axis is always perpendicular up to 15 ML where the film disintegrates.

Possibly the observed tetragonal distortion of the fcc lattice [3] induces an extra structure related anisotropy supporting a perpendicular easy axis.

Perpendicularly magnetized materials are potentially useful for high density magnetic data storage. Thermomagnetic writing in fcc Fe/Cu(100) has been shown to be feasible together with subsequent reading of the written information by spin-polarized photoemission, using for both processes - heating and photoemission - the same pulsed KrF excimer laser. At present, for magnetic recording purposes perpendicularly magnetized hcp Co/Pt(111) superlattices are actively investigated in many laboratories due to their unique property of having a Kerr rotation which increases towards shorter wavelengths.

Fig. 2 illustrates that the 1 ML film does not consist of superparamagnetic islands as observed in similar systems for not well annealed rough interfaces [13]. In superparamagnetism the magnetization scales above the blocking temperature with $\mu(T)H/kT$ where $\mu(T)$ is total magnetic moment of the particle. Since the magnetization curve shows no hysteresis effect at all at 30 K this condition is fulfilled. At 260 K the saturation field is clearly smaller than at 30 K: a fact which is incompatible with superparamagnetism both because the $1/kT$ factor and $\mu(T)$ are smaller at high temperature. In contrast, for a non-superparamagnetic ferromagnetic film the smaller saturation field finds a simple explanation, because $H_{sat} = 4\pi M$ (for a film with shape anisotropy only) and M at 260 K is smaller by roughly a factor 7 compared to 30 K, as Fig. 2 shows. The Curie temperature of the 1.2 ML fcc Fe/Cu(100) film is about 270 K.

A further important observation from Fig.1 is that the films with perpendicular easy axis are magnetically saturated at remanence, i.e., they consist of a single domain. This is remarkable because 1) the classical theory of Kooy and Enz [14] predicting single domain structure below a critical thickness d is found to apply (gain in demagnetizing energy ($\sim d^2$) does not compensate for the cost of domain wall energy ($\sim d$) and, secondly, the unavoidable disruption of the overlayer due to terraces in the substrate surface separated by steps is ignored by the domain structure. Interestingly, similar observations have been made in in-plane magnetized systems [15].

The experimental determination of the magnetic ordering temperature in thin films is even more problematic than in 3 dimensions: whenever the film is not in full saturation at $H = 0$ a change for instance in the spin-polarization P of the photoelectrons is bound to be influenced primarily by domain formation and not by temperature. On the other hand, an external magnetic field acts like a magnetic anisotropy and thus possibly fakes a Curie temperature higher than the one at $H = 0$ leading to a tailing of the magnetization which must be expected to be even more serious than in 3 dimensions. Being aware of these pitfalls the Curie temperature of fcc Fe/Cu(100) films more than 5 ML thick - where no dispute about the epitaxial nature of the system exists - is found to be close to 300 K. Since in metallic films $t > 5$ ML the bulk properties of the material are fully developed - which can be

tested e.g. by comparing the magnetic properties of epitaxial films of bcc Fe/Ag(100) with those of the bulk metal [16] - this value is considered to represent the bulk value of T_c for epitaxial fcc Fe/Cu(100).

ACKNOWLEDGEMENTS

We thank H.C.Siegmann for his continued interest in this work. The financial support by the Schweizerische Nationalfonds is gratefully acknowledged.

REFERENCES

- 1) Magnetism in Ultrathin Films; Special issue of Applied Physics A (Editor: D. Pescia): Appl. Phys. A49, 437-523 (1989); Appl. Phys. A42, 547-619 (1989)
- 2) D.A.Steigerwald and W.F.Egelhoff jr., Phys.Rev.Lett. 60, 2558 (1988); D.Pescia, M.Stampanoni, G.L.Bona, A.Vaterlaus, F.Meier, G.Jennings, and R.F.Willis, Phys. Rev.Lett. 60, 2558 (1988).
- 3) S.H.Lu, J.Quinn, D.Tian, and F.Jona, Surf.Sci. 209, 364 (1989)
- 4) F.Bloch, Z.Physik 61, 206 (1930)
- 5) C.A.Neugebauer, Z.Physik 176, 207 (1963)
- 6) U.Gradmann, Appl. Phys. 3, 161 (1974)
- 7) M.Campagna, D.T.Pierce, F.Meier, K.Sattler, and H.C.Siegmann, Adv. Electronics and Electron Physics 41, 113 (1978)
- 8) C.Herring and C.Kittel, Phys. Rev. 81, 869 (1951)
- 9) J.M.Kosterlitz and D.J.Thouless, Progr. Low Temp. Physics VII B, 371 (1978)
- 10) V.I.Pokrovskii and M.V.Feigel'man, Zh. Kksp.Teor.Fiz. 72, 557 (1977) (Sov. Phys. JETP 45, 291 (1977))
- 11) J.G.Gay and R.Richter, J. Magn. Magn. Mat. 1990 (to be published)
- 12) L.Néel, Compt. Rend. Acad. Sci. 237, 1468 (1953); L.Néel, J. Phys. Radium 15, 225 (1954); for a review see: I.S.Jacobs and C.P.Bean, in "Magnetism" (Editors: G.T.Rado and H.Suhl), Academic Press 1963, Vol. III, p.314 ff.
- 13) C.J.Gutierrez, H.D.Wieczorek, Z.Q.Quin, and J.L.Walker, J.Magn.Magn.Mat. 1990 (to be published)
- 14) C.Kooy and U.Enz, Philips Res.Rep. 15, 6 (1960)
- 15) H.P.Oepen, J.Magn.Magn.Mat. 1990 (to be published)
- 16) M.Stampanoni, Appl.Phys. A49, 449 (1989)

FERROMAGNETIC RESONANCE STUDIES OF BCC EPITAXIAL ULTRATHIN

Fe(001)/Cu(001) BILAYERS AND Fe(001)/Cu(001)/Fe(001) TRILAYERS

Z. Celinski, B. Heinrich, J.F. Cochran, K. Myrtle and
A.S. Arrott

Surface Physics Laboratory, Physics Department
Simon Fraser University, Burnaby B.C., Canada V5A-1S6

We have epitaxially grown a new phase of Cu, bcc Cu on bcc Fe(001). This fact allowed us to investigate bilayers of Fe(001)/Cu(001), Cu(001)/Fe(001) and trilayers of Fe(001)/Cu(001)/Fe(001) grown on Ag(001) single crystal substrates using Ferromagnetic Resonance. The role of bcc Cu on the magnetic properties (magnetic moment and anisotropies) of Fe(001)/Cu(001) bilayers and Fe(001)/Cu(001)/Fe(001) trilayers is reported. Magnetic coupling between Fe layers separated by a bcc Cu interlayer was investigated as a function of the interlayer thickness and temperature. The crossover from ferromagnetic to antiferromagnetic coupling was observed for Cu interlayers thicker than 8 ML.

In this paper we report Ferromagnetic Resonance (FMR) measurements on ultrathin Fe(001)/Cu(001) and Cu(001)/Fe(001) bilayers and Fe(001)/Cu(001)/Fe(001) trilayers. These structures were prepared using Molecular Beam Epitaxy (MBE) on the (001) face of bulk silver single crystals. The Ag (001) surfaces were oriented within 0.25° of the [001] crystallographic direction. The epitaxial growth was carried out in the low 10^{-10} Torr range. Reflection High Energy Electron Diffraction (RHEED) and a thickness monitor were used to control the growth process. Auger Electron Spectroscopy (AES) was used to monitor coverage quality. Cu grows on Fe(001) and Ag (001) in a metastable bcc structure for the first 10 - 11 monolayers (ML). Details of the growth of bcc Fe/Cu structures were presented in separate paper at this School¹ and by Heinrich et al.².

The magnetic properties of Fe/Cu and Fe/Cu/Fe structures were determined by 36 GHz FMR measurements carried out at room, dry ice and liquid nitrogen temperatures. The samples, 15mm in diameter were used as the endplate of a TE₀₁₂ (doughnut mode) cylindrical cavity which gave constant sensitivity independent of the orientation of the magnetic field in the plane of the specimen. We used standard lock-in amplifier detection techniques with 176 Hz field modulation to detect the signal and 60 kHz repeller modulation to stabilize the frequency of the klystron to the resonant frequency of the cavity containing the sample. Measurements were carried out with a constant voltage on the detector diode, using an approach similar to that of Feher³.

From a magnetic point of view our structures are ultrathin, i.e. the thickness of each magnetic layer is smaller than the exchange length¹ (33Å for Fe). This fact causes all of the spins within the layer to be aligned parallel to one another. Each Fe layer responds as a unit with its own magnetic properties. The total intensity of the FMR signal (doubly integrated field derivative of the absorption or χ'') is directly proportional to the total magnetization of the specimen⁴

$$I \propto M_s d \frac{[H_{\text{FMR}} + (4\pi M_s)_{\text{eff}}]}{[2H_{\text{FMR}} + (4\pi M_s)_{\text{eff}}]}$$

where M_s is the saturation magnetization, d is the thickness of the film, H_{FMR} is the FMR field (the zero crossing of the field derivative of the power absorption) and $(4\pi M_s)_{\text{eff}}$ is an effective demagnetizing field. By collecting FMR data over the same effective range of the applied external field H (i.e. from $H_{\text{FMR}} - 3.5\Delta H$ to $H_{\text{FMR}} + 3.5\Delta H$ where ΔH is the FMR linewidth (FWHM)) we are able to investigate the effect of the Cu overlayer on the magnetic moment of the Fe layer. At 77K we have found that the total magnetic moment in the sample Ag/5Fe/10Cu/20Au (5Fe means 5 ML of Fe etc.) is smaller (by appr. 9.4%) than the corresponding total magnetic moment in the reference sample Ag/5Fe/20Au used in all of our measurements. A 9.4% decrease, measured at LN₂ temperature, in the total magnetic moment of the 5ML thick Fe films corresponds to a decrease of $1.0\mu_B$ per interface atom, assuming that the magnetization of the reference sample is equal to 21.55 kOe⁴. From the resonance condition one can determine the effective demagnetization field $(4\pi M_s)_{\text{eff}} = 4\pi M_s - H_u$, where H_u is the uniaxial perpendicular field. The uniaxial field in the sample Ag/5Fe/10Cu/20Au is always larger than in the reference sample, see Table I. The in-plane 4th order anisotropy¹ K_1 for an Fe/Cu bilayer was only slightly larger than the value of K_1 for the reference sample. Magnetic parameters of the standard 5Fe/20Au sample and the bilayers 5Fe/12Cu and 9Cu/10Fe are shown in Table I.

TABLE I. Magnetic parameters of the Fe/Cu and Cu/Fe bilayers. The $2K_1/M_s$ is the strength of the in-plane fourth - order anisotropy field (Ref.5).

| Sample | $(4\pi M_s)_{\text{eff}}$ (kG) | | $2K_1/M_s$ (kOe) at 77K |
|------------------|-----------------------------------|--------|-------------------------------|
| | at 295K | at 77K | |
| Ag/5Fe/20Au | 6.10 | 6.93 | 0.220 |
| Ag/5Fe/10Cu/20Au | 3.08 | 1.72 | 0.280 |
| Ag/9Cu/10Fe/20Au | 13.50 | 13.75 | 0.285 |

We have studied the exchange coupling between Fe layers separated by bcc Cu using the trilayer structure 5Fe/xCu/10Fe for $x=5,6,7,8,9,9.5,11.6,12.6,13.7$. Two Fe layers with different magnetic properties are needed to observe the acoustic and optical modes¹. In our case this was achieved by using 5 and 10 ML Fe films which exhibit different $(4\pi M_s)_{\text{eff}}$, see Table I. The positions and intensities of both modes depend in a complicated way on the properties of the individual layers and on the strength of the exchange coupling A^{AB} , for a detailed discussion see¹. We calculated A^{AB} by means of a least squares fitting

routine using as starting parameters the magnetic properties of the Fe/Cu and Cu/Fe bilayers along with the detailed theoretical model of exchange coupled ultrathin magnetic bilayers⁵.

Antiferromagnetic coupling² was observed for Cu interlayers thicker than 8ML. At room temperature these samples showed both the acoustic and optical FMR modes. For trilayers with $x=9, 9.5$ and 11.6 ML the exchange coupling A^{AB} was so strong at 77K that only the acoustic mode was observed. Strong antiferromagnetic coupling decreases the intensity of optical mode and shifts it to high magnetic fields which are beyond our experimental limits. At room temperature the maximum antiferromagnetic coupling occurred at ~ 11 ML (see Fig.1). It is worth mentioning that during the growth process Cu undergoes a structural reconstruction for thicknesses above 10-11ML. Our results show that antiferromagnetic coupling does not depend on the structural change in the Cu interlayer. For all temperatures we observed ferromagnetic coupling in trilayers with Cu interlayer thickness between 5 and 8ML. Only the acoustic mode was observed for samples having 5 and 6ML of Cu. The sum of the moments from 5Fe/Cu and Cu/10Fe bilayers is close to the measured moment in these trilayers. The trilayers with 7 and 8ML thick interlayers have a small enough ferromagnetic coupling that both the acoustic and optical modes could be observed allowing one to determine the ferromagnetic exchange coupling A^{AB} . Fig. 1 shows the thickness dependence of the exchange coupling on the Cu interlayer thickness.

We have studied the exchange coupling as a function of temperature in trilayers with 8 and 13.7ML thick Cu interlayer (see Fig. 2). The sample

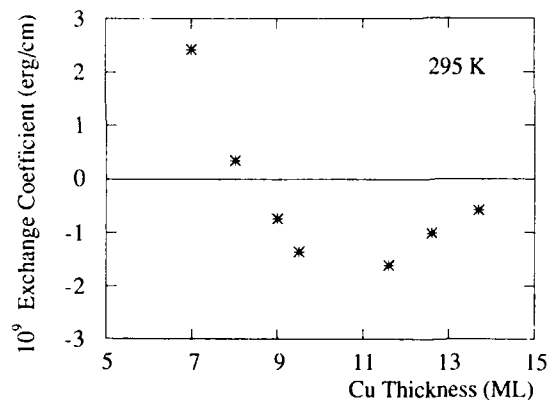


Fig.1 The exchange coupling coefficient A^{AB} in Fe/Cu/Fe trilayers as a function of Cu interlayer thickness at room temperature.

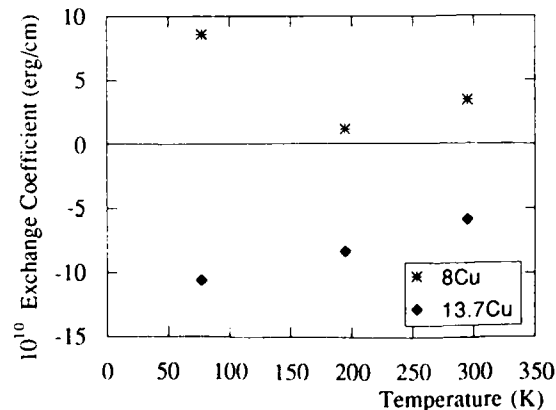


Fig. 2. The exchange coupling coefficient A^{AB} as a function of temperature in Fe/Cu/Fe trilayers with 8 and 13.7 ML thick Cu interlayer.

with 13.7ML of Cu exhibited a monotonically increasing antiferromagnetic coupling (almost a factor of 2) when the temperature decreased from 295 to 77K. The 8ML Cu sample exhibited a non monotonic change of ferromagnetic coupling between 295 and 77K (see Fig.2). This is not a surprising result if we assume that the exchange coupling is electronic in nature. This 8ML sample is very close to the thickness where the coupling changes from ferromagnetic to antiferromagnetic. The changes in band structure induced by thermal expansion can easily effect the balance between ferromagnetic and antiferromagnetic tendencies. From magnetization measurements we have estimated that the change of the magnetic moment in 5Fe/10Cu and 9Cu/10Fe bilayers is not greater than 20 to 25% between 295 and 77K. This result suggests that the exchange coupling mechanism is not due to dipole interactions but is caused by electronic properties.

Recently ^{6,7,8} a great deal of attention has been paid to the antiferromagnetic coupling in the Fe/Cr/Fe system. Comparing the bcc Fe/Cu/Fe and bcc Fe/Cr/Fe systems we note that the Cu interlayer couples the Fe layers approximately as strongly (for equivalent interlayer thicknesses) as Cr. The maximum of antiferromagnetic coupling in Cr occurs around 6ML while in Cu it occurs at 11ML. Therefore the antiferromagnetic coupling through Cu is more spatially expanded than in Cr. Unlike Cr the Cu does not have any holes in its d band and therefore the strength and spatial extent of the antiferromagnetic coupling in Cu is a surprise and challenge to theoretists.

We have found that: (1) A Cu overlayer decreases the magnetic moment in Fe/Cu and Cu/Fe bilayers, approximately $1.0\mu_B$ per interface atom. (2) Uniaxial perpendicular fields and the in-plane 4th order anisotropy K_1 in the Fe layer were only weakly affected by the Cu overlayer. (3) Magnetic coupling in bcc Fe(001)/Cu(001)/Fe(001) trilayers changes from ferromagnetic to antiferromagnetic for Cu interlayer thicknesses between 8 to 9 ML. (4) The maximum of antiferromagnetic coupling occurred at ~ 11 ML of Cu. (5) The antiferromagnetic coupling is not affected by the lattice transformation observed for Cu interlayers thicker than 10 - 11ML. (6) Ferromagnetic and antiferromagnetic coupling exhibits strong temperature dependence. This suggests that the source of the magnetic coupling is of a electronic nature.

ACKNOWLEDGEMENTS

The authors would like to thank the National Science and Engineering Research Council of Canada for financial support without which this work would not be possible.

REFERENCES

1. B.Heinrich, A.S.Arrott, J.C. Cochran, Z. Celinski, K.Myrtle, this issue
2. B.Heinrich, Z.Celinski, J.F.Cochran, W.B.Muir, J.Rudd, Q.M.Zhong, A.S.Arrott, K.Myrtle, J.Kirschner, Phys.Rev.Lett., **64**, 673, 1990
3. G.Feher, Bell Syst. Tech. J., **36**, 449, 1957
4. B.Heinrich, A.S. Arrott, J.C.Cochran, K.B.Urquhart, K.Myrtle, Z.Celinski, Q.M.Zhong, Mat.Res.Soc.Symp.Proc., **151**, 177, 1989
5. B.Heinrich, S.T.Purcell, J.R.Dutcher, K.B.Urquhart, J.F.Cochran, A.S.Arrott, Phys.Rev.B, **38**, 12879, 1988
6. M.N.Baibich, J.M.Broto, A.Fert, F.Nguyen Van Dan, E.Perroff, P.Etienne, G.Creuzet, A.Friedrich, J.Chazelas, Phys.Rev.Lett. **61**, 2472 (1988)
7. J.J.Krebs, P.Lubitz, AChaiken, G.A.Prinz, Phys.Rev.Lett., **63**, 1645, 1988
8. J.Barnas, P.Grunberg, J.Magn.Magn.Mater. (to be published)

LASER ABLATION DEPOSITION OF METALLIC THIN FILMS

James P. Gavigan*

Laboratoire Louis Néel - C.N.R.S.
25 av. des Martyrs
B.P. 166X - 38042 Grenoble Cedex, France

INTRODUCTION

Laser ablation deposition (LAD) is a thin film preparation technique in which a high powered laser beam impinges on a target causing the ejection of material which is subsequently collected on an appropriately placed substrate resulting in the growth of a thin film. In principle, this is a very elegant and simple technique compared to other established vacuum deposition methods (sputtering, electron gun & thermal evaporation, etc..) and discussion of its many advantages (e.g. congruent deposition & composition control, high deposition rates, ablation of any material,...) can be found in the literature¹. However, coupled with its versatility are the very complex problems of: 1) the laser-matter interaction which varies drastically with both laser parameters (wavelength λ , pulse length τ , irradiance I ,...) and the optical/thermophysical properties of the target material, and 2) the non-equilibrium processes governing the expansion and interactions of the ejected material and the subsequent nucleation and growth of a thin film. In spite of the huge body of literature which exists on various aspects of LAD, unfortunately no complete coherent description has been formulated which could serve as a practical guide.

In this paper therefore, the aim is to discuss some of the LAD processes in the case of metals and to try to extract some practical guidelines from available experimental results. In the field of nanostructured magnetic materials, the most exciting possibility for LAD is in the growth of epitaxial films and multilayers of compounds such as those between rare earths and transition metals (as well as ferromagnetic oxides). Epitaxial films of YNi_5 have recently been grown on sapphire substrates using this technique².

LASER - METAL INTERACTION

In this section, aspects of the laser - metal interaction are considered in the light of commonly available laser parameters: i.e. wavelengths in the range 10.6 μm (CO_2 laser) to 193 nm (Excimer/ArF laser),

* Post-doctoral research fellow of the Commission of the European Communities.

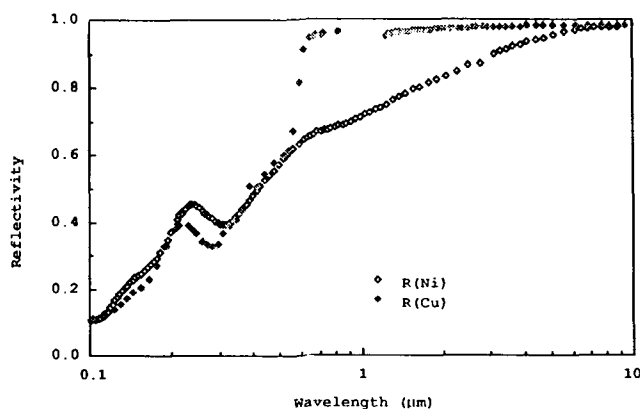


Figure 1. Reflection coefficient of Cu and Ni as a function of wavelength, calculated using experimental optical constants³.

irradiances (fluences) up to 10^{12} Wcm^{-2} (100 Jcm^{-2}) and pulse durations from a few picoseconds up to a millisecond.

The interaction of an intense laser pulse with a metal target is highly non-linear, involving extreme transient phenomena associated with the target's optical and thermal properties (temperature dependence of reflectivity, thermal conductivity, heat capacity,...), phase changes (melting, vaporisation, critical state, plasma formation & its interaction with laser pulse) and mechanical response (recoil-pressure-induced melt ejection, shock wave spall,...). In a metal, the absorption of light energy is a purely pyrolytic (thermal) process (as opposed to a photolytic process which involves bond breaking, photo-ionization, etc), provided the rate of arrival of incident energy is on a time scale longer than the relaxation time for electron-electron (10^{-16} s) and electron-phonon interactions (10^{-14} s)³. This condition is satisfied by most types of laser radiations except perhaps femtosecond pulses and giant laser pulses for plasma fusion studies which can generate irradiances greater than 10^{17} Wcm^{-2} ⁴. The laser pulse therefore acts primarily as a heat source at the target surface, but the generation of appreciable evaporation for thin film deposition depends very much on the afore mentioned transient conditions produced by the laser.

Quasi-equilibrium situation

For low incident irradiances ($\approx 10^6 \text{ Wcm}^{-2}$), evaporation is a rate-limited process and is directly proportional to the exponential temperature dependence of the vapour pressure; i.e. surface melting and evaporation occur under quasi-equilibrium conditions. The amount of energy absorbed depends on the surface reflectivity $R (= [(n-1)^2 + k^2]/[(n+1)^2 + k^2])$, n & k are the optical constants) which in turn depends on wavelength (λ) (figure 1), temperature (T) and to some extent on surface morphology. R normally decreases with decreasing λ (figure 1) making U.V. wavelengths more favourable. Note that on melting, metals show a drop in reflectivity as do solid surfaces with increasing rugosity⁵. The surface temperature is determined by the volume of metal (v) heated by the absorbed energy and its thermophysical properties. For a uniform surface irradiance, v is proportional to the thickness of the heated layer. Two situations are possible: 1) in the first case, when $l_0 \geq l_T$ (where $l_0 = \lambda/4\pi k$ is the optical absorption depth and $l_T = \sqrt{2Dt}$ is the thermal diffusion depth, where t is the pulse duration, $D = \kappa/C_v\rho$ is the thermal diffusivity,

κ is the thermal conductivity, C_v is the heat capacity and ρ is the density), then $v \propto l_0$; 2) in the second case when $l_0 < l_T$, $v \propto l_T$. For metals, a typical value of l_0 is 20 nm while typical values of $l_T \approx 1 \mu\text{m}$ (ns pulses) and $\approx 50 \text{ nm}$ (ps pulses), with D in the range $0.1 - 1 \text{ cm}^2\text{s}^{-1}$; i.e. $l_0 < l_T$. The average temperature rise in the heated layer is given by $\Delta T = [I^\circ\text{C}] / [C_v \rho \sqrt{2D\tau}]$ where I is the absorbed portion of the incident irradiance. If the amount of energy absorbed by the effected volume equals or surpasses the heat of sublimation H_s , then a fully developed evaporation regime establishes itself which is characterized by the threshold $I_{thr} = H_s \rho \sqrt{D/\tau}$. Carrying out an order of magnitude calculation (taking $H_s = 10 \text{ kJg}^{-1}$, $\rho \approx 10 \text{ gcm}^{-3}$, $D \approx 0.5 \text{ cm}^2\text{s}^{-1}$), one gets values of I_{thr} equal to 10^6 , 10^8 and 10^{10} Wcm^{-2} for respectively ms, ns and ps pulse durations.

Breakdown of quasi-equilibrium

In what has been stated so far, a quasi-equilibrium situation has been assumed. In reality, for thin film deposition, when working in a fully developed evaporation regime, this is far from being the case. Thus the above description can only be considered as a poor approximation. Indeed, under intense laser irradiances, the normal optical response of a metal is no longer valid as all target materials breakdown into a highly absorbing state (heating rates can reach over 10^{12} Ks^{-1} resulting in surface temperatures of several thousands of Kelvin in less than a nanosecond). A number of authors have commented on this fact^{1,6-8} of which ref.7 includes a coherent explanation based on a metal-insulator transition of the melt which becomes a liquid dielectric as the interaction drives the temperature to values of the order of the critical temperature T_c (the temperature above which a substance has no liquid - vapour transition; i.e. a substance cannot exist in the liquid state above T_c regardless of pressure). The recoil pressure of the ejected material which permits the melt to reach the critical state is of the order of 10^3 atm .^{7,9}

In the quasi-equilibrium situation considered above, the thermo-physical properties C_v , κ , ρ , etc were assumed to be constant, but the extreme transient temperatures attained for fully developed evaporation demand the consideration of their temperature dependence. A comprehensive

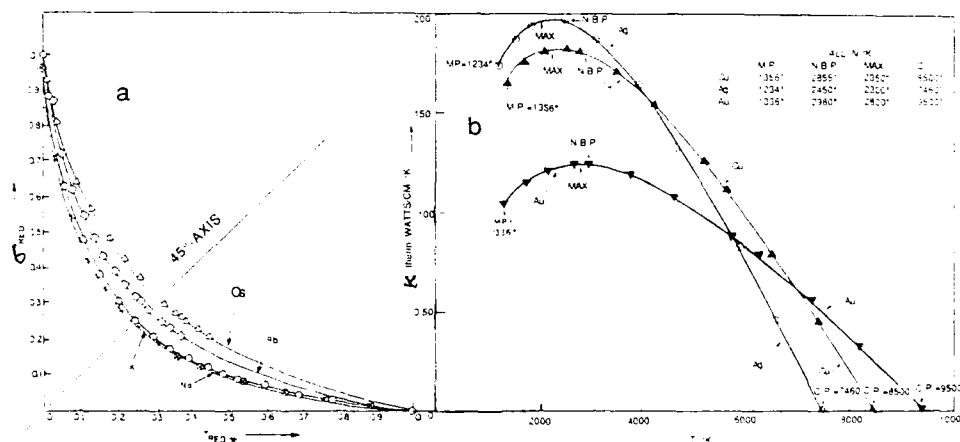


Figure 2. a) Reduced electrical conductivity $\sigma_{RED} = \sigma_{mp} / \sigma_T$ versus reduced temperature, $(T - T_m) / (T_c - T_m)$ for K, Na, Rb & Cs; b) thermal conductivity versus T for Cu, Ag & Au with listed values of melting point, normal boiling point, curve maximum and critical point¹⁰.

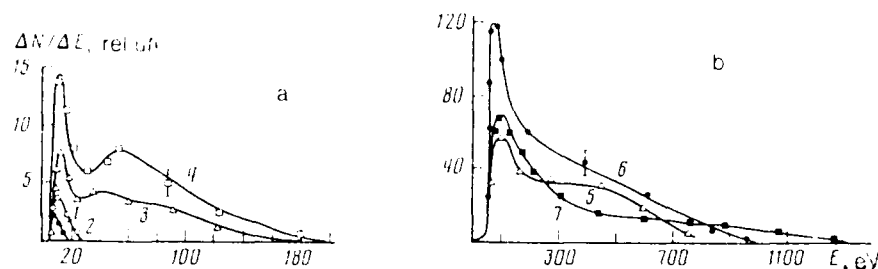


Figure 3. Energy spectra of Co atoms for $I = 1) 9.10^7$ 2) 1.10^8 3) 2.10^8 4) 3.10^8 5) $2.5.10^9$ 6) $3.5.10^9$ 7) 5.10^9 Wcm^{-2} .

review article by Grosse¹⁰ for example, discusses the electrical (σ) and thermal (κ) conductivities of metals over their entire liquid range from the melting point T_m to the critical temperature T_c (figure 2). σ decreases exponentially to reach zero at T_c (note that σ is related to the optical constants via $n\kappa = \mu\sigma\lambda/c$ where μ is the permeability) and that κ varies in a parabolic manner increasing from T_m to a maximum before gradually falling off to zero at T_c . Such behaviour is consistent with the results and interpretation of ref.7.

PLASMA PRODUCTION

A feature of LAD is that the ejected vapour often appears as a luminous plume just above the target impact region. In this section, the nature of this expanding plume and its influence on the interaction processes is considered.

An interesting paper by Bykovskii et al¹¹ reports a detailed study of the neutral and ionic composition of the plume issuing from several metal targets (e.g. see figure 3) for irradiances up to 10^{10} Wcm^{-2} . At and above I_{thr} , the plume is essentially composed of neutral species ($E \approx 10$ eV, $v \approx 1000$ ms^{-1}) with a second higher threshold corresponding to the appearance of an ionic component (plasma). Further increasing I increases the plasma density which in turn will increasingly absorb the incoming laser pulse through inverse Bremsstrahlung processes, possibly resulting in total screening of the target. In such a situation, the laser energy goes into heating the plasma, generating high kinetic energy excited neutral and ionic species which play an important role in the growth mechanism of the thin films. The energy spectra of both ions and neutrals can reach up to a few keV, the average ion energy always being higher than that of the neutrals. Experiments also show that increasing I translates into an increased kinetic energy of the expanding plume rather than an increase in the proportion of excited state species.

Note that a plasma is characterized by a frequency ω_p where $\omega_p^2 = [4\pi e^2 n_e]/m_e$ such that any frequency less than ω_p is absorbed (n_e is the particle density in the plasma). Thus the cut-off plasma densities for a Co_2 ($\lambda = 10.6$ μm), a Nd:YAG ($\lambda = 1.06$ μm) and an excimer ($\lambda = 120$ nm) are respectively $n_e = 10^{19}$, 10^{21} and 10^{23} cm^{-3} ⁴. This means that for a given irradiance value, more energy is coupled directly to the target for U.V. wavelengths resulting in a much higher plasma density than for I.R. wavelengths. Further discussion of the properties of these laser produced plasmas can be found in 4, 8 and in a series of three papers by Gapanov and co-workers¹²⁻¹⁴.

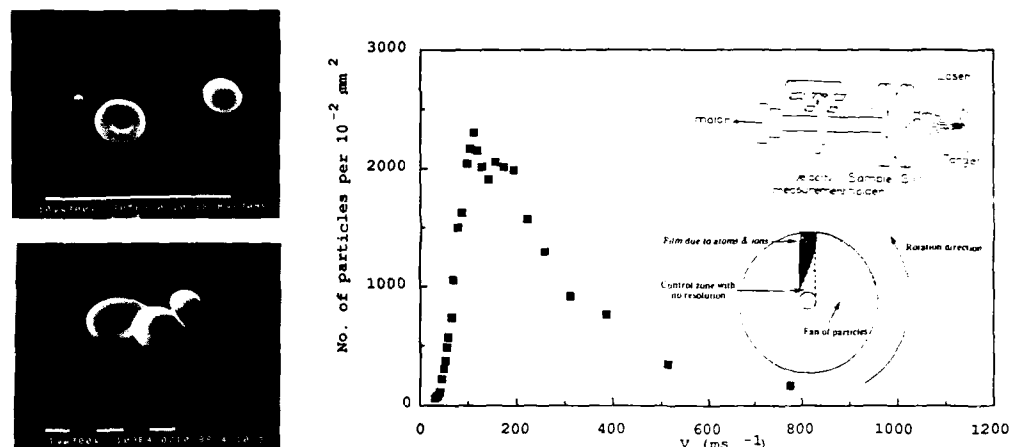


Figure 4. Electron microscope images of deposited metal droplet particles, with a measured velocity distribution for an Y deposit ($1.064 \mu\text{m}/20 \text{ ns}$, 10 Jcm^{-2}); insets show rotating substrate device and schematic diagram of a typical deposit.

MELT EJECTION

The major inconvenience of LAD is due to the recoil pressure of the escaping vapour plume acting like an acoustic "jack hammer" on the melt surface with the resulting effect of flushing out the liquid metal from the impact region, giving rise to a crater and a spray of liquid droplets of size $0.1\text{--}10 \mu\text{m}$ (figure 4). These droplet particles can constitute a mass an order of magnitude greater than that of the ejected vapour and are deposited on the substrate spoiling the film quality. This melt ejection is obviously a threshold limited phenomenon (depending on melt density, surface tension, recoil pressure,..) and it has been modeled by a number of authors¹⁵⁻¹⁶. Unfortunately, it always occurs when operating in practical thin film preparation conditions with fully developed evaporation. Other contributing mechanisms than the above have been suggested^{1,8,17} as well as several possible methods for solving the problem^{1,14,18}. Given that the average velocity of the droplets ($\approx 200 \text{ ms}^{-1}$ - figure 4) is orders of magnitude lower than that of atomic and ionic species ($10^4\text{--}10^5 \text{ ms}^{-1}$), the idea of a mechanical velocity filter is a simple and feasible solution to the problem. The idea consists of intercepting the droplet particles in their flight path from the target to the substrate. The choice of a maximum

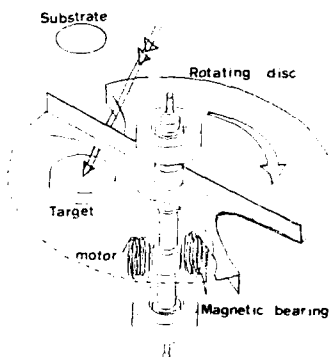


Figure 5. Diagram of a prototype UHV compatible velocity filter designed to rotate at 500 Hz.

cut-off velocity of 1000 ms^{-1} and of a typical target-substrate distance of 10 cm, determines a shutter time of 1 ms. This can be achieved by rotating a disc ($r = 10 \text{ cm}$) with a 5 cm slit at 800 Hz (circumferential velocity of $\approx 500 \text{ ms}^{-1}$) (figure 5)¹⁹.

CONGRUENT EVAPORATION/DEPOSITION

Congruent evaporation of a multicomponent target is achieved using LAD due to the fact that with intense laser pulses, temperatures of several thousands of degrees are reached almost instantaneously resulting in the simultaneous evaporation of all elements irrespective of their equilibrium vapour pressure versus temperature behaviour. It also depends on the complete thermal cycle associated with melting and resolidification being faster than the time necessary for appreciable segregation or fractionation of the different species to occur via atomic diffusion. Using values for $D = 0.5 \text{ cm}^2\text{s}^{-1}$ and a typical value for D_{atom} (the atomic diffusion coefficient)

Table I. Melt depth, resolidification & diffusion of metals versus τ

| Pulse duration: τ | 35 ps | 20 ns | 1 ms |
|---|----------------------|---------------------------|-----------------------------|
| Melt lifetime: t_{melt} | 1 ns | 1 ms | 300 ms |
| Melt depth: $\sqrt{2D\tau}$ | 60 nm | 1.5 μm | 0.3 mm (300 μm) |
| Solidification vel: u | 100 ms^{-1} | 10^{-3} ms^{-1} | 10^{-4} ms^{-1} |
| diffusion distance: $\sqrt{[2D_{\text{atom}}\gamma/u]}$ | 1.4 \AA | 36 nm | 0.1 μm |

Note: Typical values of 0.5 & $5 \times 10^{-5} \text{ cm}^2\text{s}^{-1}$ were taken for respectively D & D_{atom} .

for liquid metals of $5 \times 10^{-5} \text{ cm}^2\text{s}^{-1}$,²⁰ one can see in Table I that the diffusion distance ($= \sqrt{[2D_{\text{atom}}\gamma/u]}$, where γ is the inter-atomic distance $\approx 2 \text{ \AA}$) associated with the passing of the solidification front (at a speed u) is much less than the melt depth. In the case of ns and more so ms pulses, diffusion distances of greater than γ may lead to some segregation to the surface, but in spite of this, stoichiometric deposition is still maintained, even by ablating with repetitive rastering of the laser beam over the same target surface region.

PLUME - SUBSTRATE INTERACTION

The laser produced plume which can have particle densities up to 10^{20} cm^{-3} , expands rapidly into the vacuum towards the substrate and can give rise to instantaneous deposition rates of up to $10^{10} \text{ \AA s}^{-1}$, a condition not possible in other vacuum deposition techniques. Such a situation gives rise to an "effective vacuum" a few orders of magnitude lower in terms of impurity incorporation¹. These large particle fluxes are characterized by a high degree of supersaturation, $\Delta\mu = kT \ln(P/P_e)$ (where T is the plasma temperature and P & P_e are the actual and equilibrium pressures in the plume. Metev and Meteva²¹ have proposed a kinetic model for the nucleation and growth of thin films for such far-from-equilibrium conditions. They propose an analytical expression to predict the mean monolayer coverage at which a film becomes continuous as a function of deposition conditions and material (film & substrate) properties.

Given the presence of high energy species in the plume, partial sputtering of the substrate and resputtering of the film may occur, giving rise to a collisional region at the substrate surface which acts as a thermalizing zone for the incoming flux. It has been suggested that such a condition favours epitaxial growth. Congruent deposition is also favoured

since the collisional region acts as a remixing zone to compensate for any segregation that may occur in the inertial expansion of the plume from the target to the substrate. Note however that for the appropriate LAD conditions, the tendency in any case is for no segregation to occur due to the high supersaturation: i.e. the inertial expansion is diffusive hydrodynamic with the mean free path $\bar{m} \ll$ the target - substrate distance d , compared to a more conventional situation of a free molecular flux, where with $\bar{m} > d$, expansion can lead to segregation.

Other parameters play an important role in the plume - substrate interaction, such as substrate temperature and morphology and parameters particular to a given experimental situation (such as the interaction chemistry of the ablated elements and the elements in the substrate, etc.). In fact this whole area of LAD is the least disposed to a systematic type study as is evident from the few reports in the literature. Indeed, a general description of the kinetics of thin film growth for equilibrium conditions is itself an enormous task whose present status is far from complete.

DISCUSSION AND CONCLUSIONS

At this point, some general statements can be made about LAD of metallic thin films.

Firstly, the choice of laser wavelength is not critical so long as the irradiances are high enough to cause fully developed evaporation of the target. The most practical lasers from this point of view are pulsed nanosecond Q-switched Nd:YAGs and excimers with energy per pulse of the order of a Joule, which easily generate the necessary irradiances and can be operated at high repetition rates. The disadvantage of going to ps pulses is that the threshold irradiance increases, similar energies per pulse as for ns are harder to attain, evaporation is less efficient and the damage threshold for the laser optics is more critical. For ms pulses, while the evaporation is more efficient, the melt ejection problem is considerably worse due to the large melt depth. Furthermore, the necessary irradiances (depending on the focusing), require very large pulse energies ($\approx 10 - 10^3$ Joules). Such lasers are more suited to industrial type applications such as drilling and cutting given the large crater depths per pulse (up to a millimeter). Nonetheless, they still can be used to deposit films, and, as the average energy of the species in the plume is low (≈ 0.5 eV) compared to working with shorter pulses, one can get very smooth films and sharp interfaces due to the absence of high energy induced damage and mixing^{14,21}. However, deposition rates of $0.1 \mu\text{m}$ per pulse¹⁴ exclude the growth of ultrathin films of nanometer dimensions.

One process however, which is sensitive to wavelength is the laser pulse - plume interaction. Given that I.R. wavelengths are more easily absorbed than the visible or U.V., they will generate higher kinetic energy species (through plasma heating) but lower particle densities. On this basis, choice of wavelength will depend on the trade-off between the beneficial effects on the film growth mechanism²² and the induced damage of energetic particles. In practice, LAD will always generate particles of non-thermal energies (≥ 1 eV) even for near-threshold ablation, thus giving high adatom mobility on the substrate and favouring epitaxy in the absence of very high energy species (≥ 100 eV). The epitaxial YNi_5 films of ref.2 were grown for such near-threshold ablation conditions.

Another advantage of near-threshold ablation is that much less melt ejection of droplets occurs than for far-above-threshold ablation. However, deposition rates are low. It is also possible to reduce the amount of melt ejection by defocusing the laser beam to irradiate a large surface area.

While melt ejection will still occur¹⁶, the droplets will follow laterally divergent trajectories from the evaporating surface normal²³ (i.e. the direction of expansion of the vapour plume), as opposed to emerging as a collimated jet for a tightly focused beam. In such a situation, the deposited droplet density will be a strong function of the target - substrate distance. Such reduction in droplet deposition is also corroborated by experimental results showing a ϕ^{-1} dependence for crater depth per pulse at a fixed irradiance, where ϕ is the irradiated spot diameter²⁴.

In spite of these facts, if one wishes to exploit the versatility of LAD for a wide variety of materials, it is much better to have a process-parameter-independent means of dealing with the droplets such as the velocity filter described above (figure 5).

In conclusion, it may be said that LAD is a very powerful thin film preparation technique, the potential of which is only beginning to be exploited in the field of magnetic thin films and multilayers. Some of its aspects have been discussed in this paper with particular reference to metals, with the aim of identifying some general trends to act as guidelines for its use in the growth of droplet-free, ultra-thin, epitaxial films. An extensive review of LAD can be found in the paper by Cheung and Sankur¹, including discussions of other aspects of the technique not addressed in this paper.

ACKNOWLEDGEMENTS

The author is indebted to his collaborators at the Laboratoire Louis Néel (D. Givord, J.P. Rebouillat, Y. Souche, A. Liénard, O. Cugat and O.F.K. Mc Grath) with whom he has worked on LAD of metallic thin films for the past 20 months.

REFERENCES

1. J.T. Cheung and H. Sankur, Growth of thin films by laser-induced evaporation, CRC Critical Rev. in Sol. Stat. and Mat. Sci. 15:63 (1988).
2. J.P. Gavigan, D. Givord, A. Liénard, O.F.K. McGrath, J.P. Rebouillat and Y. Souche, Congruent evaporation and epitaxy in thin film laser ablation deposition (LAD) of rare earth transition metal elements and compounds, Mat. Res. Soc. Symp. Proc. Symposium on Laser Ablation for Material Synthesis, San Francisco, April 1990, to be published.
3. J.N. Hodgson, "Optical absorption and dispersion in solids", Chapman and Hall LTD, London (1970).
4. H. Hora, "Non linear plasma dynamics at laser radiation", Springer-Verlag lecture notes in Physics 102, Berlin/Heidelberg/New York (1979).
5. F. Cabannes, Propriétés optiques à haute température. Facteurs d'émission, in : "Les hautes températures" Vol. 2, G. Chaudron and F. Trombes eds., Masson et Cie, Paris (1973).
6. J.F. Ready, Effects due to absorption of laser radiation, J. Appl. Phys. 36:462 (1965).
7. V.A. Batanov, F.V. Bunkin, A.M. Prokhorov and V.B. Tedorov, Evaporation of metallic targets caused by intense optical radiation, Soviet Phys. JETP 36:311 (1973).
8. H. Sankur and J.T. Cheung, Formation of dielectric and semiconductor thin films by laser assisted evaporation, Appl. Phys. A 47:271 (1988).
9. V.S. Ban and B.E. Knox, Vaporization of antimony and tellurium in the vicinity of the critical point, J. Chem. Phys. 51:524 (1969).
10. A.V. Grosse, Electrical and thermal conductivities of metals over their entire liquid range, Rev. Hautes Tempér. et Réfract. 3:115 (1966).

11. Yu.A. Bykovskii, S.M. Sel'nov, E.A. Sotnichenko and B.A. Shestakov, Mass-spectrometric investigations of the neutral particles of a laser plasma, Sov. Phys. JETP 66:285 (1987).
12. A.D. Abhsakhalyan, Yu.A. Bityurin, S.V. Gapanov, A.A. Gudkov and V.I. Luchin, Processes occurring in an erosion plasma during vacuum deposition of films. I. Properties of a laser erosion plasma in the inertial expansion stage, Sov. Phys. Tech. Phys 27:969 (1982).
13. A.D. Abhsakhalyan, Yu.A. Bityurin, S.V. Gapanov, A.A. Gudkov and V.I. Luchin, Processes occurring in an erosion plasma during vacuum deposition of films. II. Interaction of laser erosion products with the solid surface, Sov. Phys. Tech. Phys 27:973 (1982).
14. S.V. Gapanov, A.A. Gudkov and A.A. Fraerman, Processes occurring in an erosion plasma during vacuum deposition of films. III. Condensation in gas flows during laser vaporization of materials, Sov. Phys. Tech. Phys 27:1130 (1982).
15. M. Von Allmen, Laser drilling velocity in metals, J. Appl. Phys. 47:5460 (1976).
16. V.A. Batanov and V.B. Fedorov, Flushing out the liquid phase - a new mechanism of producing a crater in planar fully developed evaporation of a metallic target by a laser beam, JETP Lett. 17:247 (1973).
17. R. Kelly and J.E. Rothenberg, Laser sputtering part III The mechanism of the sputtering of metals low energy densities, Nucl. Instr. and Meth. B 7/8:755 (1985).
18. H. Dupendant, J.P. Gavigan, D. Givord, A. Liénard, J.P. Rebouillat and Y. Souche, Velocity distribution of micron-size particles in thin film laser ablation deposition (LAD) of metals and oxide superconductors, Appl. Surf. Sci. 43:369 (1989).
19. J.P. Gavigan, D. Givord, A. Liénard, J.P. Rebouillat and Y. Souche, to be published.
20. N. H. Nachtrieb, Diffusion in liquid metals, in : "Liquid Metals", S.Z. Beer ed., Marcel Dekker Inc., New York (1972).
21. J.T. Cheung and H. Sankuuz, Semiconductor epitaxy and bandgap engineering by pulsed laser ablation, Mat. Res. Soc. Symp. Proc., Symposium on Laser Ablation for Material Synthesis, San Francisco, April 1990, to be published.
22. K.H. Müller, Role of incident kinetic energy of adatoms in thin film growth, Surf. Sci. 184:L375 (1987).
23. J.M. Baldwin, Comment on "Laser evaporation and elemental analysis", J. Appl. Phys., 44:3362 (1973).
24. M. Eyett and D. Bäuerle, Influence of the beam spotsize on ablation rates in pulsed laser processing, Appl. Phys. Lett. 51:2054 (1987).

Exchange Coupled Films for Magneto-Optic Applications

R. J. Gambino

IBM, T.J.Watson Research Center, Yorktown Heights, NY 10598

ABSTRACT

Exchange coupled bilayers are used to provide improved Kerr effect signals in magneto-optic storage media. The effective bias obtained by coupling one film to another can be used to control the switching characteristics of the medium. In simple systems the coupling can be characterized by an interfacial wall energy. When the magnetic layers are thin compared to the wall width, however, the wall energy model is not expected to hold.

INTRODUCTION

Magneto-optic digital information storage uses the Kerr rotation of the medium for data readout. The medium must also have certain magnetic characteristics suitable for stable information storage including perpendicular easy axis magnetic anisotropy, a square loop, and a high coercivity at ambient temperatures. It is sometimes difficult to find a single material with both good readout properties and good storage properties. This has lead to the suggestion^{1,2} that the medium be made of two materials exchange coupled together. One with good square loop properties is used to store the information (called the storage layer, ST). The other serves as a transducer for magneto-optic readout of the stored information (called the readout layer, RO). The RO layer must have a large Kerr rotation at the wavelength of interest but it need not be optimized with respect to coercivity or squareness. The magneto-optic (MO) Kerr effect only samples the magnetic state of the surface within the optical penetration depth. This makes it possible, in principle, to exchange couple two layers so that one largely controls the information storage characteristics while the other provides a larger Kerr effect readout signal.

Exchange coupling to improve the signal/noise ratio (SNR) at the wavelength of interest is not the only application in MO storage media. Other applications come from the effective bias field that one exchange coupled layer exerts on another. These effects are a consequence of the energy of the domain wall at the interface between the two exchange coupled layers. The effective bias field influences the switching properties of the couple and may be used in direct overwrite systems which make it possible to write or erase data without switching the applied magnetic field. Several direct overwrite systems using various combinations of exchange coupled films have been demonstrated^{3,4}. The adjustment of the exchange wall energy is an important requirement of making these systems practical⁵.

A third type of MO system where exchange coupling is important is in magnetic multilayers. These are multilayer stacks of a magnetic element, typically cobalt, with a

nonmagnetic metal in between. There is interest in these materials for MO applications because they have perpendicular anisotropy and square loops when the Co layers are in a certain thickness range⁶. This anisotropy seems to be associated with the interface between the magnetic and the nonmagnetic metal. One relevant question is are the magnetic layers exchange coupled in these systems? Recent results suggest that in at least some of these systems⁷ the intermediate layer element has a magnetic moment and is antiferromagnetically ordered. The magnetic moment and optical properties of the filler metal also influence the MO properties of the multilayer⁸.

In this short review the emphasis will be on a simple model which considers the exchange coupling in terms of the wall energy at the interface between two layers. The limitations of this model when the wall width is greater than the film thickness will be discussed. The use of magneto-optic techniques for extracting information about the wall structure will also be described.

EXPERIMENTAL PROCEDURE

Films of amorphous alloys of the rare earth metals (RE) and the magnetic transition metals (TM) were typically prepared by evaporation of the constituent elements from individual electron beam sources. A multitarget sputter gun deposition system was used in some cases as described elsewhere². In all cases the layers were deposited without breaking vacuum between layers. The films were characterized at room temperature on a vibrating sample magnetometer and magneto-optic Kerr loops were made at room temperature with the light incident on the films surface as well as at the film substrate interface. Faraday loops were also made at room temperature on the same apparatus on all samples that were thin enough (> 80 nm) using a HeNe laser operating at 633 nm. Selected samples were studied in a magneto-optic spectrometer in the wavelength range of 450 to 750 nm. The optical dewar is equipped with a 70 kG split coil superconducting selenoid and the sample temperature can be controlled from 1.2 to 300 K.

EXCHANGE COUPLED BILAYERS

The simplest kind of couple to consider is a high Kerr rotation readout layer with a low coercivity and a high coercivity storage layer where both layers have perpendicular easy axis anisotropy with $Q \geq 1$ ($Q \equiv H_K/4\pi M_s$ where H_K is the anisotropy field). The switching field which is the effective coercive field of the couple has been treated by considering the energy difference between the initial and final states. There are three types of systems depending on whether the films of the couple are on the same (Type II) or opposite (Type I) sides of compensation or Type III in which the rare earth subnetworks are oppositely oriented when the TM subnetworks are pointing the same direction (see Figure 1). We will only consider the Type I couple here; the other cases are treated in references 1 and 2. In a Type I couple, Fig. 1, the upper layer is TM dominated and has net magnetization M_1 and the lower layer is RE dominated and has net magnetization M_2 . In a large applied field the net magnetization of both layers will point in the field direction as shown in the figure as state 2. The subnetwork magnetizations in the two layers are pointing in opposite directions in the two layers. Since the spins of a given sublattice are ferromagnetically exchange coupled, it is energetically unfavorable for the spins to change direction abruptly at the interface. Thus a wall must form at the interface in which the spins change direction gradually. The energy per unit area of the wall σ_w is the main barrier to switching the sublattices to antiparallel orientation and thus largely determines the switching field. As with a 180° Bloch wall the wall energy is given by:

$$\sigma_w = 4\sqrt{AK_u} \quad (1)$$

where A is the exchange stiffness and K_u is the anisotropy energy. The wall will form in the lower anisotropy material, in most cases, because the wall energy is lower there.

The wall width for a 180° Bloch wall is given by:

$$\delta = \sqrt{A/K_u} \quad (2)$$

so if the low anisotropy layer is very thin the wall width may exceed the layer thickness and the simple interface wall model¹ would no longer be expected to be valid.

To use a RO layer to read the stored data it is essential that the films be strongly coupled. In other words, the field to switch from state 1 to state 2, H_{12} must be greater than the field needed to reverse both layers together, H_{14} . The switching field of the bilayer is calculated, following Kobiyashi et al¹ from the difference in free energy in the initial and final states. In the initial state, Type I state 1, the total free energy is :

$$E_1 = +M_{s1}t_1H - M_{s2}t_2H \quad (3)$$

The final state, Type I state 2, has the free energy:

$$E_2 = -M_{s1}t_1H - M_{s2}t_2H + \sigma_w \quad (4)$$

where M_{si} is the saturation magnetization of the i th layer, t_i is the thickness of the i th layer, H is the applied field and σ_w is the interfacial wall energy per unit area. When the free energy difference between states 1 and 2 equals the coercive energy given in this case by $2M_{s1}t_1H_{c1}$ because only layer 1 is switching, then the field $H = H_{12}$ will be needed to switch the couple. Therefore:

$$E_1 - E_2 = 2M_{s1}t_1H_{c1} \quad (5)$$

$$H_{12} = + \frac{\sigma_w}{2M_{s1}t_1} - H_{c1} \quad (6)$$

When both layers switch together the wall term drops out because the wall is the same in both the initial and final states. The switching field is given by:

$$H_{14} = \frac{M_{s1}t_1H_{c1} + M_{s2}t_2H_{c2}}{M_{s1}t_1 + M_{s2}t_2} \quad (7)$$

The switching field in this case is a weighted average of the coercivities of the individual layers where the weighting factors are the $M_s t$ products.

The results of a study of the thickness dependence of the Kerr signal and the effective coercivity, H_{14} are shown in Figs. 2 and 3. The RO layer was an amorphous film of Nd₂₀ Tb₅ FeCo₇₅ with a Kerr rotation of about 34 mrad at 633 nm and a coercivity of 0.9 kOe. The ST layer had the composition Nd₁₀ Tb₂₀ FeCo₇₀ with a rotation of 17 mrad and H_c of 5.3 kOe. As the RO layer thickness is increased the Kerr rotation increases to the bulk value of the RO layer when its thickness is 20 nm (200 Å) or over (see Fig. 2). The coercivity decreases monotonically following the calculated switching field, H_{14} given by equation 7. The other calculated curves in this figure show the dependence of the switching field on RO layer thickness with the ST layer thickness as a parameter. This example shows that it is possible to double the Kerr rotation with a RO layer but the coercivity of the couple is about half the value of the ST layer alone. Also, this improvement can only be obtained when the total film thickness is fairly large, 160 nm (1600 Å).

Exchange coupled layers of CoPd on amorphous TbCo alloys⁹ have also been studied. When deposited as a single layer, CoPd has weak perpendicular anisotropy. This alloy¹⁰ has a high rotation at about 400 nm making it of interest for high density storage¹⁰. These systems are similar to exchange coupled RE-TM systems shown in

Fig. 1 but with the RE subnetwork magnetization vector reduced to zero in the upper layer. When the films are on opposite sides of compensation, as in the couple CoPd/Tb25Co75, the system is Type I. In the case of weak perpendicular anisotropy, however, these diagrams are only appropriate for the saturated states when the net magnetizations of both layers are forced into the direction of the applied field. Consider Type I, state 2 with the net magnetizations of the two layers pointing in the same direction. The Co subnetworks point in opposite directions so there must be a 180° domain wall between the layers in a saturating field. In the case of a simple Type I RE-TM couple, the system can relax when the field is removed so that there is no wall at the interface (Type I, state 1). If, however, the read out layer is an in-plane material its magnetization will go in-plane when the field is removed. In this case, state 1 will consist of a RO layer with its magnetization in-plane and a RE-TM layer with perpendicular spins. The spins will not turn 90° abruptly, at the interface but rather will form a wall of a different energy, σ_{w1} , in state 1. The switching field will depend on the wall energy difference $\Delta\sigma_w (= \sigma_{w2} - \sigma_{w1})$ which will always be less than the case where there is no wall in state 1. This means that H_{12} will be smaller when the RO layer is in-plane. The CoPd/TbCo couples behave more like the in-plane RO layer case with a 90° wall in zero field.

Since the polar Kerr signal is largest when the magnetization is perpendicular, an in-plane RO layer gives a weaker MO signal. On the other hand, if the in-plane RO layer is comparable in thickness to the wall width, most of the spins will have a projection on the perpendicular axis and will contribute to the polar MO signal. In fact, because the wall width is inversely dependent on the perpendicular anisotropy, Eq. 2, a low anisotropy (in-plane) material will have wider walls. The wall width in the CoPd films can be estimated from the exchange stiffness, A , the Q and M_s . The loop character of the CoPd alloy is rather like that of a bubble domain material indicating that Q is about 1 ($Q = H_k/4\pi M_s$). It is convenient to express K_u in terms of Q using the definition of $H_k = 2K_u/M_s$ so that:

$$K_u = Q(2\pi M_s^2) \quad (8)$$

Then Eq. 2 can be expressed:

$$\delta = \frac{1}{\sqrt{Q}} \sqrt{A/(2\pi M_s^2)} \quad (9)$$

For CoPd, $4\pi M_s$ is 8000 G giving $2\pi M_s^2 = 2.55 \times 10^6$ ergs/cm³ and A is 4×10^{-6} ergs/cm. If $Q = 1$ equation 9 gives a δ of 12.5 nm. Thus in the weak perpendicular anisotropy range with Q equal to or slightly less than 1, the wall width can be expected to be comparable to the thickness of the RO layer.

The Faraday rotation can be used to extract information about the portion of the CoPd film with a perpendicular orientation. Most probably, the spins in the CoPd turn from the perpendicular to the parallel direction as in a 90° domain wall. There may be however, some thickness which maintains the perpendicular orientation before the 90° wall. For simplicity, we have modeled the system by dividing each CoPd layer into two regions, perpendicular at the TbCo interface and in plane beyond a critical thickness, t_x from the interface. We can expect t_x to be of the same order of magnitude as δ but somewhat smaller because all the spins in the wall are not perpendicular. When the CoPd thickness (t_2) is less than the critical thickness (t_x) the remanent rotation (θ_{Rem}) should be equal to the saturation rotation (θ_{FSat}) because all the spins in the CoPd are perpendicular and contribute to the rotation in both cases. When $t_2 > t_x$ only the spins within the thickness t_x will contribute to the rotation in the remanent state. The difference in rotation is then given by:

$$\theta_{FSat} - \theta_{Rem} = \Delta\theta = \theta_2 \left(\frac{t_2 - t_x}{t_1 + t_2} \right) \quad (10)$$

We know θ_2 , the saturation rotation of CoPd (1.9×10^5 °/cm at 633 nm) from independent

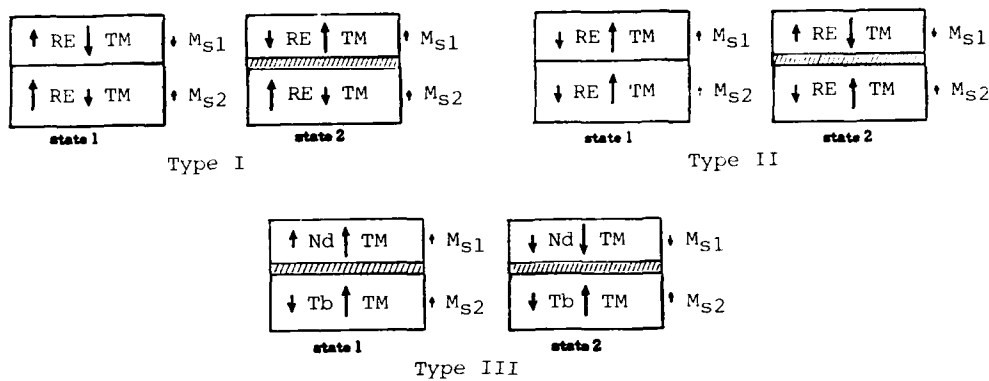


Fig. 1 Schematic representation of three types² of exchange coupled bilayers.

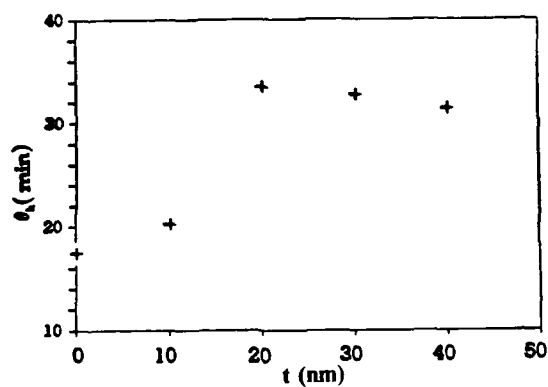


Fig. 2 The MO Kerr effect of the RO layer ($\theta_k = 34$ min) on a ST layer with $\theta_k = 17$ min as a function of the RO layer thickness².

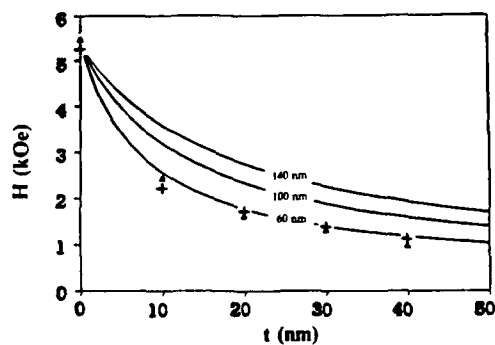


Fig. 3 The bilayer switching field, H_{14} , as a function of the RO layer thickness with the ST layer thickness as a parameter².

measurements so we can extract t_x from the thickness dependence of $\Delta\theta$. In ref. 8, t_x was shown to be typically 6 nm for a triple layer film with CoPd on both sides of $\text{Th}_{15}\text{Co}_{85}$ and 4 nm for a double layer film with CoPd deposited first. When the exchange coupling was broken by exposing the CoPd to air before the $\text{Th}_{15}\text{Co}_{85}$ deposition, t_x was zero.

CONCLUSIONS

Several kinds of magneto-optic media depend on exchange coupling to obtain improved performance. In RO/ST bilayers the improved Kerr readout signal requires that both layers switch together so that the magnetic state of the RO layer accurately reflects the magnetic state of the ST layer. This requires that the interfacial wall energy be as large as possible so that there is a large barrier to decoupling of the layers. In direct overwrite applications, the wall energy must be adjusted to an optimal value⁵. As discussed in this paper, the switching properties of the exchange coupled bilayer are a kind of weighted average of the individual film properties. The switching properties of the RO layer, therefore, are not completely irrelevant. Also, the RO layer should be as thin as possible because thickness enters into the weighting.

When the RO layer is inplane or has weak perpendicular anisotropy only a small thickness of the RO layer will remain coupled in the remanent state. Because of the low anisotropy in the RO layer a 90° wall tends to form in the remanent state. The wall width will be comparable to the thickness of the RO layer, the penetration depth of the light. However, the spins closest to the interface are perpendicular or near perpendicular so they still contribute to the polar Kerr signal. The effective thickness of this perpendicular layer in CoPd is 3 to 4 nm. In this connection, a few comments are in order on the technologically important couple of $\text{PtMnSb}/\text{TbFe}$ ¹¹. This couple is of interest because PtMnSb has the highest Kerr rotation at room temperature of any known material¹². The PtMnSb has no perpendicular anisotropy so a 90° wall would be expected in the remanent state. It may be that the MO rotation of the wall spins can account for some of the anomalous Kerr loops observed with thin (12 nm) PtMnSb layers¹³.

In multilayer metal films the individual layers are much thinner than the wall width. These systems are further complicated by the fact that the metal between the Co layers is typically nonmagnetic or antiferromagnetic. Understanding the exchange coupling in these multilayers will probably require a much more atomistic picture. Magneto-optic spectroscopy may become an important tool in the analysis of the type of coupling present in these multilayers.

Acknowledgements

The author thanks T. S. Plaskett and R. R. Ruf for their fine collaboration during several years of coupled film experiments.

References

1. T. Kobayashi, H. Tsuji, S. Tsunashima, S. Uchiyama, Japanese J. Appl. Phys. **20**, 2089 (1981)
2. R. J. Gambino, T. S. Plaskett and R. R. Ruf, IEEE Trans. Mag., **24**, 2557 (1988)
3. J. Saito, M. Sato, H. Matsumoto and H. Akasaka, Jpn. J. Appl. Phys., **26**(S26-4), 155 (1987)
4. C.-J. Lin, J. Appl. Phys. **67**, 4409 (1990)
5. T. Tokunaga, M. Taguchi, T. Fukami, Y. Nakaki and K. Tsutsumi, J. Appl. Phys. **67**, 4417(1990)
6. W. B. Zeper, F. J. A. M. Greidanus, P. F. Carcia, IEEE Trans. Magnetics, **25**, 3764 (1989)
7. S. S. P. Parkin, S. Fan, N. More and K. P. Roche, JAP **67** 5931 (1990)
8. R.J.Gambino and R.R.Ruf, J. Appl. Phys. **67**, 4784 (1990)
9. R.J.Gambino, R.R.Ruf and R.Rishi, IEEE Trans. Mag., **25**, 3749 (1989)

10. Rugar, C.-J. Lin and R. Geiss, IEEE Trans. MAG22, 2263 (1987)
11. K. Matsubara, M. Koyama, T. Koyanagi, Y. Watanabe and T. Yoshitomi, Advances in Magneto-Optics, Proc. Int. Symp. Magneto-Optics, J. Magn. Soc. Jpn. 11, Supplement S1, 213 (1987)
12. K.H.J. Buschow, P.G. van Engen, and R. Jongebreur, J. Mag. Magn. Mat., 38, 1-22(1983)
13. M. Kitada and N. Shimizu, J. Appl. Phys. 54, 7089(1983)

TEMPERATURE DEPENDENCE OF MICROMAGNETIC DOMAIN STRUCTURE IN COBALT FILMS

I.R. McFadyen and P.S. Alexopoulos

IBM Research Division
Almaden Research Center
650 Harry Road
San Jose, CA 95120-6099

INTRODUCTION

The magnetic domain structure in Co and Co-based alloys is strongly influenced by the pronounced crystalline anisotropy of hcp Co. The energy associated with this crystalline anisotropy is given by:

$$E_a = K_1 \sin^2\phi + K_2 \sin^4\phi + \dots$$

where K_1 and K_2 are the first and second anisotropy constants respectively and ϕ is the angle between the magnetisation and the c-axis. At room temperature K_1 and K_2 are both positive and K_1 is greater than K_2 , which results in a strong easy axis along the c-axis direction. At temperatures above 325°C both K_1 and K_2 are negative and the easy axis lies in the basal plane of the hexagonal unit cell. Between $\approx 245^\circ\text{C}$ and 325°C , $0 < -K_1 < 2K_2$ and the easy axis lies at an angle θ to the c-axis which is given by:

$$\theta = \arcsin(-K_1/2K_2)^{1/2}$$

Figure 1. shows the anisotropy energy as a function of temperature for various angles of the magnetisation. It is obvious from this plot that not only does the easy axis direction change from the c-axis to in-plane, but that the strength of the anisotropy decreases from its room temperature value to a minimum around 280°C and then increases again as the easy axis rotates into the basal plane.

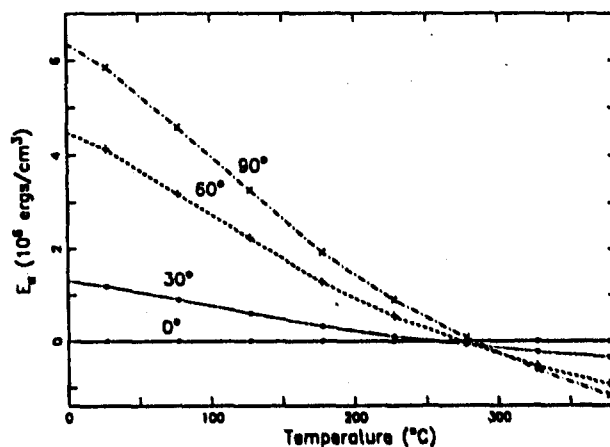


Figure 1. Anisotropy energy of Co vs temperature for various angles between M and the c-axis.

The variation of the easy axis direction with temperature has been studied by a number of groups using Lorentz electron microscopy, mostly in well annealed single crystal samples, and the rotation of the easy axis with increasing temperature has been experimentally verified^{2,3,4}. However, the effect of the change in the anisotropy direction on the domain structure of polycrystalline Co films has not been investigated on a micromagnetic scale. Neither has the effect of the change in the strength of the anisotropy on the micromagnetic domain structure been studied.

In this work the domain structures in single crystal and polycrystalline Co films have been investigated as a function of temperature; from 20°C to 316°C in the case of the single crystal sample, and from 20°C to 400°C in the case of the polycrystalline sample. The domain patterns were observed using differential phase contrast Lorentz transmission electron microscopy⁵ (hereafter called DPC).

EXPERIMENT

The single crystal sample used in this work was prepared from a single crystal Co ingot by mechanical polishing and finally ion milled to electron transparency. No annealing was carried out after the sample was thinned and as a result many crystallographic twins were seen in the sample. The polycrystalline sample was a 360Å thick R.F. magnetron sputtered Co film on a 200Å thick Cr underlayer. A Si₃N₄ membrane⁶ was used as a substrate for ease of observation in the TEM.

The microscope used for the investigation was a JEOL JEM2000FX TEM with a scanning attachment. The microscope has an eight segment position sensitive detector for DPC imaging and computer controlled image acquisition, both of which have been described elsewhere^{7,8}. The DPC technique basically maps out the integrated in-plane induction at the sample by measuring the angular deflection of the beam due to the sample at each point in a regular raster scan.

The samples were heated in situ in the microscope using a GATAN 628 single tilt heating holder. In this holder the sample is clamped between two tantalum washers to ensure good thermal contact with the resistive heating element in the holder. A thermocouple on the heating element measures the temperature at the sample with an accuracy of $\pm 10^\circ$. Throughout the experiment the pressure in the sample chamber was $\sim 10^{-6}$ torr as measured on the microscope ion gauge.

Initial domain structures within the samples were generated by applying an external magnetic field. In the case of the single crystal film the field was applied by tilting the sample in the microscope and activating the objective lens. The external field for the polycrystalline sample was provided by a commercial ac tape eraser. In this case the field was applied in the plane of the film. No magnetic fields were applied during the heating experiment itself.

RESULTS

Single Crystal Co

Figure 2 shows a series of DPC images of the domain structure in the single crystal Co film as a function of temperature. The room temperature image (2a) shows a series of domains running almost vertically across the image (the alternating areas of black and white contrast) separated by 180° walls. The slight jog of the domains to the left in the centre of the image is due to the presence of a crystallographic twin. Analysis of this image and the complimentary orthogonal DPC image indicates that the magnetisation within the domains is almost entirely parallel to the domain walls. The narrow domains on either side of the twin remain a constant width almost all the way to the twin boundaries, and only very close to these boundaries do they increase to accommodate the larger domains in the twin. This is indicative of a strong anisotropy aligning the magnetisation with the in-plane projection of the c-axis together with the minimisation of charge in the walls. As the temperature is increased the number of smaller domains decreases, probably due in part to thermal activation, and the narrow domains which attach to those in the twin change from a "wine glass" shape into a more triangular shape (fig 2b). In this case the magnetisation is still almost parallel to the wall, however a reduction in the strength of the anisotropy allows the magnetisation to rotate with respect to the c-axis and the length (and therefore total energy) of the domain wall is reduced. Note that the c-axis should still be the easy axis at this

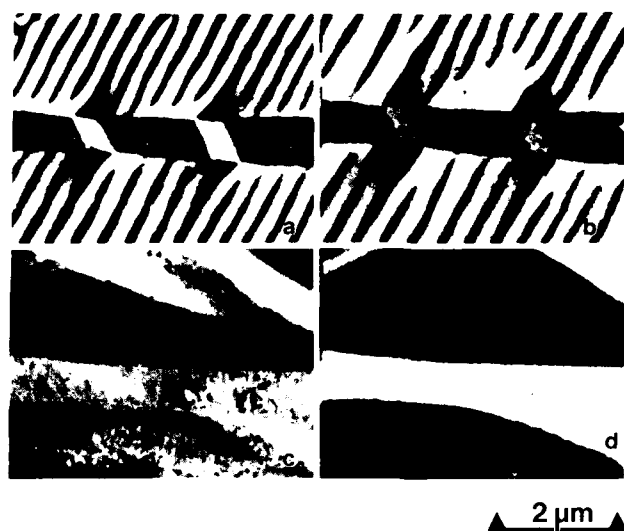


Figure 2. DPC images of single crystal Co at a) 20°C, b) & 150°C c) 270°C and d) 316°C

temperature. In figure 2c the temperature has been increased to 270°C and here the magnetisation is no longer locked to one direction within each domain but varies smoothly from point to point. At this temperature there is very little energy difference between pointing parallel or perpendicular to the easy axis (which is somewhere between the c-axis and the basal plane) (see Figure 1). At 316°C, figure 2d, the domain boundaries are running approximately horizontally and the magnetisation is now pointing at 90° to its initial direction. This is due to the increased strength of the anisotropy in the basal plane. On cooling to room temperature the original magnetisation directions are regained but the final domain structure has much wider domains than the initial room temperature structure.

Polycrystalline Co

The domain structures in the polycrystalline sample are shown in figure 3. Images 3a and 3b show two orthogonal images of the same area at room temperature. From 3a it can be seen that the domain structure consists of wide domains running from top left to bottom right with the magnetisation running in approximately the same direction. Within the domains there is a small scale ripple structure (fig 3b) which is a characteristic feature of these randomly oriented polycrystalline film and indicates a small deviation of the magnetisation to either side of the mean direction. At the domain walls the ripple on either side of the wall combine to form vortex structures which can be identified in figure 3b by their similarity to topographic features viewed from above under oblique illumination (e.g. indicated feature in fig 3b). The smaller the scale of the ripple structure in this type of material, the higher the demagnetising fields associated with it and therefore the higher the coercivity required to maintain it.

Figure 3c shows the same area of the film at a temperature of 200°C. The overall large scale domain structure remains essentially unchanged from that in figure 3b, however the small scale structure has changed quite dramatically. The ripple structure within the domains, has almost completely disappeared leaving behind only the vortex flux closure structures at the walls. After the initial loss of the small scale ripple (between 100 and 200°C) the structure remains relatively unchanged up until approximately 270°C at which point there is a marked reduction in the number of vortices along the domain walls, as can be seen in figure 3d, together with an increase in the spatial extent of the remaining vortices. The conclusion from this is that there is no strong easy axis direction at this temperature and that exchange and demagnetising effects act together to maintain the flux closure of the vortices while increasing the scale of coherently magnetised regions within these structures. As the temperature is increased further to where there is once again a strong easy axis direction a small scale ripple structure reappears (fig 3e), however, the spacing and scale of the vortices does not decrease noticeably. When the sample is cooled to room temperature (fig 3f) the large scale vortex structure persists and although a small scale ripple structure is present, it



Figure 3. Domains in polycrystalline Co at a) & b) 20°C c) 200°C d) 270°C e) 400°C f) 20°C

is very strongly influenced by the vortex structure giving rise to a much wider angular distribution of magnetisation directions within the domains than that present in the initial room temperature state.

Re-application of an in-plane ac field to the sample, such as that used to generate the initial room temperature state, produces a domain configuration with very similar ripple scale and vortex spacing and size to the initial state indicating that the changes to the film during heating are magnetic changes and not irreversible oxidation or structural changes.

CONCLUSION

It has been known for many years that the anisotropy constants of Co change rapidly with temperature in the range from room temperature up to 400°C and the effect of this change on the direction of the easy axis is well documented. In this work it has been shown that the change in the strength of the anisotropy has a noticeable effect on the domain structure of imperfect thin film single crystal Co and may in fact play a major role in the temperature dependence of domain structures in randomly oriented fine grain polycrystalline Co thin film. These results do not only relate to Co but also to the numerous Co alloys which are of particular importance in the high density recording industry today.

ACKNOWLEDGEMENTS

The authors would like to show their thanks to M. Moshref for providing the polycrystalline Co sample, and J. Paterson for preparing the single crystal sample.

REFERENCE

1. Y. Barnier, R. Pautenet, and G. Rimet, *Cobalt* No.15 (1962) 14-20
2. P.J. Grundy, *Phil. Mag.* 12 (1965) 335-345
3. M. Takahashi and T. Suzuki, *Japan. J. Appl. Phys.* 18 (1979) L1071-L1078
4. D. Watanabe, T. Sekiguchi, T. Tanaka, T. Wakiyama and M. Takahashi, *Japan. J. Appl. Phys.* 21 (1982) pp. L179-L181
5. I.R. McFadyen, *J. Appl. Phys.* 64 (1988) 6011
6. See for example Jacobs and Verhoeven, *J. Microsc.* 143 (1986) 103
7. J.N. Chapman, I.R. McFadyen and S. McVitie, to be published in *IEEE Transactions on Magnetics*, Fall 1990

HYPERFINE INTERACTION TECHNIQUES APPLIED TO THE STUDY OF SURFACES AND INTERFACES

M. Rots

*Instituut voor Kern- en Stralingsfysica, K.U. Leuven
Celestijnenlaan 200 D, B-3030 Leuven Belgium*

The combination of perturbed angular correlation spectroscopy and inert gas inclusions in metals is presented as a complementary approach for the study of magnetic surfaces or interfaces.

The attractive feature of hyperfine interaction techniques for the study of surfaces and interfaces is their ability to directly probe spatial charge distribution around the probe atom through the corresponding magnetic hyperfine field or electric field gradient. Key experiments have been reported using the nuclear methods such as NMR, Mössbauer and perturbed angular correlation spectroscopy. The NMR measurements¹ using nuclear spin polarized alkali-metal atoms on clean and oxygen covered W(110) surfaces demonstrated the observation of an average field gradient sensed by the diffusing adsorbed atoms. In recent experiments² using conversion-electron Mössbauer spectroscopy (CEMS) one could measure, by approaching the surface or an interface, the influence on the hyperfine field.

For non-magnetic sp-impurities or magnetic 3d(4d)- probe impurities in transition metals, the dominant contribution to the hyperfine field B_{hf} arises from the Fermi contact interaction, thus the local magnetization density at the nucleus. The exchange interaction between host magnetic moments and the electron screening cloud around the impurity induces a critical balance between negative and positive contributions to the hyperfine field, largely determined by the impurity charge and the size of the impurity potential. While an experimental and theoretical consensus exists on the surface enhanced magnetization, the Mossbauer work² on Fe (110) surfaces has shown that the hyperfine field at the Fe probe decreases. The predicted oscillatory behavior of the hyperfine field by going from the surface into the bulk region also contrasts with the absence of Friedel oscillations in the magnetic moment of the surface layers³. Furthermore, the important role of the broken symmetry at the surface reflects in the existence of a large electric field gradient at the surface layer, not present beneath the top two layers⁴⁻⁵.

In addition to NMR and Mossbauer spectroscopy applied to the study of surface phenomena, the application of perturbed angular correlation (PAC) techniques for probe atoms at the surface of a nonmagnetic metal was successful⁶ and able to measure the electric field gradient (efg). In those experiments, the electric quadrupole interaction detected at isolated radioactive indium atoms on Cu surfaces has given precise information on the magnitude as well as the orientation of the electric field gradient at the surface and the outermost layers. Very recently⁷, those PAC experiments have been extended to the observation of hyperfine fields at magnetic Ni(111) near surfaces positions. The results illustrate that even less than 10^{-4} of a monolayer in probe concentrations is needed, allowing the study of any magnetic

system. Furthermore, the nuclear-probe experiences an unique electromagnetic hyperfine environment which facilitates the derivation of the magnitude as well as the orientation of the surface magnetic hyperfine field over a wide temperature range. Finally, coverage of the surface with three monolayers suffices to restore the bulk hyperfine field value and to erase the electric field gradient.

Notwithstanding the success so far, the tremendous efforts needed to prepare clean surfaces and to deposit the hyperfine probe atoms on those surfaces, motivated us to look for an alternative and more practical way to reach that goal. For this purpose we refer to recent investigations⁸ dealing with the precipitation or bubble formation of rare gases in metals produced either by nuclear reaction or ion implantation. It is rather well established now⁹, that the bubbles are overpressurized and in solid phase, epitaxially aligned with the metal matrix. In the present paper, we discuss an alternative procedure and results on a search for hyperfine interaction parameters for probes at the surface of a magnetic metal, by using the interface of a rare gas inclusion in iron¹⁰.

1. Outline of the hyperfine interaction methods

The hyperfine interaction refers to the coupling of the nuclear electromagnetic moments (magnetic dipole and electric quadrupole) to the extranuclear electromagnetic fields, originating from the electronic charge distribution in the environment of the probing nucleus. Due to this hyperfine interaction (*hfi*) the energy of a particular nuclear state split up in the *m*-sublevel components and nuclear *hfi* techniques aim to measure this energy splitting which is proportional to the nuclear moment-e.m. field product, i.e. μB_{hf} and/or QV_{zz} . The measurement of the *hfi*-splitting in a particular nuclear state (see fig. 1a) can be done with the intermediate of nuclear radiation populating and depopulating this nuclear state during the decay of the radioactive nucleus. In *Mössbauer spectroscopy* the energy differences between *m*-components in the excited and the ground nuclear state, connected by the absorbed γ -radiation results in an absorption spectrum consisting of different absorption minima, their positions a direct measure of those *hfi*-splittings. The principle of the nuclear methods is similar to conventional NMR to the extent that the nuclear polarization, here governed by the Boltzmann distribution over the nuclear *m*-substates, is not destroyed by an RF-field but rather measured by the resulting anisotropy of the nuclear radiation emitted by further nuclear decay. By simple detection of nuclear radiation in a particular direction, one selects a nuclear sub-ensemble which is oriented relative to that direction. Therefore, those selected nuclei contain an unequal population of the *m*-substates and the subsequent radiation will be emitted anisotropically. In *perturbed angular correlation (PAC) spectroscopy*, thus, the *hfi*-splitting within the *m*-multiplet of a single nuclear state can be observed by measuring the time dependence of the nuclear orientation when this state is an intermediate state of a γ - γ cascade. As a result of the interference among the *m*-states (quantum beating), one may understand the frequencies in a PAC time spectrum as reflecting transitions among the *m*-substates of the intermediate state.

The nuclear methods are "*finger print*" methods identifying, through its *hfi*-parameters, the environment of a nucleus used as a nuclear probe. The interaction Hamiltonian of the static *hfi* consists generally of a magnetic dipole part, due to an external magnetic field or internal magnetic hyperfine field, and an electric quadrupole part, due to a surrounding charge distribution of non-cubic symmetry. The former results in an equidistant Zeeman splitting given by the Larmor frequency $\omega_B = g\mu_N B/\hbar$, with *g* the nuclear *g*-factor, the latter in a non-equidistant splitting dependent on the electric field gradient (*efg*) and eventually its orientation relative to a magnetic field. The electric field gradient is a second rank tensor quantity specified by five components: its magnitude V_{zz} , its asymmetry $\eta = (V_{xx} - V_{yy})/V_{zz}$ and its Euler angles (α, β, γ) defining the orientation of its principal axis system (*PAS*) relative to a laboratory system. In case of axial symmetry $\eta = 0$ and no magnetic field, the basic quadrupole frequency equals: $\omega_Q = eQV_{zz}/(4I(2I-1)\hbar)$, with *Q* the nuclear quadrupole moment and *I* the nuclear spin.

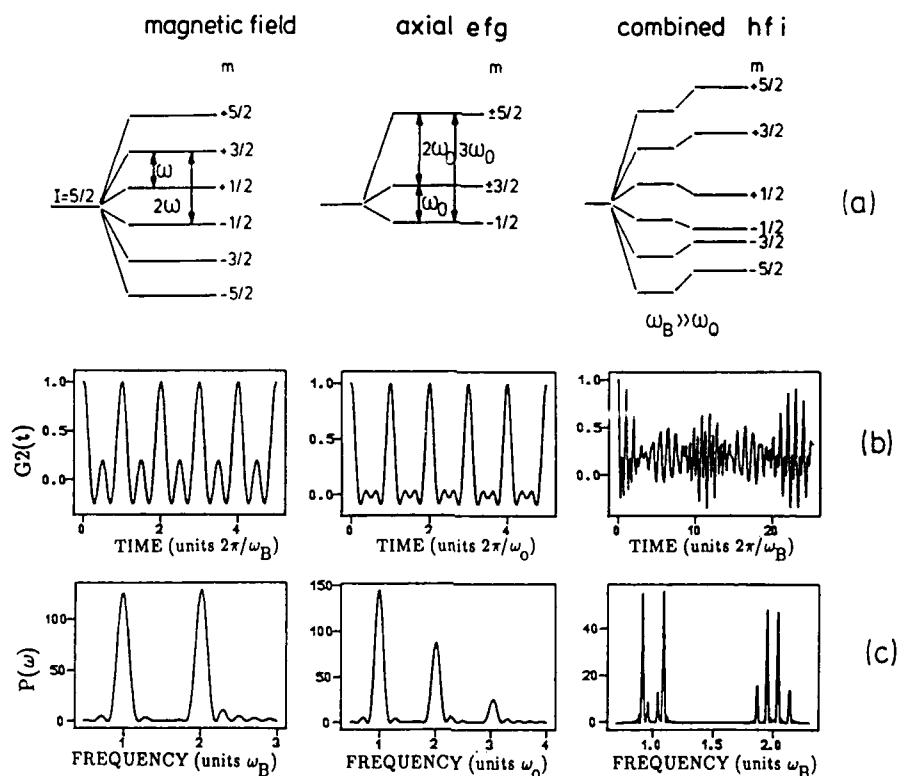


Fig.1. (a) Illustration of the hfi-splitting due to magnetic-electric- and combined interaction, (b) the corresponding PAC spectra and (c) their Fourier transforms.

In fig.1, we illustrate the hfi-splitting due to a magnetic dipole-, electric quadrupole- and combined magnetic+electric interaction. In each case the expected PAC spectrum for a polycrystalline sample is shown, along with the corresponding Fourier transform. The equidistant energy splitting in the pure magnetic case results in the appearance of two harmonic frequencies ω_B and $2\omega_B$ in the PAC spectrum. The relative intensity of both frequency components depends on the orientation of the magnetic field relative to the radiation detector plane. For instance, when the field is perpendicular to this plane the first harmonic is absent, when the field lies in plane the second harmonic is suppressed and in case of a random oriented magnetic field both harmonics are equally intense.

The PAC spectrum observed in case of a pure electric quadrupole interaction, which is due to the non-equidistant splitting, consists of three frequency components, the third frequency being the sum of the other two. For an efg with rotational symmetry ($\eta=0$) observed frequencies are ω_0 , $2\omega_0$ and $3\omega_0$, with $\omega_0=3(m^2-m'^2)\omega_Q$, their intensities also dependent on the orientation of the efg relative to the detector plane. Finally, the PAC spectrum for a combined magnetic and electric hfi can be decomposed in different frequency components dependent on ω_B , ω_Q , η and (α, β, γ) . For the collinear case ($\beta=0$) or for cases where the quadrupole interaction is small ($\omega_B \gg \omega_Q$), the diagonal approximation of the interaction Hamiltonian is sufficient and the frequency components are: $N\omega_B \pm n\omega_0 \langle \beta \rangle$, with $N=1,2$ and $n=1,2,3$, while $\langle \beta \rangle$ means the value of $P_2(\cos\beta)$ for an unique orientation or its average value in case of a random orientation of the PAS relative to the magnetic field direction. In second

order approximation, however, the symmetric frequency shifts around the Larmor frequency is lifted and up to 16 frequency components (for $I=5/2$) may be observed when ($\omega_B \approx \omega_Q$). In such cases the PAC spectrum loses structure, due to incoherent superposition. In fig.1c we illustrate the case $\omega_Q/\omega_B = 0.01$, $\eta=0$, $\beta=25^\circ$, in order to show the sensitivity of the PAC spectrum as well as the frequency shifts around the ω_B -frequency.

2. Experimental details

Polycrystalline Fe-, Al- or Mo-foils pre-implanted with krypton to a dose of 2.10^{16} ions/cm² were subsequently doped with ^{111}In to a dose of 4.10^{13} ions/cm² and post-implanted with the same initial amount of krypton. The implantation energies were matched for an optimal depth profile overlap and the implantation was performed at room temperature. Time differential PAC experiments (TDPAC), in a conventional four detector set-up, were done on the samples as-implanted as well as isochronal annealed at temperatures up to 500C. For the Fe-sample, along with zero external magnetic field measurements (random hfi samples), we performed experiments in an external field (oriented hfi samples) in the transversal as well as the longitudinal detector configuration, simultaneously. The latter configuration was intended to decouple the electric quadrupole interaction from the magnetic interaction.

The ^{111}In probe nucleus distributed as an observer in the sample, will experience a hfi depending on its environment. For instance, iron is a ferromagnet and therefore a magnetic hyperfine field will be observed fairly proportional to the local magnetization. The corresponding Larmor frequency in pure iron for ^{111}In at a substitutional site is very well known as $\omega_B = 559.6(1)\text{Mrad/s}$. At those lattice positions the electric field gradient equals zero because of cubic symmetry. Due to the presence of krypton, one

expects to observe defect sites or interface sites taken by the probe nucleus. Each of those sites will be characterized by a reduced (or enhanced) value for the hyperfine field (Fe-sample), but in addition also by a non-zero efg, because at those sites the cubic symmetry may be destroyed. Notice that the quadrupole interaction depends on the inverse cube of the probe-defect distance and therefore we sense the probe's charge environment within the first neighbour shells only.

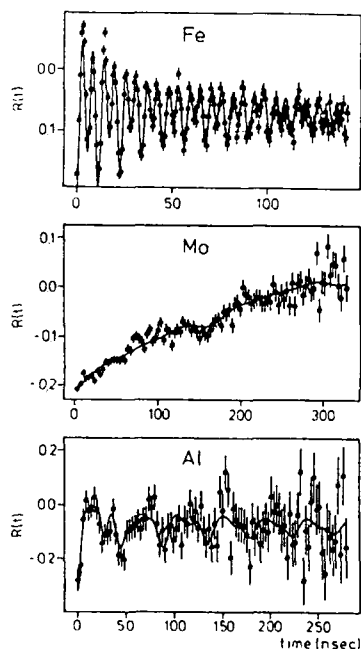


Fig.2. TDPAC-spectre for ^{111}In at krypton bubbles in Al, Mo and Fe.

3. Results

Earlier data on ^{111}In implantation in pure iron, already indicated that as-implanted the substitutional fraction is almost negligible and no structure in the PAC spectrum could be measured, without annealing. Here, we observe a well-defined spin precession pattern attributed to almost 50% of the indium probes, in an as-implanted sample containing the high Kr-dose. A typical PAC spectrum is shown in fig.2a. A reasonable fit to the data results in a magnetic interaction frequency $\omega_B = 555.8(1)\text{Mrad/s}$ of width $\delta = 1.23(3)\%$. The observed fraction of probes in this hyperfine interaction

environment remains almost unchanged during annealing below 350C. At higher annealing temperatures a completely different PAC pattern was observed, reflecting a broadly distributed hyperfine interaction, then the spin precession pattern disappears and finally the indium activity escapes from the foil at 600C. The experiments on an Al- or Mo-sample illustrate that the In probe indeed senses the presence of krypton inclusions. Those spectra are shown in fig. 2b,c and can be interpreted, because no hfi is expected in an unperturbed cubic lattice, as due to a fraction of In-probes at the Al/Kr or Mo/Kr interface. The magnitude of the electric field gradient responsible for the spin precession pattern in the fcc Al-sample equals $V_{zz}=7.1(10) \cdot 10^{17} \text{V/cm}^2$, to be compared⁶ with the surface/vacuo interface at Cu(111) $V_{zz}=10.2(15) \cdot 10^{17} \text{V/cm}^2$. The bcc Mo-sample reflects a much smaller efg value of $V_{zz}=2.6(4) \cdot 10^{17} \text{V/cm}^2$, in quite good agreement with the value $3 \cdot 10^{17} \text{V/cm}^2$ obtained¹¹ by "onplantation" of ¹¹¹Cd on a Mo(111) surface, both values, however, almost two times smaller than observed in the CEMS experiment on Fe(110), illustrating the dependence on the surface symmetry.

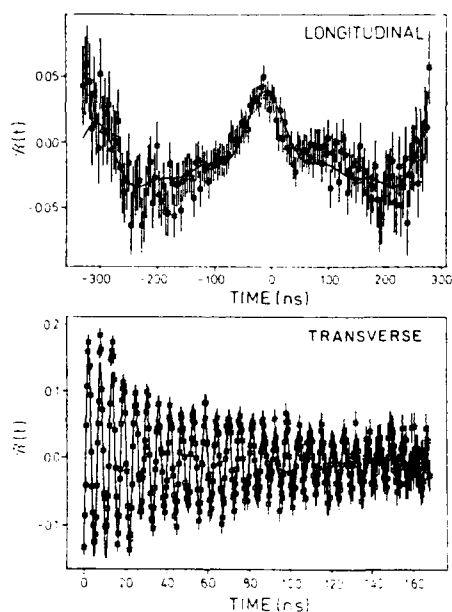


Fig.3. Spin-precession for ¹¹¹CdFe(Kr) in an external field of 0.1T.

lattice positions, where they contribute to the transversal spectrum by a well-defined precession pattern. Then the f_1 fraction should be associated to probe sites experiencing a combined interaction with $y \neq 1$, in order to produce the observed spectrum shape of the longitudinal measurement. As a consequence those probes should experience a much reduced magnetic hyperfine field, but remain almost unobservable (missing fraction) in the transversal spectrum, due to incoherent superposition of the many different frequency components.

In fact, the data could be fitted nicely in a model admitting more than one probe site and the result given by:

- a "quasi-substitutional" site (fraction 65%) with $\omega_B = 554.7(1) \text{Mrad/s}$, $\omega_Q = 0.42(14) \text{Mrad/s}$ and $\delta = 9.2(1.1) \text{Mrad/s}$;
- a "defect site" (fraction 20%) with $\omega_B = 519.9(2.2) \text{Mrad/s}$, $\omega_Q = 2.7(2) \text{Mrad/s}$ and $\delta\omega = 10(5) \text{Mrad/s}$;
- an "undefined site" (fraction 15%) with $\omega_B = 130(2) \text{Mrad/s}$ and $\delta\omega = 41(7) \text{Mrad/s}$.

Because obviously a combined magnetic and electric interaction should be considered for the present Fe(Kr) samples, we measured simultaneously the spin precession under an external magnetic field of $B_{\text{ext}} = 0.1 \text{ T}$ in both the transversal and longitudinal detector configuration, the result is shown in fig.3. The longitudinal spectrum can nicely be fitted with two quadrupole sites: $f_1 = 0.64$ with $\omega_Q = 3.53(5) \text{Mrad/s}$ and $f_2 = 0.36$ with $\omega_Q = 1.1(1) \text{Mrad/s}$, meaning however that the magnetic interaction is negligible. In view of the spectrum obtained in the transversal geometry this is an unexpected result, because a substantial fraction of probes experience a large magnetic hyperfine field. These magnetic sites contribute to the longitudinal spectrum as a time independent anisotropy, whenever the ratio $y = \omega_B / \omega_Q$ is large. This is

because an almost pure Larmor precession of the spins around the magnetic hfi-axis hardly changes the relative m-substate population and thus the angular correlation anisotropy remains unperturbed by such hfi. The f_2 fraction may correspond to probes on such "quasi-substitutional"

In addition to the above sites an almost 40% fraction of probes experience a complex hyperfine interaction and therefore escape observation. After correction for the external field we obtain for the quasi-substitutional site (s) a hf-field shift $\Delta|B_{hf}| = -6.8 \cdot 10^{-3}$ and $\langle V_{zz} \rangle = 0.13(4) \cdot 10^{17} \text{ V/cm}^2$. For the defect site (d), however, the hf-field shift equals $\Delta|B_{hf}| = -6.89(4)\%$ or -2.6 T while $\langle V_{zz} \rangle = 0.86(6) \cdot 10^{17} \text{ V/cm}^2$. The measured electric field gradient values are mean values because of their random orientation relative to B_{ext} .

The present results can be compared with CEMS data² at the Fe (110) surface, where for a clean surface $\Delta|B_{hf}| = -2.03 \text{ T}$ (first layer) or -0.11 T (second layer) has been found along with $V_{zz} = 8 \cdot 10^{17} \text{ V/cm}^2$. We suggest that both fractions showing a well-defined precession in the TDPAC pattern (quasi-substitutional and defect site) may be interpreted as originating both from the Fe/Kr-interface, the latter at the surface of the inclusion, the former in the outermost Fe layers. It is known from experiments⁵ as well as recent efg calculations¹², that the cubic charge symmetry is restored some two layers beneath the metal surface. Calculations³ of the magnetic hyperfine field, on the other hand, seem to predict substantial dependence on the symmetry of the surface. No characterization of the surface type, probed here at the Kr-inclusion, was available as yet and therefore quantitative comparison with theoretical estimates may be somewhat premature.

4. Conclusion

The hyperfine type experiments presented here are rather promising to the study of surface phenomena at an atomistic scale. The high resolving power of hyperfine interaction techniques and more specially PAC, allow to follow the mobility of atoms at the surface, their diffusion and clustering. The identification of the surface sites by their efg tensor is really exceptional among the existing surface investigation techniques. This ability has been convincingly demonstrated by the PAC work of the Konstanz group⁶⁻⁷, where they could identify terrace-, step- and in plane-sites by measuring the full efg tensor. In addition, the approach described here allows surface/interface research, with the appealing feature that it can be done without using expensive apparatus to produce clean surfaces. Indeed one only needs an ion implanter to create inert gas bubbles into the metal matrix and a probe with an affinity to occupy sites at the interface of those inclusions. The insolubility of indium in iron and aluminum may well be responsible for the relatively large fraction of interface positions observed in the present experiment.

References

1. B. Horn, E. Koch and D. Fick, Phys. Rev. Lett **53**:364 (1984)
2. M. Przybylski and U. Gradmann, Phys.Rev.Lett.**59**:1152 (1987)
3. S. Ohnishi, M. Weinert and A.J. Freeman, Phys.Rev.**B30**:36 (1984)
4. J. Koréchi and U. Gradmann, Phys.Rev.Lett.**55**:2491 (1985)
5. J. Koréchi, Hyp.Int.**40**:89 (1988), and references therein.
6. G. Schatz, R. Fink, T. Klas, G. Krausch, R. Platzter, J.Voigt and R. Wesche, Hyp.Int.**49**:395 (1988)
7. J. Voigt, R. Fink, G. Krausch, B. Luckscheiter, R. Platzter, U. Wöhrmann, X. L. Ding and G. Schatz, Phys.Rev.Lett.**64**:2202 (1990)
8. A. vom Felde, J. Fink, Th. Müller-Heinzerling, J. Pflüger, B. Scheerer and G. Linker, Phys.Rev.Lett.**53**:922 (1984)
9. H. H. Andersen, J. Bohr, A. Johansen, E. Johnson, L. Sarholt-Kristensen and V. Sarganov, Phys.Rev.Lett.**59**:1589 (1987)
10. P. Decoster, G. De Doncker and M. Rots, Phys.Rev.**B41**:6165 (1990)
11. E. Hunger, H. Haas, V. Marx and M. Menningen, in: "Nuclear Physics Applications on Material Science" E. Recknagel and J.C. Soares. ed., Kluwer Ac. Publ.(1988)
12. B. Lindgren, Hyp.Int.**34**:217 (1987)

SURFACE MAGNETOSTRICTION

R.C. O'Handley and S.W. Sun

Department of Materials Science and Engineering
Massachusetts Institute of Technology
Cambridge, MA 02139 USA

1. INTRODUCTION

The outer surface layer of a material is generally strained relative to the bulk. This may be due to the reduced coordination there or to an altered charge distribution such as tailing of some of the itinerant charge density into the vacuum¹. In 3d metals this surface charge redistribution often leaves the surface atoms more under the influence of the 3d charge which is primarily responsible for the attractive bonding interaction². Hence the lattice constant normal to the surface may decrease for the outermost atoms, e.g. by 9% for v^1 .

In epitaxial thin films and multilayers with less than perfect lattice match uniform strains up to several percent occur for the first few layers deposited. Above a critical thickness, misfit dislocations may nucleate to accommodate some of this strain. Thus in thin films there is this additional source of strain, which at the surface, combines with the intrinsic effect described above.

These surface strains can have strong effects on the preferred direction of magnetization at the surface of a magnetic material. The parameters which describe the extent to which these strains couple to magnetic properties are the magnetostriction coefficient λ_i or the magneto-elastic (ME) coupling factor B_i which are related by the elastic constant tensor c_{ij} :

$$B_i = c_{ij} \lambda_j \quad (1)$$

Magnetostriction is the anisotropic strain of a magnetic material referenced to the direction of the magnetization M . In an isotropic material the strain is given by

$$\epsilon = (3/2)\lambda_s [\cos^2\theta - 1/3] \quad (2)$$

where λ_s is the saturation magnetostriction coefficient and θ is the angle between \mathbf{M} and the strain direction. The inverse effect, piezomagnetism, indicates that a stress may cause the magnetization direction to change. This is because the stress σ contributes to the magnetic anisotropy energy density according to:

$$E_\sigma = (3/2)\lambda_s \sigma \quad (3)$$

If the product $\lambda_s \sigma$ is strong enough, the direction of magnetization may be pinned by the stress. Note that a 0.1% strain in Ni ($|\lambda_s| \approx 46 \times 10^{-6}$, $Y = 2.4 \times 10^{11} \text{ N/m}^2$) produces a ME energy density of order $1.6 \times 10^4 \text{ J/m}^3$ which is four times the magneto-crystalline anisotropy of Ni. So a modest surface strain could produce a large ME surface anisotropy. In fact the surface anisotropy of ultrathin Au-Co-Au sandwiches is believed to be due predominantly to stress³.

Just as magnetic anisotropy⁴⁻⁶ and the magnetic moment itself⁷⁻⁹ can take on unique values at the surface of a material, it is possible that the ME parameters themselves are different there. Thus, to fully appreciate the role of stress in surface magnetism, it is necessary to know the values of two of the parameters B_i , c_{ij} and λ_j at the surface: B_i^s , c_{ij}^s and λ_j^s . The magnitude of the ME effect suggests that while surface magnetic moments may differ by as much as 10% from their bulk values, surface anisotropies and ME coefficients may differ much more dramatically from their corresponding bulk values.

The fact that macroscopic strain contributes to magnetic anisotropy is a reflection of the microscopic origin of ME interactions. Magnetostriction has its origin in the asymmetry of the local crystal field as seen by the spin at a particular site. The spin senses the symmetry of the Coulomb field of its neighbors because its direction is coupled to that of the molecular orbital by spin-orbit interaction. Thus, the three microscopic ingredients necessary for magnetostriction are:

- 1) the symmetry of the magnetic orbitals must be less than spherical (i.e. $L \neq 0$).
- 2) the symmetry of the local environment (crystal field) must be less than spherical, and
- 3) the spin-orbit coupling $\xi \mathbf{L} \cdot \mathbf{S}$ must be non-zero.

Clearly a strain in the crystal field seen by an atom, such as occurs at a surface, will alter the ME coefficient and therefore alter the extent to which that strain perturbs the magnetization.

For transition metals and alloys, the magnitude of λ_s is generally below 10^{-4} and it is known to be stress dependent. Barandiaran et al.¹⁰ have determined that $(\partial\lambda_s/\partial\epsilon)$ is of order -12×10^{-6} for amorphous $(\text{Co}_{0.94}\text{Fe}_{0.6})_{75}\text{Si}_{15}\text{B}_{10}$ for bulk tensile

strains up to 1%. There is reason to believe, therefore, that the huge strains at a surface could alter the strength or even the sign of λ_s there. Mazumdar and Juretschke¹¹ have used the metallic field effect in permalloy (90-10) thin films to determine that the surface ME effect is an order of magnitude less (they measure $\eta = \partial(\ln K)/\partial \epsilon \approx \lambda_s^S/K$) than in the bulk. Szymczak¹² has used strain modulated FMR on Ni-C and Ni-Ag multilayers to show that the effective magnetostriction due to interfacial strain varies inversely as the Ni layer thickness. He finds λ_s^{eff} becomes less negative ($\lambda_s^{\text{bulk}} \approx -36 \times 10^{-6}$) as Ni thickness decreases. The present paper is concerned with the significance and measurement of surface magnetostriction.

2. MEASUREMENT OF SURFACE MAGNETOSTRICTION

2.1 Measuring surface magnetization

Surface magnetization (sampled over about 5Å at the surface) can be measured from the spin polarization of secondary electrons emitted from a magnetic surface. It has been shown¹³ that the spin polarization

$$P = (N^+ - N^-)/(N^+ + N^-) \quad (4)$$

of the true secondary electrons¹⁴ emitted from a ferromagnet (where N^+ is the number with positive spin component along a chosen axis) is equal to the polarization of the valence electrons inside the material

$$P' = (n^+ - n^-)/(n^+ + n^-) = n_B/n_V \quad (5)$$

where n^+ is the number of spin up valence electrons, $n^+ + n^- = n_V$ (= 7.68 in our case) is the total number of valence electrons, and n_B is the spin imbalance or magneton number ($n_B = 2.2, 1.7$ and $0.6 \mu_B$ for Fe, Co and Ni, respectively). Spin polarization can be measured using a Mott detector¹⁵, a LEED polarimeter¹⁶ or a diffuse scattering polarimeter¹⁷. In such instruments the spins of interest are subjected to elastic spin-orbit scattering, often by a gold target, and the resulting scattering asymmetry A about a plane containing the spin quantization direction is measured:

$$A = (N_L - N_R)/(N_L + N_R). \quad (6)$$

Here N_i ($i = L, R$) is the number of electrons detected to the left or right of the scattering plane. The polarization of the beam is related to A by the efficiency or Sherman function S of the detector

$$S = A/P \quad (7)$$

Combining Eqs. 4, 5, and 7 we have for the surface magnetization

$$M^S = (N/V)n_B\mu_B = (N/V)\mu_B n_V A/S \quad (8)$$

where $N/V = N_A \rho f/w$ is the number of magnetic atoms per unit volume, each with moment $n_B \mu_B$, N_A is Avogadro's number, ρ is the mass density, f is the fraction of the atoms present that are magnetic and w is the molar mass ($f = 0.76$ and $w = 49$ g/mole in our case).

Equation 8 has been used to determine the surface magnetization of a variety of materials by measuring the asymmetry of their secondary electron spectrum^{7,13,18}.

2.2 Measuring magnetostriction

Bulk magnetostriction is most often measured using a strain gauge, or a capacitance gauge to determine the length change along a particular direction in a material when the saturation magnetization is rotated relative to the strain direction (Eq. 2). But λ can also be determined by noting the change in magnetization in a given direction due to a stress or strain.

The differential of the Gibbs free energy of a ME system at constant temperature, $dG = -\epsilon d\sigma - B dH$, where ϵ and $B = \mu_0(H + M)$ are dependent variables, leads to the linear relations:

$$d\epsilon(\sigma, H) = (\partial\epsilon/\partial\sigma)_H d\sigma + (\partial\epsilon/\partial H)_\sigma dH = s^H d\sigma + d dH \quad (9)$$

$$dB(\sigma, H) = (\partial B/\partial\sigma)_H d\sigma + (\partial B/\partial H)_\sigma dH = d d\sigma + \mu^0 dH.$$

These equations define s^H , the compliance ($1/Y^H$) at constant field, μ^0 , the permeability at constant stress, and d , the magnetostrictivity. Eq. 9b shows that it is possible to measure d from the stress or strain dependence of B or M :

$$d = (\partial B/\partial\sigma)_H = (\partial B/\partial\epsilon)_H (\partial\epsilon/\partial\sigma)_H = s^H (\partial B/\partial\epsilon)_H \quad (10)$$

Further, integrating $d = (\partial\epsilon/\partial H)_\sigma$ shows that

$$\lambda(H) = \int d(H) dH \quad (11)$$

Thus, if we can measure $(\partial B/\partial\epsilon)_H$ at several different fields, we can get d which can be integrated to give $\lambda(H)$. It now remains to describe a simple and repeatable way to measure $(\partial B/\partial\epsilon)_H$.

2.3 Details of experiment

As yet we do not know the surface elastic constants of the material of interest. Therefore we need a method that imposes a known stress or a known strain at the surface for which we will determine either $(\partial B/\partial\sigma)_H$ or $(\partial B/\partial\epsilon)_H$, respectively. The latter

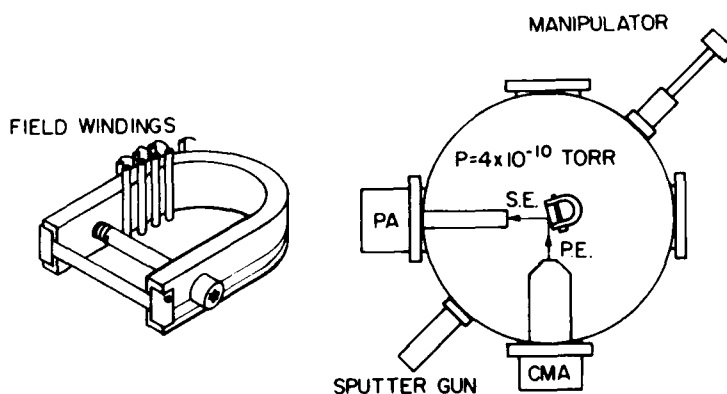


Fig. 1 Left, flexible, externally adjustable yoke holding ribbon sample. Some field windings are shown. Right, schematic of u.h.v. chamber showing primary electron (PE) source in Auger analyzer (CMA), secondary electrons (SE), and polarization analyzer (PA).

is more easily done by simply bending the sample *in situ*. If its curvature at the point of measurement is well represented by an arc, it is easy to relate the displacement to the strain at the front surface.

A sample holder has been made that allows a long ribbon of magnetic metal to be wound about a supporting yoke (Fig. 1a). The ribbon is clamped at the ends of each tyne so that it forms a flat surface across the open end of the yoke. Electrical windings are applied to the yoke and the sample can be heated to 300°C. A specially machined screw joins the tynes of the yoke a few mm behind the flat face of the sample. A 5° turn of the screw produces a 6.3 μm displacement of the tynes. Before being placed in the u.h.v. chamber the curvature and displacement of the sample were optically calibrated. When the tynes are pulled together by the screw, the ribbon can be deflected so that its front surface is either convex or concave. Surface strains up to 6×10^{-4} in increments of approximately 3×10^{-5} are achievable.

We may now combine Eqs. 8 and 10 with $B = \mu_0(H+M)$ to give

$$d^S = (\partial B / \partial \epsilon) s^H = (\mu_0 \mu_B \rho f N_A s^H / S_w) (\partial A / \partial \epsilon)_H \quad (12)$$

which, with Eq. 11, gives $\lambda^S(H)$.

The primary electron energy was 2 keV which is just above the knee of our secondary electron yield vs primary energy curve⁷. An instrumental asymmetry, linear in applied field, due to a weak fringe field above the sample face which deflects the secondary electrons up or down, has been removed from the data.

3. RESULTS

The solid line in Fig. 2 shows a typical $A(H)$ loop at $\epsilon = 0$ for the amorphous alloy $\text{Co}_{76}\text{Cr}_4\text{B}_{20}$. Detailed VSM studies on the same material show its bulk magnetization to be 82% saturated, $M = 6.2 \times 10^5$ A/m, at $H = 640$ A/m (8 Oe). With our polarimeter efficiency $S = 0.154 \pm 7\%$, the asymmetry at 8 Oe, $A = 1.93\%$, gives the surface magnetization from Eq. 8 to be within a few percent of 6.2×10^5 A/m (i.e. 82% of M_s in Table). The dotted curve shows $A(H, \epsilon)$ for a compressive stress $\epsilon = -2 \times 10^{-4}$ so the increasing magnetization indicates λ_s^S is negative. (The bulk magnetostriction of this metallic glass is also negative¹⁹, $\lambda_s^b = -3.8 \times 10^{-6}$). The surface magnetostriction is proportional to the area between these curves divided by ϵ . Because we cannot fully saturate the specimen in the uhv chamber, we can only calculate $\lambda_s^S(8 \text{ Oe})$ or estimate the saturation surface magnetostriction. Integrating the $\partial A / \partial \epsilon$ values up to $H = 8 \text{ Oe}$ gives $\lambda_s^S(8 \text{ Oe}) = -8 \times 10^{-6}$, twice the bulk value. If we estimate the strain derivative of A to decrease linearly, reaching zero at saturation, the surface magnetostriction would be as great as $\lambda_s^S = -53 \times 10^{-6}$!

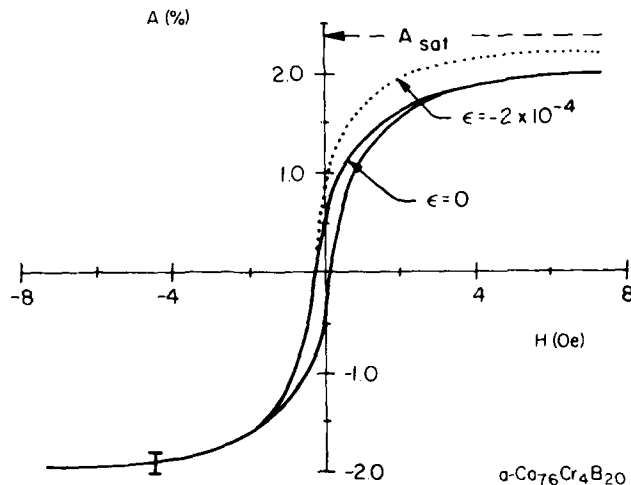


Fig. 2 Asymmetry vs applied field for zero strain and modest compressive strain at front surface of ribbon. Saturation asymmetry based on bulk measurements is indicated.

Table. Properties of amorphous $\text{Co}_{76}\text{Cr}_4\text{B}_{20}$

| | Ref. |
|---|------|
| Mass density: $\rho = 8.2 \text{ g/cm}^3$ | a |
| Saturation moment: $n_B = 1.1 \mu_B/(\text{CoCr})$ | b,c |
| Saturation magnetization: $M = 7.6 \times 10^5 \text{ A/m (S.I.)}$ ($\sigma = 93 \text{ emu/g}$, $4\pi M = 9600 \text{ Gauss}$) | b,c |
| Curie temperature: $T_C > T_X \approx 800 \text{ K}$ | c |
| Bulk saturation magnetostriction $\lambda_s = 3.8 \times 10^{-6}$ | b |
| Young's modulus $Y^H = 1/s^H = 6.2 \times 10^{10} \text{ N/m}^2$ | d |
| Valence electrons per F.U.: $n_V = 7.68$ | |
| Molar weight: $w = 49 \text{ g/mole}$ | |

- a) R. C. O'Handley, M. E. Eberhardt, K. H. Johnson, and N. J. Grant, J. Appl. Phys. **53**, 8231 (1982)
- b) Ref. 19.
- c) R. C. O'Handley, Sol. St. Comm. **38**, 703 (1981).
- d) Value given is for Metglas[®] 2714A $\text{Co}_{66}\text{Fe}_4\text{B}_{14}\text{Si}_{15}$ from Metglas Products catalogue.

We have assumed a constant (field independent) bulk value for s^H in evaluating λ^S (Eq. 12). This is incorrect on two counts. First, s^H is field dependent because of the ΔE effect. This has little effect on the $\epsilon \neq 0$ data shown in Fig. 2 because the compressive stress in a $\lambda < 0$ material tends to quench the ΔE effect. It does complicate the data for tensile stress so they were not used to calculate λ^S . Second, the assumption of a bulk elastic constant at the surface could be in error because of the huge strain and reduced bonding there. It may be more accurate to say that we have estimated the product $Y^H, s^H \lambda^S$ to be in the range -5×10^5 to $-32 \times 10^5 \text{ N/m}^2$. If, as may be the case, $Y^S < Y^B$, then we expect λ_s to be even more negative than estimated.

4. CONCLUSION

Preliminary measurements indicate that the surface magnetostriction of a cobalt-base amorphous alloy is considerably more negative than its bulk value. Much narrower limits can be put on the actual value of λ^S with experimental modification. These measurements need to be extended to other materials and particularly to single crystals where their significance may be more readily assessed. Such measurements are critical to proper understanding of magnetism at surfaces and in nanostructured materials.

5. ACKNOWLEDGEMENT

This work was supported by ONR contract Nos. N00014-86-K0257 and N00014-90-J1174. Helpful comments and assistance from Joe Woods and Craig Ballentine are gratefully acknowledged.

References

- 1) A.J. Freeman and C.L. Fu, J. Appl. Phys. **61**, 3356 (1987).
- 2) C.D. Gelatt, Jr., H. Ehrenreich, and R.E. Watson, Phys. Rev. B **15**, 1613 (1977).
- 3) C. Chappert and P. Bruno, J. Appl. Phys. **64**, 5736 (1988).
- 4) J.G. Gay and R. Richter, Phys. Rev. Lett. **56**, 2728 (1986).
- 5) M. Stamparoni, A. Vaterlaus, M. Aeschlimann, and F. Meier, Phys. Rev. Lett. **59**, 2483 (1987); N.C. Koon, B.T. Jonker, F.A. Volkening, J.J. Krebs, and G.A. Prinz, Phys. Rev. Lett. **59**, 2463 (1987), and B. Heinrich, K.B. Urquhart, A.S. Arrott, J.F. Cochran, K. Myrtle, and S.T. Purcell, Phys. Rev. Lett. **59**, 1756 (1987).
- 6) R.J. Hicken, G.T. Rado, Gang Xiao, and C.L. Chien, Phys. Rev. Lett. **64**, 1820 (1990).
- 7) D. Mauri, R. Allenspach, and M. Landolt, J. Appl. Phys. **58**, 906 (1985).
- 8) L.E. Klebanoff, S.W. Robey, G. Liu and D.A. Shirley, Phys. Rev. B **30**, 1048 (1984).
- 9) E. Tamura and R. Feder, Sol. St. Comm. **44**, 1101 (1982) and J. Korecki and U. Gradmann, Phys. Rev. Lett. **55**, 2491 (1985).
- 10) J.M. Barandiaran, A. Hernando, V. Madurga, O.V. Nielsen, M. Vasquez and M. Vasquez-Lopez, Phys. Rev. B **35**, 5066 (1987).
- 11) P. Mazumdar and H.J. Juretschke, Phys. Rev. B **19**, 672 (1979).
- 12) H. Szymczak, Proceedings of XXIV Ampere Congress, Poznan, Poland, 1988.
- 13) E. Kisker, W. Gudat and K. Schroder, Sol. St. Comm. **44**, 591 (1982) and G. Chrobok and M. Hoffmann, Phys. Lett. **57A**, 257 (1976).
- 14) D.R. Penn and S.P. Apell, Phys. Rev. Lett. **55**, 518 (1985).
- 15) J. Kessler, Polarized Electrons, Springer Verlag (Springer Verlag, Berlin, 1976).
- 16) J. Kirschner in Polarized Electrons at Surfaces, ed. by G. Hohler, Springer Tracts in Modern Physics, Vol. 106 (Springer Verlag, Berlin, 1985).
- 17) J. Unguris, D.T. Pierce and R.J. Celotta, Rev. Sci. Instrum. **57**, 1314 (1988).
- 18) J. Unguris, D.T. Pierce, A. Galejs and R.J. Celotta, Phys. Rev. Lett. **49**, 72 (1982), J.P. Woods, A. Ushioda, A. Fukuno, S.W. Sun, L. Henderson and R.C. O'Handley, J. Appl. Phys. **64**, 5446 (1988).
- 19) R.C. O'Handley and M.O. Sullivan, J. Appl. Phys. **52**, 1841 (1981).

MAGNETIC RARE EARTH ARTIFICIAL METALLIC SUPERLATTICES

J.J. Rhyne, R.W. Erwin, and J.A. Borchers
National Institute of Standards and Technology
Gaithersburg, Maryland 20899

M.B. Salamon, F. Tsui, R. Du, and C.P. Flynn
Department of Physics
University of Illinois
Urbana, Illinois 61801

INTRODUCTION

Intense interest has been generated over the past several years in the growth and properties of layered magnetic materials, both from a fundamental point of view and for applications. Layered structures have been prepared by a variety of techniques including sputtering, electro-deposition, and evaporation, and include semi-conducting, metallic, and insulating materials. These systems can consist of crystalline layers of one element or compound interleaved with layers of a different element or compound, or alternatively may be built of amorphous layers or amorphous layers alternated with crystalline layers. Depending on the materials and growth techniques, these multilayers may be produced (a) with no uniform crystallographic alignment or coherence from layer to layer, (b) with alignment of one specific crystallographic axis direction along the growth (stacking) direction, or (c) with true three-dimensional atomic order (epitaxy) in which there is multi-layer atomic registry both along the growth axis and also within the growth planes. For the purposes of this review, the term *artificial metallic superlattice* will be reserved for this latter category of true three dimensionally coherent layered structures, while the term *multilayer* will be used for layered structures in which coherence is present in less than three dimensions.

The recent refinements in computer-controlled molecular beam epitaxy (MBE) techniques for the growth of single crystal artificial superlattices of two or more distinct compositions have opened up vast possibilities for the production of tailor-made artificial superlattices with controlled film thicknesses down to atomic dimensions and with highly reproducible stacking sequences. This has provided previously unavailable opportunities to examine problems of interaction ranges, tunneling distances, and other coherent phenomena which are dependent on the superlattice periodicity. In particular, the development¹ starting in 1984 of MBE growth procedures for single crystal rare earth metal superlattices has permitted prototypical tests for verifying many of the theoretical concepts of magnetic exchange, anisotropy, and magnetostriction effects in the rare earths which could not previously be examined in as controlled a way using conventional bulk materials.

Superlattices consisting of magnetically concentrated layers (e.g., Dy) interleaved in a controlled fashion with magnetically "dead" layers (e.g., Y) offer a near-ideal opportunity to investigate these basic interactions. It should be noted that such a system is unique and can never be simulated by bulk dilute alloys because of the attendant reduction in the average exchange interaction with the decreased density of magnetic ions and the probability of some nearest neighbors even in very dilute samples. Y and Lu have similar physical and electronic properties to the magnetic heavy rare earths and because of the relatively small mismatch between the basal plane lattice parameters (e.g., 1.6% for Dy and Y), good epitaxial growth is achieved. The key to the growth of rare earth superlattices¹ (see Fig. 1 left) lies in the use of a [110] Nb buffer layer evaporated onto a [11 $\bar{2}$ 0] sapphire substrate beneath the rare earth metals. This buffer layer prevents the oxidation of the sapphire by the rare earths during growth. An Y strain-relieving overlayer is placed between the Nb and the rare earth bilayers. Y and Nb have a nearly perfect 3:4 atomic registration sequence which allows good epitaxial growth in spite of the 33% lattice parameter mismatch. Lattice parameter mismatch is a moderately serious constraint for MBE-produced materials, since this mismatch must generally be taken up by lattice dislocations. As shown in the figure for a [Dy|Y] superlattice, the thick Y layer is followed by a constant bilayer repeat sequence of ℓ of atomic planes of Dy and m atomic planes of Y. This is designated $[Dy_{\ell}|Y_m]_N$ where N is the total number of bilayers. Rare earth superlattices have been produced by similar procedures in the [Gd|Y],^{2,3} [Dy|Y],^{4-9,13} [Er|Y],¹⁰⁻¹² [Ho|Y],¹³ and [Dy|Gd]¹³ systems.

The [Dy|Y] and [Er|Y] superlattices discussed in this review were grown at the University of Illinois. During evaporation the chamber pressure was maintained in the 10^{-9} Torr range to minimize oxidation of the rare earths which were evaporated at a rate of only about 0.5-1.0 Å per second with a substrate temperature of approximately 300 C. These conditions were chosen to minimize interdiffusion of the Y and lanthanide layers. Analysis of the neutron or x-ray diffraction¹² data for the intensity of the bilayer harmonics (see next section) confirms that this interdiffusion is quite minimal and that the composition reaches

RARE EARTH SUPERLATTICE STRUCTURE

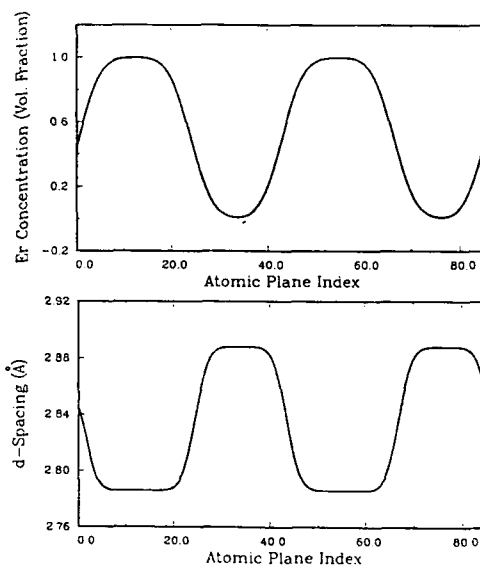
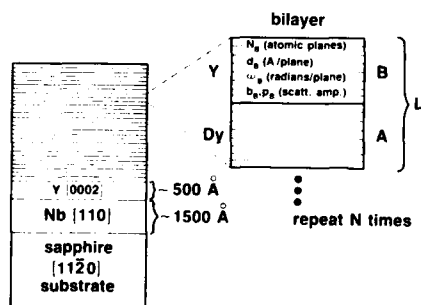


Fig. 1 (Left) Schematic drawing of the rare earth multilayer structure. The expanded view of a bilayer lists the physical parameters of the A and B layers (see text). (Right, top) The composition profile calculated from the x-ray diffraction intensities for an $[Er_{23.5}|Y_{19}]_{100}$ superlattice showing that interdiffusion is limited to approximately 5 total planes. (Right, bottom) The d-spacing variation for the same superlattice illustrating the rather abrupt transition resulting from the relatively large Er-Y lattice mismatch.

85% of the pure element (Y or Er,Dy) within about two planes on either side of the interface. (See Fig. 1 right.) The intensity analysis of the same $[\text{Er}_{23.5}|\text{Y}_{19}]_{100}$ superlattice also confirms that the d-spacing variation is quite abrupt as shown in Figure 1 (right), reflecting the relatively large (2.5%) lattice mismatch between Er and Y.

In bulk crystalline form, the lanthanide elements and their alloys with non-magnetic but chemically and electronically similar elements such as yttrium, scandium, and lutetium, have long provided a fertile area for the study of indirect exchange interactions, crystal field anisotropy, and magnetostrictive effects. The elements have weak exchange compared to the 3d transition elements as illustrated by their low ordering temperatures (e.g., Tb, $T_N = 230$ K) and have anomalously large crystal field and magnetostriction interactions which arise from the strong spin orbit coupling and highly non-spherical 4f charge distribution. The occurrence of periodic incommensurate magnetic orderings in the heavy lanthanides (except for the S state ion Gd) below their Néel temperatures is a consequence of electronic effects, in particular the occurrence of nearly two-dimensional parallel sections (nesting) on the hole Fermi surface which are spanned by a Q-vector whose magnitude which determines the initial stable periodicity of the magnetic ordering. At lower temperatures, the free energy associated with the magnetostrictive and anisotropy interactions becomes significant and strongly perturbs the basic periodic magnetic orderings leading to phase transitions to a ferromagnetic state in Tb, Dy, Ho, and Er. These transitions are largely driven by a lowering of the magnetostrictive energy arising from a coupling of the local moments to the hexagonally symmetric lattice strains. Recently it has been suggested that dipole-dipole interactions of extremely long range may be also responsible for perturbing the c-axis modulated moment states found in Ho¹⁴ and probably Er. For details and references on the fundamental orderings and interactions in the rare earth metals, one is referred to the many review works available, including, but certainly not limited to, those given in refs.¹⁵⁻¹⁷

Neutron scattering has played a seminal role in elucidating the spin structures which occur in the lanthanide metals and in providing details of the perturbations of these structures at temperatures below the Néel point and those induced by the application of external fields. Much of this work was done by W.C. Koehler and his associates at Oak Ridge starting more than 25 years ago. (See reference 15.) Recently, highly precise synchrotron radiation studies have been conducted at very close temperature intervals which have shown additional details of the magnetic ordering in Ho¹⁸ and Er¹⁹ including the occurrence of lock-in transitions in which the periodic moment wave-vector passes through a series of stair-step-like changes as the temperature is lowered, corresponding to various spin-slip states. (See references 18,19 and later discussion.) The step-like changes are in contrast to the more monotonic linear variation reported in the early neutron measurements taken with much broader temperature intervals and have been confirmed also by recent neutron scattering studies.

NEUTRON SCATTERING FROM ARTIFICIAL METALLIC SUPERLATTICES

For artificial metallic superlattices, neutron diffraction provides atomic structural information complementary to that obtained from x-ray diffraction.²⁰ In addition, the magnetic interaction of the neutron with ordered spins in the superlattice provides the opportunity to study the magnetic spin configurations and the range of coherence of the magnetism. In particular, it can be used as a probe of the propagation of magnetic phase information from a magnetically ordered layer (e.g., Dy) across the intervening "non-magnetic" Y layer to additional ordered layers.

Neutron diffraction studies on the $[\text{Dy}|\text{Y}]$ superlattices were performed in reflection geometry at the National Bureau of Standards Reactor. Neutron data were taken on a triple-axis spectrometer using $\lambda = 2.4$ Å wavelength neutrons from a (002) reflecting pyrolytic graphite monochromator and equivalent analyzer, the latter set for the elastic position to suppress background scattering. Soller slit collimators with 40'-25'-25'-40' acceptance

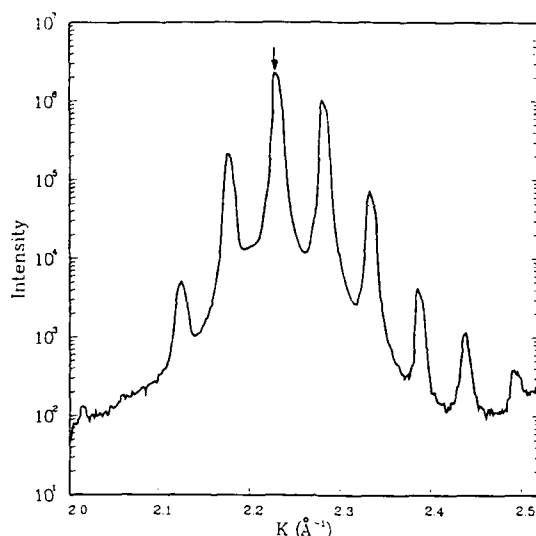


Figure 2. Room temperature x-ray (000 l) diffraction pattern for an [Er_{23.5}|Y₁₉]₁₀₀ superlattice showing the presence of harmonics up to fifth order. The arrow marks the position of the central (0002) Bragg peak.

angles were used before and after the monochromator and analyzer respectively. This produced a Q -resolution of 0.021 \AA^{-1} for scans along Q and 0.008 \AA^{-1} transverse to Q for $Q = 4\pi \sin \Theta/\lambda$ at the [0002]. For most scans, the c -axis of the superlattice, which was perpendicular to the film plane, was oriented parallel to the scattering vector, which allowed continuous scans of the wave vector Q along the (000 l) direction.

The basic unit cell of an A-B superlattice is one bilayer (e.g., one Y + one Dy layer). Considered apart from the effects of intralayer atomic ordering, the bilayer sequence would then give rise to a set of peaks along (000 l) corresponding to diffraction from the bilayer cell at evenly spaced values of $\Delta Q = 2\pi/L$ where L is the bilayer thickness. The Bragg diffraction conditions can be satisfied in two ways: (a) the above diffraction from the bilayer unit cells which can be directly observed at low angle experiments (e.g., [Mo|Si] artificial superlattices²⁰) and (b) conventional diffraction from the atomic order within the bilayers seen at large angles. In the small angle case $N-2$ subsidiary maxima, arising from diffraction by the entire superlattice, are present between the principal bilayer diffraction peaks. N is the total number of bilayers. These subsidiary maxima are only observable if the bilayer repeat sequence is nearly perfect and the spectrometer resolution is at least comparable to $2\pi/NL$. In the large angle regime, illustrated by the x-ray diffraction pattern for an [Er_{23.5}|Y₁₉]₁₀₀ superlattice in Fig. 2, the atomic order within a bilayer modulates the intensity of the bilayer Bragg peaks and has the effect of singling out a set of predominant (000 l) peaks from the infinite set of bilayer reflections. If the lattice parameter mismatch is reasonably small, these groups of peaks occur at multiples of $Q = 2\pi/\langle d \rangle$ where $\langle d \rangle$ corresponds to a weighted average d -spacing of the A and B layers of the bilayer. Other peaks (bilayer harmonics) in the neighborhood of the principal ones fall off in intensity in a manner controlled by the relative nuclear scattering amplitudes $b_{A,B}$, layer thicknesses, and the lattice parameter mismatch. The last quantity is additionally responsible for intensity asymmetry which can occur for the harmonics on opposite sides of the fundamental peak. In general, the number of harmonics present is an indication of the crystal perfection of the superlattice and the sharpness of the interface boundary. In the extreme limit of a sine wave composition modulation, only one harmonic exists.

The addition of incommensurate magnetic order, such as found in Dy and Er, produces additional principal scattering peaks of solely magnetic origin at Q 's dictated by

the magnitude of the magnetic propagation vector. The principal satellite peaks occur along the c^* direction on opposite sides of the nuclear (000 l) peaks (for the Dy structure) and are designated Q^+ and Q^- . They are again individually part of an infinite repeating set of magnetic harmonics with amplitudes controlled by factors analogous to the nuclear case -- the magnetic scattering amplitudes $p_{A,B}$ ($p_B = 0$ for Y) and the magnetic propagation vectors $\kappa_{A,B}$ in both A and B layers. Note that even though Y has no 4f magnetic electrons and is only paramagnetic, a spin density wave may be formed in the conduction band with characteristic propagation vector κ_B as discussed later. In Er superlattices, the principal moment component is parallel to the c -axis and thus gives rise to satellites along c^* about $(hk\ell)$ $\{h,k \neq 0\}$ class nuclear reflections, but not about the (000 l) peaks. (See eqn. 3.) As discussed later, at low temperature the transverse moment components order into a helix which then gives rise to weak [000 l] $^\pm$ satellites as well.

The neutron scattering intensity for the c^* direction (z) for a superlattice can be written as the sum of the coherent nuclear and magnetic scattering terms as:

$$I(Q) = S_{nuc}(Q) + S_{mag}(+Q) + S_{mag}(-Q) \quad (1)$$

where the nuclear structure factor has the form:

$$S_{nuc}(Q) = \left| \sum_{m=0}^{N-1} b_m e^{iQ \cdot \mathbf{r}_m} \right|^2 \quad (2)$$

and the magnetic structure factor can be written:

$$S_{mag}(\pm Q) = \left| \sum_{m=0}^{N-1} p_{m\perp} e^{iQ \cdot \mathbf{r}_m \pm i\phi_m} \right|^2 \quad (3)$$

b_m is the nuclear scattering amplitude of atoms in the m atomic plane, $p_{m\perp}$ is the coherent magnetic scattering amplitude proportional to the moment component perpendicular to the scattering vector, and ϕ_m is the cumulative layer magnetic phase shift or the propagating magnetization wave.

In the case of an idealized $[n_A | n_B]_N$ superlattice with perfectly sharp interfaces, the nuclear scattering intensity is:

$$S_{nuc}(Q) = \frac{\sin^2(NQL/2)}{\sin^2(QL/2)} \left\{ \frac{\sin^2(n_A Q d_A/2)}{\sin^2(Q d_A/2)} b_A^2 + \frac{\sin^2(n_B Q d_B/2)}{\sin^2(Q d_B/2)} b_B^2 \right\} \\ + 2b_A b_B \cos(QL/2) \left\{ \frac{\sin(n_A Q d_A/2) \sin(n_B Q d_B/2)}{\sin(Q d_A/2) \sin(Q d_B/2)} \right\} \quad (4)$$

where N is the total number of bilayers each of thickness $L = n_A d_A + n_B d_B$, where d is the atomic d -spacing of the respective A and B layers. The same functional form as equation (4) also describes the x-ray diffraction profile.

For a superlattice in which only the A layer contains magnetic atoms (e.g., $p_B = 0$) and for which the total magnetic phase shift across a bilayer is given by $\Phi = n_A \kappa_A d_A + n_B \kappa_B d_B$, the corresponding magnetic scattering is:

$$S_{mag}(\pm Q) = \left\{ \frac{\sin^2[N(QL \pm \Phi)/2]}{\sin^2(QL \pm \Phi)/2} \frac{\sin^2[n_A(Q \pm \kappa_A)d_A/2]}{\sin^2[(Q \pm \kappa_A)d_A/2]} \right\} \frac{p_{A1}^2}{2} \cdot (5)$$

Details of the calculation of these structure factors are given in reference⁷. Each of the above structure factors consists of a product of terms -- the first produces the infinite set of bilayer peaks and the second is a much broader envelope function (i.e., generally $N_A d_A \ll NL$) which, for the nuclear case, has its maximum on one of the bilayer Bragg peaks only if there is no lattice mismatch. The product of these two terms gives the intensity modulation of the diffracted intensity peaks as shown in Fig. 2 for the atomic structure and in Fig. 3 for the magnetic structure.

MAGNETIC SCATTERING, STRUCTURE, AND COHERENCE

Basal Plane Helical Spin Configurations

Fig. 3 shows the results of a $Q_z = (000l)$ scan around the (0002) principal Bragg peak for a $[\text{Dy}_{16}\text{Y}_{20}]_{89}$ superlattice for several temperatures near and below $T_N = 167$ K. Note that there is one temperature-independent central peak at $Q = 2\pi/\langle d \rangle$ of structural origin with one harmonic visible and displaced by $\Delta Q = 2\pi/L = 2\pi/102\text{\AA} = 0.0308\text{\AA}^{-1}$. Higher order harmonics are not visible on this scale. The magnetic scattering

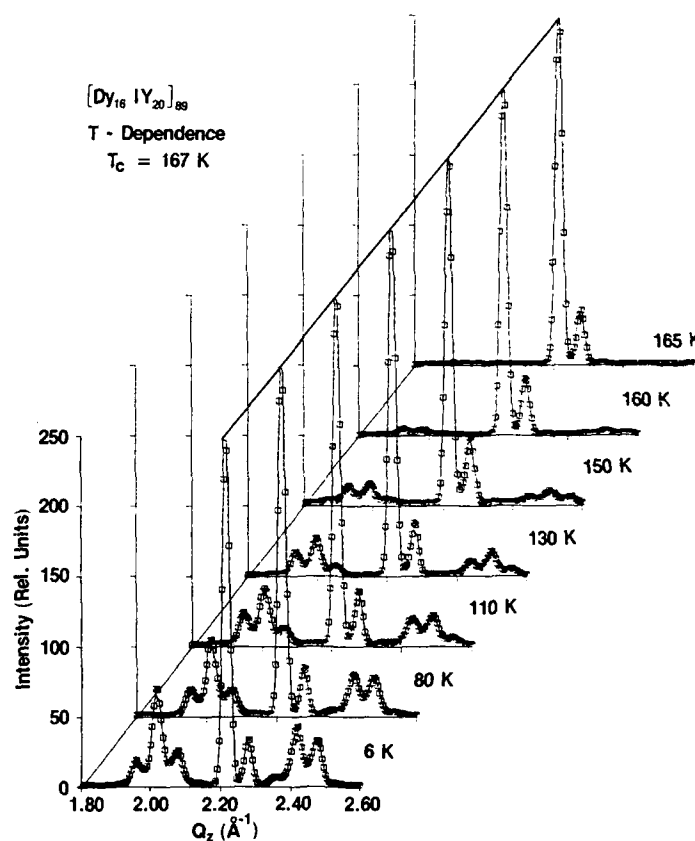


Fig. 3. Neutron diffraction scans along (000 l) in a $[\text{Dy}_{16}\text{Y}_{20}]_{89}$ superlattice for temperatures below T_N . Note the temperature independence of the (0002) peak at $Q_z = 2.215\text{\AA}^{-1}$. The small peak to the right is a bilayer harmonic. The fundamental and two bilayer harmonics are shown for both Q^- ($\approx 2.02\text{\AA}^{-1}$) and for Q^+ ($\approx 2.42\text{\AA}^{-1}$) magnetic satellites. T_c denotes the helical ordering temperature $T_N = 167\text{K}$.

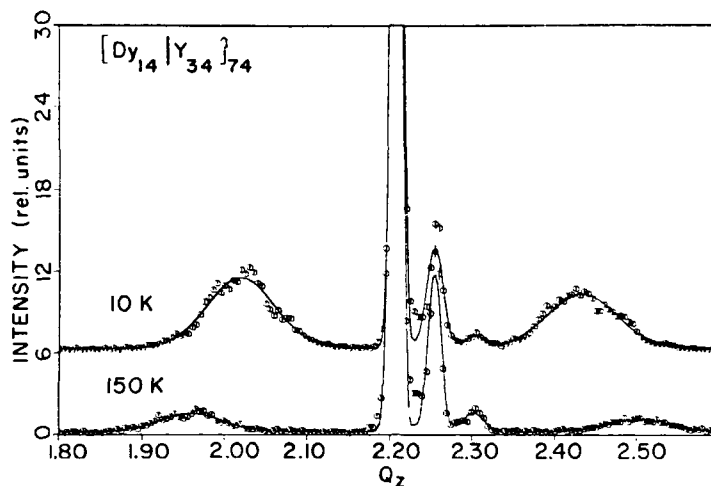


Fig. 4 Scattered intensity from a $[\text{Dy}_{14}|\text{Y}_{34}]_{74}$ superlattice showing the loss of magnetic coherence at larger Y layer thicknesses, and the concomitant peak broadening.

arising from the incommensurate spin structure gives rise to the temperature-dependent Q^- and Q^+ satellite peaks on either side of the nuclear structure peaks. As discussed later, the ferromagnetic transition which occurs at 85K in bulk Dy is suppressed in the superlattices. This would have been manifested by additional intensity appearing at low temperatures on the nuclear peaks.

The presence of the fully resolved bilayer harmonics on either side of the Q^+ and Q^- satellites as shown in Fig. 3 is dramatic evidence that the magnetic structure is coherent over many superlattice periods and is not interrupted at the layer boundaries or by the intervening Y layers. Also important is the fact that the chirality of the helix is maintained across the bilayer boundary. If the magnetic order were confined within single Dy layers, the Q width of the central magnetic satellite peak would encompass the bilayer harmonic positions rendering them unresolved. This is the case found for a superlattice of $[\text{Dy}_{14}|\text{Y}_{34}]_{74}$ (see Fig. 4) in which the coherence range has dropped to less than one bilayer due to the increased number of intervening layers of Y. (See later discussion.)

From the data of Fig. 3 the coherence ranges of the atomic (nuclear) and magnetic order can be calculated from the intrinsic Q -width of the respective nuclear and magnetic peaks after deconvoluting the instrumental resolution width. The nuclear peaks typically give a coherence range of 500-700 Å. The resulting magnetic coherence distance after correcting for the nuclear coherence ranges from 580 Å in the sample of 46 Å of Dy separated by 26.5 Å of Y, down to 245 Å in a 46 Å Dy, 56 Å Y sample, and finally to 80 Å in a 40 Å Dy, 95 Å Y specimen. All values but the last correspond to the propagation of magnetic phase coherence across multiple bilayer cells.

The decrease in the correlation length with increasing Y thickness has been examined in a series of $[\text{Dy}|\text{Y}]$ superlattices with essentially fixed Dy layer thicknesses of 15 ± 1 atomic planes (≈ 43 Å) and varying Y layer thicknesses as shown in Fig. 5. The coherence range dependence quite accurately reflects a $1/r_Y$ fall-off where r_Y is the thickness of the intervening planes (≈ 2.87 Å per plane). As discussed later, the exchange coupling in the c -direction is of finite range, and thus this behavior suggests the presence of a decorrelation mechanism (viz., Dy basal plane anisotropy, thermal disorder, etc.) that competes with the exchange and leads to the loss of coherence for increasing Y thickness. The coherence length extrapolates to the non-interacting single layer limit of one Dy layer thickness (43 Å) at approximately 140 Å of Y.

In order to examine the factors controlling long-range coherent magnetic coupling, superlattices have been examined for the dependence of the coherence on (a) the direction of the spin alignment (e.g., basal plane or c -axis), (b) the type of spin structure

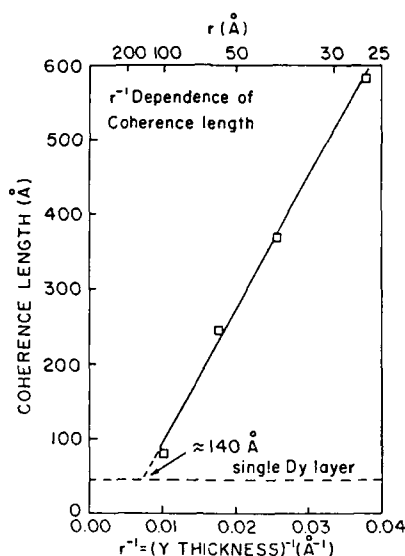


Fig. 5. The magnetic coherence length for a series of [Dy|Y] superlattices as a function of the reciprocal of the thickness of the Y layer. The number of Dy planes was held approximately constant at 15 ± 1 planes ($\sim 43 \text{ Å}$). The plot illustrates the $1/r$ fall-off of the coherence, and that the layers would become non-interacting for Y thickness greater than approximately 140 Å .

(ferromagnetic or periodic antiferromagnetic), and (c) the direction of the superlattice growth (basal plane or c-axis). The first two case studies involve varying the magnetic rare earth element and uniformly result in coherent multilayer coupling. The Dy superlattices discussed in this section are examples of basal plane helical spin structures with spins perpendicular to the propagation vector along the c^* axis, while [Er|Y] superlattices discussed in the next subsection are an example of an Ising-like incommensurate antiferromagnetic system with spins principally parallel to the c direction. [Gd|Y] superlattices are examples of a system with pure ferromagnetic coupling of spins within the layers for which either long-range ferromagnetic or antiferromagnetic interlayer coupling is found, depending on the Y thickness as shown by Majkrzak et al.²¹ The final case of rotating the growth axis relative to the spin propagation direction does in fact destroy the long-range magnetic coherence in [Dy|Y] superlattices as will be shown in a later section.

C-axis Modulated Spin Systems

Superlattices consisting of alternate layers of Er and Y represent a more complex magnetic ordering than the [Dy|Y] helical and [Gd|Y] antiferromagnetic or ferromagnetic configurations. The c-axis is the favored moment direction in Er due to a change in sign of the 4f electron quadrupole moment compared to Dy. Thus the spin alignment is parallel to the stacking direction of the superlattice and also parallel to the c-axis magnetic propagation vector. In bulk elemental form, Er initially orders at 84 K into a c-axis modulated moment structure in which the parallel (c) component of the magnetization has a sine wave amplitude modulation with a period of approximately 7 atomic layers. The transverse moment components are disordered down to 56 K and exhibit helical ordering at lower temperatures. Approximately in the same temperature range, additional harmonics signal a "squaring-up" of the c-axis modulated moment structure, until at 19 K the c-axis order becomes ferromagnetic, resulting in a conical moment state with apex angle about 27° . The scattering geometry for the Er-Y superlattice studies¹⁰⁻¹² is somewhat more complex, in that predominately basal plane reflections; for example $[10\bar{1}0]$, must be used to detect the

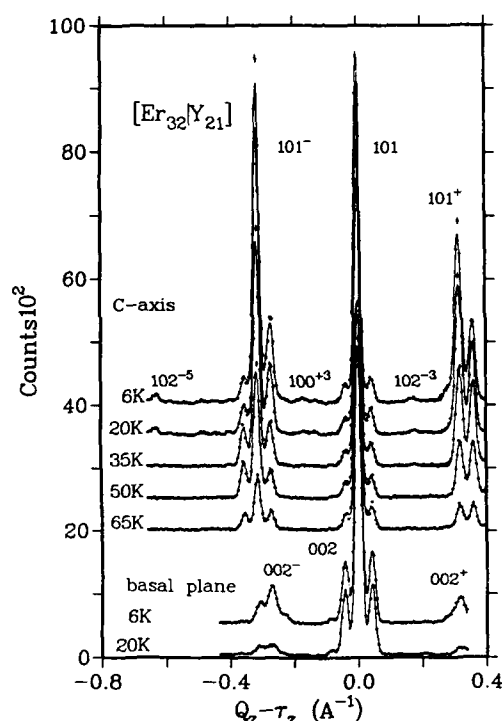


Fig. 6. Diffraction scans along the c^* direction through $(10\bar{1}0)$ and (0002) for $[\text{Er}_{32}\text{Y}_{21}]$ showing the development of a linear spin density wave with principal moment component along the c -axis. At lower temperatures the ordering "squares-up" as indicated by the appearance of higher-order harmonics [e.g., $(10\bar{1}2)^{-5}$]. Below about 30 K, the basal plane components also order as indicated by the satellites of (0002) .

c -axis moment components, since the neutron scattering is sensitive only to moment components perpendicular to Q . Basal plane ordering was detected as previously by re-orienting the sample with $[0002]$ parallel to the scattering vector.

Fig. 6 shows a composite of scans along c^* at (0002) and along c^* at $(10\bar{1}1)$ of a $[\text{Er}_{32}\text{Y}_{21}]$ superlattice demonstrating that well-defined nuclear peaks and harmonics as well as magnetic satellite peaks and harmonics are observed. The magnetic peak widths again confirm that the magnetic order is long range. The reduced intensity of the basal plane nuclear satellites results from the near equality of Er and Y scattering lengths and possible interface defects resulting from the nearly 3% lattice mismatch. The T_N for the superlattice, marked by the onset of magnetic satellites in the $(10\bar{1}0)$ scans, is 78 ± 1 K which is 7% lower than for bulk Er and similar to the reduction seen in Dy superlattices. The initial ordering is a near sinusoidal ordering of the c -axis moment components with the transverse components disordered. Below 35K, additional magnetic scattering appears which can be indexed as higher harmonics [e.g., $(10\bar{1}0)^{+3}$ and $(10\bar{1}2)^{-3,-5}$] of the fundamental magnetic satellites $(10\bar{1}1)^{\pm}$. These reflect a "squaring up" of the moment components as seen in bulk Er but at a correspondingly lower temperature than in the bulk. Below about 30 K, the basal plane moment components order into a helix; however, no conical ferromagnetic ordering is observed down to 5 K in contrast to bulk Er. The magnetic coherence range derived from the magnetic peak width, after deconvolution of the instrumental resolution, is shown in Fig. 7 as a function of the Y thickness. It is noted that the coherence range derived from the separate widths of basal plane and c -axis moment components is different. The basal plane coherence length is comparable to that found for $[\text{Dy}|\text{Y}]$ superlattices, while

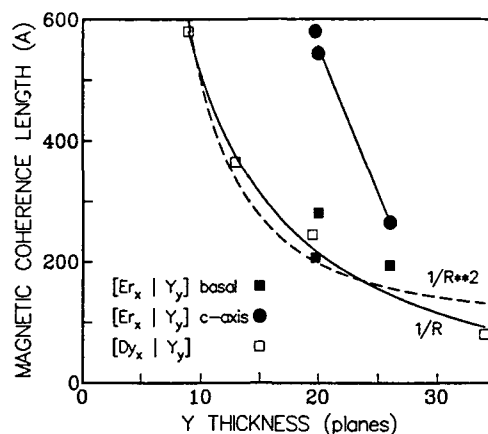


Fig. 7. Coherence length for $[\text{Er}_{32}|\text{Y}_{21}]$ and $[\text{Er}_{13}|\text{Y}_{26}]$ superlattices derived from both basal plane and c-axis moment component satellites. The basal plane values from the $[\text{Dy}|\text{Y}]$ superlattices are shown for comparison, along with $1/r_Y$ and $1/r_Y^2$ fits to the $[\text{Dy}|\text{Y}]$ data.

the c-axis values are relatively larger. The figure shows the coherence range for $[\text{Dy}|\text{Y}]$ superlattices for comparison. It is noted that the Er layer thicknesses were not held constant as was the case for the $[\text{Dy}|\text{Y}]$ superlattices in Fig. 5.

Superlattices With a Basal Plane Growth Direction

As discussed in the previous subsection, the occurrence of long-range coherent magnetism in c-axis rare earth superlattices is independent of the primary orientation of the spins and independent of whether the spin order is ferromagnetic or incommensurate antiferromagnetic. All of these systems have the common feature that the superlattice growth axis is along the c^* propagation direction of the spin system.

In order to test the dependence of the ordering on the superlattice growth direction relative to the c^* magnetic propagation vector, superlattices were prepared with the growth axis along a $[10\bar{1}0]$ basal plane direction.²² This required new preparation procedures due to the unavailability of conventional substrate materials with an appropriate lattice matching to the a-c plane of the hexagonal rare earths. Highly polished single crystal slabs of Y were used as a substrate material with the superlattice of alternate Dy and Y layers grown on top, following a thick Y buffer layer.

In the neutron scans along the a^* (growth axis) direction, the near coincidence of the Y lattice parameters and that of the superlattice prevented the direct observation of the (0002) structural peak. Instead, as illustrated in Fig. 8 for a $[\text{Dy}_{26}|\text{Y}_9]_{82}$ superlattice, the bilayer harmonics of the (0002) (enhanced by applying a magnetic field which produced ferromagnetic ordering) were scanned and their width confirmed the quality and chemical order coherence of the superlattice as shown by the $(Q_b, 0, 2.221)$ nuclear harmonics of near resolution width. Below 170 K, helical magnetic ordering was found in the basal plane of the Dy layers; however, as shown in the figure the $(0, 0, 1.995) Q^-$ magnetic satellite scanned along a^* is quite broad and there are no resolved bilayer harmonics of the magnetic ordering. Indeed the intrinsic width of this peak, after deconvolution of the resolution broadening, is $\xi = 80 \text{ \AA}$. This is quite close to the 73 \AA thickness of the Dy layers and is compelling evidence that the coherence between the helices in adjacent Dy layers is destroyed in these basal plane superlattices. This result thus established that the multiple layer coherence indeed depends on the magnetic propagation vector (c^*) being parallel to the growth axis.

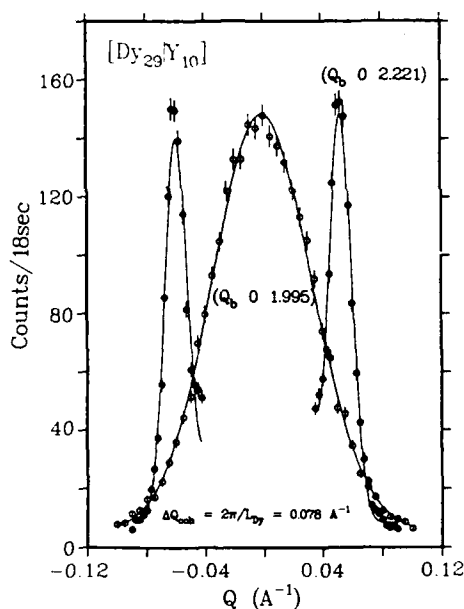


Fig. 8. Magnetic and structural peaks of the b-axis superlattice $[Dy_{26}Y_9]_{82}$ scanned along the a^* direction. The narrow resolution-limited peaks are the bilayer harmonics of the (0002), and broad peak is the helimagnetic satellite. The width of this peak corresponds to a coherence range nearly identical with the Dy layer thickness showing the loss of long-range magnetic coupling.

For the b-axis superlattices, the helical order which develops within each Dy layer also is observed to have finite range. Transverse scans show that the width of the magnetic satellite peaks along the $(11\bar{2}0)$ $[a^*]$ direction have essentially resolution width ($\xi \geq 500 \text{ \AA}$), indicating that the ferromagnetic sheets in the basal planes of each layer are uniformly ordered and probably limited in extent only by the sample size (along a) and by the layer thickness (along b). However, the coherence range measured along the c^* in-plane direction is significantly smaller and decreases with temperature to about 250 \AA below 100K . Thus the helical stacking of the a - b ferromagnetic sheets within each layer is within a finite and temperature-dependent domain size. Similar results for the range of magnetic coherence were obtained for a $[Dy_7Y_{25}]_{67}$ basal plane superlattice.

SUPERLATTICE MAGNETIC COUPLING

The above results illustrate that long-range interlayer magnetic coupling is present in superlattices for which the stacking direction is parallel to the c -axis propagation direction of the periodic magnetic system and that such coupling is destroyed for stacking sequences along basal plane directions. The interlayer exchange coupling is not simply ferromagnetic or antiferromagnetic (except for Gd superlattices) but is of a more complex form as can be demonstrated from the effective phase shift of the magnetic ordering across the Y layers. This phase shift can be calculated from the asymmetry in the intensities of the magnetic satellites Q^- and Q^+ using equation (5). This has been done for the $[Dy|Y]$ superlattices, and as shown in Fig. 9, this phase shift is not a multiple of π (as for purely ferromagnetic or antiferromagnetic interactions), but is completely prescribed by the number of interleaving Y atomic planes. The phase shift corresponds to an effective "turn angle" of 51 - 52 degrees per Y layer ($\kappa = 0.31 \text{ \AA}^{-1}$).

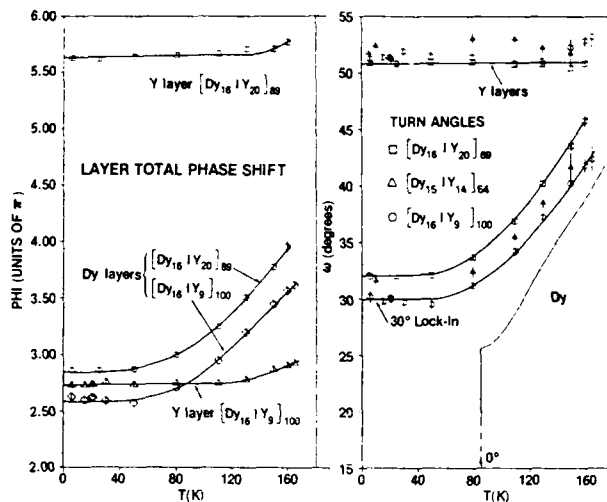


Fig. 9. (Left) Total phase shift of the spin density wave across Y and Dy layers as a function of temperature for $[Dy_{16}|Y_{20}]_{89}$ and for $[Dy_{16}|Y_9]_{100}$. Note that the Y phase shift is not a multiple of π and is independent of temperature. The Dy shift reflects the T-dependence of the turn angle (see text). (Right) Temperature dependence of the interplanar turn angle for Y and Dy layers derived from the propagation vectors, κ , for three $[Dy|Y]$ superlattices and for bulk Dy.

A theory by Yafet,²³ invoking only the RKKY interaction between Dy layers, successfully predicts chiral coherency and the correct order of magnitude for the interlayer interactions (as measured, for example, by the magnitude of the applied field required to break down helical order). However, in this calculation the Y turn angle is not a constant independent of Y thickness as observed experimentally. The model does correctly predict the cross-over from ferromagnetic to antiferromagnetic spin configurations with varying Y thickness as found in the $[Gd|Y]$ superlattices.⁹

The complexity of the ordering in $[Dy|Y]$ and $[Er|Y]$ superlattices and its dependence on propagation direction has led us to suggest¹¹ that the mechanism behind the long-range spin coupling is the stabilization of a spin density wave (SDW) in the Y and 4f lanthanide conduction bands via RKKY coupling to the 4f local moments in the lanthanide. In linear response theory¹⁵ the real space exchange coupling $J(R)$ can be expressed in terms of a Fourier transform of a q-dependent exchange $j(q)$:

$$J(R) = \sum_{q=0}^{q_{max}} j(q) e^{-i\mathbf{q} \cdot \mathbf{R}} \quad (6)$$

where $j(q)$ is in turn proportional to a conduction electron generalized susceptibility $\chi(q)$ through an exchange matrix element $j_{sf}(q)$ in the following form:

$$j(q) = |j_{sf}(q)|^2 \chi(q) / 2 \quad (7)$$

$\chi(q)$ has been calculated for Dy and Y from the band structure.^{24,25} This function exhibits strong positive maxima along the c^* direction at $q = q_{max} \neq 0$ (q = reduced wave vector), where q_{max} is only minimally different for Dy and Y and is in general prescribed by "nesting" features of parallel sheets of the Fermi surface.²⁶ In Dy and other lanthanide

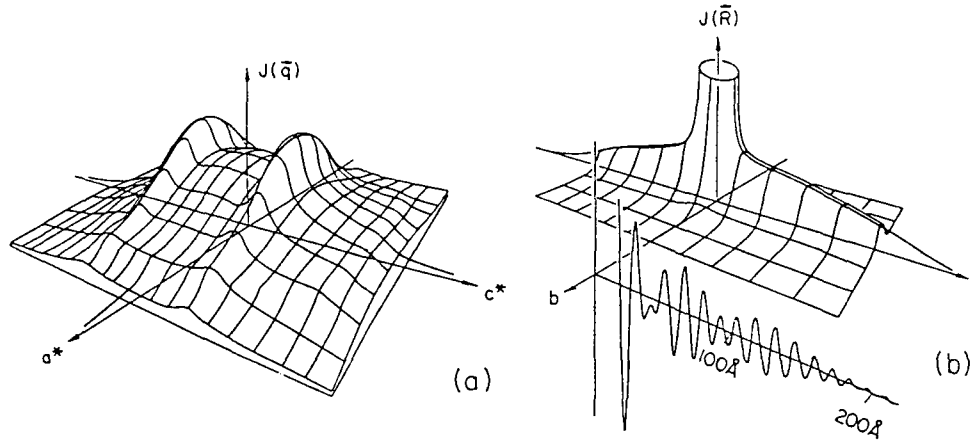


Fig. 10. (a) Schematic representation of $j(q)$ as discussed in the text for which the width along a^* reflects mainly the exchange matrix element while that along c^* reflects $\chi(q)$. (b) The envelope function for the Fourier transform real space exchange, showing the highly anisotropic spatial range. The oscillatory function is the actual transform function.

elements this calculated wave vector q_{\max} is also very close to the measured magnitude of the helical wave vector at the initial ordering temperature. In the a^* and b^* directions the peaked behavior at $q \neq 0$ is not observed and $j(q)$ falls off in a manner that reflects the core size and can be approximated by a Gaussian of width 0.63 \AA^{-1} . Using this form for $j(q)$ in the basal plane direction and that for c^* as calculated by Liu,²⁵ Flynn et al.²² have derived the three-dimensional representation for $j(q)$ shown in Fig. 10a. The real space exchange $J(R)$ calculated from eqn. 6 is also shown in Fig. 10b, along with the overall envelope function for the exchange. The salient feature of this calculation is that the range of the real space exchange coupling is highly anisotropic and extends out to beyond 130 \AA with significant amplitude in the c direction, but along the basal plane direction $J(R)$ falls rapidly to negligible values within about 12 \AA . This result clearly explains the existence of long-range coupling through Y layers exceeding 100 \AA in thickness (see Fig. 5) in superlattices grown along the c direction and also accounts for the lack of such coupling through Y layers as thin as 26 \AA in $[\text{Dy}|\text{Y}]$ superlattices with growth axis along b (Fig. 8).

MAGNETIC PERIODICITY AND SUPPRESSION OF FERROMAGNETISM

The fit of eqn. 5 to the magnetic diffraction data for the superlattices yields values of the propagation vector κ_A for the magnetic layer and a total phase shift across the bilayer Φ . From these, the layer-to-layer turn angle ω in the Dy (or Er) layers can be determined:

$$\omega_{\text{Dy}} = \frac{180}{\pi} \frac{C_o}{2} \kappa_A \quad (8)$$

Similarly, an effective turn angle can be determined for the spin density wave in Y which is the turn angle to which the $4f$ spins would lock if present. Fig. 9 (right) displays the turn angles for the Dy superlattices, while the turn angles for the c -axis modulated spin structure of the Er superlattices is shown in Fig. 11. It is noted that ω in the Y remains constant at about $51\text{-}52$ degrees/Y layer ($\kappa = 0.31 \text{ \AA}^{-1}$), corresponding closely to the peak q position in $\chi(q)$.^{24,25,27} The turn angle between the Dy planes varies with temperature as in bulk Dy,²⁸ but without the first order drop to $\omega = 0$ at 85K which signals the onset of the ferromagnetic state (suppressed by epitaxial clamping of the magnetostrictive modes in the superlattices as discussed later). This temperature dependence has been suggested to arise

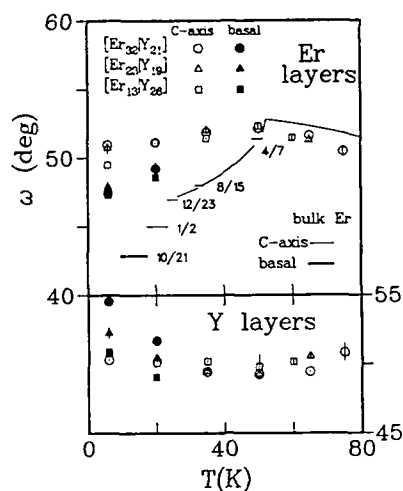


Fig. 11. The temperature dependence of the turn angles in the Er and Y layers for three [Er|Y] superlattices compared to bulk Er. The superlattice Er layer ω is "clamped" near the high-temperature lock-in value of bulk Er ($2\pi/7$). The basal plane ω appearing at low temperature has a somewhat smaller value than the c-axis ω . The ω in the Y layers is near the 50° value prescribed by the electronic structure.

from the development of superzone gaps in the Fermi surface coupled to the order parameter,²⁹ or from the effects of the magnetostrictive interactions.³² In bulk Dy at T_N , ω has the value 43.2° which decreases to 26.5° just above the first order transition to ferromagnetism at T_c .²⁸ In the superlattice $[Dy_{16}|Y_9]_{100}$ the turn angle is observed to lock-in to 30 degrees below about 50 K, presumably driven by the increase in the sixfold basal plane single ion anisotropy energy. For Er superlattices, using an analysis including the effects of strain modulation, distinct turn angles were obtained for the c-axis and the basal plane moment components which also order at different temperatures. More recent measurements at low scattering angles, for which strain modulation effects are negligible, produced identical values for the turn angles of both components as in bulk Er. As shown in Fig. 11, the c-axis turn angle is about 50° ($\approx 2\pi/7$) per layer corresponding to the high temperature initial state of bulk Er and shows relatively little temperature dependence compared to bulk Er which is given by the solid line. The plateaus in the bulk turn angle (indexed by the fractions) correspond to stable commensurate moment configurations (a spin "slip" structure) as derived by Gibbs et al.¹⁹ from an analysis of the magnetic x-ray scattering using synchrotron radiation.

The absence of the low temperature ferromagnetic transitions observed in bulk Dy at 85K and in Er at 20K is a universal characteristic of the superlattices studied and also of Dy and Er films grown on sapphire substrate with Y strain relieving layers.^{12,22,30} In the bulk elements the ferromagnetic phase transition is driven by a reduction in the magnetostrictive energy associated with the ferromagnetic state compared to the helical (or c-axis modulated) configuration.^{31,32} In Dy for example, the exchange interaction favors the helical ordered state by an energy difference of approximately 1K/atom at 0 K. This is countered by the large magnetostrictive energies which consist of two principal modes: (1) an anisotropic γ -mode strain^{33,34} that corresponds to an orthorhombic symmetry distortion of the basal plane and that is effectively "clamped" in the helical state and (2) isotropic α -mode c-axis and basal plane dilations (partially clamped in the helical state). The magnetostrictive energy reduction from allowing these strains to unclamp in the ferromagnetic state amounts to about 2 K/atom at $T = 0$ and about 1 K/atom at $T_c = 85$.

In bulk Dy, this is sufficient to overcome the equivalent exchange energy difference favoring the helical state and to drive the system ferromagnetic at 85 K. In the superlattice⁷ there is further clamping by the presence of the non-magnetostrictive epitaxial Y layers attached on either side of the Dy. This clamping strongly inhibits the γ -mode strain and is relatively weaker for the α -modes. The α mode energy (calculated to be ≈ 0.6 K/atom at 85 K⁷) is insufficient alone to drive the transition, and the clamping of the γ -mode strain forces the Dy in the superlattice to remain helical down to low T. In Er superlattices and films, the absence of the conical ferromagnetic state and the weaker temperature dependencies of the turn angles compared to bulk Er are also ascribed to magnetostrictive effects.

MAGNETIC MOMENTS AND INTERFACE DISORDER

The coherent 4f atomic magnetic moment in magnetic layers of the Dy and Er superlattices can be calculated from the observed magnetic scattering intensity relative to the nuclear intensities. The resulting temperature dependence of the moment is shown in Fig. 12 for Dy and Er superlattices and compared to a Brillouin curve ($J = 15/2$) for Dy and to the experimental bulk c-axis and basal plane moments for Er. For the Er superlattices the data analysis was based on a simple parameterization of the squaring-up process. Note that the low-T value of the c-axis moment is $8\mu_B$ as in bulk Er (total free ion moment = $9\mu_B$), and with a rapid fall-off at increasing temperatures. The 5 K basal plane moment (helical) is about $3.5\mu_B$ which is reduced from the bulk value of $4\mu_B$. For Dy, the calculated atomic moments for both superlattices fall below the Brillouin curve for the $10\mu_B$ free ion moment of Dy. The figure also shows the total overall magnetic intensity obtained from a difference pattern between scans taken at temperature (T) minus that for $T > T_N$. This difference intensity, which should include all the magnetic scattering (coherent and incoherent), does accurately follow the Brillouin curve. These results imply some degree of disordered moment, presumably in the interface layers, which does not contribute to the coherent moment. Additional evidence⁷ for this is found in a temperature-dependent weak broad

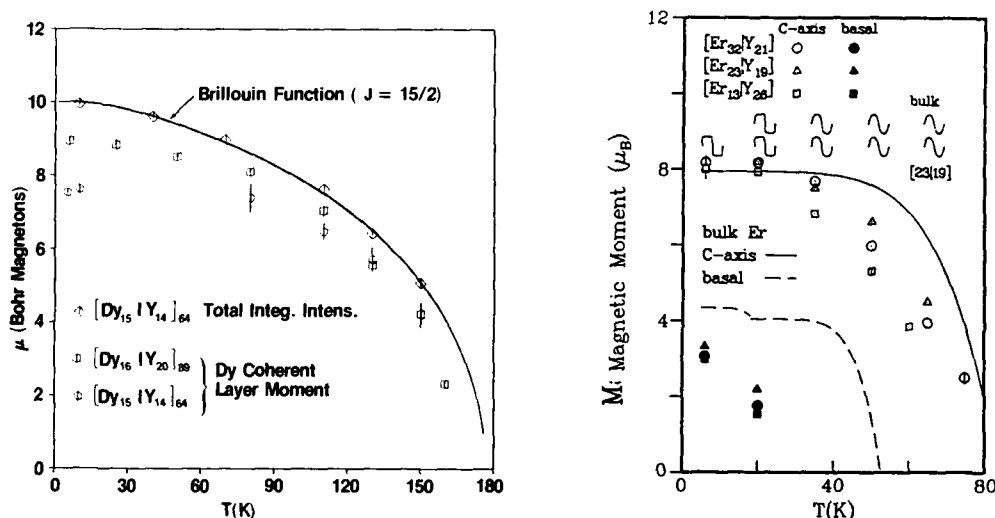


Fig. 12. (Left) Temperature dependence of the coherent Dy layer moment in $[Dy_{16}|Y_{20}]_{89}$ and $[Dy_{15}|Y_{14}]_{64}$ superlattices compared to a Brillouin function. Also shown is the total integrated magnetic intensity. (See text.) (Right) The c-axis and basal plane moment components for $[Er_{13}|Y_{26}]$, $[Er_{23}|Y_{19}]$, and $[Er_{13}|Y_{26}]$ superlattices ($T_N = 78.0, 78.5$, and 72.5 ± 1 K, respectively) compared to bulk Er ($T_N = 84$ K). The ordering temperature for the basal plane components is about half the value for bulk Er.

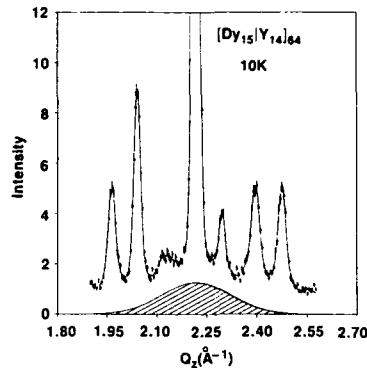


Fig. 13. Enlarged plot of the (000 l) scattering in the $[\text{Dy}_{15}|\text{Y}_{14}]_{64}$ superlattice showing the broad magnetic peak underlying the pattern at the (0002) position. This peak, reproduced by the shaded area, reflects short-range ferromagnetic correlation of the some of the moments, presumably those in the interface layers. This explains the reduced coherent layer moment (Fig. 12).

diffuse scattering which underlies the [0002] nuclear peak. This is shown by the enlarged plot in Fig. 13 for a $[\text{Dy}_{15}|\text{Y}_{14}]_{64}$ superlattice at 10 K. The shaded area is a representation of the broad incoherent scattering underlying the (0002) diffraction peak at $Q_z = 2.24 \text{ \AA}^{-1}$. The broad distribution reflects ferromagnetic moment correlations of a range of order 10 \AA . The reduction of the coherent moment in the interface layers has also been found in $[\text{Gd}|\text{Y}]$ superlattices by Majkrzak et al.³ and has been calculated directly from magnetic diffraction data on $[\text{Gd}|\text{Y}]$ using polarized synchrotron radiation data by Vettier et al.³⁵ The best fit model to the diffraction data as shown in Fig. 14 assumes the full Gd moment ($5.6 \mu_B$ for $T = 150 \text{ K}$) at the center of the Gd layer with a reduction in the planes near the interface. Interface disorder effects are presumably responsible for the decreased coherent moments in the Er superlattices also.

MAGNETIC FIELD DEPENDENCE

The response of the superlattice systems to an external applied field has been studied by both bulk magnetization and by neutron diffraction. The results of the bulk magnetization study on $[\text{Dy}|\text{Y}]$ superlattices can be found in ref. 8, and results on the $[\text{Er}|\text{Y}]$ in refs.

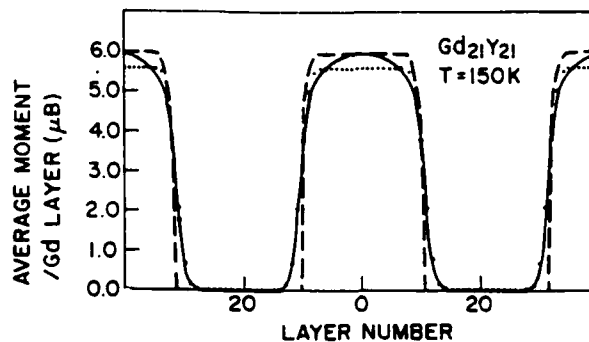


Fig. 14. Models for the spatial magnetic moment modulation in a $[\text{Gd}_{21}|\text{Y}_{21}]$ superlattice. The dashed curve follows the chemical modulation, and the solid curve, which gives the best fit to the data, represents the full $6.0 \mu_B$ moment ($T = 150 \text{ K}$) at the center of the Gd layer with a smooth decrease in the interface planes (after Vettier et al.³³).

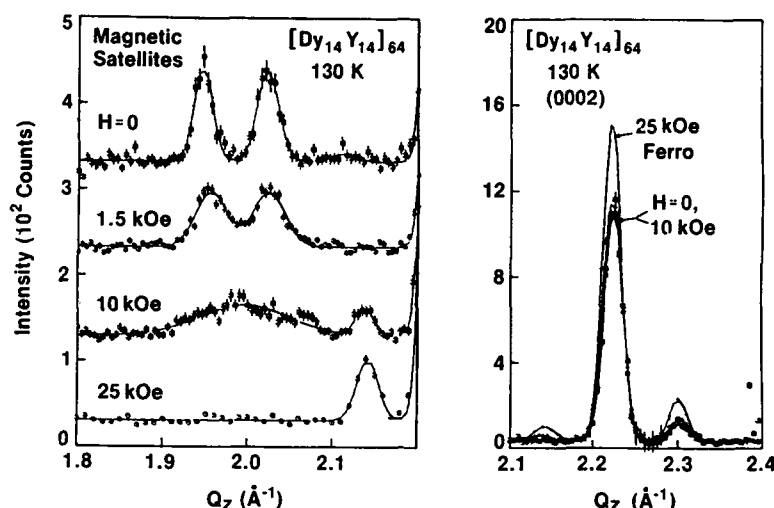


Fig. 15. (Left) Field dependence of the Q^- magnetic satellite in $[\text{Dy}_{16}\text{Y}_{20}]_{89}$ at 130 K. The satellite and magnetic bilayer harmonics are observed to broaden in low fields reflecting a loss of coherence. (Right) Only at fields higher than 10 kOe is the intra-layer helimagnetic structure gradually destroyed by the field and the resulting ferromagnetic component appears as intensity on the (0002).

11,12. The magnetization process has also been studied by neutron scattering with a superconducting magnet to apply fields in the basal plane of the c-axis growth superlattices. The effect of the field on the $[\text{Dy}_{16}\text{Y}_{20}]_{89}$ sample varied depending on the temperature.⁹ At 10 K ($0.059 T_c$), the intensity of the Q^- satellites was observed to decrease above about 3 kOe and to essentially collapse in fields of 10 kOe and higher. This corresponds to the destruction of the helix by the applied field and its conversion to ferromagnetic order. This is the same as in bulk Dy, although without a discontinuous transition as in Dy at low T. The intensity removed from the Q^\pm helix peaks reappears concomitantly as ferromagnetic intensity added to the (0002) peak and its harmonics. At higher temperature, for example 130 K ($0.77 T_c$), as illustrated in Fig. 15, the Q^- satellites are observed to first broaden increasingly with field. This corresponds to a decrease in the magnetic coherence length and at the higher fields the coherence is lost to a degree that merges the three satellite peaks into one broad maximum. This initial loss in coherence occurs before an appreciable ferromagnetic moment component is developed as shown in the figure where additional (0002) intensity is evident only above 10 kOe.

As suggested in ref. 7, this loss of coherence may arise from a Zeeman coupling of the applied field to the uncompensated moment, which is the vector sum of the moments in a Dy layer. It will be in general non-zero because of an incomplete helical period at the layer boundary. As shown in Fig. 16, the net uncompensated ferromagnetic moment can be quite large and varies with the Dy layer thickness and also with temperature because of the variation of both the turn angle and the order parameter. At temperatures near T_N it is suggested that this coupling to the helically directed (super-spiral) uncompensated moment in each layer acts like a random field and breaks the weak interlayer exchange coupling of the Dy spins. This results in independent layer helical magnetism as is reflected in a single broad magnetic satellite at the centroid of the three original zero field satellites. At low temperatures the decreased thermal spin disorder and strongly increased anisotropy and magnetostriction interactions result in a lower ferromagnetic transition field and apparently preclude the loss of coherence before the helical order is eliminated.

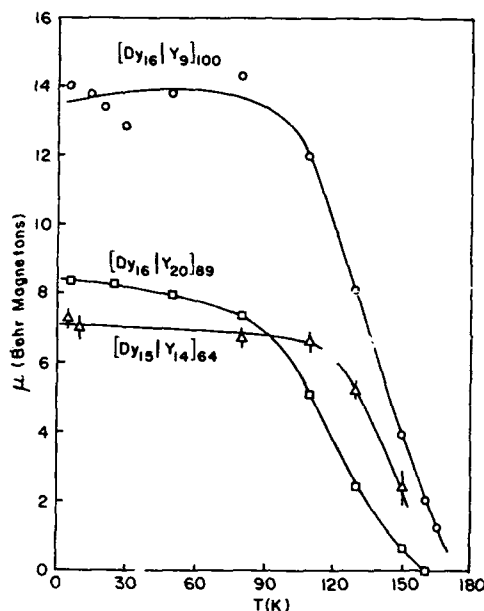


Fig. 16. Uncompensated net ferromagnetic moment resulting from the incomplete helicies in the Dy layers. It is suggested that at temperatures approaching T_N , the coupling of the applied field to this net moment destroys the long-range interlayer coupling.

This explanation is also consistent with the behavior of the $[\text{Dy}_{16}|\text{Y}_9]_{100}$ sample that has relatively less Y and a larger zero field coherence length. (See Fig. 5.) Due to the thinner Y layer this sample is expected to have a stronger interlayer exchange coupling, and it was found that there is relatively little broadening of the Q^- satellite at 130 K (or at lower T) on application of a field. This suggests that the applied field Zeeman coupling to the net moment is insufficient to break the relatively stronger c-axis exchange coupling in this sample. The onset transition fields (< 1 kOe at 10 K) for the helical to ferromagnetic conversion are lower than in the thicker Y sample, reflecting again the larger magnetostriction and anisotropic energy densities.

The magnetization of an $[\text{Er}_{13}|\text{Y}_{26}]_{100}$ superlattice as measured by both neutrons and a SQUID magnetometer is shown in Fig. 17. At low temperatures the turn angle in zero field was found to be 50.3° . As shown in the left figure (a), on application of a c-axis field ($H = 7$ kOe internal) this shifts to the commensurate value $\omega = 2\pi/7 = 51.4^\circ$ with no loss in the long-range magnetic coherence. The relatively poor resolution of the principal and superlattice peaks is a consequence of the out-of-scattering plane $(1,1,\bar{2},\xi)$ scan. At higher fields no further shift in q is observed indicating that the $2\pi/7$ state is the stable configuration. At 40 K (Fig. 17b, left), the zero field state already has the stable $\omega = 2\pi/7$ value and is thus not shifted by application of a 8 kOe field. However, larger fields strongly shift the q -centroid and produce broadening indicating a loss of coherence. This shift corresponds to the development of linear fan states with an average $\omega \approx 35^\circ$, which is significantly lower than any turn angle in bulk Er. The lower magnetoelastic energy in the superlattice due to epitaxial clamping favors the formation of a fan state instead of a direct transition to a c-axis aligned state. The fan states also appear as plateaus in the SQUID magnetization data in Fig. 17 (right) for temperatures of 20 K and higher. The magnetization step at low fields corresponds to a net moment of $1/7$ of the saturation value which is characteristic of the $2\pi/7$ commensurate lock-in state. It is noted in Fig. 17b (left) that the zero field remanent state following application of a 27 kOe field recovers the zero-field-cooled turn angle but the range of coherence is appreciably reduced.

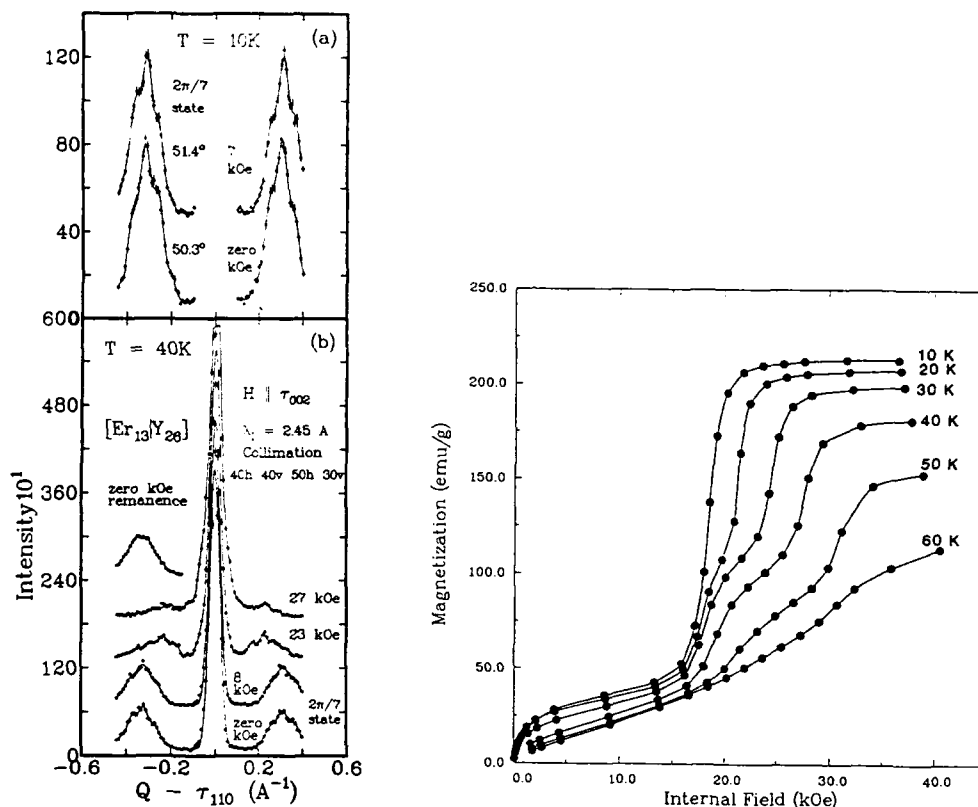


Fig. 17. (Left, a) Neutron diffraction scans along $(11\bar{2}\xi)$ for $[Er_{13}Y_{26}]$ at 10K with a c-axis applied field showing the shift in ω to the $2\pi/7$ state. (b) At 40 K the zero field $\omega = 2/7$ and there is no shift at 8 kOe. Higher fields induce fan states which are also observed in the magnetization

SUMMARY

Artificial metallic superlattices of the heavy lanthanide elements with yttrium have been shown to exhibit incommensurate (except Gd) periodic magnetic order that is coherent over several bilayer periods. The features of the ordering, including the phase and chirality coherence observed in $[Dy|Y]$ systems, suggest that the order is propagated via a spin density wave in the Y conduction bands stabilized by the 4f spins. Superlattices with the S-state ion Gd behave similarly, except that the interlayer coupling is only collinear ferromagnetic or antiferromagnetic. The existence of the long-range propagating order is found to be independent of the direction of the net moment component (viz., Dy vs. Er) as long as the stacking direction of the superlattice is parallel to the propagation vector of the magnetic structure (c^*). However, $[Dy|Y]$ superlattices produced with the growth axis in a basal plane direction are observed to have no long-range interlayer coupling consistent with the large anisotropy in the conduction electron generalized susceptibility, which leads to a large anisotropy in the real space exchange coupling range. In the $[Dy|Y]$ superlattices, the magnetic coherence length is found to be proportional to the reciprocal thickness of the intervening Y layer. In the Dy-Y superlattices, the application of an external field effects a gradual transition to an aligned ferromagnetic state. This transition is preceded at temperatures approaching T_N (in samples with relatively thick Y layers) by a loss in interlayer coupling before the helical ordering is broken.

REFERENCES

1. J. Kwo, D. B. McWhan, M. Hong, E. M. Gyorgy, L. C. Feldman, and J. E. Cunningham, Layered Structures, Epitaxy, and Interfaces, edited by J. H. Gibson and L. R. Dawson, Materials Research Society Symposia Proceedings **37** (Mats. Res. Soc., Pittsburgh, PA, 1985), pp 509.
2. J. Kwo, E. M. Gyorgy, D. B. McWhan, M. Hong, F. J. DiSalvo, C. Vettier, and J. E. Bower, Phys. Rev. Lett. **55**, 1402 (1985), J. Kwo, E. M. Gyorgy, F. J. DiSalvo, M. Hong, Y. Yafet, and D. B. McWhan, J. Mag. and Magn. Matls. **74-77**, 771 (1986).
3. C. F. Majkrzak, J. W. Cable, J. Kwo, M. Hong, D. B. McWhan, Y. Yafet, J. V. Waszczak, and C. Vettier, Phys. Rev. Lett. **56**, 2700 (1986).
4. S. M. Durbin, J. E. Cunningham, and C. P. Flynn, J. Phys. F **12**, L75 (1982).
5. J. J. Rhyne, R. W. Erwin, Shantanu Sinha, J. Borchers, M. B. Salamon, R. Du, and C.P. Flynn, J. Appl. Phys. **61**, 4043 (1987), and references therein.
6. M. B. Salamon, Shantanu Sinha, J. J. Rhyne, J. E. Cunningham, R. W. Erwin, J. Borchers, and C. P. Flynn, Phys. Rev. Lett. **56**, 259 (1986).
7. R. W. Erwin, J. J. Rhyne, M. B. Salamon, J. Borchers, S. Sinha, R. Du, J. E. Cunningham, and C. P. Flynn, Phys. Rev. B **35**, 6808 (1987).
8. J. Borchers, Shantanu Sinha, M. B. Salamon, R. Du, C. P. Flynn, J. J. Rhyne, and R.W. Erwin, J. Appl. Phys. **61**, 4043 (1987).
9. J.J. Rhyne, R.W. Erwin, J. Borchers, M.B. Salamon, R. Du, and C.P. Flynn, Physica B **159** 111 (1989).
10. R. W. Erwin, J. J. Rhyne, J. Borchers, M. B. Salamon, R. Du, and C. P. Flynn, J. Appl. Phys. **63**, 3461 (1988).
11. R.W. Erwin, J.J. Rhyne, J. Borchers, M.B. Salamon, R. Du, and C.P. Flynn, Jour. de Physique, Colloque C8, **49** 1631 (1988).
12. J.A. Borchers, Ph.D. Thesis, Univ. of Illinois, 1989; and to be published.
13. C. F. Majkrzak, Doon Gibbs, P. Boni, Alan I. Goldman, J. Kwo, M. Hong, T. C. Hsieh, R. M. Fleming, D. B. McWhan, Y. Yafet, J. W. Cable, J. Bohr, H. Grimm, and C.L. Chien, J. Appl. Phys. **63**, 3447 (1988).
14. C. C. Larsen, J. Jensen, and A. R. Mackintosh, Phys. Rev. Lett. **59**, 712 (1987).
15. R. J. Elliott, ed., "Magnetic Properties of Rare Earth Metals" (Plenum Publishing, London) 1972.
16. K. A. Gschneidner, Jr., and LeRoy Eyring, eds., "Handbook on the Physics and Chemistry of Rare Earths," (North Holland Publishing) vol. 1 - 2 (1979).
17. B. Coqblin, "The Electronic Structure of Rare Earth Metals and Alloys: The Magnetic Heavy Rare Earths" (Academic Press, London) 1977.
18. Doon Gibbs, D. E. Moncton, and K. L. D'Amico, J. Appl. Phys. **57**, 3619 (1985).
19. Doon Gibbs, Jakob Bohr, J. D. Axe, D.E. Moncton, and K. L. D'Amico, Phys. Rev. B **34**, 8182 (1986).
20. C.M. Falco, J.M. Slaughter, and B.N. Engel, this volume.
21. C. F. Majkrzak, Doon Gibbs, P. Boni, Alan I. Goldman, J. Kwo, M. Hong, T. C. Hsieh, R. M. Fleming, D. B. McWhan, Y. Yafet, J. W. Cable, J. Bohr, H. Grimm, and C. L. Chien, J. Appl. Phys. **63**, 3447 (1988).
22. C.P. Flynn, F. Tsui, M.B. Salamon, R.W. Erwin, and J.J. Rhyne, J. Phys.: Condensed Matter **1**, 5997 (1989).
23. Y. Yafet, J. Kwo, M. Hong, C. F. Majkrzak, and T. O'Brien, J. Appl. Phys. **63**, 3453 (1988).
24. R. P. Gupta and A. J. Freeman, Phys. Rev. B **13**, 4376 (1976).
25. S. H. Liu, R. P. Gupta, and S. K. Sinha, Phys. Rev. B **4**, 1100 (1971).
26. S. C. Keeton and T. L. Loucks, Phys. Rev. **168**, 672 (1968).
27. H. R. Child, W. C. Koehler, E. O. Wollan, and J. W. Cable, Phys. Rev. **138**, A1655 (1965).
28. M. K. Wilkinson, W. C. Koehler, E. O. Wollan, and J. W. Cable, J. Appl. Phys. **32**, 48S (1961).
29. R. J. Elliott, and F. A. Wedgwood, Proc. Phys. Soc. (London) **81**, 846 (1963).
30. J.A. Borchers, G. Nieuwenhuys, M.B. Salamon, C.P. Flynn, R. Du, R.W. Erwin, and J.J. Rhyne, J. de Physique, Colloque C8, **49** 1685 (1989).
31. B. R. Cooper, Phys. Rev. Letters **19**, 900 (1967), Phys. Rev. **169**, 281 (1968).
32. W. E. Evenson and S. H. Liu, Phys. Rev. **178**, 783 (1969).
33. J. J. Rhyne and S. Legvold, Phys. Rev. **138**, A507 (1965).
34. Earl Callen, J. Appl. Phys. **39**, 519 (1968).
35. C. Vettier, D. B. McWhan, E. M. Gyorgy, J. Kwo, B. M. Buntschuh, and B. W. Batterman, Phys. Rev. Lett. **56**, 757 (1986).

X-RAY CHARACTERIZATION OF MAGNETIC MULTILAYERS AND SUPERLATTICES

Charles M. Falco, J.M. Slaughter and Brad N. Engel

Department of Physics; Optical Sciences Center
University of Arizona
Tucson, Arizona 85721 USA

INTRODUCTION

In this paper we describe several x-ray diffraction techniques which we have found to be very useful for characterizing the structure of magnetic multilayers and superlattices. Examples are given from several of the magnetic and non-magnetic materials studied recently with these techniques.

HIGH-ANGLE θ - 2θ

The lattice constants of most materials of interest for use in magnetic multilayers and superlattices are a few Ångströms. Since $\lambda_x \approx 1.542$ Å for the commonly used Cu K_α radiation, this means that high symmetry crystallographic planes (e.g [110] for bcc materials, [111] for fcc, etc.) will result in diffraction at angles $2\theta \approx 35^\circ$ - 45° . Diffraction at angles in this range is referred to as "high-angle" diffraction in this paper.

Satellite Peaks

Satellite peaks in the high-angle x-ray diffraction spectra (as well as the presence of low-angle superlattice Bragg peaks), are direct evidence of composition modulation and long range structural coherence in a superlattice.^{1,2,3,4} It can be shown^{5,6} that the spacing of the satellite lines should obey the relation

$$\Lambda = \lambda_x / 2[\sin\theta_i - \sin\theta_{i+1}] \quad (1)$$

where Λ is the superlattice wavelength, λ_x is the wavelength of the x-rays, and θ_i and θ_{i+1} are the diffraction angles of two adjacent satellites. Thus, as the modulation wavelength Λ of the superlattice is decreased, the separation of the superlattice lines should increase in angle. A plot of the high-angle x-ray lines for a series of Cu/Pd superlattices is shown in Figure 1. Data of this type can be used to directly determine the modulation wavelength Λ of each superlattice sample.

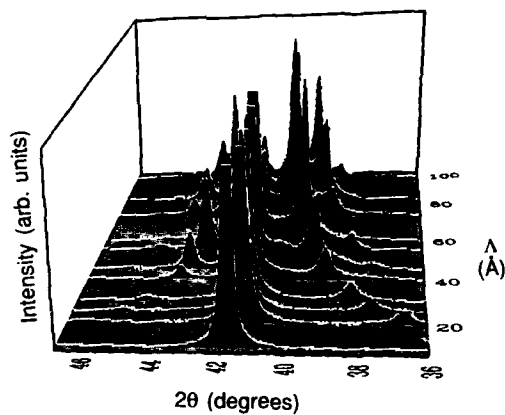


Figure 1. X-ray diffraction intensity *vs.* diffraction angle 2θ for a series of Cu/Pd superlattices of wavelength Λ .

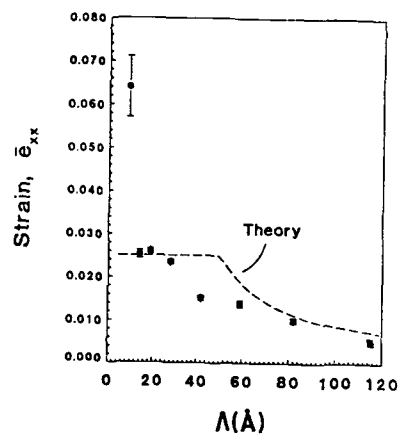


Figure 2. Wavelength dependence of the strain in a series of Mo/Ta superlattices. Dashed curve is theoretically expected behavior.

Structural Coherence Length from the Scherrer Equation

After deconvoluting instrumental broadening and the overlap of adjacent x-ray satellite peaks, the Scherrer equation,⁷ can be used to convert measured x-ray linewidths into structural coherence lengths. For example, in Fig. 1 the linewidth of the central Bragg peak ($2\theta \cong 42^\circ$) is seen to remain very narrow over the entire range of wavelengths shown, down to $\Lambda < 10 \text{ \AA}$. From these linewidths we calculate the structural coherence length perpendicular to the Cu/Pd layers to be $> 150 \text{ \AA}$ for $10 \text{ \AA} \leq \Lambda \leq 115 \text{ \AA}$. This indicates that the structure perpendicular to the layers is coherent over many interfaces in this material.¹

Different Crystal Planes

High-angle Bragg diffraction is usually made from crystal planes which are in the plane of the substrate. However, diffraction also can be made with the sample surface rotated to some other fixed angle.⁸ For example, the (211) planes in a metal with bcc structure are at an angle of 30° with respect to the (110) planes. Consequently, the sample can be mounted in a standard diffractometer at 30° with respect to the substrate normal, and θ - 2θ scans made through the (211) reflections. Knowing the structural coherence length perpendicular to the substrate and at some other angle relative to the substrate normal is sufficient to obtain a measure of the in-plane structural coherence length.

Strain

The intensity of the x ray diffraction peaks contain information about the strain in the samples. Since strain can affect the magnetic properties of a thin film, such information is desirable. If we assume that in the superlattice the scattering factor varies over the range $f(1 \pm \eta)$ and lattice spacing over the range $d_0(1 \pm \epsilon)$, and we also assume that the strain amplitude ϵ is small, we can write an expression for the ratio of the intensities of the first order satellites as⁹

$$I/I^* \approx [(\Lambda/d - 1)\epsilon + \eta]^2 / [(\Lambda/d + 1)\epsilon - \eta]^2 \quad (2)$$

Experimentally, the ratio of the first order satellite peaks, I/I^* , is obtained as a function of Λ after correcting for the Lorentz, polarization, and Debye-Waller factors in the x-ray intensities.¹⁰ By considering the elastic nature of each layer, we can convert the coherency strains ϵ obtained from Eq. (2) into parallel strains e_{par} . The perpendicular strains are converted into parallel strains by use of the definition of the Poisson ratio $e_z = -\nu e_x$, where $\nu = 1/3$ is assumed for both layers. Strains determined in this way from diffraction measurements from a series of Mo/Ta superlattices are plotted as a function of Λ in Fig. 2, where the dashed line is the theoretical curve. Except for the $\Lambda = 9 \text{ \AA}$ sample we see that the experimental data agree reasonably well with the theory. The data in Fig. 2 suggest a critical wavelength $\Lambda_c \approx 28 \text{ \AA}$, at which point misfit dislocations are introduced in the layers. Beyond this, the data show the expected decreasing of strain with further increasing Λ . Figure 2 indicates that some kind of structural transition is occurring, which would affect the physical (e.g. magnetic) properties of a superlattice. However, caution must be taken when trying to determine information about structure parallel to the interfaces from spectra obtained with a scattering vector perpendicular to the layers, as this can lead to ambiguous results.⁹

LOW-ANGLE θ - 2θ

As discussed above, for Cu K_α radiation ($\lambda_\alpha \cong 1.542 \text{ \AA}$) and typical lattice constants $a \approx 2 \text{ \AA}$, the Bragg condition for high symmetry planes is satisfied for angles

$2\theta = 40^\circ$. However, the diffraction condition also can be satisfied directly from the superlattice repeat distance Λ . Since a typical sample of interest might contain ≈ 5 -50 atomic layers in each Λ , the low-angle Bragg peaks should occur for angles $2\theta < 0.5$ -5°.

Figure 3 shows an x-ray diffraction scan at grazing incidence angle for a Mo/Si sample of $\Lambda = 126 \text{ \AA}$ ($d_{\text{Mo}} = 31.2 \text{ \AA}$; $d_{\text{Si}} = 94.8 \text{ \AA}$). At very low angles ($< 0.6^\circ$) the reflectivity of the sample approaches 1.0 due to total external reflection. The lowest order Bragg peak, occurring at $2\theta \approx 0.9^\circ$, is seen to be distorted. This is caused by refraction of the x-rays due to the slight difference of indices of refraction between the sample and air. The regularly spaced subsidiary maxima between the low angle Bragg peaks are due to the finite number of bilayers (15) in this sample. Figure 4 shows an expanded region of this data near the 5th and 6th Bragg peaks. The 13 subsidiary maxima due to the 15 bilayers in this sample can be clearly seen. The presence of such subsidiary maxima are direct evidence of the quality of the layering, since variations in layer thickness of only $\pm 0.5\%$ would obliterate these peaks. The bilayer spacing ($\Lambda = d_{\text{Mo}} + d_{\text{Si}}$) can be determined accurately from the Bragg peak positions and, by fitting model calculations to the measured curve, the thickness ratio ($\gamma = d_{\text{Mo}}/\Lambda$), r.m.s. roughness of the layers, and the thickness of oxide on the top Mo layer can be deduced.³ Unfortunately, for some materials of interest (e.g. Co/Pd), the x-ray contrast between the materials in the two layers is too small to give rise to more than one or two low angle peaks in spectra obtained using a conventional sealed tube x-ray source. Thus, the information which can be obtained from measurements of such samples is limited, unless data is taken using an intense source, such as a synchrotron.

WIDE-FILM DEBYE-SCHERRER

Wide-film Debye-Scherrer x-ray diffraction ("Read camera")^{11,12,13} measurements are very useful for studying the crystalline structure of metal-metal superlattices. The Read camera uses a glancing angle x-ray beam incident at some fixed angle with respect to the substrate (typically 5° - 50° , depending on what features are being studied), and the diffracted beams then emerge in various directions determined by the crystal structure. However, unlike the case of the θ - 2θ diffractometer, the scattered wavevector is no longer constrained to be perpendicular to the substrate in order to be detected. Thus, one photograph contains information about the crystal structure perfection both in and out of the plane of the substrate.

Figure 5 is a portion of a Read camera diffraction pattern from an MBE-grown $\Lambda = 26.4 \text{ \AA}$ Co/Pd film on a (110) GaAs substrate. Sharp spots from the single crystal Ga/As substrate are clearly visible, as are the superlattice lines from the Co/Pd sample. The angular width of the Co/Pd superlattice "spots" indicates a mosaic spread of only about $\pm 5^\circ$. In addition to the (110) spot at $2\theta \approx 40^\circ$, which would have been measured by a standard diffractometer, one also sees diffraction from the (011) and (01 $\bar{1}$) planes oriented at 60° with respect to the (110) spot. These spots all are due to diffraction from planes with the same spacing, and thus occur at the same 2θ value. However, with the Read camera it is possible to confirm that they have the proper crystallographic orientation with respect to each other, as expected of a sample which is close to single crystal in quality. At higher angles one sees the (200), (211), etc. planes, all of which lie at the correct "single crystal" values with respect to each other.

SEEMANN-BOHLIN

The Seemann-Bohlin scattering geometry is very similar to that of the wide-film Debye-Scherrer technique discussed in the previous section.^{14,15,16,17,18} However, instead of photographic film, a scintillation counter is used to detect the diffracted

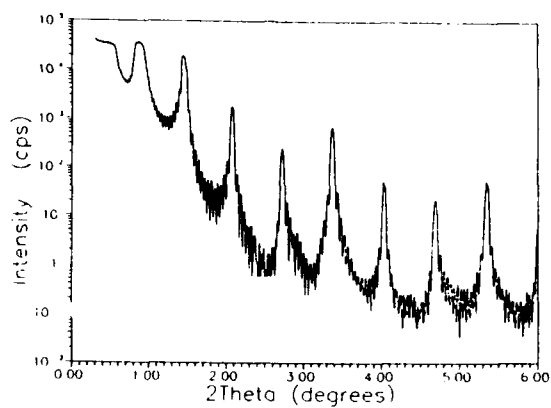


Figure 3. Low-angle x-ray diffraction intensity *vs.* 2θ for a Mo/Si multilayer of $\Lambda = 126$ Å.

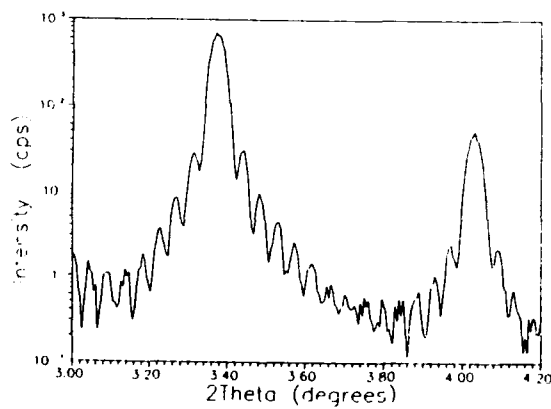


Figure 4. Expanded portion of the diffraction spectrum of Fig. 3, showing the 13 subsidiary maxima between the 5th and 6th low-angle Bragg peaks.

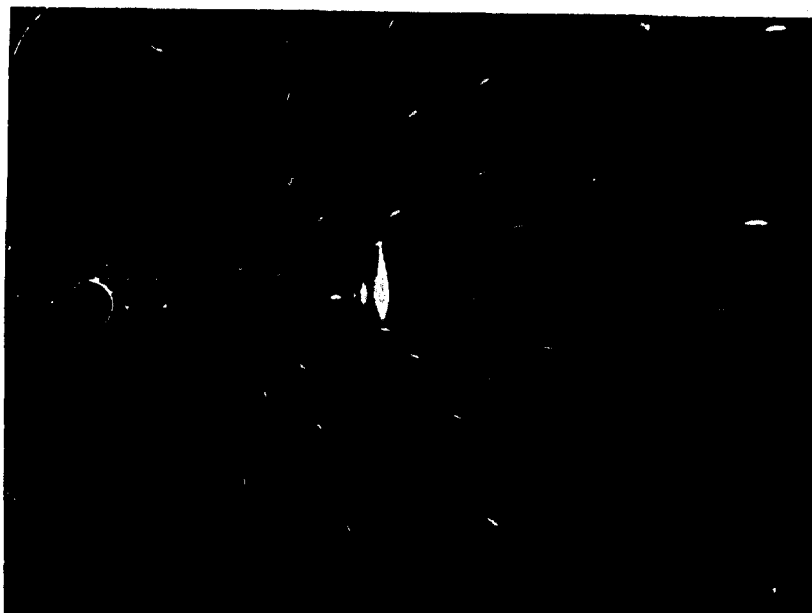


Figure 5. Portion of a wide-film Debye-Scherrer diffraction pattern from an MBE-grown $\Lambda = 26.4 \text{ \AA}$ Co/Pd superlattice. Approximately 45% of the entire pattern is shown in this Figure.

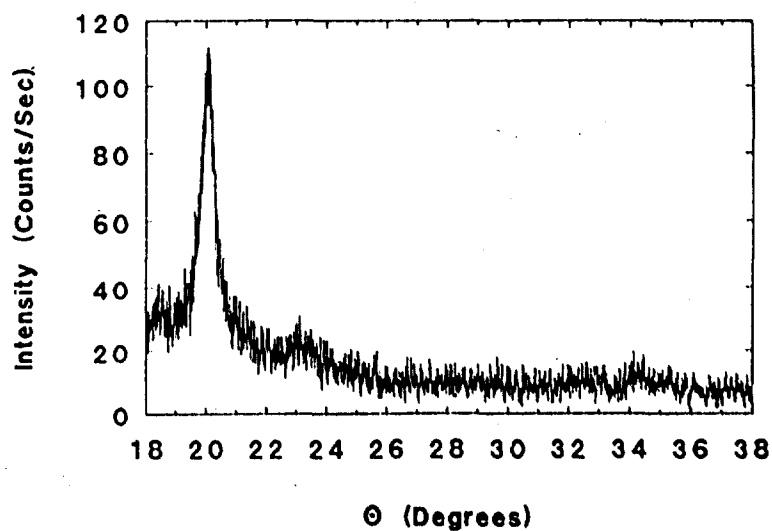


Figure 6. Seemann-Bohlin diffraction scan from a $\Lambda \approx 15 \text{ \AA}$ Pd/Co multilayer of total thickness $t \approx 160 \text{ \AA}$.

beams. This limits the diffraction information collected to that of a single arc in reciprocal space, rather than the wide area possible with a sheet of film. However, use of a counter means the sensitivity is much greater than possible with photographic film. Also, an incident beam focussing monochrometer is used, giving much higher intensities, as well as greatly increased resolution. Because the x-rays are incident on the sample at a grazing angle ω , the effective film thickness is increased by approximately $1/\sin\omega$. This enables very thin films to be studied with this technique using conventional sealed tube x-ray sources. Figure 6 is a scan made of a sputtered $\Lambda \approx 15$ Å Pd/Co multilayer on a sapphire substrate. This sample consists of 10 Co layers of $d_{\text{Co}} = 4$ Å and 11 Pd layers of $d_{\text{Pd}} = 11$ Å, for a total sample thickness of only ≈ 160 Å. In spite of the thinness of this sample, diffraction from three crystallographic planes can be resolved.

LAUE

Transmission and reflection Laue diffraction using polychromatic Mo radiation is useful for determining the symmetry of growth of multilayer thin films. The primary difficulty with Laue diffraction is the small diffraction intensity from the thin film as compared to the diffraction intensity from the substrate. This can be overcome in some cases by removing the sample from the substrate. However, strong adhesion often means that the sample is damaged in the removal process. For materials which grow best on substrates such as single crystal sapphire, removal by dissolving the substrate is not possible.

SUMMARY

We have described several x-ray diffraction techniques which are very useful for characterizing the structure of magnetic multilayers and superlattices. These techniques provide complementary information to the others, so that using a combination of them is desirable when attempting to establish structure-property relationships in magnetic multilayers and superlattices.

ACKNOWLEDGEMENTS

We gratefully acknowledge a number of students and postdocs, current and former, who have collaborated on our research program related to this article: Wayne Bennett, Ahmed Boufelfel, Craig England, Félix Fernández, Valentín García-Vázquez, Patrick Kearney, Jeha Kim, John Makous, Gino Maritato, Heidi Ruffner, Dean Schulze, Arye Shapiro, and Robert van Leeuwen. This research is supported by the AFOSR, DOE, JSOP, ONR, and Optical Data Storage Center.

REFERENCES

1. J.P. Locquet, D. Neerincx, L. Stockman, Y. Bruynseraede and I.K. Schuller, *Phys. Rev. B* **38**, 3572 (1988).
2. P.F. Carcia and A. Suna, *J. Appl. Phys.* **54**, 2000 (1983).
3. F. Fernández, C.M. Falco, P.Dhez, A. Khandar-Shahabad, L. Nénot, B. Pardo, J. Corno and B. Vidal, *Appl. Phys. Lett.* **51**, 880 (1987).
4. B. Vidal and P. Vincent, *Applied Optics* **23**, 1794 (1984).
5. K.E. Meyer, G.P. Felcher, S.K. Sinha and I.K. Schuller, *J. Appl. Phys.* **52**, 6608 (1981).
6. I.K. Schuller, *Phys. Rev. Lett.* **44**, 1597 (1980).

7. Harold P. Klug and Leroy E. Alexander, **X-Ray Diffraction Procedures for Polycrystalline and Amorphous Materials**, 2nd ed., Chapter 9 (New York, Wiley, 1974).
8. Wayne R. Bennett, Ph.D. Dissertation, University of Arizona (1985).
9. D.B. McWhan, "Structure of Chemically Modulated Films", in **Synthetic Modulated Structures**, L. Chang and B.C. Giessen, eds. (Academic Press, New York, 1985).
10. John Makous, Ph.D. Dissertation, University of Arizona (1989).
11. M. Read and D.H. Hensler, *Thin Solid Films* 10, 123 (1972).
12. L.G. Feinstein, *Appl. Phys. Lett.* 19, 137 (1971).
13. W.D. Westwood, *Thin Solid Films* 15, 15 (1973).
14. W. Parrish and M. Mack, *Acta Cryst.* 23, 687 (1967).
15. W. Parrish and M. Mack, *Acta Cryst.* 23, 693 (1967).
16. R. Feder and B. S. Berry, *J. Appl. Cryst.* 3, 372 (1972).
17. K. N. Tu and B. S. Berry, *J. Appl. Phys.* 43, 3283 (1972).
18. T. Tien, G. Ottaviani and K. N. Tu, *J. App. Phys.* 54, 7047 (1983).

THE CHARACTERIZATION OF INTERFACE ROUGHNESS AND OTHER DEFECTS IN MULTILAYERS BY X-RAY SCATTERING

S.K. Sinha, M.K. Sanyal, and A. Gibaud *
Physics Department, Brookhaven National Laboratory
Upton, New York 11973 U.S.A.

S.K. Satija and C.F. Majkrzak
National Institute for Standards and Technology
Gaithersburg, Maryland 20899 U.S.A.

H. Homma
Physics Department, Brooklyn College of CUNY
Brooklyn, New York 11210 U.S.A.

INTRODUCTION

In this paper we present some theoretical and experimental results on the characterization of roughness in thin films and multilayers by scattering techniques. Particular attention is focussed on the difference between specular and diffuse scattering and on correlated roughness between interfaces.

SPECULAR VS. DIFFUSE SCATTERING

There are two components to the scattering cross-section from a rough surface. One is a true specular component which is restricted to the specular ridge (chosen as the q_z axis in reciprocal space) and which contains the factors $\delta(q_x) \delta(q_y)$ and is a function of q_z . This component is thus limited only by the resolution width of the spectrometer in a transverse scan (rocking curve) across the specular ridge in q -space. The other is a diffuse component due to the height-height fluctuations of the interface. It is centered at $q_x=q_y=0$ but is in general broader than the instrumental resolution and gives "tails" to the rocking curves, as well as being a function of q_z . The specular reflectivity is obtained from the true specular component as ^{1,2}

$$R = R_F \exp(-q_z \tilde{\sigma}^2) \quad (1)$$

where R_F is the usual Fresnel reflectivity for a smooth surface of the same

material, \tilde{q}_z is the value of q_z inside the medium ($=\sqrt{q_i^2 - q_c^2}$, where q_c is the critical normal wavevector transfer for total reflection), and σ is the rms surface roughness. To obtain a true estimate of the global surface roughness one must subtract from the measured intensity the estimated diffuse scattering under the specular ridge, i.e. one must separate the two components (else one is measuring only a (smaller) local roughness over a region inversely proportional to the instrumental acceptance width in q -space). In practice, this can usually be done by measuring the diffuse scattering on either side of the specular ridge by slightly missetting the reflecting surface off the specular angle, although if the diffuse scattering is sharply peaked around the specular ridge (i.e. if the surface height-height correlations are long ranged) one may need very tight

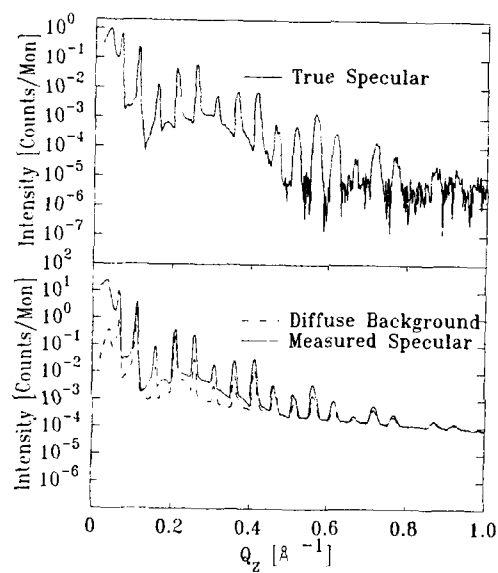


Fig. 1 (Lower) On-ridge nominal specular scattering (solid curve) and diffuse background (dotted curve) for a GaAs/AlAs multilayer at small angles. (Upper) The true (background subtracted) specular reflectivity.

resolution settings. One must also integrate over the width of the true specular peak in the rocking curve, noting that the resolution width changes continuously with q_z . Such procedures have generally not always been followed in reflectivity measurements from multilayers, resulting in probably considerable underestimates of surface roughness. As an example, we show in Fig. 1 the specular and diffuse scattering (i.e. off-specular scattering) from a GaAs/AlAs multilayer in the small angle region as measured at the National Synchrotron Light Source at Brookhaven³. Note that the difference which is the true amplitude of the specular scattering decreases much more rapidly with q_z than the "raw" intensity yielding a larger value of the roughness. Note also that the diffuse scattering also shows multilayer low angle Bragg peaks. This is due to correlated interface roughness and is discussed in the next section.

CONFORMAL INTERFACE ROUGHNESS

We now discuss the general results for scattering from a multilayer where the interfaces possess correlated or conformal roughness, in the sense illustrated in Fig. 2. We work here in the small angle limit, i.e. we neglect the crystal structure of the materials assuming only uniform electron densities in the layers separated by (rough) interfaces. This may be expressed mathematically in the following manner. If $\delta z_i(\mathbf{r})$ is the height fluctuation of interface i above its average value at lateral position \mathbf{r} in the plane, we write

$$\langle \delta z_i(0) \delta z_j(\vec{r}) \rangle = c_{ij}(\vec{r}) \quad (2)$$

If the roughness of the interfaces is truly uncorrelated, $c_{ij}(\mathbf{r}) = \delta_{ij} c(\mathbf{r})$ where $c(\mathbf{r})$ can be generally taken to be of the form $\sigma^2 \exp(-r/\xi_{||})^h$

($0 < h < 1$)¹, and the diffuse scattering will be the incoherent sum of the diffuse scattering from each interface. If on the other hand, there is a degree of conformal roughness (as in Fig. 2), we may write

$$c_{ij}(\vec{r}) = c_o(\vec{r}) + \sigma^2 \exp\left(-|z_i - z_j|/\xi_{||}\right) c(\vec{r}) \quad (3)$$

where z_i, z_j are the mean positions of interfaces i, j respectively, and $\xi_{||}$ is a conformal correlation length along the z -direction. (We have assumed, for simplicity, that the mean square roughness of each interface is the same) $C_o(\mathbf{r})$ represents a short-wavelength fluctuation on each interface which is independent of the others. Then the expression for the diffuse scattering intensity from the N interfaces in the multilayer can be shown to be given in the Born approximation by³

$$I = \frac{I_o}{q_z^2 k_o^2 \sin \alpha \sin \beta} \sum_{ij} \Delta \rho_i \Delta \rho_j e^{-iq_z(z_i - z_j)} \exp\left[-q_z^2(\sigma^2 + \delta^2|i - j|)\right] F_{ij}(\vec{q}_{||}) \quad (4)$$

while the expression for the integrated specular reflectivity in the Born approximation is given by

$$R = \frac{16\pi^2}{q_z^4} \sum_{ij} \Delta \rho_i \Delta \rho_j e^{-iq_z(z_i - z_j)} \exp\left[-q_z^2(\sigma^2 + \delta^2|i - j|)\right] \quad (5)$$

In Eqs. (4) and (5), I is the detector counts per second, I_o the incident beam intensity (we assume the sample completely intercepts the beam), k_o the wavevector of the incident radiation, α and β the angles which the incident and scattered beams respectively make with the surface,

$$\Delta \rho_i = \frac{e^2}{mc^2} (n_i^- - n_i^+) \quad (6)$$

where n_i^\pm denotes the electron density of the medium above or below the interface i , δ is the root-mean-square random error in the mean thickness of each layer compared to its nominal mean thickness, and

$$F_{ij}(q_{||}) = \iint d\mathbf{x} d\mathbf{y} \left[e^{iq_z c_{ij}(\vec{r})} - 1 \right] e^{-i\vec{q}_{||} \cdot \vec{r}} \quad (7)$$

$q_{||}$ being the component of the set momentum transfer parallel to the surface. These expressions are only valid for $q_z \gg q_c$ while near or below

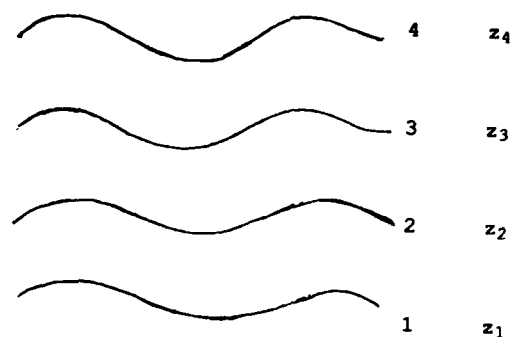


Fig. 2 Schematic showing conformally rough interfaces in a multilayer. The interfaces are denoted by 1,2,...etc. with average heights z_1, z_2, \dots above a reference $z=0$ plane.

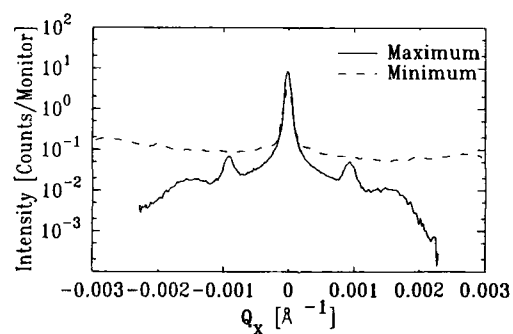


Fig. 3 Transverse scans of the diffuse scattering across the specular ridge for a Pb/Ge multilayer at a specular maximum and at a minimum.

the critical angle they have to be modified according to the Distorted Wave Born Approximation² in a manner which we shall not have space to discuss here. Eq. (6) must of course also be convolved with the instrumental resolution in order to reproduce the observed counts.

We now discuss qualitatively the structure of the scattering. The factor $e^{-q_z^2 \delta^2 |i-j|}$ arising from the cumulative deposition error δ will produce a "smearing out" along q_z of both the specular (Bragg) peaks and the diffuse scattering peaks. (In the limit of an infinite number of bilayers, the Bragg peaks would become delta functions in q_z but are broadened to Lorentzians by this factor). If ξ_1 is very large, i.e. the conformal roughness persists over all the interfaces, so that $c_{ij}(z)$ becomes more or less independent of i, j , then the factor $e^{-iq_z(z_i - z_j)}$ in the diffuse scattering will produce constructive and destructive interference between the scattering from the various interfaces, resulting in the peaks in the diffuse scattering seen in Fig. 1. Thus a transverse scan (rocking curve) across the specular ridge will show a different line shape when q_z is at a Bragg peak and when it is at a minimum between peaks. This is illustrated in Fig. 3 for a Pb/Ge multilayer⁴. The transverse scan across a q_z -minimum is fairly flat, corresponding to rather short-length scale height-height correlations which are not conformal between interfaces, while that across a Bragg peak is peaked strongly at the specular ridge, implying conformal long length-scale height fluctuations across the interfaces. The additional peaks at transverse q -values do not imply periodic order along the surfaces, but are rather a interesting manifestation of what we may call "generalized Yoneida scattering"^{2,5} (due to multiple Bragg and diffuse scattering whenever either the incident or scattered beams make an angle with the surface corresponding to total reflection or Bragg scattering).

It should be borne in mind, for crystalline multilayers, that the roughness of the interfaces is a manifestation of the height and orientation distribution of the microcrystalline grains at the interface. Thus a combination of small and wide angle data is needed for a complete micro-characterization of the grain morphology in multilayers. Detailed results will be given elsewhere³.

ACKNOWLEDGEMENTS

Work at Brookhaven was supported by US DOE contract No. DE-AC02-76CH00016.

*Permanent address - Universite du Maine, Faculte des Sciences, Route de LAVAL, 72017 Le Mans, Cedex, France.

REFERENCES

1. L. Nevot and P. Croce, Rev. Phys. Appl. **15**, 761 (1980).
2. S.K. Sinha, E.B. Sirota, H.E. Stanley and S. Garoff, Phys. Rev. **B38**, 2297 (1988); R. Pynn, to be published.
3. M.K. Sanyal, A. Gibaud, S.K. Sinha, S.K. Satija, C.F. Majkrzak, D. Newman and H. Homma, to be published.
4. Y. Yoneda, Phys. Rev. **131**, 2010 (1963); O.J. Guentert, J. Appl. Phys. **20**, 1361 (1965); A.N. Nigam, Phys. Rev. **A4**, 1189 (1965).
5. M.K. Sanyal, A. Gibaud, S.K. Sinha, H. Homma and I.K. Schuller, to be published.

MAGNETISM OF NANOSTRUCTURED RARE-EARTH MULTILAYERS

D. J. Sellmyer and Z. S. Shan

Behlen Laboratory of Physics and
Center for Materials Research and Analysis
University of Nebraska
Lincoln, NE 68588-0111

INTRODUCTION

In recent years a great deal of effort has been devoted to the study of the growth of thin-films with microstructures that lead to physically interesting and technologically useful properties.¹ Modern deposition systems increasingly have been used to produce magnetic films with controlled values of magnetization (M_S), coercivity (H_C), uniaxial anisotropy (K_U), ordering or compensation temperature (T_C), etc. Much of the driving force for this research has come from the hope that, with enough understanding and control of the microstructure and its relationship to properties, it will become easy to design magneto-optic or perpendicular recording data-storage media, or to create thin-film hard or semihard magnets which can be coupled with semiconducting integrated circuits, micromachines, microsen-sors, actuators, etc.

In this paper we review recent work in this field with particular emphasis on thin films containing rare-earth elements. The rare earths, particularly when combined with the ferromagnetic 3d transition metals (Fe, Co and Ni), form a vast array of compounds and alloys with widely variable properties. Moreover, amorphous alloys of the form a-TbFeCo and crystal-line compounds of the $Nd_2Fe_{14}B$ class constitute two of the most important magnetic materials for high-density erasable magneto-optic data storage and for high energy-product permanent magnets, respectively. In both of these applications the single-ion anisotropy of the rare earth element, plus subtle or straightforward anisotropic atomic structures, lead to a uniaxial magnetic anisotropy which is at the heart of the desired properties. An additional desirable feature of the rare earths is that their chemical sim-ilarity leads to easy substitution of one for another. By contrast, their Hund's rule interactions and the presence or absence of orbital angular mo-mentum produces a wide range of ferromagnetic or ferrimagnetic structures, when combined with 3d moment-bearing ions, and either very strong or rather weak magnetic anisotropies.

Specifically, in this paper we will focus on the use of a multi-ple-gun sputtering system, such as that shown schematically in Fig. 1, to produce thin films of RT-TM multilayers. The ability to deposit multilay-ers, with characteristic layer thicknesses in the nanometer region, gives one the hope of affecting the local atomic arrangements in ways that will

produce interesting properties. The many controllable parameters available in a deposition system (e.g., sputtering pressure, substrate temperature, deposition rate, etc.) permits a variety of multilayered structures to be grown, and some of these are illustrated in Fig. 2. A coherent layered structure, or single-crystal superlattice, is shown in Fig. 2(a). A compositionally modulated alloy (CMA), with some disorder at the interfaces, is depicted in Fig. 2(b). A variety of other multilayers are shown in Figs. 2(c)-2(f), with the latter two showing schematically ferromagnetic and ferrimagnetic examples with differing atomic structures. Additional complexity can be introduced by employing rare earth (RE) and transition metal (TM) elements when the REs possess orbital angular momentum and single-ion anisotropy. In a homogeneous amorphous RE-TM alloy such as a-TbCo, the randomness of the structure produces random easy magnetic axes, which tends to disorder the RE moments, below the spin-freezing temperature, into a frozen spin-glass-like structure. Often this is called a speromagnet, a term which is used reasonably to indicate that the disordered spin structure is caused by random magnetic anisotropy (RMA) rather than exchange fluctuations which produce a typical spin glass such as Cu-Mn. When RE/TM multilayers are considered, some rather complex magnetic structures can be envisaged and a few examples of these are shown schematically in Fig. 3. Here, an idealized RE/TM multilayer with perfectly sharp interfaces is shown in (a), and a sine-wave modulated multilayer, with $C_{RE}(z)$ and $C_{TM}(z)$ representing the atomic fractions of the RE and TM along the growth direction z , in (b). Fig. 3(c) shows some possible RE-TM amorphous alloy magnetic structures for light and heavy REs with random anisotropy, and for gadolinium with no random anisotropy. The "fanned" RE structures shown for the Nd and Dy structures result from random anisotropy in the assumed amorphous structure of the CMA.

Research on RE/TM multilayers in the last few years has been stimulated by several factors. First, there has been growing interest in magnetic and other phase transitions in physical systems which approach two or even one dimensions. Second, considerable progress has been made in understanding magnetic transitions in random systems such as spin glasses and random magnetic anisotropy (RMA) systems. In the latter case, scaling analyses have indicated the presence of a true phase transition, and theoretical work has indicated that when a coherent anisotropy is added to the

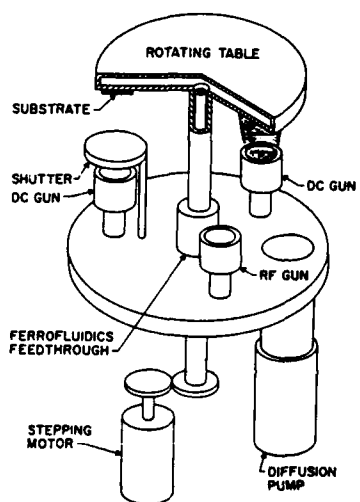


Fig. 1 Schematic of multiple-gun sputtering system.

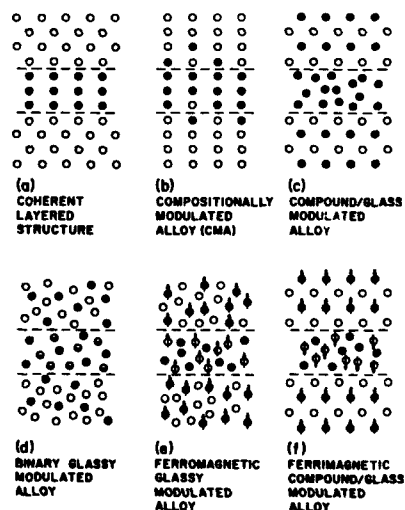


Fig. 2 Examples of multilayers.

RMA problem, the speromagnetic ordered state is converted into a ferromagnetic-like one.² Naturally, the deposition and growth of thin films does tend to produce a uniaxial anisotropy and thus there is the hope of relating recent theory to thin-film RMA systems, i.e., those containing RE ions with orbital angular momentum. Third, work in the early 1970s showed a perpendicular magnetic anisotropy (PMA) in sputtered, nominally isotropic RE-TM amorphous films. The origins of this PMA have remained controversial ever since, but it often has been claimed that anisotropic pair correlations, for example excess TM-TM pairs in the film plane or excess RE-TM pairs normal to the film plane, were the sources of the PMA. Clearly, the modern multiple-source deposition systems, such as that of Fig. 1, permit the control of the atomic pair correlations and their anisotropy, and thus allow one to investigate these questions. These circumstances have motivated the research to be outlined in the remainder of this contribution.

This article is intended to review our understanding of the physics of thin-films such as those introduced above. We do not review exhaustively all of the specific systems that have been investigated experimentally, but rather illustrate with a few examples the kinds of phenomena that have been observed. In the following sections we discuss aspects of the experimental determination of the anisotropy, summarize some systematics of PMA in RE/TM multilayers, outline a theoretical model for PMA in these systems, and discuss recent work on magneto-optics of RE/TM multilayers.³⁻⁵

MAGNETIC ANISOTROPY IN THIN FILMS

The measurement, interpretation and theoretical understanding of the magnetic anisotropy of thin films is of great importance fundamentally and for practical reasons. This section is intended to be a tutorial on definitions and measurements of anisotropy energies and fields in thin films. It has been found that there is some confusion on these concepts, even among those performing research on modern materials.

Definition and Measurement of Anisotropy

In the uniaxial case one may write the anisotropy energy per unit volume as

$$E_a = K_u \sin^2 \theta, \quad (1)$$

where θ is the angle between the magnetization (\vec{M}) and the easy axis (\hat{e}). The anisotropy constant (K_u) can be measured with a torquemeter. Here we

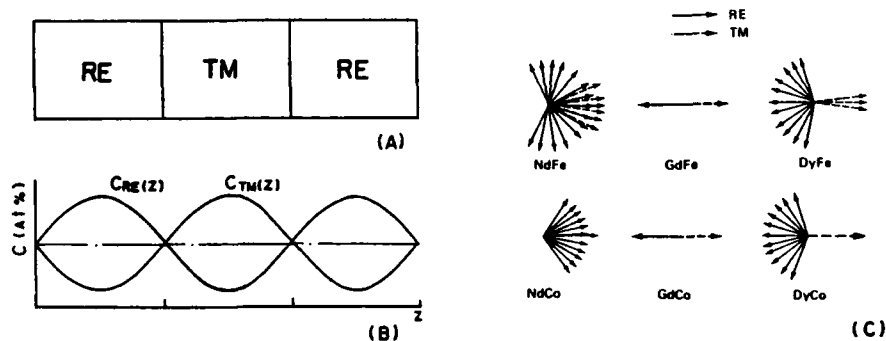


Fig. 3 Schematic diagrams of: (A) idealized multilayer with sharp interfaces; (B) sinusoidally modulated RE/TM multilayer; and (C) magnetic structures possible in RE-TM glasses and multilayers.

focus on its determination by magnetization measurements as a function of the direction of the applied field (\vec{H}_a). The measured anisotropy, or effective anisotropy, is determined by measuring the area between the parallel ($\vec{H}_a \parallel \hat{e}$) and perpendicular ($\vec{H}_a \perp \hat{e}$) magnetization curves. That is, the measured anisotropy (K'_u) is given by

$$K'_u = \left(\int_0^{M_s} \vec{H}_a \cdot d\vec{M} \right)_{\parallel} - \left(\int_0^{M_s} \vec{H}_a \cdot d\vec{M} \right)_{\perp}. \quad (2)$$

The intrinsic anisotropy (K_u) is given by

$$K_u = \left(\int_0^{M_s} \vec{H} \cdot d\vec{M} \right)_{\parallel} - \left(\int_0^{M_s} \vec{H} \cdot d\vec{M} \right)_{\perp}, \quad (3)$$

where \vec{H} is the internal field given by

$$\vec{H} = \vec{H}_a - N_d \vec{M}, \quad (4)$$

with N_d being defined as the demagnetization factor. It then follows that

$$K_u = K'_u + \frac{1}{2} (N_d^{\perp} - N_d^{\parallel}) M_s^2, \quad (5)$$

or

$$K_u = K'_u + 2\pi M_s^2 \quad (6)$$

for a thin film with a perpendicular demagnetization factor of 4π . Naturally $N_d^{\parallel} = 0$.

With the above definitions $K_u > 0$ implies perpendicular anisotropy. From Eqs. (2), (3) and (6), it can be seen that for a thin-film sample, if the $M(H_a)_{\perp}$ curve lies on or above the $M_{\parallel}(H_a)$ curve, this implies $K_u > 0$ so that the easy axis is normal to the film plane, i.e., perpendicular anisotropy exists.

Determination of Interface Anisotropy

Consider a multilayer consisting of a magnetic material (MM) and a nonmagnetic material (NM). Assume the thickness of the MM is t and the bilayer thickness is λ . If one considers a unit volume of the material with cross-section A in the plane of the film, the total measured anisotropy associated with the volume λA is

$$\lambda A K'_u = 2K_i A + [K'_v + K_{st} + K_{de}] t A, \quad (7)$$

where K_i is the interface anisotropy per unit area, K'_v is the volume anisotropy of the MM per unit volume, K_{st} is the induced volume anisotropy of the MM due to stress from either the NM or the substrate, and K_{de} is the demagnetization energy as, for example, in Eq. (6). Often one defines a total volume anisotropy as

$$K_v = K'_v + K_{st} \quad (8)$$

so that for the case of a thin film

$$\lambda K'_u = 2K_i + [K_v - 2\pi M_s^2] t. \quad (9)$$

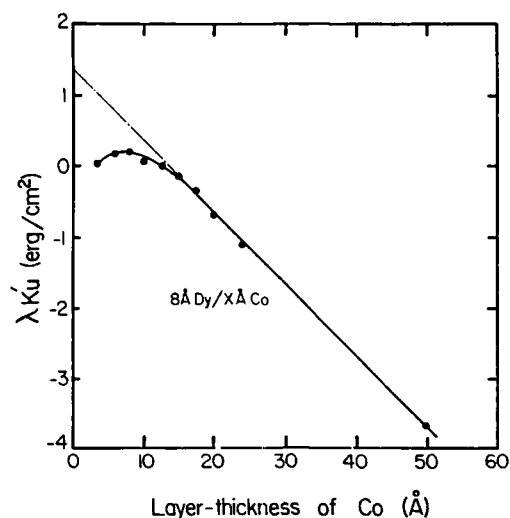


Fig. 4 $\lambda K_u'$ vs. t_{Co} for $8\text{\AA Dy}/x\text{\AA Co}$.

Figure 4 shows an example of $\lambda K_u'(t)$ for a Dy/Co multilayer at room temperature. These data, and those for many other systems such as Co/Au, Co/Cu, Co/Pt, Nd/Fe, etc. can be interpreted in terms of Eq. (9).⁵ Several points concerning such interpretations should be made.

- It is often the case, for $t \geq 10\text{-}15\text{ \AA}$, that the $\lambda K_u'(t)$ data do fall on a straight line with a slope and intercept presumably related to the second and first terms of Eq. (9), respectively.
- For $t \leq 10\text{ \AA}$, there is a general tendency for a maximum to be seen in $\lambda K_u'(t)$ and an approach to zero as $t \rightarrow 0$. This is the region where the structure exhibits significant disorder and, at least for several RE/TM multilayers, where the structure is compositionally modulated amorphous. Thus there are two distinct structural regions ($t \geq 15\text{ \AA}$, crystalline with distinct interfaces; and $t \leq 10\text{ \AA}$, highly disordered or amorphous) and the models used to interpret these structures should be clearly borne in mind.
- In the $t \leq 10\text{ \AA}$ region Eq. (9) obviously breaks down as a description of the data. This is reasonable because this region corresponds to thicknesses less than a few monolayers where, surely, it makes no sense to consider a well-defined volume anisotropy. Moreover, the demagnetization energy will be ill defined and, especially if there is disorder on the scale of several monolayers, K_i also will be poorly defined.
- Regarding the origins of PMA, the existing data often show a positive intercept of the extrapolation of the straight line. This implies that interface anisotropy favors PMA. Also, generally the slope of $\lambda K_u'(t)$ is negative so that often the demagnetization energy term dominates the K_v term, the latter of which can be positive at times. This depends on crystalline texture. Since the maximum in $\lambda K_u'(t)$ generally occurs in the range of $t \approx 4\text{-}8\text{ \AA}$, this means that it is the detailed anisotropic distribution of the constituent atoms that must be considered, rather than an idealized "sharp" boundary at the interface, as the origin of PMA.
- Occasionally a formula differing from Eq. (9) is employed for multilayers:

$$K_{eff} = 2K_s/t + K_v. \quad (10)$$

It is useful to correlate the terms in the two expressions as follows. Eq. (10) gives

$$tK_{eff} = 2K_S + K_V t \quad (11)$$

so that K_S , the surface anisotropy, is identified with K_i ; K_V in Eqs. (10) and (11) simply includes the demagnetization energy term of Eq. (9), and $K_{eff} \equiv (\lambda/t) K_U$ is an effective anisotropy which associates magnetic energy only with the magnetic material rather than with an average unit volume of the film. Given the above discussion about disorder and intermixing in the $t \sim 6 \text{ \AA}$ region it seems preferable to use Eq. (9) as compared to Eq. (10).

Determination of Intrinsic Anisotropy Fields

The concept of an anisotropy field arises in the following way. Consider a single domain particle with no domain walls and assume an anisotropy energy of the form Eq. (1). If the field \vec{H} makes an angle of α with respect to the easy axis \hat{e} , the total energy is

$$E = K_U \sin^2 \theta - HM_S \cos(\alpha - \theta). \quad (12)$$

The equilibrium position of \vec{M} is given by

$$\frac{\delta E}{\delta \theta} = 0 = 2K_U \sin \theta \cos \theta - HM_S \sin(\alpha - \theta). \quad (13)$$

Now suppose $\vec{H} \perp \hat{e}$ (i.e., $\alpha = 90^\circ$). Then

$$2K_U \sin \theta \cos \theta = HM_S \sin(90 - \theta) = HM_S \cos \theta. \quad (14)$$

$$\text{Since } M = M_S \sin \theta, \quad (15)$$

$$2K_U M/M_S = HM_S. \quad (16)$$

Defining the intrinsic anisotropy field as

$$H_K = 2K_U/M_S \quad (17)$$

leads to

$$M = \frac{H}{H_K} M_S. \quad (18)$$

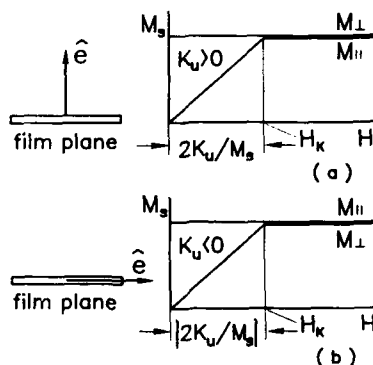


Fig. 5 M vs. H for easy axis normal to plane (a) and in-plane (b).

Thus M is proportional to H and equals M_S at a field $H = H_K$. This situation is shown in Fig. 5, where $M_{||}$ and M_{\perp} are shown in the cases where \vec{H} is parallel or perpendicular to the film plane, and the easy axis is either perpendicular or parallel to the film plane. Based on this simple mathematics, the knee field (H_K), where the "hard" direction magnetization curve intersects the "easy" direction curve, is used by various experimenters to estimate the anisotropy energy in Eq. (17) by means of a measurement of M_S and H_K . However, the situation actually is more complicated because one must account for demagnetizing fields and, further, the fact that K_U' can be positive or negative. The types of situations that can be encountered are illustrated in Fig. 6, which shows the magnetization plotted as a function of the applied field H_a . If we define H_K' to be the knee field where the magnetization in the "hardest" direction reaches M_S , then we have, for the three cases illustrated,

$$(a) \quad K_U > 0; K_U' > 0; K_U = K_U' + 2\pi M_S^2; H_K' = 2K_U/M_S \quad (19)$$

$$(b) \quad K_U > 0; K_U' < 0; K_U = 2\pi M_S^2 - |K_U'|; H_K' = 4\pi M_S \quad (20)$$

$$(c) \quad K_U < 0; K_U' < 0; K_U = |K_U'| - 2\pi M_S^2; H_K' = 2|K_U'|/M_S + 4\pi M_S \quad (21)$$

In Fig. 6, the cross-hatched area corresponds to the measured anisotropy energy, $|K_U'|$. It is clear from Eqs. (19)-(21) that a simple association of H_K' with an intrinsic anisotropy through $2K_U/M_S$ will be incorrect, and this has been done several times in the literature.

Another complicating factor that should be raised is that in general the $M(H_a)$ curves are not simple straight lines as shown in Fig. 6. They often exhibit curvature indicative of more complex forms (higher order) of anisotropy, and also the presence of a significant coercivity can lead to problems of interpretation.

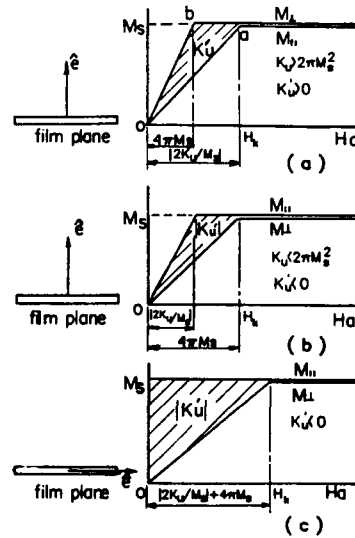


Fig. 6 M vs. H_a , the applied field.

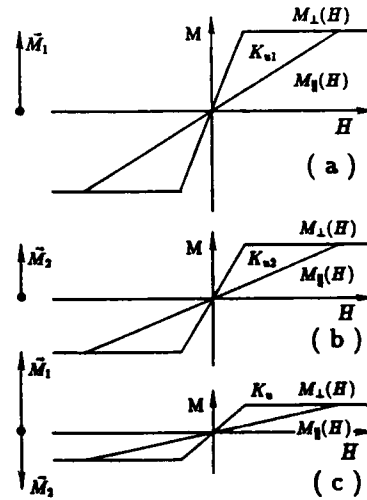


Fig. 7 $M(H)$ curves for separate (a and b) and ferrimagnetic (c) structures.

Measurement of Anisotropy Near a Compensation Point⁶

The measurement and interpretation of the anisotropy and coercivity of RE-TM amorphous alloys and multilayers, in the vicinity of the compensation temperature T_{comp} , leads to some interesting questions. T_{comp} is defined as the temperature at which $\vec{M}_{\text{RE}} = -\vec{M}_{\text{TM}}$ so the net magnetization is zero. Under these circumstances, the coercivity has been found, in many homogeneous RE-TM glasses such as Tb-Fe, to diverge. This behavior is explained crudely as follows: since the torque required to rotate the magnetization is

$$\tau \propto (\vec{M}_1 - \vec{M}_2) \times \vec{H},$$

an infinite field is required if $|\vec{M}_1 - \vec{M}_2| \rightarrow 0$.

Measurements of H_c , M_s and K_u often are plotted as a function of either temperature or composition, near T_{comp} or the compensation composition. Sometimes, but not always, the anisotropy approaches zero at the compensation point and this has led to confusion because it is thought, in the heavy RE-TM alloys, that the major source of K_u is from the RE subnetwork, and there is no reason for this to vanish as $T \rightarrow T_{\text{comp}}$. This conundrum can be explained as follows. Fig. 7 shows schematically the M_{\perp} and M_{\parallel} curves for a ferrimagnetic system where 1 represents RE and 2 represents TM. One expects that

$$K_u^{\text{total}} = K_{u1} + K_{u2} = K_{u1} = K_{u\text{RE}}.$$

However, graphically one sees that the measured anisotropy, the area between the curves, is given by

$$K_u^{\text{meas}} = K_{u1} - K_{u2} \propto |\vec{M}_1 - \vec{M}_2|,$$

since the ordinate is proportional to the difference in the subnetwork magnetizations. But since $|\vec{M}_1 - \vec{M}_2| \rightarrow 0$ as $T \rightarrow T_{\text{comp}}$, the measured value of

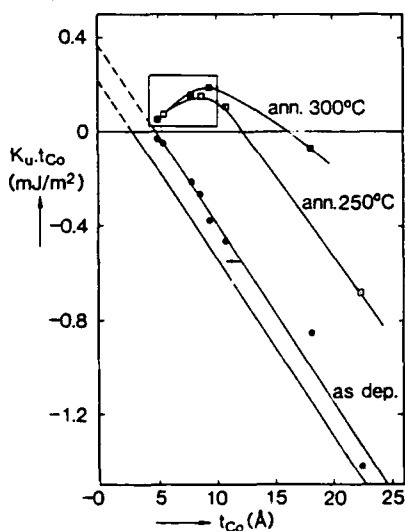


Fig. 8 $K_u t_{\text{Co}}$ vs. t_{Co} for as-deposited and annealed Co/Au (after Ref. 7).

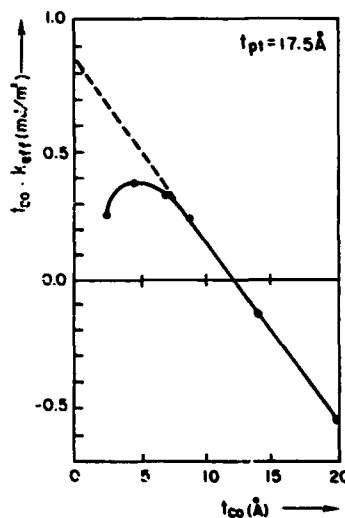


Fig. 9 $K_{\text{eff}} t_{\text{Co}}$ vs t_{Co} for Co/Pt (after Ref. 8)

(K_U^{meas}) will also approach zero and, moreover, will have no simple physical interpretation.

In several of the RE/TM multilayer systems that have been investigated, K_U^{meas} does not tend towards zero and this phenomenon involves a more complex explanation.

SYSTEMATICS OF PMA IN MULTILAYERS⁵

In this section we illustrate some systematic aspects of the experimental behavior of the magnetic anisotropy of RE and TM multilayers. For example, Figs. 8-11 show plots of $\lambda K_U'$ (or the equivalent) versus the layer thickness of the magnetic material. Several points should be noted. (1) As in Fig. 4 for Dy/Co, it is true in each case that for $t \geq 10 \text{ \AA}$, the data fall on a straight line with a slope and intercept interpretable in terms of the second and first terms of Eq. (9), respectively. (2) For $t \leq 10 \text{ \AA}$ there is a tendency for a maximum to be seen in $\lambda K_U'$ (t) and an approach to zero as $t \rightarrow 0$. In this region there is a significant disorder in the structure and, for the RE/TM cases, a structure describable as compositionally-modulated amorphous. (3) It is to be emphasized that the concept of an interface (or surface) anisotropy is a valid concept only as an intercept of data relevant to the "large" t region where the individual layers are crystalline and where distinct interfaces exist. In the "small" t region it no longer makes sense to consider an interface anisotropy K_i ; the anisotropic structure as a whole must be accounted for. (4) In Fig. 8 for Au/Co there is an upward shift towards positive $\lambda K_U'$ (PMA) after annealing. This was interpreted as resulting from a sharpening of diffuse interfaces by heat treating these two immiscible metals. The sharpened interfaces lead to an enhanced interface anisotropy K_i . (5) For RE/TM multilayers of Nd/Fe (Fig. 10), K_i is approximately independent of Nd thickness. However, for Dy/Fe (Fig. 11), the slope of the lines varies but the intercept ($2K_i$) does not. Additional data on Dy/Co show that both the intercept and slope vary as a function of RE thickness. These data are consistent with small-angle x-ray diffraction data which show a trend from more sharp to more diffuse interfaces in the series: Nd/Fe; Dy/Fe; Dy/Co.

A review and tabulation of K_i values in many RE/TM and TM/NM (NM = nonmagnetic material) multilayers has been given by Sellmyer *et al.*⁵ This tabulation will not be repeated here but we mention only some general features to be found in a variety of sputtered, evaporated, and MBE-grown multilayers. Ni multilayers with Mo and Cu tend to have negative K_i values, while Co multilayers with Pd, Au, Pt, and Cu have positive K_i values. RE/TM multilayers such as Nd/Fe, Dy/Fe, Dy/Co, Tb/Fe, and Tb/Co have

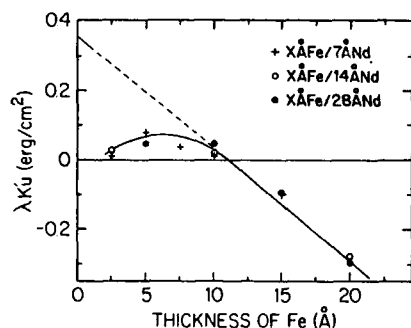


Fig. 10 $\lambda K_U'$ vs. t_{Fe} for Fe/Nd.

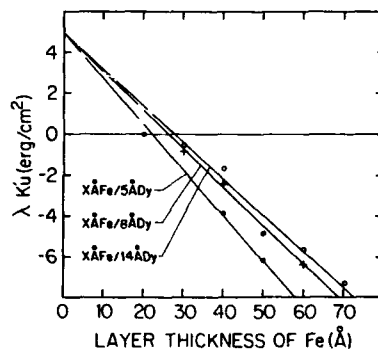


Fig. 11 $\lambda K_U'$ vs. t_{Fe} for Fe/Dy.

positive K_i values, while Er and Gd multilayers with Fe and Co have nearly vanishing values of K_i . Another point following from the data is that multilayers of the same two materials, but prepared by different methods, can have significantly different K_i values. This, again, suggests a strong sensitivity to the exact anisotropic atomic correlations.

We discuss in the following section some theoretical concepts relevant to understanding magnetic anisotropy in general. Following this we outline our recently developed model for understanding PMA in RE/TM systems in particular.

THEORETICAL CONCEPTS OF MAGNETIC ANISOTROPY³

Magnetic anisotropy arises from dipole-dipole and spin-orbit interactions and in the following we outline some of the important concepts for general structures first, and then for multilayers.

Dipole-Dipole Interactions

The long-range interaction energy between the dipoles \vec{m}_i and \vec{m}_j separated by a distance \vec{r}_{ij} is

$$\mu_{ij} = \frac{\vec{m}_i \cdot \vec{m}_j - 3 (\vec{m}_i \cdot \vec{r}_{ij}) (\vec{m}_j \cdot \vec{r}_{ij}) / r_{ij}^2}{r_{ij}^3} \quad (26)$$

The total energy from this term is

$$E_{d-d} = \frac{1}{2} \sum_i \vec{m}_i \cdot \vec{H}_i, \quad (27)$$

where \vec{H}_i is the local field at site i which does not include any contribution from \vec{m}_i . The anisotropy energy due to dipole-dipole interaction is then determined from Eq. (27) as the dipoles are aligned in various directions in the sample. The local field is calculated by Lorentz's method as discussed elsewhere, and a macroscopic field \vec{H} can be calculated.

For a thin-film magnetic sample of very large in-plane dimensions, there is a depolarization field of $-4\pi\vec{M}$ normal to the plane of the sample. This gives rise to a dipolar energy of $2\pi M^2$ which favors the in-plane direction of \vec{M} over the perpendicular direction.

The above procedure for the dipole-dipole energy breaks down for very thin films or multilayers because the macroscopic theory fails. Under these circumstances, the discrete sums in Eq. (26) must be performed to determine this energy.

Spin-Orbit Interaction

The spin-orbit interaction is given by the one-particle operator

$$H_{so} = \frac{1}{2} \alpha^2 \sigma [\vec{F}(\vec{r}) \times \vec{p}], \quad (28)$$

where α , σ , \vec{F} and \vec{p} represent the fine-structure constant, the electron spin, electric field, and momentum operators, respectively. Many years ago, Van Vleck approximated the spin-orbit energy by a short-range pseudo-dipolar term having the form of Eq. (26) except that \vec{r}_{ij} was replaced by some function $f(r_{ij})$. Néel extended this procedure to study the surface

and interface contributions to the anisotropy energy. Recently, band theory has been used to calculate the anisotropy energy for crystalline materials. Normally self-consistent spin-polarized band structure calculations are performed without spin-orbit interactions. The resulting wave functions are used to calculate matrix elements of the total Hamiltonian including H_{SO} , and the total Hamiltonian is diagonalized in a large number of points in the Brillouin zone. The anisotropy energy is obtained by performing this calculation for different directions of the magnetization, and then taking the difference. Very recent calculations for the ferromagnetic elements Fe, Co and Ni have shown that the resulting energy differences are extremely small, and that the results are only marginally reliable.

In some cases the above fundamental approach is not appropriate. Particularly when the main focus is the effect of anisotropy on the character of phase transitions, the generation of a model Hamiltonian is useful. Two areas of importance are those relevant to transition-metal ions and rare earths, which are discussed briefly below.

In the transition-metal case, the orbital angular momentum can be regarded to be quenched. Then, by second-order perturbation theory the spin-orbit Hamiltonian $\lambda \vec{L} \cdot \vec{S}$ gives for the anisotropy energy of an ion

$$E_i = D [3 S_z^2 - S(S+1)], \quad (29)$$

where D is the anisotropy constant. For the rare earths, the f electrons are localized so their orbital angular momentum is not quenched in a solid. Here, J is a good quantum number and one is interested in the ground state with $J_z = |J|$ in the crystal potential, as determined by first-order perturbation theory, for different directions of z . Keeping only the largest term in the crystal potential energy leads to the energy of the i^{th} ion as

$$E_i = \alpha_j \langle r^2 \rangle A_2^0 [3 J_z^2 - J(J+1)] \quad (30)$$

$$\approx 2\alpha_j \langle r^2 \rangle A_2^0 J_z^2, \quad J \gg 1, \quad (31)$$

where α_j is the Stevens factor, $\langle r^2 \rangle$ is the quantum mechanical average of the square of the radius of the $4f$ orbit, and A_2^0 is a crystal-field term given by

$$A_2^0 = \sum_j q_j \frac{3 \cos^2 \theta_j - 1}{r_j^3}, \quad (32)$$

where q_j is the charge on the j^{th} ion at a distance \vec{r}_j and θ_j is the angle between \vec{r}_j and the z direction. Of course, knowing or estimating the q_j values for a complex crystal is very difficult and even the signs of q_j often are controversial. Also Eq. (32) ignores the effects of the crystal field on the charge distribution of the i^{th} ion itself. This again illustrates the difficulty of first principles calculations of anisotropy energies.

Equations (29) and (31) give simple expressions for energies referred to as single-ion anisotropy. We shall use Eqs. (31) and (32), especially, in the following to determine structural effects on anisotropy in magnetic multilayers. Before doing this, however, it is useful to mention several results and calculations relevant to magnetic anisotropy in thin films and multilayers.

It should be noted that in Eq. (9), the terms K_i (or K_s), K_v , and $E_{\text{demag}} = 2\pi M_s^2$ all will become undefined if the thickness of the magnetic

layers becomes less than several monolayers. In these circumstances one must simply calculate the magnetic anisotropy, for the given structure, as a difference in total energy for the magnetization in the two relevant directions. For example, Draaisma and de Jonge found that the dipole-dipole energy deviates from the macroscopic value of $2\pi M^2$ for thicknesses less than about 12 Å. Further considerations of magnetic anisotropy in thin film systems with domains and with surface roughness have been given by Sura and Bruno, respectively. Finally, we should mention the calculations of Gay and Richter on thin layers of Fe, Ni and V. These workers found that the easy magnetization direction, for idealized monolayers, was perpendicular to the plane for Fe and V, but in plane for Ni. There is not, however, a direct correspondence between these quantitative results and real physical systems.

PMA IN AMORPHOUS RE/TM MULTILAYERS³

Recently we have devoted considerable effort to understanding the PMA of amorphous RE/TM multilayers in terms of the anisotropic pair correlations. Figure 12 shows data for the intrinsic anisotropy K_u as a function of the TM layer thickness, all data being taken at 300 K. One of the main problems in developing a model is to determine the importance of dipole-dipole versus single-ion contributions to K_u . Phenomenologically, one may write

$$K_u = \sum D_{mn} X_n X_m \langle J_n \rangle \langle J_m \rangle + \sum D_n X_n \langle J_n^2 \rangle, \quad (33)$$

where X_n is the concentration of the n^{th} type of atom and the first and second terms are due to dipole-dipole and single-ion interactions, respectively. This can be transformed into

$$K_u = f_1 M_{\text{RE}}^2 + f_2 M_{\text{TM}} + f_3 M_{\text{RE}}^2 M_{\text{TM}} + g M_{\text{RE}}^2, \quad (34)$$

where f_1 and g are complicated functions of structure. Fitting K_u data as a function of thickness, and including a structural model, can be done but it is very difficult to obtain meaningful results. However, from Fig. 12 it is obvious that, except for RE = Gd, single-ion anisotropy must be the dominant origin of PMA. This follows since there are no spin-orbit

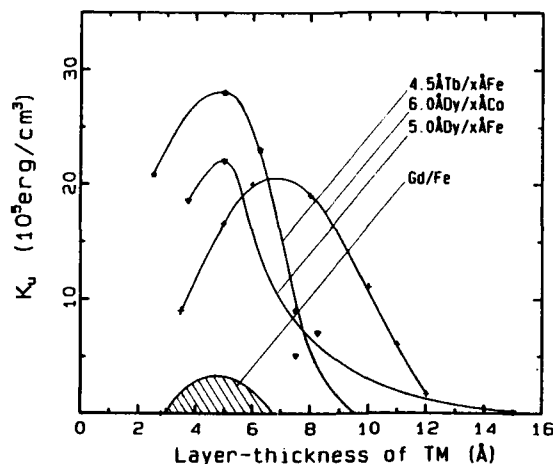


Fig. 12 K_u vs. layer thickness of TM.

interactions in the S-state ion Gd^{3+} . The K_u values for the RE ions with orbital angular momentum is about one order of magnitude larger than for Gd. Thus a model incorporating single-ion anisotropy Eq. (31) and a sinusoidal compositional modulation (relevant to the RE/TM systems considered) has been developed. In the following we outline the model and analysis for a series of Dy/Co multilayers.

The magnetization and anisotropy data are analyzed by means of models adapted to the CMF microstructure. First, a mean-field model is fitted to experimental data on homogeneous a-DyCo alloys to obtain the subnetwork magnetizations M_r and M_t , as a function of composition. The result of this is shown in Fig. 13. Then the amorphous CMF with sinusoidal compositional modulation is modeled by

$$\eta_t(t) = \eta_{t0} + (A/2) \cos(2\pi z/\lambda), \quad (35)$$

where $\eta_t(\eta_r)$ is defined to be the atomic fraction of the TM(RE). For simplicity in this development we assume equal RE and TM nominal layer thicknesses. η_{t0} is a constant and A is the peak-to-peak compositional modulation of the TM. The CMF is then divided into thin slices parallel to the interfaces with the z axis normal to them. Each slice is regarded as a two-dimensional amorphous RE-TM alloy. The CMF magnetization then can be written as an average over the slices:

$$M = \frac{1}{\lambda} \sum_i [M_t(\eta_t(z_i)) - M_r(\eta_r(z_i))] \Delta z_i. \quad (36)$$

The parameters η_{t0} and A are determined by fitting the calculated magnetization to experimental data. As an example the calculated results for 6ÅDy/tÅCo samples are shown in Fig. 14. It is seen that the calculated and experimental magnetization data agree very well. The average magnetization of Co and Dy subnetworks are also drawn in this figure. Figure 14 also shows the Co-layer-thickness dependence of the Co-atomic fraction modulation, A . The A value is only about 0.1 for the thinnest Co layer thickness of 3.5 Å and its value increases as the Co layer becomes thicker. This feature is understandable in terms of a larger mixing effect for the thinner-layer samples, which results from some combination of diffusion and roughness introduced at interfaces during fabrication. An example of the subnetwork and total magnetizations as a function of t is shown in Fig. 15.

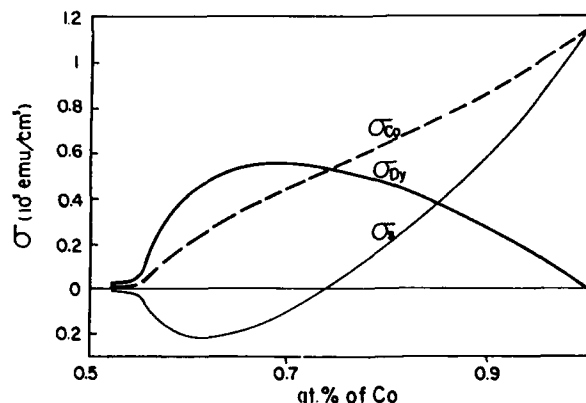


Fig. 13 Plot of subnetwork and total magnetizations for homogeneous a-DyCo alloys.

For this CMF, $6\text{\AA Dy}/6\text{\AA Co}$, it can be seen that all of the magnetizations oscillate in magnitude, and the total magnetization changes sign.

The evaluation of the anisotropy for an amorphous CMF is done on the basis of Eqs. (31) and (32). For a compositionally modulated amorphous structure, the sum over j in Eq. (32) is replaced with an integral weighted with an anisotropic pair distribution function

$$P_{ij} = \eta_j(z) R_{ij}(r) [1 + \beta_j \cos \theta_j + \dots], \quad (37)$$

where $\eta_j(z)$ is the atomic fraction of the j^{th} neighboring atom, $R_{ij}(r)$ is the isotropic part of the distribution and β_j is the lowest order anisotropic contribution. The anisotropy in the pair distribution function can arise from the composition modulation of multilayers and strains at the various interfaces.

The stress in a magnetic material gives rise to magnetoelastic anisotropy energy due to inverse magnetostriction (magnetostriction is the strain $\lambda = \Delta l/l$ in the direction of magnetization). This contribution is given by

$$E_{me} = \frac{3}{2} \lambda_s \sigma \sin^2 \theta, \quad (38)$$

where λ_s is the saturation magnetostriction, σ is the stress, and θ is the angle between M_s and σ (σ is negative for compressive stress). Knowing λ_s and σ one can find the contribution of this term to the anisotropy energy. If one assumes a magnetostriction of $\lambda = 2 \times 10^{-4}$ and a stress of $\sigma = 10^{10}$ dynes/cm², then one can obtain

$$K_u \approx \frac{3}{2} \lambda \sigma \sim 3 \times 10^6 \text{ erg/cm}^3,$$

which is the right order of magnitude. However, in the case of multilayers consisting of a magnetic metal (MM) with a nonmagnetic metal (NM), one must envision a situation in which the NM exerts a stress on the MM - thus causing a PMA as calculated above. But in the case of amorphous CMF the structure is not neatly separable into MM/NM layers with sharp interfaces. Rather one has a continuously varying composition as synthesized. This suggests that stress would play a minor role.

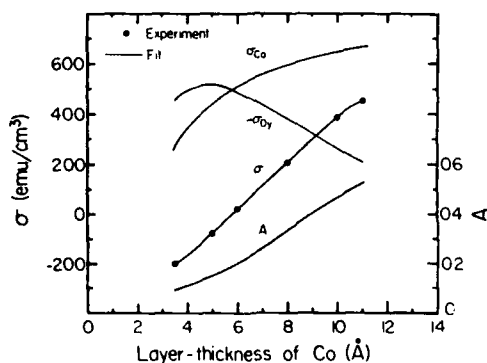


Fig. 14 Subnetwork and total magnetizations, and amplitude A , for $6\text{\AA Dy}/t\text{\AA Co}$.

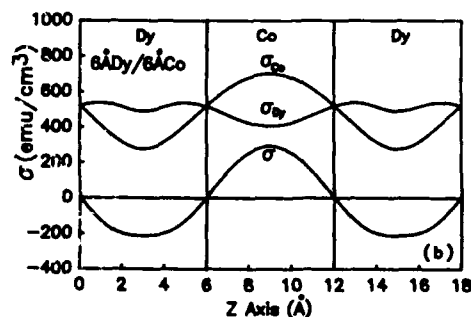


Fig. 15 Magnetization distribution along z axis for two $6\text{\AA Dy}/6\text{\AA Co}$.

In addition, Van Dover *et al.*⁹ considered carefully magnetostrictive effects in a-TbFe glasses and found that the sign of K_u did not correlate with the sign of the stress. Finally, Awano *et al.*¹⁰ found for Co/TM (TM = Cu, Ag, Au and Pd) and Fe/Cu CMF that the calculated stress-induced anisotropies are about 10 to 100 times smaller than the measured PMA. All of these results indicate that stress plus inverse magnetostriction does not play a major role in the PMA of the RE/TM multilayers. To the extent that magnetostrictive effects do play a role, it seems to be as a relatively small perturbation on the anisotropic structure and local environments, as already determined by the fabrication procedures.

The lowest order contribution to the crystal field term A_2^0 comes from the first-order term in the expansion of η from Eq. (39) about the rare-earth ion and it is proportional to A/λ . Also the first-order term in η has the maximum value at the interface and the charges q_i are expected to be most significant in the interface region. Thus, as expected, most of the anisotropy comes from the interface region. Combining the results for A_2^0 with E_i in Eq. (31), the anisotropy energy K_u for a CMF can be written as

$$K_u = \xi \frac{A}{\lambda} \langle M_{RE}^2 \rangle, \quad (39)$$

where ξ is a constant and $\langle M_{RE}^2 \rangle$ is the average of the square of the saturation magnetization of the rare-earth subnetwork in the easy direction. With ξ as an adjustable parameter, Eq. (39) is fitted to the K_u data for 6ÅDy-/tÅCo samples and the results are shown in Fig. 16. In view of the single parameter, the agreement between the experimental data and calculated results is remarkable. The fitted value of $\xi = 5.26 \times 10^{-6}$ cm leads to an average value of the single-ion anisotropy parameter $D = 2 \times 10^{-17}$ erg, which is reasonable in terms of the typical value of the single-ion random-anisotropy parameter in amorphous RE-TM alloys. Finally, this model gives similar fits for other RE/TM CMF which are published elsewhere.⁶

In concluding this discussion we have seen that when the thickness of the magnetic layer becomes smaller than several atomic diameters, significant disorder sets in for both the TM/NM and RE/TM multilayers. The

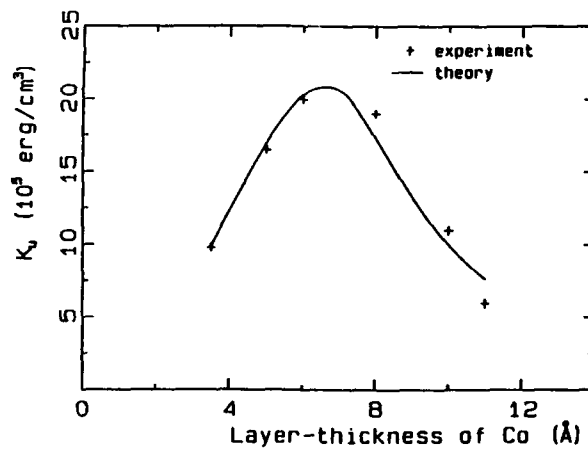


Fig. 16 Comparison of experiment and theory for $K_u(t_{Co})$ (after Ref. 3)

compositional modulation is lost in the limit $t \rightarrow 0$, where a homogeneous, isotropic film results. We have developed a model, relevant to RE/TM multilayers with significant single-ion anisotropy. Based on the similarity of the data of these multilayers and Co/Au and Co/Pt multilayers, this model is likely to be valid for such disordered multilayers as well.

MAGNETO-OPTIC PROPERTIES OF RE/TM CMF⁴

We have seen in the above sections that it is possible to understand and thus to control the magnetic anisotropy of RE/TM CMF. Since the presence of PMA in thin films is essential for erasable magnetic-optic data-storage applications, it is of interest to consider the extent to which magneto-optic (MO) phenomena can be understood and, possibly, optimized in RE/TM CMF. In the long history of the study of MO properties of materials it has been found that a quantitative understanding has been very difficult to achieve. Empirically, several classes of MO materials can be identified. These include: (1) RE and actinide intermetallic compounds with Kerr rotation (θ_K) values of about 10-15 deg, (2) TM intermetallics such as MnBi and PtMnSb for which $\theta_K \sim 1$ -2 deg, (3) Amorphous RE-TM alloys such as a-Tb₂₀Co₈₀, a-Nd₂₀Co₈₀, and a-(Gd,Tb)₂₅(Fe,Co)₇₅ for which $\theta_K \sim 0.2 - 0.4$ deg. The latter class is the one now being used in first-generation MO storage devices and systems. Studies of RE/TM CMF are in their early stages but several systems including Dy/Co and Dy/Fe have been investigated. In the remainder of the section we briefly describe the results obtained thus far.

For several reasons there is little fundamental understanding of the magnitudes of the MO properties of materials. But the theory does indicate a number of criteria which must be satisfied to obtain large MO Kerr effects (MOKE) and other appropriate properties. These include:

- (a) A large concentration of a 3d transition element (e.g., Mn, Fe, Co) so that large exchange interactions and a high Curie temperature will result.
- (b) Heavy elements with large spin-orbit interactions should be present since the off-diagonal dielectric tensor element, ϵ_{xy} , scales with the spin-orbit interaction.
- (c) There should be a large joint-density-of-states at the appropriate photon energy (e.g., 830 nm) so as to give significant optical transitions.
- (d) The dipole selection rule $\Delta l = \pm 1$ suggests that there should be a significant mixture of orbital angular momenta in the valence states so that dp or fd transitions are likely.
- (e) For a bulk or thin-film MO material one needs an appropriate anisotropy in the structure so that uniaxial anisotropy of the required strength can be achieved.
- (f) Finally, there are additional constraints such as thermal and chemical stability, appropriate coercivity, etc.

With all these conditions it is not surprising that nature has resisted the easy design of outstanding MO materials.

In addition to the above general principles, in recent years several groups have been studying "new" mechanisms to enhance the magnitude of the MOKE observed in a single MO material, or a MO/NM bilayer film, or in MO/NM multilayers. Feil and Haas showed that a resonance-shaped MOKE spectra can be produced by a plasma resonance of free carriers in a magnetic material,¹¹ and a similar effect and explanation was advanced for Fe/Cu bilayers by Katayama *et al.*¹² Reim and Weller¹³ presented data and similar arguments for TbFeCo/Cu and GdTbFeCo/Ag bilayers, and also showed that if the NM "reflecting" substrate has a low value of the complex refractive index, an enhancement of θ_K can result.

Recent work in our laboratories has been concerned with experimental MOKE studies of several RE/TM systems and theoretical treatment of the Kerr effect in two-medium layered systems. In the following we discuss briefly some of the results of Chen *et al.*¹⁴ and then conclude this section with a summary of the major results on this class of materials. Chen *et al.*¹⁴ considered two geometries: (1) a system of two thick media with a single interface (denoted as NM/MO where NM represents the nonmagnetic medium from which the light impinges at the interface on the ferromagnetic MO medium, and (2) layered systems with one thin medium on top and a thick one on the bottom. This is denoted as either [MO/NM] or [NM/MO]. The former would correspond, for example, to a MO medium with a metallic underlayer such as Ag, and the latter to an antireflection dielectric coating such as SiO₂ on top and a thick MO medium on the bottom.

For the NM/MO case, it was shown that the complex Kerr function ϕ_k is

$$\phi_k = i \frac{\epsilon_{mxy} (\epsilon_0/\epsilon_m)^{1/2}}{\epsilon_m - \epsilon_0}, \quad (40)$$

where ϵ_m and ϵ_0 correspond to diagonal components of the MO and NM media, respectively, and ϵ_{mxy} is the off diagonal component for the MO medium. Thus, for this configuration the MOKE is controlled by four physical quantities: (1) ϵ_{mxy} which has its origins in intraband and interband transitions in the MO medium, (2) $\epsilon_m^{-1/2}$ which has features similar to the energy-loss function at the plasma edge, (3) the optical matching term $(\epsilon_m - \epsilon_0)^{-1}$ which will lead to maxima when $\epsilon_m \approx \epsilon_0$, and (4) $\epsilon_0^{1/2}$ or n_0 , the index of the NM medium. Thus a small ϵ_0 , corresponding to a plasmon (ϵ_2 is small and $\epsilon_1 \approx 0$) of the NM medium, will not contribute to the enhancement of the Kerr effect unless it matches ϵ_m . It should be noted that if the NM medium is air, then $\epsilon_0 = 1$ and Eq. (40) reverts to that used by other authors.

An example of the effect of thickness variation of Dy7Å/Co5Å CMF which is deposited on a thick Ag underlayer is shown in Fig. 17. A large resonance-like peak is seen at about 3.6 eV for 108 Å CMF thickness. Figure 18 shows the Kerr rotation, for the same samples, calculated by McGahan *et al.*¹⁵ It is seen that there is rather good agreement between the experimental and calculated curves, and thus the optical constants of the system, as influenced by the plasma edge of Ag, strongly affect the energy dependence of the MOKE. A second example of the spectral and thickness dependence of

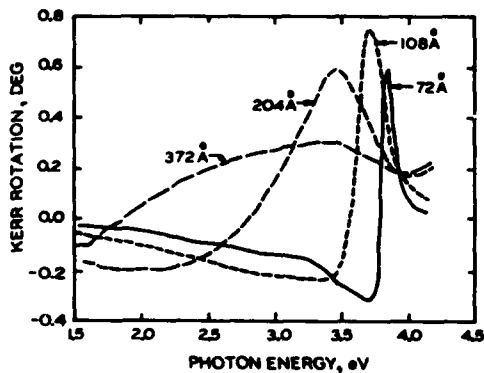


Fig. 17 Kerr rotation vs. photon energy for Dy/Co multilayers of varying thickness on Ag (after Ref. 15).

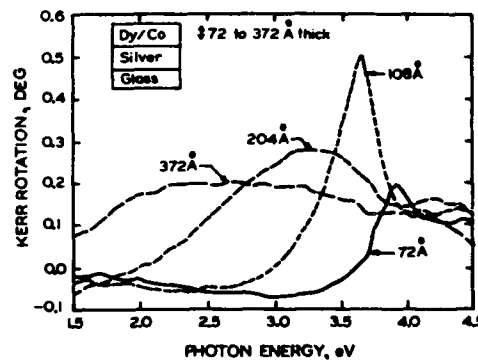


Fig. 18 Calculated Kerr rotation vs. photon energy for samples of Fig. 17 (after Ref. 15).

θ_k for a $\text{SiO}_2/(\text{Dy/Co})/\text{SiO}_2/\text{Ag}$ layered system is shown in Fig. 19. Here the SiO_2 layers are 1700 Å thick and the Dy7Å/Co5Å layers are of variable thickness. A sharp resonance-enhanced θ_k value is seen in Fig. 19.¹⁴ However, a contour plot of the signal-to-noise figure of merit,

$$\text{SNR FOM} = 100 R^{1/2} \sin 2\theta_k,$$

shows that large enhancements of θ_k by optically induced effects are not an unalloyed benefit. The maxima in the SNR FOM appear elsewhere in phase space because the reflectivity tends toward zero where θ_k gets large. Further experiments with dielectric overlayers have been performed and these also have led to large θ_k enhancements and spectral structure. One example, of Dy/Co coated with SiO_2 , is shown in Fig. 20. It is seen that θ_k changes from about 0.2 deg to 2.0 deg at 2.0 eV, and that the calculated result based on an SiO_2 thickness of about 2020 Å gives excellent agreement with experiment.

SUMMARY AND CONCLUSIONS

In this paper we have reviewed methods of measuring the intrinsic uniaxial anisotropy of thin films. We have presented some systematics on the occurrence of perpendicular anisotropy in rare-earth and transition-metal multilayers and have indicated that the detailed anisotropic pair correlations, which become significant at interfaces when the layer thicknesses approach several monolayers, lead to PMA. It is seen that concepts such as surface or interface anisotropies must be used very carefully, and that ideas such as RE-TM "pairs" as the origin of PMA are oversimplified. Aside from Gd, it was shown that single-ion anisotropy of RE ions, and probably TM ions as well, was the fundamental source of PMA in CMF.

Concerning the MO properties of RE/TM CMF, it has been shown that the magnitude of the Kerr rotation is similar to that of the TM component, viz. 0.2-0.4 deg. Significant enhancements of the MO effects are possible by the use of metallic underlayers and antireflection overlayers with special optical properties, especially if they are well matched to those of the magnetic material. A theoretical understanding of the properties, in a phenomenological sense, has been achieved, given the MO properties of the constituent layers.

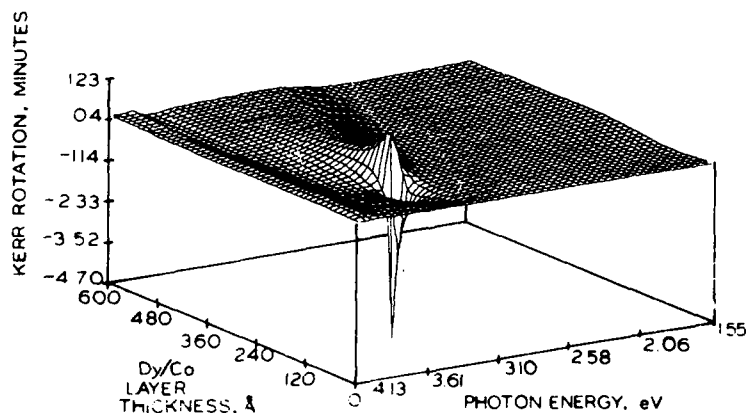


Fig. 19 Calculated Kerr rotation vs. Dy/Co layer thickness and photon energy for quadrilayer structures (see text, after Ref. 16).

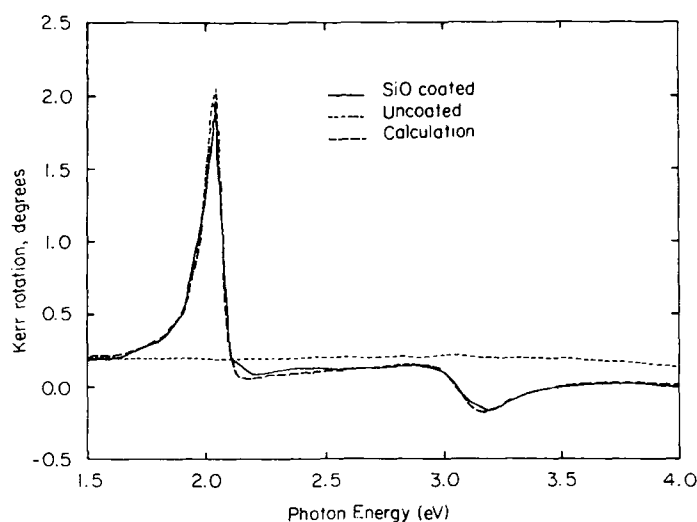


Fig. 20 Measured and calculated Kerr rotation vs. photon energy for SiO coated and uncoated Dy/Co (see text, after Ref. 17).

A significant challenge for the future is the design and growth of still more complex multilayer structures, with the required magnetic anisotropy and other properties, but with larger intrinsic MO effects. Such magnetic multilayers may have a great deal of potential for new data-storage or semihard thin-film magnetic device applications.

ACKNOWLEDGEMENTS

We are grateful for financial support to the National Science Foundation under Grants DMR-8918889 and INT-8715441. We thank J. A. Woollam, S. S. Jaswal, R. D. Kirby, J. X. Shen, L. Y. Chen, and W. A. McGahan for helpful discussions and collaboration.

REFERENCES

1. See, for example, Proc. of 34th Conf. on Mag. and Magnetic Materials, J. Appl. Phys. 67, 1990, and refs. therein.
2. D. J. Sellmyer and S. Nafis, Phys. Rev. Lett. 57, 1173 (1986) and refs. therein.
3. Z. S. Shan, D. J. Sellmyer, S. S. Jaswal, Y. J. Wang and J. X. Shen, Phys. Rev. Lett. 63, 449 (1989).
4. D. J. Sellmyer, J. A. Woollam, Z. S. Shan and W. A. McGahan, Mat. Res. Soc. Symp. Proc. 150, 51, (1989).
5. D. J. Sellmyer, Z. S. Shan and S. S. Jaswal, Mat. Sci. Eng. B 6, 137 (1990) and refs. therein.
6. Z. S. Shan, Ph.D. Thesis, University of Nebraska (1990), and to be published.
7. F. J. A. den Broeder, D. Kuiper, A. P. van de Mosselaer and W. Hoving, Phys. Rev. Lett. 60, 2769 (1988).
8. W. B. Zeper, F. Greidanus and P. F. Garcia, IEEE Trans. Mag. 25, 3764 (1989).

9. R. B. Van Dover, M. Hong, E. M. Gyorgy, J. F. Dillon, and S. D. Albiston, J. Appl. Phys. 57, 3897 (1985).
10. H. Awano, O. Taniguchi, T. Katayama, F. Inoue, A. Itoh and K. Kawanishi, J. Appl. Phys. 64, 6107 (1988).
11. H. Feil and C. Haas, Phys. Rev. Lett. 60, 1989 (1988).
12. T. Katayama, Y. Suzuki, H. Awano, Y. Mishihara and N. Kashizuka, Phys. Rev. Lett. 60, 1426 (1988).
13. D. Weller and W. Reim, Mat. Res. Soc. Proc. 150, 37 (1989).
14. L. Y. Chen, W. A. McGahan, Z. S. Shan, D.J. Sellmyer and J.A. Woollam, J. Appl. Phys. (in press).
15. W. A. McGahan, L. Y. Chen, Z. S. Shan, D.J. Sellmyer and J.A. Woollam, Appl. Phys. Lett. 55, 2479 (1989).
16. W. A. McGahan and J. A. Woollam, Appl. Phys. Commun. 9, 1 (1989).
17. L. Y. Chen, W. A. McGahan, Z. S. Shan, D.J. Sellmyer and J.A. Woollam, J. Appl. Phys. 55, 5337 (1990).

FMR STUDIES OF METALLIC MAGNETIC THIN FILMS IN LAYERED STRUCTURES

Hervé Hurdequint

Laboratoire de Physique des Solides
Université Paris-Sud
Orsay, France

INTRODUCTION

We will present and discuss, in this paper, results of FMR studies performed on metallic magnetic thin films. Specifically, the thin films studied correspond to metallic systems where a metallic ferromagnetic layer is in contact with a paramagnetic normal metal in a layered structure sample geometry. Such a layered structure geometry is well appropriate, with respect to the magnetic properties studied, for the investigation of various physical phenomena occurring *at different length scales*. Different physical questions have been addressed in our FMR studies and they will be successively discussed in the present report according to the following classification where the physical phenomena studied are ranked in increasing order of complexity: (i) in ultrathin layers of the magnetic material interface effects are expected to be revealed, in particular, in the magnetic anisotropy. One of the goals of our experimental investigation is thus to extract an information on the specific *interface-induced magnetic anisotropy*, characteristic of the interface studied. This is achieved by studying *single* magnetic layers, either "ultrathin" or "thick". (ii) we are also concerned more generally in such layered structure metallic systems with a systematic study of the *magnetic interfacial coupling* (magnetic proximity effects) between a thin *metallic* ferromagnetic film and a normal metal. (iii) finally we raise the problem of the nature of *inter-magnetic layer coupling* in metallic *multilayer* structures.

In the following we will present (in a condensed and summarized form) and discuss FMR results obtained on magnetic films constituted of (Ag/single Fe layer or Fe multilayer/Ag) sandwiches where, for this (Ag/Fe) system, the ensemble of the phenomena mentioned above has been studied in parallel and is reported, in more detail, in our previous publications (see, respectively, the references 1,2,3).

SAMPLE CHARACTERISTICS

The whole series of films whose FMR results will be reported correspond to (Ag/magnetic layer/Ag) sandwiches with a base Ag layer 550 Å thick and a top Ag layer 275 Å thick for a Fe single layer or 550 Å thick for a Fe multilayer¹. The films are deposited by sputtering on heated mica substrates. The Ag base layer is deposited on a freshly cleaved mica substrate at a

temperature $T_s \sim 150^\circ\text{C}$, then annealed in situ in vacuum ($\sim 10^{-6}$ Torr) for 1/2 hour at the same temperature. The whole metallic layered stack (Fe and Ag layers) is deposited subsequently at the same temperature T_s . The conditions of deposition used enable to get a highly textured polycrystalline Ag base layer with a preferred (111) orientation perpendicular to the film, characterized by a large lateral size (~ 2000 Å) of the crystallites and a spread of heights of these crystallites as determined through Scanning Tunneling Microscopy (STM) measurements¹. The individual thickness of the thin layers of Fe and Ag given in the following corresponds merely to a conversion of their actual time of deposition (only parameter monitored in the sputtering process) according to the following, previously determined on thick films, deposition rates: 48 Å/min for Fe and 210 Å/min for Ag. A more detailed information on the characteristics of the samples studied is given in ref. 1 and 3.

FMR RESULTS AND ANALYSIS

FMR Studies of Single Fe Layers

Reflection FMR measurements are performed at X band. The basic FMR experiment carried out consists in studying the resonance spectrum as a function of the orientation [angle $\theta_H = (\hat{N}, \hat{H})$ with respect to the film normal \hat{N}] of the applied dc field H in a plane perpendicular to the film (see the insert of Fig. 2 for a sketch of the experimental configuration). A standard field-modulation being used, the detected signal corresponds to the field derivative of the absorbed microwave power. This leads for the observed^{1,3} resonance lines to nearly antisymmetrical lines with an A/B ratio (of the amplitudes of the lobes above and below the baseline) close to but different from 1, which varies in a systematic fashion with the orientation θ_H .

Ultrathin Fe single layers. A series of ultrathin single Fe layers, with thickness t_{Fe} taking the set of values [24 Å; 36 Å; 48 Å; 80 Å] has been studied¹. As expected theoretically⁴, in these ultrathin Fe layers ("ultrathin" defined by $t_{Fe} < \lambda_s$ a characteristic exchange length λ_s^{-1} precised later) a *unique* resonance line is observed. We mention first that, for the whole series of ultrathin Fe single layers studied, the value of the A/B ratio in parallel geometry is found less than 1 (in the range [0.7; 1], corresponding³ to a positive "signal phase". This characteristic resonance line feature is commented upon in ref. 3. The data to be discussed in the following concern, primarily, the field for resonance H^{res} which is derived from the field H_0 (intersection with the baseline) and peak-to-peak linewidth ΔH^{pp} after a correction¹ relevant to the observed A/B value. Fig. 1 of ref. 1^{pp} displays the angular variation of the field for resonance $H^{res}(\theta_H)$ observed for two characteristic ultrathin Fe layers. For the (Fe 48 Å) sample, the $H^{res}(\theta_H)$ curve reflects the dominant contribution of the demagnetizing field effect (shape anisotropy) where the line cannot be observed within a few degrees around the perpendicular geometry (as our available dc field is limited to 11 kOe). By contrast, for the (Fe 24 Å) sample the resonance is now seen in perpendicular geometry ($\theta_H = 0$) with $H^{res} \approx 8.92$ kOe, which reveals the presence of a strong uniaxial perpendicular anisotropy (\hat{N} easy axis) that substantially counteracts the demagnetizing field effect.

Theoretical analysis. We consider the energy density described by:

$$E = - \vec{M} \cdot \vec{H} + 2\pi M^2 \cos^2 \theta - K \cos^2 \theta - (\vec{A}M^2) \cdot \nabla^2 \vec{M} \quad (1)$$

where \vec{M} is the saturated magnetization whose orientation is given by $\theta = (\hat{N}, \hat{M})$. The first term represents the Zeeman energy, the second the demagnetization, the fourth one the non uniform exchange energy. The third term describes an anisotropy energy: $E_{an} = -K \cos^2 \theta$, taken in the form of a uniaxial perpendi-

cular anisotropy (\hat{N} easy axis for $K > 0$), with $H_A = 2K/M$ the corresponding anisotropy field, whose effective value of the constant K will depend on the interface-induced anisotropy, stress-induced and volume magneto-crystalline anisotropy of the magnetic layer. The static equilibrium orientation θ_0 of the magnetization is thus¹ given by the following magnetostatics equation:

$$H \sin(\theta_0 - \theta_H) = (4\pi M - H_A) \cos\theta_0 \sin\theta_0 \quad (2)$$

From the Landau-Lifschitz equation of motion of the magnetization, the resonance condition for the uniform mode, as a function of the orientation θ_H , is derived:

$$(\omega/\gamma)^2 = [H \cos(\theta_0 - \theta_H) - (4\pi M - H_A) \cos^2\theta_0] [H \cos(\theta_0 - \theta_H) - (4\pi M - H_A) \cos 2\theta_0] \quad (3)$$

where γ is the gyromagnetic ratio of the precessing moments ($g=2.09$ for Fe) and θ_0 is given by eq.(2) at $H = H^{\text{res}}$. For each ultrathin Fe layer, the observed $H^{\text{res}}(\theta_H)$ is compared with the theoretically expected one (as derived from eqs.2 and 3) in terms of the *unique fitting parameter* $(4\pi M - H_A)$. We get, in each case, an overall reasonably good fit of the experimental variation except from systematic deviations (up to 0.1 kOe) towards the parallel geometry. Thus, for each ultrathin Fe layer sample, the best fit value of the parameter $(4\pi M - H_A)$ is determined and, assuming for the magnetization the bulk Fe value ($4\pi M = 21.55$ kOe), the value of the anisotropy field H_A is deduced. Results are displayed in Fig.1 where H_A is plotted versus the inverse Fe layer thickness. As discussed by Rado^{4,5A}, one may analyse the effective anisotropy constant K of such "ultrathin" Fe layers in terms of the sum of a volume contribution K_{vol} and an interface-induced one (constant K_S and symmetric interfaces in our case) inversely proportional to the magnetic layer thickness, according to:

$$K = K_{\text{vol}} + (1/t_{\text{Fe}}) 2 K_S \quad (4)$$

In summary, the principal result of this FMR study of ultrathin single Fe layers sandwiched by Ag is that the anisotropy induced at the (Ag/Fe) interface is essentially a *perpendicular uniaxial anisotropy* (\hat{N} easy axis), characterized by an effective constant $K_S \approx 1.45$ erg/cm² at room temperature whose value is deduced from the slope of the observed linear variation of H_A with $(1/t_{\text{Fe}})$.

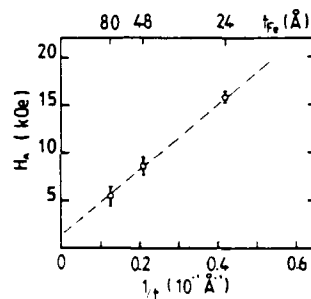


Fig. 1. Anisotropy field H_A plotted versus the inverse of the Fe layer thickness t_{Fe} .

Thick Fe single layers. A series of thick Fe layers, with thickness t_{Fe} taking the set of values [432 Å; 648 Å; 864 Å] has been studied¹. By contrast to the ultrathin layer case, the resonance spectrum of the thick Fe layer samples shows the presence, besides the principal uniform mode, of a *higher field mode* in a large angular range. This line is much less intense and dephased (essentially a B lobe is observed) as compared to the principal one. We identify this higher field mode to a non propagating (propagation wave vector purely imaginary: $k = ik_s$) surface-exchange mode, as described theoretically by Puszkarski⁶, whose energy is lower than the one of the uniform resonance mode. Fig.2 displays the observed angular variation of the field position of these two modes for the (Fe 864 Å) sample. Using the dispersion relation^{1,7} for non uniform modes ($\sim e^{i\omega t} e^{-ikz}$), derived from the energy density described in eq.1, and looking for a surface mode solution ($k = ik_s$) we may analyse the observed field splitting ($H^{res} - H^{res}_0$) of the surface mode with respect to the uniform mode. For example at $\theta_H^0 = 70$ deg where this field splitting is found equal to 0.66 kOe, using $(H^{res} - H^{res}_0) \sim (2A/M)k_s^2$, we deduce the characteristic penetration depth $k_s^{-1} \sim 190$ Å of this surface mode⁸. The constraint imposed on the allowed wave vector k_s , through the boundary conditions, would lead for this "thick" Fe layer [$th(k_s t) \sim 1$] and symmetric interfaces to $k_s = p$, i.e reflecting directly the pinning parameter p of the microwave magnetization, characteristic of the (Ag/Fe) interface considered. If p were to be described solely in terms of an interface-induced anisotropy (constant K_s) we would get [for $\theta_H = 70$ deg where $p \sim (K_s/A)$, with A the exchange stiffness constant] $K_s \sim 1.05$ erg/cm², roughly consistent with the value of K_s determined from the FMR study of the ultra thin single Fe layers.

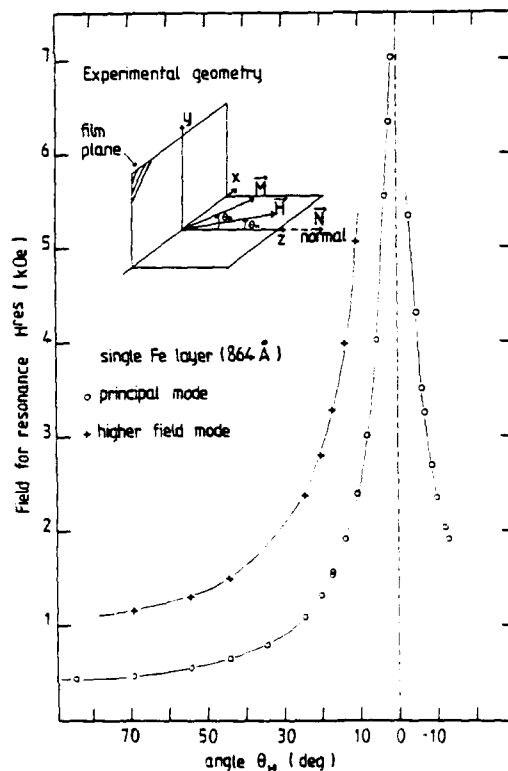


Fig. 2. Angular variation (with the angle θ_H) of the field for resonance of the two modes, the uniform mode and a higher field mode, observed in a thick (864 Å) Fe single layer sample.

Magnetic interfacial coupling. We have studied² a set of *two samples* corresponding to a thick (648 Å) Fe single layer sandwiched by Ag deposited (*same* sputtering run) on a mica substrate and on a very pure polycrystalline silver foil (25 μm thick), these two samples being called² the mica sample and the silver sample. At *room temperature*, the FMR reflection experiments performed at X band and at E band (≈ 79 GHz) indicate that the observed H_{res} of the principal uniform mode, in these two samples, can be reasonably well accounted for in terms of a uniaxial perpendicular magnetic anisotropy where H_A is found greater on the silver sample than on the mica sample. At *low temperatures* more complex phenomena² are observed: below typically T_v150 K, H_{res} monotonically shifts to *lower field* and a concomitant linewidth increase is observed for both samples. These phenomena are interpreted² in terms of the dissipative part of the magnetic interfacial coupling at the (Fe/Ag) interface which is to be associated^{8,9} with the *diffusion* of the microwave induced magnetization of the conduction electrons from one metal to the other.

FMR Studies of Fe bilayers

The following set of samples has been studied³: i) an ultrathin single Fe layer, with $t_{Fe} = 36$ Å, which serves as our control sample. ii) a series of Fe bilayers (Fe1/Ag/Fe2) with $t(Fe1) = t(Fe2) = 36$ Å, in which we have varied the Ag spacer thickness (abbreviated by t_s below) in a large range according to the following set of values [70 Å; 138 Å; 275 Å; 550 Å; 1100 Å]. Our FMR results obtained for the whole series of Fe bilayers may be summarized as follows. All the characteristics (lineshape, A/B ratio, H_{res} , ΔH_{pp}) of the resonance line observed in the Fe bilayers, and the angular variation of these characteristics, are to some degree modified *with respect*

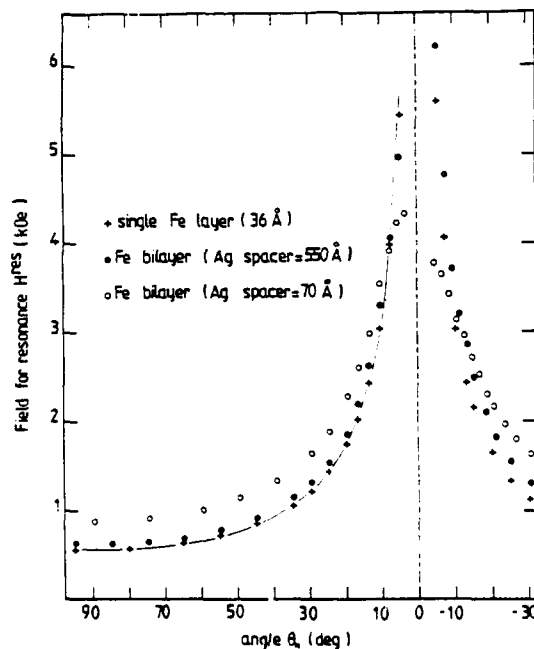


Fig. 3. Variation with the dc field orientation (angle θ_H) of the field for resonance H_{res} observed in the single Fe layer control sample and in two different Fe bilayer samples ($t_s = 70$ Å and $t_s = 550$ Å).

to the corresponding ones of the *single Fe layer control sample*. The strongest modifications occur for the thinnest Ag spacer thickness ($t_s=70 \text{ \AA}$; $t_s=138 \text{ \AA}$) and the amplitude of these effects decays monotonically with increasing t_s . A detailed account of these results is given in ref.3, where the observed (A/B) value and corresponding "signal phase" are in particular discussed. Fig.3 displays the observed angular variation of the *field for resonance* [$H^{\text{res}}(\theta_H)$] for three samples (single Fe layer and two characteristic bilayers). For the ($t_s=70 \text{ \AA}$) sample H^{res} is substantially higher in field towards the parallel geometry whereas the resonance is now seen in perpendicular geometry where it occurs at low field. It is to be mentioned also that the $H^{\text{res}}(\theta_H)$ curve of the single Fe layer is well recovered for the largest t_s (1100 \AA) bilayer sample. *Effects on the linewidth* are also observed. ΔH_{pp} , in parallel geometry, shows a substantial increase (with respect to the Fe single layer $\Delta H_{\text{pp}}=100 \text{ Oe}$) for the low values of t_s and a "recovery" for the two largest Ag t_s values. Effects on the resonance *signal intensity* is also evidenced where it is found³, in parallel geometry, that the normalized intensity (S/S_{ref}) increases monotonically (in the range [1;2]) as t_s is increased to reach a value ~ 2 for the largest t_s (1100 \AA) sample (S_{ref} is the single Fe layer intensity).

It is concluded³ from the ensemble of FMR results obtained for the Fe bilayer series that they provide evidence for the *presence of a dynamic coupling* between the precessing magnetizations of the two Fe layers. We suggest the following mechanism to be responsible for these *dynamic coupling effects*. It is to be associated with the effects of the diffusion (or more generally transport) of the *non-equilibrium* microwave-induced transverse *magnetization of the conduction electrons* present in each metal (the two Fe layers and the normal Ag metal spacer). From the thermodynamically required^{8,9} continuity of the magnetization current of the conduction electrons at each (Fe/Ag) interface, one may realize that the precessing magnetizations of the 2 Fe layers "see" each other provided that the phase memory of the conduction electron magnetization is not lost through the Ag spacer. For this to be the case, the Ag spacer thickness has to be less than the spin diffusion length δ_{eff} . A rough estimation³ of δ_{eff} , at room temperature, in our Ag layers would lead to a value typically in the range [500 \AA ; 1000 \AA], which would be consistent with the characteristic decay length of the coupling effects experimentally evidenced in the Fe bilayers. Further experimental investigations are now in progress to test the relevance of the proposed dynamic coupling mechanism and an explicit theoretical description is being elaborated.

References

1. H.Hurdequint, FMR studies of single Fe layers sandwiched by Ag, Symp.C of E-MRS 1990 Spring Meeting (May 29-June 1), Strasbourg, France (to be published in the Proceedings).
2. H.Hurdequint and G.Dunifer, Interfacial coupling between a magnetic thin film and a normal metal, J.Physique (Paris), C8-1717 (1988).
3. H.Hurdequint and M.Malouche, FMR studies of Fe bilayers and multilayers (Ag/Fe)_n: evidence for a dynamic inter-magnetic layer coupling, Symp.C of E-MRS 1990 Spring Meeting, Strasbourg, France (to be published in the Proceedings).
4. G.Rado, Phys.Rev.B26:295 (1982).
5. L.Zhang and G.Rado, Phys.Rev.B36:7071 (1987).
6. H.Puszkarski, Prog.Surf.9: 191 (1979).
7. L.J.Maksymowicz and D.Sendorek, J.Magn.Magn.Mat.37:177 (1983).
8. R.H.Silsbee, A.Janossy and P.Monod, Phys.Rev.B19: 4382 (1979).
9. H.Hurdequint, Thèse d'Etat, Université Paris-Sud, Orsay (1981).

COMPOSITIONALLY MODULATED MAGNETIC MULTILAYERS:
TEMPERATURE- AND MODULATION-DEPENDENT PROPERTIES

N.K. Flevaris¹, P. Poulopoulos¹, R. Krishnan² and M. Porte²

¹Dept. of Physics
Aristotle Univ. of Thessaloniki
54006, Thessaloniki - Greece

²Laboratoire de Magnetisme
CNRS-92195 Meudon - France

INTRODUCTION

Property modifications or enhancements observed for metallic multilayers initiated a growing interest for both fundamental questions and technological applications. Several such systems have been prepared and studied by different or complementary techniques with interesting results which, however, often exhibit considerable differences and occasionally are contradicting^{1,2}. Only with recent advancements in controlled growth techniques as well as in secondary structural characterizations it has become possible for works of different groups to be comparable.

In this contribution we will report very briefly on recent results via different techniques for magnetic, magnetooptical and optical properties of magnetic multilayered systems which have been extensively investigated with respect to their structural characteristics and growth mechanisms; there will be shown results suggesting both enhancement and (modulation-dependent) modification of properties.

EXPERIMENTAL

The multilayers were grown onto heated mica substrates by the alternate deposition of the two constituent fluxes via e-gun evaporation². The structural characterization involved x-ray diffraction² and electron microscopy techniques³⁻⁵ such as RHEED, planar (TEM) and cross-sectional (XTEM) transmission and SEM. Magnetic studies (by VSM and torque magnetometry) and Kerr-effect magnetooptical studies were also performed.

RESULTS and DISCUSSION

The magnetic studies^{1,6-9} of the most extensively studied multilayered system (Cu-Ni) had concluded that the initial report¹⁰ on enhanced moments in a Cu-Ni multilayer was false; it was based on erroneous interpretations of ferromagnetic resonance lines. However, considerable differences can be found among these works which, at least to some extent,

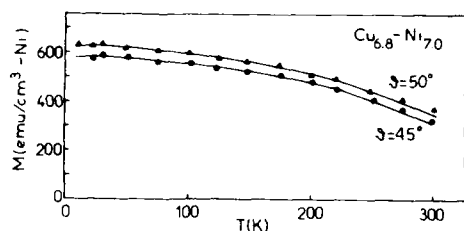


Fig.1 Magnetization densities for $\text{Cu}_{6.8}\text{-Ni}_{7.0}$ as a function of temperature for $\delta=0$ and 50° and calculated only for $\delta=0^\circ$.

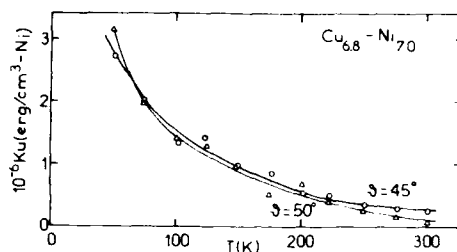


Fig.2 The first-order magnetic uniaxial anisotropy constant as a function of temperature for $\delta=0$ and 50° and calculated only for $\delta=0^\circ$.

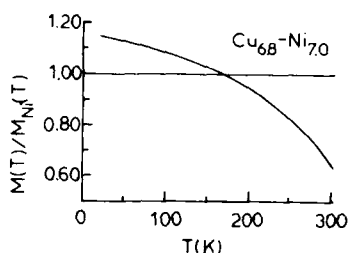


Fig.3 The magnetization density of $\text{Cu}_{6.8}\text{-Ni}_{7.0}$ normalized to that of pure Ni as a function of temperature.

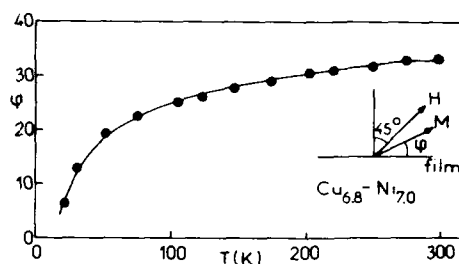


Fig.4 The angle of M (from the film plane), for $H=15$ kOe at 45° , as a function of T .

may be attributed to differences in the studied materials originating from different preparation techniques and material quality. We have studied the anisotropic magnetic behavior of a $\text{Cu}_{6.8}\text{-Ni}_{7.0}$ multilayer which has been studied structurally in a considerable detail and reasonably clear knowledge has been established for its structural characteristics^{3,4}: the notation $\text{Cu}_m\text{-Ni}_n$ will denote that the period (λ) of the composition modulation consists of m (n) atomic planes rich in Cu (Ni). The values $m=6.8$ and $n=7.0$ were determined by x-ray diffraction and both XTEM and XTED (cross-sectional electron diffraction).

The temperature dependence of the magnetization density and the first-order uniaxial magnetic anisotropy constant will be shown in Figs. 1 and 2, respectively, as determined by static torque magnetometry (TM) via the well known analytical techniques^{11,12}. The angle (θ) between the film plane and the applied magnetic field is kept constant by a nulling procedure and the required torque is measured as a function of the applied field. When $\theta=45^\circ$ it was shown^{11,12} that one can find analytical expressions to reveal M and K from (L/H) vs. H or $(L/H)^2$ vs. L curves. Also it is possible¹³ to check the measurements by repeating them at $\theta=45+\delta$. The two data sets of Figs. 1 and 2 refer to $\delta=0$ and 50° and analyzed in both cases, for $\delta=0$. The two M vs. T curves of Fig. 1 will coincide perfectly if the relation $(\sin 45/\sin 50)$ between them is considered. Thus these measurements provide an accurate representation of the T -dependent M and K for an easy-plane uniaxial ferromagnet. As seen in Fig. 2, with the initial analysis for $\delta=0$, the curve for $\theta=50^\circ$ exhibits a more pronounced increase at low temperatures indicating a possible additional feature in the anisotropy.

Figure 3 depicts the anisotropy moments $M(T)$, as function of the temperature, normalized for each T to the corresponding moment of pure bulk Ni. It is seen that this ratio becomes higher than unity at about $T=150$ K, with a highest low- T value of about 1.15. Some possible errors for such an observation would be: a) a wrongly established angle for the field, b) an underestimate for the Ni contained in the sample, c) erroneous analysis of the torque data and d) some temperature-dependent effects of the film-mica bonding.

As far as the first (a) point is concerned the analysis of Fig. 1 for $\delta=0$ and $\delta=50^\circ$ can be taken as evidence enough for sufficiently accurate experimentation. Second, the volume of Ni was determined by measuring the area and calculating the thickness as the product of the number of λ 's (as determined by counting the shutter movements during growth) and the n (assuming no interdiffusion) as determined by the techniques mentioned before and rechecked with the thickness of Ni deposited and recorded on the quartz crystal during the growth. Briefly, the most inaccurate part of these steps must be the measurement of the area of the specimen used. The fringes of the modulation observed in XTEM micrographs³ and the XTED analysis revealed m , n , m/n and $m/(m+n)$ values in excellent agreement with the values determined by x-ray diffraction. Thus, the overall uncertainty in the volume as determined here should be smaller than 5%.

Third, the analysis of the data is accurate for high temperatures for both M and K . For low T it is not safe to determine K accurately (and for this reason it is not included in Fig. 2) while it can be said that by this technique the values for M must be within about $\pm 3\%$ the real one. Finally, the temperature-dependence of the film-mica bonding stresses would not affect the M values and, as far as the K ones are concerned, it has been investigated in the past¹³ by FMR for thin films of Ni, Ni-on-Cu or $\text{Cu}_n\text{-Ni}_n$ and such a possibility can be safely ignored.

Therefore, it can be said that the observed ratio (M/M_{Ni}) of about 1.15 at low T can be considered as either an enhancement of the Ni moment in $\text{Cu}_{6.8}\text{-Ni}_{7.0}$ or, if we consider the highest possible error in estimating the Ni content and analyzing the data, at least that the Ni-rich layers have reached the bulk moment unlike any other $\text{Cu}_n\text{-Ni}_n$ multilayer or pure Ni film studied and reported thus far. In any case, considering that it is certain that some interdiffusion has occurred, such strong moments must be taken as evidence for additional contribution of the planar magnetism of the Ni layers.

The analysis of the torque data may be used to obtain also the equilibrium angle between M and the plane of the film as a function of the temperature for $H=15$ kOe and its angle $\delta=45^\circ$ as depicted in Fig. 4. It is interesting to note that as T decreases it becomes increasingly more difficult to bring M out of the plane.

Such easy plane behavior is much more pronounced than in the case of pure films of Ni deposited on mica¹³. However, it will be shown that, for $n=2$ and only for this value, it is possible to create perpendicular anisotropy in the normally easy-plane $\text{Pd}_n\text{-Ni}_n$ system of multilayers. Figure 5 shows the magnetic and magneto-optical hysteresis loops for $\text{Pd}_3\text{-Ni}_2$. (Similar observations were made for $\text{Cu}_4\text{-Co}_3$ and $\text{Pd}_4\text{-Co}_2$ multilayers. Reports on magnetic studies for these systems can be found in Refs.¹⁴⁻¹⁶ and also FMR studies for $\text{Cu}_4\text{-Co}_3$ at $T=150\text{-}300$ K have been reported earlier¹³.) It must be noted that no perpendicular component was observed for $\text{Pd}_n\text{-Ni}_n$ with $n>2$. The observation of significant differences between $\text{Pd}_n\text{-Ni}_2$ multilayers and those with $n\neq 2$ in the FMR lines has also been reported recently¹⁷.

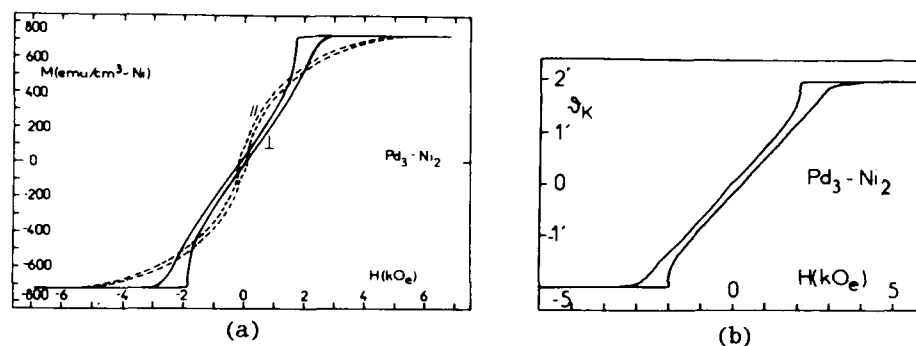


Fig.5 Magnetic (a) and magneto-optical Kerr (b) hysteresis loops for $\text{Pd}_3\text{-Ni}_2$ at room temperature.

Extensive accounts of the λ -dependent magnetic, magneto-optical and optical properties will be published elsewhere.

Acknowledgement: Work supported in part by the Greek Secretariat for Research and Technology and the EEC through the B/E Action.

REFERENCES

1. For recent reviews see: B.Y. Jin and J.B. Ketterson, *Adv. in Phys.* **38**, 189 (1989); I.K. Schuller, in "Physics, Fabrication and Applications of Multilayer Structures", P. Dhez and C. Weisbuch (eds.), Springer, Berlin (1989).
2. N.K. Flevaris, D. Baral, J.E. Hilliard and J.B. Ketterson, *Appl. Phys. Lett.* **38**, 992 (1981).
3. N.K. Flevaris and Th. Karakostas, *J. Appl. Phys.* **63**, 1228 (1988).
4. N.K. Flevaris and Th. Karakostas, in: "Alloy Phase Stability", G.M. Stocks and A. Gonis (eds.), Kluwer Academic Publs., Dordrecht (1989), p. 591.
5. N.K. Flevaris, *J. Microsc. Spectrosc. Electron.* **14**, 397 (1989).
6. E.M. Gyorgy, J.F. Dillon and D.B. McWhan, L.W. Rupp Jr., L.R. Teslardi and P.J. Flanders, *Phys. Rev. Lett.* **45**, 57 (1980).
7. J.Q. Zheng, C.M. Falco, J.B. Ketterson and I.K. Schuller, *Appl. Phys. Lett.* **38**, 424 (1981).
8. N.K. Flevaris, J.B. Ketterson and J.E. Hilliard, *J. Appl. Phys.* **53**, 2439 (1982).
9. L. Smardz and J. Baszynski, *Phys. Stat. Sol. (a)* **110**, 227 (1988).
10. B. Thaler, J.B. Ketterson and J.E. Hilliard, *Phys. Rev. Lett.* **41**, 336 (1978).
11. C.A. Neugebauer, *Phys. Rev.* **116**, 1441 (1959).
12. H. Miyazima, K. Sato and T. Mizoguchi, *J. Appl. Phys.* **47**, 4669 (1976).
13. N.K. Flevaris, Ph. D. Thesis (unpublished), Northwestern University, Evanston, USA (1983).
14. P.F. Carcia, A.D. Meinhardt and A. Suna, *Appl. Phys. Lett.* **47**, 178 (1985).
15. H.J.G. Draaisma, W.J.M. de Jonge and F.J.A. den Broeder *J. Mag. Magn. Mater.* **66**, 351 (1987).
16. A. Cebollada, J.L. Martinez, J.M. Gallego, J.J. de Miguel, R. Miranda, S. Ferrer, F. Batallan, G. Fillion and J.P. Rebouillat, *Phys. Rev. B* **39**, 9726 (1989).
17. N.K. Flevaris and R. Krishnan, *J. Mag. Magn. Mater.* (to be published).

STRUCTURAL AND MAGNETIC PROPERTIES OF EPITAXIAL Co/Pd SUPERLATTICES

Brad N. Engel, Craig D. England, Masafumi Nakada[†], Robert Van Leeuwen, and Charles M. Falco

Optical Sciences Center and Department of Physics
University of Arizona
Tucson, AZ 85721

[†]NEC Corporation
Kawasaki 213, Japan

INTRODUCTION

Recent interest in the magnetic and magneto-optic properties of transition metal/transition metal multilayers has been stimulated by the discovery of perpendicular magnetism in particular systems.^{1,2} However, partially due to the large variety of thin-film deposition methods and growth conditions, it has been difficult to obtain a clear understanding of the mechanisms of interfacial magnetic anisotropy. In order to create controlled and well characterized interfaces, we have grown a series of epitaxial Co/Pd superlattices on single-crystal GaAs(110) substrates by Molecular Beam Epitaxy (MBE). This paper describes the growth procedure, structural characterization, and the magnetic and magneto-optic properties of these superlattices. Comparisons are made to a series of non-epitaxial, polycrystalline multilayers that were simultaneously deposited on Si substrates.

GROWTH PROCEDURE

To enable epitaxial growth of the Co/Pd superlattices, GaAs (110) single-crystal substrates were chosen. The GaAs wafers were In bonded to a Mo block along with Si (111) substrates for use as Rutherford Backscattering Spectrometry (RBS) witness samples. The Si, with its lower mass, allows the thickness of both Pd and Co to be determined with RBS. These substrates also provided polycrystalline, UHV-evaporated multilayers for direct comparison with the epitaxial superlattices. The GaAs substrates were heated to ≈ 625 C for ≈ 30 minutes in UHV ($< 10^{-10}$ torr) for oxide desorption and annealing. This procedure provided a clean, smooth, and highly ordered surface as determined by both reflection high and low energy electron diffraction (RHEED and LEED) and Auger electron spectrometry (AES).

To initiate epitaxial growth, a seed layer of 6 Å of Co was deposited at 0.25 Å/s from a feedback controlled electron beam evaporator onto the room temperature substrate. This Co grows epitaxially in the metastable bcc form on GaAs (110),³ but results in a very rough surface as revealed by RHEED and LEED. To heal this surface and provide a good starting point for the superlattice growth, a buffer layer of 500 Å of Pd was then deposited at 0.15 Å/s from a high temperature effusion cell. The Pd grows as fcc (111) as determined from RHEED, LEED and x-ray diffraction. Other examples of fcc/bcc growth are in the

literature.⁴ We found that the resulting surface could be improved by raising the substrate temperature to 200 C for the last 200 Å of Pd growth. The resulting RHEED and LEED images show improved sharpness with a reduced diffuse background. We also discovered that sample rotation, ordinarily used to improve the thickness uniformity across the sample, caused faceting of the surface if performed too early in the growth. The buffer layers were therefore deposited without rotation. Details of the Pd growth are given elsewhere in these proceedings.⁵



Figure 1 RHEED patterns from the two different azimuthal directions of the final Pd superlattice layer ($d_{Co}=4\text{\AA}$, $d_{Pd}=11\text{\AA}$, $N=30$).

Following deposition of the Pd buffer layer, the substrate was cooled to room temperature and the superlattices deposited onto the rotating (10 rpm) wafers. This rotation reduces the thickness variation across the ≈ 5 cm wafer to $< 0.5\%$ and does not affect the quality of superlattice growth. RHEED was monitored during deposition and indicated single-crystal growth throughout. Figure 1 are the resulting RHEED patterns for the final Pd layer of a 30 bilayer superlattice ($d_{Co}=4\text{\AA}$, $d_{Pd}=11\text{\AA}$).

STRUCTURAL CHARACTERIZATION

In addition to using the MBE's *in situ* structural probes, the superlattice morphology and crystal structure were investigated *ex situ* with Scanning Tunneling Microscopy (STM) and x-ray diffraction. Although RHEED can provide indirect information about surface roughness, the STM gives direct real-space images of the final surface. The final surface of these superlattices was Pd, and therefore imaged well with the "in-air" STM.

A typical STM image, represented as a line scan, is shown in Figure 2. The remnants of a columnar structure are visible, with typical lateral dimensions of the individual grains $\approx 500\text{\AA}$. These grains are very flat, with measured variations in height on the order of 2\AA (an atomic layer). Because the grain diameters are on the order of the coherence length of the RHEED electron beam, these flat-topped columns are responsible for the streaked RHEED patterns seen during growth.

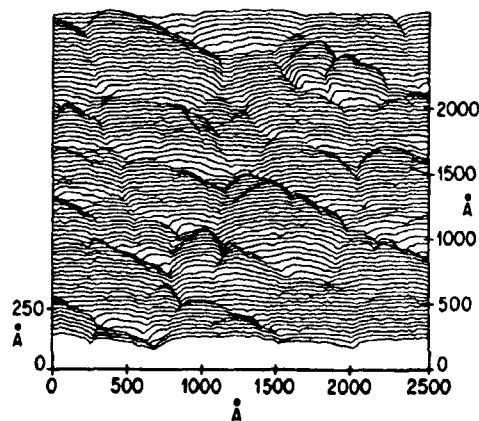


Figure 2 STM line scan of the final Pd layer ($d_{Co}=4\text{\AA}$, $d_{Pd}=11\text{\AA}$, $N=30$).

The crystal structure of the superlattices was investigated with x-ray diffraction in both high and low angle θ - 2θ geometries.

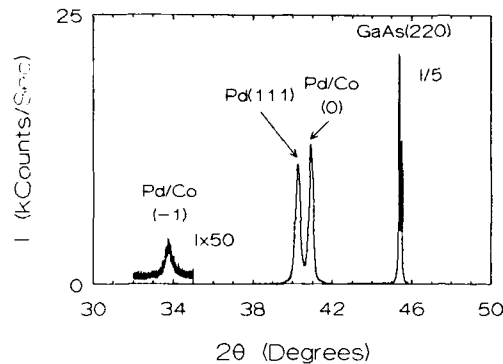


Figure 3 High angle x-ray θ - 2θ scan of an epitaxial superlattice ($d_{Co}=2\text{\AA}$, $d_{Pd}=11\text{\AA}$, $N=50$).

superlattice ($d_{Co}=2\text{\AA}$, $d_{Pd}=11\text{\AA}$). In contrast to this behavior, the x-ray diffraction from the multilayers deposited on Si (111) revealed a polycrystalline structure with no discernable superlattice satellites.

High angle rocking curves were also performed as a probe of the crystal quality and orientation. Composition modulation was confirmed in all of the structures, and a consistent determination of the bilayer period was obtained from the low-angle and high-angle superlattice peaks and RBS. Coherence lengths estimated from x-ray linewidths are consistent with a single crystal throughout the entire superlattice. Rocking curves performed on the superlattice peak produced linewidths that vary monotonically from $0.9^\circ < \Delta\theta < 1.8^\circ$ as d_{Co} increases. These narrow lines confirm the high quality of these single-crystals. Figure 3 is a high-angle θ - 2θ scan of a 50 bilayer

MAGNETIC AND MAGNETO-OPTIC CHARACTERIZATION

The magnetic and magneto-optic properties of both the epitaxial superlattices and polycrystalline evaporated multilayers were investigated with vibrating sample magnetometry (VSM) and Kerr rotation measurements. A magnetic easy-axis perpendicular to the film plane was observed for all four of the superlattices reported here ($d_{Co} \leq 12\text{\AA}$, $d_{Pd}=11\text{\AA}$).

The Kerr rotation was measured via a HeNe laser, lock-in amplifier based system with a Faraday rotator providing the necessary polarization modulation. Figure 4 displays the Kerr rotation versus applied field for both an epitaxial and polycrystalline multilayer ($d_{Co}=2\text{\AA}$, $d_{Pd}=11\text{\AA}$, $N=50$). These samples were grown simultaneously using GaAs and Si substrates respectively. The most striking difference is the increased coercivity of the epitaxial superlattice ($H_c=6.7\text{ kOe}$). It also should be noted that the spin reversal mechanism is obviously very different for the two samples. The epitaxial superlattice displays a gradual nucleation, in contrast to the abruptness of the polycrystalline multilayer. Additional information on the details of the reversal process is being gathered from measurements of the coercivity as a function of angle of the applied field. Results of this study will be reported elsewhere.

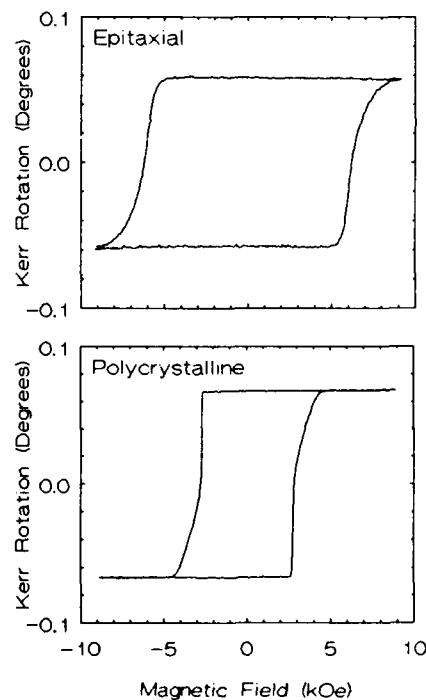


Figure 4 Kerr rotation loops for an epitaxial and polycrystalline multilayer ($d_{Co}=2\text{\AA}$, $d_{Pd}=11\text{\AA}$, $N=50$).

In addition to the differences in coercivity, the magnitude of the Kerr rotation in the epitaxial superlattices is consistently smaller than that in the polycrystalline multilayers. Although the reduction is slight, it is easily resolved with our system. This small reduction cannot easily be attributed to substrate interactions since all of the samples possess a 500 Å Pd buffer layer. VSM measurements of the total magnetization are currently being performed in search of possible differences in the overall magnetic behavior. Although these studies are not yet complete, significant polarization of the Pd has been observed. Table 1 is a summary of the structural, magnetic and magneto-optic properties of the epitaxial and polycrystalline multilayers produced to date.

Table 1. Summary of parameters. $d_{Pd}=11$ Å for all samples.

| $d_{Co}(\text{Å})$ | N | $H_c^{epi}(\text{kOe})$ | $H_c^{poly}(\text{kOe})$ | $\theta_K^{epi}(\text{deg})$ | $\theta_K^{poly}(\text{deg})$ |
|--------------------|----|-------------------------|--------------------------|------------------------------|-------------------------------|
| 2 | 50 | 6.7 | 2.8 | 0.05 | 0.07 |
| 4 | 30 | 3.4 | 1.6 | 0.10 | 0.11 |
| 8 | 15 | 0.96 | 0.83 | 0.15 | 0.16 |
| 12 | 15 | 0.41 | 0.46 | 0.20 | 0.21 |

SUMMARY

We have demonstrated the epitaxial growth of the Co/Pd fcc(111) superlattice system and contrasted the magnetic and magneto-optic behavior with that of simultaneously deposited polycrystalline multilayers. Significant differences are seen in the spin reversal process. Further measurements are needed to elucidate the mechanisms responsible for the enhanced coercivity observed in these epitaxial structures. Presently, a more complete magnetic characterization is being conducted using VSM and torque magnetometry, and will be reported in a later paper. Future work will include LEED and *in situ* Kerr rotation measurements of Co monolayers deposited on Pd to investigate interfacial strain effects.

ACKNOWLEDGEMENTS

The authors thank Masud Mansuripur, Jon Slaughter, and M.H. Wiedmann for useful discussions. This research is supported by the University of Arizona Optical Data Storage Center and the U.S. Department of Energy contract DE-FG02-87ER45297.

REFERENCES

1. P.F. Carcia, A. Suna, D.G. Onn and R. van Antwerp, *Superlattices and Microstructures* **1**, 101 (1985).
2. N. Sato, *J. Appl. Phys.* **59**, 2514 (1986).
3. G.A. Prinz, *Phys. Rev. Lett* **54**, 1051 (1985).
4. C.H. Lee, H. He, F. Lamelas, W. Vavra, C. Uher, and R. Clarke, *Phys. Rev. Lett.* **62**, 653 (1989)
5. J. Slaughter, B.N. Engel, M.H. Wiedmann, P.A. Kearney, and C.M. Falco, these proceedings.

FIRST-PRINCIPLES CALCULATION OF THE MAGNETOCRYSTALLINE ANISOTROPY ENERGY OF Co_nPd_m MULTILAYERS

G.H.O. Daalderop, P.J. Kelly and M.F.H. Schuurmans

Philips Research Laboratories
P.O. Box 80.000, NL-5600 JA Eindhoven, The Netherlands

ABSTRACT

The magnetocrystalline anisotropy energies of $\{001\}$ and $\{111\}$ oriented Co_nPd_m multilayers (with $n+m \leq 6$) have been calculated from first principles using the linear muffin-tin orbital method in the atomic-spheres approximation together with the local-spin-density approximation. While the easy axes of all $\{111\}$ Co_nPd_m multilayers considered are found to be perpendicular to the film plane, $\{001\}$ Co_nPd_m multilayers are only found to be perpendicularly magnetized if they contain cobalt as *monolayers*. The magnetocrystalline anisotropy energy is calculated to be largest for $\{111\}$ Co_1Pd_2 and decreases with increasing Co thickness. These predictions are in agreement with experiment.

INTRODUCTION

The magnetization of Co/X multilayers, where X is a late transition metal element (Pd[1] or Pt[2]) is oriented perpendicularly to the film plane if the Co layers are one or a few monolayers thick. Increasing the Co thickness the easy axis eventually changes to an in-plane direction. Measurements show that the anisotropy energy-density, K , times the Co-thickness, t , decreases approximately linearly with t , i.e., $Kt \approx 2K_S + K_V t$, where K_S and K_V are interface and volume energy-densities respectively. For thin Co layers the interface anisotropy energy apparently dominates the volume anisotropy energy and gives rise to a perpendicularly oriented magnetization. This indicates that in these multilayers the anisotropy energy of monolayers of cobalt is very different from that of bulk (hcp) cobalt.

It was pointed out by Néel more than thirty years ago that the reduced symmetry at a surface may lead to an anisotropy energy that is different from the bulk anisotropy.[3] Recently it has been shown experimentally that the magnetic anisotropy of Co/X multilayers strongly depends on the element X[4], the structure of the multilayer[5] and the mixing of Co and X elements in the vicinity of the interface [6]. Moreover, magnetoelastic energy may contribute via a thickness dependent strain of the Co layers.[7] Partly because of these effects the origin of the measured anisotropy energy is not well understood.

We have therefore examined the anisotropy energy of lattice matched multilayers with *ideal* interfaces. The results of first-principles calculations for Co_nPd_m multilayers in two different structures, $\{111\}_{\text{fcc}}$ with $n+m=3,6$ and $\{001\}_{\text{fcc}}$ with $n+m=2,4,6$ are presented. Of all multilayers considered, the anisotropy energy is largest for $\{111\}_{\text{fcc}}$ Co_1Pd_2 and decreases with increasing Co thickness. Co_nPd_m multilayers with a $\{001\}_{\text{fcc}}$ structure are found to be perpendicularly magnetized only if they contain Co as

monolayers. Where comparison is possible, these predictions are in agreement with experiment.

METHOD

Magnetocrystalline anisotropy energy (MAE) is the difference in the ground state energies corresponding to two different orientations of the magnetization density. Although in principle a relativistic current density functional theory ought to be used [8], we calculate the MAE for practical reasons within the framework of the standard local-spin-density approximation[9]. The MAE is caused by the simultaneous occurrence of exchange splitting and spin-orbit coupling in the Hamiltonian. Because the spin-orbit coupling parameter is small with respect to the exchange splitting and the bandwidth, it is treated non self-consistently.

First the Kohn-Sham equations for the scalar-relativistic spin-polarized Hamiltonian are solved self-consistently using the LMTO method in the atomic-spheres approximation (ASA)[10]. The spin-orbit coupling is then added and on diagonalizing the full Hamiltonian the eigenvalues, $\epsilon_i(\mathbf{k}, \hat{n})$, are obtained. These depend on the chosen orientation \hat{n} of the magnetization because the term $\mathbf{l} \cdot \mathbf{s}$ is not invariant under a rotation in spin-space. By employing the force-theorem[11] the MAE may be expressed as the difference in sums of Kohn-Sham eigenvalues for two different orientations \hat{n} . Each sum is performed by integration over the Brillouin Zone (BZ) using the improved tetrahedron method[12]. Using this procedure a detailed study of the MAE of the transition metal elements Fe, Co and Ni was made, and for a description of the method we refer to this work.[13]

An important contribution to the measured anisotropy energy is the magnetostatic energy difference, ΔE_D , between the two orientations of the magnetization in the multilayer geometry. It is calculated by summing classical magnetostatic interaction energies between magnetic dipoles on lattice sites.[14]

STRUCTURE

The experimental information about the multilayers from den Broeder et al.[4,5] is used to construct a model for their structure. Epitaxial [111] Co/Pd multilayers, comprising close packed planes of Pd and Co, were prepared by vapor deposition in UHV on mica substrates with a Pd buffer layer of 1000 Å.[4] Epitaxial [001] Co/Pd multilayers have been obtained by vapor deposition in UHV onto cleaved [001] NaCl with a Pd buffer layer.[5] In this case the Co and Pd layers were found to be coherent with each other. Typically the Pd layer is 20 Å thick. In the calculations coherent layers are assumed in which the in-plane lattice parameter is determined by the Pd-layer. Then the only structure parameters left undetermined are interplanar distances. These were evaluated by minimizing the total energy calculated using the full potential LAPW method[15].

In our model for the [111]_{fcc} Co_nPd_m multilayers an ABCABC stacking sequence of close packed planes is assumed. The resulting crystal structure has trigonal symmetry and a basis which consists of multiples of 3 atoms. Hexagonal lattice vectors with length a and c may be chosen to span a unit-cell, where $c = 2c_{\text{Co-Pd}} + (n-1)c_{\text{Co-Co}} + (m-1)c_{\text{Pd-Pd}}$. Here c_{A-B} denotes the distance between neighbouring A and B planes. The nearest neighbour distance between Pd atoms is taken unchanged from that calculated for the Pd (bulk) fcc lattice, and determines a and $c_{\text{Pd-Pd}}$. For Co_nPd_m multilayers the remaining two parameters are calculated for trigonal Co₃ and Co₁Pd₂, yielding $c_{\text{Co-Co}}$ and $c_{\text{Co-Pd}}$ respectively. They are found to be only slightly smaller than those that would have been obtained from close packing of hard spheres. As will be discussed, small changes in the structure parameters do not change the anisotropy energy significantly.

The structure of [001]_{fcc} Co_nPd_m multilayers is a stacking of [001] planes of an fcc lattice. The multilayer has tetragonal symmetry and a is taken to be equal to the calculated fcc Pd cubic lattice constant. The interplanar separations are found from calculations for tetragonal bct cobalt and Co₁Pd₁, yielding $c_{\text{Co-Co}}$ and $c_{\text{Co-Pd}}$.

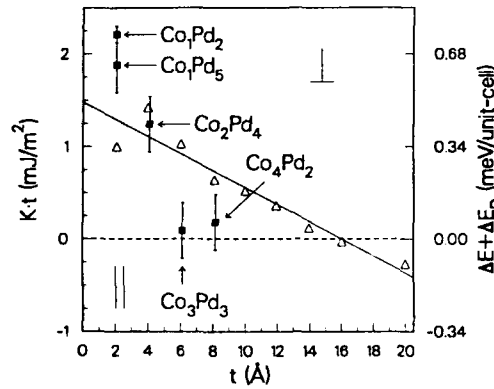


Figure 1. The anisotropy energy-density, K , times Co-thickness, t , as a function of t for [111] multilayers deposited at $T_s = 200^\circ\text{C}$ (Δ), compared with the *ab initio* calculated values. The (room temperature) experimental data are taken from den Broeder et al.[4] $K > 0$ corresponds to a perpendicularly oriented magnetization. Error bars indicate the estimated numerical accuracy of the calculation.

MAGNETIC ANISOTROPY CALCULATIONS

Previous first-principles calculations of the anisotropy energy of hcp Co have shown that the calculational results depend sensitively on the location and dispersion of degenerate energy bands near the Fermi-energy.[13] The *ab initio* calculated anisotropy energy of hcp cobalt (-0.02 meV/Co) is not in accordance with the experimental value of 0.06 meV/Co. This result was obtained using a basis including *spd* and *f* partial waves. Including only *spd* partial waves in the basis a correct easy axis was predicted with an anisotropy energy of 0.03 meV/Co. It is concluded that the accuracy of the calculations can not be claimed to be better than 0.1 meV/Co-atom. For several ferromagnetic compounds (YCo₅, MnAs and MnSb) with a larger anisotropy energy (≈ 0.2 meV/magnetic atom or larger) the easy axes appear to be predicted correctly but quantitative discrepancies with experiment are still found. The magnetocrystalline anisotropy energy of [111] Co/Pd multilayers containing monolayers of cobalt is about a half meV per unit-cell.

It is important to accurately perform the Brillouin Zone (BZ) integral of the eigenvalues $\epsilon_i(\mathbf{k}, \hat{n})$. We have found that it is possible to demonstrate the convergence of the BZ integral for unit-cells containing up to six atoms in the basis.[16] The numerical uncertainty in the results to be quoted below, is at most 0.1 (0.03) meV for unit-cells containing six (three) atoms. The results that follow are obtained using *spd* and *f* partial waves in the basis.

Co/Pd MULTILAYERS

In Fig. 1 the calculated results for Kt of $[111]_{fcc}$ Co_{*n*}Pd_{*m*} multilayers are compared with experimental results obtained at room temperature[4]. Kt multiplied by the Co area per atom (the area of a Co atom projected onto the basal plane in the bulk hcp structure), A , equals the sum of the magnetocrystalline anisotropy energy ΔE and the magnetostatic energy difference ΔE_D ($\sim -0.09n$ meV). The corresponding values for $\Delta E + \Delta E_D$ are denoted on the right-hand vertical axis. The numerical convergence of the calculated results is indicated by error bars. The dependence of the calculated MAE on the Pd thickness is small; the anisotropy energy of Co₁Pd₅ is $\sim 10\%$ smaller than that of Co₁Pd₂. A perpendicularly oriented magnetization and decreasing anisotropy energy with increasing Co thickness is predicted. However, the decrease is about a factor of three larger than observed in the experiment. For thick

Co layers the calculated slope will be determined by $\Delta E + \Delta E_D$ of strained trigonal cobalt. ΔE of strained trigonal cobalt is calculated to be less than 0.03 meV/Co atom for various c/a ratios between 2 and 2.45 (fcc) while keeping a constant, so that for thick Co layers the slope should be $\sim \Delta E_D$. This is actually found in the experimental data. We conclude that the presence of the Co/Pd interface leads to a strong preference for a perpendicularly oriented magnetization. The initial decrease of the magnetocrystalline anisotropy energy with increasing Co thickness is much larger than that calculated for strained trigonal cobalt. This indicates that the influence of the interface extends beyond the Co interface layer. For large Co thicknesses the slope will be determined by the demagnetization energy. Magnetoelastic energy, arising from strain in the Co layers, is not the cause of the very large anisotropy energy.

In Fig. 2 the calculated results for Kt of $[001]_{\text{fcc}}$ Co_nPd_m multilayers are compared with experiment[5]. Compared to the $[111]$ oriented multilayers there are two essential differences in the experimental data. Firstly, the interface anisotropy energy is strongly reduced. Secondly, an additional easy-plane anisotropy is present in the volume anisotropy, which is nearly as large as the demagnetization energy. Hence $[001]$ multilayers are only perpendicularly magnetized if they contain monolayers of cobalt.

Our calculated anisotropy energies reflect these two differences. Only Co_1Pd_3 and Co_1Pd_5 are predicted to be perpendicularly magnetized, and a strong decrease of the anisotropy energy with increasing t is also found. However, as in the calculations for $[111]$ oriented multilayers, the slope is about a factor of three larger than is found experimentally.

The dependence of the magnetocrystalline anisotropy energy, ΔE , on the structure parameters was calculated for the $[111]_{\text{fcc}}$ Co_1Pd_2 multilayer. In Fig. 3(a) the fractional change of the MAE, $\frac{\delta(\Delta E)}{\Delta E}$, is shown as a function of the fractional change in the volume of the unit-cell, $\frac{\delta\Omega}{\Omega}$. Here ΔE and Ω refer to the multilayer Co_1Pd_2 for which we have shown results in Fig. 1.

A uniform compressive strain was applied, i.e., all structure parameters were changed with the same fraction $\sim \frac{\delta\Omega}{3\Omega}$. Decreasing the volume causes a reduction of the MAE. For example, on changing the volume by -8%, the change in the MAE is only about -10 %. Assuming $K = -\frac{3}{2}\lambda\sigma$ for stress induced magnetoelastic energy, experiments on sputtered Co/Pd multilayers and Co/Pd alloys indicate a value for the magnetostriction constant $\lambda = -1.5 \cdot 10^{-4}$. [17] The calculated results yield a magnetostriction constant of about $-6 \cdot 10^{-5}$ assuming a bulkmodulus $B = 2 \cdot 10^{11} \text{ N/m}^2$.

We might expect the anisotropy energy to depend differently on $c_{\text{Co-Pd}}$ than on a . In Fig. 3(b) the change of the MAE is shown as a function of the fractional change in $c_{\text{Co-Pd}}$. Here a was kept fixed. The change of the MAE is about a factor of three larger than in Fig. 3(a) for corresponding changes in the volume, indicating that the MAE depends less on a than on $c_{\text{Co-Pd}}$. From Fig. 3 it is concluded that for a wide range of values of the structure parameters a perpendicular orientation of the magnetization is predicted.

CONCLUSIONS

In summary, we have shown that the observed preference for a perpendicularly oriented magnetization in $[111]$ oriented Co/Pd multilayers and the qualitative difference in the magnetic anisotropy between $[111]$ and $[001]$ oriented multilayers is predicted by first-principles calculations. The large value of the anisotropy energy and the preference for a perpendicular orientation of the magnetization of $[111]$ Co/Pd multilayers must be attributed to the presence of the Co/Pd interface and the resulting energy bands. Calculations for Co/X multilayers, where X = thick Ni, Cu or Ag, are in equal good agreement with experiments. [16] A determination of the anisotropy energy of coherent epitaxial multilayers at low temperatures is necessary in order to be able to make a more rigorous evaluation of the success of the calculations.

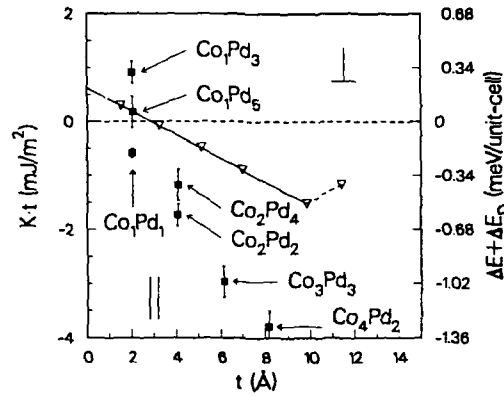


Figure 2. Kt as a function of t for coherent epitaxial $[001]$ multilayers deposited at $T_s = 50^\circ\text{C}$ (∇) [5] compared with the *ab initio* calculated values.

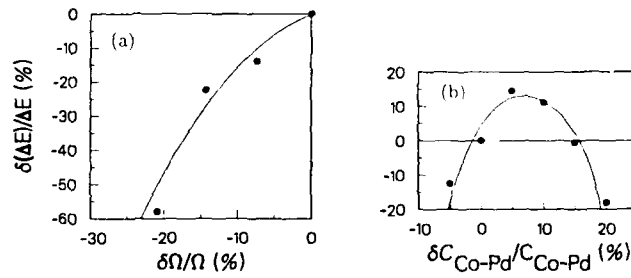


Figure 3. The fractional change in the calculated magnetocrystalline anisotropy energy of $[111]_{\text{fcc}}$ Co_1Pd_2 as a function of the fractional change in the volume, (a), and as a function of the fractional change in $c_{\text{Co-Pd}}$, the separation between interface Co and Pd layers, (b). The solid lines are a guide to the eye. The prediction of a perpendicular orientation of the magnetization is not sensitive to the particular values of the structure parameters.

REFERENCES

- [1] P.F. Carcia, A.D. Meinholdt and A. Suna, Appl. Phys. Lett. **47**, 178 (1985); H.J.G. Draaisma, W.J.M. de Jonge and F.J.A. den Broeder, J. Magn. Magn. Mat. **66**, 351 (1987).
- [2] W.B. Zeper et al., J. Appl. Phys. **65**, 4971 (1989).
- [3] L. Néel, Le Journal de Physique et le Radium **15**, 225 (1954).
- [4] F.J.A. den Broeder, W. Hoving and P.J.H. Bloemen, Proc. EMRS (1990).
- [5] F.J.A. den Broeder, D. Kuiper, H.C. Donkersloot and W. Hoving, Appl. Phys. A **49**, 507 (1989).
- [6] F.J.A. den Broeder, D. Kuiper, A.P. van de Mosselaer and W. Hoving, Phys. Rev. Lett. **60**, 2769 (1988).
- [7] P. Bruno, J. Phys. F **18**, 1291 (1988); P. Bruno and J.-P. Renard, Appl. Phys. A **49**, 499 (1989).
- [8] H.J.F. Jansen, Phys. Rev. B **38**, 8022 (1988) and references therein.
- [9] O. Gunnarsson and R.O. Jones, Reviews of Modern Physics, **61**, 689 (1989) and references therein.
- [10] O.K. Andersen, Phys. Rev. B **12**, 3060 (1975).
- [11] A.R. Mackintosh and O.K. Andersen, in *Electrons at the Fermi Surface*, edited by M. Springford (Cambridge University Press, Cambridge, 1980); M. Weinert, R.E. Watson and J.W. Davenport, Phys. Rev. B **32**, 2115 (1985).
- [12] O.K. Andersen, P. Blöchl and O. Jepsen, Bull. Am. Phys. Soc. **33**, 804 (1988); P. Blöchl, Ph.D.thesis, University of Stuttgart, (1989) (unpublished).
- [13] See for a discussion of calculations of the MAE by the authors and others: G.H.O. Daalderop, P.J. Kelly and M.F.H. Schuurmans, Phys. Rev. B **41**, 11919 (1990).
- [14] B.R.A. Nijboer and F.W. De Wette, Physica **29**, 422 (1958).
- [15] H.J.F. Jansen and A.J. Freeman, Phys. Rev. B **29**, 5965 (1984).
- [16] G.H.O. Daalderop, P.J. Kelly and M.F.H. Schuurmans, Phys. Rev. B **42**, 7270 (1990).
- [17] S. Hashimoto, Y. Ochiai and K. Aso, J. Appl. Phys. **66**, 4909 (1989).

STRUCTURAL AND MAGNETIC STUDIES IN Co-Pt MULTILAYERS

R. Krishnan, M. Porte and M. Tessier

Laboratoire de magnetisme, C.N.R.S.
92195 Meudon Cedex, France

N.K. Flevaris

Physics Department, Aristotle University
Thessaloniki, Greece

ABSTRACT

Co/Pt multilayer films have been prepared by evaporation under UHV conditions. For samples with Co layer thickness below 0.8 nm a strong uniaxial anisotropy and rectangular loop are observed. While the polar Kerr rotation decreases with the Co layer thickness, the Faraday rotation, on the contrary, is seen to increase strongly. This increase has been attributed to the presence of Co-Pt alloy layer at the interfaces formed by mixing and whose thickness has been estimated to be about 0.3 nm. Furthermore this layer is thought to play a crucial role in the origin of the uniaxial anisotropy. Faraday rotation studies are thus shown to be powerful to characterize the multilayers.

INTRODUCTION

Recently Garcia et al.¹ reported on Co/Pt multilayers (ML) which present an uniaxial anisotropy for Co layers thinner than about 1 nm and with reasonable polar Kerr rotation. This uniaxial anisotropy is attributed to the interfacial surface anisotropy which generally increases with the decreasing thickness of the magnetic film. These characteristics such as a rectangular loop along the film normal with coercivities on the order of 1 kOe, fairly high Kerr rotation in the smaller wavelength region, and finally their chemical stability make them potential candidates for the future generation of magneto-optical storage media and which has stimulated active research on these new materials in many laboratories^{2,3,4}. We describe here some results on structural, magnetic and magnetooptical studies in the Co/Pt MLs. As we have described previously, the study of the Faraday rotation is very interesting and it yields important information about the interfaces because this rotation arises from the bulk of the multilayer structure unlike the polar Kerr rotation which also would involve complex interference effects due to multiple reflections⁵. We will attempt here to correlate the Faraday rotation observed to the interface material, which in our opinion, should be playing an important role in determining the properties of these new materials.

EXPERIMENTAL DETAILS

The multilayers were deposited using a dual electron gun fitted in a UHV chamber, where the starting pressure was $1-2 \cdot 10^{-10}$ torr and which was kept below $6 \cdot 10^{-9}$ torr during film deposition. The deposition rate and the thickness of the layers were controlled individually using two quartz oscillators which had been previously calibrated. Water cooled glass or silicon wafers were used as substrates.

The thickness of the Co (d_1) layer was in the range 0.5 to 3 nm and that of the Pt (d_2) 1 to 4 nm. The number of bi-layers (n) was varied from 8 to 20. The samples will be denoted as $(d_1, d_2)^n$.

The periodicity was checked by low angle X-ray diffraction. Some samples were examined by cross sectional transmission electron microscopy (XTM). The magnetization (M) and the M-H loops were measured with a vibrating sample magnetometer (VSM). Both uniaxial anisotropy (K_u) and M were measured using a torque magnetometer in the temperature range 5 to 290K. Polar Kerr and Faraday loops were taken at $\lambda = 633$ nm, using a magneto-optical set up capable of a resolution of 10^{-4} deg.

RESULTS AND DISCUSSIONS

The multilayer structure was confirmed by the low angle Bragg reflections. Fig. 1 a and b show the XTM picture (the end on view) of two samples $(0.6, 1.6)^8$ and $(2.6, 3.2)^6$. Some crystallites are seen which are comprised of both constituents and without affecting the layering sequence or the interfaces. The diffraction pattern for the $(0.6, 1.6)^8$ sample indicates one diffraction ring which corresponds to the average lattice. No evidence of two distinct diffraction rings for the two constituents is seen.

The M-H and the magneto-optical loops were similar in general and Fig. 2 shows the Faraday loop for the sample $(0.5, 1.6)^{16}$.

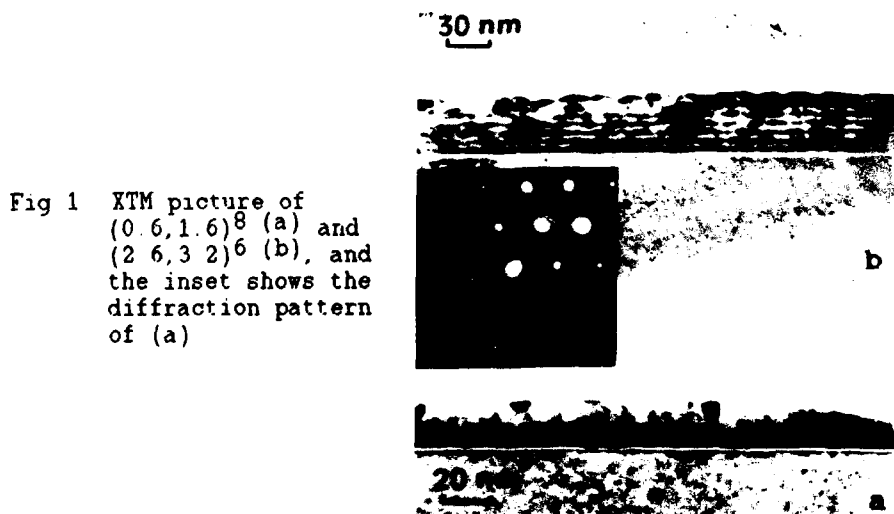


Fig 1 XTM picture of $(0.6, 1.6)^8$ (a) and $(2.6, 3.2)^6$ (b), and the inset shows the diffraction pattern of (a)

Fig. 2 Faraday loop for
(0.5, 1.6)¹⁶ sample

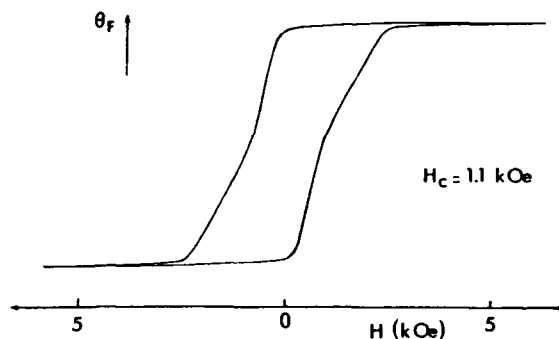


Fig. 3. shows the torque curve for the sample (0.8, 1.6)¹⁵ and the perfect uniaxial symmetry is seen

We have calculated K_U (erg cm^{-3}), in three different ways. To calculate the volume we first took into consideration only (a) d_1 , then (b) $d_1 + d_2$ and finally (c) $d_1 +$ two layers of alloy at each surface of the Co layer of thickness $\delta = 0.3$ nm each, this aspect will be discussed under the Faraday rotation studies. only for the case (a), K_U is seen to increase almost linearly with decreasing Co layer thickness. For the other two cases (more realistic) K_U seems to be less sensible to the Co layer thickness. The highest value (case a) is 1.3×10^7 erg cm^{-3} and is obtained for (0.5, 0.8)²⁰. Fig. 4 shows K_U as a function of d_1 for a fixed $d_2 = 1.6$ nm for the three cases described above.

The variation of the Faraday rotation (Θ_F) with d_1 , in our opinion, is an important aspect of our present work. Fig. 5 shows that the rotation, expressed in terms of total Co layer thickness,

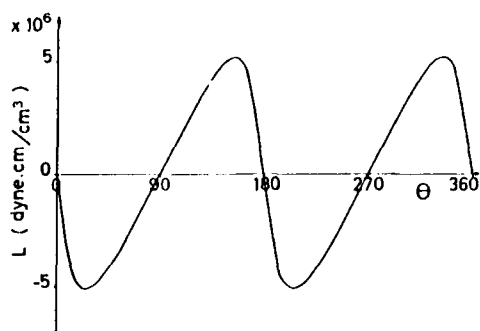


Fig. 3 Torque curve for
(0.8, 1.6)¹⁵

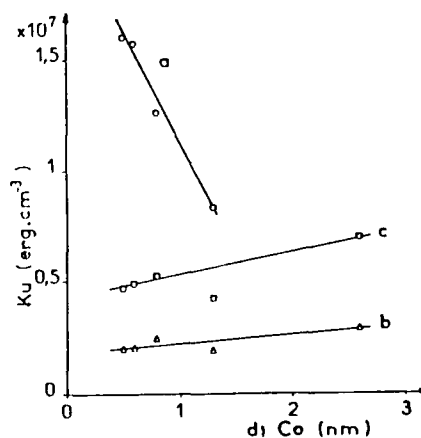
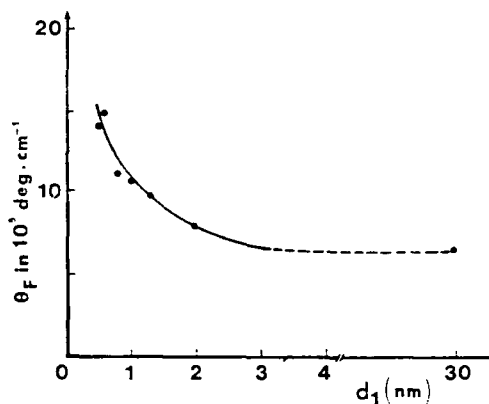


Fig. 4 K_U dependence on
 $d_1(\text{Co})$

increases in a remarkable fashion as d_1 decreases. The observed increase has been attributed to the presence of an interface layer arising from the alloying in ML with thin layers⁶. In the present case by using a simple model⁷ we have calculated the thickness (δ) of

Fig. 5 The d_1 (Co) layer dependence of the Faraday rotation with $d_2=1.6$ nm



this layer as follows. The rotation arises from not only the Co layer but also from the alloy layer. So one can write for the observed rotation, $\theta_F(\text{measured}) = \theta_F^{\text{Co}}(d_1)n + \theta_F^{\text{Co-Pt}}(\delta)2n$, where n , θ_F^{Co} , $\theta_F^{\text{Co-Pt}}$ indicate the no of bi-layers, and the rotation from Co and the alloy layers respectively. Assuming that the two rotations are equal (in the first approximation) we find that $\delta=0.3$ nm for all the ML with $d_2=1.6$ nm. This interfacial alloy layer also favours exchange coupling between the adjacent Co layers and could play a key role in the development of the uniaxial anisotropy.

In conclusion, we have prepared Co/Pt multilayers by sequential deposition in UHV. For thin Co layers rectangular loops are observed and the torque studies confirm the presence of a strong uniaxial anisotropy. The increase in the Faraday rotation observed has been attributed to the presence of a magnetic alloy layer at the interface. The study of the Faraday rotation thus has enabled us to reveal the presence of the interface material and which in our opinion could play an important role in exchange coupling the Co layers and in the appearance of the uniaxial anisotropy.

REFERENCES

1. P.F. Carcia, A.D. Meinhaldt and A. Suna, Appl. Phys. Lett., 47 178 (1985)
2. P.F. Carcia, J. Appl. Phys., 63 5066 (1988)
3. W.B. Zepper, F.J.A. Greidanus, P.F. Carcia and P.R. Fincher, J. Appl. Phys., 65 4971 (1989)
4. Y. Ochiai, S. Hashimoto and K. Aso, Jap. J. Appl. Phys., 28 L 65 (1989)
5. R. Krishnan, M. Porte, M. Tessier and J.P. Vitton, Mat. Res. Symp. Proc. Vol. 150, 63 1989
6. K. Le Dang, P. Veillet, M. Sakakima and R. Krishnan, J. Phys. F Met. Phys. 16 93 (1986)
7. R. Krishnan, M. Porte, M. Tessier, To appear in IEEE. Trans. Mag. 1990

MAGNETIC PROPERTIES OF HEXAGONAL Fe/Ru SUPERLATTICES WITH SHORT PERIODICITY

M. Piecuch¹, M. Maurer^{1*}, M.F. Ravet¹, J.C. Ousset¹,
J.M. Broto² and B. Dieny³

(1) Laboratoire Mixte CNRS Saint Gobain, CR PAM, BP 109,
54704 Pont a Mousson, (France)

(2) Service des Champs intenses Toulouse (France)

(3) Laboratoire Louis Neel, CNRS, BP 166 X, 38042 Grenoble
(France)

INTRODUCTION

The recent introduction of molecular beam epitaxy techniques in metal physics has introduced the ability to prepare new crystalline structures of elemental metals by epitaxy (pseudomorphic structures).

In this context, the case of metallic Fe is worth of attention. Indeed, besides the bcc and fcc structures, an hcp phase is obtained under high pressure¹. Only the bcc (8-coordinated) one is magnetic, whereas the fcc and hcp (12-coordinated) forms, which correspond to a volume of 11.4 \AA^3 / Fe atom, are non-magnetic. According to theoretical predictions, both fcc and hcp bulk phases should undergo a transition to a magnetic state at volume expansions of the order of 5%^{2,3}. The purpose of this paper is to discuss our present knowledge of the the magnetic properties of (0001) hcp Fe/Ru superlattices. A brief recall of the results obtained on the local structure around Fe atoms, including the interatomic distances, the nature and the number of near neighbours will be done⁴. Regarding magnetism in particular, it is essential to characterize the atomic roughness at the Fe/Ru interface layer because Ru is very efficient to destroy Fe magnetism in $\text{Fe}_x\text{Ru}_{1-x}$ hcp solid solutions^{1,5}.

In the present report, we focus on bulk magnetic properties, which are investigated by SQUID magnetometry and magnetoresistance measurements. ⁵⁷Fe Mössbauer spectroscopy in transmission geometry⁶ has been published elsewhere.

EXPERIMENTAL PROCEDURE

The (0001) Fe/Ru superlattices were either grown on (11 $\bar{2}$ 0) sapphire substrates or on freshly cleaved mica discs in a RIBER EVA 32 MBE. In every case, a Ru buffer layer of 200 Å was firstly grown

at 500°C to ensure an atomically flat and single crystalline surface and to avoid oxygen contamination from the substrate. Superlattices were then elaborated at 100 °C. The working pressure never exceeded $5 \cdot 10^{-10}$ Torrs during deposition. Magnetization measurements were performed with a SQUID. Magnetoresistance measurements were carried out in pulsed fields ($\tau=1s$) up to 35 teslas.

STRUCTURE OF THE (0001) FE/RU SUPERLATTICES

The RHEED diffraction patterns^{4,7} of the Fe layers grown on a Ru surface, ascertain that Fe planes stack pseudomorphically on the (0001) dense planes of Ru. The crystalline structure of these superlattices has formerly been discussed, with a particular emphasis on the nature of the stacking (ABAB... or ABCABC...) ^{4,7}. The conclusion was that the stacking is close to the HCP one. Diffraction experiments leads to a value of $V_{Fe} = 12.7 \text{ \AA}^3 / \text{Fe atom}$ which is surprisingly large, the atomic volume is expanded by 10% at least.

The characterization of the sharpness of the concentration gradient is particularly important. Thus, the mode of growth has to be checked. Auger electron spectroscopy results can be fitted with the hypothesis of a layer-by-layer growth without volume interdiffusion. An other insight into interface sharpness can be gained from diffraction spectra⁸. A great wealth of information on interface is for instance obtained with a superlattice Fe(2,1)/Ru(1.9). Despite all the atomic planes correspond to interfacial ones, a set of satellites is unambiguously observed at low and high angles⁸. This is a direct evidence that the interface composition is sharp at the monolayer scale.

To conclude the discussion of the structure, we can state that Fe layers are stabilized in an hexagonal structure, with an anomalous volume of $12.7 \pm 0.2 \text{ \AA}^3 / \text{Fe atom}$ corresponding to an expansion of more than 10% as compared to the γ -Fe or ϵ -Fe phases.

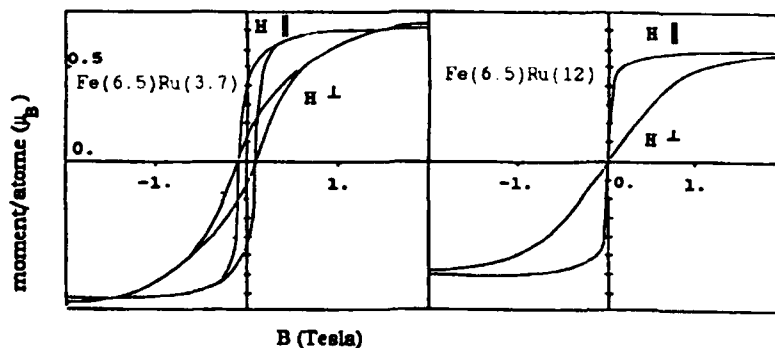


Figure 1. Hysteresis curves for two typical superlattices

BULK MAGNETIC PROPERTIES

Two different family of sample have been investigated by SQUID magnetometry. In the first family we keep the ruthenium thickness constant (around 12 atomic layers) and vary the iron thickness; in

the second one we keep the iron thickness constant (around 6.5 monolayers) and we vary the ruthenium thickness.

We first discuss the results on the second family. Two typical hysteresis curves are shown in fig.1 for a sample of around 3 Ru monolayers and a sample of 12 Ru monolayers. One can see clearly on these curves, that the coercive field is markedly larger for the sample with the thinner layer of ruthenium. This result is summarized on figure 2 where we present the coercive field versus the Ru layer thickness. To check in more details the nature of the interactions through the ruthenium layer, we present in figure 3, the first magnetization curve of a coupled sample Fe(6.5)/Ru(3.7) (field parallel to the layers).

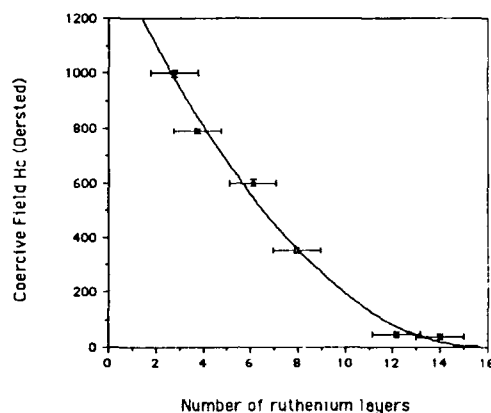


Figure 2. Coercive field versus ruthenium thickness

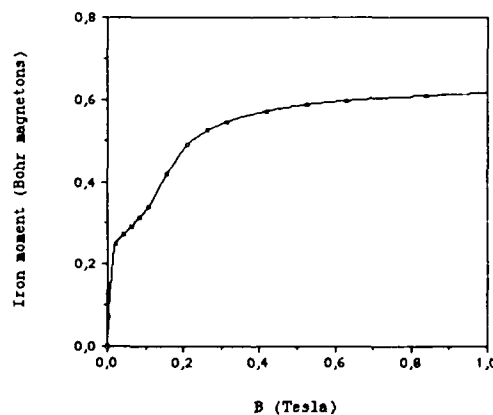


Figure 3. Low field magnetization curve of a coupled superlattice, Fe(6.5)Ru(3.7), showing the evidence of a spin flop transition

One sees clearly two steps in this curve, a spontaneous jump occurs at very low field and then a positive curvature is observed. This kind of curve is very close to those calculated by Dieny et al for antiferromagnetically coupled layers in the case of weak

anisotropy. We then conclude that antiferromagnetic coupling between adjacent layers seems to be possible for thin ruthenium interlayers. Another type of conclusion can be deduced from figure 2; it seems that the interlayer coupling becomes very weak for a ruthenium thickness of about 12 monolayers.

We have chosen this ruthenium thickness for the study of hexagonal iron since in that case only intralayer coupling plays some role for the magnetic properties.

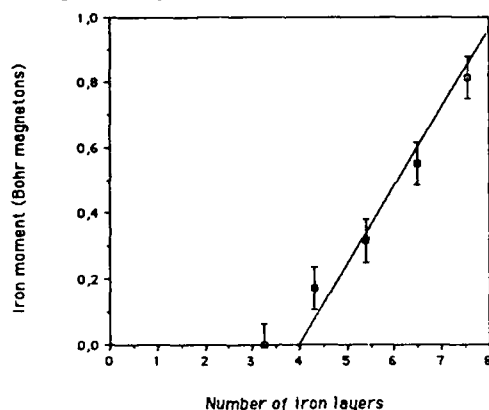


Figure 4. Iron moment versus iron thickness

Figure 4 shows the total moment of the iron layer versus the iron layer thickness. This curve reveals the absence of spontaneous magnetization for Fe layers thinner than 4 monolayers and a subsequent increase of $1.7\mu_B$ per atom in the additional layers (straight line on figure 4).

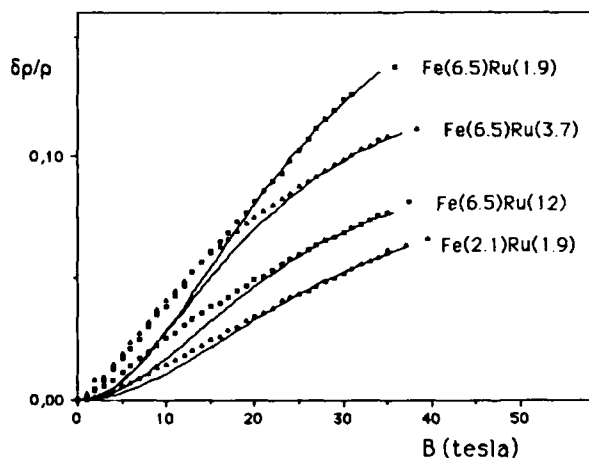


Figure 5. Magnetoresistance of some multilayers at 4.2K

As a matter of conclusion, the magnetic measurements of Fe/Ru superlattices permit to establish that the 2 Fe layers at the interface with Ru are absolutely non-magnetic whereas the next ones are fully polarized, with a moment of $1.7\mu_B/\text{Fe}$. This result must be related to a volume expansion exceeding 10% for the Fe layers due

to the pseudomorphous growth with Ru. At this stage, we must mention the likelihood of the magnetic behaviour of Fe in hcp (0001) Fe/Ru superlattices, with the results obtained independently by Liu and Bader¹⁰ for a single Fe/Ru (0001) interface; in both experiments, it is found that the magnetic interface is sharp, albeit at 2 planes apart from the chemical interface. The absence of Fe magnetism at the interfaces, which is significant owing to the sharpness of the interface at a monolayer scale, is certainly due to a strong hybridization of the Fe bands with the broader bands of Ru.

MAGNETORESISTANCE MEASUREMENTS

Figure 5 shows magnetoresistance results at 4.2K for four typical samples. The four samples have nearly the same residual resistivity of about $3\mu\Omega\text{cm}$ at 4.2K. The magnetic field is perpendicular to the current and in the film plane. One can see immediately that there is no trace of giant magneto resistance at low field.

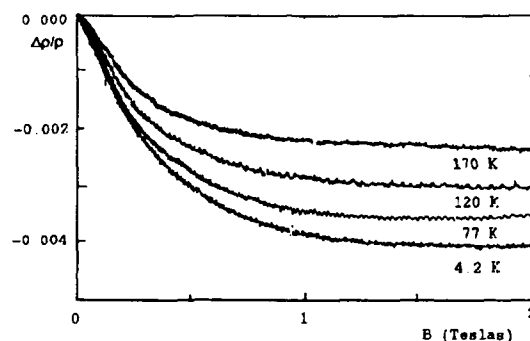


Figure 6. Low field magnetoresistance at various temperature of a rough sample

If one inspects closely the low field part, one can detect some small negative component of about 10^{-4} to $0.5 \cdot 10^{-3}$ at applied fields below 1 or 2 Teslas. This small negative part is more important in the Fe(7.5)Ru(6.5) sample (fig.6) where the residual resistivity is notably higher due to the surface roughness detected by RHEED on this kind of samples⁴. One can see also on fig.5 that the high field magnetoresistance increases with the onset of magnetic moment (from the 2.1, 1.9 sample to the 6.5, 12 sample) and also when the Ru layer thickness decreases. Then the magnetoresistance in our samples is clearly related with the magnetic properties. To gain more information, we have tentatively fitted the magnetoresistance curves with a two band model (free electrons with spin up or spin down)¹¹. This model is obviously not correct since it implies a zero magnetoresistance for the non magnetic sample and it neglect the spin flip diffusion, but it can give a preliminary account of our data. The fits are the solid lines in fig. 6. One may deduce from these curves the ratio of the spin up and spin down relaxation time which is 1.9, 2.1 and 2.4 for the three magnetic samples (Ru = 12, 3.7 and 1.9). This can be related¹¹ to an increase of the ratio

between the density of states of d electrons with spin down to the density of states of d electrons with spin up.

These results are preliminary but show that in presence of antiferromagnetic coupling, the magnetoresistance is not necessarily giant if the residual resistivities of the samples are low.

CONCLUSIONS

From a systematic study of the crystalline structure and of the local environment around Fe, we have been able to conclude that the (0001) Fe/Ru superlattices have an hexagonal structure, in which the specific volume of Fe is expanded by more than 10 % as compared to equilibrium phases. The Fe/Ru interfaces are very sharp; correlatively, the magnetic interfaces is also sharp but located at two planes apart inside the Fe layer. The magnetic Fe sites carry a large moment of $1.7\mu_B$. These results are in excellent agreement with theoretical predictions^{3,12,13} and the fact that the expanded Fe phase is observed for two different pseudomorphous epitaxies, i.e. (0001) and (11 $\bar{2}$ 2), strongly supports Kübler's prediction³ that an hcp Fe phase could correspond to a metastable state with a relatively high moment. The magnetization and magnetoresistance results suggest that there exist a coupling between the iron layers. This coupling could be antiferromagnetic but the giant magnetoresistance is not directly related to this antiferromagnetic coupling.

* Present address: Compagnie de Saint Gobain, Direction de la Recherche, Les Miroirs, Cedex 27, 92096 Paris - La Défense

REFERENCES

1. D.I.C. Pearson and J.M. Williams, J. Phys. F **9**, 1797 (1979).
2. V.L. Moruzzi, P.M. Marcus and J. Kübler, Phys. Rev. B **39**, 6957 (1989).
3. J. Kubler, Solid. State Comm. **72**, 631 (1989).
4. M. Maurer, J.C. Ousset, M.F. Ravet and M. Piecuch, Europhysics Lett. **9**, 803 (1989).
5. D.L. Williamson, S. Bukshpan and R. Ingalls, Phys. Rev. B **6**, 4194 (1972).
6. J.P. Sanchez, M.F. Ravet, M. Piecuch, and M. Maurer, Hyperfine Inter., to appear.
7. M. Piecuch, M.F. Ravet and M. Maurer, MRS Proceedings, San Francisco Spring Meeting 1990 (to appear).
8. A. De Andres, M. De Santis, D. Raoux, M. Maurer, M.F. Ravet and M. Piecuch Proceedings of: X-ray studies by Synchrotron Radiation II, Roma, 1990 and D.Raoux et al, to appear.
9. B. Dieny, J.P. Gavigan and J.P. Rebouillat, J. Phys.: Condens.Mater. **2**, 159 (1990).
10. C. Liu and S. Bader, Phys. Rev. B **41**, 553 (1990).
11. A. Fert Thesis Orsay (1970).
12. D. Knab and C. König, EMRS meeting Strasbourg (1990) to be published.
13. M.O. Selme and P. Pecheur, EMRS meeting Strasbourg (1990) to be published.

MAGNETIC STUDIES OF Fe-Si COMPOSITIONALLY MODULATED THIN FILMS

J. Tejada, B. Martínez^{*}, F. Badia, R. Ribas

Departamento de F. Fundamental, Facultad de
Física, U. de Barcelona Diagonal 647, 08028
Barcelona

^{*} Instituto de Ciencia de Materiales de Barcelona
C.S.I.C. Martí i Franqués S/N, 08028, Barcelona
SPAIN

INTRODUCTION

Among other interesting problems superlattices or multilayers are very suitable systems to study magnetic properties of ultra thin films, surface effects, periodicity effects, etc.. Due to this special properties a wide range of metallic multilayers have been studied with different techniques^{1,2,3,4,5,6}. In our case we are mainly concerned with the iron-silicon system. Early studies on the magnetic properties of amorphous $\text{Fe}_{1-x}\text{Si}_x$ thin films were performed by Y. Shimada et al.⁷ and by D. Bloch et al.⁸, in this studies the range of composition in which a ferromagnetic ordering exist is available together with some of the structural features, as a function of x , of the $\text{Fe}_x\text{Si}_{1-x}$ alloys. J.M. Alameda et al.⁹ have pointed out that the behavior of the saturation magnetization as a function of x between the values $0.66 < x \leq 0.78$ is greatly influenced by the particular conditions of the sample preparation. Clear differences are evident in the magnetic behavior of sputtered samples and evaporated samples pointing out the influence of the short range order effects.

EXPERIMENTAL AND DISCUSSION

We will describe in this part the magnetic properties of the multilayered system $\text{Fe}_{1-x}\text{Si}_x / \text{Si}$. Details about sample preparation can be found elsewhere¹⁰. The magnetic studies have been carried out as a function of the composition ($x = 0.25, 0.3$) and as function of the modulation length (λ) (thickness

TABLE I. Thickness and composition of the two series of samples

| SAMPLE | Fe ₇₅ Si ₂₅ / (Å) | Si (Å) | λ (Å) | Fe ₇₀ Si ₃₀ / (Å) | Si (Å) | λ (Å) |
|--------|--|-----------|------------------|--|-----------|------------------|
| 1 | 4.4 | 2.2 | 6.6 | 2.2 | 1.4 | 3.6 |
| 2 | 8.8 | 4.4 | 13.2 | 4.4 | 2.8 | 7.2 |
| 3 | 17.6 | 8.8 | 26.4 | 8.8 | 5.8 | 14.4 |
| 4 | 35.2 | 17.6 | 52.8 | 17.6 | 11.2 | 28.8 |

of the Fe_{1-x}Si_x layer plus thickness of the Si layer) by using conversion electron Mössbauer spectroscopy (CEMS) and SQUID magnetometry. The total thickness of the samples of about 0.1 μ m was determined by using Tolansky interferometry. The amorphous character of the samples was tested by using X-ray diffraction and by means of low angle X-ray scattering we have checked the modulated structure of the multilayered system.

MAGNETIC MEASUREMENTS

Magnetic measurements were performed in a commercial SQUID magnetometer in applied magnetic fields up to 5.5T working in the temperature range between 1.8 and 300K. The fact that the curves are not saturated at high field (see Fig. 1) can be correlated with the existence of non magnetic iron atoms as has been deduced by means of Mössbauer spectroscopy^{5,11,12}. The saturation magnetization of the samples increases as the modulation length increases reflecting that both, the exchange interactions intensity and the Curie temperature increase as

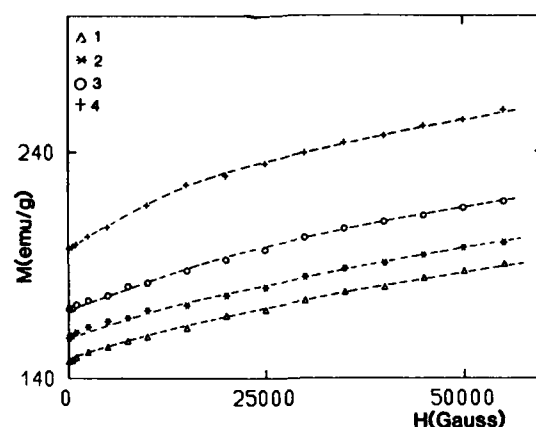


FIGURE 1. Magnetization curves as a function of λ for the Fe₇₅Si₂₅/Si samples with the external field applied parallel to the sample plane.

TABLE II. Values of the saturation magnetization and of the macroscopic uniaxial anisotropy K_0 .

| SAMPLE | Fe ₇₅ Si ₂₅ /Si | | Fe ₇₀ Si ₃₀ /Si | |
|--------|---------------------------------------|------------------------------|---------------------------------------|------------------------------|
| | μ_B/atom | K_0 (ergCm ⁻³) | μ_B/atom | K_0 (ergCm ⁻³) |
| 1 | 1.60 | 1.7×10^5 | 1.50 | 4.8×10^5 |
| 2 | 1.90 | 3.2×10^5 | 1.80 | 4.7×10^5 |
| 3 | 2.20 | 1.9×10^5 | 2.10 | 3.9×10^5 |
| 4 | 2.20 | 2.7×10^5 | 2.20 | 4.5×10^5 |

well. By means of the law of approach to magnetic saturation¹³

$$M(H) = M_0 \left(1 - \sum_{n=1}^4 a_{n/2} H^{-n/2} \right) + \kappa H + b H^{1/2} \quad (1)$$

different magnetic features of the samples were investigated. The macroscopic uniaxial anisotropy constant K_0 can be determined from the law of approach to magnetic saturation through the following relation^{14,15}:

$$A_2 = (4/15) [K_0^2 / M_0^2] \quad (2)$$

where A_2 is the coefficient of the H^{-2} term in (1) and M_0 is the saturation magnetization. The coefficient b in (1) can be calculated from the spin waves theory and it is related to the spin wave stiffness constant D through the following expression¹³.

$$b = 3.54 g \mu_B (1/4\pi D)^{3/2} K T (g \mu_B)^{1/2} \quad (3)$$

We have also studied the thermal behavior of the saturation magnetization in a constant applied field while heating the samples from 1.8 to 100K. In presence of an applied field the experimental data should be analyzed by means of the formula¹⁶:

$$M(T)/M_0 = 1 - B [F(3/2, t_H) / \zeta(3/2)] T^{3/2} - C [F(5/2, t) / \zeta(5/2)] T^{5/2} - A T^2 \quad (4)$$

Where M_0 is the saturation magnetization and the definition of the remaining functions can be found elsewhere¹⁶. Eq. (4) takes into account the effect of the applied field on the spin-wave spectrum, first studied by Holstein and Primakoff¹⁷. The spin-wave stiffness constant, D , of the dispersion law is related to the B coefficient of the modified Bloch's law given by equation (3) through the expression:

$$B = \zeta(3/2) (g \mu_B / M_0) (k_B / 4\pi D)^{3/2} \quad (5)$$

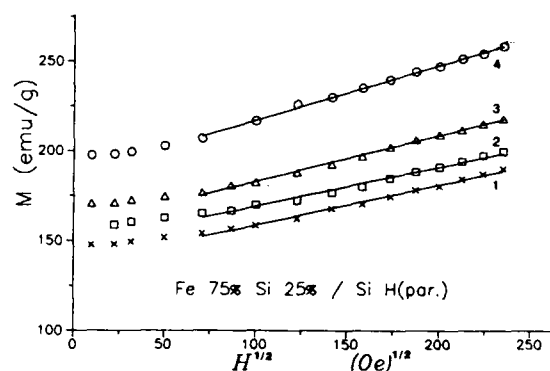


FIGURE 2. Determination of the b values from the M_0 vs. $H^{1/2}$ plots in the high field regime.

Two different regimes are clearly evidenced in the thermal behavior of the magnetization. i) A very fast decreasing of the magnetization takes place below 30K given values for the B coefficient that are around 100 times bigger than the corresponding values for crystalline materials. Similar results have been obtained in thin films integrated by other materials¹⁸ but it is still not clear what is the origin of this behavior. In a theoretical paper by Kaneyoshi¹⁹ it is shown that the effect of the surface amorphization (i.e. relaxation of the intensity of the exchange interactions at surface) may produce a thermal behavior of the magnetization that is very similar to that obtained experimentally. ii) Above $\approx 40K$ a more slowly decreasing of the magnetization is observed and in this case the values obtained for the B coefficient are more similar to that corresponding to crystalline materials.

MÖSSBAUER SPECTROSCOPY

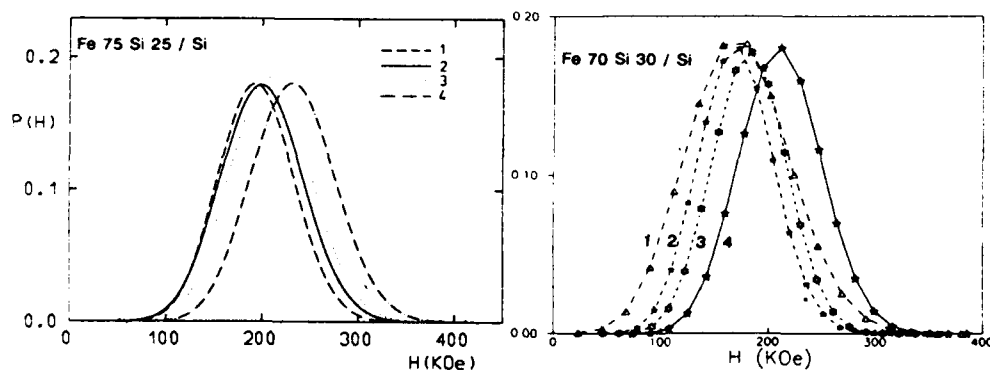
The conversion electron Mossbauer studies have been carried out by using a "home made" acetone gas detector. The single line source was 20 mCi of $^{57}\text{CoRh}$. The spectra were collected at room temperature and the experimental arrangement is that the gamma rays incoming beam is perpendicular to the substrate plane. All the spectra show 6 broad and partially overlapping lines because of the wide distribution of local environments of the iron atoms due to the chemical and structural disorder. To analyze the $P(H)$ distribution we have used a method proposed by Vincze in which $P(H)$ is assumed to be given by a binomial distribution²⁰. Furthermore we have assumed that the intensity ratio between the lines of the sextuplet is 3:4:1 as indicated by magnetic measurements. The extra contribution to the two middle lines is due to the presence of paramagnetic iron atoms in the samples because of the interdiffusion between the Si and $\text{Fe}_{1-x}\text{Si}_x$ layers in the

TABLE III. Hyperfine parameters of the different samples.

| Fe ₇₅ Si ₂₅ / Si | | | | | |
|--|----------------|----------------------|--------------------------------|---------------|---------------------|
| SAMPLE | I.S. (mm/s) | ΔE (mm/s) | $\langle H_f \rangle$ (KOe) | μ_o /atom | linewidth (mm/s) |
| 1 | 0.13(1) | 1.58(2) | 200 | 1.5 | 0.33(1) |
| 2 | 0.12(1) | 1.28(1) | 204 | 1.5 | 0.42(1) |
| 3 | 0.12(1) | 1.52(1) | 215 | 1.6 | 0.36(1) |
| 4 | 0.07(1) | 0.73(1) | 240 | 1.8 | 0.38(1) |

| Fe ₇₀ Si ₃₀ / Si | | | | | |
|--|----------------|----------------------|--------------------------------|---------------|---------------------|
| SAMPLE | I.S. (mm/s) | ΔE (mm/s) | $\langle H_f \rangle$ (KOe) | μ_o /atom | linewidth (mm/s) |
| 1 | 0.13(1) | 0.98(1) | 168 | 1.3 | 0.36(1) |
| 2 | 0.12(1) | 0.87(1) | 173 | 1.3 | 0.44(1) |
| 3 | 0.11(1) | 0.93(1) | 184 | 1.4 | 0.42(1) |
| 4 | 0.11(1) | 1.05(1) | 212 | 1.6 | 0.37(1) |

interfaces. The number of Bohr's magnetons per Fe atom has been obtained assuming a linear relation between μ_B and H_f^{21} , $H_f = 13T/\mu_B$. The fact that the $P(H)$ distributions corresponding to samples having $\lambda \leq 10\text{\AA}$ have practically the same width and values for $\langle H_f \rangle$, allows us to interpret them as due mainly to interfacial Fe atoms. Hence we assume that the interface has an extension of about 10\AA in good agreement with the results obtained by C. Dufour et al. by using low angle X-ray diffraction¹² and neutron diffraction⁶ in the Fe/Si multilayered system. Increasing the characteristic modulation length λ , the $P(H)$ distribution moves to higher fields. This increase may be due to two different causes: a) Variation of

FIGURE 3. Binomial distributions of the hyperfine fields as a function of λ .

the magnetic moments of the iron atoms. b) An increase of the exchange interactions intensity and consequently in the Curie temperatures. Since the Mössbauer isomer shift is a direct measure of the electronic charge density at the site of the Mössbauer isotope, a considerable variation of this hyperfine parameter should be detectable if a variation of the magnetic moments takes place^{22,23}.

It is evident from Table III that this is not our case, so the increase of $\langle H_f \rangle$ must be attributed to an increase of the exchange interactions intensity and consequently in the Curie temperatures²⁴.

REFERENCES

- ¹E.M. Gyorgy, D.B. Mcwhan, J.F. Dillon, L.K. Walker, J.V. Waszczak, D.P. Münser and R.H. Willies. *J. Magn. Magn. Mat.* 31-34, 915 (1983).
- ²N. Hosoi, K. Kawaguchi, T. Shinjo, T. Takada and Y. Endoh. *J. Phys. Soc. Japan.* 53, 257 (1984).
- ³B. Martínez, M.A. Moreu, A. Labarta, X. Obradors and J. Tejada. *J. Appl. Phys.* 63(8) (1988) 3206.
- ⁴H.K. Wong, H.Q. Yang, J.E. Hilliard and J.B. Ketterson. *J. Appl. Phys.* 57(1), 3660 (1985).
- ⁵B. Martínez, A. Labarta and J. Tejada. *Hyperfine Interactions* (In Press).
- ⁶C. Dufour, A. Bruson, B. George, G. Marchal, C. Vettier, J.J. Rhyne and R. Erwin. *Solid State Commun.* 69(10), 963 (1989).
- ⁷Y. Shimada and H. Kojima. *J. Appl. Phys.* 47, N 9, 4156 (1976).
- ⁸D. Bloch, P.H. Mangin, G. Marchal and Chr. Janot. *Solid State Commun.* 25, 555 (1978).
- ⁹J.M. Alameda, J.F. Fuertes, D. Givord, A. Lienard, B. Martínez, M.A. Moreu and J. Tejada. *J. de Phys.* 49, N 12, C8-1789 (1988).
- ¹⁰C.N. Afonso, A.N. Lagunas, F. Briones and S. Giron. *J. Magn. Magn. Mat.* 62 (1980) 833.
- ¹¹B. Martínez, A. Ruiz, A. Labarta, X. Obradors, F. Briones and J. Tejada. *IEEE Trans. on Magn.* MAG-23, N 5, 3581 (1987).
- ¹²C. Dufour, A. Bruson, B. George, G. Marchal and Ph. Mangin. *J. de Phys.* 49, N 12, C8-1781 (1988).
- ¹³Osamu Khomoto. *J. Appl. Phys.* 53(11), 7486 (1982).
- ¹⁴S.G. Cornellison and J.D. Sellmyer. *Phys. Rev. B*, 30, 2845 (1984).
- ¹⁵H. Zijlstra. *Experimental Methods in Magnetism*. Vol 2. Wiley. N.Y. (1967).
- ¹⁶F. Keffer. *Handbuch der physik*, Springer-Verlag. Berlin, 18, 1 (1966).
- ¹⁷T. Holstein and H. Primakoff. *Phys. Rev.* 58, 1098 (1940).
- ¹⁸Peng Chu-Bing, Dai Dao-Sheng, Fang Rei-Yi and Lin Zum-Xia. *J. Magn. Magn. Mat.* 79, 11 (1989).

- ¹⁹T. Kaneyoshi. Phys. Rev. B, 39, 557 (1989).
- ²⁰I. Vincze. Solid State Commun. 25 (1978) 689.
- ²¹J.M.D. Coey, D.H. Ryan and Yu Boliang.
J. Appl. Phys. 55 (1984) 1800.
- ²²A.M. Van der Kraan and K.H.J. Buschow.
IEEE Trans. on Mag. MAG-20,5 (1984) 1284.
- ²³A.R. Miedema and F. Van der Woude. Physica 100B (1980) 145.
- ²⁴J. Kwo, E.M. Gyorgy, D.B. McWhan, M. Hong, F.J. Disalvo,
C. Vetier and J.E. Bower. Phys. Rev. Lett. 55 (1985) 402.

MÖSSBAUER SPECTROSCOPY OF THE Fe/Ni INTERFACE

E. Colombo, O. Donzelli, G.B. Fratucello and
F. Ronconi

Dipartimento di Fisica, Università' di Ferrara
via Paradiso 12, I-44100 Ferrara, Italy

INTRODUCTION

The interfaces of magnetic thin films and multilayers exhibit characteristic behaviours which are object of increasing experimental as well as theoretical investigations. At least one of the component layers of these systems is magnetic, usually iron; in Fe-Ni thin films both the components are magnetic. Fe/Ni films grown in the fcc structure differs from all the others system in that they can exhibit the well known Invar anomalies of the corresponding disordered alloys (Window, 1973). Thin fcc $\text{Ni}_x\text{Fe}_{1-x}$ alloy films have been studied in the whole range of composition as well in the Invar region $0.32 < x < 0.39$ (Dumpich et al., 1987, 1988). Ultrathin fcc Fe-Ni films, prepared by alternating the deposition of Fe and Ni, could exhibit Invar behaviour if one takes in to account that interdiffusion can occur during evaporation of Fe on Ni creating intermixing of Ni atoms in Fe-rich regions and therefore Invar ultrathin films. This possibility has been investigated by us especially by Conversion Electrons Mössbauer Spectroscopy (Colombo et al., 1987; Fratucello et al., 1989); the Mössbauer Spectroscopy of the resonating ^{57}Fe isotope can give valuable informations of different kinds of short-range orders through the analysis of the distribution function $p(B)$ of the hyperfine fields. Our CEMS results suggest a layer by layer growth of fcc gamma-Fe on (111) Ni and that interdiffusion is confined within two monolayers ML. Contrary to alloy thin films our samples are near to the ideal structure in which one ultrathin f.c.c. film of pure gamma-Fe is interfaced with (111) f.c.c Ni: in this case the influence of the magnetic properties of pure gamma-Fe in the film should be taken in to account. We shall come back to these subjects in this paper in which results obtained in ultrathin Fe-Ni films will be shown and discussed.

EXPERIMENTAL

Fe-Ni films have been produced by thermal evaporation in vacuum (10^{-6} tor) by growing a Ni underlayer 1000 Å thick

onto different substrates, mica and mylar, held at 300 °C or at room temperature RT. Ni can pseudomorphically grow on heated mica as (111) coherent crystals containing growth faults with grain size much larger than the film thickness so that their influence on the magnetic properties is expected to be negligible; on the other hand Ni films deposited on mica at RT also show (111) texture but, owing to reduced surface diffusion, they reproduce characteristic surface defects of mica obtained by cleavage. On the contrary Ni deposited on mylar at room temperature is polycrystalline with crystal size of about 150 Å (Colombo et al., 1987); strains seem absent in this case while (111) Ni layers on mica are strained because the oxygen atoms on mica planes form a pseudohexagonal lattice with distance of 2.65 Å, 6% greater than the first nearest neighbors distance equal to 2.49 Å in bulk Ni (Fratucello et al., 1989).

The deposition of Fe-Ni bilayers follows the Ni underlayer preparation: common growth condition for any sample were deposition rate (1 Å/s) and growth temperature (25 °C); all the samples have the same multilayer structure obtained by alternating the deposition of one Fe film and one Ni film five times at room temperature to avoid bulk diffusion. The last Ni layer (overlayer) prevents the oxidation of the Fe layer; after the underlayer preparation some of the samples were simultaneously deposited, onto different substrates, to make sure equal growth conditions. Rate of growth and film thickness were measured in situ by quartz oscillators.

RESULTS

In this work we shall discuss results, prepared according to the above described process, having the following structure:

- A: mica/Ni underlayer at 300 °C / 5 Å ⁵⁷Fe/ 200 Å Ni at RT
- B: mica/Ni underlayer at 300 °C / 12 Å ⁵⁶Fe/ 5 Å ⁵⁷Fe / 200 Å Ni at RT
- C: mica/Ni underlayer at 300 °C / 6 Å ⁵⁶Fe/ 5 Å ⁵⁷Fe / 6 Å ⁵⁶Fe/ 200 Å Ni at RT
- D: mica/Ni underlayer at 25 °C / 12 Å ⁵⁶Fe/ 5 Å ⁵⁷Fe / 200 Å Ni at RT

Sample B and D were simultaneously deposited onto Ni underlayer to study the effect of the temperature on substrate and underlayer; samples B, C and D all have the same Fe total thickness of 17 Å; the total thickness of the samples is about 2000 Å.

It has been shown that pure fcc (gamma-)Fe films, 15 Å thick, can be epitaxially grown onto (001) Ni single crystals, without misfit dislocations and compressed to match the Ni lattice constant (Matthews and Jesser, 1969). We have suggested that ultrathin gamma-Fe films can also grow onto (111) Ni films up to a thickness of 15-20 Å. X-ray diffraction patterns of our samples did not show the presence of bcc phases; a single fcc phase appears corresponding to the characteristic interplanar distance of Ni (Colombo et al., 1987). As-prepared Fe_{1-x}Ni_x alloy films in the Invar region, 2000 Å thick, exhibit two distinct peaks corresponding to bcc and fcc phases in almost equal

proportion (Dumpich et al., 1987); the X-ray resolution lower bound to reveal the presence of one different phase in a crystalline matrix of atoms of nearly equal atomic weight is 5%; we have taken in to account that this value corresponds to Fe percent contribution in our samples.

CEMS spectra were obtained using a conventional constant acceleration Mössbauer spectrometer connected with a 512 multichannel analyser; the cosine smearing of the velocities was eliminated by folding double symmetric spectra.

The sampling depth of this technique is about 2000 Å, equal to the total thickness of the samples.

Fits of the spectra were obtained using the Le Caer-Dubois method (1979); the resulting hyperfine fields distribution functions $p(B)$ are shown in Fig.1.

DISCUSSION

The mean values of the hyperfine fields of the distribution function $p(B)$ in Fig. 2 are 26.1 T, 31.1 T, 31.8 T and 26.2 T for samples A, B, C and D respectively; these values cannot be fitted into the usual curve of the mean values of hyperfine fields in fcc FeNi alloys (see e.g. Dumpich, 1988, Fig. 7). In fact a magnitude of about 24 T should be expected in the Fe-rich Invar region corresponding to a possible situation of our films if they were strongly intermixed; a better understanding can be obtained by the distribution function $p(B)$ of the hyperfine fields. Ullrich and Hesse (1984) have shown that Invar alloys have a broad hyperfine fields $p(B)$; the analysis of their distribution functions indicates a number of peaks corresponding, in the framework of a magnetic model based on a Heisenberg hamiltonian, to different number n of first nearest neighbours Fe atoms giving the maximum hf at $n=9$. Moreover they pointed out that in their polarized gamma-rays Mössbauer spectroscopy, in contrary to the usually presented $p(B)$ distributions (like in this work), the vector character of the magnetic hf, and therefore its sign, was considered and found antiparallel to the normal ferromagnetic direction giving indirect evidence of the existence of antiparallel Fe-moments even at room temperature for $n=11,12$ i.e. up to pure gamma-Fe environments. On the other hand the $p(B)$ functions in thin as-prepared alloys Fe-Ni films (Dumpich et al., 1989) show only one main peak at 33.5 T and a shoulder at 31.5 assigned to the occ and fcc phase respectively; only after annealing at 850 °K they observed again the typical broad distribution of bulk Invar alloys.

Our sample A shows an intermediate behaviour because its $p(B)$ is not broad enough to be bulk-like nor sharp enough to be assigned to a well defined short-range order like the one suggested by Dumpich (1989); more than 70% of this $p(B)$ has a peak at $B=30.1$ T, 11% at 27.0 T and the remaining part gives a tail in the low-fields region; contrary to all the other samples whose Fe-thickness is 17 Å, in this sample the Fe-thickness is 5 Å, i.e. 2.5 ML. Assuming interdiffusion confined within two ML and observing that this sample has two Ni/Fe interfaces, we believe that the behaviour of $p(B)$ is due to the existence of different short-range orders on both interfaces.

Sample B clearly shows high-spin states evidenced by

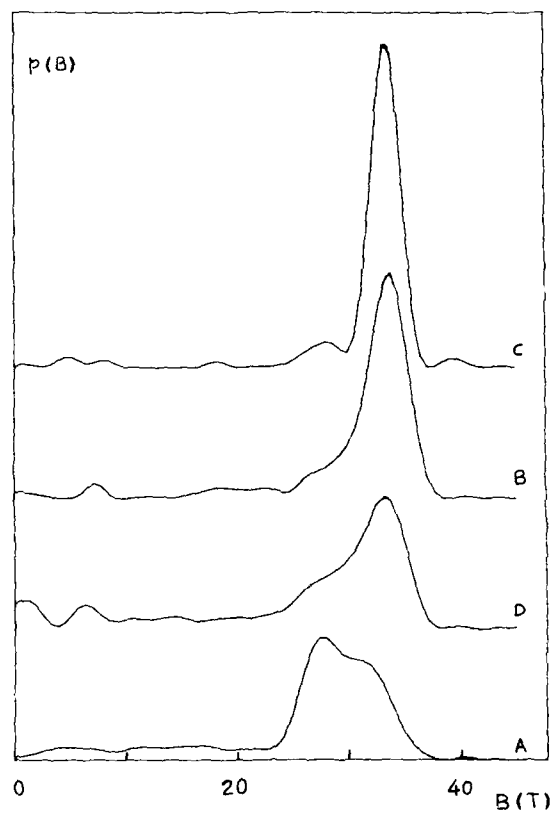


Fig. 1. Distribution functions $p(B)$ of hyperfine fields B (Tesla) in the four samples A, B, C, and D.

the dominant peak (more than 91%) in the high-fields region; even after the gaussian analysis of this peak we find the main contribution at 34.0 T (63.9%) and a second contribution at 30.4 T (27.6%). We assign the main contribution to the Ni/Fe interface; sample D, simultaneously grown with sample B, essentially shows the same hf (33.7 T, 34.2%, 27.5 T, 44.2%) with a decrease of the interface field contribution due to defects of the Ni underlayer evaporated at RT in sample D instead of 300 °C growth temperature of sample A substrate; the isomer shift in samples B and D were found equal to about 0.020 mm/sec and 0.030 mm/sec respectively giving further confirmation of the existence of local environments different from the α -Fe bcc phase.

Finally sample C shows one Zeeman sextet with hf basically at 33.5 T; sample C has not Ni/Fe interfaces and therefore the observed hf should be assigned to highly susceptible and pure gamma-Fe in the magnetic environment of the Ni multilayer structure.

CONCLUSIONS

The sharp peak of the distribution function of the hyperfine fields $p(B)$ of sample B and the fairly broad $p(B)$ of sample D, both simultaneously evaporated in the same growth conditions (temperature, pressure, growth rate and Fe/Ni multilayer structure) onto 1000 Å (111) Ni underlayers grown on mica at 300 °C and 25 °C respectively, give an indirect evidence for a layer-by-layer growth of ultrathin (17 Å) fcc Fe films on (111) Ni of sample B in a nearly perfect Fe/Ni interface having one hyperfine field equal to 34.0 T. The $p(B)$ broadening of sample D shows that as the Ni underlayer and mica substrate are rich of defects owing to lower growth temperature, than more than one short-range order is detected by Conversion Electrons Mössbauer Spectroscopy in the 2.5 ML of resonating ^{57}Fe in the interface region, and correspondingly different components of the hyperfine fields; one of two component in the high-field is again due to the Fe/Ni interface field near to a second one at 27.8 T of about the same percent contribution. The low-field contribution, not negligible (21.6 %) in sample D, gives negative isomer shift (-0.130 mm/sec) in the low-fields region and positive (0.020-0.030 mm/sec) in the high-fields region.

The sharp peak at 33.5 T of the distribution $p(B)$ of sample C, not having Fe/Ni interfaces, suggests the existence of a high-spin, highly susceptible fcc phase of pure gamma-Fe in the magnetic environment of the Fe/Ni multilayer structure of these samples.

ACKNOWLEDGEMENTS

This work has been supported by the Ministero dell'Università e della Ricerca Scientifica e Tecnologica (MURST) of Italy and by the Consiglio Nazionale delle Ricerche, Gruppo Nazionale di Struttura della Materia CNR-GNSM of Italy.

REFERENCES

- Colombo, E., Fratucello, G., and Ronconi, F., 1987, Ferromagnetism of fcc iron films grown on Nickel, *J. Magn. Magn. Mat.*, 66:331.
- Dumpich, G., Wasserman, E.F., Manns, V., Keune, W., Murayama S. and Miyako Y., 1987, Structural and magnetic properties of Fe Ni evaporated thin films, *J. Magn. Magn. Mat.*, 67:55.
- Dumpich, G., Becker, E., Schletz, K., Stamm, W., Keune, W., Kiauka, W., and Murayama S., 1988, Evidence for a high-spin Fe state in fcc $\text{Fe}_{1-x}\text{Ni}_x$ thin films in the Invar region, *J. Magn. Magn. Mat.*, 74:237.
- Fratucello, G.B., Colombo, E., Donzelli, O., and Ronconi, F., 1989, Study of the Fe-Ni interface by Conversion Electron Mössbauer Spectroscopy, *Hyp. Int.*, 45:255.
- Le Caer, G., and Dubois, J.M., 1979, Evaluation of hyperfine parameter distributions from overlapped Mössbauer spectra of amorphous alloys, *J. Phys. E*, 12:1083.
- Matthews, J.W., and Jesser, W.A., 1969, A Study of the F.C.C. to B.C.C. Transformation in Films of Iron on Nickel, *Phil. Mag.*, 20:999.
- Ullrich, H., Hesse, J., 1984, Hyperfine fields vectors and hyperfine field distributions in FeNi Invar alloys, *J. Magn. Magn. Mat.*, 45:315.
- Window, B., 1973, Invar anomalies, *J. Appl. Phys.*, 44:2853.

ANALYSIS OF AMORPHOUS DYSPROSIUM-TRANSITION METAL NANOSCALE MAGNETIC MULTILAYERS

Z. S. Shan and D. J. Sellmyer

Behlen Laboratory of Physics and
Center for Materials Research and Analysis
University of Nebraska, Lincoln, NE 68588-0111, U. S. A.

ABSTRACT

A theoretical model has been developed recently to understand the magnetic properties of compositionally-modulated films (CMF) or multilayers. In this paper, the magnetization and anisotropy and their distributions in Dy/Co CMF along the film normal are analyzed in terms of this model. Also this model is further checked by measuring the temperature dependence of magnetic properties for Dy/Co CMF and contrasting the magnetic character between Dy/Ta and Dy/Co CMFs. It is found that the calculated results are in good agreement with the experiments when the bilayer thickness is small enough ($\leq 16\text{\AA}$).

INTRODUCTION

Compositionally-modulated films or multilayers have enjoyed more and more attention in recent years for both the studies of interface magnetism and their promising applications, such as perpendicular magnetic and magneto-optical recording. We have developed a detailed model to understand the magnetization and anisotropy and their distributions along the film normal^{1,2}. In the present paper, the magnetic properties of Dy/Co CMF are analyzed in terms of this model, and also this model is further checked by measuring the temperature dependence of magnetic properties for Dy/Co CMF and comparing the magnetic properties of Dy/Ta and Dy/Co CMFs.

MODEL ANALYSES

The basic idea of this model is to divide the RE/TM CMF into thin slices each of which can be regarded as a two-dimensional amorphous film and thus the resultant magnetic properties are obtained by taking the average over the whole volume of the CMF. In this model, a modified mean-field model is used to analyze the distributions of magnetization including the total, rare earth(RE), and transition metal(TM) magnetizations, and a single-ion anisotropy model is used for analyzing the anisotropy. Some results from this model are listed below without proof. A brief discussion of the procedure for obtaining these results is given in Ref.[1] and the further details are given in Ref.[2].

(A) The atomic distribution of constituents are sinusoidal for RE/TM CMF (RE=Th, Dy, and TM=Co, Fe) when the bilayer thickness $\lambda < 16\text{\AA}$.

(B) The relationship between the intrinsic anisotropy K_u , the distributions of

RE-subnetwork magnetization and constituent atoms can be expressed as

$$K_u = \xi \langle M_{RE}(z)^2 \rangle > \frac{A}{\lambda} \quad (1)$$

for the CMF with thin layer thickness, where ξ is a constant and A is the peak-to-peak compositional modulation of the constituents. $\langle M_{RE}(z)^2 \rangle$ is the statistical average of RE-subnetwork magnetization squared over the whole sample and (A/λ) the average gradient (or anisotropic distribution) of the constituent atoms.

Layer-Thickness Dependence of the Magnetization Distribution and Anisotropy

Figure 1 illustrates the distributions of Co atom and magnetizations, which include the total, Dy- and Co-subnetwork magnetizations, along the film normal. These curves present a microscopic picture to understand the structure and magnetic behavior for Dy/Co CMF. Figure (1a) shows: (1) The Co atomic distribution C_{Co} has small fluctuations with $C_{Co(min)}=0.50$ and $C_{Co(max)}=0.62$ for $8\text{\AA Dy}/3.5\text{\AA Co}$; the nominal layer thickness of Co is only about one monolayer and the interdiffusion between Dy and Co atoms makes the distribution curve relatively flat. (2) We notice the magnetization in the central Dy region is zero because the $Dy_{1-x}Co_x$ alloy is disordered magnetically at room temperature as $C_{Co} < 55\%$. (3) In the central Co region the magnetization of Dy-subnetwork, not the Co-subnetwork, dominates. This behavior follows since $C_{Co(max)}$ is only 62% and the Dy-subnetwork has much larger magnetic moments ($gJ=7.3$) than that of Co-subnetwork ($gJ=1.5$). Figure (1b) shows: (1) Compared with $8\text{\AA Dy}/3.5\text{\AA Co}$, the Co atom distribution of $8\text{\AA Dy}/8\text{\AA Co}$ has relatively large fluctuations with $C_{Co(min)}=0.62$ and $C_{Co(max)}=0.81$. (2) The magnetization of Dy- and Co-subnetworks dominates in their own regions, respectively, and at the nominal boundary they are compensated nearly. The magnetic state of this sample is near the compensation point with small total magnetization. (3) Compared with Fig. (1a) where the Dy-subnetwork magnetization is disordered in the central Dy region, both Dy- and Co-subnetwork magnetizations are ordered in the central Dy region. The reason is that $C_{Co} \approx 0.62$ there, and the exchange interactions between Co- and the Dy-subnetworks make both subnetworks ordered and Dy moment dominates for its much larger gJ value as pointed out before.

Equation (1) indicates that the intrinsic anisotropy K_u can be calculated if the magnetization distribution of the RE-subnetwork and the amplitude of the compositional modulation are determined. We take $8\text{\AA Dy}/X\text{\AA Co}$ ($X=3.5, 6, 8, 10$) as an example and the $M_{Dy}(z)$ and A value can be found from Fig. (1a) and (1b) for $8\text{\AA Dy}/3.5\text{\AA Co}$ and $8\text{\AA Dy}/8\text{\AA Co}$. The intrinsic anisotropy K_u is fitted to the experimental data with ξ as an adjustable parameter and the result is shown in Fig. 2. The

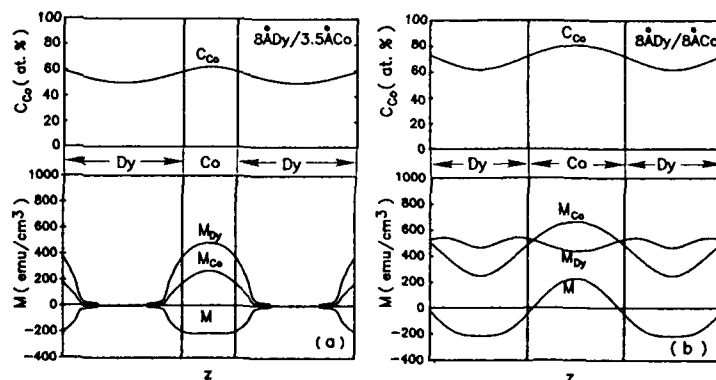


Fig. 1. The distributions of Co atoms and magnetizations for $8\text{\AA Dy}/3.5\text{\AA Co}$ (a) and $8\text{\AA Dy}/8\text{\AA Co}$ (b).

following features should be pointed out: (1) The agreement between the experimental data and calculated results is very good. (2) The rapid fall of K_u as Co layer thickness approaches 3.5 \AA is because the Dy-subnetwork magnetization is disordered in the central Dy region and A value decreases as the Co layer becomes thinner as shown in Fig. (1a). The decrease of K_u as the Co layer thickness goes to 10 \AA is because both the Dy-subnetwork magnetization and (A/λ) value decrease as the Co layer thickness becomes thicker. (3) The fitted value of $\xi \simeq 4.7 \times 10^{-6} \text{ cm}$ leads to an average value of the single-ion anisotropy parameter $D \simeq 2.2 \times 10^{-17} \text{ erg}$ which is very close to what has been found for $6 \text{ \AA Dy}/X \text{ \AA Co}$ CMF in Refs.[1, 2].

Many efforts have been made to investigate the magnetic anisotropy and its origin in the thin films. Often, three sources of anisotropy are suggested to be the candidates for PMA: these include dipolar-interaction, single-ion anisotropy and stress-induced "or magnetostrictive" anisotropy. Reference[2] gives a detailed analysis and concludes that the single-ion anisotropy of the RE ions with orbital angular momentum is the main origin of PMA. The good agreement between the experimental and calculated results for $8 \text{ \AA Dy}/X \text{ \AA Co}$ confirms once again that this conclusion is correct. To further test this model, the temperature dependence of PMA and the comparison of magnetic properties between Dy/Ta and Dy/Co CMFs are presented below.

Temperature Dependence of Magnetic Properties

Figure 3 shows the magnetic properties for $Y \text{ \AA Dy}/6 \text{ \AA Co}$ ($Y=3.5, 5, 8, 11, 14$) at 300 K and 4.2 K. It is seen clearly: (1) The intrinsic anisotropy K_u is much larger at 4.2 K than at 300 K. For example, the maximum K_u is about $1.4 \times 10^7 \text{ erg/cm}^3$ at 4.2 K and only $2 \times 10^6 \text{ erg/cm}^3$ at 300 K. This is attributed to the fact that the single-ion anisotropy of Dy ion is proportional to its magnetization squared which is well ordered at 4.2 K. (2) Both at 4.2 K and 300 K, sample $5 \text{ \AA Dy}/6 \text{ \AA Co}$, whose individual layer thickness of Dy and Co are about 2-atomic layers, has the maximum values of anisotropy. This feature can be understood in terms of Eq. (1): the individual layer thickness of about 2-atomic layers may show the largest anisotropic distribution of constituent atoms, i.e. the largest value of (A/λ) . (3) We notice that at the compensation points where the total magnetization $M=0$ at 300 K or 4.2 K, the intrinsic anisotropy K_u has a rather large value. This implies that not the total magnetization, but the Dy-subnetwork magnetization gives the major contribution to the anisotropy. All these three points are explained by our model reasonably.

Comparison of the Magnetic Properties between Dy/Ta and Dy/Co CMFs

Equation (1) shows that the intrinsic anisotropy is proportional to $\langle M_{RE}(z)^2 \rangle$ and (A/λ) . More detailed analysis indicates that the region near the nominal bound-

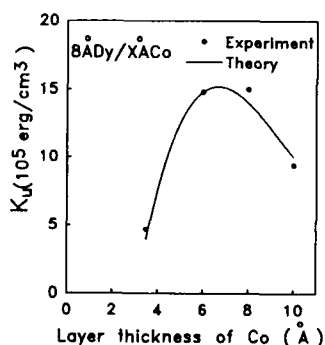


Fig. 2. A comparison between the calculated and experimental anisotropy for $8 \text{ \AA Dy}/X \text{ \AA Co}$ ($X=3.5, 6, 8, 10$).

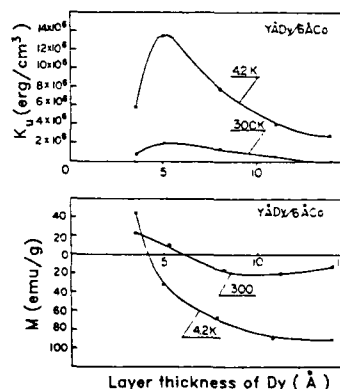


Fig. 3. Anisotropy and magnetization for $Y \text{ \AA Dy}/6 \text{ \AA Co}$ ($X=3.5, 5, 8, 10$) at 300 K and 4.2 K.

ary may give the major contribution to the anisotropy because the distribution of constituent atoms has the maximum anisotropic character there. However, if the value of Dy-subnetwork magnetization is small, this region will not contribute to the anisotropy appreciably. Samples of Dy/Ta and Dy/Co were prepared to test this behavior.

An example of hysteresis loops for $Y\text{\AA}Dy/6\text{\AA}Co$ ($Y=3.5, 5$) and $Y\text{\AA}Dy/6\text{\AA}Ta$ ($Y=3.5, 5.25$) at 4.2 K are shown in Fig. (4a) and (4b), respectively. The following features should be noticed: (1) Sample $5\text{\AA}Dy/6\text{\AA}Co$ exhibits larger total magnetization than that of $5.25\text{\AA}Dy/6\text{\AA}Ta$. Since Ta is nonmagnetic, the total magnetization of $5.25\text{\AA}Dy/6\text{\AA}Ta$ is determined uniquely by the Dy-subnetwork. However, for $5\text{\AA}Dy/6\text{\AA}Co$ the Dy- and Co-subnetwork magnetizations are coupled antiferromagnetically and Dy-subnetwork magnetization dominates. Thus the Dy-subnetwork magnetization is the sum of the total and Co-subnetwork magnetization. Consequently the Dy-magnetization of $5\text{\AA}Dy/6\text{\AA}Co$ is much larger than that of $5.25\text{\AA}Dy/6\text{\AA}Ta$. (2) $Y\text{\AA}Dy/6\text{\AA}Co$ samples exhibit much larger perpendicular anisotropy than that of $Y\text{\AA}Dy/6\text{\AA}Ta$. The reason is twofold: First, the Dy-subnetwork magnetization of Dy/Co CMF is much larger than that of Dy/Ta CMF as mentioned above; Second, the Ta is nonmagnetic and thus the Dy-subnetwork magnetization near the nominal boundary region is very small (or zero). Consequently there is no appreciable contribution of anisotropy from this region. In the central Dy region, the Dy-subnetwork magnetization may be larger, but the anisotropic distribution of constituent atoms is very weak and thus contribution of anisotropy from this region also is small. (3) Compared with $3.5\text{\AA}Dy/6\text{\AA}Ta$, sample $5.25\text{\AA}Dy/6\text{\AA}Ta$ shows a little stronger perpendicular anisotropy. This is because that $5.25\text{\AA}Dy/6\text{\AA}Ta$ sample has the individual layer thickness of about 2-atomic layers.

SUMMARY

In summary, the results from model analysis agree with experiments reasonably well. The experimental data only show the magnetic properties resulting from a statistical average over the whole sample; however, the model analysis may offer information about the micromagnetic structure. The control of the micromagnetic structure may find important applications in various magnetic or magneto-optic data-storage technologies.

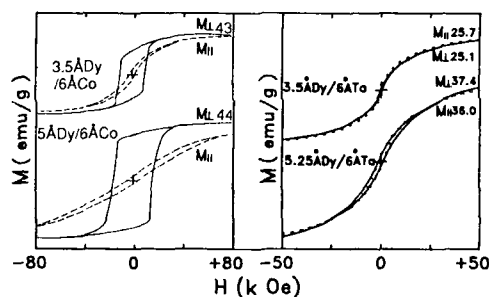


Fig. 4. A comparison of hysteresis loops between $Y\text{\AA}Dy/6\text{\AA}Co$ and $Y\text{\AA}Dy/6\text{\AA}Ta$.

ACKNOWLEDGEMENT

We are grateful for financial support of NSF under Grant DMR-8918889.

REFERENCES

1. Z. S. Shan, D. J. Sellmyer, S. S. Jaswal, Y. J. Wang, and J. X. Shen, Phys. Rev. Lett. 63, 449 (1989).
2. Z. S. Shan, D. J. Sellmyer, S. S. Jaswal, Y. J. Wang, and J. X. Shen, Phys. Rev. B, (to be published).

TRANSPORT PROPERTIES OF THIN METALLIC FILMS AND MULTILAYERS

A. FERT

Laboratoire de Physique des Solides, Université Paris-Sud
91405 Orsay Cedex, France

INTRODUCTION

The problem of electron transport in thin metallic films is an old one. The Fuchs-Sondheimer semi-classical theory [1,2] was worked out fifty years ago and the influence of the electron scattering by surfaces on the conductivity of thin films was extensively investigated in the fifties and sixties. A good report on this early stage of the transport properties of thin films is the review paper by Maissel [3] in 1970. The recent progresses of the growth techniques has revived the subject. Data on well characterized ultrathin films have shown the drawbacks of the semi-classical models and led to the development of quantum theories. Also the interplay between electron transport and magnetic properties in magnetic multilayers begins to be extensively investigated. In this article, first we present the Fuchs-Sondheimer theory of the conductivity of thin films and related experiments. Then we proceed to the recently developed quantum mechanical models, to the electron transport in multilayers, and finally to the case of magnetic multilayers.

FUCHS-SONDHEIMER SEMI-CLASSICAL THEORY OF THE RESISTIVITY OF THIN FILMS

The Fuchs-Sondheimer model [1,2] is based on the Boltzmann equation [4]:

$$\frac{e}{m} \mathbf{E} \cdot \text{grad}_{\mathbf{v}} [f^0(\mathbf{v})] = \frac{1}{\tau} g(\mathbf{v}, \mathbf{r}) + \mathbf{v} \cdot \text{grad}_{\mathbf{r}} [g(\mathbf{v}, \mathbf{r})] \quad (1)$$

where g is the departure of the distribution function of the electron gas $f(\mathbf{v}, \mathbf{r})$ from the Fermi-Dirac equilibrium distribution, i.e:

$$g(\mathbf{v}, \mathbf{r}) = f(\mathbf{v}, \mathbf{r}) - f^{(0)}(\mathbf{v}) \quad (2)$$

with:

$$f^{(0)}(\mathbf{v}) = \frac{1}{\exp \left[\frac{(\epsilon_{\mathbf{v}} - \epsilon_F)}{k_B T} \right] + 1} \quad (3)$$

$$\epsilon_v = \frac{1}{2}mv^2$$

E is the electric field and τ is the relaxation time supposed to be a function of v only. Eq.1 means that the change of $g(v,r)$ due to the acceleration of the electrons by the electric field E is balanced by the change due to scattering expressed by the term g/τ and the change due to diffusion which tends to make the distribution uniform. For a bulk metal, g is uniform, $\text{grad}_r[g] = 0$, and the standard solution is:

$$g_B(v) = \frac{eE}{m} \text{grad}_v [f^{(0)}(v)] = e\tau E \cdot v \frac{\partial f^{(0)}}{\partial \epsilon_v} \quad (4)$$

Eq.4 means that the Fermi surface is shifted in k -space by $eE\tau(v_F)/\hbar$ in the opposite direction to E . The current density is proportional to this shift,

$$j = - \frac{ne^2\tau(v_F)E}{m}$$

We now consider the case of a metallic film of thickness d . The z -axis is perpendicular to the plane of the film and the current is supposed to be in the x direction. Due to the diffuse part of the scattering by the surfaces the current density will generally be smaller near the surfaces. This means that g depends on z and that the diffusion term in Eq.1 does not vanish. Eq.1 is written as:

$$\frac{eE}{mv_z} \frac{\partial f^{(0)}(v)}{\partial v_x} = \frac{g(v,z)}{\tau v_z} + \frac{\partial g}{\partial z} \quad (5)$$

The general solution of Eq.5 is of the form:

$$g(v,z) = e\tau E \cdot v \frac{\partial f^{(0)}}{\partial \epsilon_v} \left[1 + F(v) \exp\left(\frac{-z}{\tau v_z}\right) \right] \quad (6)$$

where $F(v)$ is an arbitrary function of v to be determined by introducing appropriate boundary conditions.

The simplest assumption for the boundary conditions is to suppose that the scattering at the surfaces is entirely diffuse. The distribution function of the electrons leaving a surface must be independent of the direction of v . Eq.6 shows that this can be satisfied only if we choose $F(v)$ so that $g(v,0) = 0$ for all v having $v_z > 0$ and $g(v,d) = 0$ for all v having $v_z < 0$.

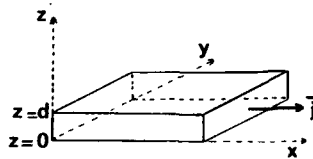


Fig.1. Thin film geometry.

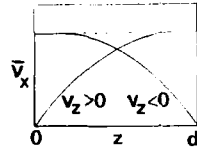


Fig. 2. Variation of the mean value of the electron velocity component along the field direction as a function of z for the electrons with $v_z > 0$ and $v_z < 0$ respectively.

There are therefore two functions g : g^+ for electrons with $v_z > 0$ and g^- for electrons with $v_z < 0$:

$$\begin{aligned} g^+(v, z) &= e\tau E \cdot v \frac{\partial f^{(0)}(v)}{\partial \epsilon_v} \left[1 - \exp\left(-\frac{z}{\tau v_z}\right) \right] \\ g^-(v, z) &= e\tau E \cdot v \frac{\partial f^{(0)}(v)}{\partial \epsilon_v} \left[1 - \exp\left(-\frac{d-z}{\tau v_z}\right) \right] \end{aligned} \quad (7)$$

With such expressions for g , the mean value of the velocity component along the field direction varies as $\{1 - \exp(-z/\tau v_z)\}$ and $\{1 - \exp(-(d-z)/\tau v_z)\}$ for the electrons with $v_z > 0$ and $v_z < 0$ respectively, as shown in Fig. 2.

The current carried by the film is given by an expression of the form:

$$J \sim \int e v_x g(v, z) d^3 v dz \quad (8)$$

to be compared to the current in an equivalent slab of the bulk metal:

$$J_0 \sim \int e v_x g_B(v) d^3 v dz \quad (9)$$

where g_B is expressed by Eq. 4. Resorting to polar coordinates:

$$\begin{aligned} v_z &= v \cos \Theta, \quad v_x = v \sin \Theta \cos \phi \\ d^3 v &= \frac{v}{m} d\epsilon_v \sin \Theta d\Theta d\phi \end{aligned}$$

one derives the ratio of conductivity of the film to that of the bulk metal:

$$\frac{\sigma}{\sigma_0} = \frac{J}{J_0} = \frac{\int_0^d dz \int_0^{\frac{\pi}{2}} d\Theta \int_0^{2\pi} d\phi \sin^3 \Theta \cos^2 \phi \left[1 - \exp\left(-\frac{d}{2\lambda \cos \Theta}\right) \cosh\left(\frac{d-2z}{2\lambda \cos \Theta}\right) \right]}{\int_0^d dz \int_0^{\frac{\pi}{2}} d\Theta \int_0^{2\pi} d\phi \sin^2 \Theta \cos^2 \phi} \quad (10)$$

where $\lambda = \tau v_F$ is the mean free path of the electrons in the bulk metal. After integrating over z and ϕ one obtains:

$$\frac{\sigma}{\sigma_0} = 1 - \frac{3}{2k} \int_1^\infty \left(\frac{1}{t^3} - \frac{1}{t^5} \right) [1 - \exp(-kt)] dt \quad (11)$$

where $t = 1/\cos\Theta$, $k = d/\lambda$ = thickness/mean free path. Approximations can be made for large and small k :

$$\frac{\sigma}{\sigma_0} = 1 - \frac{3}{8k} \quad \text{for } k = \frac{d}{\lambda} \gg 1 \quad (12)$$

$$\frac{\sigma}{\sigma_0} = \frac{3k}{4} \left(\ln \frac{1}{k} + 0.423 \right) \quad \text{for } k = \frac{d}{\lambda} \ll 1 \quad (13)$$

It is also useful to derive expressions of the resistivity as a function of d and λ . With $\rho_0 = mv_F/ne^2\lambda$, Eq.12-13 are written as:

$$\rho = \frac{mv_F}{ne^2} \left[\frac{1}{\lambda} + \frac{3}{8d} \right] \quad \text{for } \lambda \ll d \quad (14)$$

$$\rho = \frac{4mv_F}{3ne^2} \left[\frac{1}{d \left(\ln \frac{\lambda}{d} + 0.423 \right)} \right] \quad \text{for } \lambda \gg d \quad (15)$$

which gives the behavior shown in Fig.3.

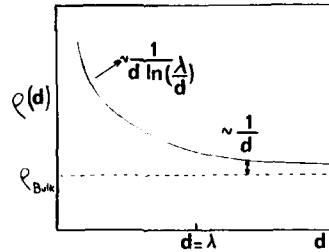


Fig.3. The Fuchs-Sondheimer resistivity as a function of the film thickness d (at fixed λ).

The limit $\lambda \ll d$ is clearly understood: there is a simple addition of scattering rates proportional to $1/\lambda$ and to $1/d$ arising from background and surface scattering respectively. In the limit $\lambda \gg d$ the result of the Fuchs-Sondheimer theory is puzzling as ρ tends to zero when the background scattering vanishes (i.e. when $\lambda \rightarrow \infty$) at fixed d . This seems unphysical: for d fixed at a finite value one would rather expect a finite surface scattering and therefore a finite residual surface resistivity. As a matter of fact the assumption of classical point electrons makes the Fuchs-Sondheimer theory incorrect in the limit $\lambda \rightarrow \infty$. Electrons with velocities almost parallel to the surfaces ($v_z/v \ll 1$) can propagate with a vanishingly small surface scattering; more precisely, for electrons with $d/\lambda < v_z/v \ll 1$, Eq.7 indicates that the function g is proportional to:

$$1 - \exp\left(-\frac{z}{\tau v_z}\right) = 1 - \exp\left(-\frac{z v}{\lambda v_z}\right) \approx \frac{dv}{\lambda v_z} \quad (16)$$

By integrating g over $\alpha = v_z/v$ down to d/λ we do obtain a current density diverging as $\ln(\lambda)$. We shall see later that, in quantum mechanical models, this divergence of the conductivity for $\lambda \rightarrow \infty$ disappears and the resistivity remains finite for finite d . This is because the quantum mechanical zero point motion excludes momentum states confined in a plane parallel to the surfaces.

Up to now we have considered the case with only diffuse scattering by the surfaces. The opposite case is that with only specular reflections at the surfaces. Specular reflections do not change the component of the velocity along the current direction and does not contribute to the resistivity. In the intermediate case, if one assumes that a fraction p of the electrons are specularly reflected while the fraction $(1-p)$ is scattered, calculations similar to those presented above for the case $p=0$ lead to:

$$\frac{\sigma}{\sigma_0} = 1 - \frac{3(1-p)}{8k} \quad \text{for } k = \frac{d}{\lambda} \gg 1 \quad (17)$$

instead of Eq.12 and

$$\frac{\sigma}{\sigma_0} = \frac{3k}{4} (1 + 2p) \left(\ln \frac{1}{k} + 0.423 \right) \quad \text{for } k = \frac{d}{\lambda}, p \ll 1 \quad (18)$$

instead of Eq.13. We see that the contribution from the surfaces decreases progressively to zero as p increases. Fig.4 shows a plot of ρ/ρ_0 versus k for several values of p .

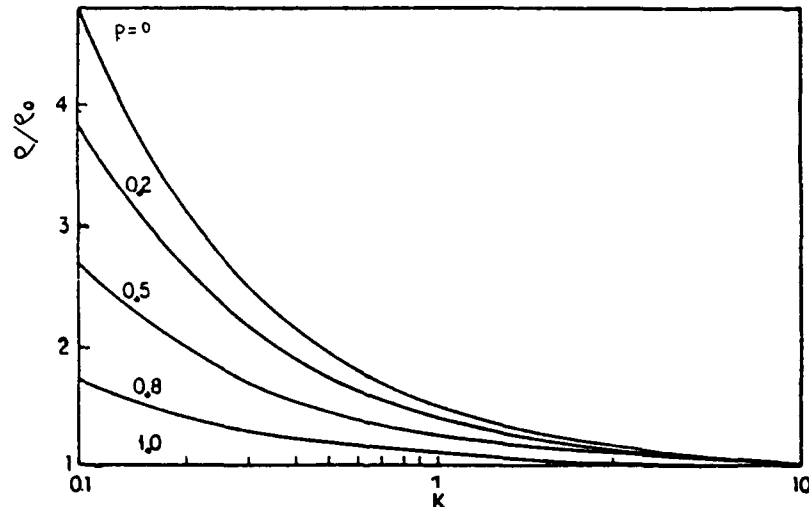


Fig.4. Ratio of the resistivity to the bulk metal resistivity as a function of $k=d/\lambda$ for several values of the proportion of specular reflection .
From Campbell.[5]

Finally we summarize the results of the Fuchs-Sondheimer theory for the temperature dependence of the resistivity of thin films. The temperature dependent phonon scattering enhances the background scattering (and therefore reduces λ), which finally reduces the coefficient $\alpha = 1/\rho \partial \rho / \partial T$ with respect to its value in the bulk material α_0 .

$$\frac{\alpha}{\alpha_0} = 1 - \frac{3(1-p)}{8k} \quad \text{for } k \gg 1 \quad (19)$$

$$\frac{\alpha}{\alpha_0} = \frac{1}{\ln\left(\frac{1}{k}\right) + 0.423} \quad \text{for } k \ll 1 \quad (20)$$

APPLICATION OF THE FUCHS-SONDHEIMER THEORY TO THIN FILMS

The experimental verification of the predictions of the Fuchs-Sondheimer theory is not as straightforward as might be expected. This is due to the difficulties in preparing clean films with well characterized surfaces and to additional effects we will discuss later.

Fig.5 shows an example of good fit between theoretical predictions and experimental results on a Sn film [6]. A good agreement has also been obtained in extensive studies on alkali metal films[3]. However, even when there is a good agreement for relatively thick films, it often deteriorates at small values of $k = d/\lambda$ (say below $k \sim 10^{-1}$), as will be discussed later. In most films the best agreement is generally obtained for $p = 0$, that is for completely diffuse scattering at the surfaces. However certain metals such as Pb, Ag and Au have values of p very close to 1, provided they have received a suitable annealing treatment. A typical behavior for "specular films" of gold with p close to 1 is shown in Fig.6. The deposition of a gold overlayer causes initially an increase of their resistance that is attributed to surface roughening. On the contrary, for "non-specular films", one observes the normal decrease of the resistance due to the increase of the film thickness. Resistivity measurements can be used to probe the surface roughness. The data of Fig.7 show that, for a copper overlayer deposited on copper, the resistivity increases for a deposition at 80K and decreases for a deposition at 300K. This clearly establishes that the surface of the overlayer is rougher for the lower temperature of deposition. For layer by layer epitaxial growth, it turns out that p is maximum when a layer has just been completed. Fig.8 shows typical oscillations of the resistivity observed in these conditions [9].

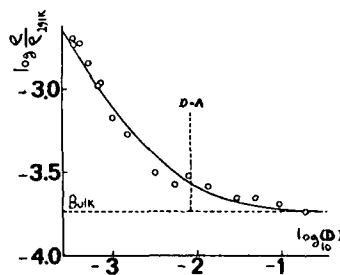


Fig.5. Log-log plot of the resistivity of Sn films at 38K versus the film thickness. The solid line is the variation predicted by the Fuchs-Sondheimer theory with $p=0$. From Andrew [6].

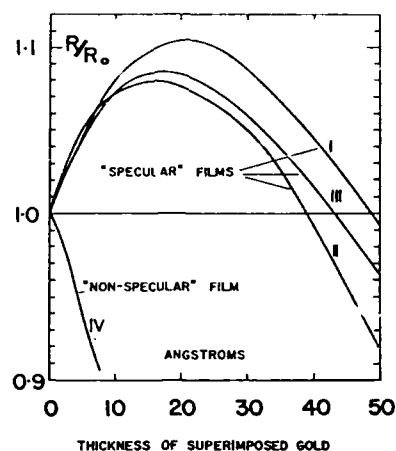


Fig.6. Change in resistance of gold films as a function of the thickness of a surimposed gold layer for "specular films" and a "non-specular film". The "non-specular" film is obtained by deposition on bismuth oxide and its high resistivity can be ascribed to diffuse scattering by its rough surface. The "specular films" are obtained by annealing "non-specular films" and their low resistivity approaches that of the bulk metal, which is the signature of flat surfaces and specular reflections. The deposition of a gold overlayer on the "specular films" causes initially an increase of resistance that is attributed to a surface roughening and a larger fraction of diffuse scattering. With further deposition of Au the resistance begins to decrease as the roughness reaches a maximum while the thickness of the conduction path is increased. The thickness of all the initial films is around 100 Å. From Lucas [8].

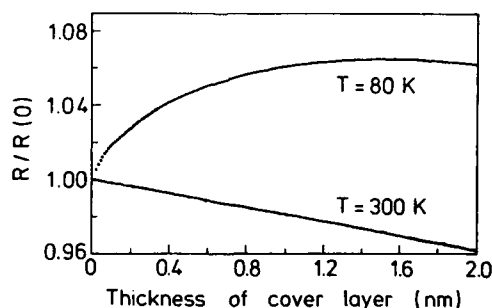


Fig.7. Change in resistance of a copper film prepared at 300K during coating with copper at 300 and 80K. From Jacob et al. [7].

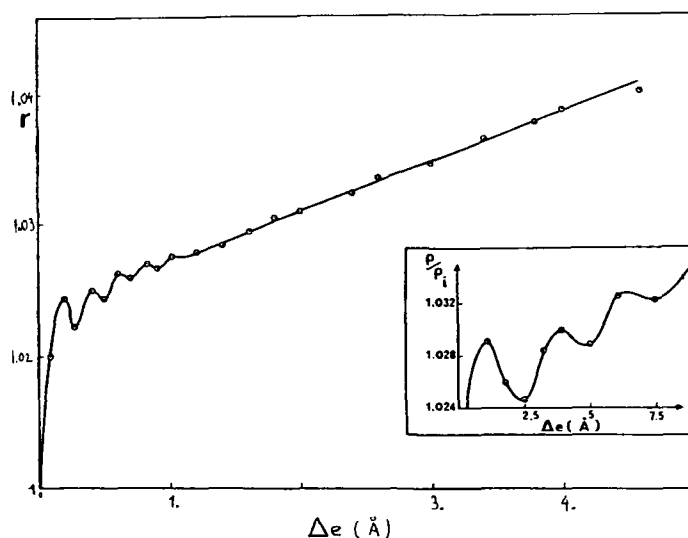


Fig.8. Oscillations of the resistivity of an annealed gold film as a function of the thickness of a surimposed gold layer. In contrast to the progressive increase in Figs. 6 and 7, the oscillations of the present case are characteristic of a layer by layer growth. The resistivity minima can be attributed to minima in the roughness for an integer number of atomic layers. From Chauvineau and Pariset [9].

There are several additional effects which also contribute to the thickness dependence of the resistivity. In polycrystalline films the most important of these effects arises from the thickness dependence of the grain size. An extension of the Fuchs-Sondheimer theory taking into account the grain boundary scattering (with some assumptions on the thickness dependence of the grain size) has been worked out by Mayadas and Shatzkes [11] and applied to many experimental results.

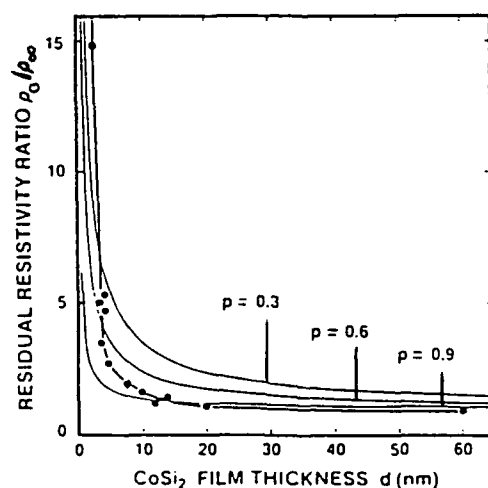


Fig.9. Low temperature residual resistivity of CoSi_2 single crystal films grown on Si(111) as a function of the film thickness. The thin lines refer to the Fuchs-Sondheimer calculations for different values of the parameter p . From Badoz et al. [10].

Nevertheless, even when these additional effects are taken into account, there are systematic departures from the theoretical predictions at small values of the parameter $k=d/\lambda$. In recent years the progress of the epitaxy techniques have enabled very thin single crystal films with long mean free path to be prepared and the departure from the Fuchs-Sondheimer theory in the regime $d/\lambda \ll 1$ to be studied. An example of experimental results obtained by Badoz et al. [11] on CoSi_2 is shown in Fig.9. The sharp upturn of the resistivity at small thickness cannot be fitted with the Fuchs-Sondheimer expressions and has been accounted for by recently developed quantum mechanical models. These models are described in the next paragraph.

QUANTUM MECHANICAL MODELS OF THE RESISTIVITY OF THIN FILMS

Full quantum mechanical treatments of conduction in thin films have recently been worked out by Tesanovic et al. [12] and Fishman and Calecki [13]. We describe the model of Fishman and Calecki. Its starting point is the following Hamiltonian for electrons (or holes) in an ideal film with perfectly plane surfaces.

$$H_0 = \frac{p^2}{2m} + V \left[Y(z - \frac{1}{2}d) + Y(-z - \frac{1}{2}d) \right] \quad (21)$$

where $Y(z)$ is the step function and V is the potential height outside the well for $z > d/2$ and $z < -d/2$. The quantization of the energy associated with the motion along the z axis gives rise to sub-bands and the energy in the sub-band v is written as:

$$E_{vk} = E_v + \hbar^2 k^2 / 2m \quad (22)$$

where k is a two-dimensional wave vector in the plane parallel to the surfaces. If the surface at $z = d/2$, for example, is rough, its equation becomes:

$$z = d/2 + f(\rho) \quad (23)$$

where ρ is a two-dimensional vector in the (x,y) plane ($f(\rho) \ll d$) and the scattering potential induced by the roughness is written as:

$$U = V \left\{ Y \left[z - \frac{d}{2} - f(\rho) \right] - Y \left(z - \frac{d}{2} \right) \right\} \approx -V f(\rho) \delta \left(z - \frac{d}{2} \right) \quad (24)$$

U is the only scattering potential in the model. There is no additional background scattering (in the notation of Fuchs-Sondheimer $\lambda = \infty$), so that the model is implicitly worked out for the case $\lambda/d \gg 1$. In particular the model cannot describe the situation with the non-uniform current density occurring in the Fuchs-Sondheimer theory for $\lambda/d \leq 1$. Thus, whereas the Fuchs-Sondheimer theory is relevant for relatively dirty systems, the Fishman-Calecki model is appropriate to describe very thin-high purity samples for which the Fuchs-Sondheimer theory is inadequate.

We now summarize the results obtained by calculating the scattering of the eigenstates of H_0 , Eq.21, by the roughness potential U , Eq.24. The simplest results are obtained in the limit $\xi k_1 \leq 1$ where k_1 is of the order of magnitude of the wave vector at the Fermi level and ξ is the correlation length of the roughness function $f(\rho)$ (for metallic films the condition $\xi k_1 \leq 1$ is obeyed if the surface profile is rough at the atomic scale). We first consider the case of a metal for which the number of occupied sub-bands N is very large. In this case the thickness dependence of the resistivity calculated by Fishman and Calecki [3] is written:

$$\rho \sim \frac{1}{d^2 \xi^2 \Delta^2} \left[1 - \frac{6}{(3 n \pi^5)^{\frac{1}{3}}} \times \frac{1}{d} \right] \quad (25)$$

This expression, for $10\text{\AA} < d < 200\text{\AA}$ and $n = 3 \times 10^{22} \text{cm}^{-3}$ is equivalent to $\rho \sim d^{-2.1}$. The experimental thickness dependence of the resistivity for the metallic films in the limit $d \ll \lambda$ is in much better agreement with $\rho \sim d^{-\alpha}$, $\alpha \lesssim 2$ predicted by the quantum mechanical models than with the variation $\rho \sim d^{-1}$ of the Fuchs-Sondheimer theory. For CoSi_2 thin films Badoz et al [10] derive $\alpha = 2.3$. Fig. 10 shows the good agreement obtained by Fishman and Calecki between their calculation (solid line) and the experimental results of Badoz et al on CoSi_2 . The best fit is obtained with $\xi = 2\text{\AA}$ for the correlation length of the roughness function, $\Delta = 4\text{\AA}$ for the root mean square of the height of the bumps on the surface and $n = 3 \times 10^{22} \text{cm}^{-3}$ for the electron density.

In the opposite limit, for $N = 1$ (one occupied subband), a variation of ρ as d^{-6} is found in the model of Fishman and Calecki. This is a well known limit for bi-dimensional semiconductors. For metals, N can be a relatively small integer only in films composed of a few ML. In this thickness range the variation of the resistivity as a function of the thickness is expected to show oscillations correlated with the change of N between integer values and superimposed to a crossover from $\alpha = 2.1$ to $\alpha = 6$. To our knowledge such quantum size effects have never been observed up to now.

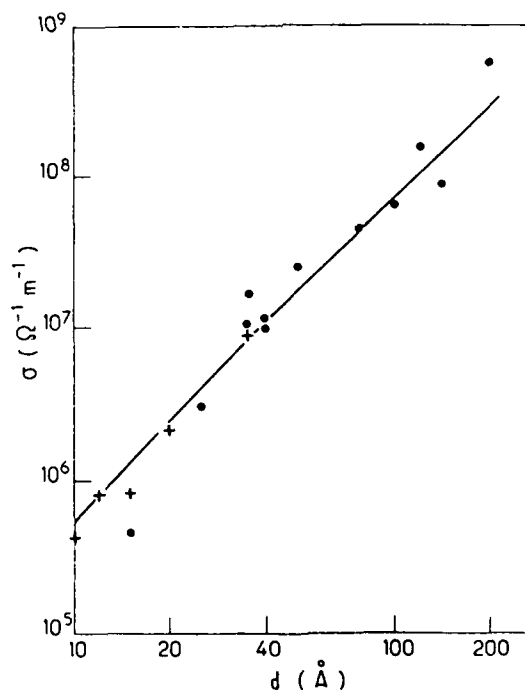


Fig. 10. Low temperature inverse residual resistivity $\sigma(d) = [\rho(d) - \rho(\infty)]^{-1}$ as a function of the film thickness d for two CoSi_2 samples. Symbols : experimental results of Badoz et al.[10]. Solid line : best fit between the data and the Fishman-Calecki model [13].

ELECTRON TRANSPORT IN MULTILAYERS

The theoretical models developed to describe the resistivity of multilayers are extensions of the Fuchs-Sondheimer theory for thin films. The simplest and most convenient model has been worked out by Carcia and Suna [14]. These authors introduce a probability p of coherent passage across an interface which is equivalent to the probability p of specular reflection in the Fuchs-Sondheimer theory. The probability of diffuse scattering at the interface is $1-p$ (this implies that the probability of specular reflection is zero). The calculation is similar to that described in 1: the functions $g^+(z)$ and $g^-(z)$, because of the interface scattering, have a minimum at the interfaces ($g=0$ at the interface if $p=0$) and vary exponentially inside the layers. The total current is obtained by integrating g over z , and Carcia and Suna [14] find for the conductivity of the multilayer:

$$\sigma(d_1+d_2)=d_1\sigma_1+d_2\sigma_2+[(\lambda_2\sigma_1+\lambda_1\sigma_2)p-\lambda_1\sigma_1-\lambda_2\sigma_2] I - (1-p^2)[\sigma_1\lambda_1J_1+\sigma_2\lambda_2J_2] \quad (26)$$

where d_1 and d_2 are the layer thicknesses, σ_1 , σ_2 and λ_1 , λ_2 are the conductivities and mean free paths of the two metals, and:

$$\begin{aligned} I &= \frac{3}{2} \int_0^1 d\mu \frac{\mu (1-\mu^2) (1-e_1) (1-e_2)}{(1-p^2 e_1 e_2)} \\ J_1 &= \frac{3}{2} \int_0^1 d\mu \frac{\mu (1-\mu^2) (1-e_1) e_2}{(1-p^2 e_1 e_2)} \\ J_2 &= \frac{3}{2} \int_0^1 d\mu \frac{\mu (1-\mu^2) (1-e_2) e_1}{(1-p^2 e_1 e_2)} \end{aligned} \quad (27)$$

with $e_i = \exp(-d_i/\lambda_i\mu)$

It is easy to check that these expressions of the conductivity bears a resemblance with the expressions of the Fuchs-Sondheimer theory. For example, for $\sigma_1=\sigma_2=\sigma_0$, $\lambda_1=\lambda_2=\lambda$, $p=0$ one obtains for s exactly Eq.11, as expected for the situation of independent thin films of thickness d and mean free path λ . The limit $k=d/\lambda \gg 1$ again gives the typical variation of the resistivity as d^{-1} , Eq.14 :

$$\rho \sim [1/\lambda + 3/8d] \quad (28)$$

When p is different from 1, the contribution from the interfaces to the resistivity decreases and, in addition, there is some averaging of the relaxation rates in the two metals. In the limit $\lambda_1, \lambda_2 \gg d_1, d_2$ the current is uniform and there is complete averaging of the relaxation rates due to interface scattering and to background scattering in the metals 1 and 2.

A more sophisticated model has been developed by Dimmich [15]. This model introduces different parameters p_1 and p_2 , where p_1 (p_2) is for the passage from metal 1 (2) to metal 2 (1), and takes into account the scattering by grain boundaries in polycrystalline films.

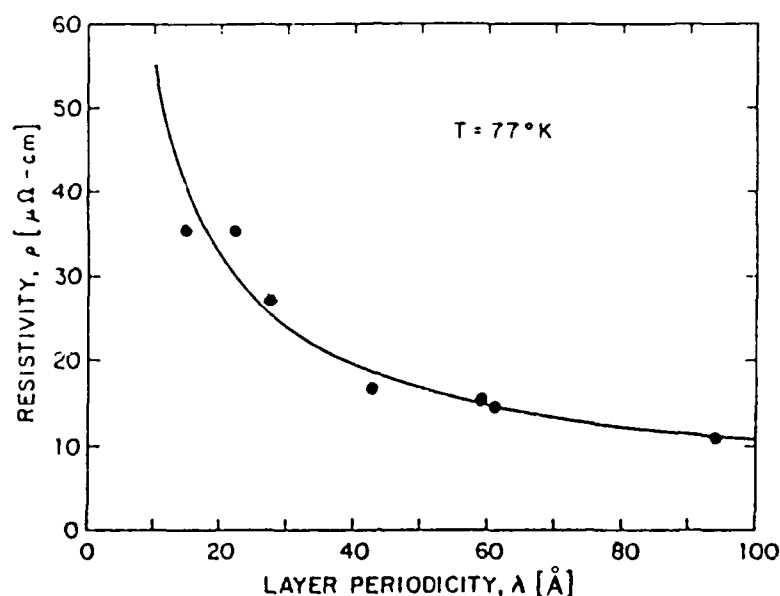


Fig. 11. Resistivity at 77 K of Pd/Au multilayers as a function of the multilayer periodicity. The solid curve is calculated from Eqs 26 and 27 with $p=0$. From Carcia and Suna [14].

There are few experimental results on the resistivity of metallic multilayers. In Fig. 11 we show the thickness dependence of the resistivity of Pd/Au multilayers at 77 K; a satisfactory fit is obtained by calculating the resistivity from Eq. 26 and 27 with $p = 0$. At room temperature it is necessary to introduce some coherent transmission ($p \neq 0$) to account for the experimental results [15]. The experimental results are too few and more extensive data are needed for a better insight into the physics of the electron transport in metallic multilayers.

Finally, as in thin films, quantum size effects are expected in multilayers as well. In a superlattice with a periodicity of n atomic planes, the Brillouin zone is reduced by a factor n in the perpendicular direction to the layers. This leads to folded dispersion curves of the electrons and to (small) gaps in the conduction band. For metallic multilayers with layer thicknesses in the ML range (and very well defined interfaces) the resulting oscillations of the resistivity as a function of the layer thickness could possibly be detected, especially in the perpendicular direction.

TRANSPORT PROPERTIES OF MAGNETIC FILMS AND MULTILAYERS

The magnetic thin films and multilayers present specific effects that are related to the interplay between electron transport and magnetism. First the transport measurements are a convenient tool to follow the field dependence of the magnetization, through the Hall effect and the magnetoresistance [16]. In addition the giant magnetoresistance of the magnetic multilayers is an interesting specific effect that we will describe in some detail. The first example of this giant magnetoresistance was found in Fe/Cr superlattices by Baibich et al. [7]. Typical results are shown in Fig. 2. This magnetoresistance is associated with the existence of antiferromagnetic exchange coupling between the Fe layers across the Cr layers (the Cr layers are non-magnetic or weakly magnetic). At zero field the magnetizations of neighbor Fe layers are antiparallel and the resistivity has its maximum value. By aligning the magnetizations of all the layers with an applied field, one reduces the resistivity. In Fig. 12 the reduction factor is almost two for the sample having the thinnest Cr layers. When the Cr thickness is increased, the magnetoresistance decreases steeply. The dependence on the thickness of Fe is

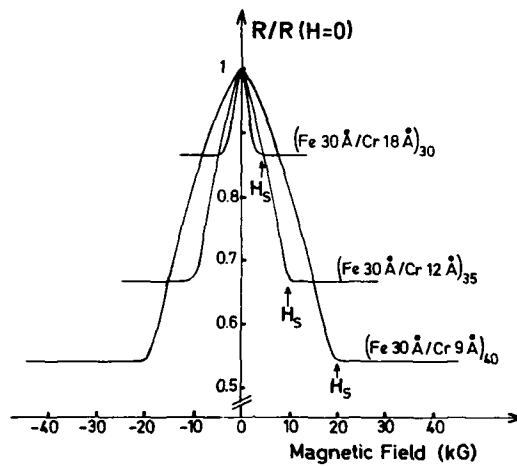


Fig.12. Magnetoresistance of Fe/Cr superlattices at 4.2K. H_s is the saturation field needed to align the magnetic moments of the iron layers. From Baibich et al.[17].

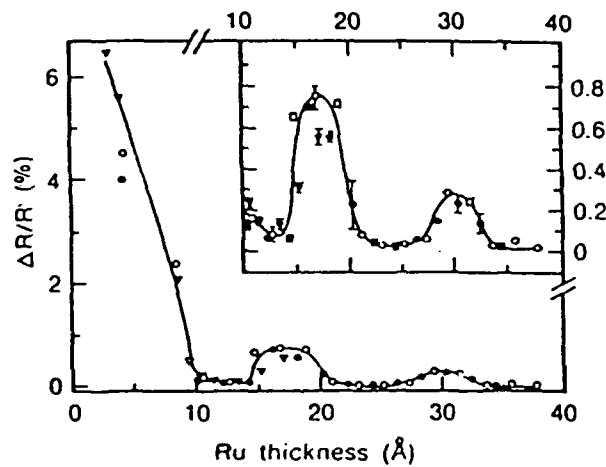


Fig.13. Maximum magnetoresistance as a function of the thickness of Ru for (Co 20 Å / Ru) multilayers. The multilayers are prepared by sputtering on Si(111) substrates at temperatures of 40°C (●), 125°C (○) and 200°C (×) From Parkin et al.[19].

less pronounced. As the temperature increases, the magnetoresistance decreases but is still very large at room temperature (around 20% in some samples). This is of interest for applications to magnetoresistive sensors.

Similar results have also been obtained for Fe/Cr multilayered structures by Binasch et al.[19], Krebs et al.[20], Parkin et al.[21], Araki et al.[22].

The giant magnetoresistance of the Fe/Cr multilayers has been ascribed to **spin dependent scattering** by the interfaces or, alternatively, by impurities or defects within the Fe layers [17, 23-25]. This spin dependence is related to the spin dependence observed for impurity scattering in ferromagnetic metals such as Ni, Fe or Co [26]. In these metals there is no spin-flip scattering at $T \ll T_c$ (because the main spin-flip scattering mechanism is via exchange interaction between the s carriers and the d electrons, that is, through creation or annihilation of spin waves), so that the current is carried by the spin \uparrow and spin \downarrow electrons in two independent channels. This is the "two-current model." [26] The two currents can be very different because certain transition metal impurities scatter the spin \uparrow and spin \downarrow electrons very differently. This is due to combined effects involving the spin splitting of the host d band, the spin splitting of the impurity d levels and the different hybridization between the host and impurity d states for the spin \uparrow and spin \downarrow directions. For example, Cr impurities in Fe scatter much more strongly the spin \uparrow electrons, which results in a ratio of 6 between the resistivities of the spin \uparrow and spin \downarrow channels, $r = \rho_{\uparrow} / \rho_{\downarrow} \sim 6$ [28].

To describe the mechanism of the magnetoresistance in the simplest way, we first consider the following limit : (i) electron mean free path λ much larger than the layer thickness, (ii) non-spin-flip scattering, that is, $T \ll T_c$. For $H > H_s$ the magnetizations of all the Fe layers are parallel, there is a spin direction that is less scattered at all the interfaces and the resulting short-circuit effect gives a low resistivity, $\rho_0 = \rho_{\uparrow}\rho_{\downarrow}/(\rho_{\uparrow} + \rho_{\downarrow})$ where ρ_{\uparrow} and ρ_{\downarrow} are the resistivity in the spin \uparrow and spin \downarrow channels. In contrast, for $H = 0$, an electron with a given spin is alternately weakly and strongly scattered, which leads to an average value of the resistivity, $\rho_1 = (\rho_{\uparrow} + \rho_{\downarrow}) / 4$. The resistivity drop from ρ_1 to ρ_0 during the magnetization of the sample can be large if ρ_{\uparrow} and ρ_{\downarrow} are very different.

Now, suppose that the thickness of Cr, t_{Cr} increases and becomes larger than the mean free path λ . From the general properties of the Boltzmann equation, the perturbation of the electron distribution function cannot extend farther than λ . For $t_{Cr} \gg \lambda$, there will be an electron layer of thickness λ around each interface affected by the scattering at this interface but completely independent of the magnetization at the other interfaces. The magnetoresistance will vanish as $\exp(-t_{Cr}/\lambda^*)$ (with λ^* of the order of magnitude of λ) [22], which explains the dependence on t_{Cr} .

The magnetoresistance is also expected to decrease as the temperature increases. This is first because the collisions with spin waves will tend to equalize the spin \uparrow and spin \downarrow currents, secondly because the reduction of λ increases t_{Cr}/λ .

Several theoretical treatments of the magnetoresistance arising from spin dependent scattering in magnetic multilayers have been worked out. The model of Camley and Barnas [23] is based on a semi-classical approach of the Fuch-Sondheimer type and proposes a numerical calculation of the magnetoresistance. The model of Ref. [24] is also semi-classical and gives analytical expressions of the magnetoresistance for some simple cases. The model of Levy and coworkers [25] is based on a quantum mechanical treatment. Typical thickness dependences predicted by this model are shown in Fig. 14.

Large magnetoresistance effects have also been found in other multilayered structures. The Co/Ru system is similar to Fe/Cr, with the same type of antiferromagnetic interlayer coupling but smaller magnetoresistance effects [19]. Like in Fe/Cr where the magnetoresistance depends strongly on the thickness of Cr, the magnetoresistance decreases steeply when the thickness of Ru increases, see Fig.13. In addition one remarks that the magnetoresistance almost disappears for thicknesses of Ru around 13 and 34 Å, which is probably due to a crossover from antiferromagnetic to ferromagnetic interlayer coupling in these thickness ranges [21].

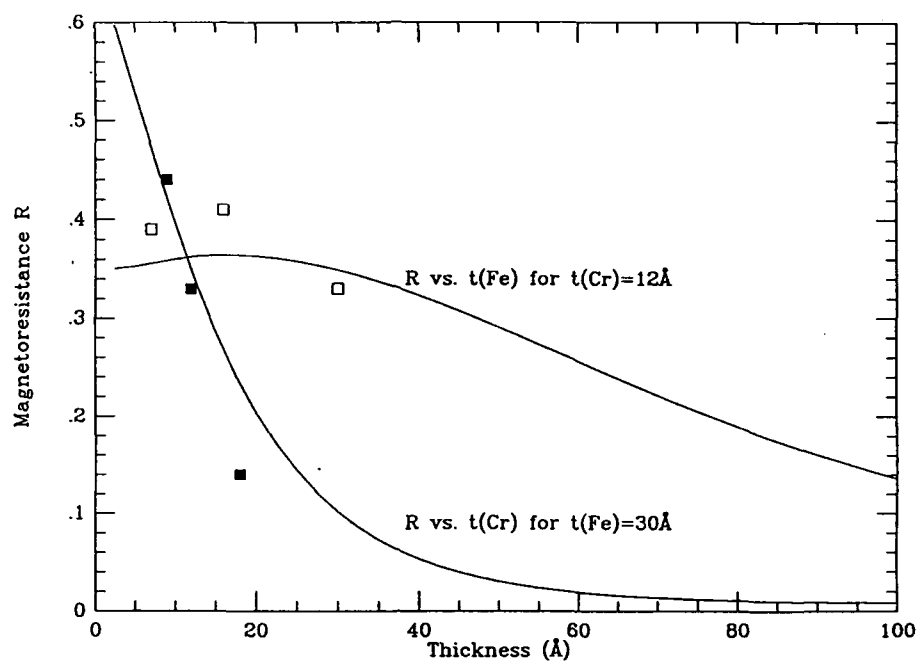


Fig.14. Calculated curves and experimental data for the dependence of the magnetoresistance of (Fe, tFe / Cr, tCr) multilayers as a function of the thickness of Fe (for tCr = 12 Å) and as a function of the thickness of Cr (for tFe = 30 Å). R is the ratio of the maximum resistivity change to the maximum resistivity and is calculated in the model of Levy et al.[23]. The experimental data are from Ref. [21].

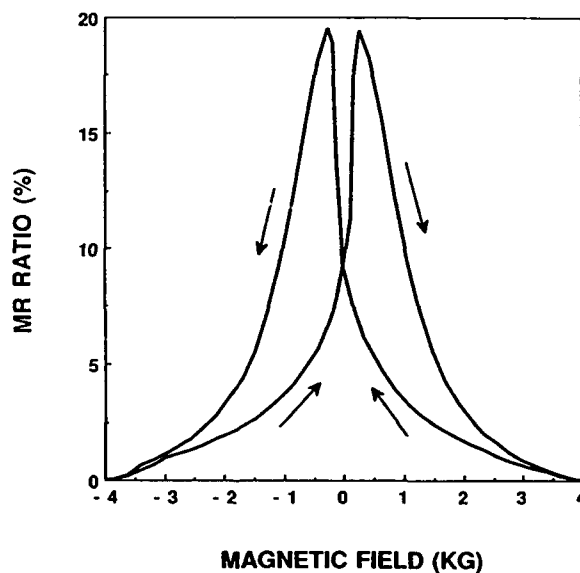


Fig.15. Magnetoresistance of a 6x(Co5Å/Ag60Å/Co60Å/Ag60Å) multilayer at 4.2K [31].

The case of Au/Co, Ag/Co and Cu/Co multilayered structures is different [27-31]. The antiparallel alignment enhancing the resistivity is not obtained by antiferromagnetic interlayer exchange but by some difference in the coercivities of the odd and even layers. The magnetization reversal does not occur at the same field in neighbor Co layers and there is a field range with some degree of disorder in the magnetizations of neighbor Fe layers. The difference in the coercivity of the neighbor layers is obtained by different thicknesses [28,30] or different crystal structures [27,31]. As a matter of fact, even without any difference between the odd and even layers, there is still some degree of antiparallel alignment and a peak of magnetoresistance during the magnetization reversal [29,31]. Interesting results, with a relatively large magnetoresistance at very small fields have been also obtained in multilayers based on permalloy and Co. In the work of Dieny et al. [30] on NiFe/Cu/NiFe structures, one of the NiFe layers is pinned by an overlayer of FeMn, while the magnetization of the second NiFe layer rotates freely. In the work of Shinjo et al. [31] on NiFe/Au/Co structures, the magnetization of the NiFe layer can be reversed at a much smaller field than that of the Co layer (a MR of 10% at Room Temperature has been obtained in these structures). In Fig.15 we show the large magnetoresistance (20% at 4.2K) recently found in Ag/Co multilayers having different thicknesses for the odd and even layers of Co [32].

REFERENCES

- 1) K. Fuchs, Proc. Camb. Phil. Soc. 1938, 34, 100.
- 2) E.H. Sondheimer, Ad. Phys. 1952, 1, 1.
- 3) L.I. Maissel, Handbook of Thin Film Technology, edited by L.I. Maissel and R. Glang (Mc Graw Hill, New York) 1970, Chapter 13, 1.
- 4) J.M. Ziman, Electrons and Phonons (Clarendon Press, Oxford) 1960, 267.
- 5) D.S. Campbell, The Use of Thin Films in Physical Investigations (Academic Press, New York) 1966, p. 299.
- 6) E.R. Andrew, Proc. Phys. Soc. A, 1949, 62, 77.
- 7) U.Jacob, J.Vancea and H.Hoffmann, Phys. Rev. B 1990, 42, 11852.
- 8) M.S.P. Lucas, Appl. Phys. Letters 1964, 4, 73.
- 9) J.P. Chauvineau and C. Pariset, Surface Science 1973, 36, 155.
- 10) P.A. Badoz, A. Briggs, E. Rosencher, F. Arnaud d'Avitaya and C d'Anterrosches, Appl. Phys. Lett. 1987, 51, 169.
- 11) A.F. Mayadas and M. Shatzkes, Phys. Rev. B 1970, 1, 1382.
- 12) Z. Tesanovic, M.V. Jaric, S. Maekawa, Phys. Rev. Lett. 1986, 57, 2760.
- 13) G. Fischman, D. Calecki, Phys. Rev. Lett. 1989, 62, 1302.
- 14) P.F. Garcia and A. Suna, J. Appl. Phys. 1983, 54, 2000.
- 15) R. Dimmich, J. Phys. F. 1985, 15, 2477.
- 16) E.D. Dahlberg, K. Riggs, G.A. Prinz, J. Appl. Phys. 1988, 63, 4270.
- 17) M.N. Baibich, J.M. Broto, A. Fert, F. Nguyen Van Dau, F. Petroff, P. Etienne, G. Creuzet, A. Friederich, J. Chazelas: Phys. Rev. Letters, 1988, 61, 2472.
- 18) A. Barthélmy, A. Fert, M. Baibich, S. Hadjoudj, F. Petroff, P. Etienne, R. Cabanel, S. Lequien, J. Appl. Phys. 1990, 67, 5908.
- 19) G. Binasch, P. Grünberg, F. Saurenbach, W. Zinn, Phys. Rev. B, 1989, 39, 4828.
- 20) J.J. Krebs, P. Lubitz, A. Chaiken, G.A. Prinz, Phys. Rev. Letters 1989, 63, 1645.
- 21) S.S.P. Parkin, N. More, K.P. Roche, Phys. Rev. Lett. 1990, 64, 1990.
- 22) S. Araki, T. Shinjo, Jap. J. Appl. Phys. 1990, 29, 621.
- 23) R.E. Camley and J. Barnas, Phys. Rev. Letters 1989, 63, 664.
- 24) A. Barthélmy, Thesis (Orsay 1990) and to be published.
- 25) P.M. Levy, K. Ounadjela, S. Zhang, Y. Wang, C.B. Sommers, A. Fert, J. Appl. Phys. 1990, 67, 5914. S. Zhang, P.M. Levy and A. Fert, to be published.
- 26) A. Fert and I.A. Campbell, J. Phys. F 1976, 6, 849; I.A. Campbell and A. Fert, Ferromagnetic Materials, edited by E.P. Wohlfarth (North Holland, Amsterdam) 1982, Vol. 3, p. 769.
- 27) J. Barnas, A. Fuss, R.E. Camley and W. Zinn, to be published.
- 28) C. Dupas, P. Beauvillain, C. Chappert, J.P. Renard, F. Triqui, E. Velu, D. Renard, J. appl. Phys. 1990, 67, 3292.
- 29) T. Takahata, S. Araki, T. Shinjo, J. Mag. Mat. 1989, 82, 287.

- 30) D.H.Mosca,A.Barthélémy,F.Petroff,A.Fert,P.A.Schroeder,W.P.Pratt,R.Laloe,
R.Cabanel,Symposium C of theE-MRS Spring Meeting(Strasbourg 1990),to
appear in J.Mag.Mat.
- 31) P.Etienne,F.Petroff,D.H.Mosca,A.Barthélémy,A.Fert,to be published.
- 32) B. Dieny, V.S. Speriosu, B.A. Gurney, S.S. Parkin, D.R. Wilhoit, K.P. Roche,
Symposium C of the E-MRS Spring Meeting (Strasbourg 1990) to appear in J.
Mag-Mag.Mat.
- 33) T. Shinjo, N. Hosiito, S. Araki, K. Mibu and S. Ogawa, Symposium C of the
E-MRS Spring Meeting (Strasbourg 1990) to appear in J. Mag-Mag.Mat.

MICROMAGNETICS OF LONGITUDINAL RECORDING MEDIA

P.S. Alexopoulos, I.R. McFadyen, I.A. Beardsley, T.A. Nguyen and
R.H. Geiss

IBM Research Division
Almaden Research Center
650 Harry Road
San Jose, CA 95120-6099

INTRODUCTION

Future needs in high density magnetic storage devices require increases both in linear and track densities. The latest 1 Gigabit per square inch areal density for longitudinal media demonstrated by IBM¹ has reduced the bit size to dimensions comparable to the characteristic micromagnetic length scales of today's media. Improvement or extension of the current recording limits requires detailed knowledge of micromagnetics and their manipulation or tailoring through the microstructure of the utilized magnetic thin films.

The recent interest in micromagnetics of "hard" magnetic materials in the recording industry was a result of the use of metal thin-film longitudinal media as a substitute for particulate oxide media for high density recording applications. While cobalt based alloyed thin film media demonstrated clear advantages in a number of areas such as: thickness uniformity, saturation magnetization, squareness, coercivity range, resolution, processing, etc., they were shown to demonstrate inferior noise performance in comparison to oxide particulate media or sputtered $\gamma\text{-Fe}_2\text{O}_3$ ². The frequency dependence of noise indicated that the measured media noise was associated with the transitions and was speculated to arise from fluctuations in the zig-zag transitions between adjacent recorded bits. Further recording studies by Y.S. Tang and E. Yarmchuk³ showed a correlation between the media noise and transition peak jitter. An early investigation of written transitions recorded on a series of cobalt based alloys using Lorentz microscopy by Alexopoulos et. al.⁴ showed that the domain wall structures observed in the transition zones are more complex than previously assumed in the literature and contain not only (180° walls) zig-zags but also vortex structures and intermediate states between the two.

Effort has been made by a number of investigators to quantify the micromagnetic structures of written bits by a set of parameters that can eventually be correlated to material microstructural parameters and functional performance. These efforts are accompanied by parallel efforts in the development of modelling using large scale numerical micromagnetic simulations. This paper presents a short review of the micromagnetic quantification and simulation studies of thin film magnetic materials performed by the authors at the IBM Almaden Research Center.

MAGNETIC CHARACTERIZATION OF THIN FILMS

The magnetic characterization of thin film magnetic media can be performed at different levels: functional performance, macromagnetic, and micromagnetic. The

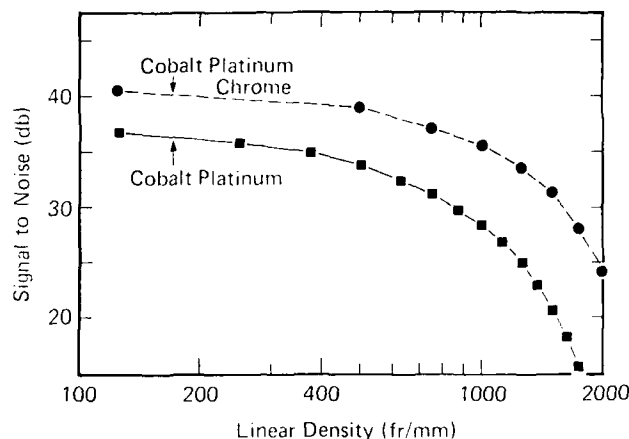


Figure 1. Signal-to-Noise Ratio of CoPtCr and CoPt thin films.

functional performance characterization determines relevant recording parameters such as media signal and noise, overwrite modulation, soft and hard errors and rates, etc.

The macromagnetic characterization techniques include: vibrating sample magnetometry, torque measurements and ferromagnetic resonance. These techniques provide measurements of macroscopic magnetic parameters such as coercivity, magnetization (remanence and saturation), squareness (S & S^*), H_k etc. These parameters represent mean values of macroscopic magnetic properties and do not provide much quantitative information on the distribution of local magnetic properties in the film. Even in cases in which the dispersion information is included in the data (example: switching field distribution or hysteresis loss torque curves) it is practically impossible to deconvolute these information in order to obtain distributions of specific parameters such as magnetic anisotropy, exchange constant etc.

While the macroscopic parameters are useful for media development they are not adequate to predict the functional performance of recording media. For example, CoPt and CoPtCr thin films with similar macromagnetic parameters (such as H_c , M_s , S, S^* etc.) can have dramatically different signal to noise ratios. Figure 1 stresses the need for understanding the micromagnetic properties of media.

Finally by the term micromagnetic characterization we mean determination of magnetic properties with spatial resolution comparable to domain wall dimensions. There are currently three types of micromagnetic measurements with adequate spatial resolution for recording media:

1. Lorentz microscopy in Fresnel, Foucault or differential phase contrast (DPC) modes.
2. Magnetic force microscopy.
3. Spin polarized electron microscopy.

Lorentz microscopy is the characterization technique employed in all of our studies. Since Lorentz microscopy is based on transmission electron microscopy, it can provide high spatial resolution information on domain structures in thin magnetic films. The conventional phase contrast techniques of Foucault and Fresnel Lorentz microscopy provide image contrast of the domains and domain walls. Differential phase contrast Lorentz microscopy (DPC), which is performed in the STEM mode, provides very high resolution (down to 100 Å) and directly measures the in-plane magnetic induction of the thin film sample and the associated stray fields integrated along the electron trajectory⁵.



Figure 2. (a) Foucault and (b) Fresnel images of magnetic track.

IMAGING OF MAGNETIC WRITTEN BITS

Lorentz electron microscopy in Fresnel, Foucault and DPC modes has been used to study the written bit patterns on cobalt-based alloys under a variety of recording conditions. Examples of Foucault and Fresnel images of magnetic tracks with uniform bit density recorded on previously DC saturated longitudinal $\text{Co}_{80}\text{Cr}_{20}$ sputtered thin films with thickness of 150 Å are shown in Figures 2a and 2b.

The Lorentz images shown in Figure 2 reveal three distinct regions in the recorded tracks: the recorded bits, the transition zones between adjacent bits and a complex structure at the sides of the bits (side-writing) which is generated by the fringing field of the inductive head. The Fresnel image (Figure 2b) shows the presence of magnetic ripple structure in all regions of the track. The structure of the ripple in the bits is very similar to that in the DC erased background indicating that the bits are in a saturated remanence state. A very complex "vortex like" domain wall structure can be observed in Figure 2b at the transition zone between oppositely magnetized bits. The transition zones were further investigated using discrete magnetic recording tracks and DPC imaging. DPC images of recorded bits on a discrete track and the induction vector map calculated from them are shown in Figures 3a and 3b.

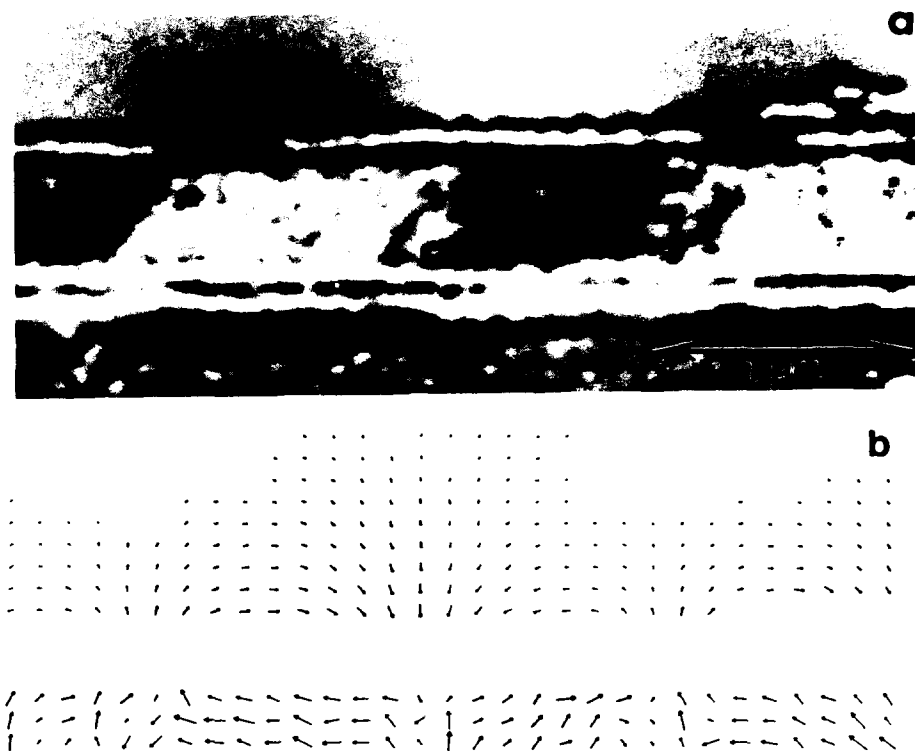


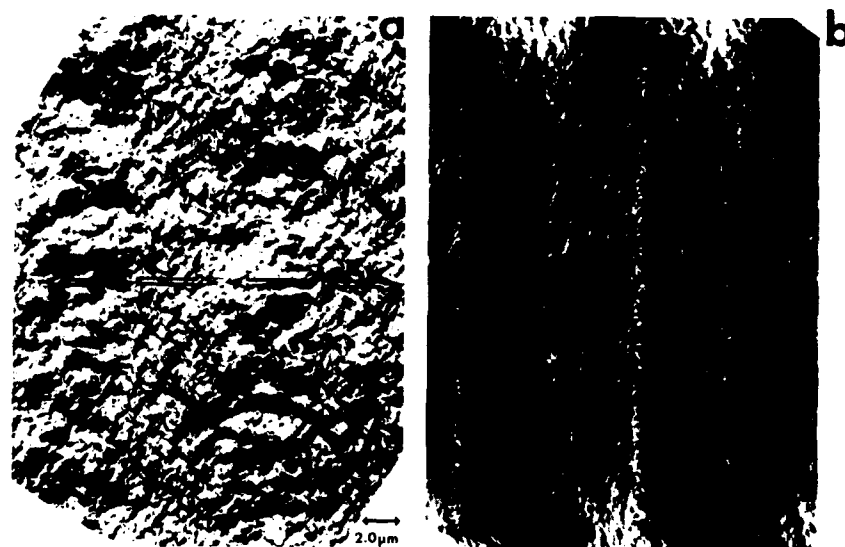
Figure 3. (a) DPC images and (b) calculated induction vector map of recorded bits on a discrete track.

A very interesting feature of the image in Figure 3a is of an apparent tilted of the transition zone. The associated induction vector map reveals that there is in fact a magnetization vortex at this point.

The type of ripple structure observed within the bit and at the transition zones is not only very much material dependent as we shall elaborate in the following section but also correlates with the functional signal-to-noise measurement. Figures 4a and 4b, for example, show Lorentz images of bits corresponding to CoPt and CoPtCr media with similar functional performance to the media shown in Figure 1. It is clear from those images that the CoPtCr (which has higher signal-to-noise ratio) has a better bit definition with smaller scale ripple structure in the bits in contrast to CoPt that shows a high density of vortices.

A three-dimensional self-consistent write process model was used to model the magnetization pattern at the edge of a written track ⁶. A vector loop model, assuming an isotropic in-plane distribution of anisotropy, was adjusted to match the remanence and coercivity of the $\text{Co}_{80}\text{Cr}_{20}$ alloy. The grid represented a $0.25 \times 0.015 \times 0.25 \mu\text{m}$ volume of medium. The head field on this grid was obtained using the 3-d finite element TOSCA model for a head-to-medium separation of $0.1 \mu\text{m}$. Except for a narrow track width, the head parameters were those of the standard thin film head used for writing. The mismatch between the pole tip widths was $1.0 \mu\text{m}$ on each side. The head was positioned with its center at the edge of the medium and a single transition was written. The maximum write field was varied between two and approximately five times the coercivity. The resultant magnetization patterns were appropriately folded and duplicated to obtain the patterns in Figure 5.

A comparison between the simulated side-written structure observed in Figure 5 and the experimental results in Figure 2 indicates very good qualitative agreement.



CoPt

CoPtCr

Figure 4. Lorentz images of bits of (a) CoPt and (b) CoPtCr media.

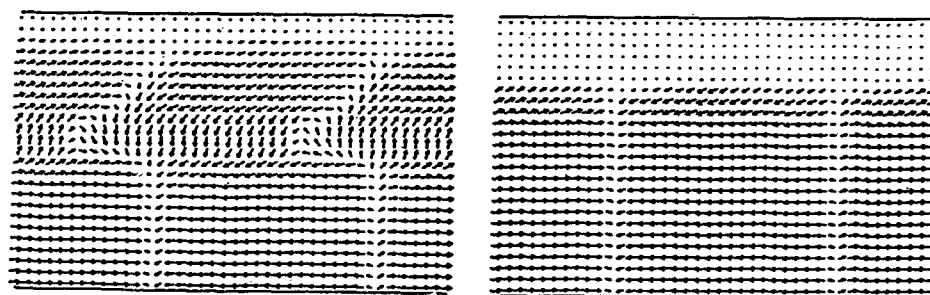


Figure 5. Simulated magnetization pattern at the edge of a written track .

QUANTIFICATION OF MAGNETIC RIPPLE STRUCTURE

The micromagnetic ripple or "feather" structure is the result of local minimization of the total magnetic energy given by the equation

$$E_{total} = E_{exchange} + E_{anisotropy} + E_{demagnetizing} + E_{Zeeman}$$

The exchange interaction in polycrystalline films has two components. The first component is the interatomic exchange and the second is the intergranular exchange which describes the interaction between neighboring crystallites. The anisotropy also has two terms: The crystalline anisotropy which, in the case of cobalt and its alloys, is strong and uniaxial with the easy magnetic axis coinciding with the *c* crystallographic direction. The stress induced anisotropy is rather small in the case of the cobalt alloys of interest and can generally be ignored. Since the recorded information is in the remanent state, the Zeeman energy term is equal to zero. The domain size is therefore determined by the competition between the magnetic forces (exchange and magnetostatic) and the local anisotropies.

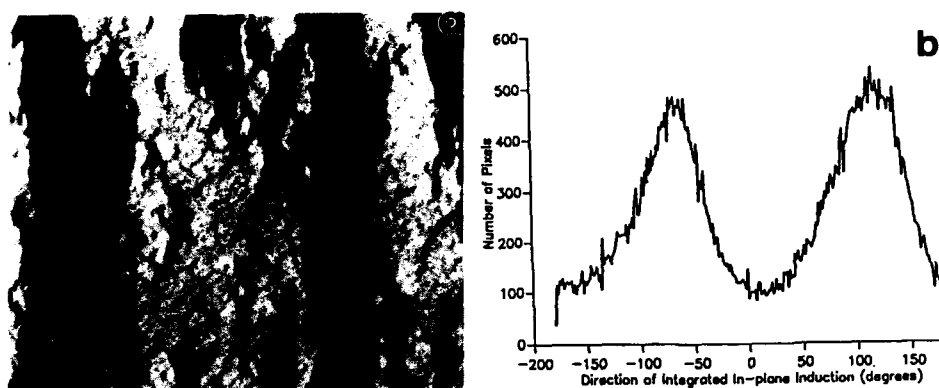


Figure 6. (a) DPC image and (b) greyscale histogram of CoPt media.



Figure 7. Effect of chemical alloying on media ripple structure.

DPC imaging can be used to quantify the angular distribution and the mean wavelength of the magnetization ripple seen in these film. Since two orthogonal DPC images provide a complete description of the magnitude and direction of the integrated in-plane induction through the film they can be used to generate an image where the intensity at each pixel is proportional to the direction of the integrated induction at that point, (using $\theta = \tan^{-1}(y/x)$). This corresponds to a directional map of the integrated induction. An image of this type is shown in figure 6a. A greyscale histogram of this image is shown in figure 6b and gives directly the number of pixels (and hence the area) within the image which has each given magnetization direction. The two peaks in the

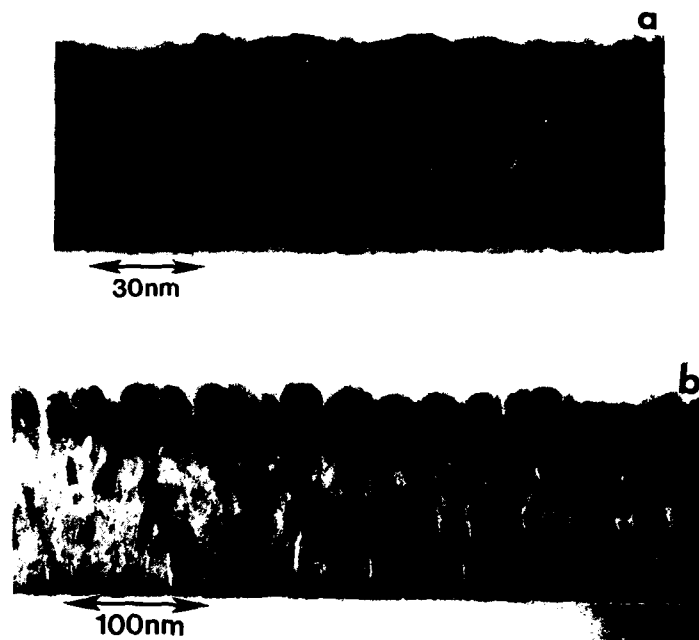


Figure 8. Cross-section TEM images showing the effect of (a) thin and (b) thick underlayers.

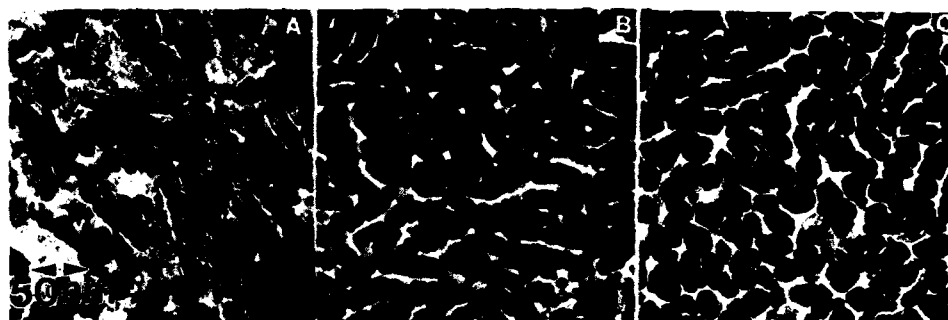


Figure 9. Plane view TEM images of microstructures of CoPtCr/Cr thin films using sputtering pressure of (a) 3, (b) 6, (c) 24 mtorr.

histogram correspond to the two magnetization directions within the film. The full width at half maximum of the peaks is a direct measure of the angular dispersion of the magnetization within the domains in the image. From directional maps of the integrated induction it is apparent that the magnetization ripple in these films is longitudinal. That is to say that the magnetization varies to the left and then to the right of the mean magnetization direction within a domain as you travel along the mean direction. In one ripple wavelength the component of magnetization at 90° to the mean direction will start at a maximum, decrease through zero to a minimum, and then increase again to a maximum. The mean wavelength of the ripple can be obtained by generating the autocorrelation function of this, transverse, component of integrated induction. For a wave of period λ the first zero crossing of the autocorrelation function corresponds to $\lambda/4$. The autocorrelation function of the transverse component of magnetization is generated by taking the DPC image corresponding to the transverse component,

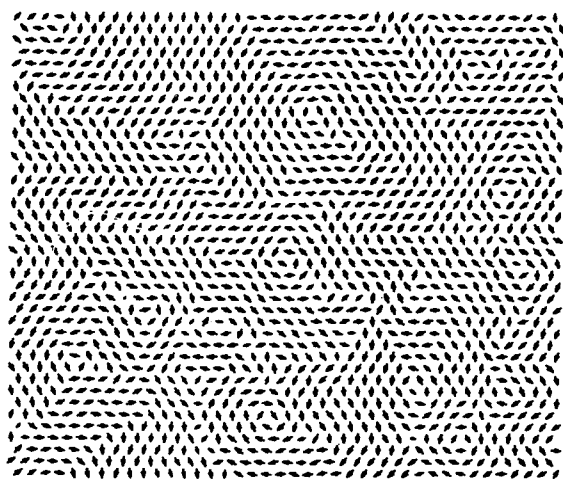


Figure 10. Simulated micromagnetic structure showing coherent magnetization regions, magnetization vortices and ripple structure.

multiplying it by a copy of itself which has been shifted by x' pixels along the mean magnetization direction and finding the resulting mean value within the region of overlap. This mean value as a function of x' corresponds to the autocorrelation function, and the first zero crossing gives the ripple $1/4$ wavelength. Hence both the angular distribution of the magnetization about the mean direction and the mean ripple wavelength can be obtained using DPC Lorentz microscopy.

MICROSTRUCTURE / MICROMAGNETICS

As discussed in the previous section, the micromagnetic structure of thin films is controlled by the degree of coupling between the magnetic forces (exchange and magnetostatic) and by the magnitude as well as the extent to which anisotropy is distributed. There is a number of ways that these interactions can be controlled through the microstructure of the thin films. This includes chemical alloying, use of nucleating underlayers, and deposition parameters.

In the case of alloying, if the films are continuous and compact, the exchange and magnetostatic interactions are both proportional to the saturation moment of the material. Therefore a reduction of the saturation moment by chemical alloying (with Cr, Pt, Ni, etc.) will result in a reduction of magnetic coupling. The chemical alloying also causes an increase in the anisotropy field strength and therefore gives rise to finer ripple structure in the thin film media (Figure 7).

A different approach in reducing the magnetic coupling between adjacent grains is the physical separation of grains or cluster of grains and this results in the reduction of magnetic domain size to the dimension of grain or cluster size. The physical separation can be achieved by manipulating the deposition parameters or by using an underlayer material.

Using the Thornton diagram as a guide, recent works on sputtered thin films showed that by varying the sputtering pressure, deposition rate, substrate temperature, film thickness, atomic mass, etc., one can either fabricate compact and continuous, or columnar porous films. Deposition of the magnetic thin film on a porous columnar underlayer replicates the physical separation of grains or column of grains in the magnetic layer. Figures 8 and 9 illustrate the effect of Cr underlayer thickness and sputtering pressure respectively. In short, the tailoring of microstructure and hence

magnetic properties and functional performance of recording media has been achieved by using a combination of alloying effects and polycrystalline epitaxy on physically separated grains or columns.

NUMERICAL SIMULATIONS

Due to the complexity of the problem, analytic solutions of the micromagnetic equation are of limited value in the investigation of micromagnetic structures of polycrystalline recording materials. Large scale numerical simulations have been used by a number of investigators as a reliable and versatile input to the experimentalists. In these simulations the film is represented as a lattice of up to 256x256 pixels, each pixel, which is treated as a dipole, represents a grain in the polycrystalline film. The dipoles act under the influence of an effective field from the local random axis anisotropy, nearest neighbor exchange, and long range dipole-dipole interactions and the dynamics of its motion are governed by the Landau-Lifshitz-Gilbert equation. The simulations can trace the magnetization distribution in the array as a function of applied field and generate simulated macromagnetic measurements, domain images and vector maps of the magnetization distribution for comparison with experimental results. An example of a micromagnetic structure is given in figure 10. Coherent magnetization regions, magnetization vortices and ripple structure are plainly visible.

CONCLUSIONS

The understanding of functional performance of recording media requires the quantification of the micromagnetics and correlation to microstructural parameters. A number of tools are now available to carry out this quantification. Numerical simulations could be invaluable in guiding experimental work and facilitating understanding of the effects of microstructural parameters on recording performance.

ACKNOWLEDGEMENT

The authors would like to thank M. Moshref, M. Krounbi, T. Yogi, V. Speriosu, I. Sanders, S. Lambert, and C. Hwang for their useful contributions to this project.

REFERENCES

1. T. Yogi, C. Tsang, T. Nguyen, K. Ju, G. Gorman and G. Castillo
To be published in IEEE Trans. Magn. Fall 1990
2. N.R. Belk, P.K. George and G.S. Mowry,
IEEE Trans. Magn. MAG-21 (1985) 1350
3. Y.S. Tang, Noise autocorrelation in magnetic recording systems,
IEEE Trans. Magn. MAG-21 (1985) 1389-1391
4. P.S. Alexopoulos and R.H. Geiss,
IEEE Trans. magn. MAG-22, (1986) 566-569
5. I.R. McFadyen, J. Appl. Phys. 64 (1988) 6011
6. I.A. Beardsley, Three dimensional model for magnetic recording,
IEEE Trans. Magn. MAG-22 (1986) 361

MO-RECORDING: THE SWITCHING PROCESS AND ITS RELATION TO THE MAGNETIC
PROPERTIES OF THIN FILMS

D. Mergel, P. Hansen, S. Klahn, D. Raasch

Philips Research Laboratories. Hamburg
P.O.B. 540840, D-2000 Hamburg 54 (FRG)

1. INTRODUCTION

Magneto-optic (MO) recording combines the advantages of optical (high storage density of about $3 \cdot 10^7$ bit/cm², contactless writing and reading) and magnetic (unlimited rewriteability) recording.^{1,2}

The thermomagnetic write process will be described in section 2 using a bubble-like model.

Thin films of rare-earth transition-metal (RE-TM) alloys with the general composition GdTb-Fe and Tb-FeCo are today's medium for MO recording (Dy-FeCo is also a candidate).³⁻⁶ Their essential properties will be briefly reviewed in section 3.

In section 4 we discuss recording experiments with RE-TM based disks concerning the write process and the domain stability in dependence on the laser power and the external magnetic field.

2. THERMOMAGNETIC SWITCHING PROCESS

In a simplified way, a magneto-optical (MO) recording system can be regarded as a CD player with polarized laser light of tunable intensity and a disk containing a hard magnetic layer with perpendicular anisotropy. The information is stored as domain pattern in the magnetic film.¹⁻¹¹

The thermo-magnetic write process is illustrated in Fig. 1. A focussed laser beam heats the magnetic layer locally to close to its Curie temperature, where the coercivity decreases and the magnetization can be reversed by a small external magnetic field, thus creating a magnetic domain. The read process utilizes the polar magneto-optical Kerr effect, such that the polarization plane of the reflected light is turned clock- or counter-clockwise according to the domain pattern.

As the MO films are magnetically hard at room temperature, they have to be heated locally by a laser beam (cmp. Fig.1) in order to write and erase domains. This process is primarily controlled by the laser-induced temperature profile, the radial and time dependence of the magnetic properties, the domain nucleation, and the domain-wall motion. Dynamic magnetization processes can only take place within the heated volume where the coercivity is sufficiently reduced.

The domain-formation process can be described in a bubble-like model^{12,13} with:

- the domain wall energy E_w (contracting), which decreases with increasing temperature:

$$E_w = 2 \pi h r \sigma_w, \quad (1)$$

- the demagnetizing energy (expanding) (simple formula for cylindrical domain):

$$E_d = 4\pi\mu_0 \cdot t \cdot r^2 (4 \pi M_s(r) M_s)/(1 + 3R/2t), \quad (2)$$

- the magnetic energy in an external field:

$$E_H = 4\pi\mu_0 \cdot t \int r^2 M_s H_{ext} dr, \quad (3)$$

- and the coercive energy (frictional)

$$E_c = 4\pi\mu_0 \cdot t \int r^2 M_s H_c dr. \quad (4)$$

The driving force for wall motion is given by:

$$F = d/dr E(T(r)); \quad E = E_w + E_d + E_H. \quad (5)$$

The domain moves for $|F| > F_c$, it expands when $F_H + F_D > F_w$ and contracts when $F_H + F_D < F_w$.

A typical radial dependence of the different reduced forces $f=F/(2\pi h^2)$ is presented in Fig. 2 for cylindrical symmetry of the domains. The curve f_{eff} represents $f_H + f_d + f_w$. The maximum temperature at the spot centre was, for the sake of simplicity, assumed to be equal to T_c . Two radial (i.e. temperature) dependences of the coercivities have been plotted: a very steep one and a relatively flat one. The position of the domain wall is determined by $f(r_{Hc})=0$ where the domain wall radius R is equal to the "coercivity radius" r_{Hc} , as indicated for the flat $H_c(T)$ -curve by the arrow.

The requirements to be fulfilled by a magnetic layer suitable for MO recording are summarized in Table 1. Requirements 1-3 are obvious from the read and write processes so far presented. The remaining requirements will be deduced in section 4 from recorder experiments on disks with amorphous rare-earth transition-metal (RE-TM) films.

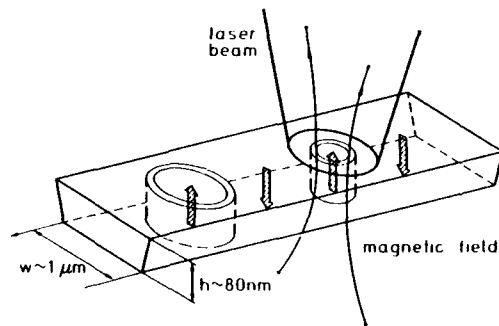


Fig. 1. (top): Creation of domains in the thermomagnetic write process.

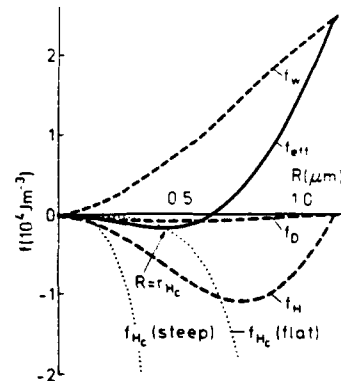


Fig. 2. (right): Radial dependence of the forces f acting on the wall of a bubble-like domain; f_d : demagnetizing force, f_w : Booh wall force, f_H : force of external magnetic field, f_c : coercive force.

Table 1. Requirements on the magneto-optic storage layer

stable micron sized domains:

1. perpendicular magnetic anisotropy

perfect stable domains with a good SNR:

4. steep H_c vs T and medium M_s

read-out with Kerr effect:

2. magneto-optically active layer with a sufficient figure of merit $R\theta^2$

5. a fine microstructure (< 50 nm) and a good lateral homogeneity

6. high coercivity and low magnetization at read-out temperature

limited write laser power:

3. $T_c = 400$ K - 600 K

Additional requirements on the disc structure:

7. long-term stability, sufficient sensitivity (high absorption, suitable thermal conductivity), low medium noise. This is achieved by a proper choice of dielectric cover layers.

3. THE MAGNETIC PROPERTIES OF AMORPHOUS RE-TM FILMS

$RE_{100-x}TM_x$ alloys containing heavy rare-earth ions like Gd, Tb, Dy show a ferrimagnetic order in the range of composition, which is of interest for MO recording. The TM moments form one magnetic subsystem and the RE moments the other one. The temperature at which the opposite sublattice magnetizations are equal in magnitude is called compensation temperature T_{comp} . It is found in the very narrow compositional range of $70 < x < 85$.¹¹ Typical compositions used in storage applications are $Gd_{20}Tb_{5}Fe_{75}$ or $Tb_{27}Fe_{65}Co_8$.

The characteristic ferrimagnetic behaviour of a RE-TM film is depicted in Fig. 3. At T_{comp} the saturation magnetization is zero, and as it is impossible to introduce energy by an external magnetic field, the coercivity becomes infinity. The Faraday rotation is mainly due to the transition metal sublattice (transitions of the 3d conduction electrons), and shows no singular behaviour at T_{comp} .

The position of the compensation temperature can be chosen by a proper composition. This effect can be used to control the saturation magnetization, the maximum of which is approximately proportional to $T_c - T_{comp}$, and the coercive field in the high temperature range where the thermomagnetic

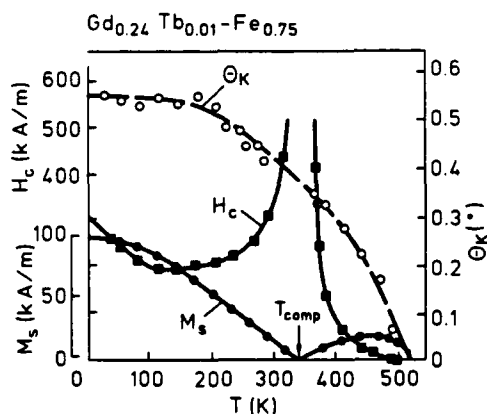


Fig. 3. Magnetic properties of a $Gd_{24}Tb_{1}Fe_{75}$ layer (50 nm) versus temperature: ●: saturation magnetization M_s , ■: coercivity H_c , ○: Kerr rotation Θ_K .

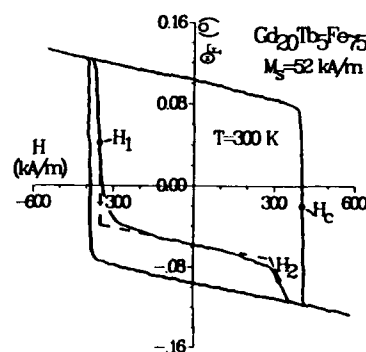


Fig. 4. Faraday loops of $1.2 \mu m$ domains in a $Gd_{20.5}Tb_{4.5}Fe_{75}$ -disk at room temp.. After saturation the usual curve is observed.⁷

switching process takes place. (This will be discussed in more detail in connection with Tab. 2.) T_C is the Curie temperature.

An experimental method was developed to measure the wall coercivity H_c^w and the wall energy σ_w .⁷ Faraday hysteresis loops were prepared from a disk containing domains of radius R (about $1\mu m$) written in a test recorder. A typical hysteresis curve is shown in Fig. 4. The switching fields H_1 and H_2 correspond to the expansion and the shrinking respectively, of the domains. The absolute values of H_1 and H_2 differ from one another, because in the first process wall energy has to be delivered by the external field, whereas the second process is supported by the wall tension. Wall coercivity and energy can be expressed by:

$$M_s H_c^w = (H_1 + H_2)/2 \quad (6a); \quad \sigma_w = \mu_0 M_s 2R \cdot [(H_1 - H_2)/2 - M_s/(1 + 3R/2t)], \quad (6b)$$

where t is the thickness of the film (Eq. (6b) derived via Eq. (5)).

4. RECORDING EXPERIMENTS

The correlation between the switching parameters in recorder experiments and the magnetic properties of the magneto-optical layer can be understood using eqs. (1) - (5) together with Fig. 2 as visual aid.

The variation of the switching field at constant domain length L with $T_C - T_{comp}$ is given in Fig. 5 for GdTb-Fe alloys.¹⁴ At lower $T_C - T_{comp}$ values the magnetization in the high temperature range where the switching occurs is lower and thus higher external magnetic fields are needed to create domains of fixed length. The theoretical curve in Fig. 5 is derived from Eqs. (1)-(6) assuming Gaussian temperature profiles. In the case of low demagnetizing forces the switching energy is mainly given by $M_s \cdot H_{ext}$ leading with $M_s = \text{const} \cdot (T_C - T_{comp})$ to a dependence $H = \text{const}/(T_C - T_{comp})$, which is very similar to the theoretical curve in Fig. 5.

Considerable experimental insight into the switching process could be gained by Lorentz electron microscopy, which is based on the deflection of electrons by magnetic stray fields perpendicular to the direction of the electron beam.¹⁵ Four Tb-FeCo and one GdTb-Fe samples with different compensation temperatures were investigated by Greidanus et al. (Table 2).¹⁴

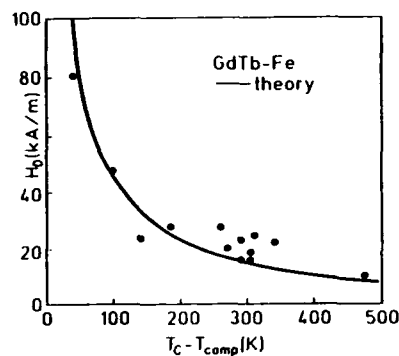


Fig. 5. Optimal external switching field H_0 for GdTb-Fe films (constant domain length).¹⁴

Layer stack of Fig. 6:
80nm AlN/45nm GdTb-Fe/Al or Ti

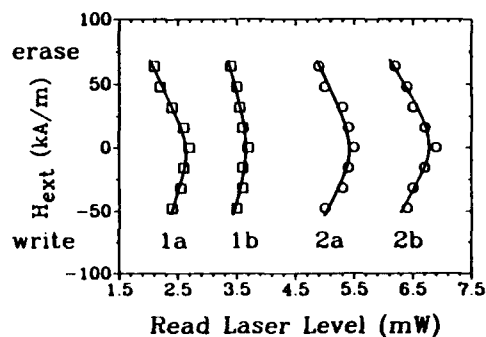


Fig. 6. Read-out without losses in SNR for GdTb-Fe disks with varying layer thicknesses at a disk velocity of 5m/s. The lines represent the calculated dependence of domain stability.⁸

1a: 21.5nm Ti, 1b: 90nm Ti,
2a: 18nm Al, 2b: 30nm Al

Table 2.a. Shape of written domains observed with Lorentz Microscopy¹⁵

| | LM | MFM |
|---|-----------|-----------|
| 1 | multidom. | multidom. |
| 2 | single | crescent |
| 3 | single | crescent |
| 4 | subdom. | subdom. |
| 5 | subdom. | |



Fig. 7. Imperfect domain shapes.
(a) multidomain (b) subdomains

Table 2.b. Composition and magnetic data of the samples of Table 2.a

| sample | composition | T _c | T _{comp} | T _{demag} | H _c (T) | M _s | M _s ^{max} |
|--------|---|----------------|-------------------|--------------------|--------------------|----------------|-------------------------------|
| 1 | Tb _{29.9} Fe _{62.6} Co _{7.5} | 450 | > T _c | > T _c | very steep | low | - |
| 2 | Tb _{27.2} Fe _{65.5} Co _{7.3} | 461 | 310 | 455 | steep | | 35kA/m |
| 3 | Tb _{23.6} Fe _{67.6} Co _{8.8} | 473 | 214 | 465 | steep | | 90kA/m |
| 4 | Tb _{21.2} Fe _{71.9} Co _{6.9} | 473 | ≤ 0 | 440 | flat | high | 170kA/m |
| 5 | Gd ₁₅ Tb _{6.5} Fe _{78.5} | 455 | 40 | | very flat | high | 120kA/m |

The composition, Curie temperature, and compensation temperature are given in Table 2.b together with their demagnetizing temperature defined as the temperature where the magnetic layer loses its 100% remanence. The decrease of the remanence in the vicinity of T_c is due to demagnetizing effects and not to an in-plane magnetization. Sample 1 does not have a compensation temperature, its M_s(T) approaches T_c like the curve in Fig. 3 approaches T_{comp}. The M_s(T) curves of the other samples look like the complete curve in Fig. 3 and exhibit a maximum M_s^{max} which is also listed in Tab. 2.b.

In samples 2 and 3 regular single domains are observed (Table 2.a). This is the desired shape and gives good signal-to-noise ratios in recorder experiments. In sample 1 not one single domain but several small domains are observed within the heated area (see Fig. 7a). The mark size is independent of the external magnetic field. The reason for this behaviour is that the coercive field rises very steeply below the Curie temperature whereas the magnetization rises only slowly. Domain growth is possible only in a very small temperature range below T_c (compare with the steep H_c vs T-curve in Fig. 3, the layer is heated above the Curie temperature) which is passed too quickly during the write process to allow continuous wall motion. In specimen 4, the demagnetizing force is predominant due to a high magnetization, leading to the formation of subdomains within the written mark (see fig. 7b) whose size is again independent of the external field.

It was found that in samples with high magnetization (where the maximum of magnetization above the compensation temperature is greater than about 120 kA/m) subdomains are built due to the high demagnetizing force.

Domain diameters in a Gd₁₅Tb_{6.5}Fe_{78.5} sample (#5 in Table 2) as observed with Lorentz microscopy show a characteristic dependence upon the applied magnetic field. At fields below 30 kA/m the mark size is independent of the applied field and contains several subdomains, indicating that the demagnetizing force Eq. (2) is predominant (in Fig. 2, f_D would have to be much greater than f_H) whereas a linear dependence at higher fields shows that the external field Eq. (3) is the decisive force there (Fig. 2 corresponds to this situation). An increase in domain size at the highest applied fields is accompanied by a significant decrease in the smoothness of the domain contour, an effect which may be explained by the small coercive field ('soft' intersection of the coercive force with f_{eff} in Fig. 2). At negative fields the domains shrink.

The domain stability was tested on GdTb-Fe based disks with different Tb content and different compensation temperatures.^{7,8} During read-out the domain patterns are heated. If the domain walls move under the applied field by only about 20 nm, this leads to a degradation of the signal-to-noise ratio by more than 1dB. The results of the recorder experiments are displayed in Fig. 6 in dependence on the applied magnetic field and the read laser level for disks with a variety of thicknesses of the different layers in the stack /AlN/GdTb-Fe/Al or Ti/.⁸

The solid curves represent the theoretical values as obtained using the magnetic parameters of the disks. A fit to the experimental data was obtained by varying an effective thermal conductivity Λ_{eff} which is given as the weighed sum of the conductivities of the layers: $\sum_i \lambda_i \cdot t_i$. As the heat capacity is not expected to depend as sensitively on the microstructure as λ , bulk values taken from literature were used in these calculations. The thermal conductivity of a layer can be obtained by varying its thickness with those of the others remaining constant. The results are: Al: 190 W/mK (bulk 240), Ti: 8W/mK (crystalline 22), AlN: 15 W/mK (bulk: 300), GdTb-Fe: 17 W/mK (crystalline: 54).

The dependence of the read-out stability was also investigated in dependence on the Tb-content.¹⁶ From the force equation (Eqs.1-6, visualized in Fig. 2) we can qualitatively understand that the read-out stability is increased with increasing Tb content (- higher coercivity, i.e. frictional force) and with increasing T_{comp} (- lower magnetization in the high temperature range, i.e. lower driving force due to Eqs. 2-3).

5. CONCLUSION

From the discussion in the previous sections we conclude, that, in order to achieve perfect domains, we need a steep H_c vs T and medium M_s (see Tab.1). We see that it is advantageous to have a ferrimagnetic medium with tunable M_s . For the stability of the domains we need a high coercivity and a low magnetization at room temperature and at read-out temperature (req.6 of Tab.1). The Kerr rotation controlling the read-out signal can be optimized by choosing a suitable stack with optical enhancement layers.

REFERENCES

1. M. Hartmann, J. Braat, B. Jacobs, IEEE Trans. Magn. MAG-20, 1013 (1984).
2. N. Imamura, S. Tanaka, F. Tanaka, Y. Nagao, IEEE Trans. Magn. MAG-21, 1607 (1985).
3. P. Hansen, J. Mag. Mag. Mat. 83, 6 (1990).
4. P. Hansen, H. Heitmann, IEEE Trans. Mag., 25, 4390 (1989).
5. S. Klahn, P. Hansen, F.J.A.M. Greidanus, 11th Int. Vacuum Conf. and 7th Int. Conf. on Solid Surfaces, Köln 1989, to be publ. in Vacuum.
6. D. Mergel, P. Hansen, S. Klahn, MASHTC 90, Dresden, G.D.R., April 23-27 (1990), to be published in Proceedings.
7. S. Klahn, D. Raasch, INTERMAG Brighton, paper DB-07 (1990).
8. D. Raasch, S. Klahn, MRS conference, C6-P1, Strasbourg, May 1990.
9. M. Hong, E. M. Gyorgy, R. B. van Dover, S. Nakahara, D. D. Bacon, and P. K. Gallagher, J. Appl. Phys. 59, 551 (1986).
10. Y. Mimura, N. Imamura, T. Kobayashi, A. Okada, Y. Kushihiro, J. Appl. Phys. 49, 1208 (1978).
11. P. Hansen, C. Clausen, G. Much, M. Rosenkranz, K. Witter, J. Appl. Phys. 66, 756 (1989).
12. P. Hansen, J. Appl. Phys. 62, 216 (1987) 63, 2364 (1988).
13. B.G. Huth, IBM J. Res. Dev. 18, 100 (1974).
14. J. H. Crasemann, P. Hansen, M. Rosenkranz, K. Witter, J. Appl. Phys. 66, 1273 (1989).
15. F.J.A.M. Greidanus, B.A.J. Jacobs, F.J.A. den Broeder H.J.M. Spruit, S. Klahn, IEEE Trans. Magn. MAG-25, 3524 (1989).

MICROMAGNETIC COMPUTATIONS OF MAGNETIZATION CONFIGURATIONS

J. P. Jakubovics

Department of Materials, University of Oxford
Parks Road, Oxford OX1 3PH, U.K.

1. INTRODUCTION

1.1 Domain walls in infinite media

Micromagnetism could be said to have begun with the Landau-Lifshitz solution for the magnetization configuration in a 180° domain wall in an infinite medium with uniaxial anisotropy.¹ The energy per unit volume for this case may be written

$$\epsilon = \epsilon_e + \epsilon_a, \quad (1)$$

where ϵ_e and ϵ_a are the exchange and anisotropy energy densities respectively;

$$\epsilon_e = A[(\nabla\alpha)^2 + (\nabla\beta)^2 + (\nabla\gamma)^2], \quad (2)$$

and

$$\epsilon_a = K(\alpha^2 + \beta^2) = K(1 - \gamma^2), \quad (3)$$

where A is the exchange constant, K is the uniaxial anisotropy constant, and α , β and γ are the direction cosines of the magnetization with respect to the cartesian coordinate axes x , y and z respectively. Eqn (3) corresponds to easy directions of magnetization parallel to $\pm z$. For the case when the medium contains a 180° domain wall, we may assume (i) that the magnetization is parallel to the yz -plane ($\alpha = 0$), and (ii) that its orientation varies with x only. The boundary conditions imposed by the anisotropy are

$$\gamma \rightarrow \pm 1 \quad \text{as} \quad x \rightarrow \pm\infty. \quad (4)$$

Condition (i) ensures that no magnetic charges are present. A magnetization configuration satisfying these conditions is called a Bloch wall. With these conditions, eqns (1)–(3) may be simplified to give

$$\omega = \int_{-\infty}^{\infty} \left[A \left(\frac{d\phi}{dx} \right)^2 + K \sin^2 \phi \right] dx \quad (5)$$

for the energy per unit area of domain wall, where

$$\phi = \arcsin \beta = \arccos \gamma. \quad (6)$$

The exact solution for $\phi(x)$ that minimises ω is

$$\cos \phi = \tanh \left(\frac{x}{\delta} \right), \quad (7)$$

where

$$\delta = \sqrt{\frac{A}{K}}. \quad (8)$$

Substituting eqn (7) into eqn (5) gives

$$\omega = 4\sqrt{AK}. \quad (9)$$

An exact solution may also be obtained in the more general case when the anisotropy includes a $\sin^4 \phi$ term, so that ω becomes

$$\omega = \int_{-\infty}^{\infty} \left[A \left(\frac{d\phi}{dx} \right)^2 + K (\sin^2 \phi + \kappa \sin^4 \phi) \right] dx, \quad (10)$$

where $K\kappa$ is the second-order anisotropy constant. The solution is²

$$\cos \phi = \frac{\sqrt{1 + \kappa \tanh(x/\delta)}}{\sqrt{1 + \kappa \tanh^2(x/\delta)}}, \quad (11)$$

valid for $\kappa > -1$, since the easy directions are not parallel to $\pm z$ when $\kappa < -1$. Substituting eqn (11) into eqn (10) gives

$$\omega = 2\sqrt{AK} \left[1 + \frac{(1 + \kappa) \arctan \sqrt{\kappa}}{\sqrt{\kappa}} \right] \quad (12)$$

when $\kappa > 0$, and

$$\omega = 2\sqrt{AK} \left[1 + \frac{(1 + \kappa) \operatorname{arctanh} \sqrt{-\kappa}}{\sqrt{-\kappa}} \right] \quad (13)$$

when $-1 < \kappa < 0$. This solution may also be used for a material in which cubic anisotropy as well as uniaxial anisotropy is present. For this case, eqn (3) may be written

$$\epsilon_a = [K_u(\alpha^2 + \beta^2) + K_c(\alpha^2\beta^2 + \beta^2\gamma^2 + \gamma^2\alpha^2)], \quad (14)$$

where K_u and K_c are the uniaxial and cubic anisotropy constants respectively, and the $\langle 100 \rangle$ crystallographic directions are assumed to be parallel to the cartesian coordinate axes. With the same constraints as above, the energy per unit area becomes

$$\omega = \int_{-\infty}^{\infty} \left[A \left(\frac{d\phi}{dx} \right)^2 + K_u \sin^2 \phi + K_c \sin^2 \phi \cos^2 \phi \right] dx, \quad (15)$$

which is equivalent to eqn (10) if

$$K_u + K_c = K, \quad (16)$$

and

$$-\frac{K_c}{K_u + K_c} = \kappa. \quad (17)$$

If no uniaxial anisotropy is present ($K_u = 0$), no solution for ϕ exists that satisfies the boundary conditions. In that case, 180° walls would be unstable and would break up into two 90° walls. However, magnetostriction is always present in real materials, the effect of which is to move the two 90° walls together in order to avoid a large magnetoelastic energy that would be present in the domain separating the 90° walls. It can be shown¹ that when $K_c > 0$, the effect of magnetostriction is equivalent to

a uniaxial anisotropy with easy axis parallel to the domain magnetizations, and an effective anisotropy constant

$$K_u = \frac{9}{4}(c_{11} - c_{12})\lambda_{100}^2, \quad (18)$$

where c_{11} and c_{12} are the usual elastic stiffness constants for a cubic crystal, and λ_{100} is the saturation longitudinal magnetostriction constant in the $\langle 100 \rangle$ directions.

1.2 The effect of surfaces

The analytic solutions given above are no longer valid for a specimen with external surfaces. In such cases the energy of the specimen becomes

$$E = E_e + E_a + E_m, \quad (19)$$

where E_e and E_a are the integrals of ϵ_e and ϵ_a respectively over the volume of the specimen, and E_m is the magnetostatic energy:

$$E_m = \frac{1}{2} \iiint_V \rho \Phi dV + \frac{1}{2} \iint_S \sigma \Phi dS, \quad (20)$$

where

$$\rho = -\nabla \cdot \mathbf{M} \quad (21)$$

is the volume charge density,

$$\sigma = \mathbf{M} \cdot \mathbf{n} \quad (22)$$

is the surface charge density, \mathbf{M} is the magnetization, \mathbf{n} is a unit vector normal to the surface, and Φ is the magnetostatic scalar potential:

$$\Phi(\mathbf{r}) = \iiint_V \frac{\rho}{|\mathbf{r} - \mathbf{r}'|} d\mathbf{r}' + \iint_S \frac{\sigma}{|\mathbf{r} - \mathbf{r}'|} d\mathbf{r}'. \quad (23)$$

In a finite specimen, a Bloch wall would generate charges on the surfaces. For a very thin film (of thickness small compared with $\sqrt{A/K}$), it becomes favourable for the magnetization to remain parallel to the surfaces. Domain walls in which this condition is satisfied are called Néel walls. However, Néel walls contain volume charges, and it is expected that in films whose thickness is not small compared with $\sqrt{A/K}$, domain walls will have more complicated structures, in which the magnetization varies with y as well as with x . No exact analytical solutions have been obtained for such cases. However, Hubert³ suggested that stray-field free magnetization configurations ($E_m = 0$) would be possible in thin films if the magnetization had one of two possible symmetries, either

$$\alpha(-y) = -\alpha(y), \quad \beta(-y) = \beta(y), \quad \gamma(-y) = \gamma(y) \quad (24)$$

('asymmetric Bloch wall'), or

$$\alpha(-x, -y) = \alpha(x, y), \quad \beta(-x, -y) = \beta(x, y), \quad \gamma(-x, -y) = -\gamma(x, y) \quad (25)$$

('asymmetric Néel wall'), where $y = 0$ at the centre of the film, and he proposed specific structures of both types. At the same time, LaBonte⁴ developed a method for the numerical computation of magnetization configurations. He computed the structure of 180° domain walls in Permalloy films of thickness in the range 50 to 200 nm, and found that they were of the 'asymmetric Bloch'-type, as shown in Fig. 3 of his paper. These walls have a curved centre (the line along which $\gamma = 0$), and the magnetization circulates in a vortex-like manner to achieve a high degree of flux closure.

1.3 Numerical computations

LaBonte's method consists of subdividing the specimen into small regions in which the magnetization is assumed to be uniform. In the specific case for which he carried out his computations, he used subdivisions in the shape of infinitely long square prisms with axes parallel to z . The film is subdivided into N_x columns and N_y rows of prisms of side Δ , $N_y\Delta$ being the film thickness, and it is assumed that the magnetization is parallel to $+z$ when $x > \frac{1}{2}N_x\Delta$ and to $-z$ when $x < -\frac{1}{2}N_x\Delta$. The exchange energy per unit length of wall is given by

$$F_e = 2A \sum_{I=1}^{N_x-1} \sum_{J=1}^{N_y} [1 - \mathbf{m}(I, J) \cdot \mathbf{m}(I+1, J)] \\ + 2A \sum_{I=1}^{N_x} \sum_{J=1}^{N_y-1} [1 - \mathbf{m}(I, J) \cdot \mathbf{m}(I, J+1)] + S, \quad (26)$$

where $\mathbf{m}(I, J)$ is a unit vector parallel to the magnetization of the prism in column I , row J , and S stands for 'surface terms', which have to be treated differently: see LaBonte⁴ for details. The anisotropy energy per unit length is

$$F_a = K\Delta^2 \sum_{I=1}^{N_x} \sum_{J=1}^{N_y} [1 - \gamma^2(I, J)], \quad (27)$$

if the material is assumed to have uniaxial anisotropy. The magnetostatic energy per unit length is given by

$$F_m = F_s + F_i, \quad (28)$$

where

$$F_s = \frac{\pi M_s^2}{K} F_a \quad (29)$$

is the sum of the magnetostatic energies of the prisms per unit length, and F_i is the energy per unit length due to the magnetostatic interactions between all pairs of prisms, given by

$$F_i = \frac{1}{2} M_s^2 \Delta^2 \sum_{I=1}^{N_x} \sum_{J=1}^{N_y} \sum_{I'=1}^{N_x} \sum_{J'=1}^{N_y} \{ A_m(I-I', J-J') [\alpha(I, J)\alpha(I', J') - \beta(I, J)\beta(I', J')] \\ + C_m(I-I', J-J') [\alpha(I, J)\beta(I', J') + \beta(I, J)\alpha(I', J')] \}, \quad (30)$$

where A_m and C_m are interaction coefficients given by LaBonte.⁴ The total energy per unit length is given by

$$F = F_e + F_a + F_m, \quad (31)$$

which must be minimised subject to the constraint

$$\mathbf{m}^2(I, J) = \alpha^2(I, J) + \beta^2(I, J) + \gamma^2(I, J) = 1. \quad (32)$$

The condition for F to be a minimum is therefore

$$\frac{\partial F}{\partial \mathbf{m}(I, J)} + 2\lambda_{I, J} \mathbf{m}(I, J) = 0 \quad (33)$$

for all I and J , where $\lambda_{I, J}$ are Lagrange multipliers. It is convenient to introduce an 'effective field'

$$\mathbf{H}(I, J) = -\frac{\partial F}{\partial \mathbf{m}(I, J)}, \quad (34)$$

so that the magnetization configuration is in equilibrium if the magnetization of each prism is parallel to the effective field acting on it. The minimisation procedure is therefore to calculate the effective field acting on each prism in turn, set the magnetization parallel to this field, and repeat this process until none of the magnetizations have to be rotated by more than a predetermined small angle. There is one difficulty that was not mentioned by LaBonte, namely that the effective field acting on a given prism depends on the magnetization of that prism, so that when the magnetization is aligned with the effective field, the effective field changes. To overcome this problem, it is necessary to carry out an iterative process at each prism, which consists of recalculating the effective field and realigning the magnetization repeatedly until a stable situation is reached, before proceeding to the next prism. This does not increase the complexity of the computation significantly, because when the effective field is recalculated, only the contribution of one prism changes. Although the initial calculation of the effective field at a new prism is time-consuming, the recalculation is very fast, and the number of iterations needed at each prism is usually small.

The purpose of this paper is to discuss ways in which this numerical method may be extended for the computation of a number of different problems.

2. INTERACTION OF PAIRS OF DOMAIN WALLS

2.1 *Domain wall symmetries*

For fixed domain magnetization directions ((eqn (4)), an asymmetric Bloch wall separating the two domains can have four possible configurations, since the centre line of the wall (where $\gamma = 0$) can curve in two directions, and for each direction, the sense of the vortex can be clockwise or counterclockwise. (Each configuration is related to the one of the others by reflection in the xz -plane, to a third by reflection in the yz -plane followed by time-reversal, and to the fourth one by a combination of both transformations.) In a film containing three domains (i.e. two parallel 180° walls), there are *six* distinctly different magnetization configurations for the two walls,⁵ as shown in Fig. 1.

In configurations A and B, the wall centre lines curve in the same direction, in C and D they curve towards each other, and in E and F they curve away from each other; in A, C and E the two vortices circulate in the same sense, and in B, D and F they circulate in the opposite sense. When a magnetic field is applied in the $+z$ direction, the walls are driven towards each other.

In the case of one-dimensional 180° walls, of structure given by eqns (7) or (11), a pair of walls can only have two possible configurations, termed winding and unwinding respectively, according to whether the magnetization in the two walls rotates in the same sense or in opposite senses. It is clear from simple qualitative considerations that unwinding walls can be annihilated more easily than winding walls, when they are driven towards each other by an applied field. In the case of pairs of asymmetric Bloch walls, it has not been possible to predict from qualitative considerations which of the configurations would be annihilated easily and which would not.

2.2 *Experimental results*

In-situ magnetization experiments have provided some experimental evidence for the behaviour of pairs of Bloch walls in thin films. Figs 2 and 3 show micrographs of two specimens of an Fe-Co-Ni-Ti alloy (Incolloy 904) recorded by R. A. Taylor⁶ in the AEI EM7 1 MV transmission electron microscope in Oxford, using an in-situ magnetizing device. The sequence in Fig. 2 shows a pair of walls that are easily annihilated in an increasing field, but they reappear when the field decreases again,

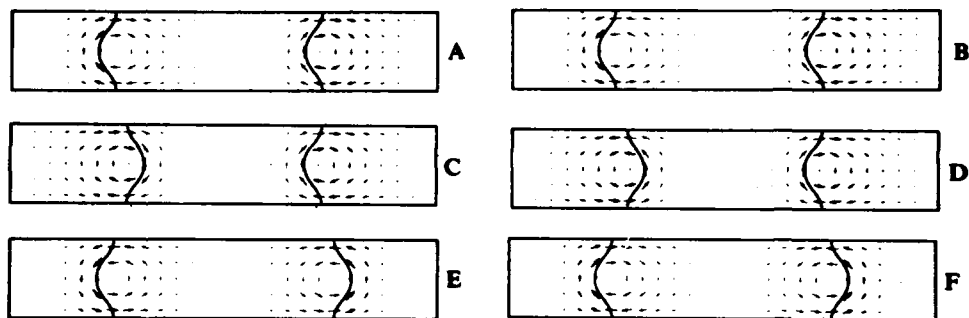


Fig. 1 The six magnetization configurations for a pair of Bloch walls. The contour lines separate regions in which $\gamma > 0$ from those in which $\gamma < 0$.

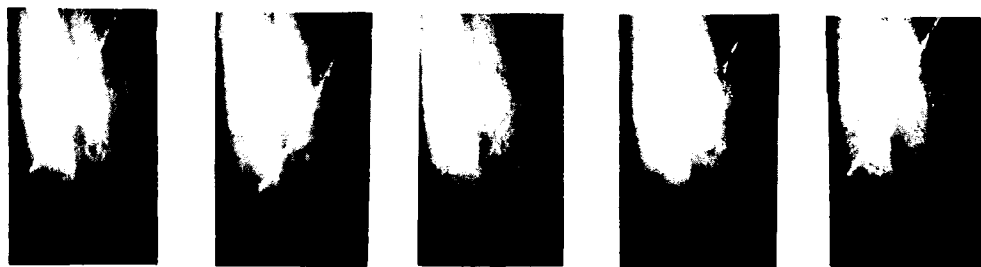


Fig. 2 Electron micrographs of an Incoloy 904 specimen. The applied field increases for the first three frames, and decreases for the last two.

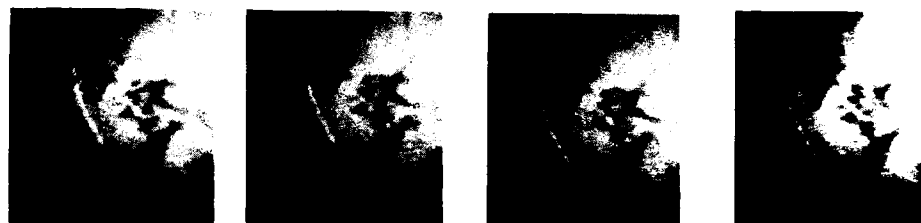


Fig. 3 Electron micrographs of an Incoloy 904 specimen. The applied field increases from left to right.

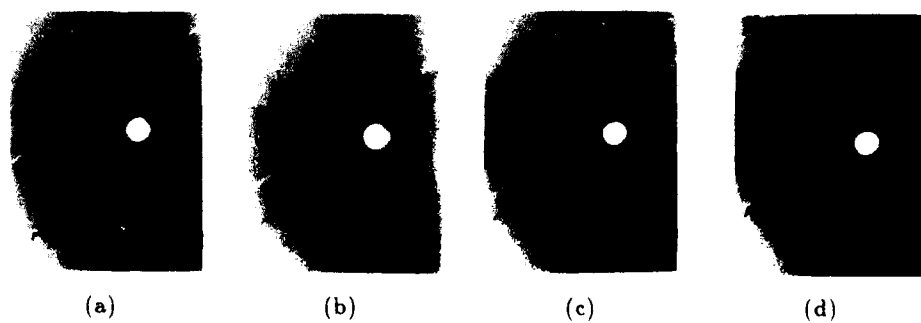


Fig. 4 Electron micrographs of a $\text{Co}_{90}\text{Zr}_{10}$ film of thickness 400 nm, in applied fields of (a) 0, (b) 2.34 Oe, (c) 3.64 Oe, and (d) 5.46 Oe. The specimen was saturated in 6.5 Oe.

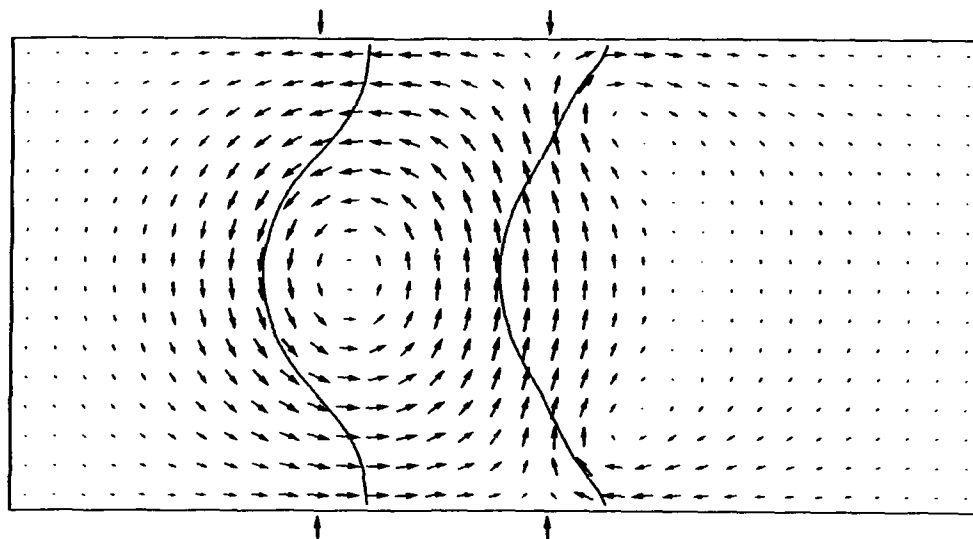


Fig. 5 Computed magnetization configuration for an iron film of thickness 200 nm for case B, in an applied field of 14 Oe.

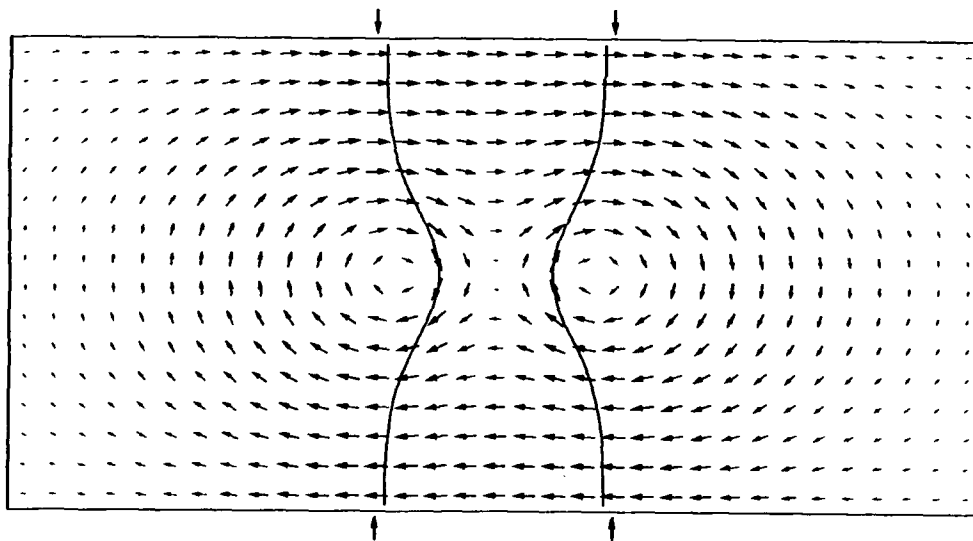


Fig. 6 Computed magnetization configuration for an iron film of thickness 200 nm for case C, in an applied field of 4 Oe.

while Fig. 3 shows a pair of walls that remain stable as the field increases, until the field reaches a critical value, causing the wall to disappear suddenly. In these micrographs, the domain walls appear as bright or dark lines, made visible by the standard technique of defocusing the objective lens. Another example, obtained by R. Wimmer⁷ using the same apparatus, is shown in Fig. 4. In this case, the walls were divided into segments that rotated in opposite directions in the field (Fig. 4(d)), before being suddenly annihilated.

2.3 Computations

These experiments did not provide enough information to enable the magnetization configuration at the domain walls to be determined. However, the 'hardness' of

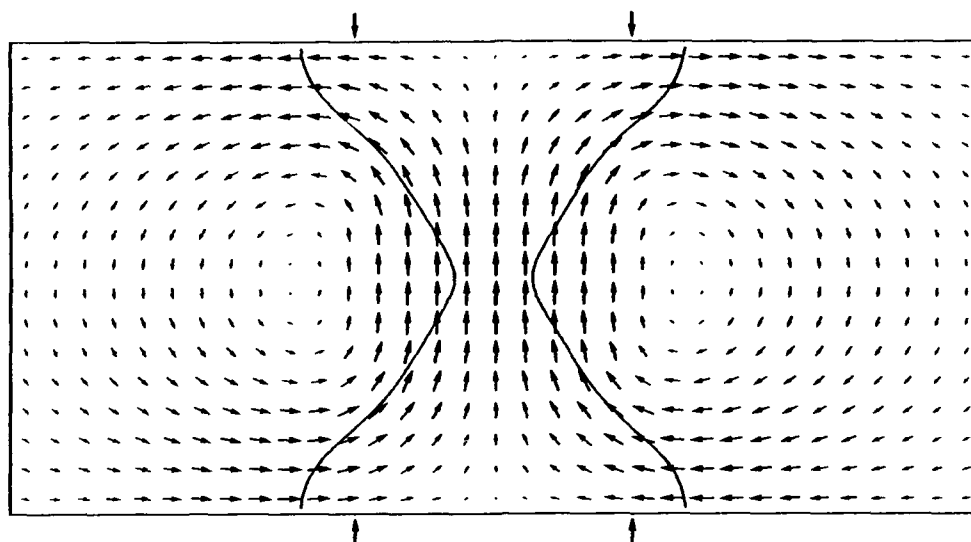


Fig. 7 Computed magnetization configuration for an iron film of thickness 200 nm for case D, in an applied field of -4 Oe.

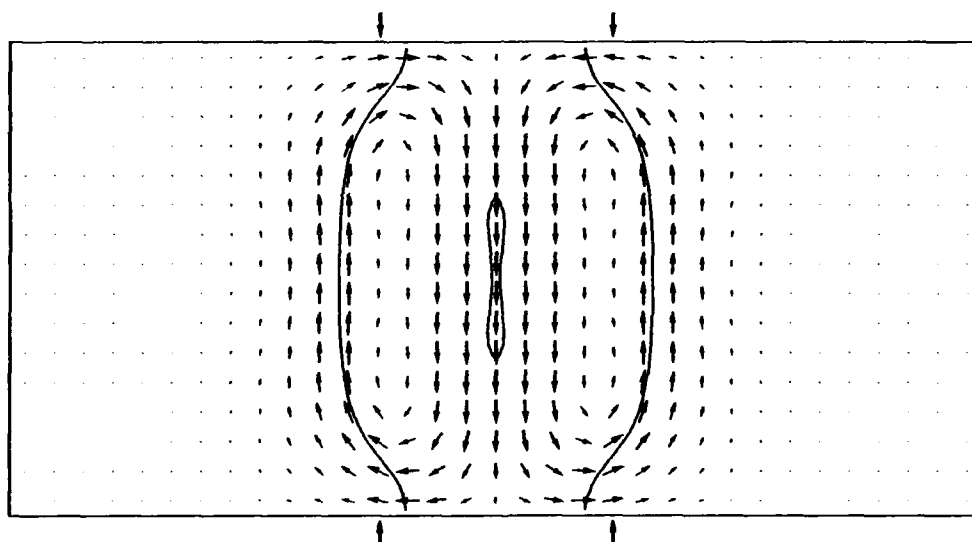


Fig. 8 Computed magnetization configuration for an iron film of thickness 200 nm for case F, in an applied field of 150 Oe.

the different wall configurations can be estimated from computations, and the results can be correlated at least qualitatively with the experiments. The method was based on that of LaBonte,⁴ with a number of modifications.⁸ (i) The symmetry of the walls about the xz -plane is well established,^{3,4} and the computations can be constrained to have this symmetry, which reduces the computation time by about a factor 4. (ii) For a pair of walls, the boundary conditions become

$$\gamma \rightarrow 1 \quad \text{as} \quad x \rightarrow \pm\infty, \quad (35)$$

cf. eqn (4) for a single wall. (iii) The starting configuration for each case must be a pair of walls of appropriate symmetry far enough from each other for a well-defined domain to exist between them. (iv) The calculations were carried out for a material with cubic

Table 1. Maximum field in Oe in which Bloch wall pairs of different types are stable

| Thickness | B | C | D | F |
|-----------|----|----|-----------|-----|
| 150 nm | 26 | 12 | 2 | 250 |
| 200 nm | 14 | 4 | ~ -2 | 150 |
| 250 nm | 7 | 0 | ~ -2 | 100 |

anisotropy. Assuming that the $\langle 100 \rangle$ directions are parallel to the coordinate axes, eqn (27) can be modified to include both anisotropies:

$$F_a = \Delta^2 \sum_{I=1}^{N_x} \sum_{J=1}^{N_y} K_u [1 - \gamma^2(I, J)] + K_c [\alpha^2(I, J) \beta^2(I, J) + \beta^2(I, J) \gamma^2(I, J) + \gamma^2(I, J) \alpha^2(I, J)]. \quad (36)$$

(v) An additional term, representing the effect of a magnetic field parallel to the $+z$ -direction, is added to the total energy. Computations were carried out for films of thickness 150 nm, 200 nm, and 250 nm, with exchange constant $C = 2A = 2 \times 10^{-6}$ erg cm $^{-1}$, cubic anisotropy constant $K_c = 10^5$ erg cm $^{-3}$, and saturation magnetization $M_s = 1700$ gauss. No stable configurations were found for cases A and E in any field. For the other four cases, stable configurations were found for applied fields up to the values shown in Table 1. It is seen that case F is much harder than the other three cases, and that in all cases, the hardness decreases with increasing film thickness. Figs 5, 6, 7 and 8 show the magnetization configurations corresponding to the values in Table 1 for films of thickness 200 nm. In these figures, as well as in Fig. 9, the arrows represent the component of magnetization in the xy -plane, and the curves pass through points where $\gamma = 0$. The width of the domain in the centre with $\gamma < 0$, marked by the two pairs of arrows outside the frame, is 97.7 nm in Fig. 5, 100.8 nm in Fig. 6, 117.8 nm in Fig. 7, and 98.9 nm in Fig. 8.

From these results, it is suggested that the walls in Fig. 2 were probably type A or E, those in Fig. 3 were probably type F or B, and that those in Fig. 4 were probably type B. This interpretation of Fig. 4 is the most likely one because of the apparent breaking up of the walls into segments of opposite polarity, indicating that the structure did not have the symmetry of C, D, E or F.

3. DOMAIN WALLS IN THICK FILMS

The recently developed experimental technique of scanning electron microscopy with polarisation analysis (SEMPA) has enabled the magnetization configuration on the surfaces of bulk materials to be determined.^{9,10,11} It was found that the magnetization had only a small component normal to the surface of the specimen even at the centres of domain walls, and that the structure of the walls at the surface was similar to that of Néel walls in thin films. In view of these experiments, it is important to develop models for the wall structure in thick films and bulk materials. The magnetization configuration of domain walls near the surface of thick films has been predicted by Hubert¹² from a consideration of the behaviour of his stray-field free model for increasing film thickness. Preliminary results of rigorous numerical calculations are given by Scheinfein *et al.*,¹¹ who used the same method as LaBonte.⁴ However, the computation time increases rapidly with increasing film thickness, and the calculation becomes impractical unless coarse subdivisions are used, which makes the results inaccurate. A possible way to overcome this problem is to subdivide the

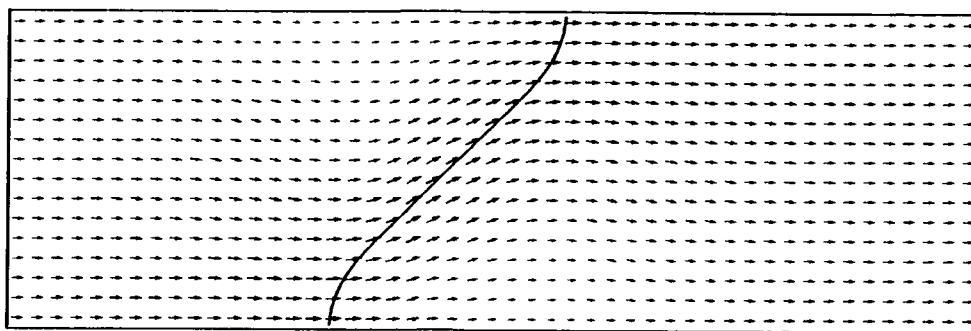


Fig. 9 Computed magnetization configuration for a 90° domain wall in an iron film of thickness 100 nm.

specimen into prisms with rectangular rather than square cross-section. Finer subdivisions can then be used near the surface, where the magnetization varies rapidly, and coarser subdivisions in the interior where the variation in the direction normal to the surface is slower. Using this method, Aharoni and Jakubovics¹³ confirmed that near each surface of thick specimens, the structure of 180° domain walls resembles one half of the vortex structure found in thin films. The two half-vortices are connected by a structure in which the magnetization is almost one-dimensional, varying only with x but almost independent of y . However, up to the largest thickness investigated so far ($3.8 \mu\text{m}$), the x -dependence was different from that given by the analytic solutions for infinite media, eqns (7) or (11). It is likely that these analytic solutions are only approached at very much larger thicknesses.

4. 90° DOMAIN WALLS

The SEMPA technique has also been used to study 90° domain walls,⁹ and it is therefore important to compute the structure of such walls. Computations for thin films have been carried out by Aharoni and Jakubovics.¹⁴ In this case one of the easy directions of magnetization is parallel to the y -axis, and the other two are in the xz -plane at $\pm 45^\circ$ to the x and z axes. The boundary conditions therefore become

$$\alpha \rightarrow \sqrt{\frac{1}{2}}, \quad \beta \rightarrow 0, \quad \gamma \rightarrow \pm \sqrt{\frac{1}{2}} \quad \text{as} \quad x \rightarrow \pm \infty. \quad (37)$$

In this case, assuming a cubic anisotropy only, the anisotropy energy becomes

$$F_a = K_c \Delta^2 \sum_{I=1}^{N_x} \sum_{J=1}^{N_y} \{ \beta^2(I, J) - \beta^4(I, J) + \frac{1}{4} [\alpha^2(I, J) - \gamma^2(I, J)]^2 \}. \quad (38)$$

In the case of a films of finite width in the x -direction, magnetic charges would be present on the faces perpendicular to x . In order to eliminate the effect of these charges, the magnetostatic energy of the wall is calculated by subtracting a uniform magnetization $M_s/\sqrt{2}$, where M_s is the saturation magnetization, from the wall structure. With these modifications, LaBonte's⁴ method may be used to compute the structure. Fig. 9 shows the result obtained for a 100 nm thick film with the same values of the material parameters as above. This structure has the symmetry of eqns (25), in contrast to 180° walls, which in films of similar thickness have the symmetry of eqns (24). However, the structure avoids both surface and volume charges quite efficiently, and has a relatively small magnetostatic energy.¹⁴

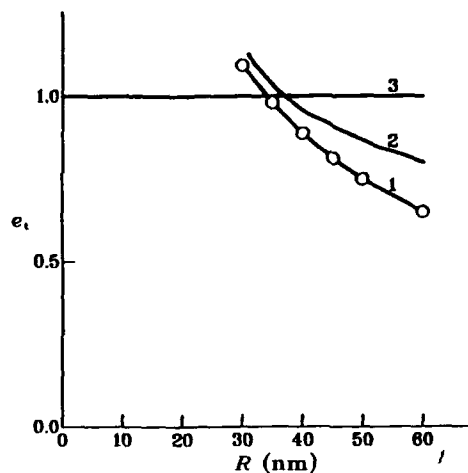


Fig. 10 Variation of the normalised total energy, e_t , with radius, R , for anisotropic spheres in zero field. Open circles and curve 1 represent the results of two-dimensional calculations. Curve 2 is taken from Fig. 5 of Stapper¹⁵, representing his two-domain state. Line 3 corresponds to saturated spheres.

5. SPHERICAL PARTICLES

The magnetization configuration is of interest not only in films, but also in small particles, since particulate magnetic media can be used in a number of applications, such as information storage and permanent magnets. For such applications, it is important to know whether particles of a given size are uniformly magnetized. The first computations aimed at determining the critical diameter of spherical particles at which a transition from uniform to non-uniform magnetization occurred was carried out by Stapper.¹⁵ However, he used a one-dimensional model in which the particles were divided into flat slices in which the magnetization was assumed to be uniform. More realistic magnetization configurations, and more reliable estimates of critical radii can be achieved by using a two-dimensional model. LaBonte's⁴ method can also be adapted to this case.¹⁶ The sphere is now subdivided in such a way that the boundaries between subdivisions are surfaces on which two of the three spherical polar coordinates are constant. The subdivision is therefore into $N_r \times N_\theta$ rings bounded by the spherical surfaces $r = (J-1)R/N_r$ and $r = JR/N_r$ ($J = 1, 2, \dots, N_r$), and the conical surfaces $\theta = (I-1)\pi/N_\theta$ and $\theta = I\pi/N_\theta$ ($I = 1, 2, \dots, N_\theta$), where R is the radius of the sphere. Within each ring, the polar components of the magnetization are assumed to be constant, so that the magnetization has cylindrical symmetry. The total energy is then the sum of the exchange, anisotropy and magnetostatic energies, plus the energy due to an applied field if one is present. Evaluation of the anisotropy energy and of the energy due to the applied field is straightforward. The exchange energy contains the sum of the energies of interaction of all pairs of rings that have a common surface, and in addition, each ring contributes a 'self-energy' because of the non-uniform magnetization (the polar, not the cartesian components being constant). The magnetostatic energy has a similar form to that for thin films, e.g. eqn (30), but the coefficients are much more difficult to evaluate, since the interaction between any two rings depends on their absolute, not relative positions, and therefore a four-dimensional rather than a two-dimensional matrix of coefficients is needed. The equations needed to evaluate the total energy are all given in ref. 16.

Magnetization configurations were computed for spheres with uniaxial anisotropy, with values of the parameters appropriate to cobalt. Fig. 10 shows a plot of the normalised total energy, e_t (i.e. the energy of the sphere divided by that of a uniformly magnetized sphere of the same radius), as a function of radius. It is seen that the two-dimensional model gives a lower energy than the one-dimensional one for all radii. The radius at which the energy of a uniformly magnetized sphere is equal to the lowest energy obtained for a non-uniformly magnetized sphere is about 34.1 nm, and below this radius the uniformly magnetized state would be favoured.

In real spheres some anisotropy is always present, but it is of interest to investigate whether useful properties could be achieved in particles with low anisotropy, since there are methods of producing spheres from amorphous materials. Computations have therefore been carried out to determine the behaviour of spheres with zero anisotropy in applied magnetic fields.^{17,18} The physical parameters were chosen to fit amorphous particles of $\text{Fe}_{75}\text{Si}_{15}\text{B}_{10}$. It was found that particles of radius 11.2 nm were uniformly magnetized even in zero applied field. In particles larger than that size the magnetization increased fairly linearly with applied field, reaching saturation in fields very close to the nucleation values predicted theoretically,¹⁹ these values increasing with increasing radius. However, for relatively small particles, the magnetization was not zero in zero applied field. For example, in spheres of radii 15 nm and 20 nm, the magnetization was 73.3% and 37.4% of the saturation value respectively. As the magnetization would be able to rotate easily on reversal of the field, these results predict a large susceptibility in particles of small anisotropy.

6. OTHER RECENT COMPUTATIONS

Two other ways of extending LaBonte's method may be mentioned. Firstly, magnetization configurations have been computed in small particles in the shape of rectangular parallelepipeds. This requires a straightforward extension of LaBonte's formulae into three dimensions, the subdivisions being in the shape of small cubes. A three-dimensional matrix is needed for the magnetostatic interaction coefficients.²⁰ Although the requirements of computer time and storage limit these calculations to fairly coarse subdivisions at present, magnetization processes in elongated particles have been modelled. The method has enabled magnetization reversal mechanisms to be studied in Ba-ferrite²¹ and $\gamma\text{-Fe}_2\text{O}_3$ ^{22,23} particles, including the effects of non-uniform applied fields such as those generated by magnetic recording heads,²⁴ and even complete hysteresis loops²⁵ to be obtained. Secondly, an extension of LaBonte's method has enabled the magnetization configuration in two-dimensional periodic structures such as stripe domains to be computed.²⁶ The only modification to LaBonte's method needed for this case is to replace individual terms making up the total energy by summations.

7. CONCLUSIONS

It has been shown that the two-dimensional numerical computation technique first used by LaBonte⁴ can be extended to a number of different problems. With faster and more powerful computers becoming available, it will be possible to model increasingly complex situations.

REFERENCES

1. C. Kittel, "Physical theory of ferromagnetic domains", *Rev. Mod. Phys.* **21**, 541 (1949).

2. A. Hubert, *Theorie der Domänenwände in geordneten Medien*, Springer-Verlag (1974).
3. A. Hubert, "Stray-field-free magnetization configurations", *Phys. Stat. Sol.* **32** 519, (1969).
4. A. E. LaBonte, "Two-dimensional Bloch-type domain walls in ferromagnetic films", *J. Appl. Phys.* **40**, 2450 (1969).
5. A. Hubert, "Interaction of domain walls in thin magnetic films", *Czech. J. Phys.* **B21**, 532 (1971).
6. R. A. Taylor, D. Phil. Thesis, University of Oxford (1981).
7. R. Wimmer, Diploma Thesis, University of Regensburg (1986).
8. J. P. Jakubovics, "Interaction of Bloch wall pairs in thin films", Proc. Int. Colloq. on Magnetic Films and Surfaces, Le Creusot, France (1988).
9. H. P. Oepen and J. Kirschner, "Imaging of magnetic microstructures at surfaces", *J. de Physique* **49** C8-1853, (1988).
10. H. P. Oepen and J. Kirschner, "Magnetization distribution of 180° domain walls at Fe(100) single-crystal surfaces", *Phys. Rev. Lett.* **62**, 819 (1989).
11. M. R. Scheinfein, J. Unguris, R. J. Celotta and D. T. Pierce, "Influence of the surface on magnetic domain-wall microstructure", *Phys. Rev. Lett.* **63**, 668 (1989).
12. A. Hubert, "Blochwände in dicken magnetischen Schichten", *Z. für angewandte Physik* **32**, 58 (1971).
13. A. Aharoni and J. P. Jakubovics, "Magnetic domain walls in thick iron films", to be published.
14. A. Aharoni and J. P. Jakubovics, "Structure and energy of 90° domain walls in thin ferromagnetic films", *IEEE Trans. Magn.*, in press.
15. C. H. Stapper, "Micromagnetic solutions for ferromagnetic spheres", *J. Appl. Phys.* **40**, 798 (1969).
16. A. Aharoni and J. P. Jakubovics, "Cylindrical magnetic domains in small ferromagnetic spheres with uniaxial anisotropy", *Phil. Mag. B* **53**, 133 (1986).
17. A. Aharoni and J. P. Jakubovics, "Magnetization curves of small isotropic spheres", *J. Appl. Phys.* **57**, 3526 (1985).
18. A. Aharoni and J. P. Jakubovics, "Approach to saturation in small isotropic spheres", *J. Magn. and Mag. Mater.* **83**, 451 (1990).
19. A. Aharoni, "Some recent developments in micromagnetics at the Weizmann Institute of Science", *J. Appl. Phys. suppl.* **30**, 70S (1959).
20. M. E. Schabes and H. N. Bertram, "Magnetization processes in ferromagnetic cubes", *J. Appl. Phys.* **64**, 1349 (1988).
21. Y. D. Yan and E. Della Torre, "The switching mechanism in BaFe particles", *IEEE Trans. Magn.* **25**, 3464 (1989).
22. M. E. Schabes and H. N. Bertram, "Ferromagnetic switching in elongated γ -Fe₂O₃ particles", *J. Appl. Phys.* **64**, 5832 (1988).
23. M. E. Schabes and H. N. Bertram, "Magnetization reversal of cobalt-modified γ -Fe₂O₃ particles", *J. Appl. Phys.* **67**, 5149 (1990).
24. M. E. Schabes and H. N. Bertram, "Effects of applied field inhomogeneities on the magnetization reversal of elongated γ -Fe₂O₃ particles", *IEEE Trans. Magn.* **25**, 3662 (1989).
25. Y. D. Yan and E. Della Torre, "Modelling of elongated fine ferromagnetic particles", *J. Appl. Phys.* **66**, 320 (1989).

26. M. Labrune and J. Miltat, "Micromagnetics of strong stripe domains in NiCo thin films", *IEEE Trans. Magn.*, in press.

DOMAIN WALLS AND WALL STRUCTURE

Floyd B. Humphrey

Boston University
Department of Electrical, Computer and
Systems Engineering
44 Cummington Street
Boston, MA 02215

The concept of a magnetic domain wall is as fundamental to the domain theory as the domains themselves. The original formulation of what we now call a Bloch Wall assumed an infinite sample, an energy of both exchange and anisotropy and recognized that the lowest energy would be when the demagnetizing field across the wall was zero. Straight forward energy minimization using the Ritz method calculated a finite, stable transition region between domains. The width of the wall was when the exchange energy just balanced the energy from anisotropy. The total energy was the sum of these two equal parts. The theory seemed clear, complete(1).

Some twenty years later, it became clear that the infinite sample assumption was in trouble. Films of vacuum evaporated Permalloy were made that were clearly too thin to contain walls because of the high demagnetizing energy at the surface(2). These "single domain" films did, indeed contain walls that could be easily detected by the Bitter Colloid technique. Calculations by Neel had already solved the problem by proposing a wall that rotated in the plane of the film confining the demagnetizing field to be across the wall(3). This Neel wall was stable in films as their thickness approached zero as long as the film was large enough to support the ever widening wall(4). When the energy of the Neel wall as a function of film thickness was compared to that of the Bloch wall, it was found that the transition between the two was for a film thickness of a few hundred angstroms. Below this transition, the Neel wall was energetically more favorable and above, the Bloch wall was more favorable.

The thickness, in Permalloy, of the Bloch-Neel wall transition was very fortuitous from an experimentalist point of view. It was at a thickness where domain walls could be seen quite well with the electron microscope using out of focus Lorentz imaging techniques. In this thickness range, the wall changed from one type to the other along the wall. Called cross-tie, these investigations were the first into wall structure(5). Unfortunately, The structure existed only over a rather narrow thickness range so that the more global effects of wall structure could not be realized. It was clear, however, that the effect of a finite sample on a Bloch wall could not be ignored.

Computers became available for modeling magnetic structures. A field free calculation of a Bloch wall in static equilibrium was made that avoided the demagnetizing energy at the surface by creating a vortex in the plane normal to the wall and surface(6). The flux of the center of the Bloch wall was "closed" by this circulation of flux either to one side of the wall or the other. At the surface, the magnetization would be parallel to the surface and perpendicular to the plane of the wall pointing one way or the other depending on which side of the wall the vortex happened to be.

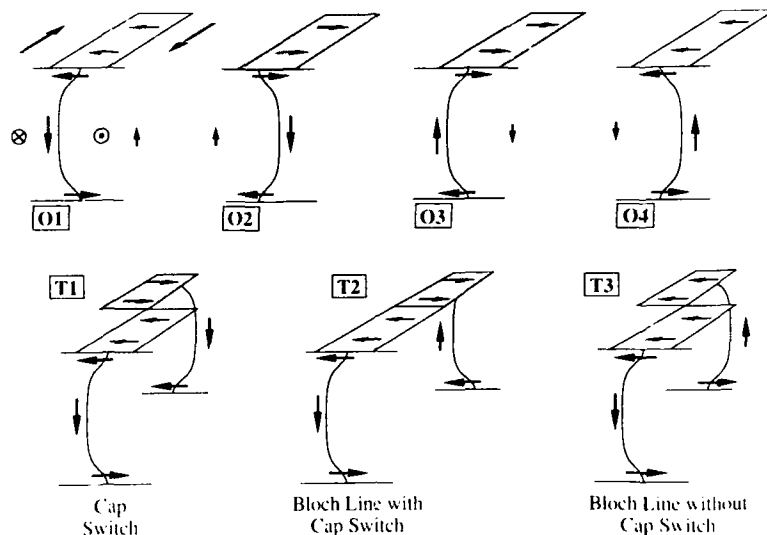


Fig. 1. Schematic of field free Bloch walls: O1, O2 down chirality; O3, O4 up chirality; O1, O3 vortex right; O2, O4 vortex left. Transition T1 is between O1 and O2; T2 between O1 and O3 and T3 between O1 and O4

All the possibilities for a field free Bloch wall(7) are shown in Fig.1A. Consider the little structure labeled O1. It illustrates a cross-section of an in-plane material at a Bloch wall. The sample, confined between the two horizontal lines, is magnetized into the paper on the left and out on the right. The Bloch wall between the two must have a chirality, i.e., a direction of rotation. For this wall it is clockwise when looking at the wall from the left. The chirality is indicated by the large arrow in the center pointing down showing the direction at the magnetization of the center of the Bloch wall. The small arrow to the right pointing up indicates the direction of the vortex flux and that the closure is on the right side of the wall. On the top surface (and, of course, on the bottom not shown) the vortex forces a little band of magnetization along to be magnetized normal to the wall in the direction of the vortex flux as shown. This stripe is shown white to indicate that an observation of the surface using the Magneto-optic Kerr Effect with the light incident normal to the wall has the analyzer adjusted to light. This same wall could have the vortex on the left side as shown in O2. Of course, the wall could have had the opposite chirality with the vortex on the right as shown in O3 or with the vortex on the left as shown in O4. These are the only possibilities for an arbitrary wall.

Transitions from one wall type to another are possible to predict as is the surface magnetization configuration that should be observed. If the wall starts as O1 and along the wall the vortex changes side to an O2 wall, then the transition should look like T1 of Fig. 1B. The cap should switch from white to

dark because the direction of the vortex flux reverses. Since the thickness of the Bloch wall part is much greater than the surface Neel part of the wall (the illustration is not to scale), a continuous wall can be expected forcing the cap to show a jog. If wall O1 changes to O3 the vortex stays on the same side so no jog is expected but the cap does switch because of the change of sign of the vortex. A Bloch line is the general name for the structure that must exist when walls of opposite chirality meet. There is a vertical Bloch line (VBL) under the surface at T2. The BL is vertical to mean that the whole wall changes chirality at that place through the thickness of the sample. Finally, if O1 changes to O4, the vortex changes side producing a jog but without a contrast change because the chirality also changed. Again, there is a VBL under the surface.

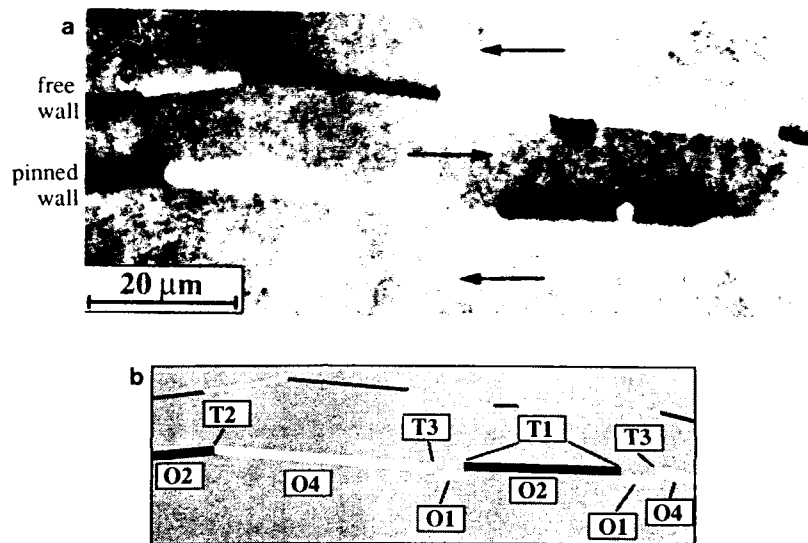


Fig.2 (a) High resolution Kerr magneto-optic micrograph in an amorphous ribbon and, (b) schematic of a with wall sections and transitions identified

Using a high resolution optical microscope equipped with an image enhancement system(8) to observe the Longitudinal Kerr Effect, these structures have all been recently identified in amorphous FeCoSiB ribbon. A section of two walls can be seen in Fig. 2A. Since the microscope is set to resolve the magnetization that is normal to the walls (vertical), the domains with magnetization along the walls are the same shade of gray. A schematic in Fig. 2B identifies the walls and transitions.

One of the walls in Fig.2A looks and is twice as wide as the other. This wall is the result of annealing the film with the wall in place(9). The anisotropy created by this annealing assumes the direction of the magnetization at the time of the anneal. Since the wall has a twist, the anisotropy assumes a twist. The wall is now pinned and will not move when small fields are applied. Since the anisotropy axis is in the shape of the wall, the anisotropy energy should be very low since the magnetization is everywhere along the anisotropy axis. The exchange energy, to balance the anisotropy, widens the wall. Since exchange energy is very nearly proportional to distance across the wall, the wall looks twice as wide.

A quasi-wall is a boundary between two domains with their magnetization in the same direction. Having a pinned wall makes the creation of quasi-walls relatively easy. Figure 3 is a Kerr micrograph of a quasi-wall under various conditions. The exact structure of the quasi-wall will depend upon how it is formed. Normally a free wall will approach a pinned wall. The resultant will depend upon their relative chirality, i.e., whether they form a winding or unwinding pair. The relative side of the vortex will also make a difference, i.e., do their vortices meet first or not at all. At this time, no one has unraveled these details for these quasi-walls.

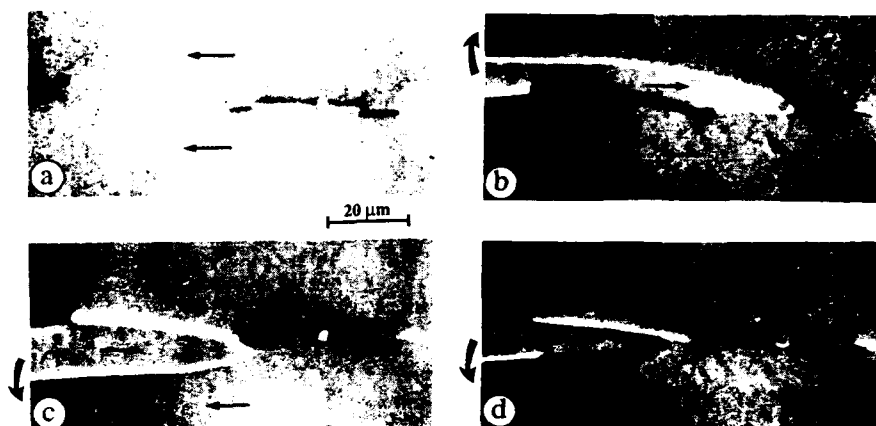


Fig. 3 Kerr magneto-optic micrograph of, (a) quasi-wall; (b) pinned wall with 2 VBL's, quasi-wall and normal wall; (c) pinned wall with VBL, quasi-wall and normal wall; and (d) pinned wall with VBL, quasi-wall, and normal wall with cap switch

Magnetic material that is spontaneously magnetized perpendicular to the surface adds a new twist to the wall(10). Bubble garnet material is a good example of this kind of material. The surface stray field creates a strong field across the wall that reverses direction in the center of the sample to be in the opposite direction at the other surface. This field puts a twist in the wall as a function of thickness through the material as illustrated in Fig. 4A. Of course, there is always the opposite chirality as seen in Fig. 4B. Also there is still the rotation of the magnetization associated with a Bloch wall. The static Bloch wall in bubble material is illustrated in Fig. 4C. Each twist is only correct along the center of the wall in each direction. The chirality of the wall is still determined by the center "spin" as before indicated by the black arrow. A change in chirality creates a VBL. The structures have been more extensively studied in this material than in the planar materials because of the profound effect the structure has on the dynamics of the walls.

In magnetic bubble memories, the expectation is that the bubble domain will be translated by gradient fields in the direction normal to the surface created by an overlay of planar material driven by a rotating in-plane field. The desire and expectation was that the bubble domains would be reproducible and easily pushed around. It was found that some bubbles did not move because their walls were filled with VBL's. Fortunately, ways were found to keep the number small so that the memory could be made to work. Even so, a small number of VBL's can make a large effect on the direction the bubble moves in respect to the direction of the gradient. Since VBL's are a rotational structure, they have a chirality. A pair of the same chirality VBL's can change the direction of motion of the bubble domain by 10-20 degrees whereas a pair with opposite chirality will make no change at all. An unwinding pair,

i.e., a pair with opposite chirality, can make the bubble domain move even after the gradient field is removed. Winding pairs are so stable that they are the basis of an attempt to make a computer memory where the information is stored in the form of VBL pair or no-pair for a "one" or "zero".

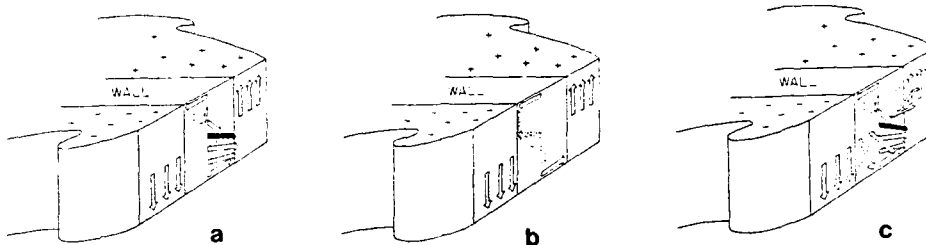


Fig. 4 Domain wall in material magnetized normal to the plane of a film (a) twist caused by the stray field from the surface domains (b) opposite chirality and (c) Bloch wall

Horizontal Bloch lines are mostly associated with moving walls since most are statically unstable(11). Remember that a cross product is in the equation of motion for the magnetic system. Therefore, a field applied to move a wall couples only to the magnetization in the wall since the magnetization in the domains is parallel to the field ($M \times H = 0$). A field applied to bubble material will cause a precession in the wall in the direction of the twist shown in Fig 4A. This precession will take one surface to the equilibrium of the opposite chirality wall. The two sections of wall with opposite chirality satisfy the definition of a BL but this time a horizontal Bloch line. It's horizontal to indicate that it runs along a wall rather across it dividing the sample through the thickness. As the wall continues to move, the HBL continues to move through the thickness confining the rotation to a limited area. When it reaches the opposite surface, the spins there make a 2π rotation. A new HBL starts at that surface to move in the opposite direction through the sample. This motion of the HBL hinders the motion of the wall. Whereas walls in planar material have a linear mobility, i.e., they move proportionally faster in higher field, walls with HBL's have a very limited linear mobility assuming a velocity that remains unchanged for orders of magnitude increase in field amplitude.

A wide variety of horizontal wall structure has been identified mostly by observing the motion of the wall. For instance, when the HBL reaches the opposite surface, the spinning of the surface magnetization during "punch through" can stop the wall for a short time. This process is very surface sensitive so that slight surface modification by ion implantation can inhibit punch-through. When the HBL gets to the "far" surface, it continues to wind up becoming a 2π HBL(12). The 2π and multiple 2π structures are statically stable, however, most samples are quickly filled with this windup. Similar structures have been seen in computer simulation but not confirmed experimentally. An HBL can also be created by a modest in-plane field on the wall. By comparing the velocity of the normal and structured wall, the chirality of structureless bubble domains can be determined.

Bloch points are the result of topological arguments. There is a clear need for something like them to explain various experimental results but no experiment has directly confirmed their existence. They also seem to fit the other structure. A domain wall is a transition between two oppositely (differently) oriented domains. A Bloch line is the transition between regions of opposite chirality within a wall. It seems reasonable that a Bloch point should be the transition between two sections of opposite chirality Bloch lines.

They are needed to provide a mechanism for the loss of VBL's in the wall. Bloch loops can create VBL's but cannot destroy them. A +/- VBL pair will annihilate. Once a winding pair, either ++ or -- is in a wall, there is no mechanism for their removal without using a Bloch point. By observing the motion of bubble domains in a rotating gradient experiment, for example, it is clear that changes are made. The most reasonable mechanism involves the nucleation of a Bloch point. When it moves, it changes the chirality of the BL. The resultant +/- pair can then annihilate. With the recent interest in the VBL memory, there is a renewed interest in Bloch points because they hold the key to the stability of the memory.

Summary

Domain walls are fundamental to the domain theory of magnetism but that does not mean that they are simple. The shape and structure that they take depends on the material and geometry. The chirality of walls is important. Wall structure exists to match chirality changes in the form of Bloch lines. Vertical Bloch lines move along walls pushed by gyrotropic forces. Horizontal Bloch lines dominate the dynamic characteristics of walls in some materials. Although it was once felt that wall structure was confined to very thin planar material and perpendicular material, it's now clear that "bulk" material has it's share of structure. The idealized Bloch wall is useful as a concept but when details are needed, expect something much more complicated.

References

1. C.Kittel "Physical Theory of Magnetic Domains", Rev. Mod. Phys. **21**, 541 (1949)
2. C. Kittel "Theory of the Structure of Ferromagnetic Domains in Films and Small Particles", Phys.Rev., **70**, 965 (1946)
3. L. Neel, "Energy des Parois de Bloch dan les Couches Minces", C.R. Acad. Sci. Paris **241**, 533 (1955)
4. S. McVitie and J.N. Chapman, "Magnetic Structure in Small Regularly Shaped Particles using Transmission Electron Microscopy" IEEE Trans. Magn. **Mag-24**, 1778 (1988)
5. A. Hubert, "Domain Wall Structures in Thin Magnetic Films", IEEE Trans Magn. **Mag-11**, 1285 (1975)
6. A. Hubert: "Stray-field-free Magnetization Configurations" Phys. Stat. Soli. **32**, 519(1969).
7. R. Schaefer, W.K. Ho, J. Yamasaki, A. Hubert and F.B. Humphrey, IEEE Trans Magn (in press)
8. F. Schmidt, W. Rave and A. Hubert, "Enhancement of Magneto-optical Domain Observation by Digital Image Enhancement", IEEE Trans. Magn. **Mag-21**, 1596 (1985)
9. J. Yamasaki, K. Mohri, K. Watari and K. Narita "Domain Wall Induced Anisotropy during Annealing in Amorphous Ribbons", IEEE Trans. Magn. **Mag-20**, 1855 (1984)
10. J.C. Slonczewski "Theory of Domain Wall Motion in Magnetic Films and Platelets", J. Appl. Phys., **44**, 1759 (1973)
11. B. MacNeal and F.B. Humphrey "Horizontal Bloch Line Motion in Magnetic Bubble Materials", IEEE Trans Magn., **Mag-15**, 1272 (1979)
12. T.J. Gallagher and F.B. Humphrey "Dynamics of Stable Horizontal Wall Structure in Magnetic Bubble Domains", J. Magn. and Mag. Mat., **15-18**, 1493 (1980)

DOMAIN WALL MULTIPLICATION IN AMORPHOUS FERROMAGNETIC ALLOYS

C. Beatrice, P. Mazzetti*, and F. Vinai

Istituto Elettrotecnico Nazionale Galileo Ferraris
GNISM-INFM, 10125 Torino, Italy

* Phys. Departement, Politecnico di Torino, 10129
Torino, Italy

ABSTRACT

The domain wall multiplication in the amorphous alloy $\text{Fe}_{81}\text{B}_{14}\text{Si}_3\text{C}_2$ is investigated as a function of stress and temperature. Optical observations of the domain pattern, performed in conjunction with a.c. permeability measurements, show that new 180° domains grow from small nuclei where the local stresses are frozen-in during the rapid quenching. Such instability of the domain structure is compared with the intrinsic dynamic instability of a single domain wall.

INTRODUCTION

It is well known that multiplication of domain walls takes place in ferromagnetic laminations when, under alternating fields, critical conditions for the amplitude of the wall displacement are obtained^{1,2}. Such an effect can be ascribed to two different types of processes. First, a wall driven beyond a certain critical velocity becomes intrinsically unstable, because the pressure exerted by the eddy current field cannot be sustained any longer through bowing of the wall profile³. This process is strictly related to the value of the wall surface energy γ_0 . Second, domain nuclei, related to defects and local stresses, can grow and develop into extended active domains. A qualitative description of these two processes is given in Figs 1a and 1b.

In a preceding paper⁴ we performed an experimental investigation on the intrinsic instability of the domain wall, by means of an optical method. This method is based on the measurement of the absolute maximum displacement that a wall, oscillating under an a.c. driving field, can attain before breaking down. It permits one to determine the specific wall energy γ_0 .

In this paper we concentrate on the role played in wall multiplication by domain nuclei, through experiments performed under different conditions of stress and temperature. We find that the critical field H_{c1} at which new domains are generated from existing nuclei is in general smaller than the field H_{c2} at which intrinsic domain wall instability takes place. However, by increasing the applied tensile stress H_{c1} tends to increase, for nuclei tend to disappear. A similar effect is observed after annealing.

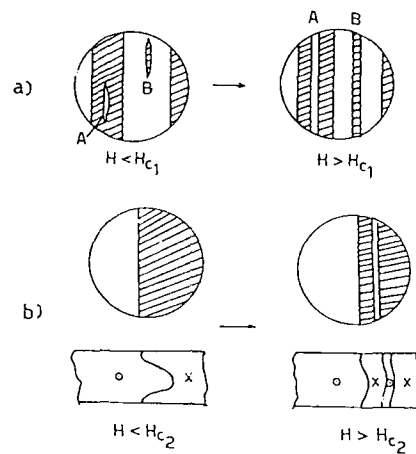


Fig. 1. 1a) Schematic representation of domain nuclei (A and B). They give rise for $H > H_{c1}$ to four moving walls. 1b) Critical bowing of a domain wall. A new domain enucleates when $H > H_{c2}$.

EXPERIMENTAL SETUP

The measurements were performed on amorphous ribbons of $\text{Fe}_{81}\text{B}_{14}\text{Si}_3\text{C}_2$ having a length of 130 mm, a width of 5 mm and an average thickness of 38 μm . In order to create a very regular domain pattern, the sample was subjected to a minimum tensile stress of 210 MPa and systematically demagnetized, through a quasi-static procedure, before each run. A sinusoidal field H , ranging in amplitude between 0.1 and 100 A/m and in frequency between 1 kHz and 50 kHz, was applied. Computer assisted data acquisition was made by two digital multimeters respectively for the applied field H and the induced signal dB/dt.

The measuring temperature ranged between 20 C and 250 C. Room temperature permeability measurements were associated with Kerr-effect optical observations of the domain pattern, in order to relate the electrical signal to the number of active domain walls.

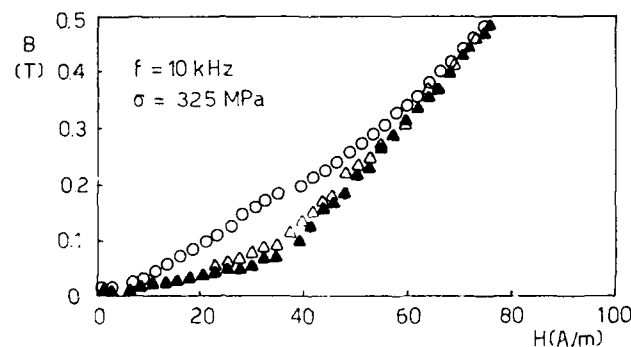


Fig. 2. Dependence of peak induction B on the driving field amplitude H , in correspondence of three different initial domain patterns: \blacktriangle 4 walls, \triangle 6 walls, \circ 10 walls. The magnetizing frequency is 10 KHz. The final number of walls is 10.

RESULTS

Domain wall multiplication in the investigated sample can be clearly recognized through the B vs. H behavior reported in Fig. 2. Let us consider the lower curve (black triangles). As demonstrated by simultaneous Kerr effect observations, an initial domain pattern, characterized by four 180° Bloch walls, evolves, upon increase of the driving field amplitude, towards a final state with ten walls. An abrupt change of slope above a certain threshold field $H_{c1} \approx 38$ A/m can be noticed. This corresponds to the full development of a nucleus into a new 180° domain. A very same effect can be put in evidence when we start with six Bloch walls (open triangles). This is not the case when we operate in order to keep a constant number of walls everywhere (open circles, ten walls). It should be stressed that, were in this case the multiplication due to the intrinsic wall dynamic instability, it would have required a much larger critical field $H_{c2} \approx 80$ A/m [4].

In Figs. 3 and 4 we have reported the B vs. H behavior at different frequencies, in correspondence of two values of applied tensile stress ($\sigma = 210$ MPa and $\sigma = 325$ MPa respectively). One can clearly see that by increasing the applied stress the wall multiplication becomes hindered, because the nucleation centres tend to disappear. A similar effect takes place upon annealing, as shown in Fig. 5. Again, by relaxing long range residual stresses the number of nuclei is reduced and the critical field increases. The role of temperature has been investigated on the annealed samples. In Fig. 5 we report the B vs. H behavior determined at $T = 158$ C. From this and other experiments we conclude that domain wall multiplication is enhanced by temperature.

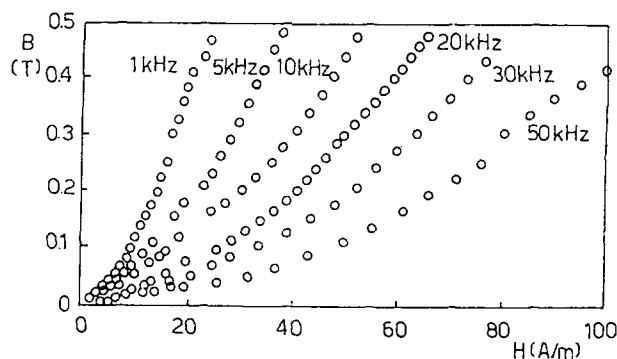


Fig. 3. B vs H curves at different frequencies. $\sigma = 210$ MPa.

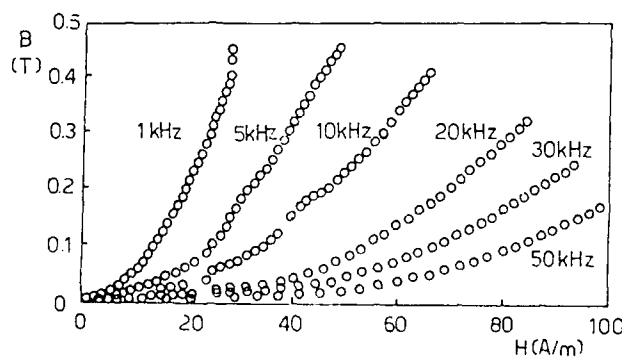


Fig. 4. B vs H curves at different frequencies. $\sigma = 325$ MPa.

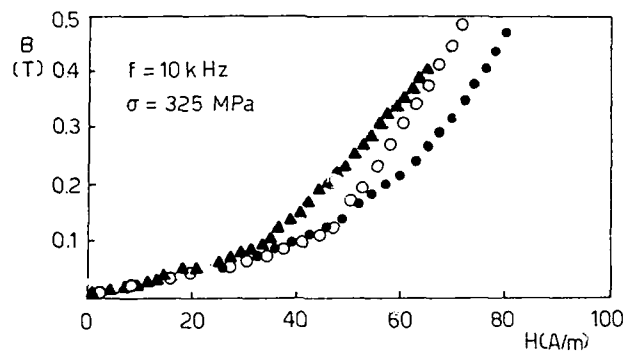


Fig. 5. B vs H curves at 10 kHz measured on : \blacktriangle as cast ribbon at room temperature, \bullet annealed ribbon at room temperature, \circ annealed ribbon at 158 C.

CONCLUSIONS

The domain wall multiplication caused by nucleation of domains from existing nuclei has been investigated in the amorphous alloy $\text{Fe}_{81}\text{B}_{14}\text{Si}_3\text{C}_2$. It is shown that the critical field H_{c1} above which new walls become active is generally smaller than the critical field H_{c2} at which intrinsic instability of a single domain wall occurs. However, annealing and/or application of a tensile stress tend to suppress domain nuclei, therefore leading to an increase of H_{c1} .

ACKNOWLEDGMENTS

It is a pleasure to thank F. Fiorillo for useful discussions.

REFERENCES

1. J. W. Shilling, and G. H. House Jr., IEEE Trans. Magn., **MAG-10** (1974) 195.
2. S. D. Washko, M. L. Osborn, and W. G. Veeraraghaven, J. Appl. Phys. **52** (1981) 1899.
3. J. E. L. Bishop, M. J. Threapleton, J. Magn. Magn. Mater. **40** (1984) 293.
4. C. Beatrice, P. Mazzetti, and F. Vinai, to appear on IEEE Trans. Magn., **MAG-26**, (1990).

ELECTRON MICROSCOPE METHODS FOR IMAGING INTERNAL MAGNETIC FIELDS AT HIGH SPATIAL RESOLUTION

J.C.H. Spence and Z.L. Wang*

Dept. of Physics
Arizona State University
Tempe
AZ. 85287 U.S.A.

*Oak Ridge National Laboratory
P.O. Box 2008
Oak Ridge
TN 37831

1. INTRODUCTION

This Advanced Study Institute is primarily concerned with magnetism in small particles, thin films, interfaces and multilayers. In other words, we are interested in the effects of boundary conditions and low dimensionality on spin systems. Before the dynamic magnetic properties of these structures can be understood, an older and simpler question often remains to be answered - what is the spatial arrangement of the spins at low temperatures on a nanometer scale? How is the three-dimensional vector field modified by the presence of boundaries, defects and interfaces? For bulk materials, we may similarly be interested in the fine details of magnetic domain structure - for example in the measurement of domain wall width, and in the mechanisms of flux pinning.

This article has two purposes. Firstly, we will provide a brief summary of the transmission electron microscope techniques which exist for the spatial mapping (imaging) of magnetisation in crystals, and outline the important physical principles on which they are based. These methods are known generically as "Lorentz microscopy", since, in a classical picture, all depend on the effects of the Lorentz force. Applications of these methods will also be described. Since other contributors have been commissioned to do so, we shall not discuss the exciting recent developments in the scanning tunnelling microscopy of magnetic materials, or the equally important spin-polarized imaging using secondary electrons in scanning electron microscopy (SEMPA). Secondly, we then summarise our recent research into a new method which holds promise for imaging the domain structure of magnetic monolayers. By allowing real-time recording of bulk samples, this method may also permit studies of dynamic properties at high temperatures.

These various magnetic field imaging techniques may be classified according to whether they require thin, electron transparent films for the transmission geometry, or bulk samples for either the reflection geometry or for the detection of back-scattered¹ or secondary electrons. Ultrahigh vacuum conditions may also be needed for the study of magnetic monolayers prepared in

surface science laboratories. We will restrict ourselves to those methods which have been developed for use in modified transmission electron microscopes. The most important modification is the creation of a field-free region around the sample. (Conventional transmission electron microscopes operate with the sample immersed in a field of about 2T). This is easily achieved in older TEM instruments where the objective lens may be switched off. The diffraction lens can then be used to form a low magnification image of the sample. On modern machines where microprocessors are used to control all the lens currents, extensive modifications may be necessary. A controllable transverse field at the sample level is also desirable for dynamic magnetisation experiments. Convenient double-tilting transmission heating stages capable of heating samples up to about 1000°C while retaining an alignment precision of less than a milliradian have also become available recently for the first time, and will be useful for the study of magnetic phase transitions. Video-rate recording systems with image intensifiers are also now available commercially for TEMs.

Since some of the most important results have come from comparisons of crystallographic and magnetic microstructures, atomic resolution transmission electron microscopy (and diffraction contrast imaging) may also be needed. This is particularly important for research on flux pinning mechanisms, on small particles, and on multilayers. In multilayers the important question arises as to how the multilayer crystallographic structure influences the magnetic domain structure, and how this differs, if at all, from that of a random substitutional alloy. As an example of the contribution which high resolution electron microscopy can make, figure 1 shows a non-magnetic multilayer film under development for possible application as an X-ray mirror². The crystalline silicon substrate can be seen, together with alternating layers of Mo (darker fringes) and amorphous silicon. This image was taken on an atomic resolution transmission electron microscope. As discussed below, contrast in the thinnest regions results from phase changes in the electron beam, and is proportional to the projected electrostatic crystal potential $V(x,y)$. In ferromagnetic materials, an additional weaker phase shift due to the magnetisation of the crystal would be superimposed on this electrostatic contrast. The interface abruptness can be estimated on an atomic scale from these images, which were recorded on a JEOL 4000 transmission electron microscope (TEM), with a point resolution of 0.17 nm.

Several reviews of the TEM imaging of magnetic materials have appeared recently^{3, 4, 5}.

2. INTERACTIONS AND CONTRAST MECHANISMS. AHARONOV-BOHM

The formation of a high resolution image which can be simply related to the strength and direction of the total magnetic field \mathbf{B} within a crystal requires at least the following: (a) A strong interaction between \mathbf{B} and the imaging radiation, (b) A convenient lens, or a sufficiently coherent radiation source to allow holography. (Incoherent projection imaging methods are limited in resolution by the available detector resolution). (c) A method of three-dimensional reconstruction of the vector potential \mathbf{A} from the projection of one component of \mathbf{A} which imaging systems provide.

Neutrons possess a usefully strong magnetic interaction, however despite active research, convenient lenses have yet to be developed. (If based on the Fresnel zone plate, the lens resolution would be equal to the width of the smallest (outermost) zone). For X-rays, however, the direct magnetic interaction is extremely weak. (X-ray topographic images do not show 180° domain walls). The projection problem for vector fields is particularly difficult, and no successful three-dimensional reconstructions of this have yet been reported.

Field emission electron sources are the brightest particle sources known to physics. Since brightness may always be exchanged for coherence, these sources therefore allow holography experiments to be conveniently undertaken. Detectors with a quantum detective efficiency close to unity are

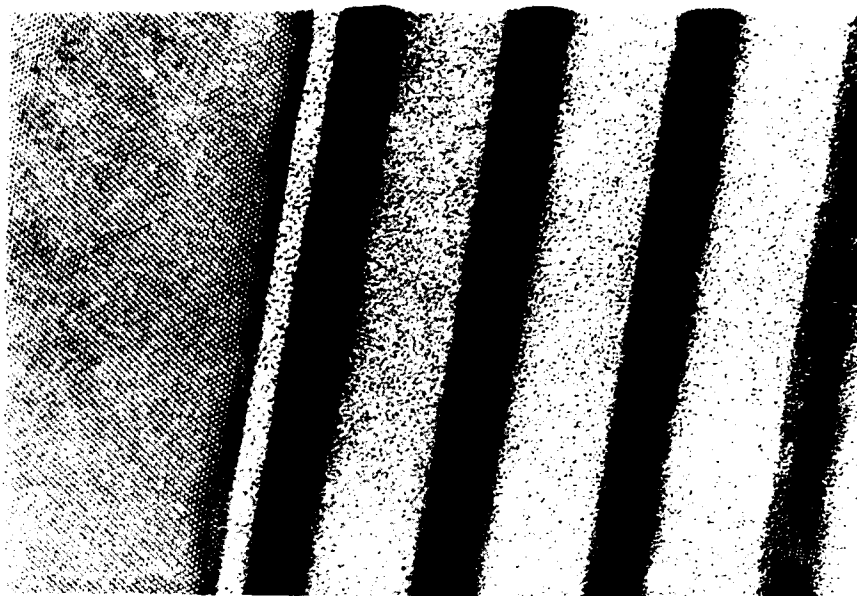


Figure 1. High resolution transmission electron micrograph of a an Mo/Si multilayer grown on (100) crystalline silicon. The silicon (111) lattice fringes can be seen (spacing 0.311 nm) . Darker layers are Mo, lighter layers are amorphous silicon.

available for electrons. Magnetic electron lenses are now commercially available for electrons whose energy is a few hundred kilovolts with a resolution as small as 0.17 nm. Also for electrons, the classical Lorentz force provides a usefully strong magnetic interaction. For the quantitative analysis of magnetic contrast images at high resolution, however, the equivalent quantum mechanical interaction is required. We now discuss the relationship between these two descriptions of the interaction, since this forms the basis of all electron microscope magnetic contrast imaging methods which use polarization insensitive electron sources and detectors.

Consider a collimated (plane-wave) electron beam traversing a thin magnetised slab of single crystal of thickness t , as shown in figure 2. Radiation from S passes through the crystal at A to the detector at D. If m is the electron mass, λ its wavelength, e the electronic charge, $V = V(\mathbf{r})$ the crystal electrostatic potential in volts, E_0 the accelerating voltage, \mathbf{A} the vector potential (with $\mathbf{B} = \text{curl } \mathbf{A}$) and \mathbf{p} the beam electron's momentum, then the Hamiltonian describing the interaction of the beam electron with the crystal potential is, in S.I. units,

$$H = \frac{1}{2m}(\mathbf{p} + e \mathbf{A})^2 - eV \quad 1$$

As discussed in section 5 this interaction, when used in the Schroedinger equation, leads to a "transmission function" for the incident electron beam of the form

$$\chi(x, y, t) = \exp\left(\frac{i\pi}{\lambda E_0} \int_0^t V(x, y, z) dz - \frac{2\pi e}{h} \int_0^t \mathbf{A}_z(x, y, z) dz\right) \quad 2$$

where h is Planck's constant. For a very thin sample (less than 20 nm thick in a 200Kv electron microscope) equation 2 gives the wave-function across the downstream face of the sample. We conclude that thin TEM samples of magnetic

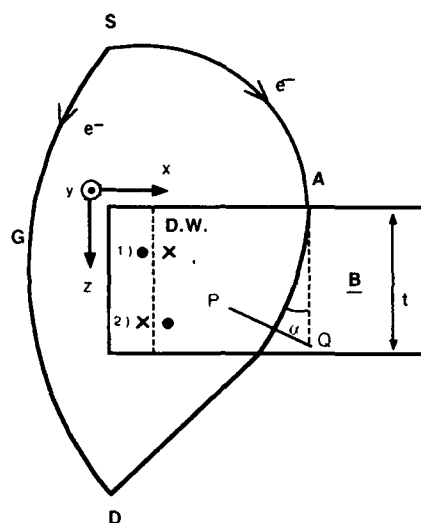


Figure 2. The geometry of Lorentz microscopy and interferometry experiments. S - electron source, D - electron detector. The path of the integral in equation 3 is SADG. A simple domain wall (D.W.) is also indicated, with two possible magnetisations.

materials are phase objects, in which the spatial variation of phase contains a large contribution from the projected scalar electrostatic crystal potential and (even for ferromagnets) a smaller contribution from the vector magnetic potential. For a foil thickness of about 100nm as used in the DPC method (see section 4), phase changes due to the magnetic interaction alone of up to 15 radians are common, so that the first-order expansion of equation 2 (the "weak phase object" approximation) cannot be made.

It is this wave-function χ which is imaged by the electron lenses in a high resolution electron microscope. In order to convert this phase variation into an intensity variation, any of the methods of optical phase contrast microscopy may be used. In conventional high resolution lattice imaging (e.g. figure 1), a special choice of objective lens focus deficit is used, so that the image becomes an in-line, bright field hologram. By introducing aberrations and a diffraction limit, these lenses also limit the resolution of the image to about 0.2 nm. Since the first term in equation 2 is much larger than the second, under high resolution imaging conditions where many Bragg beams contribute to the image we see only a projection of the electrostatic crystal potential V . If the resolution of the microscope is limited, however, by using a small central objective aperture to exclude Bragg diffracted beams, the fine lattice periodicity in $V(x,y,z)$ may be suppressed, leaving contributions only from the second (magnetic) term, from thickness variations, and from the effects of bending on the local diffraction conditions. At large defocus, the magnetic phase change produces the characteristic fringes at domain boundaries which form the basis of the Fresnel method. We note that the electrostatic and magnetic contributions to the phase of the electron wave-field can be distinguished if the sample magnetisation is reversed (for example by inverting the sample).

The first (electrostatic) term can be written in a similar form to the second (magnetic) term, since, if τ represent time, and T is the time taken for the electron to pass through the sample at velocity v ,

$$\frac{\pi}{\lambda E_0} \int_0^t V(z) dz = \frac{2\pi m e \lambda}{h^2} \int_0^t V(z = v\tau) dz = \frac{2\pi e}{h} \int_0^t V(\tau) d\tau$$

We shall also be discussing off-axis electron holographic methods for obtaining magnetic contrast. For this purpose, the phase shift between the ray SAD and the reference wave SGD shown in figure 2 is, for a constant magnetic field $\mathbf{B} = B_0 \hat{z}$,

$$\Delta\theta = \frac{2\pi e}{h} \int \mathbf{A} \cdot d\mathbf{l} = \frac{2\pi e}{h} \int \mathbf{B} \cdot d\mathbf{s} = \frac{2\pi e}{h} B_0 \Phi = \frac{2\pi e}{h} \Phi \quad 3$$

Here Stokes' theorem has been applied to the integration path SADGS, which encloses flux Φ . Since the integral of the tangential component of a gradient around a closed path is zero, the gradient of any scalar function may be added to \mathbf{A} without changing $\Delta\theta$, and this observable is therefore gauge invariant. The Aharonov-Bohm paradox arises if a compact solenoidal field is placed between the ray paths. Then the rays may pass in regions where $\mathbf{B} = 0$, but $\mathbf{A} \neq 0$. A phase-shift is nevertheless observed experimentally⁷.

The deflection of the ray AD at $z = t$ in figure 2 is thus

$$\alpha = \frac{\lambda \Delta\theta}{2\pi x} = \frac{\lambda t e B_0}{h} \quad 4$$

The hyperbolic wavefront PQ is seen to suffer a local deflection α . This is the same deflection which would be calculated using the classical Lorentz force law. For $t = 200\text{nm}$, $\alpha = 0.2\text{ mRad}$ for a typical ferromagnetic material irradiated by 100 kV electrons. This is considerably less than the Bragg angle. Internal magnetic fields within a crystalline sample containing many domains therefore produce fine structure (spot splitting) in transmission electron diffraction patterns. It is large enough, however, to alter the local diffraction conditions (i.e. the Ewald sphere orientation) of the electron beam. This provides the second important source of contrast in crystalline magnetic materials. A beam at the Bragg condition in one portion of a crystal (and hence causing that portion of a bright-field image to appear dark) may be deflected out of the Bragg condition by local magnetic fields in another, causing it to appear bright.

For thin samples containing a spatially varying field $B_y(x)$ (see figure 2) the variation of phase across the downstream face of a sample of constant thickness t between points x_1 and x_2 is given by

$$\Delta\theta(x) = \frac{2\pi e t}{h} \int_{x_1}^{x_2} B_y(x) dx \quad 5$$

The effect of a domain wall (D.W. in figure 1) is therefore akin to that of a Fresnel biprism in optics. Note, in particular, that if the integral had been taken *along* a line of \mathbf{B} (i.e. in the y direction), then $\Delta\theta = 0$. This result is used to interpret fringes in the electron holography method. In case 1) in figure 2, electrons passing through the domain whose magnetisation runs in the $+y$ direction will be deflected in the $+x$ direction, and so overlap with those deflected in the opposite direction which have passed through the other domain. The resulting interference fringes observed at large defocus delineate the domain boundary by a bright fringe, and form the basis of the technique of Fresnel mode Lorentz microscopy (for a review, see Jakubovics 1975). In case 2), a deficiency of intensity is produced. This method is the simplest method of

obtaining contrast from magnetic structures in a TEM. Because of the large defocus and high coherence required, however, the images are faint (unless a field-emission gun is used) and show poor resolution. A considerable amount of work has been devoted to the problem of extracting the variation of magnetic induction from these Fresnel fringe images (see for example 8). The number of adjustable parameters in such a "refinement" can become rather large, however. These include defocus setting, thickness t , magnetic field model parameters, magnification, field strength, inelastic scattering parameters etc. The method has therefore proven to be useful mainly for qualitative work. In the related Foucault mode, a half-plane objective aperture is used to produce in-focus phase contrast. This method complements the Fresnel mode in that, unlike the Fresnel mode, it provides a level of contrast which varies with the mean direction of magnetisation in the sample. Both therefore provide simple and useful qualitative imaging techniques for magnetic materials in TEM instruments. For both, the relationship between magnetisation and image intensity is highly non-linear (see figure 5). In general, while a knowledge of the sample magnetization fixes $\Delta\theta(x,y)$, the inversion is not unique.

3. ELECTRON INTERFEROMETRIC TECHNIQUES

Gabor's original proposal for holography described a system for electron (not optical) holography. While initially overshadowed by the spectacular successes of optical holography, work on electron holography has nevertheless continued steadily for over thirty years. Whereas most of this has been aimed at improving atomic resolution images of the electrostatic potential, it is ironic that perhaps the most successful results to date have come from the application of electron holography to the imaging of magnetic structures, as first suggested by Cohen ⁹. Dramatic results have appeared over the last decade from at least three groups, in Bologna, Tübingen and Tokyo (Hitachi). This has been chiefly due to the recent development of stable field-emission electron guns for TEM instruments. (These were previously available only for ultra-high vacuum STEM machines). The field of electron holography has recently been reviewed ¹⁰. The field-emission gun provides sufficient coherence and intensity to allow the recording of as many as 500 fringes in a few seconds onto film. The finest fringes so far recorded appear to be less than 1 nm, however other material's dependent factors limit the resolution of the method for magnetic samples, as further discussed below. For good separation of the real and conjugate images one requires a carrier frequency about three times higher than the highest spatial frequency of interest in the image. The magnetic lenses of the microscope provide some magnification, and, if the reconstruction is completed using laser illumination, a further magnification equal to the ratio of the electron to laser radiation wavelengths is obtained. The use of an electrically charged fine wire beyond the sample as a beam-splitter ¹¹ has now become established as the most versatile and convenient experimental arrangement. (Amplitude division of wavefront, using a thin crystal at the Bragg condition, has also been used ¹⁰). By placing this wire between two grounded vertical plates in the selected area aperture position, an electron biprism is created. The sample is then illuminated by two virtual point sources. Interpretation is greatly simplified, however, if it is also arranged for one of the incident waves to pass only beyond the edge of the sample ¹². The result may then be interpreted as an off-axis electron hologram. Then, if the film detector is arranged to be conjugate to a plane a distance Δf beyond the lower sample surface, the wavefield beyond the sample where the two wavefields overlap is

$$\Psi(x, y) = \chi'_{\Delta f}(x, y, t + \Delta f) + \exp\left(-\frac{2\pi i x}{S}\right) \quad 6$$

Unit magnification has been assumed, and $\chi'_{\Delta f}$ is related to χ by the Fresnel

free-space propagator¹³. Here s is related to the voltage on the biprism, and so is under the control of the experimenter. Information on the spatial variation of the magnetic potential is thus encoded in the intensity variation of the fringes $\Psi\Psi^*$.

From equation 3 we see that the phase shift between the transmitted wave and the reference wave will be π if the enclosed flux amounts to $h/2e = 4.13 \times 10^{-15}$ Wb, or one quantum of flux (one fluxon). ("Phase amplification" by n is also possible, in which fringe maxima are produced for every change of h/ne in enclosed flux¹²). The reconstructed holograms show contour maps of the phase variation $\Delta\theta$ in the specimen. Changes of 2π typically occur over distances of about 50 nm. As discussed following equation 5, these contours may be interpreted directly as magnetic lines of force, since the phase change along them is zero. Unfortunately, what is imaged in both the holographic and DPC methods is the total field B , including stray fields outside the sample (H is not necessarily zero outside a ferromagnet) rather than the desired magnetisation M .

Figures 3 and 4 show examples of reconstructed holograms for a small cobalt particle¹⁴, and for a cobalt magnetic recording medium on which digital bits have been recorded¹⁵. The cobalt film thickness was $t = 45$ nm, and the bit length 5 microns, with $M_r = 890$ G and $H_c = 340$ Oe. Leakage fields outside the

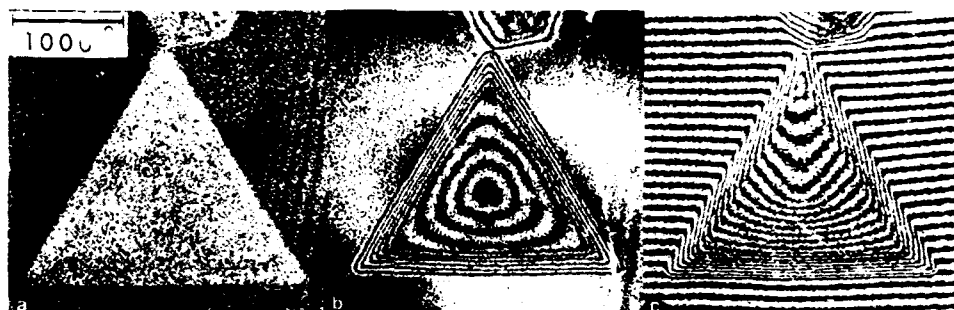


Figure 3. In-focus image (left), phase contrast, reconstructed hologram (middle) and original interferogram (right) from a truncated tetrahedral particle of cobalt with (111) faces¹⁴.

film (on its side) are seen above figure 4(a). From this work it was confirmed that the width of the transition region was proportional to $M_r t / H_c$. In figure 3 are seen the interferogram and reconstructed hologram from triangular cobalt particles. The interferogram can be used to show that the magnetisation runs anticlockwise in (b) (particles with clockwise magnetisation were also found). From the known shape of the particles, it could be concluded that the outer fringes in 3(b) are due to thickness changes, and the inner to magnetisation. It is postulated that at the central point the dipole moment is vertical. A cross-tie domain wall has also been imaged by this method (and compared with Lorentz images) in a thin film of Permalloy¹². Single fluxons have been imaged entering the surface of a superconducting lead film¹². The method is thus a quantitative one since, if the sample thickness is accurately known, absolute values of flux density (averaged through the sample thickness) may be determined. Against this important advantage over the Fresnel and Foucault methods must be set the disadvantage that, in order to obtain an unobstructed reference wave, only sample regions near an edge may be studied. In thicker samples, inelastic scattering also reduces fringe contrast.

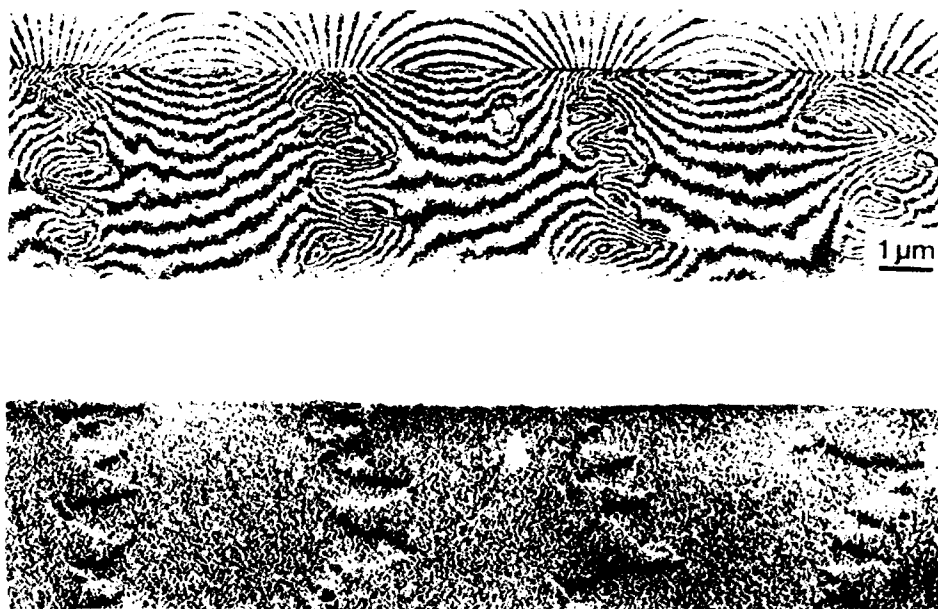


Figure 4. The upper figure shows the reconstructed phase-contrast hologram of a thin film of cobalt, on which has been recorded alternating "bits" of magnetisation (shown by arrows). The upper fringes are stray fields beyond the edges of the "tape". The lower figure shows the corresponding Fresnel image ¹⁵.

Field-emission TEM instruments are now available commercially for this work, at a cost of over \$10⁶. Some must be modified by the installation of a biprism, and facilities provided for eliminating the objective lens field. A controllable transverse field may also be required at the sample, and a heating stage is desirable. As an alternative, an instrument which uses an electrostatic objective lens and a field-emission gun has also been built ¹⁶. These workers have pointed out that, if a minimum detectable phase shift of $2\pi/100$ is assumed, equation 3 suggests that the lateral resolution will ultimately be limited by the weakness of the field in the sample and the noise properties of the electron image recording, rather than the resolution of the electron microscope.

4. DIFFERENTIAL PHASE CONTRAST (DPC) IN STEM

While the reciprocity theorem of optics ensures that both the Fresnel and Foucault modes of Lorentz microscopy may be employed in a Scanning Transmission Electron Microscope (STEM), these instruments also offer new possibilities for phase contrast imaging. The most successful for magnetic materials has been the DPC mode ¹⁷, based on the use of a quadrant detector ¹⁸. In STEM, a sub-nanometer sized probe (generated by a field-emission gun) is scanned over a thin sample, and some portion of the transmitted intensity is then used to form the scanning image. In the DPC mode an axial circular detector is used, divided into four quadrants, and the image formed from differences between the signals arriving at opposite sectors. For example, if the quadrants are labelled A,B,C,D (clockwise), then the signals $X = (A+B)-(C+D)$ and $Y = (A+D)-(B+C)$ give difference signals measuring the x and y field components running normal to the cut in the detector. For normalisation, these may each be divided by the total signal $(A+B+C+D)$. The resulting signal will

normally be zero, unless an internal magnetic field is present to deflect the beam slightly over the detector. The difference signal X , for example, can be seen from geometrical optics to be proportional to α , and hence to $B_y(x)$ from equations 4 and 5 (and similarly for Y , which gives B_x). Care must be taken, however, to ensure accurate "de-scanning", so that the diffraction pattern does not move due to the scan displacement of the probe. A fuller analysis¹⁹, based on the wave-optical formulation of phase-contrast image formation for a pair of semi-circular detectors shows that the difference signal is proportional to the gradient of the sample phase function $\Delta\theta(x)$ taken in the direction normal to the cut in the detector. Thus if the detector cut runs in the y direction,

$$\frac{\partial \Delta\theta(x)}{\partial x} = \frac{2\pi e t B_y(x)}{h} = \frac{2\pi\alpha}{\lambda} \quad 7$$

In a digital STEM system all four signals may be processed and displayed simultaneously, or stored. Thus it is possible in DPC to obtain a map of the two-dimensional (x and y) vector field, projected through the sample.

This important result indicates one of the main advantages of the DPC method by comparison with Fresnel and Focault methods - its linearity. It can be shown¹⁹ that the ideal DPC detector is a first moment detector whose response is proportional to spatial frequency. Such a detector gives a linear image whose intensity is proportional to the phase gradient (and hence to $B_y(x)$), even for the "strong" phase object of equation 2. For more practical quadrant detectors, nonlinear effects even in strong phase objects have been found to be appreciable only for very narrow domain walls in very thick samples, in which the phase-gradient may change very rapidly. Figure 5 shows calculations comparing Fresnel, Focault and DPC images for an assumed variation of induction across a pair of 180° domain walls, illustrating the linearity of DPC. Note the similarity of the DPC image to $B_y(x)$. In geometrical terms, non-linear effects are found to be important if the Lorentz deflection exceeds about 20% of the illumination half-angle²⁰. For very high resolution work the properties of the probe become important, and deconvolution procedures must be considered.

Apart from its desirable linearity, the DPC method may be used in thicker samples than the holographic method, since inelastic scattering is less deleterious. It also allows real-time observation of a live image, without the delays involved in holographic reconstruction, so that features of interest may be sought before recording. Useful DPC images have also been obtained without using a field emission gun on a conventional TEM instrument (with scanning attachment)²¹.

The DPC technique has now been applied to many materials, including vortex walls in soft Ni-Fe-Co-Ti magnetic alloys²². The subject of DPC imaging in STEM has been reviewed recently²³. Figure 6 shows an example of the reconstruction of a vector field map, obtained by DPC.

5. MAGNETIC CONTRAST FROM BULK SAMPLES IN THE REFLECTION GEOMETRY

In this section we consider an approach to the problem of imaging magnetic domains on the surface of a bulk crystal. The techniques so far described all require the use of thin films. If these are prepared from bulk material, the magnetic domain structure may change during sample preparation - for example any perpendicular magnetisation may be lost. While no three-dimensional mapping techniques exist for bulk materials, their surfaces may be studied in the Bragg (reflection) geometry in any modern electron microscope. The experimental arrangement is similar to RHEED. By

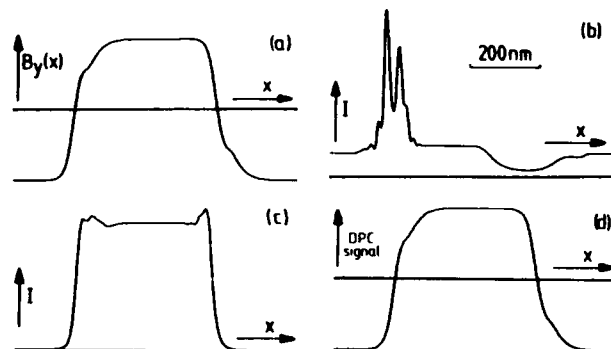


Figure 5. In (a) is shown the variation of induction across a pair of 180° domain walls in a film of permalloy 12nm thick, according to one theoretical model ³⁴.

(b) shows the calculated image in the Fresnel mode.

(c) shows the calculated image in the Foucault mode.

(d) shows the calculated differential phase contrast (DPC) image ³⁵.

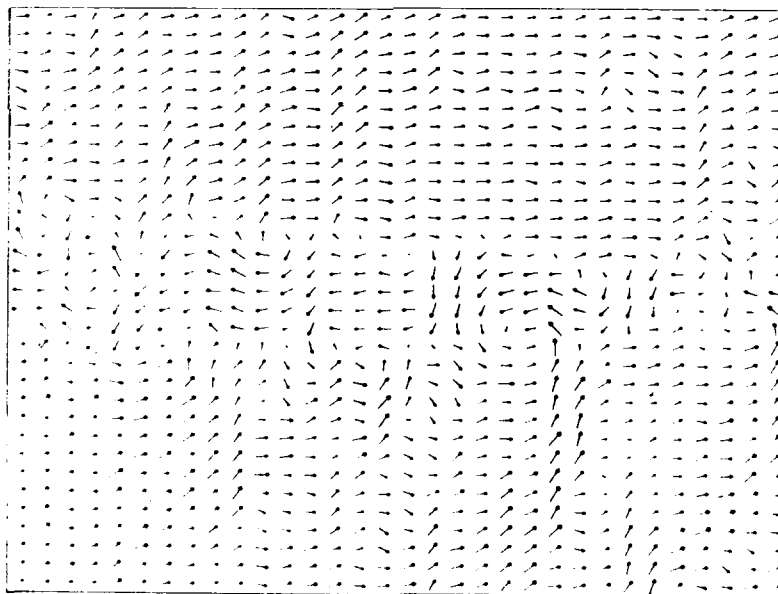


Figure 6. DPC vector map of magnetisation across a reversal domain in $\text{Co}_{85}\text{Pt}_{15}$ ²⁰. This vector image was obtained from two successive DPC images. The detector has been rotated by 90° between images. Each image gives one component (normal to the cut in the detector) of the field. The width of the image is 4.46 microns.

selecting the reflected Bragg beam by passing it through a small aperture for imaging, the mode known as Reflection Electron Microscopy (REM) is obtained.

The development of molecular-beam epitaxy and other controlled crystal growth techniques has now made possible the fabrication of magnetic monolayer systems on bulk substrates of great theoretical and practical interest, which might be studied by this method. These low-dimensional spin systems present challenging theoretical problems in electronic structure calculations, such as the computation of spin-polarized photocurrents and magnetic anisotropy. For device applications, the possibilities of developing "vertical" magnetic recording media of very high density, and uses of the magnetoresistance effect have both attracted considerable interest. Systems such as Fe on Cu, Fe on Ni, Fe on Ag, Fe on Au, Ni on NaCl, Fe on W, Co on Cu and Fe on GaAs have been extensively studied amongst others²⁴. The mechanisms of monolayer growth have been studied by LEED microscopy (LEEM) and STM. Magnetic properties have also been studied by photoelectron diffraction, Auger spectroscopy, spin-polarized photoemission, SEXAFS and surface energy loss spectroscopy.

An example of an REM image of GaP is shown in figure 7, and a fuller discussion of this imaging mode (for non-magnetic materials) can be found elsewhere²⁵. In surface science, spectacular REM "movie" images have been obtained of surface phase transformations on the silicon (111) surface at 830 °C in an ultra-high vacuum electron microscope²⁶. We now wish to consider the application of the REM method to crystalline magnetic materials, and assume that a crystal surface has been prepared *in situ*, in which the magnetic domain size is smaller than the crystal grain size. (For fine-grained bulk polycrystalline magnetic materials this is not usually so, and the REM method is therefore unlikely to be useful). An in-situ U.H.V. preparation chamber attached to a TEM or STEM will therefore be required for experimental tests of the following calculations²⁷.

We are therefore led to consider the effect of the Lorentz force on the diffraction conditions of a beam in the RHEED geometry²⁵. For a 120kV electron beam incident on Fe, the angular deflection along the beam path is about 0.4 mRad for a path length of 200nm, so that the corresponding change in diffraction conditions may be considerable, leading to appreciable diffraction contrast in an REM image. The effect may be enhanced at the surface resonance condition. We now test this contrast mechanism, using detailed multiple electron scattering calculations.

As a model system, we consider a monolayer of Fe on the (110) bulk GaAs surface, with the electron beam at glancing incidence running approximately along [001] in the plane of the surface. If terms in the square of the small vector potential A in equation 1 are neglected, the non-relativistic Schrodinger equation becomes

$$\nabla^2 \psi + \frac{8\pi^2 m e}{h^2} V + E_0 \psi + \frac{2\pi i e}{h} \mathbf{A} \cdot \nabla \psi = 0 \quad 8$$

We have shown elsewhere²⁸ that this equation may be solved by the multislice recursion method²⁹ under the usual approximations if the "transmission function" for a thin slice is taken to be

$$\chi = \exp\left(\frac{j\pi}{\lambda E_0} \int_{z_0}^z V(x, y, z) dz - \frac{2\pi i e}{h} \int_{z_0}^z A_z dz\right) \quad 9$$

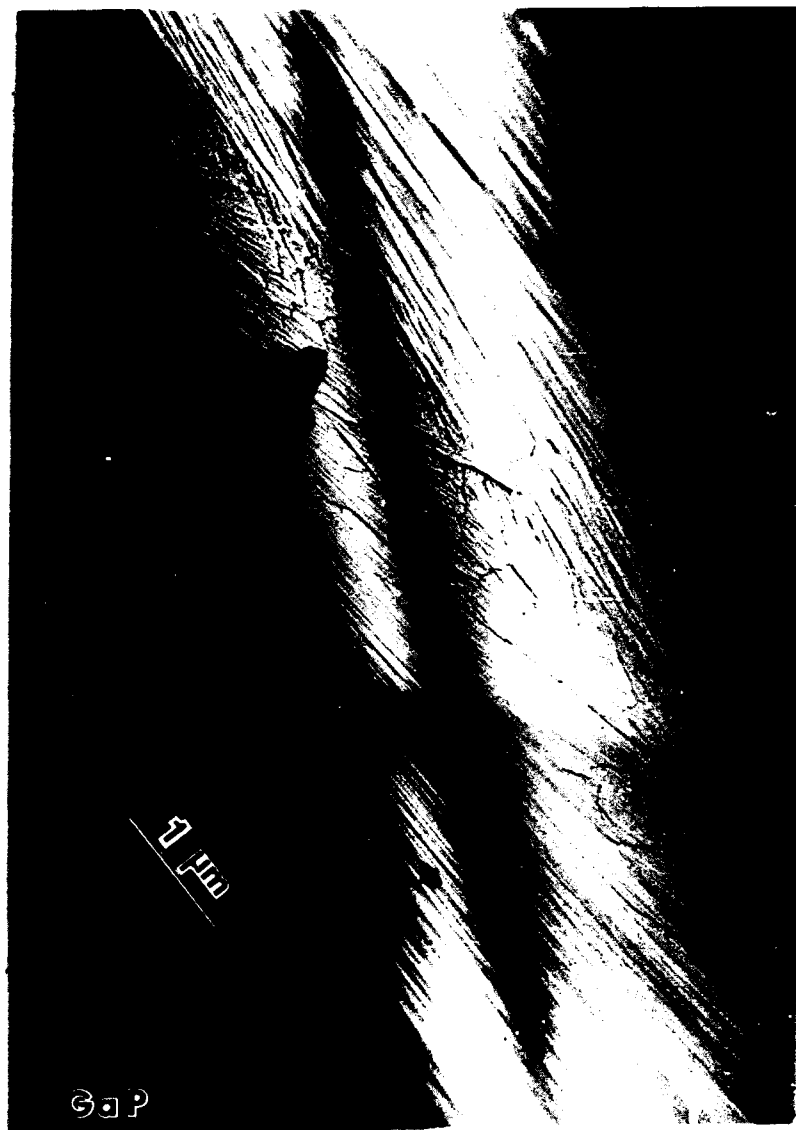


Figure 7. REM image of a cleaved crystal of GaP. This was obtained on a Philips EM400 TEM. Surface steps, and the image (and its mirror reflection) of an opaque particle are seen. (courtesy of Dr. N. Yamamoto). The image is foreshortened in the beam direction by about 40.

The first term is the conventional phase-grating term used in the multislice algorithm - the second describes the effect of a weak magnetic field inside the sample. The electron wavefield ϕ_{n-1} on the [001] plane before traversing a slice is related to that (ϕ_n) after the slice by

$$\phi_n(x, y, z) = [\phi_{n-1}(x, y, z_0) \chi] * P(x, y) \quad 10$$

where $P(x, y)$ is a free-space Fresnel propagation function

$$P(x, y) = \frac{i}{\lambda \Delta z} \exp\left(\frac{j\pi(x^2 + y^2)}{\lambda \Delta z}\right) \quad 11$$

Δz is the thickness of the slice, and the asterisk denotes convolution.

The results given below were obtained using the artificial superlattice method for RHEED, as described in detail elsewhere³⁰, where it is compared with other methods. Unlike differential equation, slice, or Bloch-wave methods which assume perfect translational symmetry in the plane of the surface, our method takes slices approximately normal to the electron beam (which lies almost in the plane of the surface). The advantage of this approach is that discontinuities such as surface steps, emerging dislocations, inclined stacking faults and surface roughness generally may easily be incorporated into the calculation.

A slab of crystal, together with an adjoining vacuum space was made artificially periodic in the [110] direction (normal to the surface), as shown in figure 8. The height h of this crystal/vacuum slab (one period) was either 8nm or 16 nm. This limit on the incident beam width results in a spread of the diffracted beams over an angular range of about 0.5 mR. Slices of thickness 0.28267 nm were taken normal to [001], the approximate beam direction, and the multi-slice recursion algorithm used to calculate the resulting RHEED pattern. The calculation was continued until any perturbations due to the starting condition had decayed. (For further discussion of RHEED calculations by the multi-slice method, see²⁵). Typical computation times on our Vax station were 1 hour, with a 32 X 1064 array of "beams", for a distance of 110 nm along the beam path. The large number of dynamically coupled "beams" results from the use of the artificial superlattice - the number of true reciprocal space rods included in the calculation was 32. Scattering factors for neutral atoms were taken from the International Tables for X-ray Crystallography. Calculations were performed for the (440), (660) and (880) specular beams. No absorption effects were included. The figures show either the real-space intensity distribution of the wave-field on a plane normal to the beam near the surface of the crystal, or the Fourier Transform of this complex real-space wave-field in steady state. The latter gives the rocking curve which would be obtained using a coherently filled cone of illumination. Since radiation from a point source reflected from an atomically smooth surface gives rise to a point diffraction pattern in RHEED (in the absence of thermal vibration), this rocking curve is the same as that which would be obtained from an extended incoherent illumination source.

A perfect lattice match was assumed between the Fe and GaAs, and misfit dislocations and other defects neglected. All Fe atoms in the top monolayer were placed on bulk GaAs sites, in view of the very small misfit of the two crystals. We have assumed an internal magnetic field of $B = 2T = 20$ kGauss for the Fe layer, and zero in the GaAs. (For a discussion of the measured magnetic and growth properties of this system, see³¹). For simplicity in the calculations the magnetic structure of the domain boundary is taken to be completely abrupt. Domain boundary structure may therefore actually introduce additional broadening in the images.

It will be seen from figure 8 that there are three important directions for B . Boundaries may run in any direction. Case 1 produces negligible Lorentz force. Case 2 results in a change in azimuth, while case three results in change

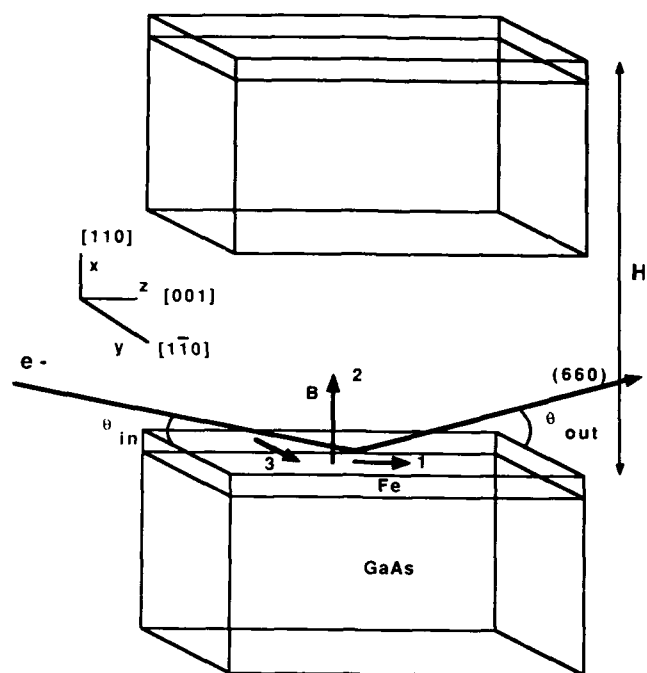


Figure 8. Geometry used for RHEED calculations, showing three directions for **B**. The RHEED calculations take slices normal to $[001]$, the approximate beam direction. The crystal slab and vacuum space is periodically continued in the $[110]$ direction.

in the beam elevation θ . Because of the vertical mirror plane of symmetry normal to $[1\bar{1}0]$, a reversal of **B** in case 2 produces identical deflections from the $[001]$ beam direction and identical diffraction conditions, and therefore no contrast across a domain boundary. We therefore consider case 3 first.

Figure 9(a) shows the wavefield intensity distribution inside the crystal for the (440) specular condition at 120 Kv. at successive increments of 27.15 nm along the beam path. The sense of the internal magnetic field has been reversed after panel E, causing a small local change in θ_{in} and diffraction conditions.

Figure 9(b) shows a similar calculation for the (660) specular beam. The beam is incident in the $[1\bar{1}0]$ plane, and makes an angle of approximately $90^\circ - \theta_{in}$ with the $[110]$ surface normal direction, where (non-relativistically)

$$\theta_{in}^2 = \theta_B^2 - (V_0/E_0) \quad 12$$

with V_0 the mean inner potential for the surface layer, and θ_B the Bragg angle for the specular beam. For pure GaAs, $V_0 = 13.2 \pm 0.6$ eV³². Equation 12 gives the approximate RHEED Bragg condition for monolayer systems on a GaAs substrate - the precise position of intensity maxima along the reciprocal lattice rod for monolayers can only be obtained from multiple-scattering calculations. Equation 12 can be expected to be most in error for high energies and very small angles, where the electron flux is confined to the monolayer whose mean inner potential differs from that of the substrate. For certain voltages and materials the rocking curve maxima may not occur at the Bragg angle.

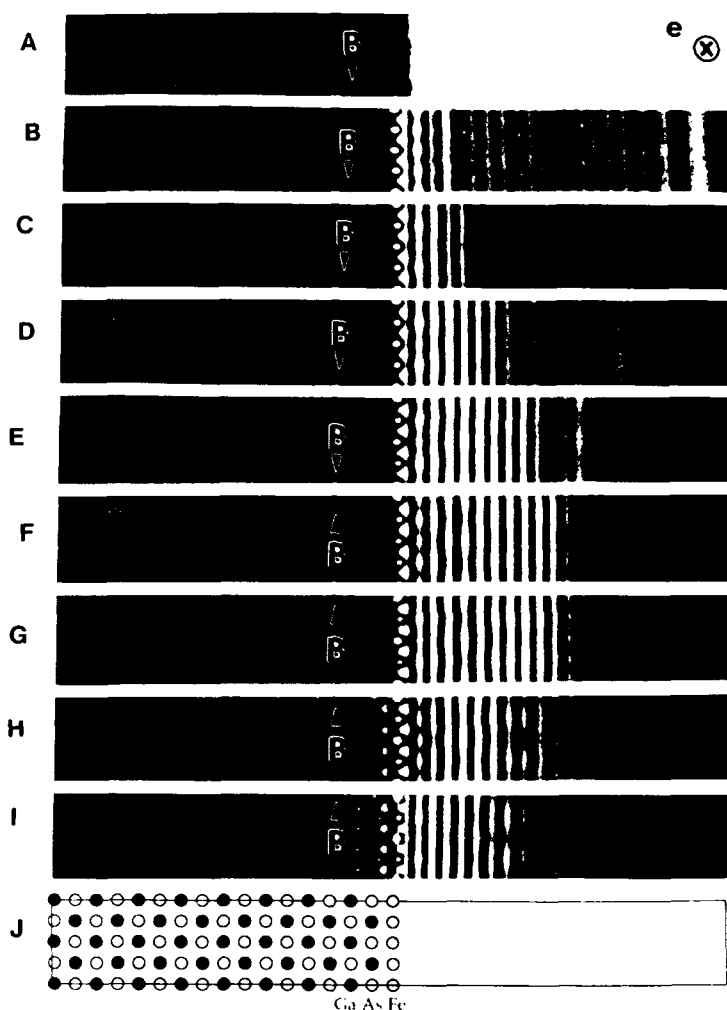


Figure 9. (a). The two-dimensional real-space electron intensity distribution for 120 kV electrons incident on a monolayer of Fe on the GaAs (110) surface. Beam direction approximately normal to the page, satisfying the (440) specular condition. Each panel A - I shows the wavefield at increments of 27.15 nm along the beam path, with the first panel A at 27.15 nm and the last (I) at 244.35 nm. The direction of the 2T magnetic field is indicated.

We see from figure 9 that if the small (440) grazing angle of incidence is used, the penetration of the wavefield is about one layer, and is confined mainly to a thin sheet of intensity in the Fe monolayer. For the (660) beam (figure 9(b)) however, the penetration is increased considerably to several layers. The use of higher angle beams thus produces less foreshortening $F = 1/\sin\theta_{out}$ in the REM image, at the cost of deeper penetration into the sample. (The respective foreshortening factors in figures 9(a) and (b) are 86 and 42). These calculations do not include an absorption potential, which would have the effect of reducing the penetration still further. Absorption is also responsible for the depletion of the transmitted wave, which can be seen splitting off in the last panel (I) of figure 9(a).

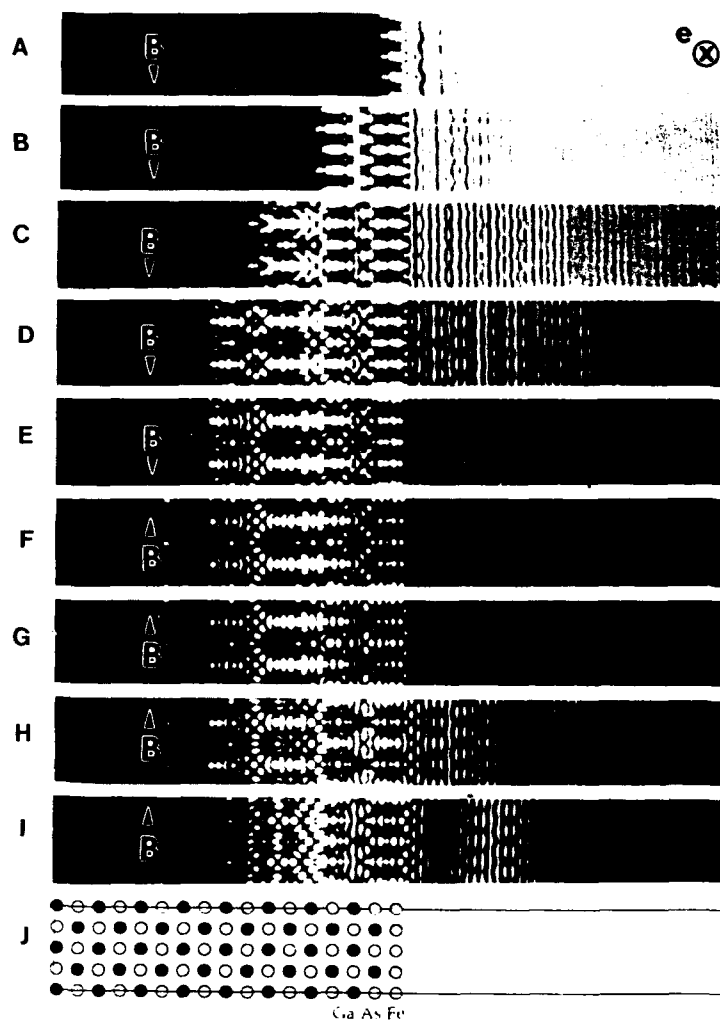


Figure 9. (b). Similar to figure 9 (a), but for the (660) specular reflection. [001] azimuth. Penetration is much greater. The structure is indicated below, with the position of the surface also shown.

Figure 10 shows the integrated intensities of the same (440) and (660) specular beams shown in figure 9 as a function of z -coordinate along the [001] beam path. The intensity shown is the integral of the intensity along the beam path from the beginning of the crystal, so that a constant slope represents the steady state condition. The magnetic field is reversed at T. The width of the perturbed region R shown is found to be about 88nm for the (440) monolayer case and 75 nm for the (660) beam. The width of this perturbation required to re-establish the steady state may be taken as a rough measure of the resolution of the REM magnetic contrast, in the most unfavorable case, where a magnetic domain boundary crosses the beam path at right angles.

Figure 11 (a) shows computed rocking curves for the (440) specular beam ($\theta_{in} = 11.6$ mR) for cases two and three, with $B = \pm 2T$. These were obtained by Fourier transform of the steady-state wave function, usually the last slice. For a typical experimental incident beam divergence, all of the rocking curve shown

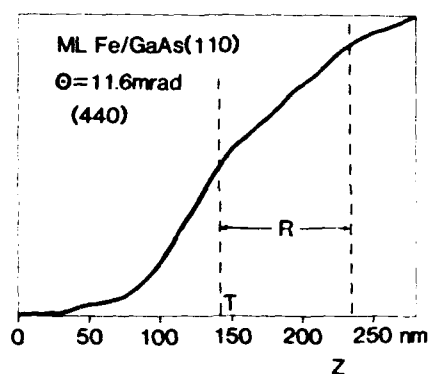


Figure 10. (a) Intensity, integrated along the beam path, of the (440) specular beam from a monolayer of Fe on GaAs (110) as a function of distance along the beam path. The 2T surface magnetic field direction (normal to the page) is reversed at T. The distance R may be taken as an approximate estimate of "resolution" for this sample in this direction.

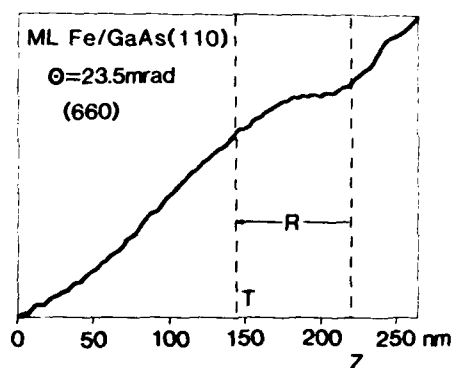


Figure 10. (b) Similar to figure 10(a), but for the (660) specular beam. Taken from the data of figure 9.

would contribute to the REM image. From the curve areas, we find the change in intensity due to the reversal of B across a domain boundary to be 28% in case 3. Figure 11 (b) shows similar results for the (660) beam. In this case the intensity change is reduced to 26% due perhaps to the greater penetration of the beam into the GaAs bulk. Here $\theta_{in} = 23.5$ mR.

Figure 12 shows similar calculations for the (110) surface of bulk iron. In figure 12 (a) is shown the RHEED rocking curve for the (660) specular beam, while figure 12 (b) shows the (880) specular beam. As expected, much larger RFM contrast (59%) across a case 3 magnetic domain is obtained from the more deeply penetrating (880) beam than from the (660) beam (23%).

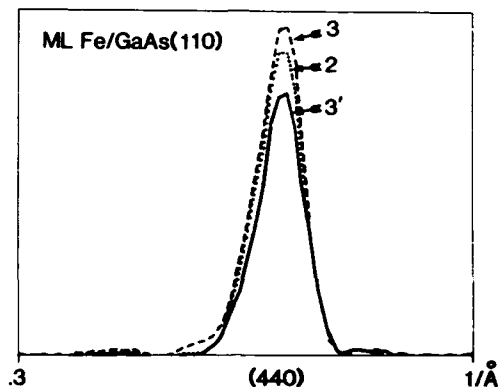


Figure 11. (a) RHEED Rocking curve for (440) specular beam at 120 kV. Monolayer of Fe on GaAs (110). Curve 3 - computed with \mathbf{B} along $[1, -1, 0]$, in the plane of the surface, normal to the beam. Curve 3' - direction of \mathbf{B} reversed. Curve 2 - case 2 in figure 1, along $[110]$. (No change on reversal due to symmetry). Steady state condition. Azimuth $[001]$. $B = \pm 2T$.

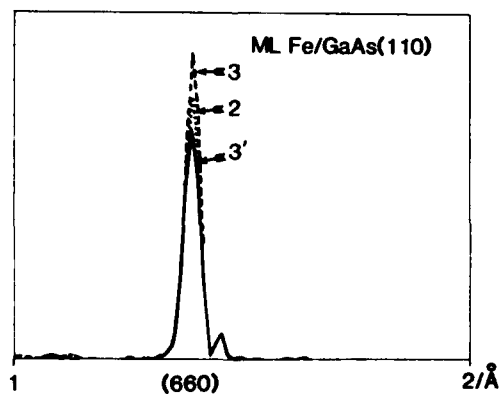


Figure 11. (b) Similar to 4 (a) for (660) specular reflection. Intensity scale is arbitrary. Abscissa is in inverse Angstroms.

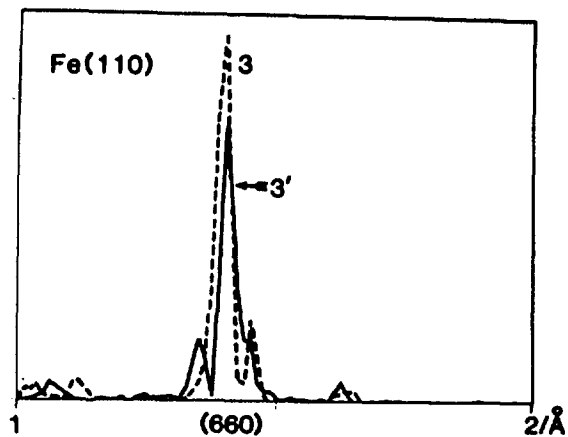


Figure 12. (a) As for figure 11, but showing the (660) specular RHEED beam reflected from the bulk Fe (110) surface at 120 kV.

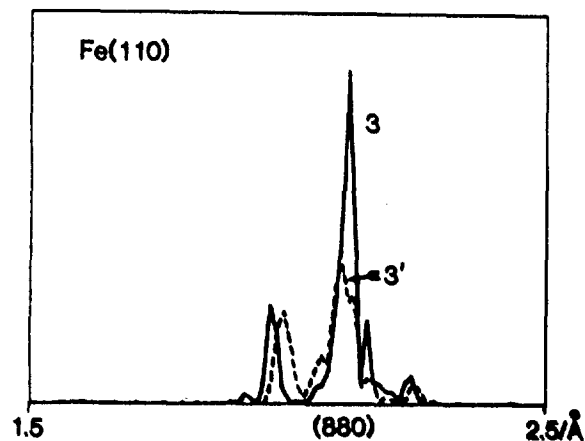


Figure 12. (b) As for figure 12 (a), but showing the (880) specular RHEED rocking curve from the bulk (110) Fe surface.

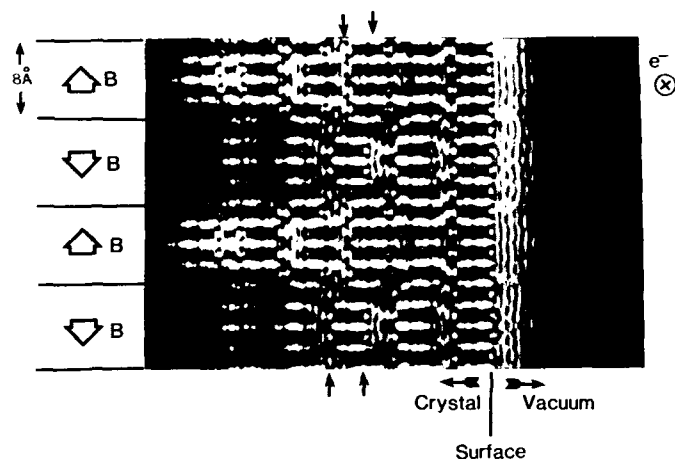


Figure 13. (a) Magnetic domain boundary parallel to $[001]$ beam direction, which is into the page. (660) specular condition at 120 kV on Fe (110). Directions of B shown. The periodic domain width is 0.8 nm. Steady state condition.

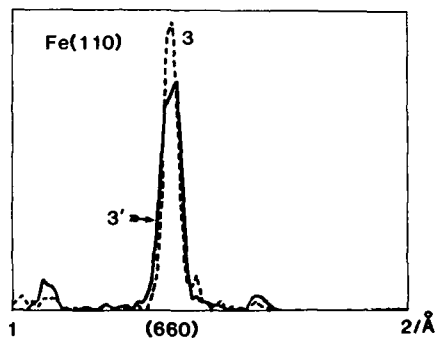


Figure 13. (b). Rocking curves for figure 13(a). Curve 3 has B parallel to $[1-10]$, curve 3' has the sense of B reversed.

For the special case of a boundary running parallel to the beam in case 3, the resolution may be very high, since there is then no foreshortening across the boundary. Figure 13 (a) and (b) shows calculations for this case for the (110) surface of iron, with the electron beam into the page. In figure 13 (a) it will be seen that the Lorentz force acts to increase θ_{in} in the uppermost domain, leading to slightly increased penetration. Figure 13 (b) shows the corresponding rocking curves. (It differs from figure 12 (a) because of the transverse spreading of the wave between domains in figure 13 (b)). A similar boundary in case 2 might be expected to produce a narrow band of contrast along the beam path where the wavefields from adjacent domains overlap. A contrast difference between domains in case 2 may be obtained by tilting the incident beam slightly off the symmetry plane. The resolution limit for images of domain boundaries running parallel to the beam may thus be equal to that set by chromatic aberration in REM. This is about 1 nm at 100 kV, measured normal to the beam.

These calculations take no account of the inelastic background present in RHEI due to plasmon excitation. Recent dynamical inelastic calculations³³ show that inelastic scattering makes a most important contribution to the so-called "resonance" condition. At the optimum condition (close to the (660) specular condition for bulk (110) GaAs at 120kV) the total elastic plus inelastic scattering within the (660) rocking curve is more than twice that due to elastic scattering alone, while the total scattering at resonance increases by a factor of more than two over the non-resonance condition. The dominant processes are surface plasmon excitation and phonon scattering. We expect the small-angle plasmon scattering to contribute to the magnetic diffraction contrast, but the larger angle phonon scattering to produce a slowly varying background.

6. CONCLUSIONS

Several powerful TEM techniques now exist for the spatial mapping of magnetic fields within thin films. The simplest of these, the Fresnel and Focault modes, may be used with slight modifications to most modern TEM instruments. They are mainly useful for demonstrating the existence of domain walls, and to trace their direction at low resolution. For higher resolution, quantitative work, the DPC method in STEM appears to be the most versatile method available at intermediate cost and complexity, being suitable for the thicker samples likely to be of greatest interest to materials scientists. The most dramatic detailed, quantitative images of the internal fields in small particles and thin films have, however, been obtained by the more complex and costly electron holographic method. This method is restricted to the edges of very thin samples, but may eventually allow both the lattice image and the magnetic image to be obtained simultaneously. In addition we may expect that the cost of field-emission TEM machines will fall in the near future as these gain popularity for other purposes.

Our calculations for magnetic contrast in REM suggest that magnetic domain boundaries may be expected to give usefully large contrast changes in reflection electron microscope images of monolayer films of iron at 120 kV. Contrast of about 28 % is predicted for a reversal of the magnetic field within a monolayer of iron on GaAs. The effects of inelastic scattering might be expected to reduce this somewhat, however this is difficult to predict without more extensive dynamical inelastic scattering calculations since it appears that inelastic scattering makes a strong contribution to the resonance intensity. While the penetration of the wavefield increases from one to about seven atomic layers in going from the (440) to the (660) specular condition, the loss of magnetic contrast is small and a desirable reduction in foreshortening is obtained. Thus higher order beams appear most useful for imaging, whilst the confinement of the electron wavefield to the magnetic surface monolayer found at low angles may find application in the study of channelling effects.

The resolution of REM images of domains depends on the direction of the boundary, and is greatest in the direction normal to the beam for a boundary running parallel to the beam. For boundaries normal to the beam, perturbations in the image extend for about 80 nm along the beam path.

The ability to image these systems in an electron microscope would allow the study of the interaction and pinning of two-dimensional magnetic domains with surface defects such as steps and dislocations, and of their temperature dependence. The required ultra-high vacuum electron microscopes, are now operating in a few laboratories ²⁷.

Acknowledgments

Work supported by NSF grant DMR88-13879 (J.C.H.S., P.I.) and the ASU-NSF national center for HREM at Arizona State University. We are grateful to Drs. I. McFadyen, A. Tonomura, H. Lichte and M.B. Stearns for useful discussions.

References

1. Jurek, K. & Zaveta, K. *JEOL NEWS* 26E, 17 (1988).
2. Stearns, D.G., Stearns, M.B., Cheng, Y., Stith, J.H. & Ceglio, N.M. *J. Appl. Phys.* 67, 2415 (1990).
3. Chapman, J.N. *J. Phys. D* 17, 623 (1984).
4. Jakubovics, J.P. *Electron Microscopy in Materials Science* 1-pp. 1303 (Commission of the European Communities, Brussels, 1975).
5. Missiroli, G.F., Pozzi, G. & Valdre, U. *J. Phys. E: Sci Instr.* 14, 649 (1981).
6. Aharonov, Y. & Bohm, D. *Phys. Rev.* 115, 485 (1959).
7. Tonomura, A., *et al.* *Phys. Rev. Letts.* 48, 1433 (1982).
8. Tsukahara, S. & Kawakatsu, H. *J. Magn. Magn. Mater.* 36, 98 (1983).
9. Cohen, M.S. *J. Appl. Phys.* 38, 4966 (1967).
10. Matteucci, G., Missiroli, G.F. & Pozzi, G. *IEEE Trans on Magnetics.* MAG-20, 1870 (1984).
11. Mollenstedt, G. & Wahl, H. *Naturwiss.* 55, 340 (1968).
12. Tonomura, A., *et al.* *Phys. Rev. B* 25, 6799 (1982).
13. Spence, J.C.H. *Experimental high resolution electron microscopy.* (Oxford University Press, New York, 1988). Second edition.
14. Tonomura, A., Matsuda, T., Endo, J., Arie, T. & Mihama, K. *Phys. Rev. Letts.* 44, 1430-1433 (1980).
15. Osakabe, N., *et al.* *Appl. Phys. Letts.* 42, 746 (1983).
16. Frost, B. & Lichte, H. *Inst. Phys. Conf. Ser.* 93, 267 ("EUREM 88") (1988).
17. Chapman, J.N., Wadell, E.M., Batson, P. & Ferrier, R.P. *Ultramicrosc.* 3, 203 (1978).
18. Dekkers, N.H. & de Lang, H. *Philips Tech. Rev.* 37, 1 (1977).
19. Morrison, G.R. & Chapman, J.N. *Optik* 64, 1 (1983).
20. McFadyen, I.R. *Personal communication.* (1990).
21. McFadyen, I.R. *Proc. 47 th Electr. Micros. Soc. Am. (G. Bailey, Ed.) San Francisco Press.* 568 (1989). See also *J. Appl. Phys.* 64, p.6011 (1988) for details of the use of DPC on a conventional TEM.
22. Chapman, J., Morrison, G.R., Jakubovics, J.P. & Taylor, R.A. *J. Magn. and Mag. Mat.* 49, 215 (1985).
23. Chapman & J.N. *J. Phys. D* 17, 623 (1983).
24. Gardiner, T.M. *Thin Solid Films* 105, 213 (1983).
25. Wang, Z.L., Liu, J., Lu, P. & Cowley, J.M. *Ultramicrosc.* 27, 101 (1989).
26. Tanishiro, Y., Takayanagi, K. & Yagi, K. *J. Microsc.* 142, 211 (1986).
27. Drucker, J.S., Krishnamurthy, M., Hembree, G., Hong, L. & Venables, J. *Proc. 47 th Electr. Micros. Soc. Am. (G. Bailey, Ed.) San Francisco Press.* p.208 (1989).
28. Wang, Z.L. & Spence, J.C.H. *Surface Science.* in press, (1990).
29. Cowley, J.M. *Diffraction Physics* (North-Holland, New York), (1981).
30. Peng, L.M. & Cowley, J.M. *Acta Cryst. A* 42, 545 (1986).
31. Prinz, G.A., Rado, G.T. & Krebs, J.J. *J. Appl. Phys.* 53, 2087 (1982).
32. Yamamoto, N. & Spence, J.C.H. *Thin Solid Films* 104, 43 (1983).
33. Wang, Z.L., Liu, J. & Cowley, J.M. *Acta Cryst. A* 45, 325 (1989).
34. Jakubovics, J.P. *Phil Mag* B37, 761 (1978).
35. Chapman, J.N., Morrison, G.R., Jakubovics, J.P. & Taylor, R.A. 68, 197 (1983).

SCANNING TUNNELING MICROSCOPY AND FORCE MICROSCOPY APPLIED TO MAGNETIC MATERIALS

Nicolás García

Dpto. Física de la Materia Condensada
Universidad Autónoma de Madrid
Cantoblanco, 28049-Madrid, Spain

and FISINTEC, Ruperto Chapí 19
28100 Alcobendas, Madrid, Spain

ABSTRACT

This paper covers, in this workshop, the part related with Tunneling Microscopy; i.e. Scanning Tunneling Microscopy (STM) and Atomic Force Microscopy (AFM). The lectures give a review of the field, but these notes will be more limited to the application of magnetic materials. The version of AFM in magnetism is known as the Magnetic Force Microscopy (MFM). Therefore we present STM applied to polarized electrons and some MFM results applied to recent experiments in magnetic materials and to high temperatures superconducting materials. However there are excellent reviews and comprehensive books that we reference and the reader can follow any specific field with the references quoted.

INTRODUCTION

STM is a technique that we all owe to the discovery of the instrument by Binnig, Rohrer, Gerber and Weibel¹. This discovery deserved the 1986 Nobel Prize in Physics² and today the application of the instrument has extended to many areas of Physics, Chemistry and Biology³. It is always interesting to know how an important discovery was done for this purpose. We direct the reader to the Chapter by García in Ref.2 where part of the text of the Nobel Lecture given by Binnig and Rohrer is presented. We also direct the reader to Ref. 3 which is a very comprehensive book about "STM and Related Methods" and represents the Lectures and Seminars of a NATO ASI Series that took place in Erice (Italy) in 1989; it was organized by Behm, García and Rohrer. For those who want to know what is STM and its perspectives this is the appropriate book. There are also some other good reviews and Proceedings of Conferences to which we refer and that can be followed for additional information in particular topics.

Here we also present a program, as was followed in the lectures, with the more adequate references to follow in each session in case that the reader wants to look at it in more detail.

LECTURES PROGRAM

(A) Lecture on STM

1. STM: Apparatus, mode of operation and recording Microscopy and Spectroscopy. Resolution of the devices and some examples. Refs. 2,3,4.
2. Theory of the tunneling current and its derivatives. Refs. 2,3,5,9-13.
3. Interaction Forces between the tip of an STM and the surface. Refs. 2,3,14.
4. Can STM give information in an atomic scale by measuring the tunneling current between two magnetic electrodes (ferro or antiferromagnetic)? Theory of tunneling between magnetic electrodes. Do s and d orbitals have the same tunneling probabilities? Discussion of a new experiment in Basel University on tunneling between spin polarized electrodes (Refs. 15-17). We will also discuss this point in detail in these notes and see also discussions in this School.

(B) Lecture on MFM (N. García and J.J. Sáenz).

1. AFM: Forces and its measurement, operation modes force and force gradient measurements. Refs. 2,3 (Chapt. VIII), 18-20.
2. Repulsive, short range, forces and attractive, long range van der Waals, forces. Their analysis and compensations. Refs. 2,3,18-20.
3. Resolution of AFM. Can AFM provide atomic resolution? Refs. 2,3,7-9,21.
4. MFM: Measuring magnetic forces in the 10^{-9} to 10^{-7} Newtons. Refs. 2,3,22-27.
5. Theory of the MFM: Dipolar magnetic forces, anisotropy magnetic forces and van der Waals forces. Separation of the different contribution forces to obtain a clean magnetic information. Refs. 3,22,24.
6. MFM experiments in the 100Å to 1000Å resolution. Refs. 3,22,23,25-28.
7. Magnetic volume needed to measure magnetic forces. Are magnetic forces destructive of the surface to be measured? In certain cases they are. Application of MFM to high Tc superconductors. An experiment in the Institut for Physical Problems in Moscow (Ref. 27).

We believe that by following the lecture program given above according to the references quoted, the reader can have a broad and also specialized view of the STM, AFM and MFM fields. In any case I repeat one of the preferred sentences of H. Rohrer: "STM is a small, micro instrument for a big imagination".

In what follows we will describe a little the use and operation of STM as well as its application to s-polarized electrons^{15,17}. We will also discuss and describe MFM^{22,25} and its application to high Tc superconductors²⁷.

A. LECTURE ON STM

View of STM Operation and Performance

To proceed further we take a description of the basic principles of operation, basic instrumentation, imaging applications and localized spectroscopy in STM from the lectures Notes by García in Ref.2.

Physical Principles of Operation

The quantum mechanical tunneling phenomenon which underlies STM has already been extensively exploited by solid state physicists in the context of thin oxide and other insulating films^{29,30}. The situation for electron tunneling between two planar conducting electrodes in the presence of a bias voltage V is shown schematically in Fig. 1. A simple trapezoidal tunneling barrier, related to the work functions ϕ_1 and ϕ_2 is employed and for simplicity we assume that the bias voltage V is small compared to the effective barrier height $\phi \approx (\phi_1 + \phi_2)/2$. In these circumstances the tunneling current density j for free electrons is given by the expression³¹.

$$j = (e^2/\hbar) (Q/4\pi^2s) \cdot V \cdot \exp(-2Qs) \quad (1)$$

where $Q = (2m\phi\hbar^2)^{1/2}$ is the inverse decay length of the wave function outside the surface. Compared with typical oxide film tunneling barrier heights of below 1 eV, the effective height for vacuum tunneling is usually a few eV.

The simple expression (1) has to be modified at larger bias voltage where the barrier height becomes a function of V but the dominating exponential dependence on barrier height and width remains. For non-free electron situations, the exponential pre-factor has to be altered to take account of density of state effects. It can be seen from Fig.1 that the main contribution to the current depends on the density of filled states just below the Fermi level, E_{F1} , and the density of empty states just above the Fermi level, E_{F2} , since these electrons experience the minimum barrier height. This energy

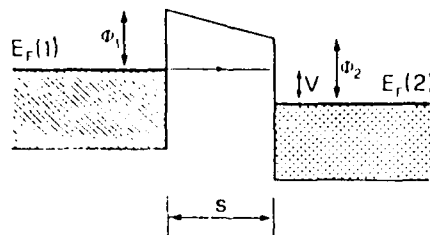


Fig. 1. Schematic energy diagram for a tunneling junction with a trapezoidal barrier (ϕ_1, ϕ_2) of thickness s .

selectivity allows the density of states on either side of the Fermi level to be explored by observing the current voltage characteristic and is exploited in classical tunneling spectroscopy of insulating films^{29,30}

The STM technique depends crucially on the extreme sensitivity of the tunneling current to the separation distance s (it typically decreases by about one order of magnitude for each 1 Å increase in s). Of course the planar geometry assumed in Fig. 1 no longer strictly applies. It is assumed that the tunneling current is confined to a filament between the apex of the tip and the specimen surface, whose own deviation from strict planarity are often the essential subject of interest. This is the crucial theory for the fantastic performance. Further discussion of more sophisticated and realistic tunneling theories for the STM situation can be seen in Refs. 2,3,5,9-13.

The most frequently used mode of operation is illustrated schematically in Fig. 2, taken from Binnig and Rohrer⁵. In this mode the tip is scanned laterally across the surface, whilst its z position is controlled in order to keep the tunneling current I constant. Contours of constant tunneling current can then be obtained which, on a surface which is chemically and electronically uniform will yield an image of the surface topography limited by the instrumental resolution.

Electronic or chemical inhomogeneities will also produce features in the scanned images. Such inhomogeneities can arise at foreign surface atoms as indicated schematically in Fig.2 or at special surface features such as steps or other defects. The local electronic or chemical variations can be distinguished from simple height changes by I vs V or I vs s measurements (see later section on localised spectroscopy). These measurements provide for example information on local variations in tunneling barrier height or density of states which are vital in analysing the images.

Another procedure which can be useful in some situations is to check the reproducibility of the image scan or I vs s scan. Although the STM generally causes no appreciable specimen damage (see later section), its occasional occurrence may be signalled by apparent image changes or hysteresis effects.

Basic Instrumentation

A schematic diagram of the instrumentation for STM is shown in Fig. 2 due to Binnig and Rohrer⁵. As indicated there the equipment must be well protected from external vibration by a vibration filter system. The most serious vibrations are those which excite resonances of the system itself and change the tip-sample separation s . With increasing design experience, particularly the move towards microscopes of smaller physical size, the vibration problem is now less severe. In one of the successful designs³², the necessary mechanical isolation is achieved simply by mounting the instrument on a stack of metal plates and separated from its neighbour by a viton damper. It is also useful in the

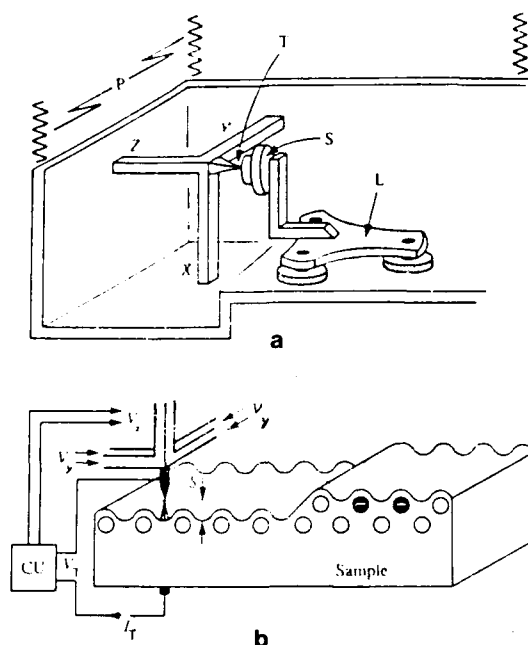


Fig. 2. Schematic of a tunneling microscope and its operation. The tip T of the microscope depicted in (a) is scanned over the surface of a sample S with a piezoelectric tripod (X,Y,Z). The rough positioner L brings the sample within reach of the tripod. A vibration filter system P protects the instrument from external vibrations. In the constant tunneling current mode of operation, a voltage V_z is applied to the Z piezoelectric element by means of the control unit CU depicted in (b) to keep the tunneling current constant while the tip is scanned across the surface by altering V_x and V_y . The trace of the tip, a y-scan, generally resembles the surface topography. Electronic inhomogeneities also produce structure in the tip trace, as illustrated on the right above two surface atoms having excess negative charge. Figure reproduced from Refs. 2,5.

tip-position control loop to employ a low-pass filter, limiting the tip motion to frequencies below the lowest mechanical mode frequency. This can restrict the imaging speed particularly on rough surfaces. But many other devices have been depicted depending on the everyone needs.

The sample positioning and scan drive system has obviously also to be designed to minimise vibration effects. This is difficult to reconcile with the desire to be able to select from a reasonably large surface of perhaps millimetre dimensions, a specifically chosen small area for high resolution imaging. Coarse positioning of the sample has been achieved in a number of ways including the piezo-electric walker or louse³⁻⁵ shown in Fig. 2a, as well as mechanical pushers³⁻⁵ and screw reduction drives. The fine, three-

dimensional, highly controlled motion of the tip which is required for high resolution imaging is usually provided by some form of the piezo-electric tripod shown schematically in Fig. 2a. A more compact design, which may have advantages if the area to be scanned is not too large, replaces the tripod by a single piezo-electric tube fitted with several electrodes to produce the necessary deflections. If distortion free images are to be produced, careful attention to calibration of the piezo response at different scanning speeds is often required.

The tip is evidently a very crucial component. Its structure can influence the image, not only in determining the resolution attainable but also, in extreme cases, it may contribute to the final result just as significantly as the structure of the sample under investigation. Tips are generally made by grinding or etching wires of tungsten (and on occasion stainless-steel, iridium or gold). Further in-situ tip shaping experiments can often be useful, particularly after damage through accident contact with the sample. These procedures usually depend on removing the tip to a few 100 Å of the surface and applying a pulse + 100 V or more. More systematic studies of tip structure and its influence on STM images are possible by field ion microscopy.

Computer control of the various STM imaging and microscopy operations is essential for efficient operation. Ideally, however, this should also be integrated with a data acquisition, processing and display system. The basic requirements for such a system, together with examples of the significance of background subtraction, filtering and enhancement have been presented⁶. Anyone who studies the STM literature will quickly appreciate the enormous part played by sophisticated image processing and display in improving the quality of the published images. As always however, these procedures have their danger unless are used intelligently.

Imaging Applications

The number of significant and high quality STM images already published means that it would be impractical to give a comprehensive review of the results here. We will simply outline what has been achieved in the main fields explored so far, drawing attention to points which seem to be of wider significance either for surface science or for general STM imaging.

The technological importance of semiconductor surfaces has ensured that a considerable effort has gone into the study of their structure and reconstruction. In many of these cases, including the best known example of the 7x7 reconstruction of the (111) surface of Si (for details see the chapter by Gibson²), the basic elements of the surface structure had already been worked out on the basis of LEED, photoemission, ion-channeling or transmission diffraction data. Nevertheless even for regions of perfect structure, the STM images have supplied important confirmatory information on points of detail, particularly over the outermost and ad-atoms in the 7x7 structure. Furthermore, the images obtained from such known structures have been

extremely useful both experimentally and theoretically in separating the topographical and electronic contributions to the STM image contrast. In imperfect regions such as where the surface reconstruction encounters a surface step^{2,5}, or where different domains of surface reconstruction form in the same region, the high resolution information provided by the STM is unrivalled. However, other high resolution techniques such as REM imaging (see Chapter by Cowley²) and LERM imaging (see chapter by Bauer and Teliéps²) may retain an advantage where it is desired to follow in real time the dynamics of surface phase transitions at temperatures.

Surface structures and reconstructions have now been observed on a considerable variety of other surfaces particularly of metals such as Au and Pt and including situations with monotomic surface steps, close packed atomic corrugations or where ad-atoms are present, e.g., O on Ni, Au on Si. With metal surfaces or then relatively large sample-tip distances are employed, the images are largely due to surface topography. However as indicated schematically in Fig. 3 adapted from Binnig and Rohrer⁵, the contours of equal tunneling current need not follow the surface topography exactly. In semiconductors the image contribution from electronic effects such as varying local density of states (LDOS) at the surface is geneally more significant. For instance, there is an apparent but not real height difference between the two halves of the unit cell in the Si 7x7 structure. As shown in the next section, these effects can sometimes be unravelled by careful local spectroscopy. An even more striking case of spurious topography are the giant corrugations observed in graphite¹⁴. These may be due to extremely low density of states at the Fermi level in this case. However they may also be a consequence of actual physical contact between tip and surface since the typical barrier height measured is only a few tenths of a volt or less.

The STM has already been applied to a number of specimens not previously accessible by any kind of high resolution imaging. These include surfaces under air at atmospheric pressure, under water and saline solutions and under various other electrolytes. Another novel and exciting new

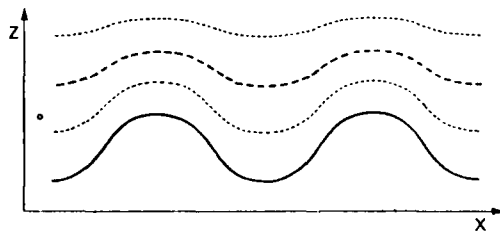


Fig. 3. Expected STM-equicurrent lines (dashed lines) above an atomically corrugated surface (solid line). The different spacings of the equicurrent lines at the protrusions and in the valleys can be described by a varying effective tunneling barrier height.

application is to the imaging of organic molecular structures which would be severely damaged by more energetic electrons. More recent work has included imaging of stearic acid, purple membrane and of Langmuir-Blodgett films. (See Chapter by García in Ref.2 and references therein).

Localized spectroscopy in the STM

As mentioned above, given sufficiently stable conditions, the feed-back loop employed to maintain the tip-sample distance can be briefly interrupted to permit measurement of tunneling current I vs separation distance at constant bias V , or of I vs V at constant s . The first of these measurements gives a value for the effective barrier height. The second measurement yields density of states information near the Fermi level and is a kind of spectroscopy based on elastic tunneling.

A most impressive demonstration of the power of elastic tunneling spectroscopy was given by Hamers et al.³³ who were able to probe the density of states with a resolution of 3 Å inside the unit cell of the Si(111) 7x7 reconstruction. Their results show the very striking variations which occur within the unit cell. Hamers et al. were able to relate the measurements to the presence of surface states previously observed in UV and inverse photoemission spectroscopy. Detailed analysis of these results indicated not only the presence of the electron state responsible for the difference in STM contrast in the two halves of the unit cell but also provided direct evidence for the presence of a stacking fault in one half, as required by the Takayanagi model (see chapter by Gibson, Ref. 2).

In principle it may be possible also to carry out inelastic tunneling spectroscopy^{29,30} in the STM. In this case the tunneling electron loses some characteristic amount of energy, e.g. by exciting a vibration in a molecule adsorbed on the surface. It might then be feasible to identify various adsorbed species from their spectra. Unfortunately the expected signal strengths are very weak and although the technique is thought to be possible, it will undoubtedly be extremely difficult.

Spin-Polarized electrons with STM (SPSTM)

One of the very interesting points in Surface Science is surface magnetism because its influence on technological devices (see other authors contributions in this field in these lectures). One of the goals that STM scientist have been pursuing for long time is to distinguish in the tunneling current the magnetic polarization of the electrons. This is a very hard task because as indicated by Saenz et al²²:

"One of the most challenging problems nowadays in several laboratories using scanning tunneling microscopy (STM) is the characterization of the magnetic properties of surfaces. It would be very interesting to observe, with very high resolution, the surface domain structure of materials of interest in magnetic information technology³⁴. We believe that

it is not simple to solve this problem with the STM. To observe a domain wall we should perform (x,y) scans of ≈ 0.01 - $1\mu\text{m}$. The variation of current (or tip-sample distance z), when the STM is operated in the constant z (or constant current) mode, is expected to be of $\approx 10\%$ ³⁵ (or, at most, ≈ 1 Å). It is possible that in this case the surface topography will hide these tiny effects. There is no way, given the irregularities and surface defects observed in STM experiments, to distinguish ≈ 1 -Å tip displacement associated to a change in the spin configuration in the surface when the tip scans over several hundred nanometers. We present in this communication a way of observing magnetic domain structure based on the idea of measuring magnetic forces with an atomic force microscope¹⁸ (AFM)".

The difficulty of performing SPSTM gives us²² the opportunity of discovering MFM but with 100-1000 Å lateral resolution. However many things can be achieved with imagination and insistance. Recently in a paper by Wiesendanger et al¹⁶ it seems that the problem of SPSTM has been partially solved. This has been done by using a clever build high polarized CrO_2 tip (see Gambino on the Special Session of Spin-Polarized Vacuum Tunneling in this School) and by choosing a clever and adequate surface $\text{Cr}(100)$ that seems to present a topological antiferromagnetic model³⁶ so that the spin in alternate terraces emerging at the surface has opposite sign. To describe the experiment we mainly follow Ref. 16 and quote it.

"This topological antiferromagnetism of the Cr surface (Fig. 4) is compatible with both the absence of magnetization observed by spin-resolved photoemission³⁷ which arises from the cancellation between oppositely magnetized terraces within the diameter of the light spot, as well as with the existence of spin-split surface states detected by energy - and angle-resolved photemission³⁸ which are due to majority- and minority-spin states inside each ferromagnetic terrace. The topological antiferromagnetism of the $\text{Cr}(001)$ surface provides an ideal test structure for SP-STM experiments.

Our topographic STM studies of the $\text{Cr}(001)$ surface also strongly support this microscopic model with terraces separated predominantly by monoatomic steps. The mechanically and electrolytically polished $\text{Cr}(001)$ surface was prepared in

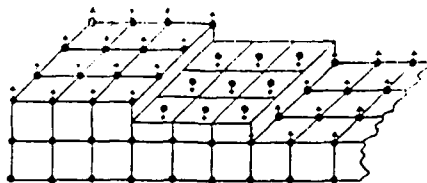


Fig.4. Topological antiferromagnetic order of $\text{Cr}(001)$ surface with terraces separated by monoatomic steps. Different terraces are magnetized in opposite directions. Only surface spins are indicated (Figure taken from Ref. 36).

situ over a time period of several months by cycles of Ar^+ - ion etching and annealing. A $p(1 \times 1)$ LEED pattern was obtained characteristic of a clean $\text{Cr}(001)$ surface³⁸. Only small traces of oxygen and nitrogen could be detected by x-ray photoelectron spectroscopy. The average width and shape of the observed terraces were found to depend on the annealing conditions, whereas the preferred occurrence of monoatomic steps was independent of the preparation conditions. The experimental determination of the monoatomic step-height value yields 0.149 ± 0.008 nm, in good agreement with half of the cubic unit-cell height of 0.144 nm for bcc Cr.

After replacing the tungsten tip by a CrO_2 tip, the STM images of the $\text{Cr}(001)$ surface showed qualitatively the same topographic structures, i.e. terraces separated by monoatomic steps. Surprisingly, these monoatomic steps could still be imaged with a remarkably high spatial resolution, although the CrO_2 tips appear macroscopically rather blunt. However, we find two different experimental results with CrO_2 tips compared to tungsten tips.

First, a positive sample bias voltage of at least 2 V had to be applied in order to get a stable tunneling current of 1 nA. The I vs V characteristics, which were recorded to investigate the bias-voltage dependence in more detail, showed the typical appearance of semiconductor-vacuum-metal tunneling than that for metal-vacuum-metal tunneling. This observation is consistent with results from spin-resolved photoemission from similar CrO_2 films showing low intensity in the photoemission spectra near E_f ³⁹. We therefore operated the STM always in a regime of maximum spin polarization of the CrO_2 , which is found at about 2 eV below E_f ³⁹.

Second, a periodic alternation of the measured monoatomic step heights between larger and smaller values compared to the mean single step-height value of 0.144 nm is observed (Fig.5). To support this experimental result, we have analyzed the step heights from individual line scans of over twenty STM raw data images obtained in the constant-current model. Care was taken to analyze only measured line scans (line scans in the x or y direction) and not oblique line scans where the exactness of the determination of the step-height values can suffer from the interpolation procedure necessary to get the topographic height values along these oblique line scans. It should be noted that the step-height values determined from topographic STM images might sometimes fluctuate within a few percent; however, a periodic alternation of the step-height values, as reproducibly observed in different line scans (independent measurements) with the CrO_2 tip on the $\text{Cr}(001)$ surface, has never been found in topographic STM images measured with a tungsten tip. Furthermore, the deviation from the single step-height value determined with a CrO_2 tip can be as large as $\pm 15\%$ which is outside the range of scatter of the monoatomic step-height values measured with a tungsten tip. Therefore, we conclude that the observed periodic alternation of the single step-height values is characteristic for STM experiments performed with CrO_2 tips on a $\text{Cr}(001)$ surface.

We interpret this periodic alternation of the monoatomic step-height values as being due to an additional contribution

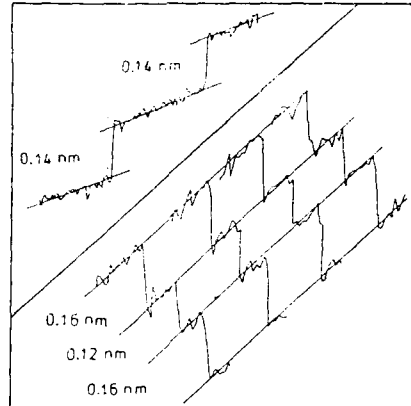


Fig. 5. Arbitrarily chosen (not successive) single-line scans over the same three monatomic steps taken from the STM image which was obtained with a CrO_2 tip. The same alternation of the step-height values (0.16, 0.12, and again 0.16 nm) in all single-line scans is evident. The line scans are 22 nm long. Inset: For comparison, a single line scan over two monatomic steps taken from the STM image which was obtained with a tungsten tip. In this case, the measured step-height value is constant and corresponds to the topographic monoatomic step height. This line scan is 70 nm long. (From Ref. 16).

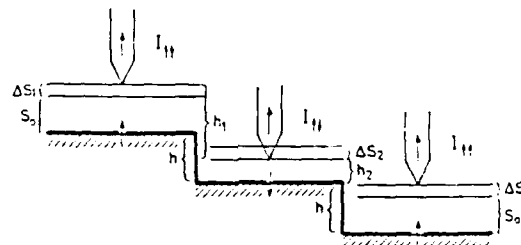


Fig. 6. Schematic drawing of a ferromagnetic tip scanning over alternately magnetized terraces separated by monatomic steps of height h . An additional contribution from SP tunneling leads to alternating step heights $h_1 = h + \Delta_{S1} + \Delta_{S2}$ and $h_2 = h - \Delta_{S1} - \Delta_{S2}$. (From Ref. 16).

from SP tunneling. Assume, as sketched in Fig. 6, that the CrO_2 tip is first scanning over a terrace having the same direction of magnetization as the front part of the CrO_2 tip. The tunneling current I_{11} will then be increased due to a contribution from SP tunneling¹⁵.

$$I_{11} = I_0 (1 + P) \quad (2)$$

where I_0 would be the tunneling current without this contribution and P is the effective spin polarization of our tunneling junction. Since the STM is operated at constant current, and additional contribution to the tunneling current leads to a corresponding increase Δ_{s1} of the mean distance S_0 between the tip and the sample surface. If the CrO_2 tip is scanning over a terrace having the opposite direction of magnetization, the tunneling current I_{11} will be decreased:

$$I_{11} = I_0 (1 - P) \quad (3)$$

leading to a corresponding decrease Δ_{s2} of the distance between tip and sample. The measured single step-height values therefore alternate between $h_1 = h + \Delta_{s1} + \Delta_{s2}$ and $h_2 = h - \Delta_{s1} - \Delta_{s2}$, where h is the topographic monoatomic step height. The relationship between

$$P = \frac{I_{11} - I_{11'}}{I_{11} + I_{11'}} \quad (4)$$

and Δ_{s1}, Δ_{s2} is given by

$$P = \frac{\exp(A\sqrt{\phi}\Delta_{s1}) - \exp(-A\sqrt{\phi}\Delta_{s2})}{\exp(A\sqrt{\phi}\Delta_{s1}) + \exp(-A\sqrt{\phi}\Delta_{s2})} = \frac{\exp(A\sqrt{\phi}\Delta_s) - 1}{\exp(A\sqrt{\phi}\Delta_s) + 1} \quad (5)$$

where ϕ is the mean local tunneling barrier height, $\Delta_s = \Delta_{s1} + \Delta_{s2}$, and $A \approx 1 \text{ eV}^{1/2} \text{ \AA}^{-1}$. Equation (5) represents a relationship between the effective spin polarization P and the quantities ϕ and Δ_s which are directly measurable with the STM. Apart from the determination of the changes of the single step-height value, measurements of ϕ are necessary to derive P . We have determined ϕ from the slope of local $\ln I$ vs s characteristics. The value of ϕ lies between 3 and 5 eV for all of over one hundred $\ln I$ vs s characteristics which were measured with different sample bias voltages between + 2.5 and + 3.5 V. These ϕ values indicate that clean conditions for the tip and the sample surface were achieved, whereas anomalous low ϕ values were reported for contaminated surfaces of either tip or sample³. Therefore, we have confidence that the derived values for the polarization P cannot greatly be affected by surface contamination. Taking $\Delta_s = 0.22 \pm 0.01 \text{ nm}$ and an average value of $4 \pm 0.5 \text{ eV}$ for ϕ , we derive values for P of $(20 \pm 10)\%$. The tip-to-sample distance at 1-nA tunneling current and a sample bias voltage of + 2.5 V was determined to be about 0.5 nm¹⁶.

However the value of the polarization P is very obscure because it is not the sample nor the tip polarization. Also the theory used is for S-electrons¹⁵ and is not used¹⁶ correctly. By using adequately the existing calculations by Fu and Freemann⁴⁰ it is possible to obtain much more

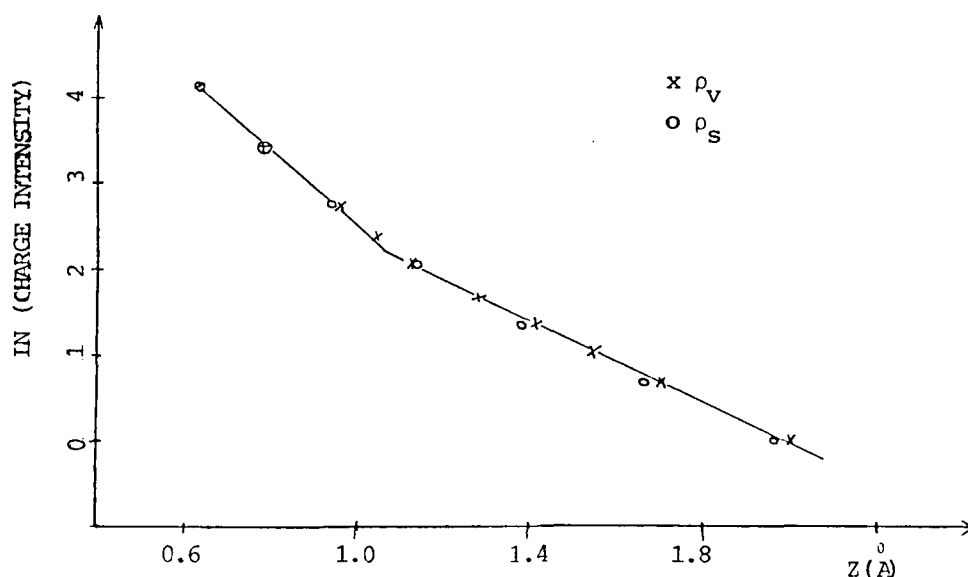


Fig. 7. Valence charge density \times and spin charge density \circ as falling away from the surface $z = 0$ on top site. The large slope (4.4 \AA^{-1}) at small values of z corresponds to d-electrons. The smaller slope (2.3 \AA^{-1}), at large z is dominated by s-electrons. At large distances $\rho_v \approx \rho_s$, so that all the s-charge at Fermi level is polarized. (Charge units are 10^{-3} electrons/(a.u.)³).

information that reported in Ref.16 by using the experimental data¹⁶. For that reason I would like to make the following clarifying comments.

1. The applied voltage in the experiment is large, 2.5 V. Therefore the barrier used to analyze the data should be trapezoidal and not square as has been used (16). We find, from the data analysis, that $P = (16 \pm 8)\%$. Also this is a joint tip-barrier-sample polarization (see for this the illuminating paper by Slonczewski (15)); i.e. P is not the tip, neither the sample polarization.
2. The self consistent calculation for Cr(001) have been done by Fu and Freeman (40). In Fig. 7 we show the valence charge density ρ_v and the spin density ρ_s as falling off outside the surface. Notice that at long distances the charge is built only by s-electrons from the Fermi level and that $\rho_s \approx 0.9 \rho_v$. This is what STM is measuring and it is remarkable that even at a tip-sample distance of $\approx 7 \text{ \AA}$ a direct ferromagnetic coupling is observed. This implies that s-electrons play an important role in coupling ferromagnetically at long distances and d-electrons do not play any role. This role played by s-electrons is crucial to understand the magnetic coupling in ferro/para/ferro trilayers⁴¹⁻⁴² as has been shown by García and Hernando⁴³.

3. The topological antiferromagnetic model of Ref. 36 does not imply that the spins are normal to the surface, in fact it is not possible to give the spin direction without the spin polarized STM experiment (16). If the tip is polarized normal to the surface the STM measures the normal component of the spin. We find that by using a polarization of the tip of 90 % (see Ref. 39), 90% polarization of the surface (Fig. 7 from Fu and Freeman calculations⁴⁰) and Slonczewski theory¹⁵ the observed value of P should be larger than 50%, but only 16% is measured. We calculate that the normal and parallel to the surface spin components are 32 % and 68% and surface magnetostriction⁴⁴ may play an important role. We propose that a spin-polarized STM experiment with tip polarization parallel to the surface should show a larger effect in the tunneling current than in the case of normal tip polarization¹⁶.

The results reported in SP-STM open such an interest that a special version in this School was arranged. The reader interested is addressed to the resumé made by Hathaway in this School Notes.

We also want to mention that the problem of SP-STM has only been solved in a very first step for a very special antiferromagnetic configuration, but for the use of ferromagnets it still is open, and no way has been depicted as the state of the art up today.

B. LECTURE ON MAGNETIC FORCE MICROSCOPY (MFM)
(With J.J. Sáenz, Universidad Autónoma de Madrid)

MFM represents an application of AFM¹⁸ to magnetism and was first studied and proposed by Sáenz et al²². Its applications to many magnetic materials and in particular to magnetic recording materials have been proven to be of much use with a resolution in the 100-1000Å.

In order to proceed for describing the basis of the MFM as well as the physical insight of this instrument we describe two papers in this field that give a general broad idea of what and how much magnetic information can be obtained with this techniques.

From J.J. Sáenz et al²² in Journal of Applied Physics it can be reported:

"We present in this communication a way of observing magnetic domain structure based on the idea of measuring magnetic forces with an atomic force microscope¹⁸ (AFM). In the AFM technique a sharp tip attached to a tiny cantilever is used to map the contours of a sample surface. Instead of measuring the current as in STM, the force between tip and sample is used as the control parameter. Forces are detected by measuring the deflection of the lever. This paper presents a theoretical analysis of the finger prints of the magnetic forces and the associated motion of the cantilever for different spin configurations. The influence of some experimental conditions in the performance of the AFM as a magnetic profiling device is also discussed. As we will see,

domain resolution of the order of $0.01 \mu\text{m}$ can be achieved with this technique, even on rough surfaces. Preliminary experimental results that appear to prove the theoretical proposals are reported.

In the magnetic version of the AFM, images are obtained by measuring the interaction force between a singledomain magnetic microtip and a magnetic sample. When the tip is moved parallel to the surface, it will follow the changes of the normal component of the tip-sample force. The interaction force can be estimated by assuming a direct interaction between the permanent magnetic moments μ_1 and μ_2 , per unit volume, corresponding to the tip and sample, respectively. Provided the gap distance z between tip and sample is larger than say $\approx 10 \text{ \AA}$, the interatomic forces can be neglected as long as we are considering a tip with a radius of the order of nanometers¹⁴ (these kind of forces should be taken into account for very large macroscopic-tip-radius¹⁹). Within these approximations, the normal force F , acting on the tip, will be given by

$$F(z) = \int_{\text{tip}} d^3\vec{r}_1 \int_{\text{sample}} d^3\vec{r}_2 f_z(\vec{r}_1 - \vec{r}_2), \quad (6a)$$

where $f_z(\vec{r})$ is the interaction force between two magnetic dipoles, $\vec{\mu}_1$ and $\vec{\mu}_2$, at a distance $\vec{r} = \vec{r}_1 - \vec{r}_2$:

$$f_z(\vec{r}) = \left(\frac{\mu_0}{4\pi} \right) \frac{\partial}{\partial z} \left(\frac{3(\vec{r}\vec{\mu}_1)(\vec{r}\vec{\mu}_2)}{r^5} - \frac{(\mu_1\mu_2)}{r^3} \right) \quad (6b)$$

and μ_0 is the vacuum permeability. Because of the dipolar behaviour of the magnetic force given by Eq. (6), when the tip is over a region of uniform magnetization (constant magnetic field), there is not normal force acting on it. The forces manifest themselves when the tip approaches a domain wall separating two regions of different magnetizations (in general, any region of nonuniform magnetization). The main features of the force acting on the tip as it goes across a domain wall can be illustrated with the simple model sketched in Fig. 8, where we consider two infinite antiparallel domains separated by a sharp domain wall. The force distribution around the domain wall will depend on the orientations of the tip and sample magnetizations, characterized by the angles θ_1 , ψ_1 and θ_2 , ψ_2 , respectively. A very important point associated with the long-range force given by Eq. 6 is that, as long as the size L of the single-domain particle at the end of the tip is large compared to the gap distance z , the tip force does not depend on z . Therefore, one can work at relatively long distances from the surface and in contrast with the STM, it is not necessary to have a welldefined z value. By assuming a spherical magnetic tip (with a radius $L \gg z$), the tip sample force as a function of the tip distance x to the domain wall takes the simple form

$$F(x) = F_0(ax_r + b)/x^2_r + 1), \quad (7)$$

where $x_1 = x/L$ and $F_2 = 8/\pi\mu_0\mu_1\mu_2L^2$; a and b are constants that

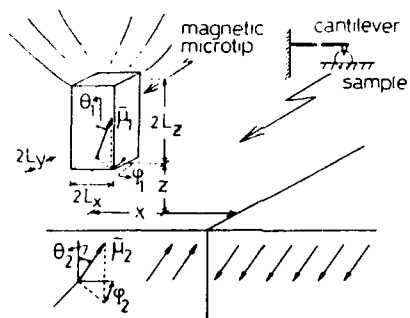


Fig. 8. Scheme of the magnetic version of the atomic microscope (from Ref. 22).

depend on the spin configuration. In Fig. 9 we have plotted the reduced force F/F_0 as a function of x_r for different spin configurations. These results are obtained for a spherical magnetic tip, but can be generalized to an arbitrarily shaped single-domain particle used as the tip. For example, we have calculated the forces induced on a needlelike tip like that shown in Fig. 8. Our results show that Eq. (7) remains approximately valid, provided $L^2 = L_x L_y$, $x_r = x/L_x$, and $L_z \gg z$. In Fig. 9 (d) we have plotted the calculated force or tip displacement profile assuming different wall widths⁴³. Provided the domain wall width would be of the order or higher than L , it would be possible to get information, not only of the domain distribution on the sample surface, but also of the domain wall itself. An interesting point is that the AFM would be able to obtain information about the thermodynamic

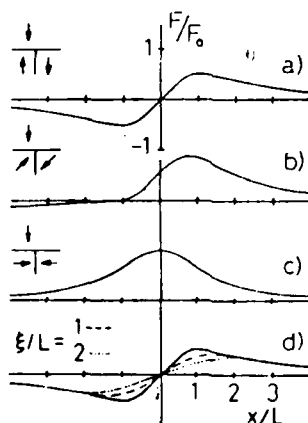


Fig. 9. Calculated forces F/F_0 vs the distance x/L between a spherical tip and a domain wall separating two antiparallel domains for different spin configurations. (a) - (c) correspond to a sharp domain wall. (d) is the same as (a) but for different wall widths z/L . (From Ref. 22).

properties of a magnetic sample through the dependence of ζ (or the magnetic correlation length) and μ with the temperature. From this point of view, we can interpret Fig. 9(d) as the expected behavior of an AFM profile as the temperature increases.

To simulate the influence of these forces in an AFM experiment, consider that the base of the lever is kept fixed with respect to the sample. When the tip approaches a domain wall, it will suffer a normal displacement given by the solution of $K(d-z) + F(x,z) = 0$, K being the force constant of the lever and d the tip sample distance in the absence of forces. In our case the displacement Δz will be given by $\Delta z = F/K$, and is independent (for $L_z \gg z$) on the exact distance between tip and sample. This is very important, because the magnetic AFM will not be sensitive to the surface roughness, as long as the surface roughness is small compared to L_z . Another point is that Fig. 9 could be taken approximately as a plot of the tip displacement that would be observed in an experiment, just by noting that $F/F_0 = \Delta z/\Delta z_0$, $\Delta z_0 = F_0/K$ being the maximum amplitude of the displacement. The sensitivity of the AFM will be controlled by the magnitude of Δz_0 with respect to the amplitude of thermal oscillations, $z_T \approx \sqrt{(K_B T/K)}$. Taking μ_1 and μ_2 typically of the order of a Bohr magneton μ_B per atom, we have $F_0 \approx 10^{-14} L^2 N$ and $z_0 \approx 10^{-14} L^2 / K$ Å (K given in $N m^{-1}$ and L in Å). At room temperature the condition $\Delta z_0 > \Delta z_T$ is equivalent to a condition that relates the force constant of the lever K and the lateral dimensions of the magnetic tip: $K > 10^{-8} L^4 N m^{-1}$ (L in Å). By assuming that this sensitivity condition is satisfied, the most useful measure of the performance of the AFM as a magnetic profiling device will be the lateral resolution parallel to the surface. In other words, what is the minimum domain size D which can be distinguished with this technique? A measure of this resolution could be the width of the region

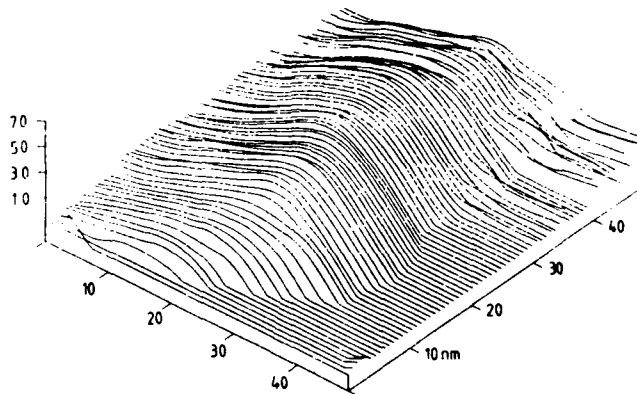


Fig.10. Deflection of the lever is plotted as a function of the tip position on the Ni sample. The interaction force between sample and lever was attractive. The AFM was operated in the constant force model, i.e., the displayed lines are equipotential lines. (From Ref. 22).

in which the force changes as the tip goes across a domain wall. As we have seen, this characteristic length is of the order of the lateral tip dimension in the scanning direction L . From the sensitivity condition given above, we see that the force constant of the lever imposes a lower limit to the AFM lateral resolution. For example, for typical force constants $K \approx 0.01-1 \text{ N m}^{-1}$ we would have $L_{\min} > 50-100 \text{ \AA}$ (or forces $F_0 > 10^{-11}-10^{-10} \text{ N}$).

We have tried to measure magnetic forces with our FM, which is operated in air. In order to simulate the situation presented in Fig. 8, we have chosen a ferromagnetic Ni foil as a sample and an electrochemically rolled and etched Ni lever with an integrated ferromagnetic tip. As an example of various measurements, Fig. 10 shows the obtained line scans, which are very similar to the asymmetric lines shown in Fig. 9(d). The interaction force in this case was attractive. The right side of the scans in Fig. 10 are flat, indicating that small forces are out of apparatus resolution. We have checked very carefully the topography of this Ni foil by STM measurements, also performed in air. Typical structures have a height of 5-10 nm. However, the structures observed by magnetic interactions (Fig. 10) show a deflection of the cantilever beam in the range of 60 nm. Therefore, no correlation between the height of the structures in the topographic and magnetic images is observed. It is very difficult to calculate the force constant of the lever K because of the unknown elastic constant of rolled and etched thin ferromagnetic Ni foil used as a lever and the effects arising from the interactions within the tunneling junction. Nevertheless, from the width of the structure in Fig. 10, we estimate a monodomain tip of $L \approx 500 \text{ \AA}$ (i.e., a maximum force $F_0 \approx 10^{-14} \text{ N}$, $L^2 \approx 3 \times 10^{-9} \text{ N}$) and from the deflection of the cantilever beam $\Delta z_0 \approx 500 \text{ \AA}$, we obtain $K \approx 0.05 \text{ N m}^{-1}$, which satisfy very well the sensitivity condition of the AFM versus thermal oscillations. By taking into account the roughness of the estimation, the order of magnitude of K seems to be a reasonable value in comparison with others reported before in AFM experiments ($\approx 0.05-0.2 \text{ N m}^{-1}$)¹⁸. Our experimental results show a good reproducibility for the repulsive as well as the attractive interaction between tip and sample. Since these interactions can be observed for a wide range of tip-sample separation (more than 10 nm), we conclude that we measure long-range forces, which cannot be attributed solely to the attractive van der Waals forces. This strongly suggests the magnetic nature of the observed interaction. Finally, we would like to add that we were also able to observe oscillating force-sample position curves. These experiments were performed on rapidly quenched Fe-Nd-B samples, where the domain size is known to be much smaller than the typical sizes ($0.1-2 \mu\text{m}$) in Ni."

In the above work only dipole forces were considered however, one should also consider, for the tip-sample van der Waals and anisotropy forces. Van der Waals forces are non magnetic and are due to induce electric dipole interactions between tip and samples. When the tip has a radius of $\approx 500 \text{ \AA}$ these forces can be important and can be used to distinguish between magnetic and topography effects. The study and

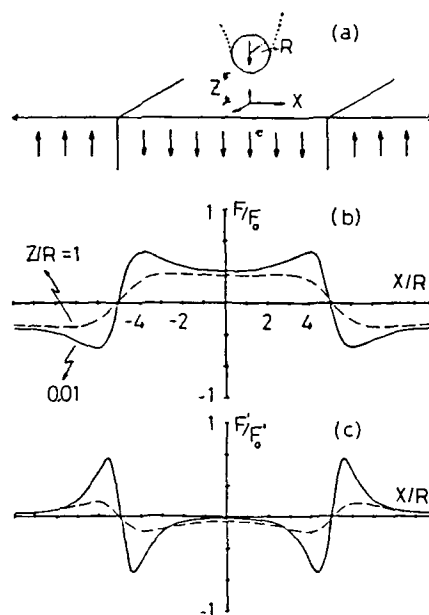


Fig. 11. Magnetic imaging by force microscope of an isolated strip-like domain. (a) Schematic view of the geometry analyzed, (b) represents the calculated magnetic dipolar forces F/F_0 vs the distance, $x = X/R$, between a spherical tip and the sample magnetization for two different tip-sample spacings $z = Z/R$, and (c) represents the force gradients F'/F'_0 ($F'_0 = F_0/R$) corresponding to (b).

discussion of van der Waals interactions as applied to MFM as well as the anisotropy forces was studied by Sáenz, García and Slonczewski²⁴. In what follows we describe the description of the above forces as discussed in Ref. 24.

"In this work we discuss the forces involved in a magnetic force microscope (MFM) and its relevance in the interpretation of the experimental results. In particular, we discuss the contrast mechanism in the magnetic images obtained by Martin et al.²⁸ in a recent experiment on laser-written domains in a thin TbFe film.

We have discussed before²² the basic principles and performance of the force microscopy as a magnetic profiling device. The main features of the forces acting on the tip as it goes across a domain can be illustrated with the simple model sketched in Fig. 11(a). We will consider antiparallel domains with sharp domain walls. The force distribution around a domain wall depends on the relative orientation of tip and sample magnetizations²² and, for simplicity, we will consider the case of orientations normal to the surface.

In any experiment which involves force measurements we should include the contribution of van der Waals forces. For

a distance Z of separation between tip and sample surfaces, which is less than the tip radius R , the van der Waals forces can be given approximately by¹⁹.

$$F_w \approx - \frac{A}{6R} \left(\frac{R}{Z} \right)^2 = - \frac{A}{6R} \frac{1}{z^2} \quad (8)$$

where A is a constant of the order of $\approx 5 \times 10^{-20}$ J (this is a lower limit estimation) and $z = Z/R$. In general, for submicron tip radius, we can neglect the van der Waals contribution as compared to the magnetic forces.

Together with the dipolar force, there is another kind of magnetic force associated to the local changes of the sample magnetic moments induced by the magnetic field of the tip. It is possible to estimate the contribution of this force just by adding to the energy density inside the sample the contribution of the anisotropy energy. The energy density now takes the form⁴⁴

$$\Phi \approx (1/2)\beta M_1^2 \sin^2(\theta) - M_1 H, \quad (9)$$

where β is the anisotropy constant. We assume the condition $\beta \gg 1$, which is usually satisfied by materials having stripe domains. The equilibrium value of the angle θ is determined by the condition $\partial\Phi/\partial\theta = 0$. The total magnetic force, in this case, is obtained, as in the former case, by taking the energy gradient in the z direction after integration over the sample. For magnetic fields H much smaller than the coercivity H_c ($H \ll H_c \approx \beta M_1$), it can be seen that the new contribution to the magnetic force is given by

$$F_{an} \approx - (\pi^2 M_2 / 8 H_c) [F_0 / (z+1)^4] \quad (10)$$

This force is always attractive and does not change as the tip goes across a domain wall. Moreover, as in the case of F_d , for small tip-sample distance this force is almost constant and the only effect on the lever motion would be a constant shift of the displacements obtained before.

Up to now, we have discussed the relevant forces in magnetic force microscope. However, we have assumed an operation mode of the microscope in which the lever would follow the changes in the tip-sample force. However, it is also possible, to use, instead of the force, the force gradient as the control parameter. In Fig. 11 (c) we show the force gradient corresponding to the force given in Fig. 11(b). This would be the expected behavior in an experiment performed at a constant tip-sample spacing. As before, in this operation mode (constant z) the only effect of the other forces would be a constant shift in the force gradient and would have no effect in the analysis of the experimental results.

The situation changes if the experiment is performed in such a way that the gap distance is adjusted to keep constant the force gradient. Recently, Martin et al.²⁸ have obtained high-resolution images of domains, working in the constant gradient mode (See Fig. 12). In this working model, the

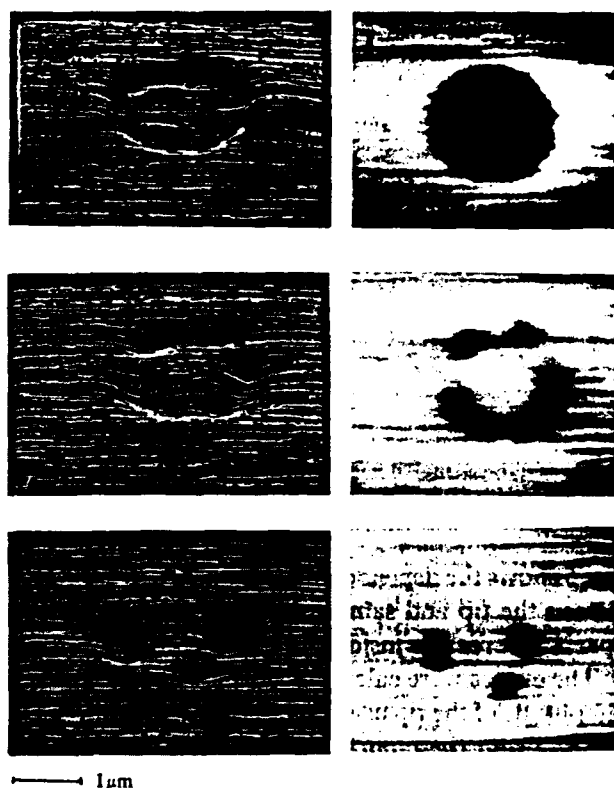


Fig. 12. High magnification magnetic images of laser written marks which consist of multiple domains due to the low bias field used during writing.

displacements the lever depends, not only on the dipolar force, but also on the van der Waals and "anisotropy" contributions. We can estimate the expected order of magnitude of the different contributions to the total gradient in the case of the experiments by Martin et al.²⁸. The sample used in their experiments consisted of 500-Å-thick $Tb_{19}Fe_{81}$ with magnetization $M_1 = 109 \text{ emu/cm}^3$ and a coercivity $H_c = 5.1 \text{ kOe}$. The sample had sufficient perpendicular anisotropy to ensure a magnetization normal to the surface. For a magnetized tip of iron we will assume a typical magnetization of $M_2 \approx 2 \times 10^3 \text{ emu/cm}^3$. Substituting these values, after differentiation of Eqs. (8) and (6), we have

$$F'_w \approx \frac{1}{R^2} - \frac{1}{z^3} \left(\frac{N}{m} \right),$$

$$F'_{an} \approx 10^{-4} R \frac{1}{(z+1)^5} \left(\frac{N}{m} \right)$$

and, at the peaks near the domain walls [see Fig. 11(c)],

$$F'_d \approx 10^{-4} R (N/m),$$

where R is given in Å. For a tip radius $R \approx 1000$ Å and typical tip-sample distances of $z \approx 0.1-0.5$ (Ref. 28) (remember that all distances are in units of R) we obtain $F'_w \approx 10^{-7} - 10^{-3}$ N/m and $F'_{an} \approx 10^{-2} - 10^{-1}$ N/m. These values are larger than the $\approx 10^{-3} - 10^{-4}$ N/m observed experimentally²⁸. This difference could indicate that the magnetization of the tip is actually smaller than that we have assumed. It is worth noting, that although the van der Waals forces are very small, their gradient is not negligible compared with that of magnetic forces, and even dominates near the surface.

In order to understand the main features in a constant gradient experiment, we have shown in Fig. 13 the qualitative effect of the additional gradients on the curves given in Fig. 11(c). Let us assume that we scan the tip at a large constant gradient, in such a way that the van der Waals dominates over the magnetic gradients. In this case the tip displacements, necessary to compensate the changes of the dipolar gradients as we go through a domain wall, will be very small. On the other hand, if we start at a large distance from the surface (i.e., small gradients), the tip displacements, necessary to keep the small gradient fixed, will be very large. This is in qualitative agreement with the observed behavior in the experiments by Martin et al.²⁸. However, from the above discussion we would expect strong peaks on either side of the domain boundaries. Moreover, for very large domain sizes ($D \gg R$), the dipolar force will be negligible far from the domain walls²². Then we would expect that the force, and the force gradient, inside and outside the domain walls would be the same (notice that the van der Waals and "anisotropy" contributions should be independent of the sign of the sample magnetizations) This is in contrast with the smooth experimental behavior obtained by Martin et al. They also deduced different values for the force and force gradients inside and outside the laser-written domains.

The contrast mechanism in the experimental magnetic images is not clear. The absence of strong peaks at the domain boundaries indicates that the observed structure is not associated to the dipolar forces discussed before. (It is worth noting, that for large domain sizes, as it is the case in the experiments, there are not significant differences between circular domains and the strip-like domains we have

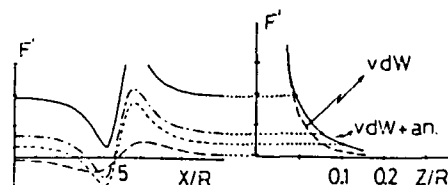


Fig. 13. Qualitative effect of the van der Waals and anisotropy gradients on the curves given in Fig. 11(c).

studied). The experimental behaviour could be explained if the magnetization or anisotropy inside and outside the written domains were different. A slightly smaller magnetization inside the domain (as a result of heat treatment during experimental sample preparation) could account for the difference in force gradient, as well as for the fairly uniform contrast across the domain interior".

There is actually much work carried on to study magnetic heads with MFM²³⁻²⁸. In particular we want to stress a recent method developed by Schönenberger et al²⁶ that shows, in an elegant way, how to separate magnetic structure from topography. We recommend to read Rohrer contribution in Ref.3 that is basically followed here.

"Generally, short-range repulsive forces are used to image surface structures by force microscopy. This contact method can achieve atomic resolution on hard materials or on surfaces where the atoms are laterally fixed by strong bonds. The forces are controlled and monitored by the deflection of the cantilever carrying the probe tip. The long-range forces, on the other hand, are usually probed dynamically by the vibrations of the cantilever. These are noncontact methods. The measurements yield force derivatives: F/s from the shift of resonance frequency, and higher-order derivatives from the entire frequency spectrum of the vibrating cantilever⁵.

The method of Schönenberger et al. is based on the fact that magnetic forces due to a magnetization pattern vary slowly with distance at distances which are small or comparable to the dimension of the magnetic probe²². They introduce an additional force, the coulomb force, obtained by applying a voltage between tip and sample, as control interaction. The coulomb force diverges at small distance with $\approx s^{-2}$. The magnetic force F_m , on the other hand, saturates at $F_{m,0}$ (see Fig. 14); we approximate the slow variation of the magnetic force with distance by $dF_m/ds < F_m(s)/l$, where l is the lateral extension of a magnetic domain. One can then always find a distance s_0 such that $dF_c/ds \gg dF_m/ds$, even if $F_c(s_0)$ might be smaller than $F_m(s_0)$. Without magnetic forces, $dF/ds = dF_c/ds = \text{const}$ is essentially a topography. The magnetic forces induce only a small deviation, $\delta s/s_0 = 1/6(F_m/F_c)(s_0/l)$. The lateral variation of the force on a constant dF/ds surface, however, is dominated by the lateral variation of F_m . The total force on a $dF/ds = \text{const}$ surface is

$$F(s) = F_c(s) + F_m(s) = F_c(s_0) + F_m(s) (1 + 1/3(S_0/l)) \quad (11)$$

Since $F_c(s_0) = \text{const}$, the force image reflects the magnetic force up to a correction of order s_0/l ".

Applications have also been made of the MFM to measure superconductors. Due to the fact that a superconductor is diamagnetic, there is a magnetic interaction between tip-superconductor that can give information on critical fields, etc. Prof. Khaikin and collaborators in the Institut for Physical Problems of Moscow have cordially presented the information that we describe here.

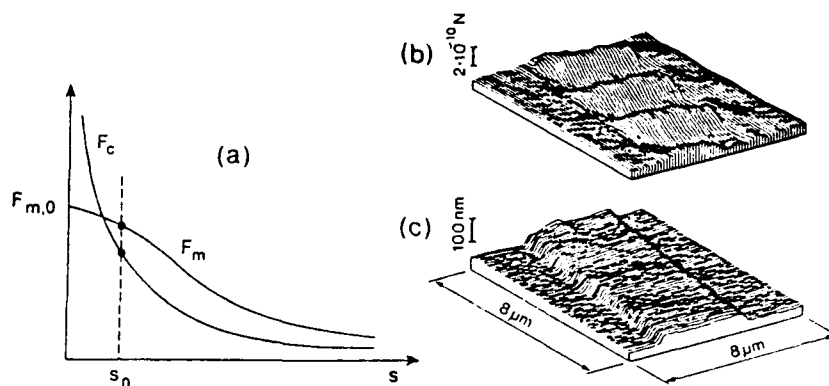


Fig. 14. (a) Distance dependence of magnetic and coulomb forces. (b) and (c) give the magnetic force image and topography (as a $dF/ds = \text{const}$ image), respectively, at a stripe of alternatively up and down-oriented magnetic bits.

Application of Magnetic Force Microscopy to High-Tc Superconductor.

(A.P. Volodin, M.V. Marchevsky, M.S. Khaikin (Institute for Physical Problems of Moscow)).

"The magnetic force microscope (MFM) is based on the idea of measuring magnetic forces with usual atomic force microscope²². Forces acting between a ferromagnetic tip and the sample are recorded by measuring the deflection of a lever. In the present letter we describe the first experiments with the low-temperature MFM as a tool for investigation of the High-Tc superconductor.

The absence of any magnetic flux in a superconductor independently of the initial conditions of the Meissner effect as it is called, is a fundamental property of superconductivity. Let's consider the single domain ferromagnetic tip near the surface of a superconductor. There exist the mutual repulsion between this tip as elementary magnet and a superconductor. The simplest way of understanding the repulsion is to think of image poles under the superconductor. The real tip and it's mirror image would in the absence of the superconductor, produce above the surface just the same field distribution as produced by real tip alone the superconductor. In case of absence of the local perturbations of superconductivity the repulsive force depends on the distance from the tip to the surface of the superconductor only. The scanning would in this case produce the topogram of the surface. But our research objective has been to try to use the MFM to measure the superconducting structure of High-Tc superconductor. The local perturbation of superconductivity would produce the changing in the repulsive force, which deflects the lever of the MFM. If such a deflections are more less then the surface roughness, we get

the image of the superconducting structure of the specimen as a result of scanning.

Our MFM closely resembles a previous bimorph STM design in our group⁴⁶. Magnetic force sensor was cut from 20- μm Ni wire and electrochemically etched to a tip of less than 100-nm radius. MFM was operated in the variable deflection mode, in which tunneling was used to detect the lever motion.

We have performed our preliminary MFM measurements on film of $\text{Bi}_2\text{Sr}_2\text{CaCu}_2\text{O}_x$ at 77.6 K. The film with the thickness $\approx 1\ \mu\text{m}$ and $T_c = 86\ \text{K}$ was fabricated by laser sputtering. The roughness of the film was less than 30 nm, as it was measured by STM.

Fig. 15 shows MFM images, obtained for different distances from the tip to the surface of the superconductor at 77.6 K. The direction of the Z axis displays the deflection of the lever proportional to the repulsive force, acting between a ferromagnetic tip and the sample. The divisions are 2 μm on the X and Y axis and 100 nm on the Z axis. The second and third images were measured 480 and 530 nm farther to the sample than the top image. All images in Fig. 15 show some perturbations and a smooth regions. A higher magnification

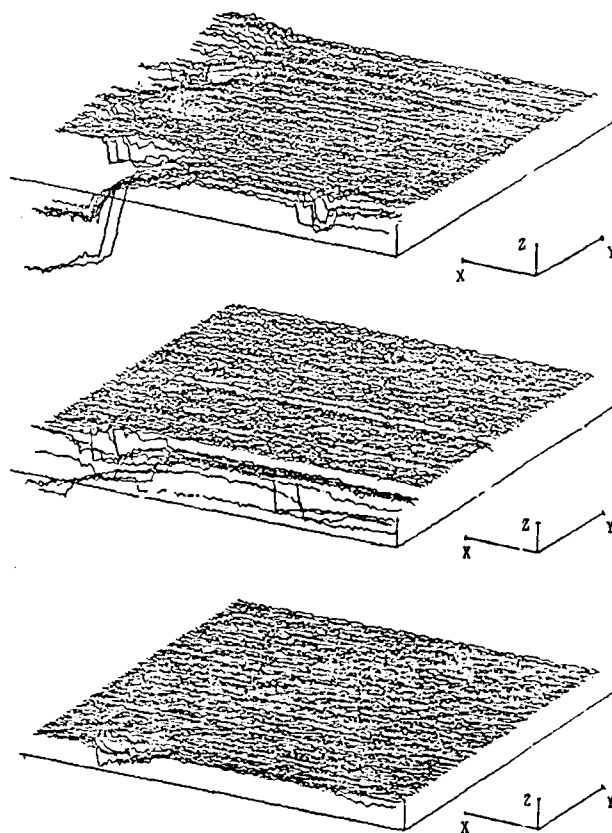


Fig. 15. See text.

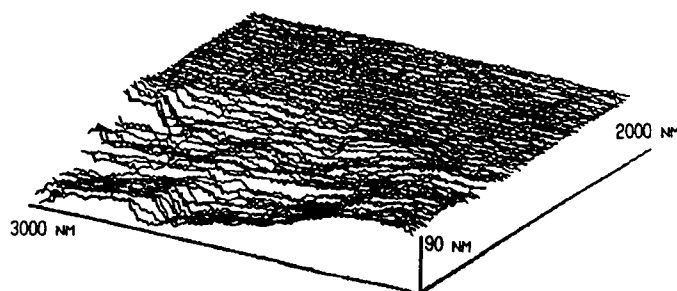


Fig. 16. See text.

by a factor 3) image of the perturbed region on the bottom Fig. 15 imaged in Fig. 16. The perturbed regions correspond to the diminishing of repulsive forces. The typical value of the sensor deflection diminishes in ≈ 6 times from the top to the bottom image. The magnetic nature of the repulsive forces is proven by measuring this force as a function of tip sample separation. These observations when combined with the room temperature result, which shows the absence of any forces, acting at this range of the distances indicate the superconducting nature of the phenomenon. The perturbed regions may be treated as the regions with the disturbances in the superconductive properties of the sample. The possible physical reasons for the existence of such a regions could be the imperfections in the sample structure or more complex phenomena of the magnetic field penetration into the High-Tc superconductor, which is caused by the tip.

It is shown that the low-temperature MFM may be used to investigate the distributions of the superconductive phase on the surface of the superconductors".

WARNINGS AND FUTURE

This finishes our lecture notes on STM and MFM. But there are some warnings and future work that will be interesting to discuss:

1. MFM can be destructive if the tip or the sample are soft materials comparatively to each other. For example magnetic domains can be shifted by passing the tip because of the larger molecular influencing the sample. Experimental results have shown this effect⁶⁵.
2. In order to measure magnetic forces one needs to have a large enough magnetic volume otherwise forces are too weak and the cantilevers in MFM with electric constant ≈ 1 N/m can not be bend; i.e. the force is not large enough. This limitate the resolution because the volumen of the tip should be of the order of spheres of $100 - 1000\text{\AA}$ minimum. By the same taken it will be difficult to apply MFM to thin magnetic layers.

3. MFM may be able to measure direct exchange forces if a clever experiment is thought.

4. The problem of measuring magnetic properties with atomic resolution is only possible with STM, with MFM it is not possible. Although there is a door open with the experiment of Ref. 16, this is far from being solved for any magnetic conducting material. We want to establish here, for the first time, that this is only possible through surface magnetostriiction⁴⁸ (see the lecture by O'Handley).

5. There are also many finite size effects that are in its way to be studied by STM and related techniques³. Recently, for example, it has been proposed⁴⁹ that an STM could be used, by resonant tunneling to count electrons (Coulomb blockade) and in this way to establish a quantum standard of current.

6. As said in the beginning STMs and related instruments are small, simple, cheap, and everybody can build one for his personal needs. So it is a small, versatile instrument for a big imagination.

ACKNOWLEDGEMENTS

I want to thank the organizers for inviting me to the School in Crete where I learned a lot of magnetism and new problems. I also got to know new interesting people in the School and this is what life is all about.

REFERENCES

1. G. Binnig, H. Rohrer, Ch. Gerber and E. Weibel, Appl. Phys. Lett. 40, 178 (1982).
2. N. García, Scanning Tunneling Microscopy and Spectroscopy in NATO, ASI, Series B, Vol. 191, (Ed. A. Howie and U. Valdrè). Review Article.
3. Scanning Tunneling Microscopy and Related Methods. NATO, Series E, Vol. 184. Editors J. Behm, N. García and H. Rohrer. This is a comprehensive book on the topic.
4. G. Binnig, and H. Rohrer, Rev. Mod. Phys. 59, 615 (1987).
5. Two issues of the IBM Journal of Research and Development dedicated to STM, Volume 30, Nos 4 and 5 (1986).
6. Proceedings of the First STM Conference. Surface Sci. 181, (1987), Ed. N. García.
7. Proceedings 2nd STM Conference. J. Vac. Sci. Technology A6(2) 1988, Ed. R.M. Feenstra.
8. Proceedings 3rd STM Conference, Journal of Microscopy Vol. 152 (1989), Ed. W.M. Stobbs.
9. Proceedings 4th STM Conference. J. Vac. Sci. Technol. A5(2) (1990), Ed. T. Ichinokawa.
10. J. Bardeen, Phys. Rev. Lett. 6, 57 (1961).
11. J. Tersoff and D.R. Hamann, 50, 1998 (1983); Phys. Rev. B 31, 805 (1985).
12. N. García, C. Ocal and F. Flores, Phys. Rev. Lett. 50, 2002 (1983) and Ref. 5, n°5, page 533.
13. N.D. Lang, Phys. Rev. Lett. 56, 1164 (1986); Phys. Rev. Lett. 55, 230 (1985).
14. J.M. Soler, A.M. Baró, N. García and H. Rohrer, Phys. Rev. Lett. 57, 444 (1986).

15. J.C. Slonczewski, Phys. Rev. B 39, 6995 (1989).
16. R. Wiesendanger, H-J. Güntherodt, G. Güntherodt, R.J. Gambino and R. Ruf, Phys. Rev. Lett. 65, 247 (1990).
17. N. García, Comment submitted to Phys. Rev. Lett.
18. G. Binnig, C.F. Quate and Ch. Gerber, Phys. Rev. Lett. 56, 930 (1986).
19. J.N. Israelachvili, Intermolecular and Surface Forces, Academic Press (1985).
20. F.O. Goodman and N. García, Roles of the Attractive and Repulsive Forces in AFM, Phys. Rev. B, August Issue (1990).
21. E. Meyer, H. Heinzelmann, H. Rudin and H-J. Güntherodt, Zeitschrift für Physics B (1990).
22. J.J. Sáenz, N. García, P. Grütter, E. Meyer, H. Heinzelmann, L. Rosenthaler, H.R. Hidber and H.-J. Guntherodt, J. Appl. Phys. 62, 4293 (1987).
23. Y. Martin and H.K. Wickrama Singhe, Appl. Phys. Lett. 50, 1455 (1987).
24. J.J. Sáenz, N. García and J. Slonczewski, Appl. Phys. Lett. 53, 1449 (1988).
25. P. Gutter, Ph.D Thesis, University of Basel, 1989.
26. C. Schönenberger, Ph.D Thesis, Swiss Federal Institut of Technology Zürich (1990) and to be published in J. Appl. Phys.
27. A.P. Volodin, M.V. Marchevsky and M.S. Khaikin, Application of MFM to High-Tc Superconductors (to be published). This will be discussed in these Notes.
28. Y. Martin, D. Rugar and H.K. Wickramasinghe, Appl. Phys. Lett. 52, 244 (1988).
29. C.B. Duke, "Tunneling in Solids", Academic Press, New York (1969).
30. E.L. Wolf, "Principles of Electron Tunneling Spectroscopy", Oxford University Press, Oxford 1985.
31. J. Simmons, J. Appl. Phys. 34, 1973 (1963).
32. Ch. Gerber, G. Binnig, H. Fuchs, O. Marti and H. Rohrer, Rev. Sci. Instrum. 52, 221 (1986).
33. R.J. Hammers, R.M. Tromp and J.E. Demuth, Phys. Rev. Lett. 56, 1972 (1986).
34. J.H. Kryder and A.B. Bortz, Physics Today, 37, 20 (1984).
35. A. Modinos, in Field Thermoionic and Secondary Electron Emission Spectroscopy (Plenum Press, New York 1984), page 157.
36. S. Blügel, D. Pescia and P.H. Dederich, Phys. Rev. B 39, 1392 (1989).
37. F. Meier, D. Pescia and T. Schriber, Phys. Rev. Lett. 48, 645 (1982).
38. L.E. Klebanoff, S.W. Robey, G. Liu and D.A. Shirley, Phys. Rev. B 30, 1048 (1984).
39. K.P. Kämper, W. Schmitt, G. Guntherodt, R.J. Gambino and R. Ruf, Phys. Rev. Lett. 59, 2788 (1987).
40. C.L. Fu and A.J. Freeman, Phys. Rev. B 33, 1755 (1986).
41. J. Krebs, P. Lubitz, A. Chaiken and G.A. Prinz, Phys. Rev. Lett. 63, 1645 (1988).
42. B. Heinrich, Z. Celinski, J.F. Goghran, W.B. Muir, J. Rudo, Q.M. Zhong, A.S. Arrot and K. Myrtle, Phys. Rev. Lett. 64, 673 (1990). See also same authors in this School.
43. N. García and A. Hernando, Coupling Ferromagnets Through Paramagnetic Layers: Direct Exchange Coupling Plus a

- Magnetic Pump Mechanism. (Preprint submitted to Physical Review Letters, 24 August 1990).
44. R.C. O'Handley and S.W. Sun, in this School.
 45. See L.D. Landau and E.M. Lifshitz, Electrodynamics of Continuous Media (Pergamon, London, 1960).
 46. A. P. Volodin, G.A. Stepanjan, M.S. Khaikin, V.S. Edelman, Prib. Tekh, Eksp. 5, 185 (1989).
 47. H.J. Mamin, D. Rugar, J.E. Stern, R.E. Fontana and P. Kasiraj, Appl. Phys. Lett. 55, 318 (1989).
 48. N. García, STM and Surface Magnetostriction (to be published).
 49. F. Guinea and N. García, Phys. Rev. Lett. 65, 281 (1990).

Special Session on Spin-Polarized Vacuum Tunneling

(This session was organized to address the numerous questions that arose at the end of the lecture by N. Garcia, when he reported on an experimental observation of vacuum tunneling of spin-polarized electrons with the scanning tunneling microscope,¹ on the Cr(001) surface. Participants included N. Garcia, Universidad Autonoma de Madrid, R. Gambino, IBM, T. J. Watson Research Ctr., F. Meier, ETA Zürich-Festkörperphysik, R. Victora, Eastman Kodak Research Labs, and K. Ounadjela, University of Strasbourg. K. Hathaway, Naval Surface Warfare Ctr., MD served as chairman for the session and assembled these contributions from the participants.)

The session began with a discussion of theoretical and experimental investigations of the Cr (100) surface:

Hathaway: Freeman and coworkers performed a seven layer Cr(001) slab calculation using the full-potential augmented-plane-wave method (FLAPW) and reported results on the charge density, magnetic moment, spin density and hyperfine contact field.² They find a ferromagnetic surface layer with antiferromagnetic coupling between layers in the [001] direction. The layer-projected magnetic moments within each muffin tin sphere from the surface to the center layer are 2.49, -1.29, 0.89, and -0.89 Bohr magnetons, respectively.

Victora: Victora and Falicov calculated the electronic and magnetic structures of the Cr(001) surface using a tight-binding scheme, with single-site, full orbital interactions treated self-consistently.³ A ferromagnetic surface was predicted: spin polarizations were 3.00 (surface), -1.56, 1.00, -0.93, 0.86, -0.85 (center) Bohr magnetons. The calculated surface electronic structure yielded binding energies and dispersions which were consistent with the (non-spin-polarized) photoemission data of Klebanoff et. al.,⁴ subject to the usual difficulties with many-body effects and unknown transition matrix elements.

Meier: In contrast, photoemission work by Meier, Pescia, and Schriber, using spin-polarized photoelectron detection, found no evidence for ferromagnetic order in the Cr(100) surface.⁵ In this case ferromagnetic order means an alignment of all magnetic surface moments along the same direction and not just a truncation of the antiferromagnetic order of bulk chromium which results in oppositely magnetized surface regions if adjacent (100) planes are exposed to the vacuum. Minute amounts of oxygen incorporated into the chromium subsurface were observed to give rise to ferromagnetic order.

Ounadjela: Recently, Blügel, Pescia, and Dederichs⁶ have studied, within the framework of spin density functional theory two possible magnetic structures for the surface of bcc (001) Cr:

i) antiferromagnetic order 1 (A01) in which spin orientations are ferromagnetic within each (001) plane and alternate antiferromagnetically in the [001] direction perpendicular to the surface.

ii) antiferromagnetic order 2 (A02) in which the (001) surface layer of spins is ordered in a c(2x2) antiferromagnetic structure, leading to a frustration of the spins on the first subsurface layer.

A comparative study of the total energies of these two magnetic structures clearly shows that the ground state of A01 is lower and thus it is the more stable magnetic structure. A more realistic topological configuration was considered consisting of a surface structure of (001) terraces separated by single atomic layer steps, with alternate terraces magnetized in opposite directions. From the observed environmental insensitivity of the antiferromagnetic coupling between Cr near neighbors, it can be inferred that the existence of steps does not perturb the bulk induced topological antiferromagnetic order. These calculations and observations reconcile the various theoretical calculations and the photoemission experiments showing spin-split states with the spin-polarized photoemission measurements in which no net magnetization was measured for the Cr (001) surface.

The session then proceeded to a discussion of the experimental results reported in Ref. 1.:

Gambino: Spin polarized scanning tunneling microscopy (SP-STM) was recently demonstrated for the first time.¹ The tip used in these experiments was made from a thin film of CrO_2 , a ferromagnet with a Curie temperature of 392K and $2\mu_B$ per formula unit. It is a metallic conductor with a typical resistivity in thin film form of $40 \mu\Omega\text{cm}$ at 4.2K and $200\mu\Omega\text{cm}$ at 300K. A band structure calculation shows that the compound is a half metallic ferromagnet with a gap of about 2 eV in the minority spin band and the Fermi energy passing through the majority spin d band.⁷ The calculation thus predicts that CrO_2 is a ferromagnetic metallic conductor with 100% spin polarized electrons at the Fermi energy and these electrons have mainly d character. Subsequent spin polarized photoemission experiments⁸ on a sputter cleaned surface of CrO_2 showed 100% spin polarization but only at about 2eV below E_F . Very little density of states was observed at E_F in contrast to the ground state band structure calculation. In spite of the unexplained inconsistency between the calculation and the experiment, the spin-polarized photoemission results showed that CrO_2 can provide a 100% spin-polarized electron current.

The CrO_2 films for both the spin-polarized photoemission and the SP-STM experiments were prepared by the same chemical vapor deposition method. The main reaction is the decomposition of CrO_3 vapor to CrO_2 and oxygen on a heated substrate. The starting material, CrO_3 , is toxic, corrosive and a strong oxidant so the method was developed to minimize the quantity of chemical used and to confine the reaction to a small apparatus. The reaction chamber consists of a small fused quartz beaker about 8 cm high and 8 cm in diameter. The reactor is placed on a flat heater and the bottom of the reactor is covered with granular CrO_3 . The top of the reactor is fitted with a nonsealing fused quartz cover, to which the substrates are clamped. The top heater, in contact with the top cover, is brought to 390C before the CrO_3 is vaporized by heating the bottom heater to about 200C. The deposition of CrO_2 is very dependent on the substrate. Any substrate with the rutile (TiO_2) structure will serve to nucleate the growth of CrO_2 , however, amorphous substrates or surfaces tend to grow Cr_2O_3 under the same deposition conditions.

To fabricate the thin film tips for STM it was necessary to deposit on a silicon substrate. A nucleation layer of 200Å of polycrystalline TiO_2 was first deposited on the Si by rf sputtering. The substrates were then coated with 0.5 to 1.0 μm of CrO_2 using the CVD method outlined above. The (111) Si substrates were cleaved so as to produce intersecting (111) planes. The

cleavage crack propagates through the CrO_2 film so that the tip is formed at the intersection of two cleavage cracks. The Si is etched back 1-2 μm by carefully dipping the tip into a solution of HF and HNO_3 .

Garcia: The variation in distance for keeping the tunneling current constant for successive terraces, when using a polarized ferromagnetic CrO_2 tip, is a clear indication that the terraces alternate magnetization orientation. Furthermore the magnetization has a component perpendicular to the surface, otherwise the effect would not be observable in the tunneling current. This indicates that the Cr is antiferromagnetic with the spin alternation taking place in half a lattice constant in the (100) direction. These results seem to be in agreement with the calculations by Freeman's group² as well as with the model proposed by Blügel et. al.⁶

The fact that stable current can be established for low voltages (10meV) for a W tip, but stable current is only observed at 2eV for a CrO_2 tip indicates that the CrO_2 tip is semiconducting. This implies that the bulk band structure calculations for CrO_2 do not hold at the surface. Perhaps what happens is that the oxygen content at the surface is smaller and a real gap or quasi-gap appears at the Fermi level in the surface region. Then the tunnel current will come from the majority spin in the CrO_2 . This could be consistent with the photoemission experiments by Güntherodt et. al.,⁷ which showed nearly 100% spin-polarization for energies 2eV below the Fermi level.

The conclusion reached by Wiesendanger et. al.¹ in their analysis of the experimental data, that the polarization of the Cr(100) surface is 20 per cent, is unjustified because the theory that they use is much too approximate. They do not apply all the consequences of the theory of Slonczewski⁹ for s-wave ferromagnetic tunneling. In this theory the polarization enters as the joint polarization of the ferro- or antiferromagnet with the tunnel barrier, i. e. the polarization of the ferromagnet is masked by the tunnel barrier. This effect is not taken into account by the analysis of Ref. 1.

Also, in order to quantitatively evaluate the polarization of the sample and the tip, a more refined calculation of the spin polarization of the integrated tunnel current should be done, especially considering the difference in contributions from the d and s electrons. This can only be done by performing a band structure calculation with minimization of total energy and looking at the extension out of the surface of the tails of the d and s wavefunctions for the waves involved in tunneling. This case involves not only states at the Fermi level but states from the Fermi level to the 2eV applied voltage at which the experiments are performed. The conjunction of such calculations with spin-polarized scanning tunneling microscopy is a very powerful technique to study atomic magnetism.

In conclusion I would like to state that spin-polarized scanning tunneling microscopy is now possible with atomic resolution and a new door opens to understanding ferromagnetic problems and ferromagnetic coupling with atomic resolution.

REFERENCES

1. R. Wiesendanger, H.-J. Güntherodt, G. Güntherodt, R. J. Gambino and R. Ruf, *Phys. Rev. Lett.* **65**, 247 (1990).
2. C. L. Fu and A. J. Freeman, *Phys. Rev.* **B33**, 1755 (1986).
3. R. H. Victora and L. M. Falicov, *Phys. Rev.* **B31**, 7335 (1985).
4. L. E. Klebanoff, R. H. Victora, L. M. Falicov, and D. A. Shirley, *Phys. Rev.* **B32**, 1997 (1985).
5. F. Meier, D. Pescia, and T. Schriber, *Phys. Rev. Lett.* **48**, 645 (1985).
6. S. Blügel, D. Pescia, and P. H. Dederichs, *Phys. Rev.* **B39**, 1392 (1989).
7. K. Schwarz, *J. Phys. F* **16**, L211 (1986).

8. K. P. Kamper, W. Schmitt, G. Güntherodt, R. J. Gambino and R. Ruf,
Phys. Rev. Lett. **59**, 2788 (1990).
9. J. C. Slonczewski, Phys. Rev. **B39**, 6995 (1989).

MAGNETIC IMAGING VIA SCANNING ELECTRON MICROSCOPY

WITH POLARIZATION ANALYSIS[†]

R.J. Celotta, M. Scheinfein, J. Unguris and D.T. Pierce

Electron and Optical Physics Division
National Institute of Standards and Technology
Gaithersburg, Maryland 20899

INTRODUCTION

Scanning Electron Microscopy with Polarization Analysis (SEMPA) is a relatively new technique for obtaining images of magnetic microstructure. We will summarize the method and give a few examples of its application in this brief paper. A new review of the technique provides extensive additional information and references [1].

As in the magneto-optic Kerr technique, SEMPA images the magnetization of the sample directly, while Lorentz electron microscopy or magnetic force microscopy display magnetic structure through their sensitivity to magnetic fields. SEMPA was suggested as a technique [2,3] following the demonstration [3] that secondary electrons scattered from a ferromagnet by a high energy electron beam exhibited the spin polarization characteristic of the magnetization of the solid. It was envisioned that the highly focused electron beam of a scanning electron microscope could be rastered across a magnetic surface and a magnetization map would be obtained by measuring the polarization of the secondary electrons which are generated, as depicted in Fig 1. We use high efficiency polarization detectors based on the low energy diffuse scattering of electrons from a Au target [4] to measure all three components of magnetization. Other embodiments of SEMPA at KFA Jülich [5], Hitachi [6] and Stanford [7] use Mott or LEED polarization detectors.

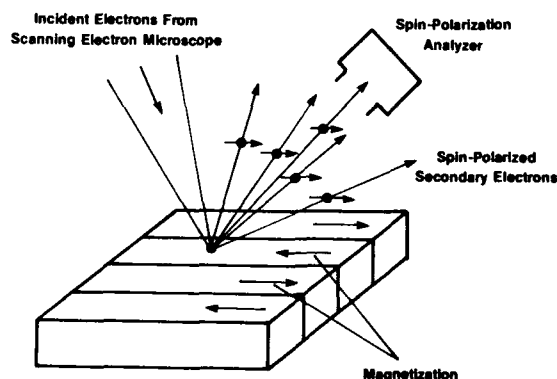


Fig. 1 A schematic representation of a SEMPA microscope.

SEMPA offers the ability to image the magnetic microstructure of solid samples with a resolution considerably better than optical techniques. A resolution of 40 nm has already been demonstrated for SEMPA [5] and 10 nm appears obtainable. This is to be contrasted with 1 μm resolution for the magneto-optical Kerr effect and about 10 nm for Lorentz microscopy when samples are thinned to less than 300 nm. Because SEMPA is based on measuring the polarization of secondary electrons which originate in the top few nm of the solid, it is intrinsically a surface analytic technique. As such, it requires that thick non-magnetic overlayers be removed and that measurements be made in an ultra-high vacuum environment. An advantage of the surface sensitivity is that very thin magnetic layers can be analyzed with no loss in signal. Because the magnetization images are obtained simultaneously with the topographic image, but are independent of the topographic measurement, the effect of surface physical structure on magnetic structure can be ascertained. Typically, a scanning Auger microscope is used so that an elemental map of the surface composition is also available. The time required for SEMPA imaging varies considerably depending on the magnetization and the resolution required. SEMPA images generally take a few minutes to acquire, although coarse (64x64) images can be obtained in one second for favorable cases. Both ferromagnetic and ferrimagnetic conductors can be imaged.

OBSERVATION OF THE (0001) SURFACE OF hcp COBALT

As an example of the three dimensional imaging capability of SEMPA, we show in Fig. 2 measurements [8] of the magnetic microstructure of a single crystal of Co that has been oriented so that its easy axis (c-axis) lies

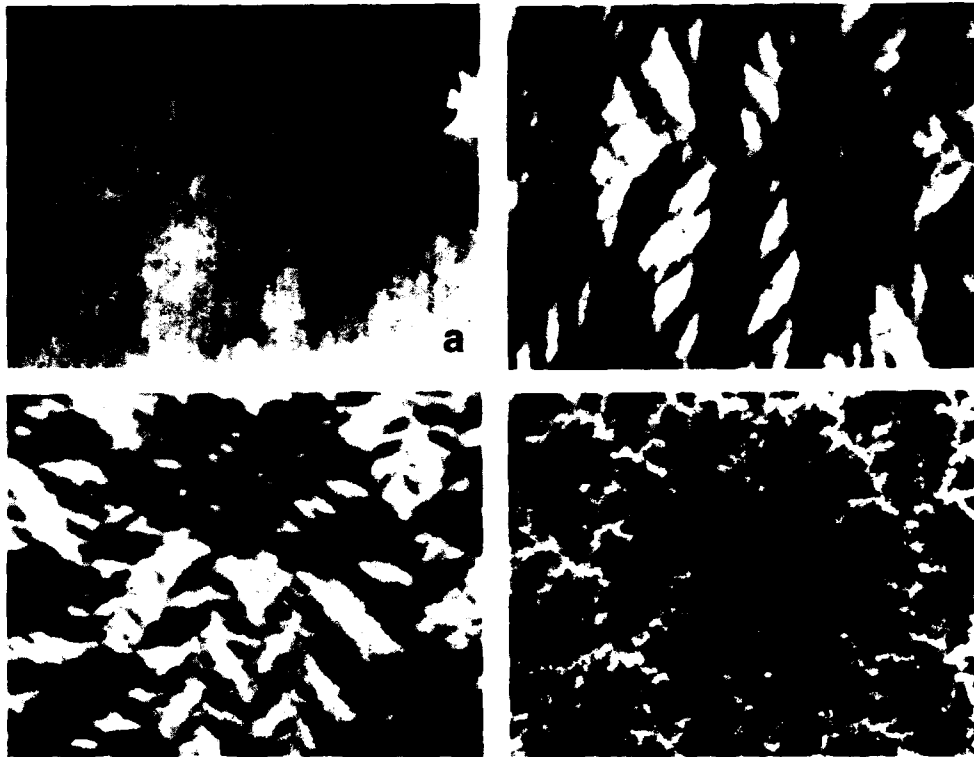


Fig. 2 Images of the topography (a) and the domain structure of the Co (0001) showing magnetization components (b) M_x along the horizontal and (c) M_y along the vertical in-plane directions, and (d) M_z in the out-of-plane direction. Each image is 18 μm wide.

perpendicular to the surface. Figure 2 (a) is the normal SEM topographic image obtained from the full secondary signal. Figures 2 (b), (c) and (d) show the M_x , M_y , and M_z components of the magnetization vector, respectively. The data are represented by a linear gray scale with white (black) indicating the maximum of the magnetization in the positive (negative) direction. Hence in the dendritic pattern of Fig. 2 (d), the white (black) areas represent magnetization out of (into) the crystal surface. The very different pattern shown by the in-plane magnetization components of Fig. 2 (b) and (c) can be analyzed by converting the value of these two components at each point to an in-plane angle and a magnitude. The angles appear quantized in roughly 60° increments which we speculate is related to a weak six-fold magnetocrystalline anisotropy. These patterns are very similar to those observed by the Kerr technique [9].

SURFACE DOMAIN WALLS IN Fe

The magnetostatic energy associated with magnetization perpendicular to the surface generally forces the magnetization at the surface to lie in the surface plane. Only for strong perpendicular anisotropies, as in Co above, do we see an out-of-plane component. For domain walls, this effect is seen in the rotation into the surface plane of the near-surface moments at the termination of a bulk Bloch wall. This results in a transition from a Bloch wall to a Néel wall within a length from the surface corresponding to approximately the width of a bulk Bloch wall. Figure 2 shows a SEMPA line scan across a 180° wall in Fe(100) between domains which are oriented in the $\pm y$ direction. The M_y component is directed along the domain direction. No perpendicular (M_z) component is observed. The M_x component shows the in-plane rotation of the magnetization for the surface Néel wall. The solid line is the result of our micromagnetics model calculation [10], broadened by the 70 nm beam probe width for this measurement. The calculation uses only the bulk values for the magnetization, the magnetocrystalline anisotropy and the exchange coupling constant. No magnetostriction or surface anisotropy terms were included. The excellent agreement obtained here, and in other systems with a wide range of magnetic parameters, gives us a high degree of confidence in our model calculations.

TbFeCo MAGNETO-OPTIC RECORDING MEDIA

The examples discussed so far have been ferromagnetic systems. The

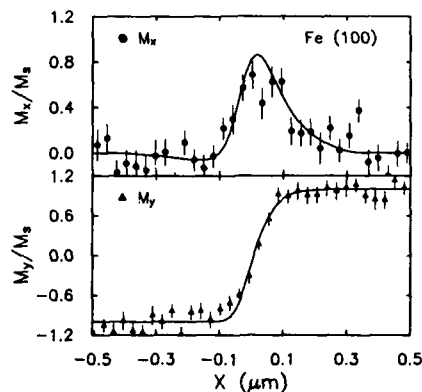


Fig. 3 Magnetization profile for 180° surface domain wall in Fe(100).

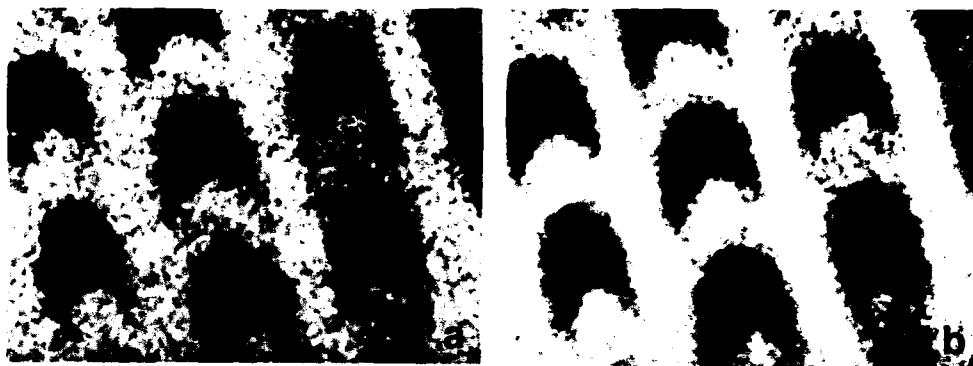


Fig. 4 The M_x (a) and M_y (b) magnetization components of laser written bits in a TbFeCo magneto-optic recording medium. Each image is $6.7 \mu\text{m}$ wide.

TbFeCo medium, as used for thermomagnetic writing in magneto-optical recording, is a ferrimagnetic system with its transition metal and rare earth sublattices antiferromagnetically aligned. A typical thermomagnetic material will have its compensation temperature, where the magnetization is zero, near room temperature. Figure 4 shows room temperature SEMPA images [11] of bits written in just such a material. The crescent shaped bits are created by reversing the applied magnetic field while the media is moved under a circular laser spot which provides local heating. We are able to see the domain structure even though there is no net magnetization because the secondary electrons analyzed in SEMPA come preferentially from the 3-d valence electrons in these alloys. The use of the Lorentz, MFM, and Bitter techniques near the compensation temperature is difficult because of the very small magnetic fields produced. SEMPA is being used here to study the size and shape of the written bits and the structure of their boundaries as a function of material and writing parameters.

REFERENCES

- † This work was supported in part by the Office of Naval Research.
1. M.R. Scheinfein, J. Unguris, M.H. Kelley, R.J. Celotta and D.T. Pierce, *Rev. Sci. Instrum.* **61**(10), October 1990.
2. R.J. Celotta and D.T. Pierce, in *Microbeam Analysis 1982*, ed. by K.F.J. Heinrich, (San Francisco Press, 1982) p. 469
3. J. Unguris, D.T. Pierce, A. Galejs and R.J. Celotta, *Phys. Rev. Lett.* **49**, 72 (1982).
4. M.R. Scheinfein, D.T. Pierce, J. Unguris, J.J. McClelland, R.J. Celotta and M.H. Kelley, *Rev. Sci. Instrum.* **60**, 1 (1989).
5. H.P. Oepen and J. Kirschner, *Phys. Rev. Lett.* **62**, 819 (1989).
6. K. Koike, H. Matsutama and K. Hayakawa, *Scanning Micro. Intern.*, Supp. **1**, 241 (1987).
7. T. VanZandt, R. Browning, C.R. Helms, H. Poppa, M. Landolt, *Rev. Sci. Instrum.* **60**, 3430 (1989).
8. J. Unguris, M.R. Scheinfein, R.J. Celotta and D.T. Pierce, *Appl. Phys. Lett.* **55**, 2553 (1989).
9. A. Hubert, R. Schäfer and W. Rave, *Chin. J. Phys. Suppl.* (to be published).
10. M. R. Scheinfein, J. Unguris, D.T. Pierce and R. J. Celotta, *J. Appl. Phys.* **67**, 5932 (1990).
11. M. Aeschlimann, M.R. Scheinfein, J. Unguris, F.J.A.M. Greidanus, S. Klahn (to be published).

ATOMIC SCALE PROBE INTO HIGH-T_c SUPERCONDUCTORS USING SCANNING TUNNELLING MICROSCOPY

J. Nogues and K.V. Rao

Dept. of Condensed Matter Physics
Royal Inst. of Technology, Stockholm, Sweden

INTRODUCTION

Scanning Tunneling Microscopy (STM) has proved to be one of the most versatile techniques to study various surface properties of metallic as well as semiconducting materials directly in real space with atomic resolution [1,2]. When using STM, an atomically sharp metallic tip is advanced near enough (a few Å) to the surface so that the sample wave function overlaps and the vacuum tunnelling resistance between surface and tip becomes finite and measurable.

The tunnelling current is critically dependent on the wave function overlap. The two main modes of operation of an STM are "topography" and "spectroscopy". In the first mode of operation as the tip is scanned across the sample with an applied voltage (typically 0.01-2 V), the tunnelling current between the sample and the tip is maintained constant via a feedback circuit to the z-piezo which adjusts appropriately the sample-tip distance. The correction feedback voltage thus faithfully images the surface topology with a vertical resolution of about 0.01-0.1 Å and a lateral resolution around 1-2 Å. In the 'spectroscopic' mode of operation the I-V characteristics due to tunneling between the tip and the sample at a fixed location are obtained [2,3].

Since the discovery of high temperature superconductors [4], extensive STM studies have been carried out on these oxide materials to obtain both structural and electronic information. The potential of STM was first exploited by Garcia et al.[5] to investigate microstructural details like homogeneity, and conductivity across the 'twin-boundary' planes inside each grain of a sintered bulk Y-Ba-Cu-O based superconductor with T_c close to 85K. Since then, extensive STM studies have been carried out by various research groups on a whole class of Y-, Bi-, and Tl-based high-T_c materials mainly to understand the importance of granularity in both bulk and thin film forms [6,7], growth mechanisms [8,9], metal-semimetal conduction characteristics, especially across the Y-based material [10-14], surface degradation [12] etc.

The mechanism for high critical temperature superconductivity is still unknown. In order to understand the possible mechanism of fundamental importance are the knowledge of the density of states near the Fermi-surface, and the superconducting

energy gap [15]. Several techniques have been used to study these properties, electron tunnelling spectroscopy being the most powerful among them. Conventional electron tunnelling with planar insulating barriers has not so far provided a consistent unambiguous information for the oxide superconductors [16]. On the other hand both point contact and vacuum tunnelling using STM - the so called Scanning Tunnelling Spectroscopy or the STS-method - which probes small, almost atomic scale, areas on the surface of the sample have produced significantly reproducible data leading to a local information of the energy gap [16,17]. By STS, Bi-based superconductors are found to be easier to tunnel through probably because their surface properties do not degrade so easily as in the case of the Y-based materials. The energy gap values, $2 \Delta/kT_c$, obtained on the Bi- and Tl-based materials using point contact tunnelling are more clearly determined [17,18] and has been usually found to be in the range 4-6 which is slightly higher than the expected BCS-value.

Fabrication of thin films of high- T_c superconductors with desirable functional properties has been reported up to now mostly for films deposited on expensive and exotic substrates such as SrTiO_3 or MgO single crystals of chosen orientations. Studies on suitably chosen buffer layers on inexpensive substrates such as mica or glass are rather scarce [19] but of considerable interest. However, it is clear that the functional properties and growth process of superconducting films on such substrates depends very much on the morphology of the buffer layers and the nature of the substrate.

In this paper we present the salient features of some of our STM studies of the topology and tunnelling spectroscopy along and normal to the Cu-O planes of monocrystals of $\text{Bi}_2\text{Sr}_2\text{CaCu}_2\text{O}_{8+x}$. In addition preliminary topological studies of the morphology of buffer layers of Au and Pt on mica as a function of film thickness are also presented.

EXPERIMENTAL DETAILS

Single crystals of nominal composition $\text{Bi}_2\text{Sr}_2\text{CaCu}_2\text{O}_{8+x}$ studied in the present work were prepared by the floating zone technique [20], kindly made available to us by Dr. Balbashov at the Moscow Power Institute. The monocrystals, approximately $10 \times 2 \times 0.3 \text{ mm}^3$, had its c-axis growth perpendicular to the thinner dimension.

The thin-film buffer layers of Au and Pt of thickness 1000-3000 Å were rf-sputter deposited on mica substrates (maintained at about 500 C, or room temperature) at a rate of 1 Å/sec and in an argon atmosphere of typically 2 mTorr pressure with a bias field of about 155 V for a target-substrate distance of about 3.5 cm.

For the topological and spectroscopic characterization three types of STM's were used: The first one has a single piezo-tube to drive the tip. This piezo-tube rests on a stack of four 2mm thick stainless steel plates separated from each other by rubber vitons which dampen the external mechanical vibrations by four orders of magnitude. Initially, the tip-sample approach is made by means of a differential micrometer until the electronics takes over at the appropriate stage. The second one consists of two concentric piezotubes, one for scanning and the other for thermal compensation as well as internal sample translation. This set-up makes the microscope rather insensitive to thermal drifts and thus enables us to carry out dynamic temperature dependent property-studies. In this instrument the tip-approach is done by inertial motion which avoids many of the problems of the mechanical approach systems between 4K to 300K.

Together with the small size of this microscope (the overall dimensions being that of a 5cm long cylinder of 1.5 cm diameter) the above described arrangement makes the STM stable with hardly any need for damping [21]. The third STM used for low temperature tunnelling studies, in collaboration with Prof. Vieira at Autonoma University at Madrid, consists of a single piezo-tube rigidly thermally anchored in the inner chamber of a ^4He cryostat, where-in He gas is introduced to achieve thermal equilibrium. This STM can operate in the temperature range 1.4K to 300K. The tip-sample approach is made by means of a micrometric screw, driven from outside the cryostat, and which can be mechanically decoupled after the tunnelling current is established [12]. In our experiments the first two microscopes were used for topographic studies, at ambient conditions, of the single crystals and thin film buffer layers. In the first two STM's we used W tips either mechanically ground or electrochemically etched in NaOH. In our tunneling studies with the third STM Pt-Rh tips were used.

RESULTS AND DISCUSSIONS

Figure 1 shows the X-ray diffraction pattern obtained for the monocrystal $\text{Bi}_2\text{Sr}_2\text{CaCu}_2\text{Cu}_{8+x}$ produced by the floating zone technique. From the X-ray data we determine the unit cell parameters of this well oriented to be $a = 5.45 \text{ \AA}$, $b = 5.46 \text{ \AA}$ and $c = 30.81 \text{ \AA}$. From microstructural SEM and STM studies we find the monocrystal to consist of a stack of plates packed along the growth axis. Low field ac-, and dc susceptibility measured perpendicular to the c-axis show almost complete flux shielding at helium temperatures even at fields of the order of a few hundred Oersteds, with $T_c = 80\text{K}$ at the onset of diamagnetism. The microstructural investigations using STM

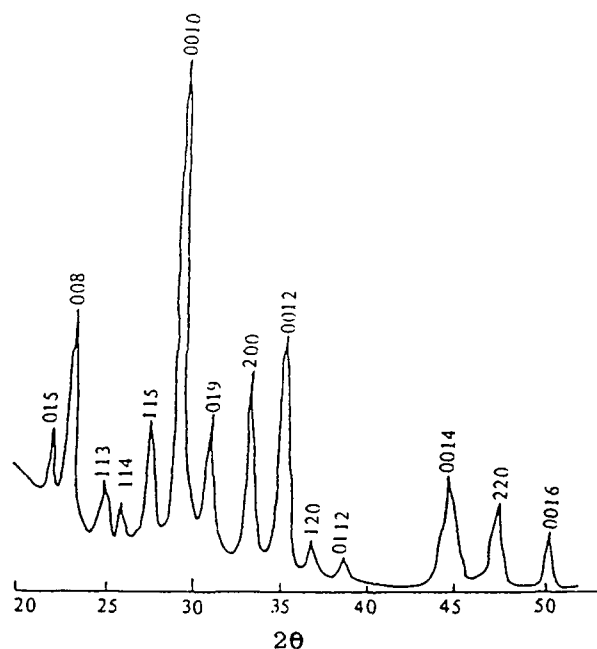


Fig 1. X-ray diffraction pattern for the Bi-based monocrystal produced by floating zone technique.

carried out in air at room temperatures was possible on freshly cleaved samples using tunneling voltages in the range 0.1-1 V and tunnelling currents between 1-2 nA. Even smaller tunnelling voltages could be used but we found that it was much easier to tunnel in the above mentioned voltage range. The existence of cleavable plane implies that scanning will be more likely to occur through a specific face of the crystal. At many areas of the surface rough features are found in agreement with SEM observations (fig. 2a). Another common feature is a layered structure with micron size smooth surface regimes as seen in fig. 2a. In our STM studies, shown in fig 2b, we observe steps of several hundred Å clearly divided into smaller steps in multiples of the lattice constant. Such macrosteps are a usual feature of the growth of crystal surfaces. In the places where flat areas are found we often observe steps of one or two times the lattice constant as seen clearly in fig.3. Unfortunately, in our STM studies we have not been able to image the superstructure of the a-b plane which characterizes the $\text{Bi}_2\text{Sr}_2\text{CaCu}_2\text{O}_{8+x}$ monocrystals [22].



Fig 2a. SEM observation of the surface of a Bi-based monocrystal produced by floating zone technique.

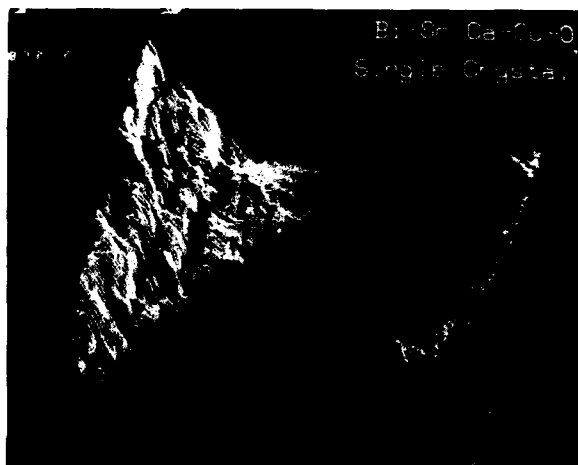


Fig 2b. STM topography of an area of the Bi-based monocrystal produced by floating zone technique showing steps of several hundred Å divided into smaller steps.



Fig 3. STM image in the flat areas of the Bi-monocrystal showing a steps of one or two times the lattice constant.

The I-V characteristics of the monocrystal of $\text{Bi}_2\text{Sr}_2\text{CaCu}_2\text{O}_{8+x}$ were carried out at helium temperatures both for orientations parallel as well as perpendicular to the Cu-O planes. In our measurements the Pt-Rh tip was touching the surface of the sample in order to obtain measurable currents at low voltages. From the measured I-V curves the conductance (dI/dV) was numerically calculated. The obtained data is not free from the usual problems concerning STS on high- T_c superconductors. In fig 4 manifestations of several of these problems can be observed, viz: a) broadening of the peaks of the conductance, b) slight asymmetry of the dI/dV curve, c) leakage currents at zero voltage, and d) peak structure at high voltages. The first three points indicated above are quite well accounted for by the lifetime broadening effects, and the asymmetrical insulating barriers model, which have been used [see ref.17 and the references therein] to fit our dI/dV data. The peak structure observed at higher voltages (the fourth point above) is probably due to S-I-S tunnelling, as discussed in detail in ref. 17, and not from charging effects. Taking into account the above possible effects on the tunneling characteristics, an energy gap of about 20 mV can be deduced from our data for both parallel and

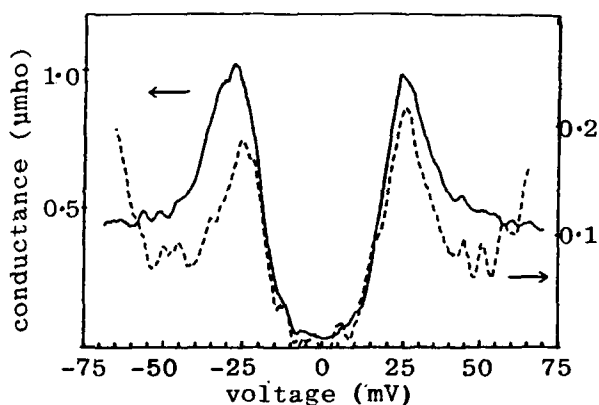


Fig 4. Conductance curves obtained at 4.2K for the Bi-based monocrystal with the STM-tip perpendicular (solid curve) and parallel (dashed curve) to the Cu-O planes.

perpendicular directions with respect to the *c*-axis. Thus the anisotropy in our sample is found to be quite small from the gap measurements as has also been observed before in some cases [16]. The energy gap we observe for the Bi-monocrystal is determined to be $2\Delta/k_B T_c = 6$ which is in good agreement with some previous measurements [17,18 etc.]. Detailed discussions of the above studies are presented in ref. 17. It is important to point out that in our STM studies on a 120K Tl-based bulk superconductor we have obtained remarkable, almost ideal, I-V characteristics with none of the above described effects [17]. The value obtained for the energy gap in this case was 3.5, a value perhaps fortuitously in agreement with the expectations from the BCS formalism.

Next we present our preliminary studies of the topology of buffer layers of Au and Pt on mica substrates. Clearly the morphology of these buffer layers will have an important indelible effect on the superconducting films grown on them. We thus would require an epitaxial growth of the buffer layers with as little, if not negligible, effect on the over layers. The present study is thus intended to optimize the thickness of the buffer layer and determine the conditions for possible epitaxial or film growth with a well defined directional property. The topography of thin films of 3000Å Au and 1000Å Pt were studied at room temperature in air. As shown, fig 5a, in the X-ray diffraction pattern of 1000Å Pt (sputtered at 0.01 mTorr with a rate of 1 Å/sec on a mica substrate held at room temperature) an epitaxial growth of the film along (1,1,1) direction is obtained. However, in the STM topography of these films we observe, fig 5b, quite a rough surface usually with several tenths of Å corrugations which are randomly distributed without any correlation among them. Further studies of Pt-films grown at different substrate temperatures is desirable. The 3000Å Au films deposited at room temperature showed a marked tendency to island formation. As seen in fig. 6 these islands are oval shaped and of different sizes usually about 100 Å wide and several hundreds of Å in length with their heights typically between 10 and 50 Å. Such island formation has already been reported for Au deposited on mica when the deposition temperature is not so high [19]. This may be so, because at room temperature the possibility of migration for the Au atoms is very small, and therefore

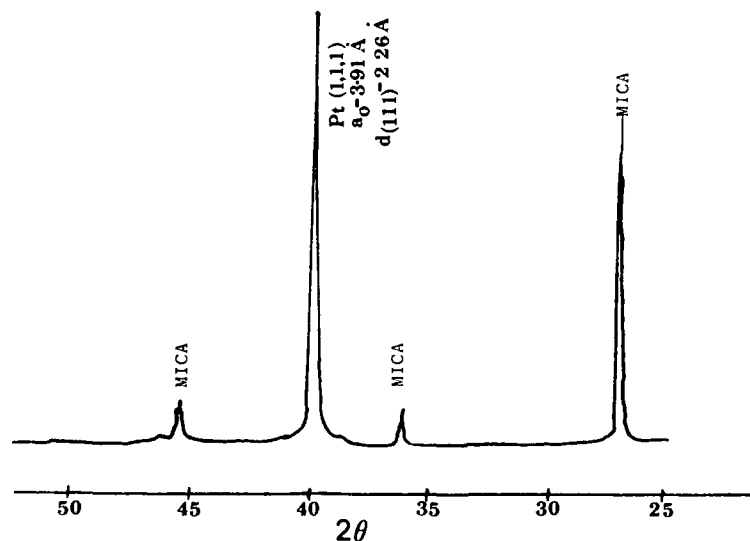


Fig 5a. X-ray diffraction of 1000 Å Pt showing oriented growth on mica substrate at room temperature.

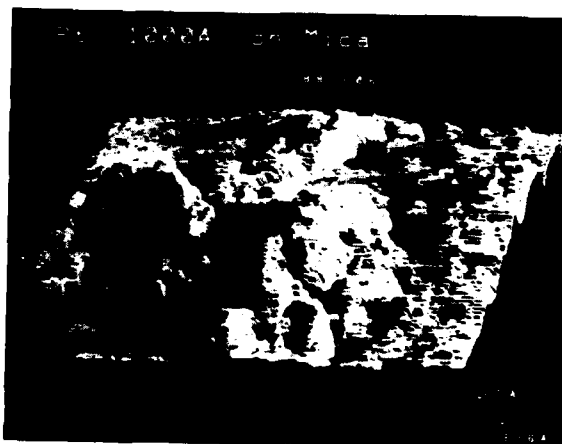


Fig 5b. STM topography of the 1000 Å Pt-film sputtered on mica at room temperature.

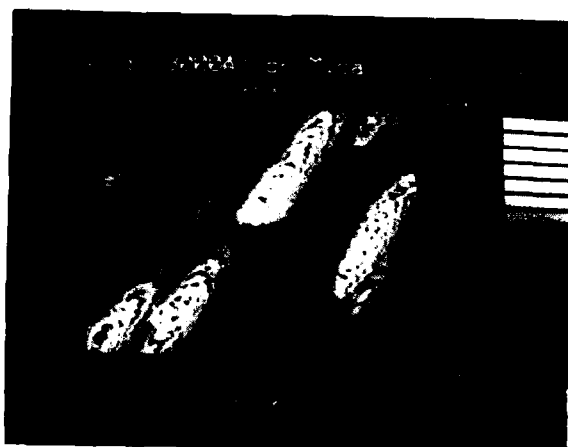


Fig 6. STM-depth profile topography of a Au-film deposited on mica with island growth.

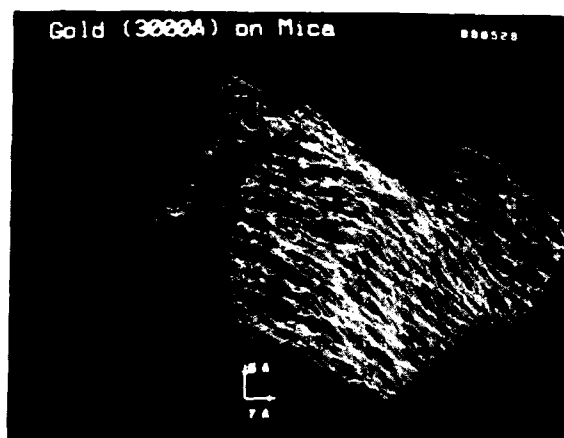


Fig 7. STM topography of a Au-film on mica showing atomic steps on top of one of the island-growth. ($V_t = 0.05\text{V}$; $I_t = 1\text{ nA}$)

they coalesce into islands. In fig. 7 the STM topography of the 3000 Å Au film shows some atomic steps on top of one of these islands. Clearly more systematic studies of these buffer layer films are needed before useful high-Tc films can be deposited on them. Such studies are now in progress.

In summary, we have presented three types of STM studies on high-Tc related work: 1) surface topology and growth pattern of Bi-based monocrystal grown by the floating zone technique, demonstrating the layered structure and growth mechanism at the surface in steps of unit cell dimensions or their multiples, 2) STS local electron-tunnelling at helium temperatures determining the superconductivity energy gap for the Bi-based monocrystal along both the c-axis and the a-b plane to be of the same order of 20 mV thus implying a small anisotropy, and 3) the topography of Pt and Au buffer layers on mica. While the Pt films showed an epitaxial growth even at a thickness of 1000 Å, it is found that Au films less than 3000 Å thick tends to form islands of about 300 x 100 x 40 Å with some monatomic steps on them. These island formations are probably due to the low deposition substrate temperature.

ACKNOWLEDGEMENTS

This research has been supported by the Swedish National Board for Technical Development, STU, and the Swedish Natural Science Research Council (NFR). One of us (JN) wishes to thank the Spanish Government for a F.P.I.-scholarship.

REFERENCES

1. G. Binnig and H. Rohrer, *Helv. Phys. Acta* **55**, 726 (1982)
2. G. Binnig and H. Rohrer, *IBM J. Res. Develop.* **30**, 355 (1986)
3. Ruud M. Tromp, *J. Phys.: Condens Matter* **1**, 10211 (1989)
4. J.G. Bednorz and K.A. Muller, *Z. Phys.* **B64**, 189 (1986); M.K. Wu, J.R. Ashburn, C.J. Thorng, P.H. Hor, R.L. Meng, L. Gao, Z.J. Huang, Y.Q. Wang, and C.W. Chu, *Phys. Rev. Lett.* **58**, 908, (1987)

5. N. Garcia, S. Vieira, A.M. Baro, L. Vazquez, J. Gomez, A. Aguilo, S. Bourgeal, A. Buendia, J. Tornero, M. Hortal, M.A. Lopez de la Torre, M.A. Ramos, R. Villar, K.V. Rao, D.-X. Chen, and J. Nogues, Proc. of 1st European Workshop on High-Tc Superconductors and Potential Applications. EEC-Brussels 1987, page 97; see also Z. Phys. B70, (1988) 9. See also: K. Naukkarinen, A. Arlauskas, L. Grönberg, R. Laiho, J. Vanhatalo, J. Mat. Sci 24, 1203 (1989)
6. R.C. Jaklevic, L. Elite, W. Shen, J.T. Chen, J. Vac Sci & Tech A6 448, (1988)
7. M.C. Gallagher, J.G. Adler, J. Vac Sci & Tech A8, 464 (1990)
8. H.J. Scheel, Ph. Niedermann, J. Crystal growth, 94, 281 (1989)
9. Ph. Niedermann, H.L. Scheel, W. Sadowski, J. Appl. Phys 65, 3274 (1989); see also: R. Laiho, M. Aarnio, L. Heikkilä, H. Snellman, I. Kirshner, and I. Hataz. J. Microscopy 152, 408 (1988)
10. C.J. Chen, C.C. Tsuei, Solid State Commun. 71, 33 (1989)
11. D. Anselmetti, H. Heinzelmann, R. Wiesendanger, H. Jenny, H.G. Guntherodt, M. Dueggelin, R. Guggenheim, Physica C153-155, 1000 (1988)
12. S. Vieira, M.A. Ramos, A. Buendia, A.M. Baro, Physica C153-155, 1004 (1988)
13. A.D. Kent, I. Maggio-Aprile, Ph. Niedermann, O. Fischer Phys. Rev B39, 12363 (1989)
14. M.C. Gallagher, J.G. Adler, Physica C162-164, 1129 (1989)
15. C.B. Duke, Tunneling in Solids (Academic Press, 1969)
16. For recent review see: J.R. Kirtley, Int J Mod. Phys B4, 201 (1990) and references therein
17. S. Vieira, J.G. Rodrigo, M.A. Ramos, N. Agrait, K.V. Rao, Y. Makino, and J.L. Costa, J. Appl. Phys, 67, 5026 (1990)
18. T. Hasegawa, H. Suzuki, S. Yaegashi, H. Takagi, K. Kishio, S. Uchida, K. Kitazawa, K. Fueki, Japanese J. Appl. Phys 28, L179 (1989)
19. C.E.D. Chidsey, D.N. Loiacono, T. Sleator, S. Nakahara Surface Science 200, 45 (1988)
20. A. M. Balbashov, E.A. Antonova, A.S. Nigmatulin, S.G. Karabashev, K.W. Kiseleva, O. W. Alexandrov, Superconductivity: Physics, Chemistry, Engineering, Vol.2, 57 (1989) (in Russian)
21. J. Lyding, S. Skala, J.S. Hubacek, R. Brockenbrough, G. Gammie, Rev. Sci. Instr. 59, 1897 (1988)
22. M.D. Kirk, J. Nogmi, A.A. Baski, D.B. Mitzi, A. Kapitulnik, T.H. Geballe, C.F. Quate, Science 242, 407 (1988) ; see also: Appl. Phys. Letters 52, 2071 (1988)

MAGNETIC ANISOTROPY

H.J.F. Jansen

Department of Physics
Oregon State University
Corvallis OR 97331, USA

ABSTRACT

Magnetic anisotropy reflects deviations from spherical symmetry on a macroscopic or a microscopic level. The macroscopic effects are easily calculated from Maxwell's equations and the susceptibility of the material. Microscopic effects are much harder to obtain, since they involve the details of the electronic structure. A relativistic description of the electrons is necessary to explain microscopic magnetic anisotropy. Single particle effects are due to the spin to own orbit coupling in the relativistic form of the kinetic energy. Intra-atomic many body effects find their origin in the Pauli principle, which causes a coupling of the orbital magnetic moments according to Hund's second rule. Relativistic corrections to the electron-electron interaction lead to a coupling of the magnetic moments of the electrons, and an effective inter-atomic coupling of the atomic moments. All these ingredients are necessary for a discussion of microscopic anisotropy. In this paper we will give an overview of these concepts within the framework of density functional theory.

INTRODUCTION

Solids interact with magnetic fields in many different ways¹. Materials can be diamagnetic, paramagnetic, ferromagnetic, etc. Magnetism plays an important role in many applications. Without permanent magnets it would be impossible to produce electricity, use engines, and so on. In all the applications it is not only important that there is some kind of magnetic response of the material, but also that this response depends on the orientation of the material with respect to the external fields. For example, this magnetic anisotropy stabilizes bar magnets because it makes it highly unlikely that the north and south pole will interchange. Without magnetic anisotropy we would not have useful magnets!

The shape of a sample is the most important cause of magnetic anisotropy. This is easy to understand if one assumes

that the magnetic energy of a solid is given by the sum of dipole-dipole interactions between all the local atomic moments. This interaction decays with the inverse third power of the distance between the magnetic dipoles. The number of dipoles increases with the square of the distance, and hence the total contribution of all magnetic dipoles in a shell of a certain radius decreases like the inverse of this radius. The corresponding summation over all shells is therefore conditionally convergent, making it plausible that the answer will depend on the way we perform this summation. As a result, the shape of the sample is important. Shape anisotropy is a macroscopic phenomenon.

There are several microscopic aspects of magnetic anisotropy. In a free atom, the values of the spin moment, the orbital moment, and the total moment are determined by Hund's rules if the Russell-Saunders coupling scheme is applicable. This certainly is true for the transition metals. The orbital moment of a transition metal atom in a solid is almost always quenched, but still has a small non-zero value. The orbital moment is locked in with the crystalline structure. The spin moment on the other hand is locked in by the external magnetic field. Spin-orbit coupling connects these two moments and hence leads to a coupling of the direction of the external magnetic field and the crystal symmetry.

Intra-atomic correlation between the orbital angular momenta is described by Hund's second rule. Inter-atomic correlation is a coupling of the motion of an electron on one atom and another electron on a neighboring atom. The latter effects will be of short range, but might lead to a correlation of the magnetic moments on neighboring atoms and hence also yield a coupling between magnetic effects and crystalline directions. Even in a mean-field approach there is a coupling between the magnetic moments of electrons on different atoms due to the Breit interaction between the electrons. At large distances this interaction is mainly of a dipole-dipole nature, but for near neighbors higher order terms might play a role. The dipole-dipole interaction is of a microscopic origin, but in the macroscopic limit gives rise to shape anisotropy. At present, there is no description of inter-atomic correlations and of near field corrections to the dipole-dipole interaction, and we can only hope that their effects are small.

BASIC QUANTITIES

In order to avoid confusion, we briefly review the terms used in the theory of magnetism². The magnetic flux density $\mathbf{B}(\mathbf{r})$ (or magnetic induction) is the basic quantity in the theory of magnetism. The units of the magnetic induction are the Gauss (Gaussian system) or the Tesla (Rationalized MKSA system). It can be measured by determining the torque on a magnetic dipole or by investigating the trajectories of charged particles, which are deflected by this flux density. According to Maxwell's equations, a flux density is caused by currents and is related to the total current density $\mathbf{J}(\mathbf{r})$ by

$$\nabla \times \mathbf{B} = \frac{4\pi}{c} \mathbf{J}$$

The main problem in applying Maxwell's equations to solids is related to the different length scales in a solid. On one hand there are the currents due to the electrons revolving around the nuclei, and on the other hand there are macroscopic currents on a large scale. The microscopic currents are localized, and their resulting flux densities can be approximated for most of the material, at locations further away than a few atomic distances by

$$\mathbf{B} \approx \frac{3\hat{\mathbf{r}} (\mathbf{r} \cdot \mathbf{m}) - \mathbf{m}}{r^3}$$

The only thing we need to know of the atom is its magnetic moment \mathbf{m} . Spin can be easily included in this stage. The average macroscopic magnetization or magnetic moment density $\mathbf{M}(\mathbf{r})$ is defined by

$$\mathbf{M}(\mathbf{r}) = \sum_i N_i(\mathbf{r}) \mathbf{m}_i$$

where $N_i(\mathbf{r})$ is the average number of atoms of type i per unit volume. Changes in $N_i(\mathbf{r})$ are on a length scale much larger than the distance between the atoms and hence $N_i(\mathbf{r})$ is considered to be a macroscopic quantity. The magnetic field $\mathbf{H}(\mathbf{r})$ (measured in Oersteds or Ampere-turns per meter) is related to \mathbf{B} and \mathbf{M} by

$$\mathbf{H} = \mathbf{B} - 4\pi \mathbf{M}$$

and only depends on macroscopic currents through

$$\nabla \times \mathbf{H} = \frac{4\pi}{c} \mathbf{J}_m$$

where $\mathbf{J}_m(\mathbf{r})$ now denotes the macroscopic current density. The properties of the material determine the relation between \mathbf{B} and \mathbf{H}

$$\mathbf{B} = \mathbf{F}(\mathbf{H})$$

and all microscopic information is contained in the function $\mathbf{F}(\mathbf{H})$. This is a convenient way of separating macroscopic quantities and microscopic, material dependent quantities.

SHAPE ANISOTROPY

The shape of a sample is the most important factor giving rise to anisotropy. We will assume that the sample has a surface of width zero, and that $\mathbf{F}(\mathbf{H})$ is different in the sample and outside. If outside is vacuum, we simply take $\mathbf{F}(\mathbf{H}) = \mathbf{H}$, or $\mathbf{M} = 0$. If there are no macroscopic currents, it is possible to define a

magnetic scalar potential Φ which is related to \mathbf{H} by

$$\mathbf{H} = - \nabla \Phi$$

and which obeys the equation

$$\Delta \Phi = 4 \pi \nabla \cdot \mathbf{M}$$

It is easy to find the solution for the magnetic scalar potential as a function of the magnetization

$$\Phi = - \int_V \frac{\nabla \cdot \mathbf{M}(\mathbf{x}')}{|\mathbf{x} - \mathbf{x}'|} d^3x' + \oint_S \frac{\hat{n}' \cdot \mathbf{M}(\mathbf{x}')}{|\mathbf{x} - \mathbf{x}'|} d^2S'$$

The first term describes an integration over the total volume V of the sample, while the second term pertains to an integration over the surface S of the sample. If \mathbf{M} is constant throughout the material the magnetic scalar potential depends only on the surface term. The resulting magnetic field \mathbf{H}_s has a direction opposite to the direction of \mathbf{M} and is therefore called a demagnetizing field. Since it is mainly related to a surface integral, it depends strongly on the shape of the sample.

If we artificially build up the magnetization in the material from zero, we need a certain amount of energy to create this magnetization and its demagnetizing field. This self energy of the demagnetizing field is in its turn strongly dependent on the direction of the magnetization with respect to the shape of the sample. As a consequence, rod like shaped materials have a direction of magnetization along the long axes, and plate like materials are magnetized in plane³. Again, the energies involved are large compared to other sources of shape anisotropy. For an infinite, perfect plane the anisotropy energy, e.g. the difference in energy between magnetization in plane and perpendicular to the plane, is $2\pi M^2$. If the plane is not perfectly flat, however, this number will be different. Therefore, subtracting the shape anisotropy for multilayer films has to be done with care.

CRYSTALLINE ANISOTROPY

It is easy for a theorist to construct a perfectly spherical sample of iron or nickel. The macroscopic shape of such a sample does not lead to any anisotropy in the response of this sample to a magnetic field. In experiments with such a sample one still would find magnetic anisotropy though. The local arrangement of the atoms in the sample is not spherical, but has a lower symmetry. As a consequence, it is found experimentally that the preferred direction of the magnetization in iron is along the $\langle 100 \rangle$ axis, while in nickel it is along a $\langle 111 \rangle$ axis. If one assumes such a microscopic anisotropy to exist, it is easy to explain experimental results measuring the magnetization of iron or nickel along different axis. Obviously, one needs single crystals for these experiments and for a non-ideal sample one somehow has to subtract the large effects of the shape of the sample.

Crystalline anisotropies have already been measured a long time ago⁴. The values depend very strongly on temperature and on

composition (for alloys). A microscopic theory of crystalline anisotropy has to be consistent with these observations, and this is not straightforward. The spin-orbit parameter in iron is about 4 mRy, which corresponds to 600K. One expects therefore a dramatic reduction in the anisotropy at these temperatures, as is seen experimentally. This simple consideration, however, cannot explain why higher order anisotropy coefficients sometimes change sign before they become very small.

ANISOTROPY ENERGY

The anisotropy energy can be measured in different ways³. Here we mention only two techniques, which (in principle) can be mimicked directly in density functional calculations. The first possibility is to determine the difference in area between magnetization curves along two directions. This difference is equal to the magnetization energy. In density functional calculations this means calculating the total energy of a solid as a function of the strength and the direction of the applied field. This is not a feasible approach, however, since the differences in energy are much smaller than the numerical errors in the calculations. The second possibility is to measure the field H_0 for which the magnetization along an arbitrary direction becomes equal to the saturation magnetization. This value can be related to the magnetization energy. This approach is not feasible either in a density functional approach, since the values of the field H_0 are very small and again are not reliable due to numerical errors accumulating in the calculations.

Both approaches assume that the value of the saturation magnetization is not field dependent for fields on the order of H_0 . This is a realistic assumption, since for iron and nickel H_0 is on the order of 0.04T, which corresponds to 0.2 microRy. This is a very small value compared to the spin-orbit parameter, which is typically a few mRy. The experimentally measured change in saturation magnetization is indeed small. This change can be neglected in a first order approach to evaluate the anisotropy energy. Actual density functional calculations therefore are performed by specifying the direction of the spin moment and obtain the change in total energy as a function of this direction.

RELATIVISTIC THEORY

Quantum field theory⁵ is the proper framework to discuss relativistic electrons interacting with electromagnetic fields⁶. It is common to use simple models to obtain anisotropy energies. In order to decide whether such a simple model is meaningful, it is not sufficient that this model reproduces experimental data. One also has to show that the model is a limiting case of a precise theory. Quantum field theory is the fundamental theory for electrons and phonons and its prediction of the value of the Lamb shift is one of the most precise known to date.

The state of a system is given by a state vector $|a,b\rangle$, where a denotes the quantum state of the electrons and b the quantum state of the photons. The energy is calculated from

$$\begin{aligned}
E[a, b] = & \langle a, b | \int d^3r H(\mathbf{r}) + \\
& -e \int d^3r \phi_{\text{ext}}(\mathbf{r}) : \psi^\dagger(\mathbf{r}) \psi(\mathbf{r}) : + \\
& -e \int d^3r \mathbf{A}_{\text{ext}}(\mathbf{r}) : \psi^\dagger(\mathbf{r}) \vec{\alpha} \psi(\mathbf{r}) : | a, b \rangle
\end{aligned}$$

with a Hamiltonian density given by

$$\begin{aligned}
H(\mathbf{r}) = & : \psi^\dagger(\mathbf{r}) \left(\frac{\hbar c}{i} \vec{\alpha} \nabla + (\beta - 1) m c^2 - \right. \\
& \left. e \phi(\mathbf{r}) + e \vec{\alpha} \mathbf{A}(\mathbf{r}) \right) \psi(\mathbf{r}) : + H_{\text{rad}}(\mathbf{r})
\end{aligned}$$

The field operators $\psi^\dagger(\mathbf{r})$ and $\psi(\mathbf{r})$ describe the creation and destruction of an electron at \mathbf{r} . The field operators $\phi(\mathbf{r})$ and $\mathbf{A}(\mathbf{r})$ pertain to the photons.

The external fields are on one hand due to the nuclei, but also can include fields external to the sample. It is a good approximation to treat all these external fields as classical, fixed quantities. This certainly is true for external fields, which are of macroscopic origin. But also the interaction with the nuclei can be treated this way since the mass of the nuclei is much larger than the mass of the electrons. This is only a a-posteriori justification: we know that quantum chemistry gives good results. One can expect difficulties for hydrogen and heavy fermion materials.

DENSITY FUNCTIONAL THEORY

There is nothing mysterious about density functional theory. The basic Hohenberg-Kohn theorem⁷ can be derived very easily in the following way. In order to find the ground state energy we have to minimize the energy $E[a, b]$ over all quantum states $|a, b\rangle$. An important consideration is that the external fields couple only to the charge density

$$\rho(\mathbf{r}) = -e \langle a, b | : \psi^\dagger(\mathbf{r}) \psi(\mathbf{r}) : | a, b \rangle$$

and the current density

$$\mathbf{j}(\mathbf{r}) = -e c \langle a, b | : \psi^\dagger(\mathbf{r}) \vec{\alpha} \psi(\mathbf{r}) : | a, b \rangle$$

We now perform the minimization in two steps. First we select arbitrary values for the charge density and current density and minimize the expectation value of the Hamiltonian using all states $|a, b\rangle$ which are compatible with these densities. This defines a functional $F[\rho, \mathbf{j}]$:

$$F[\rho, \mathbf{j}] = \min \langle a, b | \int d^3r H(\mathbf{r}) | a, b \rangle$$

where the minimum is taken over all states $|a,b\rangle$ consistent with ρ and \mathbf{j} . This functional does not depend on external quantities and, in principle, can be calculated for once and for all. Next, we take the external world into account and minimize over all possible values of the densities ρ and \mathbf{j} to get the true ground state of the system

$$E_0 = \min \left\{ F[\rho, \mathbf{j}] + \int d^3r \rho(\mathbf{r}) \varphi_{\text{ext}}(\mathbf{r}) - \frac{1}{c} \int d^3r \mathbf{j}(\mathbf{r}) \mathbf{A}_{\text{ext}}(\mathbf{r}) \right\}$$

Some care has to be taken in defining the space of allowed densities⁸, but apart from that there are no special problems. The main difficulty, of course, is that one cannot obtain an analytic expression for F , and therefore approximations are necessary.

At this point we want to eliminate the photon contributions. For each state a of the electrons we find the minimum configuration of the photons. This introduces an effective electron-electron interaction:

$$\begin{aligned} & \frac{1}{2} \frac{e}{|\mathbf{r} - \mathbf{r}'|} : \psi_{\kappa}^+(\mathbf{r}) \psi_{\lambda}^+(\mathbf{r}') \\ & \left\langle \delta_{\lambda\mu} \delta_{\kappa\nu} - \frac{1}{2} \tilde{\alpha}_{\lambda\mu} \tilde{\alpha}_{\kappa\nu} - \right. \\ & \left. \frac{1}{2} \frac{[\tilde{\alpha}_{\lambda\mu}(\mathbf{r} - \mathbf{r}')][\tilde{\alpha}_{\kappa\nu}(\mathbf{r} - \mathbf{r}')]}{(\mathbf{r} - \mathbf{r}')^2} \right\rangle \\ & \psi_{\mu}(\mathbf{r}') \psi_{\nu}(\mathbf{r}) : \end{aligned}$$

which was originally discussed by Breit^{9,10}. We have lost the photon fields, but we have to pay the price of carrying around a term in the Hamiltonian containing four electron field operators. One insoluble problem is replaced by another, but the latter one can be approximated more easily.

The current density $\mathbf{j}(\mathbf{r})$ is a quantity without an obvious physical interpretation. Using the Gordon decomposition⁶, this current can be approximated by

$$\begin{aligned} \mathbf{j}(\mathbf{r}) \approx & -c\mu_B \langle \nabla \times : \psi^+(\mathbf{r}) \tilde{\Sigma} \psi(\mathbf{r}) : \\ & + \frac{1}{i} : \psi^+(\mathbf{r}) [\nabla - \tilde{\nabla}] \psi(\mathbf{r}) : \rangle \end{aligned}$$

where the first term is related to the spin of the electrons and the second term to the real current of the electrons. The coupling of the external field to the first term can be expressed like

$$- 2 \int d^3r \mathbf{B}_{\text{ext}}(\mathbf{r}) \mathbf{S}(\mathbf{r})$$

If the external magnetic induction is constant, the coupling to the second part of the current becomes

$$- \mathbf{B}_{\text{ext}} \int d^3r \mathbf{L}(\mathbf{r})$$

and we see that the magnetic induction only interacts with the magnetization density

$$\mathbf{M}(\mathbf{r}) = \mathbf{L}(\mathbf{r}) + 2 \mathbf{S}(\mathbf{r})$$

Therefore, at this point we will only use the charge density ρ and the magnetization density \mathbf{M} . It is useful to separate the magnetization density in the spin and orbital components, because the spin part is easier to describe in density functional theory and because for transition metals the orbital part is often very small.

There are two terms which play a role in F : the kinetic energy of the interacting electrons and the Coulomb energy of these electrons. These two terms can be approximated by the kinetic energy of a system of non-interacting particles which has the specified densities, and the classical electrostatic energy of such a system. The non-interacting kinetic energy is given by

$$K_{\text{ni}}[\rho, \mathbf{M}] = \min_{|a, b\rangle} \langle a, b | \int d^3r : \psi^\dagger(\mathbf{r}) \left(\frac{\hbar^2 c}{i} \vec{\alpha} \cdot \nabla + (\beta - 1) m c^2 \right) \psi(\mathbf{r}) : | a, b \rangle$$

where the minimum is taken over all states $|a, b\rangle$ consistent with ρ and \mathbf{M} . The classical electrostatic energy is given by

$$\begin{aligned} U_{\text{H}}[\rho, \mathbf{M}] = & \frac{1}{2} \iint d^3r d^3r' \frac{\rho(\mathbf{r}) \rho(\mathbf{r}')}{|\mathbf{r} - \mathbf{r}'|} + \\ & \frac{1}{2} \iint d^3r d^3r' \frac{1}{|\mathbf{r} - \mathbf{r}'|^3} \langle \mathbf{M}(\mathbf{r}) \mathbf{M}(\mathbf{r}') - \\ & 3 \frac{[\mathbf{M}(\mathbf{r}) \cdot (\mathbf{r} - \mathbf{r}')][\mathbf{M}(\mathbf{r}') \cdot (\mathbf{r} - \mathbf{r}')]}{(\mathbf{r} - \mathbf{r}')^2} \rangle \\ & - \frac{4\pi}{3} \int d^3r \mathbf{M}^2(\mathbf{r}) \end{aligned}$$

These two terms define the most important parts of the functional F , and the remainder is called the exchange-correlation energy, E_{xc} . This name is incorrect, since the remainder also contains the difference in kinetic energy between the interacting and non-interacting system. All many-body effects are contained in the exchange-correlation energy. It is a formidable problem to obtain analytic expressions for this energy. Fortunately, several simple approximations for E_{xc} exist. It is surprising that these forms

give very good results for the ground state properties of most materials, as long as f electrons do not play an important role. Apparently, hybridization (which is accounted for in the non-interacting kinetic energy) is a more important factor in the determination of the cohesive energy of many solids than correlation (as expressed in E_{xc}). A similar conclusion is not necessarily true for the anisotropy energy!

The term in the functional F which is the most time consuming to evaluate is the kinetic energy of the non-interacting reference system. The traditional way to obtain this energy is to solve the Kohn-Sham equations^{11,6}

$$\left\langle \frac{\hbar}{i} \vec{\alpha} \cdot \nabla + (\beta - 1) m c^2 - e V_{\text{eff}}(\mathbf{r}) + \mu_B \mathbf{B}_{\text{eff}}^{\text{orb}}(\mathbf{r}) \cdot \frac{\mathbf{r} \times \nabla}{i} + \mu_B \mathbf{B}_{\text{eff}}^{\text{sp}}(\mathbf{r}) \cdot \vec{\Sigma} \right\rangle \phi_n(\mathbf{r}) = \epsilon_n \phi_n(\mathbf{r})$$

in a self-consistent way. The effective potentials and magnetic fields can be defined by

$$V_{\text{eff}}(\mathbf{r}) = \frac{\delta F}{\delta \rho} + \phi_{\text{ext}}(\mathbf{r})$$

$$\mathbf{B}_{\text{eff}}^{\text{sp}}(\mathbf{r}) = \frac{\delta F}{\delta \mathbf{S}} + \mathbf{B}_{\text{ext}}$$

$$\mathbf{B}_{\text{eff}}^{\text{orb}}(\mathbf{r}) = \frac{\delta F}{\delta \mathbf{L}} + \mathbf{B}_{\text{ext}}$$

assuming that the functional derivatives exist. It is also possible to arrive at these equations without using functional derivatives. After solving the Kohn-Sham equations one evaluates the charge and magnetization densities from

$$\rho(\mathbf{r}) = -e \sum_{n \text{ occ}} |\phi_n(\mathbf{r})|^2$$

$$\mathbf{S}(\mathbf{r}) = -\frac{1}{2} \mu_B \sum_{n \text{ occ}} \phi_n^+(\mathbf{r}) \vec{\Sigma} \phi_n(\mathbf{r})$$

$$\mathbf{L}(\mathbf{r}) = -\mu_B \sum_{n \text{ occ}} \phi_n^+(\mathbf{r}) \frac{(\mathbf{r} - \mathbf{r}_0) \times \nabla}{i} \phi_n(\mathbf{r})$$

A complication arises because the effective potentials depend on the densities. Therefore, one combines the search for a minimum in the total energy and the evaluation of the kinetic energy. A self-consistent solution of the Kohn-Sham equations, in which the charge and magnetization densities used to construct the effective potentials are identical to the densities obtained from these equations, also yields the densities for which the total energy is minimized. One starts by guessing an approximate form of the charge and magnetization densities. The resulting output densities are obtained and in a systematic way the input

densities are improved until they match the output densities within a prescribed precision.

It is tempting to use the eigenvalues and eigenvectors of the effective non-interacting Kohn-Sham equations to calculate other properties of the interacting electron system. This is an approximation, however, and the results will only be correct in first order. The discrepancies between the outcome of such calculations and the true many-body calculations is hard to predict. Nevertheless, using the eigenvalues as a guide to interpret data from photo-emission and de Haas-van Alphen measurements is very useful.

EFFECTS LEADING TO ANISOTROPY

Relativistic effects important for crystalline anisotropy come into play in all three terms of the functional F . In the non-relativistic case the Kohn-Sham equations are ordinary Schrodinger equations, but in the relativistic case they are replaced by Dirac equations. The Dirac equations can be expanded as a Taylor series in the fine structure constant α and the terms in second order include

$$\frac{1}{c^2} \vec{\sigma} \cdot (\nabla V_{\text{eff}}) \times \nabla$$

which for a spherical potential couples the spin to the orbit of the electrons. It is important to recognize that this constitutes a coupling between the spin of an independent particle and its own orbit, and that this is essentially a single-particle effect. All simple bandstructure models to calculate the anisotropy energy are based on this consideration. Changes in the total energy as a function of the direction of the applied field are related to changes in the energy eigenvalues of the Kohn-Sham equations. One then hopes to relate the anisotropy energy to changes in the Fermi surface (and, in general, near band crossings) as a direction of the applied field. In all cases where the orbital moment is sufficiently quenched, these single particle models will give good answers.

Relativistic effects also modify the effective electron-electron interaction. This was already shown a long time ago by Breit. The classical electrostatic Coulomb energy has the form as given before, which contains a dipole-dipole interaction between the different electrons. This integral depends very strongly on the shape of the sample. If we replace the magnetization in this expression by its average value, this term yields the shape anisotropy as calculated before⁶. One can subtract this term, and the difference can be reduced to the form we had before with $\mathbf{M}-\mathbf{M}_0$ in stead of \mathbf{M} . Cross terms integrate to zero and hence can be neglected. This dipole-dipole interaction between the electrons also leads to an effective interaction between atomic moments. The contributions of all individual electron pairs are added together and result in dipolar and quadrupolar (and higher order) effective inter-atomic interactions. This also leads to a large class of models to calculate the magnetic anisotropy. These models are especially useful when the orbital moments are not quenched, as in many rare earth compounds.

Relativistic effects in the exchange correlation potential are probably less important for magnetic anisotropy. As mentioned before, in a free atom Hund's rules are a direct consequence of Pauli's principle. Although in a solid the angular momentum is usually quenched, it is still non-zero, and some remnants of Hund's rules will be present. The traditional forms of the exchange-correlation energy do not include these effects. This is the main reason why density functional calculations are less successful when rare earth atoms are present or for free atoms. Crystal field models for the magnetic anisotropy include these orbital moments and are yet another way to give a simplified description of magnetic anisotropy. Additionally, inter-atomic correlations might be important for the effective inter-atomic interactions mentioned in the previous paragraph.

NON-INTERACTING KINETIC ENERGY

We will first discuss the effects of the spin to own orbit coupling in the kinetic energy of the electrons. At this time we ignore the Breit corrections to the electron-electron interaction and orbital terms in the exchange-correlation energy. Hence we use the traditional local density approach for the electronic structure. In analogy with experiment, we assume that we have an applied magnetic field larger than H_0 , which causes a complete alignment of the magnetization with the external field. Rotating this field will change the total energy of the sample, but not the external energy, and the changes in total energy are equal to the changes in anisotropy energy. Assuming that the magnetization is always parallel to the external field, we write the total energy in the local density approximation as

$$E[\rho, \mathbf{S}] = K_{ni}[\rho, \mathbf{S}] + U_H[\rho] + E_{xc}[\rho, |\mathbf{S}|] +$$

$$\int d^3r \rho(\mathbf{r}) \varphi_{\text{ext}}(\mathbf{r}) - \int d^3r \mathbf{B}_{\text{ext}} \cdot \mathbf{S}(\mathbf{r})$$

The only term which depends on the direction of the magnetization, $\hat{\mathbf{B}}$, is the non-interacting kinetic energy. This direction $\hat{\mathbf{B}}$ can be taken as a parameter for the calculations. The ground state charge and spin density corresponding to $\hat{\mathbf{B}}$ are ρ_B and \mathbf{S}_B , and the total energy is

$$E_{an}(\hat{\mathbf{B}}) = E[\rho_B, \mathbf{S}_B]$$

Differentiating this expression with respect to $\hat{\mathbf{B}}$ leads to

$$\frac{\partial E_{an}}{\partial \hat{\mathbf{B}}} = \frac{\delta E}{\delta \rho} \frac{\partial \rho}{\partial \hat{\mathbf{B}}} + \frac{\delta E}{\delta \mathbf{S}} \frac{\partial \mathbf{S}}{\partial \hat{\mathbf{B}}} + \frac{\partial K_{ni}}{\partial \hat{\mathbf{B}}}$$

Since the charge and spin density used in this expression minimize the total energy, the first two terms are zero, and only the change in the kinetic energy due to a change in $\hat{\mathbf{B}}$ is important. The effect of changes in the charge and spin density come only in to play in second order and hence can be neglected.

Therefore, the effective potentials entering in the Kohn-Sham equations can be calculated once for a reference direction $\hat{\mathbf{B}}_0$ and the equations of motion we have to solve are

$$\left\langle \frac{\hbar c}{i} \vec{\alpha} \cdot \nabla + (\beta - 1) m c^2 - e V_{\text{eff}}^0(\mathbf{r}) + \mu_B \hat{\mathbf{B}} \cdot \mathbf{B}_{\text{eff}}^{0,sp}(\mathbf{r}) \right\rangle \phi_n(\mathbf{r}) = \epsilon_n \phi_n(\mathbf{r})$$

The non-interacting kinetic energy is calculated from

$$K_{\text{ni}} = \sum_{n, \text{occ}} \int d^3r \phi_n^+(\mathbf{r}) \left\langle \frac{\hbar c}{i} \vec{\alpha} \cdot \nabla + (\beta - 1) m c^2 \right\rangle \phi_n(\mathbf{r}) = \sum_{n, \text{occ}} \epsilon_n - \int d^3r \rho(\mathbf{r}) V_{\text{eff}}^0(\mathbf{r}) - \int d^3r S(\mathbf{r}) B_{\text{eff}}^{0,sp}(\mathbf{r})$$

and since the last two terms are constant, we only have to evaluate the change in the sum of the energy eigenvalues and we can write

$$E_{\text{an}}(\hat{\mathbf{B}}) = \sum_{n, \text{occ}} \epsilon_n(\hat{\mathbf{B}})$$

PREVIOUS CALCULATIONS

The earliest review article on the subject of magnetic anisotropy in iron, nickel, and cobalt was written more than fifty years ago by van Vleck¹². He assumed that the atoms had a certain atomic magnetization, and that the inter-atomic interaction of these magnetizations could be expended in dipolar and quadrupolar terms. Using a dipolar interaction only, the sign of K_1 will be negative for fcc and bcc lattices, which is correct for nickel, but wrong for iron. Quadrupolar terms will change this conclusion. His model could explain the order of magnitude of the anisotropy energy, and van Vleck maintained that the coupling of angular momentum vectors of different atoms is a vital ingredient.

The first calculations based on a band model were performed by H. Brooks¹³, who used a tight-binding model of the three t_{2g} bands in iron and nickel. Spin-orbit interactions were included using the atomic value of the spin-orbit parameter. His results give the correct order of magnitude for nickel, but are unclear for iron. In the abstract of his paper, H. Brooks already remarks that the neglect of the Russell-Saunders coupling within the atom is a chief weakness of his work.

Subsequent calculations of the anisotropy energy in the transition metals almost always consider only the single particle effects. Some examples are given in references 14, 15, and 16, but this list is by no means complete. These calculations take

the band structure into account in a more sophisticated way, and recently calculations have become very reliable. Nevertheless, the differences in the results between different authors are large. For example, the energy difference between in-plane and out of plane magnetization for an iron monolayer is given as -40 (reference 17), 340 (reference 18), and around 4 (reference 19) 10^{-5} eV/atom! The results are clearly sensitive to details of the calculations. The results for bulk iron and nickel are too large^{20,21} for calculations which are probably not well converged, but a recent precise LMTO calculations²² gives for both nickel and iron -0.5 microRy/atom, while the experimental values of the anisotropy energy are 2.7 microRy/atom for nickel and -1.4 microRy/atom for iron. The theoretical values are too small and have the wrong sign for nickel.

PROBLEMS IN CALCULATING THE CHANGE IN KINETIC ENERGY

It is surprising that the results for the magnetic anisotropy for iron, nickel, and cobalt are so different when calculated by different groups. This is a reflection of the numerical problems involved in these calculations. The changes in energy are very small compared to the electronic excitation energies, and the magnetic anisotropy is the results of an almost cancellation of two large terms.

The changes in the energy eigenvalues due to a change in the direction $\hat{\mathbf{B}}$ cause a change in Fermi energy and Fermi surface. If the Fermi energy has an error of 1 microRy, it will make the calculated results for the magnetic anisotropy energy of iron and nickel meaningless. For materials with a small value of the anisotropy energy it is useful to calculate the free energy

$$F(\mu, \hat{\mathbf{B}}) = U(\mu, \hat{\mathbf{B}}) - \mu N(\mu, \hat{\mathbf{B}})$$

It is easy to show that

$$U(\mu, \hat{\mathbf{B}}) - U(\mu_0, \hat{\mathbf{B}}_0) = \\ F(\mu_0, \hat{\mathbf{B}}) - F(\mu_0, \hat{\mathbf{B}}_0) + \rho(\mu - \mu_0)^2$$

with an error which is of second order in the change in chemical potential. Calculations for iron and nickel have shown that this approximation is very good in those cases²³. The advantage of expressing the anisotropy energy as the difference of the free energies is that one is now able to write the anisotropy energy as a integral over the Brillouin zone according to

$$\sum_{\mathbf{nk}} \langle \epsilon(\mathbf{nk}) - \mu_0 \rangle \theta(\mu_0 - \epsilon(\mathbf{nk}))$$

We have analyzed the differences in the integrant as a function of the direction $\hat{\mathbf{B}}$. The maximum values of this difference are on the order of the spin-orbit parameter, but the values are rapidly oscillating. One important reduction of the numerical errors is to first add the results of all points in the Brillouin zone which were equivalent before the introduction of

the spin-orbit coupling in the equations of motion. This leads to a large cancelation. Because a rotation in reciprocal space is equivalent to a counter rotation of the magnetic induction, we can write the anisotropy energy in the form

$$\sum_{\mathbf{nk}}^{1/48} \sum_{\text{rotations}} \langle \epsilon(\mathbf{nk}, R \hat{\mathbf{B}}) - \mu_0 \rangle \theta(\mu_0 - \epsilon(\mathbf{nk}, R \hat{\mathbf{B}}))$$

One only has to take into account all proper rotations, inversion symmetry (if present) simply gives a factor two. The differences in this integrant as a function of $\hat{\mathbf{B}}$ have large values near band crossings, especially when degenerate bands are involved. But there are still oscillations on the scale of about one percent of the Brillouin zone, and the integrated value is small, unless the crossing happens to be within a few mRy from the Fermi energy. Because of the small scale of the oscillations in the integrant, a very dense mesh in reciprocal space is needed to perform the integrations, about a million points in the first Brillouin zone for a bulk material! Reference 22 presents these convergence properties very nicely.

ESTIMATES OF THE ORDER OF MAGNITUDE OF THE VARIOUS EFFECTS

Spectroscopic data²⁴ for atoms are a good starting point to discuss the order of magnitude of the various terms leading to magnetic anisotropy. The magnitude of the effective magnetic induction coupling to the spins in a free atom corresponds to an energy of about 1.7 eV²⁵, while the effective induction coupling to the orbital angular momentum is about 1 eV. Spin-orbit energies are much smaller, on the order of 0.05 eV. This shows that Hund's rules describe iron very well, and that the sequence of importance is spin moment, orbital moment, total moment. Expanding the functional F near its minimum for an atomic potential then takes the form

$$F[\rho, \mathbf{L}, \mathbf{S}] = A[\rho] + B[\rho, \mathbf{S}] + C[\rho, \mathbf{S}, \mathbf{L}] + D[\rho, \mathbf{S}, \mathbf{L}, \mathbf{SL}]$$

where A is the largest term determining the atomic configuration (e.g. 3d⁶, 4s² for iron). The next term determines the magnitude of the spin magnetic moment and is a few eV for iron. The third term sets the orbital moment and is about 0.5 to 1 eV. If the total energy is minimal for zero net spin, this term should minimize at a zero value of the orbital moments. The last term represents the effects of spin-orbit coupling.

Adding the nuclear potential due to the neighboring atoms will change the density at the minimum. Since the band-width of iron is about 2 eV, the second term will still cause the total energy to minimize at a non-zero value of the spin-density. The band-width is larger than the third term, however, and as a result the orbital moment is quenched. The question is if without spin-orbit coupling (the last term) the orbital angular momentum would be quenched completely or not.

The g factor in iron is 2.091²⁶, leading to $\langle L \rangle = 0.10$ in the solid. If we assume that the effective induction coupling to the orbital angular momentum is proportional to $\langle L \rangle$, we find that this effective field corresponds to an energy of about 0.05 eV.

This is large enough to give an important contribution, as our model calculations have shown²⁷.

MODEL CALCULATIONS TO OBTAIN THE EFFECTS OF AN ORBITAL EFFECTIVE INDUCTION

The effects of an effective magnetic induction coupling to the orbital angular momentum can be easily investigated in a simple model²⁷. We consider the iron d electrons to be in a crystal field with strength Dq . This crystal field accounts for the hybridization with the s and p electrons on neighboring atoms. Spin-orbit coupling is introduced in a straightforward manner in this model, and the strength of the spin-orbit coupling is a free parameter. In addition, we include a magnetic induction B , which couples to $2S$, twice the spin, and αL , where α is another parameter in our model. B represents the effective induction due to exchange and correlation effects. $\alpha=1$ corresponds to a complete coupling of this effective induction to the orbital angular momentum. This is clearly an unphysical situation, since the exchange only acts on the spins. We therefore expect α to be small. The 10 by 10 Hamiltonian of this model is diagonalized, and the eigenvalues are occupied with a probability given by a Fermi-Dirac distribution, in which the temperature is replaced by the band-width W of the d bands. The chemical potential is determined by equating the total number of electrons to N . The anisotropy energy is calculated from the sum of the eigenvalues weighted with this Fermi-Dirac like distribution. This model description of the magnetic anisotropy contains six parameters and is certainly very simple. The results obtained from these model calculations should be considered with great care.

Realistic values of the band-width, the effective induction, and the crystal field splitting can be obtained from bandstructure calculations. The number of d electrons, N , in iron is somewhere between 6.5 and 7.0 and cannot be defined more precisely because spherical symmetry is broken in a solid. If we set $\alpha=0$, we find that the anisotropy energy increases with the fourth power of the spin-orbit coupling parameter, as expected. But for realistic values of the other parameters the sign of K_1 is wrong, and the correct magnitude of the anisotropy energy is obtained for a value of the spin-orbit coupling parameter three times larger than the atomic value. For a normal value of the spin-orbit parameter the anisotropy energy is too small by two orders of magnitude.

The anisotropy energy also depends strongly on the value of Dq . If the crystal field splitting is chosen in such a way that a majority band of one symmetry type is degenerate with a minority band of the other symmetry the value of K_1 has the correct order of magnitude when the spin-orbit coupling constant has a normal value. For the sign of K_1 to be correct, Dq has to be negative, which is contradictory to the results of bandstructure calculations. In such calculations, there is a strong dependency of the parameters on the position in the Brillouin zone. Degeneracies as mentioned above do occur, but only in a small portion of the Brillouin zone, which reduces its effects considerably.

If we choose realistic values of all parameters, the anisotropy energy depends very strongly on the value of α . If we set $\alpha=0.04$, which is a reasonable value based on the arguments in the previous section, we obtain the correct sign and magnitude of K_1 . The g-factor is also correct in that case, but K_2 is still too small. Also the change in saturation magnetization is too small in this case. Our general conclusion is that with $\alpha=0$ the model calculations do not give good results for the anisotropy energy, but that for small values of α it is possible to obtain the experimental values. These model calculations hence do not exclude the possibility that an effective induction coupling to the orbital angular momentum is necessary.

Recently, results of ab initio calculations including an orbital term²⁸ have become available for iron, nickel, and cobalt²⁹. The results of these calculations for the orbital moments are still inconclusive. Compared with the results from reference 22 the value for the orbital moment of iron only has improved somewhat, for cobalt it is now correct, but for nickel has a larger error. Results for the magnetic anisotropy energy are not available, but here one expects a much greater improvement because the effects are highly non-linear.

AKNOWLEDGEMENT

The research on magnetic anisotropy at Oregon State University is supported by ONR under Grant No. N00014-89-J-1165.

REFERENCES

1. R.M. White, "Quantum Theory of Magnetism" (Springer-Verlag, Berlin, 1983).
2. J.D. Jackson, "Classical Electrodynamics" (Wiley, New York, 1975).
3. B.D. Cullity, "Introduction to Magnetic Materials" (Addison-Wesley, Reading, 1972).
4. R.M. Bozorth, "Ferromagnetism" (D. van Nostrand, Toronto, 1951).
5. F. Mandl and G. Shaw, "Quantum Field Theory" (Wiley, New York, 1984).
6. H.J.F. Jansen, Phys. Rev. B38, 8022 (1988).
7. P. Hohenberg and W. Kohn, Phys. Rev. 136, B864 (1965).
8. E.H. Lieb, in "Density Functional Methods in Physics", edited by R.M. Dreizler and J. da Providencia (Plenum, New York, 1985).
9. G. Breit, Phys. Rev. 34, 553 (1929); 39, 616 (1932).
10. H.A. Bethe and E.E. Salpeter, "Quantum Mechanics of One- and Two-Electron Systems" (Plenum, New York, 1977).
11. W. Kohn and L.J. Sham, Phys. Rev. 140, A1133 (1965).

12. J.H. van Vleck, Phys. Rev. 52, 1178 (1937).
13. H. Brooks, Phys. Rev. 58, 909 (1940).
14. G.C. Fletcher, Proc. Phys. Soc. 67A, 505 (1954).
15. N. Mori, J. Phys. Soc. Jpn. 27, 307 (1969); N. Mori, Y. Fukuda, T. Ukai, ibid. 37, 1263 (1974).
16. E.I. Kondorskii and E. Straube, Zh. Eksp. Teor. Fiz. 63, 356 (1972) [Sov. Phys. - JETP 36, 188 (1973)].
17. J.G. Gay and R. Richter, Phys. Rev. Lett. 56, 2728 (1986); J. Appl. Phys. 61, 3362 (1987).
18. W. Karas, J. Noffke, and L. Fritsche, J. de Physique C (1989).
19. C. Li, A.J. Freeman, H.J.F. Jansen, and C.L. Fu, unpublished.
20. H. Eckardt, L. Fritsche, J. Noffke, J. Phys. F 17, 943 (1987).
21. P. Strange, H. Ebert, J.B. Staunton, and B.L. Gyorffy, J. Phys. Cond. Matt. 1, 3947 (1989).
22. G.H.O. Daalderop, P.J. Kelly, M.F.H. Schuurmans and H.J.F. Jansen, J. de Physique Colloq. C8, suppl. 12, 93 (1989); G.H.O. Daalderop, P.J. Kelly, and M.F.H. Schuurmans, unpublished.
23. G.H.O. Daalderop, private communication.
24. C.E. Moore, "Atomic Energy Levels", volume II, p49 (NSRDS-NBS 35, Washington, 1971).
25. H.J.F. Jansen, unpublished.
26. E.P. Wohlfarth, in "Ferromagnetic Materials", volume I, edited by E.P. Wohlfarth (North-Holland, Amsterdam, 1980).
27. H.J.F. Jansen, J. Appl. Phys. 64, 5604 (1988).
28. O. Eriksson, thesis; O. Eriksson, M. Brooks, and B. Johansson, unpublished.
29. O. Eriksson, private communication.

RANDOM ANISOTROPY IN MAGNETIC MATERIALS

J. R. Cullen

Naval Surface Warfare Center
10901 New Hampshire Ave., White Oak
Silver Spring, MD 20903-5000 USA

ABSTRACT

A study is made of the effects of random anisotropy on the magnetic properties of ferromagnets. The first section deals with the destruction of long range order in bulk materials due to random uniaxial anisotropy. Succeeding sections deal with random anisotropy confined to surfaces of and interfaces between ferromagnetics. Finally, a model of random multiaxial anisotropy which gives rise to a discrete set of easy directions in space is discussed. The latter model is applied to crystalline alloys of rare earths and to crystalline pseudobinaries of rare earths and transition elements.

I. INTRODUCTION

Random anisotropy has been on the magnetism scene for about as long as anisotropy itself. Indeed, the earliest experimental work on magnetic material was almost exclusively performed on polycrystalline samples, which are a large subclass of random anisotropy materials, given the random orientation of the crystallites. One of the first theoretical studies of the effects of random anisotropy was that of Harte¹ who suggested this as the origin of the magnetic ripples seen on the surfaces of thin films.

Systematic investigation of the effects of random uniaxial anisotropy dates to the work of Harris et al² who suggested that random uniaxial crystalline electric fields coupled to rare earth spins via spin orbit coupling could account for the decreased Curie temperatures of rare earth-iron amorphous alloys. They modelled these amorphous alloys by means of the Hamiltonian,

$$H = - \sum_{i,j} J_{ij} S_i \cdot S_j - \sum_i D_i [(S \cdot \xi_i)^2 - \frac{S^2}{3}] \quad (1)$$

Here J is the exchange coupling, D_i is the strength of the uniaxial anisotropy, treated as a positive constant. ξ is a unit vector taken as a random function of the site variable. The distribution in directions of ξ was taken by Harris et al, and by succeeding workers to be uniform. This is a very important feature of the model. Any texturing, that is, any tendency for a set of easy directions to predominate, drastically changes the most significant prediction based on this model, namely, the destruction of long range magnetic order in three or fewer dimensions. But we are getting ahead of our story. Harris et al treated the statistical mechanics of amorphous alloys using this H and mean field theory. They found a reduction in Curie temperature and remnant magnetization from those of their pure (no random anisotropy) counter-parts. To obtain the reduction in T_c for a $Tb_{33}Fe_{67}$ compared to crystalline $TbFe_2$ (about forty percent), the authors had to choose D to be the same size or larger than J . This is hardly likely, unless J itself is drastically reduced from its crystalline value.

Subsequent work has shown that the effects of the randomness of the easy axes in H are much more profound than simply a reduction in T_c and in remnant magnetization. Not long after the model Hamiltonian, Eq. (1), was introduced, it was shown by Imry and Ma³ that random magnetic fields acting in a system of ferromagnetically coupled spins destroy long range order. Since random uniaxial anisotropy acts in this context like a random magnetic field, the Imry and Ma result applies to the model of equation (1). This was shown more explicitly by Alben and Chi⁴ and Alben et al⁵ using a scaling argument. Later still, Chudnovsky⁶ and Chudnovsky and Serota⁷ demonstrated the breakdown of long range magnetic order using a continuum form of equation (1), in which the vectors S_i and ξ_i were replaced by field variables $S(\vec{x})$ and $\xi(\vec{x})$, respectively. Since their method is most easily extended to calculate physical quantities like the susceptibility and the spin-spin correlation function, it is repeated here. Also, the method can be used to study the effects of random surface and random interface anisotropy, which are the subjects of the second part of these lectures.

There are, of course, other sources of anisotropy besides the single-ion type. Chief among them are anisotropic exchange and dipole-dipole coupling. The latter are especially interesting in amorphous and crystalline alloys because they contribute to the random anisotropy and significantly alter the shapes of correlated regions in amorphous random-anisotropy magnets. In crystalline random anisotropy magnets with uniaxial symmetry the dipole-dipole force can actually stabilize long range magnetic order, if the spins are forced to lie in the plane perpendicular to the unique axis.⁸

This stabilization of long range order in crystalline alloys is one example of the effect that the crystalline lattice generates on the magnetic properties of alloys. Other examples include completing anisotropy alloys like $Tb_x Dy_{1-x}$, $R_y R' Al_2$ where R and R' are rare earth atoms with opposite signs of their Stevens factors. In these systems the randomness is discreet, i.e., only a finite set of directions are possible easy directions of magnetization. In the context of Eq. (1), ξ_i is restricted to lie along a finite set of axes, albeit randomly. Long range order, i.e., a net remanent magnetization is maintained in these models, but there is short-range ordering of the transverse spin components, and consequent reduction in remanent magnetization. We will discuss a simple example of this discreet random anisotropy, $Tb_x Dy_{1-x}$, later in these lectures.

II. BREAKDOWN OF LONG RANGE MAGNETIC ORDER IN BULK MATERIALS

Most of the interesting physical properties of the Random Anisotropy Model, Eq. (1), are preserved in the continuum form of the model, in which the spins are taken as vector fields of constant magnitude, and ξ_i is replaced by a unit vector field $\xi(\vec{r})$, where (\vec{r}) is a continuous spatial variable. For simplicity, we assume planar spins. For the exchange term, in which the summations are confined to nearest neighbors,

$$J \sum_{\langle ij \rangle} S_i \cdot S_j = S^2 J \sum_{\langle ij \rangle} \cos \phi_{ij}, \quad (2)$$

where ϕ_{ij} is the angle between the directions of spins at center points i and j of a random arrangement of spheres, say, representing the positions of the magnetic atoms of an amorphous material. If the exchange J is much greater than the anisotropy energy D (which will be taken to hold throughout these lectures), then the variations in ϕ_{ij} will be small; we can expand it in a Taylor's series about its local value,

$$\phi_{ij} = \phi_i - \phi_j = \phi_i - (\phi_j + \vec{r}_{ij} \cdot \nabla \phi_i + \dots)$$

We now define a field $\phi(\vec{r})$ and take $\phi_i = \phi(\vec{r})$, expand the cosine in Eq. (2) keeping terms to second order in $\phi(\vec{r})$,

$$\sum_{ij} J_{ij} S_i \cdot S_j \rightarrow -\frac{1}{2} \sum_{ij} J_{ij} (\vec{r}_{ij} \cdot \nabla \phi)^2$$

At each point i , it is possible to find a set of axes such that the right-hand side of the above expression is reducible to a sum of squared terms;

$$\sum_{ij} J_{ij} S_i \cdot S_j \rightarrow -\frac{1}{2} [A_{xx} (\frac{\partial \phi}{\partial x})^2 + A_{yy} (\frac{\partial \phi}{\partial y})^2 + A_{zz} (\frac{\partial \phi}{\partial z})^2],$$

where the A_{xx} etc depend on the position i . Since the principal axes (x , y , z) will vary randomly from site to site, the A 's are random functions of position. We are going to ignore this type of randomness; it is not essential to the nature of the magnetic order, as long as the exchange integrals J_{ij} are predominantly ferromagnetic. Replacing the fluctuating A_{xx} etc. by some average A , we arrive at the final form for the exchange energy:

$$E_{ex} = + \frac{1}{2} A \int (\nabla \phi)^2 d^3 r, \quad (3)$$

where the sum over the sites i has been replaced by an integral over the coordinates \vec{r} . The form taken by the anisotropy energy is more transparent, because it is a single-site energy:

$$E_{anis} = \int D(\vec{r}) \cos^2 (\phi(\vec{r}) - \zeta(\vec{r})) d^3 \vec{r}$$

For the purpose of this section, namely, to demonstrate the absence of long range magnetic order in a bulk random-anisotropy system, we can ignore the spatial dependence of $D(\vec{r})$. Then, we finally arrive at the form of the energy function first used by Chudnovsky to discuss the magnetic correlations in the RAM:

$$E = E_{ex} + E_{anis} = + \frac{A}{2} \int (\nabla \phi)^2 d^3 \vec{r} - \int D \cos^2(\phi - \zeta) d^3 \vec{r} \quad (4)$$

For the realistic case in which spins are not confined to a plane, the functional for the energy is more complicated. The exchange energy density $\frac{A}{2} (\nabla \phi)^2$ is replaced by:

$$\frac{A}{2} (\nabla \Theta)^2 + \frac{A}{2} \sin^2 \Theta (\nabla \phi)^2,$$

the anisotropy energy density becomes

$$Y_2^* (S \cdot \zeta),$$

where Y_2^* is the second order spherical harmonic with cylindrical symmetry. Because no new physical insight is gained by complicating the problem using these expressions, we restrict ourselves in this section to Eq. (4), the planar model. When the number of degrees of freedom of the spin variables is important, as in the case of additional interactions from dipole forces, it is more convenient to use spin-wave variables anyway.

We proceed to the problem of examining the possibility of long-range order at zero temperature. First, from the necessary condition that the energy of the ground state be a minimum with respect to variations in ϕ ,

$$\frac{\delta E}{\delta \phi} = 0, \quad (5)$$

we obtain

$$-A \nabla^2 \phi - D \sin 2(\phi - \zeta) = 0 \quad (6)$$

It is convenient to write Eq. (6) in the form

$$\phi(\vec{r}) = - \frac{D}{A} \int d^3 r' G(r, r') \sin 2(\phi - \zeta). \quad (7)$$

$$\text{where } G(r, r') = \frac{4\pi}{(r-r')} \quad (8)$$

Note that Eq. (7) is not an explicit solution of (6), since the right hand side contains the unknown, ϕ . However, it is impossible to determine ϕ exactly for a given distribution of ζ in any case. Since we really want the correlations among the ϕ 's for an ensemble of $\zeta(r)$, it is only certain averages of ϕ that we need. The most important of these is the squared average deviation in ϕ ,

$$Q = \langle (\phi(\vec{r}_1) - \phi(\vec{r}_2))^2 \rangle \quad (9)$$

Using Eq. (7), an expression for Q can be found in terms of the correlation function.

$$\langle \sin 2(\phi(1)) - \zeta(1) \sin 2(\phi(2) - \zeta(2)) \rangle, \quad (10)$$

where $\langle \rangle$ denote an average over ζ . The angles ζ vary much more rapidly than does ϕ , because the exchange is so much stronger than the anisotropy, not permitting rapid variation in ϕ . Also, there is no correlation among the ζ , except of course auto-correlation, so the above expression reduces to

$$v \langle \sin^2 (\phi - \zeta) \rangle \delta(\vec{r}_1 - \vec{r}_2) \quad (11)$$

v is the average volume of an atom.

Now, averaging ζ around the unit circle,

$$\langle \sin^2 (\phi - \zeta) \rangle = \frac{1}{2},$$

independent of ϕ . Then, the right hand side of the expression for Q , i.e.,

$$Q = \frac{v}{2} \left(\frac{D}{A} \right)^2 \int d^3f (G(r_1 - f) - G(r_2 - f))^2 \quad (12)$$

is independent of ϕ , and can be evaluated. It is easiest to do this using Fourier transforms of the Green's functions. When the separation $(r_1 - r_2)$ is much greater than the cube root of the atomic volume, in three dimensions we find

$$Q = \frac{v}{2} \left(\frac{D}{A} \right)^2 |r_1 - r_2|. \quad (13)$$

This is the central result of this section. Equation (12) expresses the fact that the average deviation in spin direction continues to grow as the separation increases. The coefficient in front of $|r_1 - r_2|$ in (12) can be taken as the correlation length for the model. This connection can be made more precise. The spin-spin correlation function is defined as

$$\langle S(r_1) \cdot S(r_2) \rangle = S^2 \langle \cos(\phi(r_1) - \phi(r_2)) \rangle \quad (14)$$

The right-hand side of (14) can be written in exponential form

$$\langle \cos(\phi(1) - \phi(2)) \rangle = \exp \left(- \frac{1}{2} Q \right) \quad (15)$$

Thus, the correlation function is a decaying exponential in $|r_1 - r_2|$ and the correlation length is

$$R_c = \frac{4}{v} \left(\frac{A}{D} \right)^2 \quad (16)$$

If we use known values of A for iron (2×10^{-6} erg/cm), and estimate v as 10^{-21} cm³, R_c is of the order of 50-100 Å for rare earth-iron alloys ($D \approx 10^6$ erg/cm³).

Thus, for the RAM, in three dimensions, there is no long range order, and the order parameter (the spin direction) correlations decay exponentially. The result can be shown to be true also when the planar restraint is lifted from the spins. The modifications which take place when a magnetic field is present or when there is a net easy direction (as may happen in crystalline alloys) is reviewed in a paper by Chudnovsky, Serota and Sallow. In this paper, we are concerned with modifications to the model which describe surfaces and interfaces.

111. SURFACES AND INTERFACES

The central result of the last section, namely, that in the absence of any coherent anisotropy and in zero applied magnetic field, the random anisotropy model exhibits no long range order, depends crucially on two

features. The first of these is complete isotropy of the randomness, which we already mentioned. The second requirement of the continuum form of the model is that the random anisotropy be uniformly dense and translationally invariant. We wish to consider cases when the latter condition is not fulfilled. Let us begin with a model in which a ferromagnet, which fills the half space $Z > 0$ is subjected to randomly oriented easy axes, but only in a small region $0 < Z < Z_0$, (see Figure 1). The model was actually invoked to describe the magnetic behavior of iron (Fe) films grown epitaxially on GaAs substrates. The first one or two layers of the Fe were shown to have been contaminated with Ga and As; these were pictured as altering in a random manner the crystalline electric fields seen by the orbits of the Fe electrons. Through the spin orbit coupling, the electronic spins are coupled to the surface by a random uniaxial anisotropy energy. The spins, however, are confined to the xy plane by demagnetizing fields. The appropriate energy functional is then a generalization of equation 4,

$$E = \int \left(\frac{A}{2} (\nabla\phi)^2 - D(z) \cos^2 (\phi - \xi) \right) d^3r, \quad (16)$$

Where the integral is taken over the half-plane $Z > 0$. Again, taking the variation in E , δE , due to an arbitrary variation in ϕ , $\delta\phi$, to be zero, we obtain

$$A \nabla^2 \phi = 0, \quad Z > 0 \quad (17a)$$

and

$$\frac{\partial \phi}{\partial Z} = \frac{D_s}{A} \sin 2(\phi - \xi), \quad Z = 0 \quad (17b)$$

Here, we have introduced the surface anisotropy density D_s , by writing

$$D(z) = \delta(z) D_s \quad (18)$$

in equation (16). Note that D_s has units of energy per area. This surface anisotropy is estimated to be from 0.1 to 1.0 erg/cm² for Fe, depending on the substrate.

The solution of equations (17a) and (17b) may be written

$$\phi(\vec{r}) = \frac{D_s}{4\pi A} \int d^2r^1 G_s(\vec{r}, \vec{r}^1) \sin[2(\phi - \xi)], \quad (19)$$

where the integration is taken on the surface $Z^1 = 0$. The surface Green's function is

$$G_s(\vec{r}, \vec{r}^1) = \frac{1}{V} \sum_{\vec{k}} \sum_q e^{\frac{i\vec{k} \cdot \vec{\zeta} \cdot \vec{\zeta}^1}{k^2 + q^2}} \cos qz \cos qz^1 \quad (20)$$

$\vec{\zeta}$ and $\vec{\zeta}^1$ are two-dimensional vectors representing the x and y coordinates. \vec{k} is also two-dimensional. V is the volume of the half-space. The procedure to follow at this point is very similar to that of section II. We form the quantity Q , (see equation (8)).

$$Q = \langle (\phi(\vec{r}_1) - \phi(\vec{r}_2))^2 \rangle \quad (21)$$

where again the average is over the ensemble of angle variables ξ . Upon substituting for G_s in (19), the \vec{r}^1 integration and the q summations may be done, leading to

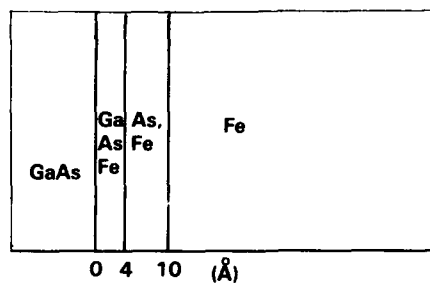


Figure 1

An example of a system giving rise to random anisotropy near a surface. A film of single-crystal Fe is grown epitaxially on GaAs. Although the lattice matching is excellent, there is an interfacial region of one or two layers in which Ga and As have reacted with Fe. Also, As has diffused into interstitial positions in and near the interface. These effects create randomly oriented crystal fields at Fe sites in and near the interfacial region. The region of random anisotropy is a layer 10 Å thick at the surface.

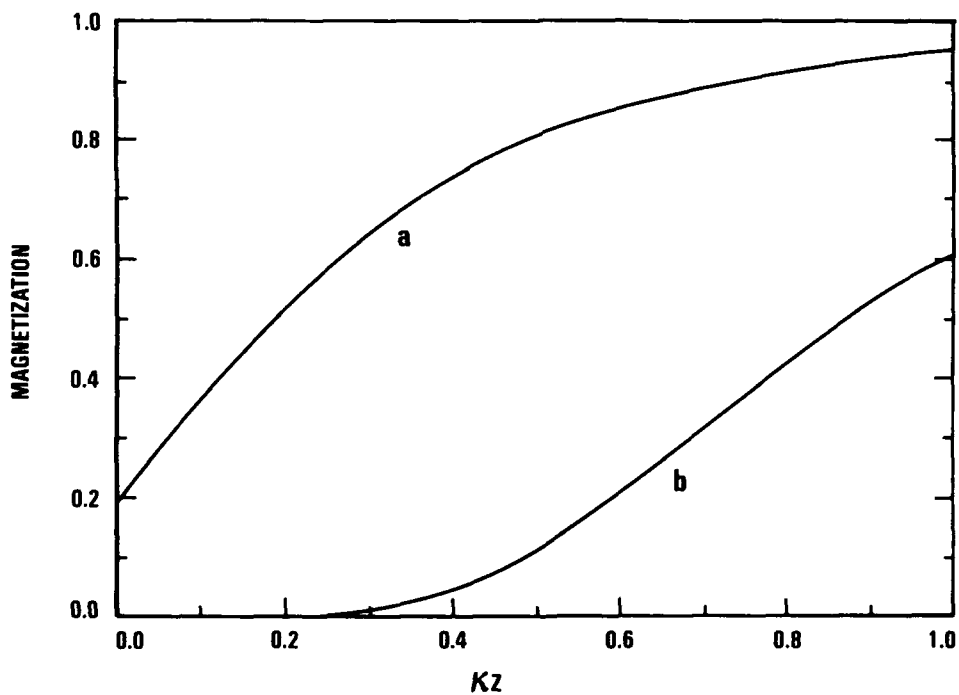


Figure 2

The magnetization versus distance from the surface as calculated from the random surface anisotropy model given in the text. Results for weak and strong surface anisotropy are shown, κ is the reciprocal of the ferromagnetic domain wall width.

$$Q = l^2 \left(\frac{D_s}{A} \right)^2 \int \frac{dk}{k} |(e^{ik\vec{r}_1} e^{-kz_1} - e^{ik\vec{r}_2} e^{-kz_2})|^2, \quad (22)$$

where $\vec{r} = (\vec{\rho}, z)$ and similarly for \vec{r}_2 .

Let us now imagine two points \vec{r}_1 and \vec{r}_2 in the half space, for which $|\vec{q}_1 - \vec{q}_2| > |z_1 - z_2|$, (see figure 2). We then place $z_1 = z_2$ in the integrand of equation (22), thus obtaining

$$Q(\vec{r}_1, \vec{r}_2) = 2 \left(\frac{D_s}{A} \right)^2 \int_0^\infty \frac{dk}{k} e^{-2kz_1} (1 - J_0(k|\vec{q}_1 - \vec{q}_2|)), \quad (23)$$

where J_0 is the Bessel function of zeroth order. l^2 is the surface area over which the easy axes are correlated. For large $|\vec{q}_1 - \vec{q}_2|$, the contribution to (23) from the J_0 term is negligible, except for $k < |\vec{q}_1 - \vec{q}_2|^{-1}$, where $J_0 \rightarrow 1$. Thus, Q is given to a good approximation by

$$Q(\vec{r}_1, \vec{r}_2) = 2 \left(\frac{D_s}{A} \right)^2 l^2 \int_{a/|\vec{q}_1 - \vec{q}_2|}^\infty e^{-2kz_1} \frac{dk}{k}, \quad (24)$$

which, for $|\vec{q}_1 - \vec{q}_2| > z_1$, is, to leading order

$$Q(\vec{r}_1, \vec{r}_2) = 2 \left(\frac{D_s}{A} \right)^2 l^2 \ln \frac{|\vec{q}_1 - \vec{q}_2|}{az_1} \quad (25)$$

and a is a constant of order unity. If we consider two points r_1 and r_2 such that $\vec{q}_1 = \vec{q}_2$ but $z_2 > z_1$, we find, after setting $\vec{q}_1 = \vec{q}_2$ in equation (22), that Q is again a logarithmic function of the separation $(z_2 - z_1)$,

$$Q(r_1, r_2) = 2 \left(\frac{D_s}{A} \right)^2 l^2 \ln \frac{|z_2 - z_1|}{bz_1}, \quad (26)$$

where b is another constant of order unity. Thus, random anisotropy imposed on the surface of a ferromagnet causes the spin-spin correlation function to exhibit a power-low dependence on the spin separation:

$$\langle S(r_1) \cdot S(r_2) \rangle = \exp \left[-\frac{1}{2} Q(r_1, r_2) \right] = \left(\frac{z_1}{|r_1 - r_2|} \right)^p, \quad (27)$$

$$\text{with } p = \left(\frac{D_s l}{A} \right)^2 \quad (28)$$

To understand the significance of this result, we must contrast it with that of the previous section, in which we found that the correlation function decayed exponentially with separation, and again with the correlations in a ferromagnet where there is long range order,

$$\langle S_1(r_1) \cdot S_2(r_2) \rangle_r \sim \langle S \rangle^2 \text{ as } |r_1 - r_2| \rightarrow \infty \quad (29)$$

The power-low dependence of the correlation function which we have just found, therefore, implies that our system has no long range order but an infinite correlation length. The situation is somewhat like that of the three-dimensional ferromagnet at its Curie point. The critical coordinate in the case at hand is not the temperature relative to the Curie temperature, but instead is the crystalline anisotropy of the underlying material, which, however small, is always present. In the case of crystalline Fe, for example, this energy density is of order 10^5 erg/cm³. The crystalline anisotropy restores the long range order destroyed by the

surface disorder. When this type of energy is added to equation (16), the resulting equation for ϕ which replaces (17a) is highly nonlinear. Deep in the interior of the sample however, ϕ can be considered as small, when measured with respect to one of the easy crystalline axes, and the equation may be linearized. The surface Green's function is modified so that the denominator in equation (20) is now of the form $k^2 + \kappa^2$, where κ is the reciprocal of the bulk domain wall thickness:

$$\kappa \sim (K/A)^{1/2}. \quad (30)$$

Now, for the spin-spin correlation at large spin separation, at a distance Z from the surface,

$$Q = P \frac{e^{-2\kappa Z}}{\kappa} \left(1 - \frac{2}{\kappa^2 |r_1 - r_2|^2} \right) \quad (31)$$

The magnetization, which can easily be obtained from the infinite-separation limit of the correlation function, i.e.,

$$\langle S \rangle^2 = \lim_{|r_1 - r_2| \rightarrow \infty} \langle \vec{S}(r_1) \cdot \vec{S}(r_2) \rangle = \exp - \frac{1}{2} Q(\infty). \quad (32)$$

is

$$gu_B \langle S \rangle = \exp - \frac{1}{4} Q(\infty) = \exp \left(- \frac{P}{4} \left(\frac{e^{-2\kappa Z}}{\kappa} \right) \right) \quad (33)$$

Plots of $\langle S \rangle (Z)$ for two different values of P are given in figure (2). As the equations indicate, and as can be seen from the figure, the magnetization is almost restored when Z is equal to κ^{-1} , however, there is still some lack of saturation until well beyond this point. The random anisotropy of the surface depletes the magnetization to a depth of approximately a domain wall width, which is approximately 100 Å in Fe. This model was used to explain the anomalous decrease in magnetization observed in Fe films grown on GaAs.¹⁰ Other physical quantities, such as the susceptibility and the anisotropy energy, should also behave anomalously as a result of the surface randomness, in a way which reflects the influence of the disorder on the scale of a domain wall width, even though the random anisotropy is confined to the first one or two layers at the surface.

CONCLUSION

Random uniaxial anisotropy at the surface of an isotopic ferromagnet causes the destruction of long-range ferromagnetic order but the spin-spin correlation length is infinite. The anisotropic ferromagnet retains long range order with a reduced magnetization. The reduction in magnetization and anisotropy energy is greatest at the surface and becomes small only at distances from the surface which are greater than the bulk domain wall width.

REFERENCES

1. K. J. Harte, Journ. Appl. Phys. 39, 1503 (1968).
2. R. Harris M. Plschke, and M. Zuckerman, Phys. Rev. Lett. 31, 160 (1973).
3. Y. Imry and S. Ma, Phys. Rev. Lett 35, 1399 (1975).
4. R. Alben, J. Becker, and M. Chi, Journ. Appl. Phys. 49, 1653 (1978).
5. R. Alben, J. Budnick, and S. Cargill, in "Metalic Glasses," American Society for Metals, Metals Park, OH, (1978).
6. E. Chudnovsky and R. Serota, Phys. Rev. 26, 2697 (1982).
7. E. Chudnovsky, R. Serota, Phys. Rev. 16, 4181 (1983).
8. J. Cullen, J. Appl. Phys. 6, 4413 (1987).
9. E. Chudnovsky, S. Serota, and W. Saslow, Phys. Rev. B33, 251, (1986).
10. J. Cullen, K. Hathaway, and J. M. D. Coey. J. Appl. Phys. 63, 3649 (1988).

PERPENDICULAR AND IN-PLANE ANISOTROPY IN AMORPHOUS Tb-Fe

Michael J. O'Shea

Cardwell Hall
Kansas State University
Manhattan, KS 66506-2601, USA

INTRODUCTION

During the last two decades amorphous Tb-Fe has been a much studied system both because it has been a testing ground for theories of random anisotropy and because of its magneto-optical storage applications.

A microscopic single ion anisotropy associated with the rare-earth is present in Tb-Fe alloys whose direction and magnitude vary from site to site.¹ This is a result of the random electric field gradients at the rare earth site generated by the positional disorder of its neighbors in an amorphous solid. In high fields the Tb moments do not line up with the applied field but rather form a "fan" about the field direction.²⁻⁴ The exchange between the Tb and Fe is antiferromagnetic and this interaction leads to a fanning of the Fe moments as well.^{4,5} The magnetic order is collinear only if the rare-earth is isotropic (no orbital angular momentum) as is the case for Gd-Co. In zero field, neutron scattering results⁶ indicate that no long-range ferromagnetic order is present for Tb-Fe alloys as expected from theory.^{7,8}

The discovery of a perpendicular anisotropy⁹ in rare-earth-transition metal (RE-TM) films has opened the door to a number of applications, the most important of which is magneto-optical recording (see Refs. 10, 11 and references therein). The perpendicular anisotropy allows for high storage densities and readout of magnetic bits is done by the rotation of polarization of low power laser light via the Kerr effect. The composition of the film is chosen so that its compensation point (where the Tb and Fe "sublattice" magnetizations are equal and opposite) is close to room temperature. The coercivity is large under these conditions. Writing is achieved by heating a small spot on the film with a higher power laser. This results in a shift away from the compensation point due to the different dependencies of the Tb and Fe "sublattice" magnetizations on temperature. The coercivity is now much smaller and the magnetic bit may be reversed by the application of a small field.

Tb_xFe_{1-x} amorphous alloys have been studied over the composition range $x=0.75$ down to as low as $x=0.02$.¹²⁻¹⁸ Tb/Fe multilayers have also been

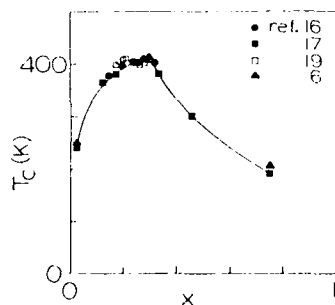


Figure 1. Transition temperature T_c versus x for Tb_xFe_{1-x}

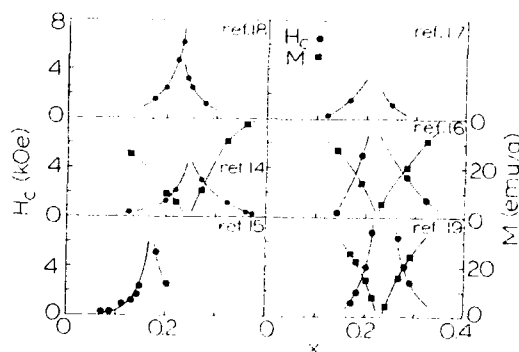


Figure 2. The coercivity and magnetization as a function of composition

studied.^{19,20} Figure 1 shows the transition temperature versus composition for homogeneous films prepared by different workers and thin multilayer films. As can be seen the data fall on or close to the same line indicating that variations in sample preparation technique and even a layering of the film (≤ 20 Å layer thickness) does not change the transition temperature significantly for a given Tb concentration. The transition temperature decreases for large x due to the weaker exchange associated with Tb and also the increasing effects of random magnetic anisotropy. There is a maximum in T_c at $x \sim 0.30$ and it again decreases for small x . Similar behavior is seen in a number of Fe-rich amorphous alloys²¹ (Fe-Zr, Fe-Sc, Fe-Hf) as the concentration of diluting element is decreased and is associated with the appearance of strong exchange fluctuations in Fe-rich alloys. Figure 2 shows the magnetization and coercivity versus composition at room temperature. As can be seen, these quantities and also the position of the compensation point show some variation among different workers indicating (in contrast to the transition temperature) that these quantities do depend on preparation method. Also the perpendicular anisotropy and in-plane anisotropy depend on sample preparation conditions and we discuss these below.

PERPENDICULAR ANISOTROPY

For a smooth homogeneous magnetic film the isotropic symmetry is broken by the surfaces of the film leading to demagnetization effects which result in an in-plane anisotropy. The demagnetizing field is $-4\pi M_s$ when the magnetization (assumed here to be saturated) is perpendicular to the film plane and close to zero when the magnetization is in the film plane. Perpendicular anisotropy can result from a number of causes as we discuss below and its presence and strength can be determined in a number of ways. Torque measurements are one of the most direct ways. Denoting the angle the magnetization makes with a perpendicular to the film as θ the simplest macroscopic energy incorporating a perpendicular anisotropy is

$$\epsilon = 2\pi M_s^2 \cos^2 \theta + K_u \sin^2 \theta. \quad (H = 0) \quad (1)$$

The first term represents the demagnetization energy and the second term is a uniaxial anisotropy. Differentiating equ. 1 yields the torque

$$\Gamma = (K_u - 2\pi M_s^2) \sin 2\theta. \quad (2)$$

which is zero in equilibrium. The solutions are $\theta = 0, \pi/2, \pi, 3\pi/2$. If $K_u > 2\pi M_s^2$ then the $\theta = 0, \pi$ solutions minimize the energy giving a magnetization perpendicular to the film. The anisotropy constant is defined as

$$K = K_u - 2\pi M_s^2 \quad (3)$$

and so is positive for a perpendicular anisotropy and negative for an in-plane anisotropy. If the intrinsic anisotropy, $K_u = 2\pi M_s^2$ ($K = 0$) then higher order terms in the anisotropy ($\sin^4 \theta$) become important. Some nice examples of this for CoCr are discussed in ref. 22. A magnetic field H is applied at some angle θ_H measured from a perpendicular to the film to measure the torque. This leads to a torque

$$\Gamma = MH \sin(\theta_H - \theta) \quad (4)$$

This torque may be measured and yields the magnitude and symmetry of the macroscopic anisotropy K_u . The chosen field is usually large enough that $\theta_H \approx \theta$ giving $\Gamma = K \sin 2\theta \approx K \sin 2\theta_H$. If $MH > K$, this will occur. The amplitude of the torque curve gives K_u and its sign may be found from the initial slope of the torque curve. For the example shown in Fig. 3, K is 6×10^5 ergs/cm³ (note that the sign convention used in Fig. 3 for the torque curve marked 1 hour is such that the negative slope at $\theta_H = 0$ corresponds to a positive K_u i.e., perpendicular anisotropy). Other torque methods²³ to determine K_u have been suggested. Also techniques such as ferromagnetic resonance²⁴ and hysteresis loops may be used^{25,26} and give good estimates of the anisotropy strength. In the case of hysteresis loop measurements, the difference in areas (to the left of the hysteresis loop in the first quadrant) for loops taken perpendicular to, and in the plane of, the sample gives K_u (after a demagnetization correction). The applied field must be large enough to saturate the sample for this method to be reasonably accurate. This is not possible close to the compensation point where the coercivity is large as has been emphasized by van Dover²⁶ and coworkers and Shan and Sellmyer.²⁰

Preparation conditions that affect the perpendicular anisotropy of Tb-based films are listed in Table 1. As can be seen a number of preparation parameters can be varied to change K_u . The microstructure of the nominally amorphous film, the stress in the film and the amount of gas absorbed in the film can be changed when preparation parameters such as V_B , T_s , α and P_a are changed. These changes in turn affect the value of K_u .

For example a compressive stress can be induced by evaporating onto a substrate at an angle³² or sputtering under preparation conditions of low²⁹ Ar pressure. This compressive stress leads via the magnetoelastic effect to a perpendicular anisotropy. Stress is not however, a requirement for perpendicular anisotropy. Takagi and coworkers²⁹ have removed their Tb-Fe samples from the substrate and although the perpendicular anisotropy is reduced it is still substantial. van Dover and coworkers²⁶ have also argued

Table 1. Preparation Parameters which affect the value of K_u

| Preparation | Alloy ^a | Param. varied | Effect on K_u^b | Author (ref.) |
|-----------------|----------------------------|----------------------------|------------------------------------|---------------------|
| Modified Sputt. | TbFe | Tb content | Maximum | van Dover et al(26) |
| Thermal coevap. | TbFe | | Maximum | Imamura et al(28) |
| RF sputt. | TbFe | | Maximum | Takagi et al(29) |
| DC sputt. | TbFe | | Complex | Hellman et al(30) |
| RF sputt. | TbFe | | Complex | Chen et al(31) |
| DC sputt. | TbGdCo | | Complex | Sato et al(27) |
| Thermal evap. | TbFeCo | Depos. angle, α | Decrease | Lee and Lee (32) |
| Thermal coevap. | TbFe(Co) | | Decrease | Shin (33) |
| Modified sputt. | TbFe | Subs. temp., T_s | Decrease ($T < 0^\circ\text{C}$) | van Dover et al(26) |
| RF sputt. | NdFe | | Max. at 260°C | Suzuki (34) |
| RF sputt. | TbCo | Subst. bias, V_b | Complex | Tokunaga et al(35) |
| RF sputt. | GdTbCo | | Complex | Heitmann et al(36) |
| RF sputt. | GdTbCo | Ar gas pres., P_a | Complex | Heitmann et al(36) |
| RF sputt. | NdFe | | Complex | Suzuki (34) |
| DC sputt. | TbGdFe | N, O, H ₂ O gas | Decrease | Heitmann et al(37) |
| RF sputt. | NdFe | Nd content | Max. at 40% | Suzuki (34) |
| e-beam evap. | Fe(Pr, Nd, Sm, Gd, Dy, Er) | | Complex | Miyazaki et al(38) |
| Ion beam mix. | TbFe(Co) | Xe ion dose | In-plane anis | Yan et al(39) |
| DC sputt. | Tb/Fe | Multilay struc. | Complex | Sato et al(19) |
| RF and DC | Dy/Co | Co layer thick. | Maximum | Shan et al(40) |
| RF and DC | Tb/Fe | Fe layer thick | Maximum | Shan et al(20) |
| RF sputt. | TbFe/AlO | Multilay struc. | Complex | Krishnan et al(41) |

^aAlloys written with a slash, e.g. Tb/Fe, are multilayer alloys.

^bWe have indicated whether the value of K_u increases, decreases or has a maximum, minimum or is more complex as a function of the parameter varied.

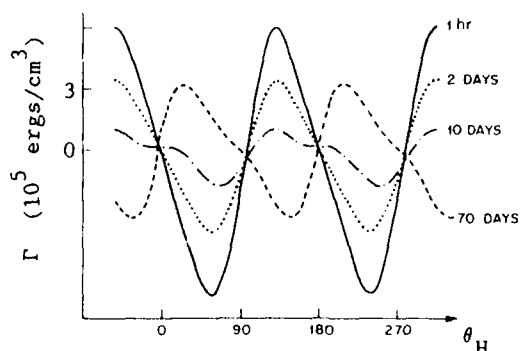


Figure 3. Torque as a function of magnetic field direction at various times in a TbFeCo alloy (ref. 52).

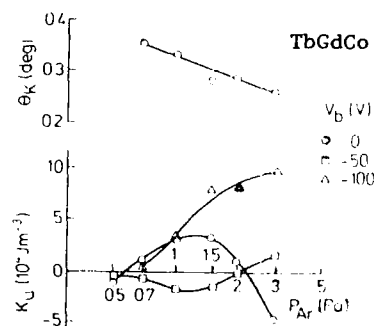


Figure 4. Dependence of K_u and θ_K on Ar sputtering pressure and subst. bias (ref. 36).

that stress cannot account for all the perpendicular anisotropy they observe in their Tb-Fe films. The effect of substrate bias and Ar sputtering pressure are somewhat complicated as can be seen from Fig. 4. The effect of substrate bias is thought to be through its effect on selectively resputtering atoms on the surface of the film. Such a process would change the nature of the pair ordering in the film and so affect the perpendicular anisotropy. The ways in which microstructure such as pair ordering can arise has been discussed by Gambino⁴² and we take up pair ordering again below. Columnar structure appears in RE-TM films which have perpendicular anisotropy but this structure is not present in all films with such anisotropy. When present this type of microstructure can contribute to the perpendicular anisotropy and a model due to Bernstein⁴³ is able to reproduce the magnitude of K_u .

The strength of the perpendicular anisotropy is also affected by the type of microscopic anisotropy present, e.g. single ion anisotropy such as that found in Tb amorphous alloys. Sato²⁷ has shown that the perpendicular anisotropy varies with Tb content and Miyazaki and coworkers³⁸ have shown that systematic changes in the perpendicular anisotropy occur when the species and concentration of anisotropic rare-earth are changed. van Dover and coworkers²⁶ emphasize that the perpendicular anisotropy changes smoothly through the compensation point exhibiting a maximum at $x \sim 0.20$.

Layered alloys have been a testing ground for the pair ordering origin of perpendicular anisotropy. In RE-TM alloys one has a 'forced' RE-TM pair ordering perpendicular to the layers and the density of these pairs increases as the layer thickness is decreased. Sato¹⁹ and Shan and Sellmyer have shown that for Tb/Fe multilayer films the largest values of coercivity and perpendicular anisotropy occur for the smallest layer spacing in agreement with the pair ordering model. The value of K_u falls off as the layer thickness approaches the width of the Tb-Fe interface, i.e., where the film crosses over from being a layered alloy to a homogeneous alloy. The anisotropy of the rare-earth is also important with Gd/Fe multilayer films showing a smaller anisotropy.¹⁹ More recently Shan⁴⁰ and coworkers have used a model involving the single ion anisotropy of anisotropic rare-earths and pair ordering in multilayers to explain in some detail the perpendicular anisotropy in Dy/Co layered alloys.

The magneto-optical (MO) properties of rare-earth alloys are important because of their MO recording media applications and so have been studied in some detail. Both Kerr and Faraday rotation of polarized light produced by a RE-TM film are affected by preparation conditions.^{14,18,33,36,44-49} For example the Kerr rotation angle θ_k decreases³⁶ with increased Ar pressure when sputtering GdTbCo (Fig. 4) because less Co is incorporated into the film at higher Ar pressures. While many of the preparation parameters that affect K_u also affect the Kerr rotation, there is no simple relation between them.

Finally many of the properties of RE-TM films show a time dependence because of their reactivity.⁴⁹⁻⁵³ Figure 3 shows torque curves for a TbFeCo film which initially has a perpendicular anisotropy but after aging has an in-plane (negative K_u) anisotropy. This is often exacerbated by the porous nature of the film. Various types of oxide and metal coatings have been quite successful in protecting the films.^{51,53}

IN-PLANE ANISOTROPY

Tb-Fe films can also have an in-plane anisotropy in the sense that it is not only energetically favourable for the magnetization to lie in the plane of the film, but also to have an easy direction within the plane of the film. At least two sources of in-plane anisotropy can be identified in rare-earth amorphous alloys, anisotropic microstructure (most likely in-plane pair ordering) and stress associated with the film-substrate contact.

Figure 5a shows the in-plane torque for a Tb-Fe alloy prepared by DC sputtering. In this experiment the sample is field-cooled from room temperature to low temperatures.^{54,55} This field is then removed and a (usually) smaller field is applied and rotated in the plane of the sample. As can be seen a fixed anisotropy is present since cooling the sample at 0° or -90° leads to the same torque pattern. Note that the perpendicular anisotropy of the previous section is also a fixed anisotropy. Both stress involving the contact between the film and substrate and microstructure such as pair ordering could contribute to this in-plane anisotropy.

Figure 5b shows similar measurements for a sample with the same composition and as can be seen the torque curve shifts when the cooling field direction is changed. Such an anisotropy is movable and so cannot be due solely to anisotropic structural ordering such as pair ordering in the plane of the sample. This effect is remarkable in that the alloy maintains a memory of its field-cooling direction even after the magnetization has been rotated through 360° .

A clue to the origin of this movable uniaxial anisotropy comes from the fact that it appears in NiO, pure Ni and NiFe films.⁵⁶⁻⁵⁹ Such films have been studied in some detail and models involving inhomogeneous alloys with anisotropy centers and involving antiferromagnetic interactions were not able to explain these results. A suggestion involving stress between the film and substrate appears the most likely option for these films. Stress in the film is expected to depend on sample preparation conditions and could explain the observation of movable anisotropy in one Tb-Fe sample (sample B) and its absence in another sample (sample A). A discussion of this is given in the review by Soohoo⁶⁰ for these films. Such a mechanism for sample B in which an applied field creates a certain stress field in the film via the magneto-elastic effect, which is frozen in on cooling the sample to low temperatures,

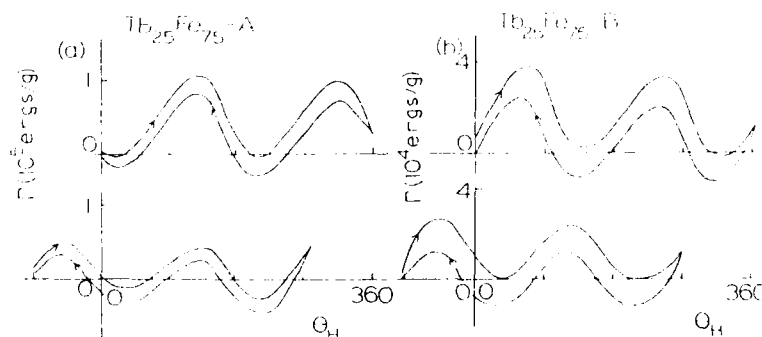


Figure 5. In-plane Torque for two Tb-Fe samples, A and B. The upper torque curves in each case are taken after cooling the sample with the field along $\theta = 0^\circ$ to 2 K and the lower ones were taken after cooling the sample with the applied field along -90° .

will produce an anisotropy. If the stress is relaxed at higher temperatures when the magnetic field is removed then it is controlled by the magnetic field and movable.

FUTURE DIRECTIONS

A number of preparation parameters have been shown to affect the perpendicular anisotropy of RE-TM films. The most important of these is RE-TM pair ordering. This ordering and thus the perpendicular anisotropy may be controlled by preparing the film in multilayer form and varying the layer spacing.

A movable in-plane anisotropy has been found in Tb-Fe films and is thought to be due to control of stress within the film by an applied field. It has been shown that stress may also contribute to the perpendicular anisotropy so the interesting possibility of a movable perpendicular anisotropy also exists. Such an anisotropy is unlikely to exist in multilayer alloys where pair ordering dominates the perpendicular anisotropy.

ACKNOWLEDGMENTS

I have benefited from discussion with A. Fert, W. Saslow and D.J. Sellmyer and support from NATO for visits to Orsay.

REFERENCES

1. R. Harris, M. Plischke and M.J. Zuckermann, Phys. Rev. Lett. 31, 160 (1973); R.W. Cochrane, R. Harris and M.J. Zuckermann, Phys. Rep. 48 1, (1978).
2. J. J. Rhyne, J. H. Schelleng and N.C. Koon, Phys. Rev. B10, 4672 (1974).
3. J. M. D. Coey, J. Appl. Phys. 49, 1646 (1978).
4. K. Moorjani and J. M. D. Coey, Chapter VI, Magnetic Glasses, Elsevier Press, 1984.
5. J. P. Eymer, A. Fnidiki, R. Krishnan, M. Tessier and J. P. Vitton, Phys. Rev. B 38, 11931 (1988).
6. M. L. Spano and J. J. Rhyne, J. Appl. Phys. 57, 3303 (1985) and M. L. Spano and J. J. Rhyne, J. Appl. Phys. 61, 4100 (1987).
7. E. Pytte, Phys. Rev. B 18, 5046 (1978).
8. R. A. Pelcovits, E. Pytte and J. Rudnick, Phys. Rev. Lett. 40, 476 (1978); R. A. Pelcovits, Phys. Rev. B 19, 465 (1979).
9. P. Chaudhari, J.J. Cuomo and R.J. Gambino, Appl. Phys. Lett. 22, 337 (1973).
10. R. M. Carey, D. M. Newman and B. W. J. Thomas, p. 213, of Proc. of 4th Conf. on Physics of Materials, eds. W. Gorzkowski, H. Lachowicz and H. Szymczak, World Scientific (1988).
11. M. H. Kryder, J. Magn. Mater. 83, 1 (1990).
12. J.J. Rhyne, S.J. Pickart, H.A. Alperin, Phys. Rev. Lett. 29, 1562 (1972).
13. N. Heiman, A. Onton, D. F. Kyser, K. Lee and C. R. Guarnieri, AIP Conf. Proc. 24, 573 (1974).
14. C.D. Wright, P.J. Grundy and E.T.M. Lacey, IEEE Trans. MAG-23 162 (1986).
15. P. Bernstein, and C. Gueugnon, J. Appl. Phys. 55, 1760 (1984).
16. J. C. Suits, D. Rugar and J. R. Lin, J. Appl. Phys. 64, 252 (1988).
17. H. A. Alperin, J. R. Cullen, A. E. Clark and E. Cullen, Physica a, 86-88B, 767 (1977) and A.I.P. Conf. Proc. 29, 186 (1976).
18. A. Takenouchi, E. Shichi, T. Rato, S. Tsunashima, S. Uchiyama and N. Imanura, J. Appl. Phys. 55, 2164 (1984).
19. N. Sato, J. Appl. Phys. 59, 2514 (1986) and N. Sato and K. Habu, J. Appl. Phys. 61, 4287 (1987).

20. Z.S. Shan and D.J. Sellmyer, J. Appl. Phys. 67, 5713 (1990).
21. K. Fukamichi, T. Goto, H. Komatsu and H. Wakabayashi, p. 354 of Proc. of 4th conf. on Physics of Materials, eds. W. Gorzkowski, H. Lachowicz and H. Szymczak, World Scientific (1988).
22. Horst Hoffmann, IEEE Trans. Magn. Vol. MAG-22, 472 (1986).
23. H. Miyajima, K. Sato and T. Mizoguchi, J. Appl. Phys. 47, 4669 (1976).
24. R.F. Soohoo, Glassy Metals, ed. R. Hasegawa, CRC press (1983).
25. G. Hadjipanayis, D. J. Sellmyer and B. Brandt, Phys. Rev. B 23, 3349 (1981).
26. R. B. van Dover, M. Hong, E. M. Gyorgy, J. F. Dillon, Jr. and S. D. Albiston, Jour. Appl. Phys. 57, 3897 (1985).
27. R. Sato, N. Saito and Y. Togami, Japan. Jour. Appl. Phys. 24, L266 (1985).
28. N. Imamura, Y. Mimura and T. Kobayashi, Japan. Jour. Appl. Phys. 15, 179 (1976).
29. H. Takagi, S. Tsunashima and S. Uchiyama, J. Appl. Phys. 50, 1642 (1979).
30. F. Hellman, R. B. van Dover, S. Nakahara and E. M. Gyorgy, J. Magn. Mater. 81, 234 (1989).
31. T. Chen, D. Cheng and G. B. Charlan, IEEE Trans. MAG-16, 1194 (1980).
32. Y. H. Lee and S. S. Lee, J. Appl. Phys. 64, 6803 (1988).
33. S. C. Shin, J. Appl. Phys. 61, 3340 (1987).
34. T. Suzuki, Jour. Magn. Mater. 50, 265 (1985).
35. T. Tokunaga, M. Harada, M. Ohkoshi, S. Honda and T. Kusuda, IEEE Trans. MAG-22, 940 (1986).
36. H. Heitmann, M. Hartmann, S. Klahn, M. Rosenkranz, H. J. Tolle and P. Willich, J. Appl. Phys. 61, 3331 (1987).
37. H. Heitmann, A. M. J. Spruijt, P. Willich and H. Wilting, J. Appl. Phys. 61, 3343 (1987).
38. T. Miyazaki, K. Hayashi, S. Yamaguchi, M. Takahashi, A. Yoshihara, T. Shimamori and W. Wakiyama, J. Magn. Mater. 75, 243 (1988).
39. Z.H. Yan, B.X. Liu and H.D. Li, Nucl. Inst. Meth. Res., B19, 700 (1987).
40. Z. Shan, D. J. Sellmyer, S. S. Jaswal, Y. J. Wang and J. X. Shen, Phys. Rev. Lett. 63, 449 (1989).
41. R. Krishnan, M. Porte, M. Tessier, J. P. Vitton and Y. Le Cars, Jour. Magn. Mater. 78, 333 (1989).
42. R. J. Gambino, Current Topics on Non-Crystalline Solids, eds. M. D. Baro and N. Clavaguera, p41, World Scientific Pub. Co. (1986).
43. P. Bernstein, J. Appl. Phys. 53, 8052 (1982).
44. A. M. Toxen, T. H. Geballe and R. M. White, 64, 5431 (1988).
45. R. A. Allen and G. A. N. Connell, J. Appl. Phys. 53, 2353 (1982).
46. M. Akihiro, T. Satoh, J. Tada and T. Satoh, IEEE tran. Magn. Mag 22, 928 (1986).
47. V. Reim, R. J. Gambino, R. R. Ruf and T. S. Plaskett, J. Appl. Phys. 61, 3349 (1987).
48. M. Naoe, N. Kitamura and T. Hirata, J. Appl. Phys. 61, 3337 (1987).
49. K. Aratani, T. Kobayashi, S. Tsunashima and S. Uchiyama, J. Appl. Phys. 57, 3903 (1985).
50. F. E. Luborsky, J. Appl. Phys. 57, 3592, (1985).
51. M. Miyazaki, I. Shibata, S. Okada, K. Ito and S. Ogawa, J. Appl. Phys. 61, 3326 (1987).
52. M. Hong, D. D. Bacon, R.B. van Dover, E.M. Gyorgy, J.F. Dillon, Jr. and S.D. Albiston, J. Appl. Phys. 57, 3900 (1987).
53. M. Hartmann, K. Witter, J. Reck and H. J. Tolle, IEEE Tran. Magn. Mag. 22, 943 (1986).
54. M. J. O'Shea and A. Fert, Europhy. Lett. 9, 283 (1989).
55. M. J. O'Shea, K. M. Lee and A. Fert, J. Appl. Phys. 67, 5769 (1990) and references therein.
56. R. J. Prosen, J. O. Holmen and B. E. Gran, J. Appl. Phys. 32, 91s (1961) and Jour. Appl. Phys. 33, 1150s (1962).
57. J. M. Lommel and C. D. Graham Jr., J. Appl. Phys. 33, 1160s (1962).

- 58. T. Matcovich, E. Korostoff and A. Schmeckenbecher, Appl. Phys. 32, 93s (1961).
- 59. S. S. Lehrer, J. Appl. Phys. 34, 1207 (1963).
- 60. R.F. Soohoo, Magnetic Thin Films, Harper and Row (1965).

MAGNETOSTRICTION IN AMORPHOUS FERROMAGNETS

A. Hernando, M. Vázquez[°], J. Barandiarán* and G. Rivero

Instituto de Magnetismo Aplicado. RENFE-UCM. Las Rozas (Madrid), Spain

[°] Instituto de Ciencia de Materiales. CSIC. Madrid, Spain

* Dpto. Electricidad y Electronica, Fac. Ciencias. Un. Pais Vasco. Lejona, Spain

INTRODUCTION

The change in length of a sample upon magnetization is a common phenomenon in all materials and it is known as linear magnetostriction. The macroscopic magnetostriction reflects the existence of interactions between the local spin direction and the local strain. The physics underlying such magnetoelastic coupling can be understood from the concept of local magnetic anisotropy. The atomic magnetic moment is coupled to the atomic charge distribution through the spin-orbit interaction. On the other hand the electronic cloud interacts with the charge of the neighbouring atoms. When both neighbourhood atomic distribution and electronic charge distribution are anisotropic the total energy depends on the spin direction. This local anisotropy, known as single-ion coupling, should be proportional to the spin-orbit interaction strength. Two-ion coupling originated by anisotropic exchange interaction is the second source of local magnetic anisotropy. For this case the strength of the anisotropy is also governed by the strength of the spin-orbit interaction (1,2). If we consider uniaxial local anisotropies they can be described by an energy term as $D\cos^2\theta$ where θ is the angle between the magnetic moment and the local easy axes. For 3-d ferromagnets D is typically 10^5 erg/cm³ whereas it reaches a value of 10^7 erg/cm³ for 4f samples. This difference in D values is a natural consequence of difference in atomic weight and therefore in spin-orbit interaction strength. The local anisotropy, being originated by electrical forces, is expected to change under local strains which change the arrangement and distances of neighbour atomic sites. The strain derivative of the local anisotropy is the magnetoelastic coefficient, B , which explains the linear magnetostriction phenomenon.

In single-crystals the local easy axes lie along the same macroscopic direction. Therefore ferromagnetic exchange and anisotropy are perfectly compatible, and the macroscopic anisotropy and magnetostriction coincide with the local ones. Notice that in amorphous ferromagnets the direction of the local easy axes fluctuates with correlation length $L \approx 10\text{\AA}$. In this case local anisotropy tends to destroy ferromagnetic order. Nevertheless it is well known that, for 3d-based amorphous, ferromagnetic exchange overcomes local anisotropy, ferromagnetic order is achieved and the macroscopic anisotropy vanishes. It is now well established that the distribution of local easy axes decreases the macroscopic anisotropy which is zero when the correlation length of the directional fluctuations becomes much smaller than the exchange correlation length (3). The more striking characteristic of amorphous ferromagnets is that the average macroscopic magnetostriction does not vanish: In other words the average local or structural anisotropy is zero but the average strain

derivative of the anisotropy is different from zero. The way in which this average procedure has to be done is an open and difficult subject (4).

METHODS OF MEASUREMENT

The shape of amorphous alloys and the value of magnetostriction to be measured determine the most convenient method. In the following, frequently used techniques are briefly reviewed.

-Strain-gage extensimetry. This method, developed by Goldman (5) in 1947, made use of the strain dependence of the resistivity of a strain-gage cemented on the magnetostrictive sample. The use of this method is limited by the gage sensitivity and the geometry of the sample. Obviously, it is not useful in amorphous wires.

-Three-terminal capacitance dilatometer. In this method, based on the Whiddington ultramicrometer, the magnetostrictive displacement is measured as a change of a capacitance of a condenser, having one plate mechanically coupled with the sample. The device described by Tsuya et al (6) has a sensitivity of 0.1 nm, allowing the measurement of ribbons with magnetostriction constant of at least 10^{-7} . A great advantage of this dilatometer is the possibility to perform magnetostriction measurements over a wide range of temperature.

-Cantilever capacitance method. This is an adaptation of above method, designed to measure the magnetostriction of thin films sputtered, evaporated or electrodeposited, when it is not possible to eliminate the substrate. In this method an air condenser is formed by a fixed electrode and one end of sample-substrate system, which is rigidly fixed on the other end. If the substrate is thin enough, the change in length produced when the magnetostrictive sample is magnetized, causing a bending of the system sample-substrate, and thereby, a change in the capacitance of the condenser (7).

-Ferromagnetic resonance. This method was introduced by Smith and Jones (8) in 1963. When uniaxial stress is applied to a magnetostrictive sample, a shift of frequency of ferromagnetic resonance can be measured. In a dynamic version of this method, a periodic strain is applied by means of an ultrasonic transducer. The strain modulation causes the change of the anisotropy field since the magnetoelastic resonance is modulated. The high sensitivity of this method allows to measure values as small as 10^{-9} .

-Small-angle magnetization rotation. This method was reported by Narita et al. in 1980 (9). It is based on the fact that, in a magnetostrictive ribbon, saturated along its longitudinal axis, under the simultaneous action of a longitudinal field, H_z , and a tensile stress, the magnetization, M_z , rotates a small angle, θ , out of the axial direction when a transverse field, H_y , is applied. Hernando et al. (10) have proposed using an alternating current following through the ribbon to produce H_y . This method makes it possible to measure values of as low as 10^{-9} ; however, it seems to fail in ribbons with high magnetostriction.

-Direct Wiedemann effect. As is well known, the Wiedemann effect consists of the magnetostrictive torsional strain induced by applying simultaneously an axial H_z and a transverse H_y , H_y being produced by a current, I , flowing along the ribbon. This effect was proposed in 1986 (11), as a method for directly measuring λ . According to these authors, the maximum torsional deflection, is roughly given by the inverse of the half thickness times the magnetostriction constant.

-Dependence of initial susceptibility on the tensile stress. This method made use of the dependence of the initial susceptibility or the anisotropy energy on applied stress. The experimental device consists of a conventional system to apply tensile stress to the sample, combined with magnetizing Helmholtz coils or a solenoid, and a sense coil to measure magnetization. This method is very simple and sensitive, but it applies only to samples with negative values of λ . If positive values are to be measured, a magnetic anisotropy perpendicular to the ribbon axis is needed.

EXPERIMENTAL DEPENDENCIES OF MAGNETOSTRICTION

a) Compositional dependence

Typical compositions of amorphous alloys is $(TM)_{100-x}M_x$ where TM and M represent tran-

sition metals and metalloids respectively. x usually ranges between 20 and 30. Some particular alloys also include small amounts of rare earth elements.

Taking into account values of the magnetostriction, amorphous alloys can be classified into two general groups: Fe and Co based alloys (12). Fe rich alloys exhibit positive magnetostriction in the range of values of the order of 10^{-5} at room temperature. This value depends somewhat on the kind of metalloid and on the x ratio. Addition of Ni makes the magnetostriction decrease. On the other hand, Co rich alloys are magnetostrictively negative in nature and values are of the order of 10^{-6} . Nevertheless, for these alloys λ changes in a quite decisive way on small additions of other elements. As in the case of Fe based alloys, the presence of Ni reduces λ . But on addition of Fe atoms the magnetostriction not only decreases but also changes the sign of λ . Typical composition for zero magnetostriction is $(\text{Co}_{0.95}\text{Fe}_{0.05})_{100-x}\text{M}_x$.

Addition of small amounts of RE elements (around 5%) does not increase significantly the value of the magnetostriction in Fe rich alloys although it could play an important role concerning the magnetic coupling. Quite recently, the addition of Cu and Nb elements has been proven itself important in the achieving of nanocrystalline structures (13). In this case as-quenched samples exhibit high magnetostriction ($\approx 10^{-5}$). The value is significantly reduced upon thermal treatment ($\approx 10^{-7}$).

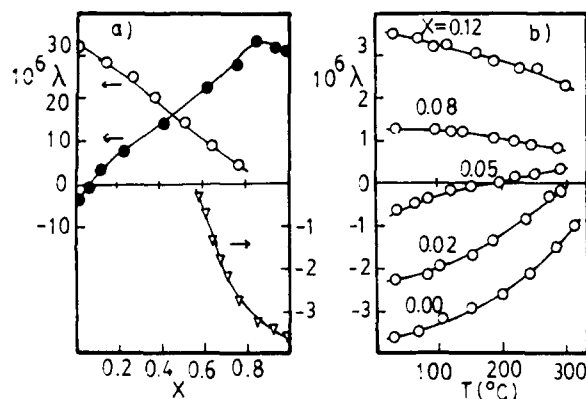


Fig.1 a) Composition Dependence of λ for $(\text{Fe}_x\text{Co}_{1-x})_{80}\text{B}_{20}$ (●), $(\text{Fe}_x\text{Ni}_{1-x})_{80}\text{B}_{20}$ (○) and $(\text{Co}_x\text{Ni}_{1-x})_{75}\text{Si}_{15}\text{B}_{10}$ alloys (14) b) Temperature dependence for the $(\text{Fe}_x\text{Co}_{1-x})_{75}\text{Si}_{15}\text{B}_{10}$ alloy (15).

b) Temperature dependence

Reported experimental temperature dependence of Fe and Co rich alloys show that in both cases the magnetostriction decreases monotonically towards zero at the Curie point for either positive or negative values respectively. Nevertheless, disagreement with such behavior is found for some Co-rich alloys containing other elements such as Fe. In this case, a temperature compensation for the magnetostriction is found far below the Curie point suggesting the competition between positive and negative contributions. The temperature dependence of both saturation magnetization, J_s , and magnetostriction have been thought to arise from the single-ion, α , and two-ions, β , mechanisms of anisotropy. A general expression for the temperature dependence of λ is the following: $\lambda(T) = -\alpha J_s^2(T) + \beta J_s^2(T)$

Where α and β coefficients that do not depend solely on the composition. Measurements of λ near and below the Curie point have yielded an critical exponent, κ , $\lambda(T) \propto (T_c - T)^\kappa$. It was found that κ ranges between 2 and 3 times the value of the critical exponent for saturation magnetization (16).

c) Structural relaxation

The stabilization of the magnetostriction constant is quite important for technological applications where this magnitude is involved. As is well known, thermal treatments modify the local atomic arrangement of amorphous alloys giving rise to modifications of intrinsic magnetic properties. In the case of magnetostriction, these changes are small in magnitude ($\approx 10^{-7}$) and can be detected only in nearly-zero magnetostriction alloys. A general feature is that as the microstructure relaxes to more stable states, the magnetostriction changes towards positive values and in fact it can change sign when the initial value is negative (10). On the other hand, structural relaxation can be so important that it alters the microstructure giving rise to the appearance of nanocrystalline units. In this case a drastic reduction of λ is probably obtained due to the parallel collapsing anisotropic effect. Moreover, amorphous local atomic arrangement can also be modified from the very beginning just by changing the fabrication parameters that define the quenching (in case of metallic glasses) or deposition (electrodeposited alloys) rates. Consequently, these fabrication parameters also determine the corresponding magnetostriction values.

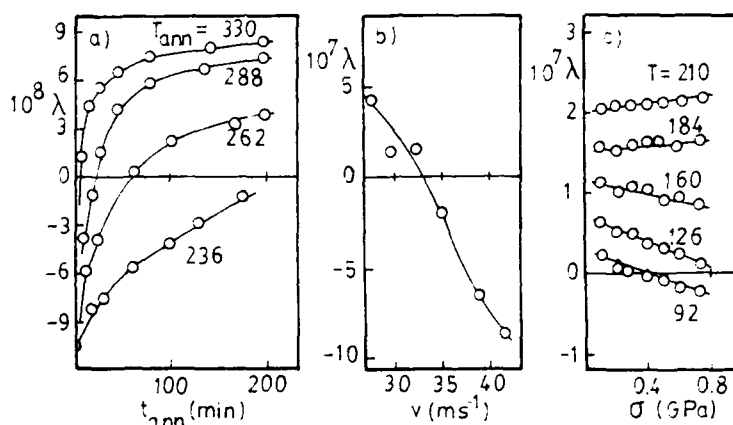


Fig.2 - Dependence of λ on: a) Thermal treatments for the $\text{Co}_{58}\text{Fe}_5\text{Ni}_{10}\text{B}_{16}\text{Si}_{11}$ alloy (10). b) Velocity at the wheel surface during fabrication for the $\text{Co}_{80}\text{Nb}_8\text{B}_{12}$ alloy (17) and c) Applied tensile stress at different temperatures for the $(\text{Co}_{0.94}\text{Fe}_{0.06})_{75}\text{Si}_{15}\text{B}_{10}$ alloy (18).

d) External Agents

It has been recently reported that λ for those Co-rich alloys exhibiting nearly zero magnetostriction is susceptible to modification when samples are submitted to applied stresses. This effect has been measured by different groups and it appears that the derivative of λ on applied tensile stress is always negative and of the order of 10^{-10}MPa^{-1} . λ can change sign. Finally as has been recently found, λ seems to depend also on the applied field in the technically saturated magnetic state. Nevertheless, results are not conclusive since λ would either increase or decrease with the applied field after different reported measurements.(19-20)

THEORY

Magnetostriction of metallic glasses has been explained on the basis of the quantum mechanical theory of Callen and Callen for crystalline materials with localized moments with two dif-

ferent contributions: single ion crystal field effects and two ions anisotropic exchange. The temperature dependence of each contribution is different. For instance a M_s^3 dependence of λ_s is expected up to $T \approx 0.8 T_c$ for single ion contributions of aniaxial symmetry and M_s^2 variation for anisotropic exchange (two-ion) contributions. The single ion contribution of uniaxial symmetry has been shown to be the only one in Fe rich glasses (21). This supports the idea of localized moments and interactions upon which the theory of Callen and Callen is built. In Co-rich glasses, however, the two-ion contributions are needed for explaining the compensation points in λ_s (T). This fact, somewhat contradicts the starting hypothesis because exchange in Transition Metal-Metalloid alloys is indirect (via conduction electrons). The itinerant model (band theory) has also been used to explain such anomalies, but a modified theory, the so called "Split band model" only accounts for some characteristics in the Ni-rich part of the composition diagrams. Some improvement to the Callen and Callen theory has been done taking into account the amorphous structure and calculating both "cluster" electric field (23-24) or pair interactions (25). More recently, phenomenological models taking into account the elastic interaction between adjacent zones with different orientation of anisotropy easy axis (26) or the fluctuations in a medium range scale (27) of the magnetostriction constant, have been developed in order to explain the stress dependence of the magnetostriction.

APPLICATIONS

Two types of applications for metallic glasses can be used: those having high saturation induction and low price are used as magnetic cores for transformers and electric motors. On the other hand specially designed materials for electronic and sensing applications must have special features but the price is not a restriction. In this group we deal the influence of magnetostriction on the magnetic properties (27). Large magnetostriction Fe-based glasses are very suitable for sensing force, torque and other mechanical quantities. The "figure of merit" of such alloys is related to the "magnetoelastic coupling coefficient" which reaches values very close to unity (0.98 for carefully annealed $\text{Fe}_{81}\text{B}_{13.5}\text{Si}_{3.5}\text{C}_2$) (28), indicating that all the elastic energy provided to it is transformed into magnetic energy (or viceversa). As defined by Savage and Spano (29) the figure of merit of metallic glasses is given by the relative susceptibility change per unit deformation and depends on λ , the Young's modulus and the strength of the magnetic anisotropy present in the alloy. The possibility of reducing the anisotropy to very low levels while maintaining high values of λ improves sensitivity of metallic glasses three orders of magnitude more than any other known material. Very low magnetostriction glasses (Co-rich ones) are suitable for magnetic field sensing applications (30) and for small core transformers (31). The low magnetostriction ($\lambda_s \approx 10^{-7}$) glasses show susceptibilities in the range of 10^6 and very good frequency response making them ideal materials for flux gate magnetometer cores or force transformer cores. In such applications the influence of annealing, stress, field etc. on the value of magnetostriction is very important in order to get the desired properties of the glasses.

REFERENCES

- 1) E.R. Callen and H.B. Callen Phys. Rev. 129, (1963) 158
- 2) J. Cullen and Adel Moral T. Magn. Magn. Mat. 83, (1990) 157
- 3) R.C. O'Handley J. Applied Physics 62 (10), (1987) R-49
- 4) J. Furthmuller, M. Fähnle and G. Herzer. J. Phys. F 16 (1986) L225
- 5) J.E. Goldman, Phys. Rev. 72 (1947) 529
- 6) N. Tsuya, K.I. Arai, Y. Shiraga, M. Yamada and T. Masumoto Phys. Stat. Sol. a) 31 (1975) 557
- 7) E. Klokholm IEEE Trans. Magn. MAG-12 (1976) 819
- 8) A.B. Smith and R.V. Jones J. Appl. Phys. 34 (1963) 1283
- 9) K. Narita, J. Yamasaki and H. Fukunaga IEEE Trans. Magn. MAG-16 (1980) 435
- 10) A. Hernando, M. Vazquez, V. Madurga and H. Krönmüller J. Magn. Magn. Mat. 37 (1983) 161
- 11) C. Nuñez de Villavicencio, M. Vazquez, V. Madurga and A. Hernando, J. Magn. Mat. 59 (1986) 333
- 12) R.C. O'Handley in "Amorphous Metallic Alloys" Ed. F.F. Luborsky, Butterworths Monographs in Materials, London 1983, p. 257
- 13) Y. Yoshizawa, S. Oguma and K. Yamanchi, J. Appl. Phys 64 (1988) 6044

- 14) M. Vazquez, A. Hernando and O.V. Nielsen *J. Magn. Magn. Mat.* 61 (1986) 390
- 15) V. Madurga, M. Vazquez, A. Hernando and O.V. Nielsen *Sol.State Comm.* 52 (1984) 710
- 16) M. Vazquez, A. Hernando, and H. Krönmüller *Phys. State Sol.* 133 (1986) 167
- 17) V. Madurga, J.M. Barandiaran, M. Vazquez, O.V. Nielsen, A. Hernando *J. Appl. Phys.* 61 (1987) 3228
- 18) J.M. Barandiaran, A. Hernando, V. Madurga, O.V. Nielsen, M. Vazquez and M. Vazquez-Lopez *Phys. Rev. B* 35 (1987) 5066
- 19) A. Hernando, M. Vazquez, J.M. Barandiaran, and W.J. van Hettum *J. Physique C* 8 (1988) 1333
- 20) L. Kraus and P. Duhaj, *J. Magn. magn. mat.* 83 (1990) 337
- 21) R.C. O'Handley and M.O. Sullivan *J. Appl. Phys* 52 (1981) 1841
- 22) H. Szymczak *IEEE Trans Magn. MAG-14* (1978) 847
- 23) M. Fähnle, and T. Egami *J. Appl. Phys.* 53 (1982) 2319
- 24) E. duTremolet de Lacheisserie, *J. Magn. Magn. Mat* 69 (1987) 102
- 25) J. Furthmüller, M. Fähnle and G. Herzer, *J. Magn. Magn. Mat.* 69 (1987)
- 26) A. Hernando, M. Vazquez, G. Rivero, J.M. Barandarian, O.V. Nielsen and A. Garcia-Escorial *J. Phys. Condens. Matter*, 2 (1990) 1129
- 27) A. Hernando, M. Vazquez, and J.M. Barandiaran, *J. Phys. E.* (1988) 1129
- 28) C. Modzelewski, H.T. Savage, L.T. Kabawff and A.E. Clark, *IEEE Trans Magn. MAG-17* (1981) 2837
- 29) H.T. Savage and M.L. Spano *J. Appl. Phys.* 53 (1982) 8092
- 30) O.V. Nielsen, J.R. Petersen, B. Hernando, J. Gutierrez, and F. Primdahl, *Proc. of the Soft Magnetic Materials 9, El Escorial (Spain) September 1989*
- 31) G. Herzer and H.R. Hilzinger in "Magnetic Properties of Amorphous Metals" A. Hernando et al. Editors Science Pub. (1987) p. 354

ANDERSON LOCALIZATION IN 3-DIMENSIONAL AMORPHOUS ALLOYS: EVOLUTION
WITH THE CONTENT OF MAGNETIC IONS

J. Filippi, B. Barbara, V.S. Amaral*, J.B. Sousa*,
J.M. Moreira*, A.G.M. Jansen**

Laboratoire Louis Néel
CNRS, 166 X, 38042 Grenoble Cedex, France

* Centro de Fisica da Universidade do Porto
INIC, 4000 Porto, Portugal

** Max Planck Institut
Hochfeld Magnetlabor, 166 X, 38042 Grenoble Cedex, France

• Bolseiro do INIC para Doutorado

In a disordered system conduction electrons have a diffusive motion due to the random scattering from atoms. These collisions are predominantly elastic and then the electron wave functions retain their phase for long distances. It is therefore possible that two partial electrons waves, starting from one point and experiencing scattering in a time reversed sequence with respect to each other, get back to their origin and interfere constructively. This coherent backscattering of electron waves through closed paths leads to the existence of quantum corrections to the transport coefficients, in particular to the resistivity, which increases due to these mechanisms^{1,2}. In an amorphous metal with typical resistivities up to a few hundred $\mu\Omega\text{cm}$, these corrections are small and can be treated theoretically as a perturbation to the classical transport problem. We then have the phenomenon of weak localization. General expressions for the magnetoresistance including all the contributions can be found in refs 1 and 3.

We present here a systematic study of the effect of magnetic scattering weak localization in the amorphous system $\text{Dy}_x\text{Y}_{1-x}\text{Ni}$. Starting from YNi which is non-magnetic, the random substitution of Y by Dy introduces interactions between localized and delocalized magnetic states creating an electron-band polarization. In order to focus our attention directly on the effect of independent magnetic ions, we prepared diluted alloys with $x = 0, 0.01, 0.03, 0.074$ and 0.118 , using triode magnetron sputtering. The thickness of the samples is typically $20\mu\text{m}$ and they have resistivities around $200\mu\Omega\text{cm}$. We measured the longitudinal magnetoresistance ($I // B$) in Bitter coils up to 22 Tesla (only 11 T for $x = 0.074$ in a superconducting coil) and temperatures between 1.3 and 20 K using a high resolution (10^{-5}) DC method.

The results for YNi given, in Fig. 1, show the characteristic features of the magnetoresistance due to weak localization under strong spin-orbit scattering : $\Delta\rho/\rho$ is positive, increasing like \sqrt{B} up to a temperature independent maximum⁴ around 20 Tesla, the maximum

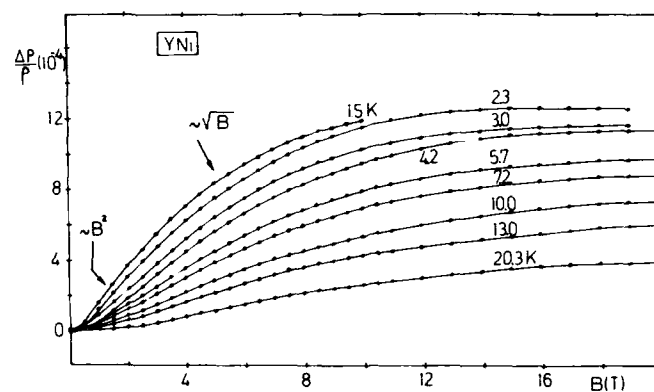


Fig.1. Magnetoresistance of YNi at the indicated temperatures, characteristic of weak localization under strong spin-orbit scattering.

measuring field for this sample. At low fields $\Delta\rho/\rho$ starts parabolically. At higher temperatures $\Delta\rho/\rho$ is smaller because the dephasing due to the inelastic scattering from phonons increases with temperature. In this way the magnetic field will have a smaller effect, as more interferences were suppressed by inelastic scattering.

Let us now consider the effect of the inclusion of magnetic impurities. We expect that the increase of magnetic scattering and of the corresponding dephasing should reduce the $\Delta\rho/\rho$ contribution of localization, like the increase of temperature in the non-magnetic sample (YNi). Furthermore, the increase in the magnetic polarization in an applied field reduces spin disorder scattering, thus producing a direct negative magnetoresistance contribution⁵. This term goes approximately like M^2 where M is the average magnetic moment of the impurities, ultimately saturating at sufficiently high fields. The magnetoresistance $\Delta\rho/\rho$ is therefore given by the sum of the weak localization contribution and the direct magnetic term, always negative.

Fig. 2 shows $\Delta\rho/\rho$ at 4.2 K for all the studied samples. For the two samples richer in Dy ($x = 0.074$ and 0.118) we clearly see the direct effect of spin alignment by the magnetic field, saturating at negative values. This means that the direct magnetic contribution dominates localization at these high fields. However, as shown by the complete curve obtained with the sample $x = 0.118$ above 8 Tesla (when the direct magnetic effect is nearly saturated) $\Delta\rho/\rho$ is slightly increasing, showing that weak localization effects are still present. Decreasing the magnetic concentration ($x = 0.03$ and 0.01), $\Delta\rho/\rho$ is now positive at the highest fields showing the dominance of localization. For $x = 0.01$ we can clearly see the magnetoresistance maximum around 16 Tesla, due to spin-orbit scattering. The position of this maximum does not change with temperature in the studied temperature range, as should be expected⁴.

Surprisingly, in all the magnetic samples at low fields $\Delta\rho/\rho$ has an initial positive slope (associated with localization) much larger than in YNi. Furthermore this positive slope increases with magnetic concentration. To elucidate this problem, we present in Figs. 3 and 4 the low field data of $\Delta\rho/\rho$ for $x = 0.03$ and 0.074 at several

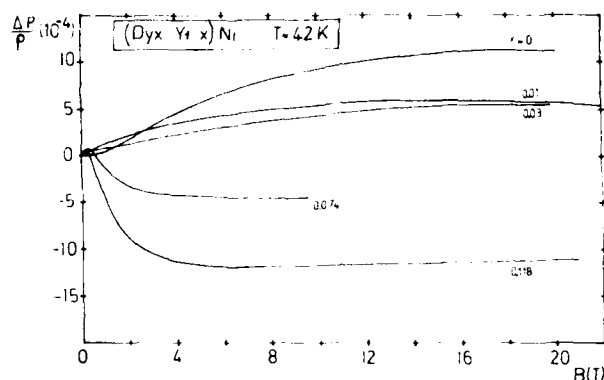


Fig.2. Magnetoresistance for all the samples studied at 4.2 K. The negative direct magnetoresistance dominates at high concentrations of Dy. At high fields the weak localization behaviour is still observed. At low fields the positive localization term dominates in all samples, with a slope increasing with magnetic concentration.

temperatures. From Fig. 3 we conclude that lowering the temperature increases both the negative direct contribution ($\propto -M^2$) and the positive initial slope, in the same manner as through an increase of magnetic concentration. The curve at 1.36 K is very revealing: after a positive start (localization), $\Delta\rho/\rho$ reaches a maximum and then decreases to a negative minimum (competition with the direct negative contribution) before recovering the initial behavior with positive slope above about 3 Tesla (magnetization almost saturated). Then the

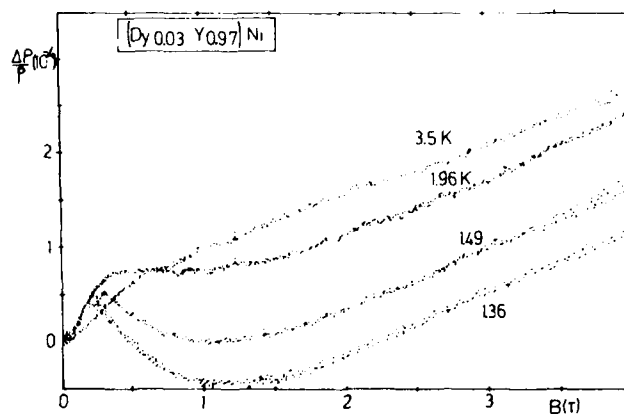


Fig.3. Magnetoresistance for $x = 0.03$ at the indicated temperatures. The coexistence of localization and the direct magnetic term is observed. At low fields and above saturation, localization dominates the $\Delta\rho/\rho$ behaviour.

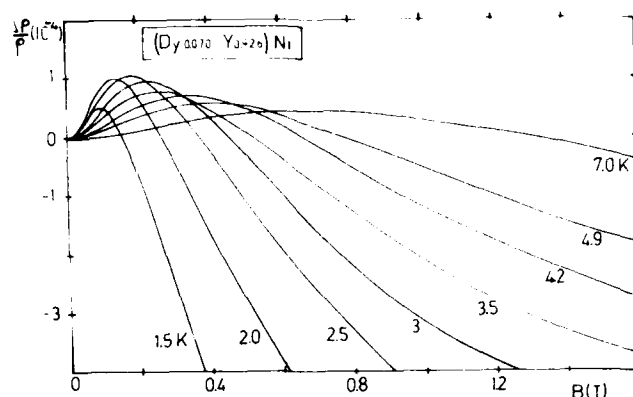


Fig.4. Magnetoresistance for $x = 0.074$ at the indicated temperatures. The positive initial slope increases with decreasing temperature.

only term that changes with the field is due to localization. Qualitatively the same phenomena occurs at higher temperatures and above saturation the result is almost an upward shift of the curves due to the decrease in the negative direct contribution. In Fig. 4, for $x = 0.074$, we illustrate in greater detail the systematic increase of the initial slope with decreasing temperature and the displacement of the low field maximum.

Our results clearly show a dramatic increase in the weak localization contribution to the magnetoresistance when magnetic impurities are added to the non-magnetic amorphous alloy YNi. In principle one should expect the opposite effect, due to the progressive dephasing caused by magnetic spin-flip scattering. In the framework of the available weak localization theory, the only possible explanation can be found in the pronounced enhancement of the Zeeman spin-splitting due to the interaction between localized and delocalized magnetic states which leads to a significant increase of the amplitude of the weak localization magnetoresistance⁶.

ACKNOWLEDGEMENTS

We are very pleased to thank T. Fournier from the Laboratoire de Cristallographie-CNRS, Grenoble, for the chemical analysis of the samples. This work was partially supported by the INIC - JNICT/CNRS Scientific exchange program, and by a grant from Reitoria da Universidade do Porto, Fundação Gomes Teixeira is gratefully acknowledged. The Portuguese work is part of the IFIMUP programo.

REFERENCES

- 1 - G. Bergmann, Phys. Reports 107, n°1, 1 (1984)
- 2 - P.A. Lee and T.V. Ramakrishnan, Rev. Mod. Phys. 57, 287 (1985)

- 3 - D. Baxter, R. Richter, M.L. Trudeau, R.W. Cochrane and J.O. Strom-Olsen, J. Physique 50, 1673 (1989)
- 4 - J.B. Bieri, A. Fert, G. Creuset and A. Schuhl, J. Physics F 16 2099, (1986)
- 5 - M.T. Beal Monod and R.A. Weiner, Phys. Rev. 170, 552, (1968)
- 6 - M.L. Trudeau and R.W. Cochrane, Phys. Rev. B 38, 5353, (1988)

ON THE LAW OF APPROACH TO SATURATION

IN THE SERIES OF AMORPHOUS ALLOYS $a\text{-Dy}_x\text{Gd}_{1-x}\text{Ni}$

V.S. Amaral⁽¹⁾, J. Filippi⁽²⁾ and B. Barbara⁽²⁾

(1) Centro de Fisica da Universidade do Porto INIC
4000 Porto, Portugal

(2) Laboratoire Louis Néel, CNRS
166X 38042 Grenoble-Cedex, France

The lack of complete alignment of magnetic moments of amorphous alloys in the presence of a large magnetic field is essentially due to the disorder of local anisotropy directions. In the framework of a powerful real space model, Chudnovsky et al (1-4) have shown that the law of approach to saturation in amorphous alloys must display two field regimes. The field where the cross-over from one regime to another occurs, depends on the exchange interaction and the size of regions in which local anisotropy directions are correlated. In this paper we analyse high field magnetization curves of the series of amorphous alloys $\text{Dy}_x\text{Gd}_{1-x}\text{Ni}$ (with $x = 1, 0.75, 0.50, 0.25, 0.1$) in the framework of this model. Measurements have been performed at the Service National des Champs Intenses, Grenoble, at 4.2 and 1.5 K up to 150 kOe. The interesting point concerning this series is the possibility to change the local anisotropy to exchange ratio D/J from ≈ 1 (for DyNi) to ≈ 0.1 (for GdNi). We have seen that the cross-over predicted by Chudnovsky (3) varies with this ratio D/J in a way so that the size of regions in which anisotropy directions are correlated remains constant and equal to ≈ 2.7 mean interatomic distances.

Raw magnetization results obtained at 4.2 K are represented by fig. 1. Qualitatively they show that the saturation becomes more difficult when the ratio D/J (i.e. x) increases. The Pauli paramagnetic susceptibility has been estimated on the Gd-richest sample from the superimposed slope, $dM/dH \approx \text{constant}$ in large enough field. For other samples it has been estimated from the high temperature susceptibility using the form $\chi = \chi_0 + C/(T-\theta)$. Within error bars, we always found the same value, $\chi_0 = (8 \pm 1) \cdot 10^{-4} \mu_B/\text{kOe}$. When comparing the experimental data to theoretical results, it is important to take into account the Pauli contribution to the magnetization especially in Gd-based systems where $\chi_0 H$ is of the same order than $\Delta M = M_S - M_{\text{obs}}(H)$ (here M_S represents the saturation magnetization and M_{obs} the observed one).

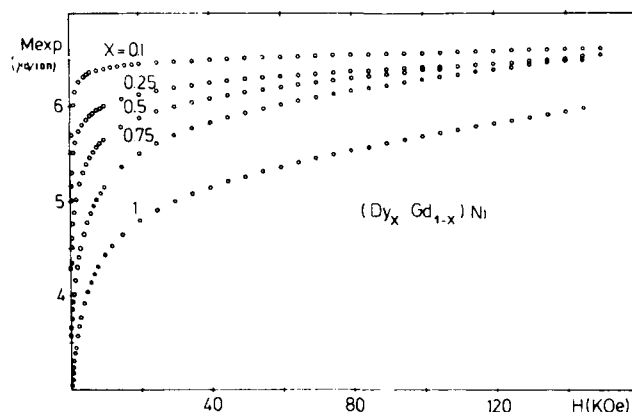


Fig. 1. Raw magnetization curves measured at 4.2 K on different samples of the series a-Dy_xGd_{1-x}Ni.

The first part of this paper is devoted to the system a-Dy_{0.1}Gd_{0.9}Ni in which the ratio D/J is of the order of 0.1, that is small enough to satisfy the assumption of the theory of Chudnovsky et al (1-4). Fig. 2 shows an excellent fit of the magnetization curve of this sample to the general formula (3) $M = M_S + \chi_0 H - \Lambda^2 / 15P(1+P)^3$, (1), where $\Lambda = KR_a^2 \sqrt{M_S} / A$ and $p = R_a \sqrt{(H+H_C) M_S} / 2A$. Interestingly we found only one set of parameters allowing to fit this curve: $\Lambda^2 = 0.63 \mu_B^2$, $M_S = 6.52 \mu_B$, $H_C \approx 0$, $H_{C0} = 2A / M_S R_a^2 = 224$ kOe and $\chi_0 = 8.2 \cdot 10^{-4} \mu_B / \text{kOe}$. The first verification of the expression (1) shows that i) although the cross-over between the $1/\sqrt{H+H_C}$ and the $1/H^2$ regimes occurs at the field $H \sim H_{C0}$ which is larger than our maximum measuring field (150 kOe), the parameter H_{C0} can accurately be determined; ii) the correlation length of anisotropy directions R_a can be evaluated to be $R_a = 2.4$ compared to the rare-earth/rare-earth mean distance.

This detailed analysis will now be completed by the study of the other samples ($x > 0.1$) which satisfy Chudnovsky's assumption $D \ll J$ less and less when x increases. First of all it appeared that the magnetization curves of these samples could not be fitted to the expression (1). We, therefore, tried to test separately the square-root regime (already observed in many other systems (5-9)) and then another regime in higher fields. For that we first derived the expression $\delta M = M_S + \chi_0 H - M = B / \sqrt{H+H_C}$, (1) to obtain $M = M_S - 2^{1/3} B^{2/3} (dM/dH)^{1/3}$ and then we plotted M vs $(dM/dH)^{1/3}$, to get the values of M_S and B (see table 1 and fig. 3). The coherent anisotropy field often present in amorphous alloys is determined from the plot of $(M_S - M)^{-2}$ vs H (see fig. 4). According to the expression (1) we should get a straight line with the slope B^{-2} and the intercept with the H -axis at $-H_C$. The values obtained for B agree very well with those obtained from the precedent fit (table 1) and the values obtained for H_C are sufficiently small (compared to D) not to

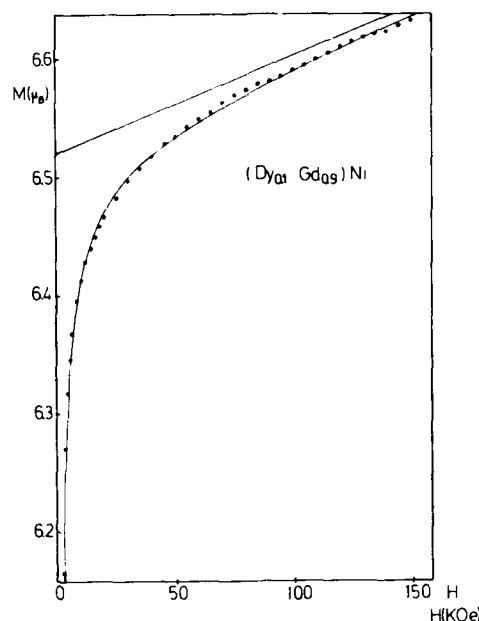


Fig. 2. Measured magnetization of $a\text{-Dy}_{0.1}\text{Gd}_{0.9}\text{Ni}$ (data points). The straight line represents the Pauli paramagnetic susceptibility $M = \chi_0 H$. The curve passing through the data point is the fit to the theory of ref (3).

perturb on a sizable way the continuous symmetry characteristic of disordered systems. Deviations from straight lines in fig. 3 and 4 clearly show that the range of validity of the $1/\sqrt{H+H_C}$ law is limited to applied fields smaller than H^* which is of the order of 20 kOe (see table 1). Above this field and up to our maximum measuring field of 150 kOe, we have shown that our data can very well be fitted to a mean field HPZ model(10). This is easily understandable for two reasons i) the predicted highest field regime $\Delta M \propto 1/H^2$ requires even larger fields to be reached and ii) our measuring field are nevertheless large enough so that the transverse correlation length is small enough to authorize a mean field approach. The D/J values obtained from this fit(10) are quoted on table 2.

One of the most interesting feature of the Chudnovsky's theory is the link existing between magnetic quantities and the volume of correlated anisotropy directions $\Omega/a^3 = (60 \pi/\sqrt{2}) B \sqrt{a^3}/M_S J^{3/2}/D^2$. Knowing B , M_S , D/J and J (from the paramagnetic Curie temperature $\theta_p = ZJ/6 \text{ kJ}$) we deduced the values of Ω for each sample (table 2). It is very interesting to see that the mean dimension of these regions $R_a \approx 2.7a$ is found the same for each sample (for $Z = 6$). Furthermore the position and width of the first peak of X-ray patterns of these sample give $a \approx 2.5 \text{ \AA}$ and $d \approx 15 \text{ \AA}$ (d = mean extension of regions with coherent scattering of X-rays). The agreement between $R_a \approx 2.7 \times 2.5 \approx 6.8 \text{ \AA}$ and $d/2 \approx 7.5 \text{ \AA}$ is surprisingly good. As expected R_a is always smaller than the ferromagnetic correlation length,

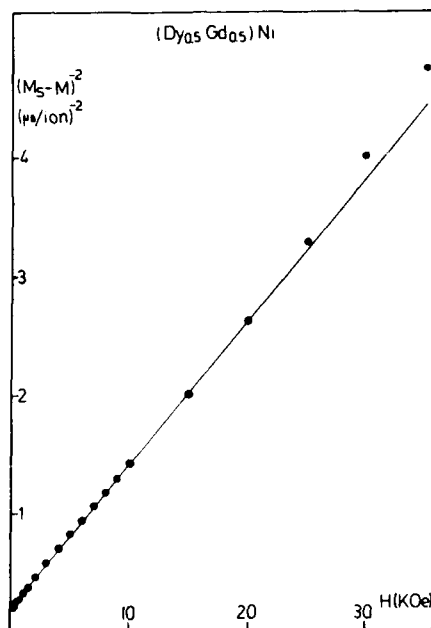


Fig. 3. An example of $(M_s - M)^{-2}$ vs H plot for $x = 0.5$. The slope gives the parameter $B = (\sqrt{2}/60\pi) \sqrt{M_s/a^3} (\Omega/a^3) D^2/J^{3/2}$ and the intercept with the M axis gives M_s the saturation magnetization.

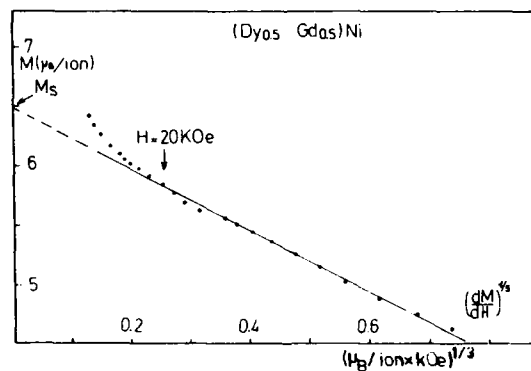


Fig. 4. An example of M vs $(dM/dH)^{1/3}$ plot for $x = 0.5$. The slope gives the parameter B and the intercept with the H -axis gives the parasitic uniform anisotropy field H_c .

Table 1. Parameters obtained for the series $a\text{-Dy}_x\text{Gd}_{1-x}\text{Ni}$ from the plots described in the text. The Pauli susceptibility χ_0 has been estimated by two independent methods (the error bars never exceed $10^{-4} \mu_B/\text{kOe}$).

| x | $B (\mu_B \text{kOe}^{1/2})$ | $M_s (\mu_B)$ | $H_c (\text{kOe})$ | $H^* (\text{kOe})$ | $\chi_0 (\mu_B/\text{kOe})$ |
|------|------------------------------|---------------|--------------------|--------------------|-----------------------------|
| 1 | 4.9 | 5.80 | 2.81 | 17 | 8 |
| 0.75 | 4.6 | 6.45 | 2.69 | 13 | 8 |
| 0.5 | 2.9 | 6.49 | 1.84 | 22 | 8 |
| 0.25 | 1.3 | 6.39 | 0.92 | 10 | 8 |
| 0.1 | 0.46 | 6.55 | 0 | 19 | 8 |

Table 2. Evolution across the series of the paramagnetic temperature θ_p , the local anisotropy to exchange ratio $D/J(10)$, the correlation volume of anisotropy directions (normalized by the number of nearest neighbours Z). For $Z = 6$ we get $R_a \approx 2.7$ interatomic distances. The ferromagnetic correlation length R_f deduced from J/D and R_a is also given. * This value rather small is difficult to determine. It is somewhat different from the one of ref. 10 in which we used only the HPZ model.

| x | $\theta_p (\text{K})$ | D/J | $\Omega/a^3 \cdot 1/\sqrt{Z}$ | R_a/a | R_f/a | $R_f (\text{\AA})$ |
|------|-----------------------|-------|-------------------------------|---------|---------|--------------------|
| 1 | 14 | 0.95 | 8.5 | 2.7 | 2.6 | 6.5 |
| 0.75 | 25 | 0.74 | 9.3 | 2.8 | 4.4 | 11.0 |
| 0.5 | 38.5 | 0.55 | 8.5 | 2.7 | 8.0 | 20.0 |
| 0.25 | 51.5 | 0.32 | 9.7 | 2.9 | 23.0 | 57.5 |
| 0.1 | 58.6 | 0.10* | 8.3 | 2.7 | 240 | 600 |

$R_f = (60 \pi / \Omega) (A/K)^2$ where $\Omega \approx R_a^3$, $A = J/2a$ and $K = D/a^3$ (table 2). Taking for the mean distance between rare earth atoms $a \approx 2.5 \text{ \AA}$ we get correlations length ranging between 7 \AA to 600 \AA in our series of alloys. Small angle neutron scattering experiments on these samples should allow to check this findings for alloys with $x \leq 0.25$. For smaller x -values (i.e. for $\text{Dy}_{0.1}\text{Gd}_{0.9}\text{Ni}$) small angle neutron scattering experiments should be resolution limited.

We have analysed the high field magnetization curves of the series of amorphous alloys $a\text{-Dy}_x\text{Gd}_{1-x}\text{Ni}$ ($0.1 \leq x \leq 1$) in the framework of the theory of Chudnovsky et al(1). For $x \geq 0.25$ (anisotropy to exchange ratio $D/J \geq 0.32$) we have found the existence of a cross-over between the $1/\sqrt{H}$ regime and another regime in larger fields. On the other hand the gadolinium richest sample ($x = 0.1$, $D/J \approx 0.1$) shows a nice fit to the global expression of Chudnovsky(2) which includes both $1/\sqrt{H}$ and $1/H^2$ regimes. One of the consequences of this study is the determination, from magnetic measurements, of the mean correlation length of local anisotropy direction $R_a \approx 2.8a$ where a is the mean interatomic distance. This value agrees surprisingly well with the size of region with short range atomic order as determined by X-ray scattering.

ACKNOWLEDGEMENTS

We are grateful to E. Chudnovsky for very interesting discussions, and also for pointing out to us that the theory of the approach to saturation in amorphous alloys has been in similar terms discussed in Ref [11]. This work was partially supported by the INIC-JNICT/CNRS scientific exchange program and by a grant from Reitoria da Universidade do Porto, Fundação Gomes Teixeira is also acknowledges.

(1) Bolseiro do INIC para Doutoramento.

REFERENCES

1. E.M. Chudnovsky and R.A. Serota
Phys. Rev. B26, 2697 (1982) ; J. Phys. C16, 4181 (1983)
2. E.M. Chudnovsky, W.M. Saslow and R.A. Serota
Phys. Rev. 33, 251 (1986).
3. E.M. Chudnovsky, J. Magn. Magn. Mat. 79, 127 (1989).
4. For a review see E.M. Chudnovsky
J. Appl. Phys. 64, 5770 (1988).
5. D.J. Sellmeyer and S. Nafis, J. Appl. Phys. 57, 3584 (1985).
6. K.M. Lee, M.J. O'Shea and D.J. Sellmeyer
APS March meeting 1988, New Orleans.
7. M.J. O'Shea, K.M. Lee and A. Fert
J. Appl. Phys. 67, 2, 5769 (1990).
8. M.J. Park, S.M. Bhagat, M.A. Manheimer and K. Moorjani
Phys. Rev. B33, 2070 (1986).
9. P.M. Gehring, M.B. Salamon, A. del Moral and J.I. Arnandas
Phys. Rev. B41, 9134 (1990).
10. J. Filippi, B. Dieny and B. Barbara
Sol. State Comm. 53, 523 (1985).
11. V.A. Ignatchenko, R.S. Iskhakov and J.V. Popov
Zh. Eksp. Teor. Fiz. 82, 1518 (1982)
(Sov. Phys. JETP 55, 878 (1982)).

MAGNETORESISTANCE OF AMORPHOUS $U_{1-x}Sb_x$ FILMS

P.P. Freitas^{1,2} and T.S. Plaskett³

1-INESC, R. Alves Redol 9-3, 1000 Lisbon and

2-IST, Av. Rovisco Pais, Lisbon 1000 Portugal

3-IBM Research Division, T.J. Watson Research Center

P.O. Box 218, Yorktown Heights, NY 10598 USA

Amorphous $U_{1-x}Sb_x$ films were prepared by DC magnetron sputtering following our quest for amorphous U systems where the U is optically and magnetically active¹⁻³. This paper describes the transport and magnetic properties of these amorphous ferromagnets that show a 26% magnetoresistance anisotropy at saturation and at low temperature. This is a striking result since typical amorphous ferromagnets have magnetoresistance anisotropies not in excess of 1% at best. This quantity is defined as $(\rho_{\parallel} - \rho_{\perp})/\rho_{\perp}$ where ρ_{\parallel} and ρ_{\perp} are the resistivities at saturation when the magnetization is parallel or perpendicular to the current direction, and $\rho_{\perp} = (1/3)\rho_{\parallel} + (2/3)\rho_{\perp}$. Our results also show large excess resistivity at $\pm H_c$ when the field is applied perpendicular to the current, where H_c is the coercive field. This excess resistivity may be caused by the distortion of current lines by domain walls and scales with the square of the tangent of the Hall angle⁴.

Crystalline USb and U_3Sb_4 compounds order antiferromagnetically ($T_N = 213K$) and ferromagnetically ($T_c = 146K$) respectively⁵. All the Th_3P_4 compounds (U_3Sb_4 , U_3P_4 and U_3As_4) show anomalously large Hall angles⁶, Kerr rotations⁷ and resistivity and magnetoresistance anisotropies⁸. The 5f electrons are responsible for the U magnetic moment, that reaches $1.8\mu_B$ in U_3Sb_4 , while p-f and d-f hybridization plays a role in the highly anisotropic nature of the magnetic and transport properties.

The films are 2000Å thick and are overcoated with a 400Å SiO_2 passivation layer. Sample composition was checked by wet chemical analysis. X-ray data show the films to be amorphous, with none of the Bragg peaks correspondent to U_3Sb_4 and USb polycrystalline material. The U-U distances in the amorphous sample cannot be determined from our data alone. However, and as we shall see, the magnetic properties of these amorphous films are similar to those of crystalline U_3Sb_4 . This means that short-range order creates an environment where the U-U distances in the amorphous material are comparable to those found in the close packed Th_3P_4 type of body centered cubic crystal structure characteristic of

Table 1. Curie temperature, magnetic moment and coercive fields of amorphous $U_{1-x}Sb_x$ films

| X | T _c (K) | μ/μ_B | H _c (KOe) |
|------|--------------------|-------------|----------------------|
| 0.37 | 98 | 0.8 | 2 0 |
| 0.55 | 132 | 1.2 | 2 0 |
| 0.64 | 90 | 0.8 | 1 8 |

U_3Sb_4 compounds. In this case the U-U distance is 4.25\AA . According to the Hill plot⁹, it is this distance that determines the existence of a magnetic moment in the U atom.

Table 1 shows the Curie temperature, magnetic moment and coercive fields for three of the measured samples. Notice that the $x=0.55$ sample has a Curie temperature and a magnetic moment close to those quoted for crystalline U_3Sb_4 ($x=0.56$).

Ferromagnetism is still observed for $x=0.37$ and $x=0.64$ while the crystalline USb compound ($x=0.5$) is already antiferromagnetic.

All samples show large Hall angles reaching 20° at low temperature, values similar to those reported for the crystalline compounds⁶.

The coercive field H_c has a thermally activated temperature dependence similar to that found for amorphous Tb-Fe ferromagnets¹⁰, and reaches 20KOe at 10K.

Another feature of the low temperature magnetization of these materials is its dependence on the field cooling or zero-field cooling process. This is similar to what is found in spin-glasses and random-ferromagnets.

Transport properties were measured on rectangular samples typically 10 mm long, 2-3mm wide and 2000\AA thick. Collinear contacts were used and care was taken to avoid sample crystallization upon contact preparation. Sample resistivity at 10K ranges from 281 to $558\ \mu\Omega\text{cm}$ for $0.36 < x < 0.65$ respectively. These values are quite high even for an amorphous material, and are caused by the large effective masses of 6d and 5p conduction electrons. This is also the reason for the large resistivities found in the crystalline USb and U_3Sb_4 compounds⁵. Magnetoresistance measurements were done at 15K in a continuous flow cryostat and using an electromagnet (0-20kOe). One of the samples was measured in a superconducting magnet in fields up to 60kOe, to compare magnetoresistance and magnetization hysteresis cycles.

The resistivity of ferromagnets can be written as a sum of an isotropic spin-disorder term, $\rho_{sd} = \rho_{dis} - \alpha m_l^2$, and an anisotropic term related to the spin-orbit interaction, $\rho_{ani} = -\beta m_l^2$. Here ρ_{dis} is the magnetic resistivity well above T_c , m_l is the moment averaged over the mean-free path distance, and m_l is the component of m_l perpendicular to the current direction; α and β are constants.

$$\rho = \rho_{dis} - \alpha m_l^2 - \beta m_l^2 \quad (1)$$

The $-\beta...$ term describes the magnetization rotation with respect to the current direction, and is responsible for the resistivity anisotropy at saturation. This term predicts maxima in ρ_{\perp} at $\pm H_c$ when magnetization reversal occurs through rotation processes.

The $-\alpha...$ term is isotropic and reflects the spin correlations between U atoms on neighbor sites. Its behavior has been described in detail by Senoussi¹¹ for Ni-Mn spin-glasses. It is also responsible for the giant transverse hysteresis found in U-Tb random ferromagnets².

A third mechanism leading to low field magnetoresistance in crystalline or amorphous ferromagnets was introduced by Berger³. He showed that current lines are distorted by twice the Hall angle at 180° domain walls oriented perpendicular to the current direction. This gives rise to excess ohmic resistivity at H_c , $\Delta\rho/\rho_s$, scaling with β'^2 where β' is the tangent of the Hall angle and ρ_s the ρ_\perp value at saturation(no walls),

$$\frac{\Delta\rho}{\rho_s} = C\beta'^2 \quad (2)$$

C is a constant of order unity depending on the wall configuration. Eq.2 assumes that the wall spacing is much smaller than the sample width. This mechanism leads to peaks in ρ_\perp at the coercive field caused by the distortion of the current lines by the walls.

Fig.1 shows the resistance behavior versus applied field, at 10K, for the $x=0.55$ sample. The data was taken with the field applied in the plane of the sample either parallel or perpendicular to the current.

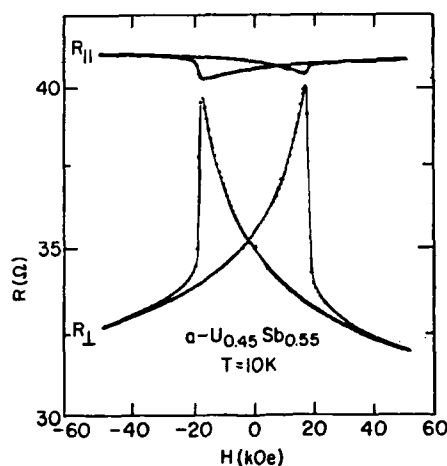


Fig.1-Magnetoresistance at 10K, for fields applied in the plane of the sample, either parallel or perpendicular to the current. Notice the 26% resistivity anisotropy at saturation and the large excess resistivity in ρ_\perp at $\pm H_c$.

First notice the giant resistance anisotropy observed at saturation and at this temperature, with

$$\frac{\Delta\rho}{\rho_o} = \frac{\rho_{\parallel} - \rho_{\perp}}{\rho_o} = 26\% \quad (3)$$

This means that $\beta \gg \alpha$ in these systems. This resistance anisotropy at saturation exceeds by far typical values found for transition-metal¹⁶ and rare-earth containing amorphous ferromagnets¹⁵.

Second, notice the sharp peaks of ρ_{\perp} at $\pm H_c$. These may correspond to the large excess resistivity predicted by Eq.3 since these samples have very large Hall angles with $\beta' \approx 0.13$. Third, but not least important, notice that there is only a slight variation in ρ_{\parallel} during magnetization reversal.

Let us start with the ρ_{\parallel} data. The upper curve in Fig.1 shows that ρ_{\parallel} never departs more than 1.5% from its saturation value during magnetization reversal. This is to be compared to a 26% decrease in the saturation resistivity when the magnetization becomes perpendicular to the current. We conclude that it is energetically favourable for magnetization reversal to proceed mainly through domain wall displacement, with the net magnetization direction induced by the applied field. In this case the current distortion mechanism will not contribute since domain walls are essentially parallel to the current.

Consider now the ρ_{\perp} curve. The net magnetization is now perpendicular to the current. This leads to domains with walls perpendicular to the current, and then the two sharp peaks observed at $\pm H_c$ can either be caused by current distortion at domain walls or by the anisotropic $-\beta m_{\perp}^2$ term. Since the magnetization reversal occurs mainly through domain wall motion as concluded above, the anisotropic term should give only a slight 1-2% increase in ρ_{\perp} over the magnetization reversal process. This cannot explain the 23% increase in ρ_{\perp} at $\pm H_c$ compared to the ρ_{\perp} saturation value. This leaves Eq.3 and the current distortion model as a good candidate to explain the sharp peaks of ρ_{\perp} observed at $\pm H_c$.

In Fig.2 we plot $\Delta\rho/\rho_s$ versus β'^2 for all our amorphous $U_{1-x}Sb_x$ samples. For comparison, we added data for a-U-Sb-Mn¹², a-Gd-Co³, a-Tb-Fe-Co¹³ and crystalline MnBi films³, and bulk Co at 4.2K¹⁴. The solid line corresponds to Eq.3 with $C=1$. We find a remarkable scaling of $\Delta\rho/\rho_s$ with β'^2 over four orders of magnitude in all these different systems. This shows that this mechanism involving the distortion of current lines by walls is probably responsible for the large excess resistivities found for ρ_{\perp} in the a- $U_{1-x}Sb_x$ systems.

Having explained the nature of the large excess resistivity in the perpendicular resistivity, we are still left with an intriguing phenomena, the large resistivity anisotropy at saturation.

Consider the anisotropic magnetoresistance caused by an anisotropic scattering cross section. In this case different resistivity values at saturation are obtained, depending on the angle between the magnetization and the current. This effect has been discussed in detail for 3d transition metals and 4f rare-earths. These existing models do not seem to apply to the present results.

For localized moments in amorphous rare-earths the magnetoresistance anisotropy arises from the quadrupole spin polarization¹⁵. This model also involves the hybridization of the 5d states with the conduction electrons. As the 5d admixed states lie close to the 4f shell they feel strongly the orbital anisotropy of this shell. This feature can be compared with p-f mixing in the actinides. Typical $\Delta\rho/\rho_c$ values predicted by this model are in the 10^{-3} to 10^{-4} range, almost two orders of magnitude smaller than the effects reported here.

The light actinides can also be viewed as transition-like metals with hybridized 5f-6d narrow bands superimposed on a broad 7s conduction band. For 3d tran-

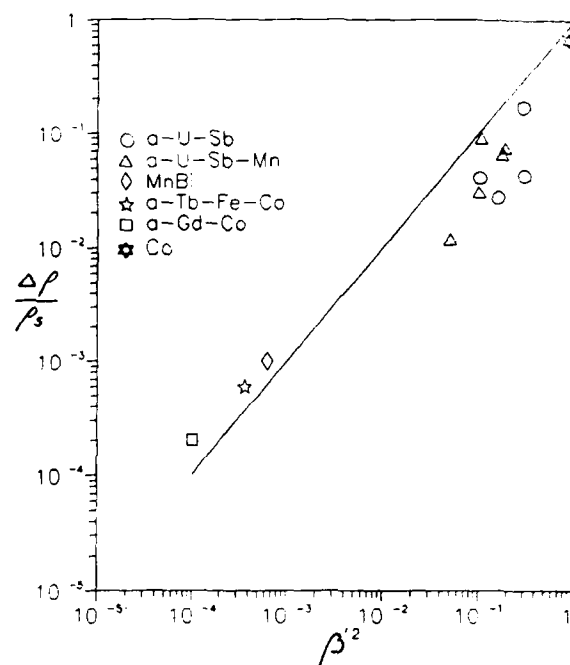


Fig.2-Plot of the excess resistivity $\Delta\rho/\rho_s$ at H_c versus the β'^2 where β' is the tangent of the Hall angle for different types of systems. The solid line corresponds to Eq.3 with $C=1$.

sition metals, and due to the spin-orbit interaction, the cross-section for electron scattering by impurities depends on the angle between the magnetization and the current directions¹⁶. This mechanism can lead to $\Delta\rho/\rho_0$ values of the order of 10^{-2} to 10^{-1} such as those found in the transition metal alloys, and of the order of those we find in the $U_{1-x}Sb_x$ amorphous films. The existing model for 3d metals uses spin-orbit interaction in perturbation theory to determine the perturbed spin-up and spin-down wave functions. Second, the two spin sub-bands are assumed to conduct in parallel (two-current model). The first hypothesis will certainly not work for the 5f systems where spin-orbit is much larger than in the 3d metals. Also, there is no proof for the validity of the two current model in the 5f systems.

This means that the observed giant resistivity anisotropy in these 5f amorphous systems cannot be described within existing models. We hope that this work will stimulate theoretical studies leading to the understanding of this phenomena.

ACKNOWLEDGEMENTS

We thank T.McGuire, T.Penney, S.von Molnar, R.Gambino, J.M.D.Coey and L.Berger for helpful comments during different stages of this work.

REFERENCES

- 1-P.P.Freitas and T.S.Plaskett, Phys.Rev.Lett.64,2184(1990)
- 2-J.M.D.Coey, P.P.Freitas and T.S.Plaskett, Phys.Rev.B41,9585(1990)
- 3-P.P.Freitas,T.S.Plaskett, J.M.Moreira and V.S.Amaral, J.Appl.Phys.64,5453(1988)
- 4-L.Berger, J.Appl.Phys.49,2156(1978)
- 5-J.Fournier and R.Troc. in Handbook on the Physics and Chemistry of the Actinides, A.J.Freeman and G.H.Lander,ed. (North-Holland,Amsterdam,1985),p.29
- 6-Z.Henkie,Bull.Acad.Polan.Sci.,Ser.Sci.Chim.20,531(1972)
- 7-W.Reim,J.Schoenes and P.Wachter, IEEE Trans.Mag. MAG-20,1045(1984)
- 8-Z.Henkie.Physica 102B,329(1980)
- 9-H.H.Hill, in Plutonium 1970 and other Actinides, W.N.Miner,ed. (The Metallurgical Society of the AIME,New York,1970),p.2
- 10-J.J.Rhyne,J.H.Schelleng and N.C.Koon,Phys.Rev.B10,4672(1974)
- 11-S.Senoussi, Phys.Rev.Lett.56,2314(1986)
- 12-P.P.Freitas and T.S.Plaskett, J.Appl.Phys.(May 1990)
- 13-P.P.Freitas, L.V.Melo and T.S.Plaskett. in Proceedings of INTERMAG'90
- 14-V.R.V.Ramanan and L.Berger, J.Appl.Phys.52,2211(1981)
- 15-A.Fert,R.Azomosa,D.H.Sanchez, and D.Spanjaard, Phys.Rev.B11,5040(1977)
- 16-O.Jaoul,I.A.Campbell and A.Fert,J.Magn.Magn.Mater.5,23(1977)

ABSENCE OF TEMPERATURE-DRIVEN FIRST-ORDER PHASE TRANSITIONS
IN SYSTEMS WITH RANDOM BONDS

A. Nihat Berker and Kenneth Hui*

Department of Physics
Massachusetts Institute of Technology
Cambridge, Massachusetts 02139, USA

Temperature-driven first-order phase transitions are converted to second-order phase transitions by the introduction of infinitesimal bond randomness, in spatial dimensions $d \leq 2$ or $d \leq 4$, respectively for systems composed of discrete or continuous microscopic degrees of freedom. Above these dimensions, this phenomenon still occurs, but requires a threshold amount of bond randomness. This quenched-fluctuation-induced criticality occurs for phase transitions involving a symmetry breaking. If no symmetry breaking is involved at the first-order transition, the phase transition is eliminated under the above conditions.

QUENCHED-FLUCTUATION-INDUCED CRITICALITY

A general renormalization-group argument for the above effects is presented here. To be precise, a first-order phase transition is any phase boundary point where the thermodynamic phases that are bounded coexist. A second-order phase transition is any phase boundary point where the thermodynamic phases that are bounded do not coexist; it is presumed (and empirically verified) that, at such a point, the macroscopic change from one thermodynamic phase to another is mediated (in the absence of coexistence) by long-range correlations (and the attendant critical singularities). The argument here is the extension, via the visualisation of global renormalization-group flows, of an argument originally presented¹ for the effect of bond randomness on tricritical and critical-endpoint systems. Independently and simultaneously, Aizenman and Wehr's rigorous mathematical work² has shown that in $d=2$ quenched randomness results, quite generally, in the elimination of discontinuities in the density conjugate to the random interaction.

The renormalization-group mechanism³⁻⁵ for temperature-driven first-order phase transitions is depicted in Fig. 1(a). In this figure, J_1 is a dimensionless coupling constant, i.e.

$$J_1 = K_1/kT, \quad (1)$$

with K_1 (with dimension of energy) being the coupling constant fixed by the

* Current address: Department of Chemistry, University of California, Berkeley, California 94720, USA

underlying physical system, so that J_1^{-1} is proportional to temperature T . J_2 represents the interactions generated under renormalization-group transformations. Under such transformations, an initial system at the phase transition (point A in Fig. 1(a)) flows to the fixed point F^* . This fixed point occurs at zero temperature, where the statistical mechanics simplifies to ground states crossing each other. At F^* , the correlation length ξ equals zero, so that $0 < \xi < \infty$ on renormalization-group trajectories flowing into F^* , including the point A. In fact, the renormalization-group flow topology of Fig. 1(a) is required for first-order phase transitions because, by contrast, a fixed point occurring at finite (non-zero, non-infinite) temperature and trajectories flowing into such a fixed point have $\xi = \infty$, implying critical (second-order) behavior.⁶

Similarly, a quenched-random-bond system, with a distribution $\{J_1\}$ of bond strengths given, for example, by the range \mathcal{A} in Fig. 1(b) maps, under the renormalization-group transformations, onto the range \mathcal{B} in the same figure. (Underlying the latter statement is that the renormalization-group transformation is a non-singular local transformation, namely that a localized set of interactions fix, smoothly, the renormalized interaction of a locality.) Note that in the neighborhood of what was F^* , the segment \mathcal{B} exhibits, at low temperature (strong coupling), randomness transverse to what was the first-order (coexistence) boundary. Thus, we effectively have a random-field situation where the arguments of Imry and Ma apply.

Imry and Ma⁷ have argued, and it is now generally accepted, that random fields destroy first-order coexistence in spatial dimensions $d \leq 2$ for systems composed of $n=1$ component spins (Ising models) and $d \leq 4$ for systems composed of $n \geq 2$ component spins (e.g., XY and Heisenberg models). The Imry-Ma mechanism is that would-be coexistent phases become indistinguishable, as it becomes energetically favorable to nest arbitrary domains of each in the other. The applicability of this mechanism is seen by comparison of the random-field energy lowering and domain-wall energy gain in the formation of arbitrary domains. Similarly, their two categories can be expanded to include, respectively, systems composed of discrete microscopic degrees of freedom (e.g., Potts models, melting in registry with a substrate) and systems composed of continuous degrees of freedom (e.g., melting in a free-standing environment, liquid-crystal transitions).

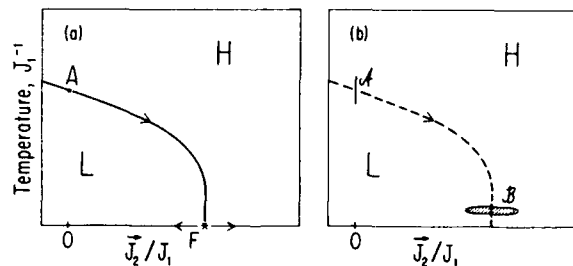


Fig. 1. (a) Renormalization-group mechanism for temperature-driven first-order phase transitions. The strong-coupling fixed point F^* has an eigenvalue exponent equal to dimensionality, $y=d$, along its direction of instability (Ref. 3). (b) The system with random bonds distributed over range \mathcal{A} maps, under repeated renormalization-group transformations, onto range \mathcal{B} . The dashed line shows the phase boundary, given by the renormalization-group flows of average interactions.

Accordingly, in our case, the original random bonds $\{J_1\}$ remove the temperature-driven first-order transitions for $d \leq 2$ and $d \leq 4$ respectively, since removal of coexistence in the renormalized system implies the same for the original system. In Fig. 1(a), if the thermodynamic phase L involves a symmetry breaking with respect to the phase H, random bonds $\{J_1\}$ will not remove this symmetry breaking (the persistence of symmetry breaking under bond randomness can be seen by Peierls-type arguments), nor induce it in H. Thus, a boundary of singularities will continue to exist between L and H. This boundary will not be a first-order phase boundary because of the preceding argument, and thus has to be a second-order (critical) phase boundary. By contrast, if there is no symmetry breaking between the two phases, the boundary between them should be simply eliminated by the bond randomness.

In the higher dimensions complementing the above conditions, $d > 2$ for the discrete degrees of freedom and $d > 4$ for the continuous degrees of freedom, the Imry-Ma argument indicates first-order coexistence at low temperatures in the presence of infinitesimal random fields. Calculations on the random-field problem show that a threshold amount of random-field strength is required for the coexistence to disappear, as shown in Fig. 2 reproduced here from McKay and Berker.⁸ In our present consideration, this is equivalent to a threshold extent of range \mathcal{B} in Fig. 1(b), in turn requiring a threshold extent of range \mathcal{A} in the same figure. Accordingly, in the high-dimension regimes, a threshold amount of bond randomness is required to convert a temperature-driven first-order transition into second-order, presumably via a tricritical point, when it involves a symmetry breaking (or, to eliminate it, presumably via an isolated critical point, when it does not involve a symmetry breaking).

It will be seen in the following that this simple, very general reasoning is supported by works on specific systems.

In the previous work,¹ this argument was in fact tested by an approximate renormalization-group calculation on the Blume-Emery-Griffiths (spin-1 Ising) model,^{9,4}

$$-\beta\mathcal{H} = \sum_{\langle ij \rangle} J_{ij} s_i s_j + K \sum_{\langle ij \rangle} s_i^2 s_j^2 - \Delta \sum_i s_i^2, \quad s_i = 0, \pm 1, \quad (2)$$

where $\langle ij \rangle$ indicates summation over all nearest-neighbor pairs of sites i and j of a hypercubic lattice. The renormalization-group recursion of the quenched probability distribution of interactions,⁸

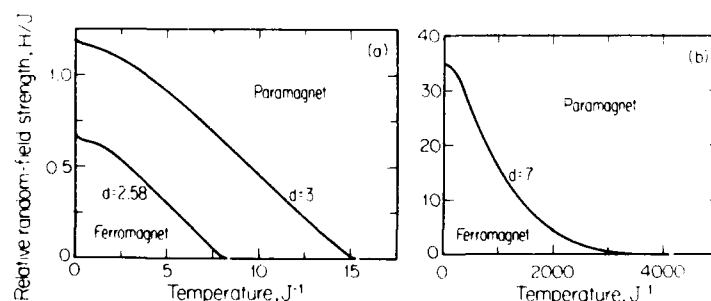


Fig. 2. Calculated phase diagrams, from McKay and Berker,⁸ for the random-field Ising model for dimensionalities $d=2.58$, 3, and 7. The ferromagnetic phase at non-zero random field (i.e. off the horizontal axis) vanishes at $d=2$.

$$\mathcal{P}'(\vec{V}') = \int \left[\prod_{\langle ij \rangle} d\vec{V}_{ij} \mathcal{P}(\vec{V}_{ij}) \right] \delta(\vec{V}' - \vec{R}(\{\vec{V}_{ij}\})) , \quad (3)$$

where $\vec{V}_{ij} = (J_{ij}, K_{ij}, \Delta_i, \Delta_j)$ and \vec{R} are the local recursion relations, was effected by approximating the renormalized distribution \mathcal{P}' by 16 bins and by using the Migdal-Kadanoff approximation for the local recursion relations.

In agreement with the a priori argument, it was found¹ that, under random bonds $\{J_{ij}\}$ in $d=2$, all first-order transitions involving symmetry breaking are converted to second-order, and all first-order transitions not involving symmetry breaking are eliminated. This is illustrated in Figs. 3(a,b) for systems that have tricritical ($K/J=0$) and critical-endpoint ($K/J=1$) phase diagrams before the application of randomness. Thus, both tricritical points and critical endpoints are eliminated by bond randomness. It was also found¹ that, in $d=3$, the first-order phase transitions recede gradually with the introduction and increase of bond randomness $\{J_{ij}\}$.

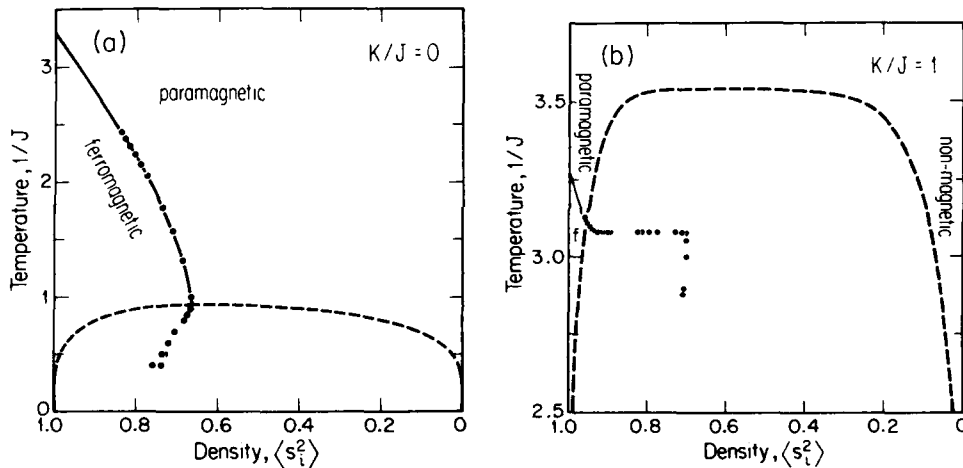


Fig. 3. (a) Effect of bond randomness on a tricritical phase diagram of the Blume-Emery-Griffiths model, from Ref. 1. The curves are calculated for the pure system, with the dashed curve enclosing the coexistence region of the first-order transition. The dark circles are the calculated phase-boundary points for the random-bond system with $\mathcal{P}(J_{ij}) = [\delta(J_{ij} - J + \sigma) + \delta(J_{ij} - J - \sigma)]/2$, $\sigma = J/4$. The lowest phase-boundary point is split, because of the more than 14-digit accuracy in chemical potential needed to reach the phase boundary from either side.

(b) Effect of bond randomness on a critical-endpoint phase diagram of the Blume-Emery-Griffiths model, from Ref. 1. The curves are calculated for the pure system, with the dashed curve enclosing the coexistence region of the first-order transitions between the ferromagnetic (f) and non-magnetic phases and between the paramagnetic and non-magnetic phases. The latter does not involve symmetry breaking and is eliminated by the bond randomness. The dark circles are the calculated phase-boundary points for the random-bond system with $\mathcal{P}(J_{ij}) = [\delta(J_{ij} - J + \sigma) + \delta(J_{ij} - J - \sigma)]/2$, $\sigma = J/4$.

Furthermore, it was realized¹ that the disappearance of tricriticality under bond randomness in $d=2$ has an important consequence for q -state Potts models,

$$-\beta\mathcal{H} = J \sum_{\langle ij \rangle} \delta_{s_i s_j}, \quad s_i = 1, 2, \dots, q, \quad (4)$$

where $\delta_{s_i s_j} = 1$ (0) for $s_i = s_j$ ($s_i \neq s_j$). The renormalization-group solution⁵ of these models is imbedded in the Potts-lattice-gas models,¹⁰ where as the number of states q is increased, a critical fixed point and a tricritical fixed point approach each other, merging and annihilating at q_c , thereby clearing the way for renormalization-group flows to a first-order fixed point for $q > q_c$. With the introduction of bond randomness, in $d=2$, tricriticality should be eliminated and this mechanism for the changeover of the transitions from second-order to first-order cannot occur. Thus, it was concluded¹ that random-bond Potts models have second-order transitions for all q in $d=2$, namely q_c is changed from 4 to ∞ by bond randomness. In fact, independently and simultaneously, Aizenman and Wehr's rigorous mathematical work² has shown that there is no latent heat at the phase transition of random-bond Potts models for all q in $d=2$.

To continue our discussion to $d > 2$, we define q_c to be the number of states of the Potts model where, for fixed randomness, the transition changes from second-order to first-order (in $d=2$, $q_c=4$ for zero randomness and $q_c=\infty$ for any bond randomness). In $d > 2$, since bond randomness causes first-order phase transitions to recede only gradually, infinitesimal bond randomness should not convert finite first-order behavior to second-order (in contrast to $d=2$). Thus, in any given $d > 2$, q_c will increase, with increasing bond randomness, continuously from its non-random value. However, since we have argued that, for any system, first-order coexistence can be eliminated by a threshold amount of bond randomness (cf. our discussion above centered around Fig. 2), for any $q > q_c$ Potts model, the first-order transition can be converted to second-order with application of enough bond randomness, presumably with an intermediate tricritical point.

The above has been seen with Monte Carlo numerical simulations. In $d=2$, for the $q=5$ Potts model, Wilson and Vause¹¹ have reported a "termination" of the first-order phase transition for a quenched site dilution (which is equivalent to bond randomization) of only 2.6% on the square lattice and of only 1.4% on a Penrose lattice. We believe that this is consistent, within the limits of numerical simulation, with our predicted change in $d=2$ from first-order to second-order behavior with infinitesimal bond randomization. In $d=3$, for the $q=3$ Potts model, Wilson¹² has reported a change from first-order to second-order behavior, via a tricritical point, for a quenched site dilution of 13.5% and for a quenched bond dilution of 23.5% on the cubic lattice.

Finally, the generality of our argument is seen via yet another model. In previous work, Murthy¹³ has found that in the $d=2$ N -component Ashkin-Teller model, first-order transitions are converted to second-order by the introduction of bond randomness.

CONCLUDING REMARKS; EXPERIMENTAL PROSPECTS

The conversion of first-order phase transitions to second-order, by the introduction of quenched disorder (in infinitesimal amount in $d=2$) is conceptually rather fascinating. (Also note the interesting diametric opposition of the quenched-fluctuation-induced second-order transitions here to the well-studied annealed-fluctuation-induced first-order transitions.¹⁴) At the most phenomenological level, an a posteriori explanation is that

locally strong or weak couplings pin down the ordered or disordered phases, respectively, and prevent phase separation (a.k.a. phase coexistence). At the same time, correlations of the ordered phase propagate (via convoluted paths) and increase as temperature is lowered, causing criticality.

Furthermore, this effect points to literally infinitely many new universality classes of criticality, for example with the criticality of $q > 4$ Potts models^{1,2} in $d=2$ and the tricriticality and criticality of $q \geq 3$ Potts models¹² in $d=3$. These unexplored systems should excite experimentalists on fundamental grounds. Moreover, the interest for possible device applications of the phenomenon presented in this paper is (i) the avoidance of the hysteresis of first-order transitions and (ii) the introduction of the large response functions of second-order transitions. However, this brings us to a practical question: It may be difficult to prepare an experimental system with random bonds without also random fields (these actual random fields couple, randomly at each locality, to the differently broken symmetry states, whereas the effective random fields of our argument couple, randomly at each locality, to the symmetry unbroken and broken states, without distinguishing between the latter). In $d=3$, this is not a concern, since ordering persists under the actual random fields¹⁵ for systems with discrete degrees of freedom and the above effect should take place due to the bond part of randomness. In $d=2$, however, ordering is destroyed by the actual random fields, which should therefore be avoided.

There are ways to create random-bond systems without actual random fields. Systems with quenched vacancies are the simplest examples. Doping crystals with atoms of different sizes has been effected for KMnF_3 undergoing structural transition,¹⁶ and it appears that the effect we present here was seen. Finally, we propose here an experimental method that would be applicable to complex fluids: If two laser beams are crossed within the sample, after being reflected from rough surfaces, a static random distribution of local temperatures will be created, which by Eq.(1) is equivalent to a random-bond situation.

ACKNOWLEDGEMENTS

We thank M. Aizenman, K. Nelson, R. Shankar, and J. Wehr for useful discussions. This research was supported by the National Science Foundation under Grant No. DMR-87-19217 and by the Joint Services Electronics Program under Contract No. DAAL 03-89-C0001.

REFERENCES

1. K. Hui and A.N. Berker, Phys. Rev. Lett. **62**, 2507 (1989); erratum **63**, 2433 (1989).
2. M. Aizenman and J. Wehr, Phys. Rev. Lett. **62**, 2503 (1989).
3. B. Nienhuis and M. Nauenberg, Phys. Rev. B **13**, 2021 (1976).
4. A.N. Berker and M. Wortis, Phys. Rev. B **14**, 4946 (1976).
5. B. Nienhuis, A.N. Berker, E.K. Riedel, and M. Schick, Phys. Rev. Lett. **43**, 737 (1979).
6. K.G. Wilson and J. Kogut, Phys. Rep. C **12**, 75 (1974).
7. Y. Imry and S.-k. Ma, Phys. Rev. Lett. **35**, 1399 (1975).
8. S.R. McKay and A.N. Berker, J. Appl. Phys. **64**, 5785 (1988).
9. M. Blume, V.J. Emery, and R.B. Griffiths, Phys. Rev. A **4**, 1071 (1971).
10. A.N. Berker, S. Ostlund, and F.A. Putnam, Phys. Rev. B **17**, 3650 (1978).
11. W.G. Wilson and C.A. Vause, Phys. Lett. A **134**, 360 (1989).
12. W.G. Wilson, Phys. Lett. A **137**, 398 (1989).
13. G.N. Murthy, Phys. Rev. B **36**, 7166 (1987).

14. P. Bak, S. Krinsky, and D. Mukamel, Phys. Rev. Lett. 36, 52 (1976).
15. I.B. Ferreira, A.R. King, V. Jaccarino, J.L. Cardy, and H.L. Guggenheim, Phys.Rev. B 28, 5192 (1983).
16. U.J. Cox, A. Gibaud, and R.A. Cowley, Phys. Rev. Lett. 61, 982 (1988).

MAGNETIC BEHAVIOR OF DILUTED MAGNETIC SEMICONDUCTORS

W.J.M. de Jonge and H.J.M. Swagten

Department of Physics, Eindhoven University of Technology (EUT)
Eindhoven, The Netherlands

ABSTRACT

The magnetic characteristics of Diluted Magnetic Semiconductors are reviewed and related to the exchange interactions and mechanisms. The relevance of the long-range interactions in II-VI DMS is emphasized. An analytical expression for the radial dependence is derived from the freezing temperature and compared with theoretical predictions. The magnetic properties of Fe-DMS are summarized and interpreted on the basis of the dominant crystal field splitting effects. Recent studies on IV-VI Mn DMS are presented with the emphasis on the new phenomena of carrier induced ferromagnetism.

INTRODUCTION

Diluted Magnetic Semiconductors (DMS) or, as they are sometimes called, Semimagnetic Semiconductors, are a relatively new class of materials, consisting generally of a nonmagnetic host in which a controlled fraction of cations is replaced by magnetic ions. The fundamentally as well as technologically interesting and characteristic features of DMS have attracted considerable attention during the past years and are directly related to the coupling between the two interacting subsystems: the electronic system of the carriers and the (diluted) magnetic system of paramagnetic ions. Most of the investigations have been devoted to the class of the II-VI compounds diluted with Mn, such as $\text{Cd}_{1-x}\text{Mn}_x\text{Te}$, $\text{Zn}_{1-x}\text{Mn}_x\text{Te}$, $\text{Hg}_{1-x}\text{Mn}_x\text{Te}$ and corresponding selenides and sulfides although also compounds like $(\text{Cd}_{1-x}\text{Mn}_x)_2\text{As}_3$ and $(\text{Zn}_{1-x}\text{Mn}_x)_2\text{As}_3$ have been studied. Recently also results have been reported on DMS containing other transition metal magnetic ions, such as Fe, Co. Extensive reviews on the semiconducting as well as the magnetic properties of specifically II-VI DMS have appeared recently^{1,2}.

As for the semiconducting properties, striking effects were observed such as: a giant Faraday rotation, anomalous and large magneto-resistance effects as well as significant bandstructure modification in moderate magnetic fields^{1,2}. Generally spoken, these effects can be traced back to the field enhancement and polaron formation brought about by the interaction between carriers and magnetic ions.

Magnetically the behavior of these systems^{1,2} originates from the interactions between the magnetic ions, which are in general mediated by the carriers. Typically these interactions are antiferromagnetic (AF) and long ranged (with significant and systematic variations in range depending on covalency or bandgap). A spin-glass phase is found at low magnetic ion concentrations (Mn^{2+} as well as Fe^{2+} and Co^{2+}) extending to the very dilute limit. At higher concentrations sometimes AF ordered regimes are reported. Since the carrier concentration is in general relatively low ($n, p < 10^{19} \text{ cm}^{-3}$), the well known Ruderman Kittel Kasuya Yoshida (RKKY) interaction, which is proportional to the carrier density, is too small to account for the interaction between the magnetic ions. A number of alternative physical mechanisms, involving different bands, might be responsible for these interactions. A substantial number of papers have been devoted to this subject^{1,4}. Recent theoretical results seem to indicate that, at least for the interactions between nearest neighbors, superexchange might be the dominant mechanism⁴. These nearest-neighbor interactions cannot, however, be responsible for the observed spin-glass transition in the dilute limit, which is claimed to be triggered primarily by the long-range part of the exchange interaction⁵.

As we quoted above, the carrier concentration in the II-VI DMS is generally rather low. Several IV-VI DMS however exhibit a much higher carrier concentration in the range of 10^{19} – 10^{21} cm^{-3} , caused by deviations from stoichiometry. In contrast to the II-VI DMS some of these systems, such as $\text{Sn}_{1-x}\text{Mn}_x\text{Te}$ and $(\text{PbGe})_{1-x}\text{Mn}_x\text{Te}$, show ferromagnetic ordering phenomena, implicating a rather different exchange mechanism. Furthermore Story et al.⁶ reported the observation of a carrier concentration induced ferromagnetic transition in $\text{Pb}_{0.25}\text{Sn}_{0.72}\text{Mn}_{0.03}\text{Te}$ (PSMT) above a critical concentration p_{crit} . Analogous effects were reported recently for other compositions including $\text{Sn}_{1-x}\text{Mn}_x\text{Te}$. This striking demonstration of the influence of the carrier concentration on the magnetic properties is facilitated by the significant range of carrier concentrations which can be realised in this system. A RKKY interaction between localized moments, resulting from intra-band scattering of the charge carriers by the magnetic moments, seems to be the only interaction that is strong enough and sufficiently long ranged to explain the magnitude of the observed critical temperatures in these IV-VI compounds. The abrupt change in T_c at the critical hole density p_{crit} is PbSnMnTe , however, cannot be understood by the original RKKY model, modelled for free (parabolic) electrons. A modified RKKY model was proposed by Swagten et al.⁷, in which also carriers which are located at different regions of the Brillouin zone contribute to the RKKY interaction. The intriguing increase of interactions at p_{crit} is then attributed to the entrance of the Fermi-level into a second set of heavy hole valence bands, located along the Σ -axis. On the basis of this more realistic two valence band model a satisfactory description of the carrier concentration dependence in these IV-VI DMS can be obtained.

This paper is focussed on the magnetic behavior of DMS. Since, as we quoted before, excellent reviews have appeared on the II-VI Mn-diluted compounds, we will emphasize a few items which have not yet been included i.e. the relevance of long-range interactions, Fe-diluted II-VI DMS and the IV-VI DMS introduced above.

Exchange interactions

In DMS two subsystems can be distinguished. The carrier subsystem, characterised by a band structure, and the system of magnetic ions (Mn^{++} or other transition metal ions) which can be treated as isolated, with energy levels of the relevant d orbitals superimposed on the band structure.

One of the basic ingredients, which determines the cooperative magnetic behavior in these systems, is the exchange interaction between the magnetic ions (d-d

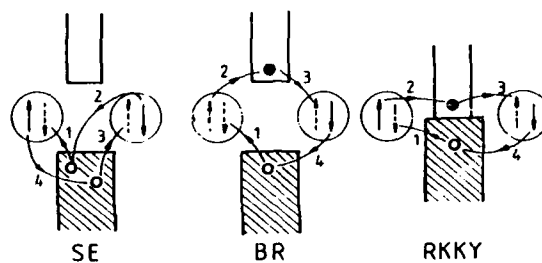


Fig. 1

Schematic representation of the exchange processes superexchange (SE), Bloembergen-Rowland (BR) and Ruderman-Kittel-Kosuya-Yosida (RKKY). The filled valence bands, empty conduction band, Mn spin states and transitions are shown; based on Ref. 4.

interaction). Since direct overlap of the 3d wave functions can be neglected in these structures, interaction can only take place via indirect processes. The indirect exchange can be regarded as consisting of three processes. First, a exchange between the d-electrons of the localized magnetic moments and the s- or p-orbitals of the band electrons exists, which is referred to as sp-d exchange or alternatively sp-d hybridisation. Secondly, a direct interaction between the polarized electrons takes place, which is followed by secondary sp-d exchange processes with other magnetic moments. Because of the important role of the charge carriers in these processes, the band structure of the electrons (or holes), together with the number of charge carriers and the interatomic distances between the manganese ions completely determines which indirect exchange mechanism is dominant. The various processes are schematically illustrated in Fig. 1. An elaborate review on the indirect exchange mechanisms is given by Larson et al.⁴ who concluded from theoretical calculations that in II-VI Mn DMS superexchange (involving only two hole processes in the valence band, see Fig. 1) is the dominant Mn-Mn exchange mechanism, while the one hole-one electron process (Bloembergen-Rowland mechanism) accounts for only a few percent, and the contributions of two electron processes, involving only carriers at the Fermi-level (RKKY mechanism), is negligible. For IV-VI DMS, however, the latter mechanism is the dominant mechanism, at least for higher carrier concentrations, as we shall see later on.

II-VI DMS

Relevance of the long-range of the interaction

From the available data on a large number of Mn-DMS a rather characteristic behavior can be deduced⁸⁻¹⁰. The essential features (for low Mn concentration x) are:

1. Curie-Weiss behavior of the magnetic susceptibility, $C/(T-\Theta)$, at high temperatures, with negative Θ indicating antiferromagnetic Mn-Mn interactions.
2. A cusp or kink in the low temperature χ , indicating a spin-glass like transition at a temperature T_F which decreases continuously with the Mn concentration x even in the limit $x \rightarrow 0$.
3. A continuous magnetic contribution to the zero-field specific heat C_m with a broad maximum in the ^4He temperature region, shifting to higher T with x , indicating a range of exchange splitted Mn energy levels.
4. A field dependence of the magnetization indicating AF Mn-Mn interactions, in some cases accompanied with discrete steps¹⁰.

Originally the magnetic behavior has been interpreted as arising from interactions between Mn-ions, situated at nearest neighbor sites (NN) in the host lattice *only*¹¹. The use of this model was strongly supported by the early observation that the spin-glass transition was restricted to DMS with a magnetic ion concentration *x* above the percolation limit, x_c , of the host lattice. From this observation it was concluded that the transition was induced by short range AF (nearest neighbor) interactions causing topological frustration effects due to the cubic symmetry of the host lattice. Subsequent calculations on the basis of this conjectured short-range interaction only, however, did not yield a consistent set of interaction parameters, explaining all the data simultaneously.

The most convincing evidence for the long-range character of the exchange interaction (that is the extension beyond nearest neighbors) is provided by the observation of the transition to the spinglass state at the so-called freezing temperature T_F for Mn concentrations far below the percolation limit x_c , which amounts to 17% for f.c.c. structures. This behavior, which was first noted¹² in $(\text{CdMn})_3\text{As}_2$ has been documented since for almost all known DMS¹³. This extension of T_F down to zero in the dilute limit cannot be understood on the basis of nearest neighbor interactions, but strongly indicates the existence of a long-ranged interaction as the driving mechanism behind this transition. It should be noted at this point that a transition to a spin-glass state in these type of materials (which is supported by experimental evidence¹⁴) is of fundamental interest on itself, since spin-glass transitions in random arrays coupled only by AF interactions represent a new type of spin-glass^{5,15}.

If one accepts the nature of the transition as a spin-glass freezing, then a scaling analysis should be applicable. Such a scaling analysis generally exploits the fact that for a continuous random distribution it is assumed that $R_{ij}^3 x = \text{const}$, where R_{ij} denotes a typical distance between the ions. Implementation of this expression in a model for spin-glass freezing, given a known functional form for the radial dependence of the exchange interaction, then yields a theoretical prediction for $T_F(x)$ which can be compared with experimental data. Details of this procedure can be found elsewhere for a continuous as well as a discrete distribution of ions¹⁶. In the spirit of earlier analyses¹⁷ the spin-glass-freezing condition is based on the conjecture that T_F is related to the interaction energy at the average distance (\bar{R}) between the magnetic ions, e.g.,

$$k_B T_F \approx J(\bar{R}) S^2. \quad (1)$$

Given a power-law dependence of the interaction, the concentration dependence of T_F can be expressed as

$$\ln(T_F) \sim \frac{n}{3} \ln(x) \text{ for } J(R) = J_0 R^{-n}. \quad (2)$$

As the power-law behavior of $J(R)$ is chosen somewhat arbitrarily (although inspired by earlier theoretical predictions³) it may be replaced by more adequate functional forms. However, it describes the data remarkably well in the whole concentration range as is shown in Fig. 2, where the freezing temperature for a number of Mn DMS is plotted versus concentration.

This analysis therefore provides a probe for the spatial extension of the d-d interaction strength in the various systems, which can hardly be obtained any other way. The results can be used subsequently to calculate the magnetic behavior, as summarized before, and for comparison with the theoretical predictions concerning physical mechanisms, chemical trends, etc.

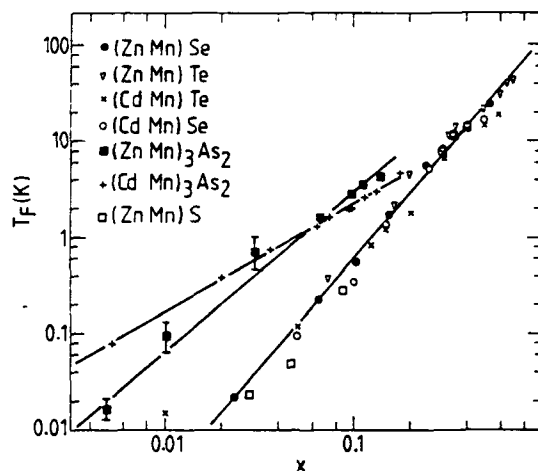


Fig. 2

Freezing temperatures as a function of the Mn-concentration x for several DMS on a logarithmic scale; the drawn lines yield the power dependences $J(R) \sim R^{-n}$ (see Table I); see Ref. 9,16,18,40.

The calculation of the thermodynamic properties of an infinite, random ensemble of spins, all coupled to each other by a long-ranged AF interaction $J = -|J_0|R^{-n}$, requires an approximative calculation method. It was shown that the so-called Extended Nearest Neighbour Pair Approximation (ENNPA) is particular useful for this purpose¹⁸. The essential ingredient of this approximation, first suggested by Matho¹⁹, is the assumption that the partition function of the ensemble of random spins can be factorized into the contribution of pairs. In this case a pair consists of a Mn-spin coupled to its neighbouring Mn-spin, which can be located anywhere as prescribed by the statistics in a random array.

Since the size of this paper is rather limited we will not report on the results for each DMS system in detail. Instead we exemplify the results by the figures 3-5, which all refer to (CdMn)Te. Results for other systems show basically the same features. We would like to emphasize that no efforts have been undertaken yet to adjust the parameters in order to obtain a better overall fit to the data.

From the comparison shown in figures 3-5 we would like to conclude that, on the whole, the agreement between calculated results, using reported values for the interaction, and the data is fair and shows that a model which includes the long-range nature of the interaction is in principle capable of explaining the overall magnetic behavior in DMS. A more detailed comparison can be found in the references^{8-10,16}.

As quoted in the introduction, Larson et al.⁴ found theoretically that superexchange is the dominant mechanism contributing to the d-d exchange. They were able to calculate J_{NN} and J_{NNN} in CdMnTe and the detailed results were used to construct a simplified so-called three level model, in which only the most relevant characteristics of the electronic structure are contained and which permits the extension of their results to other DMS. The relevant levels are schematically indicated in Fig. 6 and determine together with the hopping parameter V_{dp} , (characterizing the hybridisation between Mn d-orbitals and anion p-orbitals contained in the valence band), the strength of the NN exchange. Introducing a simplified k dependence of the levels yields an R dependence of the exchange $f(R_{ij})$ which is claimed to be "material insensitive", that is independent of electronic

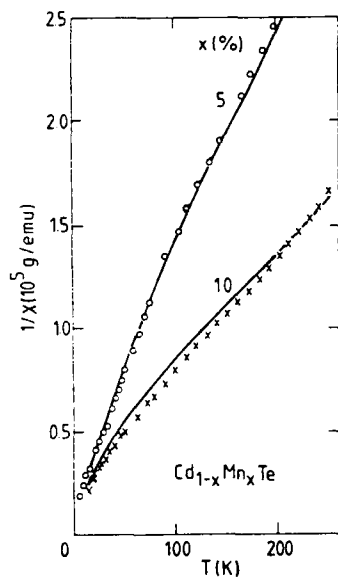


Fig. 3

Inverse high temperature susceptibility¹¹ of (Cd,Mn)Te; solid lines are ENNPA calculations with $J(R) = -10 R^{6.8} K$.

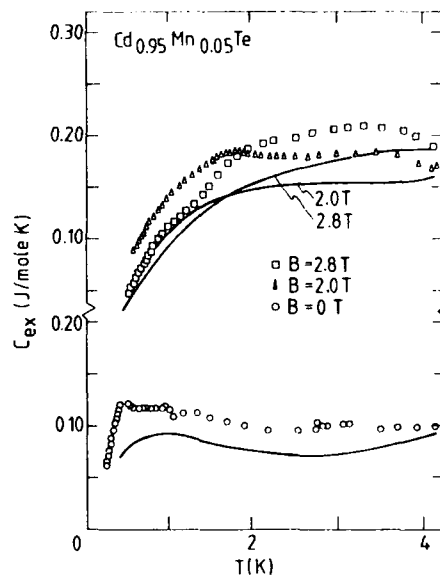


Fig. 4

Magnetic specific heat of $Cd_{0.95}Mn_{0.05}Te$ ¹¹; Solid lines represent ENNPA calculations using $J(R) = -10 R^{6.8} K$.

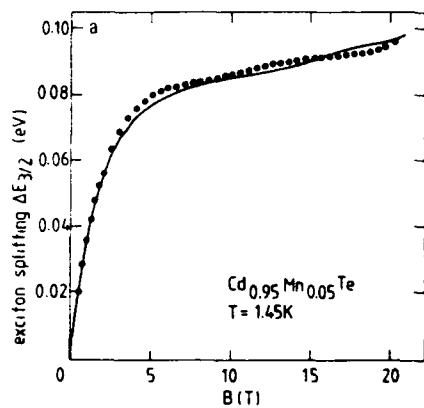
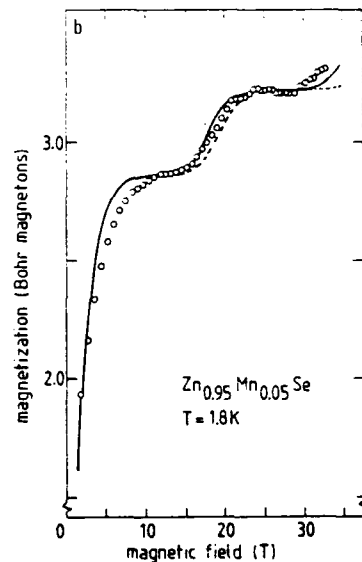


Fig. 5

- (a) Magnetization of $Cd_{0.95}Mn_{0.05}Te$ as monitored by exciton splitting⁴¹; the solid line represents the ENNPA with $J(R) = -10 R^{6.8} K$.
 (b) Magnetization of $Zn_{0.95}Mn_{0.05}Se$; the solid line represents the ENNPA with $J_{NN} = -13 K$ and $J = -7 R^{6.8} K$; see Ref. 16.



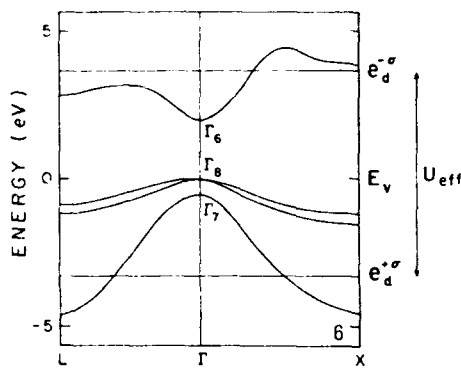
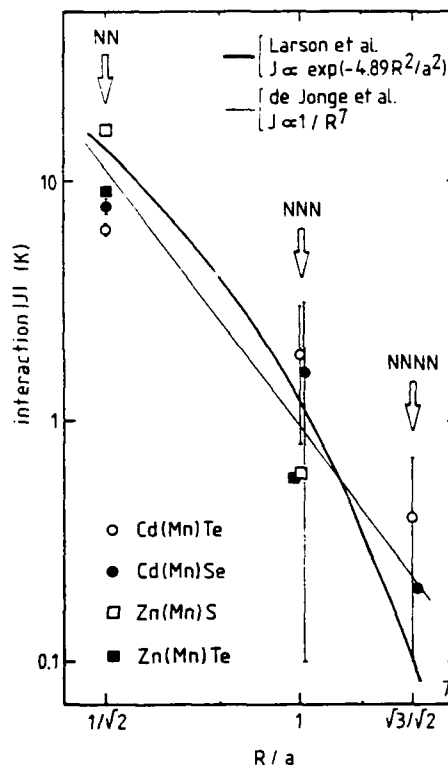


Fig. 6

Schematic illustration of the Mn-majority (e_d^-) and minority (e_d^+) levels, within a zinc-blende based bandstructure; from Ref. 4.

Fig. 7

Radial dependence of the exchange interaction $|J|$ based on Lasson's superexchange model⁴ ($\sim \exp(-4.89 R^2/a^2)$) and a scaling analysis of $T_F(x)$ ($\sim R^{-7}$) by de Jonge et al.⁵, compared with experimental data^{42,43,10}.



structure details within a class of materials closely related by symmetry:

$$J(R_{ij}) = -2V_{dp}^4 \left[\left[E_d + U - E_v \right]^{-2} U^{-1} + \left[E_d + U - E_v \right]^{-3} \right] f(R_{ij}), \quad (3)$$

where for $f(R_{ij})$ in CdMnTe-like symmetry is suggested

$$f(R_{ij}) = 51.2 \exp -4.89 R_{ij}^2 \quad (4)$$

It has been shown⁴ that the chemical trends, contained in the effects of anion and cation substitution on the energy levels and V_{dp} , compare very well with the experimental data as tabulated in Table I, demonstrating convincingly the applicability of the model.

Of particular interest to us in the present context are the predictions related to the spatial extension of the exchange; i.e. the "universality" of $f(R_{ij})$ within a certain class of materials and the actual quantitative decay of $f(R_{ij})$.

From the results shown in Fig. 2 and tabulated in Table I, indeed a remarkable universal behavior of the radial dependence (characterized by n) can be observed for certain classes of materials, thus corroborating the expectations. In particular the universal behavior of the large class of wide gap materials $A_{1-x}Mn_xB$ where $A = Cd, Zn$ and $B = S, Se, Te$ is impressive, in view of the rather wide variety of bandgap, hybridization, lattice constants and NN exchange constants found in this class. We note parenthetically that the *coalescence* of the freezing temperatures as function of x for all these materials, as is apparent in Fig. 2, represents an additional remarkable

Table I

| material | $d_{NN}(\text{\AA})$ | $E_g(\text{eV})$ | $-J_{NN}^*$ (K) | n^{**} | $-J_{NNN}^\dagger$ (K) |
|-------------------------------------|----------------------|------------------|--------------------|------------|---------------------------|
| ZnMnS | 3.83 | 3.8-3.9 | 16 | 7.6 | $\sim 0.7, 0.6$ |
| ZnMnSe | 4.00 | 2.8-3.0 | 12 | 6.8 | ~ 0.7 |
| ZnMnTe | 4.31 | 2.3-2.8 | 9 | 6.8 | 0.6 |
| CdMnS | 4.12 | ~ 2.5 | 10 | ~ 6.8 | |
| CdMnSe | 4.28 | 1.5-2.5 | 8 | ~ 6.8 | 0.1-3.1 |
| CdMnTe | 4.58 | 1.5-2.7 | 6 | ~ 6.8 | 0.8-3.0 |
| HgMnSe | 4.30 | ~ 0 | 6 | 5 | |
| HgMnTe | 4.55 | -0-1.1 | 5 | 5 | |
| $(\text{ZnMn})_3\text{As}_2$ | 2.94 | ~ 1 | 100 | 4.5 | ~ 20 |
| $(\text{CdMn})_3\text{As}_2$ | 3.17 | $\sim 0-0.2$ | 30 | 4.0 | ~ 5 |
| ZnFeS | | 3.8 | | | |
| ZnFeSe | | 2.8 | 22 | 12 | |
| ZnFeTe | | 2.4 | | | |
| CdFeSe | | 1.8 | 19 | | |
| CdFeTe | | 1.6 | | | |
| $\text{HgCd}_y\text{Fe}_x\text{Se}$ | | | 18 | | |
| HgFeSe | | 0 | 18 | | |
| HgFeTe | | 0 | | | |

* see Ref. 9,10,18,27,44

** see Ref. 5,16,40,23

† see Ref. 9,10,16,18,40,42,43

feature. This behavior seems at variance with the common wisdom that the freezing transition should be proportional to the driving interaction.

As for the actual quantitative decay of $J(R)$ it should be noted that, apart from the analytic radial dependence of $J(R)$ obtained from $T_F(x)$ as shown before, direct experimental data on interactions beyond nearest neighbors is almost unavailable. Some data on the relative strength of next nearest neighbors (NNN) have been obtained from very careful analysis of neutron scattering results²⁰ (in concentrated DMS) and steps in the high field magnetization¹⁰ (a technique which we will discuss in some more detail in relation to Fe-DMS). These data, together with the results from the $T_F(x)$ analysis (which in principle includes all more distant neighbour interactions), as well as the prediction of Larson et al.⁴, are shown in Fig. 7. Obviously, the Gaussian decay suggested by Eq. (2) and the power-law dependence employed in the present analysis do not agree. We have to recall, however, that the Gaussian decay is only claimed to be valid up to roughly the fourth neighbour while the power law behavior probes mainly the tail of the interaction. The comparison in Fig. 7 shows that the deviations between the experimental exchange interaction probed by $T_F(x)$ and the prediction based on superexchange are irrelevant in the plotted range, certainly when compared with the inaccuracy of the data obtained by other methods. We therefore conclude that these data yield additional support for the superexchange mechanism and demonstrate the usefulness of the present analysis of $T_F(x)$.

Fe based II-VI DMS

The vast majority of the experimental effort so far has been devoted to Mn-DMS. The magnetic behavior of these systems shows common characteristics, described earlier, which can be understood on the basis of a random array of localized isotropic Mn^{2+} spins coupled by long ranged AF interactions.

In several aspects Mn^{2+} , with its degenerate 6A_1 spin-only ground state, represents a rather simple case, since all phenomena involving orbital momentum are absent. Fe^{2+} on the other hand represents a much more general case since it possesses both spin and orbital moment ($S = 2$ and $L = 2$). As in the Mn case, Fe can be substituted for the group II ion and contributes its $4s^2$ electrons to the typical $(s-p^3)$ bonding. Since the exchange is intimately related to the location of the magnetic ion levels with respect to the band structure, substitution of Fe instead of Mn might affect the character and strength of these interactions, since the Fe^{2+} d^6 level may be located far above the valence band, in contrast to the Mn^{2+} levels²¹.

Also, the magnetic properties are expected to be substantially different from Mn-type DMS. This difference can be ascribed to the different energy scheme of Mn^{2+} and Fe^{2+} ions, as is shown in Fig. 8. Substitutional Fe^{2+} has a d^6 configuration. The ground state of the Fe^{2+} free ion (5D) is split by a tetrahedral crystal field into a 5E orbital doublet and a higher lying 5T orbital triplet (separated from 5E by $10 Dq$ is the crystal-field parameter)²². Spin-orbit interaction splits the 5E term into a singlet A_1 , a triplet T_1 , a doublet E , a triplet T_2 , and a singlet A_2 (the energy separation between these states is approximately equal to $6\lambda^2/10Dq$, where λ is the spin-orbit parameter). Thus the ground state of the isolated Fe^{2+} ion in zero field is a magnetically inactive singlet A_1 resulting in Van Vleck-type temperature independent paramagnetism. Exchange interactions and magnetic fields will of course modify this energy-scheme as was shown by numerical calculations²³. Starting point for the calculations was the Fe-Fe pair Hamiltonian:

$$\mathcal{H} = \mathcal{H}_{CF} + \mathcal{H}_{so} + \mathcal{H}_{exch} + \mathcal{H}_B, \quad (5)$$

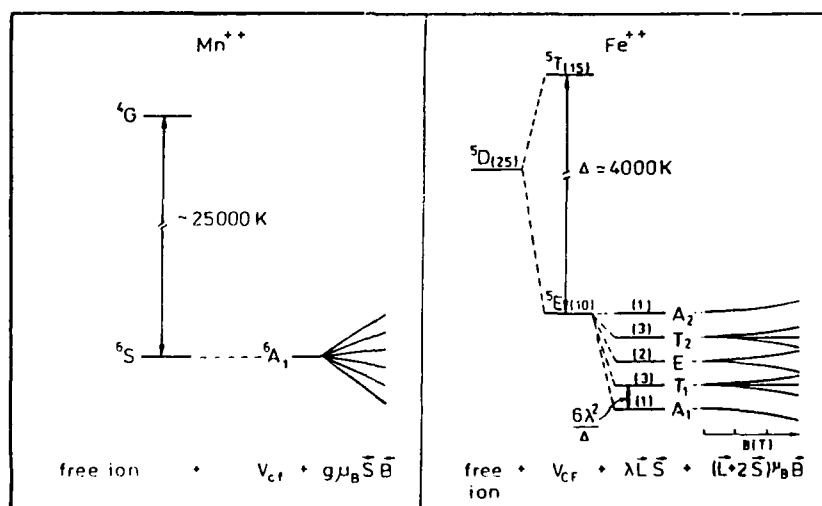


Fig. 8

Schematic illustration of the low-lying energy levels of non-interacting Mn^{2+} and Fe^{2+} .

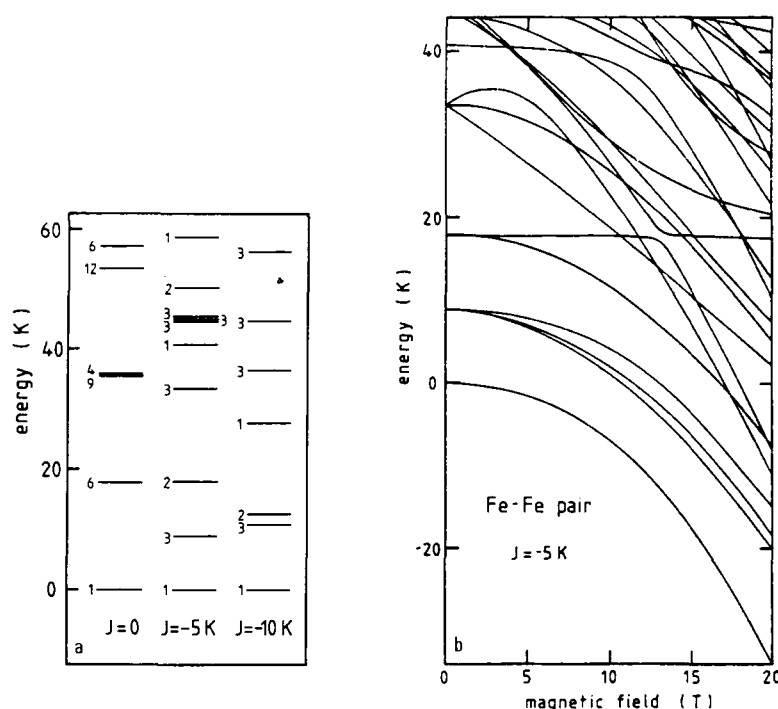


Fig. 9

The influence of exchange interaction (a) and magnetic field (b) on the low-lying energy levels of Fe²⁺; see Ref. 23.

where

$$\begin{aligned} \mathcal{H}_{\text{exch}} &= -2JS_1 \cdot S_2, \\ \mathcal{H}_{\text{so}} &= \lambda S_1 \cdot L_1 + \lambda S_2 \cdot L_2, \\ \mathcal{H}_B &= (L_1 + L_2 + 2S_1 + 2S_2) \cdot \mu_B B, \end{aligned}$$

and \mathcal{H}_{CF} is the crystal-field term. J is the exchange constant, S and L are spin and orbital momentum operators, respectively. The indices i and j refer to the ions of the pair. The behavior of the levels as a function of J and external field is illustrated in Fig. 9. Based on this results calculations of the thermodynamic properties of diluted samples can now be performed within the ENNPA outlined before.

Experiments so far are restricted to ZnFeSe, CdFeSe and HgFeSe and in this section we will shortly review the characteristics of the magnetic behavior. A comprehensive review will be published shortly²⁴.

Probably the most direct confirmation of the conjectured energy level scheme (see Fig. 9) is obtained from far infrared transmission experiments in zero field as well as in applied field²⁵. Transitions from the ground level to excited levels were indeed observed. The first excited level appears at about 20 K above the singlet ground state. No direct shift or splitting due to exchange coupled pairs could be detected, indicating the dominant influence of the crystal field splitting in this case.

Representative results for C_m , M and χ are reproduced in Fig. 10-12. Susceptibility experiments²⁶ yield a Curie-Weiss behavior at high temperatures with a negative Curie-Weiss Θ , indicating an antiferromagnetic exchange coupling with a strength (See Table I) considerably larger than the Mn-DMS. No temperature

independent v. Vleck behavior has been observed in the low-temperature susceptibility²³, because of inevitable (small) amounts of paramagnetic impurities ($x \approx 10^{-4}$). Instead, a kink has been observed in some samples which tentatively has been ascribed to a freezing transition. Only for ZnFeSe the data points allow an analysis of $T_F(x)$ to obtain information on the radial dependence of the exchange, as applied for Mn-DMS. In doing so one has to realize, however, that we are dealing here with a singlet ground state which makes the interaction energy (Eq. 1) less effective. Implementing the pair correlation function in the exchange energy ($J(\underline{R}) < S_o \cdot S_R > \approx kT_F$) it has been shown that the data indicate a radial dependence of J for ZnFeSe similar to the one observed in the Mn analogue ($J(R) \approx J_o R^{-7}$).

The exponential low temperature onset of C_m observed for diluted samples, followed by a maximum at about 10 K as shown in Fig. 12, resembles a Shottky-type anomaly brought about by the gap between ground state and excited states. The decrease of C_m/x with x indicates the relevance of the Fe^{2+} - Fe^{2+} interaction, since for isolated ions C_m would scale with x . The magnetic field dependence (not shown) in fields up till a few Tesla is small and hardly exceeds the experimental accuracy, in marked contrast with Mn-DMS and again demonstrating the dominant influence of the ground state splitting.

If the exponential onset of C_m is due to zero field splitting of the Fe^{2+} levels then C_m can be expressed as²⁸

$$C_{Schottky}(T) = xR(g_1/g_o)(\Delta E/kT)^2 \exp(-\Delta E/kT), \quad (6)$$

with $g_1/g_o=3$, denoting the degeneracy of the levels, which schematically represents the lowest levels of the Fe^{2+} ion (singlet ground state and a threefold degenerate state at ΔE). Within the framework of this simplified model a plot of $\ln(C_m T^2)$ versus T^{-1}

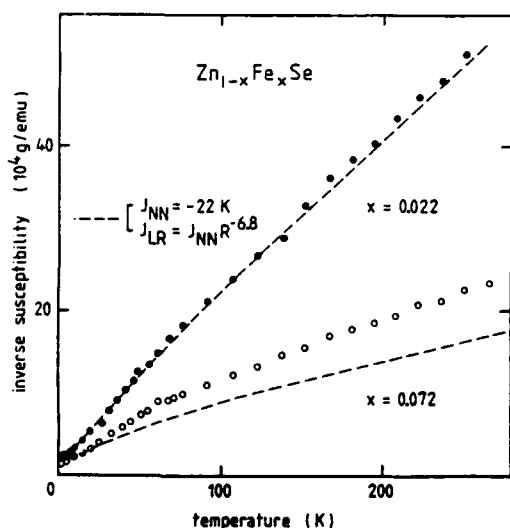


Fig. 10

Inverse high-temperature susceptibility of $Zn_{0.978}Fe_{0.022}Se$ and $Zn_{0.928}Fe_{0.072}Se$. The dashed line represents the ENNPA ($J = -22 R^{-6.8} K$); see Ref. 23.

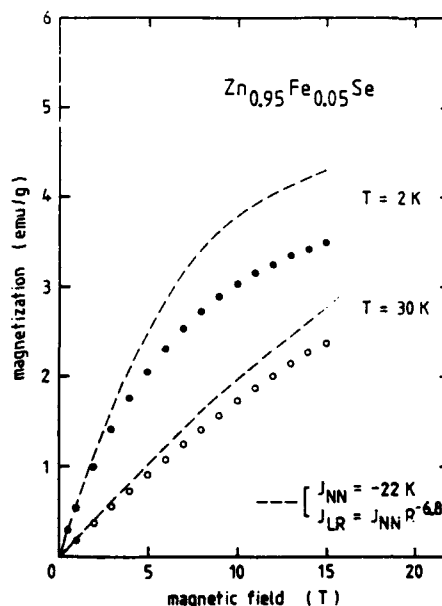


Fig. 11

Magnetization of $Zn_{0.995}Fe_{0.005}Se$ at $T = 2 K$ and $30 K$; the dashed line represents calculations within the ENNPA ($J = -22 R^{-6.8} K$); see Ref. 23.

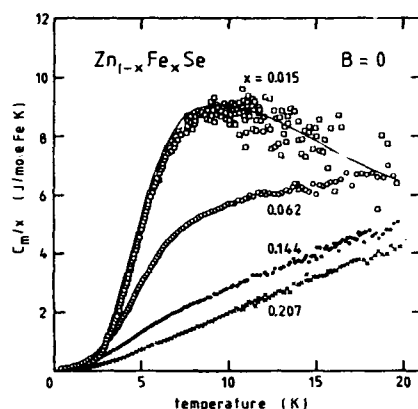


Fig. 12

Magnetic specific heat (C_m/x) of $Zn_{1-x}Fe_xSe$; the solid line represents calculations within the ENNPA ($J = -22 R^{-5.3} K$) for $x = 0.015$; see Ref. 23.

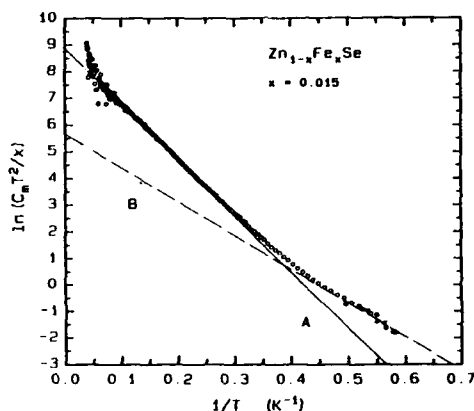


Fig. 13

Magnetic specific heat of $Zn_{0.985}Fe_{0.015}Se$ shown as $\ln(C_m T^2/x)$ versus T^{-1} , illustrating the contribution of singles (A) and pairs (B); see Ref. 27.

would result in a straight line with a slope determined by ΔE . Extrapolation to $T = \infty$ will yield the value for g_1/g_0 . The data for the various compounds²⁷, illustrated in Fig. 13 for the case of $ZnFeSe$, indeed show a linear part below C_{max} . For low Fe-concentrations, where Eq. (6) would apply these plots yield, ΔE in the range 20-25 K, in accordance with data from spectroscopic experiments²⁵, and g_1/g_0 in the range 2-4. Quite surprisingly, these data also show the contribution of exchange coupled NN pairs at low temperatures. As can be seen from Fig. 9 the exchange coupling reduces the gap ΔE , resulting in a reduced slope for C_m , as is indeed observed. Detailed low temperature C_m measurements might therefore provide an additional method to obtain values for the nearest neighbor interactions in these systems.

As we quoted before, for Mn-DMS the high field magnetization data can provide a direct determination of J_{NN} through the stepwise increase of the contribution of exchange coupled AF pairs to the magnetization¹⁰. At zero field the coupled spins are AF aligned with total spin $S_T = 0$ and do not contribute to the magnetization. Increasing the field will create new ground states by level crossing with states with increasing S_T (and magnetization) until, at fields comparable with the exchange energy, the parallel configuration is reached. The process is illustrated in Fig. 14.

Obviously the situation is completely different for Fe^{2+} . However, despite the complexity of the energy level scheme, it has been shown recently²⁹ that also in the Fe^{2+} case magnetization steps should be detectable, and could be used to determine J_{NN} , provided that J_{NN} exceeds a certain critical interaction strength J_{crit} . The calculations were based on the Hamiltonian (5) and performed for different directions of the external field. The resulting variation of the levels as well as the pair magnetization is shown in Fig. 14. The actual physical process is rather complex and J_{crit} results from a delicate interplay between crystal field, exchange and magnetic field. For $J < J_{crit}$ a relatively large degree of mixing repulses the ("v Vleck") ground state in such an amount that excited states cannot intersect. In Fig. 15 the calculations are compared with the experimental data for fields up to 15 T showing that the steps, if they can be observed, are outside the measured regime.

Summarizing the experimental results so far one can conclude that the overall magnetic behavior of the investigated Fe-DMS is similar and can be fairly well understood from the crystal field model of Fe^{2+} introduced in this section,

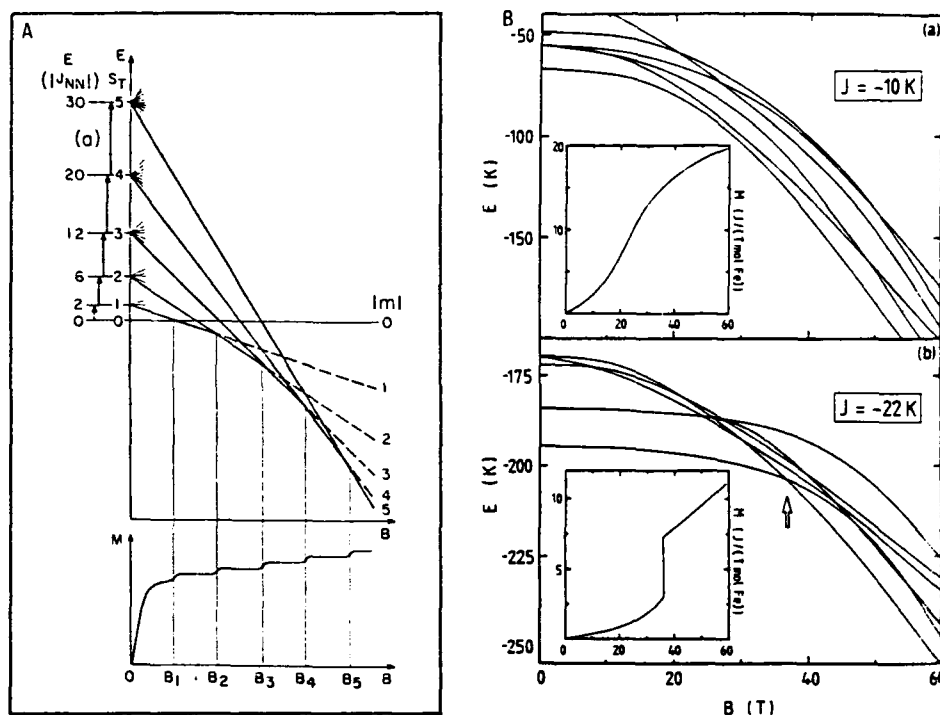


Fig. 14

- (A) Energy-level diagram of a Mn^{2+} -pair, showing the existence of steps in the magnetization at low temperatures; from Ref. 10.
- (B) Low-lying energy levels and magnetization, at $T = 0$ (see insets), of the Fe^{2+} pair for B along the crystallographic $[111]$ axis; (a) $J = -10$ K, (b) $J = -22$ K, the arrow indicates the position of the magnetization step; see Ref. 29.

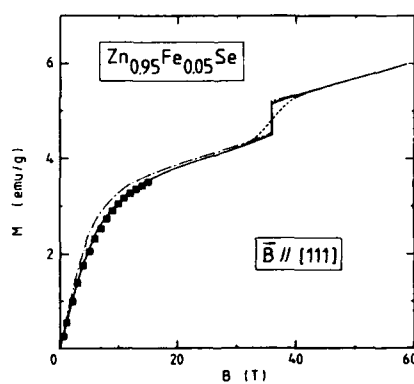


Fig. 15

Magnetization of $Zn_{0.95}Fe_{0.05}Se$ for B along the crystallographic $[111]$ axis, using ENNPA with $J = -22$ R^{-5.8} K ($T = 0$, —; $T = 1.5$ K, ---) and the cluster approximation with $J = -22$ K ($T = 0$, - · - · -), the squares represent data from Ref. 23.

supplemented with AF NN exchange. The few available data for this exchange parameter seem somewhat higher than in the corresponding Mn-DMS, which is, however, not inconsistent with a somewhat larger hybridization (V_{dp} in Eq. 1). Influence of location of the F_e^{2+} energy levels with respect to the band structure could not be found so far in the magnetic data. In the schematic representation of the Fe levels the 6d electrons occupy the e, and t, orbitals deeply in the valence band (like Mn) while the 6th electron occupies the e, orbital. This orbital is reported²¹ to vary considerably in location with respect to bandgap going from HgFeSe to CdFeSe. The reported similar behavior of these compounds seems to indicate that the hybridization of this orbital is rather weak and does not contribute to the magnetic coupling.

IV-VI DMS

In this section we will report on carrier induced magnetic interactions as observed in (PbSn)MnTe (PSMT) in various compositions, including SnMnTe. These alloys belong to the larger family of IV-VI DMS of which Pb alloys³⁰ as well as Sn alloys³¹ have been extensively studied in the past. From these studies it appears that the IV-VI family can roughly be divided into two groups. One group, mainly Pb alloys, with, as grown, carrier concentrations around 10^{18} cm^{-3} , resembles magnetically the II-IV DMS, although the AF interactions are weaker. Another group includes the Sn and Ge alloys, with, as grown, carrier concentrations around 10^{20} cm^{-3} , which are known as ferromagnets. The first observation of Story et al.⁶, that in (PbSn)MnTe an increasing carrier concentration transforms the system from essentially paramagnetic to ferromagnetic, has shed new light on this historical distinction. Viewed in a wider perspective, this was the first observation of the fact that the carrier concentration can be a relevant parameter in the magnetic phase diagram. It should be noted that the possibility to vary the carrier concentration reversibly over a relatively wide range (10^{19} - 10^{21} cm^{-3}), by introducing a slightly non stoichiometric composition by thermal annealing in a Te-rich or Sn-rich atmosphere, is a basic condition for this type of research.

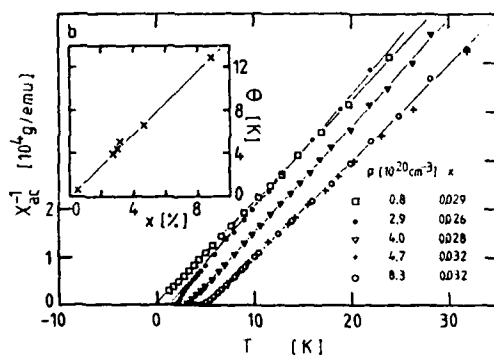


Fig. 16

Inverse ac susceptibility (χ_{ac}^{-1}) for $\text{Pb}_{0.25}\text{Sn}_{0.75}\text{Mn}_{0.03}\text{Te}$ and several carrier concentrations (p); the Curie-Weiss temperature (Θ) as a function of the Mn concentration (x), in the ferromagnetic regime, is inserted; see Ref. 7.

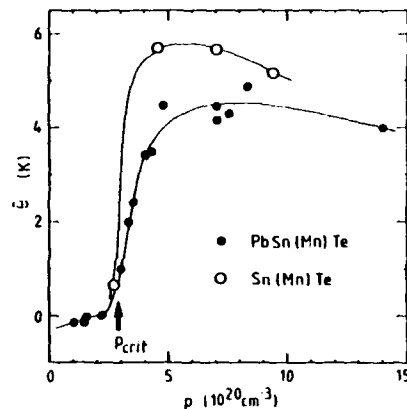


Fig. 17

Curie-Weiss temperature Θ ($\equiv \Theta \cdot 0.03/x$ used for small variations in Mn-concentration) as a function of the carrier concentration p , for $\text{Pb}_{0.25}\text{Sn}_{0.75}\text{Mn}_{0.03}\text{Te}$ (full circles) and $\text{Sn}_{0.97}\text{Mn}_{0.03}\text{Te}$ (open circles); the lines are guides to the eye only; see Ref. 7,32,33.

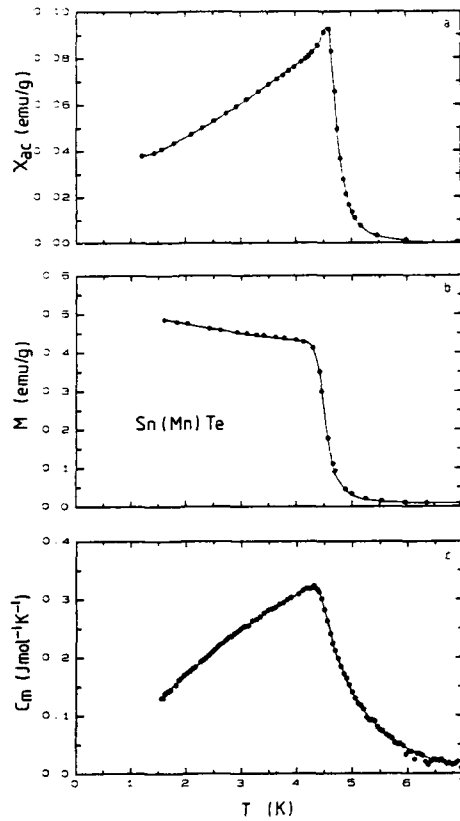


Fig. 18

AC susceptibility (a), magnetization for $H_{DC} = 5$ G (b), and magnetic specific heat (c) of $\text{Sn}_{0.97}\text{Mn}_{0.03}\text{Te}$, $p = 7-10 \times 10^{20} \text{ cm}^{-3}$; see Ref. 33.

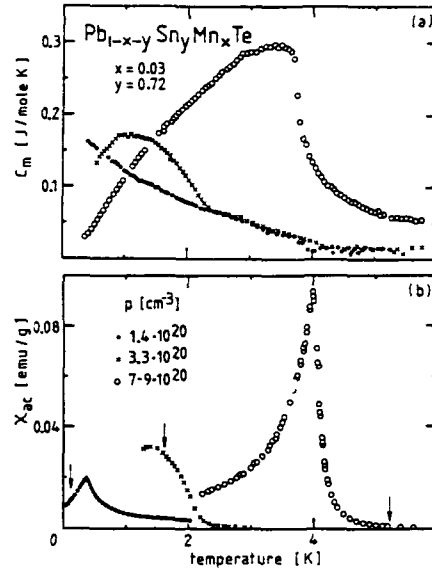


Fig. 19

Low temperature magnetic specific heat C_m (a) and ac susceptibility χ_{ac} (b) of $\text{Pb}_{0.25}\text{Sn}_{0.72}\text{Mn}_{0.03}\text{Te}$, for 8 carrier concentrations p ; the arrows in χ_{ac} indicate the Curie-Weiss temperature; see Ref. 7,32.

In order to illustrate some of the major results we will use data obtained from PSMT^{6,32} as well as recent results for SnMnTe (SMT)³³ to actualize this compilation. Fig. 16 illustrates the behavior of PSMT as function of the carrier-concentration p , as probed by the high temperature susceptibility χ . The influence of p can be clearly observed and the Curie Weiss Θ , which measures the interaction strength, shows a dramatic increase at p_{crit} , as is shown in Fig. 17, which also contains data for SMT. The actual phase transition observed in χ_{ac} , magnetization and C_m is shown in Fig. 18 for SnMnTe with carrier-concentrations in the range of $(7-10) \times 10^{20} \text{ cm}^{-3}$, the range to which earlier investigations were restricted. In this range indeed a transition to a ferromagnetic like ordered state is observed. When the carrier concentration is reduced, the transition shifts (proportional to Θ in Fig. 17) to considerable lower temperatures, as shown in Fig. 19.

Only the RKKY interaction between the (diluted) Mn ions, mediated by the free carriers (see Fig. 1), seems of sufficient strength and range to establish a long range ferromagnetic ordering in these systems. The RKKY exchange between ions on two lattice points at a distance R_j through carriers in a band denoted by i can be written as^{7,34}:

$$J_i(R_j) = \left[\frac{m_i}{m_e} J_{sp-d,i}^* \right] \frac{m_e}{128 \pi^3 \hbar^2} \left[\frac{a_0^2}{j^2} \right] F(z_{i,j}), \quad (7)$$

with

$$F(z_{i,j}) = [\sin(z_{i,j}) - z_{i,j} \cos(z_{i,j})]$$

and with $z_{i,j} = 2k_{i,F}R_j$, where $k_{i,F}$ is the Fermi wave number for the i -th band, m^* is the effective mass, $J_{sp-d,i}$ is the exchange constant between the Mn-ion and band i , and a_0 is the lattice parameter. The resulting Curie Weiss Θ is given by

$$\Theta = \frac{2S(S+1)x}{3k_B} \sum_{j \geq 1} J_i(R_j) \quad (8)$$

The characteristic behavior of $J^{RKKY}(R_j)$ is shown in Fig. 20. The resulting Θ from such an interaction, containing contributions from carriers in one band only, will, however, never result in a steplike increase at p_{crit} .

Triggered by observations from Hall effect studies³⁵ and the pressure dependence³⁶ of T_c , indicating the importance of contributions of carriers from other bands, Swagten et al.⁷ presented a first interpretation of the threshold dependence of T_c at p_{crit} , based on a realistic two band model for these compounds. The two bands denoted by VB1 and VB2 are located at the L point and along the Σ direction. The top of VB1 is higher than the top of VB2 and m_1^* , the effective hole mass of VB1 is much smaller than m_2^* of VB2 (see Fig. 21). The total d-d exchange is now assumed to be the sum of the contributions from the carriers in each band, each with their own effective mass. For low carrier concentrations $p < p_{crit}$, E_F is located in the top of VB1, at p_{crit} the Fermi-level enters also the top of VB2. The increase of $J(R)$, and thus Θ , at p_{crit} is due to the large effective mass of VB2 ($m_2^*/m_1^* \approx 20!$) as follows from equation 7. Calculations based on this simple model⁷, and using estimated values for the parameters (notably $m_1^* = 0.05 m_e$, $m_2^* = 1.00 m_e$, $\Delta VB = 0.6$ eV, $J_{sp-d,1} = J_{sp-d,2} = 0.3$ eV and an exponential decay of J_{RKKY} to account for the finite mean free path), yielded a fair agreement with the experimental data as shown in Fig. 22. Recent more detailed calculations of Story et al.³⁷ based on actual band structure calculations confirmed this result for PSMT.

Although it is gratifying to conclude that a rather crude and simple two band RKKY model is capable of explaining one of the most intriguing features of this quaternary alloy, i.e. the carrier induced ferromagnetism, the quantitative agreement,

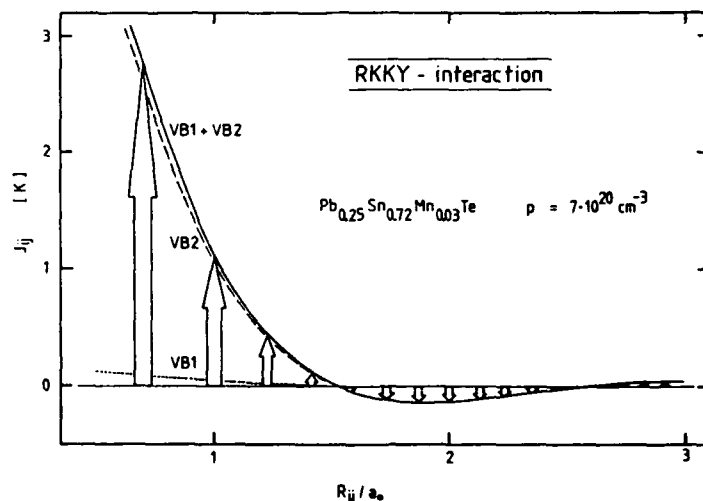


Fig. 20

Schematic behavior of the RKKY-interaction for $p = 7 \cdot 10^{20} \text{ cm}^{-3}$ and $a_0 = 6.347 \text{ \AA}$.

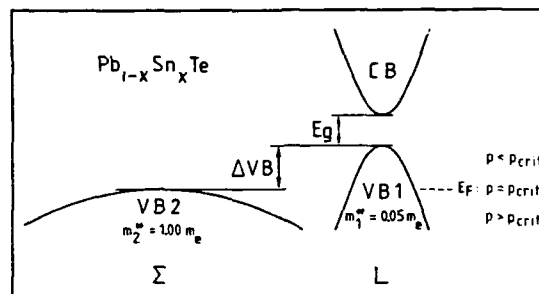


Fig. 21

Schematic illustration of the band structure of $Pb_{1-x}Sn_xTe$ used in the model calculations as described in the text; see Ref. 7.

specifically in the ferromagnetic regime, may be somewhat fortuitous. The absolute magnitude of Θ in that region depends directly on the value for the sp-d exchange constants J_1 and J_2 , for which no experimental data are available. A further verification of the validity of the model is also found in an extension of the composition range (Pb-Sn), which yields a slight shift in p_{crit} brought about by the variation in ΔE_{VB} . PbMnTe and SnMnTe can be considered as the limiting cases in the composition range of PbSnMnTe. On the basis of our model the contrasting magnetic behavior of these compounds might be understood from the difference in hole concentration. Since SnMnTe has a band structure comparable with PSMT it was conjectured that, if the model holds, a reduction of p would yield a transformation of this ferromagnet to a paramagnet. Such a transition was indeed observed recently³³ as shown in Fig. 17. The same mechanism might also be responsible for the substantial decrease of the (ferromagnetic) Θ in $(Ge_{1-x-y}Pb_y)_{0.9}Mn_{0.1}Te$ with increasing Pb content, particularly since it was reported to be accompanied by a simultaneous decrease of the carrier concentration³⁸.

The RKKY d-d exchange interaction is in general a radially oscillating function, decaying with R^{-3} and changing sign with a periodicity of $\pi/2k_F$, as can be seen from equation (7). In Fig. 20, $J(R)$ is shown for one specific carrier-concentration p (and thus for one k_F since $p^{1/3} \sim k_F$). Increasing p would yield faster oscillations as a

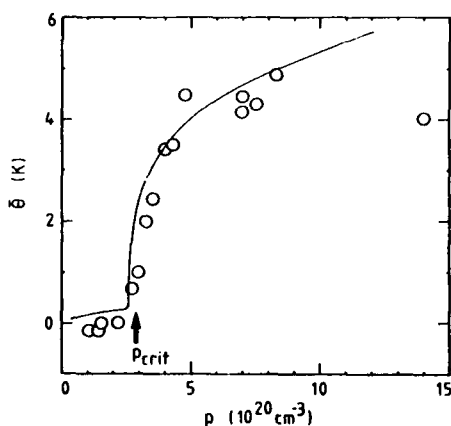


Fig. 22

Calculations of the Curie-Weiss temperature in the modified RKKY-model using $m_1^* = 0.05$, $m_2^* = 1$, $J_{spd} = 0.92$ eV; the data for $Pb_{0.25}Sn_{0.75}Mn_{0.03}Te$ are shown as open circles.

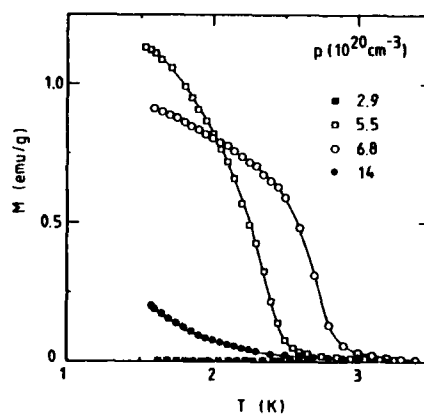


Fig. 23

Magnetization ($H = 10$ G) of $Pb_{0.25}Sn_{0.75}Mn_{0.03}Te$ for several carrier concentrations p .

function of R and a shift of the first node to smaller R_j . This oscillatory behavior of $J(R)$ gives rise to the existence of two magnetic regimes (not to be confused with carrier induced ferromagnetism discussed above) depending on the ratio between the average distance \bar{R} between the magnetic ions ($\sim x^{-1/3}$) and the distance R_j at which the first node in $J(R)$ occurs ($\sim p^{-1/3}$). Calculation shows that for the present structures, this ratio equals 1 for $x/p \sim 10^{-23}$. For larger x/p the short-range ferromagnetic interactions outweigh the oscillatory behavior. For smaller x/p competition might be expected, giving rise to a spin-glass behavior. We note in passing that the latter situation is encountered in the canonical metallic spin-glasses like Cu(Mn), because of the extremely high carrier concentration p . In the present IV-VI semimetals the transition from one regime to another might very well be found in the dilution range studied.

Experimental evidence on the existence of different magnetic regimes as discussed above is scarce. Escorne et al.³⁹ claimed to have observed a transition to a spin-glass state in SMT with $p = 5 \cdot 10^{20} \text{ cm}^{-3}$, when reducing the magnetic concentration x . Recently, the complementary situation has been observed, illustrated in Fig. 23 by the behavior of the magnetization. Increase of the carrier concentration in $\text{SnMn}_{2.2}\text{Te}$ yields, after an initial increase of the ferromagnetic transition temperature T_c , according to the behavior in Fig. 17, a sharp decrease at high carrier concentration, accompanied by a breakdown of the proportionality between Θ and T_c , indicating a change of ordering mechanism. Further research is however necessary before pertinent conclusions can be drawn.

Concluding we would like to remark that one of the essential results of the present study, i.e. the explicit demonstration of the relevance of separate contributions from carriers in different regions of the Brillouin zone, might also be relevant for alternative interaction mechanisms which have been proposed for other classes of diluted magnetic semiconductors.

ACKNOWLEDGEMENTS

We would like to acknowledge the fruitful discussions and cooperation with R.R. Gałazka, A.T. Twardowski, T. Story and K. Kopinga.

REFERENCES

1. J.K. Furdyna, Diluted magnetic semiconductors, J. Appl. Phys. 64: R 29 (1988).
2. J.K. Furdyna and J. Kossut, "Diluted magnetic semiconductors", Academic, Boston MA (1988).
3. C.E.T. Gonçalves da Silva and L.M. Falicov, Theory of magnetic properties of rare earth compounds, J. Phys. C 5: 63 (1972); W. Geertsma, C. Haas, G.A. Sawatzky and G. Vertogen, Long-range exchange interactions, Physica 86-88 B: 1039 (1977).
4. B.E. Larson, K.C. Hass, H. Ehrenreich and A.E. Carlsson, Theory of exchange interactions and chemical trends in diluted magnetic semiconductors, Phys. Rev. B 37: 4137 (1988).
5. W.J.M. de Jonge, A. Twardowski and C.J.M. Denissen, The relevance of long-range interactions in diluted magnetic semiconductors, in: "Diluted magnetic (semimagnetic) semiconductors", R.L. Aggarwal, J.K. Furdyna, S. von Molnar, eds., M.R.S., Pittsburgh (1987).
6. T. Story, R.R. Gałazka, R.B. Frankel and P.A. Wolff, Carrier-concentration-induced ferromagnetism in PbSnMnTe , Phys. Rev. Lett. 56: 777 (1986).

7. H.J.M. Swagten, W.J.M. de Jonge, R.R. Galazka, P. Warmenbol and J.T. Devreese, Hole density and composition dependence of ferromagnetic ordering in Pb-Sn-Mn-Te, Phys. Rev. B 37: 9907 (1988).
8. P.H. Keesom, Low-temperature specific heat of the diluted magnetic semiconductors $M_{1-x}^{(IIb)}Mn_x^{(VIA)}$ with $x < 0.1$: $M^{(IIb)} = Zn, Cd$ or Hg and $X^{(VIA)} = S, Se$ or Te , Phys. Rev. B 33: 6512 (1986); M. Escorne, A. Mauger, R. Triboulet and J.L. Tholence, Magnetic properties of $Cd_{1-x}Mn_xTe$ at low temperatures, Physica 107 B: 309 (1981).
9. J.K. Furdyna, N. Samarth, R.B. Frankel and J. Spalek, Static magnetic susceptibility of $Zn_{1-x}Mn_xSe$, Phys. Rev. B 37: 3707 (1988);
10. S. Foner, Y. Shapira, D. Heiman, P. Becla, R. Kershaw, K. Dwight and A. Wold, Magnetization steps in dilute magnetic semiconductors to 55 T: Mn^{2+} pair saturation in $Cd_{1-x}Mn_xTe$ and steps in $Zn_{1-x}Mn_xSe$, $Zn_{1-x}Mn_xTe$, and $Cd_{1-x}Mn_xSe$, Phys. Rev. B 39: 11793 (1989).
11. R.R. Galazka, Shoichi Nagata and P.H. Keesom, Paramagnetic-spin-glass-antiferromagnetic phase transition in $Cd_{1-x}Mn_xTe$ from specific heat and magnetic susceptibility measurements, Phys. Rev. B 22: 3344 (1980).
12. C.J.M. Denissen, H. Nishihara, P.A.M. Nouwens, K. Kopinga and W.J.M. de Jonge, Spin-glass behavior of $(Cd_{1-x}Mn_x)_3As_2$, J. M.M.M. 54-57: 1291 (1986).
13. M.A. Novak, O.G. Symko, D.J. Zheng and S. Oseroff, Spin freezing below the nearest neighbor percolation concentration in $Cd_{1-x}Mn_xTe$ and $Cd_{1-x}Mn_xSe$, Phys. Rev. B 33: 6391 (1986).
14. S.P. McAlister, J.K. Furdyna and W. Girit, Magnetic susceptibility and spin-glass transition in $Zn_{1-x}Mn_xTe$, Phys. Rev. B 29: 1310 (1984).
15. J.A. Mydosh, The spin-glasses: some recent experiments, in: Proc. of 3rd Int. Conf. on Phys. of Magn. Mat., W. Gorzkowski, H.K. Lachowicz and H. Szymczak, eds., World Scientific, Singapore (1986).
16. A. Twardowski, H.J.M. Swagten, W.J.M. de Jonge and M. Demianiuk, Magnetic behavior of the diluted magnetic semiconductor $Zn_{1-x}Mn_xSe$, Phys. Rev. B 36: 7013 (1987).
17. J.L. Tholence and R. Tournier, Susceptibility and remanent magnetization of a spin-glass, J. Phys. (Paris) Colloq. 35, C4: 229 (1974).
18. C.J.M. Denissen, H. Nishihara, J.C. Gool and W.J.M. de Jonge, Magnetic behavior of the semimagnetic semiconductor $(Cd_{1-x}Mn_x)_3As_2$, Phys. Rev. B 33: 7637 (1986).
19. K. Matho, Pair approximation to the Rudermann-Kittel-Kasuya-Yoshida free energy, J. Low Temp. Phys. 35: 165 (1979).
20. T. Giebultowicz, B. Lebeck, B. Buras, W. Minor, H. Kepa and R.R. Galazka, Neutron scattering studies of $Cd_{1-x}Mn_xTe$, J. Appl. Phys. 55: 2305 (1984).
21. A. Mycielski, Fe-based semimagnetic semiconductors, J. Appl. Phys. 63: 3279 (1988).
22. G.A. Slack, S. Roberts and J.T. Vallin, Optical absorption of Fe^{2+} in CdTe in the near and far infrared, Phys. Rev. 187: 511 (1969).
23. H.J.M. Swagten, A. Twardowski, W.J.M. de Jonge and M. Demianiuk, Magnetic properties of the diluted magnetic semiconductor $Zn_{1-x}Fe_xSe$, Phys. Rev. B 39: 2568 (1989).
24. A. Twardowski, Magnetic and optical properties of Fe-based semimagnetic semiconductors, in: "Diluted magnetic semiconductors", M. Jain, ed., World Scientific Press, Singapore (1990).
25. A.M. Witowski, A. Twardowski, M. Poheman, W.J.M. de Jonge, A. Wieck, A. Mycielski and M. Demianiuk, FIR Optical investigations of Fe-based semimagnetic semiconductors, Solid State Comm. 70: 27 (1989).
26. A. Twardowski, A. Lewicky, M. Arciszewska, W.J.M. de Jonge, H.J.M. Swagten and M. Demianiuk, Magnetic susceptibility of iron-based semimagnetic semiconductors: high-temperature regime, Phys. Rev. B 38: 10749 (1988);

- A. Lewicky, J. Spalek and A. Mycielski, Magnetic susceptibility and specific heat of semimagnetic semiconductors $\text{Cd}_{1-x}\text{Fe}_x\text{Se}$, $\text{Hg}_{1-x}\text{Fe}_x\text{Se}$ and their mixtures, J. Phys. C 20: 2005 (1987).
27. A. Twardowski, H.J.M. Swagten and W.J.M. de Jonge, Low-temperature specific heat of the diluted magnetic semiconductor $\text{Hg}_{1-x-y}\text{Cd}_y\text{Fe}_x\text{Se}$, Phys. Rev. B 42, to be published (1990).
 28. E.S.R. Gopal, "Specific heats at low temperatures", Heywood books, London (1966).
 29. H.J.M. Swagten, C.E.P. Gerrits, A. Twardowski and W.J.M. de Jonge, Magnetization steps in iron-based diluted magnetic semiconductors, Phys. Rev. B 41: 7330 (1990).
 30. M. Escorne, A. Mauger, J.L. Tholence and R. Triboulet, Magnetic and transport properties of $\text{Pb}_{1-x}\text{Mn}_x\text{Te}$ spin-glass, Phys. Rev. B 29: 6306 (1984); M. Gorska and J.R. Anderson, Magnetic susceptibility and exchange in IV-VI compound diluted magnetic semiconductors, Phys. Rev. B 38: 9120 (1988).
 31. M.P. Mathur, D.W. Deis, C.K. Jones, A. Patterson, W.J. Carr and R.C. Miller, Magnetic studies of the alloy system SnTe-MnTe , J. Appl. Phys. 41: 1005 (1970); M. Inoue, H. Fun, M. Fukuoka and H. Yagi, Magnetic transitions in degenerate semiconductor, J. Phys. Soc. Japan 49: 835 (1980).
 32. W.J.M. de Jonge, H.J.M. Swagten, R.R. Gałazka, P. Warmenbol and J.T. Devreese, Carrier induced magnetic interaction in the diluted magnetic semiconductor PbSnMnTe , IEEE trans. on magn. 24 (6): 2542 (1988).
 33. W.J.M. de Jonge, H.J.M. Swagten, S.J.E.A. Eltink and N.M.J. Stoffels, Carrier concentration dependence of the magnetic interactions in Sn(Mn)Te , Semicond. Sci. Technol. 5: 5131 (1990).
 34. M.A. Ruderman and C. Kittel, Indirect exchange coupling of nuclear magnetic moments by conduction electrons, Phys. Rev. 96: 99 (1954); K. Yosida, Magnetic properties of Cu-Mn alloys, Phys. Rev. 106: 893 (1957); T. Kasuya, A theory of metallic ferro- and antiferromagnetism on Zener's model, Prog. Theor. Phys. 16: 45 (1956).
 35. M. Ocio, Hall coefficient and mobility in $\text{Pb}_{1-x}\text{Sn}_x\text{Te}$ with high carrier densities, Phys. Rev. B 10: 4274 (1974).
 36. T. Suski, J. Igalsen and T. Story, Ferromagnetism of $(\text{Pb}, \text{Sn}, \text{Mn})\text{Te}$ under high pressure, J. M.M.M. 66: 325 (1987).
 37. T. Story, private communication.
 38. T. Hamasaki, Magnetic properties of $(\text{Ge}, \text{Pb})_{1-x}\text{Mn}_x\text{Te}$, Solid State Comm. 32: 1069 (1979).
 39. A. Mauger and M. Escorne, Transport properties and spin disorder in the degenerate ferro-spin-glass $\text{Sn}_{1-x}\text{Mn}_x\text{Te}$, Phys. Rev. B 35: 1902 (1987).
 40. H.J.M. Swagten, A. Twardowski, W.J.M. de Jonge, M. Demianiuk and J.K. Furdyna, Magnetic properties of $\text{Zn}_{1-x}\text{Mn}_x\text{S}$, Solid State Comm. 66: 791 (1988).
 41. R.L. Aggarwal, S.N. Jasperson, P. Becla and R.R. Gałazka, Optical determination of the antiferromagnetic exchange constant between NN Mn^{2+} -ions in $\text{Cd}_{0.95}\text{Mn}_{0.05}\text{Te}$, Phys. Rev. B 32: 5132 (1985).
 42. B.E. Larson, K.C. Hass and R.L. Aggarwal, Effects of internal exchange fields on magnetization steps in diluted magnetic semiconductors, Phys. Rev. B 33: 1789 (1986).
 43. Y. Shapira, S. Foner, D. Heiman, P.A. Wolff and C.R. McIntyre, Narrowing and fine structure of the magnetization steps of DMS in pulsed magnetic fields, Solid state Comm., 70: 355 (1989).
 44. R.R. Gałazka, W. Dobrowolski, J.P. Lascaray, N. Nawrocki, A. Bruno, J.M. Bruto and J.C. Ousset, NN exchange constants in $\text{Hg}_{1-x}\text{Mn}_x\text{Te}$, $\text{Hg}_{1-x}\text{Mn}_x\text{Se}$ and other semimagnetic semiconductors, J. M.M.M. 72: 174 (1988).

Intermetallic Compounds and Crystal Field Interactions

J. M. D. Coey

Department of Pure and Applied Physics
Trinity College
Dublin 2, Ireland

INTRODUCTION

Intermetallic compounds form when two or more metallic elements or metalloids occupy distinct sites in a specific structure. For example, AB_3 is a disordered alloy (solid solution) when A and B occupy the sites of an fcc lattice more or less at random, but it becomes an intermetallic compound with the ordered $AuCu_3$ structure when the A atoms are all located on one of the four sc sublattices, so that each A is surrounded by 12 B nearest-neighbours.

Binary intermetallics involve two metals, and there are more than 2000 possible combinations in the periodic table. But not every binary phase diagram includes intermetallic compounds however; some pairs of elements like La and Fe are so incompatible as to be quite immiscible in any proportion, whereas others, like Ag and Au or Ni and Pd are so similar that they dissolve mutually in any proportion to give a complete range of fcc solid solution. Intermetallics form best when the constituent atoms have rather different sizes and electronegativity. An example of a binary phase diagram is shown in Fig.1. There are four compounds of Y and Fe: Y_2Fe_{17} , Y_6Fe_{23} , YFe_3 and YFe_2 . Intermetallics are typically 'line compounds' which have a well-defined stoichiometry and exhibit little or no variability in composition.

With three elements, the number of possible combinations exceeds 45000, but this vastly exaggerates the number of possible ternary intermetallics. The three constituents have all to be sufficiently different in size and electronegativity to seek distinct sites, each having a characteristic chemical environment. Otherwise we end up with a *pseudobinary* $A_n(B_m-xC_x)$, where B and C occupy a site, or set of sites more or less at random. Conversely, one way of generating ternaries from complex binary structures is to arrange for preferential occupancy of different sites by different atoms, $A_nB_mC_p$. Another way is to introduce small foreign atoms on interstitial sites in a binary structure.

The more elements there are involved, the more difficult it becomes to find structure types with distinct sites for the different elements. Quarternaries are relatively rare, partly from lack of research and partly because it is not easy to choose four metals sufficiently different from one another to avoid the formation of a pseudoternary.

Here our concern is with intermetallic compounds of interest in applied magnetism. For applications, one is generally interested in materials that are magnetically-ordered at room temperature, hence the focus is on alloys of iron or cobalt. Iron, cobalt and nickel are the three ferromagnetic elements having Curie points well above room temperature. However, the magnetism of 3d elements is quite sensitive to alloying with other elements, which generally tend to destroy the 3d moment. The nickel moment, being the smallest of the three, is most easily destroyed. This is also true of 4f elements, which behave as early transition elements in their alloys, although they bear a magnetic moment in the 4f shell. The 4f shell is also the main

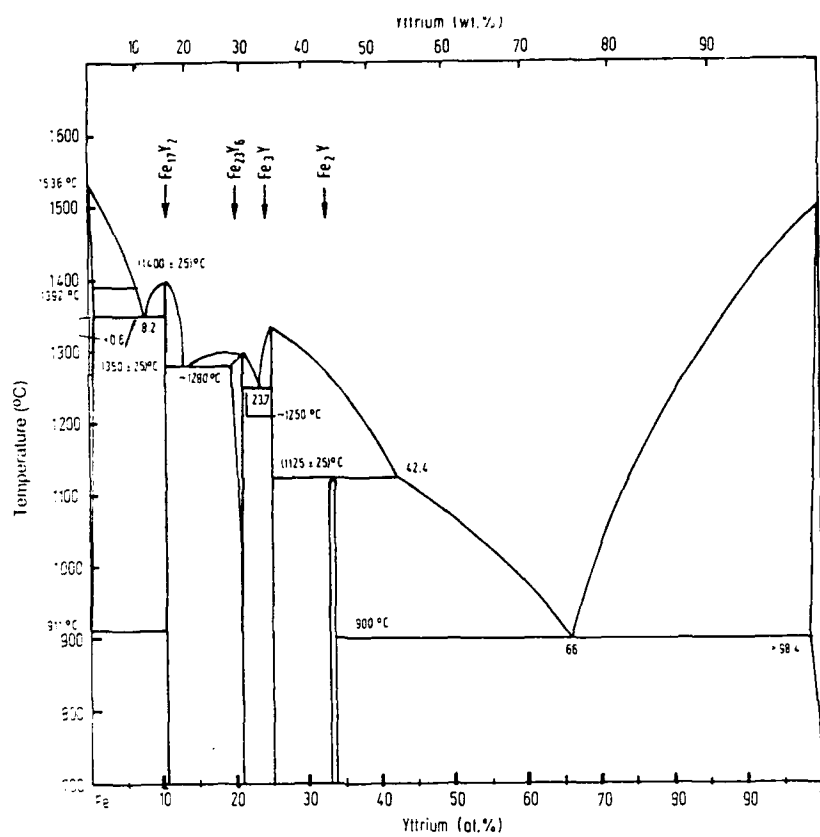


Fig. 1 The yttrium-iron phase diagram.

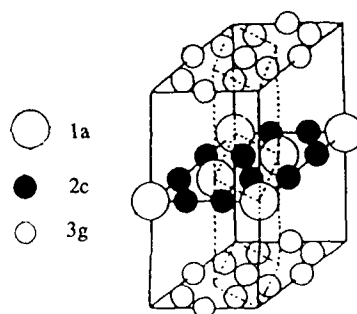


Fig. 2 The crystal structure of CaCu_5 .

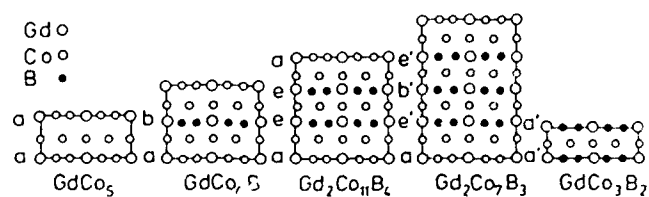


Fig. 3 Some ternary boride structures derived from CaCu_5 (GdCo_5) by preferential substitution.

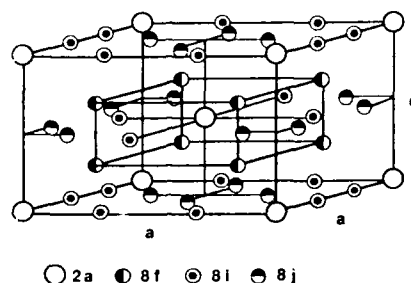


Fig. 4 The ThMn_{12} structure.

source of magnetocrystalline anisotropy in many intermetallics, via the crystal field interactions which are discussed in a later section. A strong anisotropy field is indispensable for permanent magnets. We now look at some intermetallic compounds of interest in magnetism, focusing on compounds of 4f and 3d elements.

INTERMETALLIC COMPOUNDS

A Binaries

RCu_5 : The hexagonal CaCu_5 structure is one of the simplest, and a number of other intermetallic structures can be derived from it. It does not form with iron, so the compounds of interest here are RCu_5 , and SmCo_5 in particular. The rare earth is in a special position (1a) with hexagonal point symmetry 6/mmm, and a large uniaxial electric field gradient ($A_2^0 = -200 \text{ K} \cdot a_0^{-2}$ [1]). There are two types of cobalt sites; 2c in the layers containing the rare earth, and 3g in the alternate layers (Fig. 2). A large series of related ternary structures may be generated by replacing the Co in some of the rare earth layers by another element such as boron, as shown in Fig. 3. For example, in RCu_4B , the 2c atoms in alternate R layers are replaced by boron.

ThMn_{12} : The ThMn_{12} structure is tetragonal, with space group $I4/mmm$ and $Z = 2$ (Fig 4). There is a single rare earth site (2a) in a highly symmetrical special position having point symmetry 4/mmm, but a relatively weak uniaxial electric field gradient. There are three transition metal sites (8f, 8i and 8j). The ThMn_{12} structure is related to that of CaCu_5 by replacing some of the rare earths by a closely-spaced pair (dumbbell) of transition metal atoms, according to the relation $\text{RT}_{12} = 2\text{RT}_5 - \text{R} + 2\text{T}$. Half of the transition metal atoms on 2c sites of the CaCu_5 cell become equivalent to the substituting dumbbell atoms to form the 8i sites, one third of the 3g and the other half of the 2c sites form the 8j site and the remaining 3g atoms form the 8f site. Furthermore the c-axis of the CaCu_5 structure becomes the a-axis of the ThMn_{12} structure [2]. The relation between the unit cells is shown in Fig 5a. The ThMn_{12} structure is not found for binaries of the rare earths with Fe or Co, but it can be stabilized by small additions of third elements (see below). ThMn_{12} itself is antiferromagnetic, with a Néel point far below room temperature (120 K).

$\text{Th}_2\text{Zn}_{17}$ and $\text{Th}_2\text{Ni}_{17}$: The R_2T_{17} compounds exist in two, closely related structure types, which differ in the stacking sequence of the elementary atomic planes. Again, some of the 1a atoms in the CaCu_5 structure are replaced by transition metal dumbbells, this time according to the relation $\text{R}_2\text{T}_{17} = 3\text{RT}_5 - \text{R} + 2\text{T}$, as illustrated in Fig. 5b. The $\text{Th}_2\text{Zn}_{17}$ structure is rhombohedral with $Z = 1$, although it is normally indexed on a hexagonal cell with $Z = 3$. There is a single rare-earth site 6c, with point symmetry 3m, and four transition metal sites, 18f, 18h, 9d and 6c, the latter being the dumbbell site. The $\text{Th}_2\text{Ni}_{17}$ structure has a similar hexagonal structure with $Z = 2$. Now there are two inequivalent rare earth sites 2b and 2d, both with point symmetry $\bar{6}m2$, and four transition metal sites 12j, 12k, 6g and 4f. The $\text{Th}_2\text{Zn}_{17}$ structure is favoured by the larger rare earths at the beginning of the lanthanide series, whereas the $\text{Th}_2\text{Ni}_{17}$ structure is favoured by the smaller rare earths, towards the end of the series. The iron compounds have remarkably low Curie temperatures (Fig 6), but the Curie points of the cobalt compounds are close to 1200 K; $\text{Sm}_2\text{Co}_{17}$ and its derivatives have long been used to make high-quality permanent magnets.

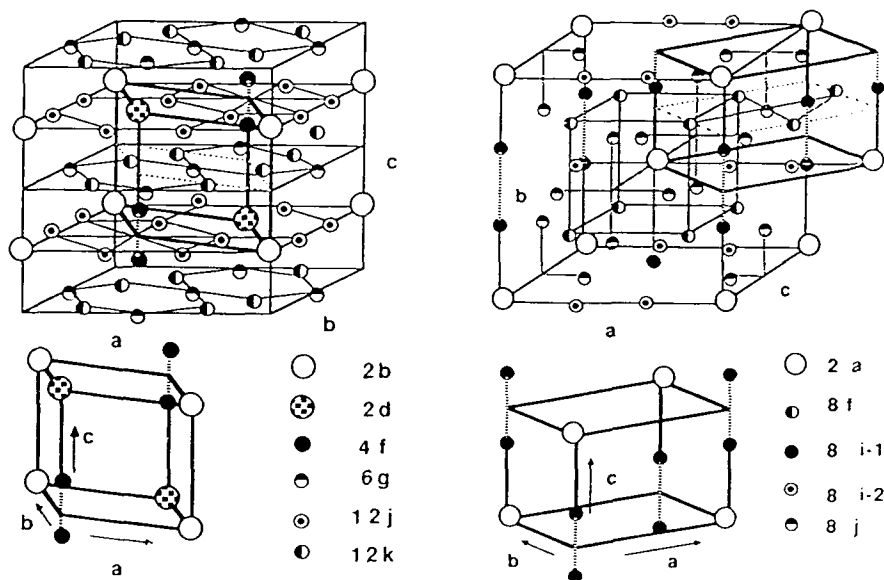


Fig. 5 Unit cells of the $\text{Th}_2\text{Ni}_{17}$ structure (left) and the ThMn_{12} structure (right) with the CaCu_5 cell marked by bold lines. The lower part indicates the $R \rightarrow 2T$ substitution sites in the CaCu_5 cell.

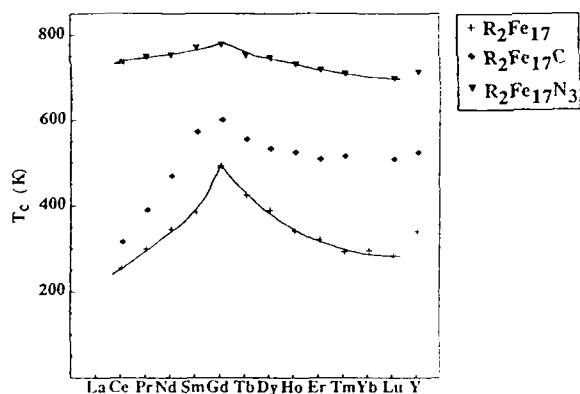


Fig. 6 Curie temperatures of R_2Fe_{17} , $\text{R}_2\text{Fe}_{17}\text{C}$ and $\text{R}_2\text{Fe}_{17}\text{N}_{3-\delta}$.

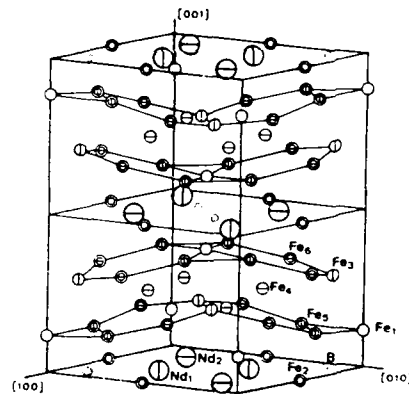


Fig. 7 Crystal structure of $\text{R}_2\text{Fe}_{14}\text{B}$.

B Ternaries[3]

$\text{Nd}_2\text{Fe}_{14}\text{B}$. This is a true ternary structure, not simply related to any existing binary; it is illustrated in Fig 7a. $Z = 4$, so there are 68 atoms in the unit cell. The main symmetry elements in the space group $P4_2/mmm$ are the 4_2 screw axes along the vertical cell edge, and two perpendicular mirror planes 110 and $\bar{1}\bar{1}0$ that are parallel to c . The two rare-earth sites $4f$ and $4g$ each have mm point symmetry, and Fig. 7b illustrates how they are disposed in the planes at $z = 0$ and $z = 1/2$, which they share with the boron ($4f$) and one of the iron sites ($4c$). Boron is coordinated by six irons that form a trigonal prism, a structural element typical of transition-metal borides. Four of the remaining iron sites are sandwiched between these rare-earth/boron planes. Iron atoms on $4e$, $8j_1$, $16k_1$ and $16k_2$ sites form two kagomé networks of distorted hexagons and triangles, while the last iron site, $8j_2$ is sandwiched between them in a hexagonal antiprism. The rare-earth sites are each surrounded by distorted

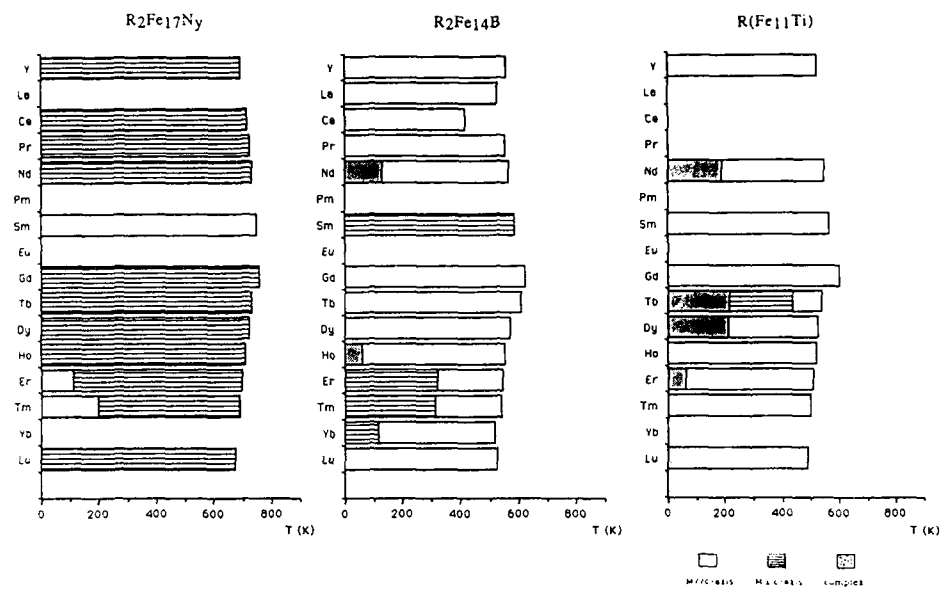


Fig. 8 Magnetic properties of $R_2Fe_{17}N_{3-\delta}$, $R_2Fe_{14}B$ and $R(Fe_{11}Ti)$.

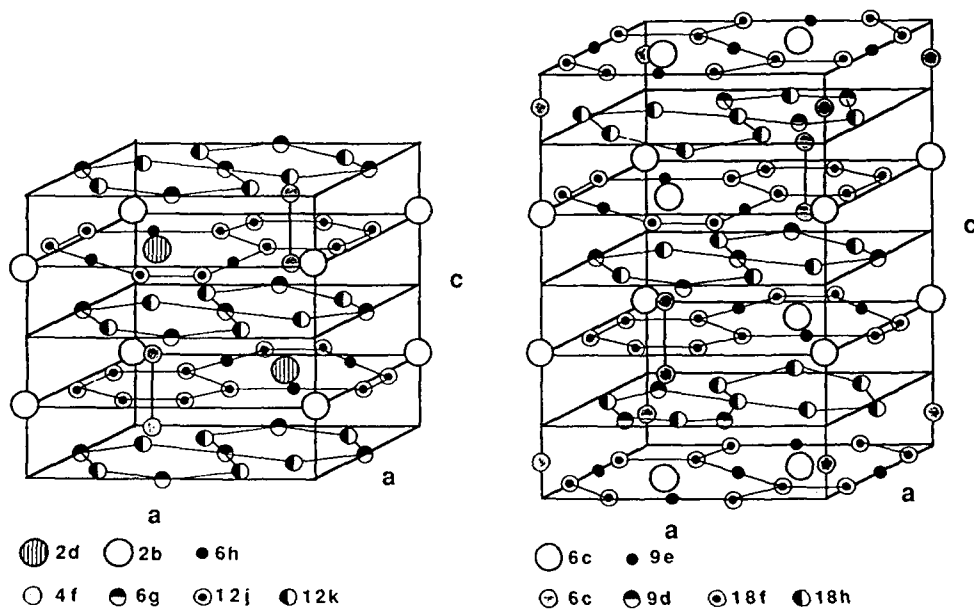


Fig. 9 The Th_2Ni_{17} and Th_2Zn_{17} crystal structures. The interstitial sites occupied by carbon or nitrogen are 6h and 9e.

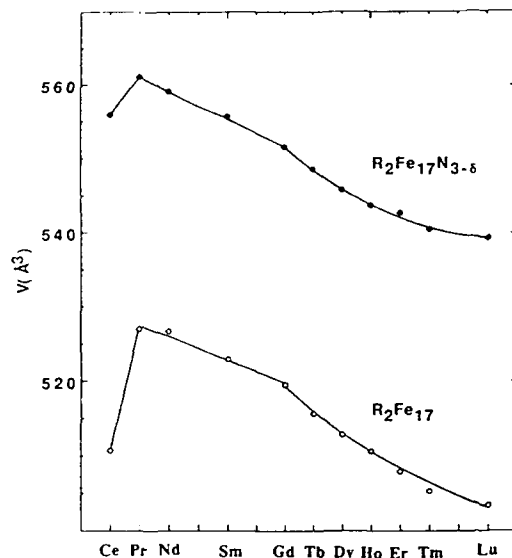


Fig. 10 Unit cell volumes for R_2Fe_{17} and $R_2Fe_{17}N_{3.5}$.

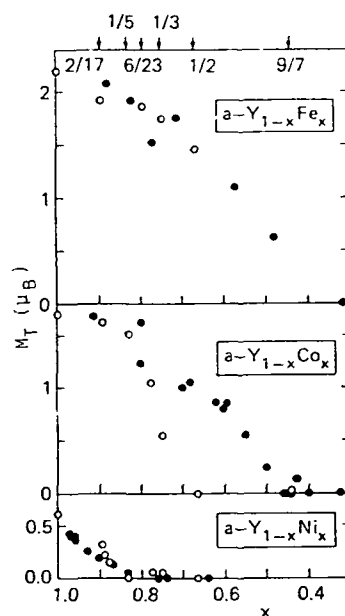


Fig. 11 Concentration dependence of the average 3d moment in crystalline (o) and amorphous (●) alloys of yttrium with iron, cobalt and nickel.

hexagonal prisms of iron, like the Sm in $SmCo_5$ ($CaCu_5$ structure). All rare earths from La to Lu, plus Y (but not Eu or Sc) will form the $R_2Fe_{14}B$ phase with iron. Cobalt can replace iron completely for the lighter rare earths, up to Tb, and partial substitution is possible for heavier ones [4]. $R_2Fe_{14}B$ is actually the only rare-earth iron compound which exists across the rare earth series from La to Lu. The magnetic properties of the series are summarized in Fig. 8. A_{20} is positive at both rare earth sites in the structure, with an average value of $300K a_0^{-2}$.

$R(Fe_{11}Ti)$. Another family of potentially-useful magnetic materials is derived from the $ThMn_{12}$ structure of Fig. 4 [5]. The RFe_{12} end-member does not exist for any rare earth, but the structure forms quite readily for $R(Fe_{12-x}M_x)$ when $M = Ti, V, Cr, Mn, Mo, W, Al$ or Si and x is in the range $1 < x < 4$. Ti, V and Mo atoms have a strong preference for the 8i sites in alloys with $1 < x < 2$, and the distribution of Fe and M atoms over these sites appears to be random. It is the M site preference that formally allows us to classify these alloys as ternaries rather than pseudo-binaries, but the distinction is a fine one. The magnetic properties of the series are summarized in Fig 8.

$R_2Fe_{17}N_{3.5}$. This newly-discovered series of intermetallics illustrates a different structural principle for deriving a ternary from a binary: introduction of interstitial atoms. Nitrogen can be introduced from the gas phase into the lattice of R_2Fe_{17} intermetallics, to produce interstitial compounds with structures related to those of the parent compounds [6]. For example, the interstitial site in the Th_2Zn_{17} structure is the 9e site in the rare earth planes. (Fig 9). Not all these sites are filled, and δ is typically 0.4. A similar series of ternary carbides also exists, with many more vacant interstitial sites (δ is about 2). Both carbon and nitrogen interstitials dilate the unit cell and increase the Curie temperature, but the effect for the nitrides is quite spectacular. The increase in cell volume is 6-7% (9% for Ce) (Fig. 10), and the magnetic ordering temperatures are some 400 °C higher than for the 2:17 parent compounds (Fig 6). The Fe-Fe exchange interactions are increased by a factor 2.6 in the nitrides, whereas the R-Fe exchange is only slightly weakened [7]. At room temperature all compounds exhibit easy-plane anisotropy, except for Sm, which has strong c-axis anisotropy equivalent to an

anisotropy field of 14 Tesla [8]. These materials have excellent potential for a new generation of bonded permanent magnets. The magnetic properties of the series are summarized on Fig. 8. The average value of A_{20} is about $-150 \text{ K.}\text{\AA}^{-2}$.

MAGNETIC MOMENTS and EXCHANGE INTERACTIONS

The simplest way of taking into account the effect of alloying on the magnetic moment involves counting the number of electrons present. The magnetic valence model of Williams et al [9] is based on the idea of *strong ferromagnetism*. A strong ferromagnet is one where the d-band is spin-polarized to the greatest possible extent, so that there are only minority spin electrons at the Fermi level. The chemical valence of an atom is $N^\uparrow + N^\downarrow$, where N^\uparrow and N^\downarrow are the numbers of valence electrons with spin up and spin down. The magnetic moment in units of μ_B is $m = N^\uparrow - N^\downarrow = 2 N^\uparrow - Z$. But N_{3d}^\uparrow is precisely 5 for strong ferromagnets (i.e. the 3d band is spin polarized to the maximum possible extent) so that the magnetic valence Z_m defined by $Z_m = 2 N_{3d}^\uparrow - Z$ is always an integer. The moment m is therefore $Z_m + 2N_{sp}^\uparrow$ where N_{sp}^\uparrow is the number of electrons in the sp^\uparrow conduction band, which is practically unpolarized.

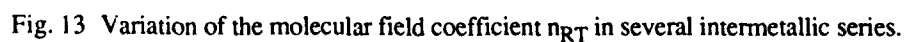
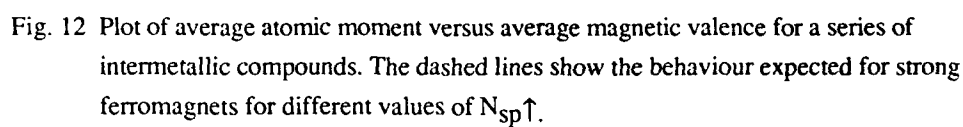
In an alloy, the average magnetic moment per atom $\langle m \rangle$ is deduced by replacing Z_m by its average value $\langle Z_m \rangle$ over all atoms present. N_{3d}^\uparrow is 5 for atoms to the right of iron in the 3d series, but it is *zero* for the early transition elements including the whole rare earth series, because replacement of an atom of Fe, Co or Ni by one of these elements removes five 3d states from below the Fermi level E_F and introduces five states above E_F . Z is 3 for B, Y, and the rare earths, 4 for C, Si, Ti ..., 8 for Fe, 9 for Co and 10 for Ni. N_{sp}^\uparrow is a small number in the range 0.3 - 0.6.

The model predicts that when a transition element T is alloyed with an other element M to form an alloy T_xM_{1-x} , the average moment falls steadily with decreasing x , reaching zero at a critical concentration for the appearance of magnetism x_c which depends on the valence of M; if it is trivalent (e.g. a rare earth), the model predicts $x_c = 0.5$ for Fe, 0.6 for Co and 0.8 for Ni. These values are borne out by studies of many amorphous alloy series, where the composition x may be varied continuously (Fig. 11). Results for a number of intermetallics are assembled in Fig 12 [3]. Weak ferromagnets, such as Fe, for which N_{3d}^\uparrow is < 5 are distinguished by their position below the line. The low nickel moment and the high critical concentration x_c make Ni alloys less attractive for magnetic applications than either Co or Fe alloys, even though the Ni compounds may be strong ferromagnets and the Fe compounds are often weak ferromagnets. A weak ferromagnet is one where 3d electrons of both spins are present at the Fermi level. Dilution usually pushes the iron compounds towards strong ferromagnetism. The Co compounds are always strong.

Intermetallic compounds of 3d and 4f elements are of great interest in magnetism because of the magnetocrystalline anisotropy provided by the crystal field interaction of the rare earth partner. These intermetallics exhibit a rich variety of spin structures and magnetic transitions including spin reorientations and compensation points (temperatures where the magnetizations of the rare earth and transition metal sublattices exactly cancel). These phenomena can be understood, and to a large extent predicted, by modelling the exchange and crystal-field interactions. The chemical similarity of the rare earths means that long isostructural series are available, sometimes covering the whole series from La to Lu. These properties could be exploited to realize a number of interesting nanocrystalline structures, such as multilayers of YCo_5 and YNi_5 , where magnetic and nonmagnetic layers of the same structure alternate, or multilayers where the anisotropy direction changes by 90° from layer to layer.

We now consider briefly the exchange coupling. There are a great number of exchange interactions between atoms on each site and the neighbouring atomic shells, which are usually represented by the Heisenberg Hamiltonian $H_{ij} = -2J_{ij}S_i \cdot S_j$. The exchange integral J_{ij} couples the spins of two nearby atoms. It is positive for a ferromagnetic interaction and negative for an antiferromagnetic interaction, and its magnitude falls rapidly with increasing distance between the atoms.

The principal magnetic interaction in an R-T intermetallic is due to direct overlap of the 3d shells of atoms on neighbouring sites. These interactions are very sensitive to structure and cell volume, particularly for Fe. The ferromagnetic interactions are strongest for Co, and significantly weaker for Fe and Ni. Usually they are all lumped together in terms of an



effective exchange interaction J_{TT} (often quoted as J/k , in units of K) or molecular field coefficient n_{TT} (usually expressed in units of μ_0) so that the contribution to the effective field B_{ex} at the T sublattices due to the T sublattices themselves is $n_{TT}M_T$. These parameters may be deduced directly from the Curie temperatures of intermetallic compounds with nonmagnetic rare earths (e.g. Y) using the molecular field expressions $T_C = N_T n_{TT} 4S^*(S^*+1)\mu_B^2/3k = 2Z_T J_{TT} S^*(S^*+1)/3k$, where N_T is the number of T atoms $/m^3$ and Z_T is the effective number of nearest neighbours. S^* is an effective spin quantum number deduced from the zero-temperature magnetic moment $m(0) = g\mu_B S^*$.

The other magnetic interactions that are important in R-T intermetallics are those between R and T atoms and R - R interactions. In terms of the molecular field theory, the effective average fields acting on R and T sublattices are

$$B_{ex}^T = n_{TT} M_T + n_{RT} \gamma M_R$$

and
$$B_{ex}^R = n_{RT} \gamma M_T + n_{RR} \gamma^2 M_R$$

where n_{TT} , n_{RT} and n_{RR} are the molecular field coefficients which have the same units as μ_0 and are generally expressed as a multiple of μ_0 , $\gamma = 2(g-1)/g$ (i.e. γ projects out the spin part of the rare earth moment). The R-R interactions are usually neglected in T-rich intermetallics, so the problem is then to determine n_{RT} . Several methods are available: one is to use the Curie temperature to deduce n_{RT} from a two-sublattice molecular field model. Then

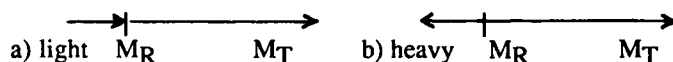
$$T_C = (1/2)[T_T + (T_T^2 + 4T_{RT}^2)^{1/2}]$$

where
$$T_T = N_T n_{TT} 4S^*(S^*+1)\mu_B^2/3k$$

and
$$T_{RT} = (N_T N_R)^{1/2} n_{RT} \gamma [2g(S^*(S^*+1)J(J+1))]^{1/2} \mu_B^2/3k$$

Another method is to fit the temperature-variation of the rare-earth sublattice magnetization measured by a local probe such as Mössbauer spectroscopy; yet another method is to measure the energy splitting between magnetic sublevels of the same or different J multiplets by a technique such as inelastic neutron scattering [10]. In any case, it is found that n_{RT} is *not a constant* across the rare earth series [11], but it seems to decrease monotonically by a factor of 2 approximately from the beginning to the end (Fig. 13). This is because the R-T interaction proceeds indirectly via the rare-earth 5d electrons. The 4f-5d interaction is ferromagnetic, but the 5d-3d coupling is antiferromagnetic for 3d transition elements in the second half of the series.

Hence the transition metal spin is coupled antiparallel to the rare earth spin. Because of Hund's rules, this means that the magnetizations of the transition metal and rare earth are coupled *parallel* for the light rare earths ($J = L - S$), and *antiparallel* for the heavy rare earths ($J = L + S$), as shown below. This rule has been confirmed by studies of countless R-T intermetallics.



Intermetallic compounds of the light rare earths are of interest when the largest magnetic moment is required at the lowest cost, for example in permanent magnets (the light rare earths are one or two orders of magnitude more abundant than the heavy rare earths). The compounds of the heavy rare earths are useful when a small net moment is required, for example in perpendicular magnetic recording.

Some further remarks: There is a tendency for the Co-rich compounds to have higher Curie temperatures than either iron or nickel counterparts. The Co - Co exchange tends to be rather independent of structure or Co moment, in the range $130 < J < 150$ K or $n_{TT} \sim 1100 \mu_0$. By contrast, the Fe - Fe exchange is unpredictable. In those structures where it is exceptionally low (e.g. 2:17), it may be enhanced by substitutions that dilate the lattice. The 3d magnetocrystalline anisotropy (K_1) is usually of opposite sign in isostructural iron and cobalt compounds. In a uniaxial structure where the iron is easy axis, the cobalt is normally easy plane and *vice versa*.

CRYSTAL FIELD INTERACTIONS

Crystal-field interactions arise when the orbitals of the electrons with unpaired spin on an atom are subject to a non-spherical potential due to the electronic charges of neighbouring atoms, or even of different electronic shells of the same atom. The energy-levels, and hence the populations of the orbitals are modified by the 'crystal-field' associated with the non-spherical potential, and as a result of spin-orbit coupling, some 'easy' directions of magnetization of the atom are lowered in energy. Adding together the contributions of all the atoms in the solid produces the macroscopic 'magnetocrystalline anisotropy'.

In the case of the rare-earths, the electrons with unpaired spin are localized in the 4f shell. The potential which they experience is due, in principle, to all other charges in the solid. In insulators it is traditional to calculate this potential by point-charge sums (sometimes allowing for the polarizability of the orbitals involved). In metals however this approach is inappropriate, because of the rapid screening of any charge by conduction electrons. In fact, most of the crystal-field potential experienced by 4f electrons is due to the 6s, 6p and 5d electrons of the same atom [12]. Regardless of its origin, the crystal field potential can be expressed in terms of an expansion which reflects the point symmetry of the rare earth site. The parameters in the expansion are determined empirically, and the effect of placing different rare earths in the potential can be calculated. This empirical approach to rare earth crystal field interactions allows us to relate the properties of the members of an isostructural series of rare earth intermetallics.

The leading terms in the expansion represent the interaction of the quadrupole moment of the 4f orbitals with the electric field gradient, the second derivatives of the potential. Charge distributions for the trivalent rare earth atoms are illustrated in Fig. 14. Except for Gd^{3+} , which is a half-filled shell ($4f^7$) and therefore spherical, these distributions are either oblate ($Pm^{3+}, Sm^{3+}, Er^{3+}, Tm^{3+}, Yb^{3+}$) or prolate (all the rest). Eu^{3+} is omitted because it has $J = 0$. In an electric field gradient of a given sign, atoms of the two groups will be aligned with their moments either parallel or perpendicular to the field gradient axis; this axis coincides with a 3-fold or higher axis of local point symmetry of the atomic site, if one is present, otherwise the electric field gradient (a second order tensor) will have three unequal principal components, the biggest of which defines the local easy or hard axis.

We now develop these ideas more formally: The Hamiltonian for a single rare earth ion having a localized moment and a well-defined magnetic quantum number J is

$$H_R = H_C + H_{SO} + H_{ex} + H_{cf} + H_{mag}$$

Here H_C includes the intra-atomic Coulomb interactions that result in states with well-defined L and S . H_{SO} is the spin-orbit interaction, $\lambda L \cdot S$, that couples L and S together to form J . $H_{ex} = 2M_B S \cdot B_{ex}$ is the exchange interaction. Since it is normally larger in magnitude than the crystal field term H_{cf} , the M_J states can be taken as the basis set for considering the electrostatic crystal field interaction. The final term, $H_{mag} = \mu_B (L + 2S) \cdot B_0$, represents coupling of the rare earth moment with an internal or external magnetic field.

The crystal field term H_{cf} is the interaction of the charge distribution in the 4f shell with the potential created by the rest of the crystal. That potential $V(r, \theta, \phi)$ can be expressed as a sum of normalized tesseral harmonics $Z_n^m(\theta, \phi)$

$$eV(r, \theta, \phi) = \sum_{n=0}^6 \sum_{m=0}^n A_n^m [r^n Z_n^m(\theta, \phi) / C_{nm}]$$

where C_{nm} is a numerical constant and all the information about the crystal is contained in the crystal field coefficients A_n^m . The index m runs over integers $0 \leq m \leq n$, and covers terms in $\sin \phi$ and $\cos \phi$ when $m \neq 0$ (an extra index s or c is sometimes included). The index n can take the values 2, 4 and 6 for the rare earth series. A convenient way of evaluating the matrix elements of the potential for the wavefunctions corresponding to a particular value of J is the method of *operator equivalents* introduced by Stevens, and described in some detail by Hutchings [13]. The tesseral Harmonics in the expansion of the potential are expressed in Cartesian coordinates, and then replaced by operators involving J_x, J_y, J_z and J^2 . For

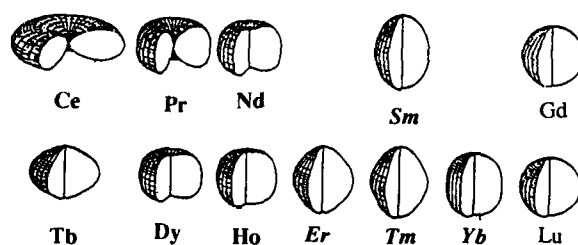


Fig. 14 Normalized angular distributions of 4f charge density for the trivalent rare earth series with $J_z = J$. From Thole, quoted in ref. 12.

Rare earths in italics have $\alpha_J > 0$, while those in bold type have $\alpha_J < 0$.

example, $r^2 Z_2^0 / C_{20}$ which can be written as $3z^2 - r^2$, is replaced by $\langle r^2 \rangle \alpha_J O_2^0 = 3J_z^2 - J(J+1)$. The crystal field Hamiltonian is then written in the form

$$H_{cf} = \sum_{n=0}^6 \sum_{m=0}^n B_n^m O_n^m$$

The number of terms in the expansion is limited by the point symmetry of the rare-earth site. The parameters B_n^m combine information on the potential created by the distribution of charge in the solid and the form of the charge distribution of the 4f shell. Specifically

$$B_n^m = \theta_n \langle r^n \rangle (1 - \sigma_n) A_n^m$$

where θ_n is a reduced matrix element known as the Stevens coefficient for the rare-earth ion in question (denoted as α_J , β_J , γ_J for $n=2, 4, 6$ respectively), $\langle r^n \rangle$ is the average over the 4f wavefunctions, σ_n is a shielding factor. The coefficients A_n^m describe the crystal field produced by the surroundings of the rare earth ion, and should change little in an isostructural series of compounds with different rare earths.

One way of evaluating A_n^m , which is of very limited use in a metal because of the presence of conduction electrons, is from the *point charge model*. Charges q_i are associated with the atomic sites ($R_i \Theta_i \Phi_i$), and

$$A_n^m = -\{4\pi e / (2n+1) C_{nm}\} \sum_i q_i Z_n^m(\Theta_i \Phi_i) / R_i^{n+1}$$

For example, $A_2^0 = -\{e/4\} \sum_i q_i (3\cos^2\Theta_i - 1) / R_i^3$

The point charge model can be improved by allowing for the screening effect of the conduction electrons, for example in the Thomas-Fermi approximation. It is mainly used in metals as a way of estimating the ratios of terms of the same order n , when it is impossible to deduce them unambiguously from experiment.

The leading term $B_2^0 O_2^0$ in the expansion of the crystal field interaction in uniaxial materials is particularly important, because it is the sign of this term, the product of the signs of α_J and A_2^0 , that determines whether the rare earth has hard- or easy-axis anisotropy.

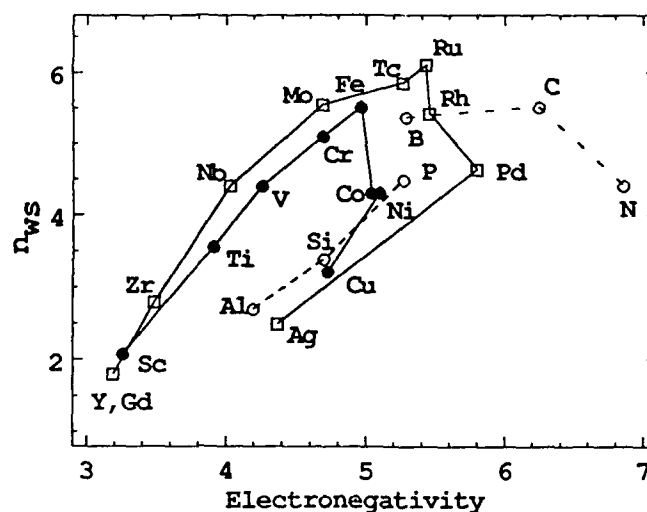


Fig. 15 Normalized charge density at the Wigner Seitz cell boundary versus Miedema's electronegativity parameter [12].

Easy-axis anisotropy is required for permanent magnets. The sign of A_2^0 is decided by the crystal structure, but that of α_J depends on whether the shape of the 4f charge distribution is prolate or oblate. Values of α_J , β_J and γ_J for the rare-earth series are listed in Table 1. Note that the sign of α_J for Sm is opposite to that for Pr or Nd. A crystal with positive A_2^0 will exhibit an easy axis 4f contribution to the anisotropy when $R = \text{Pr or Nd}$, but easy-plane anisotropy when $R = \text{Sm}$.

Recent progress has been made in obtaining crystal field coefficients from full band structure calculations of metals, taking account of the screening effect of distant charges. Coehoorn [12] has also proposed a simple way of estimating the sign and magnitude of A_{20} in a qualitative manner. The idea is to consider the Wigner Seitz cell around the rare-earth atom, and to look at the charge density given by the Miedema parameter n_{ws} . The requirement of continuity across the cell boundary imposes some shape on the rare earth valence electron charge density, which is mainly responsible for A_{20} . The result is simply that A_{20} is positive if neighbours with the highest n_{ws} lie on the z-axis through the rare earth atom, and A_{20} is negative if neighbours with the highest n_{ws} are in the xy plane around the atom. The parameter n_{ws} shows no simple correlation with electronegativity, except in very limited sequences of atoms (Fig 15).

Another way of regarding the terms of different order in the crystal field Hamiltonian is as the interaction between the multipole moments of the 4f distribution and the appropriate component of the potential created by the rest of the solid. Terms with $n = 2, 4, 6$ correspond to the quadrupole, hexadecapole and the 64-pole interactions.

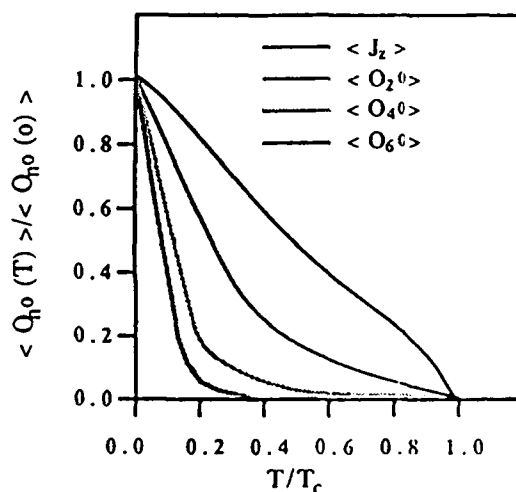
The relative strengths at $T = 0$ of the terms in the crystal field with $m = 0$ and $n = 2, 4$ and 6 for different rare-earths in a particular crystal structure are represented by the products $\theta_n \langle r^n \rangle \langle O_n^m \rangle$. These quantities are also displayed in Table 1. The sign of the fourth order terms are relevant in determining, in a tetragonal structure for example, whether 100 or 110 is the easier direction. Fourth and sixth order terms are usually insignificant in comparison to the second order terms at room temperature and above, because of the high powers of J_z that appear in the fourth and sixth order Stevens operators. $\langle J_z \rangle$ falls with increasing temperature, tending to zero at the Curie point. Figure 16 illustrates the point, comparing the temperature variation of $\langle J_z \rangle$, $\langle O_2^0 \rangle$, $\langle O_4^0 \rangle$ and $\langle O_6^0 \rangle$ calculated for Er in $\text{Er}(\text{Fe}_{11}\text{Ti})$. The higher order terms may be crucial for determining the ground state magnetic structure at zero temperature.

Returning to the ferromagnetic transition metals, the crystal field acting there on the unshielded 3d electrons is stronger than the spin-orbit interaction. The orbital moment is largely quenched, but single-ion anisotropy can arise when some residual orbital contribution remains. The effect is typically an order of magnitude smaller than for the rare-earth series, but the contribution of the 3d element to the total magnetocrystalline anisotropy is significant

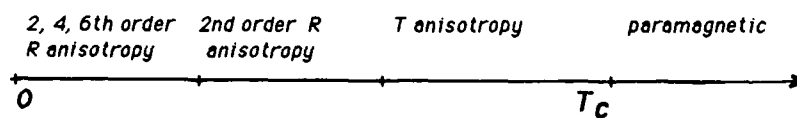
Table 1

| | J | S | γ | $\langle r^2 \rangle \alpha_J O_{20}$ | $\langle r^4 \rangle \beta_J O_{40}$ | $\langle r^6 \rangle \gamma_J O_{60}$ |
|-----|------|-----|----------|---------------------------------------|--------------------------------------|---------------------------------------|
| Ce | 5/2 | 1/2 | -1/2 | -0.74 | 1.51 | - |
| Pr | 4 | 1 | -1/2 | -0.71 | -2.12 | 5.9 |
| Nd | 9/2 | 3/2 | -3/4 | -0.26 | -1.28 | -8.6 |
| Sm | 5/2 | 5/2 | -5 | 0.40 | 0.34 | - |
| Sm* | 7/2 | 5/2 | -9/26 | 0.33 | -0.19 | 2.0 |
| Gd | 7/2 | 7/2 | 1 | - | - | - |
| Tb | 6 | 3 | 2/3 | -0.55 | 1.20 | -1.3 |
| Dy | 15/2 | 5/2 | 1/2 | -0.52 | -1.46 | 5.6 |
| Ho | 8 | 2 | 2/5 | -0.20 | -1.00 | -10.0 |
| Er | 15/2 | 3/2 | 1/3 | 0.19 | 0.92 | 9.0 |
| Tm | 6 | 1 | 2/7 | 0.45 | 1.14 | -4.0 |
| Yb | 7/1 | 1/2 | 1/4 | 0.43 | -0.79 | 0.7 |

*Excited state. $\langle r^n \rangle$ values from A J Freeman and J P Desclaux J Magn Magn Mat 12 11 (1979)

Fig. 16 Thermal variation of operators calculated for Er in Er(Fe₁₁Ti).

because 3d atoms are the major constituents of the alloys of interest here. The 3d anisotropy can be estimated in the framework of extensive band structure calculations, but it is usually phenomenologically represented by a term $K_1 \sin^2 \theta$ where θ is the angle between the 3d moment and the c axis. Temperature dependence of the 3d anisotropy is typically less pronounced than that of the second-order 4f term. It is often useful to distinguish three regions of temperature for rare earth transition-metal intermetallic compounds where different terms in the anisotropy are responsible for determining the magnetic structure, as shown below:



At the lowest temperatures, the second, fourth and sixth order rare earth anisotropy can all be important, and complex noncollinear magnetic structures may be the result. On raising the temperature, the influence of the fourth and sixth order terms will rapidly decline, leaving the second order rare earth terms as the principal source of magnetocrystalline anisotropy. This is often the situation at room temperature, and the second-order rare earth anisotropy is the key to understanding the magnetism of most of the $R_2Fe_{14}B$ series. Finally, at higher temperatures the more rapid decline of the rare earth magnetization compared with that of the transition metal can lead to a situation where the iron or cobalt anisotropy is the dominant term up to T_c . The magnetic structure of $R_2Fe_{14}B$ and $R_2Fe_{17}N_3$ (Fig.8) can be understood in terms of this scheme, bearing in mind that K_{1T} and A_2^0 are opposite in sign in the two structures.

Two other sources of anisotropy should be mentioned. One arises because the magnetic dipole interaction is anisotropic; the mutual interaction of two dipoles depends on their orientation with respect to the vector joining them. If the dipoles are parallel, their interaction will be a factor of 2 greater when $\mathbf{m} \perp \mathbf{r}$ than when $\mathbf{m} \parallel \mathbf{r}$. The sum of these two-ion contributions can give a contribution to the magnetocrystalline anisotropy in non-cubic structures. Typical dipolar fields are < 1 T.

Finally, shape anisotropy should be mentioned although it is not related to atomic scale magnetism. An elongated particle will prefer, all else being equal, to have its magnetization lie along the long axis, thereby minimizing the self energy in the demagnetizing field. The difference between the demagnetizing field in the easy and hard directions is less than $\mu_0 M_s$ (~ 1 T).

Modelling the Interactions

In analysing the magnetic properties of R-T intermetallic compounds, we are obliged to resort to phenomenological models whose parameters are determined by experiment. One day it may be possible to predict the magnetic properties of a crystal from a knowledge of its structure and chemical composition by numerical solution of Schrodinger's equation. But by then magnetism will have lost its appeal for physicists. In the meantime we endeavour to develop models with a small number of experimentally-determined parameters which can describe a range of compounds or phenomena such as Curie temperature, magnetic structure, temperature dependence of magnetization or anisotropy field [14].

Modelling of exchange interactions is done in the *molecular field approximation* [15]. This consists of replacing the interaction $-2J_{ij}S_i \cdot S_j$ summed over each pair of spins by the interaction, $-2\mu_B S_i B_{ex}$, of each moment with an effective 'molecular' field B_{ex} acting at its site. The molecular field is determined self-consistently, and it is proportional to $\langle S_z \rangle$. The molecular field theory of magnetism is the prototype mean field theory. It yields values of the critical exponents that are appropriate for four dimensions, but which differ somewhat from those observed for three-dimensional systems.

The compounds that concern us here have two magnetic sublattices, composed of rare earth and transition metal atoms. This is already a simplification because there can be several sublattices of each kind if the structure includes inequivalent crystallographic sites. The effective fields acting on each sublattice are B_{ex}^R and B_{ex}^T , defined earlier in terms of the molecular field coefficients n_{TT} , n_{RT} and n_{RR} .

The temperature-dependence of the magnetization of the two sublattices are given by the Brillouin functions;

$$M_T(T) = M_T(0) B_S(g_S \mu_B B_{ex}^T / kT)$$

$$M_R(T) = M_R(0) B_J(g_J \mu_B B_{ex}^R / kT)$$

where

$$B_J(x) = 1/(2J) \{ (2J+1) \coth[(2J+1)x/2J] - \coth[x/2J] \}.$$

S in the above equations must be replaced by the effective spin S^* . Self-consistent solutions are sought in terms of the molecular field coefficients n_{TT} and n_{RT} (n_{RR} is usually neglected). Typical temperature dependence of the sublattice magnetizations for an R-T alloy are shown in Fig. 17.

If the rare-earth is nonmagnetic, the Curie point is found by solving the equations for B_{ex}^T and $M_T(T)$ in the limit $x \ll 1$. Then we find the result quoted earlier: $T_c = n_{TT} C_T$, where $C_T = N_T g^2 S^* (S^* - 1) \mu_B^2 / 3k$ and N_T is the number of atoms per cubic metre. The relation between the microscopic and macroscopic exchange parameters J and n is $J =$

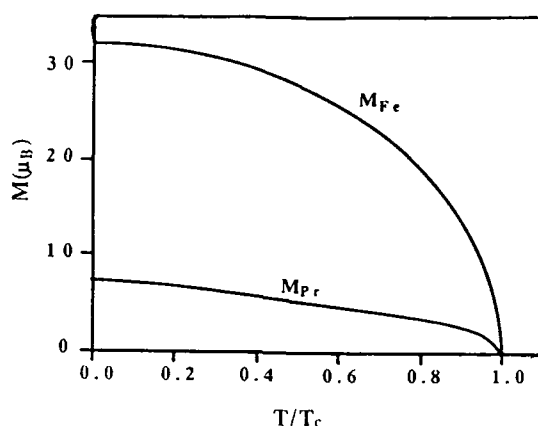


Fig. 17 Sublattice magnetization in $\text{Pr}_2\text{Fe}_{14}\text{B}$.

$(N_T g^2 \mu_B^2 / 2Z)n$. Also $B_{cx} = 2ZSJ / g\mu_B$. When the rare-earth is magnetic, solution of the equations gives the expression for T_c given earlier.

The crystal field acting on the rare-earth will have some influence on the results of the molecular field calculation. Instead of acting on a $(2J+1)$ -fold degenerate energy level, the crystal field ground state may be a doublet or even a singlet, but the effect on results such as those in Fig. 17 is slight. In any case, the molecular field theory takes no account of spin wave excitations, and provides an inaccurate, mean-field description of the behaviour in the critical region around T_c . Yet, despite the shortcomings, it does offer a really useful basis for modelling the magnetic properties of two-sublattice magnets so long as it is not forgotten that the molecular field coefficients are just empirical parameters.

The *anisotropy energy* can be expressed as a series of terms involving the orientation of the total or sublattice magnetization with respect to the crystal axes. In a tetragonal crystal the expression is

$$E_a = K_1 \sin^2 \theta + K_2 \sin^4 \theta + K_3 \sin^6 \theta + K_2' \sin^4 \theta \cos 4\phi + K_3' \sin^6 \theta \cos 4\phi$$

whereas in an hexagonal crystal the corresponding expression is

$$E_a = K_1 \sin^2 \theta + K_2 \sin^4 \theta + K_3 \sin^6 \theta + K_3' \sin^6 \theta \cos 6\phi$$

The dominant term for the 3d anisotropy is $K_{1T} \sin^2 \theta$, which leads to an easy axis when K_{1T} is positive and a hard-axis when K_{1T} is negative. Units of K are J m^{-3} .

Related to the anisotropy energy is the concept of *anisotropy field*. The anisotropy energy is somehow equivalent to that produced by an effective field B_a acting along the easy direction. The analogy is useful, but inexact because the angular variation of magnetic energy is as $-MB_a \cos \theta$. The anisotropy field is defined as that needed to saturate the magnetization in a direction perpendicular to the easy axis. The orientation of the magnetization is given by the condition $dE/d\theta = 0$, so the condition $\theta = \pi/2$ yields $B_a = 2(K_1 + 2K_2 + 3K_3)/M_s$. The anisotropy field sets an upper limit on the coercivity $\mu_0 H_c$; achievable coercivities rarely exceed 20% of B_a .

Finally, there exist relations between the terms in the crystal field Hamiltonian for the rare earth sublattice and the K 's in the above equations. For the tetragonal case these are:

$$K_{1R} = -\{(3/2)B_2^0 \langle O_2^0 \rangle + 5B_4^0 \langle O_4^0 \rangle + (21/2)B_6^0 \langle O_6^0 \rangle\}$$

$$K_{2R} = (7/8)\{5B_4^0 \langle O_4^0 \rangle + 27B_6^0 \langle O_6^0 \rangle\}$$

$$K_{3R} = -(231/16)B_6^0 \langle O_6^0 \rangle$$

$$K'_{2R} = (1/8)\{B_4^{4c} \langle O_4^0 \rangle + 5B_6^{4c} \langle O_6^0 \rangle\}$$

$$K'_{3R} = -(11/16)B_6^{4c} \langle O_6^0 \rangle$$

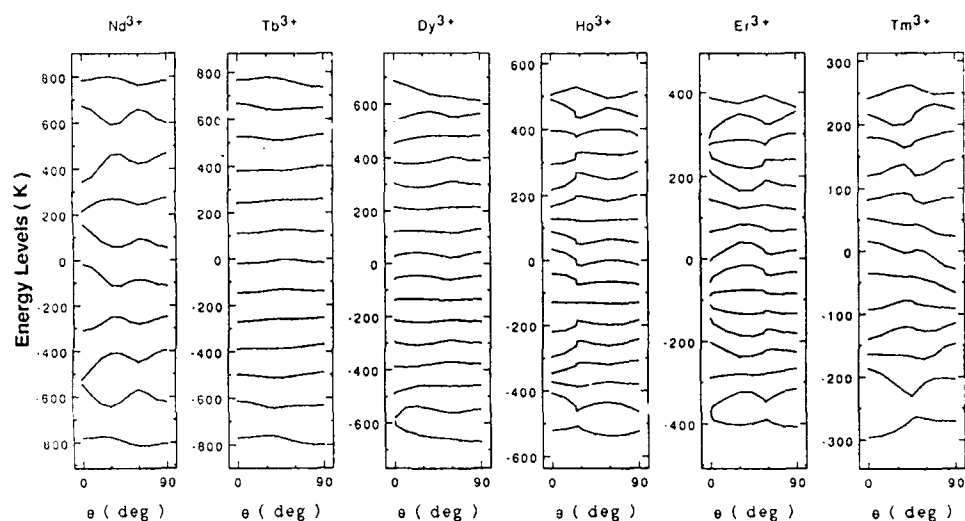


Fig. 18 Theoretical energy level schemes calculated for R^{3+} in $R(Fe_{11}Ti)$.

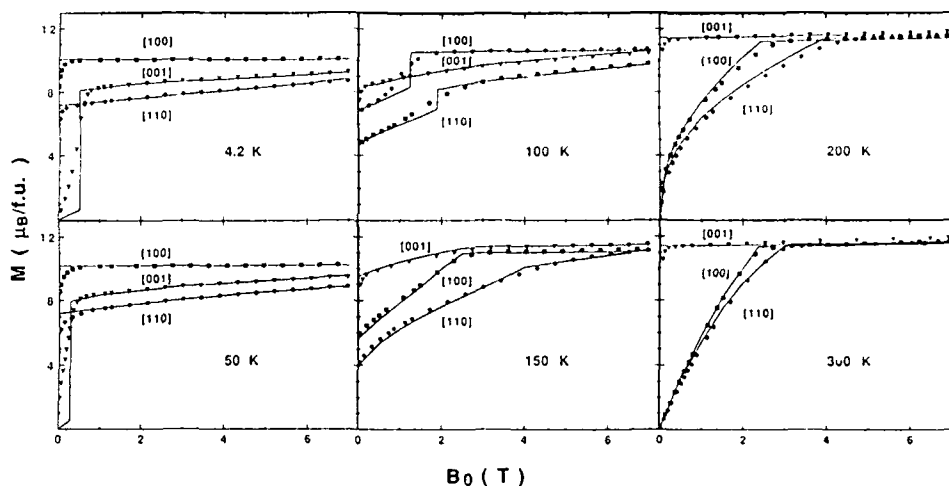


Fig. 19 Experimental (points) and calculated (lines) magnetization curves of $Dy(Fe_{11}Ti)$ at six temperatures[18].

Relations are similar in the hexagonal case, except that $K'_{2R} = 0$, and

$$K'_{3R} = (1/16)B_6^{6c}\langle O_6^0 \rangle$$

However, there is no straightforward relation between $\{B_n^m\}$ and $\{K_i\}$ in a two-sublattice magnet if the sublattices do not remain rigidly collinear in the applied field.

Magnetization curves in different directions on single crystal samples, and spin reorientation transitions as a function of temperature or applied field can be analysed in terms of a set of empirical anisotropy constants $\{K_i\}$. A spin reorientation begins when K_1 changes sign, and the angle between the moment direction and the c-axis is given by minimizing the energy E_a as

$$\sin \theta = \{(-K_2 \pm [K_2^2 - 3K_1K_3]^{1/2})/3K_3\}^{1/2}$$

or if K_3 is negligible by

$$\sin \theta = (-K_1/2K_2)^{1/2}$$

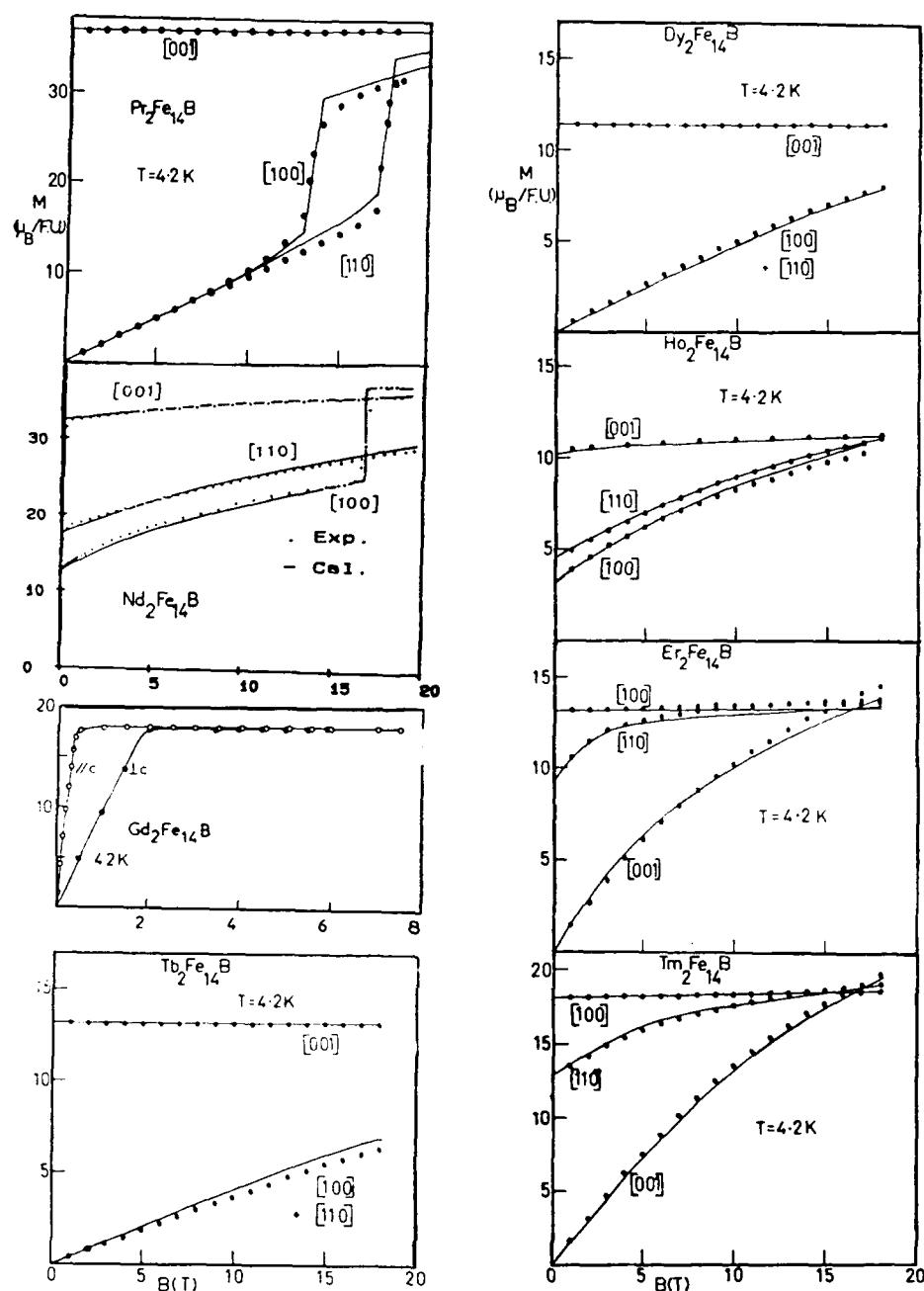


Fig. 20 Magnetization curves measured on single crystals of $R_2Fe_{14}B$. The solid lines are fits from the model described in the text [19].

Experimental Determination of the Crystal Field: A complete specification of the crystal field is a challenging task. Expressions for the crystal field hamiltonian at the rare earth sites in the intermetallic structures we have been considering are as follows.

$$4/mmm : (ThMn_{12}) \quad H_{cf} = B_2^0 O_2^0 + B_4^0 O_4^0 + B_4^4 O_4^4 + B_6^0 O_6^0 + B_6^4 O_6^4$$

$$6/mmm : (CaCu_5) \quad H_{cf} = B_2^0 O_2^0 + B_4^0 O_4^0 + B_6^0 O_6^0 + B_6^6 O_6^6$$

$$\text{or } \bar{6}m2 : (Th_2Ni_{17})$$

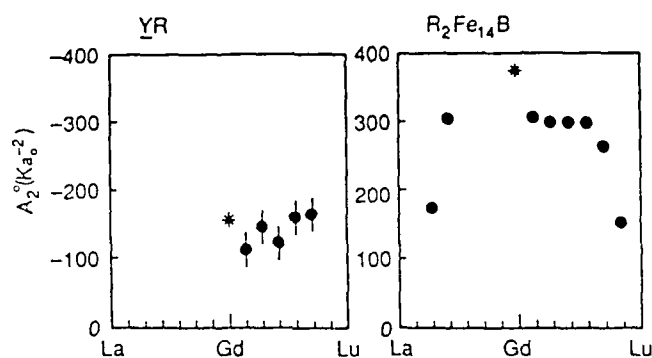


Fig. 21 A_2^0 crystal field parameters at R sites in hcp Y (left) and in $R_2Fe_{14}B$ (right) [12].

Table 2. Crystal Field Parameters for $R_2Fe_{14}B$

| | A_{20} | A_{22}^s | A_{40} | A_{44}^c | A_{60} | A_{64}^c | | A_{20} | A_{22}^s | A_{40} | A_{44}^c | A_{60} | A_{64}^c |
|----|----------|------------|----------|------------|----------|------------|-----|----------|------------|----------|------------|----------|------------|
| Pr | 176 | -116 | 3 | -9 | -7 | -42 | 179 | 351 | 3 | 8 | -7 | -4 | |
| Nd | 304 | -200 | -15 | 43 | -2 | -33 | 308 | 605 | -13 | -41 | -2 | -13 | |
| Tb | 304 | -200 | -15 | 43 | -2 | -33 | 308 | 605 | -13 | -41 | -2 | -13 | |
| Dy | 292 | -192 | -14 | 42 | -1 | -20 | 296 | 581 | -12 | -39 | -1 | -8 | |
| Ho | 298 | -196 | -9 | 26 | -1 | -19 | 302 | 593 | -8 | -24 | -1 | -7 | |
| Er | 292 | -222 | -16 | 37 | -1 | -6 | 296 | 689 | -14 | -39 | -1 | -3 | |
| Tm | 258 | -205 | -12 | 35 | -2 | -27 | 262 | 617 | -11 | -33 | -2 | -10 | |
| Yb | 151 | -100 | -7 | 22 | -1 | -17 | 154 | 303 | -6 | -20 | -1 | -6 | |

Units of A_{nm} are Ka_0^{-n} : The first six values are for the 4f site, the second six are for the 4g site.

Table 3. Crystal Field Parameters for $R(Fe_{11}Ti)$

| A_{20} | A_{40} | A_{44} | A_{60} | A_{64} | ($K \cdot a_0^{-n}$) |
|----------|----------|----------|----------|----------|------------------------|
| -32.3 | -12.4 | 118 | 2.56 | 0.64 | |

$$3m : (Th_2Zn_{17}) \quad H_{cf} = B_2^0 O_2^0 + B_4^0 O_4^0 + B_4^3 O_4^3 + B_6^0 O_6^0 + B_6^3 O_6^3 + B_6^6 O_6^6$$

$$mm : (Nd_2Fe_{14}B) \quad H_{cf} = B_2^0 O_2^0 + B_2^{2s} O_2^{2s} + B_4^0 O_4^0 + B_4^{2s} O_4^{2s} + B_4^{4c} O_4^{4c} \\ + B_6^0 O_6^0 + B_6^{2s} O_6^{2s} + B_6^{4c} O_6^{4c} + B_6^{6s} O_6^{6s}$$

The number of independent crystal field parameters is just four in $SmCo_5$, but 18 in $Nd_2Fe_{14}B$ (9 for each 4f or 4g site).

The most direct way of determining the crystal field parameters is by measuring the crystal field energy levels directly. These (calculated) energy levels are shown in Fig 18 for the case of $R(Fe_{11}Ti)$. The effect of the crystal field is superimposed on the Zeeman splitting due to the exchange field B_{ex}^R . Crystal field effects are most pronounced for non-Kramers ions with small J - values. Inelastic neutron scattering has been used to probe the lowest levels of the ground-state J multiplet [16] (and the relatively low-lying $5/2 \rightarrow 7/2$ intermultiplet transition in Sm [10]). However the range of energy transfer available does not span the range of energy shown in Fig. 5.

Another approach is to fit an axis \rightarrow plane spin reorientation transition, or to fit the value of the anisotropy field. It is assumed that the temperature variation of $K_1 T$ is known from measuring, for example, the isostructural yttrium compound. An effective value of A_{20} is obtained in this way; Examples are analysis of the spin reorientations in $R_2Fe_{17}N_3$ ($R=Er, Tm$), which yield $A_{20} = -60 \text{ K a}_0^{-2}$, or the anisotropy field of $Sm_2Fe_{17}N_3$, which yields $A_{20} = -180 \text{ K a}_0^{-2}$ [17].

For a more accurate set of crystal field parameters, a more complete set of data is required. Magnetization curves of a single crystal can be measured along the principal crystallographic directions as a function of temperature, and fitted (see Fig 19 for $Dy(Fe_{11}Ti)$) [18]. Note that this data includes discontinuous jumps in magnetization known as first order magnetization processes when the field is applied in a certain direction. Torque curves may also be fitted in a similar way. When more parameters are required, as in the case of $Nd_2Fe_{14}B$, it is necessary to consider data on a suite of isostructural compounds (see Fig 20), often making judicious approximations regarding the higher-order crystal field terms. The variation of A_{20} across the series is shown in Fig 21, and some sets of A_{nm} are shown in Tables 2. and 3 [19].

CONCLUSIONS

Despite the structural and magnetic complexity of rare earth transition metal intermetallics, it is possible to deduce exchange parameters which vary in a consistent and reasonable manner across a series of compounds of different rare earths, and to deduce sets of series. The key features of the magnetic behavior including spin reorientations and first order magnetization processes are explained in terms of the model. The modelling that has been built up for these long series of isostructural intermetallics provides a good basis for predicting the properties of any new R-Fe or R-Co binaries or ternaries that may be discovered in future.

ACKNOWLEDGEMENTS

The author is grateful to many colleges who have participated in different parts of this work but in particular to Dr Li Hong-shuo and D.P.F Hurley for help in preparing this manuscript. Most of this work has been supported by the European Commission in particular through the EURAM programme.

REFERENCES

- 1 de Wijn H W, van Diepen A M and Buschow K H J, *Phys. Stat. Sol.* **b76**, 11 (1976)
- 2 Hong-shuo Li, Bo-ping Hu, Cadogan J M, Coey J M D and Gavigan J P, *J. Appl. Phys.* **67** 4838 (1990)
- 3 Hong-shuo Li and J. M. D. Coey in *Ferromagnetic Materials* ed. Buschow K H J, (North Holland, Amsterdam) vol 5. in press
- 4 Buschow K H J, in *Ferromagnetic Materials*, ed. Wohlfarth E P and Buschow K H J, (North Holland, Amsterdam, 1988) vol 4, Ch.1
- 5 Buschow K H J and De Mooij D B, in *The Concerted European Action on Magnets* ed Mitchell I V, Coey J M D, Givord D, Harris I R and Hanitsh R, (Elsevier, London) p.63
- 6 Coey J M D and Sun Hong, *J. Magn. Magn. Mater* **87**, L 251 (1990)
- 7 Sun Hong, Coey J M D, Otani Y and Hurley D P F, *J. Phys. Condens. Matter* **2**, 6465 (1990)

- 8 Katter K, Wecker J, Schultz L and Grössinger R, J. Magn. Magn. Mater. (to be published).
- 9 Williams A R, Moruzzi V L, Malozemoff A P and Terakura K, IEEE Trans. Magn. **MAG 19** 1983 (1983)
- 10 Moze O, Caciuffo R, Li Hongshuo, Hu Boping, Coey J M D, Osborn R and Taylor A D, Phys. Rev. B **42** 1940 (1990)
- 11 Belorizky E, Frémy M A, Gavigan J P, Givord D and Li H S, J. Appl. Phys. **61** 3971 (1987)
- 12 Coehoorn R Phys. Rev. B. (1990) in press
- 13 Hutchings M T, Solid State Physics **16** 227 (1964)
- 14 Cadogan J M, Gavigan J P, Li Hongshuo J Phys **F18** 779 (1988)
- 15 Smart J S *Effective field theories of magnetism* (Saunders, Philadelphia, 1966) 188pp.
- 16 Löwenhaupt M, Sosnowska I and Frick B, Phys Rev B **42** 3866 (1990)
- 17 Hu Boping, Li Hongshuo, Sun Hong, Lawler J F and Coey J M D, Solid State Commun **76** 587 (1990)
- 18 Hu Bo-Ping, Li Hong-Shuo, Gavigan J P and Coey J M D, Phys. Rev. B **41** 2221 (1990)
- 19 Coey J M D, Li Hongshuo, Gavigan J P, Cadogan J M and Hu Boping in *The Concerted European Action on Magnets* ed Mitchell I V, Coey J M D, Givord D, Harris I R and Hanitsh R, (Elsevier, London) p.63

CRYSTAL-FIELD AND EXCHANGE INTERACTIONS

IN HARD MAGNETIC MATERIALS

J.J.M. Franse and R.J. Radwanski

Natuurkundig Laboratorium der Universiteit van Amsterdam
Valckenierstraat 65, 1018 XE Amsterdam, The Netherlands

1. Introduction

The detailed description of the magnetic behaviour of the 4f-3d intermetallics is a long-standing problem of which the solution is hampered by the complex interactions and the large number of parameters that is involved. The basic principles behind the magnetic properties of these compounds are quite well understood: the Curie temperature of the 3d-rich compounds is mainly governed by the 3d-3d exchange interactions, whereas the extraordinary large magnetocrystalline anisotropy is a special feature of the magnetic rare-earth ions. The 3d and 4f moments are coupled by exchange interactions that are usually described in a molecular-field type of model. The interactions between the rare-earth spins are assumed to be weak compared to the interactions mentioned so far.

The study of rare-earth transition-metal intermetallic compounds has a number of interesting aspects. By the wide range of intermetallics with different stoichiometries and with different rare-earth elements, modifications of magnetic properties of 3d transition-metal and 4f rare-earth ions can be investigated systematically. These studies illuminate the complex interactions in which the 3d and 4f electrons are involved. In case of the 4f ions these interactions can be distinguished into interactions of the 4f electrons with the surrounding electric charges and those with the surrounding electron spins. These two interactions can be represented by the crystalline electric field and an exchange field, respectively. Magnetism of the 3d ions is mainly discussed in terms of the energy-band parameters.

The technical interest in this class of materials is closely connected to the huge magnetic anisotropy that is found in many of the 3d-4f interme-

tallics. This anisotropy originates from the rare-earth ions and is transferred by the 3d-4f exchange interactions to the 3d ions. This anisotropy is the fundamental parameter behind the coercive field.

The largely anisotropic magnetic properties of compounds involving rare-earth ions originate from the existence of non-quenched orbital moments. In the quantum formalism, the 4f shell is represented by wavefunctions on the basis of the total angular momentum J and its components M_J : $|J, M_J\rangle$. The appropriate Hamiltonian, which determines these wavefunctions includes several terms associated with the various relevant interactions. The interactions of the 4f electrons with the surrounding electric charges is described in terms of the crystalline electric field (CEF). This field can eventually be modulated by magnetoelastic phenomena associated with magnetostriction. The interaction of the 4f electron spin with the surrounding spins is treated in terms of an isotropic Heisenberg-type Hamiltonian that is approximated by an effective field originating from the spin surrounding and that is denoted by the molecular (or exchange) field.

The intrinsic magnetic properties of $R_2T_{14}B$ compounds can be qualitatively understood in terms of **exchange interactions** and **magnetocrystalline anisotropy**. The **exchange interactions** take place between all unpaired spins in the 3d-4f system. These interactions are generally considered to be of the Heisenberg type. Because there are three kinds of spin pairs, the exchange interactions are formally described by three different exchange-interaction parameters: J_{TT} , J_{RT} and J_{RR} . The strength of these interactions decreases in the sequence mentioned. J_{TT} is positive and leads to ferromagnetic coupling between the 3d spins. In the iron- and cobalt-based compounds this interaction turns out to be strong enough to produce an almost exact parallel alignment of the 3d magnetic moments at low temperatures. This interaction primarily governs the temperature dependence of the 3d moment and the value of T_c of a 3d-4f compound. The interaction parameter J_{RT} is responsible for the internal magnetic structure. Its negative sign reflects an antiparallel coupling of the 4f and 3d spins and leads to a parallel alignment of the 3d and 4f moments in case of light rare earths and to an antiparallel alignment for the heavy rare earths. The 3d-4f interaction dominates the temperature dependence of magnetic moment and magnetocrystalline anisotropy of the rare-earth ions.

2. Crystal-field interactions

The 4f electrons, that are considered as well localized and separated from other positive and negative charges, experience an electrostatic potential $V_{CF}(r)$ that originates from the surrounding charge distribution.

In case there is no overlap between this charge distribution and the wave functions of the 4f state, V_{CF} can be expanded in terms of the spherical harmonics, Y_n^m with $m \leq n$. The values of n in this expansion are limited to $n \leq 6$ as higher-order multipole terms do not enter into the Hamiltonian of the rare-earth ion because of the electronic density configuration of the 4f shell. For details see Hutchings (1964) and Fulde and Loewenhaupt (1988).

Since for the rare-earth ions the spin-orbit interaction is much larger than the crystal-field and exchange interactions, it is generally sufficient to consider the lower multiplet J , given by Hund's rule. This limitation results in a substantial simplification in computations. Most of the interpretations are made within this ground-state multiplet. Samarium is a typical example of an ion where the analysis requires the involvement of higher multiplets. For this case the Racah algebra has been employed.

Within the ground-state multiplet the crystal-field Hamiltonian is written in the conventional form:

$$H_{CF} = \sum_n \sum_m B_n^m O_n^m(J_z) \quad (2.1)$$

where the summation goes over n and m and where the parameters O_n^m are the Stevens equivalent operators and B_n^m the crystal-field parameters. Evaluation of these crystal-field parameters is the subject of an analysis of the experimental data. The parameters B_n^m can be written as:

$$B_n^m = \theta_n \langle r^n \rangle A_n^m \quad (2.2)$$

in which terms related to the 4f ion, $\theta_n \langle r^n \rangle$, and the term related to the surrounding charges, A_n^m , have been separated. The coefficients A_n^m are known as the crystal-field coefficients, θ_n is the appropriate Stevens factor and $\langle r^n \rangle$ is the mean of the n -th power of the 4f radius. In eq.2.2, the screening factors, that might occur in theoretical calculations of the crystal-field coefficients, are included in the coefficients A_n^m . Values for the average value $\langle r^n \rangle$ over the 4f wave function have been computed on the basis of Dirac-Fock studies of the electronic properties of the trivalent rare-earth ions by Freeman and Desclaux (1979).

For cubic symmetry the crystal field is described by two parameters

$$H_{CF} = B_4 (O_4^0 + 5 O_4^4) + B_6 (O_6^0 - 21 O_6^4) \quad (2.3)$$

whereas for the hexagonal symmetry, e.g. the CaCu_5 and the $\text{Th}_2\text{Ni}_{17}$ type of structures, four crystal-field parameters are needed:

$$H_{CF} = B_2^0 O_2^0 + B_4^0 O_4^0 + B_6^0 O_6^0 + B_6^6 O_6^6 \quad (2.4)$$

For the rhombohedral symmetry (e.g. the $\text{Th}_2\text{Zn}_{17}$ type of structure) two extra terms appear in eq.2.4: $B_4^3 O_4^3$ and $B_6^3 O_6^3$.

For the $\text{Nd}_2\text{Fe}_{14}\text{B}$ type of structure the expression reads as:

$$H_{CF} = B_2^0 O_2^0 + B_4^0 O_4^0 + B_4^4 O_4^4 + B_6^0 O_6^0 + \\ + B_6^4 O_6^4 + B_2^2 O_2^2 + B_4^2 O_4^2 + B_6^2 O_6^2 + B_6^6 O_6^6 \quad (2.5)$$

The last four terms in eq.2.4 appear as the local symmetry of the rare-earth ion is lower than tetragonal, i.e. orthorhombic.

3. Exchange interactions and the molecular (exchange) field

In compounds with magnetic rare-earth elements, the electronic structure around the Fermi level is not expected to differ significantly from the yttrium compounds with the same stoichiometry as the number of conduction electrons and the lattice parameters are rather similar. The 4f states of the 4f atom can be discussed in the atomic limit and consequently the f states do not contribute to the DOS near E_F . From a formal point of view, one can write the molecular field acting on the R moment as:

$$B_{\text{mol}}^R = B_{\text{mol}}^{RT} + B_{\text{mol}}^{RR} = n_{RT} M_T + n_{RR} M_R \quad (3.1)$$

$$B_{\text{mol}}^T = B_{\text{mol}}^{TT} + B_{\text{mol}}^{RT} = n_{TT} M_T + n_{RT} M_R \quad (3.2)$$

Although the 4f magnetic moments are often larger than the magnetic moments of the 3d transition metals, the internal field acting on the rare-earth moment and originating from the 3d sublattice dominates that originating from the 4f sublattice. This dominance is due to the much smaller value of the intra-sublattice molecular-field coefficient n_{RR} compared to that of inter-sublattice molecular-field coefficient n_{RT} . In the analysis of most of the rare-earth compounds with iron or cobalt, the contribution to the molecular field from the 4f-4f interactions is ignored. Since it is the spin rather than the moment that is involved in the interactions, it is useful to introduce the exchange field, B_{ex}^{RT} that acts on the rare-earth spin, similar as done in the previous section. The relation between B_{mol}^{RT} and B_{ex}^{RT} can be written in the form:

$$B_{\text{mol}}^{RT} = \frac{2(g-1)}{g} B_{\text{ex}}^{RT} \quad (3.3)$$

This relation results from a comparison between two expressions for the exchange Hamiltonian:

$$\mathcal{H}_{\text{ex}} = g\mu_B J \cdot B_{\text{mol}}^{\text{RT}} \quad \text{and} \quad \mathcal{H}_{\text{ex}} = 2(g-1)\mu_B J \cdot B_{\text{ex}}^{\text{RT}} \quad (3.4)$$

This field is a measure for the strength of the interaction between different species of the spins in the 3d-4f intermetallics. For gadolinium compounds, $B_{\text{mol}}^{\text{Gd}} = B_{\text{ex}}^{\text{Gd}}$ as the Gd moment is a spin moment only.

Within a molecular-field formalism the field $B_{\text{ex}}^{\text{RT}}$ can be expressed as:

$$B_{\text{ex}}^{\text{R}} = \frac{\sum J_{\text{RT}} S_{\text{T}}}{\mu_B} \quad (3.5)$$

where the summation runs over all transition metal neighbours of the rare-earth spin.

In a further step this field can be related to the interactions between nearest neighbours. Assuming this interaction to be isotropic one gets:

$$B_{\text{ex}}^{\text{RT}} = \frac{J_{\text{RT}} S_{\text{T}} z_{\text{RT}}}{\mu_B} \quad (3.6)$$

where J_{RT} is the exchange integral between the 3d and 4f spins and where z_{RT} is the number of transition metal spins in the nearest-neighbours surrounding of a rare-earth atom. The evaluation of the molecular field, the exchange field and the parameter J_{RT} is the main purpose of the analysis of the experimental data. The restriction to the nearest neighbours in eq.3.6 gives the possibility to correlate the values for $B_{\text{ex}}^{\text{RT}}$ between the different series.

4. Electronic structure of the 4f ions in the $R_n T_m$ compounds

The 4f ion is described within a single ion Hamiltonian that takes into account the spin-orbit, crystal-field and exchange interactions:

$$\mathcal{H}_{\text{R}} = \mathcal{H}_{\text{s-o}} + \mathcal{H}_{\text{CF}} + \mathcal{H}_{\text{ex}} + H_{\text{Z}} \quad (4.1)$$

where \mathcal{H}_{CF} already has been discussed in eqs 2.3 - 2.5, where the exchange Hamiltonian has been introduced in section 3 and where H_{Z} stands for the Zeeman magnetostatic energy term taking into account the effect of external fields.

For most of the rare-earth ions, the spin-orbit interaction strongly dominates the other terms. In that case, J is a good quantum number and, in a first approximation, the Hamiltonian

$$\mathcal{H}_{\text{R}} = \mathcal{H}_{\text{CF}} + \mathcal{H}_{\text{ex}} \quad (4.2)$$

can be considered. The eigenvalues and eigenfunctions follow from the diag-

onalization of this Hamiltonian in terms of the $|J, J_z\rangle$ functions in a straightforward way, provided that the relevant CF and exchange field parameters are known. By inelastic neutron scattering experiments the energy difference between the ground state and some excited levels can be measured, for instance, and by a "guess and trial" method, the relevant crystal-field and exchange parameters are obtained. In general, the experimental information is too limited in view of the large number of parameters that is involved in the microscopic description even with the simple Hamiltonian given by eq.4.2. Other techniques are invoked for that reason, for instance, high-field magnetization studies on single-crystalline samples, Mossbauer and NMR studies etc. Combination of the results from these different experimental techniques and inspection of the systematics across the 4f series is essential for getting reliable and physically meaningful sets of crystal-field and exchange parameters.

For a quantitative understanding of the magnetic properties of these materials the two key interactions are: the exchange parameter J_{RT} and the second-order crystal-field parameter at the rare-earth sites. A comparison of these two interactions throughout the $R_2Fe_{14}B$ series indicates that most of the compounds belong in first approximation, to the limiting case where the magnetic interactions dominate the crystal-field splitting. Both interactions, however, are equally important for a description of the magnetization curves. Although the theoretical concepts behind the crystal-field and isotropic exchange interactions are rather straightforward, the evaluation of their numerical values is far from simple. Nevertheless, the overall features are now quite well understood for the whole series of the 2:14:B compounds. Two general reviews that include a basic description of the magnetism of 3d-4f intermetallic compounds and that provide a good insight into their general properties have been written by Buschow (1977) ("Intermetallic compounds of rare-earth and 3d transition metals") and by Kirchmayr and Poldy (1979) ("Magnetic properties of intermetallic compounds of rare earth metals"). More recent articles by Buschow (1986) and Coey (1986, 1987) review the magnetic properties of the 2:14:B compounds in particular.

5. References

- Buschow K H J (1977), Rep.Prog.Phys.40, 1179.
- Buschow K H J (1986), Materials Science Reports 1.
- Coey J M D (1986), J.Less-Common Met.126, 21.
- Coey J M D (1987), Physica Scripta T19, 426.
- Freeman A J and Desclaux J P (1979), J.Magn.Magn.Mat.12, 11.
- Hutchings M T (1964), Solid State Phys.16, 227.

FIRST ORDER MAGNETIZATION PROCESSES

Giovanni Asti

Dipartimento di Fisica
Università di Parma
Parma, Italy

INTRODUCTION

The magnetization curve of a ferromagnetic crystal is normally continuous in the region preceding saturation, where the magnetization process takes place by reversible rotation of the magnetization vector \vec{M} . However when the anisotropy constants fall within certain ranges, irreversible rotations of \vec{M} are possible implying first order transitions between inequivalent magnetization states - hereafter referred as FOMP, for first-order magnetization processes (Asti and Bolzoni 1980) -. In fact, depending on the values of the anisotropy constants, the system may admit two or more inequivalent minima of free energy E for different magnetization directions; so it is evident that an applied magnetic field \vec{H} of suitable intensity and orientation can induce a transitions between these minima. In principle in the case of FOMP we expect to observe minor hysteresis loops around the critical field for which the two states have equal energy. But it is difficult to observe hysteresis in FOMP even at low temperatures (Melville et al. 1976, Ermolenko and Rozhda 1978). The reason is probably associated with the very low coercivity inherent in this type of magnetization process.

UNIAXIAL SYMMETRY

A very special but important case is that of uniaxial symmetry. In this case the free energy of the system is

$$E = K_1 \sin^2 \vartheta + K_2 \sin^4 \vartheta + K_3 \sin^6 \vartheta - HM_c \cos(\vartheta - \varphi) \quad (1)$$

where K_1 , K_2 , K_3 are the anisotropy constants and ϑ and φ are the orientation angles of the magnetization vector \vec{M} and the magnetic field \vec{H} with respect to the symmetry axis, c , respectively.

FOMPs occur when the anisotropy constants fall within certain ranges, which depend on the direction of the magnetic field. For most purposes it is enough to consider the cases of \vec{H} parallel or perpendicular to the c -axis, hereafter indicated as the A-case and P-case respectively. The general case is relevant when considering the effects

of FOMP in polycrystalline materials (see below). The equilibrium equation for the P-case turns out to be

$$h = 2m(1+2xm^2+3ym^4)K_1/|K_1|, \quad (2)$$

where $m=M/M_s$ is the reduced magnetization, $h=2H/H_{A1}$ the reduced field and $H_{A1}=2K_1/M_s$ the c-axis anisotropy field. Using eq. (2) and the condition that the total energy is equal in the two phases, we obtain the equation for the critical magnetization

$$(3m^2+2m+1)x+(5m^4+4m^3+3m^2+2m+1)y+1=0. \quad (3)$$

The equations for the A-case are easily deduced from the P-case by the use of a transformation, called the $K \rightleftharpoons R$ transformation, of the anisotropy constants into conjugate quantities. This transformation is a symmetrical dual correspondence and is obtained by imposing on the energy expressions the same formal dependence on the reduced magnetization m , for the A and P cases. So one obtains the following linear transformation

$$R_1 = -K_3 - 2K_2 - 3K_1, \quad R_2 = K_2 + 3K_3, \quad R_3 = -K_3 \quad (4)$$

In terms of reduced variables $x=K_2/K_1$, $y=K_3/K_1$, $\bar{x}=R_2/R_1$ and $\bar{y}=R_3/R_1$, it becomes

$$\bar{x} = (-x-3y)/(1+2x+3y), \quad \bar{y} = y/(1+2x+3y), \quad (5)$$

The inverse transformation has obviously the same form.

Two types of FOMP are distinguished, depending on whether the final state after the transition is the saturation state (type-1 FOMP) or not (type-2 FOMP). From the equality of the total energy in the two states and from the equilibrium equations one obtains the conditions for the occurrence of the two types of FOMP. Fig. 1 summarizes the results giving the complete diagram of FOMP in the planes of reduced anisotropy constants x and y for the two cases $K_1 > 0$ and $K_1 < 0$. The various regions are distinguished by the labels A1, A2, P1, P2, P1C, A1C which specify the magnetic field direction (A, axial; P, planar) and the type of FOMP (1 and 2), and easy-cone regions with type-1 FOMP (A1C, P1C). The areas that are conjugated in the $K \rightleftharpoons R$ transformation are shaded in the same way. The analysis of the equations also provides the values of the reduced critical field h_{c2} and critical magnetization m_{c2} as functions of the coordinates x , y and the sign of K_1 .

Similar diagrams can also be obtained in terms of the anisotropy coefficients $\chi_{l,m}$ which appear in the expansion of the anisotropy energy in spherical harmonics. It is known in fact that there are advantages in using this representation when analyzing the temperature dependence of magnetocrystalline anisotropy, because of the congruence with the Callen and Callen (1966) theory. The FOMP diagrams in terms of the ratios $u = \chi_{4,0}/\chi_{2,0}$ and $v = \chi_{6,0}/\chi_{2,0}$ are reported in fig. 2, for the cases $\chi_{2,0} > 0$ and $\chi_{2,0} < 0$. These diagrams, besides the type of FOMP, give the lines of constant h_{c2} and m_{c2} . These plots can be used in analyzing experimental observations of FOMP, and allow precise evaluations of the ratios of the anisotropy coefficients. It is of interest to consider a typical trajectory of the representative point with varying temperature as predicted by the $1/(1+1)/2$ power law according to the Callen and Callen (1966) theory. This yields $u \propto m^7$, $v \propto m^{18}$ so that the line described by the representative point is a curve of the type $v = cu^{18/7}$, with c constant. Fig 2 reports a typical curve for $c=1$.

MEASUREMENTS IN HIGH MAGNETIC FIELDS

With only a few exceptions, as is the case of ferrites (Asti et al. 1978) and of $\text{Pr}_2(\text{Fe,Co})_{17}$ (Shanley and Harmer 1973, Melville et al. 1976), magnetic fields above the limit of ordinary laboratory electromagnets are necessary to investigate this type of magnetic phenomena. As a matter of fact rare earth-intermetallic compounds having H_{C2} above 15 Tesla are fairly common. The only way to carry out magnetic measurements at very high magnetic fields is by using pulsed methods. The main problem arising with the use of pulsed field apparatus, in performing magnetic measurements, are connected with the inherent difficulty to dominate the various noise sources. Despite this there are several reasons why a pulsed field could be used for magnetic measurements: i) in a single shot it is possible to measure the whole magnetization curve from zero up to the maximum field; ii) the continuous and regular variation of the field is a favorable condition for detecting sudden changes such as those associated with a transition; iii) the experimental set-up is relatively simple and economical.

The use of single crystal samples is obviously the most favorable condition for detecting the transition and a unique way to achieve precise evaluations of the critical magnetization M_{C2} (or M_1 and M_2 , in the case of type-2 FOMP). However, the orientation of the crystal in the magnet in most cases appears to be quite critical for performing precise measurements, because of the strong sensitivity of H to deviations from perfect alignment: for instance a deflection by only two degrees of the applied field direction from the basal plane in PrCo gives rise to a displacement of H_{C2} by 2 Tesla (Asti et al. 1980).

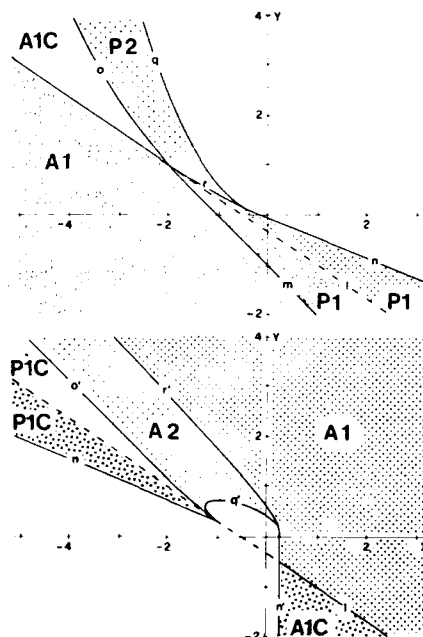


Fig. 1. Diagram of FOMP in the planes of reduced anisotropy constants $x=K_2/K_1$, $y=K_3/K_1$. Upper and lower figures refer to the cases $K_1 > 0$ and $K_1 < 0$, respectively.

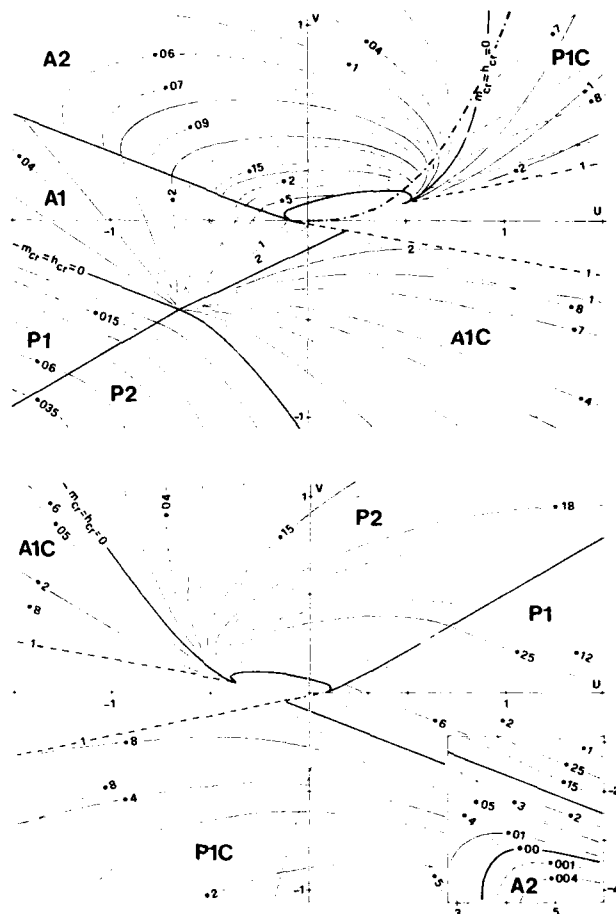


Fig. 2. Lines of constant values for the reduced critical magnetization, m_{cr} (dashed lines) and reduced critical magnetic field, h_{cr} (full lines), in the planes of reduced anisotropy coefficients $u = \chi_{4,0} / \chi_{2,0}$, $v = \chi_{6,0} / \chi_{2,0}$. Top and bottom figures refer to the cases $\chi_{2,0} > 0$ and $\chi_{2,0} < 0$ respectively. The different regions are distinguished as in fig. 1. The spacing between the values relative to the contiguous lines of m_{cr} and h_{cr} , changes only when crossing a line labelled by its value. The rectangle on the bottom right shows a part of the plane $\chi_{2,0} < 0$ with an expanded scale and with the origin ($u=v=0$) in the same point. The curve ----- is an example of the $1(1+1)/2$ power law for the temperature dependence of the anisotropy. The equation of the curve is $v = cu^{1/2}$ with $c=1$.

THE SINGULAR POINT DETECTION TECHNIQUE

The inherent high sensitivity of the pulsed field method for detecting transitions is more and more enhanced if one observe the successive derivatives of magnetization M with respect to the field H , or to time. This is indeed the principle at the basis of the singular point detection technique (SPD) (Asti and Rinaldi 1974), an experimental method that allows to reveal the singularities associated with the field induced magnetic transitions, utilizing polycrystalline specimens. The SPD theory was originally developed for measurements of the hard direction anisotropy fields and has been subsequently extended to the case of FOMP (Asti 1981, Asti and Bolzoni 1985). Usually SPD measurements are easily performed in pulsed fields by direct differentiation of the signal from the pick-up coil. For a random orientation, in the case of a P-type FOMP, there is a discontinuity in the differential susceptibility, dM/dH , equal to

$$\Delta \chi = (M_s/H_{cr}) (m_2 - m_1)^2 / (\sqrt{1 - m_1^2} - \sqrt{1 - m_2^2}) \quad (6)$$

where m_1 is the critical magnetization, i.e. the lower limit, and m_2 the upper limit of m at the transition. In the case of A-type FOMP the discontinuity is in the slope of the differential susceptibility, d^2M/dH^2 , and turns out to be

$$\Delta \chi' = (M_s/H_{cr}^2) (m_2 - m_1)^3 / (\sqrt{1 - m_1^2} - \sqrt{1 - m_2^2})^2 \quad (7)$$

PrCo_5 is a clear example of the application of SPD techniques to the study of FOMP (Asti et al. 1980). Another case is that of $\text{Nd}_2\text{Fe}_{14}\text{B}$: figure 4 shows the progressive change with decreasing temperature of the SPD signal, d^2M/dH^2 (Asti et al. 1984).

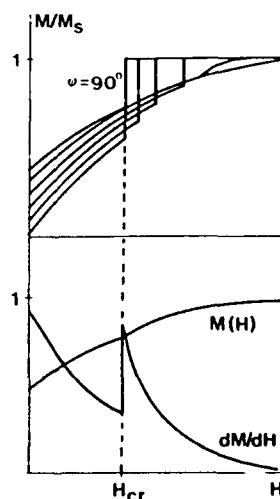


Fig. 3. (Top) Magnetization curve $M(H)$ of an easy axis uniaxial single crystal at various orientations close to $\varphi = 90^\circ$, where φ is the angle of magnetic field direction with respect to the c-axis. The FOMP transition is progressively displaced to higher fields with decreasing φ . From left to right the various curves in the figure refer to $\varphi = 90^\circ, 86^\circ, 82^\circ, 78^\circ, 74^\circ$ and 70° . (Bottom) $M(H)$ and first derivative dM/dH for a polycrystalline aggregate having crystallites oriented at random.

located at H_A is modified until, at 200 K, a sharp positive peak appears that grows more and more with the further decrease of the temperature. Clearly the positive peak is an approximation of the delta function representing the derivative of the discontinuity in the differential susceptibility given by eq. (6). Other examples are intermetallic compounds of ThMn_{12} structure (Li et al. 1988, Deriu et al. 1989, Solzi et al. 1988).

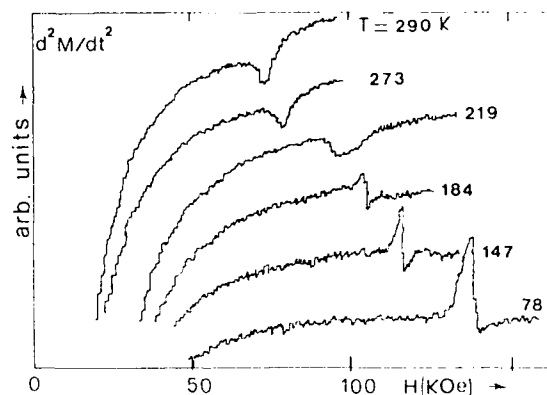


Fig. 4. Progressive change with decreasing temperature of the SPD signal, d^2M/dH^2 , for a magnet of $\text{Nd}_2\text{Fe}_{14}\text{B}$. As is evident, the downward cusp located at $H=H_A$ is modified until, at 200 K, a sharp positive peak appears that grows continuously.

REFERENCES

- Asti G., 1981, IEEE Trans. Mag. MAG-17, 2630.
 Asti G. and F. Bolzoni, 1980, J. Magn. Magn. Mat. 20, 29.
 Asti G. and F. Bolzoni, 1985, J. Appl. Phys. 58, 1924.
 Asti G. and S. Rinaldi, 1974, J. Appl. Phys. 45, 3600.
 Asti G., F. Bolzoni, F. Licci and M. Canali, 1978, IEEE Trans. Mag. MAG-14, 883.
 Asti G., F. Bolzoni, F. Leccabue, R. Panizzieri, L. Pareti and S. Rinaldi, 1980, J. Magn. Magn. Mat. 15-18, 561.
 Asti G., F. Bolzoni, F. Leccabue, L. Pareti and R. Panizzieri, 1984, Nd Fe Permanent Magnets - Their Present and Future Applications, Rep. and Proc. of a Workshop Meeting, Brussels, October 25, 1984, ed. I.V. Mitchel (Commission of the Europ. Commun., 1984), p. 161.
 Callen H. B. and E. Callen, 1966, J. Phys. Chem. Solids 27, 1271.
 Deriu, A.; G. Leo, O. Moze, L. Pareti, M. Solzi and R.H. Xue, 1989, Hyperfine Interactions, 45, 241.
 Ermolenko A. S. and A. F. Rozhda, 1978, IEEE Trans. Mag. MAG-14, 676.
 Li, H.S., B.P. Hu, J.P. Gavigan, J.M.D. Coey, L. Pareti and O. Moze, 1988, J. Phys. (France) 49, 541.
 Melville D., W. I. Khan and S. Rinaldi, 1976, IEEE Trans. Mag. MAG-12, 1012.
 Shanley, C.W., and S. Harmer, 1973, AIP Conf. Proc. 18, 1217.
 Solzi, M., L. Pareti, O. Moze and W.I.F. David, 1988, J. Appl. Phys. 64, 5084.

STRUCTURE AND PROPERTIES OF NOVEL TERNARY FE-RICH RARE-EARTH CARBIDES

T.H. Jacobs (a) and K.H.J. Buschow (a,b)

(a) Kamerlingh Onnes Laboratory
2300 RA Leiden, The Netherlands

(b) Philips Research Laboratories
5600 JA Eindhoven, The Netherlands

INTRODUCTION

The compounds of the type R_2Fe_{17} (R = rare earth) have been studied extensively during the last few decades. A large number of experimental methods has been used to investigate their magnetic and crystallographic properties^{1,2}. These compounds are not suitable as starting materials for permanent magnets because of their too low Curie temperature and their in-plane easy magnetization axis. During recent investigations we have found that the R_2Fe_{17} structure can take up a certain amount of carbon³, leading to a drastic change in their magnetic properties. In this paper we will show a few examples of these changes and discuss the possibility of using these new compounds as starting materials for permanent magnets.

CRYSTAL STRUCTURE

The intermetallic compounds R_2Fe_{17} crystallize into two structures. The first half of the rare-earth series (from Ce to Gd) obtains the rhombohedral Th_2Zn_{17} type of structure while the second half of the series (from Tb to Lu) obtains the hexagonal Th_2Ni_{17} type. The former structure consists of a repeated stacking in the c direction of three $CaCu_5$ layers, whereas the latter consists of two layers, every third R atom being replaced by a Fe dumbbell in both cases.

Alloying with carbon leads to an increase in the lattice parameters of both structure types, a saturation taking place for high carbon concentrations ($x \geq 1$ in $R_2Fe_{17}C_x$), as can be seen in fig. 1 for $Y_2Fe_{17}C_x$. This lattice expansion indicates that carbon atoms occupy interstitial holes in the lattice. This has been confirmed by neutron diffraction experiments on $Nd_2Fe_{17}C_x$ ⁴, which showed that carbon occupies the 9c position of the rhombohedral structure type close to the rare-earth atoms. Full occupation of these sites would lead to the formula composition $R_2Fe_{17}C_4$ as is shown in fig. 2.

We have also observed a carbon-induced transition from the hexagonal to the rhombohedral structure for some rare-earth elements (fig. 1). This is due to the increase in unit cell volume because the rhombohedral structure type is obtained by the compounds with the larger rare-earth atoms and the hexagonal one by the smaller rare-earth atoms. In the case of $Y_2Fe_{17}C_{0.8}$, with a carbon concentration just at the transition between the rhombohedral and hexagonal structure, no superstructure lines of either crystal structure were seen in our x-ray diagrams. Electron diffraction and HRTEM experiments showed that we had not obtained a carbon-stabilized $CaCu_5$ structure type, but they revealed a special kind of disorder in these samples which has been extensively discussed elsewhere^{5,6}.

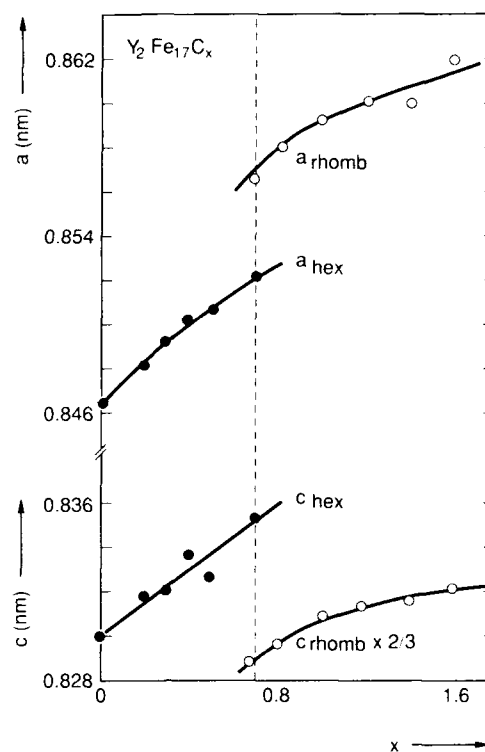


Fig. 1. Lattice constants as a function of increasing carbon concentration. To compare the c -axes of both structure types we multiplied the rhombohedral one by $2/3$.

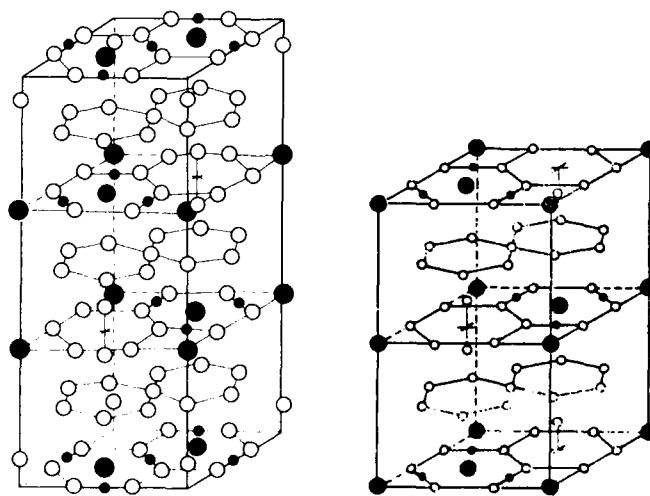


Fig. 2. The hexagonal $\text{Th}_7\text{Ni}_{17}$ (left) and rhombohedral $\text{Th}_7\text{Zn}_{17}$ (right) crystal structure of $\text{R}_2\text{Fe}_{17}\text{C}_x$. Open dots represent iron atoms, large filled dots the rare-earth atoms and the small ones the C atoms.

MAGNETIC PROPERTIES

Magnetic ordering temperature and magnetization

As already mentioned in the introduction, one of the main reasons why the R_2Fe_{17} compounds were never serious candidates for permanent magnet materials is their too low Curie temperature, for some rare-earth metals even being below room temperature. The up-take of carbon leads to a drastic increase in T_c , as can be seen in fig. 3. The values obtained for $R_2Fe_{17}C$ are comparable with those obtained on $R_2Fe_{14}C$ compounds. We saw that above a certain carbon concentration the T_c does not increase any further. This concentration is different for every rare-earth atom, about $x=1$ for the first half of the rare-earth series to about $x=1.5$ for the second half, depending also on the annealing temperature.

The R_2Fe_{17} compounds have the highest magnetic moment per iron atom of all binary R - Fe compounds. This combined with the large ratio of Fe to R atoms leads to a high moment per formula unit. The introduction of carbon into the lattice has hardly any effect on the Fe moments. ($M \approx 2.0 \mu_B$ / Fe atom at 4.2 K.) This has been observed by ^{57}Fe Mössbauer spectroscopy and by magnetic measurements on $Y_2Fe_{17}C_x$ (Y being a non-magnetic atom)^{8,9}. The saturation magnetization of all $R_2Fe_{17}C$ compounds has also been measured in high fields (35 T) at $T = 4.2$ K⁷. The conclusion was that the magnetic moments of the rare-earth atoms were very close to the free ion values $\mu_R = g_J \mu_B$.

To obtain information on the coupling strength between the R and Fe sublattice we can make use of two different methods⁷. Firstly, a simple relation can be derived between the Curie temperatures and the interaction constant using a mean-field model. Secondly, we can perform high-field magnetization measurements on powder particles that can rotate freely and thus can orient themselves in the field applied. The way of obtaining the interaction constant using this technique has been described in detail elsewhere⁷. For the $R_2Fe_{17}C$ compounds both methods led within 10 % to the same results. For the $R_2Fe_{14}C$ compounds however, the discrepancy was almost 30 %.

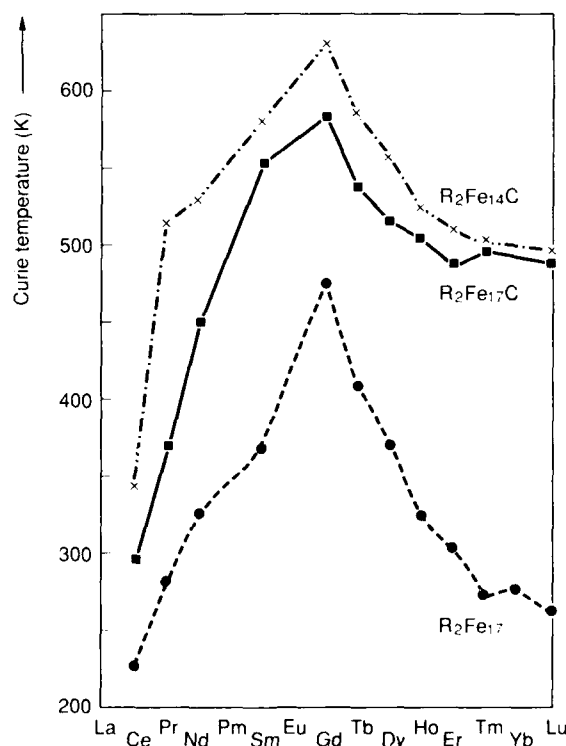


Fig. 3. Magnetic ordering temperature of R_2Fe_{17} , $R_2Fe_{17}C$ and $R_2Fe_{14}C$.

The second reason why the R_2Fe_{17} compounds are not good starting materials for permanent magnets is the relatively low in-plane magnetocrystalline anisotropy of the Fe sublattice. There are a few rare-earth elements which favour an easy c-axis at low temperatures because of the shape of their 4f charge cloud ($\alpha_1 > 0$ for $R = Sm, Er, Tm$). For instance, Tm in Tm_2Fe_{17} is able to overrule the iron sublattice anisotropy, but only up to a certain temperature at which a spin reorientation takes place. The addition of carbon leads to an increase in this spin reorientation temperature⁹. This is due to an increase in the magnetocrystalline anisotropy of the rare-earth atom which e.g. has been observed by ^{169}Tm Mössbauer spectroscopy. In fig. 4 the A_2^0 parameter which is a measure of this anisotropy is shown. It can be seen that for $x = 0$ the contributions of the two different Tm sites in the hexagonal Tm_2Fe_{17} compound are rather small and have a different sign. For increasing carbon concentration both contributions become negative and increase in absolute value. This increasing negative value indicates that the rare-earth sublattice anisotropy is becoming stronger and will be able to overrule the iron sublattice anisotropy up to a higher temperature. In fig. 4 results from ^{155}Gd Mössbauer spectroscopy on $Gd_2Fe_{17}C_x$ can also be seen⁸. Gd itself does not contribute to the magnetocrystalline anisotropy because of its spherical symmetric 4f charge cloud, but we can use this compound for measuring the lattice contribution to the magnetocrystalline anisotropy. The rhombohedral compound $Gd_2Fe_{17}C_x$ has only one rare-earth site which has a negative value of the A_2^0 parameter. After correcting the Gd and Tm data for the same amount of screening, the results of the two types of Mössbauer measurements may be compared with each other, which is done in fig. 4.

Because of the low magnetizations of the ferrimagnetic compounds $Tm_2Fe_{17}C_x$ and $Er_2Fe_{17}C_x$, the only possible candidate for permanent magnet material is the ferromagnetic compound $Sm_2Fe_{17}C_x$. High-field magnetization measurements at 4.2 K on powder of $Sm_2Fe_{17}C_1$ aligned at room temperature can be seen in fig. 5. With the external field parallel to the alignment direction we found the highest magnetization. This indicates that no spin reorientation has taken place between 4.2 K and room temperature, the easy magnetization axis being already along the c-axis at room temperature⁷. X-ray measurements on the same aligned powders indeed showed an easy c-axis as can be seen in fig. 6. The x-ray diagrams are taken parallel and perpendicular to the alignment direction. The first one only shows (00l) reflections while the second one only shows (hk0) reflections. Also SPD (Singular Point Detection) measurements have been performed on this material which are shown in fig. 7 as a function of temperature. With this technique an anisotropy field of about 5 T at room temperature has been found for $Sm_2Fe_{17}C_1$ ¹¹.

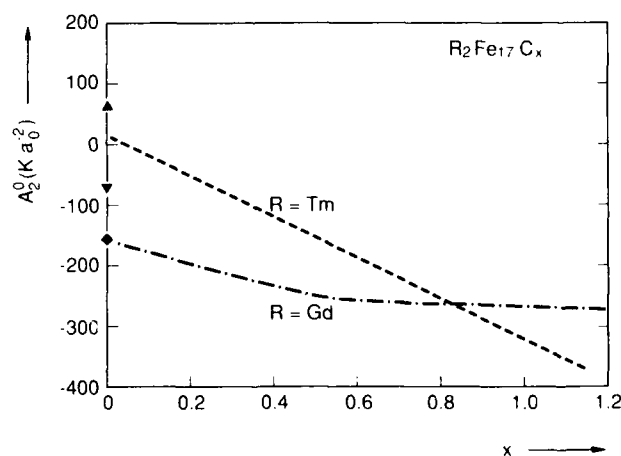


Fig. 4. Composition dependence of A_2^0 observed by ^{155}Gd Mössbauer spectroscopy in $Gd_2Fe_{17}C_x$, and by ^{169}Tm Mössbauer spectroscopy in $Tm_2Fe_{17}C_x$. The data for $Gd_2Fe_{17}C_x$ are those of ref. [10] after correction for screening. The data for $Tm_2Fe_{17}C_x$ are mean values for both Tm sites⁹.

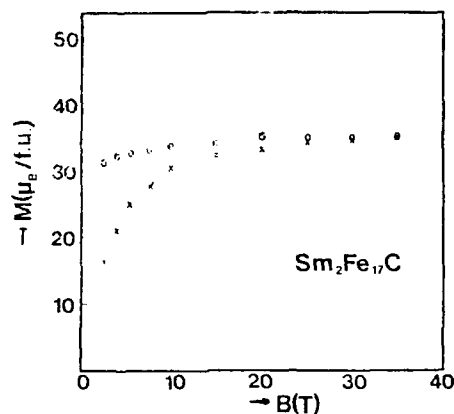


Fig. 5. Field dependence of the magnetization at 4.2 K in $\text{Sm}_2\text{Fe}_{17}\text{C}_{11}$. The symbols 0 and X apply to measurements made with the external field direction parallel and perpendicular to the alignment field.

In conclusion we can say that the intrinsic properties of the $\text{R}_2\text{Fe}_{17}\text{C}_x$ compounds are good enough for permanent magnet applications, although investigations still have to be carried out in order to obtain the right microstructure which is needed for high coercivity.

ACKNOWLEDGEMENT

Part of this work has been supported by the Stichting voor Fundamenteel Onderzoek der Materie (FOM).

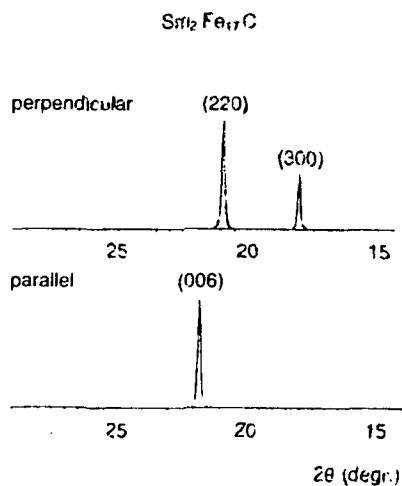


Fig. 6. X-ray diffraction diagrams of magnetically aligned powder of $\text{Sm}_2\text{Fe}_{17}\text{C}_{11}$, taken parallel and perpendicular to the alignment direction.

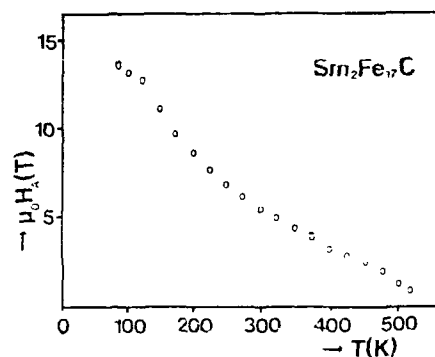


Fig. 7. The temperature dependence of the anisotropy field of $\text{Sm}_2\text{Fe}_{17}\text{C}$.

REFERENCES

1. K. Strnat, G. Hoffer and A. E. Ray, Magnetic properties of rare-earth-iron intermetallic compounds, *IEEE Trans. Magn.* MAG-2:489 (1966).
2. K. Kumar, RETM₅ and RE₂TM₁₇ permanent magnets development, *J. Appl. Phys.* 63:R13 (1988).
3. D. B. de Mooij and K. H. J. Buschow, Formation and magnetic properties of the compounds $\text{R}_2\text{Fe}_{14}\text{C}$, *J. Less-Common Met.* 142:349 (1988).
4. R. B. Helmholtz and K. H. J. Buschow, Crystallographic and magnetic structure of ternary carbides of the type $\text{Nd}_2\text{Fe}_{17}\text{C}_x$, *J. Less-Common Met.* 155:15 (1989).
5. W. Coene, F. Hakkens, T. H. Jacobs, D. B. de Mooij and K. H. J. Buschow, High energy electron diffraction and x-ray diffraction studies on magnetic materials of the type $\text{Y}_2\text{Fe}_{17}\text{C}_x$ ($0 \leq x \leq 1.6$), *J. Less-Common Met.* 157:255 (1990).
6. W. Coene, F. Hakkens, T. H. Jacobs and K. H. J. Buschow, High resolution imaging of stacking sequences in $\text{Y}_2\text{Fe}_{17}\text{C}_x$ ($0.6 \leq x \leq 1.6$) magnetic material, *Phil. Mag. B* accepted for publication.
7. X. P. Zhong, R. J. Radwanski, F. R. de Boer, T. H. Jacobs and K. H. J. Buschow, Magnetic and crystallographic characteristics of rare-earth ternary carbides derived from R_2Fe_{17} compounds, *J. Magn. Magn. Mater.* 86:333 (1990).
8. T. H. Jacobs, M. W. Dirken, R. C. Thiel, L. J. de Jongh and K. H. J. Buschow, Magnetic properties of $\text{Gd}_2\text{Fe}_{17}\text{C}_x$, *J. Magn. Magn. Mater.* 83:293 (1990).
9. P. C. M. Gubbens, A. M. van der Kraan, T. H. Jacobs and K. H. J. Buschow, Magnetic properties of the ternary carbides $\text{Tm}_2\text{Fe}_{17}\text{C}_x$, *J. Magn. Magn. Mater.* 80:265 (1989).
10. M. W. Dirken, R. C. Thiel, L. J. de Jongh, T. H. Jacobs and K. H. J. Buschow, Effect of carbon take-up on the crystal-field effects in rare-earth compounds R_2Fe_{17} , *J. Less-Common Met.* 155:339 (1989).
11. X. C. Kou, R. Grössinger, T. H. Jacobs and K. H. J. Buschow, Magnetocrystalline anisotropy and magnetic phase transition in $\text{R}_2\text{Fe}_{17}\text{C}_x$ based alloys, *J. Magn. Magn. Mater.* (1990) at the press.

GRANULAR SOLIDS

C.L. Chien

Department of Physics & Astronomy
The Johns Hopkins University
Baltimore, Maryland 21218

Abstract

Granular metals consist of nanometer size metal granules embedded in an immiscible medium. They display a rich variety of physical properties as a result of their unique nanostructure and extra degrees of freedom. They are also suitable for the exploration of finite-size effects, enhanced and tailored properties of fundamental interest and for technological applications. Granular magnetic solids of elemental metals and alloys will be discussed. Single-domain characteristics, superparamagnetic relaxation, enhanced ferromagnetic properties, granular alloys and spin glasses are some of the topics covered.

1. Introduction

Granular metal solids^{1,2} are one particular kind of artificially structured materials (ASM's), of which superlattices, modulated solids³ and amorphous solids are some of the more widely known examples. ASM's contain intricate structure on the nanometer scale and extra degrees of freedom with which the physical properties can be manipulated to achieve tailored materials for applications and for explorations of physical phenomena. Granular solids are usually in the form of small metal granules embedded in an immiscible medium which may be insulating or, less frequently, metallic. The relevant extra degrees of freedom are the granule size, which can be controlled by process conditions, and metal volume fraction (x_v), which can be experimentally varied between 0 and 1. Because of their unique nanostructures, granular solids display a particularly rich variety of interesting conducting, superconducting, optical, magnetic, mechanical and other physical properties.

For most common metals (e.g. Fe, Au, Co, Cu), the ultrafine solid granules can be made as small as 10 to a few hundred angstroms. This size range is much smaller than that achievable by traditional metallurgical and chemical methods. This is also the size range where finite-size effects, single-domain magnetic properties, enhanced superconducting transition temperature, and other phenomena may be observed.

Many granular solids consist of a metal and an insulator, the latter includes SiO_2 , Al_2O_3 , MgO , etc. Granular solids are therefore also nanocomposite materials, which can reap benefits from both components. Since these insulators are usually mechanically harder, and more wear and corrosion resistant than the metal companion, granular metals exhibit superior auxiliary properties in addition to their attractive physical properties.

Most of the granular metal solids studied to date consist of a single element metal (e.g. Au, Fe, Co, Cu) and selected insulators (e.g. Al_2O_3 , SiO_2 , MgO). Granular solids, as opposed to homogeneous alloys, are realized because these metals and insulators are immiscible with each other. In these granular metals, the metals are generally crystalline, whereas the insulators are usually amorphous. The important area of ultrafine metallic alloys remains largely unexplored, despite the fact that alloys, both crystalline and amorphous, have generally proven to be more useful. We have recently succeeded in the fabrication of granular alloys of Fe-Ni, Fe-B, and Fe-Cu, which are respectively a stable crystalline alloy, an amorphous and a metastable crystalline alloy.⁴ Therefore the feasibility of granular metals can be extended far beyond elemental metals, to include many alloys of technological importance. One faces a different and more formidable challenge in achieving granular metals in a metallic medium.⁵ This is because most metals, such as Fe, form alloys or compounds with almost any other metal. The loss of immiscibility prevents the successful formation of granular metals in a metallic medium. However, these difficulties can be avoided in some cases, as will be described later.

In this paper, we will primarily discuss the magnetic properties of a variety of granular magnetic solids. These results will be complimented by other nanostructure-induced properties. We will present extensive results of single element (e.g. Fe, Ni) granules in an insulating matrix. Some recent results of granular alloys, both stable (e.g. Fe-Ni alloys) and metastable (crystalline and amorphous), and results of granular metals embedded in a metallic medium, will also be discussed. Finally, in addition to our results on ferromagnetic magnetic granules, some recent studies of spin-glass granules will also be presented.

2. Fabrications and Characterizations

Granular solids can be made by sputtering, co-deposition, evaporation under high pressure, and other methods. Of those, sputtering has been demonstrated to be the most versatile. In sputtering, one can employ a variety of target configurations: a single homogeneous target, co-sputtering from two separated targets, or a composite target with slabs of materials pieced together. We have primarily used the first two target configurations in conjunction with magnetron sputtering. The base pressure in the chamber is in the 10^{-8} torr range using either a diffusion pump or a cryopump. Deposition is carried out in an Ar atmosphere with a pressure near 4 mtorr regulated by an MKS gas flow system. Most of the samples have been deposited by rf sputtering, or in some cases by dc sputtering at rates of about 2 $\mu\text{m/hr}$. The substrate has been maintained at a fixed temperature between 77 K and 900 K. Since the nanostructures of granular metal solids are strongly influenced by the process conditions, deposition parameters such as deposition rate, sputtering pressure and substrate temperature must be tightly controlled. The total film thicknesses are usually in the range of a few μm 's.

Because the density of the metal granules is generally different from that of the matrix they are embedded in, the metal volume fraction can be quite different from the atomic composition. For example, $\text{Fe}_{50}(\text{SiO}_2)_{50}$ in atomic percent is equivalent to $\text{Fe}_{21}(\text{SiO}_2)_{79}$ in volume percent. The all important metal volume fraction must of course be established using electron microprobe, Auger spectroscopy, energy-dispersive x-ray analysis or wet chemistry.

Since the intricate structure of granular solids exists only on the nanometer scale, the use of transmission electron microscopy (TEM) is imperative. Examples of TEM micrographs are shown in Fig. 1 and elsewhere in this paper. The nanostructure of the specimens with low volume fractions consists of isolated metal granules embedded in the medium. For high melting point metals (e.g. Fe, Ni, Au, W), the granules are equiaxial in shape, having sizes in the nanometer range with a rather narrow size distribution (Fig.1). For specimens with high volume fractions, the metallic grains form a connecting network, enclosing isolated regions of the second, usually insulating, medium.

X-ray and electron diffraction are additional techniques used to establish the structure of the ultrafine metal particles. For granules of such small size, the diffraction peaks are quite broad, since the peak width scales inversely with the particle size. Examples of x-ray diffraction data are shown in the Fig. 2. Despite the broad peaks, the diffraction data unequivocally show the crystal structure and lattice parameter of the granules, in spite of their small sizes.

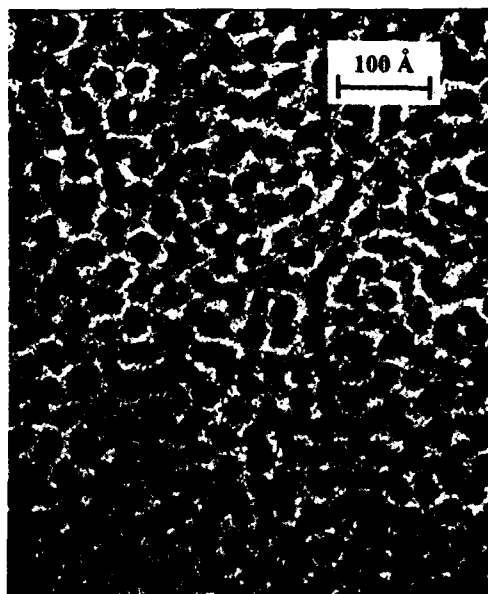


Fig.1. Bright-field TEM micrograph of granular $(\text{Fe}_{50}\text{Ni}_{50})_{40}(\text{SiO}_2)_{60}$ deposited at 150 C.

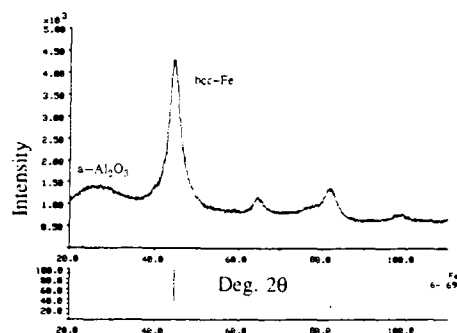


Fig.2. X-ray diffraction pattern of granular $\text{Fe-Al}_2\text{O}_3$.

In the cases of magnetic granular solids, the magnetic properties provide additional information about the granule sizes and their distribution. Finally, for granular solids containing Fe, ^{57}Fe Mössbauer spectroscopy is a powerful tool for the examination of a wide range of characteristics of the granules.⁶⁻⁸

3. Nanostructure-induced Properties

For many physical properties, the metal volume fraction x_v ($0 \leq x_v \leq 1$) and the granule size are of crucial importance. For the samples with small values of x_v , the metal granules are isolated from each other and protected by the insulating matrix. Electrically, granular solids with low x_v are insulating, apart from tunneling among metallic grains, which is of course interesting in its own right. In magnetic granular solids, all such granules are single domain. On the other hand, for samples with large values of x_v , the metal granules form an infinite network, exhibiting metallic conductivity and bulk magnetic properties, since the conducting paths and magnetic closure structure are readily facilitated.

The percolation threshold (x_p) is the volume fraction at which an infinite network of metal granules first forms. Experimentally, for a wide variety of granular metal solids, the value of x_p has been found to lie in the range of 0.5 - 0.6. Qualitatively, such values of x_p can be understood by noting that the packing fractions of spheres in closed-packed structures (e.g. fcc, bcc, hcp) are in this range. Theoretically, Sheng⁹ has established more rigorously the experimentally observed values of x_v .

Finite-size effects can be profitably studied in granular metals. Below x_p , the isolated granules are suitable for the exploration of finite-size effects in particle size. One can study the properties of ultrafine crystals and the deviation from those of bulk solids. Size-dependent behaviors of melting, lattice dynamics, magnetic ordering are some of the examples. Above x_p , the dimension of the infinite network of connecting granules is probably less than three. It may be possible to study finite-size effects associated with fractional dimension and different correlation length scales.

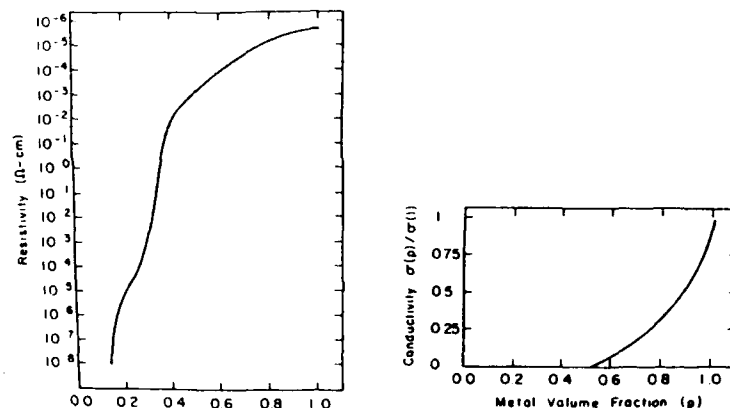


Fig.3. Resistivity (in log scale) and conductivity of a typical granular metal as a function of metal volume fraction.

Granular metal solids exhibit large changes in most properties when x_v is varied, particularly across x_p . One property that is readily appreciated is electrical conductivity. As shown in Fig. 3, by varying x_v the conductivity can be easily changed over 12 orders of magnitude, of which 3 orders of magnitude occur above x_p . Therefore by varying x_v , one can tailor the conductivity to any value desired, a manifestation of the extra degrees of freedom. Many other properties of granular metals are also affected significantly by the metal volume fraction. Qualitatively one can anticipate the following general trends. As one varies x_v from 0 to 1, properties that are associated with metal (e.g. conductivity and thermal conductivity) would increase, whereas those characteristic of the insulators (e.g. hardness, wear resistance and corrosion resistance) would decrease. In many cases, there would be prominent effects due to percolation when x_p is crossed. Magnetically, the samples with $x_v < x_p$ exhibit "hard" magnetic properties (e.g. high coercivity) due to the single-domain nature of the particles, whereas at $x_v > x_p$, much "softer" magnetic properties result.⁹

Some of the nanostructure-induced properties of granular solids will be described in greater detail later. Here, as an example, let us examine the mechanical properties, microhardness in particular, of the granular Ni-Al₂O₃ system.¹⁰ Those samples were thin films of about 5 μ m thick deposited on Al₂O₃ substrates. Hardness was determined by using an Anton Paar NHT-4 microindenter. Since Al₂O₃ is harder than Ni, the hardness is expected to take on higher values as one increases the content of Al₂O₃. This is indeed observed as shown in Fig. 4. One also observes a sharp increase in hardness near $x_p \approx 0.5$, the percolation threshold, below which amorphous Al₂O₃ forms a continuous network. Interestingly, the hardness also

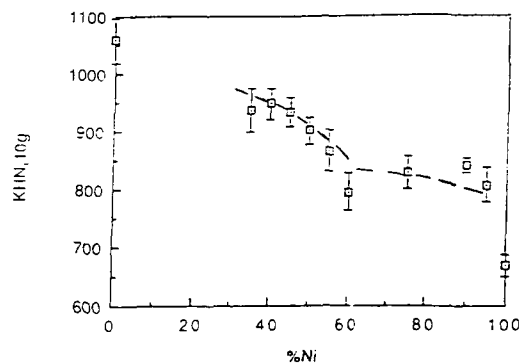


Fig.4. Hardness of granular Ni-Al₂O₃.

increases rapidly when only small amounts of Al_2O_3 are first introduced into Ni. This is because in these high volume fraction samples, Al_2O_3 exists as isolated grains dispersed in Ni, acting as pinning sites for dislocations in the Ni medium. Consequently, one derives a large increase in hardness from only a small amount of Al_2O_3 . Since Ni is already a metal of considerable hardness, the enhancement of the hardness in Ni- Al_2O_3 , while impressive, is not dramatic. In the case of a softer metal such as Ag, a much larger enhancement results.

4. Single-domain Particles and Superparamagnetism

The magnetic properties of granular solids are dominated by nanostructures. As mentioned earlier, the percolation threshold (x_p) divides regimes of very different nanostructure. For metal volume fraction (x_v) well below x_p , one observes the magnetic behavior of single-domain particles. At $x_v > x_p$, granular magnetic solids exhibit bulk magnetic properties. At $x_v \approx x_p$, they display particularly unusual magnetic characteristics, such as giant magnetic coercivity.

For ultrafine magnetically ordered particles, there exists a critical size below which the granules can acquire only single magnetic domains even in zero magnetic field.^{11,12} The critical sizes for Fe, Ni, and Co are of the order of a few hundreds of angstroms depending on the shape of the particle. The magnetic axis of a single-domain particle is determined by the magnetic anisotropy energy (CV) of the particle, where C is total magnetic anisotropy energy per unit volume and V is the volume of the particle. Along the magnetic axis, parallel and antiparallel orientations are energetically degenerate, separated by an energy barrier of CV. At low temperatures, the magnetic axes of the single-domain particles are randomly oriented and frozen. This leads to a zero magnetization of the sample. Under a large external field, all the magnetic axes will be aligned, giving rise to the saturation magnetization (M_s). When the external field is turned off, one measures the remanent magnetization (M_r) which generally obeys $M_r = \frac{1}{2} M_s$, because the magnetic axes are randomly oriented over a hemisphere and $\langle \cos \theta \rangle = \frac{1}{2}$. These features are shown in Fig. 5. In fact $M_r = \frac{1}{2} M_s$ at $T = 0$ K is an experimental signature expected for all samples with well-separated ultrafine particles and randomly distributed magnetic easy axes.⁷

At sufficiently high temperatures, the magnetic anisotropy energy barriers of the single-domain particles are overcome by thermal energy, and superparamagnetism occurs. Under these conditions the magnetic vector of each particle is not fixed but fluctuates rapidly; i.e., all the moments in the single-domain particle rotate in unison. Ferromagnetic signatures, such as spontaneous magnetization, coercivity and remanence will be absent. Since the magnetic anisotropy energy of an isolated particle is proportional to the volume of the particle, superparamagnetism is observed only in ultrafine particles. In the simplest analysis, superparamagnetic relaxation can be described by the Arrhenius law¹¹

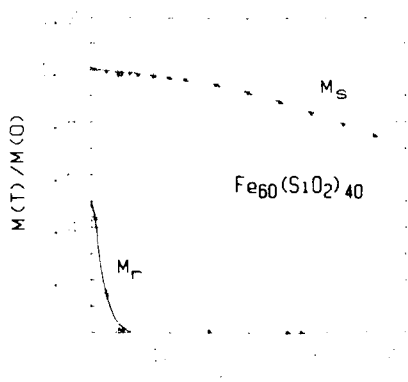


Fig. 5. Normalized magnetization (M_s) at 50 kOe and remanent magnetization (M_r) of $\text{Fe}_{60}(\text{SiO}_2)_{40}$ as a function of temperature.

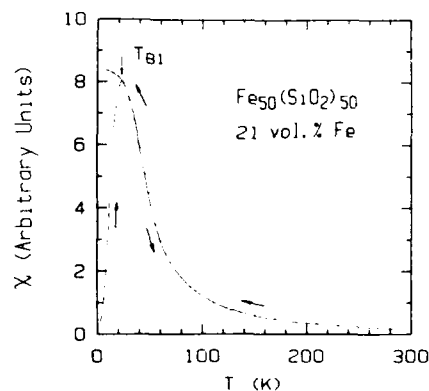


Fig. 6. Typical zero-field-cooled and field-cooled magnetic susceptibility vs temperature curve with an applied field of 50 Oe.

$$\tau = \tau_0 e^{CV/k_B T}, \quad (1)$$

where k_B is the Boltzmann constant, and T is the temperature. The value of τ_0 , related to the natural frequency of gyromagnetic precession, has been estimated to be in the range of 10^{-9} to 10^{-13} sec. The value of C includes the anisotropy energies from several contributions: magnetocrystalline, shape, surface, stress, etc. Superparamagnetic behavior can be observed, using an instrument with a characteristic measuring time (τ_i), at temperatures above the blocking temperature (T_{Bi}), which is defined by

$$T_{Bi} = \frac{CV}{k_B [\ln(\tau_i/\tau_0)]}. \quad (2)$$

It should be noted that the relaxation time may be more accurately described by a stretched exponent rather than a simple Arrhenius law. This leads only to a minor modification of Eq. (2).

Superparamagnetism and the associated blocking phenomenon have been observed in magnetic granular materials by several techniques.^{6-8,11-15} However, if only one measuring time is employed, τ_0 and CV cannot be independently determined. The situation is vastly improved if one can employ *two* measuring techniques with widely different characteristic times. The two techniques we employed were SQUID magnetometry and ^{57}Fe Mössbauer spectroscopy with characteristic times of $\tau_1 \approx 10$ sec and $\tau_2 \approx 10^{-8}$ sec, respectively.⁷ Furthermore, by extrapolation from the results of the low-field measurements, the characteristics at zero applied field can be extracted.

The magnetization of $\text{Fe}_{50}(\text{SiO}_2)_{50}$ ($x_v = 21\%$) under $H_a = 50$ Oe is shown in Fig. 6; both the zero-field-cooled (ZFC) and field-cooled (FC) data are shown. It is evident that above T_{B1} , the FC and the ZFC data are the same and reversible. Below T_{B1} , the ZFC and FC data are totally different. In ^{57}Fe Mössbauer spectroscopy, the value of T_{B2} can be determined by noting the temperature at which the magnetic hyperfine interaction first appears.

One obtains from Eq. (2)

$$\frac{T_{B1}}{T_{B2}} = \frac{\ln(\tau_2/\tau_0)}{\ln(\tau_1/\tau_0)}, \quad (3)$$

which is *independent* of the sample. Equation (3) can be rewritten as

$$\tau_0 = \tau_1^{1/[1-(T_{B2}/T_{B1})]} \tau_2^{1/[1-(T_{B1}/T_{B2})]}. \quad (4)$$

A large number of granular samples with low x_v have been measured by both techniques.⁷ As shown in Table I the same ratio $T_{B1}/T_{B2} \approx 0.35$ has been obtained for *all* granular samples, indicating that τ_0 is essentially *independent* of sample. Using $\tau_1 \approx 10$ sec, $\tau_2 \approx 10^{-8}$ sec, and $T_{B1}/T_{B2} \approx 0.35$, one obtains $\tau_0 \approx 1.4 \times 10^{-13}$ sec. This is a physically reasonable value. There have been claims that the Arrhenius law can not adequately describe the magnetic relaxation process in magnetic granular systems, because the τ_0 value obtained is too small⁸ (10^{-18} s). In our study, the fact that T_{B1}/T_{B2} remains essentially the same for different samples and an adequate ($\tau_0 \approx 10^{-13}$ s) value is obtained indicated that the Arrhenius law remains a good approximation. Of course, if a stretched exponential relaxation time is assumed, the τ_0 value will be modified.

Table I

Deposition temperatures, blocking temperatures obtained from SQUID (T_{B1}), Mössbauer (T_{B2}), and the ratio (T_{B1}/T_{B2}) for various granular samples.

| Sample (atomic %) | Deposition temperature (K) | SQUID T_{B1} (K) | Mössbauer T_{B2} (K) | Ratio T_{B1}/T_{B2} |
|--|----------------------------|--------------------|------------------------|-----------------------|
| Fe ₅₀ (SiO ₂) ₅₀ | 300 | 30 | 86 | 0.349 |
| Fe ₆₀ (SiO ₂) ₄₀ | 300 | 58 | 167 | 0.347 |
| Fe ₆₀ (SiO ₂) ₄₀ | 670 | 158 | 448 | 0.353 |
| Co-sputtered Fe-(SiO ₂) | 300 | 14 | 123 | 0.358 |

From Eq. (2) we can also obtain the magnetic anisotropy energy

$$CV = k_B T_{B1} [\ln(\tau_1/\tau_2) / (1 - T_{B1}/T_{B2})]. \quad (5)$$

Since the term inside the bracket of Eq. (5) is a constant, CV scales linearly with the blocking temperature. The average diameters of the small particles obtained from TEM are 25 and 38 Å for Fe₅₀(SiO₂)₅₀ and Fe₆₀(SiO₂)₄₀, respectively. Consequently the magnetic anisotropy constant C is about 1×10^7 erg/cm³. This value is about two orders of magnitude larger than bulk magnetocrystalline anisotropy of Fe ($K_1 = 1 \times 10^5$ erg/cm³),¹¹ indicating that magnetocrystalline anisotropy energy is *not* the main contribution to the magnetic anisotropy in these granular systems.

The essential feature of Eq. (2) is that T_B is proportional to CV. In Fig. 7, the values of T_B , measured by a SQUID magnetometer, of various granular alloys (Fe₅₀Ni₅₀)—Al₂O₃ are plotted as a function of the cube of the mean particle radius.⁴ The linear relation indicates that the total magnetic anisotropy energy density C is indeed independent of the particle size.¹¹ Using $\ln(\tau_{\text{SQUID}}/\tau_0) \approx 30$, we obtain $C = 3 \times 10^7$ erg/cm³, which again is much larger than the value of the magnetocrystalline anisotropy energy for bulk Fe₅₀Ni₅₀ ($K_1 = 1 \times 10^4$ erg/cm³). Thus it is apparent that the total anisotropy energy in granular magnetic solids is dominated by contributions (e.g. stress and surface) *other* than the magnetocrystalline anisotropy.

We next turn to coercivity. Below T_B , single domain particles exhibit ferromagnetic characteristics including coercivity (H_c) and remanence. Coercivities of single domain particles are generally much larger than that of bulk material. The temperature dependence of H_c is dominated by superparamagnetic relaxation which leads to¹⁶

$$H_c(T) = H_c(0) \left(1 - \sqrt{\frac{T}{T_B}}\right). \quad (6)$$

This \sqrt{T} dependence has been observed in many granular Fe specimens.^{17,18}

Above T_B , where the thermal energy surpasses the magnetic anisotropy energy, the moments of the particles fluctuate freely as if in a paramagnetic system with each particle bearing a giant moment. The ferromagnetic characteristics, such as coercivity and remanence will be absent. In such a superparamagnetic state, the magnetization curve $M(H)$ of a non-interacting system with uniform particle size is described by the Langevin function:¹¹

$$M = p M_s L\left(\frac{\mu H}{k_B T}\right) = p M_s \left[\coth\left(\frac{\mu H}{k_B T}\right) - \frac{k_B T}{\mu H} \right], \quad (7)$$

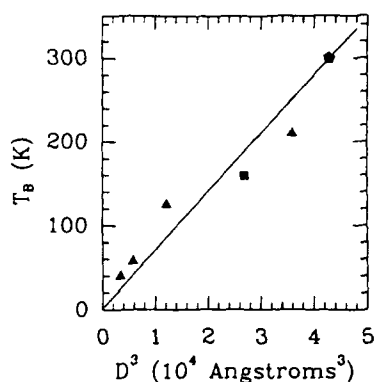


Fig.7. Blocking temperature (T_B) vs the cube of the diameter for various samples of granular $(\text{Fe}_{50}\text{Ni}_{50})\text{-Al}_2\text{O}_3$. Triangles, squares and pentagons indicate substrate temperatures of 100, 300 and 450 C respectively.

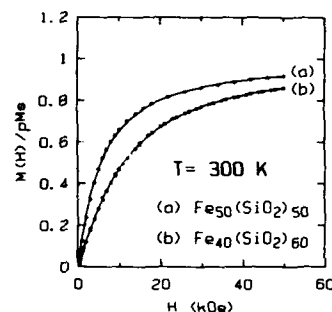


Fig.8. Normalized magnetizations vs magnetic field at 300 K. The lines are theoretical curves obtained with log-normal size distribution.

where p is the volume fraction of the magnetic particles, $\mu = M_s V$ is the magnetic moment of a single particle with volume V , and H is the external field. Because μ is large ($\approx 10^2 - 10^3 \mu_B$), saturation of the magnetic moments cannot be accomplished particularly at $T \gg T_B$.

In all real systems, there are size distributions. The resultant magnetization should be given by

$$M = pM_s \int_0^\infty L\left(\frac{M_s V H}{K_B T}\right) f(V) dV, \quad (8)$$

where L is the Langevin function as before and $f(V)$ is size distribution. Assuming spherical particles of diameter D for simplicity, a log-normal size distribution,

$$f(D) = \frac{1}{\sqrt{2\pi\ln\sigma}} \exp\left[-\frac{(\ln D - \ln \bar{D})^2}{2(\ln\sigma)^2}\right], \quad (9)$$

is most often used. This log-normal distribution is just a Gaussian function in logarithmic scale, and subjected to normalization

$$\int_0^\infty f(D) d(\ln D) = 1. \quad (10)$$

Thus by fitting the experimental data $M(H)$ to Eq.(8), one can obtain the distribution characterized by \bar{D} and σ . Two such examples are shown in Fig. 8, from which $\bar{D} = 19 \text{ \AA}$, $\sigma = 1.21$ have been obtained for $\text{Fe}_{40}(\text{SiO}_2)_{60}$, and $\bar{D} = 23 \text{ \AA}$, $\sigma = 1.3$ for $\text{Fe}_{50}(\text{SiO}_2)_{50}$. The sizes are in good agreement with TEM determinations. Note that even with a field of 50 kOe, saturation magnetization cannot be obtained at 300 K.¹⁹

Other distinctive features of granular magnetic systems are the susceptibility (χ) and its temperature dependence. For conventional paramagnetic systems with atomic moments, χ has the well-known Curie-Weiss form of

$$\chi = \frac{np_{\text{eff}}^2 \mu_B^2}{3k_B(T-\theta)} \quad (11)$$

Consequently, $1/\chi$ will be linear in T . In the case of granular magnetic systems at $T > T_B$, one obtains, using Eq. (7),

$$\chi = \frac{pVM_s^2(T)}{3k_BT} \quad \text{for } \mu H < k_BT, \quad (12)$$

for non-interacting granules. By including interactive effects, following Chantrell and Wohlfarth,²⁰

$$\chi \propto \frac{M_s^2(T)}{T-T_0}. \quad (13)$$

Because of the temperature dependence of $M_s(T)$, $1/\chi$ is not linear in T . This is indeed observed as shown in Fig. 9. The T_0 values obtained are 10 K and 26 K for $\text{Fe}_{40}(\text{SiO}_2)_{60}$ and $\text{Fe}_{50}(\text{SiO}_2)_{50}$ respectively.

Having obtained T_0 for the samples, one can now deduce $M_s(T)$, the temperature dependence of the spontaneous magnetization of the ultrafine ferromagnetic particles. In the Fig. 10, we plot $\sqrt{\chi(T-T_0)}$, which is proportional to M_s of the ultrafine Fe particles, against $T^{3/2}$. At temperatures higher than 150 K, the data can be well described by straight lines, i.e., M_s follows Bloch's law:

$$M_s(T) = M_0(1-BT^{3/2}). \quad (14)$$

A noticeable departure from Eq. (14) at low temperatures where an enhancement of χ is observed. This is caused by the effect of size distribution. Even above the effective blocking temperature, some large particles at the tail of the particle distribution still remain magnetically blocked, which will generate a nonvanishing internal field and enhance the magnetic susceptibility.

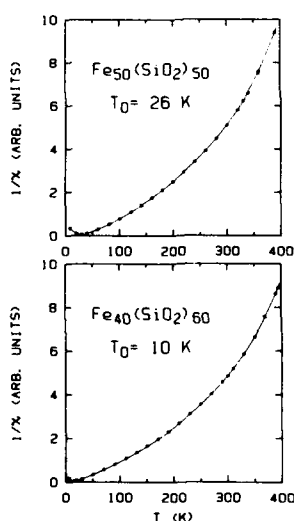


Fig.9. Inverse susceptibilities vs temperature under a field of 5 Oe. The T_0 values were obtained from extrapolation.

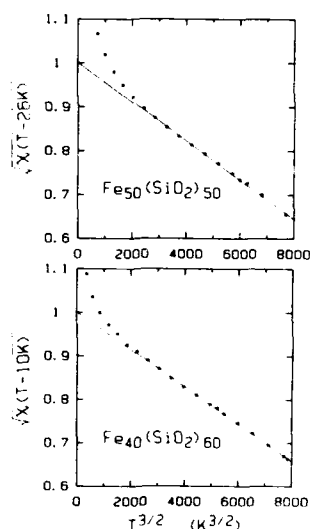


Fig.10. $\sqrt{\chi(T-T_0)}$, which is proportional to $M_s(T)$, as a function of $T^{3/2}$.

The fact that $T^{3/2}$ dependence is observed indicates spin-wave excitation despite the small size of the ferromagnetic particles. However, the spin-wave constant B of the granular Fe particles is very different from that of the bulk Fe. The spin-wave constants B obtained from Fig. 10 are $4.30 \times 10^{-5} \text{ K}^{2/3}$ and $4.46 \times 10^{-5} \text{ K}^{2/3}$ for $\text{Fe}_{40}(\text{SiO}_2)_{60}$ and $\text{Fe}_{50}(\text{SiO}_2)_{50}$, respectively, considerably larger than the value of $3.3 \times 10^{-6} \text{ K}^{2/3}$ for bulk Fe. There are several possibilities for the increase. Theories and experiments^{21,22} on magnetic thin films have shown that the fluctuation of the surface moments is larger than that of interior moments so that the B constants for the surfaces are 2-3.5 times larger than that for the interior. In the case of ultrafine Fe particles with diameter of 20 Å, the portion of surface atoms exceeds 50%, assuming that the surface layer consists of two atomic layers. Thus a large B value observed in the Fe particles is, in part, a consequence of the abundance of the magnetic surfaces. The other effect which may change the B constant is the finite size effect. It plays at least two roles in the magnetic properties of the ultrafine particles. First, the physical properties such as spin wave spectrum may be substantially altered from the bulk case, causing a softening of the spin waves. Second, the geometrical size causes a cutoff of the spin waves with wavelength larger than the physical dimension of the particles.

5. Enhanced Ferromagnetic Properties of Granular Fe Systems

Granular Fe-SiO₂ samples have been fabricated across the entire metal volume fraction range¹⁷ $0 \leq x_v \leq 1$ to reveal the evolution of magnetic properties. The superparamagnetic properties have been briefly discussed above. Here we will examine the ferromagnetic properties. In Fig. 11 we show the coercivity (H_c) at 2 K, 77 K and 300 K for a set of samples of granular Fe-SiO₂ deposited on room temperature substrates. The H_c data at 2 K are close to the ground-state properties. Below the percolation threshold ($x_v < x_p$), one observes a giant enhancement of H_c , reaching a peak of 2500 Oe. As x_v is increased further, H_c precipitously drops to a value of about $H_c \approx 50$ Oe, which is close to the value of sputtered bulk Fe. H_c remains at that value from $x_v = 60\%$ to 100%. As shown in Fig. 12, for a given sample of $x_v < x_p$, H_c decreases with temperature due to the temperature dependence described in Eq.(6).

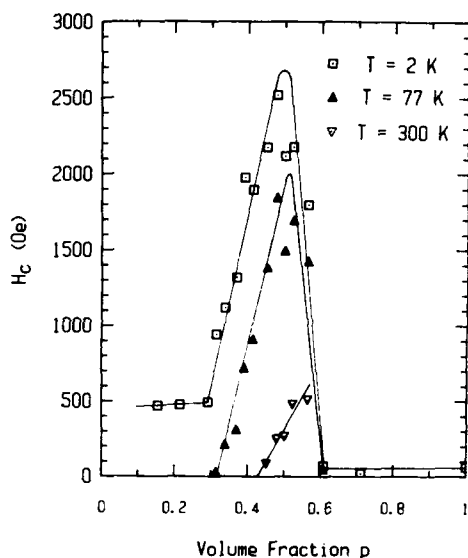


Fig. 11. Magnetic coercivities at 2, 77 and 300 K of granular Fe-SiO₂ films deposited onto room temperature substrates as a function of Fe volume fraction.

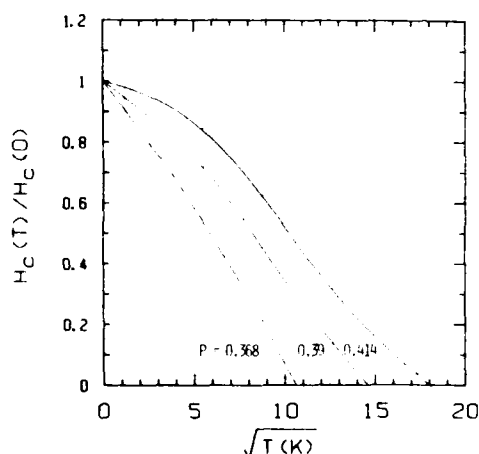


Fig. 12. Temperature dependence of the normalized coercivity for samples with volume fraction 36.8%, 39% and 41.4%.

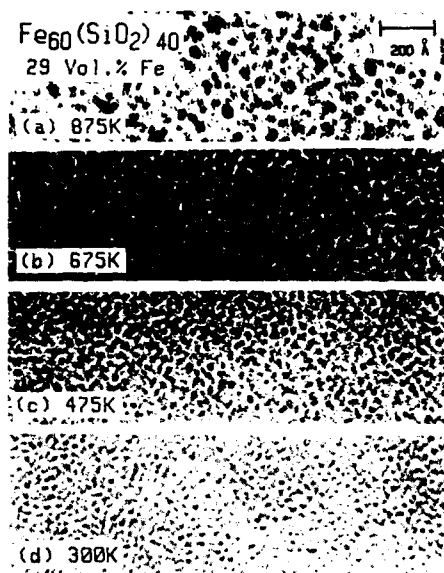


Fig. 13. TEM micrographs of granular $\text{Fe}_{60}(\text{SiO}_2)_{40}$ (29 vol.% Fe) films prepared at various substrate temperatures : (a) 875 K, (b) 675 K, (c) 475 K and (d) 300 K.

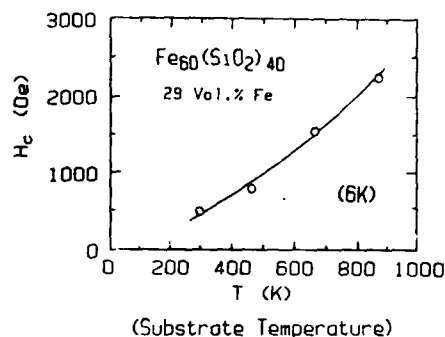


Fig. 14. Variation of coercivity of $\text{Fe}_{60}(\text{SiO}_2)_{40}$ (29 vol.% Fe) at 6 K with substrate temperatures.

For samples deposited at room temperature, larger particle sizes are realized in samples with higher values of x_v . Therefore, the observed increase of H_c may be associated with the increase of particle size. This indeed is supported by the following experiment. We deposited samples with the same volume fraction (29%) at temperatures of 300 K, 475 K, 675 K and 875 K. The high substrate temperatures effectively enlarge the particles as shown in Fig. 13. The values of H_c for these samples increase rapidly with particle size as shown²³ in Fig. 14.

There are two anomalies in the behavior of H_c in the granular Fe-SiO₂ system. First, the experimental results establish that H_c increases dramatically with particle size. Second, extremely high H_c values (at least 2500 Oe) are achieved.

According to conventional theories,^{11,12} for single domain Fe particles the rotation-in-unison mode of magnetization reversal is more favorable than buckling and curling modes. In this mode, the zero-temperature coercivity H_{c0} is $2K_1/M$, where M is the magnetization and K_1 is the magnetocrystalline anisotropy constant, which is independent of size. But $2K_1/M$ gives a coercivity of only 600 Oe. The chain-of-spheres fanning mode could provide a maximum H_c of 2700 Oe for an infinitively long chain in a random system, these extreme particle shapes and morphology were not revealed in the TEM micrographs.

However, it must be recognized that almost all the existing models assume free-standing particles dispersed in a nonbonding medium. In the granular Fe-SiO₂ system, the particles are strongly bonded to the insulating matrix and may be subjected to very large stresses. For small particles, a large portion of the Fe atoms are at or near the surface, and the fraction of surface atoms increases with particle size. The metal-insulator interfaces may dominate the coercivity in such systems. Under a reversing field, the moment reversal may well begin first at the surface and then propagate throughout the particle.

If the high H_c and magnetization already realized can be further improved, granular Fe-SiO₂ offers much promise as a magnetic recording medium. For high density recording, the amplitude and width are proportional to $\sqrt{M_r H_c}$ and $\sqrt{1/H_c}$ respectively where H_c is the coercivity and M_r is the remanent magnetization. Larger H_c and M_r thus assure better recording characteristics. Some common recording media and their magnetic properties are shown in Table II.²⁴⁻²⁶ The low temperature values of H_c and M_r of granular Fe-SiO₂ have already exceeded those listed in Table II, if only the excellent properties can be preserved to room temperature. Another important consideration is that of recording noise, which roughly scales with the particle size. Granular Fe-SiO₂, containing ultrafine particles, enjoys great advantage in this regard.

Table II
Magnetic Characteristics of $\gamma\text{-Fe}_2\text{O}_3$, CrO_2 and Granular Fe-SiO_2

| | H_c | M_s |
|--------------------------------|--------------|-----------|
| $\gamma\text{-Fe}_2\text{O}_3$ | 300—550 Oe | 80 emu/g |
| CrO_2 | 600—800 Oe | 80 emu/g |
| Granular Fe-SiO_2 | 1000—1100 Oe | 160 emu/g |

The coercivity data shown in Fig. 11 are from samples deposited onto room-temperature substrates, where the metal granules are relatively small ($\leq 70 \text{ \AA}$). Consequently, H_c at room temperature is much reduced, primarily because of superparamagnetic relaxation. Since the relaxation rate depends sensitively on the particle size through Eq. (1), even a modest increase of V (e.g. a factor of 2) would drastically alter the temperature dependence of the magnetic properties.

The composition $\text{Fe}_{75}(\text{SiO}_2)_{25}$ with $x_v = 0.42$ was chosen for further exploration²⁷ because a maximum in H_c has been achieved near that volume fraction as shown in Fig. 11. A number of process conditions such as sputtering gas pressure, deposition rate, substrate temperature were varied in order to increase the granule size. Of those, the substrate temperature was found to be most effective. As shown in Fig. 15, for samples deposited at $77 \text{ K} \leq T_s \leq 400 \text{ K}$, the granules are about 40 \AA . Above $T_s = 400 \text{ K}$, granule sizes increase with increasing T_s . The samples deposited at $T_s = 575 \text{ K}$ contain grains of about 60 \AA , and $T_s = 775 \text{ K}$ yields grains of about 150 \AA .

By increasing the granule size, as facilitated by higher T_s , the coercivity is dramatically affected in both magnitude and temperature dependence. As shown in Fig. 16, H_c at 6 K increases from 1.5 kOe to about 3 kOe as T_s is increased from 300 to 775 K . For samples with $T_s > 800 \text{ K}$, H_c at both 6 and 300 K decreases precipitously, due to sintering between the granules. The partially connected granules effectively allow the formation of multidomain structures, thus reducing H_c . A maximum of H_c at both 6 and 300 K is achieved with $T_s = 775 \text{ K}$. The values of H_c of 3 kOe (at 6 K) and 1.1 kOe (at 300 K) are among the highest for Fe particles. The high value at 300 K together with a large magnetization of 160 emu/g are particularly encouraging for possible recording media applications.

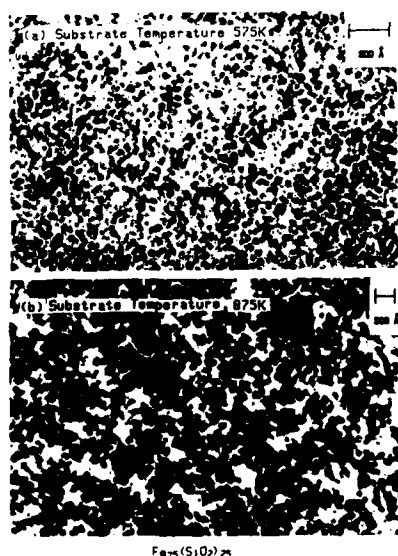


Fig. 15. TEM micrographs of $\text{Fe}_{75}(\text{SiO}_2)_{25}$ ($x_v = 0.42$) sputtered at substrate temperatures of (a) 575 K and (b) 875 K .

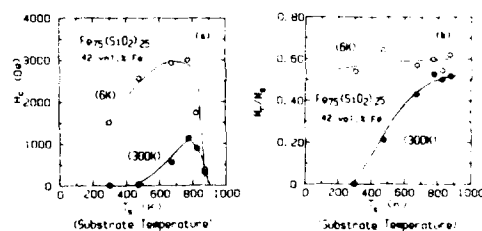


Fig. 16. Variations of (a) coercivity and (b) squareness of $\text{Fe}_{75}(\text{SiO}_2)_{25}$ ($x_v = 0.42$) at 6 and 300 K as a function of substrate temperatures.

Finally, it should be mentioned that the superior magnetic properties of the granular solids are microstructure controlled and can be tailored through process conditions. The insulating matrix (e.g., SiO_2 , Al_2O_3) greatly enhances the chemical stability of the magnetic particles, and the wear and corrosion resistance of the media. Furthermore, since vapor deposition is the most effective method of making granular metal films, the fabrication, dispersion, and protection of the ultrafine granules, as well as coating onto desired surfaces suitable for device applications, are achieved in a *single* process.

6. Granular Alloy Systems

Almost all studies of granular materials performed to date have been restricted to systems involving a single elemental metal. Ultrafine metal alloys, both crystalline and amorphous, remains largely unexplored despite the fact that alloys have almost always proven to be more useful and interesting than their pure metallic constituents. On the other hand, the fabrication of granular alloys presents additional challenges over those posed by pure elemental granular materials. It is not assured that metals will alloy in the form of ultrafine particles, instead of forming individual grains of each of the metals. Further difficulties may be encountered in the fabrication of ultrafine particles in which the alloy composition does not appear in the equilibrium phase diagram, for example, amorphous or metastable crystalline alloys. We have recently succeeded in the fabrication of granular alloys of Fe-Ni, Fe-Co, Fe-B, and Fe-Cu in a variety of matrices.⁴ Of these, Fe-Cu is an example of a metastable crystalline alloy and Fe-B is amorphous.

In Fig. 7, we show that the blocking temperature (T_B) of various granular $(\text{Fe}_{50}\text{Ni}_{50})\text{-Al}_2\text{O}_3$ samples are proportional to CV as expected. The value of $C = 3 \times 10^7$ ergs/cm³ is much larger than the magnetocrystalline anisotropy energy for bulk $\text{Fe}_{50}\text{Ni}_{50}$ ($K_1 \approx 1 \times 10^4$ ergs/cm³). Below the blocking temperature, granular magnetic systems exhibit ferromagnetic behavior. The coercivity of the $(\text{Fe}_{50}\text{Ni}_{50})_x(\text{Al}_2\text{O}_3)_{1-x}$ alloy system is shown in Fig. 17. The value of the coercivity changes smoothly as the metal content is increased, and drops off sharply at the percolation threshold. This is precisely the expected behavior of H_c in granular magnetic system when the percolation threshold is crossed. It also underscores the anomalous features of H_c in granular Fe-SiO₂ which are shown in Fig. 17 for comparison. It should be mentioned that very similar behavior is also observed in the $(\text{Fe}_{50}\text{Ni}_{50})_x(\text{SiO}_2)_{1-x}$ system.

The case of granular metastable crystalline Fe-Cu alloys is particularly challenging. Under equilibrium conditions, Fe and Cu have negligible solubility in one another, and form no intermetallic compounds. We have demonstrated that, by vapor quenching, metastable $\text{Fe}_x\text{Cu}_{1-x}$ can be formed at any composition.²⁸ For $x < 0.65$, all of those alloys are fcc. The magnetic ordering temperature of metastable Fe-Cu is shown in Fig. 18. Above the percolation threshold

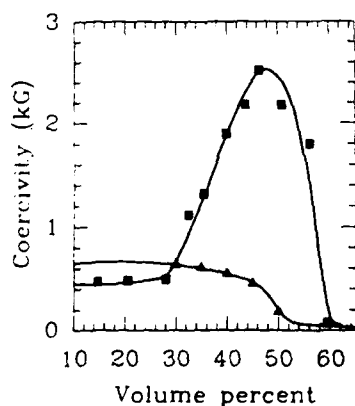


Fig. 17. Coercivity vs volume fraction for granular Fe-SiO₂ (squares) and granular $(\text{Fe}_{50}\text{Ni}_{50})\text{-Al}_2\text{O}_3$ (triangles).

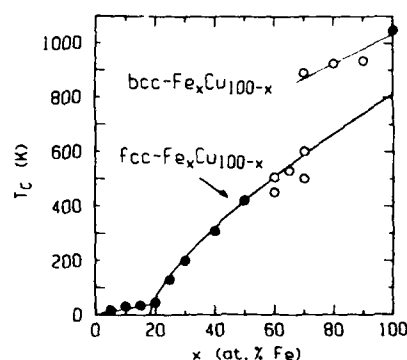


Fig. 18. Magnetic ordering temperature of metastable fcc Fe-Cu Alloys.

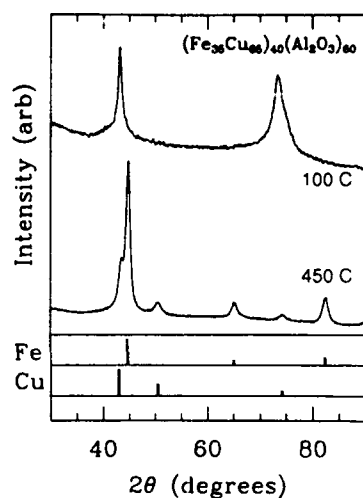


Fig. 19. X-ray diffraction patterns of granular $(\text{Fe}_{35}\text{Cu}_{65})_{40}(\text{Al}_2\text{O}_3)_{60}$ deposited at 100 °C and 450 °C, and the standard patterns for Fe and Cu.

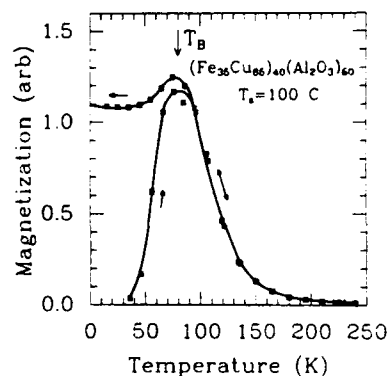


Fig. 20. Field-cooled and zero-field cooled magnetization of granular $(\text{Fe}_{35}\text{Cu}_{65})_{40}(\text{Al}_2\text{O}_3)_{60}$ deposited at 100 °C. The applied field was 5 Oe.

($x = 0.19$), these alloys are ferromagnetic with an ordering temperature rising sharply with Fe content. We will discuss samples of the metastable alloy $\text{Fe}_{35}\text{Cu}_{65}$ with $T_c = 250$ K. Because of the inherent metastability of this alloys, we have managed to fabricate granular $\text{Fe}_{35}\text{Cu}_{65}$ only within a limited range of process conditions. Samples of $(\text{Fe}_{35}\text{Cu}_{65})_{40}(\text{Al}_2\text{O}_3)_{60}$ have been deposited at various values of T_s . The x-ray diffraction patterns of two of these samples are shown in Fig. 19. If the substrate are maintained at 100 °C, the metastable fcc phase, which has been observed in pure sputtered Fe-Cu films, can be achieved, as seen in the upper curve. However, at higher substrate temperatures the metal segregate forming isolated grains of fcc Cu and bcc Fe. The lower curve in Fig. 19 is typical of this case; peaks due to both of the pure metal phases are clearly visible. The sample deposited at 100 °C was found to have a blocking temperature of $T_B = 80$ K, as shown in Fig. 20. Below T_B coercivity is observed, with a value of $H_c = 620$ G at 4.2 K. These results further confirm the granular nature of the metastable $\text{Fe}_{35}\text{Cu}_{65}$ alloys.

7. Granular Fe in a Metallic Medium

Ultrafine Fe particles containing a single magnetic domain exhibit magnetic properties that are strikingly different from those of bulk Fe. For Fe particles in an insulator such as SiO_2 and Al_2O_3 , these samples are generally poor electrical conductors and often insulating. New applications may exist for materials which combine the high magnetization and coercivity of single-domain Fe particles together with a highly conducting matrix. Such a system, unfortunately, cannot easily be obtained by co-deposition, since Fe readily forms alloys or compounds with almost any metal. However, there are actually a few metallic elements with which Fe is essentially immiscible. Copper is one such example as mentioned above. Although Fe and Cu are immiscible, homogeneous metastable $\text{Fe}_x\text{Cu}_{1-x}$ alloys over the entire composition range can be made by sputtering.²⁸ Because of the metastable nature of such Fe-Cu alloys, recrystallization will occur at elevated temperatures, with a transformation into separated phases of bcc Fe and fcc Cu. In the process, Fe forms small particles whose sizes can be controlled by the annealing conditions. In this manner the magnetic properties of these materials can be optimized.⁵

Typical behavior for the evolution of the magnetic properties at room temperature is shown in Fig. 21 for the case of $\text{Fe}_{45}\text{Cu}_{55}$, as it goes through an annealing sequence of 10 min at each annealing temperature (T_A). The as-prepared metastable fcc $\text{Fe}_{45}\text{Cu}_{55}$ alloy is a soft fer-

romagnet ($T_C=360$ K), with a very small H_C (< 10 Oe) and a squareness ratio ($SQ=M_R/M_S$) of less than 5% at room temperature. Up to $T_A = 250$ °C, the magnetic properties do not change appreciably. However, the value of H_C increases dramatically between $T_A = 250$ °C and $T_A = 300$ °C, reaches $(H_C)_{max}=526$ Oe for $T_A=350$ °C and then decreases as T_A is increased further. The value of SQ behaves similarly, reaching a maximum of 40%, also at 350°C.

The associated evolution of the crystal structure and microstructure of the sample during the annealing process has been determined by X-ray diffraction and TEM with its accompanying electron diffraction, as shown in Fig. 22 and 23. The fcc structure is preserved up to $T_A=250$ °C. Following annealing at 300°C, however, the bcc α -Fe lines suddenly appear, signaling the recrystallization of the metastable alloy into fcc Cu and bcc Fe. Thus the dramatic increase in H_C at $T_A=300$ °C is the direct result of the appearance of the α -Fe phase. As T_A is increased past 300°C, the diffraction lines become progressively narrower due to the growth in

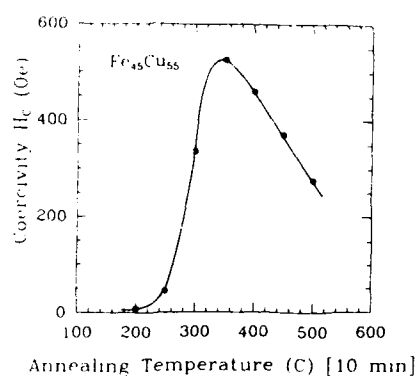


Fig.21. Room temperature coercivity of $Fe_{45}Cu_{55}$ after annealing at T_A for 10 min.

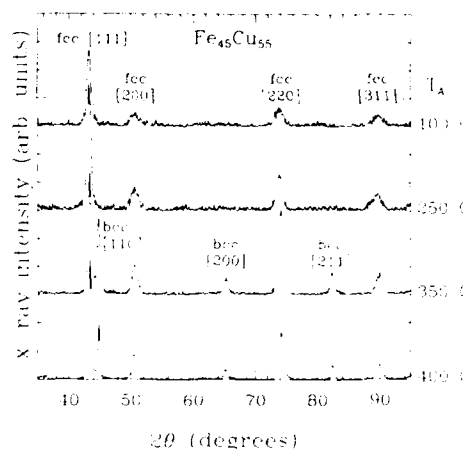


Fig. 22. X-ray diffraction patterns of $Fe_{45}Cu_{55}$ after annealing at T_A for 10 min.

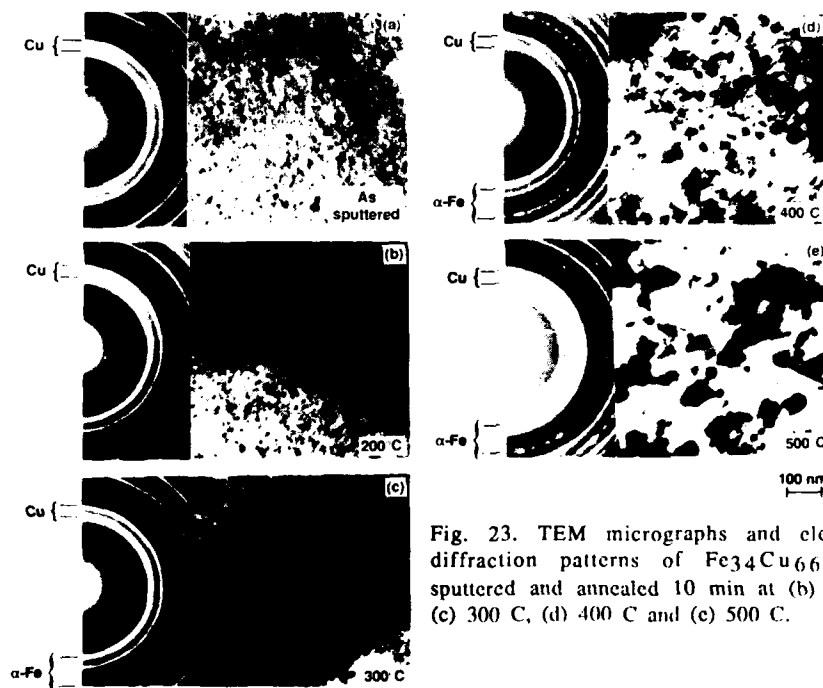


Fig. 23. TEM micrographs and electron diffraction patterns of $Fe_{34}Cu_{66}$ (a) as sputtered and annealed 10 min at (b) 200 °C, (c) 300 °C, (d) 400 °C and (e) 500 °C.

grain size, which increases from 15nm at $T_A=300^\circ\text{C}$ to 60 nm at $T_A=500^\circ\text{C}$. Eventually, when the critical size is exceeded or Fe grains come into contact, the enhanced magnetic properties begin to deteriorate.

8. Granular Spin-glass Systems

More recently, we have begun a study of granular spin glass systems. This is motivated by the fact that the critical dimension²⁹ for spin glass ordering is believed to be between 2 and 3. Spin glass ordering is observed in 3d systems, but as one reduces the spin glass film thickness, the spin glass transition (T_g) shifts to low temperature due to finite size effects.³⁰ For sufficiently thin samples, where the correlation length exceeds the film thickness (e.g. 60 Å), 2d behavior has been observed.³¹ We used multilayer of CuMn/Al₂O₃ to study the finite size effects. In order to illustrate the scaling behavior of T_g , we have plotted the reduced temperature $\varepsilon=[T_g(\infty)-T_g(w)]/T_g(\infty)$ versus the layer thickness w on a log-log scale in Fig. 24. We have found that all of the data can be described by the simple finite-size scaling relation

$$\frac{T_g(\infty)-T_g(w)}{T_g(\infty)} = \varepsilon = A w^{-\lambda} = \left[\frac{w}{w_0}\right]^{-\lambda}, \quad (15)$$

with $\lambda = 0.64 \pm 0.07$, $A = 6.7 \pm 0.25$, and $w_0 = 19.5 \pm 1.1$ Å. The solid line represents those calculated results. The value of $\lambda = 0.64$ is quite close to the value which was obtained by Kenning, Slaughter, and Cowen³⁰ for the thicker films in that study: $\lambda=0.63\pm0.15$ for $w\geq 150$ Å.

In ferromagnetic films, no deviation of T_c can be observed until the films are only a few atomic layer thick. In contrast, it is remarkable to note that significant deviations from the bulk value of $T_g(\infty) = 34$ K may be observed even in the samples with a thick spin-glass layer ($w = 1250$ Å). Specifically it is the large value of the constant A (or the zero-temperature correlation length w_0) which is responsible for the effect, and which in turn makes this measurement possible. While theoretical calculations focus on scaling behavior and critical exponents, the large value of w_0 has not been addressed.

The non-linear susceptibility is defined as

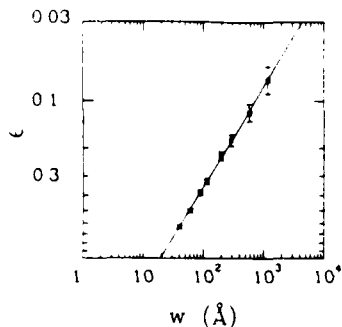


Fig.24. Reduced temperature $\varepsilon = [T_g(\infty) - T_g(w)]/T_g(\infty)$ vs w , the layer thickness of Cu₉₂Mn₈.

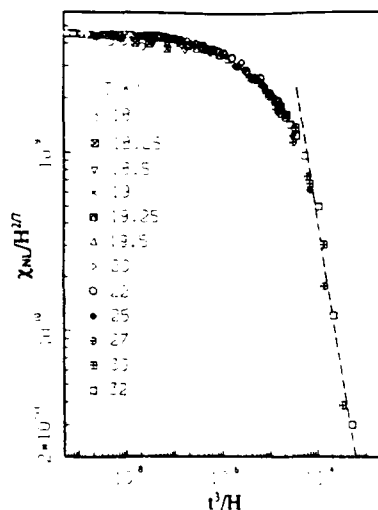


Fig.25. Scaling plot for CuMn with thickness $w = 60$ Å, where $t = (T-T_g)/T_g$, $\delta=7$, $\phi=6$, and $T_g=17.5$ K.

Table III

Experimental and theoretical values of the spin-glass critical exponents.

| Exponent | 60 Å | 88 Å | Bulk | 2D Ising |
|----------|-------------|---------------|---------------|-----------------|
| δ | 7 ± 0.5 | 7.1 ± 0.2 | 4.4 ± 0.2 | (6.6) |
| ϕ | 6 ± 1 | 6 ± 1 | 3.9 | (6.2) |
| β | 0.86 | 0.85 | 0.9 | (0.95) |
| γ | 5.1 | 5.2 | 3.0 | 5.3 ± 0.3^a |
| ν | 3.4 (d=2) | 3.4 (d=2) | 1.6 ± 0.2 | 3.6 ± 0.1^b |
| η | 0.5 | 0.49 | 0.11 | (0.53) |

a: ref. 32

b: ref. 33

$$\chi_{nl}(H,T) = \chi_l(T) - M(H,T)/H \quad (16)$$

where $\chi_l(T)$ is the linear susceptibility. We expect χ_{nl} to obey the single-parameter scaling relation

$$\chi_{nl}(H,T) \propto H^{2\delta} f(t/H^{2\phi}) \quad (17)$$

Here, $t = (T - T_g)/T_g$, δ and ϕ are spin-glass critical exponents which are related to the susceptibility exponent by $\gamma = \phi(1 - 1/\delta)$, and f is a scaling function. Excellent scaling behavior is revealed by the choices of $T_g = 17.5 \pm 0.25$ K, $\delta = 7.0 \pm 0.5$, and $\phi = 6 \pm 1$ as shown in Fig. 25, where we plot $\chi_{nl}/H^{2\delta}$ vs $t^{\phi/2}/H$.

Table III summarizes the critical exponents we have obtained from χ_{nl} for thin layers and bulk spin glasses. The quantities with errors are the directly determined values, whereas those without error are derived from the scaling laws. As seen in Table III, our results suggest such a dimensional crossover. The experimental temperature range for the thin-layer sample is clearly well within the 2D regime.

In the spin glass granular system of $\text{Cu}_{92}\text{Mn}_8$, no spin glass transition can be observed for particle size of about 15\AA , consistent with finite size effects observed in layered spin glasses. For samples above the percolation threshold, spin glass ordering exists but with a depressed T_g according to the metal volume fraction. These very interesting preliminary results indicate a new realm for the exploration of granular magnetic systems.

9. Finite-size Effect in Lattice Dynamics

Finite-size effects in nanometer-size crystals can lead to physical properties markedly different from those of the bulk material.³⁴ In many cases, the increased importance of the surface in these nanocrystalline materials is responsible for the observed changes. For example, different binding conditions for surface atoms can lead to stresses or strains which propagate throughout the lattice of nanocrystals, altering the lattice spacing. Similarly, the restricted geometry of such systems can lead to a phonon spectrum not normally found in the bulk material. Consequently, the lattice dynamics and melting behavior of nanocrystals has been for many years a topic of great interest in condensed matter research.

Experimentally, unambiguous finite size effects are difficult to observe. First of all, the fabrication of nanocrystals, their protection from reaction with atmosphere, and their dispersion into a suitable matrix are challenging requirements. The experimental techniques which measure finite size effect must be able to discriminate against a very large background due to the matrix and other irrelevant phases in the specimen. For this reason, Mössbauer spectroscopy is an ideal tool for measuring multiphase samples since it only probes the local environment of the absorbing nucleus and is not adversely affected by the macroscopic properties of the

material as whole. This allows a simple and direct comparison between atoms in the bulk material and in small particles.

Most recently, Hayashi et al.³⁵ used Mössbauer spectroscopy to study the Debye temperature of 6.6 nm Fe particles bound in a matrix and found no different from that of bulk Fe. Thus much smaller particle sizes appear to be a necessary requirement for the possible observation of such effects. In our case, inspection of Transmission Electron Microscopy pictures revealed all samples to have a narrow distribution of grain sizes, with mean diameter 1.5 nm and 2.5 nm for Fe-SiO₂ with 15 vol% and 30 vol% Fe, respectively. These sizes are smaller than any other Fe nanocrystals studied for finite size effects.

In a Mössbauer experiment, the mean-square displacement $\langle x^2 \rangle$ of the Mössbauer atom determines the f-fraction (or recoilless fraction) of atoms which participate in the recoilless absorption of gamma-rays. $\langle x^2 \rangle$ in turn can be related to the temperature of the solid by the Debye model, which establishes a relation between f and Debye temperature. On a typical plot of Mössbauer data showing gamma-ray absorption versus shift velocity, f is proportional to the area A under the absorption peaks. In the case of Fe, such an analysis leads to:

$$\Theta \approx -11.6 \left(\frac{d \ln f}{dT} \right)^{-1/2} \approx -11.6 \left(\frac{d \ln A}{dT} \right)^{-1/2} \quad (T > \frac{\Theta_D}{2}) \quad (17)$$

Here Θ_D can be directly obtained from the slope of a $\ln A$ vs. T curve, without the painstaking corrections to the background counts that are needed for an accurate determination of f. The high temperature requirement $(T > \frac{\Theta_D}{2})$ amounts to $T > 200$ K for Fe. All the granules in the samples used here are small enough and well isolated so that they are all superparamagnetic at $T > 200$ K. Thus the Mössbauer spectra of these samples for $T > 300$ K never includes the complications of magnetic hyperfine interactions.

The Debye temperature (Θ_D) for bulk Fe is found to be 388 ± 20 K, in good accord with previous published results. However, Θ_D for nanocrystalline Fe sharply decreases with decreasing particle size to 344 ± 16 K and 259 ± 18 K for 2.5 nm and 1.5 nm particles in SiO₂, respectively. This is the largest decline of Debye temperature observed in microcrystals by the Mössbauer effect, with a 35% change from the bulk value for the smallest particle size.³⁶

In Fig. 26 we plot $\Theta_D(d)/\Theta_D(\infty)$ versus particle size d. The solid line is the theoretical result using a self-consistent Einstein model with the Morse potential. Excellent agreement is evident in the magnitude of the decrease, in excess of 30% for particle size around 1.5 nm.

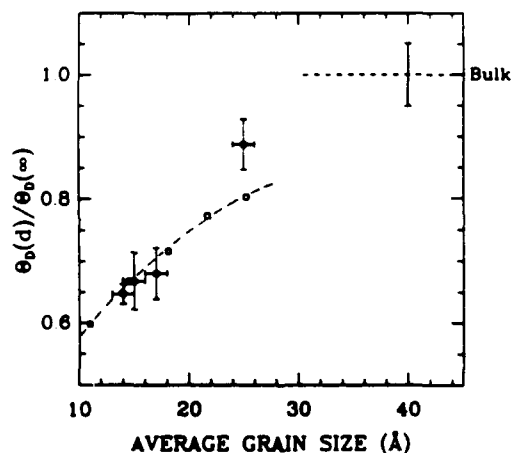


Fig. 26. $\Theta_D(d)/\Theta_D(\infty)$ versus particles size d for the theoretical calculation (open squares) and Mössbauer measurements (filled circles).

10. Applications

The applications of granular solids utilize several unique characteristics of these systems: extra degrees of freedom (granular size and metal volume fraction), enhanced physical properties due to finite-size effects, tailored properties and nanocomposite nature. The following are a few examples of possible applications:

1. Magnetic recording medium: By capitalizing on single-domain properties, one can realize high magnetization and tunable giant coercivity in granular magnetic solids with characteristics comparable to, or better than those of the existing medium. Together with enhanced hardness, wear and corrosion resistance, granular magnetic solids are promising media for recording disk applications.

2. Thin Film Resistors: Since the resistivity of granular metals can be varied over many orders of magnitude by simply changing the metal volume fraction, thin film resistors, particularly those with high resistance, can be readily achieved.¹

3. Environmental Resistant Coatings: The nanocomposite nature of granular metal solids leads to much better wear and corrosion resistance as well as hardness, while maintaining metallic characteristics. In many applications where metallic thin films are used, granular metal films can substantially strengthen the integrity of the thin films.

4. Thermometry and Sensors: The resistivity of granular metals with low metal volume fraction displays a universal temperature dependence and highly reproducible magnetic field dependence. Granular metal films can be used as thermometers at ultra-low temperatures (<1 K) and as sensors for magnetic field.³⁷

11. Summary

Granular magnetic solids are a good example of artificially structured materials. Starting from two very ordinary materials, Fe and SiO₂ for example, granular Fe-SiO₂ may be produced and seen to display a rich variety of physical properties. Below the percolation threshold the magnetic properties of an assembly of isolated single-domain particles of nanometer sizes have been studied in considerable detail. Across the percolation threshold, enhanced magnetic properties, particularly coercivity, have been uncovered. The improved properties show potential for applications, among them, as magnetic recording media. Further exploration of granular magnetic solids of other magnetic elements and alloys are in progress.

Acknowledgments Several colleagues have contributed to the results in this paper. Among them are Dr. G. Xiao now at Brown University, Dr. S.H. Liou now at the University of Nebraska, Dr. R.C. Cammarata, T.E. Schlesinger, A. Gavrin, F.H. Streitz, J.R. Childress and J.N. Taylor at the Johns Hopkins University, Dr. Ping Sheng and Dr. M.Y. Zhou at Exxon Research and Engineering. This work is supported by ONR Contract No. N00014-85-K-0175

References

1. B. Abeles, in *Applied Solid State Science: Advances in Materials and Device Research*, eds. R. Wolfe (Academic, New York, 1976). P.1
2. B. Abeles, P. Sheng, M.D. Coutts and Y. Arie, *Adv. Phys.* **24**, 407 (1975).
3. See e.g.: *Synthetic Modulated Structures*, eds. L.L. Chang and B.C. Giessen (Academic, New York, 1985).
4. A. Gavrin and C.L. Chien, *J. Appl. Phys.* **67**, 938 (1990).
5. J.R. Childress and C.L. Chien, *Appl. Phys. Lett.* **56**, 95(1990).
6. S. Morup, H. Topsøe and B.S. Clausen, *Phys. Scr.* **25**, 713 (1982).
7. G. Xiao, S.H. Liou, A. Levy, J.N. Taylor and C.L. Chien, *Phys. Rev. B* **34**, 7573 (1986).
8. J.L. Dormann, J.L. Tholence, L. Bessais and D. Villers, *J. Magn. Magn. Mater.* **54-57**, 173 (1986).

9. P. Sheng, *Phys. Rev. Lett.* **45**, 60 (1980).
10. T.E. Schlesinger, A. Gavrin, R.C. Cammarata and C.L. Chien (to appear)
11. See e.g. A.H. Morrish, *Physical Principles of Magnetism* (Wiley, New York 1965).
12. I.S. Jacobs and C.P. Bean, in *Magnetism III*, edited by G.T. Rado and H. Suhl (Academic, New York, 1963) p. 275.
13. Y. Goldstein and J.L. Gittleman, *Solid State Commn.* **9**, 1197 (1971).
14. J.L. Gittleman, Y. Goldstein and S. Bozowski, *Phys. Rev.* **B5**, 3609 (1972).
15. J.L. Gittleman, B. Abeles and S. Bozowski, *Phys. Rev.* **B9**, 3891 (1974).
16. E.F. Kneller and F.E. Luborsky, *J. Appl. Phys.* **34**, 656 (1963).
17. G. Xiao and C.L. Chien, *Appl. Phys. Lett.* **51**, 1280 (1987).
18. G. Xiao and C.L. Chien, *J. Appl. Phys.* **63**, 4252 (1988).
19. Gang Xiao and C.L. Chien, *J. Appl. Phys.* **61**, 3308 (1987).
20. R.W. Chantrell and E.P. Wohlfarth, *J. Magn. Magn. Mater.* **40**, 1(1983).
21. D.L. Mills, *Comments Solid State Phys.* **4**, 28 (1971); *Comments Solid State Phys.* **4**, 95 (1972).
22. D.T. Pierce, R.J. Celotta, J. Unguris, and H.C. Siegmann, *Phys. Rev.B* **26**, 2566 (1982).
23. S.H. Liou and C.L. Chien, *J. Appl. Phys.* **63**, 4240 (1988).
24. See e.g. M.H. Kryder and A.B. Bortz, *Physics Today*, **37**,20 (1984).
25. W.T. Maloney, *IEEE Trans. Magn.* **MAG-17**, 3196 (1981).
26. G. Bate, *J. Appl. Phys.* **52**, 2447 (1981).
27. S.H. Liou, C.L. Chien, *Appl. Phys. Lett.* **52**, 512 (1988).
28. C.L. Chien, S.H. Liou, D. Kofalt, W. Yu, T. Egami, and T.R. McGuire, *Phys. Rev.* **B33**, 3247 (1986).
29. K. Binder and A.P. Young, *Rev. Mod. Phys.* **58**, 801(1986).
30. G.G. Kenning, J.M. Slaughter and J.A. Cowan, *Phys. Rev. Lett.* **59**, 2596 (1987).
31. A. Gavrin, J.R. Childress, C.L. Chien, B. Martinez and M.B. Salamon, *Phys. Rev. Lett.* **64**, 2438 (1990).
32. W.L. McMillan, *Phys. Rev. B* **29**, 4026 (1984).
33. R.P. Singh and S. Chakravarty, *Phys. Rev. Lett.* **57**, 245 (1986).
34. E.g. W.P. Halperin, *Rev. Mod. Phys.* **58**, 533 (1986).
35. M. Hayashi, I. Tamura, Y. Fukano, and S. Kanemaki, *Surface Science*, **106**, 453 (1981).
36. J.R. Childress, C.L. Chien, M.Y. Zhou and Ping Sheng, (to be published).
37. K.M. Unruh, B.M. Patterson, J.R. Beamish and N. Mulders and I. Shah, *J. Appl. Phys.* (to appear).

ULTRAFINE MAGNETIC PARTICLES

G. C. Hadjipanayis, S. Gangopadhyay, L. Yiping

University of Delaware
Department of Physics and Astronomy
Newark, Delaware 19716

C. M. Sorensen and K. J. Klabunde

Kansas State University
Department of Physics
Manhattan, Kansas 66506

I. INTRODUCTION

Fine magnetic particles are scientifically and technologically very important. The particles are of great scientific interest in developing a better understanding of magnetic phenomena. From the technological point of view, they find wide applications in many types of materials including magnetic tapes, ferrofluids, catalysts, medical diagnostics, drug delivery systems, and pigments in paints and ceramics.^{1,2} Magnetic particles are also found in the cells of some animals and in some bacteria which help them to navigate in geomagnetic fields.²

Research on fine magnetic particles started in late 1940's^{3,4} and peaked in the 1950's. One of the milestones of that development was the emergence of domain theory⁵ which led to the concept of single domain particles⁶ and magnetic anisotropy contributions giving rise to permanent magnet behavior⁷ and superparamagnetism.⁸ More recently the potential application of fine magnetic particles in magnetic recording media⁹ has reactivated experimental and theoretical research in these systems. In Japan¹⁰ a five year research and development project on ultrafine magnetic particles (UFM) has been supported by the government to obtain further basic knowledge and technology for utilizing UFM's as a new category of materials. Today fine particles are being used in magnetic recording media in the form of acicular γ -Fe₂O₃, cobalt-modified γ -Fe₂O₃, iron, chromium dioxide, iron nitride, and barium ferrite particles (for perpendicular recording materials). These particles are single domain and have high magnetization, large coercivity, narrow size distribution, good dispersibility and high mechanical strength to ensure a strong output and a low signal noise.

There are several techniques for the preparation of fine particles including chemical reduction^{7,11-14}, thermal¹⁵, spark erosion¹⁶, aerosolization¹⁷, vapor deposition^{9,18,19}

and sputtering²⁰⁻²². Most of these studies so far have been made on transition metal based systems. Elongated Fe and Fe-Co fine particles ($\ell/d > 10$ with $\ell = 30$ nm) with H_c about 1000 Oe have been produced by electrodeposition into mercury.⁷ A higher coercivity (~ 2140 Oe) has been obtained²² in elongated, but coarser Fe particles ($\ell/d \sim 65$, $\ell \sim 130$ nm; produced by reducing goethite (FeOOH) particles with hydrogen gas). Reduction of transition metal ions by NaBH_4 or KBH_4 has been used^{11,12-14} to prepare fine crystalline Fe, Fe-Co, Fe-Co-B and Fe-Ni-B particles having sizes in the range 10-100 nm with $H_c \sim 200$ -1000 Oe and $M_s \sim 100$ -140 emu/g, with the lower values corresponding to amorphous particles. Amorphous Fe-C particles with a size of 8.5 nm have been prepared by thermal decomposition of iron pentacarbonyl.¹⁵ Spark erosion¹⁶ was also used to prepare amorphous Fe(Co)-Si-B particles in the range 5 nm - 25 μ . Very recently, aerosol pyrolysis has been used to prepare fine iron-oxide and barium ferrite particles¹⁷ with interesting magnetic properties. The latter particles have also been produced in glassy matrices.²³ Gas evaporation is the most widely used technique^{9,10} for the production of fine particles with a size range between several nanometers to micrometers. With this technique, narrow size distributions can be achieved,¹⁸ leading to coercivities as high as 1580 Oe and saturation magnetizations up to 200 emu/g²⁴. A similar behavior has also been observed in granular solids where crystalline $\text{Fe}^{20,21}$ and amorphous Fe-Si^{25} fine particles have been embedded in insulating SiO_2 and BN matrices by sputtering. In Fe-SiO_2 the room temperature coercivity was 1500 Oe reaching a value beyond 2500 Oe upon cooling to 4.2 K.²⁰ Sputtering onto sputter-etched polymer substrates has also been used²² to prepare crystalline Fe, Fe-Co and amorphous Fe-B and Co-B particles.

The magnetic properties of fine particle prepared by different techniques have been found to be different from the bulk. In ultrafine indium particles quantum size effects were found to affect the spin paramagnetism of small particles leading to a saturating magnetic moment at relatively low fields.²⁶ The reports are controversial on the size dependence of magnetization. Luborsky et al²⁷ claimed that M_s of ultrafine Fe particles prepared by electrodeposition was invariant with size even for particles 1.5 nm in size, where 50% of the atoms are on the surface, indicating a complete ferromagnetic coupling. However, for most of the Fe-based particles studied, a thin oxide coating has been found to protect the metallic core from further oxidation. In these particles Tamura et al²⁸ found the hyperfine field coming from the interface Fe atoms to be about 8% larger than the value of bulk Fe, indicating a larger moment for the Fe interface atoms. A similar observation has been made by Shinjo et al²⁹ in Fe thin films. The possible presence of a nonmagnetic (dead) layer in the surface layers remains a controversial issue.^{30,31} Berkowitz et al³² postulated the existence of a non-magnetic layer of 0.6 nm to explain the dependence of M_s on particle size in $\gamma\text{-Fe}_2\text{O}_3$ particles. However, as pointed out by Morrish et al³³ and Coey et al³⁴ the surface spin structure of fine particles is canted and this can account for their lower magnetization. The spontaneous magnetization and Curie temperature of $\text{Fe}_{75}\text{Si}_{15}\text{B}_{10}$ alloys have been found to decrease monotonically from ribbons to particles with decreasing particle size.³⁵ Berkowitz and Walter³⁵ attributed this to differences in short range order with an increased number of metalloid atoms around the Fe sites in fine particles.

In the past three years we have developed and refined some techniques for preparation of fine magnetic particles in the size range 2-500 nm with reasonable particle size control. Extensive characterization studies have yielded some fundamental knowledge of magnetic behavior for such small particles, and have uncovered some novel, perhaps unexpected magnetic properties.

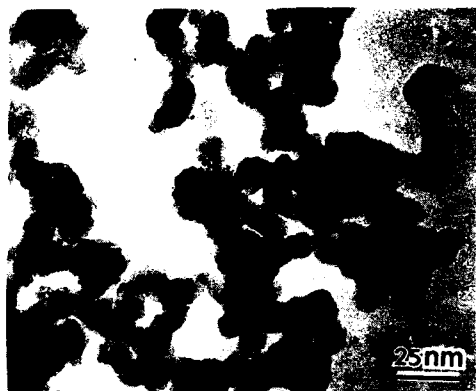


Figure 1. Bright field micrograph showing the morphology of Fe particles.

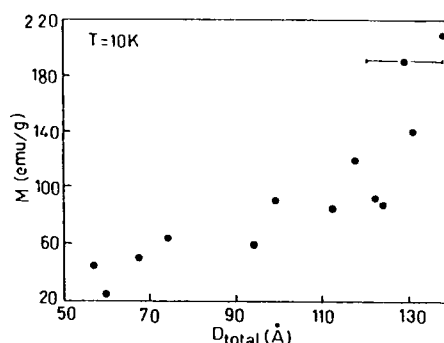


Figure 2. Magnetization as a function of particle size.

Throughout this work we have investigated two broad classes of materials: (1) Theories³⁷ and experiments have shown that the fluctuation of surface moments are larger than those of the interior so that B of the surface atoms is about 2-3.5 times larger than the interior. The problem, however, might be more difficult because of the possible lattice softening of the small particles³⁸ (and therefore softening of spin waves) and the geometrical size effect limiting the value of the spin wave wavelength.²¹ Additional studies are needed to clarify this issue.

The smaller particles showed a superparamagnetic behavior with a blocking temperature, T_B , below 300 K. Above T_B no hysteresis was observed (Fig. 3a). The increase in H_c with particle size at 300 K is due to thermal effects observed in particles with size below the single domain particle size (Fig. 3a). At 10 K, thermal effects are negligible and a different behavior is observed; H_c decreases from 3400 Oe to ~ 1500 Oe as the particle size is increased from 25 to 100 Å (Fig. 3b). The smallest particles had a coercivity of 3.4 kOe at 10 K, which decreased down to negligible values at 150 K, whereas the magnetization did not change drastically with temperature. At room temperature the maximum H_c was 900 Oe corresponding to a M_s of 150 emu/g and a corrected particle diameter of 11 nm. The strong temperature dependence of coercivity (Fig. 3c) is discussed later using Mössbauer spectroscopy.

The Mössbauer spectrum of an Fe sample with core diameter of 96 Å is shown in Fig. 4. Two magnetic hyperfine splitting patterns were found at a temperature of 85 K and below, which were attributed to α -Fe and a mixture of Fe_3O_4 and $\gamma\text{-Fe}_2\text{O}_3$. Above 85 K a broad absorption band due to Fe-oxide is superimposed on the α -Fe spectrum. The expected quadrupole splitting due to superparamagnetic particles was absent. Several explanations have been proposed to explain this behavior. Haneda et al³⁸ and Tamura et al²⁸ explained this broad absorption by assuming the existence of an asymmetrical uniaxial anisotropy in each Fe-oxide grains because of the presence of an unidirectional anisotropy due to the interaction with the metallic core. Because of this, the hyperfine field does not vanish even in the superparamagnetic state. The broad absorption band is explained by the distribution in the average hyperfine field because of the distribution in particle size. For

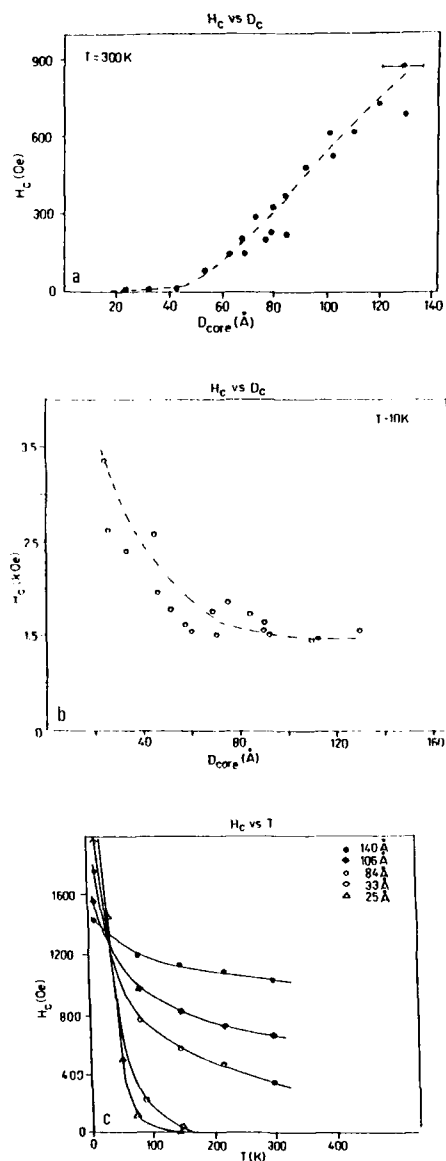


Figure 3. (a) Dependence of coercivity on particle size at $T = 300$ K. (b) Decrease in coercivity with increase in particle size at $T = 10$ K for Fe particles. (c) Temperature dependence of coercivity in Fe particles.

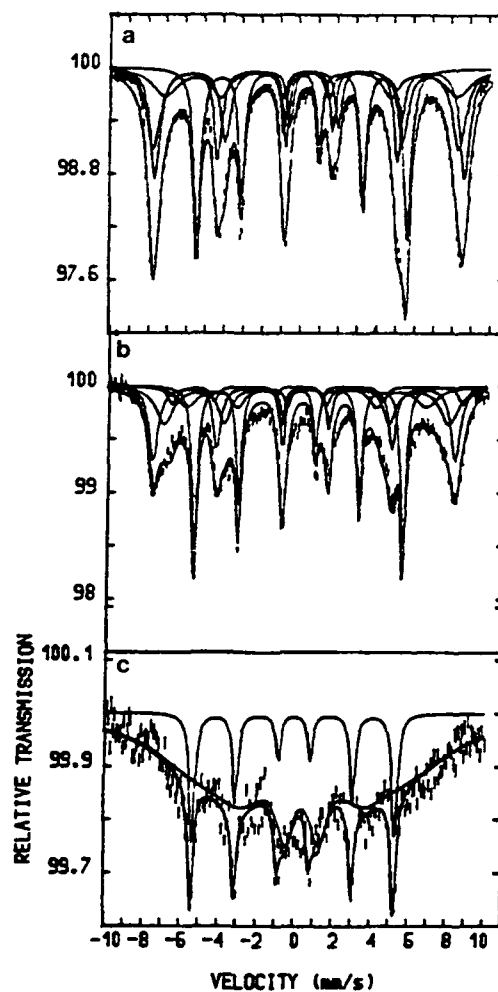


Figure 4. Mössbauer spectra in Fe particles with a size of 96 Å, (a) $T = 10$ K, (b) $T = 85$ K, (c) $T = 300$ K.

Small metallic particles. In this work a critical feature with which we have spent considerable effort has been to develop chemical means of protection from oxidation. Without such protection small metallic particles are doomed to complete oxidation during study and/or use. (2) Small metal boride and oxide particles. In this work, in contrast to metallic particles, the challenge has been to develop means of obtaining desired particle sizes, morphologies, and chemical compositions.

So far our work has been very successful, both scientifically and technologically. We managed to produce fine Fe-based particles with high coercivities and unique properties which in most cases cannot be explained by existing models. In this article we will focus on the techniques of vapor deposition, reduction of metal ions and aerosolization.

II. VAPOR DEPOSITION TECHNIQUES

A. Fe-Smoke

In the evaporation-deposition technique, the deposition metal is vaporized in the presence of an inert gas. The metal vapors undergo collisions with the inert gas atoms resulting in vapor cooling, which causes a decrease in its mean free path leading to particle nucleation. Thereafter occurs the growth process which results in coagulation of the particles to form agglomerates which are then collected on a cold Cu substrate. Gas pressure below 10 torr results in the formation of fine particles with sizes of a few hundred angstroms.

We have studied in some detail the properties of fine Fe, Co and Ni particles prepared by evaporation in an Ar atmosphere at pressures in the range of 0.5 to 8.0 Torr. After deposition, the samples were subjected to a few hours soak in a diluted air-argon mixture to passivate their surface. The specimen was then removed to the atmosphere, weighed, and immobilized and sealed from further contact with the atmosphere by mixing with molten wax in a quartz capsule. In this paper we will concentrate only on Fe particles.

X-ray and selected area diffraction patterns (SAD) showed mostly the presence of α -Fe lines and a few Fe_2O_3 lines with the oxide lines being very diffuse.³ The particle size measured from dark field micrographs was smaller than that of bright field indicating the presence of an oxide shell coating the metallic Fe core. This was further observed in bright field micrographs where rings of different contrast are seen around the core particles. Clusters of particles appeared in the electron micrographs when the deposits were sufficiently thick. No tendency for long chain formation was observed (Fig. 1). Most of the particles had nearly spherical shape with a total diameter in the range 5 - 20 nm. The core diameter range was 2.5-17 nm. This range falls in the single domain regime which for Fe is about 15 nm.⁶

The highest value of M_s was 200 emu/g for particles with an average size of 14 nm; this is 90% of the bulk value (220 emu/g). It was observed that as the particle size increased the apparent magnetization also increased (Fig. 2) because the oxide coating of constant thickness constituted a smaller fraction of the volume of larger particles. The temperature dependence of magnetization shows a common trend in all fine particles. For Fe fine particles,³⁶ the magnetization can be fitted to the $BT^{3/2}$ law³⁹ predicted by the spin wave theory but with a value of the spin wave constant B much higher than in bulk Fe ($B_{Fe} \sim 3.3 \times 10^{-6} \text{ K}^{2/3}$). Xiao and Chien²¹ found a similar behavior in Fe granular solids with $B \sim 4.5 \times 10^{-5} \text{ K}^{2/3}$.

magnetic above 85 K, the sample as a whole shows an H_c of 507 Oe even at room temperature which increases to 1613 Oe at cryogenic temperatures where both the shell and the core show magnetic hyperfine splitting. When the oxide shell around the Fe core becomes superparamagnetic above 85 K, it affects the magnetization of Fe-core significantly through exchange interactions. In the smaller particles where the core is small enough, the fluctuation of the moment in the superparamagnetic oxide shell succeeds in making the whole particle soft. In the bigger particles, where the oxide-to-Fe ratio is much lower, the thermal fluctuations of the oxide moment are not strong enough to make the magnetic core magnetically soft and hence the coercivity is much higher at room temperature.

The coercivity of these Fe particles can not be explained by any of the existing models of magnetic hysteresis assuming the values of M_s and K for bulk Fe. These particles behave like they have a large effective anisotropy an order of magnitude higher than bulk Fe. We believe that the magnetic hysteresis properties are controlled by the nature and magnetic state of the surface layer and its interaction with the metallic Fe core.

III. REDUCTION OF METAL IONS BY NaBH_4

Ultrafine transition metal boron particles were synthesized by reduction of metal salts with NaBH_4 in aqueous solution.^{13,14,40} Amorphous high boron content powders are usually produced by dropping the NaBH_4 solution into the FeCl_3 solution. However, if the two solutions are mixed in a Y-junction, a low B concentration powder is obtained which is also crystalline. The particle size can be varied by changing the concentration of solvent and solution. Normally a low concentration solution leads to larger particles. Also the use of ethanol instead of water leads to smaller particles because of the faster reaction rate.

The systems we have studied include Fe-B, Fe-Ni-B, Fe-Co-B and Co-B particles. First we studied the magnetic properties of Fe-B particles, then picked a particular Fe-B sample and gradually replaced Fe with Ni or Co to observe how the magnetic properties were changed. The magnetic and structural properties of these particles are briefly discussed below.

A. Fe-B particles

X-ray diffraction (XRD) patterns showed that the particles were amorphous for boron concentrations more than 20 at.%, otherwise they were crystalline. TEM showed that particles formed chainlike structures and their average monomer size ranged from 30 to 50 nm. H_c increased with decreasing particle size (Fig. 5). For a given size, H_c increased with increasing boron concentration, reached a maximum of more than 1000 Oe near 15 at.% B, and then decreased. M_s displayed the opposite behavior with a minimum value of about 60 emu/g. We believe this is due to the surface oxidation of these particles. As size decreases, the surface to volume ratio increases hence oxidation increases to yield smaller M_s . The oxidized layer enhances the effective surface anisotropy which yields larger H_c . At higher B concentration the particles became amorphous and this change in morphology caused H_c to drop while M_s increased.

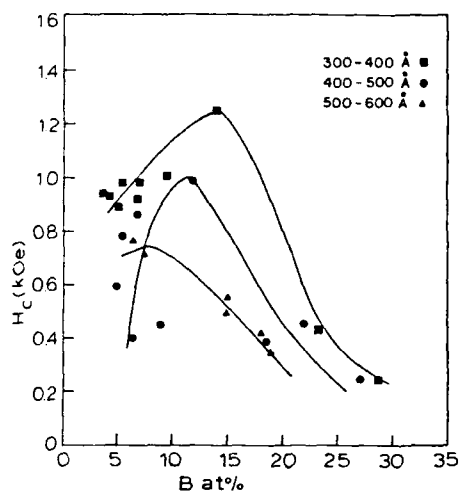


Figure 5. Coercivity of Fe-B particles versus the boron content.

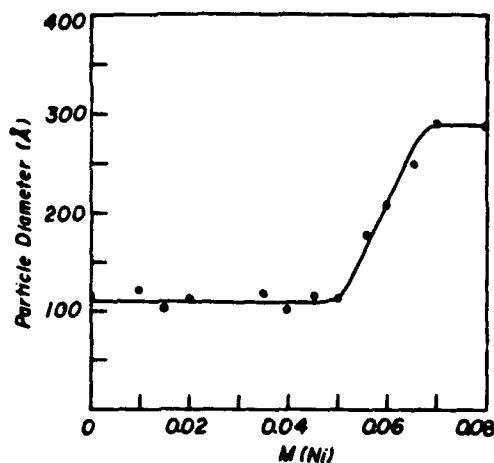


Figure 6. Particle size and boron content of Fe-Ni-B particles as a function of Ni molarity.

B. Fe-Ni-B particles

For this study¹³ we have chosen a Fe-B sample with Fe/B = 20 (at) which showed the largest H_c (1050 Oe). We then replaced Fe with Ni. Unfortunately, the boron concentration in the particles also changed (Fig. 6). Regardless of this, we studied the magnetic properties as a function of nickel salt molarity, $M(\text{Ni})$, of the solutions used to make the particles. XRD patterns showed that the particles became amorphous when $M(\text{Ni}) \geq 0.05$ M and at the same time the particle size increased from a constant value of 10 nm to 30 nm for $M(\text{Ni}) > 0.07$ M. H_c at 10 K showed an initial increase, reached a maximum of about 1550 Oe for $M(\text{Ni}) = 0.015$ M, then decreased for higher $M(\text{Ni})$ (Fig. 7). We concluded that a small amount of Ni addition into the Fe-B system increased the magnetic anisotropy and that caused H_c to increase. M_s data showed a monotonic decrease for the range $M(\text{Ni}) = 0$ to 0.07 M. After that, it sharply dropped to almost zero. At higher boron concentrations Ni-B becomes nonmagnetic.

C. Fe-Co-B

Fine Fe-Co-B particles were produced by a two step procedure. First, a 0.8M NaBH_4 aqueous solution was added dropwise to a 0.4M mixed FeCl_3 and CoCl_2 aqueous solution while the pH value of the solution was kept at 8. The black precipitates were rinsed with distilled water and acetone, and dried in an Ar atmosphere chamber.

All the as-made powders were amorphous except those with boron content lower than 10 at%. With varying Fe:Co ratio, the amount of boron was found to vary in the range 5-30 at%. The dependence of Co and B content and particle size on the Fe:Co ratio is shown in Fig. 8. The particle size obtained was in the range of 20-30 nm. The saturation magnetization of as-made powders was relatively low, with a

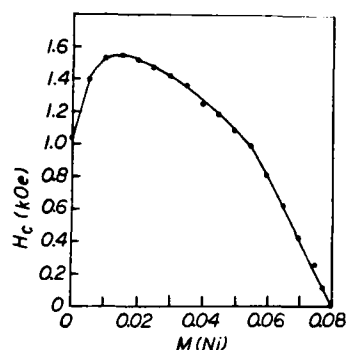


Figure 7. Coercivity as a function of Ni concentration.

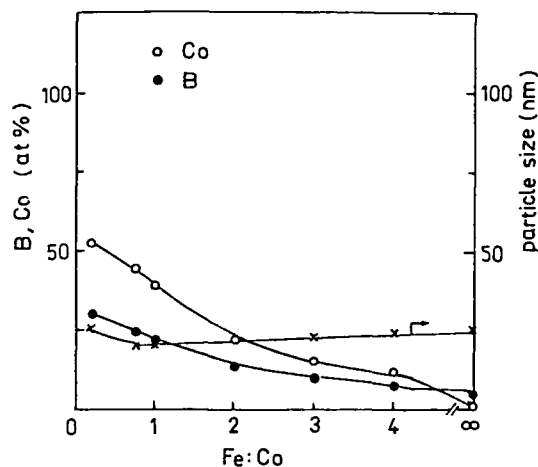


Figure 8. Dependence of chemical composition and particle size on Fe:Co ratio in Fe-Co-B particles.

maximum value of about 90 emu/g. A coercivity of about 1100 Oe at 300 K was found in an as-made crystalline sample with boron content of about 10 at%.

The magnetic properties of amorphous and crystallized isolated particles as a function of Fe:Co ratio are shown in Fig. 9. The maximum saturation magnetization obtained is 160 emu/g for a sample made with Fe:Co=4 which corresponds to 10 at% B. This is much different from bulk Fe-Co alloys where the maximum was obtained at 30 at% Co,⁹ but similar to the Nd-Fe(Co)-B alloys where the maximum is about 12 at% Co.⁴¹ The saturation magnetization of any composition corresponds to 75-80% of that of bulk iron-cobalt alloys. The other 20% is probably an oxide, but none of the oxide peaks were detected by X-ray diffraction may be because they are too broad and difused. The maximum coercivities obtained for the isolated particles were 1655 Oe at 10 K in a 25 at% Co powder, and 1940 Oe at 300 K in a 35 at% Co sample. The maximum coercivity is shifted to Co-rich powders when the temperature is increased from 10 K to 300 K.

The coercivity as a function of temperature for both annealed isolated and pressed particles is shown in Fig. 10. An anomalous behavior is observed with the temperature coefficient of coercivity depending on the Fe:Co ratio. When the powders contain only one transition metal, such as Fe-B, CoB¹⁴ the temperature coefficient of coercivity is negative, with the coercivity at low temperatures being greater than that at higher temperatures. However, when the powders contain both Fe and Co, regardless of composition, the coefficient gradually changes to positive as shown in Fig. 10. The temperature coefficient of coercivity in pressed powders is always found to be negative with different ratio of Fe:Co similar to that for most bulk magnets.⁹

In summary, these systems display a wide variety of phenomena. Oxide layers seem to be more important in the iron systems. Co and perhaps Ni have poor magnetic properties until annealed to stoichiometric or crystalline phases. Most likely two different sources of anisotropy and hence H_c are involved. Future work

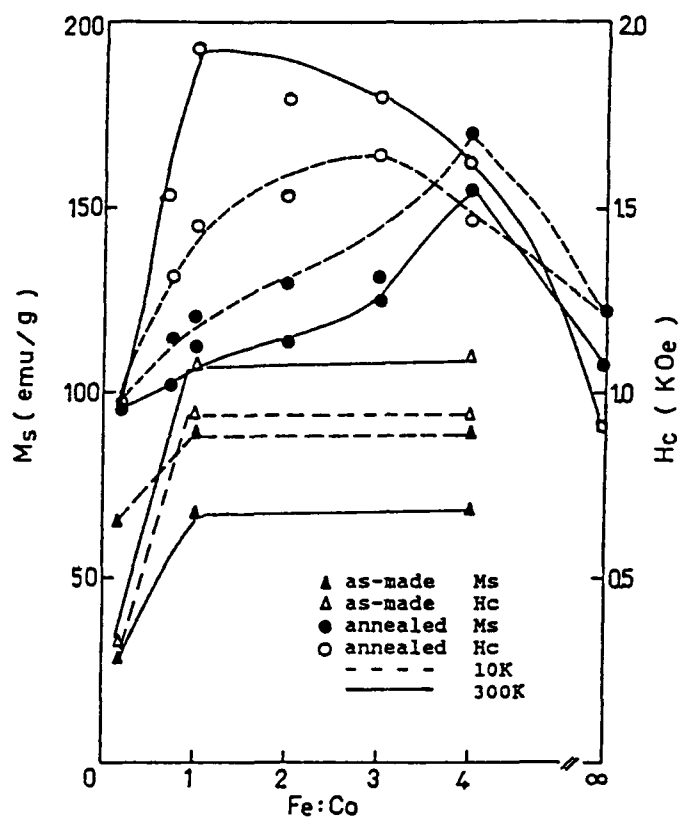


Figure 9. Magnetic properties of amorphous and crystallized Fe-Co-B particles.

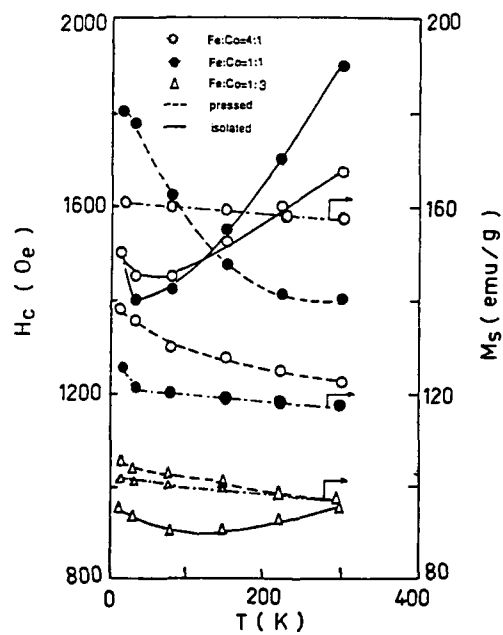


Figure 10. Coercivity of annealed Fe-Co-B particles as a function of temperature.

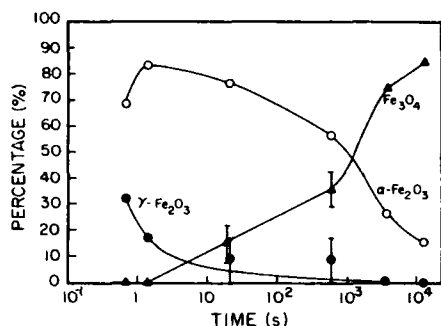


Figure 11. Phase formation in aerosol sprayed iron oxide particles.

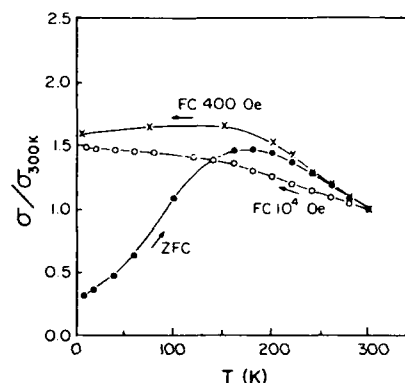


Figure 12. Thermomagnetic data in as-made barium ferrite particles showing a spin-glass type behavior.

will be concerned with comparing these systems further and controlling the surface chemical features.

IV. AEROSOL SPRAY PYROLYSIS

By aerosolizing, drying and baking aqueous solutions of pure and mixed metal salts, we can create nearly any metal oxide or mixed metal oxide particles conceivable.^{42,43} An aerosol generator was used¹⁷ to synthesize the fine particles from aqueous solutions of pure and mixed metal salts. The solution was fed to a constant output atomizer (Model 3075, TSI, St. Paul, MN) operated by a nitrogen gas flow of 2.6L/min at a pressure of 35 psi. The liquid drop aerosol stream passed through a diffusion dryer to remove water and then was heated to 800°C as it passed through a tube furnace. The aerosol particles were collected on cover glasses by thermophoresis after they passed through the tube furnace. Powder samples were obtained by scraping the particles off the cover glasses. Further heat treatment was also made in a nitrogen environment at 800°C.

A. Iron Oxides

Iron oxide particles with median diameter about 100 nm were created by spray pyrolysis of $\text{Fe}_2(\text{SO}_4)_3$ solutions.^{44,17} The phases produced could be changed from γ to α - Fe_2O_3 to Fe_3O_4 by heating in either air or N_2 (Fig. 11). The magnetic properties of the particles directly followed from the phases present and their bulk properties. This project developed our technique and demonstrated the importance of the diffusion drier, without which the particles were hollow spheres.

B. $\text{BaO} \cdot 6\text{Fe}_2\text{O}_3$

Barium ferrite was created from an aqueous solution of Ba and Fe^{3+} nitrates. A novel phase was found in the as-received samples. These spherical particles were

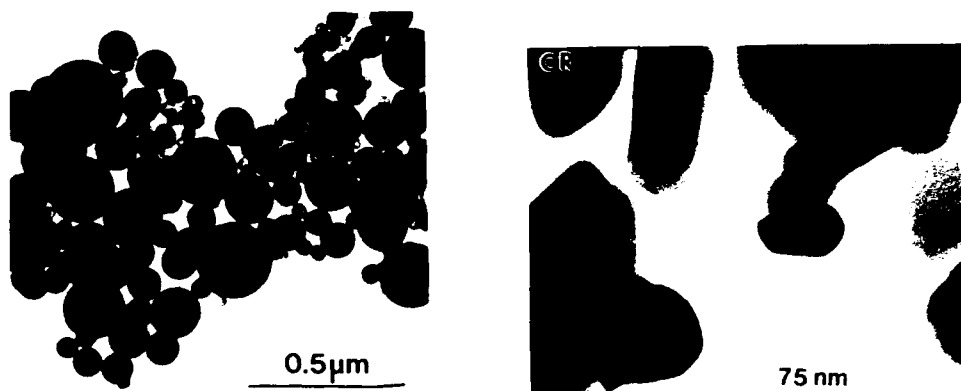


Figure 13. Structure morphology of amorphous and crystallized barium ferrite particles.

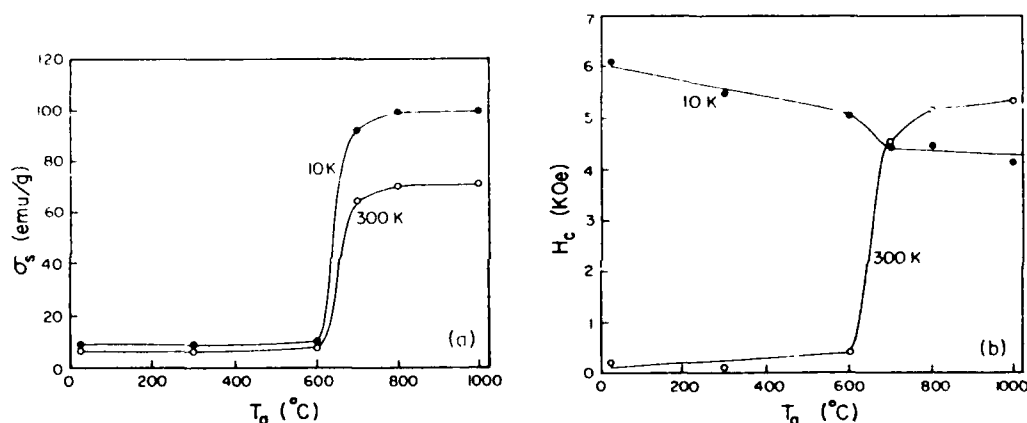


Figure 14. Magnetic properties of crystallized barium ferrite particles.

amorphous with a diameter about 100 nm and displayed a spin glass behavior (Fig. 12). Upon annealing at 800°C, the sample became crystalline, with hexagonal morphology (Fig. 13) and the usual bulk magnetic properties of barium ferrite (Fig. 14). This work demonstrated two important aspects of this spray pyrolysis techniques: (1) the ability to create mixed oxides using short times and low temperatures compared to standard, time consuming milling-sintering techniques; and (2) the small size allows for quick quenching into metastable states which in this case led to an heretofore unknown phase.

CONCLUSIONS AND FUTURE DIRECTION

Our studies so far have been very successful. We have developed and refined several techniques for preparation of fine magnetic particles with a size in the range of 2-500 nm depending on the procedure. Extensive characterization studies have

yielded some fundamental knowledge of magnetic behavior for such small particles and have uncovered some novel, perhaps unexpected properties. We have produced magnetically hard Fe and Fe-B particles which possess an anisotropy and coercivity one to two orders of magnitude higher than in bulk. Most of the particles made are coated by a surface layer oxide which is very important technologically and theoretically. The magnetic state of the surface layer and its interaction with the metallic core are found to affect the magnetic properties of the particle significantly.

There is still much to be learned about magnetic effects in small particles. The nature and magnetic state of surface layers and their effect on the particles' anisotropy and magnetic hysteresis need to be clarified. There is also a great need for systematic studies in order to understand better the magnetic hysteresis behavior. In the past the oversimplified theories of single domain particle and fanning have been used to explain the coercivities of particles even though microstructure and magnetic properties did not support the idea. The hysteresis behavior of these particles is rather complex and can not be explained by existing models. Thus, a new approach to these problems is needed.

ACKNOWLEDGEMENTS

This work has been supported by NSF-CHE-9013930. We are grateful to Dr. Kostikas and his colleagues at Demokritos in Athens, Greece for the Mössbauer measurements.

REFERENCES

1. E. Matijevic, MRS Bulletin, Volume XIV, 19 (1989).
2. M. Ozaki, MRS Bulletin, Volume XIV, 35 (1989).
3. L. Neel, Compt. Rend. 221, 1550 (1947).
4. R. Steinitz, Powder Met. Bull. 3, 124 (1948).
5. C. Kittel, Revs. Modern Phys. 21, 541 (1949).
6. A. H. Morrish, "The Physical Principles of Magnetism", John Wiley, New York (1965).
7. F. E. Luborsky, J. Appl. Phys. 32, 1715 (1961).
8. C. B. Bean and J. D. Livingston, J. Appl. Phys., 30, 1205 (1959).
9. A. Tazaki, S. Tomiyana, S. Eto, J. J. Appl. Phys. 4, 707 (1965).
10. C. Hayashi, J. Vac. Sci. Technol. A5, 1375 (1987).
11. T. Miyahara and K. Wawakauri, IEEE Trans. Magn. MAG-23, 2877 (1987).
12. I. Dragieva, G. Gavrilov, D. Buchkovand, M. Slavecheva, J. Less Comm. Metals 67, 375 (1979).
13. S. G. Kim, J. R. Brock, J. Coll. Interf. Sci. 116, 431 (1987).

14. S. Nafis, G. C. Hadjipanayis, C. M. Sorensen and K. J. Klabunde, IEEE Trans. Mag., 25, 3641 (1989); and to appear in J. Appl. Physics.; L. Yiping, G. C. Hadjipanayis, C. M. Sorensen and K. J. Klabunde, J. Magn. Magn. Mat., 79, 321 (1989).
15. J. van Wonerghem, S. Morup, S. W. Charles, S. Welles and J. Villadsen, Phys. Rev. Lett. 55, 410 (1985).
16. A. E. Berkowitz, J. L. Walter and K. F. Wall, Phys. Rev. Lett. 49, 1481.
17. a. Z. X. Tang, S. Nafis, C. M. Sorensen, G. C. Hadjipanayis and K. J. Klabunde, J. Magn. Magn. Mat., 80, 285 (1989). b. Z. X. Tang, S. Nafis, C. M. Sorensen, G. C. Hadjipanayis and K. J. Klabunde, IEEE Trans. Magn., 25, 4236 (1989).
18. C. G. Granqvist and R. A. Buhrman, J. Appl. Phys. 47, 2200 (1976).
19. A. Tasaki, M. Oda, S. Kashu and C. Hayashi, IEEE Trans. Mag. MAG-underline15, 1540 (1979).
20. G. Xiao, C. L. Chien, J. Appl. Phys., 61, 3308 (1987).
21. G. Xiao, C. L. Chien, J. Appl. Phys., 51, 1280 (1987).
22. S. Ohnuma, Y. Nakanouchi, C. D. Graham and T. Masumoto, IEEE Trans. Magn. MAS-21, 2038 (1985); AMG-22, 1098 (1986). A. L. Oppergard, F. J. Darnell and H. C. Miller, J. Appl. Phys. 32, 1845 (1961).
23. L. C. Nanna, S. Aarj, E. E. Anderson, APS Bulletin, 31, 976 (1989).
24. Y. W. Du, J. Wu, H. Lu, T. Wang, Z. Q. Hu, H. Tang and J. C. Walker, J. Appl. Phys. 61, 3314 (1987).
25. R. L. Holtz, A. S. Edelstein, C. R. Gossett, preprint.
26. F. Meier and P. Wyder, Phys. Rev. Lett., 30, 181 (1973).
27. F. E. Luborsky and P. E. Lawrence, J. Appl. Phys., 32, 2315 (1961).
28. I. Tamura and M. Hayashi, Surf. Sci., 146, 501 (1984).
29. T. Shinjo, T. Shigematsu, N. Hosaito, T. Iwasaki, T. Takai, Japan J. Appl. Phys. 21, L220 (1982).
30. A. S. Edelstein, B. N. Das, R. L. Holtz, N. C. Koon, M. Rubinstein, S. A. Wolf and K. E. Kihlstrom, J. Appl. Phys. 61, 3320 (1987).
31. A. Tasaki, M. Takao and H. Tokunaga, J. J. Appl. Phys. 13, 271 (1974).
32. A. E. Berkowitz, W. J. Schuele and P. J. Flanders, J. Appl. Phys. 39, 1261 (6C6), 301 (1987).
33. A. H. Morrish, K. Haneda and P. J. Schiurer, J. de Physique, C6, 301 (1976).
34. J. M. D. Coey and D. Khalafella, Phys. Stat. Sol. (A) 11, 229 (1972).

35. A. E. Berkowitz and J. L. Walter, *Mat. Sci. Eng.* 55, 275 (1982).
36. S. Gangopadhyay, E. B. Dale, G. C. Hadjipanayis, C. M. Sorensen and K. J. Klabunde (in preparation).
37. D. L. Mills, *Comm. Solid State Phys.* 4, 28 (1971).
38. K. Haneda and A. H. Morrish, *Nature*, 282, 186 (1979).
39. C. Kittel, "Introduction to Solid State Physics," John Wiley, New York (1966).
40. S. Linderoth, S. Morup and M. D. Bentzon, *J. Magn. Mang. Mat.* 83, 457 (1990).
41. Y. Maisuura, S. Hirose et al, *Appl. Phys. Lett.* 46, 308 (1985).
42. T. T. Kodas, *Adv. Mat.* 180 (1989).
43. M. Ramamurthi and K. Leong, *J. Aerosol. Sci.* 18, 175 (1987).
44. S. Nafis, Z. X. Tang, E. B. Dale, C. M. Sorensen, G. C. Hadjipanayis and K. J. Klabunde, *J. Appl. Phys.* 64, 5835 (1988).

MAGNETIC NANOMETER SYSTEMS AND MÖSSBAUER SPECTROSCOPY

A. H. Morrish and X. Z. Zhou

Department of Physics
University of Manitoba
Winnipeg, MB R3T 2N2, Canada

1. INTRODUCTION

At the one extreme, atoms and molecules have been investigated a very long time and a vast amount of knowledge has been garnered using sophisticated experimental and theoretical techniques. At the other extreme, condensed matter has been intensively studied over the past few decades and much is now known about its properties. The phase transition between these two extremes is much less well known; conditions appear to be ripe for a widespread surge of interest in nanometer systems of atoms and molecules.

A nanometer system may be defined as matter that has one, two, or three dimensions severely restricted in size. To date, most attention has focused on thin films (one restricted dimension) or on ultrafine particles (three restricted dimensions); however, filamentary or wire structures (two restricted dimensions) no doubt will become more topical in the future.

All nanometer systems possess, of course, diamagnetism and a sizeable fraction also display paramagnetism. A much smaller class are said to be magnetic, a term that implies strongly-coupled magnetic dipoles are present; examples are materials exhibiting ferromagnetism, ferrimagnetism, and antiferromagnetism. Magnetic nanometer systems, by owning an extra accessible property, can be probed by additional methods. One of the most important of these is Mössbauer spectroscopy; this is the subject matter of this chapter.

Since the discovery of the Mössbauer effect in 1958, several experimental arrangements have been developed. By far the commonest used set up is a transmission geometry (called Transmission Mössbauer Spectroscopy, or TMS). Besides offering simplicity, TMS often provides all the data required. In addition, various scattering techniques, including polarized Mössbauer spectroscopy, have been successfully demonstrated (for a review, see, for example, Wagner¹). Although more information is obtained, frequently the price is increased experimental difficulties, lengthy data-collection times, and more complex analyses. As a consequence, scattering methods have not found widespread adoption. An exception is Conversion-Electron Mössbauer Spectroscopy,

or CEMS. Only TMS and CEMS will be considered in this article. Both some advantages and limitations of these techniques will be discussed by considering several examples of one and three dimensional magnetic nanometer systems.

2. MAGNETIC ULTRAFINE PARTICLES

Particles less than 1.0 nm in size are probably better called clusters; after all many atoms and ions are about 0.1 nm in diameter and some are significantly larger. The number of atoms in a cluster can be determined by some mass spectroscopy method. Some clusters may be present in a host, for example dilute alloys; whether or not such clusters actually occur would seem to depend on the preparation conditions. Powders generally consist of a range of particle sizes; some may lie in the subnanometer region. Some individual particles may have an outer layer of subnanometer crystallites, for instance, metal particles passivated by an oxide. Although, some analyses of Mössbauer spectra have considered that clusters may be present, clear cut evidence is lacking. Magnetic subnanometer particles have the potential to be objects of future investigations.

The lower limit for a nanometer particle then is in the vicinity of 1 nm; the upper limit is much more contentious. An average diameter of 1000 nm (1 μ m) enters the micron-size region and would seem to be too large. Perhaps a figure around 100 nm is acceptable. There is already a substantial literature on particles in the micron range. Even though these particles are usually in their bulk crystalline form, a number of interesting new properties, including surface effects, have been observed.

A number of methods are available to make nanometer particles and clusters: some are new technologies, others are not so new. Some of these ultrafine particles may be in non-equilibrium crystalline, quasi-crystalline, icosahedral and amorphous phases. As such they may possess physical properties that differ greatly from those of bulk material and that may lead to new applications. These prospects are responsible for the current excitement and activity in nanometer particles.

A few ways to produce nanometer particles will now be described briefly in order to provide some flavor of the principles involved; the listing is incomplete. Evaporation into an inert gas (argon, helium, etc) at a reduced pressure has produced metallic particles that resist clustering but form a lace-like pattern.² Atomic agglomeration has also been achieved in cold liquids, for example after evaporation nanometer iron particles have been prepared in cold pentane.³ Fine metallic particles have been embedded in glass (SiO_2) by sputtering.⁴ Direct formation by hydrothermal synthesis starting with a mixture of nitrate salts and aqueous NaOH has been used to make barium ferrite particles.⁵ Chemical coprecipitation has long been a favorite technique; an alkaline solution is added to a salt of the selected ions and the suspension formed is dried and heated.⁶ Another approach is a three-component micro-emulsion technique that consists of two immiscible liquids, water and a hydrocarbon, together with a surfactant that reduces the interfacial tension. Nanometer Fe_2O_3 particles were made by adding $\text{Fe}(\text{NO}_3)_3$ to the water, using 2-ethyl hexanol as the hydrocarbon, and sorbitane mono-oleate as the surfactant. The mixture was emulsified by ultrasonic agitation and then $\text{Fe}(\text{OH})_3$ was precipitated by adding NH_4OH . The dried precipitate was calcined at $\sim 250^\circ\text{C}$; particles as small as 5 nm were made by changing the iron nitrate concentration.⁷

Another avenue is via metal-organic complexes. Their hydrolysis has produced

ultrafine $\text{SrFe}_{12}\text{O}_{19}$ particles.⁸ A resin method for hexaferrite particles is promising. First ammonia is added to an aqueous solution of iron nitrate and the precipitate, after washing, is dissolved in citric acid. Transition metal and alkaline earth oxides are next added to form the metal-organic (citrate) salt. Then ethylene glycol is added and the solution is slowly evaporated until a viscous residual forms that solidifies after heating at $\sim 300^\circ\text{C}$. The organic matter is ignited by heating at 450°C for a few hours; the residual provides the hexaferrites.⁹

In a melting process, sometimes called glass crystallization, a molten mixture of oxides, for example, B_2O_3 , BaO , and Fe_2O_3 , is quenched between brass rollers spaced $100\ \mu\text{m}$ apart so rapidly that the glassy state is retained. Then by heating $\sim 600^\circ\text{C}$ Ba ferrite crystals are precipitated; the particle size, controlled by changing the heat treatment, has a narrow size distribution.¹⁰

Lasers have been brought into play. A CO_2 TEA (transversely excited atmospheric) laser has induced dielectric breakdown of carbonyl vapors; nanometer particles then form.¹¹ Also, metal substrates inside the throat of a high-pressure nozzle have been vaporized by pulsed lasers to produce metallic clusters.¹²

The list could go on and on. The common thread in all these methods is first the creation of an intimate mixture of the chosen atomic or molecular species and second the induction of the phase transition to the nanometer particles at as low a temperature as feasible.

There is, of course, quite a different approach to the production of small particles, viz the grinding and crushing of bulk material. This is indeed the process often used to make the particles of ferrofluids or of magnetic inks. However, the particle size is usually larger than $10\ \text{nm}$. Moreover, the particles are irregular in shape and possess strains and imperfections; to some degree these conditions can be alleviated by a suitable heat treatment.

3. TRANSMISSION MÖSSBAUER SPECTROSCOPY

Many experimental techniques can and should be used to investigate ultrafine particles, including x-ray, electron, and neutron diffraction and various kinds of magnetic measurements. Mössbauer spectroscopy provides data that may just confirm or complement those obtained by other methods. Sometimes however the Mössbauer information is unique; it is especially powerful for the study of magnetic nanometer particles.

The most convenient experimental arrangement is Transmission Mössbauer Spectroscopy, or TMS. To obtain a Mössbauer spectrum the γ -rays must be emitted or absorbed without loss of energy by the recoil of the nucleus; these events are called the recoil-free (or recoilless) fraction. This process is possible in a solid because there is a certain probability that no phonons will be excited or absorbed when a γ -ray is emitted or absorbed by a nucleus. The recoilless fraction depends on the binding energy (or Debye temperature) of the solid, the energy of the γ -ray, the temperature, and the mass of the solid.

In a typical TMS setup, a radioactive source that emits a monoenergetic γ -ray is chosen. Identical nuclei in an absorber may have the degeneracy in their energy

levels lifted by hyperfine magnetic field and quadrupole interactions. The energy of the emitted γ -rays can be tuned to match those of the absorbing nuclei by imparting a velocity to the source (Doppler modulation). A Mössbauer spectrum then consists of the number of γ -rays detected in a counter plotted against the velocity of the source. Absorption lines are then observed for those velocities at which recoilless resonant excitations have taken place.

Of the many nucleides that can be used for the Mössbauer effect, several are of interest for magnetic materials. These include the transition elements ^{61}Ni , ^{151}Eu , ^{155}Gd , ^{161}Dy , and ^{166}Eu and even some non-transition elements such as ^{119}Sn , ^{121}Sb , and ^{125}Te . There are often experimental difficulties, including short half-lives, small recoilless fractions that may require cooling to liquid-helium temperatures, and, especially for the non-transition elements, small hyperfine magnetic field splittings. By far the most popular and easiest isotope to use is ^{57}Fe , which descends from its parent, ^{57}Co , by K-capture. All the examples to be given in this chapter are for the ^{57}Fe isotope.

The roles of source and absorber can of course be interchanged; this arrangement is called emission Mössbauer spectroscopy. It is particularly useful for ultrafine particles in surface studies. For example, the nature of the surface or epitaxial deposition of cobalt on $\gamma\text{-Fe}_2\text{O}_3$ ¹³ and Fe_3O_4 (magnetite)¹⁴ particles have been investigated by this technique. It is also possible to replace a radioactive source by synchrotron radiation, a procedure that may find greatly increased use for high-resolution experiments in the future.

Today, most ^{57}Fe sources are ^{57}Co diffused into a rhodium foil (the host). The 14.4 keV Mössbauer γ -ray has a relatively narrow linewidth and remains monoenergetic (unsplit) down to liquid helium temperatures. Further, relatively strong sources ~ 100 mCi can be made that lie within an area ~ 6 mm in diameter. Other hosts can be used for the source; some even have narrower linewidth γ -rays. However, some of these sources deteriorate with age, are not monoenergetic at low temperatures, or are difficult to manufacture.

For the ^{57}Fe nucleus, the Mössbauer transitions are between the ground state with $I = \frac{1}{2}$ and the first excited state with $I = \frac{3}{2}$. A hyperfine magnetic field will then split the ground state into two levels and the excited state into four levels. Since only $\Delta m = \pm 1, 0$ transitions are allowed, an ^{57}Fe Mössbauer spectrum usually consists of six lines. When the quadrupole interaction is small compared to the hyperfine magnetic field interaction, the absorption lines are shifted slightly. Occasionally, the hyperfine field and quadrupole interactions are comparable and then the $\Delta = \pm 2$ transitions may occur; the spectra for nanometer FeF_2 particles are a contemporary example.¹⁵ There is also a shift of the spectrum that is made up of two contributions. One is the second-order Doppler shift that depends on the temperature and the other is the isomer shift that depends on the chemical composition of the material.

Analysis of an ^{57}Fe Mössbauer spectrum provides values for the hyperfine magnetic field, the quadrupole splitting, and the isomer shift. These not only vary from material to material, but are different for different crystallographic sites within the same material. Thus, the hyperfine parameters act as fingerprints; they permit not only the identification of the phase or phases present in a material but also give the occupancy of the various lattice sites.

These features are of general interest both for bulk and for nanometer-sized materials; the reader may wish to find more details elsewhere. Many books have been written on Mössbauer spectroscopy; one of the more readable and useful ones, although now rather old, is by Greenwood and Gibb.¹⁶ A overview of the role that ⁵⁷Fe Mössbauer spectroscopy plays in phase identification and site occupancy has been completed recently.¹⁷

4. TMS OF MAGNETIC NANOMETER PARTICLES

The use of TMS to study magnetic nanometer particles will be illustrated with a few specific examples. These have been chosen to demonstrate some of the ways that TMS provides pertinent data and at the same time to indicate some of the problems that arise.

As a first example, some NiFe₂O₄ (nickel ferrite) powders with varying particle sizes will be considered. These particles were prepared by chemical precipitation followed by a heat-treatment at relatively low temperatures for lengthy times. By changing the thermal conditions during the heat-treatment of the precipitates, powders with different particle size distributions were obtained.¹⁸ Electron-microscope photographs of three samples (a), (b) and (c), are shown in Fig. 1. The particle shapes may be described as irregular spheres. The average particle size and the distribution in size as estimated from the photographs are listed in Table 1.

X-ray diffraction patterns of the three samples, taken using Co K α radiation, are shown in Fig. 2. The broadening of the lines for the smallest particles, sample(a), is evident by visual inspection. Application of the Scherrer formula to the measured line broadening gave the average sizes listed in the third column of Table 1. For samples (b) and (c) these sizes are considerably less than those determined by electron microscopy. It appears that the x-ray data measures the crystallite size and that the larger particles are composed of several crystallites. The electron photomicrographs also suggest that



Fig. 1. Electron microphotographs of NiFe₂O₄ nanometer particles prepared by chemical precipitation. Samples (a), (b) and (c) were made by altering the final thermal conditions.

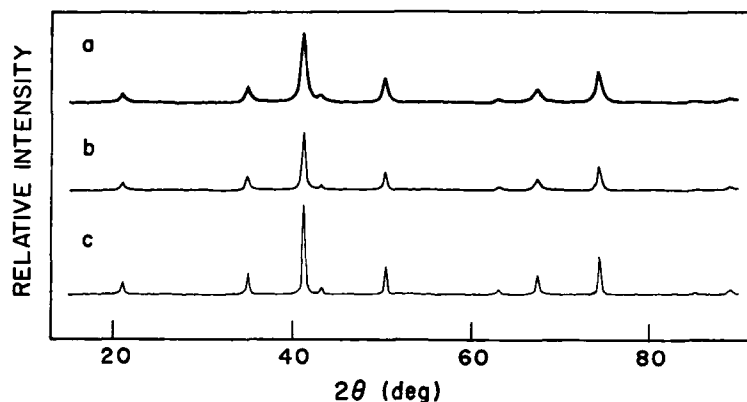


Fig. 2. Cu K α x-ray diffractometer traces for the NiFe₂O₄ powders corresponding to Fig. 1 (a), (b) and (c), respectively.

Table 1. Size Data for NiFe₂O₄ Powders Made by Chemical Precipitation Followed by Different Thermal Treatments.

| Sample | Particle Size (nm) | Crystallite Size (nm) |
|--------|--------------------|-----------------------|
| (a) | 25 \pm 5 | 25 |
| (b) | 80 \pm 20 | 40 |
| (c) | 130 \pm 20 | 50 |

some agglomeration of the particles takes place. All these features complicate the study of nanometer particles.

Absorbers for TMS were made by suspending the Ni ferrite particles in benzophenone, an organic [(C₆H₅)₂CO] that melts at a relatively low temperature ($\sim 48^\circ$ C). The spectra obtained for the three samples at room temperature are shown in Fig. 3. Each spectrum consists of two six-line overlapping subpatterns that correspond to ⁵⁷Fe nuclei in tetrahedral (A) sites or in octahedral (B) sites. The location of the minimum of each subpattern line for sample (c) is indicated by the bar diagrams; these are the same as those observed for bulk Ni ferrite. Comparison of the spectra gives some idea of the influence of particle size. For sample (a) the lines are clearly asymmetrically broadened and in addition the hyperfine field splitting is slightly reduced.¹⁸ Mørup and Topsøe¹⁹ have proposed a mechanism, called collective magnetic excitations, that may account for this behavior. In essence, the magnetization is thermally excited to oscillate about the direction of the minimum energy. This leads to an average smaller hyperfine field; the maximum reduction is about 10 to 15%.²⁰

Other mechanisms have been proposed for hyperfine-field differences between nanometer particles and bulk materials. One is a surface effect and is related to the

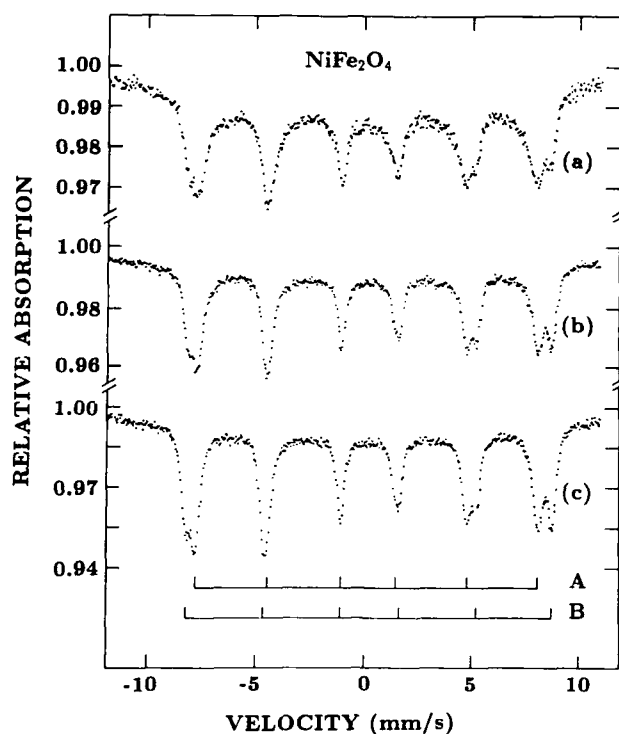


Fig. 3. Room-temperature ^{57}Fe Mössbauer spectra for the NiFe_2O_4 samples (a), (b), and (c).

reduction in atomic neighbors. For nanometer particles, which have a large surface to volume ratio, this effect may turn out to be very important, especially at higher temperatures. Some evidence for this mechanism has been found. For example, in $\alpha\text{-Fe}_2\text{O}_3$ particles the hyperfine field at the surface, although close to the bulk value at 4.2 K, decreases more rapidly than that of the bulk at higher temperatures.²¹

Another proposed mechanism concerns ferro- and ferrimagnets. Nanometer particles of these materials are often single domains. Since the demagnetization field is parallel to the hyperfine field direction, a small increase in the measured hyperfine field may be expected. For multidomain particles this enhancement will be smaller and perhaps zero. Some evidence for this demagnetization effect is provided by spectra of iron particles.²²

In yet another mechanism, dubbed superferromagnetism, the magnetic interaction between particles is proposed to be responsible for large decreases in the hyperfine field.²³ A mean-field theory has given an excellent fit to data on nanometer particles of goethite (FeOOH).²⁴

An extreme situation occurs when the thermal agitation produces magnetization directional changes between the various energy minima that are faster than the Larmor precession period. Then the hyperfine field averages to zero in a Mössbauer experiment; an ^{57}Fe spectrum consequently consists of a central singlet or, if the quadrupole interaction is non-zero, a doublet. This mechanism, called superparamagnetism, may be considered in a sense to be the extreme limit of collective magnetic excitations. Unlike paramagnetism, the process in a single particle is not considered to be chaotic; an ensemble of particles may, however, be behaving chaotically. Superparamagnetism is quenched below a characteristic temperature, called the blocking temperature. It depends on the anisotropies in the materials, the particle size, and the experimental measuring technique.²⁵ When the relaxation times are comparable to the Larmor precession time, broadened lines with characteristic shapes are observed.²⁶

Earlier, the essential role that recoilless events play in a Mössbauer spectrum is to be obtained was stated. Nanometer particles have very small masses, so that their recoil energy, at least in principle, should make a Mössbauer spectrum unobservable. To focus the discussion, iron particles made by the aerosol technique (evaporation into a helium gas at ~ 2 torr) will be considered. These particles were passivated by slow oxidation; a surface layer was identified as either Fe_3O_4 , $\gamma\text{-Fe}_2\text{O}_3$, or a mixture of the two. The particle size was ~ 30 nm, or about the same size as the NiFe_2O_4 particles of sample (a) in Figs. 1-3. A Mössbauer absorber was made by holding the passivated iron particles between two plastic circular-shaped pieces. The Mössbauer spectra obtained as a function of temperature are shown in Fig. 4. At room-temperature, essentially no recoilless absorption is observed; a similar result has been reported before.²⁷ At $T=77$ K (liquid-nitrogen temperature) a well-defined hyperfine-field split spectrum is observed. Here the outer lines are associated with the predominant iron-oxide phase; the line at $v \simeq -6$ mm/s is one of the outer lines of the $\alpha\text{-Fe}$ subpattern. The absorption areas, hence the recoilless fraction f , is intermediate to these extremes at the intervening temperatures.

In order to see whether the binder was the important difference, the aerosoled iron-iron oxide particles were suspended in benzophenone. Then, at room temperature, a split spectrum was obtained that was similar to one for the unsupported particles at $T \cong 235$ K. Although the recoilless factor, f , is therefore increased, it is still smaller than that for sample (a) of the Ni ferrite particles. The different preparation methods may provide the answer. When an aqueous method is employed, the particles seem to adhere more to each other, perhaps by van der Waal's forces or by interstitial water; the agglomerate of particles so formed then share the recoil energy.²⁸

The measurement of f provides a way to study the dynamic properties of nanometer particles. The usual procedure is to measure the Mössbauer absorption area, which is proportional to f , as a function of temperature keeping all other experimental conditions constant. Various models have been used to interpret the data.²⁹

If the particles are assumed to be harmonic oscillators of mass M bound by the restoring force constant q , then the frequency of oscillation will be

$$\omega = (q/M)^{1/2}$$

The force constant, q , is a measure of the interparticle interaction and the binding of the suspending medium. Since q is assumed to be a constant, the dynamic motion can be characterized by an Einstein temperature $\Theta_E = \hbar\nu/k = (\hbar/k)(q/M)^{1/2}$. The mean

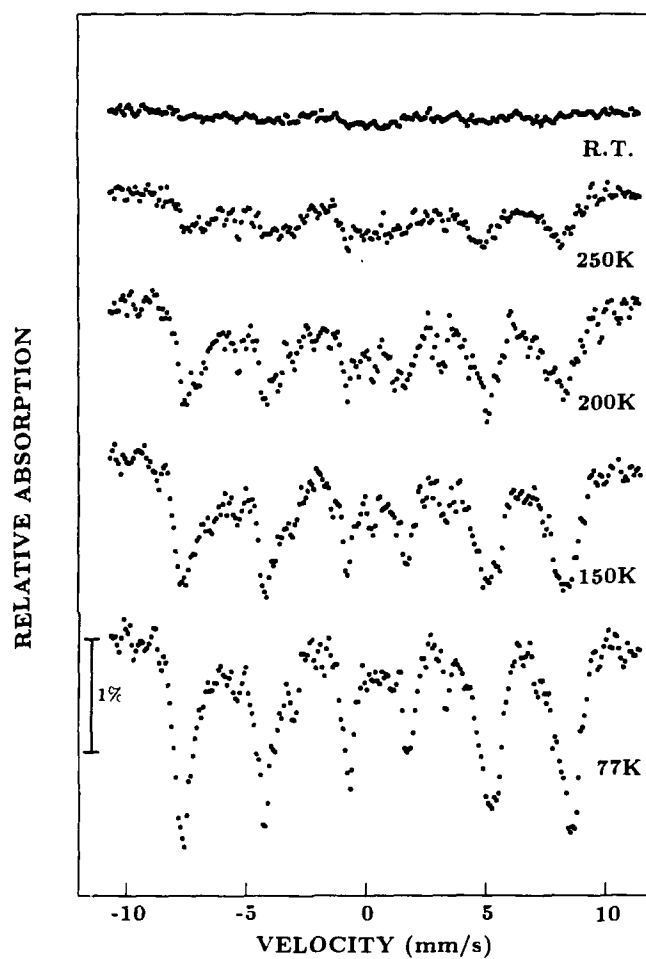


Fig. 4. Mössbauer spectra at various temperatures of iron particles passivated by an outer covering of iron oxide. The iron particles were made by evaporation into a helium gas at a reduced pressure. The iron oxide coating was produced by slow oxidation. The relative absorption has the same scale for each spectrum, as indicated by the bar. The particle size was about 30 nm. The statistics were $\sim 2 \times 10^6$ counts per channel.

square vibration amplitude, $\langle x^2 \rangle$, is

$$\langle x^2 \rangle = \frac{\hbar}{2M\omega} \left(\frac{2}{\exp(\hbar\omega/kT) - 1} + 1 \right);$$

if $kT \gg \hbar\omega$, valid except at very low temperatures, then

$$\langle x^2 \rangle = kT/q \quad (1)$$

The recoilless fraction, f , is given by

$$f = \exp(-4\pi^2 \langle x^2 \rangle / \lambda^2)$$

where λ is the wavelength of the γ -ray. Therefore, the fraction of the particles that undergo a recoil after absorbing a γ -ray is

$$f^{part} = \exp(-4\pi^2 kT/q\lambda^2). \text{ or}$$

$$f^{part} = \exp(-\alpha T) \quad (2)$$

where $\alpha = 4\pi^2 k/q\lambda^2$.

If the motion of the lattice atoms behaves as a three-dimensional Debye system, then the total recoilless fraction, f^{total} , will be given by

$$f^{total} = f^{part} f^{Debye} \quad (3)$$

where

$$f^{Debye} = \exp \left[-\frac{6E_R}{k\Theta_D} \left(\frac{1}{2} + \left(\frac{T}{\Theta_D} \right)^2 \int_0^{\Theta_D/T} \frac{x dx}{e^x - 1} \right) \right]$$

where E_R is the recoil energy and Θ_D is the Debye temperature of the material.

If the particles are large agglomerates or if the binder is rigid, $\alpha \simeq 0$ and $f^{part} = 1$. Otherwise α is expected to be appreciable.^{30,31}

In spite of its simplicity, the Debye model has been remarkably successful in solid-state physics. For nanometer particles some modifications may permit the continued use of this theory. If the nanometer lattice is softer than the bulk one, then Θ_D can be adjusted to a smaller value. If some phonons are no longer excited, changes in the lower and upper cut-off frequencies of the Debye spectrum can be made. It is possible that the lattice at the surface is softer than in the interior; then different Θ_D may be used for the two regions. Of course, future studies may show the need to develop a theory that is more sophisticated than Debye's model.

The last, but important, application of TMS that will be presented here, is the study of the magnetic structure and anisotropies in nanometer particles. As an example, when an external magnetic field produced by a superconducting solenoid is applied along the propagation direction of the ^{57}Fe γ -rays, the spectra of samples (a) and (c) of the NiFe_2O_4 particles (Table 1) obtained at just below room temperature are shown in Fig. 5 (a) and (b), respectively. The applied field of 6.65 T adds to the

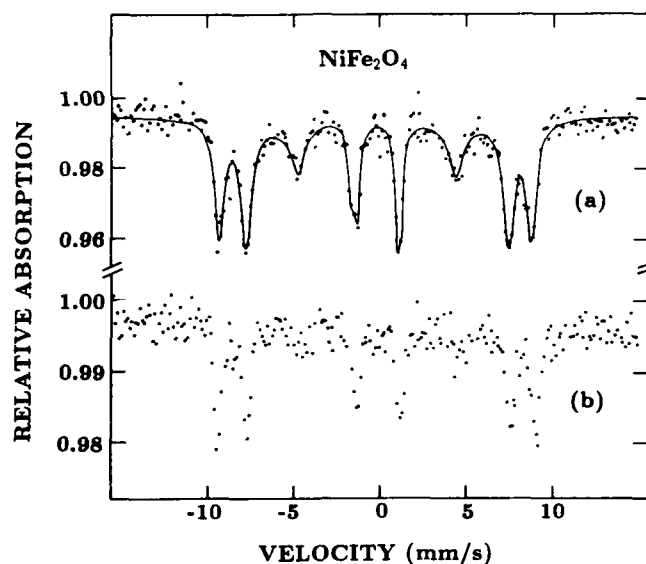


Fig. 5. Mössbauer spectra just below room temperature ($T \approx 280$ K) of NiFe_2O_4 particles in a magnetic field applied parallel to the γ -ray direction of propagation. Here (a) is for sample (a) and (b) is for sample (c) of Table 1.

hyperfine field at the A sites and subtracts from that at the B sites. The result is that the first and the sixth lines the A- and B-site subpatterns are clearly resolved; the other lines overlap. The most interesting feature of the spectra however is the presence of the second and fifth absorption lines. In a collinear magnetic system, if the magnetization lies along the direction of the external field (magnetic saturation), then the $\Delta m = 0$ transitions are forbidden; consequently the second and fifth lines should be absent. Since the lines are present the implication is that either the magnetic structure is not collinear or else a large anisotropy is preventing the rotation of a collinear magnetization. The relatively larger second and fifth line absorptions for the smaller particles [Fig. 5(a)] as compared to the larger particles [Fig. 5(b)] may imply a surface phenomena; however a volume effect can not be ruled out.³²

One way to resolve the surface versus volume quandary is to incorporate iron enriched in the ^{57}Fe isotope into the outer layers of each particle. Unfortunately this is easier said than done. First, steps must be followed to ensure that the enriched iron forms part of the lattice of the particle. Second, uniform diffusion of the enriched iron throughout the particle must be avoided. Even if the diffusion constant for ^{57}Fe in the bulk materials is known (and it may not be), it doesn't follow that this diffusion constant is the same for a nanometer particle. Several years ago we experimented with various procedures including heat treatments; after three years of efforts we obtained what we considered to be satisfactory samples of ^{57}Fe surface-enriched $\gamma\text{-Fe}_2\text{O}_3$ particles. The conclusion reached from Mössbauer spectra was that there is surface canting of the ionic magnetic moments in $\gamma\text{-Fe}_2\text{O}_3$ nanometer particles.³³

5. CONVERSION-ELECTRON MÖSSBAUER SPECTROSCOPY

Conversion-Electron Mössbauer Spectroscopy (CEMS) has a simple basis. First, recoilless γ -rays from a source are absorbed resonantly by ^{57}Fe nuclei in an absorber; this stage is the same as for TMS. Second, on deexcitation of these excited ^{57}Fe nuclei an energetic electron may be produced. Third, those electrons that emerge from the absorber into a detector are counted.

A complication with CEMS is the number of processes that can produce a countable electron; the main ones are indicated in Fig. 6. The most likely process, with about a 81 % probability, is ^{57}Fe deexcitation by emission of a K-shell conversion electron with an energy of 7.3 keV. If this electron is travelling towards the surface from a location within ~ 100 nm from the surface it may be emitted, as indicated in the upper part of Fig. 6. Deexcitation by emission of L-shell or M-shell conversion electrons, with energies of 13.6 and 14.3 keV, have probabilities of 9 and 1 %, respectively. These more energetic electrons may escape from nuclei more than 100 nm below the surface (see Fig. 6). Finally, deexcitation may occur by emission of a 14.4 keV γ -ray with the remaining probability, ~ 9 %.

Several secondary processes may produce a detectable electron. About 60 % of the K-shell conversion electrons are accompanied by an L-shell Auger electron with an energy of 5.4 keV. If both the K conversion electron and the L Auger electron are

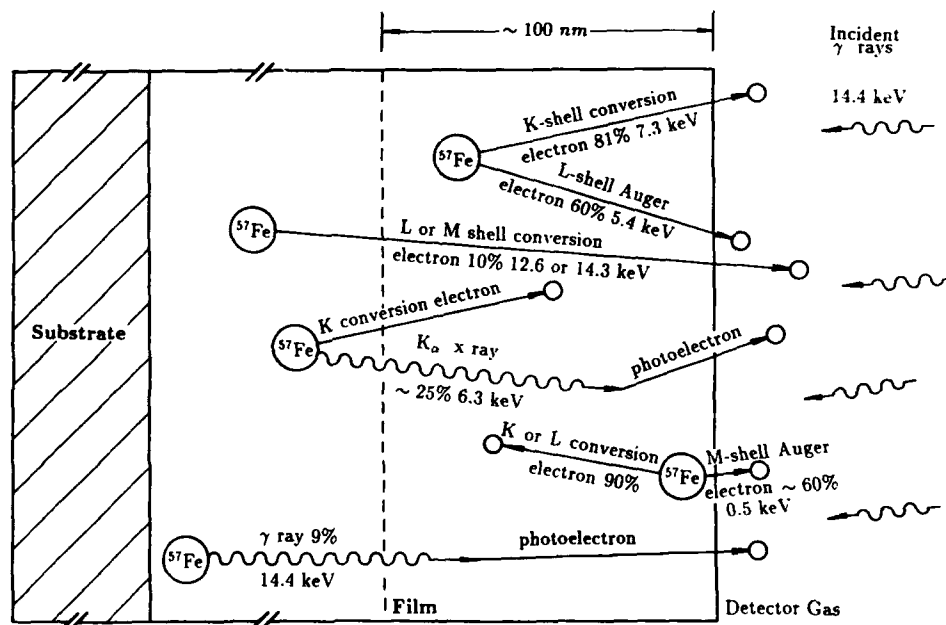


Fig. 6. Schematic to illustrate the main CEMS events in a film that lead to electrons that enter the detector. The thickness of the film more than ~ 100 nm from the surface and of the substrate are not to scale. Photons (γ - or x-rays) are indicated by wavy lines and electrons by straight lines.

emitted into the detector they are in coincidence and will produce one count. About 25 % of the K-shell conversion electrons are accompanied by a $K\alpha$ x-ray, 6.3 keV in energy. Either this $K\alpha$ x-ray or the 14.4 keV γ -ray may produce a photoelectron while traversing the absorber. These events, which may be counted, can start from a considerable distance below the surface. Finally, the emission of M-shell Auger electrons has a 60 % chance of occurrence after deexcitation via a K- or L-shell conversion electron: since these electrons have an energy of 0.5 keV, they may escape and be detected only if they start from within the topmost 2 nm surface layer. The above mechanisms are also illustrated in Fig. 6. Although this long list still does not exhaust all the possible processes, the detection probabilities of the remaining events are small.

The flux of electrons that emerge from the surface depends on the electron energies, the direction of travel, and on the absorber composition, which may be iron, an iron alloy, or an iron compound. Early theories assumed an exponential absorption law and the Fermi-age equation, but later work uses the Monte Carlo statistical method coupled with extensive computing.³⁴ There is an extensive literature on this subject; the several references given should permit the interested reader to locate the other relevant papers.

The calculations indicate that the resonant flux escaping into the detector mainly consists of K conversion electrons (~ 50 %) and Auger electrons (~ 22 %): some of these are in coincidence so that the total number of counts is reduced by about 10 %. The L conversion electrons contribute ~ 18 %, the photoelectrons from the $K\alpha$ x-rays and the 14.4 keV γ -rays about 5 % each, and the other processes the rest.

Some time ago, Swanson and Spijkerman³⁵ described a gas flow proportional counter suitable for CEMS. Our detector is a modified and improved version. One of our room-temperature CEMS detectors is shown at the left of Fig. 7. An easy disassembly, shown in Fig. 8, permits insertion of the absorber inside the detector. A helium-4% methane gas flows through the detector at 1 atm pressure and at a flow rate of 25 cm³/s. Electrons are detected with close to 100 % efficiency but x- or γ -rays are virtually not detected. In order to reduce non-resonant electrons, the body of the detector is machined out of a suitable plastic, such as lucite or perspex. The low average Z number greatly reduces the chance that secondary electrons will enter the chamber. In order to sweep the electrical charges out of the chamber, the inside of the detector is covered with a thin aluminum coating, either by evaporation or by using a thin foil, and is connected to ground potential.

Both larger and smaller detectors that employ essentially the same design have been made. The larger detectors accommodate larger disk-shaped absorbers, useful if the amount of ⁵⁷Fe present is small, as in bubble garnet films.³⁶ Smaller detectors with smaller absorbers ensure that the γ -rays from the source are better collimated. The solid angles used always produce some angular dispersion, as indicated by the incoming γ -rays drawn in Fig. 6.

A furnace attached to the absorber is shown on the right of Fig. 7. CEMS spectra have been obtained up to 540 K;³⁷ no doubt further modifications could raise this upper temperature limit. Smaller versions of the detector inserted into a suitable dewar have allowed operation below room temperatures. At liquid-nitrogen temperatures, no methane is used. Then the pulse heights in the helium gas are reduced and make a CEMS spectrum difficult to obtain unless a large amount of ⁵⁷Fe-enriched iron is present.

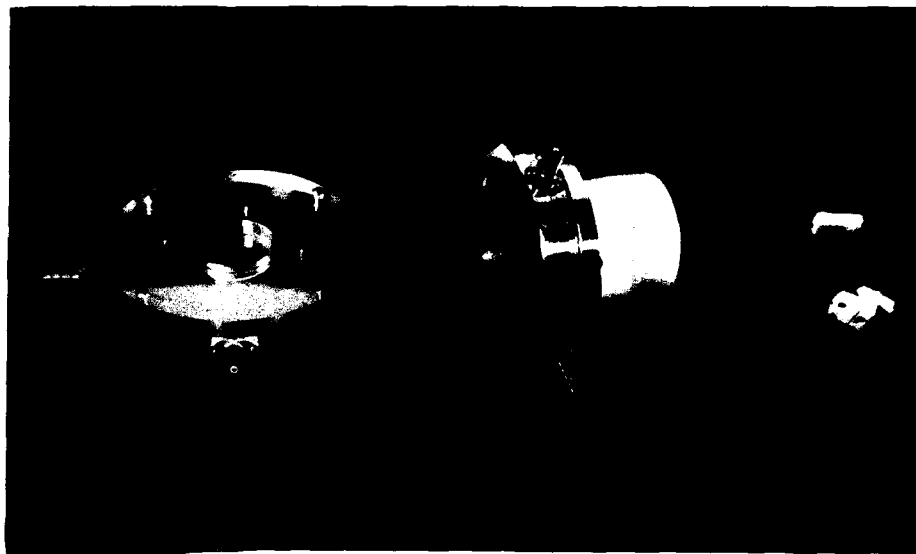


Fig. 7. Two gas CEMS detectors. The gas entry port is on the left of the room-temperature detector; the exit is a small hole 140° away in the side wall. The detector at the right has a furnace attached to the sample holder; the flow through gas remains close to room temperature.



Fig. 8. The room-temperature CEMS detector disassembled. The four $25\ \mu\text{m}$ -diameter tungsten wires for the high voltage (usually about $1000\ \text{V}$) are just visible in the part at the right. The detector body was machined out of lucite and the inside was then covered by aluminum, either by evaporation, as on the right, or by a thin foil, as on the left.

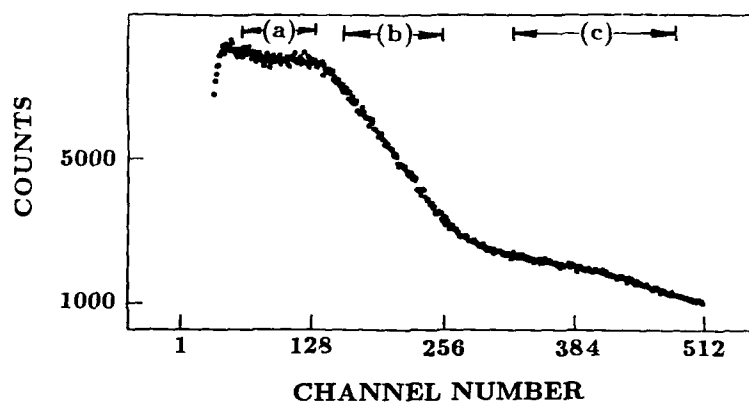


Fig. 9. The pulse height distribution in the CEMS detector. The channel number is proportional to the electron energy.

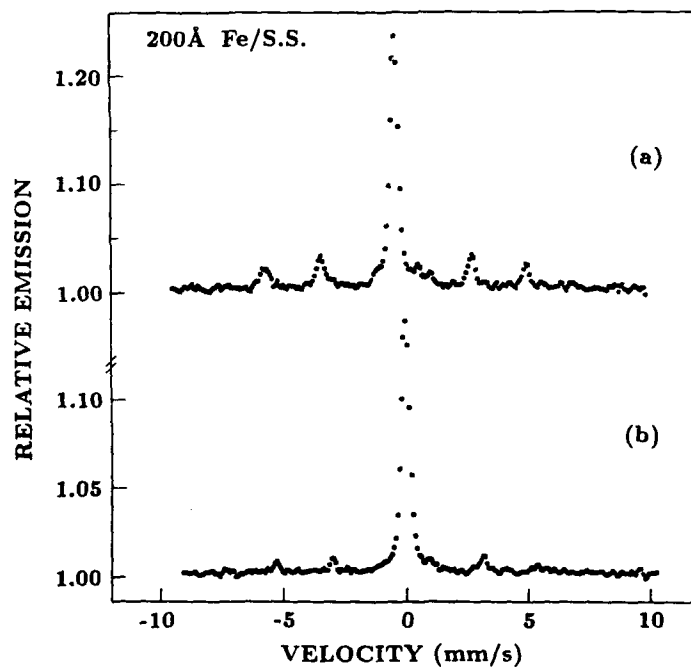


Fig. 10. Spectra obtained by CEMS for a 20 nm film of α -Fe on a stainless steel disk. In (a) only a narrow band of electron energies are counted; in (b) a wide window is used.

The distribution in pulse heights, which are proportional to the electron energies, is shown for a natural iron film, 80 nm thick, evaporated onto a stainless steel substrate in terms of channel numbers in Fig. 9. Although in principle the detector can be used to count all the electrons (integral mode), in practice an electronic window selects a range of pulse heights to be counted. For example, the window indicated by (b) in Fig. 9 will only count electrons with energies in a range in the 7 keV region; hence most Auger electrons will not be included.

A CEMS spectrum for a 20 nm thick film of natural iron on a stainless steel backing is shown in Fig. 10 (a); the window has been set to the channels indicated by (c) in Fig. 9. The central peak is the contribution from the paramagnetic stainless steel. The hyperfine split lines for the α - ^{57}Fe are clearly visible. Since the isotope ^{57}Fe has a natural abundance of only 2.25 %, the use of iron enriched to better than 90 % in ^{57}Fe will provide a multiplicative factor of at least 40. Then a film of 0.5 nm or even less in thickness should be detectable by CEMS; this conclusion seems to be in accord with that reached by Petrera et al.³⁵ The spectrum of Fig. 10(b) was obtained with a wide window starting at the beginning of (a) and ending at the end of (c) of Fig. 9. It is interesting to note that the resolution has deteriorated, probably because a smaller percentage of the resonant events occur in the 20 nm α -Fe layer.

In spite of the large number of different processes in CEMS and the straggling in energy as the electrons traverse the material towards the surface, information as a function of depth can be obtained. In one method, CEMS spectra are taken after various thicknesses of the surface have been etched off. This approach has proved to be valuable in the study of ion-implantation in magnetic garnet films.^{36,39} In another method, CEMS spectra are obtained after the deposit, usually by evaporation, of an overlayer of some other material; the thickness of this overlayer can be progressively increased. Both these techniques, however, destroy the sample.

A non-destructive approach is to measure the CEMS spectra as a function of electron energy. In a gas detector, such as ours, this can be accomplished by changing the range of pulse heights counted, that is, by altering the window. CEMS spectra obtained for a 80 nm film of natural α -Fe on a stainless steel substrate are shown in Fig. 11 for the (a), (b), and (c) windows indicated in Fig. 9. The spectra in Fig. 11 (d) was obtained by widening the window to cover the entire range from (a) to and including (c). The Mössbauer parameters obtained for the α -Fe subpattern are listed in Table 2 together with the relative areas of the stainless steel subpattern. The

Table 2. Data for CEMS Spectra of 80 nm Thick Natural Iron Film on Stainless Steel.

| Window | H_{hf} (T) | δ^a (mm s ⁻¹) | Θ^b (°) | $A_{SS}/(A_{SS} + A_{Fe})$ (%) |
|--------|--------------|----------------------------------|----------------|--------------------------------|
| (a) | 32.9 | -0.001 | 88 | 46 |
| (b) | 32.9 | 0.002 | 79 | 28 |
| (c) | 32.9 | 0.002 | 79 | 17 |
| (d) | 32.9 | 0.004 | 82 | 34 |

^a The isomer shift, δ , is relative to an α -iron calibration foil.

^b The angle, Θ , is the direction that the average hyperfine field (and also the magnetization) makes with the normal to the plane of the film.

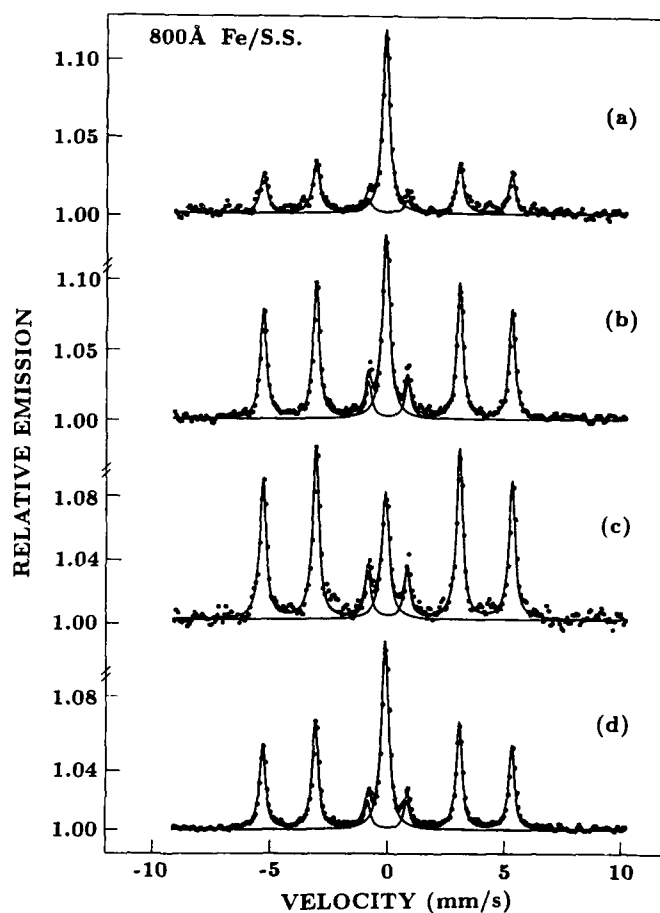


Fig. 11. CEMS spectra for an absorber with a 80 nm thick film of alpha iron on a stainless steel substrate. Spectra (a), (b), and (c) correspond to the windows (a), (b) and (c) indicated in Fig. 10. Spectrum (d) is obtained with a wide window, starting at the beginning of (a) and ending at the end of (c).

hyperfine field is constant and the isomer shift is essentially zero for all the window settings. However, the hyperfine field direction and therefore also the magnetization is slightly closer to the plane of the film for the lower energy electrons, which presumably have their origin closer to the surface. The largest signal, as compared to the stainless steel, is obtained for window setting (c); these data seem to be consistent with an earlier report by Nakagawa et al.⁴⁰

Much better energy resolution for differential or depth-selective CEMS, sometimes referred to as DCEMS, can be achieved by using a magnetic or electric energy selector and then detecting the electrons with a channeltron or a scintillation counter. Several devices have been successfully built that have utilized β -ray spectrometer or particle electrostatic analyzer technology developed for nuclear physics. Then by measuring the CEMS spectra in different narrow energy ranges and by using a deconvolution procedure information concerning different depths below the surface has been obtained.⁴¹ Additional advantages of these techniques are that the absorbers can be cooled to liquid-helium temperatures and that angular measurements can be made. The main drawbacks are the time and expense in building and bringing the analyzer into operation and the low count rates.

6. CEMS OF MAGNETIC NANOMETER SYSTEMS

Since the K-conversion electrons, the most copious ones, sample depths of ~ 100 nm, the question arises as to how the powerful CEMS and DCEMS techniques can be usefully applied to nanometer magnetic systems. We will attempt to answer this question with a few examples together with some suggestions for future experiments.

Amorphous ribbons of alloys can be made by rapid quenching using the single-roller technique. These ribbons upon annealing become crystalline; these crystallites may be of nanometer sizes. In Fig. 12, TMS and CEMS spectra of $\text{Fe}_{81}\text{B}_{13.5}\text{Si}_{3.5}\text{C}_2$ ribbons are shown for the amorphous state and after annealing at various temperatures, T_A , for 20 min in flowing helium gas.⁴² The onset of crystallization occurs at a lower value of T_A (~ 670 K) than in the bulk (~ 710 K), as observed by the appearance of the sharp peaks. The various crystallization products can be followed as a function of the annealing treatment.

Sometimes when amorphous ribbons are made, small crystalline particles are embedded in the amorphous matrix. These may be on the surface and can be detected with CEMS. In a $\text{Fe}_{90}\text{Zr}_{10}$ glass, α -Fe and Fe_3Zr crystallites were observed as hyperfine-split CEMS subpatterns, primarily at the shiny surface (the one opposite to the spinning wheel); these crystallites were not observed by TMS.⁴³

Amorphous ribbons of $\text{Fe}_{73.5}\text{CuNb}_3\text{Si}_{13.5}\text{B}_9$ upon annealing at relatively low temperatures develop crystallites with sizes below about 10 nm. This material then possesses excellent soft magnetic properties. CEMS permits the onset of crystallization to be monitored and also the identification of the compositions of the phases produced.⁴⁴

If films are supported on thick substrates, TMS is no longer possible since the 14.4 keV γ -rays will not reach the detector. It is usually not convenient and often impossible to remove this substrate so that only CEMS can be used to obtain a Mössbauer spectrum. In some Fe_3O_4 films made by sputtering under various substrate temperature and oxygen flow conditions, films as thin as 100 nm thick and with grain sizes

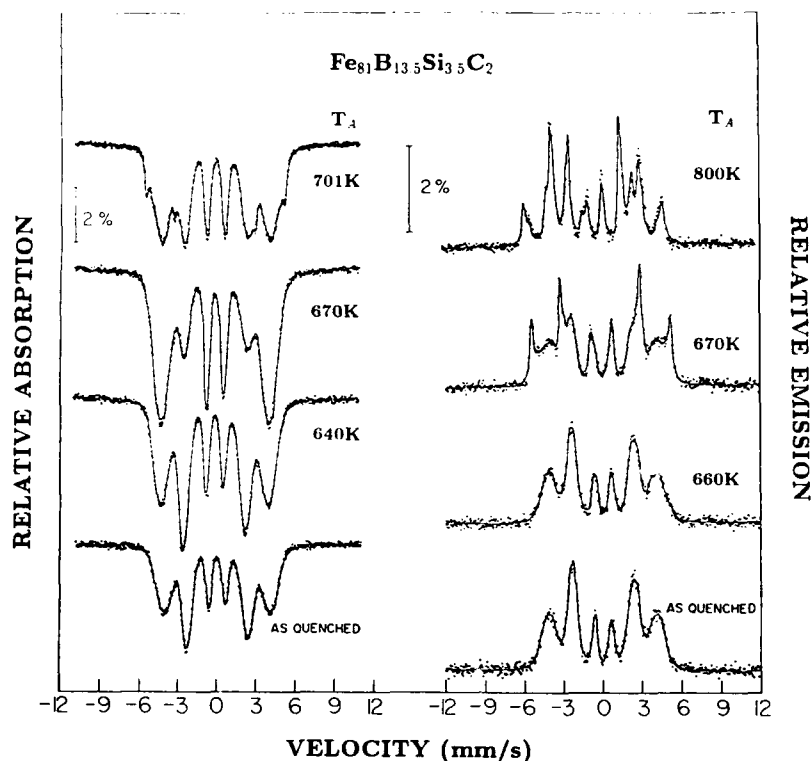


Fig. 12. TMS (at the left) and CEMS (at the right) spectra at room temperature of a $\text{Fe}_{81}\text{B}_{13.5}\text{Si}_{3.5}\text{C}_2$ ribbon in the amorphous state and after annealing at various temperatures, T_A , as indicated. Note the sharp peaks that correspond to partial crystallization appear in the CEMS spectrum for 670 K whereas they are not present in the TMS spectrum until $T_A=701$ K. Complete crystallization has occurred for $T_A=800$ K.

as small as 12 nm have been studied by CEMS. The change in magnetization was correlated with the observed superparamagnetism and with varying iron populations on the crystallographic sites.⁴⁵

Even when the substrate is relatively thin, if the films are ~ 100 nm or less in thickness, stacking of samples is necessary to observe a TMS spectrum. Again CEMS may be the only practical way to get a Mössbauer spectrum with acceptable statistics in a reasonable time.

A subject of current interest is multilayer films. These consist of alternate layers of different materials; each layer has a certain number of monolayers, as little as 2 or 3 and as many as 20 or so. If the substrate is too thick for TMS, CEMS must be employed. The hyperfine parameters of the interfacial monolayers may differ from those for the interior layers. Since the multilayer stacking can be large, a CEMS spectrum should be capable of resolving at least 2 or 3 subpatterns.

Methods to deposit clusters on surfaces are under development at the present. It should be possible to investigate clusters in the 0.5 to 1 nm range by CEMS; for

clusters below 0.5 nm iron enriched in ^{57}Fe may be required. It will be interesting to study the superparamagnetism and recoilless fractions of such systems.

ACKNOWLEDGEMENTS

Many researchers have contributed to the study of ultrafine particles and thin films in this laboratory over the past 25 years; we wish to mention in particular the stimulating ongoing collaboration with Professor K. Haneda of Ishinomaki Senshu University, Japan. Some financial support for the preparation of this article was provided by the Natural Sciences and Engineering Research Council of Canada.

REFERENCES

1. F. E. Wagner, Applications of Mössbauer scattering techniques, *J. Phys. Colloq.* C6:37 (1976).
2. A. Tasaki, M. Oda, S. Kashu, and C. Hayashi, Metal tapes using ultra fine powder prepared by gas evaporation method, *IEEE Trans. Mag.* MAG-15:1540 (1979).
3. C. F. Kernizan, K. J. Klabunde, C. M. Sorensen, and G. C. Hadjipanayis, Magnetic properties of nanometer-scale iron particles generated by ion atom clustering in cold pentane, *Chem. of Mat.* 2:70 (1990).
4. G. Xiao and C. L. Chien, Enhanced magnetic coercivity in magnetic granular solids, *J. Appl. Phys.* 63:4252 (1988).
5. M. Kiyama, T. Takada, N. Nagai, and N. Horiishi, Formation of hexagonal plate-like particles of $\text{Ba}_{12-2x}\text{Ti(IV)}_x\text{Co(II)}_x\text{O}_{19}$ with $0 \leq x \leq 1.2$, *Adv. Ceramics* 15:51 (1985).
6. K. Haneda, C. Miyakawa, and H. Kojima, Preparation of high coercivity $\text{BaFe}_{12}\text{O}_{19}$, *J. Am. Ceram. Soc.* 57:354 (1974).
7. P. Ayyub, M. Multani, M. Barma, V. R. Palkar, and R. Vijayaraghavan, *J. Phys. C.* 21:2229 (1988).
8. K. Haneda, C. Miyakawa, and K. Goto, Preparation of small particles of $\text{SrFe}_{12}\text{O}_{19}$ with high coercivity by hydrolysis of metal-organic complexes, *IEEE Trans. Mag.* MAG-23:3134 (1987).
9. F. Licci and T. Besagni, Organic resin method for highly reactive and homogeneous hexaferrite powders, *IEEE Trans. Mag.* MAG-20:1639 (1984).
10. B. Shirk and W. R. Buessem, Magnetic properties of barium ferrite formed by crystallization in a glass, *J. Am. Ceram. Soc.* 53:192 (1970); H. Laville and J. C. Bernier, Micromagnetism in a new $\text{BaO} \cdot \text{Fe}_2\text{O}_3 \cdot \text{B}_2\text{O}_3$ glass, *J. Mat. Sci.* 15:73 (1980).
11. C. W. Draper, Ultra-fine metal particle formation via pulsed laser breakdown of carbonyl vapors, *Metal. Trans. A.* 11:349 (1980).
12. D. M. Cox, D. J. Trevor, R. L. Whetten, E. A. Rohlfs, and A. Kalder, Magnetic behavior of free-iron and iron oxide clusters, *Phys. Rev. B* 32:7290 (1985).
13. A. Ouchi, K. Watanabe, M. Kiyama, T. Shinjo, Y. Bando, and T. Takada, Mössbauer studies of cobalt absorbed $\gamma\text{-Fe}_2\text{O}_3$ particles using ^{57}Co , in: "Ferriters: Proc. Third Int. Conf.," H. Watanabe, S. Iida, and M. Sugimoto, eds., Center for Academic Publications, Japan (1981).
14. M. P. Sharrock, P. J. Picone, and A. H. Morrish, Mössbauer emission spectroscopy study of cobalt-surface doped acicular magnetite particles, *IEEE Trans. Mag.* MAG-19:1466 (1983).

15. K. Haneda, X. Z. Zhou, A. H. Morrish, R. J. Pollard, and T. Majima, Mössbauer study of ultrafine FeF_2 particles, *Hyperfine Int.* (1990).
16. N. N. Greenwood and T. C. Gibb, "Mössbauer Spectroscopy," Chapman and Hall Ltd., London (1971).
17. A. H. Morrish, Mössbauer spectroscopy as used in structural chemistry, *Structural Chem.* in press.
18. K. Haneda, H. Kojima, and A. H. Morrish, Preparation and magnetic properties of small NiFe_2O_4 particles, *J. Jpn. Soc. Powder and Powder Metall.* 30:1 (1983). (In Japanese).
19. S. Mørup and H. Topsøe, Mössbauer studies of thermal excitations in magnetically ordered microcrystals, *Appl. Phys.* 11:63 (1976).
20. S. Mørup, Magnetic hyperfine splitting in Mössbauer spectra in microcrystals, *J. Magn. Magn. Mat.* 37:39 (1983).
21. T. Shinjo, M. Kiyama, N. Sugita, K. Watanabe, and T. Takada, Surface magnetism of $\alpha\text{-Fe}_2\text{O}_3$ by Mössbauer spectroscopy, *J. Magn. Magn. Mat.* 35:133 (1983).
22. I. Tamura and M. Hayashi, Mössbauer effect study of the internal magnetic field in small iron particles, *J. Magn. Magn. Mat.* 31-34:945 (1983).
23. S. Mørup, Mössbauer spectroscopy studies of ultrafine particles of crystalline and amorphous materials, in "Proc. Int. Symp. Physics of Magnetic Materials," M. Takahashi, S. Maekawa, M. Gondo, and H. Nosé, eds., World Scientific Publishing Co. Ltd., Singapore (1987).
24. S. Mørup, M. B. Madsen, J. Franck, J. Villadsen, and C. J. W. Koch, A new interpretation of Mössbauer spectra of microcrystalline goethite: "Super-ferromagnetism" or "Super-spin-glass" behavior?, *J. Magn. Magn. Mat.* 40:163 (1983).
25. K. Haneda and A. H. Morrish, Mössbauer spectroscopy of magnetic small particles with emphasis on barium ferrite, *Phase Trans.* (1990).
26. M. Blume, Stochastic theory of lineshape: generalization of the Kubo-Anderson model, *Phys. Rev.* 174:351 (1968).
27. K. Haneda and A. H. Morrish, Oxidation of aerosoled ultrafine iron particles, *Nature* 282:186 (1979).
28. J. M. D. Coey and D. Khallafalla, Superparamagnetic $\gamma\text{-Fe}_2\text{O}_3$, *Phys. Status Solidi (a)* 11:229 (1972).
29. P. J. Picone, K. Haneda, and A. H. Morrish, Dynamic and magnetic excitations in ultrafine particles, *J. Phys. C.* 15:317 (1982).
30. G. von Eynatten and H. E. Bömmel, Size and temperature dependence of the Mössbauer Debye-Waller factor of iron microcrystals, *Appl. Phys.* 14:415 (1977).
31. M. Hayashi, I. Tamura, Y. Fukano, S. Kanemaki, and Y. Fujio, Mössbauer effect study of lattice vibration of small iron particles, *J. Phys. C.* 13:681 (1980).
32. A. H. Morrish and K. Haneda, Surface magnetic properties of fine particles, *J. Magn. Magn. Mat.* 35:105 (1983).
33. A. H. Morrish, K. Haneda, and P. J. Schurer, Surface magnetic structure of small $\gamma\text{-Fe}_2\text{O}_3$ particles, *J. Phys. Colloq.* C6:301 (1976).
34. M. J. Tricker, L. A. Ash, and T. E. Cranshaw, A neglected mechanism in the interpretation of conversion electron Mössbauer spectra, *Nucl. Instr. and Meth.* 143:307 (1977); D. Liljequist, T. Ekdahl, and U. Bäverstam, Analysis of the electron transport in conversion electron Mössbauer spectroscopy (CEMS), *Nucl. Instr. and Meth.* 155:529 (1978); F. A. Deeny and P. J. McCarthy, Conversion electron, auger electron, and "resonant" photo-electron production and transmission in ^{57}Fe backscatter electron Mössbauer spectroscopy, *Nucl. Instr. and Meth.*

- 166:491 (1979); D. Liljequist, The analysis of natural ^{57}Fe abundance absorbers in conversion electron Mössbauer spectroscopy, Nucl. Instr. and Meth. 179:617 (1981); F. Salvat and J. Parellada, Theory of conversion electron Mössbauer spectroscopy (CEMS), Nucl. Instr. and Meth. B1:70 (1984); T. S. Lee, T. D. Placek, J. A. Dumesic, and B. J. Tatarchuk, Electron intensities obtained during back-scattered-Mössbauer spectroscopy, Nucl. Instr. and Meth. B18:182 (1987).
35. K. R. Swanson and J. D. Spijkerman, Analysis of thin surface layers by Fe-57 Mössbauer backscattering geometry, J. Appl. Phys. 41:3155 (1970).
 36. P. J. Picone and A. H. Morrish, CEMS characterization of ion-implanted bubble garnets, J. Appl. Phys. 53:2471 (1982).
 37. X. Z. Zhou and A. H. Morrish, Simple high-temperature proportional detector for conversion-electron Mössbauer spectroscopy, Nucl. Instr. and Meth. B18:215 (1987).
 38. M. Petrera, U. Gonser, U. Hasmann, W. Keune, and J. Lauer, Are monolayers detectable by conversion electron Mössbauer spectroscopy (CEMS)?, J. Phys. Colloq. C6:295 (1976).
 39. P. A. Smit, H. A. Algra, and J. M. Roberston, Effect of ion-implantation on magnetic-properties of a garnet as studied by Mössbauer spectroscopy, Appl. Phys. 22:299 (1980); A conversion electron Mössbauer spectroscopy study of ion-implanted bubble garnets, J. Appl. Phys. 52:2364 (1981).
 40. H. Nakagawa, Y. Ujihira, and M. Inaba, Possibility of depth selective CEMS with a gas flow proportional counter, Nucl. Instr. and Meth. 196:573 (1982).
 41. U. Bäverstam, T. Ekdahl, Ch. Bohm, B. Ringström, V. Stefansson, and D. Liljequist, Depth selective Mössbauer-effect measurements by means of scattered electrons, Nucl. Instr. and Meth. 115:373 (1974); D. Liljequist and B. Bodlund-Ringström, On the interpretation and practical analysis of depth selective conversion electron Mössbauer spectra, Nucl. Instr. and Meth. 160:131 (1979); T. Shigematsu, H. -D. Pfannes, and W. Keune, Depth-selective conversion-electron Mössbauer spectroscopy, Phys. Rev. Lett. 45:1206 (1980); T. Yang, A. Krishnan, N. Benczer-Koller, and G. Bayreuther, Surface magnetic hyperfine interactions in Fe_2O_3 determined by energy-resolved conversion-electron Mössbauer spectroscopy, Phys. Rev. Lett. 48:1292 (1982); D. Liljequist and M. Ismail, Depth-selective ^{57}Fe conversion-electron Mössbauer spectroscopy. I. Theory-improved accuracy, angular effects, Phys. Rev. B31:4131 (1985); D. Liljequist, M. Ismail, K. Saneyoshi, K. Debusmann, W. Keune, R. A. Brand, and W. Kiauka, Depth-selective ^{57}Fe conversion-electron Mössbauer spectroscopy. II. Experimental test-angular effects, accuracy, Phys. Rev. B231:4137 (1985); Zs. Kajcsos, Ch. Sauer, A. Holzwarth, R. Kurz, W. Zinn, M. A. C. Ligtenberg, and G. van Aller, Improvements in ^{57}Fe depth-selective conversion electron Mössbauer spectroscopy by applying a low-noise scintillation electron detector, Nucl. Instr. and Meth. B34:383 (1988).
 42. N. Saegusa and A. H. Morrish, Atomic rearrangements and crystalline transformations in amorphous $\text{Fe}_{81}\text{B}_{13.5}\text{Si}_{3.5}\text{C}_2$, Phys. Rev. B26:305(1982); Surface atomic arrangements and crystalline transformations in $\text{Fe}_{81}\text{B}_{13.5}\text{Si}_{3.5}\text{C}_2$ ribbons, Phys. Rev. B26:6547 (1982).
 43. Z. S. Wronski, X. Z. Zhou, A.H. Morrish, and A. M. Stewart, Magnetic micro-crystals and surface layers in as-quenched and hydrogenized $\text{Fe}_{90}\text{Zr}_{10}$ glass, J. Appl. Phys. 57:3548 (1985).
 44. K. Haneda, private communication.
 45. C. Ortiz, C. Hwang, A. H. Morrish, and X. Z. Zhou, Microstructure and conversion electron Mössbauer studies of M decrease in Fe_3O_4 films, J. Mater. Res. 5:824 (1990).

SOME TOPICS IN FINE PARTICLE MAGNETISM

Ami E. Berkowitz

Physics Department and Center for Magnetic Recording Research
University of California, San Diego
La Jolla, CA 92093

ABSTRACT

Recent progress in several areas of fine particle magnetism are discussed. These are: microstructure and morphology of particles, estimates of H_K distributions in particle assemblies, intrinsic surface magnetization of $\gamma\text{-Fe}_2\text{O}_3$ particles, anisotropy enhancement by surface treatment, and the long range magnetization order in assemblies of nominally superparamagnetic Fe particles in granular films.

INTRODUCTION

It is a simple matter to state the requirements for understanding the magnetic and hysteresis properties of magnetic fine particles systems. First, one must have an accurate model of magnetization reversal and high field behavior in individual particles. Then it is necessary to take account of the distribution of properties present in a given sample and of the magnetostatic interactions among the particles. Finally, the effects of temperature and measuring time should be included. Although there has been enormous progress over the past fifty years in developing models that are extremely helpful in thinking about these issues, it is probably accurate to say that there are very few, if any, fine particle systems whose measured properties can be confidently explained. For the most part, one is forced to fit observed properties into formalisms containing enough adjustable parameters to give reasonable agreement with the data. The results may be quite accurate, but we really cannot evaluate this because the samples are generally not well enough characterized, and even if they were, the models simply cannot take into account the enormous range of properties in a given sample and the effects of magnetostatic interactions. These factors underlie the importance of obtaining data on extremely well characterized assemblies or on single particles. If such data were available, they would provide a strong incentive to exploit the currently available numerical analysis techniques.

The topics considered are: the variety and nature of microstructural and morphological features of $\gamma\text{-Fe}_2\text{O}_3$ particle assemblies; H_K distributions and their effects; intrinsic surface magnetization of $\gamma\text{-Fe}_2\text{O}_3$ particles; some properties of surface treated particles; and the particle interactions evidenced in granular films. Much, but not all, of the work described involves particles used in magnetic recording media.

MICROSTRUCTURE AND MORPHOLOGY IN $\gamma\text{-Fe}_2\text{O}_3$

The term "cooperative" may be used to describe magnetization reversal in fine particles where rotation is initiated and proceeds uniformly over the whole particle. These well known reversal modes¹ were analytically derived for ideal particle shapes (ellipsoids of revolution)

and include coherent reversal, curling and fanning. For many years, magnetization reversal in samples of acicular $\gamma\text{-Fe}_2\text{O}_3$ particles used in recording tapes was described in terms of these cooperative modes, particularly the fanning mechanism. The reason for using the fanning mechanism was a very logical one—it fit various data better than the other models. However, the fanning mechanism was calculated for a particle consisting of a chain of spheres whose interactions were purely magnetostatic, whereas $\gamma\text{-Fe}_2\text{O}_3$ particles are elongated single crystals.²⁻⁴ Furthermore Knowles' work^{5,6} on single particles indicated a distribution of anisotropy fields, H_K , that was not consistent with a simple fanning mode. Finally, it has been amply demonstrated²⁻⁴ that these $\gamma\text{-Fe}_2\text{O}_3$ particles show a variety of microstructural and morphological features that suggest heterogeneous nucleation of magnetization reversal at sites of lower energy on the particles due to asperities, pits, defects, etc. The justification for noting this past work is that it helped to encourage more recent numerical approaches to explain the properties of acicular $\gamma\text{-Fe}_2\text{O}_3$ particles.⁷⁻⁹ These recent calculations have taken a more realistic view of particle morphology and have indicated that significant deviations from the cooperative modes do exist. Since these calculations require substantial computer time, it is not likely that they will be extended to arrays of real particles. However, it is now quite clear that anomalous microstructural and morphological features of $\gamma\text{-Fe}_2\text{O}_3$ fine particles can influence their magnetic behavior and that numerical calculations of these effects are quite feasible.

H_K DISTRIBUTIONS

In any fine particle sample, the anisotropy fields, H_K , of the individual particles are bound to be distributed. $H_K = 2K/M$, where K is the anisotropy energy density which may arise from shape anisotropy, magnetocrystalline energy, stress/magnetostriction effects, or surface anisotropy energy. Generally, the way this distribution is handled is to assume a reversal mechanism for the particles and then fit the hysteresis measurements, e.g., H_C or the fractional remanent magnetization, M_R/M_S , with a satisfactory distribution. One problem with this procedure, noted above, is that one really doesn't know what the reversal mechanism is or whether the same mechanism operates for all the particles. We have adopted a somewhat different method for estimating the H_K distribution in samples of nominally randomly oriented particles for which there is strong evidence that H_K is predominantly uniaxial.^{10,11} Instead of using hysteresis data, for which the magnetization distributions in the particles are generally unknown, we use Mössbauer or magnetization data taken in fields, H_a , comparable to H_K for which it is quite reasonable to assume each particle is uniformly magnetized. Under these conditions the Stoner-Wohlfarth¹² model for randomly oriented particles with uniaxial anisotropy is operative and universal curves can be calculated for M/M_S , P_T , and P_L versus H_a/H_K , where P_T and P_L are the Mössbauer polarizations in fields transverse and parallel to the γ -ray propagation direction. These curves are shown in Fig. 1. Thus one measures the relevant

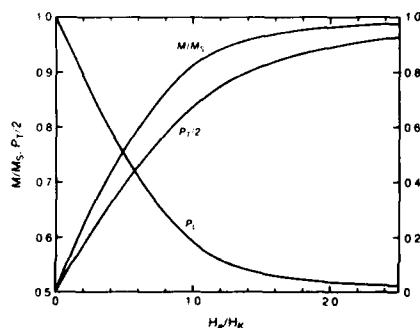


Fig. 1. Relative magnetization and Mössbauer polarization for random, single domain, uniaxial particles. The field is either along the γ -ray propagation direction (P_L , right hand scale) or transverse to this direction (P_T left hand scale). (Ref. 10)

magnetization or Mössbauer quantities in a particular H_a and determines an average H_K from these universal curves. There is an advantage in using the Mössbauer data in that the saturation magnetization need not be known (as H_a increases, $P_T \rightarrow 2.0$ and $P_L \rightarrow 0$) as is the case for the magnetization measurements. Another advantage of the Mössbauer approach

Table I. Room temperature magnetic data and anisotropy fields determined by magnetization (V) and Mössbauer effect (Mö) at applied fields H_a . The remanence ratio (M_R/M_S) was obtained after exposure to 10.6 kOe, where M_S is the moment at 10.6 kOe. All fields are in kOe. (Ref. 10)

| SAMPLE | M_R/M_S | H_C | H_a | H_K (Mö) | H_K (V) |
|---|-----------|-------|-------|------------|-----------|
| Large $\gamma\text{-Fe}_2\text{O}_3$ | 0.46 | 0.33 | 0.70 | - | 1.5 |
| | | | 1.8 | 1.9(2) | 1.6 |
| | | | 3.0 | 2.1(2) | - |
| Small $\gamma\text{-Fe}_2\text{O}_3$ | 0.41 | 0.28 | 0.66 | - | 1.4 |
| | | | 1.8 | 1.5(2) | 1.7 |
| | | | 3.0 | 2.0(2) | 1.9 |
| Precursor (reduced $\gamma\text{-Fe}_2\text{O}_3$) | 0.44 | 0.31 | 0.63 | - | 1.3 |
| | | | 1.8 | 1.2(2) | 1.7 |
| | | | 3.0 | - | 2.1 |
| 4% Co | 0.48 | 0.73 | 1.25 | - | 2.6 |
| | | | 1.8 | 2.2(2) | 2.9 |
| | | | 3.0 | 2.5(3) | 3.2 |
| Magnetite | 0.42 | 0.36 | 0.90 | - | 1.9 |
| | | | 1.8 | 2.4(2)A | 2.3 |
| | | | 3.0 | 2.2(3)B | 2.4 |
| | | | | - | |

is that H_K 's of different sublattices in the same sample may be distinguished if there is sufficient splitting in the Mössbauer spectrum. Table I shows H_K values for various samples determined at different applied fields for Mössbauer and magnetization measurements. The shape anisotropy fields for the $\gamma\text{-Fe}_2\text{O}_3$ samples are expected to be about 2kOe from electron micrographs. The H_K 's tend to increase with increasing H_a . This is due to the fact that one samples more of the high range of the H_K distribution as H_a is increased. Thus, it is possible to estimate the width of the H_K distribution by evaluating H_K at different H_a .¹¹ Figure 2 shows the fit obtained when the H_K determined from the magnetization data at $M/M_S = .75$ in a transverse field (using Fig. 1 to get H_K), is used to calculate the first quadrant magnetization curve from the Stoner-Wohlfarth formalism. The fit is quite satisfactory even when M_R/M_S is somewhat less than the Stoner-Wohlfarth value of 0.5.

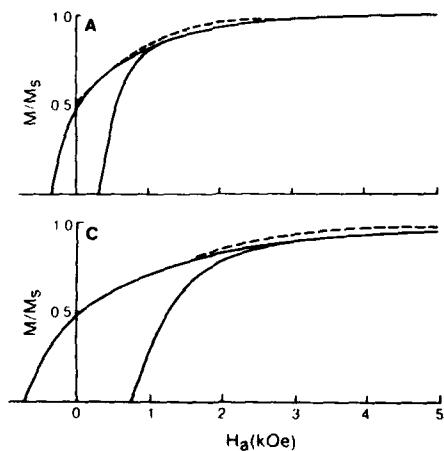


Fig. 2. Experimental magnetization (solid line) vs. applied field for two particle samples (A: large $\gamma\text{-Fe}_2\text{O}_3$; C: 4% Co adsorbed on partially reduced $\gamma\text{-Fe}_2\text{O}_3$). The dashed line shows the first, quadrant data calculated as described in the text and is not shown when it overlaps experimental data. $M/M_S = 1$ at $H_a = 10.6$ kOe. (Ref. 10)

It was noted above that Fig. 1 can be used to determine H_K at different H_a to estimate the width of the H_K distribution. This was done for a series of samples as a function of temperature.¹¹ H_K was determined for $M/M_S = .75$ and $.90$ to sample the "middle and "high" ranges of the H_K distribution. The slope at remanence

$$\chi_g = \Delta\sigma/\Delta H_a|_{H_a \rightarrow 0} = 2/3 (\sigma_s/H_a) \quad (1)$$

was used to sample the low end of the H_K distribution. Eq. (1) follows from the assumption of randomly oriented, non-interacting, identical, single domain particles with uniaxial anisotropy.¹² The temperature dependence of these data was particularly illuminating when examined together with the temperature dependence of M_R/M_S and H_C . It was possible to distinguish a significant superparamagnetic component in passivated Fe particles. The relative contributions of shape and magnetocrystalline anisotropy could also be inferred from these data. The results for Co-surface-treated particles will be discussed below.

A further refinement of the use of first quadrant data was to least squares fit with a complete distribution.¹³ This was done for various samples using log-normal, Gaussian and Lorentzian distributions. The fits for all samples were very good, as shown in Fig. 3. Table II shows

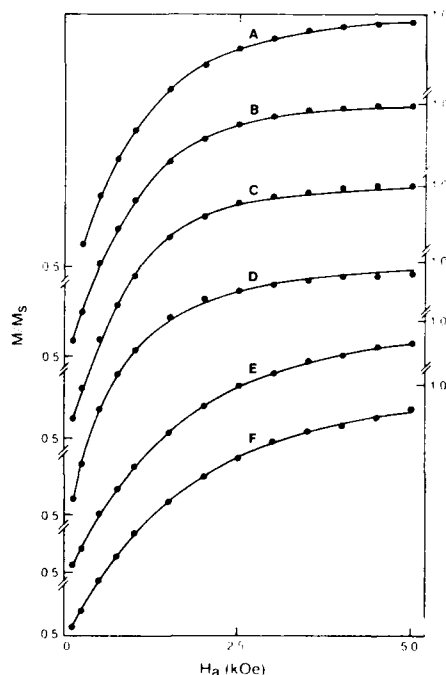


Fig. 3. Log-normal distribution fits (solid lines) to selected data (filled circles) obtained from continuous moment vs. field curves for A: magnetite; B: large γ -Fe₂O₃; C: small γ -Fe₂O₃; D: precursor (reduced γ -Fe₂O₃); E: 4% Co adsorbed on precursor; F: 16% Co adsorbed on precursor. (Ref. 13)

Table II. Best least-squares fit parameters to moment vs. field data for the log-normal distribution. All fields are in kOe, except s, in Oe. The calculations were performed with Oe units. The numbers in parentheses are the statistical standard deviations. (Ref. 11)

| Sample | Log-normal | | Lorentzian | | Gaussian | |
|---|-------------------------|----------|------------|----------|----------|----------|
| | $\langle H_K \rangle_G$ | σ | H_{KC} | Γ | H_{KC} | Γ |
| Magnetite | 1.59(2) | 1.88(3) | 1.41(5) | 1.3(1) | 1.48(6) | 3.1(2) |
| Large γ -Fe ₂ O ₃ | 1.49(4) | 1.54(6) | 1.43(5) | 0.7(1) | 1.54(1) | 1.74(8) |
| Small γ -Fe ₂ O ₃ | 1.40(4) | 1.53(7) | 1.34(3) | 0.6(1) | 1.43(4) | 1.7(1) |
| Precursor | | | | | | |
| (reduced γ -Fe ₂ O ₃) | 1.23(3) | 2.6(1) | 0.91(5) | 1.66(8) | 0.8(3) | 3.8(8) |
| 4% Co | 2.70(2) | 1.92(3) | 2.43(1) | 2.40(6) | 2.65(1) | 4.9(1) |
| 16% Co | 2.93(3) | 1.98(3) | 2.58(5) | 2.7(1) | 2.88(1) | 5.5(2) |

Table III. Model determination of H_C , compared to experimental values. (Ref. 11)

| Sample | Log-Normal | Lorentzian | Gaussian | Experimental |
|--|------------|------------|----------|--------------|
| Magnetite | 530 | 530 | 500 | 360 |
| Large γ -Fe ₂ O ₃ | 550 | 570 | 530 | 330 |
| Small γ -Fe ₂ O ₃ | 520 | 530 | 480 | 330 |
| Precursor (reduced γ -Fe ₂ O ₃) | 350 | 370 | 390 | 310 |
| 4% Co | 900 | 910 | 880 | 730 |

the parameters for the three distributions. The relative FWHM was quite large in all cases. Also, for all except the Co-surface-treated particles, the H_K determined from Fig. 1 at $M_R/M_S = .75$ agreed well with the average value calculated from the full distribution. The distributions were used to calculate H_C 's on the Stoner-Wohlfarth model. Table III gives the results. The values for all distributions are quite similar for each sample. The surprising result is that the calculated H_C is rather close to the measured values. In fact the agreement is probably better than obtained for similar samples by other approaches. This result certainly does not prove that reversal in these systems is by coherent rotation. It simply indicates that when an H_K distribution derived from first quadrant data as described, i.e., folded into the Stoner-Wohlfarth formalism, surprisingly good agreement with measured H_C is produced. The main point demonstrated by this H_K distribution work is that H_K distributions are broad and this breadth dictates H_C as much as does the specific reversal mechanism. Thus, estimates of H_C based on "average" particle dimensions from electron micrographs can be very misleading.

INTRINSIC SURFACE MAGNETIZATION IN γ -Fe₂O₃

It is to be expected that the surface magnetization of γ -Fe₂O₃ and other ferrites with the spinel structure should differ from that of the volume. The different coordination of atoms at the surface should strongly modify the superexchange interaction responsible for the magnetic coupling of the two sublattices present. This expectation was confirmed by the work of Morrish and Haneda.¹⁴ γ -Fe₂O₃ particles are prepared by oxidizing Fe₃O₄ particles at temperatures of order 300°C. Morrish and co-workers adsorbed ⁵⁷Fe, the Mössbauer active isotope, onto the surface of Fe₃O₄ particles and then oxidized them to γ -Fe₂O₃. ⁵⁷Fe is present in natural Fe at about 2% abundance. Thus, by coating the surface of particles with ⁵⁷Fe it is possible to insure that a major fraction of the Mössbauer spectrum represents surface cations. When a Mössbauer spectrum is obtained for a sample magnetically saturated in the direction of the γ -ray emission, the 2nd and 5th lines of the spectrum, representing the $\Delta m = 0$ transition of the split nuclear energy levels, vanish. They found that when a field of 5T was applied at temperatures from 4-300K, a significant fraction of these lines remained, indicating that the surface spins were canted from the applied field direction. It was also observed that phases other than γ -Fe₂O₃, containing Fe and O, were present. Subsequent work by the same group showed that non-enriched γ -Fe₂O₃, as well as other spinel ferrites, showed increased canting as the particle size decreased.¹⁴ This, of course, would be consistent with a surface-spin canting model. It was subsequently suggested¹⁵ that surface spin canting should have an important influence on magnetization reversal in these particles due to the exchange coupling of these surface spins with those in the interior.

Recently we have repeated these experiments.¹⁶ The γ -Fe₂O₃ particles were a standard current commercial grade, average length 2500Å with an aspect ratio of ~8/1. ⁵⁷Fe was adsorbed on the particles' surfaces from solution at 100°C. Two concentrations of ⁵⁷Fe were examined, 2% and 10% of total cation content. Mössbauer data were obtained in fields from 0 to 6T applied collinear with the γ -ray direction at temperatures from 4.2 to 300K. Typical results are shown in Figs. 4 and 5 comparing the standard and ⁵⁷Fe surface enriched samples. No phases other than γ -Fe₂O₃ were found. The $p(H)$ for the standard and surface enriched samples were the same, even though 50% of the spectrum from the 2% ⁵⁷Fe surface enriched sample came from the surface. There is

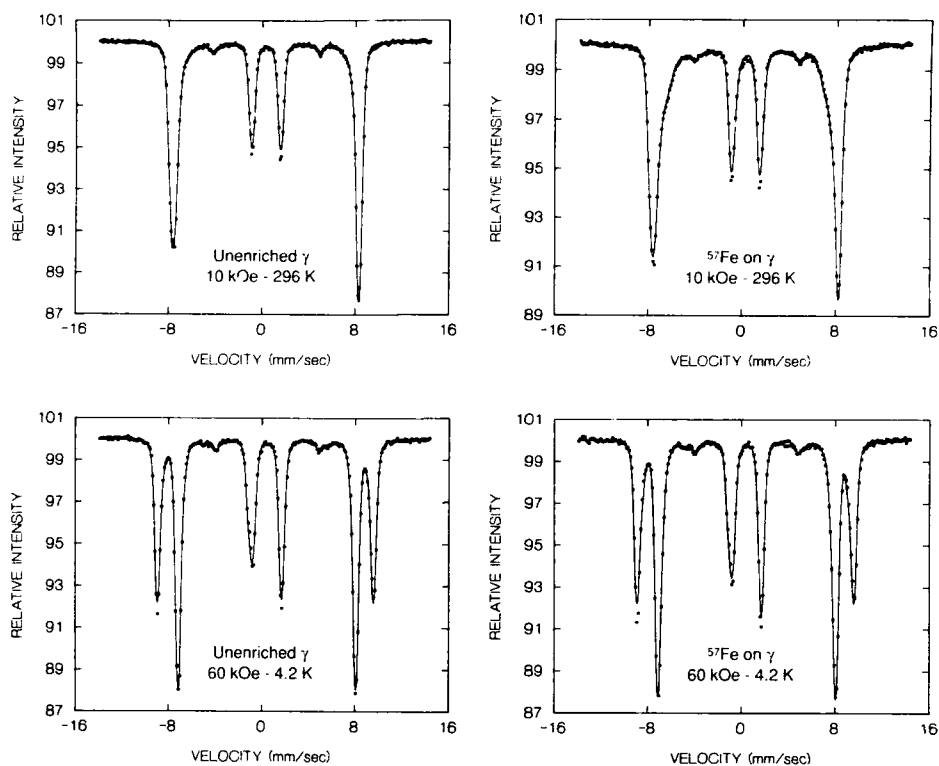


Fig. 4. Mössbauer spectra for untreated $\gamma\text{-Fe}_2\text{O}_3$ and for ^{57}Fe surface enriched $\gamma\text{-Fe}_2\text{O}_3$ obtained at 10 kOe, 296K and at 60 kOe, 4.2K as indicated on figures. Fields applied parallel to γ -ray direction.

a small degree of canting, which is the same in both samples, and increases with decreasing temperature. Therefore, there is no preferential surface spin canting. The difference between our data and the prior work may be that our samples showed no evidence for the presence of very small particles as a result of the ^{57}Fe enrichment process. Small particles noted in the previous samples may have contributed canted spins as a result of the inverse dependence of canting on particle size.¹⁴

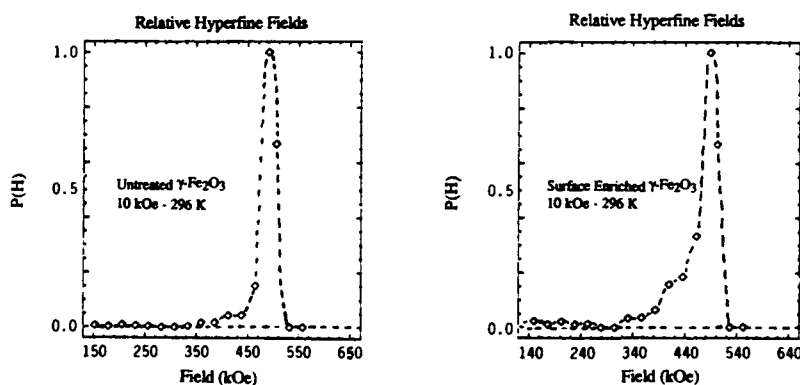


Fig. 5. Hyperfine field distribution $p(H)$, for untreated $\gamma\text{-Fe}_2\text{O}_3$ and for ^{57}Fe surface enriched $\gamma\text{-Fe}_2\text{O}_3$. From data obtained at 296K in field of 10 kOe applied parallel to γ -ray direction.

The only difference between the spectra of the treated and untreated samples was that the ^{57}Fe surface treated samples showed a small degree of tailing of the outer lines toward smaller hyperfine fields. This tailing amounted to about 5% of the area of the hyperfine field distribution at 300K. There was no difference at 4.2K. In view of the expectation that there should be some type of magnetization difference at the particles' surfaces, it is tempting to ascribe this temperature dependent tailing to weaker surface hyperfine fields. Thus, even though the surface and interior spins have the same T_c , the surface magnetization decreases at a faster rate due to weaker exchange. If this is indeed the case, we would expect the crystalline anisotropy at the surface to be weaker. This could have important consequences for initiating magnetization reversal at the surface of the particles. At present, this is conjecture. It may be that the tailing simply accompanies the small volume canting observed. It may be possible to resolve this question with Mössbauer measurements on surface enriched films.

ENHANCED ANISOTROPY BY SURFACE TREATMENT

There have been several examples reported in which the net anisotropy of fine particles has been enhanced by surface treatment with inorganic or organic compounds. Due to the extreme difficulty in characterizing the chemical and microstructural details of the surfaces of assemblies of particles with dimensions $< 10^3\text{\AA}$, reliable models of the origin of the increased anisotropy have not been produced. Aside from the general interest in these problems as examples of current investigations of surface sensitive properties, there is a strong technological motive. One of the most widely used particulate media in high density magnetic recording is Co-surface-treated Fe oxide.¹⁷ Thus, an increased understanding of the mechanisms for enhancing surface anisotropy can have important technological benefits for both particulate and film recording media.¹⁸

Co-Surface-Treated Fe-Oxide: There are two varieties of these particles. In one, the precursor is $\gamma\text{-Fe}_2\text{O}_3$ and the surfaces are treated with both Co^{2+} and Fe^{2+} ions. In the other case, which we will discuss, the precursor is a reduced $\gamma\text{-Fe}_2\text{O}_3$ which contains $\approx 10\text{-}15\%$ Fe^{2+} ions and the surface is treated from solution only with Co^{2+} ions.¹⁷ The surface treatment essentially consists of precipitating Co out of solution onto the precursor particles at a low enough temperature ($\sim 100^\circ\text{C}$) to preclude substantial diffusion of the Co into the particles' interiors. Co in the particle volume increases H_c , but with a strong temperature dependence and a loss of uniaxial anisotropy. Both these latter features minimize the suitability of these particles for recording media. When the Co is confined to the particle surface in the amount of $\sim 4\%$ of total cation content, H_c increases from about 325 Oe to ~ 750 Oe, temperature dependence of H_c is not much larger than that of pure $\gamma\text{-Fe}_2\text{O}_3$, and the uniaxial character is essentially maintained at room temperature. The question is "How does this H_c increase arise from the Co-surface-treatment?" Two principal possibilities exist. First, Co^{2+} has a large single ion anisotropy.¹⁹ Thus, it is quite reasonable to assume that the exchange coupling of the Co^{2+} to the nearest neighbor Fe ions exerts a "drag" on the spins when magnetization is reversed, increasing H_c . This could increase H_c no matter whether the spin configuration is coherent or heterogeneous during reversal. Aharoni²⁰ has discussed a special case of this mechanism. Some difficulties with this mechanism are the lack of significant temperature dependence for H_c and the apparent retention of uniaxial anisotropy. The other possibility is that there are low energy sites on the particles surfaces where reversal initiates in a heterogeneous manner. The Co^{2+} increases the anisotropy of these sites and makes for higher nucleation fields for reversal in a cooperative mode. The low temperature dependence is again a problem here. We have examined a series of Co-surface-treated Fe-oxides containing 4, 8 and 16% Co with high resolution transmission electron microscopy, Mössbauer measurements, magnetization and x-ray measurements. The results were:

- (1) The Co-containing layer is epitaxial.¹⁷
- (2) Only a fraction of a monolayer of Co produces the maximum H_c .
- (3) The symmetry of the enhanced anisotropy is not uniaxial at low temperatures.¹¹

- (4) The normalized temperature dependence of the enhanced anisotropy is essentially the same as that of the precursor.¹¹ Since the temperature dependence of the precursor anisotropy principally arises from Fe^{2+} , it is likely that Co^{2+} replaces Fe^{2+} on the surface.
- (5) When the first quadrant magnetization data are fit,¹³ the H_K distribution is rather wide, but the Stoner-Wohlfarth H_C calculated from this distribution is in excellent agreement with the measured value. Probably, this agreement is a consequence of the wide H_K distribution.
- (6) Analysis of Mössbauer measurements on a Co-treated, ^{57}Fe surface enriched sample show that the surface spins are not rigidly pinned even in a relatively weak (1.8 kOe) field.²¹

We are still trying to establish whether the low hyperfine field tailing is reduced with Co-surface treatment. If so, it would point to an effective increase of exchange field at the surface Fe sites, thus supporting the model whereby reversal is initiated at surface sites because of weaker exchange. This may be resolved by temperature dependent Mössbauer data which are now being collected. Generally, then, the basic mechanism of anisotropy enhancement by Co-surface treatment of reduced $\gamma\text{-Fe}_2\text{O}_3$ is still not clear. However, it seems likely that a simple model of a "Co-ferrite shell" is not suitable.

H_C Enhancement by Sodium Metaphosphate Surface Treatment: There have been several reports^{22,23} that surface treatment of partially reduced $\gamma\text{-Fe}_2\text{O}_3$ with $(\text{NaPO}_3)_n$ can produce remarkably high H_C , up to 2500 Oe. Furthermore, the $\text{Na}(\text{PO}_3)_n$ could be washed off in water with a reversion of H_C to its precursor value, ~400 Oe. We are attempting²⁴ to reproduce these fascinating results with a modest amount of success thus far. We used particles of average size 0.6 μm long x 0.1 μm dia., of composition $(\gamma\text{-Fe}_2\text{O}_3)_{0.73}(\text{Fe}_3\text{O}_4)_{0.27}$ with an initial H_C of 440 Oe. We find a rather narrow "window" for H_C enhancement using an alkaline 0.25M $(\text{NaPO}_3)_6$ solution. When the $(\text{NaPO}_3)_6/\text{Fe}$ oxide ratio is 0.2, H_C increases to 580 Oe. When the ratio is 0.1, H_C increases to 680 Oe. There is no increase when the ratio is ≥ 0.5 . When exposed to air, H_C of the treated particles slowly decreases, in agreement with the previous work. Most likely, this decrease results from hydrolysis of the additive. It also seems likely that the $(\text{NaPO}_3)_6$ ring must be broken by hydrolysis in order to effect an H_C increase. Much more structural and Mössbauer work (with ^{57}Fe enriched surfaces) must be done in order to begin to model this behavior. Polymeric polyphosphate chains will also be used. Obviously, an unstable H_C has little technological interest, but understanding the phenomenon could certainly lead to the development of compounds producing stable anisotropy enhancement.

Surface Treatment with Organics: In an earlier study,^{25,26} it was determined that particles of ferrite spinels such as NiFe_2O_4 , $\text{Ni}_x\text{Zn}_{(1-x)}\text{Fe}_2\text{O}_4$, and CoFe_2O_4 showed highly anomalous properties when coated with strongly bonded organic surfactants such as oleic acid. These properties included H_C values that were much larger than expected from intrinsic magnetic properties, shifted loops when field cooled, and a large fraction of magnetically ordered spins that were not collinear with fields as high as 12T. This behavior disappeared when the organic coating was removed by gentle heating. These particles were coated by grinding them in a carrier liquid in which the surfactant was dissolved. Thus, the surfactant was bonded to essentially virgin cleaned surfaces. This produced extremely strong bonds that could not be broken by any chemical means. This strong bonding to fresh surfaces was essential to produce the observed behavior. We and other investigators¹⁴ noted that when spinel particles were prepared and then treated with the surfactants, the effects were very much weaker. However, since the particles were produced by grinding, there was the possibility that particle defects were responsible for the anomalous magnetic behavior. Recent high resolution TEM and other structural work²⁷ has demonstrated that these particles are single crystals. Therefore the anomalous properties arises from surface, not volume, origins. This has encouraged us to continue examination of organic coatings for H_C enhancement. This will likely emphasize thin film work to minimize characterization problems with particles.

PARTICLE INTERACTIONS IN GRANULAR FILMS

Granular films are prepared by co-sputtering a metal and an insulator such as SiO_2 or Al_2O_3 . The resulting film consists of metal particles or particle clusters in an insulating matrix. The sizes of the particles increase with increasing metal/insulator concentration and with substrate temperature. Investigation of these films was initiated in the 1960's by Abeles and co-workers.²⁸ They established that below about 50% metal, the films' conductivity could be described by a tunneling or electron hopping mechanism among non-connected particles or clusters. Above 50% metal concentration, percolation of the metal particles or clusters resulted in a metallic conductivity. Recently, Chien and co-workers²⁹ have reported extensively on the magnetic properties of Fe/SiO_2 granular films prepared by sputtering from composite Fe/SiO_2 sources. Their Fe particles had diameters ranging from 40-60Å, increasing with Fe concentration. Most interesting was their finding of a strongly temperature dependent H_C which reached a maximum value just below percolation at about 50% Fe. The maximum H_C at 4.2K was 2500 Oe and dropped to 500 Oe at 90K. These films were sputtered at 20°C. When the substrate temperature was raised to 500°C,³⁰ the Fe particles had diameters of order 100Å, and $H_C(4.2) = 3000$ and $H_C(290) = 1000$ Oe. These H_C values together with the decreased temperature dependence indicated a possible potential for magnetic recording substrates. It seems likely from this work and similar investigations³¹ that the H_C values arise from clustering of the Fe particles which rises to a maximum just before percolation, e.g., shape anisotropy is involved. In the low Fe non-percolating concentrations, the granular films' behavior was similar to that of superparamagnetic assemblies of particles.

We have prepared Fe-SiO_2 granular films by sputtering slowly (~0.3Å/s) from separate Fe and SiO_2 sources as the substrates rotated above each source in turn.^{32,33} The substrates were Si wafers with ~350Å



Fig. 6. Bright field micrograph of cross-section of 19 vol. % Fe sample. Note that thickness of sample increases from top to bottom of micrograph.

surface layer of amorphous silicon nitride. "Windows" of silicon nitride were provided in the substrates by selectively etching the Si. Thus TEM could be performed on the same substrates used for the magnetic measurements. Films below 33% Fe were non-percolating as determined from a negative temperature coefficient of resistance and from high resolution TEM both of planar and cross-section views. Fig. 6 shows an example of a cross-section view. The particles appear to be well dispersed with a rather uniform particle diameter of about 40Å. Average particle spacing is about 80Å center-to-center. This finding confirms previous work by Logothetis, et al.³⁴ who concluded that granular films prepared from dual substrates consisted of well-dispersed, relatively uniform sized particles. They further demonstrated that particle size could be controlled more or less independently of metal concentration by adjusting the rate at which the substrates passed over the targets. The magnetic properties of our Fe-SiO₂ granular films differed significantly from those prepared from composite targets at fast sputtering rates. Fig. 7 shows the temperature dependence of H_C for various compositions. Although H_C is strongly temperature dependent as in the films prepared from composite targets, the other magnetic properties were quite different. The maximum H_C occurs at a lower % Fe. The value of the maximum H_C at 4.2K is much lower. The hysteresis loops were very square, as shown in Fig. 8 with sharp reversal and high remanence ratios; this was the case at all temperatures from 4.2→290K. Finally, Fig. 9 shows a Lorentz TEM taken at 290K. Large domains are visible with clear ripple patterns. The domain pattern shifted as expected as the in-plane field was changed. All these features are consistent with a long-range ordered magnetic film, not an assembly of dispersed 40Å Fe particles. A 40Å Fe particle would have a blocking temperature of 4.6K using the Néel relation¹

$$1 < \ln(2t'f_0) \quad 2kT/VM_S H_K$$

taking $t' = 100$ sec measuring time, $f_0 = 10^9$ sec⁻¹, and H_K determined from the magnetocrystalline anisotropy of Fe. This blocking temperature would seem to account for the steep H_C decrease above 4.2. One can account for the value of H_C at 4.2K arising primarily from the magnetocrystalline anisotropy energy of an assembly of randomly oriented single domain Fe particles¹

$$H_C = .64K/M, = 188 \text{ Oe}$$

The larger measured value could arise from a Lorentz field of $\approx 10^3$ Oe produced by oriented 40Å Fe particles on an fcc lattice. This would enhance H_C. However, the behavior at high temperatures, particularly at 290K, is very puzzling. These films are composed of well dispersed

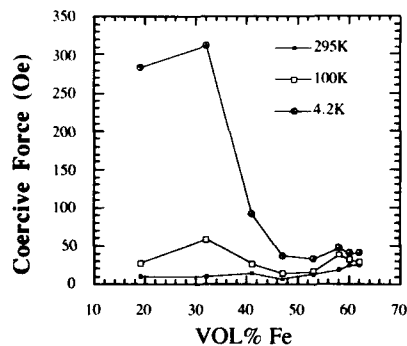


Fig. 7. Coercive force as a function of Fe concentration at 295K, 100K and 4.2K. Samples on nitrided Si. (Ref. 32)

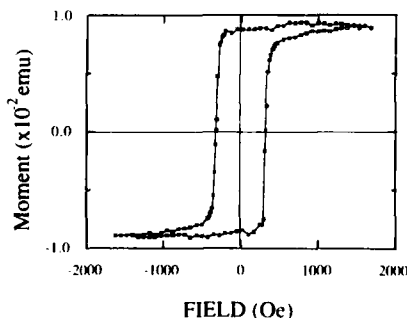


Fig. 8. Hysteresis loop for the 32 vol % Fe sample taken at 4.2K. Sample on nitrided Si. (Ref. 32)

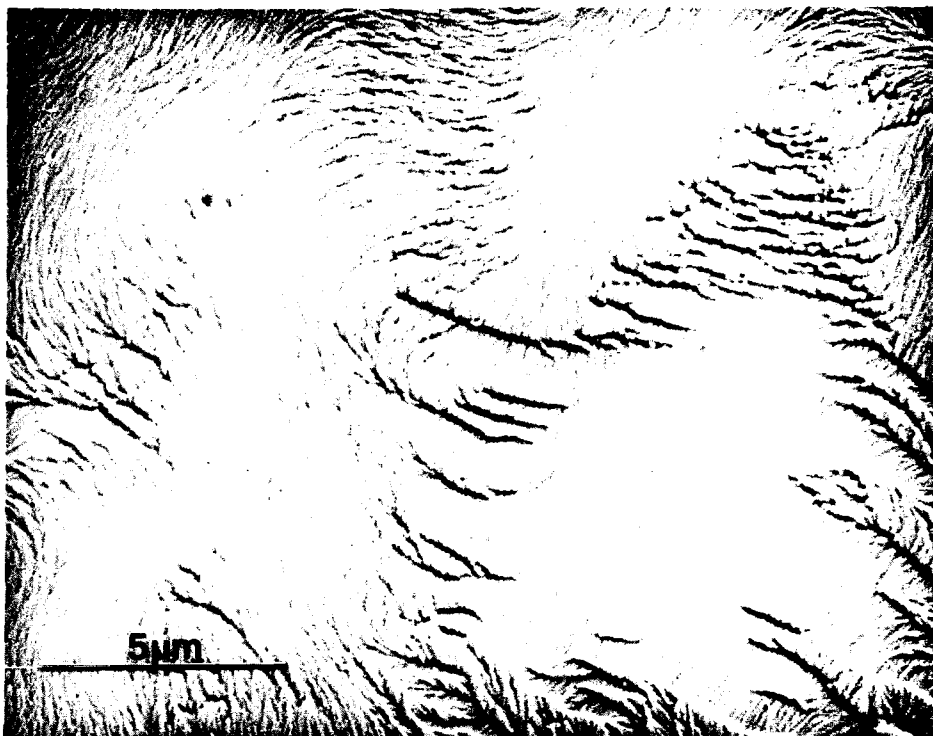


Fig. 9. Lorentz micrograph of the 19 vol. % Fe sample on Si nitride membrane. Ripple structure of large oppositely magnetized domains is visible. (Ref. 32)

particles almost 300K above their blocking temperature. What interaction is responsible for the highly ordered square loop behavior? At 290K, these particles should have a relaxation time $< 10^{-9}$ sec if magnetocrystalline anisotropy dominates. Thus they should appear superparamagnetic even in Mössbauer spectra; they do not. The Mössbauer spectrum shows sharp lines for virtually pure Fe. A hint of a possible explanation may arise from the following energy considerations:

$$H_{\text{dipolar}} < 2 \times 10^3 \text{ Oe. } \therefore E_{\text{dipolar}} \leq -m \cdot H \approx 1.1 \times 10^{-13} \text{ ergs}$$

$$\text{at } 4.2\text{K, } kT = 5.9 \times 10^{-16} \text{ ergs; at } 300\text{K, } kT = 4.2 \times 10^{-14} \text{ ergs}$$

Therefore, at 300K, $E_{\text{dipolar}} / E_{kt} \sim 3$

Thus a metastable ordered state at 290K may exist. Obviously, a great deal more investigation is required to make a meaningful estimate of the origin and magnitude of the interactions among these Fe particles in granular films.

SUMMARY AND CONCLUSIONS

A few topics in fine particle magnetism have been discussed. For the most part, they illustrate the dominance of fine microstructural features in determining magnetic behavior of individual particles. The distribution of properties among particles in an assembly obviously determines the behavior of the system, and simple means for estimating the distribution of H_K were discussed. Intrinsic surface properties can differ from the bulk and it is possible that they strongly influence magnetic reversal. Surface properties can also be altered by various treatments, resulting in enhanced anisotropy. However, the mechanisms of surface anisotropy enhancement are still unknown due to the difficulty in characterizing particles' surfaces. Finally, remarkable interactions among dispersed nominally superparamagnetic Fe particles in a SiO_2 matrix produce a surprising strong long range order which has to be explained.

ACKNOWLEDGMENTS

All of the work described above was performed by a number of colleagues whose skill and wisdom are greatly appreciated. In particular, we thank M. Carey, P. J. Flanders, M. Foster, E. L. Hall, C. Leroux, D. Margulies, F. T. Parker, G. Podolsky, and S. Slade. Much of this work was supported under contract NSF-DMR-87-07421.

REFERENCES

- 1) For a review, see E. Kneller in "Magnetism and Metallurgy," eds. A. E. Berkowitz and E. Kneller (Academic Press, 1969), Vol. 1, Chap. 8.
- 2) A. E. Berkowitz, R. P. Goehner, E. L. Hall and P. J. Flanders, J. Appl. Phys. **57**, 3928 (1985).
- 3) A. E. Berkowitz, E. L. Hall and P. J. Flanders, IEEE Trans. Magn. **23**, 3816 (1987).
- 4) E. L. Hall and A. E. Berkowitz, J. Mater. Res. **1**, 836 (1986).
- 5) J. E. Knowles, IEEE Trans. Magn. **17**, 3008 (1981).
- 6) J. E. Knowles, IEEE Trans. Magn. **20**, 84 (1984).
- 7) M. Shabes and H. N. Bertram, J. Appl. Phys. **64**, 1347 (1988).
- 8) Y. D. Yan and E. Della Torre, J. Appl. Phys. **66**, 320 (1989).
- 9) D. R. Fredkin and T. R. Koehler, J. Appl. Phys. **67**, 5544 (1990).
- 10) F. T. Parker and A. E. Berkowitz, IEEE Trans. Magn., **25**, 3647 (1989).
- 11) A. E. Berkowitz, F. T. Parker, S. B. Slade and G. Podolsky, J. Appl. Phys., **67**, 5155 (1990).
- 12) E. C. Stoner and E. P. Wohlfarth, Proc. Roy. Soc. (London), **A240**, 599 (1948).
- 13) F. T. Parker and A. E. Berkowitz, J. Appl. Phys., **67**, 5158 (1990).
- 14) A. H. Morrish and K. Haneda, J. Magn. Magn. Mat., **35**, 105 (1983).
- 15) A. E. Berkowitz, IEEE Trans. Magn., **22**, 466 (1986).
- 16) F. T. Parker, M. W. Foster, D. Margulies and A. E. Berkowitz, submitted to the 35th M³ Conference, San Diego, Nov. 1990.
- 17) A. E. Berkowitz, F. T. Parker, E. L. Hall and G. Podolsky, IEEE Trans. Magn., **24**, 2871 (1988).
- 18) A. E. Berkowitz and R. M. White, Mater. Sci. and Eng., **B3**, 413 (1989).
- 19) J. C. Slonczewski, Phys. Rev., **110**, 1341 (1958).
- 20) A. Aharoni, J. Appl. Phys., **63**, 4605 (1988).
- 21) F. T. Parker and A. E. Berkowitz, submitted to the 35th M³ Conference, San Diego, Nov. 1990.
- 22) F. Itoh, M. Satou and Y. Yamazaki, IEEE Trans. Magn., **13**, 1385 (1977).
- 23) F. Itoh and M. Satou, Japan. J. Appl. Phys., **14**, 2091 (1975).
- 24) F. E. Spada and A. E. Berkowitz, submitted to the 35th M³ Conference, San Diego, Nov. 1990.
- 25) A. E. Berkowitz, J. A. Lahut, I. S. Jacobs, L. M. Levinson, and D. W. Forester, Phys. Rev. Lett., **34**, 594 (1975).
- 26) A. E. Berkowitz, J. A. Lahut and C. E. VanBuren, IEEE Trans. Magn., **16**, 184 (1980).
- 27) A. C. Nunes, E. L. Hall and A. E. Berkowitz, J. Appl. Phys. **63**, 5181 (1988).
- 28) B. Abeles, P. Sheng, M. D. Coatts and Y. Arie Adv. Phys. **24**, 407 (1975). C. L. Chien, G. Xiao, S. H. Liou, J. N. Taylor, and A. Levy, J. Appl. Phys. **61**, 3311 (1987).
- 29) G. Xiao and C. L. Chien, Appl. Phys. Lett. **51**, 1280 (1987).
- 30) S. H. Lion, C. H. Chen, H. S. Chen, A. R. Kortan and C. L. Chien, Mat. Res. Soc. Symp. Proc. **132**, 191 (1989).
- 31) R. L. Holtz, P. Lubitz, and A. S. Edelstein, Appl. Phys. Lett. **56**, 943 (1990).
- 32) M. J. Carey and A. E. Berkowitz, Paper S8.17, MRS Spring Meeting, San Francisco, April 1990.
- 33) M. J. Carey, F. T. Parker and A. E. Berkowitz, submitted to the 35th M³ Conference, San Diego, Nov. 1990.
- 34) E. M. Logothetis, W. J. Kaiser, H. K. Plummer and S. S. Shinozaki, J. Appl. Phys. **60**, 2548 (1986).

MÖSSBAUER STUDIES OF FINE Fe-BASED PARTICLES

Steen Mørup

Laboratory of Applied Physics
Technical University of Denmark
DK-2800 Lyngby, Denmark

INTRODUCTION

Mössbauer spectroscopy is a technique which gives many different types of information about the nearest environments of nuclei in solids. The isomer shift is related to the electron density at the nuclei, the quadrupole splitting is proportional to the electrical field gradient and the magnetic hyperfine splitting is proportional to the total magnetic field at the nucleus. Moreover, the temperature dependence of the spectral area gives information about the vibrational amplitude of the atoms. Thus a Mössbauer spectrum elucidates the valence state of the atoms, the local symmetry, the magnetic properties and the lattice vibrations.

It is noticeable that the information obtained from a Mössbauer spectrum is not an average over all atoms, but atoms in different environments give separate contributions to the spectrum. Therefore it is often possible in studies of ultrafine particles to distinguish surface atoms from atoms in the interior of the particles. Another advantage of Mössbauer spectroscopy in studies of fine particles is that it is well suited for *in situ* studies, i.e. studies of the samples in a desired gas or gas mixture. This makes the technique very useful for studies of catalysts, but also for studies of other microcrystalline materials because small particles of, for example, metals and alloys are often very reactive and easily oxidize when exposed to air.

In studies of ultrafine magnetic particles it is of particular interest that Mössbauer spectroscopy is very sensitive to superparamagnetic relaxation phenomena. This short review will mainly focus on these effects, which will be illustrated by measurements of small iron-containing particles in mercury. More comprehensive reviews of Mössbauer studies of small particles have been published elsewhere ¹⁻⁴.

STUDIES OF ULTRAFINE MAGNETIC PARTICLES

A unique feature of ultrafine magnetic particles is that the magnetization direction is not fixed as in large crystals, but fluctuates spontaneously. This is due to the fact that the magnetic anisotropy energy is proportional to the particle volume, and for very small particles it may therefore be comparable to the thermal energy even below room temperature. For a particle with uniaxial anisotropy the energy is given by:

$$E(\Theta) = KV \sin^2\Theta \quad (1)$$

where K is the magnetic anisotropy energy constant, V is the volume, and Θ is the angle between the magnetization vector and the easy direction of magnetization. According to Eq. (1) the two energy minima at $\Theta = 0$ and $\Theta = \pi$ are separated by an energy barrier with the height KV .

The superparamagnetic relaxation frequency, τ^{-1} , i.e. the rate at which the magnetization vector passes the energy barrier is given by ^{1,2,3,5}:

$$\tau = \tau_0 \exp \left\{ \frac{KV}{kT} \right\} \quad (2)$$

where τ_0 is of the order of 10^{-10} – 10^{-12} s and depends little on temperature. T is the temperature and k is Boltzmann's constant.

The Mössbauer spectrum is very sensitive to the superparamagnetic relaxation time, τ . In the case of ^{57}Fe Mössbauer spectroscopy the spectrum consists of six lines when the relaxation time is long compared to the Larmor precession time of the nucleus ($\approx 10^{-8}$ – 10^{-9} s). For very short relaxation times the magnetic hyperfine splitting collapses and the spectrum then consists of one or two lines. When the relaxation time is comparable to the nuclear Larmor precession time the spectrum consist of broadened lines. Thus, according to Eq. (2) the Mössbauer spectrum of a sample of ultrafine particles may change drastically as a function of temperature.

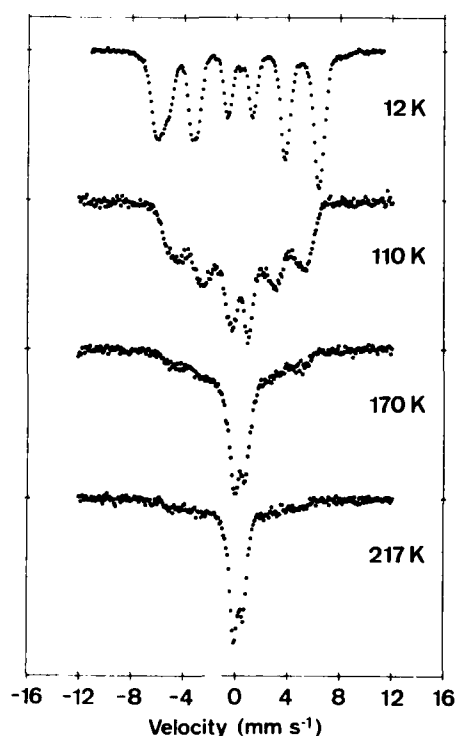


Figure 1. Mössbauer spectra of iron-containing particles in mercury at various temperatures. (Ref. 8)

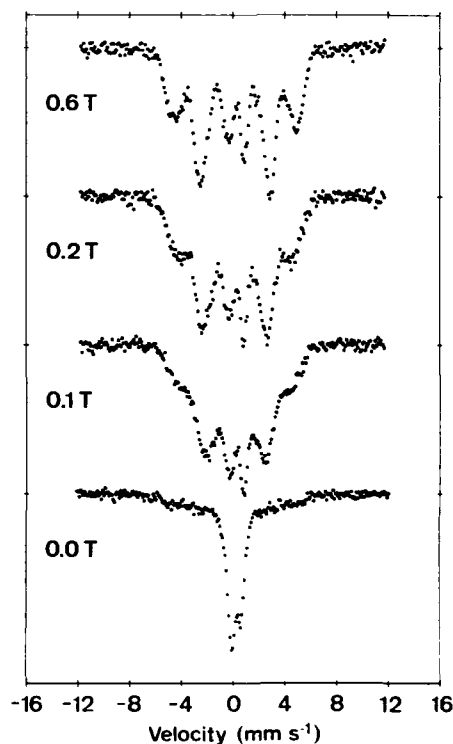


Figure 2. Mössbauer spectra of iron-containing particles in mercury at 217 K at various applied magnetic fields. (Ref. 8)

As an example, Figure 1 shows Mössbauer spectra of iron-containing particles in mercury at different temperatures. The sample was prepared by electrolytic deposition of ^{57}Fe in a mercury cathode ^{7,8}. A drop of the iron-containing mercury was pressed to a thin film which was frozen in liquid nitrogen and used as a Mössbauer absorber. At 12 K the spectrum is magnetically split indicating a long relaxation time. At higher temperatures the lines become broadened and at 217 K the magnetic hyperfine splitting has collapsed indicating that $\tau < 10^{-9}$ s at this temperature. In the intermediate range the spectra contain both a magnetically split component and a collapsed component indicating a distribution in relaxation times. This is a very typical feature of Mössbauer spectra of ultrafine magnetic particles and reflects the distribution in particles size in the sample.

Before these Mössbauer measurements were carried out it was believed that such particles of iron in mercury consist of $\alpha\text{-Fe}$. However, the spectrum obtained at 12 K shows a significantly larger magnetic hyperfine field ($\sim 38\text{--}40$ T) than $\alpha\text{-Fe}$ (~ 34 T). Moreover, the spectrum is asymmetric (e.g. line no. 1 is broader than line no. 6) indicating that iron atoms are present in more than one type of environments. These results suggest that the iron atoms are present in a (metastable) iron-mercury alloy. This conclusion illustrates how Mössbauer spectroscopy can give information about the structure of small particles that may be difficult to characterize by other techniques. At 12 K application of a magnetic field of 4 T parallel to the gamma ray direction led to the disappearance of lines no 2 and 5. This indicates that the material is ferromagnetic.

The collapse of the magnetic hyperfine splitting with increasing temperature, illustrated in Figure 1, might be explained by a low Curie temperature of the Fe-Hg alloy. However, studies of the magnetic field dependence of the spectra make it possible to distinguish between superparamagnetic behaviour and a transition from a magnetically ordered state to a paramagnetic state. This is because the spectrum of a paramagnetic material above 80 K is only little affected by small external magnetic fields whereas such fields induce a substantial magnetic hyperfine splitting in the spectra of small ferromagnetic particles which exhibit fast superparamagnetic relaxation.

The magnetic energy due to the interaction of a small ferromagnetic particle with an external magnetic field, \vec{B} , is given by:

$$E = -\vec{\mu} \cdot \vec{B} \quad (3)$$

where $\vec{\mu}$ is the magnetic moment of the particle. For moderate external magnetic fields ($B \gtrsim 0.1$ T) μB is often large compared to kT and therefore the magnetic anisotropy energy can normally be neglected⁹. The average magnetization of a superparamagnetic particle is then proportional to the Langevin function:

$$L(\mu B/kT) = \coth(\mu B/kT) - kT/\mu B \quad (4)$$

and the total observed magnetic field at the nucleus is given by:

$$\vec{B}_{\text{obs}} = \vec{B}_0 L\left(\frac{\mu B}{kT}\right) + \vec{B} \quad (5)$$

where \vec{B}_0 is the saturation hyperfine field. The magnetic moment is typically of the order of $10^3\text{--}10^5$ Bohr magnetons and therefore the sample is nearly magnetically saturated even in an external field of the order of 1 T at room temperature.

For applied fields $B > 2kT/\mu$ one can use the approximation ^{1,2,3,9}:

$$L\left(\frac{\mu B}{kT}\right) \approx 1 - \frac{kT}{\mu B} \quad (6)$$

and one then finds the induced magnetic hyperfine field:

$$\begin{aligned} \vec{B}_{\text{ind}} &= \vec{B}_{\text{obs}} - \vec{B} \\ &\approx \vec{B}_0 \left[1 - \frac{kT}{\mu B} \right] \end{aligned} \quad (7)$$

Thus a plot of B_{ind} as a function of B^{-1} should give a straight line with slope $B_0 kT/\mu$ from which B_0 and μ can be estimated^{1,2,3}.

Figure 2 shows spectra of the iron-mercury sample at 217 K in various applied magnetic fields. It is clearly seen that a substantial magnetic splitting is induced by application of relatively small external fields. This gives evidence for the presence of

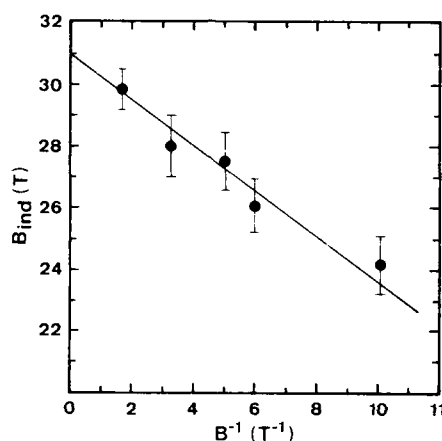


Figure 3. A plot of the induced hyperfine field as a function of the reciprocal applied magnetic field obtained from the spectra at 217 K shown in Fig. 2.

small superparamagnetic particles in the sample. Figure 3 shows a plot of B_{ind} as a function of B^{-1} . From the fit of the results with a straight line (in accordance with Eq. (7)) we find $B_0 = 31 \pm 1$ T and $\mu = (1.8 \pm 0.4) \cdot 10^{-19}$ JT⁻¹. The value of B_0 is smaller than that for α -Fe at 217 K (≈ 33 T). Thus the saturation hyperfine field decreases more rapidly with increasing temperature than in α -Fe. This indicates that the alloy has a lower Curie temperature than α -Fe. If the iron atoms are assumed to possess a magnetic moment of about 2 Bohr magnetons the value of μ corresponds to about 10000 iron atoms per particle. If these iron atoms were present in α -Fe this would correspond to a particle size of the order of 6 nm. However, since the particles also contain Hg the present particles must be larger than 6 nm.

Below the temperature, at which the spectrum becomes magnetically split (the so-called blocking temperature) the magnetic hyperfine splitting in the spectrum of a sample of ultrafine particles is affected by collective magnetic excitations, i.e. fluctuations of the magnetization vector in directions close to an easy direction of magnetization. It can be shown that these fluctuations lead to an observed magnetic hyperfine field at the nucleus is given by^{1,2,3,6,10}:

$$B_{\text{obs}} \approx B_0 \left(1 - \frac{kT}{2KV} \right) \quad (8)$$

This reduction in the magnetic hyperfine splitting relative to B_0 as well as the influ-

ence of superparamagnetic relaxation in the vicinity of the blocking temperature depend on the value of the energy barrier, KV . Thus the energy barrier, KV , can be determined from either the influence of superparamagnetic relaxation or collective magnetic excitations on the Mössbauer spectra. If the saturation magnetization, M , of the material is known the particle volume, $V = \mu/M$, can be determined from the magnetic field dependence of the spectra above the blocking temperature, and the value of the magnetic anisotropy energy constant can then be calculated.

In the above discussion it has been assumed that the magnetic interaction between the particles is negligible. Often this is not the case. In fact a strong magnetic interaction can result in an ordering of the magnetic moments of small particles which otherwise would have been superparamagnetic. This phenomenon is called superferromagnetism¹¹. The temperature dependence of the average magnetization of a system of interacting particles has been calculated using a modified Weiss molecular field theory^{4,6,11}. Below a certain temperature, T_p , the magnetic interaction between the particles leads to ordering of the magnetic moments. Above T_p the particles are superparamagnetic. If the relaxation is fast, the magnetic hyperfine splitting in the Mössbauer spectrum is proportional to the average magnetization, $\langle M \rangle$. The reduced magnetization, $b(T) = \langle M \rangle / M$, can be calculated from the equation:

$$b(T) = L \left\{ \frac{3T_p}{T} \left[\frac{B_0(T)}{B_0(T_p)} \right]^2 b(T) \right\} \quad (9)$$

This model has been applied to explain the magnetic behaviour of interacting particles of goethite (α -FeOOH)¹¹.

In the case of iron-containing particles in mercury it has been found, that if the particles are concentrated by application of a strong magnetic field gradient at room temperature and subsequently frozen, the spectrum is magnetically split at 217 K. This result shows that the particles have agglomerated and form a superferromagnetic state.

CONCLUSIONS

The examples discussed above illustrate that Mössbauer spectroscopy is a very useful technique for studies of the magnetic properties of ultrafine particles. From the temperature dependence of the spectra the value of the energy barrier, KV , can be determined, and from the magnetic field dependence of the spectra above the blocking temperature the magnetic moment of the particles can be calculated. If the magnetic interaction between the particles is significant this can also be elucidated by Mössbauer spectroscopy studies. Moreover, information about the structure of the particles and the valence state of the atoms can be obtained. In several cases it has also been shown that the magnetic properties of surface atoms can be studied.

Mössbauer spectroscopy is thus one of the most powerful techniques that can be applied for studies of ultrafine iron-containing particles, and it has been successfully used for numerous studies of small particles in catalysts, soils, biological materials, ferrofluids, magnetic tapes etc.

REFERENCES

1. S. Mørup, J.A. Dumesic, and H. Topsøe, in "Applications of Mössbauer Spectroscopy", Vol II, Ed. R.L. Cohen (Academic Press, New York, 1980), p. 1.
2. S. Mørup, H. Topsøe, and B.S. Clausen, *Phys. Scripta* 25, 713 (1982).
3. S. Mørup, in "Mössbauer Spectroscopy Applied to Inorganic Chemistry", Vol. II, ed. G.J. Long (Plenum Press, New York, 1987), p. 89.
4. S. Mørup, *Hyp. Int.* (in press).
5. L. Néel, *Ann. Geophys.* 5, 99 (1949).

6. S. Mørup, J. Magn. Magn. Mater. 37, 39 (1983).
7. J. van Wonerghem, S. Mørup, S.W. Charles, and S. Wells, J. Magn. Magn. Mater. 65, 276 (1987).
8. S. Linderøth, S. Mørup, A. Meagher, S. Wells, J. van Wonerghem, H.K. Rasmussen, and S.W. Charles, J. de Physique 49, C8-1827 (1988).
9. S. Mørup, P.H. Christensen, and B.S. Clausen, J. Magn. Magn. Mater. 68, 160 (1987).
10. S. Mørup and H. Topsøe, Appl. Phys. 11, 63 (1976).
11. S. Mørup, M.B. Madsen, J. Franck, J. Villadsen, and C.J.W. Koch, J. Magn. Magn. Mater. 40, 163 (1983).

MÖSSBAUER STUDIES OF FINE PARTICLES OF Fe-Cr-B

A. Kostikas¹ V. Papaefthymiou² A. Simopoulos¹,
Y.P. Li³ and G.C. Hadjipanayis³

¹NCSR "Demokritos", 153 10 Ag. Paraskevi, Greece

²Physics Department, University of Ioannina
Greece

³Department of Physics and Astronomy, University
of Delaware

INTRODUCTION

The magnetic properties of fine metallic particles have been extensively investigated during the last decade [1,2,3]. The interest in this subject has both fundamental and technological aspects. Magnetic metallic particles with dimensions of 5 to 50 nm are predominantly single domain ferromagnetic particles with characteristic magnetic properties as e.g. saturation magnetization and magnetic anisotropy which depend on the method of preparation and may be considerably different from that of bulk materials. Moreover, the large fraction of surface to volume atoms leads to modified magnetic interactions while the comparable values of magnetic anisotropy and thermal energy per particle cause superparamagnetic behavior. From the point of view of applications fine magnetic particles are used in ferrofluids, magnetic recording and catalysis.

A common method of preparation of fine metallic particles is the reduction of the appropriate metal salts by KBH_4 or NaBH_4 . This method was already known and used about thirty years ago for the preparation of Fe and Fe-Co particles [4] and more recently in several investigations [3,5]. A characteristic feature of this method is that due to coprecipitation of B, the produced particles are amorphous for boron concentrations approximately above 20 percent. Metallic or alloy phases can then be produced by annealing [6]. Another feature of the morphology of fine metallic particles which influences the magnetic properties is the formation of oxide layers due to free or controlled exposure to air or oxygen. Exposure to oxygen pressure of a few mbar has been used for the creation of a passivation layer [7].

The studies of magnetic metallic fine particles reported so far deal almost exclusively with ferromagnetic metals, namely, Fe, Co and Ni. It is clearly of interest to extend

these investigations to systems containing Cr, which may significantly modify the magnetic properties due to the introduction of antiferromagnetic interactions. In fact the magnetic phase diagram of Fe-Cr alloys [8] goes from antiferromagnetic alloys at high Cr concentrations through spin glass to ferromagnetic alloys as the concentration of Cr decreases. In this report we present results of a study of Fe-Cr-B particles prepared by KBH_4 reduction. We focus on the data obtained by Mössbauer spectroscopy on samples in the as-prepared state as well as after annealing at progressively higher temperatures. The inferences of these results for the magnetic state of the particles are then discussed in conjunction with information obtained from other experimental techniques.

EXPERIMENTAL METHODS

Fine particles of Fe-Cr-B were produced by adding dropwise aqueous solution of NaBH_4 to a mixed FeCl_3 and $\text{CrCl}_3 \cdot 6\text{H}_2\text{O}$ aqueous solution under vigorous stirring. The black precipitate was rinsed in water and acetone in an Ar atmosphere oven at 50°C . The chemical composition of the samples was determined by DC plasma emission spectroscopy, and was found generally to correspond to the relative compositions of Fe, Cr and B in the solutions. The samples used in this study had the composition $\text{Fe}_{51}\text{Cr}_{23}\text{B}_{26}$. Thermal treatment was done in evacuated quartz tubes at temperatures between 600 and 1000°C . From TEM micrographs it was found that the particles were roughly spherical with an average diameter of 200 Å.

Mössbauer spectra were obtained with a constant acceleration spectrometer at temperatures from 4.2 to 300 K. Magnetization was measured with a SQUID magnetometer in fields up to 5 T.

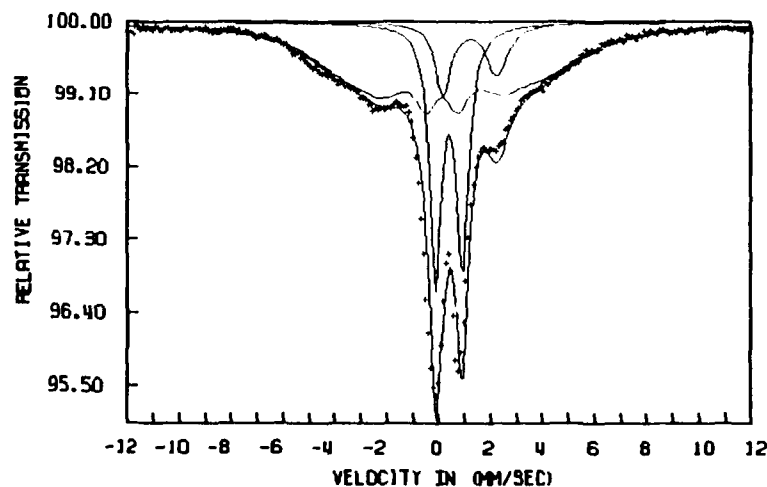


Fig. 1 Mössbauer spectrum of as-prepared particles of Fe-Cr-B at 85 K.

RESULTS AND DISCUSSION

The Mössbauer spectrum of as-prepared particles at 85 K is shown in Fig. 1. An essentially similar result, but with greater asymmetry in the central doublet was observed at room temperature. The spectrum can be analyzed as a superposition of two quadrupole split doublets and a broad line magnetic hyperfine pattern as shown by the solid line.

The results of annealing at temperatures of 680, 800, 900 and 1000°C are demonstrated in the room temperature Moessbauer spectra shown in Fig. 2 and 3a. In the sample annealed at 680°C an α -Fe component is identified together with two quadrupole doublets with parameters that are characteristic of Fe^{3+} and Fe^{2+} . The hyperfine parameters of the spectral components and their relative area are summarized in Table 1. In the sample annealed at 800°C the α -phase component has disappeared and the Fe^{2+} component is increased. The sample annealed at 900°C contains almost exclusively the Fe^{2+} phase. These results may be compared with DSC measurements which show that at the Cr content of the samples studied here, an exothermic peak appears near 650°C. The Moessbauer data indicate that in the first stage of crystallization α -Fe appears but annealing at higher temperatures results predominantly in the formation of an as yet unidentified phase containing Fe^{2+} .

To elucidate further the properties of the Fe^{2+} phase we have obtained spectra of the sample annealed at 900°C at 85 and 4.2 K. The results are shown in Fig. 3. At 85 K the spectrum consists of a quadrupole doublet with parameters similar to those of the RT spectrum and a broad hyperfine magnetic pattern. Complete magnetic hyperfine splitting is observed at 4.2 K. The average effective magnetic field is 25.0 T.

The nature of the chemical composition and the magnetic state of the main phase present in the samples annealed at 800

Table 1. Mössbauer parameters of Fe-Cr-B fine particles annealed at various temperatures

| Annealing Temp. °C | Phase | i.s.(a) mm/s | ΔE_Q mm/s | Percent area |
|--------------------|------------------|-----------------|----------------------|--------------|
| 680 | α -Fe | 0.0 | 0.0 | 11 |
| | Fe^{2+} | 1.11 | 2.02 | 65 |
| | Ox.1 | 0.43 | 0.69 | 18 |
| | Ox.2 | 0.58 | 1.29 | 6 |
| 800 | Fe^{2+} | 1.10 | 2.0 | 85 |
| | Oxide | 0.48 | 1.0 | 15 |
| 900 | Fe^{2+} | 1.13 | 2.03 | 100 |
| 1000 | Fe^{2+} | 1.09 | 2.06 | 79 |
| | Oxide | 0.63 | 0.78 | 21 |

(a) relative to iron metal at room temperature.

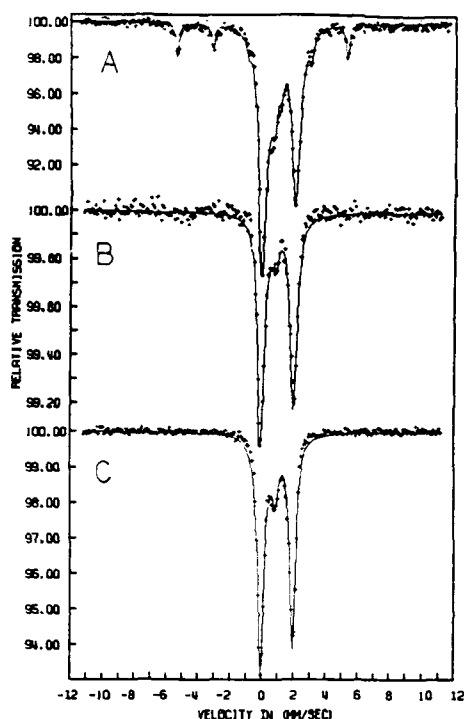


Fig.2 Room temperature Mössbauer spectra of Fe-Cr-B samples annealed at 680 °C (A) 800 °C and 1000°C (C).

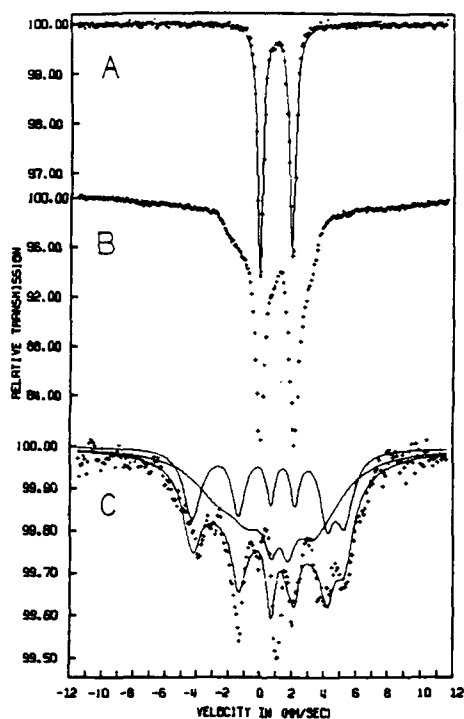


Fig.3 Mössbauer spectra of an Fe-Cr-B sample annealed at 900°C at RT (A), 85 K (B) and 4.2 K (C).

to 1000°C is not readily identified. As already mentioned, the Moessbauer parameters are typical of ionic high spin Fe^{2+} . Previously reported results on crystallization of amorphous fine particles of Fe-B [6] show the appearance of Fe_2B . The boron concentration, however, is higher in the latter case, 38 percent. In a crystallization study of amorphous metals Klein et al. [9] have reported that in melt spun samples with composition $\text{Fe}_{65}\text{Cr}_{15}\text{B}_{20}$, heat treatment at 1000°C produces first Fe_3B and then Fe_2B and $\alpha\text{-Fe}$. Our Mössbauer results, however, exclude these assignments since the observed phase is paramagnetic at room temperature. An ionic iron species could result from oxidation. In fact the Cr spinel FeCr_2O_4 has a magnetic transition temperature at 69 K and values of the effective field and quadrupole splitting comparable with our results [10]. At room temperature, however, the quadrupole splitting collapses practically to zero. We note also that the formation of a surface coating of FeCr_2O_4 on borohydride reduced iron powders has been reported as a technique for protecting the fine iron particles from oxidation [11]. Another possibility is a spinel type compound with formula CrFe_2O_4 with Cr in a 4^+ state in analogy with the spinel TiFe_2O_4 [12] but this type of chromium spinel has not been reported in the literature. The identification, therefore, of the Fe^{2+} is at present uncertain. We note only that a similar component has

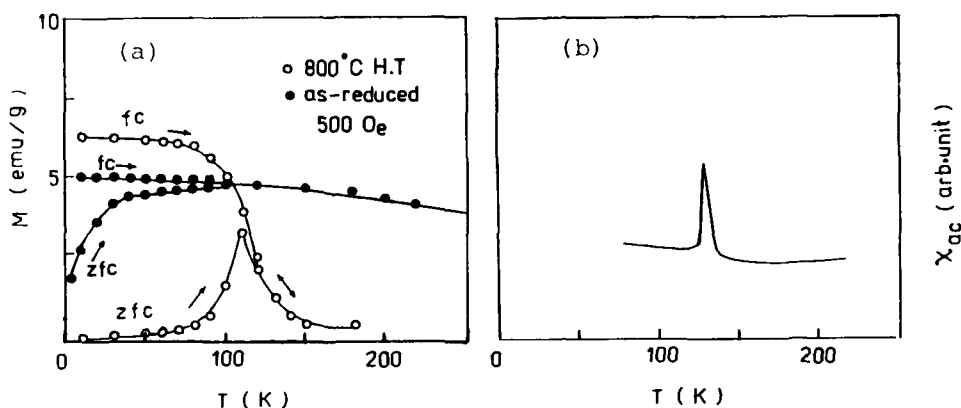


Fig. 4 (a) Temperature dependence of magnetization for FC and ZFC samples.
(b) AC susceptibility versus temperature for a sample annealed at 800°C.

been observed in Mössbauer spectra of fine particles of Fe-B prepared in a similar way [13].

We turn now to the question of the magnetic state of the particles annealed at 900°C. The Mössbauer spectra indicate the onset of magnetic hyperfine splitting near 85 K. This may be due to a magnetic transition or a blocking of superparamagnetic particles. The magnetization data offer information regarding this point. The temperature dependence of the magnetization for a sample heat treated at 800°C and measured in a field of 50 mT under zero field cooled and field cooled conditions is shown in Fig. 4(a). The occurrence of a transition at 110 K is clearly indicated. A similar conclusion can be drawn from AC susceptibility data which show a well defined peak at 120 K (Fig. 4b). The shape of the magnetization data is typical of the behavior of spin glass or superparamagnetic systems. In a study of magnetic relaxation of Fe-(SiO₂) granular films Gang Xiao et al. [14] have suggested that in the case of a superparamagnetic system the blocking temperature depends on the characteristic time of the method of observation (~ 10 s for a SQUID, $\sim 10^{-8}$ for Mössbauer) and have found that the ratio of the two temperatures is constant ($T_B^{\text{SQUID}}/T_B^{\text{MOSS}} \sim 0.35$) and independent of samples. On the other hand, the same authors, from measurements on amorphous Fe₇Pd₇₃Si₂₀, a well-known spin glass, have found the two temperatures rather close to each other. Our Mössbauer data are not detailed enough to give a value of the blocking temperature, but it is clear that it will be in the vicinity of 100 K, a value similar to that found from the magnetization experiments. This then would support a spin glass transition in our system. It must be added that above the transition temperature the magnetization data for two temperatures, 220 and 300 K, coincide when plotted vs H/T , as expected from a superparamagnetic system.

A detailed description of the magnetic measurements will be published elsewhere. We note only here, in closing, an additional remarkable result which supports the conjecture of a spin glass state. Below the transition temperature a large

increase in magnetic anisotropy is observed in the samples annealed above 800°C, yielding coercivity values of about 2.3 T for a ZFC sample and strongly displaced loop for FC samples.

CONCLUSIONS

The main features of the properties of Fe-Cr-B fine particles prepared by NaBH₄ reduction, as revealed by Moessbauer spectroscopy are summarized as follows:

(a) As-prepared particles consist of a mixture of a magnetic phase, probably amorphous, and two paramagnetic phases.

(b) Annealing at temperatures above ~800°C results in crystallization with a dominant component of high spin ionic Fe²⁺. The chemical constitution of this phase is at present uncertain. This result differs from the findings of previous investigations in Fe-B fine particles.

(c) The development of magnetic hyperfine splitting near 85 K indicates the occurrence of a transition. In conjunction with magnetization and AC susceptibility measurements, it is suggested that this is a spin glass transition. A dramatic increase of anisotropy and coercivity is observed at low temperatures.

Acknowledgements

This work was supported in part by NSF Grant CHE-8706954.

REFERENCES

1. K. Haneda and A.H. Morrish, Surface Sci. 17:584 (1978).
2. J. van Wonterghem,, S. Morup, C.J.W. Koch, S.W. Charles and S. Wells, Nature 322:622 (1986).
3. A. Watanabe, T. Uehori, S. Saitoh and Y. Imaoko, I.E.E.E. Trans on Magnetics MAG-17, 1455 (1981).
4. A.L. Oppegard, F.J. Darnell and H.C. Miller, J. Appl. Phys. 32:184 (1961).
5. D. Buchkov, S. Nikolov, I. Dragieva and M. Slarcheva, J. Magn. Magn. Mat. 62:87 (1986).
6. S. Linderoth, S. Morup, C.J.W. Koch, S. Wells, S.W. Charles, J. Van Wonterghem and A. Meagher, J. de Physique 49:C-1369 (1988).
7. I. Tamura and M. Yayashi, Surface Science 146:501 (1984).
8. See e.g. Landolt-Bornstirn, New Series, Vol. III 19/9 p. 342, Springer Verlag 1986.
9. H.P. Klein, M. Ghafari, M. Ackermann, U. Gonser and H.G. Wagner, Nucl. Instr. Meth. 199:159 (1982).
10. F. Hartmann-Boutron and P. Imbert, J. Appl. Phys. 39:775 (1968).
11. A. Balz, W.O. Freitag, A.P. Greifer and V. Suchodolski, J. Appl. Phys. 52:2457 (1981).
12. S.K. Banerjee, W. O'Reilly and C.E. Johnson, J. Appl. Phys. 1289 (1967).

13. V. Papaefthymiou et al. (to be published).
14. Gang Xiao, S. H. Liou, A. Levy, J.N. Taylor and C.L. Chien,
Phys. Rev. B34:7573 (1986).

CHEMICAL PREPARATION OF AMORPHOUS Fe—Cr—B PARTICLES

C. Bender Koch, S. Linderöth, and S. Mørup

Laboratory of Applied Physics
Technical University of Denmark
DK-2800 Lyngby, Denmark

The precipitates formed by addition of aqueous NaBH_4 solutions to $\text{Fe}^{3+}/\text{Cr}^{3+}$ solutions have been investigated by Mössbauer spectroscopy. Variation of the NaBH_4 addition rate (2.7, 5.0, and 9.8 cm^3/min) shows that at the highest addition rate formation of amorphous FeCrB alloys is suppressed. Increasing volumes of NaBH_4 solution added at constant rate ($\sim 5.4 \text{ cm}^3/\text{min}$) shows that large volumes of NaBH_4 also suppress formation of amorphous alloys. Addition of the same volumes of NaBH_4 solution with a constant rate ($\sim 5.4 \text{ cm}^3/\text{min}$) to metal salt solutions of different initial pH shows that a low initial pH suppresses the formation of amorphous alloys.

INTRODUCTION

The preparation of amorphous iron-based alloys by chemical reduction of metal salts in aqueous solution is well established¹. Regarding morphology and composition the chemical reduction method is an interesting alternative to other methods of producing amorphous alloys (liquid-quench, vapour deposition, sputtering etc.) because they are produced as ultrafine particles and because alloys with chemical compositions differing from those obtainable using other methods may be produced. The parameters influencing the chemical reaction are, of course, very different from those influencing the other methods (melt composition, cooling rate etc.). Previous studies²⁻⁶ have demonstrated that changes in the aqueous solution parameters (metal salt concentration, pH of the solution during the alloy formation) have a strong influence on the composition of the alloys. These studies indicate that systematic investigations of the influence of solution parameters on precipitate properties may be useful in order to understand the reaction. In this report we present preliminary studies of 1) the effect of addition rate of NaBH_4 solution, 2) the effect of amount of NaBH_4 solution added to the metal salt solution, and 3) the effect of initial pH of the metal salt solution on the formation of ternary Fe—Cr—B alloys.

EXPERIMENTAL

The precipitates were produced by dropwise addition of aqueous 0.8 M NaBH_4 solution to an aqueous solution of FeCl_3 and CrCl_3 . The metal salt solution was prepared by mixing of equal volumes (100 cm^3) of 0.4 M FeCl_3 and 0.05 M CrCl_3 (i.e. a total metal concentration of 0.225 M and a Fe:Cr ratio of 8:1 in the mixed solution).

Prior to mixing of the two salt solutions the pH was adjusted to a predetermined pH by addition of 1 M HCl.

- Three series of samples were prepared:
- 1) The effect of NaBH_4 addition rate was investigated by addition of 200 cm^3 NaBH_4 to 200 cm^3 metal salt solution with an initial pH of 1.00. Addition rates of 2.7, 5.0, and $9.8 \text{ cm}^3/\text{min}$ were used.
 - 2) The effect of total amount of NaBH_4 added was investigated by adding 100, 200, 250, and 300 cm^3 , respectively, to 200 cm^3 metal salt solution with an initial pH of 1.00. An addition rate of $5.4 \pm 0.4 \text{ cm}^3/\text{min}$ was used.
 - 3) The effect of different initial pH values were investigated by adjusting the pH of the salt solution to 0.50, 0.75, 1.00, and 1.14, respectively. 200 cm^3 NaBH_4 was added with a rate of $5.4 \pm 0.4 \text{ cm}^3/\text{min}$ to 200 cm^3 salt solution.

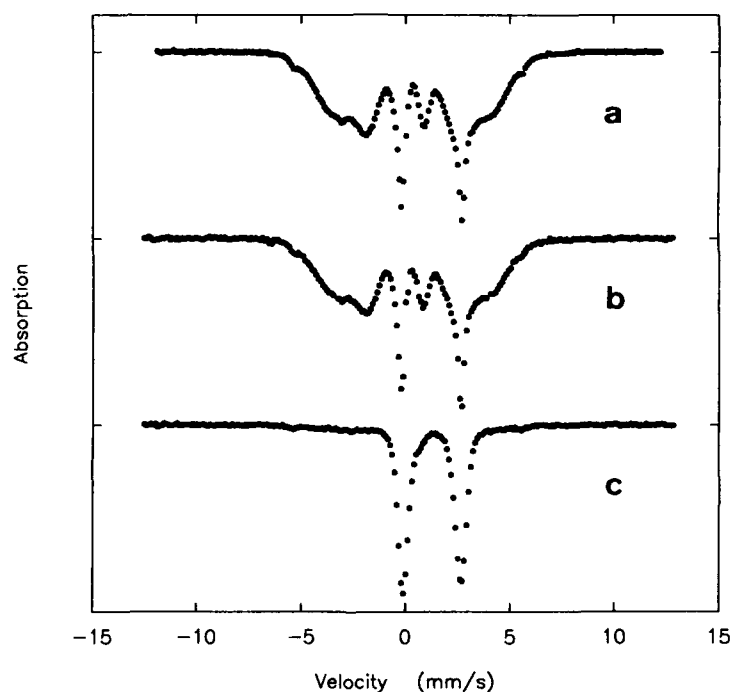


Figure 1. Mössbauer spectra of precipitates from Series 1 (different addition rates of NaBH_4). a, b, and c correspond to 2.7, 5.0, and $9.8 \text{ cm}^3/\text{min}$, respectively.

All the reactions follow a common pattern: The initial dark green solution turns light green upon addition of the first few cm^3 of NaBH_4 solution and simultaneously the pH of the solution decreases. Upon further addition of NaBH_4 the solution again turns dark green and the pH increases. As a precipitate forms at even higher pH (> 2) the solution turns very dark.

The precipitates were washed with water and investigated as frozen suspensions at 80 K using a conventional acceleration Mössbauer spectrometer. Isomer shifts are given relative to $\alpha\text{-Fe}$ at room temperature.

RESULTS AND DISCUSSION

The Mössbauer spectra obtained from the precipitates produced in Series 1 are shown in Fig. 1. The precipitate produced at the highest addition rate is dominated by a ferrous doublet with very broad lines and a small amount of ferric doublet. The

amount of alloy produced is very small. At lower addition rates the amorphous alloy ($B_{hf} \sim 23.6$ T, $2\epsilon \sim 0$, and $IS \sim 0.29$ mm/s) is the dominant component in the spectra with a small amount of a ferrous doublet with sharp lines and minor amounts of a crystalline alloy (lines 1 and 6 at about ± 5.5 mm/s). Variation of the addition rate of $NaBH_4$ causes some change of the final pH (pH increases from 7.8 to 8.1 with increasing addition rate) and this may be expected to cause a decrease in the amount of alloy formed (see Series 2 below). However, following addition of approximately half of the total amount of $NaBH_4$ the difference in pH is much greater (pH 5.3, 5.5, and 7.0 with increasing addition rate). Thus, the results suggest that the period of time which the solution is at a pH favourable for alloy formation is much shorter for the highest addition rate and other routes for precipitating becomes dominant.

Addition of increasing amounts of $NaBH_4$ causes an increase in the final pH. In Series 2 the final pH increased from 6.9 to 7.4, 8.8, and 9.1, respectively. The Mössbauer spectra of the precipitates are shown in Fig. 2. Addition of 100 cm^3 produces a precipitate dominated by a ferrous doublet with very broad lines. A small amount of amorphous alloy is also formed. Increasing the volume to 200 cm^3 produces a precipitate showing a dominant contribution from an amorphous alloy, small amounts of a sharp ferrous doublet and minor amounts of crystalline alloys. Addition of 250 and 300 cm^3 produces precipitates with Mössbauer spectra dominated by ferrous doublets, small amounts of a ferric doublet and minor amounts of amorphous alloy. The hyperfine field of the amorphous alloy formed following addition of 100 and 200 cm^3 $NaBH_4$ is 25.8 T and 23.6 T, respectively, indicating that the Cr and B contents differ significantly. Assuming that the alloys formed following addition of 100 cm^3 $NaBH_4$ still is present in the precipitate formed following addition of 200 cm^3 $NaBH_4$ this suggest that the latter is rather inhomogeneous. The dominantly ferrous precipi-

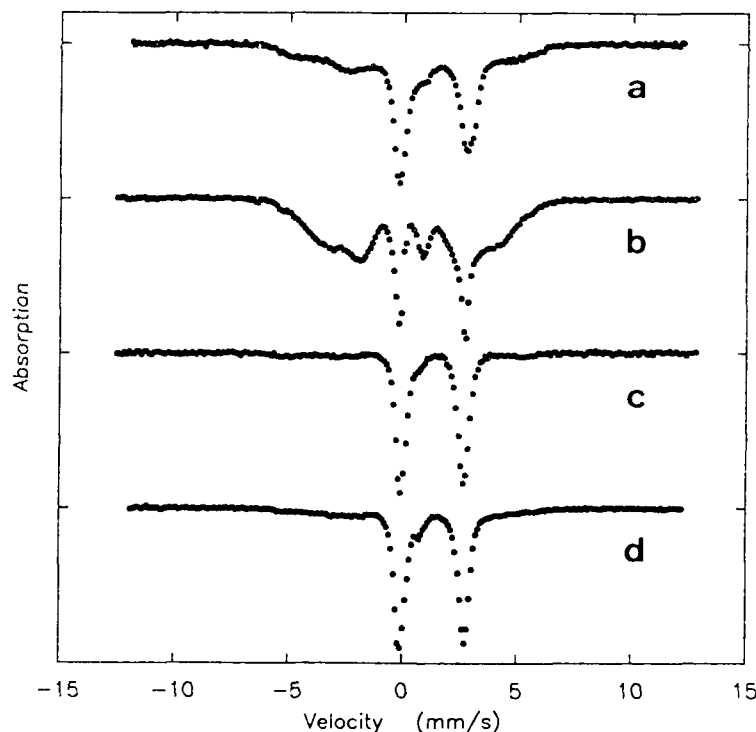


Figure 2. Mössbauer spectra of precipitates from Series 2 (increasing amounts of $NaBH_4$ added). a, b, c, and d corresponding to addition of 100, 200, 250, and 300 cm^3 $NaBH_4$ solution, respectively.

tate formed following addition of 250 and 300 cm³ NaBH₄ is presumably due to extensive precipitation of basic ferrous compounds at pH above approx. 8.

Addition of 200 cm³ NaBH₄ to 200 cm³ of metal salt solution with different initial pH (Series 3) also causes a change in the final pH of the solutions. However, the difference in the final pH of the solutions is only moderate (pH 7.7, 7.7, 7.4, and 7.8, respectively, with increasing initial pH). The precipitates formed in the solution with an initial pH of 0.50 exhibits a Mössbauer spectrum (Fig. 3a) dominated by a ferrous doublet with very broad lines. With increasing initial pH an increase in the relative spectral area due to amorphous alloys is noted (Fig. 3). The difference in hyperfine field of the alloy formed at initial pH of 0.75, 1.00, and 1.14 (30.0, 23.6, and 23.5 T, respectively) indicates a change in the chemical composition of the alloys. Thus, the present results indicate that also the initial hydrolysis reactions in the metal salt solution is an important parameter.

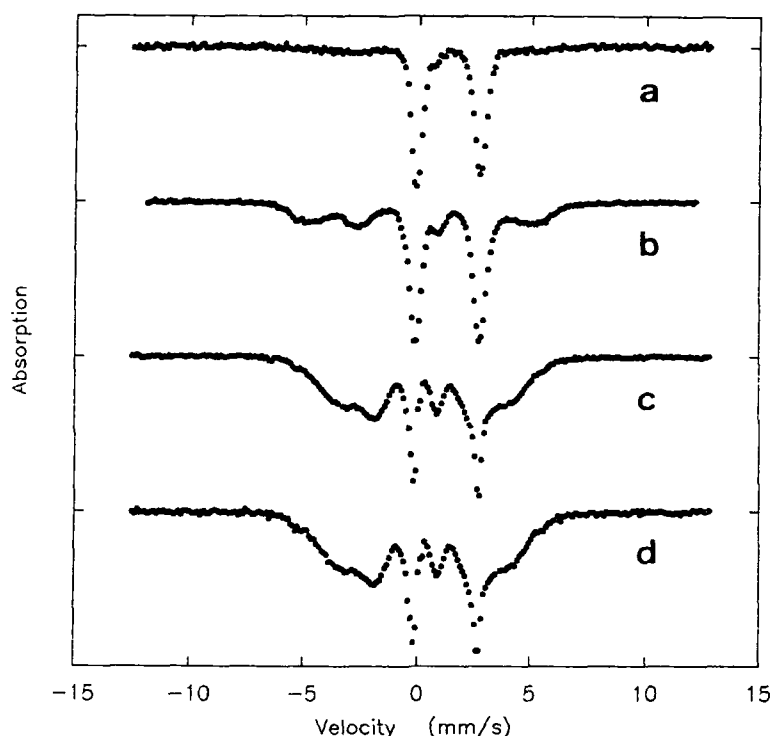


Figure 3. Mössbauer spectra of precipitates from Series 3 (different initial pH of metal salt solutions). a, b, c, and d corresponding to an initial pH of 0.50, 0.75, 1.00, and 1.14, respectively.

REFERENCES

1. J. van Wonerghem, S. Mørup, C.J.W. Koch, S.W. Charles, and S. Wells, *Nature* 322:622 (1986).
2. A. Inoue, J. Saida, and T. Masumoto, *Metall. Trans.* 19A:2315 (1988).
3. S. Wells, S.W. Charles, S. Mørup, S. Linderroth, J. van Wonerghem, J. Larsen, and M.B. Madsen, *J. Phys.: Cond. Matt.* 1:8199 (1989).
4. S. Linderroth, S. Mørup, and M.D. Bentzon, *J. Magn. Magn. Mat.* 83:457 (1990).
5. S. Linderroth and S. Mørup, *J. Appl. Phys.* (in press).
6. S. Linderroth, S. Mørup, and S.A. Sethi (this meeting).

COMPOSITION AND STRUCTURE OF Fe-Ni-B ALLOY PARTICLES

PREPARED BY CHEMICAL REDUCTION WITH NaBH_4

S. Linderroth, S. Mørup and S.A. Sethi

Laboratory of Applied Physics
Technical University of Denmark
DK-2800 Lyngby, Denmark

Fe-Ni-B alloy particles have been prepared by reducing transition metal ions in an aqueous solution by addition of an aqueous solution of NaBH_4 . The amount of amorphous and crystalline phases is shown to depend on the NaBH_4 molarity and the pH in the salt solution. Amorphous alloy particles with the boron content ranging between 9 and 19 at. % have thereby been prepared.

INTRODUCTION

After van Wonerghem et al.¹ reported that amorphous transition metal-boron alloys can be produced by chemical reduction in aqueous solutions a number of studies have dealt with the magnetic and structural properties of these ultrafine particles²⁻⁷. The purpose of several studies has been to determine the parameters that govern the reduction processes, and through that knowledge facilitate the control of e.g. the boron content in the particles. If the alloy particles are prepared by adding the transition metal ion solution to an aqueous alkali metal borohydride solution, the alloys produced contain 35-42 at. % boron^{1,2}. Wells et al.⁵ showed that by mixing the other way around the boron content in the particles could be reduced to below 30 at. %. They found that the boron content depended on the concentration of the NaBH_4 solution added to the metal ion solution, with the boron incorporated in the particles decreasing with increasing molarity of the NaBH_4 solution. The boron stabilizes the amorphous phase and the decrease of the boron content leads in some cases to the appearance of crystalline phases⁵.

Recently, Linderroth et al.^{6,7} have shown that if the pH in the transition metal ion solution is controlled during the reaction the boron content in the particles may also be controlled. By this new method amorphous alloy particles with boron contents between 14 and 30 at. % have been prepared⁷.

Here we report on a study on Fe-Ni-B alloy particles where both the concentrations of the NaBH_4 solution and the pH of during the reaction have been varied.

EXPERIMENTAL

The chemically produced alloy particles were prepared by adding 100 ml aqueous solution of NaBH_4 to 200 ml aqueous solution containing 0.16 M FeSO_4 and 0.04 M NiCl_2 . For the preparations two molarities of the NaBH_4 solution were

employed; 0.15 M and 0.25 M, respectively. When added to the metal ion solution the pH in that solution quickly raised from the initial value of about 3. To control the pH during the reaction 0.1 M HCl or 0.1 NaOH was added during the reaction, depending on the pH value heading for. After the addition of the NaBH_4 was completed the black precipitate produced was washed carefully in distilled water several times before a final wash in acetone. Part of the acetone-wet precipitate was transferred to a small container and was subsequently frozen to liquid nitrogen temperature. The remaining sample was transferred to a passivation rig where it was dried and passivated at room temperature in a flow of an oxygen-containing nitrogen gas. The passivated samples were employed for chemical analyses, performed by photo absorption spectroscopy and wet-chemical analysis. The frozen samples were used for Mössbauer spectroscopy studies.

The Mössbauer spectroscopy measurements were performed with a 50 mCi ^{57}Co source in rhodium attached to a constant acceleration spectrometer. The investigated samples were placed in a liquid nitrogen cryostat and kept at about 80 K. Zero velocity is defined as the centroid of the spectrum of a room temperature measurement on a thin $\alpha\text{-Fe}$ foil. The Mössbauer spectra were fitted with Lorentzian lines by a least-squares method.

RESULTS AND DISCUSSION

Employing NaBH_4 aqueous solutions with borohydride concentrations of 0.15 M and 0.25 M samples were prepared with pH ranging between 3 and 8, with steps of 1. The Mössbauer spectra, obtained at 80 K, of these samples are shown in Figure 1.

The spectra for pH = 3 are very similar in the two situations, and can be seen to consist of two sextets; one with sharp absorption lines and another with broad lines. The former sextet had a magnetic hyperfine field of about 34.4 T, a negligible quadrupole shift and an isomer shift of about 0.12 mms^{-1} . This component corresponds to $\alpha\text{-Fe}$, possibly partly substituted with Ni. The overall chemical analysis yielded an Fe to Ni ratio of about 7, i.e. the ratio is about twice of that in the aqueous solution. The broad sextet with a hyperfine field of about 29 T, corresponds to an amorphous Fe-Ni-B alloy. The broad absorption lines are due to a distribution of hyperfine parameters.

For the two different NaBH_4 molarities the spectra depend slightly differently on the pH. With a NaBH_4 molarity of 0.15 the Mössbauer spectra reveal only a single sextet with broad lines for pH between 4 and 7, while for a NaBH_4 molarity of 0.25 also a sharp-lined component, due to a crystalline phase, is present.

Considering first the 0.15 M experiment, the sample prepared with pH = 4 was found to have the composition $\text{Fe}_{68}\text{Ni}_{14}\text{B}_{18}$. The magnetic hyperfine field was deduced to be about 28.5 T. Sostarich et al.⁸ have determined the hyperfine field at the iron site at 4.2 K for $(\text{Fe}_x\text{Ni}_{1-x})_{80}\text{B}_{20}$ ribbons prepared by the melt-spin method, and they, similarly, deduced a hyperfine field of about 28.5 T, for $x \approx 80$. The amorphous structure seems, thus, to be similar for the particles and the ribbons.

From Figure 1 it is seen, that an increase of pH first leads to a decrease, later an increase of the magnetic hyperfine splitting of the spectra. This can also be seen from Figure 2, where the hyperfine fields for the component with broad absorption lines are shown as a function of pH for both series of experiments. The magnetic hyperfine fields reaches a minimum around a pH of 5. From the chemical analyses it can be concluded that this is due to a maximum in boron content around this pH value. The maximum boron content was found to be 19 at. %.

For a pH value of 7 the deduced hyperfine field is about 29.0 T, which is remarkably high considering the Fe/Ni ratio to be 0.8 as estimated from chemical analysis. For $(\text{Fe,Ni})_{80}\text{B}_{20}$ ribbons, prepared by the liquid-quench technique, this Fe/Ni ratio result in a magnetic hyperfine field of about 27.2 T at 4.2 K (ref. 8). The

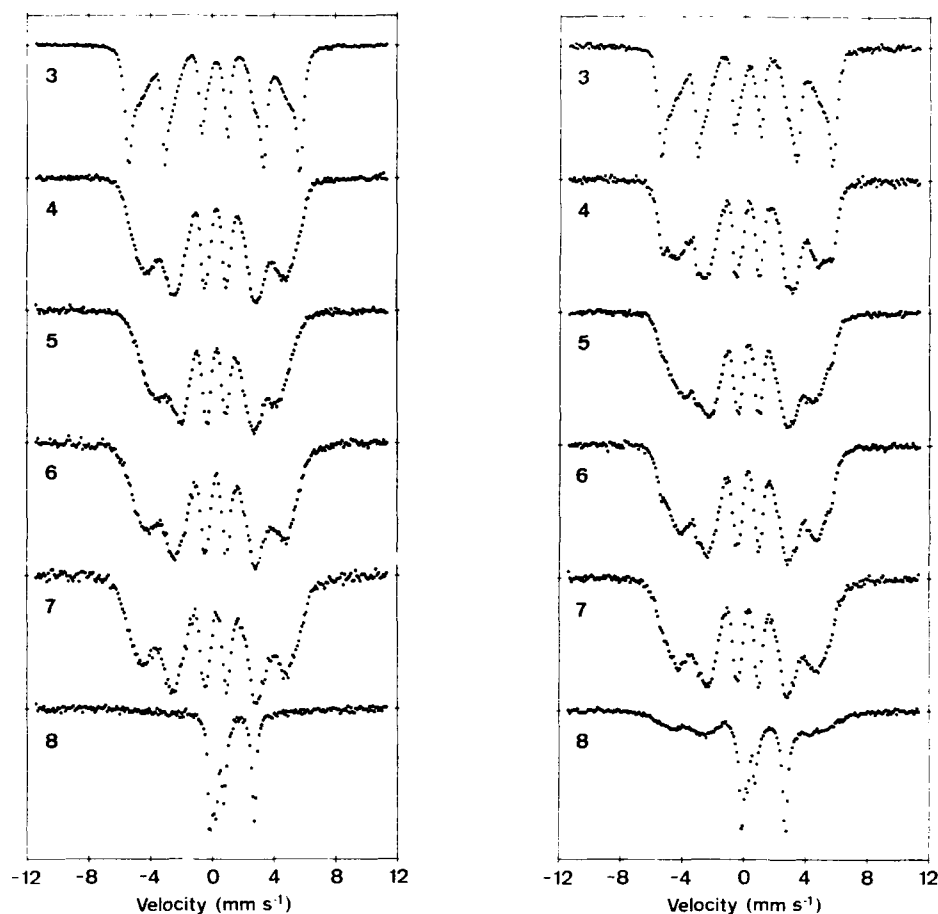


Figure 1. Mössbauer spectra obtained at 80 K for Fe-Ni-B alloy particles prepared with addition of 0.15 M (left figure) and 0.25 M (right figure) NaBH_4 in aqueous solution to an $\text{Fe}_{80}\text{Ni}_{20}$ salt solution controlled at the indicated pH values.

high Ni content decreases the Curie temperature from about 700 K for the Ni-free sample to about 500 K (ref. 8), which would lead to an even lower hyperfine field at 80 K than the about 27 T. The reason for the considerably higher hyperfine field in our sample is a low boron content. The sample prepared with pH equal 7 was found to contain only 9 at. % boron. Thus, through control of concentrations and pH we have been able to prepare an amorphous (Fe,Ni)-B alloy with only 9 at. % boron.

If the pH is forced to be 8 during the addition of NaBH_4 the Fe and Ni precipitates and do not become reduced by the NaBH_4 . For a pH value of 8 the Mössbauer spectrum in Figure 1 is seen to consist of Fe^{3+} and Fe^{2+} .

When the NaBH_4 molarity is increased from 0.15 to 0.25, the Mössbauer spectra all reveal some crystallinity in the samples. This is in accord with the observations by Wells et al.⁵, who observed that the boron content decreased and the degree of crystallinity increased with an increase of the molarity of NaBH_4 solution.

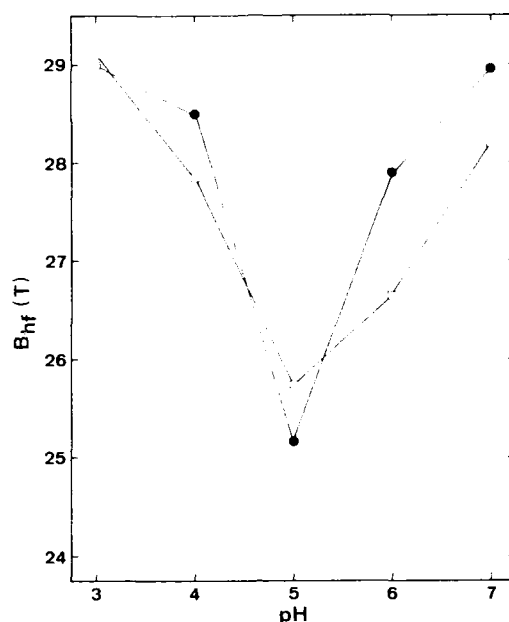


Figure 2. The magnetic hyperfine field for the amorphous component versus pH prepared with a NaBH_4 molarity of 0.15 (●) and 0.25 (□). Open/closed symbols are for partly/completely amorphous samples.

CONCLUSIONS

Fe-Ni-B alloy particles have been prepared by reduction of the transition metal ions by addition of an aqueous NaBH_4 solution. It has been demonstrated that the alloy compositions are sensitively dependent on pH as well as the NaBH_4 concentration. Using a NaBH_4 molarity of 0.15 the particles become amorphous for pH in the range 4 to 7, while a molarity of 0.25 yields partly crystalline samples. By control of the two parameters an amorphous Fe-Ni-B alloy with as little as 9 at. % boron has been produced.

REFERENCES

1. J. van Wonerghem, S. Mørup, C.J.W. Koch, S.W. Charles, and S. Wells, *Nature* 322: 622 (1986).
2. S. Linderroth, S. Mørup, A. Meagher, J. Larsen, M.D. Bentzon, B.S. Clausen, C.J.W. Koch, S. Wells, and S.W. Charles, *J. Magn. Magn. Mat.* 81: 138 (1989).
3. A. Inoue, J. Saida, and T. Masumoto, *Metall. Trans.* 19 A: 2315 (1988).
4. L. Yiping, G.C. Hadjipanayis, C.M. Sorensen, and K.J. Klabunde, *J. Magn. Magn. Mat.* 79: 321 (1989).
5. S. Wells, S.W. Charles, S. Mørup, S. Linderroth, J. van Wonerghem, J. Larsen, and M.B. Madsen, *J. Phys.: Cond. Matt.* 1: 8199 (1989).
6. S. Linderroth, S. Mørup, and M.D. Bentzon, *J. Magn. Magn. Mat.* 83: 457 (1990).
7. S. Linderroth and S. Mørup, *J. Appl. Phys.* (in press).
8. M. Sostarich, S. Dey, P. Deppe, M. Rosenberg, G. Czjzek, V. Oestreich, H. Schmidt, and F.E. Luborsky, *IEEE Trans. Mag.* MAG-17: 2612 (1981).

QUANTUM EFFECTS IN ULTRAFINE Nd-Fe-B PARTICLES

M.A. López Quintela, J. Rivas, L. Liz and I. Winter

Depts. of Physical Chemistry and Applied Physics
University of Santiago de Compostela
E-15706 Santiago de Compostela, Spain

INTRODUCTION

The production of ultrafine particles, that is, particles in the 10-100 Å interval, is a topic of great interest because of their peculiar behavior which differentiates them from the bulk material¹. One of the main differences is the existence of quantum size effects in the optical properties of the particles².

In the last few years, several production methods for ultrafine particles have been developed. These methods consist, fundamentally, in obtaining the particles in a supporting medium (solid, liquid or gas) using techniques such as thermal evaporation, colloidal systems, ion and laser bombardment, etc.

In particular, the preparation of colloidal systems of magnetic particles by chemical methods, such as precipitation³, reduction⁴, etc. presents great possibilities.

One of the problems which arises with these chemical methods is to achieve control over the size of the particles. To solve this, different procedures, which go from the simple addition of substances which hinder growth in a specific stage of the process (as in the case of the addition of gelatin in the production of Ag metallic particles⁵), to using compartmentalized media (such as microemulsions, surfactant solutions, vesicle, etc.⁶) for the chemical process, have been proposed.

In the present work we have first studied, the use of microemulsions as a way of controlling the growth of magnetic particles produced by the reduction of Fe^{2+} and Nd^{3+} salts by NaBH_4 . Secondly, we have studied the influence of size on the optical absorption of colloidal suspensions of magnetic particles, observing the existence of quantum effects when the size of the particle is sufficiently reduced.

EXPERIMENTAL PROCEDURE

The following procedure was developed for obtaining the magnetic particles of NdFeB. A solution with an adequate ratio of the metallic cations Fe^{2+} and Nd^{3+} was mixed with another of borohydride. There were two ways of mixing the solution, one was the dropwise addition of the reduction

agent solution onto the one with the metallic ions and the other was by rapidly and directly mixing them using a *tee-junction*. This way, we obtained fine particles with different Nd/Fe/B ratios and with sizes between 100 and 400 nm. In order to control the growth of the particles we carried out the reaction in the presence of microemulsions. In this case, we mixed two identical microemulsions, one containing the reduction agent and the other the metallic salts. We found that the real size of the particles (≈ 450 nm) was determined by the size of the droplets which made up the microemulsion. In this work the microemulsions we used were water in oil microemulsions composed of heptane/water/aerosol-OT (sodium bis-(2-ethyl,hexyl)sulphosuccinate) with a concentration of 0.1 M in aerosol-OT (AOT) and different ratios $R = [H_2O]/[AOT]$. For this type of microemulsion, the size of the water droplets may be calculated as a first approximation by using the equation: $r(\text{radius of the droplets})/\text{nm} = 0.175 R + 1.5$.

The optical absorption measurements were carried out with a KONTRON UV-VIS spectrophotometer (model UVIKON 930).

For the dynamic light scattering measurements, the optical source was an argon ion laser operating at 514.5 nm. The scattered light was collected at the appropriate angle by high quality commercial goniometer (ALV SP-81) and was focused on a photomultiplier cathode (EMI-9863). For the study, the scattering angle was fixed at 90°. The photomultiplier signals were passed to 10 ns amplifier-discriminator units. Single photon counting pulses were processed by a digital correlator (ALV-5000 Multiple Tau Correlator).

RESULTS

1. Size control

In order to observe the control exerted by the microemulsions on the size of the particles, we first prepared different samples in aqueous solution, this is, without the control medium. In tables 1, 2, we show the results obtained from laser light scattering as a function of time for colloidal solutions produced with concentrations $C_A: [FeCl_2] = 1.9 \times 10^{-4}$ M, $[NdCl_3] = 3.7 \times 10^{-6}$ M, $[NaBH_4] = 8.8 \times 10^{-4}$ M (table 1); $4C_A$ (table 2).

We can observe: 1) the particles obtained using this procedure are always $\approx 0.1 \mu\text{m}$ and the size increases noticeably with the concentration of reactives used. 2) The colloidal solutions are not stable and they suffer an aggregation process with time. This phenomenon can be observed in the electron micrographs shown in figure 1 where we can see the particles as obtained and after the aggregation process. 3) From tables 1, 2, we can also deduce that the quasimonodispersity observed at low concentrations disappears with time as well as with the increase of the concentrations (see figure 1.a).

Table 1. Variation of the hydrodynamic radius of particles formed in aqueous solution for C_A concentrations.

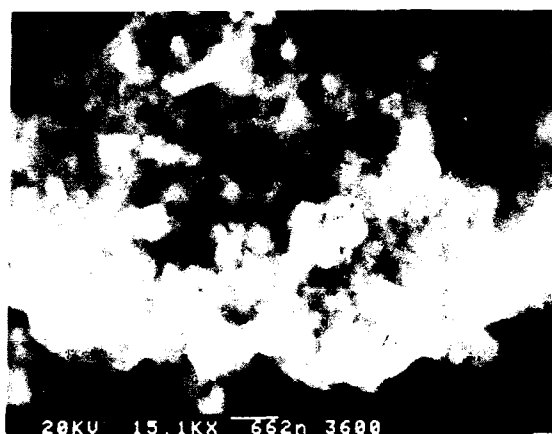
| time/min | \bar{r}_H | observations |
|----------|-------------|--------------|
| 5 | 160 | m |
| 8 | 164 | m |
| 18 | 172 | m |
| 28 | 182 | m |
| 62 | 201 | m |
| 102 | 243 | p |

m=quasi-monodispersity; p=polydispersity

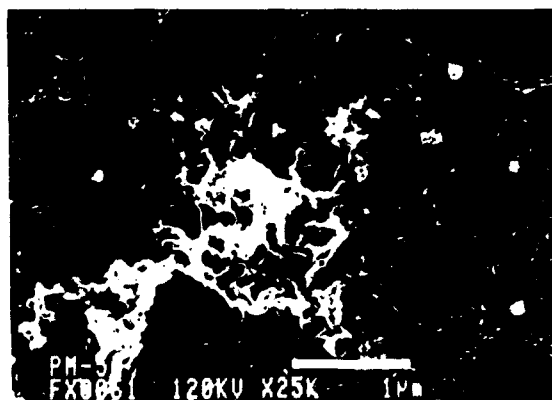
Table 2. Variation of the hydrodynamic radius of particles formed in aqueous solution for $4C_A$ concentrations.

| time/min | \bar{r}_H | observations |
|----------|-------------|--------------|
| 5 | 433 | m |
| 7 | 477 | m |
| 10 | 540 | p |
| 15 | 668 | p |
| 20 | 948 | vp |
| 25 | 3150 | vp |

vp=very polydisperse



a



b

Fig. 1. Electron micrographs of particles formed in aqueous solution (concentration = $100 C_A$).

a. - as obtained

b. - after the aggregation process

Table 3. Variation of the hydrodynamic radius of particles formed in microemulsion for $\approx C_A$ concentration.

| time/min | \bar{r}_H | observations |
|----------|-------------|--------------|
| 30 | 5.6 | m |
| 50 | 6.1 | m |
| 140 | 7.1 | m |

Afterwards, we prepared samples in microemulsions with concentrations similar to the ones used in water but referred to the total volume of the solution (see table 3). Firstly, we can observe that the particles obtained are now a lot smaller than those obtained in water and that the growth is a lot slower despite the fact that the effective concentrations used are ≈ 10 times higher than in the aqueous solution experiments because the reaction for the formation of the particles takes place only in the water microdroplets which make up the microemulsion. When effective concentrations similar to those of the aqueous solutions are used ($\approx C_A/10$) we obtain quasimonodisperse colloidal solutions which do not change noticeably with time and are stable for periods of several weeks. It can also be observed that the hydrodynamic radius of the particles obtained coincides with that of the microdroplets of the microemulsion, this confirms that microemulsions are an idoneous means for controlling growth.

There are two factors which may influence growth control. Firstly, the rapid nucleation and initial growth reaction⁸ takes place inside the water microdroplets which limit this initial growth (hindering growth). Secondly, once the particles have been formed, they are protected by a surfactant layer and by steric repulsion they do not allow that the latter collisions produce the aggregation phenomena detected in aqueous colloidal solutions (stabilization of colloidal solutions).

2. Quantum effects

We have also studied the influence of particle size on the optical properties. For this, we performed experiments by means of UV-VIS spectrophotometry in the wavelength range $200 < \lambda \text{ (nm)} < 500$. According to the sizes of the particles we have mentioned, we can differentiate three behaviors depending on the size/wavelength ratio:

- 1) Rayleigh region: $r/\lambda \ll 1$ (r =radius on an spherical particle).
- 2) Mie region: $r/\lambda = 1$.
- 3) Optical region: $r/\lambda \gg 1$.

Therefore for the particles obtained in water ($r \approx 100\text{--}400\text{nm}$) we must expect a Mie behavior from the spectrophotometric observations. In figure 2 we clearly observe a continuous drop in the absorbance superimposed to resonances of the Mie type. For particles which are smaller than these wavelengths, such as those obtained in microemulsions ($r/\lambda < 1$) we can expect a monotonous drop in the absorbance (Rayleigh region) due to the fact that the effective cross-section of the particles decreases. In figure 3 we present a characteristic spectrum obtained for the ultrafine particles. As can be seen, the behavior is not of the Rayleigh type and two maxima appear in this wavelength interval which can be attributed to the existence of quantum effects due to the small size of the particles. These effects, which have been found in other semiconducting ultrafine particles, are associated by most authors with the separation of the energy levels in the conducting band of the semiconductor because of the small dimensions of the particles. Consequently, they are called Q-particles. According to this interpretation,

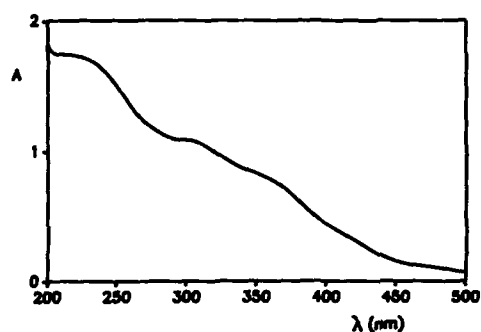


Fig. 2. Absorption spectrum of colloidal NdFeB obtained in water ($r \approx 300\text{nm}$) showing the existence of Mie resonances.

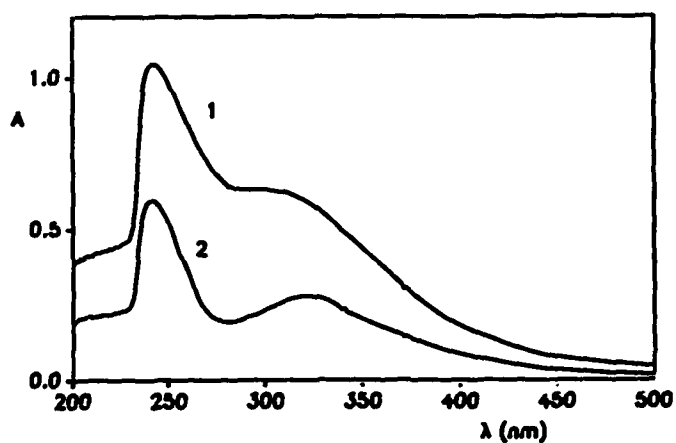


Fig. 3. Absorption spectra of colloidal NdFeB obtained in microemulsions ($R=13$) showing the presence of quantization effects.
Concentration: $1 \equiv C_A$, $2 \equiv 6C_A$.

the quantum effects should disappear when we increase the size of the particles. This is so, we observe that for particles of around 15 nm this effect disappears and we only see the continuous band corresponding to the electronic absorption of this semiconducting material.

From what has been mentioned we can conclude the following: Firstly, that microemulsions adequately control the growth of magnetic particles and permit the formation of stable colloidal solutions. Secondly, that varying the size of the microdroplets, ultrafine particles of different sizes can be obtained. Thirdly, that the optical properties have been studied and the existence of quantum phenomena has been detected for the smaller particles ($\leq 8-10$ nm).

ACKNOWLEDGEMENTS

M.A.L.Q and J.R. wish to acknowledge funding from the Spanish CICYT N.MAT89-0425-C03. We also want to acknowledge Professor K. Schätzel's assistance in letting us use his laser light scattering equipment.

REFERENCES

1. J. Davenas and P.M.Rabette, eds. "Contributions of Cluster Physics to Material Science and Technology-From Isolated Clusters to Aggregated Material", Martinns Nijhoff Publ., Dordrecht (1986).
2. J. Giraldo, *in*: "Thin Films and Small Particles", M. Cardona and J. Giraldo, eds., p.138, World Scientific, Singapore (1988).
3. E. Matijevic, *in*: "Recent Advances in Magnetism and Magnetic Materials", H. L. Huang and P. C. Kuo, eds., p.117, World Scientific, Singapore (1988).
4. S. Mørup, J. van Wonerghem, A. Meagher and C. J. W. Koch, *IEEE Trans. Magn.* 23:2978 (1987).
5. U. Kreibitz *in*: "Metal Clusters", F. Träger and G. zu Putlitz, eds., p.139, Springer Verlag, Berlin (1986).
6. J. B. Nagy, E. G. Deronane, A. Gourgue, N. Lufimpadio, I. Ravet and J. P. Verfaillie, *in*: "Proc. Int. Symp. Surf. Sol.", New Delhi, India (Aug. 18-22, 1986).
7. J. D. Nicholson and J. H. R. Clarke, *in*: "Proc. Int. Symp. Surf. Sol.", K. Mittal and B. Lindman, eds., p.1663, Plenum Press, New York (1984).
8. M. A. López Quintela, J. Rivas, I. Winter and W. Knoche, *in*: "Int. Symp. on Amorphisation by Solid State Reaction", Grenoble, France (Feb. 21-23, 1990).

MAGNETIZATION REVERSAL IN CLUSTERS OF MAGNETIC PARTICLES

P.V. Hendriksen, S. Mørup, G. Christiansen and K.W. Jacobsen

Laboratory of Applied Physics
Technical University of Denmark
DK-2800 Lyngby, Denmark

The energy barrier of reversal of the magnetic moments in a system of interacting magnetic particles has been evaluated for different geometric arrangements. It is found that introducing a neighbor particle to a linear chain lowers the energy barrier of reversing the magnetic moments substantially.

INTRODUCTION

Magnetic interactions between microcrystals are of interest because of their influence on the characteristics of technologically important materials like magnetic recording media and ferrofluids. Chains of magnetic microcrystals have also been observed in biological systems, for instance in magnetotactic bacteria¹. In the present work the energy barrier of reversing the magnetic moments in chain-like configurations of magnetically interacting particles has been evaluated. Especially the influence of a neighbor particle to a linear chain has been studied by considering a simple system containing five identical particles in the two configurations shown in fig. 1.

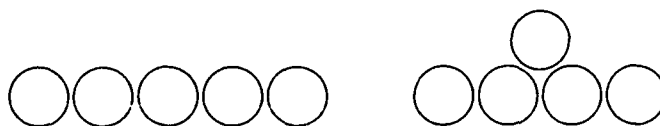


Figure 1. The linear chain and the neighbor configuration of the cluster.

THEORY

The magnetic interaction between the particles is assumed to be of the dipole-dipole kind, i.e. the total interaction E , is given by:

$$E = \frac{\mu_0}{4\pi} \sum_{i,j} \left[\frac{\bar{\mu}_i \cdot \bar{\mu}_j}{r_{ij}^3} - \frac{3(\bar{\mu}_i \cdot \bar{r}_{ij})(\bar{\mu}_j \cdot \bar{r}_{ij})}{r_{ij}^5} \right] \quad (1)$$

where i, j are particle indices, $\bar{\mu}_i$ is the magnetic moment of a particle and \bar{r}_{ij} is the vector from particle i to particle j . The summation is over all pairs of particles.

Another contribution to the energy of the system arises from magnetic anisotropy of the particles. However, the aim of this work was to study the influence of magnetic dipole interaction on the magnetic properties of the system, and therefore the anisotropy energy has been neglected.

METHOD

The linear chain obviously has two energy minima – with magnetic moments aligned along the chain pointing right or left. To evaluate the energy barrier separating these two minima one needs to "force" the system in a continuous way from one minimum to the other by constraining only one parameter. This can be done, for instance, by requiring a specific magnetization in the chain direction, and change this magnetization step by step between the values corresponding to the two minima. For each value of the magnetization the dipole orientations corresponding to the minimum value of the energy are found. If the configurations corresponding to different magnetizations represent a geometrical continuous way between the two energy minima the estimated energy barrier is the lowest one separating the two minima.

The minimum energy configuration for each magnetization is found by computer simulation. Running a Monte-Carlo simulation with the Metropolis-algorithm the accepted configurations represent a canonical ensemble². The minimum energy configuration is then found by a "simulated annealing"³ in which the temperature of the ensemble is gradually reduced. In the limit of very slow annealing the system will be trapped in the minimum energy configuration.

RESULTS

The minimum energy configurations of a system containing 5 particles in a chain corresponding to different constrained magnetizations, M , are shown in figure 2. The corresponding energies are shown in figure 4. Figures 3 and 5 show minimum energy configurations and corresponding energies of the system in the neighbor configuration. The energy barriers of reversal of the magnetic moments are summarized in table 1. ΔE_{tot} is the barrier of reversing all the magnetic moments, and ΔE_1 is the barrier for reversing only one of the magnetic moments. In the linear configuration the "cheapest" way of reversing the magnetic moment of one particle is by reversing all the magnetic moments, whereas in the neighbor configuration the magnetic moment of the neighbor particle is (almost) reversed when the system is forced between the two minima corresponding to magnetizations of -4.8 and -3.0 (see fig. 5). The global energy minimum of the system, E_{min} , indicates that the linear configuration is energetically favorable compared to the neighbor configuration.

Table 1. ΔE_{tot} is the barrier of reversing all the magnetic moments. ΔE_1 is the barrier of reversal of one of the magnetic moments. E_{min} is the minimum of the total energy. The energies are given in units of $\mu_0 \mu^2 / r^3$.

| | ΔE_{tot} | ΔE_1 | E_{min} |
|------------------------|-------------------------|--------------|------------------|
| 5 particles, linear. | 0.364 | 0.364 | -0.711 |
| 5 particles, neighbor. | 0.161 | 0.018 | -0.565 |

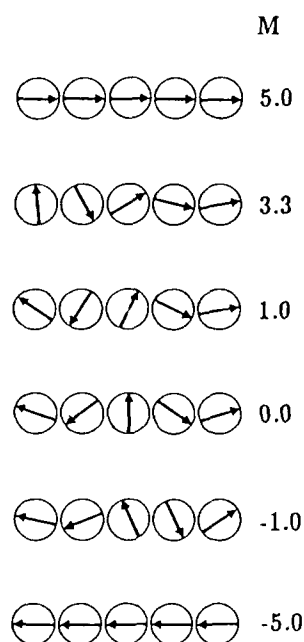


Figure 2. Minimum energy configurations in the linear system. The upper and the lower configurations are the global minima. M is the magnetization along the chain in units of μ .

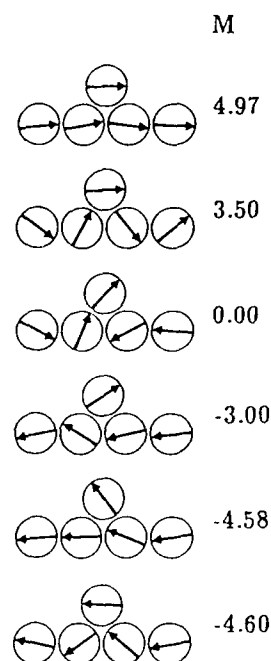


Figure 3. Minimum energy configurations in the neighbor system. M is the magnetization along the chain in units of μ .

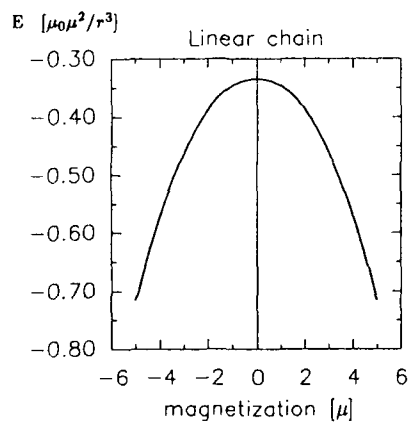


Figure 4. Energy versus magnetization in the linear system.

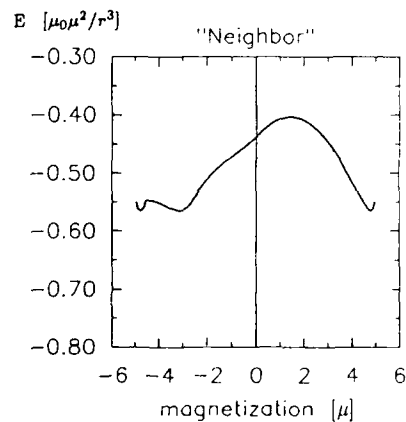


Figure 5. Energy versus magnetization in the neighbor system. The magnetization may also be reversed in a different way, which results in a curve given as the mirror image of the shown curve with respect to $M = 0$.

DISCUSSION

The results given in figures 2 – 5 and table 1 show that the neighbor configuration has an energy barrier of reversal of all the magnetic moments which is more than a factor of two lower than in the case of the linear configuration. At some magnetizations the magnetic field at the site of the neighbor particle is very small because of an outbalancing effect of the fields originating from the particles right and left of the neighbor particle (fig. 4). This leads to a very low energy barrier of reversing the magnetic moment of the neighbor particle ($\Delta E_{\text{neighbor}} \approx 1/20 \Delta E_{\text{linear}}$). Similar results are found when 7 particles are studied.

Tronc et al.⁴ have by means of Mössbauer spectroscopy studied the superparamagnetic relaxation times of different geometric configurations of 90 Å maghemite particles. They found that the relaxation times depend on the detailed geometric arrangement of the particles – especially they noted a faster relaxation when the number of nearest neighbors in the system was increased. They suggested that it is the magnetic dipole interaction between the particles that accounts for the dependence of the relaxation time on the geometrical arrangement of the particles.

For non-interacting particles the superparamagnetic relaxation time (τ) is often written:

$$\tau = \tau_0 \exp(\Delta E/kT) \quad (2)$$

where ΔE is the energy barrier of reversal of the magnetic moment. Such an expression is valid in the case where the magnetic anisotropy is responsible for the energy barrier⁵. If the form of this expression holds also when the energy barrier arises from magnetic dipole interactions between the particles the results of the computer simulations can be interpreted in terms of relaxation times.

The computer simulations presented in this article suggest that magnetic interactions between the particles might very well be the explanation of the results of Tronc et al.⁴. Deviations from the simple linear structure (introduction of one neighbor) certainly lowers the energy barrier of reversal of the magnetic moments, and assuming eq. (2) to hold, this corresponds to faster superparamagnetic relaxation.

CONCLUSIONS

The energy barrier of reversing the magnetic moments in a system of particles interacting by magnetic dipole-dipole interactions can be found by computer simulation methods. Deviation from the linear structure introduced by placing one particle of the system as a neighbor to the linear chain (instead of placing it at the end of the chain) leads to a significant reduction of the energy barrier of magnetization reversal. The magnetic moment of the neighbor particle is reversed much easier than when the particle is placed at the end of the chain. Introducing the neighbor particle complicates the appearance of the system energy as a function of magnetization – local minima are introduced and degenerations occur (different configurations possess the same energy and magnetization).

REFERENCES

1. R.B. Frankel, R.P. Blakemore, and R.S. Wolfe, *Science* 205, 1355 (1979).
2. K. Binder in "Monte Carlo Methods in Statistical Physics", Ed. K. Binder (Springer-Verlag, Berlin, 1978).
3. S. Kirkpatrick, C.D. Gelatt Jr., and M.P. Vecchi, *Science* 220, 4598, 671, (1983).
4. E. Tronc, J.P. Jolivet and J. Livage, *J. Chem. Research* (S), B6 (1987).
5. L. Néel, *Ann. Geophys.* 5, 99 (1949).

ELECTRIC AND MAGNETIC PROPERTIES OF SMALL SYSTEMS

Sigurds Arajs

Department of Physics and Center for Advanced Materials
Processing, Clarkson University
Potsdam, N.Y., 13676 USA

ABSTRACT

Importance of small physical systems is briefly described. The influence of the size on the physical properties is illustrated by the electrical conduction measurements on thin Cr and Ni films on glassy surfaces and by magnetic studies on small α -Fe₂O₃ particles.

Small physical systems are nanostructured materials which lie between the domains of atoms and molecules and the long range macroscopic solid substances. Specific examples of small physical systems are atomic clusters, small particles, thin films and wires, interfaces, organic conductors, composite phases, etc. Such materials are found in nature and can also be created artificially as new technologically promising materials with special properties. The nanostructured systems are of great fundamental and also practical interest. From the fundamental viewpoint, in such systems it is possible to explore quantum size effects on physical properties due to observable energy level quantization. Furthermore, in small systems one can observe the birth of cooperative physical behavior. Obviously, one Fe atom is not ferromagnetic, two Fe atoms do not form a ferromagnetic system but - definitely - an aggregate of 10^3 Fe atoms possess ferromagnetic characteristics. This type of questioning applies to other cooperative properties, such as superconductivity, melting, etc. In small systems a sizeable number of particles of the system are in the surface environment causing special surface effect manifestation on physical properties. In addition to the above topics, small systems also offer opportunities for fundamental investigations on a variety of tunneling phenomena in composite materials, phase transitions, and crossovers in 2d and 3d materials, investigations of moment reversal in magnetic aggregates, etc.

From an applied viewpoint, small physical systems are of significant interest for making new composite materials and magnetic fluids, for activities in the areas of powder metallurgy, catalysis, chemisorption, etc. Lastly, the general developments in the high technology fields require decreasingly smaller components and miniaturization making small physical systems useful materials for these purposes.

It is impossible in a short space to discuss the above topics in detail. Therefore, below we present few selected topics where clear

effects of small system aspects can be seen in the behavior of their physical properties.

One interesting area of small system manifestation is the study of electrical conduction in very thin metallic films deposited on glass surfaces. When a metal is evaporated on such a surface, first small disconnected islands are formed which upon additional evaporation become larger, come closer together, become partially connected ("inverse Swiss cheese model"), and eventually form a continuous film. The electrical conduction undergoes drastic changes as the evaporation process proceeds from the island distribution to a full normal film of certain grain structure. Islands separated far from each other give an electrically insulating material. As the islands grow and come closer together, the electrical conduction mechanism is some kind of tunneling process. As the average thickness increases in the tunneling regime, the film enters the percolation regime and undergoes an insulator-metal transition.

Recently we have investigated the above conduction processes in Cr and Ni films deposited by evaporation on glassy surfaces. Figure 1 shows a typical plot of electrical conductivity of a Ni film at 300 K as a function of average film thickness d . The region A is associated with the tunneling conduction. The insulator-metal transition occurs in the region B which gradually becomes the region C where the conductivity is dominated by the grain boundary and surface roughness scattering. The above boundaries were determined by a sliding least-squares fits of appropriate equations describing the conduction in these regions. The region B is of particular recent interest because for a 2d system the electrical resistance in this regime should behave as $R \sim (d - d_c)^{-t}$, where d_c is the critical thickness and t the critical index. Recently Zabolitsky¹ has theoretically determined $t/\nu = 0.973 \pm 0.005$, where ν is the correlation length exponent. Using $\nu = 4/3$ gives $t = 1.297 \pm 0.005$. Experimental confirmation of the value of t has so far involved mostly model percolating systems and an arbitrary selection of the bounds for the percolation regime. We have performed a unified continuous analysis of the conduction in various regimes of d . In this manner we have found $t = 1.27 \pm 0.10$, $d_c = 3.8 \pm 0.2$ nm for Ni films and $t = 1.34 \pm 0.11$, $d_c = 1.64 \pm 0.20$ nm for Cr films. These values are in a reasonable agreement with the theoretical predictions. A typical plot of R for Ni in the insulator-metal transition region is shown in Fig. 2.

Another interesting example of the influence of the size of the physical system on the magnetic properties is the size dependence of the Morin temperature in α -Fe₂O₃ particles. The bulk α -Fe₂O₃ possesses a corundum type crystal structure with an antiferromagnetic spin ordering. This material exhibits a first order magnetic transition at $T_M^0 = 263$ K. The superscript 0 implies that the general Morin temperature, T_M^H , which depends on the magnetic field H , has been extrapolated to the zero field case. Between this transition and the Néel temperature $T_N = 961$ K, α -Fe₂O₃ has a weak ferromagnetism due to slight spin canting out from the basal plane. Below T_M^0 the spins are aligned antiferromagnetically along the c -axis. It turns out that T_M^0 is sensitive to stresses and also is dependent of the size of the physical system. We have prepared good quality annealed α -Fe₂O₃ particles using techniques described elsewhere². The values of T_M^H for these particles were determined by magnetization measurements as a function of H . By extrapolating to $H \rightarrow 0$, T_M^0 values were calculated. Figure 3 shows a plot of T_M^0 vs. $1/d$, where d is the average particle diameter. This plot clearly demonstrates the size effect of T_M^0 . In fact, extrapolations of these data to $d \rightarrow \infty$ give the correct $T_M^0 = 264 \pm 2$ K for bulk α -Fe₂O₃ while $T_M^0 = 0$ case corresponds to the observed onset of super-

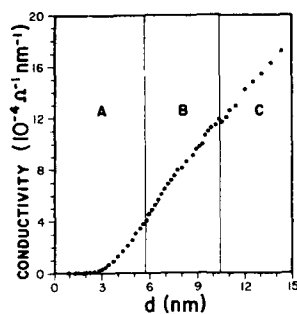


Fig. 1 - Electrical conductivity of a Ni film at 300 K function of average thickness

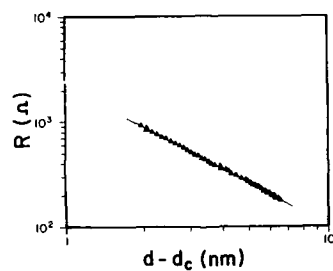


Fig. 2 - Electrical resistance of a Ni film in the insulator-metal regime

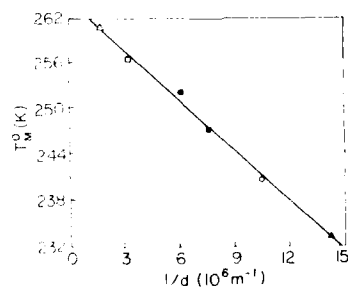


Fig. 3 - Size effect of the Morin transition in $\alpha\text{-Fe}_2\text{O}_3$ particles

paramagnetism in this system. It should be remarked that at the present time there is no satisfactory theory for this interesting size effect on T_M^0 in the α Fe_2O_3 system.

References

1. J.D. Zabolitsky, Phys. Rev. B30: 4077 (1984).
2. G.J. Muench, S. Arajs, and E. Matijevic, phys. stat. sol.(a): 92: 187 (1985).

EXISTENCE OF A FREQUENCY CUT-OFF IN THE SPIN WAVE SPECTRUM OF SMALL
MAGNETIC PARTICLES

N. García

Dpto. Física de la Materia Condensada
Universidad Autónoma de Madrid, 28049-Madrid Spain

I have calculated the spin wave spectra of a small spherical particle using the Heisenberg model for a ferromagnetic system. The main finding is that due to the finite dimension of the particle of diameter D_p there is a cut-off in the dispersion relation of the spin waves of the particle. It is the fact that there cannot be spin waves of wave lengths larger than the dimension of the particle.

The cut-off in the space is

$$k_c = \pi/D_p \quad (1)$$

and this gives a cut-off frequency in the continuous approximation

$$\hbar \omega_c = D(\pi/D_p)^2 \quad (2)$$

where D is the spin wave stiffness that reads,

$$D = 2JSa^2 \quad (3)$$

where J is the exchange coupling, S is the spin and a the interlayer spacing. For iron $D \sim 150 \text{ meV.Å}^2$. For a 30Å diameter particle $\hbar\omega_c \approx 1.5 \text{ meV} \approx 18^\circ\text{K}$. This would be observable with neutron scattering [1]. Also from equation (2) we observe that the cut-off frequency varies as in $1/D_p^2$.

This effect should introduce a stabilization of the particle magnetization with temperature and could be the explanation for the high relaxation times observed in small magnetic particle systems.

REFERENCE

1. J.J. Rhine. private communication.

MECHANICALLY ALLOYED PERMANENT MAGNETS

Ludwig Schultz

Siemens AG, Research Laboratories
D-8520 Erlangen, FRG

ABSTRACT

Mechanical alloying is applied to prepare Nd-Fe-B and Sm-Fe-TM-type permanent magnets (TM: transition metals). Starting from elemental powders, the hard magnetic phases are formed by milling in a planetary ball mill and a successive solid-state reaction at relatively low temperatures. For Nd-Fe-B, the magnetically isotropic particles are microcrystalline, show a high coercivity (up to 20 kOe for ternary alloys and above for Dy-substituted samples) and can be either used for making bonded magnets or compacted to dense isotropic magnets by hot uniaxial pressing. Magnetically anisotropic samples are formed by die-upsetting. With regard to grain size, magnetic properties, compaction and formation of anisotropy, the mechanically alloyed material is comparable with rapidly quenched Nd-Fe-B. The mechanical alloying process has also been applied to prepare magnetic material of 3 new Sm-Fe-TM phases. In Sm-Fe-V with the ThMn_{12} crystal structure, coercivities up to 11.8 kOe, in Sm-Fe-Zr with the PuNi_3 crystal structure coercivities up to 14.8 kOe and in A2-phase Sm-Fe-Ti giant coercivities up to 64 kOe (at room temperature) were achieved.

INTRODUCTION

About 15 years ago mechanical alloying has been developed as a new technique of combining metals¹. It circumvents many of the limitations of conventional alloying and creates true alloys of metals (or metal/non-metal composites) that are difficult or impossible to combine otherwise. Whereas in conventional alloying the mixing of the elements takes place in the melt and the solid alloy is formed by solidification, mechanical alloying uses an interdiffusional reaction, which is enabled by the formation of ultrafine layered composite particles during the milling process in a high-energy ball mill. The metal powder particles are trapped by the colliding balls, heavily deformed and cold-welded leading to characteristically layered particles (Fig.1a). Further milling refines the microstructure more and more (Fig.1b). Depending on the thermodynamics of the alloy system, on the mechanical workability of the starting powders and on the milling conditions, the interdiffusional reaction to form the alloy can either take place during the milling or a following heat treatment is needed.

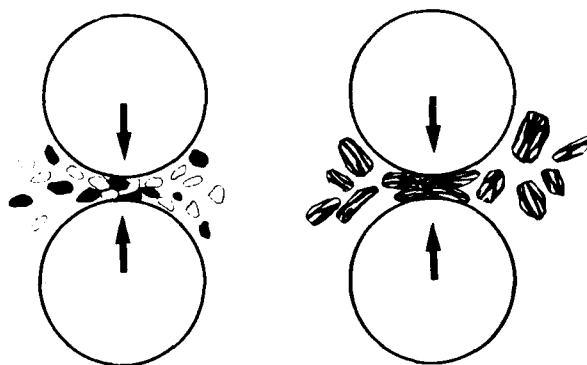


Fig. 1. Mechanical alloying: formation of layered powder particles.

Examples for mechanically alloyed materials are high-strength superalloys, oxide-dispersion-strengthened aluminum alloys, light metals and intermetallic phases (for a recent overview see ²). Besides this, mechanical alloying can also be applied as a non-equilibrium processing tool to produce metastable alloys as amorphous metals ²⁻⁴ or even quasicrystalline powders ⁵. In this contribution the formation of microcrystalline rare-earth permanent magnets by mechanical alloying is reported. The first part covers the formation of Nd-Fe-B magnets and the second part describes the formation of new and possibly metastable hard magnetic phases in Sm-Fe-TM (TM: transition metal) systems.

Nd-Fe-B MAGNETS

Mechanical alloying of Nd-Fe-B powder is performed in a planetary ball mill under an argon atmosphere. The elemental powders are mixed and poured into a cylindrical milling container together with 10 mm diameter steel balls. The ball milling first produces powder with a layered microstructure of Fe and Nd. The submicron boron powder remains undeformed. It is caught by the colliding Fe and Nd particles which are cold-welded and is, therefore, embedded in the Fe/Nd interfaces. Further milling leads to a refinement of the layered microstructure. The crystallite size of the Fe as derived from X-ray diffraction (Fig. 2a) lies in the range of 20 to 40 nm. An atomic mixing by deformation during milling does not occur ⁶. There are no hints that either a crystalline or an amorphous Fe-Nd phase is formed during milling (Fig. 2a). Thermodynamic calculations show that for Fe-Nd the difference of the free enthalpies between the amorphous phase and the layered composite is positive over the whole composition range ⁷, thus preventing an interdiffusional reaction. Therefore, by mechanical alloying, a layered Fe-Nd composite is energetically favored. The hardmagnetic Nd₂Fe₁₄B phase is formed by a heat treatment (Fig. 2b). Because of the extremely fine microstructure of the milled powders, the reaction can take place at relatively low temperatures or with short reaction times. Optimum coercivities are obtained after an annealing at 700 °C for 15 to 30 minutes ⁶. The grain size of the Nd₂Fe₁₄B phase is then about 50 nm.

Fig. 3 is a schematic representation of the processing of the milled powder and the resulting magnet types. Annealing of the as-milled material results in magnetically isotropic powders, which can be used to produce resin-bonded permanent magnets (MM1; MM: "Magnemill"). Isotropic compacted magnets (MM2) can be obtained either from as-milled or from pre-reacted powders by hot uniaxial pressing ⁸. A pressure of 1 kbar at a temperature above 600 °C is sufficient to get fully dense material. Magnetically anisotropic samples (MM3) can be prepared from compacted isotropic magnets by

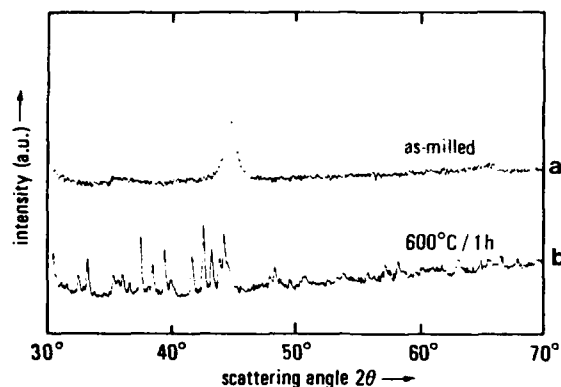


Fig. 2. X-ray diffraction patterns of Nd-Fe-B powder
a) after 30 h milling and
b) after 30 h milling and 1 h at 600 °C heat treatment.

texturing via hot deformation (die-upsetting; Fig. 3) in a similar way as has been shown before for rapidly quenched material⁹. In our experiments, 5 mm diameter samples are uniaxially compressed to half their height within a 7 mm diameter die at 700 °C. Crushing of these samples can produce magnetically anisotropic powder.

Fig. 4 shows the demagnetization curves of all three types of magnets produced from mechanically alloyed Nd₁₆Fe₇₆B₈ powder. The resin-bonded sample (MM1) exhibits a coercivity of 15.3 kOe (the magnetization values relate only to the magnetic powder). The compacted sample (MM2) shows a similar coercivity (15.4 kOe). The hot deformation to form the anisotropic sample (MM3) reduces the coercivity to 11.5 kOe, but improves the remanence, the squareness of the magnetization loop and the energy product. The demagnetization curves parallel and perpendicular to the press direction of an anisotropic sample are shown in Fig. 5. The difference in the curve shape clearly demonstrates that the sample is now magnetically anisotropic. The ratio of the remanences measured parallel and perpendicular to the press direction, which is a measure of the degree of alignment, is 1.8. Applying a further optimized processing, coercivities of 18.5 kOe for the compacted isotropic and of 15.3 kOe for the anisotropic sample have been obtained. Also the degree of alignment of the anisotropic magnets can be considerably improved by increasing the deformation ratio¹⁰.

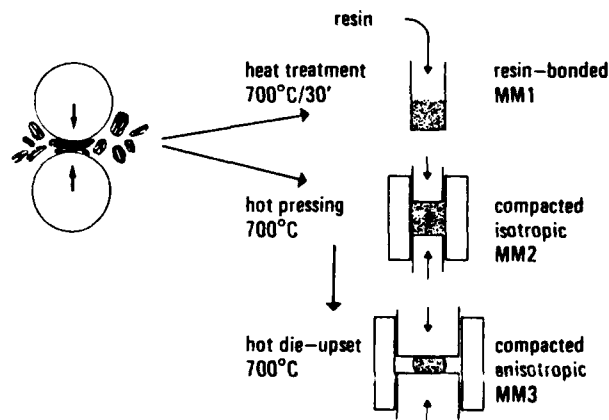


Fig. 3. Preparation of Nd-Fe-B magnets from mechanically alloyed powder.

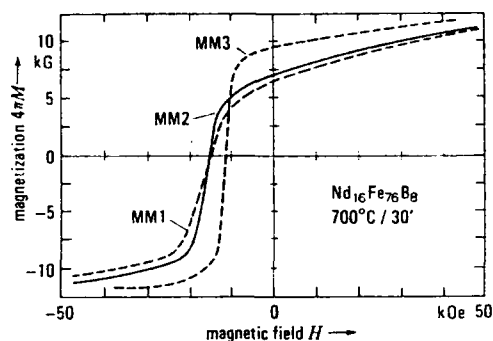


Fig. 4. Demagnetization curves of comparably prepared resin-bonded (MM1), compacted isotropic (MM2), and anisotropic (MM3) $\text{Nd}_{16}\text{Fe}_{76}\text{B}_8$ magnets.

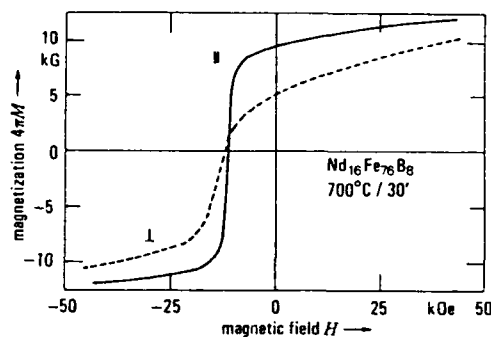


Fig. 5. Demagnetization curves measured parallel and perpendicular to the press direction of mechanically alloyed and hot die-upset $\text{Nd}_{16}\text{Fe}_{76}\text{B}_8$ magnets.

As it is well known for powdermetallurgically produced [11] and rapidly quenched samples [12], a Dy substitution increases the coercivity strongly. Fig. 6 shows the coercivity and the remanence of mechanically alloyed $(\text{Nd}_{1-x}\text{Dy}_x)_{15}\text{Fe}_{77}\text{B}_8$ samples versus the Dy content. Since the samples with a high Dy content had to be reacted at a higher temperature to avoid a two-step demagnetization curve we choose the reaction conditions which showed the highest coercivity for each composition. Therefore the reaction time and temperature varied from 10 minutes to 1 hour and, respectively, from 700 to 800 °C. Contrary to powdermetallurgically produced samples where a maximum coercivity is achieved for $x = 0.6$ [11], our samples show a continuous increase of the coercivity from 1.27 T for the ternary $\text{Nd}_{15}\text{Fe}_{77}\text{B}_8$ sample to 5.6 T for the $\text{Dy}_{15}\text{Fe}_{77}\text{B}_8$ sample. Parallel to this the remanence of these magnetically isotropic samples decreases from 0.8 T to 0.29 T.

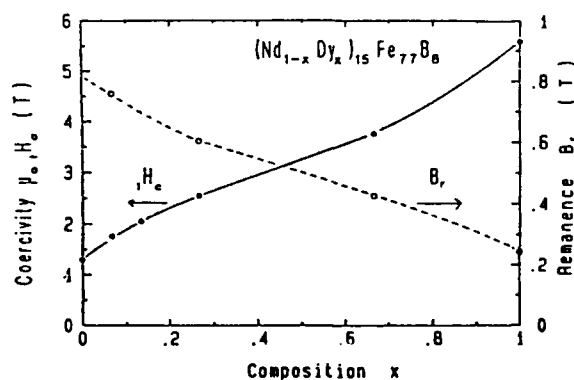


Fig. 6. Coercivity and remanence of mechanically alloyed $(\text{Nd}_{1-x}\text{Dy}_x)_{15}\text{Fe}_{77}\text{B}_8$ samples versus Dy content.

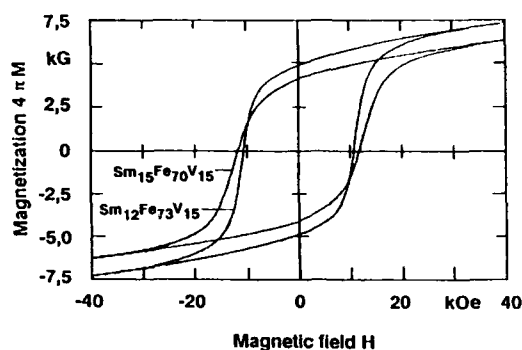


Fig. 7. Hysteresis loops of resin-bonded $\text{Sm}_{15}\text{Fe}_{70}\text{V}_{15}$ and $\text{Sm}_{12}\text{Fe}_{73}\text{V}_{15}$ samples mechanically alloyed and annealed for 30 minutes at 700°C .

Sm-Fe-TM MAGNETS

After the detection of the $\text{Nd}_2\text{Fe}_{14}\text{B}$ phase with its superior hard magnetic properties in 1983, it took several years before it was realized that further phases exist, which might be suitable for permanent magnets. In order to possess a high saturation magnetization and a high crystal anisotropy, these phases must have a high content of Fe (or Co) and must contain rare earth elements. Also only non-cubic phases exhibit a uniaxial crystal anisotropy. Since the binary phase diagrams have been searched for permanent magnet materials without success (with the exception of the Sm-Co system), one has to look for ternary phases, including metastable phases which are not described in the ternary phase diagrams and can only be prepared by non-equilibrium preparation processes like rapid quenching or mechanical alloying. In the following we report on the hard magnetic properties of 3 Sm-Fe-TM phases (TM = V, Ti, Zr) with different crystal structures, which all show high or ultrahigh coercivities. The samples were prepared from the pure elements by mechanical alloying and a subsequent heat treatment. For Sm-Fe-TM alloys, mechanical alloying leads to the formation of an amorphous phase or to a two-phase material of primary Fe plus amorphous phase. The hard magnetic phases are formed during a heat treatment in the temperature range from 600 to 900°C for annealing times between 15 min and 1 h. Depending on the alloy system, the crystallization or reaction process can either lead to equilibrium or metastable phases with a nano- or microcrystalline microstructure. For the magnetic measurements, the resulting powder particles are embedded in epoxy resin to form magnetically isotropic resin-bonded magnets. The unreacted powder can also be hot-compacted to isotropic dense magnets.

1:12 MAGNETS

Besides the Sm-Co and the RE-Fe-B systems, the best investigated RE-containing phases, which are suitable for permanent magnets, are the 1:12 phases ($\text{Sm}(\text{Fe},\text{TM})_{12}$) with the ThMn_{12} crystal structure which was first revealed by Bodak et al.¹³. The magnetic properties of these phases were investigated by Müller for $\text{RE}(\text{Fe},\text{Mo})_{12}$ ¹⁴, Buschow for $\text{Sm}(\text{Fe},\text{V})_{12}$ ¹⁵ and Ohashi et al. for $\text{Sm}(\text{Fe},\text{Ti})_{12}$ ¹⁶. A detailed investigation of the primary magnetic properties of the $\text{RE}(\text{Fe},\text{Mo})_{12}$ alloys shows that a useful uniaxial anisotropy is only found for the RE = Sm compounds. This is also true for the other new phases presented here. The anisotropy field H_A of $\text{Sm}(\text{Fe},\text{Mo})_{12}$, for example, is about 90 kOe, which is higher than that of $\text{Nd}_2\text{Fe}_{14}\text{B}$ and is, therefore, very promising for achieving high coercivities.

At the beginning, we prepared 1:12 magnets with compositions close to the nominal composition ¹⁷, obtaining coercivities up to about 5 kOe. This value of coercivity corresponds to nearly stoichiometric, microcrystalline Nd-Fe-B, where coercivities of 4 to 5 kOe were found. As in the case of Nd-Fe-B, the microcrystalline 1:12 magnets obviously need a secondary grain boundary phase for an effective magnetic hardening. This is demonstrated in Fig. 7 for mechanically alloyed $\text{Sm}_{15}\text{Fe}_{70}\text{V}_{15}$ and $\text{Sm}_{12}\text{Fe}_{73}\text{V}_{15}$ samples. These 1:12-type magnets exhibit coercivities of 11.7 or 10.6 kOe, respectively, at room temperature. An X-ray analysis ¹⁸ shows the presence of a secondary SmFe_2 phase, which separates the 1:12 grains as a grain boundary phase, as demonstrated by TEM investigations ¹⁹. The saturation magnetization of the 1:12 phase materials is about 10 kG which leads to remanences of the magnetically isotropic material of 4 kG for the sample with a high amount of second phase and of 4.9 kG for the sample with the reduced Sm content, resulting in an energy product of 5.2 MGOe. As shown before in general for the 1:12 magnets ¹⁴, a Co substitution can rise the saturation magnetization to 12 or 13 kG. The remanence also exhibits a corresponding increase.

THE A2 PHASE IN THE Sm-Fe-Ti SYSTEM

We tried to reproduce the beneficial effect of an increased Sm content on coercivity also for the 1:12-type Sm-Fe-Ti system. Surprisingly, the remanence of the samples dropped rapidly to rather small values (1 kG at 16 at% Sm ²⁰), but at even higher Sm contents (20 at% Sm) a new and probably metastable phase is formed, which, earlier, has only been reported for thin sputtered films ²¹. Fig. 8 shows the demagnetization curves of magnetically isotropic resin-bonded $\text{Sm}_{20}\text{Fe}_{70}\text{Ti}_{10}$ and $\text{Sm}_{26}\text{Fe}_{64}\text{Ti}_{10}$ samples prepared by mechanical alloying and annealing for 30 min at 725 °C. The $\text{Sm}_{20}\text{Fe}_{70}\text{Ti}_{10}$ sample shows a room-temperature intrinsic coercivity H_c of 50.3 kOe and a remanence of 3.0 kG. There is only a small step in the demagnetization curve at very low fields indicating the presence of a small amount of a soft magnetic phase. The $\text{Sm}_{26}\text{Fe}_{64}\text{Ti}_{10}$ sample even shows a coercivity of over 64 kOe which belongs to the highest coercivities ever observed at room temperature. The metastability of this material was discussed for rapidly quenched samples ²². The crystal structure of this new

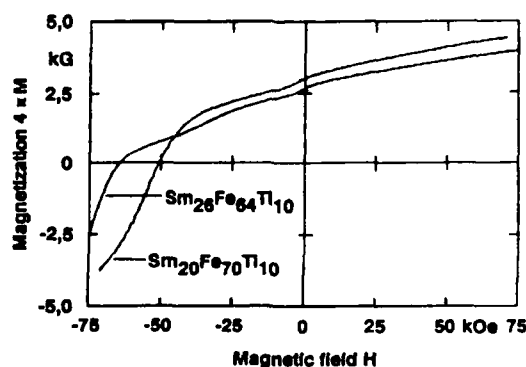


Fig. 8. Room-temperature demagnetization curves of resin-bonded $\text{Sm}_{20}\text{Fe}_{70}\text{Ti}_{10}$ and $\text{Sm}_{26}\text{Fe}_{64}\text{Ti}_{10}$ samples prepared by mechanical alloying.

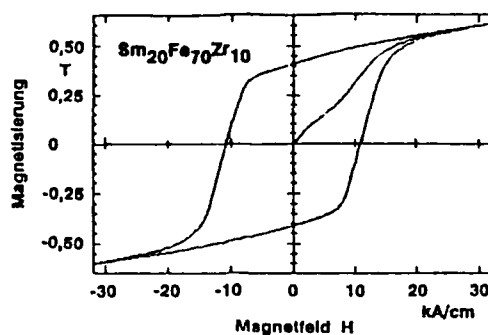


Fig. 9. Demagnetization curve of a resin-bonded $\text{Sm}_{20}\text{Fe}_{70}\text{Zr}_{10}$ sample prepared by mechanical alloying.

phase is hexagonal with $a = 2.014$ nm and $c = 1.2334$ nm. It resembles the A2 phase recently found in the Nd-Fe system ($\text{Nd}_5\text{Fe}_{17}$). Its exact composition is not yet known, since it is still open, whether the Ti atoms occupy the Fe or the RE sites.

THE Sm-Fe-Zr SYSTEM

In the Sm-Fe-Zr system neither the 1:12 nor the A2-phase was observed for mechanically alloyed samples with a high Sm content. Instead of this, a $\text{Fe}_3(\text{Sm},\text{Zr})$ phase forms with the rhombohedral PuNi_3 crystal structure. Also this phase proved to be hard magnetic when prepared as a microcrystalline material by mechanical alloying (Fig. 9). Its coercivity is 13.5 kOe and the remanence is 4.1 kG. A slightly modified composition even resulted in a coercivity of 14.8 kOe.

CONCLUSIONS

These results demonstrate that mechanical alloying is a useful technique to prepare permanent magnets. For Nd-Fe-B, magnets can be obtained with properties that are comparable to rapidly quenched material. For Sm-Fe-TM alloys, three new hard magnetic phases were found. Moderate coercivities of 12 to 15 kOe were obtained for Sm-Fe-V with the ThMn_{12} crystal structure and for Sm-Fe-Zr with the PuNi_3 crystal structure, whereas A2-Phase Sm-Fe-Ti samples reached 64.5 kOe. It is, therefore, predicted that the mechanical alloying process will get its share on the growing rare earth permanent magnet market.

ACKNOWLEDGEMENTS

The author is grateful to K. Schnitzke, J. Wecker and M. Katter for stimulating discussions. This work has been supported by the German Ministry for Research and Technology.

REFERENCES

1. J. S. Benjamin, Sci. Amer. 234:40 (1976).
2. E. Arzt and L. Schultz (eds.), "New Materials by Mechanical Alloying Techniques", DGM Informationsgesellschaft, Oberursel (1989).

3. C. C. Koch, O. B. Cavin, C. G. McKamey and J. O. Scarbrough, *Appl. Phys. Lett.* 43:1017 (1983).
4. L. Schultz, "Formation of amorphous metals by solid-state reactions", *Phil. Magazine B*, 61:453 (1990).
5. J. Eckert, L. Schultz, and K. Urban "Formation of quasicrystals by mechanical alloying", *Appl. Phys. Lett.* 55:117 (1989).
6. L. Schultz, J. Wecker, and E. Hellstern, "Formation and properties of NdFeB prepared by mechanical alloying and solid-state reaction", *J. Appl. Phys.* 61:3583 (1987).
7. L. Schultz and J. Wecker, "Hard Magnetic properties of Nd-Fe-B formed by Mechanical Alloying and Solid State Reaction", *Mater. Sci. Eng.* 89:127 (1988).
8. L. Schultz, K. Schnitzke, and J. Wecker, "Mechanically alloyed isotropic and anisotropic Nd-Fe-B magnetic material", *J. Appl. Phys.* 64:5302 (1988).
9. R. W. Lee, *Appl. Phys. Lett.* 46:790 (1985).
10. S. Heisz and L. Schultz, "Isotropic and anisotropic Nd-Fe-B-type magnets by mechanical alloying and hot pressing", *Appl. Phys. Lett.* 53:342 (1988).
11. M. Sagawa, S. Hirosawa, K. Tokuhara, H. Yamamoto, S. Fujimura, Y. Tsubokawa, and R. Shimizu, *J. Appl. Phys.* 61:3559 (1987).
12. F. E. Pinkerton, *J. Magn. Magn. Mater.* 54-57:5879 (1986).
13. O. I. Bodak and D. O. Beresjuk, *Dopovidi Akademii nauk Ukrainskoi Radjanskoi Socialisticeskoi Republiki, Ser. A*, 3:82 (1981).
14. A. Müller, "Magnetic Material R, Fe, Mo, (Co) with ThMn₁₂ structure", *J. Appl. Phys.* 64:249 (1988).
15. K. H. J. Buschow, "Physico-chemical properties of ternary rare earth base alloys and their relation to permanent magnet applications", *Proc. 9th Int. Workshop on Rare-Earth Magnets and their Applications*, Bad Soden, September 1987, Deutsche Physikalische Gesellschaft, Bad Honnef, p. 453 (1987).
16. K. Ohashi, T. Yokoyama, R. Osugi, and Y. Tawara "The magnetic and structural properties of R-Ti-Fe ternary compounds", *IEEE Trans. Mag.* MAG-23:3101 (1987).
17. L. Schultz and J. Wecker, "Coercivity in ThMn₁₂-type magnets", *J. Appl. Phys.* 64:5711 (1988).
18. L. Schultz, K. Schnitzke, and J. Wecker, "High coercivity in mechanically alloyed Sm-Fe-V magnets with a ThMn₁₂ crystal structure", *Appl. Phys. Lett.* 56:868 (1990).
19. C. Koestler, private communication.
20. K. Schnitzke, L. Schultz, J. Wecker, and M. Katter, "Sm-Fe-Ti magnets with room-temperature coercivities above 50 kOe", *Appl. Phys. Lett.* 56:587 (1990).
21. N. Kamprath, N. C. Jiu, H. Hegde, and F. J. Cadieu, "Magnetic properties and synthesis of high H_c Sm-Ti-Fe", *J. Appl. Phys.* 64:5720 (1988).
22. M. Katter, J. Wecker, L. Schultz, and R. Grössinger, "Preparation of highly coercive Sm-Fe-Ti by rapid quenching", *Appl. Phys. Lett.* 56:1377 (1990).

MELT-SPUN MAGNETS

Frederick E. Pinkerton

Physics Department
General Motors Research Laboratories
Warren, MI 48090-9055

Abstract

The discovery of high performance melt-spun Nd-Fe-B magnets ushered in a new era in permanent magnets. Since then, melt-spinning has proven to be a powerful and versatile technique for magnetic hardening, and a commercially viable alternative to conventional powder metallurgy (sintering) processing. Although most often viewed as a means of making amorphous metals, its success in fabricating permanent magnets depends instead on its ability to produce nanocrystalline material: crystalline compounds with submicron grain sizes. The wide variety of materials amenable to melt-spinning makes it an excellent research tool for exploring the potential as permanent magnets of compounds having favorable intrinsic magnetic properties, and evaluating the effects of compositional variations and additives on their hard magnetic properties. As a non-equilibrium process it is capable of fabricating magnetically hard metastable compounds which are difficult or impossible to make by more conventional means. Most recently, melt-spinning has been used to magnetically harden Sm-Fe-V and Sm-Fe-Ti alloys.

Introduction

Early interest in rapid quenching of permanent magnet materials was stimulated by Clark, who generated significant room temperature intrinsic coercivity ($H_{ci} = 3.4$ kOe) by annealing sputtered amorphous TbFe₂ films [1]. Adaptation of melt-spinning to rapidly quench rare earth-iron alloys was pioneered by Croat and Herbst [2], who obtained $H_{ci} = 8.5$ kOe in binary Nd-Fe_{1-x} alloys, and by Koon and Das [3], who obtained similar coercivity in (La_{0.5}Tb_{0.5})₁₀Fe_{73.8}B_{16.2}. This early work came to fruition when Croat et al. discovered rapidly quenched Nd-Fe-B permanent magnets [4] with $H_{ci} = 20$ kOe based on the new ternary compound Nd₂Fe₁₄B [5]. Similar results were reported by Hadjipanayis et al. [6] for a Pr-Fe-(B, Si) alloy. So successful has this work proven that Delco Remy Division of General Motors Corporation has become the first commercial producer of melt-spun Nd-Fe-B magnets at its new MAGNEQUENCH plant in Anderson, Indiana.

Melt-spinning

Figure 1 illustrates the conceptual simplicity of melt-spinning. Pre-alloyed ingot is inductively melted in a quartz or refractory ceramic crucible which has a ~0.6 mm diameter orifice at the bottom. After a brief soak at 100-150°C above the melting temperature to ensure temperature uniformity, the crucible is pressurized with 15-35 kPa of argon gas to force the molten metal through the orifice. The jet of molten metal impinges onto the circumference of a rapidly spinning quench wheel, which in our research apparatus is solid copper (for high thermal conductivity and heat capacity) with a thin chrome plating (for abrasion resistance). The jet feeds a stationary pool of liquid metal at the point of contact with the wheel, while the wheel extracts the solidifying metal from the pool as a thin, 1-mm-wide rapidly quenched ribbon. An inert gas atmosphere (or vacuum) protects the rare earth from oxidation during high temperature processing.

Much of the versatility of melt-spinning lies in its ability to alter the quench conditions by adjusting the surface velocity v_s of the quench wheel [2,4]. With all other parameters held fixed, v_s determines the rate at which ribbon is extracted from the pool, with higher surface velocities producing thinner, more rapidly cooled ribbons. The average cooling rate, or quench rate, can be as large as 10^6 K/s.

While useful, the concept of average quench rate should not be taken too literally: Of much greater importance is the thermal history of each volume element of the ribbon. This thermal history depends not only on the ribbon thickness (or equivalently v_s), but in general varies even across the thickness of an individual ribbon [4], since the wheel surface of the ribbon is more rapidly quenched than the free surface, especially in thick ribbons. The magnetic properties thus represent the average properties across the ribbon thickness.

Magnetic properties and microstructure

Demagnetization curves for crushed, compacted Nd-Fe-B ribbon samples quenched at various wheel velocities [4] are shown in Figure 2. Maximum H_{ci} occurs over a fairly narrow range of average quench rates near $v_s = 19$ m/s, corresponding to ribbons about $35 \mu\text{m}$ thick. H_{ci} decreases in ribbons quenched either too quickly ("overquenched") or too slowly ("underquenched"). The energy product $(BH)_{max}$ (the maximum product of the magnetic induction B and the field H in the second quadrant of the B - H loop) is also indicated in Figure 2. This figure of merit reaches 14 MGOe for optimally quenched ribbons.

The key to high coercivity is to maximize the content of nanocrystalline $\text{Nd}_2\text{Fe}_{14}\text{B}$. H_{ci} is largest when the $\text{Nd}_2\text{Fe}_{14}\text{B}$ grain size across the entire ribbon thickness falls within the limits 20-80 nm [4]. H_{ci} is reduced in overquenched ribbons ($v_s > 19$ m/s) by the formation of a layer of magnetically soft amorphous Nd-Fe-B at the quench surface, and very high quench rates produce thin, entirely amorphous ribbons with negligible coercivity. Optimum magnetics can be recovered from overquenched ribbons by crystallization of the amorphous material near 700°C [4]. Underquenching ($v_s < 19$ m/s) occurs when inadequate quenching at the free surface allows the growth of oversized $\text{Nd}_2\text{Fe}_{14}\text{B}$ grains. Grains with diameters greater than about 150 nm have reduced coercivity [7], and decreasing v_s increases the volume fraction of magnetically soft oversized $\text{Nd}_2\text{Fe}_{14}\text{B}$. Underquenched material cannot be recovered, since it has already been excessively heated during melt-spinning.

Optimally quenched Nd-Fe-B ribbons have a simple two-phased microstructure, [8] as illustrated by the transmission electron micrograph in Figure 3. Randomly oriented spheroidal 50-nm-diameter grains of the matrix $\text{Nd}_2\text{Fe}_{14}\text{B}$ phase are separated by a thin film (typically 3 nm thick) of non-crystalline Nd-rich, boron-depleted eutectic whose composition is about 70% Nd. This simple microstructure reflects the non-equilibrium nature of melt-spinning. Because $\text{Nd}_2\text{Fe}_{14}\text{B}$ forms peritectically at 1155°C [9], equilibrium cooling from the liquid (for example in ingots) first precipitates iron as the primary crystal above the peritectic temperature, producing a multiphased mixture with large quantities of undesirable second phases

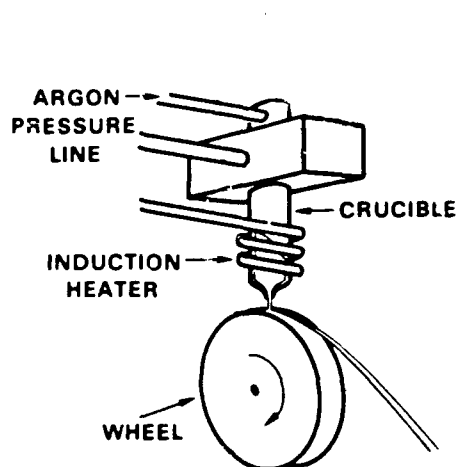


FIG. 1. The melt-spinning process.

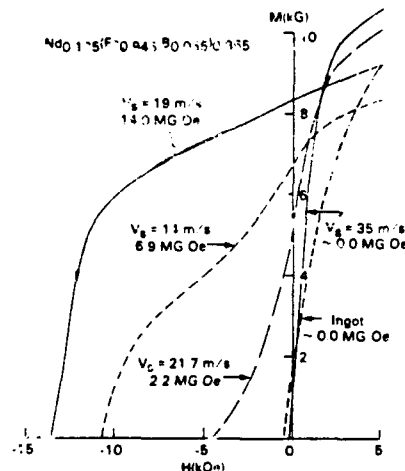


FIG. 2. Demagnetization curves for melt-spun Nd-Fe-B prepared at various wheel speeds v_s (Ref. 4).

[10]. Rapid quenching circumvents phase separation by supercooling the liquid to below the peritectic temperature, where $\text{Nd}_2\text{Fe}_{14}\text{B}$ crystallizes directly. The $\text{Nd}_2\text{Fe}_{14}\text{B}$ grains grow until they nearly impinge, whereupon the remaining Nd-enriched liquid solidifies between the grains. The intergranular phase is amorphous as a consequence of the difficulty in crystallizing a thin film of liquid [8]. An identical microstructure is obtained in over quenched-annealed ribbons: The Nd-rich film is molten at 700°C , and is unable to crystallize upon resolidification.

As the microstructure implies, practical melt-spun magnets are made at compositions somewhat Nd-rich from the $\text{Nd}_2\text{Fe}_{14}\text{B}$ composition. H_{ci} increases with increasing Nd content, but at the expense of remanence as the volume fraction of $\text{Nd}_2\text{Fe}_{14}\text{B}$ decreases [4]. The composition can thus be tailored to maximize either coercivity or remanence (but not both). A good balance between remanence and coercivity is obtained at about 13.5 at. % Nd.

Rapid nucleation and grain growth during melt-spinning (or annealing of overquenched ribbon) does not provide a mechanism for preferred orientation of the crystallographic c-axes (the magnetic easy axis). The bulk magnetic properties are isotropic, i.e. independent of the direction in which the sample is magnetized. A few reports of partial alignment in ribbons have been published [11-14], however the coercivities and hysteresis loop shapes achieved so far are not as good as those of the isotropic ribbons. Alignment can be induced in $\text{Nd}_2\text{Fe}_{14}\text{B}$ ribbons by hot deformation, as will be described below.

Grain size and coercivity

The grain size in optimally quenched ribbons, 20 to 80 nm, is less than the theoretical diameter $D_c = 150$ nm, below which an isolated spherical $\text{Nd}_2\text{Fe}_{14}\text{B}$ grain will be single domain [8]. Lorentz images of the domain walls in thermally demagnetized ribbons using electron microscopy have confirmed that every grain smaller than 150 nm consists of a single magnetic domain, with the domain walls pinned at or in the intergranular phase [8]. These are not simple 180° domain walls, but rather represent a more complex domain structure reflecting the random misalignments of neighboring grains.

Initial magnetization and remagnetization studies show that the domain walls remained pinned at the intergranular phase at all stages of the magnetization and demagnetization process. Moment reversal occurs by switching the magnetization of individual grains, or at most small groups of grains [15], presumably by insertion and propagation of a domain wall. While the intergranular phase itself can pin the domain wall, these results, together with Lorentz microscopy, suggest that an important contribution to H_{ci} is the resistance to the formation of a domain wall within grains smaller than D_c [15]. Comparison of initial magnetization and demagnetization also reveals that magnetic interactions between neighboring grains are important: The applied field needed to reverse a particular grain depends on the magnetization states of its neighboring grains [16].

The ribbons can be considered as a system of interacting single-domain particles, where high coercivity arises from the nanocrystalline particle size and the optimum configuration of wall pinning in an intergranular phase. The details of the origin of coercivity, and of the domain structure and magnetization behavior, however, are not well understood, and represent an important area for further research.

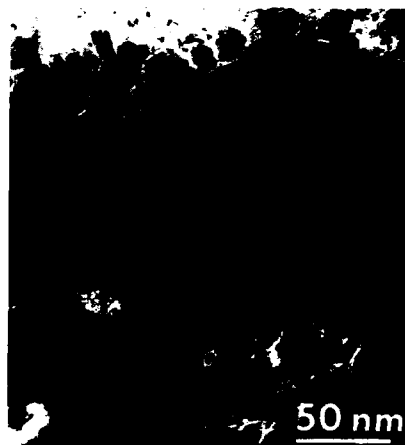


FIG. 3. Transmission electron micrograph of optimally quenched Nd-Fe-B ribbons (Ref. 8). The arrow highlights the amorphous intergranular phase.

Melt-spun R-Fe-B

Elemental substitutions for part or all of the rare earth, transition metal, and metalloid components in melt-spun Nd-Fe-B have been extensively studied. These generally fall into two categories: (1) Substitutions which alter the intrinsic magnetic properties of the $R_2Fe_{14}B$ phase (for example, substituting Co for some of the Fe to increase the Curie temperature [17, 18]), and (2) additive elements introduced in small quantities (~ 1 at. %) which concentrate in the grain boundary phase (for example, adding 0.5 at. % Cu to increase H_{ci} [19]).

The $R_2Fe_{14}B$ phase forms for all of the rare earths except Eu [20], and several R-Fe-B alloys have large coercivities when melt-spun. The saturation magnetizations are high for the light rare earths, where the rare earth-iron moments couple ferromagnetically (parallel), and are relatively low for the heavy rare earths due to the antiferromagnetic R-TM coupling [20]. The H_{ci} values achieved [4] generally reflect the anisotropy field H_A of the $R_2Fe_{14}B$ phase [20]. $Pr_2Fe_{14}B$, with intrinsic magnetic properties similar to those of $Nd_2Fe_{14}B$, has very similar hard magnetic properties [4]. Tb and Dy are especially noteworthy because even at room temperature the magnetocrystalline anisotropy fields are huge, estimated at 150 kOe for $Dy_2Fe_{14}B$ and 220 kOe for $Tb_2Fe_{14}B$ [21]. The melt-spun ribbons have correspondingly enormous room temperature coercivities [22]: 64 kOe for Dy-Fe-B and 96 kOe for Tb-Fe-B, as shown in Figure 4. To the best of our knowledge, this is the highest room temperature coercivity ever reported for a permanent magnet material.

Among compounds having the $R_2Fe_{14}B$ crystal structure, only Co substitutes fully for Fe, and both Nd-Co-B [17, 18] and Pr-Co-B [23, 24] alloys have been magnetically hardened by melt-spinning. A coercivity of 25 kOe was obtained in melt-spun Pr-Co-B [23], reflecting the 100 kOe anisotropy field of $Pr_2Co_{14}B$ [25]. Similarly, although it is more difficult to form than Nd-Fe-B, the carbide magnet Nd-Fe-C has been melt-spun [26], yielding $H_{ci} = 10$ kOe.

Hot deformation

Practical bulk magnets are made from the loose ribbon flakes by one of several consolidation techniques. In the first and simplest process, coarsely ground ribbon powder is mixed with a binding agent (such as epoxy), cold pressed, and cured [27]. This bonded magnet, designated MQ1, has isotropic magnetic properties identical to those of the constituent ribbons, except for a reduction in the magnetization reflecting the 15% by volume of non-magnetic binder. The second quadrant demagnetization curve of a bonded magnet is shown in Figure 5, together with an optical micrograph showing the arrangement of the individual ribbon fragments. The powder retains high H_{ci} after grinding by virtue of its nanocrystallinity—each powder particle contains about 10^9 individual grains, so the damage introduced by grinding affects only the small volume fraction of grains on the particle's surface. Small and complex net shape magnets can be made by pressing, compression molding, or injection molding. This

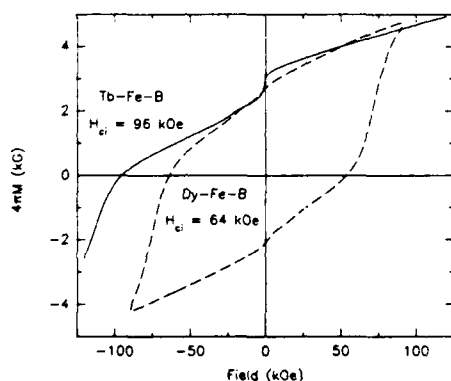


FIG. 4. Hysteresis loops for Tb-Fe-B ribbons (solid line) and Dy-Fe-B ribbons (dashed line).

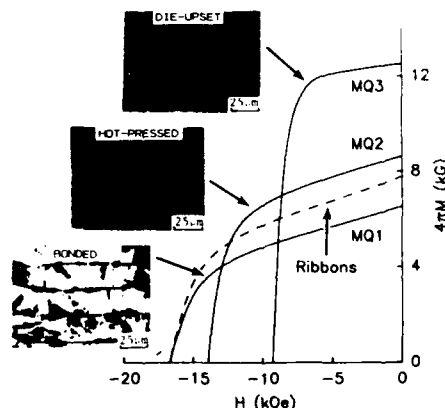


FIG. 5. Demagnetization curves for bonded, hot pressed, and die upset Nd-Fe-B magnets (courtesy C. D. Fuerst and E. G. Brewer). The deformation of individual ribbons can be seen in the optical micrographs (Ref. 20).

contrasts with large grained ($\sim 10\text{ }\mu\text{m}$) sintered magnets, where H_{ci} is severely degraded by grinding. The powder is likewise very stable against degradation when handled and stored for long periods in air.

Fully dense MQ2 magnets are fabricated by hot pressing [27, 28]. Crushed ribbons (without a binder) are placed inside a die cavity and heated to about 750°C . At this temperature the Nd-rich intergranular phase is molten, or at least viscous, allowing the ribbons to deform as the $\text{Nd}_2\text{Fe}_{14}\text{B}$ grains slide past each other. When pressed at 10^6 Pa , the ribbons flow to fill the voids, as indicated by the optical micrograph in Figure 5. The second quadrant demagnetization, shown in Figure 5, closely resembles that of the starting ribbons, except that a small degree of anisotropy is observed with the preferred direction favoring the press direction. This is attributed to partial die upsetting in the deformed regions, as discussed below.

Magnetically aligned MQ3 magnets are obtained by die upsetting [27, 28]. A fully dense MQ2 precursor is placed into an oversized die cavity, heated to $\sim 750^\circ\text{C}$, and uniaxially pressed. The magnet flows radially outward to fill the die, while the height is reduced by a factor of two or more. During hot deformation, alignment is induced parallel to the press direction, giving the high magnetization in the press direction shown in Figure 5. The lateral deformation is apparent from the thinned ribbons shown in the accompanying micrograph. The alignment mechanism is purely crystallographic: No magnetic field is applied during processing. Alignment is believed to arise from a combination of anisotropic grain growth and grain rotation of individual grains. The originally equiaxed $\text{Nd}_2\text{Fe}_{14}\text{B}$ grains grow preferentially along the basal plane orientation into coin-shaped grains about 300 nm in diameter and 60 nm thick [29]. Lubricated by the molten intergranular phase, the grains rotate while sliding during deformation, such that the a -planes orient along the direction of flow [30]. The resulting c -axis (easy axis) alignment is along the press direction, perpendicular to the flow. By virtue of the crystallographic alignment, domain walls run continuously from grain to grain, forming extended domain structures comprising many grains. Lorentz microscopy indicates that the walls become pinned where they interact with the intergranular phase along the grain edges [29]. Extruded magnets, which experience linear flow, tend to show radial alignment [31]. Energy products as large as 45 MGOe have been obtained by die upsetting [32].

New Materials

Melt-spinning has been used to explore the permanent magnetic properties of a variety of promising new compounds. Coehoorn et al. have reported $H_{ci} = 4\text{ kOe}$ for a $\text{Nd}_4\text{Fe}_{78}\text{B}_{18}$ alloy, in which the major phase is believed to be Fe_3B , with $\text{Nd}_2\text{Fe}_{14}\text{B}$ present as a secondary phase to provide magnetic hardness [33]. This alloy enjoys the advantage of a low Nd content and a relatively high remanence, $B_r = 12\text{ kG}$; however, the coercivity is limited.

The announcement of a new $\text{SmFe}_{12-y}\text{Ti}_y$ ($T = \text{Mo, V, Ti, Ta, W, Si}$) phase having the ThMn_{12} structure and possessing favorable intrinsic magnetic properties [34] stimulated several groups to magnetically harden it by melt-spinning. Pinkerton and Van Wingerden reported $H_{ci} = 7.8\text{ kOe}$ in melt-spun Sm-Fe-V [35], and Strzeszewski et al. obtained $H_{ci} = 7.7\text{ kOe}$ for Sm-Fe-Ti [36]. More recently, $H_{ci} = 11\text{ kOe}$ was reported for melt-spun Sm-Fe-(Ti, V) [37]. So far none of this class of compounds has been made into a permanent magnet by conventional sintering process.

The existence of a second, as yet unidentified, new phase in the Sm-Fe-Ti system was reported by Kamprath et al. [38], who fabricated sputtered films with coercivities as high as 38 kOe . This new material is believed to be based on a metastable phase, as attempts to synthesize the major phase by conventional equilibrium processing have been unsuccessful [39]. Recently H_{ci} values similar to those of the sputtered films have been reported using melt-spinning [39]. The demagnetization curves, however, show the presence of a substantial quantity of a magnetic impurity phase which degrades the magnetic properties. This may be ascribed in part to the inherent difficulty of melt-spinning Sm-based materials: Sm has a low melting temperature and high vapor pressure, and some Sm is lost by vaporization during high temperature processing. Stoichiometry is more difficult to control than for the other rare earths. Also, even rapid quenching has difficulty entirely suppressing the equilibrium phase separation to Sm(Fe,Ti)_2 and Sm(Fe,Ti)_{12} before the alloy cools below 800°C . The best results to date for this new metastable compound, $H_{ci} = 50\text{ kOe}$, have been achieved by the technique of mechanical alloying, which employs lower processing temperatures [40].

Summary

The power and versatility of melt-spinning as a technique for magnetically hardening a variety of potential permanent magnet materials has led to its increasing popularity as a research tool. Its use led to the discovery of $\text{Nd}_2\text{Fe}_{14}\text{B}$ permanent magnets, and it has helped

evaluate the potential of several other new magnetic phases. The ability to produce a high performance magnetic powder has proven advantageous for many motor applications. High performance aligned Nd-Fe-B magnets can be prepared from ribbons by hot deformation. Melt-spinning continues to play an important role in the search for new magnetic materials.

Acknowledgment

The author wishes to thank E. G. Brewer, C. D. Fuerst, J. F. Herbst, G. P. Meisner, R. K. Mishra, C. P. Murphy, and D. J. Van Wingerden for valuable discussions.

References

1. A. E. Clark, *Appl. Phys. Lett.* **23**, 642 (1973).
2. J. J. Croat, *Appl. Phys. Lett.* **39**, 357 (1981); J. J. Croat, *J. Magn. Magn. Mater.* **24**, 125 (1981); J. J. Croat and J. F. Herbst, *J. Appl. Phys.* **53**, 2404 (1982); J. J. Croat, *J. Appl. Phys.* **53**, 3161 (1982).
3. N. C. Koon and B. N. Das, *Appl. Phys. Lett.* **39**, 840 (1981).
4. J. J. Croat, J. F. Herbst, R. W. Lee, and F. E. Pinkerton, *Appl. Phys. Lett.* **44**, 148 (1984); *J. Appl. Phys.* **55**, 2078 (1984).
5. J. F. Herbst, J. J. Croat, F. E. Pinkerton, and W. B. Yelon, *Phys. Rev. B* **29**, 4176 (1984).
6. G. C. Hadjipanayis, R. C. Hazelton, and K. R. Lawless, *J. Appl. Phys.* **55**, 2073 (1984).
7. F. E. Pinkerton, *IEEE Trans. Magn.* **MAG-22**, 922 (1986).
8. R. K. Mishra, *J. Magn. Magn. Mater.* **54-57**, 450 (1986).
9. Y. Matsuura, S. Hirosawa, H. Yamamoto, S. Fujimura, M. Sagawa, and K. Osamura, *Jpn. J. Appl. Phys.* **24**, L635 (1985).
10. K. H. J. Buschow, *Mater. Sci. Rep.* **1**, 1 (1986).
11. R. Coehoorn and J. Duchateau, *Mater. Sci. Eng.* **99**, 131 (1988).
12. Guo-hau Tu, Z. Altounian, D. H. Ryan, and J. O. Ström-Olsen, *J. Appl. Phys.* **63**, 3330 (1988).
13. T. Kuji, R. C. O'Handley, and N. J. Grant, *Appl. Phys. Lett.* **54**, 2487 (1989).
14. Y. Otani, H. Sun, J. M. D. Coey, H. A. Davis, A. Manaf, and R. A. Buckley, *J. Appl. Phys.* **67**, 4616 (1990).
15. F. E. Pinkerton and D. J. Van Wingerden, *J. Appl. Phys.* **60**, 3685 (1986).
16. F. E. Pinkerton, *J. Appl. Phys.* **63**, 5427 (1988).
17. J. Wecker and L. Schultz, *Appl. Phys. Lett.* **51**, 697 (1987); **54**, 393 (1989).
18. C. D. Fuerst and J. F. Herbst, *J. Appl. Phys.* **63**, 3324 (1988); *Appl. Phys. Lett.* **52**, 1358 (1989).
19. J. F. Herbst, C. D. Fuerst, R. K. Mishra, C. B. Murphy, and D. J. Van Wingerden, private communication.
20. J. F. Herbst, R. W. Lee, and F. E. Pinkerton, *Ann. Rev. Mater. Sci.* **16**, 467 (1986).
21. S. Hirosawa, Y. Matsuura, H. Yamamoto, S. Fujimura, M. Sagawa, and H. Yamauchi, *J. Appl. Phys.* **59**, 873 (1986).
22. F. E. Pinkerton, *J. Magn. Magn. Mater.* **54-57**, 579 (1986).
23. C. D. Fuerst, J. F. Herbst, and F. E. Pinkerton, *J. Appl. Phys.* **64**, 5556 (1988).
24. J. Wecker and L. Schultz, *Appl. Phys. Lett.* **54**, 393 (1989).
25. R. Grössinger, R. Krewenka, H. R. Kirchmayr, S. Sinnema, Y. Fu-Ming, H. Ying-Kai, F. R. De Boer, and K. H. J. Buschow, *J. Less-Common Metals* **132**, 265 (1987).
26. R. Coehoorn, J. P. W. B. Duchateau, and C. J. M. Denissen, *J. Appl. Phys.* **65**, 704 (1989).
27. R. W. Lee, *Appl. Phys. Lett.* **46**, 790 (1985).
28. R. W. Lee, E. G. Brewer, and N. A. Schaffel, *IEEE Trans. Magn.* **21**, 1958 (1985).
29. R. K. Mishra and R. W. Lee, *Appl. Phys. Lett.* **48**, 733 (1986).
30. R. K. Mishra, T.-Y. Chu, and L. K. Rabenberg, *J. Magn. Magn. Mater.* **84**, 88 (1990).
31. C. J. Yang and R. Ray, *J. Appl. Phys.* **63**, 3525 (1988).
32. J. J. Croat, *J. Less-Common Met.* **148**, 7 (1989).
33. R. Coehoorn, D. B. de Mooij, and C. de Waard, *J. Magn. Magn. Mater.* **80**, 101 (1989).
34. D. B. de Mooij and K. H. J. Buschow, *Philips J. Res.* **42**, 246 (1987).
35. F. E. Pinkerton and D. J. Van Wingerden, *IEEE Trans. Magn.* **25**, 3306 (1989).
36. J. Strzeszewski, Y. Z. Wang, E. W. Singleton, and G. C. Hadjipanayis, *IEEE Trans. Magn.* **25**, 3309 (1989).
37. Y. Wang, G. C. Hadjipanayis, A. Kim, N. C. Liu, and D. J. Sellmyer, *J. Appl. Phys.* **67**, 4954 (1990).

38. N. Kamprath, N. C. Liu, H. Hegde, and F. J. Cadieu, *J. Appl. Phys.* **64**, 5720 (1988).
39. M. Katter, J. Wecker, L. Schultz, and R. Grössinger, *Appl. Phys. Lett.* **56**, 1377 (1990).
40. K. Schnitzke, L. Schultz, J. Wecker, and M. Katter, *Appl. Phys. Lett.* **56**, 587 (1990).

SOLID NdFeB MAGNETS MADE BY
GAS ATOMIZATION AND EXTRUSION

Edward J. Dulis and Vijay K. Chandhok

Crucible Research Center
Crucible Materials Corporation
Pittsburgh, PA

INTRODUCTION

Currently the three methods that are used to make solid NdFeB magnets for commercial production are as follows:

- (1) Vacuum-induction melt, argon gas atomize to powder, jet mill, magnetically orient, cold press, sinter, and heat treat.
- (2) Vacuum-induction melt, cast into ingots, rough grind and pulverize, jet mill, magnetically orient, cold press, sinter, and heat treat.
- (3) Vacuum-induction melt, melt spin to ribbon, pulverize, hot press (MQ2), and hot work (MQ3).

Methods (1) and (2) are used to make almost all of the NdFeB anisotropic magnets made in the U.S. today. The MQ2 (isotropic) and MQ3 (anisotropic) magnets are reportedly increasing in commercial production.

A new method of producing a radially oriented magnet has been developed that involves the hot extrusion of gas atomized powder.^{1,2} This process offers several important advantages.

GAS ATOMIZATION PROCESS

An outline of the process used to make gas atomized NdFeB powder is as follows:

- (1) vacuum melting a preset alloy charge
- (2) pouring the molten metal into a tundish that has a pouring nozzle at the base to control the stream of metal flowing into the atomizing chamber

- (3) impinging the metal stream in the atomizing chamber with a high pressure argon gas stream that breaks the metal stream into droplets, and
- (4) solidifying the fine droplets enroute to the liquid argon quench bath at the base of the argon filled atomizing chamber, Figure 1.

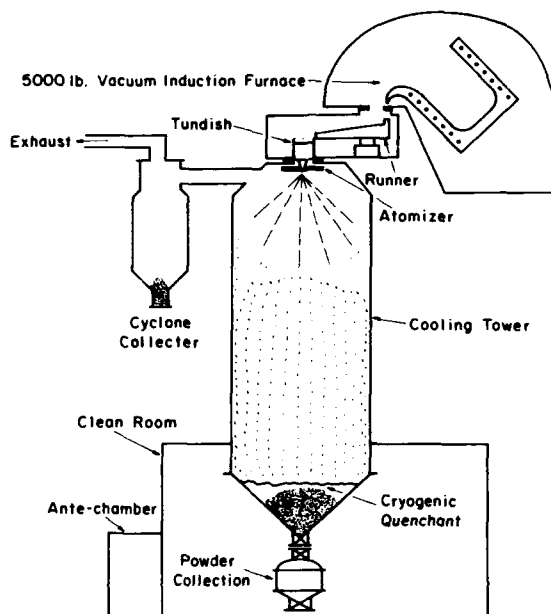


Fig. 1. Gas Atomization Unit

The powder is collected in a clean room located at the base of the atomizing chamber.

Gas atomization offers a distinct advantage over ingot casting in that solidification segregation is eliminated and less cold work is required to pulverize to the required fine particle size of 2 to 3 microns. The detrimental effect of cold work on magnetic properties is well known. Stadelmaier and his coworkers reported on the detrimental effects of cold work for sintered and crushed NdFeB magnetic materials.³ Even with the use of small molds in the ingot casting process the solidification rate is substantially slower than that found in gas atomized powder. Indeed, even in the gas atomized powder the dendritic arm spacing and solidification rates are related to the particle sizes. Gas atomization produces spherical powder particles that contain a range of particle sizes, Table I and Figure 2. The microstructures of the particles of various diameters, Figure 3, shows that the dendritic arm spacing is related to the particle size, Figure 4. The relationship of dendritic arm spacing to solidification rate is also shown. The microstructures reveal a dendritic $\text{Nd}_2\text{Fe}_{14}\text{B}$ phase surrounded by a neodymium-rich, interdendritic structure. The interdendritic neodymium-rich phase is observed in all the particles, and the size of this phase increases with increasing particle size or slower solidification rate. It is interesting that even in this high-solidification-rate range, dendritic segregation occurs.

Cryogenic quenching of gas atomized powder serves two important functions. The first is that sintering of the particles is significantly minimized so that clusters of particulates are avoided. A second advantage is the avoidance of a lengthy cooling period for the mass of particles (particularly for large size heats). Exposure of NdFeB powder to the air before it is thoroughly cooled results in oxidation damage that is detrimental to the final magnet.

Table I. Particle Size Distribution of Spherical Powders Made by the Atomization Process

| Particle Size (Microns) | Distributions (%) Regular |
|----------------------------|------------------------------|
| 250 to 600 | 32.5 |
| 150 to 250 | 20.2 |
| 75 to 150 | 18.7 |
| 45 to 75 | 8.3 |
| <45 | 19.3 |

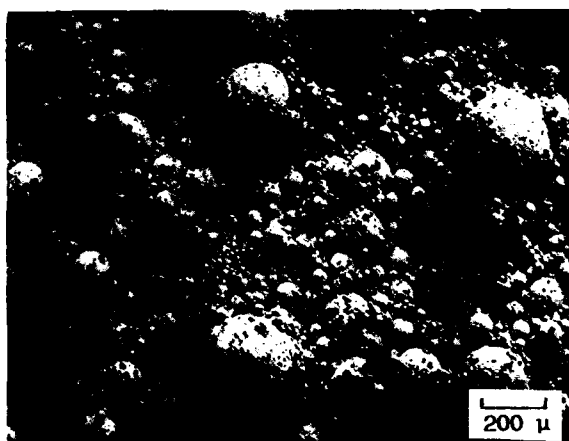


Fig. 2. Argon Atomized NdFeB Alloy Powder

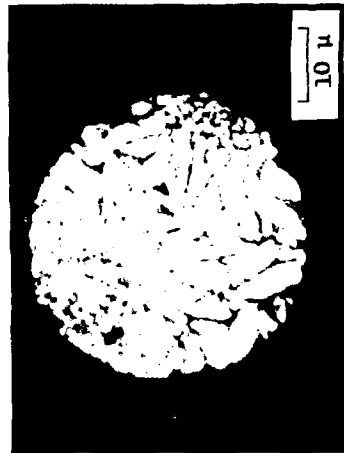
The gas atomized, cryogenically quenched spherical powder particulates are jet milled to a size of 2 to 3 microns. The jet milled powder is then magnetically aligned and cold pressed, followed by vacuum sintering. Commercially produced anisotropic NdFeB magnets by the aforementioned process have a BH_{max} of 26 to 35 MGOe.



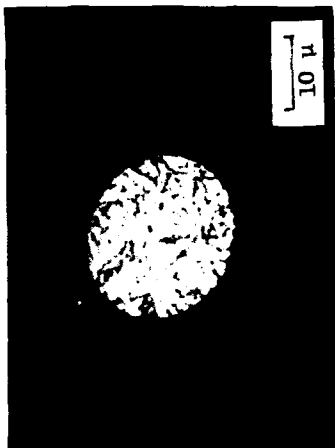
(a) Particle Diam. 275 μ
DAS 10 μ



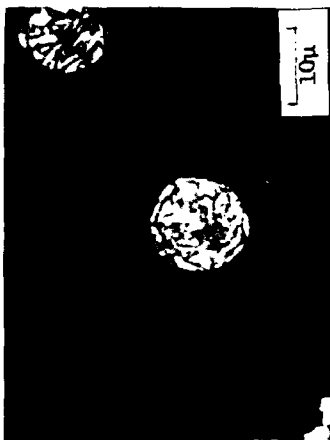
(b) Particle Diam. 53 μ
DAS 3 μ



(c) Particle Diam. 30 μ
DAS 1.7 μ



(d) Particle Diam. 17 μ
DAS 0.7 μ



(e) Particle Diam. 10 μ
DAS 0.5 μ

Fig. 3. Dendritic Microstructures Related to Various Particle Sizes

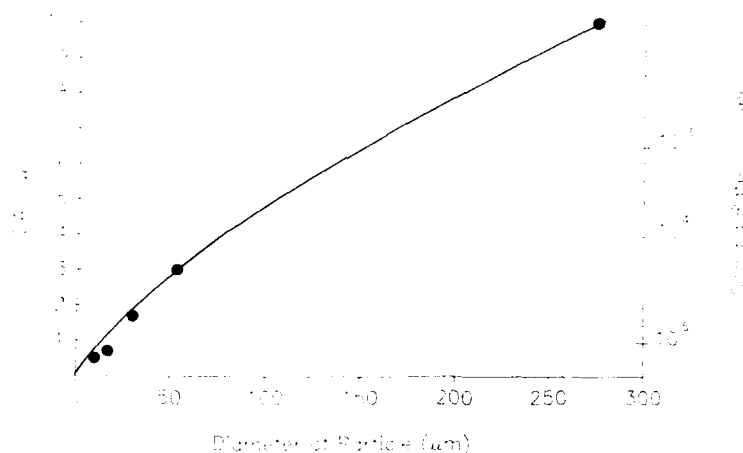


Fig. 4. Relationship of Particle Size, Dendritic Structure, and Solidification Rate for NdFeB Powder

NdFeB MAGNETS BY HOT EXTRUSION

Hot extrusion offers an advantageous process for compacting NdFeB powder. The process results in a crystallographic preferred orientation that is related to magnetic preferred orientation. Studies were made on the effects of extrusion temperature, extrusion ratio, and grain size, and on the subsequent magnetic properties of the magnets produced. The advantages of the hot extrusion process over the conventional sintering process include the elimination of crushing, grinding, milling, magnetic aligning, cold pressing and sintering. An additional advantage is that a radially oriented magnet can be fabricated by extrusion.

Gas atomized powder of different NdFeB compositions were loaded into cylindrical steel cans that were then evacuated and sealed. The cans were heated to temperatures in the range of 840 to 1038°C and extruded as shown in Figure 5. Extrusion ratios were 3.4:1 to 19:1. Extrusion ratio is defined as the ratio of the starting to the final cross sectional area. In addition to cylindrical shapes, rectangular and hollow circular shapes were also extruded. Test specimens were machined from the extruded bars to determine magnetic properties.

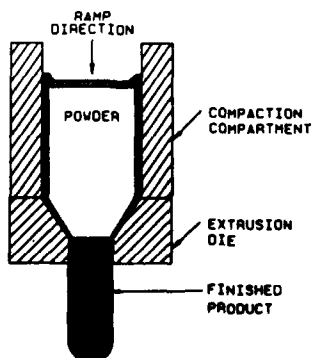


Fig. 5. Schematic of the Compaction/Extrusion Process

During hot extrusion, a crystallographic, preferred orientation is imparted by the mechanical deformation process. X-ray diffraction patterns on $\text{Nd}_2\text{Fe}_{14}\text{B}$ samples from isostatically compacted and from extruded material show the characteristic increase in intensity of diffraction lines indicating preferred orientation, Table II. Pole figure analyses in the $\langle 410 \rangle$ direction indicates that the c-axis of the tetragonal $\text{Nd}_2\text{Fe}_{14}\text{B}$ lies in the plane normal to the axis of the extruded cylinder.¹ The magnetic property data relating to the X-ray diffraction findings, Table III, show that hot isostatically compacted magnets were magnetically isotropic and that the extruded magnets were magnetically anisotropic, with the maximum properties in the radial direction. This finding relates to the development of the crystallographic preferred orientation of the c-axis in the radial direction during the extrusion process.

Table II. X-ray Diffraction Data for a $\text{Nd}_2\text{Fe}_{14}\text{B}$ Magnet in the Extruded and Unextruded Conditions¹

| Index (hkl) | 2 θ (Degree) | Intensity (Arbitrary Unit) | |
|----------------|------------------------|----------------------------|----------|
| | | Unextruded | Extruded |
| 212 | 30.5 | 4.42 | 4.18 |
| 220 | 31.5 | 3.82 | 4.05 |
| 311 | 38.6 | 4.83 | 6.47 |
| 124 | 41.7 | 5.48 | 3.80 |
| 105 | 44.8 | 4.35 | 2.80 |
| 313 | 46.0 | 4.98 | 4.12 |
| 224 | 48.6 | 4.38 | 4.58 |
| 410 | 49.7 | 5.34 | 7.70 |
| 304 | 50.4 | 4.96 | 6.45 |
| 314 | 51.7 | 5.55 | 4.60 |

Table III. Magnetic Properties of Extruded and Unextruded $\text{Nd}_2\text{Fe}_{14}\text{B}$ Magnets¹

| Measuring Direction | B_r (kG) | H_c (kOe) | H_{ci} (kOe) | BH_{max} (MGoe) | H_k (kOe) |
|------------------------|---------------|----------------|-------------------|----------------------|----------------|
| Unextruded* | | | | | |
| Axial | 5.8 | 2.8 | 4.3 | 4.8 | 1.0 |
| Radial | 5.3 | 2.8 | 4.4 | 4.2 | 0.9 |
| Radial | 5.3 | 2.7 | 4.4 | 3.9 | 0.8 |
| Extruded | | | | | |
| Axial | 4.1 | 3.2 | 8.4 | 3.2 | 1.5 |
| Radial | 7.8 | 5.9 | 9.4 | 12.4 | 3.4 |
| Radial | 7.98 | 5.9 | 9.4 | 12.8 | 3.5 |

*Unextruded means that the magnet was consolidated but did not pass through the extrusion die.

The microstructure of extruded samples showed a fine equiaxed grain size of the order of 2 to 7 microns. The fine equiaxed grain structure persisted for extrusion temperatures below 950°C. For higher extrusion temperatures, grain growth occurred that was accompanied by a decrease in intrinsic coercivity. The coarse dendritic structure of the larger particles of gas atomized spherical particulates was recrystallized to a uniform fine grained structure in the extruded material. Inasmuch as the final grains were equiaxed and

uniform in size, as well as being very fine in size, a dynamic recrystallization mechanism is postulated.

The effect of extrusion temperature and extrusion ratio on the magnetic properties, Table IV, shows that the intrinsic coercivity is strongly dependent on the extrusion temperature. The higher the extrusion temperature, the lower the intrinsic coercivity.^{1,2} The effect of extrusion ratio is minimal in the range of 10.6:1 to 18.9:1.

Table IV. Effect of Extrusion Temperature and Ratio on Magnetic Properties

| Extrusion Conditions | | Test Direction | B _r kG | H _c kOe | H _{ci} kOe | BH _{max} MGoe |
|-------------------------|--------|-------------------|----------------------|-----------------------|------------------------|---------------------------|
| Temp. (°C) | Ratio | | | | | |
| 840 | 10.6:1 | Axial | 3.1 | 3.0 | 15.8 | 2.4 |
| | | Transverse | 8.0 | 7.2 | 17.8 | 14.5 |
| 871 | 10.6:1 | Axial | 3.9 | 3.3 | 14.5 | 3.2 |
| | | Transverse | 7.2 | 6.3 | 14.8 | 11.6 |
| 927 | 10.6:1 | Axial | 4.0 | 3.3 | 14.5 | 3.4 |
| | | Transverse | 7.2 | 6.1 | 13.7 | 10.8 |
| 982 | 10.6:1 | Axial | 4.1 | 3.5 | 13.0 | 3.6 |
| | | Transverse | 7.1 | 6.0 | 13.7 | 10.8 |
| 1038 | 10.6:1 | Axial | 3.5 | 2.9 | 11.6 | 2.6 |
| | | Transverse | 7.1 | 5.9 | 11.8 | 10.9 |
| ----- | | | | | | |
| 927 | 10.6:1 | Axial | 4.0 | 3.3 | 14.5 | 3.4 |
| | | Transverse | 7.2 | 6.1 | 13.7 | 11.2 |
| 927 | 13.8:1 | Axial | 3.6 | 3.1 | 13.9 | 2.7 |
| | | Transverse | 7.1 | 6.1 | 14.0 | 10.9 |
| 927 | 16.0:1 | Axial | 3.6 | 3.1 | 14.1 | 2.9 |
| | | Transverse | 7.0 | 6.0 | 13.9 | 10.8 |
| 927 | 18.9:1 | Axial | 3.8 | 3.2 | 14.3 | 3.2 |
| | | Transverse | 7.1 | 6.0 | 13.9 | 10.8 |

All of the aforementioned studies were on extruded cylindrical shapes. To study the properties of extruded hollow cylinders, an 8-inch (20.3 cm) OD outer can and a 2-7/8-inch (7.3 cm) OD inner can by 20-1/2-inches (52 cm) long was prepared from 1/4-inch (0.64 cm) thick mild steel by welding. The can was filled with 140 pounds of powder of the following composition: neodymium - 31.6%, dysprosium - 2.6%, boron - 1.07%, iron - 64.7%. The cans were outgassed and sealed prior to heating to 927°C for extrusion. The extruded hollow bars were 3-inch (7.6 cm) OD by 2-1/8-inch (5.4 cm) ID so that the extrusion ratio was 14.4:1. Samples machined from the hollow bars showed the following properties, Table V.

Table V. Properties of Extruded Hollow Bar

| <u>Direction</u> | <u>B_r</u> <u>kG</u> | <u>H_c</u> <u>kOe</u> | <u>H_{ci}</u> <u>kOe</u> | <u>BH_{max}</u> <u>MGoe</u> |
|------------------|-----------------------------------|------------------------------------|-------------------------------------|--|
| Axial | 4050 | 3400 | 17000 | 3.6 |
| Transverse | 7100 | 6200 | 16200 | 11.4 |

These properties compare very favorably with those found in solid cylindrical bars.

To investigate the effect of the extrusion on the magnetic properties of a rectangular cross section magnet, a 3-1/4-inch (8.3 cm) diameter container was filled with powder and extruded at 871°C through a rectangular die opening of 0.5-inch (1.3 cm) by 1.66-inch (4.2 cm). The extrusion ratio was 10:1. The magnetic properties parallel to the extrusion direction and perpendicular to the extrusion direction in the long (1.66-inch, 4.2 cm) and short (0.5-inch, 1.3 cm) directions, are as follows, Table VI:

Table VI. Magnetic Properties of Fe-28.2 Nd-2.9 Dy-1.1B Magnets Extruded in Rectangular Die [0.5-inch, (1.3 cm)] by [1.66-inch, (4.2 cm)] at 871°C

| <u>Direction</u> | <u>B_r</u> | <u>H_c</u> | <u>H_{ci}</u> | <u>BH_{max}</u> |
|------------------|----------------------|----------------------|-----------------------|-------------------------|
| Extrusion | 4.3 | 3.7 | 16.3 | 4.0 |
| (1.66-inch) | 7.1 | 6.05 | 16.1 | 10.8 |
| (0.5-inch) | 8.2 | 7.2 | 16.95 | 15.02 |

The properties compare favorably with those of cylindrical bars and, indeed, in the short direction showed outstanding properties. Further work could lead to interesting combinations of shape/magnetic properties that could be used in magnet design.

The corrosion resistance of extruded magnets as compared to sintered magnets that had a low oxygen content was investigated using an autoclave environment. After the autoclave exposure of 100% humidity at 110 to 115°C and 5 to 10 psi for 18 and 40 hours, the weight loss of the sintered and extruded NdFeB magnets were as follows, Table VII:

Table VII. Comparison of the Corrosion Rate for Extruded and Sintered NdFeB Magnets

| <u>Magnet</u> | <u>Weight Loss (mg/cm²)</u> | |
|---------------|--|---------------|
| | <u>18 Hrs</u> | <u>40 Hrs</u> |
| Sintered | 60.8 | 213 |
| Extruded | 0.28 | 0.91 |

These test results indicate that extruded magnets have very good corrosion resistance.

REFERENCES

1. B. M. Ma, V. K. Chandhok, and E. J. Dulis; IEEE Trans. on Mag., Vol. MAG-23, No. 5, 1987, p. 2518.
2. R. F. Krause, B. M. Ma, and V. K. Chandhok: Hard and Soft Magnetic Materials with Applications Including Superconductivity, ASM International, 1987, p. 35.
3. H. H. Stadelmaier and N. C. Liu; Materials Letter 4, 1986, p. 304.

THE ROLE OF MICROSTRUCTURE IN PERMANENT MAGNETS

G. C. Hadjipanayis

University of Delaware
Department of Physics and Astronomy
Newark, Delaware 19716

I. INTRODUCTION

In the last ten years major advances in magnetic materials have been appearing at an accelerating pace.^{1,2} Permanent magnets have developed from AlNiCo with $(BH)_m \sim 8$ MGOe to the strong rare-earth magnets of SmCo₅ ($(BH)_m \sim 20$ MGOe), Sm₂(Co,Fe,Cu,Zr)₁₇, $((BH)_m \sim 30$ MGOe) and the recently discovered Nd-Fe-B super-magnets with $(BH)_m$ up to 50 MGOe. The remarkable progress that has been made in magnetic materials has been brought about by an interplay between experimental measurements and theoretical models.⁴ However, we are still far away from a complete understanding of magnetic hysteresis. This is mainly due to the complexity of the effect. Coercivity is a structure sensitive property and since the microstructure depends critically on composition, heat-treatment and other processing techniques, the coercivity varies considerably even in the same magnet prepared at different labs. The Stoner and Wohlfarth model⁵ for single domain particles helped significantly in understanding the origin of magnetic hysteresis in permanent magnets. But, this oversimplified theory is often used incorrectly to describe the hysteresis behavior of more complex systems where a "domain wall pinning"⁶ or a "nucleation of reverse domains"⁷ model would be rather more appropriate. This has been brought about by the lack of microstructural data which are essential for the discussion of magnetic hysteresis behavior.

In this paper we discuss the importance of microstructure in determining the coercivity of several hard magnets which were chosen to represent the three major magnetization reversal mechanisms that are commonly observed in permanent magnets.

II. MAGNETIC HYSTERESIS

A. Hysteresis Loop

A ferromagnetic material is characterized by the phenomenon of hysteresis or irreversibility in magnetization M as shown in Fig. 1. The value which the magnetization acquires at high magnetic fields H is called saturation magnetization M_s . After the removal of the field, the magnetization does not reduce to zero but to a

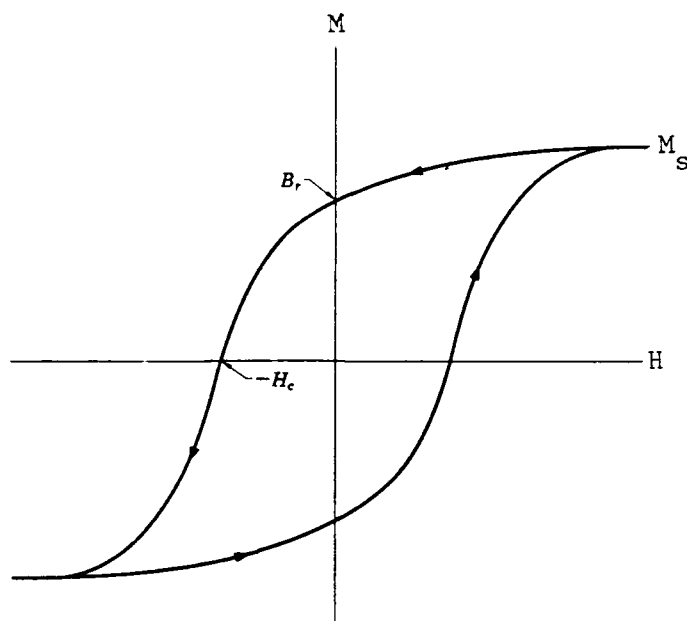


Figure 1. Hysteresis loop.

definite value called remanent magnetization or remanence M_R . The reverse field required to bring the magnetization to zero is called coercive force or coercivity H_c . Weiss⁸ was the first one to explain this irreversibility by assuming the existence of "domains" inside which the magnetization is saturated, but various domains have different directions of magnetizations so that in the absence of the field there is no net magnetization. The boundary layers between these domains are known as "domain walls".

Materials with coercivities greater than 100 Oe are usually referred to as hard magnetic materials while those with coercivities less than 10 Oe are known as soft materials. Permanent magnet materials must have a large H_c to resist demagnetization, a high magnetization to produce a large magnetic induction and a high Curie temperature to resist thermal demagnetization. The first two properties are incorporated into another parameter known as maximum energy product $(BH)_m$ which characterizes the strength of the magnet. For a ring-shape magnet one can show⁹ that

$$(B_m H_m) V_m = H_g^2 V_g \quad (1)$$

where V is the volume and the subscripts m and g specify the magnet and air-gap, respectively. Eqn. (1) shows that the larger the energy product, the smaller the volume of the magnet required to produce a fixed magnetic field in the air-gap. For a square hysteresis loop ($M_r = M_s$), the theoretical limit of energy product is given by

$$(BH)_m = \left(\frac{4\pi M_s}{2} \right)^2 \quad (2)$$

B. Theories of Magnetic Hysteresis

Magnetic hysteresis can be induced by hindrances either to domain wall motion or to magnetization rotation by anisotropic energy barriers. The three major magnetization reversal mechanisms are (i) the "single domain particle" where magnetization is rotated against anisotropic barriers, (ii) the "domain wall pinning" where domain walls are pinned by inhomogeneities within the grains and (iii) the "nucleation of reversed domains" where nucleation takes place at magnetically softer regions with large local demagnetizing fields or domain walls are pinned at grain boundaries. These models are discussed below.

1. Single Domain Particle Model

Below a critical diameter $D_c = 1.4\gamma/M_s^2$ where γ is the domain wall energy, the single domain structure is of lower energy at zero field than a multidomain structure.¹⁰ Stoner and Wohlfarth⁵ calculated the field dependence of the magnetization for non-interacting single domain particle (SDP) possessing a certain form of anisotropy (shape, magnetocrystalline or stress). The total energy of a particle with uniaxial anisotropy K and magnetization M_s in a field H is the sum of magnetocrystalline anisotropy E_k and the magnetostatic energy E_m :

$$E_t = K \sin^2(\phi - \theta) - HM_s \cos \theta. \quad (3)$$

In an equilibrium state, the magnetization of the particle in a given field H points to the direction where E_t is minimum leading to

$$\frac{1}{2} \sin 2(\phi - \theta) + h \sin \theta = 0 \quad (4)$$

where $h = HM_s/2K$ and θ and ϕ are the angles between the field H and magnetization with the easy axis. Eqn. (4) provides a relation between the reduced field h and θ and ϕ . In the final analysis θ is given as a function of ϕ and h , $\theta = \theta(\phi, h)$, and the reduced magnetization is given by $m = M/M_s = \langle \cos \theta \rangle$. Stoner and Wohlfarth⁵ solved the problem numerically and calculated hysteresis loops for various values of ϕ . For a random array of uniaxial non-interacting single domain particles the reduced remanence $m(0)$ and reduced coercivity h_c were found to be 0.5 and 0.48, respectively, leading to $H_c = 0.96K/M_s$.

The SDP model is only applicable to special cases where the single domain particles are dispersed in a non-magnetic matrix so that they do not interact with each other. However, large discrepancies have been observed between the theoretical and experimental value of coercivity in fine powders,¹¹ indicating other possible modes of incoherent rotation in which all spins do not remain parallel. The most important of these models are the magnetization fanning, curling and buckling.⁴

2. Domain Wall Pinning

According to this model,⁹ magnetic hysteresis is due to hindrances to domain wall motion which are caused by various inhomogeneities. A full pinning theory has two major components: calculations of how the individual forces from many particles combine to provide a net force on a unit area of wall. At $H = 0$ the domain wall

will be in a position which minimizes the total energy E_t of the system. For an area A of a 180° domain wall interacting with an inhomogeneity of interaction energy $U(x)$, the total energy in a magnetic field H is given by

$$E_t = U(x) - 2HMAx \quad (5)$$

where M is the magnetization per unit volume and x is the distance the wall has moved after the application of the field H . The equilibrium state can be found by minimizing E_t . At absolute zero there is no thermal activation and the coercivity corresponding to this energy barrier is given by the value of the magnetic field required to push the wall past the energy barrier:

$$H_o = \frac{1}{2MA} \left(\frac{dU}{dx} \right)_{max} \quad (6)$$

At any other temperature there is always a finite probability that the wall will cross the energy barrier through thermal activation in a lower field than H_o .

It is obvious from these discussions that the coercivity can be calculated only when the exact form of the interaction energy is known. For this the nature and distribution of inhomogeneities through the sample must be known. Domain wall pinning has been examined for different inhomogeneities including inclusions,¹² precipitates,¹³ stacking faults,¹⁴ antiphase boundaries¹⁵ and dislocations.¹⁶ Paul¹⁷ has recently used the theory to predict the coercivity due to the domain wall pinning by planar precipitates embedded in a matrix with different magnetic properties. Hilzinger and Kronmüller¹⁸ have studied the interaction between a domain wall and randomly distributed defects by statistical theory and by computer simulations.

3. Nucleation of Reverse Domains – Localized Pinning

The nucleation theory was used to explain the large values of H_c in particles that are large enough to contain domain walls which can move easily through the particles. Coherent rotation cannot be used because $H_c \ll 2K/M_s$. In the absence of domain wall pinning at the particle's surface, the only other alternative is that one or more domain walls are nucleated in the particle; the wall then moves through the particle and reverses its magnetization. Kronmüller¹⁹ has used the micromagnetic theory to determine the nucleation fields H_N for reverse domains. Recently it has been suggested²⁰ that the coercivity of this type of materials is given by

$$H_c = H_N = c \left(\frac{2K}{M_s} \right) - N_{eff} M_s \quad (7)$$

where c and N_{eff} depend strongly on the microstructure of the magnet. The values of nucleation fields can be significantly reduced in real materials where surface irregularities with large demagnetizing fields and defects with lower anisotropy are present. This explains the lower values of coercive fields (in systems where magnetic anisotropy is predominant) which are much less than $2K/M_s$, provided of course that H_N is identified with the coercive field.

The nucleation theory is valid if no residual domains are present. If this is the case then "nucleation" events and "unpinning" events are not qualitatively different. This might be the case in magnets where the pins are not randomly located within

the grains of the sample but are localized along grain boundaries; the "nuclei" might be considered as sections of domain walls pinned at grain boundaries.

Characteristic differences have been observed in the initial magnetization curves and minor loops of materials with different types of magnetization reversal.⁴ In nucleation-type materials the initial magnetization is characterized by a high susceptibility and the hysteresis loop shows a rectangular shape. The coercive field increases more or less linearly with increasing field and it saturates at fields which are usually less than H_c . In "domain wall pinning" materials a small and reversible change of initial magnetization is observed for applied fields $H_a \leq H_c$. For $H_a \geq H_c$ the magnetization and coercivity increase rapidly to saturation. In "single domain particle" materials a behavior which is a mixture of the other two is observed.

4. Conclusions

It is obvious from the previous models that H_c is a structure sensitive property, and must be correlated with the microstructure in order to understand the origin of magnetic hardening. For this purpose transmission electron microscope studies are unique in allowing the structure morphology, the crystal structure and chemical composition of small regions of the samples down to the microscopic level (50-100Å) to be determined simultaneously. In addition, for the case of magnetic materials Lorentz microscopy is another powerful technique allowing the simultaneous observation of magnetic domain structure and microstructure which then leads to identification of possible domain wall pinning sites.

III. EXPERIMENTAL TECHNIQUES

A. High Resolution Analytical Electron Microscopy

The techniques of high resolution electron microscopy²¹ and high spatial resolution microanalysis are used to characterize the microstructure at a line resolution of 0.2 nm or better, and the microchemistry at approximately the 10 nm level. Crystallographic data are obtained by electron diffraction techniques including both selected area diffraction (SAD), which provides high angular resolution but limited spatial resolution, and convergent beam electron diffraction (CBED) which provides three dimensional crystallographic information, accurate lattice parameter data, and crystal symmetry from very small volumes. Energy dispersive x-ray analysis (EDS) and electron energy loss spectrometry (EELS) are used to obtain data on the chemical composition of the various phases and boundaries where possible.

B. Magnetic Domain Studies

Lorentz electron microscopy is used to study the magnetic domain structure of magnetic materials and the interaction of domain walls with inhomogeneities. There are two techniques in observing the magnetic domain structure²²; the *Fresnel* method where domain walls are imaged and the *Foucault* method where magnetic domains are imaged. In the Fresnel technique (Fig. 2a) the incident electron beam is deflected by the horizontal component of the magnetization parallel to the specimen plane because of the Lorentz force ($F = q\vec{v} \times \vec{B}$). The transmitted beam will therefore diverge or converge according to the direction of the local magnetization

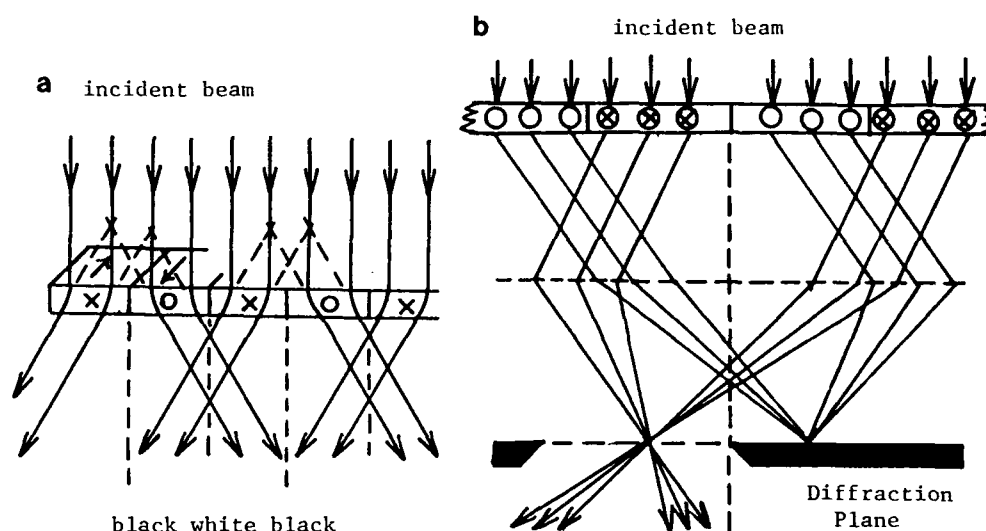


Figure 2. Lorentz microscopy; (a) Fresnel and (b) Foucault techniques.

vector. To observe the domain walls it is necessary to defocus or overfocus the objective lens so that a plane above or below the specimen plane is in focus. Because of the electron distribution below the specimen, the domain walls appear as alternate dark and bright lines. The difference between the underfocused and overfocused images is that the line contrast reverses as the image plane is moved from one side of focus through the other. The Foucault technique makes use of the fact that the diffraction spots are split. The objective aperture can be used to block out one of the split central beams (Fig. 2b) and the magnetic domains appear as alternate dark and light bands.

C. Typical Microstructure Study

In a typical study, a bright field image of the specimen under two beam conditions is obtained and regions or defects of interest are identified. Selected area diffraction combined with dark field microscopy provide information about the crystallographic orientation and the crystal structures of the phases present. Convergent beam electron diffraction provides high spatial resolution crystallographic data from regions as small as 2-5 nm. Energy dispersive x-ray analysis and electron energy loss analysis is then used to characterize the chemical composition of the various phases observed. High resolution lattice and structural imaging of the interfaces between different phases completes the microstructural characterization. Lorentz microscopy of that region would then determine the distribution of domain walls in the area of interest. Changes in the domain wall pattern as the sample is subjected to successively larger magnetizing fields would determine the ability of the defect to impede domain wall motion and thereby determine the contribution of that defect structure to the coercivity. In this fashion, material characteristics can be directly

related to magnetic properties which would aid in evaluating theoretical models and optimizing magnetic properties.

IV. TYPICAL EXAMPLES OF HARD MAGNETS-MICROSTRUCTURE

In this section we discuss the microstructure of some magnets believed to represent the main three categories of magnetic hardening discussed earlier. In the Single Domain Particle-Type magnets we included (i) the Nd-rich Nd-Fe alloys where $\text{Nd}_2\text{Fe}_{14}\text{B}$ particles are embedded in a non-magnetic matrix and (ii) CoPt where tetragonal CoPt nuclei are observed with three equivalent c-axes. The Domain Wall Pinning magnets include (i) the precipitation hardened 2:17 magnets where domain walls are pinned at the 1:5 walls of a cellular microstructure and (ii) Fe-Pt-Ni where domain walls are pinned at intersections of the tetragonal lamellae. In Nucleation Type magnets the microstructure of Nd-Fe-B magnets is discussed where domain walls move easily inside the grains and interact strongly with intergranular phases where the reverse domains are nucleated. Finally we also discuss the microstructure of Rapidly Solidified Nd-Fe-B magnets where fine single domain particles (grains of a few hundred Å) are believed to interact with each other.

A. Single Domain Particle-Like

1. As-Cast Nd-Rich-Fe Based Alloys

TEM results in $\text{Nd}_{80}\text{Fe}_{15}\text{B}_5$ revealed²³ sets of fine needle particles embedded in a non-magnetic Nd-rich matrix within the grains of annealed samples, as shown in Fig. 3. The size of these fine needles is about 100 Å and are believed to be the 2:14:1 phase which is responsible for the high coercivity. For a random distribution of single domain particles with uniaxial anisotropy, the coercivity is given by

$$H_c = 0.96 K/M_s \quad (8)$$

where K is the anisotropy constant and M_s the saturation magnetization. Using the values of M_s, K reported²⁴ for the 2:14:1 phase ($M_s = 1270$ emu/cc, $H_A = 2$ K/ $M_s = 68$ kOe) the predicted coercivity according to Eq. (8) is 32.6 kOe. These values are larger than the experimentally observed maximum value which was only 16 kOe. This difference may be due to several reasons including particle interactions, incoherent processes⁴ and domain wall pinning in the larger particles which are observed in this alloy.

2. Co-Pt

Equiatomic CoPt alloys can be quenched from a high temperature to retain a disordered f.c.c. cubic structure with a low coercivity.²⁵ Aging at lower temperatures (below 700°C) produces an ordered tetragonal phase of type AuCu I with $(\frac{c}{a}) \sim 0.97$. The c-axis is an easy axis of magnetization with an anisotropy constant of about 10⁷ erg/cc. Upon ordering the alloys become magnetically hard.

In the early stages of ordering, ordered regions of diameter 50 - 100 Å were found²⁶ with their c-axes oriented at random parallel to one of the three original

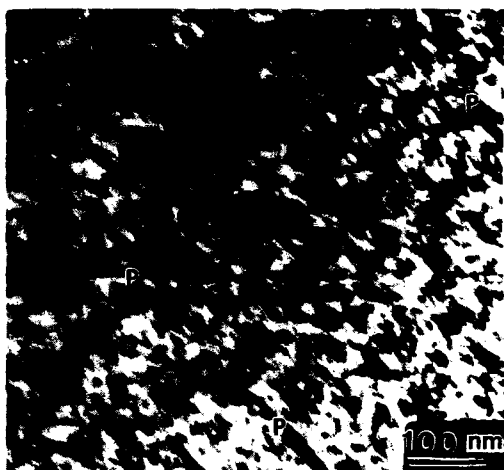


Figure 3. $\text{Nd}_2\text{Fe}_{14}\text{B}$ precipitates (needle nuclei P) embedded in a non-magnetic Nd-rich matrix.

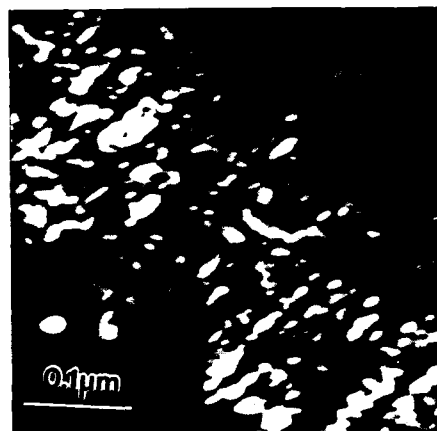


Figure 4. Ordered CoPt nuclei with the tetragonal AuCuI structure.

disordered cubic "a" axes and the measured coercivity is 350 Oe. At an intermediate aging stage the nuclei start aligning in groups as shown in Fig. 4. The ordered nuclei have a ratio of $\frac{\text{length}}{\text{width}} = 2$, with a length of 80-100 Å and a coercivity of 2500 Oe. In the optimum high coercivity (3-5 kOe) state, particles with the same c-axis having a diameter of ~200 Å group together on {100} planes with their c-axes at 45° to the {110} plane. In the overaged state like particles coalesce to form lamellae of one particular c-axis, the other two orientations being consumed. The measured coercivity is decreased to 200 Oe because of the coarsening of the microstructure.

Conventional domain walls could not be seen in an optimum $\text{Co}_{52}\text{Pt}_{48}$ sample with Lorentz microscopy. We strongly believe that the observed coercivity is due to incoherent magnetization rotation processes induced by strong interactions among the particles. This is further suggested by the large values of reduced remanence observed in these alloys. The large values of the reduced remanence ratios are explained in terms of exchange interactions⁴⁸ between particles of different c-axis. This interaction being proportional to the overall sample magnetization (λM) modifies the Stoner and Wohlfarth magnetization curves of single domain particles and allows the reduced remanence ratio to be higher than 0.5.

B. Domain Wall Pinning Type Magnets

1. Precipitation Hardened 2:17 Type Magnets

(i) Magnetic Properties

Precipitation hardened $\text{Sm}_2(\text{Co}, \text{Fe}, \text{Cu}, \text{Zr})_{17}$ type-magnets can be classified in two different groups; those which have coercivities around 6 kOe and those whose coercivity is greater than 10 kOe. The hard magnetic properties of these sintered magnets are achieved through a complex heat-treatment²⁷ consisting of a homogenization heat-treatment at around 1200°C followed by an aging at around 800°C, a slow cooling to 400°C and then quenching to room temperature.

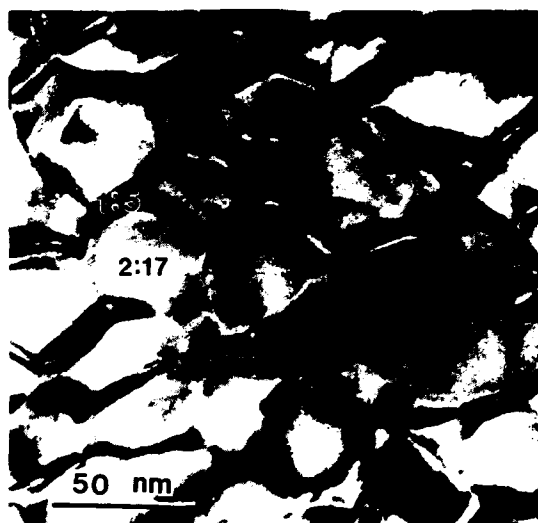


Figure 5. Cellular microstructure in precipitation hardened magnets with lower coercivity.

The low and high H_c magnets show slightly different initial magnetization curves. The initial curve of low H_c magnets is characteristic of uniform domain wall pinning materials. The initial curve of higher H_c magnets²⁸ shows a larger increase at low fields but not as much as that observed in SmCo_5 and Nd-Fe-B magnets. This kind of behavior indicates a non-uniform domain wall pinning with an additional contribution from localized pinning at grain boundaries. Kerr effect studies show corrugated domain walls which tend to ignore grain boundaries and are pinned in the interior of grains. In the high H_c materials, however, some domain walls have been observed to pile up at grain boundaries after the application of a magnetic field indicating an additional contribution to H_c from localized domain wall pinning at grain boundaries.²⁸

(ii) Microstructure and Magnetic Domain Structure

A fine "cellular" microstructure with different cell sizes have been observed in these materials.²⁹⁻³¹ The cell size is in the range of 500-600 Å and the cell boundaries are approximately 60 Å thick. Selected area electron diffraction with dark field microscopy showed that the cell interiors have the 2:17 rhombohedral structure while the cell boundaries have the 1:5 hexagonal structure (Fig. 5). The 2:17 phase can be obtained from the hexagonal 1:5 phase by the ordered replacement of a third of all samarium atoms. Whether the rhombohedral or hexagonal modification of 2:17 is obtained depends on whether this replacement occurs such that the resulting stacking sequence is ABCABC... or ABAB... type.

Several thin platelets have been observed within the cells and these are twin-oriented along the (0001) plane. Changes in the 2:17 rhombohedral stacking sequence are possible and this can lead to the twin structure ABCABACB... This

twinning is formed to release some of the lattice strain energy present because of the coexistence of the 1:5 and 2:17 phases. The cellular microstructure appears to be formed of approximately equiaxed-cells when viewed perpendicular to the c-axis. However the cells appear rhombic when viewed parallel to the c-axis. This behavior indicates that the cell boundaries are oblique to the basal plane and lie along pyramidal planes. The reason for this is the mismatch between the 2:17 rhombohedral and the 1:5 hexagonal lattice.³² The addition of Cu decreases the mismatch along the c-axis but increases the mismatch along the a-axis leading to the formation of the cellular structure.

The microstructure of high coercivity is characterized by larger cells (~ 1000 Å) which are superimposed on a "lamellae" structure (Fig. 6).³³ This type of microstructure is obtained after a prolonged heat-treatment at 830°C instead of 800°C. According to Raberberg³⁴ the lamellae have the 1:3 rare-earth phase and lie along (0001) planes. On the other hand, Fidler et al.³⁵ claimed a 2:17 hexagonal structure for the lamellae.

Energy dispersive X-ray analysis showed that Cu concentrates in the cell boundaries while Zr concentrates in the thin lamellae (referred to as Z-phase). The 2:17 rhombohedral cells are enriched in Fe.

Lorentz electron microscope studies³¹ on thermally demagnetized samples show "wavy" magnetic domains following the 1:5 cell boundaries (Fig. 7). The domains appear to be smaller (4000 Å wide) in the higher H_c materials and are not affected by the presence of lamellae. The wavy nature of the domain walls does not change after the application of a magnetic field indicating that they are pinned at the 1:5 cell boundaries.

(iii) Magnetic Hardening Models

Microstructure measurements at different stages of the heat-treatment have shown that the cellular and lamellar structure form during the prolonged heat-treatment at around 800°C. In the subsequent heat-treatment the structure morphology of the magnets *does not change*.³⁶ However, EDS studies show an increase in the Cu content of the cell boundaries during the slow cooling to 400°C. The higher Cu-content of the cell boundaries dilutes the magnetic properties of the SmCo_5 phase and a decrease in domain wall energy is expected. According to Nagel³⁷ the domain wall energy of $\text{Sm}(\text{Co,Cu})_{5-7.5}$ alloys decrease with increasing Cu content. It thus appears that here is a large gradient in domain wall energy γ across the cell boundaries which can qualitatively explain the high coercivity.

2. Fe-Pt-Ni

Ordering in $\text{FePt}_{0.7}\text{Ni}_{0.3}$ is similar to that of $\text{Co}_{52}\text{Pt}_{48}$ so that the change of microstructure through the course of ordering will not be presented here. However, the crystal morphology of the sample (Fig. 8) in its optimum state (H_c 1400 Oe) closely parallels the intermediate state of $\text{Co}_{52}\text{Pt}_{48}$. The bright field micrograph (Fig. 8) shows lamellar traces with multiantiphase domain boundaries. The lamellar traces lie along {110} directions and they are in twin relations with their c-axis at 90° to that of the tetragonal matrix.³⁸ Fig. 9 is an overfocussed image of the same area shown on Fig. 8. Each lamellar trace is decorated with black and white contrast

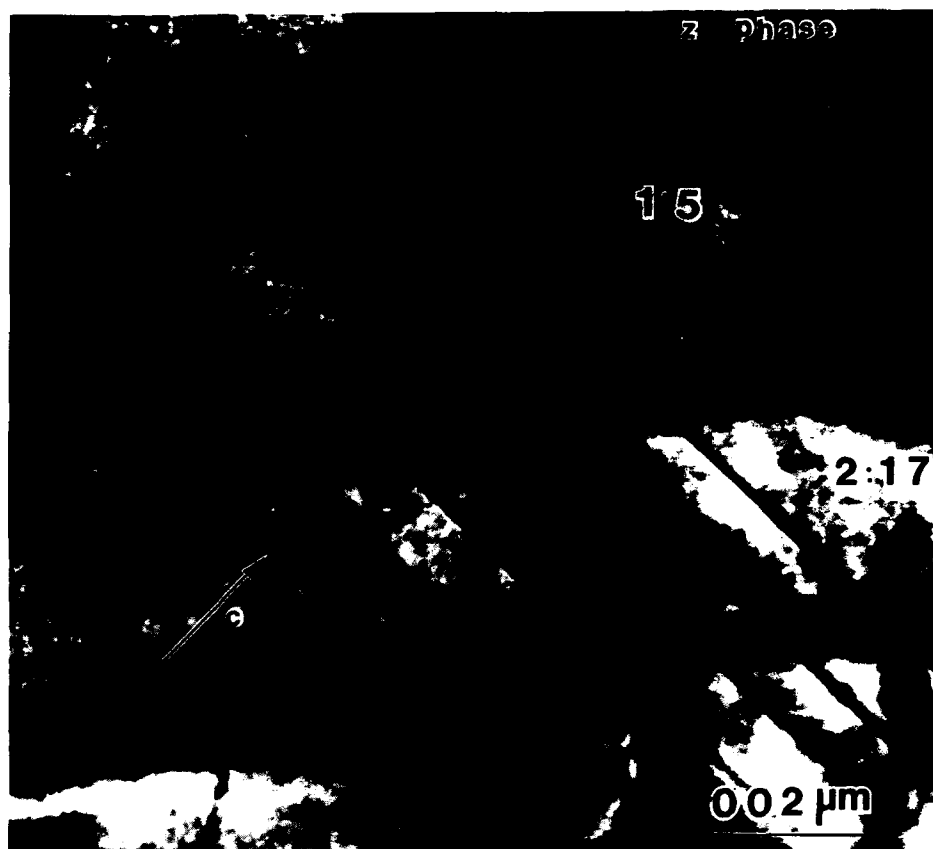


Figure 6. Coexistence of cellular structure with thin lamellae in precipitation hardened magnets with higher coercivity.



Figure 7. Magnetic domains in precipitation hardened magnets.

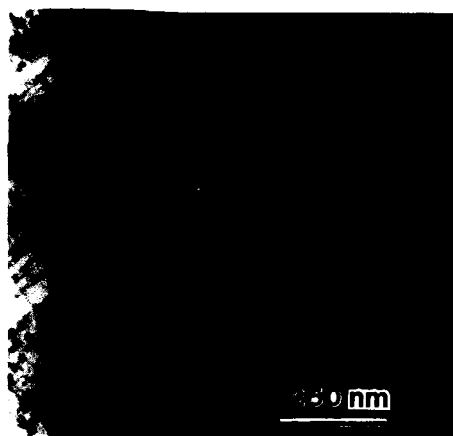


Figure 8. Bright field micrograph showing lamellae with tetragonal Au-CuI structure in $\text{FePt}_{0.7}\text{Ni}_{0.3}$.



Figure 9. Scanning electron micrograph showing the microstructure of a sintered magnet. The bright areas are Nd-rich phases and Nd-oxides.

and these are identified as 90° domain walls, since the c-axis rotates through 90° in crossing from the lamellae to the matrix. The long black and white lines, parallel to the $[001]$ are 180° domain walls. They are determined from the matrix whose c-axis and therefore the easy direction of magnetization is parallel to $[001]$. When a 180° domain wall crosses a lamellar trace the black and white contrast of the lamellae reverses. After the application and removal of a field of 2000 Oe the domain walls are displaced and in the new remanent state seem to show preference in crossing 90° lamellar junctions.

From the picture of the experimental observations a model has been set up to explain the magnetic hardening in $\text{FePt}_{0.7}\text{Ni}_{0.3}$. It is assumed that the lamellar junctions are the pinning centers of domain walls because they lower both the domain wall and demagnetization energy. When a 180° wall crosses a lamellar junction it is not necessary to have a domain wall segment and uncompensated poles within the lamellae. A linear variation of coercivity with temperature is predicted through continuous pinning of domain walls provided the intrinsic effects are not important.

C. Nucleation Type Magnets

1. Sintered Nd-Fe-B Magnets

(i) Magnetic Properties

Record values of energy product were obtained in sintered magnets where $(BH)_m$ exceeding 40 MGOe.⁴² The initial magnetization curves show a steep increase of magnetization at low field which is characteristic of nucleation-type (localized domain

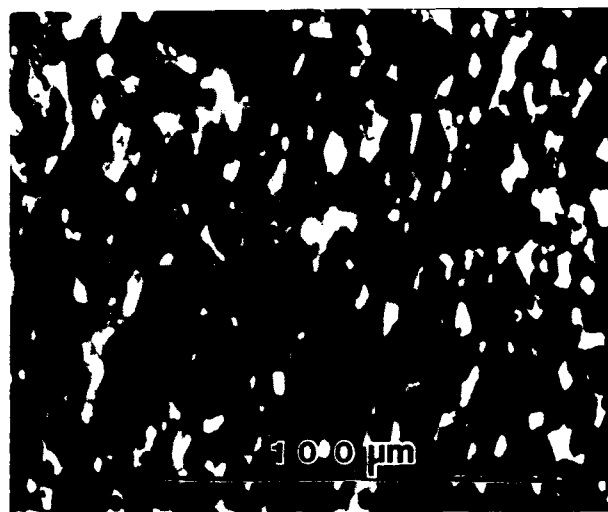


Figure 10. Scanning electron micrograph showing the microstructure of a sintered magnet.

wall pinning).⁴³ When the samples are ac demagnetized the “effective initial” curve is different and it lies below that of the thermally demagnetized samples. This indicates that after the application of a field the domain wall distribution changes and some of the walls are engaged with different and stronger pinning sites (around the grain boundaries) making it more difficult to completely saturate the sample. This was further suggested by the coercivity behavior which was found to be strongly dependent on applied field. In thermally demagnetized samples H_c increases initially slowly and then more rapidly with the applied field. In ac demagnetized samples a different behavior is observed. The coercivity is practically negligible until a critical field where it starts increasing rather drastically to saturation.

(ii) Microstructure Studies

Scanning electron microscope studies on sintered magnets show a microstructure (Fig. 10) consisting of a 2:14:1 majority phase and some other intergranular phases⁴⁴ discussed below. The major phase present is the tetragonal $\text{Nd}_2\text{Fe}_{14}\text{B}$ with $a = 0.880 \text{ nm}$ and $c = 1.22 \text{ nm}$. Fig. 11 shows a high resolution TEM lattice image of this phase with a spacing of 1.22 nm corresponding to the spacing of the basal (001) planes of $\text{Nd}_2\text{Fe}_{14}\text{B}$. No defects have been observed within the 2:14:1 phase and this is consistent with the observation that domain walls move easily inside the 2:14:1 grains. The $\text{Nd}_{1+c}\text{Fe}_4\text{B}_4$ phase was found to have an incommensurate tetragonal structure with $a = 0.709 \text{ nm}$ and $c = 14.46 \text{ nm}$. Grains of this phase were always characterized by a very high density of planar faults with a high density of dislocations associated with the faults. These faults and the dislocations are

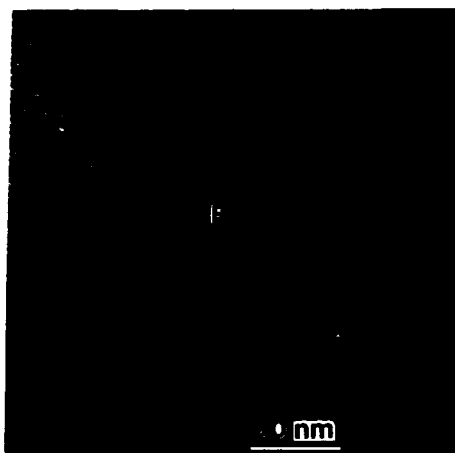


Figure 11. High resolution lattice image showing the 2:14:1 phase (F) and Nd-rich phase (G).

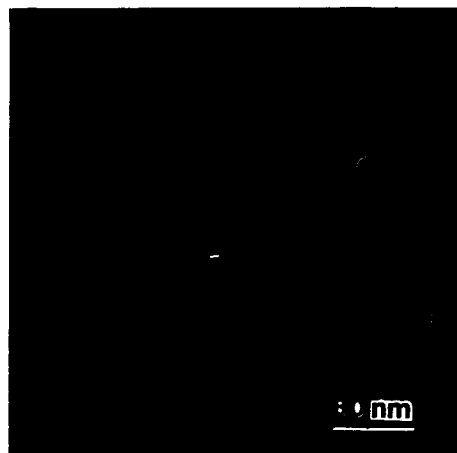


Figure 12. High resolution TEM micrograph showing the $\text{Nd}_{1+x}\text{Fe}_4\text{B}_4$ phase (C) and 2:14:1 phase (E).

readily seen in Fig. 12 along with lattice fringes corresponding to the 2.74 nm spacing of the (001) planes. At least two phases with a high Nd content (55 - 85 wt% Nd) were detected by CBED and EDS. One of these phases with its associated diffraction pattern is shown in Fig. 13. This phase has been identified as BCC with $a = 1.14$ nm, and EDS analysis gave a Nd-content of about 85 wt%. Electron energy loss spectroscopy (EELS) did not detect boron. Other high Nd-content regions gave diffraction patterns suggesting a hexagonal structure. The Nd-rich phases have been observed at some grain boundaries and most frequently at triple grain boundary junctions. Small amounts of α -Fe were found, sometimes as small well-defined grains about 6.0 nm in size densely packed in a matrix with about 25 wt% Nd, as aggregates of larger grains about 60-100 nm in size, or, as mentioned above, as even smaller grains in a $\text{Nd}_2\text{Fe}_{14}\text{B}$ matrix.

In sintered magnets, domain walls are always found to end at grain boundaries (Fig. 14(a)). The domain walls are found to interact with inclusions [Fig. 14(b)] and with intergranular phases at grain boundaries [Fig. 14(c)]. The latter interaction is believed to be the strongest; very high fields had to be applied to move the walls away from grain boundaries. The intergranular phases are also believed to be the regions where reverse domains are nucleated according to the nucleation theory.

D. Rapidly Solidified Nd-Fe-B Magnets

The highest coercivities reported in R-Fe-B magnets have been obtained³⁹⁻⁴⁰ in melt-spun samples with values exceeding 15 kOe. As it will be discussed later, the high coercivities are due to the fine grain microstructure consisting of $\text{R}_2\text{Fe}_{14}\text{B}$

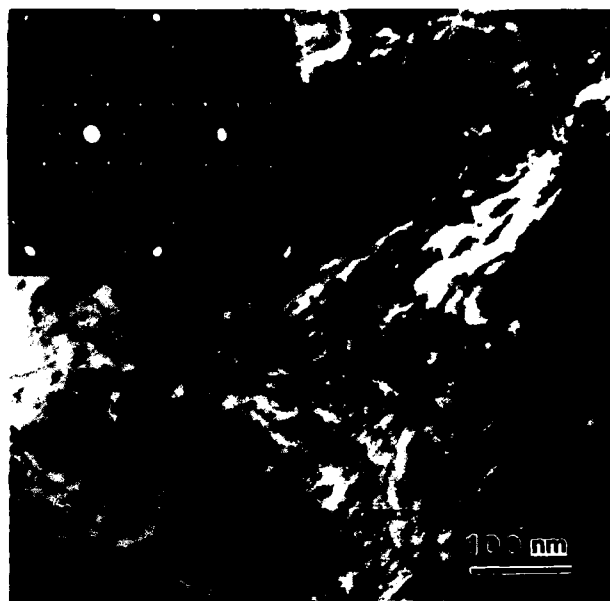


Figure 13. TEM micrograph showing a Nd-rich phase.

tetragonal grains.⁴¹ The energy product of ribbon samples is rather low (12 MGOe) because of the isotropic nature of samples. The behavior of the ribbon samples is different with the magnetization showing a slower but steady increase with field. Such behavior has also been observed in isotropic magnets and is due to the random orientation of grains (and therefore magnetic domains).

Transmission electron microscope studies on heat-treated Nd-Fe-B ribbons showed⁴⁵ the same phases as in sintered Nd-Fe-B magnets but with a much smaller grain size (Fig. 15). The grain size in melt-spun ribbons ranges from 250-4000 Å whereas that in sintered magnets is much greater than 1 μ (10-50 μ). This fine microstructure is characteristic of rapid solidification processes and leads to coercivities much higher than those observed in sintered magnets. The secondary phases are not distributed around the 2:14:1 grains but rather they are found at intersections of several R₂Fe₁₄B grains. No amorphous phases have been observed around the grain boundaries as reported by some researchers.⁴⁶ From the microstructure results⁴³ it is clear that samples with several phases and particularly more Nd-rich phase have a higher H_c . This result is in disagreement with the nucleation model, which would predict a lower H_c as the density of defects is increased. However, the above observation is consistent with domain wall pinning at the disturbed layers of 2:14:1 grains neighboring the Nd-rich grains.

Lorentz microscope studies of ribbons showed two types of magnetic domains.⁴⁷ For samples at the optimum state (grains ~ 800 Å) domain walls are found to be

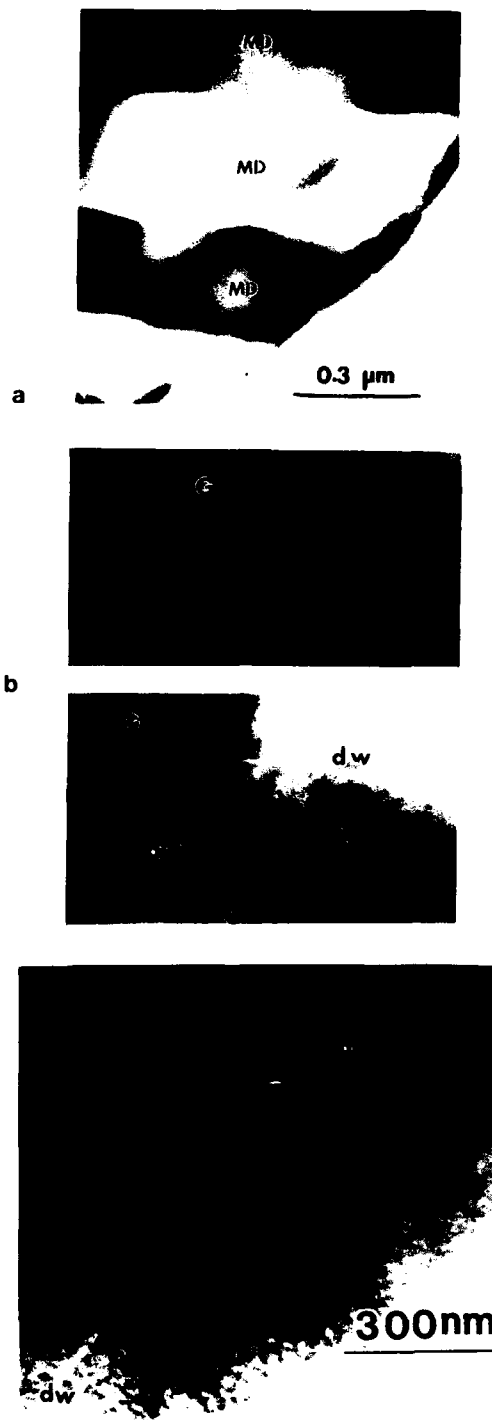


Figure 14. (a) Magnetic domains in sintered magnets. Domain walls (dw) interacting with (b) inclusions (G) and grain boundaries (L) and (c) with intergranular phases at grain boundaries (P).

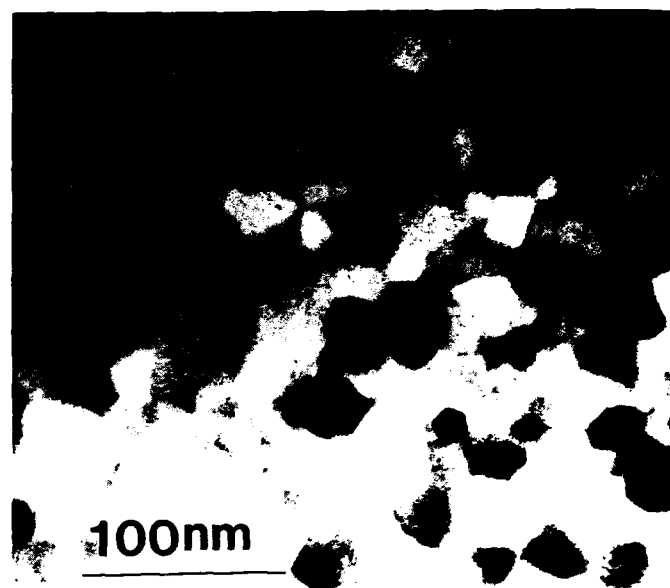


Figure 15. Microstructure of melt-spun Nd-Fe-B magnets.

clustered around grain boundaries (Fig. 16a). No domain walls were observed to cross grain boundaries and run into different grains. For much coarser grains, several domains are observed in each grain. On the other hand, for samples with very fine grains, large domains, referred to as "interaction domains,"⁴⁷ (Fig. 16b) are observed in addition to regular domains (which are the grains themselves). These large "multigrain domains" are due to interactions between the magnetic moments of neighboring grains which are expected to be enhanced for very small domains. The magnetic hysteresis of these samples may be explained by strongly interacting single domain particles.

V. SUMMARY

From the previous discussions, it is obvious that microstructure is very important in determining the coercivity of anisotropic magnetic materials. For these materials the coercivity is found to increase substantially with grain size as observed in rapidly solidified microcrystalline R-Fe-B alloys. In "single domain type" magnets coherent rotation requires the single domain particles to be embedded in a non-magnetic matrix and be further apart. When the particles are next to each other (like in CoPt and rapidly solidified Nd-Fe-B) interactions must be taken into account and these can lead to large values of reduced remanence. High coercivity domain wall pinning usually takes place in a fine uniform microstructure which consists of either two anisotropic phases (like in the 2:17 magnets) or the same anisotropic phase which is twinned oriented (like in Fe-Pt-Ni). In "nucleation-type" magnets the microstructure within grains is very clean free of any defects but the grains are decorated with other intergranular phases which are found to interact strongly with domain walls.

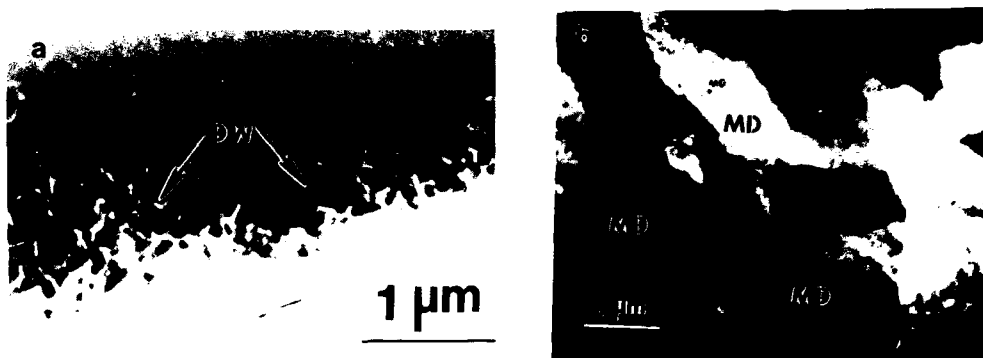


Figure 16. Lorentz microscopy in melt-spun ribbons showing (a) domain walls clustered at grain boundaries and (b) large multigrain domains known as interaction domains.

ACKNOWLEDGEMENTS

This work was supported by DOE DE-FG02-90ER45413 and the U.S. Army Research Office.

REFERENCES

1. R. M. White, *Science*, **229**, 11 (1985).
2. J. D. Livingston, General Electric, Report No. 80CRD139 (1980).
3. K. H. J. Buschow, in "Ferromagnetic Materials", E. P. Wohlfarth and K. H. J. Buschow, eds., North Holland, Amsterdam (1988) Vol. 4, p. 1.
4. H. Zijlstra, in "Ferromagnetic Materials," E. P. Wohlfarth, ed., North Holland, Amsterdam (1982) Vol. 3, p. 37.
5. E. C. Stoner and E. P. Wohlfarth, *Phil. Trans. R. Soc. London Ser A* **240**, 599 (1948).
6. P. Gaunt, *Phil. Mag. B* **34**, 775 (1976).
7. H. Kronmüller, *J. Magn. Magn. Mat.* **7** 341 (1978).
8. P. Weiss, *J. Phys.* **6**, 661 (1907).
9. B. D. Cullity, "Introduction to Magnetic Materials," Addison-Wesley, London (1972).
10. J. D. Livingston, *J. Appl. Phys.* **52**, 2544 (1981).
11. F. E. Luborsky, *J. Appl. Phys.* **32**, 1715 (1961).

12. M. Kersten, Phys. Z44, 63 (1943).
13. J. Fidler and H. Kronmüller, Phys. Stat. Sol. (a) 56, 545 (1979).
14. D. J. Craik and E. Hill, Phys. Lett. 48A, 157 (1974).
15. H. R. Hilzinger and H. Kronmüller, Phys. Lett. 51A, 59 (1975).
16. H. Trauble, in "Modern Probleme der Metallphysik," Vol. 2, A. Seeger, ed., Springer-Verlag, Berlin (1966).
17. D. I. Paul, J. Appl. Phys. 53, 2362 (1981).
18. H. R. Hilzinger and H. Kronmüller, J. Magn. Magn. Mater. 2, 11 (1976).
19. H. Kronmüller, Proc. 6th Internat. Symp. on Magnetic Anisotropy and Coercivity in Rare-Earth-Transition Metal Alloys, Baden, Austria (1982).
20. M. Sagawa, S. Hirosawa, J. de Physique, C8, 617 (1988). A. H. Morrish, "The Physical Principles of Magnetism," John-Wiley, New York (1967) p. 337.
21. G. Thomas and M. J. Goringe, "Transmission Electron Microscopy of Material," John Wiley, New York (1979).
22. R. Carey and E. D. Isaac, "Magnetic Domains and Techniques for their Observation," Academic Press Inc., New York (1966).
23. E. W. Singleton, A. Tsoukatos and G. C. Hadjipanayis, J. Appl. Phys. (in press).
24. D. Givord, H. S. Li and J. M. Moreau, Sol. Stat. Commun. 50, 497 (1984).
25. R. A. McCurrie and P. Gaunt, Proc. Int. Confer. on Magnetism, 780 (1964).
26. G. Hadjipanayis and P. Gaunt, J. Appl. Phys. 50, 235 (1979).
27. A. E. Ray, Proceedings of 7th Int. Workshop on Rare-Earth Cobalt Perm. Magn. and Their Applications, 261 (Beijing, 1983).
28. G. C. Hadjipanayis, E. J. Yadlowsky and S. H. Wollins, J. Appl. Phys. 53, 2386 (1982).
29. J. Fidler and P. Skalicky, J. Magn. Magn. Mat. 27, 127 (1982).
30. R. K. Mishra, G. Thomas, T. Yoneyama, A. Fukuno and T. Ojima, J. Appl. Phys. 52, 2517 (1981).
31. G. C. Hadjipanayis, R. C. Hazelton, K. R. Lawless and L. S. Horton, IEEE Trans. Magn. MAG-18, 1460 (1982).
32. J. D. Livingston and D. L. Martin, J. Appl. Phys. 1350, (1977).
33. G. C. Hadjupanayis, Proceeding of 6th Int. Workshop on Rare-Earth Cobalt Perm. Magn. and Their Applications, 609 (Baden, 1982).

34. L. Rabenberg, R. K. Mishra and G. J. Thomas, J. Appl. Phys. 53, 2389 (1982).
35. J. Fidler and P. Skalicky, Proceedings of 6th Int. Workshop on Rare-Earth Cobalt Perm. Magn. and Their Applications, 585 (Baden, 1982).
36. G. C. Hadjipanayis, R. C. Hazelton, S. H. Wollins, A. Wysierkierski and K. R. Lawless, Proceedings of 6th Int. Workshop on Rare-Earth Cobalt Perm. Magn. and Their Applications, 667 (Baden, 1982).
37. H. Nagel, J. Appl. Phys. 50, 1026 (1979).
38. P. Gaunt, Physica, 86-88B, 1472 (1977).
39. G. C. Hadjipanayis, R. C. Hazelton and K. R. Lawless, Appl. Phys. Lett. 43, 797 (1983); J. Appl. Phys. 55, 2073 (1984).
40. J. J. Croat, J. F. Herbst, R. W. Lee and F. E. Pinkerton, J. Appl. Phys. 55, 2078 (1984).
41. J. F. Herbst, J. J. Croat, J. D. Pinkerton and W. Yelon, Phys. Rev. B29, 4176 (1984).
42. M. Sagawa, S. Fujimura, H. Yamamoto, Y. Matsuura and K. Hiraga, IEEE Trans. Magn. MAG-20, 1584 (1984).
43. G. C. Hadjipanayis and A. Kim, J. Appl. Phys. 63, 3310 (1988).
44. J. Fidler and K. G. Knoch, J. Magn. Magn. Mat. 80, 48 (1989).
45. G. C. Hadjipanayis, Can. J. Phys. 65, 1200 (1987).
46. R. K. Mishra, J. Magn. Magn. Mat. 54-57, 450 (1986).
47. G. C. Hadjipanayis, and W. Gong, J. Magn. Magn. Mat. 66, (1987).
48. E. Callen, Y. J. Liu and J. R. Cullen, Phys. Rev. B16, 263 (1977).

LORENTZ MICROSCOPY STUDIES IN PERMANENT MAGNETS

Josef Fidler

Institute of Applied Physics
Technical University Vienna
Wiedner Hauptstr. 8-10
A-1040 Vienna, Austria

INTRODUCTION

Electron microscopic techniques including the observation of magnetic domains have become more important for the characterization of soft and hard magnetic materials. For the development of new magnetic materials the knowledge of the interaction between the magnetic domain structure and the microstructure is important for a better understanding of the magnetic properties. The size and shape of the magnetic domains are determined by the total free energy (magnetic stray field energy plus domain wall energy) and depend on the magnetic properties (magnetization, magnetocrystalline anisotropy and magnetostriction) and on the shape of the magnet. The mobility of domain walls in an external magnetic field determines the shape of the magnetic hysteresis curve. The intrinsic coercive force iH_c , which is a characteristic parameter of the hysteresis curve, strongly depends on the interaction force between domain walls and the microstructure of the material. In order to improve the magnetic properties of soft magnetic materials with a low coercive force and of hard magnetic materials with a high coercive force investigations of the microstructure and the domain structure are necessary.

The purpose of this paper is to briefly show Lorentz electron microscopic results on new permanent magnetic materials, since in the light of the historical development of hard magnetic materials the improvement of the coercivity is closely related with a better microstructural understanding of the mechanisms leading to higher coercive forces.

ELECTRON MICROSCOPIC METHODS TO STUDY MAGNETIC MATERIALS

Electron microscopy is widely being used to study and characterize magnetic materials. The oldest and most commonly used techniques for magnetic domain observation are the light optical techniques. The lack of the poor spatial resolution leads to the application of electron optical techniques for domain and microstructural investigation. The different microscopic techniques for microstructural and magnetic domain observation are listed in Table 1. The electron optical methods (Lorentz electron microscopy) for domain observation are based on the fact that electrons are deflected because of the Lorentz-force of the magnetic strayfield outside the specimen or the magnetization inside the domains ^{1,2}. Two types of

Table 1. Comparison of microscopic techniques used for microstructural and magnetic domain investigations of magnetic materials

| METHODS | MICROSTRUCTURE | MAGNETIC DOMAINS |
|--|---|---|
| Light optical microscope (LOM) | Grain boundaries Large precipitates and inclusions | Bitter technique Kerr technique Faraday technique |
| Scanning electron microscope (SEM) | Grain boundaries Precipitates X-ray microanalysis | Strayfield technique (Type 1) Tilted specimen techn. (Type 2) e ⁻ -polarization techn. (SEMPA) |
| Scanning transmission electron microscope (STEM) | Defect analysis Precipitates X-ray microanalysis | Split detector technique |
| Convent. transmission electron microscope (CTEM) | Defect analysis Precipitates X-ray microanalysis | Fresnel technique Foucault technique Holographic interference techn. |
| Field ion microscope (FIM) | Phase analysis | |
| Atom probe analysis (AP) | | |
| Magnetic force microscopy (MFM) | Surface topography | Strayfield contrast |

techniques are distinguished in the case of conventional scanning electron microscopy. The magnetic contrast is produced whether by external stray fields (Type 1) or by internal magnetic induction (Type 2). These techniques are widely used to study the surface domain structures of magnetic recording materials and soft magnetic materials³. Differential phase contrast together with STEM is a new method for domain observation⁴⁻⁶. The advantage of this method, where double or quadrant detectors are used, is the possibility to study the domain wall thickness and the magnetization distribution very accurately. An advantage of conventional TEM is to identify crystal lattice defects or small precipitates and the magnetic domain structure simultaneously. The magnetic contrast is produced whether by defocusing (Fresnel technique) or by shifting the objective aperture diaphragm (Foucault technique)². Examples for the interaction between crystal lattice defects and precipitates, respectively, and magnetic domain walls are shown in Figure 1a. The defocused micrograph shows besides dislocations, stacking faults and grain boundaries the pinning of magnetic domain walls (marked by arrows) at microtwin-boundaries in a Mn-Al-C permanent magnet material, which was produced by an extrusion process. The interaction force and the density of such pinning centres for magnetic domain walls determine the coercive force. Maximum interaction between domain walls and precipitates occur, when domain wall thickness and diameter of precipitates are comparable⁷. Crystallization centres in amorphous, soft magnetic alloys deteriorate the magnetic properties. Such an interaction in a partly crystallized Fe-Ni-B ribbon is shown in Figure 1b. The crystallization and the change of the magnetic domain structure was studied in-situ by heating the specimen within the electron microscope⁸. Special care has to be taken in order to study the magnetic domain structure under controlled conditions, and the specimen has to be shielded from the high magnetic field of the objective pole piece. In top-entry goniome-

ter stages the specimen must be withdrawn to a position of a low magnetic field ^{9,10}, and in side-entry stages shielded objective pole pieces have to be used ¹¹. The electron optical techniques for domain investigation, described so far, can be performed on conventional electron microscopes after being adapted for domain observation ¹². Such optional attachments are commercially available from electron microscope manufacturers. Other electron optical techniques need a more expensive and intricate instrumentation. Holographic interference electron microscopy, together with a field emission gun, have been used for magnetic domain investigation ¹³. Lines according to the direction of magnetization are directly observed as contour fringes which overlap individual bright field micrographs. The recent development of scanning electron microscopy with polarization analysis (SEMPA) has made the direct observation of magnetic structures with submicron spatial resolution possible ^{14,15}. Other microanalytical techniques based on field ion microscopy and atom probe analysis have recently been used and were reported to analyse the different phases of permanent magnetic materials, such as AlNiCo-, FeCrCo- and RE-cobalt/iron - magnets ¹⁶⁻¹⁸.



Fig. 1. Electron micrographs showing crystal lattice defects and magnetic domain walls (marked by arrows) in a Mn-Al-C magnet (FRESNEL image) (a) and magnetic domains in a partly crystallized Fe-Ni-B ribbon (FOUCAULT image) (b).

ELECTRON MICROSCOPY OF RARE EARTH PERMANENT MAGNETIC MATERIALS

Modern permanent magnets are based on rare earth (RE) - transition metal intermetallic compounds with hexagonal or tetragonal crystal symmetry and exhibiting rather large uniaxial magnetic anisotropy, such as SmCo_5 , $\text{Sm}_2\text{Co}_{17}$ and $\text{RE}_2\text{Fe}_{14}\text{B}$, with RE=Nd, Pr, Dy and Tb. The condition of high magnetocrystalline anisotropy is necessary, but not sufficient in order to achieve good permanent magnetic properties. The microstructure of the magnet is another factor controlling the hard magnetic properties, i.e. the coercivity. Two different mechanisms, explaining the coercivity, are distinguished:

- (a) Pinning of magnetic domain walls
- (b) Nucleation and expansion of reversed magnetic domains

Besides other analytical techniques, such as chemical analysis, magnetic measurements, X-ray analysis and X-ray diffraction, electron microscopy is increasingly used to characterize such materials after different steps of processing (i.e. sintering, annealing). The occurrence of nucleation or pinning depends on the microstructure of the magnet.

A typical example of a domain wall pinning controlled $\text{Sm}(\text{Co}, \text{Fe}, \text{Cu}, \text{Zr})_{7.5}$ magnet is shown in the bright field electron micrograph and the Lorentz electron micrograph of Figure 2. The coercivity is determined by the pinning field of magnetic domain walls at a continuous, cellular precipitation structure (Figure 2a) ¹⁹⁻²³. In high coercivity magnets ($iH_c > 1000$ kA/m) the microstructure consists of three phases, the cell interior phase A, the cell boundary phase B and the platelet phase C, whereby the optimum cell size for highest coercivity is in the order of 100 to 200 nm. The Foucault micrograph of Figure 2b shows that the cellular precipitation structure acts as attractive pinning centre for the magnetic domain walls during the magnetization reversal ²⁴. It is obvious that the size, the composition and the completeness of the continuous cellular precipitation structure determines the coercivity.

Nd-Fe-B based permanent magnets exhibit outstanding hard magnetic properties at room temperature, but their application is limited by the low Curie temperature of the hard magnetic phase $\text{Nd}_2\text{Fe}_{14}\text{B}$, which results in a high temperature dependence of the coercive field. The high irreversible thermal losses are reduced by partial substituting Co for Fe and Dy for Nd and adding small amounts of additional elements. The high magnetocrystalline anisotropy at room temperature of the $\text{Nd}_2\text{Fe}_{14}\text{B}$ (ϕ)-phase primarily determines the intrinsic coercivity and substituents such as Dy, which increase the anisotropy field, effectively increase the coercive field. An other possibility to enhance the coercivity is to add a small amount (<1 wt.%) of dopants, such as Al, Ga, Mo, V, Nb or other refractory

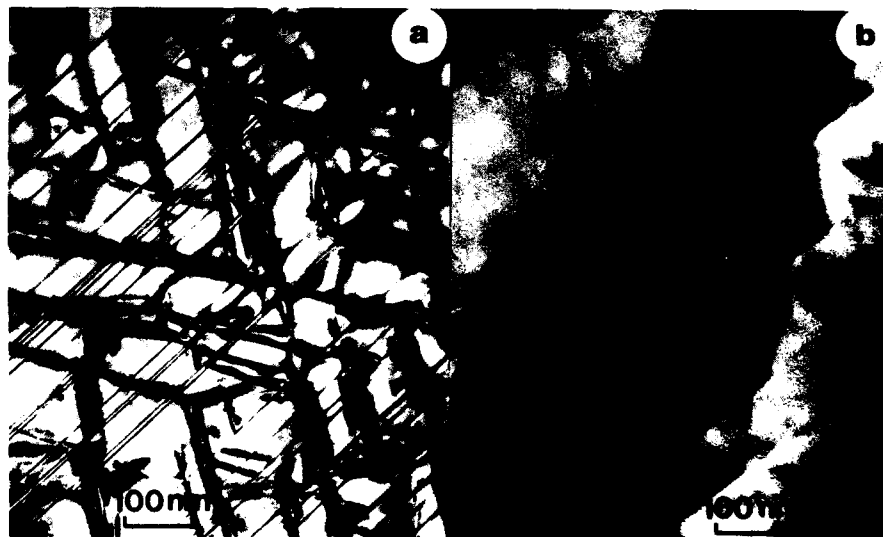


Fig. 2. Electron micrographs showing the cellular precipitation structure of a $\text{Sm}(\text{Co}, \text{Fe}, \text{Cu}, \text{Zr})_{7.5}$ magnet (a). The Foucault micrograph shows the attractive domain wall pinning at the continuous precipitation structure in the demagnetized state (b).

elements. The influence of the dopants on the coercive field is not fully understood, but it is agreed that the increase of coercivity (up to 30%) is due to a microstructural effect, since the anisotropy field only slightly changes (mostly decreases) ²⁵. Four different processing techniques for RE-Fe-B magnets are distinguished:

- (1) Powdermetallurgical sintering-process
large grain size (up to 15 μm), multiphase microstructure
- (2) Process derived from melt-spun materials
small grain size (50 nm), "two-phase microstructure"
- (3) Mechanically alloyed magnets
small and medium grain size (50 - 500 nm), multiphase microstructure
- (4) Cast, hot pressed or extruded magnets
grain size and microstructure similar to (1)?

Depending on the processing technique RE-Fe-B based permanent magnets exhibit a complex, multiphase microstructure ²⁶. The grain size of the magnets also strongly depends on the processing technique. It is agreed that similar to SmCo_5 -magnets the coercivity of Nd-Fe-B based magnets is controlled by the nucleation field and expansion field for reversed magnetic domains ^{27,28}. Magnets prepared by the melt-spinning technique and by the mechanically alloying process exhibit a fine-grained microstructure. Several Lorentz electron microscopic investigations have been undertaken to show the magnetic domain walls in melt-spun RE-Fe-B ²⁹⁻³³. The Fresnel micrograph of Figure 3a shows the magnetic domain structure of a textured $\text{Nd}_{4.5}\text{Fe}_{77}\text{B}_{18.5}$ -flake which is in the order of 80-100 nm, whereas the approximate grain size is in the order of 20-25 nm. Grain size and optimum hard magnetic properties strongly depend on the preparation conditions such as the wheel speed ³⁴. In RE-Fe-B magnets a non magnetic layer phase between the Φ -grains is desirable in order to increase the expansion field of reversed domains and to decrease the coupling field between neigh-



Fig. 3. Defocused FRESNEL micrographs showing the magnetic domain structure of a melt spun $\text{Nd}_{4.5}\text{Fe}_{77}\text{B}_{18.5}$ -flake (a) and of a sintered Nd-(Fe,Co)-B:Ga magnet (b).

bouring grains. Figure 3b shows a grain boundary junction of three ϕ -grains separated by a non magnetic Nd-rich phase in a Nd-(Fe,Co)-B:Ga magnet. Domain walls are visible only in the hard magnetic grains.

Besides chemical analysis, X-ray analysis and magnetic measurements also metallography together with analytical electron microscopy (AEM) and high resolution electron microscopy (HREM) and Lorentz electron microscope investigations are necessary for a better understanding of the mechanisms leading to high coercivities in rare earth permanent magnet materials.

Acknowledgements

This work is part of the CEAM-2 stimulations EC-programme and was partly supported by the Austrian Forschungsförderungsfonds FWF (P6935P) and by the Ministry for Science and Research (BRITE/EURAM Project BREU-0150-M).

References

1. J. P. Jakubovics, Phil. Mag., 10: 277 (1964).
2. P. J. Grundy and R. S. Tebble, Advances in Physics, 17: 153 (1968).
3. G. A. Jones, J.M.M.M., 8:263 (1978).
4. J. N. Chapman, P. E. Batson, E. M. Waddell, and R. P. Ferrier, Ultramicroscopy, 3:203 (1978).
5. J. N. Chapman, Materials Science and Engineering, B3:355 (1989).
6. K. Tsuno and M. Inoue, Optik, 4:363 (1984).
7. R. A. Taylor, J.M.M.M., 15-18:1173 (1980).
8. J. Fidler and P. Skalicky, Appl.Phys.Lett., 39:573 (1981).
9. U. Valdre, J.Sci.Instrum., 41:327 (1964).
10. R. A. Taylor, Electron Microscopy, 4:38 (1980).
11. K. Tsuno and T. Taoka, Jap.J.Applied Physics, 22:1041 (1983).
12. K. Tsuno, M. Inoue and K. Ueno, Materials Science and Engineering, B3:403 (1989).
13. A. Tonomura, T. Matsuda, J. Endo, T. Arii, and K. Mihama K, Phys.Rev.Lett., 44:1430 (1980).
14. K. Koike and Hayakawa, J.Appl.Phys., 57:4244 (1985).
15. J. Unguris, G. G. Hembree, R. J. Celotta, and D. T. Pierce, J.M.M.M., 54:1629 (1986).
16. A. Hütten and P. Haasen, J. de Physique, C7:205 (1986).
17. M. G. Hetherington, G. D. W. Smith, and J. P. Jakubovics, Metallurgical Transactions, A 17A:1629 (1986).
18. F. Zhu, P. Haasen, and R. Wagner, Acta Metall., 34:457 (1986).
19. J. Fidler, P. Skalicky, and F. Rothwarf, IEEE Trans.Magn., 19:2725 (1983).
20. G. C. Hadjipanayis, J.Applied Physics, 55:2091 (1984).
21. J. D. Livingston, IEEE Trans.Magn., MAG-14:668 (1978).
22. R. K. Mishra, G. Thomas, T. Yoneyama, A. Fukuno, and T. Ojima, J.Appl. Phys., 52:2517 (1981).
23. L. Rabenberg, R.K.Mishra, and G. Thomas, J.Appl.Phys., 53:2389 (1982).
24. J. Fidler, Phil.Mag., B46:565 (1982).
25. W. Rodewald and W. Fernengel, IEEE Trans. Magn., MAG-24:1638 (1988).
26. J. Fidler and K. G. Knoch, J.M.M.M., 80:48 (1989).
27. H. Kronmüller, K.D. Durst, and M. Sagawa, J.M.M.M., 74:291 (1988).
28. D. Givord, Q.Lu, M.F.Rossignol, and P. Tenaud, J.M.M.M., 83:183 (1990).
29. R. K. Mishra, J.M.M.M., 54-57:450 (1986).
30. C. D. Meekison, J.P. Jakubovics, A. Kostikas, D. Niarchos, and V. Papefthymiou, IEEE Trans. Magn., in print.
31. J. Bras, J. Degauque, M. Fagot, and K. Biyadi, J.M.M.M., 83:203 (1990).

32. P. J. Grundy, D.G. Lord, S.F.H. Parker, and R.J. Pollard, in
"Concerted European Action on Magnets", I. V. Mitchell, J.M.D.
Coey, D. Givord, I.R. Harris and R. Hanitsch, eds., Elsevier,
London, p.405 (1989).
33. G. C. Hadjipanayis, see Ref. 32, p. 418.
34. R. Coehoorn, D.B. De Mooij, and C. Waard, J.M.M.M., 80:101 (1989).

COERCIVITY IN HARD MAGNETIC MATERIALS

D. Givord, Q. Lu*, M.F. Rossignol

Laboratoire Louis Néel, CNRS, 166X
38042-Grenoble-cedex, France

INTRODUCTION

Coercivity is the essential property characterizing hard magnetic materials, in particular with respect to normal ferromagnets. It exists when low field domain wall motion does not take place, either the magnetization being already saturated in zero field, or domain walls being pinned at structural heterogeneities. In these two cases, the magnetic configuration of the system is an energy minimum in the field, although it may not be the lowest energy minimum. This energy minimum vanishes at $H = H_C$, the coercive field. Then magnetization reversal takes place and the system reaches the lowest energy state.

It is well established that the existence of coercivity is linked to that of magnetic anisotropy. This is shown in the first section, in a simple model due to Stoner and Wohlfarth (1948), where magnetization is assumed to be uniform and magnetization reversal can only occur by coherent rotation. H_C is then calculated to be equal to H_A the anisotropy field.

However, in real systems, non-uniform magnetization processes are actually involved in magnetization reversal and H_C is much weaker than H_A . In particular, in the case of shape anisotropy, magnetization reversal occurs through collective processes which involve all the magnetic moments. These are discussed in the second section of this paper.

In the presence of magnetocrystalline anisotropy, collective processes do not lead to any reduction in H_C . Yet, the coercive field is still much weaker than H_A . This may be attributed to the influence of structural defects ; at defect positions, a small volume of inverted magnetization may nucleate and magnetization reversal may develop from there. The mechanisms which govern these processes are not well understood and their discussion represents the essential part of the present paper. Different models to account for nucleation, nucleus expansion and domain wall propagation are presented. Experimental methods to approach coercivity mechanisms are described and they are applied to various categories of hard magnetic materials.

* Permanent address: Department of Physics, University of Nanjing, Nanjing, China.

ORIGIN OF COERCIVITY

Stoner-Wohlfarth model

A simple approach to coercivity in a saturated system is that of Stoner and Wohlfarth (1948) (SW) in which coherent rotation of the magnetization is assumed, i.e. uniform magnetization is preserved during magnetization reversal. For a uniaxial system, the energy in an applied magnetic field H can be written as :

$$E(\theta) = -\mu_0 M_S H \cos(\pi - \theta_H - \theta) + K_1 \sin^2 \theta + E_D \quad (1)$$

where M_S is the spontaneous magnetization, θ the angle between M_S and the easy axis c , θ_H the angle between H and c (with the definition that $\theta_H = 0$ when M_S and H are antiparallel), K_1 the 2nd order anisotropy constant, and E_D represents the dipolar energy. If the sample is an ellipsoid of revolution whose major axis coincides with the c -axis, E_D can be written as:

$$E_D = \mu_0/2 [N_{//} M_S^2 + (N_{\perp} - N_{//}) M_S^2 \sin^2 \theta] \quad (2)$$

where $N_{//}$ and N_{\perp} are the demagnetizing factors along c and perpendicular to c .

The equilibrium solutions for θ are deduced from :

$$\partial E / \partial \theta = -\mu_0 M_S H \sin(\pi - \theta_H - \theta) + K_1' \sin 2\theta = 0 \quad (3)$$

and

$$\partial^2 E / \partial \theta^2 = \mu_0 M_S H \cos(\pi - \theta_H - \theta) + 2K_1' \cos 2\theta > 0 \quad (4)$$

where :

$$K_1' = K_1 + \mu_0 (N_{\perp} - N_{//}) M_S^2 \quad (5)$$

is an effective anisotropy constant including shape and magnetocrystalline anisotropies. If the applied magnetic field is initially antiparallel to the magnetization (i.e. $\theta_H = 0$), the absolute minimum of energy, which corresponds to a parallel coupling between the moments and the field, is obtained for $\theta = \pi$:

$$E(\pi) = -\mu_0 M_S H + (\mu_0/2) N_{//} M_S^2 \quad (6)$$

However, as long as $H < 2K_1'/\mu_0 M_S$, a second minimum exists corresponding to antiparallel alignment of the magnetization and the field ($\theta = 0$) :

$$E(0) = \mu_0 M_S H + (\mu_0/2) N_{//} M_S^2 \quad (7)$$

The two minimum energy states are separated by an energy maximum (Figure 1):

$$E(\theta) = K_1' + (\mu_0 M_S H)^2 / 4K_1' + (\mu_0/2) N_{//} M_S^2 \quad (8)$$

where $\theta = \arccos(\mu_0 M_S H / 2K_1')$

As H reaches the value of the effective anisotropy field

$$H = H_A' = 2 K_1' / \mu_0 M_S = 2 [K_1 + \mu_0 (N_{\perp} - N_{//}) M_S^2] / \mu_0 M_S \quad (9)$$

the energy barrier is reduced to zero. If the magnetization was initially antiparallel to the field, it then rotates abruptly into the field direction : the coercive field H_C is calculated to be equal to the effective anisotropy field H_A .

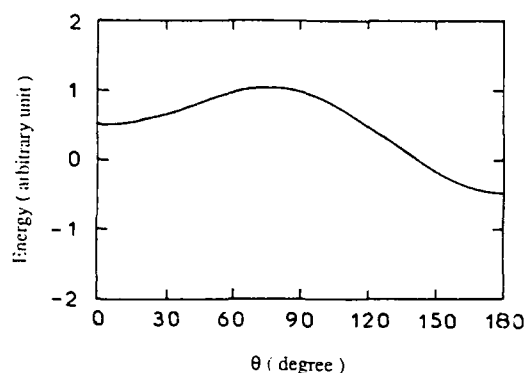


Figure 1. Energy barrier at the origin of coercivity in the SW model.

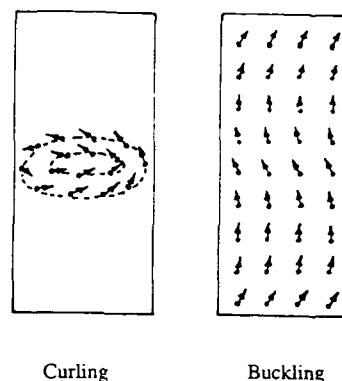


Figure 2. Schematic representations of non-uniform magnetization reversal processes.

Saturated versus non-saturated states

In order to discuss magnetization reversal mechanisms, it is important to compare the stability of a uniform magnetization state with respect to a non-uniform magnetization state. The moment configuration of a ferromagnetic system in zero applied magnetic field is determined by the interplay between exchange interactions, anisotropy energy and dipolar energy. Exchange and anisotropy favour the formation of a state of uniform magnetization where the moments are aligned along a unique direction. On the other hand, in any sample of finite size, dipolar interactions tend to stabilize a state of non-uniform magnetization. The balance between these energy terms depends on the sample volume. Uniform magnetization is favoured below a certain critical size which has been evaluated by Kittel (1949) : considering a sphere of radius R , the energy in the saturated state is compared to that obtained when a planar wall divides the sphere into two equal parts. Assuming in the latter case that the dipolar energy is reduced by a factor of 2, it is readily deduced that the critical radius for uniform magnetization is :

$$R_{\text{uni}} = 9\gamma / \mu_0 M_s^2 \quad (10)$$

where γ is the domain wall energy and M_s the spontaneous magnetization. The values of R_{uni} deduced for hexagonal cobalt, SmCo_5 and $\text{Nd}_2\text{Fe}_{14}\text{B}$ are listed in table I.

A more elaborate approach has been developed by Brown (1969), allowing lower and upper limits for R_{uni} to be evaluated. Other magnetization configurations exist, for which magnetic poles are practically eliminated, having lower dipolar energy than multi-domain states. These configurations may only occur in systems with an exceedingly small magnetocrystalline anisotropy, because the magnetic moments are then distributed over all directions of space. One such configuration,

Table I

| | Co | SmCo ₅ | Nd ₂ Fe ₁₄ B |
|--------------------------------------|-----|-------------------|------------------------------------|
| R_{uni} (nm) | 35 | 750 | 100 |
| $R_{\text{uni}}^{\text{upper}}$ (nm) | 220 | 1100 | 240 |

magnetization curling, is favoured for samples of ellipsoidal or cylindrical shape and the critical radius R_{uni} is found to be less than 150 Å (Zijlstra, 1982) in the case of iron.

In the presence of magnetocrystalline anisotropy, the state of non-uniform magnetization of lowest energy is always a multi-domain state : as the magnetization is in fact uniform, except within the domain walls, this state allows the dipolar energy to be decreased without paying too much in exchange and anisotropy energies. Considering a simple two-domain state with a planar wall, upper values for R_{uni} are given by :

$$R_{uni}^{upper} = 14 \left[(\gamma/\mu_0 M_s^2) + \sqrt{\pi/2} (\gamma/\sqrt{K\mu_0 M_s^2}) \right] \quad (11)$$

Values obtained in different materials are listed in table I.

COERCIVITY IN SHAPE ANISOTROPY SYSTEMS

Magnetization reversal processes

The possible stability of a saturated magnetic state in zero applied field means that the saturated state corresponds to an energy minimum, i.e. a certain coercivity exists. However, this does not imply that magnetization reversal occurs by coherent rotation. In particular, in a system where shape anisotropy is large, uniform magnetization costs much more energy when the magnetization is perpendicular to the easy direction than when it is parallel to it. The problem is thus to determine the exact mechanisms involved in magnetization reversal. This could in principle be found with the help of micromagnetism theory which assumes a continuous medium and localized magnetic moments, and is probably a good approximation in most systems where the exchange interactions are much larger than anisotropy, so that any deviation from magnetic saturation extends over several interatomic distances. However, the calculations involve the numerical solution of non-linear differential equations, which has been successfully obtained only for some rather idealized systems. The calculations become simpler close to magnetic saturation, where the equations can be linearised. It is then possible to determine the magnetization modes which are involved in nucleation (first departure from saturation) and the coercive field H_c is taken to be equal to the nucleation field H_n , which is equivalent to assuming that nucleation leads to complete magnetization reversal. Within this approximation, magnetization reversal has been studied in various simple systems. For a prolate ellipsoid, three modes are in principle possible (Frei et al., 1957; Aharoni, 1958; Aharoni, 1963). The first one is coherent rotation, and the associated nucleation field is given by the relation (9). The two other modes, magnetization curling and magnetization buckling (figure 2), correspond to collective non-uniform magnetization processes, which allow the dipolar energy associated with shape anisotropy to be decreased at the expense of exchange interactions. For curling, the nucleation field is :

$$H_n = 2K_1/\mu_0 M_s - N//M_s + kM_s/2S^2 \quad (12)$$

In this relation, k is a parameter of the order of 1 which depends on the shape of the ellipsoid (Aharoni 1966), and S is equal to R/R_0 , where R is the minor half axis of the ellipsoid, R_0 is a fundamental length defined by $R_0 = (4\pi A/\mu_0 M_s^2)^{1/2}$ and A is the exchange constant. The nucleation field is dependent on the sample volume. For each value of k , a certain critical minor half axis R_c exists such that magnetization reversal occurs by coherent rotation for $R < R_c$ and by magnetization curling for $R > R_c$. For $R \sim 10 R_c$, and neglecting magnetocrystalline anisotropy, H_n is typically 1/10 of the coercive field predicted for coherent rotation.

The third mode, buckling, does not significantly change the results obtained for coherent rotation and curling (Aharoni, 1958).

For other sample shapes, there may be other processes involved in magnetization reversal (Zijlstra, 1982; Aharoni, 1986), but, in every case, coherent rotation tends to occur for small sample volumes, and non-uniform magnetization processes for large volumes.

Comparisons with experimental data

Shape anisotropy is at the origin of coercivity in AlNiCo magnets, where the microstructure schematically consists of elongated magnetic Fe-Co particles (typical size $200 \times 200 \times 2000 \text{ nm}^3$) dispersed in a non-magnetic or almost non-magnetic matrix.

In Fe and Fe-Co whiskers (Luborsky, 1964; De Blois et al, 1959) coercivities of 500 Oe, amounting to 90 % of the values predicted for curling, have been measured.

The relation (12) has been used to describe the temperature dependence of H_c in $\gamma\text{-Fe}_2\text{O}_3$ particles (Figure 3) (Eagle and Mallison, 1967). In this system, the volume dependence of the coercivity is also in agreement with magnetization curling (Figure 4). However, in particles of smaller diameter which have been obtained more recently, the coercivity is not significantly larger, contrary to what would be theoretically expected (Berkowitz, 1990). This suggests that the actual magnetization reversal mechanisms are more complex than simple curling.

COERCIVITY IN SYSTEMS WITH LARGE MAGNETOCRYSTALLINE ANISOTROPY

Brown Paradox (Brown, 1945)

The processes described in the previous section allow the dipolar contribution to the energy barrier involved in magnetization reversal to be reduced. In the case of high magnetocrystalline anisotropy systems, they do not lead to any reduction in the energy barrier and thus are no longer relevant. Let us assume, in this instance, that a field antiparallel to M_s is applied and compare coherent rotation to other possible processes. Magnetization reversal not occurring by coherent rotation would imply that for some $H < H_A$, departure from saturation occurs somewhere with an

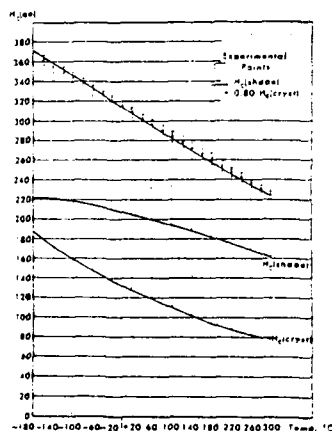


Figure 3. Temperature dependence of H_c in $\gamma\text{-Fe}_2\text{O}_3$ particles (after Eagle and Mallison, 1967).

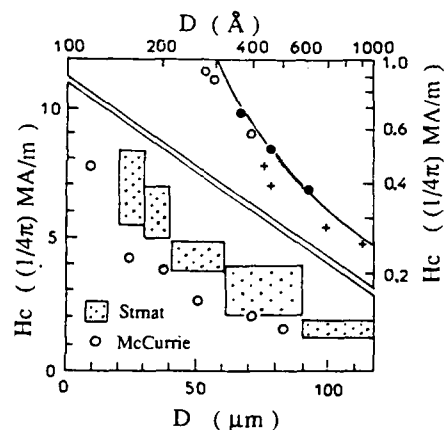


Figure 4. Volume dependence of H_c in $\gamma\text{-Fe}_2\text{O}_3$ (Eagle and Mallison, 1967) and SmCo_5 particles (McCurrie and Carswell, 1971).

associated loss in exchange energy. Expressing this loss for a given moment μ as $\Delta_s^\mu(\theta)$ and neglecting dipolar energy leads to the energy :

$$E_\mu(\theta) = - \mu_0 \mu H \cos(\pi-\theta) + K_1 v_{at} \sin^2\theta + \Delta_s^\mu(\theta) \quad (13)$$

where v_{at} is the volume of an atom. The first two terms are analogous to those in relation (1) describing coherent rotation. The additional term $\Delta_s^\mu(\theta)$ is positive whatever the θ value may be, which means that any departure from saturation leads to an increase in the energy of the system, i.e. the saturated state is a minimum energy state. It results that magnetization reversal should occur by coherent rotation, with H_c being equal to H_A , and this should apply to any material where magnetocrystalline anisotropy is present, whatever the sample volume may be in particular.

The experimental results do not correspond to this expected behaviour. H_c is actually always much smaller than H_A . This is known as the Brown paradox (Brown, 1945). This discrepancy between theoretical and experimental values of H_c can be attributed to the influence of structural defects and it is discussed below.

Magnetization Reversal from the Saturated state : nucleation, propagation

In materials which are homogeneous in the bulk, magnetization reversal is found to involve the nucleation of a small volume of inverted magnetization in a region where exchange interactions and/or magnetocrystalline anisotropy are reduced, i.e. $H_n \ll H_A$. Nucleus expansion follows nucleation, it is determined by the strength of the propagation field H_p . $H_c = H_n$ or $H_c = H_p$, depending whether $H_n > H_p$ or $H_n < H_p$.

It is found in addition that the coercive field, is dependent on the crystallite size : in bulk materials, it is in general several orders of magnitude less than H_A , and it amounts to values of the order of $H_A/5$ for particle diameters around 1-5 μm (Figure 4). Schematically, this effect may be understood by considering that magnetization reversal in a bulk material develops from the defect position where H_c is an absolute minimum. However, if the sample considered is divided into many small crystallites, H_c becomes equal to the value, averaged over all crystallites, of the minimum coercive field in each crystallite.

It is thought that the above effects describe coercivity in sintered magnets such as ferrites, SmCo_5 and NdFeB magnets, where the microstructure is formed of small magnetic crystallites between which the exchange interactions may be neglected. The coercive field in these magnets reach values which amount to a significant fraction of the anisotropy field.

Coercivity due to pinning of domain walls

There exists an alternative way of developing coercivity in materials where the nucleation of reversed domains occurs in low fields but where microstructural heterogeneities lead to a domain wall energy that is dependent on the wall position. In such systems, the domain walls tend to be pinned in the places where their energy is minimum. A domain wall which sweeps the entire sample meets all the different pinning sites and thus the sites which determine coercivity are those for which the pinning is the strongest, i.e. for which H_c is maximum. This is unlike the case of nucleation-propagation discussed in the previous section, where coercivity is determined by the sites for which H_c is minimum.

For strong pinning and thus a large coercivity to occur, large variations in wall energy are necessary and this requires, as above, high magnetocrystalline anisotropy. In particular, in $\text{Sm}(\text{CoCuFeZr})_{7-8}$ alloys, it has been reported that the domain walls are pinned at the interfaces between SmCo_5 and $\text{Sm}_2\text{Co}_{17}$ phases where a large discontinuity in anisotropy occurs (Fidler and Skalicky, 1982). The coercive field at room temperature is of the order of 4 T, similar to the coercive field in other Sm-Co magnets.

MICROSTRUCTURE AND COERCIVITY

In this section, the link existing, in high magnetocrystalline anisotropy systems, between microstructure and coercivity is illustrated by simple models.

Nucleation and propagation from the saturated state

In a system formed of saturated crystallites, let us assume that a negative magnetic field (opposed to the initial direction of magnetic saturation) is applied. As the strength of the field is increased, nucleation occurs at some defect. Due to the alteration of the magnetic properties in the region where nucleation occurs, the wall created at the boundary of the nucleus tends to be pinned and the propagation field, H_p , required for the wall to penetrate into the bulk of the crystallite may be large.

From a general point of view, the nucleation and propagation fields are obtained from the Gibbs free energy describing the system, Φ , writing that for any atom i :

$$d\Phi / d\theta(i) = 0 \quad (14)$$

with

$$d^2\Phi / d\theta(i) \leq 0 \quad (15)$$

where $\theta(i)$ represents the angle of the moment i with respect to the easy axis. For solution of the associated differential equations to be possible, simple descriptions of the physical system must be proposed. In particular, in a one-dimensional model, the free energy reduces to the simple expression (Kronmüller and Hilzinger, 1976) :

$$\Phi = \int_{-\infty}^{\infty} [A(d\theta/dz)^2 + K(z)\sin^2\theta + \mu_0 M_s H \cos\theta] dz \quad (16)$$

where θ is only dependent on the atom position z .

Within such a model, different profiles for the anisotropy defect have been proposed (Aharoni, 1960; Abraham and Aharoni, 1960; Kronmüller, 1987) leading to slightly different expressions for the nucleation field. Typically, for a defect of width $d \sim 2r_0$, in which the anisotropy is assumed to be negligible :

$$H_n \sim H_A \delta / \pi r_0 \quad (17)$$

where δ is the domain wall width. This expression indicates that the nucleation field decreases with increasing defect width (Figure 5).

In these one-dimensional calculations, the propagation field H_p is found to be (Hilzinger and Kronmüller, 1975; Friedberg and Paul, 1975) :

$$H_p \sim H_A 2\delta / 3\pi r_0 \quad (2\pi r_0 > \text{or} \sim \delta) \quad (18)$$

$$\text{or, } H_p \sim H_A \pi r_0 / \delta \quad (2\pi r_0 \ll \delta) \quad (19)$$

In general H_p is weaker than H_n . It is often argued for this reason that in real systems, magnetization reversal from the saturated state is actually controlled by nucleation.

Expansion of an existing nucleus

In the above model, the increase in wall area associated with propagation is not considered. This phenomenon tends to impede wall

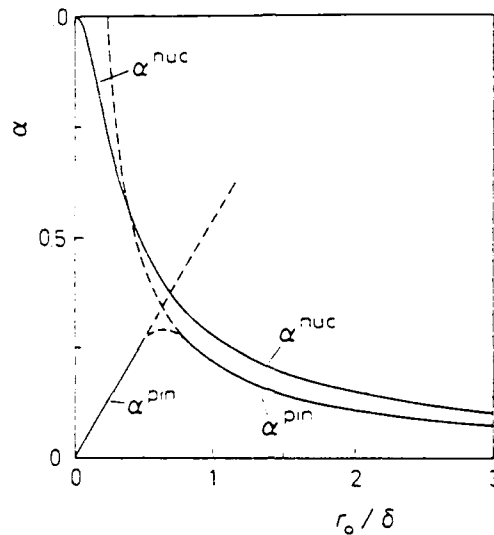


Figure 5. Variation of the parameter $\alpha^{\text{nuc}} = H_n/H_A$ or $\alpha^{\text{pin}} = H_p/H_A$ as a function of the parameter r_0/δ (r_0 is the defect width) (Kronmüller and Durst, 1989).

propagation and thus provides another possible mechanism for the existence of coercivity. Assuming that the material properties are homogeneous (i.e. the pinning of domain walls due to the heterogeneous character of the magnetic properties is now neglected), the energy of the system becomes (Elbaz et al., 1991b):

$$E = -2\mu_0 M_s H v + \gamma s \quad (20)$$

where γ is the domain wall energy, v and s are the volume and surface of the nucleus respectively. One may consider for simplicity a nucleus of conical shape, thus :

$$E = -2\pi r^2 z \mu_0 M_s H / 3 + \gamma \pi r \sqrt{z^2 + r^2} \quad (21)$$

where r is the radius of the cone basis and z its height. It appears that two modes must be considered for nucleus growth. The mode I correspond to the nucleus growing at constant r (figure 6). The energy variation as a function of z is shown in figure 7 for different values of the applied field. The mode II corresponds to the classical idea of nucleation with z and r increasing together at a constant z/r ratio (figure 6). In this instance an energy maximum is reached since the surface term is dominant at small z (and r) whereas the volume term is dominant at large z (figure 7).

Assuming that the nucleus is initially created at a defect position whose size is defined by the radius r_0 , r_0 can be considered as a minimum value for r . In low fields, the nucleus expands within mode I until the energy minimum is reached and it is stable in this situation. For :

$$H = \sqrt{\frac{3}{2}} \frac{\gamma}{\mu_0 M_s r_0} = \frac{1}{\sqrt{6}} \frac{\delta}{r_0} H_A, \quad (22)$$

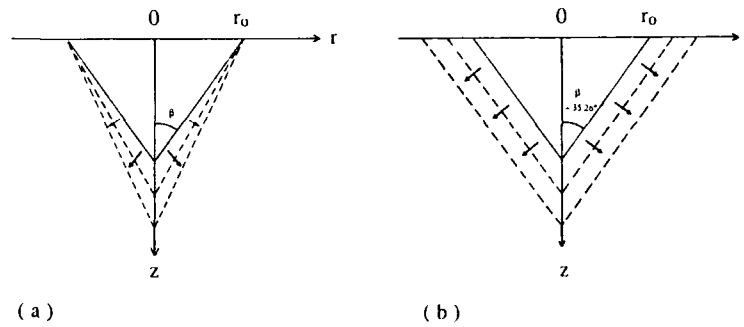


Figure 6. Growth modes for a conical nucleus. Mode I : z increases at constant r_0 . Mode II : z and r increase at constant z/r ratio.

the curves describing the energy variations are tangential at a point P which corresponds to the energy minimum in mode I and to the energy maximum in mode II (figure 7). This defines the coercive field, as the nucleus may now expand to infinity without the need to overcome any energy barrier, thus a cross-over from mode I to mode II occurs at point P. At P, $\cos\beta = \sqrt{2/3}$, i.e. β , the half-angle of the cone, is equal to 35.26° which corresponds to a cone with maximum volume at constant surface. The ratio between energy gained in the field and domain wall energy lost is thus optimized.

For $r_0 \sim \delta$, H_c amounts to $\sim 0.4 H_A$, which shows that a significant coercive field may indeed be obtained in this model.

Pinning at magnetic heterogeneities in bulk materials

Let us now consider the case where coercivity originates from domain

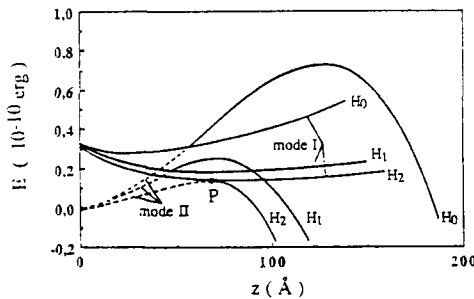


Fig. 7. Energy variation as a function of z for the two growth modes of a conical nucleus.

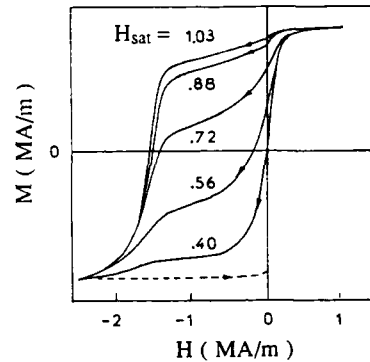


Fig. 8. Demagnetization curves at 300K in a NdFeB sintered magnet, for increasing values of an initial saturation field H_{sat} .

wall pinning. The usual way of describing interactions of domain walls with pinning sites is to treat the walls as deformable membranes. The propagation field required to unpin a domain wall from a unique pinning site is (Kersten, 1943) :

$$H_p = f/2\mu_0 M_s S \quad (23)$$

where f ($=S \partial\gamma/\partial z$) is the maximum restoring force exerted on the wall and S the wall area pinned for the considered pinning site. S decreases with increasing pin density, which means that the associated propagation field tends to increase. However, in a bulk system, a distribution of pin sites exists. If the pin sites were distributed uniformly, the wall energy would not depend on its position and $H_p = 0$. Pinning is thus due to the fluctuations in the pin sites distribution. It appears then that the pin site densities required to obtain significant values of the coercive field are of the order of $\rho \sim 10^{20} \text{ cm}^{-3}$ (Gaunt, 1988). Such very large values suggest that pinning is actually due to extended heterogeneities. To evaluate H_c in this instance one may express the energy of a 180° domain wall in a one dimensional model, and the coercive field is thus given by relations (18) or (19) for propagation fields. These relations indicate that the pinning efficiency varies as r_0/δ for narrow heterogeneities ($r_0 \ll d$) but as δ/r_0 for wide heterogeneities ($r_0 > \text{or} \sim \delta$). For $\delta \sim r_0$, a maximum value is obtained for H_p , it corresponds to $H_p \sim 0.3 H_A$ (Figure 4). This value is less than that obtained in the case of nucleation. However, as already mentioned, the sites which determine coercivity are those for which H_p is maximum. As temperature is varied, it may be that different pinning sites are involved so that δ/r_0 is a constant and pinning efficiency remains maximum. This behavior is unlike the one expected for nucleation where, coercivity being determined by the nucleation sites where H_n is minimum, the same sites may be involved at different temperatures.

EXPERIMENTAL ANALYSIS OF COERCIVITY MECHANISMS IN SYSTEMS WITH LARGE MAGNETOCRYSTALLINE ANISOTROPY

A better understanding of magnetization reversal mechanisms in hard magnetic materials may be obtained from the comparison of experimental behaviors with those expected in the different models described in the previous section. Dipolar fields present within matter may also be evaluated by such an analysis. These may be very large and thus significantly affect the measured value of the coercive field, since the magnetic properties of hard magnetic materials are, by nature, strongly heterogeneous.

Development of coercivity

The development of coercivity may be studied in systems where the magnetization state obtained after thermal demagnetization is a multi-domain state. This is the case for instance in SmCo_5 and NdFeB sintered magnets. A positive saturation field is applied and the demagnetization curve is then measured. Such curves obtained in NdFeB magnets at 300K for increasing values of H_{sat} are shown in figure 8. It can be seen that they are composed of two regions. The first occurs at weak negative fields, the magnetization decreases very quickly, its variation is reversible and corresponds to free displacement of walls. The second region occurs at larger negative fields, of the order of the magnet coercive field, and in this case, the magnetization variation is irreversible. As H_{sat} increases, the contribution of the first region can be seen to decrease with the consequential increase of that of the second region. This behaviour reveals that a proportion n_g of grains has full coercivity, whilst a proportion $(1-n_g)$ remains in the multi-domain state. The variation of n_g as a function

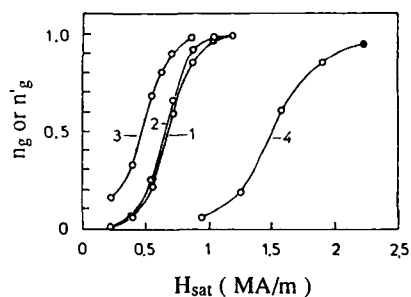


Fig.9. Proportion of crystallites n_g that are coercive as a function of H_{sat} (1: 175K, 2: 300K, 3 :400K) or n'_g as a function of H_{sat}^{inv} (4: 175K).

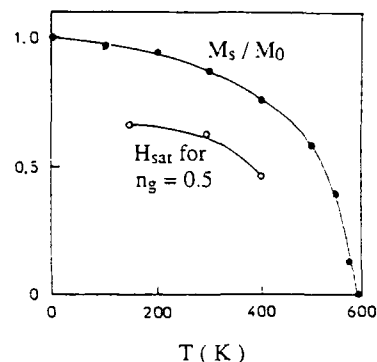


Fig. 10. Temperature dependence of H_{sat} required to obtain $n_g = 0.5$, compared to $M_s(T)$ in $Nd_2Fe_{14}B$.

of H_{sat} is shown in figure 9. The value of H_{sat} required to develop coercivity in a given proportion of grains is weakly temperature dependent between 4.2 K and 400 K, and it appears to be proportional to the value of the spontaneous magnetization (Figure 10). This result shows that the development of coercivity is not related to mechanisms involved in magnetization reversal, but is determined by the strength of dipolar fields in the magnet. The mean value of these dipolar fields, corresponding to $n_g = 0.5$, is approximately equal to 0.60 MA/m (figure 9). Since the measurements were performed on needle-shaped samples where the macroscopic demagnetizing field is negligible, this value represents the strength of internal dipolar fields only.

The dipolar field values so obtained may be compared to calculated values. The internal dipolar field acting on a given crystallite is the sum of the crystallite's self-demagnetizing field and of the Lorentz field. In principle, one would expect these two fields to almost cancel each other since the magnetization state is almost saturated and homogeneous. To understand the large value of 0.6 MA/m found experimentally, it must be considered that it is not the mean value of the dipolar field which controls the crystallite magnetic saturation. Indeed, a domain wall is present in a given crystallite until the applied field overcomes the dipolar field in any part of it. Large fluctuations may exist in the dipolar field and the value 0.6 MA/m should be regarded as the mean value of the maximum dipolar field in each crystallite.

Evaluation of the strength of the dipolar interactions involved during magnetization reversal

The dipolar field determined in the above section is not equal to the dipolar field, H_d^{vol} , acting during magnetization reversal when $H \sim H_C$. Indeed, the magnetization states in these two experimental situations are quite different. In order to evaluate the strength of H_d^{vol} , Givord et al [1991] have proposed a procedure whereby a magnetization state is obtained which resembles more closely the state of the magnet in the vicinity of the coercive field. Starting from a thermally demagnetized state, an initial saturation field is applied whose strength is such that the volume of the saturated crystallites amounts to approximately half the total volume of the sample. The field direction is then inverted. The magnetization of the saturated crystallites remains unchanged, while that of the other crystallites is aligned along the field (Figure 11). The

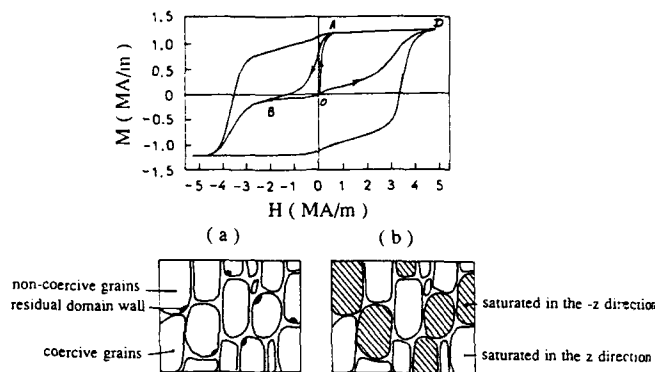


Figure 11. Description of the procedure used to evaluate the strength of the dipolar field H_d^{vol} acting in a magnet during magnetization reversal.

resulting magnetization is very weak, the magnetization state obtained being composed of two equivalent populations of crystallites respectively magnetized along and opposite to the applied field. The inverse field H_{sat}^{inv} is then increased in order to obtain saturation, eliminating domain walls in the crystallites whose magnetization is along H . The field H_{sat}^{inv} required to obtain $n_g = 0.5$ is now 1.3 MA/m (figure 9), much larger than the value 0.60 MA/m required to obtain $n_g = 0.5$. This increase in the dipolar field can be attributed to the strongly heterogeneous character of the magnetization state where the bulk magnetization is zero but the magnetization of every crystallite is saturated. Since this magnetization state applies also to the hysteresis loop in the vicinity of $H = H_C$, the field 1.3 MA/m can be regarded as an estimate of H_d^{vol} . However it must be realized that the strength of the fluctuations in the dipolar field depends obviously on the volume over which the field is averaged and these volumes are not the same for the two magnetization states considered here : the volume involved during saturation of a crystallite is the minimum volume within which a domain wall may be present, i.e. it corresponds to the single-domain particle size ; the volume involved during magnetization reversal, in the vicinity of H_C , is the activation volume. Larger fluctuations in the dipolar field are a priori expected in a volume of the order of the activation volume which is much smaller (see later in this section) than the single-domain particle size. Thus, the dipolar field here determined represents probably a minimum value for H_d^{vol} .

Temperature dependence of the coercive field

To analyse the temperature dependence of H_C experimentally observed, it is usual to express H_C/M_S as :

$$H_C / M_S = \alpha H_A / M_S - N_{eff} M_S \quad (24)$$

Sagawa et al. (1987, 1988) and Hirosawa et al (1989) have analysed the temperature dependence of H_C in NdFeB sintered magnets with α being taken as a fitting parameter which is temperature independent. Although the physical meaning of such a hypothesis is not clear in a system where magnetization reversal develops from the saturated state (The coefficient α is expected to be temperature independent only in the case of pinning, see previous section), a good agreement with experimental results was obtained as illustrated in figure 12. The deduced value of the parameter α is 0.37; the value of the parameter N_{eff} is 1 which corresponds to a dipolar field of 1.25 MA/m, in good agreement with the value deduced from H_{sat}^{inv} .

According to Kronmüller et al. (1988,1989) α should really be expressed as :

$$\alpha = \alpha_K \alpha_\psi \quad (25)$$

where α_K is the fundamental parameter describing the magnetization reversal mechanism (previous section) and α_ψ is a numerical coefficient which represents the effect of the angular dependence of the coercive field convoluted with the angular distribution of crystallite orientation (see further in this section). This analysis has been applied to sintered NdFeB magnets (Kronmüller et al., 1988, 1989). To test the possibility of a nucleation mechanism, magnetization reversal is assumed to occur by coherent rotation in the activation volume. Then, $\alpha_\psi \sim 0.7$ is expected, and the curves presented in figure 13 indicate that $\alpha_K \sim 0.9$. This high value of α_K implies that the dimension of the defect is very small ($r_0 \sim 10\text{\AA}$). The dipolar interactions are found to be very large ($N_{\text{eff}} = 1.6 - 1.8$), leading according to this analysis to a strong reduction in the coercive field. Assuming that pinning occurs in these magnets, $\alpha_\psi \sim 1$ is expected. Considering wide heterogeneities, the formalism is similar to the one describing nucleation (see previous section). It is thus deduced that $\alpha_K \sim 0.6$. This large value is incompatible with such a mechanism. Similarly, the value of α_K deduced in the case of narrow heterogeneities is incompatible with the pinning mechanism.

The same analysis has been applied to $\text{Sm}(\text{CoCuFeZr})_{7.6}$ magnets. In these magnets, a cellular structure of rhombohedral $\text{Sm}_2\text{Co}_{17}$, surrounded by 1:5 hexagonal cell boundaries, is present (Rabenberg et al., 1982; Hadjipanayis et al., 1982; Fidler et al., 1983; Ray et al., 1987). Durst (1986) has shown that the coercive field is proportional to the anisotropy difference between the 2:17 and 1:5 phases. This behavior corresponds to the one expected for the maximum propagation field resulting from pinning at the boundaries between both phases (It was argued above that the maximum propagation field should be proportional to H_A because $\Delta K = K$ has been assumed). It suggests therefore that the coercivity mechanisms in NdFeB magnets and $\text{Sm}(\text{CoCuFeZr})_{7-8}$ ones are different.

In the above analysis, the effect of thermal activation was not considered. This may significantly influence the temperature dependence of

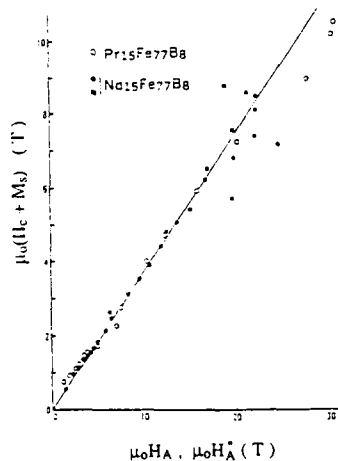


Fig. 12. Coercive field H_c in RFeB magnets as a function of H_A^* . H_A^* is defined as $\Delta E_A/M_s$ where ΔE_A is the anisotropy energy.

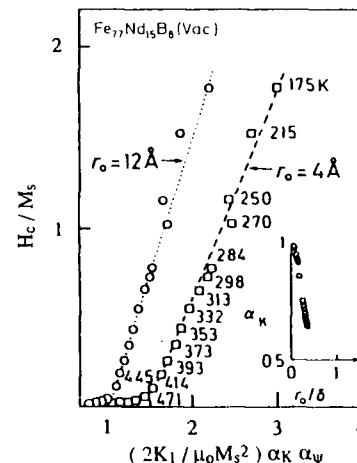


Fig. 13. Test for the temperature dependence of H_c in NdFeB magnets. α_K is deduced from relation (17) describing nucleation (Kronmüller et al., 1989).

H_c since magnetization reversal occurs when the difference in energy Δ , between the energy minimum and the energy maximum in the applied magnetic field, may be thermally activated. In the case where the increase in wall area required for wall expansion determines coercivity, the energy barrier Δ between the equilibrium state of minimum energy E_{\min} and the state of maximum energy, E_{\max} , from which magnetization reversal develops, may be expressed as (see relation (20)) [Elbaz et al., 1991b]:

$$\Delta = -2\mu_0 M_s H (v_{\max} - v_{\min}) + \gamma(s_{\max} - s_{\min}) + \Delta E_{\text{dip}} \quad (26)$$

where the indices min and max refer to the minimum and maximum energy states respectively and ΔE_{dip} represents the variation in dipolar energy when the system is excited from E_{\min} to E_{\max} . ΔE_{dip} may be expressed as $-N_{\text{eff}} M_s^2$ to be consistent with . As shown below, thermal activation occurs for $E_{\max} - E_{\min} \sim 25kT$, thus :

$$H_c = [(\gamma s_{\max} - \gamma s_{\min}) + 25kT] / \mu_0 M_s v - N_{\text{eff}} M_s \quad (27)$$

where $v = 2(v_{\max} - v_{\min})$ is the activation volume according to the relation (52). From above, v_{\min} and s_{\min} correspond to wall expansion within mode I, v_{\max} and s_{\max} within mode II. In this latter mode, s_{\max} is proportional to $v_{\max}^{2/3}$. At sufficiently high temperature, it appears that v_{\min} and s_{\min} may be neglected with respect to v_{\max} and s_{\max} , thus :

$$H_c = \alpha' \gamma / \mu_0 M_s v^{1/3} - N_{\text{eff}} M_s - 25kT / \mu_0 M_s v \quad (28)$$

where α' is a temperature independent geometric factor.

These relations have been successful in analysing the temperature dependence of H_c in Ferrites and NdFeB magnets (sintered as well as prepared from melt-spun ribbons) (figures 14 and 15) (Givord et al., 1988a, Tenaud, 1988). For this purpose, α' has been considered as a free parameter and the activation volume has been deduced from magnetic-after effect measurements. Good agreement was obtained for the different systems studied with α' being of the order of 0.3-0.5. The coefficient N_{eff} is approximately 1 in sintered magnets, but it is less in NdFeB magnets prepared from melt-spun ribbons where it may even be that dipolar interactions reinforce coercivity. It has been suggested (Givord et al., 1991) that the interactions between crystallites (residual exchange or dipolar) are larger in this latter magnets than in sintered magnets. In the

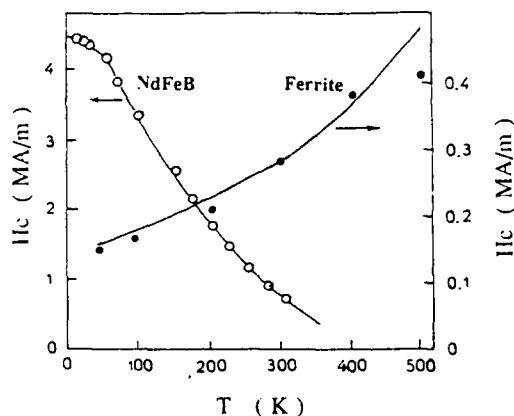


Figure 14. Temperature dependence of H_c in Ferrites and NdFeB sintered magnets (Full line : calculated). (Givord et al., 1990).

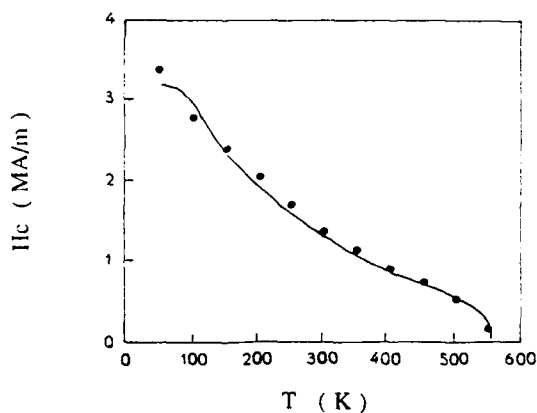


Figure 15. Temperature dependence of H_c in NdFeB magnets prepared from melt-spun ribbons (Full line: calculated) (Givord et al., 1990).

magnetization configuration corresponding to E_{\min} , the minimization of such interactions is then essential and ΔE_{dip} is reduced or even becomes positive. It may be noted that the existence of interactions between crystallites is also consistent with the evidence that collective processes are involved during magnetization reversal (Viadieu, 1988).

Concluding this section, the different models tested to analyse the temperature dependence of H_c suggest that, in all categories of sintered magnets and in NdFeB magnets prepared from ribbons, magnetization reversal may be determined by nucleation mechanism or expansion of an existing nucleus. It appears unlikely that pinning of a rigid domain wall is involved since the value of H_c is significantly higher than the maximum value then calculated. On the opposite, pinning may be at the origin of coercivity in $\text{Sm}(\text{CoCuFeZr})_{7-8}$ magnets.

Angular dependence of the coercive field in magnets

In usual experimental conditions, the coercive field is measured in a field antiparallel to the magnetization. When the field is applied at an angle θ_{CH} from the easy direction, the value of H_c is different. On the one hand, the coupling energy of the magnetization with the field, is reduced by a factor $\cos\theta_{\text{CH}}$. On the other hand, due to the non-collinearity between M_s and H , a torque is exerted which may induce a certain moment rotation towards the field direction, i.e. the physical system is modified and this may further affect the value of H_c . The analysis of these effects may help in understanding coercivity mechanisms.

Behaviors expected in various models. One may define a function $g(\theta_{\text{CH}})$ which represents the angular dependence of H_c :

$$H_c(\theta_{\text{CH}}) = H_c(0) g(\theta_{\text{CH}}). \quad (29)$$

For coherent rotation, the function $g(\theta_{\text{CH}})$ has been calculated by Stoner and Wohlfarth [STO 48] :

$$g(\theta_{\text{CH}}) = 1 / [\sin^{2/3}\theta_{\text{CH}} + \cos^{2/3}\theta_{\text{CH}}]^{3/2} \quad (30)$$

As θ_{CH} varies between 0° and 90° , the nucleation field decreases from H_A to $H_A/2$ and increases again up to the initial value (figure 16a).

The angular dependence of the coercive field has never been calculated exactly in the case of nucleation at defects. The same approximation as in the previous section may be made, assuming coherent rotation of the moments in the activation volume. The angular dependence of $H_c(\theta_{\text{CH}})$ is then given by the relation (30).

In the case of pinning, one can assume that the coercive field is much weaker than the anisotropy field. The rotation of the moments towards the field may thus be neglected, and the energy barrier is simply :

$$\Delta = \partial\gamma / \partial z v - 2\mu_0 M_s H v \cos\theta_{\text{CH}} \quad (31)$$

Relation (31) indicates that the active part of the field is $H\cos\theta_{\text{CH}}$, i.e. the coercive field exhibits a $1/\cos\theta_{\text{CH}}$ dependence (figure 16b). As H_c starts to become a significant fraction of H_A , the moments at both ends of the wall rotate towards the field direction. The angular dependence of H_c then calculated is not as strong, in particular at large angles, as that calculated in the case where the reversible rotation of the moments from c can be neglected (Elbaz et al., 1991a).

A similar angular dependence of H_c is obtained in the case where magnetization reversal involves the expansion of an already formed nucleus through domain wall propagation.

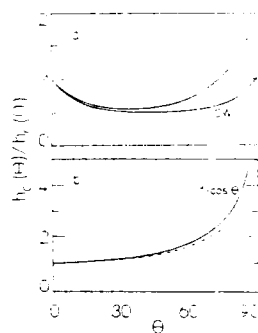


Figure 16. Calculated angular dependence of the coercive field in magnets a) SW b) pinning, without any rotation of the moments, or allowing for moment rotation (Elbaz et al., 1991a).

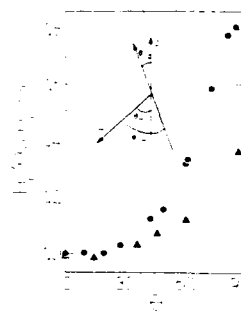


Figure 17. $H_c(\theta_H) / H_c(0)$ in RFeB magnets ●:Nd₁₇Fe₇₅B₈ ▲:Nd₂₀Fe₇₁Al₂B₇ Inset: definition of the angles involved in the analysis.

Experimental results. Measurements of the angular dependence of the coercive field in magnets are in general performed in the following way (Kronmüller et al., 1987b, Givord et al., 1988b) : the sample is cut in the shape of a thin cylinder whose axis is perpendicular to the alignment z -axis of the magnet, the magnetization is saturated in a positive field applied along z , a negative field is applied along a direction perpendicular to the cylinder axis, at a certain angle θ_H from z (figure 17, inset). In figure 17, $H_c(\theta_H) / H_c(0)$ is shown for a NdFeB sintered magnet with $H_c = 8.7$ kOe at 300K (Elbaz et al. 1991a). $H_c(\theta_H)$ steadily increases as θ_H increases and attains a value equal to 1.8 times the $\theta_H = 0$ value. For comparison, $H_c(\theta_H)$ is also shown for an Al-doped magnet in which the room temperature coercivity is 17.2 kOe (Kronmüller et al. 1988). The increase in H_c is much smaller for this magnet which has a larger H_c / H_A ratio.

Analysis. $H_c(\theta_H)$ may be calculated considering that all the crystallites which constitute a magnet have the same coercive field h_c and that magnetization reversal occurs independently within the different crystallites. The probability for a crystallite to be oriented at an angle θ_{CH} from H (applied at an angle θ_H from c) is (Givord et al., 1988b) :

$$dp_{\theta_H}(\theta_{CH}) = \int_0^{2\pi} f(\theta_{CZ}) \sin\theta_{CZ} d\alpha d\theta_{CZ} \quad (32)$$

where $f(\theta_{CZ})$ is the angular distribution of crystallite c -axes with respect to the z -axis, α is an angle in a plane perpendicular to H and θ_{CZ} is deduced from θ_{CH} and α through :

$$\cos\theta_{CZ} = \cos\theta_{CH} \cos\theta_H - \sin\theta_{CH} \sin\theta_H \sin\alpha \quad (33)$$

The function $N_{\theta_H}(\theta_{CH}) = dp_{\theta_H}(\theta_{CH}) / d\theta_{CH}$ characterizes the crystallites angular orientations with respect to H , it may be deduced from $f(\theta_{CZ})$ and the irreversible susceptibility is :

$$\chi^{irr} = 2 M_S \cos \theta_{CH} N_{\theta_H}(\theta_{CH}) / (dh_C/d\theta_{CH}) \quad (34)$$

(Givord et al., 1985). The value θ_{CH}^{max} for which χ^{irr} is maximum shows which crystallites are involved in magnetization reversal at $H = H_C$, and the coercive field is thus :

$$H_C = h_C(\theta_{CH}^{max}) \quad (35)$$

This approach has been used to calculate the angular dependence of H_C for the different mechanisms envisaged above. Assuming coherent rotation, H_C practically does not depend on θ_H (Figure 18). This is because h_C is weakly angle dependent for $20^\circ < \theta_{CH} < 70^\circ$, and the irreversible susceptibility is always dominated by crystallites within this range of angles. In the case where $1/\cos \theta_{CH}$ dependence applies (i.e. pinning or expansion of a nucleus), an increase of H_C with θ_H by approximately a factor of 2 is obtained. If a certain rotation of the moments away from their easy direction occurs, the increase of H_C with θ_H is not as strong (Figure 18).

In NdFeB magnets for which $H_C \sim 10$ kOe at room temperature (Figure 17), the increase in H_C with θ_H corresponds approximately to the one calculated for a $1/\cos \theta_{CH}$ dependence in individual crystallites. For $H_C \sim 17$ kOe, the reduced increase in H_C with θ_H can be attributed to a non-negligible rotation of the moments into the field direction. This is consistent with the fact that the coercive field at large angles amounts to approximately one third the anisotropy field of the Nd₂Fe₁₄B phase. The same type of analysis has already been applied successfully to SmCo₅ and Ferrite magnets (Givord et al., 1988b).

Finally, a decrease in H_C as θ_H increases occurs at small θ_H values in PrFeB magnets (Elbaz et al., 1991a; Grönefeld, 1990). This cannot be interpreted within the above analysis and has been tentatively attributed to the relative decrease, at low temperature, of the dipolar interactions with respect to other interactions.

The above results show that a better agreement with experimental data is obtained in models involving domain wall propagation and leading to $1/\cos \theta$ dependence, or close to it, than in models involving coherent rotation of the magnetization. Combining this with the conclusion of the above section, suggests that magnetization reversal actually occurs through expansion of an existing nucleus. However, it must also be noted that nucleation might be a complex process for which the schematic description used here (coherent rotation of the magnetization in a small volume) is inadequate.

Magnetic after-effect in sintered Nd-Fe-B magnets

Formalism. In its saturated magnetic state, a magnet is in a metastable state. It tends to reach the state of minimum energy, and, under

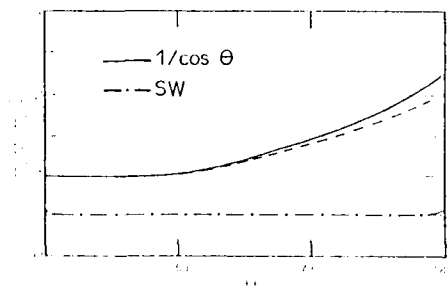


Fig. 18. Calculated angular dependence of H_C in different models (see text).

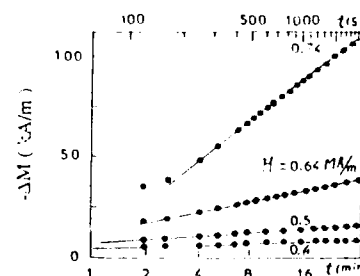


Fig 19. Typical time dependence of the magnetization in RFeB magnets.

the effect of thermal activation, the magnetization may vary with time. The magnetization variation becomes important when the applied magnetic field approaches the coercive field and the energy barrier Δ to be overcome is reduced. In all instances, thermal activation encourages magnetization reversal which develops in a small volume termed the activation volume (Wohlfarth, 1985). The size of the activation volume may be evaluated from the comparison between the field and time dependences of the magnetization (Wohlfarth, 1985 ; Givord et al., 1987).

Let $f(\Delta)$ be the distribution of energy barrier Δ . The magnetization variation associated with overcoming the barriers between Δ and $\Delta+d\Delta$ is :

$$dM = - 2 M_s f(\Delta) d\Delta \quad (36)$$

The magnetic viscosity is defined as the time dependence of the magnetization :

$$S = - dM / d(\ln t) = 2 M_s f(\Delta) d\Delta / d(\ln t) \quad (37)$$

where it is assumed that $f(\Delta)$ is a constant, i.e. the distribution is very broad [Street and Wooley, 1949]. It is in general observed that the magnetization has a logarithmic variation with time, which shows the validity of this hypothesis. In order to evaluate $d\Delta / d\ln t$, the relaxation time τ associated with a given energy barrier Δ must be determined. For an Arrhenius law :

$$\tau = \tau_0 \exp(\Delta/kT) \quad (38)$$

where τ_0 is the minimum characteristic time for magnetization reversal ($\tau_0 \sim 10^{-11}$ s).

The probability for magnetization reversal between time 0 and time t is :

$$P = 1 - \exp (-t / \tau). \quad (39)$$

The properties of the exponential function are such that P is almost 0 as long as $t < \tau$ and almost 1 for $t > \tau$. It may thus be written approximately that (Préjean and Souletie, 1980) :

$$D = kT \ln (t / \tau_0) \quad (40)$$

i.e. thermal activation may be considered to be equivalent to an energy term :

$$E_{act} = kT \ln (t / \tau_0) \quad (41a)$$

For typical values of t , between 0.1 s and 1000 s, the logarithmic factor is approximately constant and equal to 25. It results that :

$$E_{act} \sim 25 kT . \quad (41b)$$

Using (41), relation (37) may be rewritten :

$$S = - dM / d(\ln t) = 2 M_s k T f(\Delta) . \quad (42)$$

Considering now the field dependence of the magnetization, the irreversible susceptibility, χ^{irr} , may be written using (36) as :

$$\chi^{irr} = 2 M_s f(\Delta) (\partial D / \partial H)_T \quad (43)$$

In this relation, it is assumed that no thermal activation occurs. From an experimental point of view, it cannot be eliminated, but Estrin et al. (1989) have shown that it is equivalent to measure χ^{irr} at constant dM / dt .

The viscosity coefficient S_v is then defined as :

$$S_v = S / \chi^{irr} = kT / (\partial\Delta / \partial H)_T \quad (44)$$

Activation volume. Relation (44) indicates that $(\partial\Delta / \partial H)_T$ is the essential parameter deduced from magnetic after-effect measurements and we turn now to its evaluation in the different models considered in the previous section. For coherent rotation, the energy barrier Δ is :

$$\Delta = KV (1 - H/H_A)^2 \quad (45)$$

and thus :

$$(\partial\Delta / \partial H)_T = - \mu_0 V M_S (1 - H/H_A) \quad (46)$$

where V is the sample volume which may be identified with v , the activation volume, since coherent rotation involves, by definition, all the moments in the system. It has to be noted that $(\partial\Delta / \partial H)_T$ is proportional to $(H_A - H)$. However, Victora (1989) has shown that the above result is valid only for H applied exactly along the magnetization direction. A more general result is :

$$\Delta = 4 K V [2 (H_A - H) / 3H_A]^{3/2} \sin\theta_0 \cos\theta_0 \quad (47)$$

where θ_0 represents the angle of the magnetization with respect to \mathbf{c} , at the energy maximum and is related to the angle θ_H of H with \mathbf{c} by $\tan\theta_0 = -\tan^{1/3}\theta_H$. It results that :

$$(\partial\Delta / \partial H)_T = - 6KV (2/3H_A)^{3/2} \sin\theta_0 \cos\theta_0 (H_A - H)^{1/2} \quad (48)$$

which for $\theta_H \sim 15^\circ$ is approximately :

$$(\partial\Delta / \partial H)_T \sim - 0.5 \mu_0 V M_S (1 - H/H_A)^{1/2} \quad (49a)$$

i.e. $(\partial\Delta / \partial H)_T$ varies as $(H_A - H)^{1/2}$ instead of $(H_A - H)$. H_c is of the order of $H_A/2$ for $\theta_H \sim 15^\circ$ and above, and thus :

$$(\partial\Delta / \partial H)_T \sim 0.3 \mu_0 V M_S. \quad (49b)$$

For nucleation, it may be assumed, as above, that coherent rotation of the moments take place in the activation volume (Kronmüller et al., 1987b). Then (49b) should hold with V being replaced by v , the activation volume.

In the case of pinning, the energy barrier is readily deduced from the basic formula (23), to be :

$$\Delta = \partial\gamma / \partial z v - 2\mu_0 M_S H v \quad (50)$$

where $v = s dz$ is the activation volume, s the area pinned, dz the domain wall displacement from the energy minimum to the energy maximum. As long as the domain wall structure is not modified by the applied field, $(\partial\Delta / \partial H)_T$ is field independent :

$$(\partial\Delta / \partial H)_T = - 2\mu_0 M_S v. \quad (51)$$

The same result is obtained in the case where coercivity is controlled by the volume expansion of the already formed nucleus.

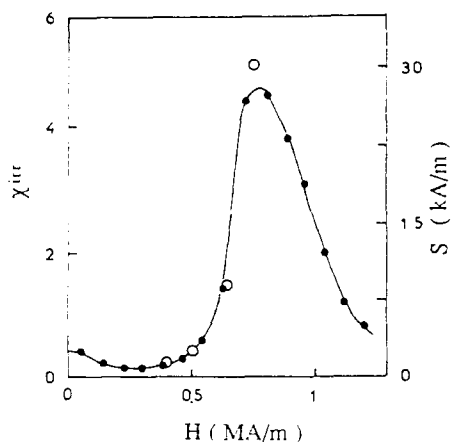


Figure 20. Field dependence of the viscosity S (o) and irreversible susceptibility χ_{irr} (o) in a NdFeB magnet.

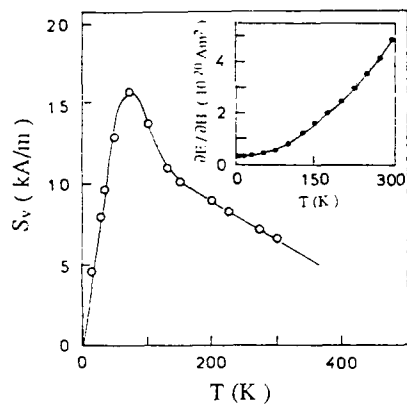


Figure 21. Temperature dependence of the viscosity coefficient S_v in a NdFeB magnet. Inset : Temperature dependence of $\partial\Delta/\partial H$.

Thus for the various mechanisms discussed here, it appears that the size of the activation volume is of the order of (Wohlfarth, 1985 ; Street et al., 1987 ; Givord et al., 1987):

$$v \sim - (\partial\Delta/\partial H)_T / \mu_0 M_s \quad (52)$$

which is the simple relation generally used to evaluate v from experimental data.

Experimental analysis of magnetic after-effect measurements. Typical time dependence of the magnetization at 300 K in a Nd-Fe-B magnet is shown

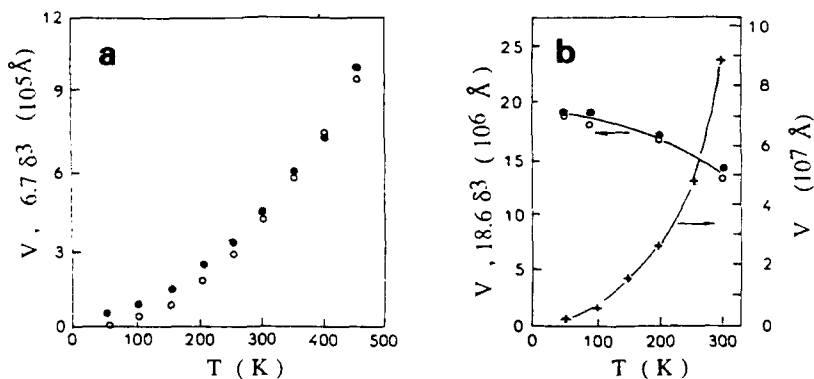


Figure 22. Thermal variation of the activation volume v (o) in various magnets compared to the thermal variation of δ^3 (o) a) NdFeB magnets prepared from melt-spun ribbons . b) sintered ferrites (also shown Ba-Ferrites for recording (+)).

in figure 19 (Givord et al., 1987). The logarithmic law obtained indicates that the distribution $f(E)$ is approximately a constant in the range of activation energies corresponding to these measurements. The slope of the straight lines in figures such as figure 19 corresponds to the viscosity $S = -dM/d\ln t$. The field dependence of S obtained is shown in figure 20. S is maximum when the applied field is close to the coercive field. The irreversible susceptibility χ^{irr} appears to be approximately proportional to S (figure 20), thus showing that the viscosity coefficient $S_v = S/\chi^{irr}$ is approximately field independent. The temperature dependence of S_v exhibits a maximum at about 75 K (figure 21). In a magnet where H_C , at 300 K, is equal to 0.8 MA/m, S_v at 75 K reaches about 16 kA/m. The field derivative of the energy barrier $\partial\Delta/\partial H$, deduced from S_v (relation 44) increases continuously with temperature (figure 21, inset).

The temperature dependences of the activation volume, deduced from $\partial\Delta/\partial H$ determined experimentally (relation 52), are shown, as typical examples, in figure 22 for NdFeB magnets prepared from melt-spun ribbons, sintered ferrites and Ba-ferrites used for magnetic recording. The size of the activation volume in all these systems is much lower than the size of the magnetic particles, in agreement with the fact that magnetization reversal is not a collective process but involves domain wall nucleation and propagation. The thermal variation of the cube of the domain wall width, δ^3 in hexagonal ferrites and $Nd_2Fe_{14}B$ is also shown in the figure 22. The activation volume is of the order of $10\delta^3$ and the temperature dependences of v and δ^3 are similar. This is particularly striking since v and δ^3 increase with temperature in NdFeB magnets but decrease in ferrites magnets.

A qualitative interpretation may be proposed to account for this phenomenon. All the results already described show that magnetization reversal involves non-uniform magnetization processes. The domain wall width δ is precisely the length which characterizes such processes. The additional consideration that the shape of the activation volume is such as to reduce dipolar interactions, implies that the dimensions of the activation volume must vary in unison. Combining these two arguments leads to $v \sim \delta^3$, as observed experimentally. However, it must be pointed out that the activation volume is compared here to a parameter which characterizes the perfect material and the interpretation proposed is thus questionable if coercivity is controlled by nucleation or propagation of a rigid domain wall, since in such instances, magnetization reversal is expected to be determined by the magnetic properties of a part of the material which is not representative of the bulk. This once more favors magnetization reversal through nucleus expansion for the systems discussed here (sintered magnets, NdFeB magnets of different categories, hard magnetic particles for recording,...). It would be important to measure magnetic-after effect in $Sm(Co-Cu-Fe-Zr)_{7-8}$ magnets, where coercivity is thought to be due to pinning of domain walls.

REFERENCES

- Abraham C. and Aharoni A., 1960, Phys. Rev., 120:1576
- Aharoni A. and Shtrikman S., 1958, Phys. Rev., 109:1522
- Aharoni A., 1960, Phys. Rev., 119:127
- Aharoni A., 1963, Phys. Rev., 131:1478
- Aharoni A., 1966, Phys. Stat. Sol., 16:3
- Aharoni A., 1986, IEEE Trans. Mag., MAG-22:478
- Berkowitz A., 1990, private communication
- Brown Jr. W.F., 1945, Rev. Mod. Phys., 17:15
- Brown Jr. W.F., 1969, Ann. New York Acad. Sci., 147:463
- De Blois R.W. and Bean C.P., 1959, J. Appl. Phys., 30:225S
- Eagle D.F. and Mallison J.C., 1967, J. Appl. Phys., 38:995

- Elbaz D., Givord D., Hirosawa H., Missell F., Rossignol M.F. and Villas-Boas V., 1991a, *J. Appl. Phys.* (to appear)
- Elbaz D., Givord D., Nozieres J.P., Missell F., Rossignol M.F. and Villas-Boas V., 1991b, (to be published)
- Estrin Y., McCormick P.G. and Street R., 1989, *J. Phys. Condens. Matter*, 1:484
- Fidler J. and Skalicky P., 1982, in *Proc. Int. Workshop On R.E. Permanent Magnets and their Applications*, J. Fidler Ed., T. U. of Vienna.
- Frei E.H., Shtrikman S. and Treves D., *Phys. Rev.*, 1957, 106:446
- Friedberg R. and Paul D.I., 1975, *Phys. Rev. Lett.*, 34:1234
- Gaunt P., 1988, *Can. J. Phys.*, 65:1194
- Givord D., Liénard A., Perrier de la Bâthie R., Tenaud P. and Viadieu T., 1985, *J. de Phys. (Paris)*, C6:313
- Givord D., Lienard A., Tenaud P. and Viadieu T., 1987, *J. Magn. Magn. Mat.*, 67:L281
- Givord D., Tenaud P. and Viadieu T., 1988a, *IEEE Trans. Mag.*, 24:1921
- Givord D., Tenaud P. and Viadieu T., 1988b, *J. Magn. Magn. Mat.*, 72:247
- Givord D., Lu Q., Rossignol M.F., Tenaud P. and Viadieu T., 1990, *J. Magn. Magn. Mat.*, 83:183
- Givord D., Lu Q., Rossignol M.F., Taylor D., 1991, *J. Magn. Magn. Mat.* (to be published)
- Grönefeld M., 1990, Thesis, Uni. of Stuttgart
- Hadjipanayis G.C., 1982, in *Proc. Int. Workshop On R.E. Permanent Magnets and their Applications*, J. Fidler Ed., T. U. of Vienna.
- Hilzinger H.R. and Kronmüller H., 1975, *Phys. Lett.*, 51A:59
- Hirosawa S., Tsubokawa Y. and Shimizu R., 1989, in *Proc. 10th Int. Workshop on R.E. Magnets and Their Applications*, The Society of Non-Traditional Technology, Tokyo, 465
- Kersten M., 1943, *Phys. Z.*, 44:63
- Kittel C., *Rev. Mod. Phys.*, 1949, 21:541
- Kronmüller H. and Hilzinger H.R., 1976, *J. Magn. Magn. Mat.*, 2:3
- Kronmüller H., 1987, *Phys. Stat. Sol. (b)*, 144:385
- Kronmüller H., Durst K.D. and Martinek G., 1987b, *J. Magn. Magn. Mat.*, 69:149
- Kronmüller H., Durst K.D., Hock S. and Martinek G., 1988, *J. Phys. (Paris)*, 49:C8-623
- Kronmüller H. and Durst K.D., 1989, in *Concerted European Action on Magnets*, I.V. Mitchell, J.M.D. Coey, D. Givord, I.R. Harris and R. Hanitsch ed., Elsevier Applied Science, London, 392
- Luborsky F.E. and Morelock C.R., 1964, *J. Appl. Phys.*, 35:2055
- Mc Currie R.A. and Carswell G.P., 1971, *Phil. Mag.*, 23:333
- Prejean J.C. and J. Souletie, 1980, *J. Phys. (Paris)*, 41:1335
- Rabenberg L., Mishra R.K. and Thomas G.J., 1982, *J. Appl. Pys.*, 53:2389
- Ray A.E., Soffa W.A., Blachere J.R. and Zhang B., 1987, *IEEE Trans. Mag.*, MAG-23:2711
- Sagawa M., Hirosawa S., Yamamoto H., Fujimura S. and Matsuura Y., 1987, *Jap. J. of Appl. Phys.*, 26:785
- Sagawa M. and Hirosawa S., 1988, *J. Phys. (Paris)*, 49:C8-617
- Stoner E.C. and Wohlfarth E.P., 1948, *Phil. Trans. Roy. Soc. (London)* 240A:599
- Street R. and Wooley J.C., 1949, *Proc. Phys. Soc.*, 62A:562
- Street R., Day R.K. and Dunlop J.B., 1987, *J. Magn. Magn. Mat.*, 69:106
- Tenaud P., 1988, Thesis, Université de Grenoble
- Viadieu T., 1988, Thesis, Université de Grenoble
- Victoria R.H., 1989, *Phys. Rev. Lett.*, 63:457
- Wohlfarth E.P., 1985, *J. Phys. F*, 14:L155
- Zijlstra H., Permanent magnets : theory, in *"Ferromagnetic Materials"*, vol. 3, E.P. Wohlfarth Ed., North-Holland, Amsterdam (1982)

MICROMAGNETISM AND MAGNETIZATION PROCESSES IN MODERN MAGNETIC MATERIALS

Helmut Kronmüller

Max-Planck-Institut für Metallforschung
Institut für Physik
Heisenbergstr. 1
7000 Stuttgart 80
Federal Republic of Germany

1. INTRODUCTION

The conventional magnetization processes in macroscopic specimens are reversible rotations and domain wall displacements, where the latter ones take place reversibly at low fields and irreversibly by Barkhausen jumps at fields comparable to the coercive field (Kneller, 1962; Chikazumi, 1964; Träuble, 1966). The scenario is quite different in the case of micro- and nanocrystalline materials which have become very important for sintered and melt-spun permanent magnets, soft magnetic materials as well as for magnetic multilayers (Croat et al., 1984; Sagawa et al., 1984; Hadjipanayis et al., 1983; Hadjipanayis and Kim, 1988).

The magnetization processes in these materials show a multitude of different mechanisms depending on material constants, orientation and value of applied fields, grain size and shape, and on the microstructure of the ensembles of grains.

The relation between magnetization processes and the microstructure has been found to be the keystone for a basic understanding of the hysteresis loop of modern magnetic materials (Kronmüller, 1987; Kronmüller et al., 1988a, 1988b). The theoretical background for a description of these phenomena is the continuum theory of micromagnetism as developed by Landau and Lifshitz (1935), Brown (1940, 1941), Néel (1950) and Kittel (1949). The more recent progresses dealing with the interaction between microstructure and magnetic properties are reviewed in papers of Kronmüller (1966, 1972, 1978). The importance of microstructural effects becomes obvious if we consider the coercive field, H_c , of different types of alloys.

In magnetically soft, amorphous materials H_c may be as small as $H_c \sim 0.1$ A/m whereas in hard magnetic materials values of $H_c \sim 4000$ kA/m have been obtained. This variation of H_c by nearly a factor of 10^6 represents a fascinating problem in the field of material development to be treated by micromagnetism.

The complexity of the whole problem becomes obvious if we consider the different types of permanent magnets developed during the last two decades. The discovery of the hexagonal intermetallic compounds Co_5Sm and $\text{Co}_{17}\text{Sm}_2$ in 1972 started a new type of permanent magnet materials known as the rare earth-transition metal alloys. Here the Co_5Sm magnets are produced as sintered magnets, magnetically hardened by the nucleation mechanism (Strnat 1978) whereas the $\text{Co}_{17}\text{Sm}_2$ based

magnets are produced from the as-cast alloy by annealing treatments where a Cu enriched 5:1 phase is precipitated in an Fe enriched 17:2 phase (Ray 1984, Hadjipanayis 1982). The grain size in the Co₅Sm sintered magnets is of the order of 5 - 10 μ m whereas the precipitation structure in the 17:2 magnets shows pyramidal cell structures of diameter 100 nm. In this case the magnetic hardening occurs by the pinning of domain walls at the cell walls of the 5:1 precipitates.

Another very interesting example of a new hard magnetic material is the tetragonal intermetallic compound Fe₁₄Nd₂B as produced by Croat et al. (1984) by melt-spinning and by Sagawa et al. (1984) by casting. As in the case of the CoSm alloys magnets with grain sizes of \sim 100 nm are produced from the melt-spun material and sintered magnets with grain sizes 4 - 10 μ m from the as-cast material. It is a matter of controversy up to now which hardening mechanism in the case of the melt-spun material governs the coercive field: Domain wall pinning or nucleation of reversed domains.

A fundamental property of H_c is its dependence on the grain diameter D which is shown qualitatively in Fig. 1 for perfect and imperfect particles. Here we may distinguish four different regions:

1. In very small so-called superparamagnetic particles with $D < d_{th} \sim 3 - 5$ nm the reversion of M_s takes place by a thermally activated process.
2. In particles with $d_{th} < D < d_{crit}$ the reversion of M_s is independent of size and takes place by a uniform rotation process.
3. In larger particle sizes $d_{crit} < D < D_{crit}$ an inhomogeneous rotation process (curling mode) with decreasing critical fields takes place.
4. In large particles $D > D_{crit}$ the single domain particles transform into multidomain particles where the reversion of M_s takes place by domain wall displacements.

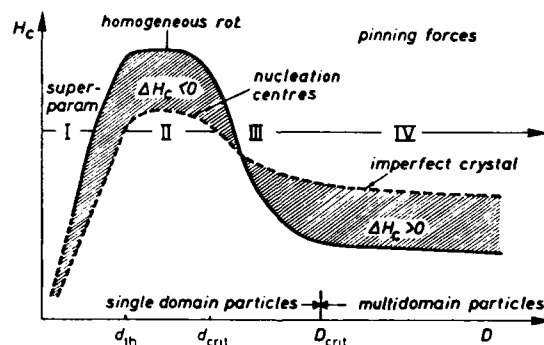


Fig. 1. Qualitative dependence of H_c on the particle diameter D . The four ranges determined by the critical diameters for thermal activation (d_{th}), transition to inhomogeneous rotation (d_{crit}) and the formation of multidomain particles (D_{crit}). The behaviour for perfect (—) and imperfect (-----) particles is visualized.

It is of interest that in small particles $D < D_{crit}$ microstructural defects lead to a decrease of the coercive field whereas in large particles the coercive field is increased by microstructural defects. In the latter case the defects act as pinning centres for domain walls whereas in small particles they act as magnetically soft regions where the nucleation of reversed domains easily takes place. The deteriorating effect of microstructural defects on the coercive field of sintered magnets is

demonstrated by Fig. 2 where we present the ratio of the experimental coercive field and the theoretical nucleation field of different hard magnetic materials. The most surprising result of this representation is the small progress achieved within a period of 40 years. It is evident that starting with the famous Alnico magnets via Ba-Ferrites up to the most modern magnet of $\text{Fe}_{14}\text{Nd}_2\text{B}$ it has not been possible to improve the magnets from a theoretical point of view. The deteriorating effects of the microstructure obviously could not be reduced. Accordingly, it seems to be the most important task in future to understand and to eliminate the deteriorating effects of the microstructure. In the following chapters we shall give a quantitative treatment of the different types of microstructural defects leading to a reduction of the coercive field.

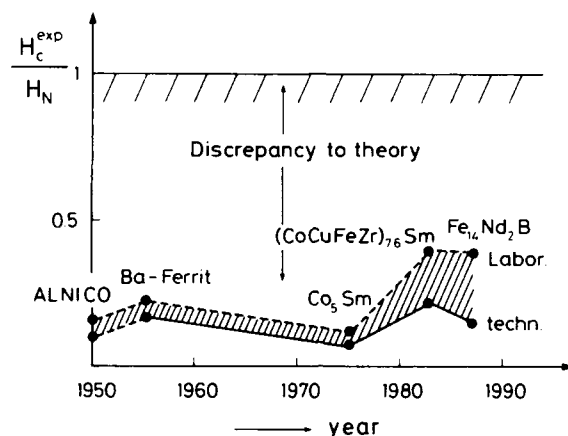


Fig. 2. The ratio H_c^{exp}/H_N of prominent magnetic systems (---◆---◆--- = laboratory magnets, —◆—◆—◆— = technical magnets).

2. MICROMAGNETIC EQUATIONS

Micromagnetism has been proven to be a rather effective tool for the study of magnetic states and magnetization processes on length scales say above several lattice parameters. Within the framework of this theory the spontaneous magnetization

$$\underline{M}_s = |\underline{M}_s| \begin{pmatrix} \gamma_1 \\ \gamma_2 \\ \gamma_3 \end{pmatrix} \quad (2.1)$$

is described by its modulus, M_s , and the direction cosines, γ_i , with respect to a cartesian coordinate system. In the special case of a uniaxial crystal we may write $\gamma_1 = 0$, $\gamma_2 = \sin \phi$, $\gamma_3 = \cos \phi$, where ϕ denotes the angle between \underline{M}_s and the c-axis. The total magnetic Gibbs free energy density of a small magnetic particle is composed of four terms

$$\phi'_t = \phi'_{\text{ex}} + \phi'_K + \phi'_S + \phi'_H, \quad (2.2)$$

which are given by the following expressions:

1. Exchange energy

$$\phi'_{\text{ex}} = A(\nabla\phi)^2 \quad (2.3)$$

(A = exchange constant).

2. Magnetocrystalline energy

$$\phi_K^i = K_1 \sin^2 \phi + K_2 \sin^4 \phi + K_3 \sin^6 \phi + \dots \quad (2.4)$$

3. Stray field energy

$$\phi_S^i = - \frac{1}{2} \underline{H}_s \cdot \underline{M}_s \quad (2.5)$$

The stray field \underline{H}_s is derived from a potential U by $\underline{H}_s = - \nabla U$, where U obeys Poisson's equation

$$\Delta U = 4\pi \operatorname{div} \underline{M}_s \quad (2.6)$$

with the solution

$$U(\underline{r}) = (-) \int \frac{\operatorname{div} \underline{M}_s d^3 r'}{|\underline{r} - \underline{r}'|} + \int \frac{\underline{M}_s \cdot d\underline{f}'}{|\underline{r} - \underline{r}'|} \quad (2.7)$$

where the first term takes care of the magnetic volume charges $(-) \operatorname{div} \underline{M}_s$ and the second term of the magnetic surface charges $\underline{M}_s \cdot \underline{n}$ (\underline{n} = surface normal).

4. Magnetostatic energy in an internal field, \underline{H}

$$\phi_H^i = - \underline{M}_s \cdot \underline{H} \quad (2.8)$$

Here \underline{H} denotes an internal field

$$\underline{H} = \underline{H}_{\text{ext}} + \underline{H}_d \quad (2.9)$$

which is composed of the external field $\underline{H}_{\text{ext}}$ and a demagnetizing field, \underline{H}_d , exerting from fixed surface charges of a macroscopic specimen. Here we have introduced two types of stray fields. \underline{H}_s results from an individual particle and is determined by (2.7) with \underline{M}_s the distribution of magnetization within the particle. \underline{H}_d is the stray field being due to all other particles and in particular being due to the macroscopic external surfaces of an ensemble of particles. If we consider a magnetization process of one individual particle we allow for the dependence of \underline{H}_s on the magnetization process, however, consider \underline{H}_d as a constant demagnetizing field of the surroundings of the particle. Insofar, \underline{H}_d is treated similarly as the external field and does not depend on the magnetic state of the particle under consideration.

Micromagnetic equilibrium conditions are obtained from a minimization of the total Gibbs free energy with respect to the direction cosines γ_i or ϕ . From the variational problem

$$\delta \phi_t = S \int \{ \phi_{\text{ex}}^i + \phi_K^i + \phi_S^i + \phi_H^i \} d^3 r = 0 \quad (2.10)$$

the equilibrium condition

$$[\underline{M}_s \times \underline{H}_{\text{eff}}] = 0 \quad (2.11)$$

follows, with an effective field

$$H_{\text{eff},i} = - \frac{2A}{M_s} \Delta \gamma_i - \frac{1}{M_s} \frac{\partial \phi_K}{\partial \gamma_i} + H_{\text{ext},i} + H_d + H_{s,i}, \quad (2.12)$$

where the first term corresponds an effective field due to the exchange energy and the second term describes the so-called crystal field

$$H_K = - \frac{1}{M_s} \frac{\partial \phi_K}{\partial \gamma_i}. \quad (2.13)$$

Actually, the torque equation (2.11) has to be solved together with Poisson's equation (2.6) which establishes an integro-differential equation. Furthermore, the additional condition $\sum \gamma_i^2 = 1$ has to be taken into account. In the case of one-dimensional problems in uniaxial crystals where $\gamma_1 = \sin \phi$, $\gamma_2 = 0$ and $\gamma_3 = \cos \phi$, and the internal field \underline{H} lies under an angle ψ with respect to the c-axis the equilibrium condition writes

$$\begin{aligned} 2A \frac{d^2 \phi}{dz^2} - \{K_1 + 2K_2 \sin^2 \phi + 3K_3 \sin^4 \phi\} \sin 2\phi + (H_{\text{ext}} + H_d) \sin(\phi - \psi) \\ + \frac{1}{2} M_s \left\{ (H_{s,x} + \frac{\partial H_{s,x}}{\partial \phi}) \cos \phi - (H_{s,z} - \frac{\partial H_{s,z}}{\partial \phi}) \sin \phi \right\} = 0. \end{aligned} \quad (2.14)$$

Eq. (2.11) and Eq. (2.14) represent the basic equation for treating one-dimensional magnetization states and processes of small particles. Four types of magnetization processes may be derived from the equilibrium equations:

1. Nucleation processes.
2. Macroscopic reversible rotations.
3. Instability processes (FOMP).
4. Domain wall displacements.

In single domain particles the first processes may occur successively, whereas in multidomain particles reversible rotation and domain wall displacements may take place simultaneously.

3. NUCLEATION AND INSTABILITY FIELDS IN SINGLE DOMAIN PARTICLES

Nucleation fields are obtained from the micromagnetic equation (2.14) as the Eigenvalue, where for the first time \underline{M}_s starts to deviate from its original orientation parallel to the c-axis. The nucleation field, H_N , depends on the magnetization mode leading to a reversion of \underline{M}_s . Fig. 3 gives a review of the three main magnetization modes: uniform rotation, curling and buckling. For a derivation of the nucleation fields of these three magnetization modes we consider a free particle with demagnetization factors N_{\parallel} and N_{\perp} , parallel and perpendicular to the c-axis. In this case the stray field terms are given by

$$H_d = 0, H_{s,x} = - N_{\perp} M_s \sin \phi, H_{s,z} = - N_{\parallel} M_s \cos \phi. \quad (3.1)$$

The nucleation fields are obtained from the linearized micromagnetic equations taking care of the special conditions of the magnetization modes:

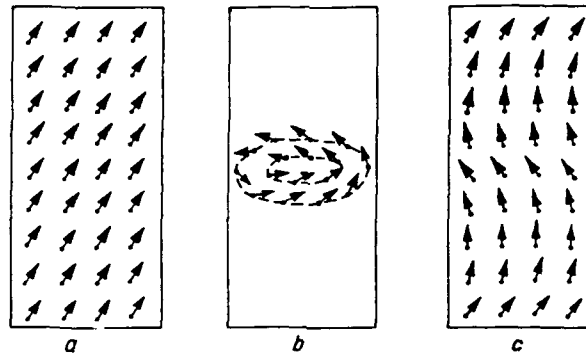


Fig. 3. Review of the main nucleation modes. a) uniform rotation, b) curling, c) buckling.

1. Uniform rotation

The equilibrium condition for vanishing exchange energy and an applied field antiparallel to \underline{M}_s writes ($\phi_A = 0$, $H_d = 0$):

$$d\phi_t'/d\phi = \left[(2K_1 + (N_\perp - N_\parallel) M_s^2) \cos \phi + 2(2K_2 \sin^2 \phi + 3K_3 \sin^4 \phi) \cos \phi - H_{\text{ext}} M_s \right] \sin \phi = 0. \quad (3.2)$$

Eq. (3.2) has a trivial solution $\phi = 0$ for $H_{\text{ext}} < H_N$, i.e., the magnetic state does not change, and a nontrivial solution obtained by putting the bracket term = 0 for $\phi \rightarrow 0$:

$$H_N = \frac{2K_1}{M_s} - M_s (N_\parallel - N_\perp) = \frac{2(K_1 + K_d)}{M_s} \quad (3.3)$$

with

$$K_d = \frac{1}{2} M_s^2 (N_\perp - N_\parallel). \quad (3.4)$$

At $H_{\text{ext}} = H_N$ the magnetization starts to deviate from the c-axis. The type of further rotation depends on the second derivative. For $d^2\phi_t'/d\phi^2 < 0$, which holds for $K_1 + K_d > 4K_2$, the magnetization rotates spontaneously into the opposite direction of the c-axis. For $d^2\phi_t'/d\phi^2 > 0$ which holds for $K_1 + K_d < 4K_2$, the magnetization rotates reversibly out of the c-axis and the instability occurs at an angle of (Kronmüller 1985, Herzer et al. 1986)

$$\sin^2 \phi_N = - \frac{1}{6} (K_1 + K_d - 4K_2) / K_2; \quad (3.5)$$

and an instability field of

$$H_N^I = \frac{4}{3 \cdot \sqrt{6}} \frac{K_2}{M_s} \left[2 + \frac{K_1 + K_d}{K_2} \right]^{3/2} \quad (3.6)$$

The two types of hysteresis loops for $H_N = H_N^I$ and $H_N > H_N^I$ are shown in Fig. 4. A further modification of the hysteresis loop takes place if the external field is applied under an angle ψ_0 with respect to the negative c-axis. In this case \underline{M}_s rotates reversibly up to an angle (see Fig. 5)

$$\operatorname{tg} \phi_N = (\operatorname{tg} \psi_0)^{1/3}, \quad (3.7)$$

where \underline{M}_s spontaneously rotates into the opposite direction. The instability field of this process is approximately given by Stoner and Wohlfarth (1948) and Kronmüller et al. (1987):

$$H_N^I(\psi_0) = \frac{2(K_1 + K_d)}{M_s} \frac{1}{[(\cos \psi_0)^{2/3} + (\sin \psi_0)^{2/3}]^{3/2}} \times$$

$$\times \left[1 + \frac{2K_2}{K_1 + K_d} \frac{(\operatorname{tg} \psi_0)^{2/3}}{1 + (\operatorname{tg} \psi_0)^{2/3}} \right]. \quad (3.8)$$

The minimum instability field is obtained for $\psi_0 = \pi/4$ and is given by

$$H_N^{\min} \left(\frac{\pi}{4} \right) = \frac{K_1 + K_d + K_2}{M_s}. \quad (3.9)$$

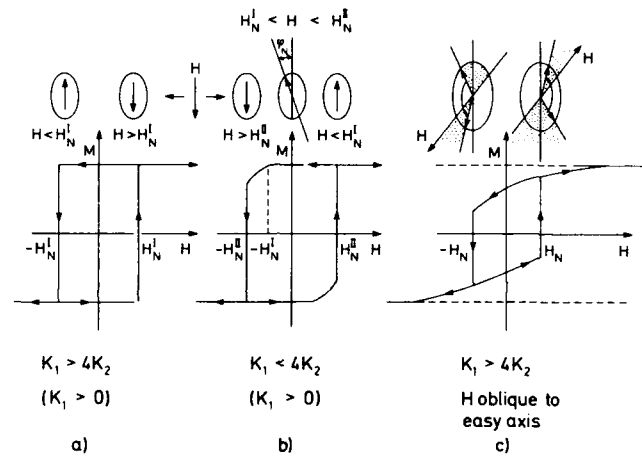


Fig. 4. Hysteresis loops in uniaxial crystals for $K_1 \gtrless 4K_2$ and for oblique applied magnetic fields.

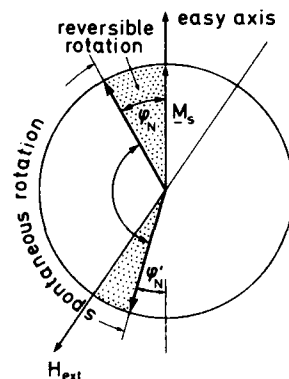


Fig. 5. Orientation of \underline{M}_s shortly before and after the spontaneous rotation under an oblique applied field.

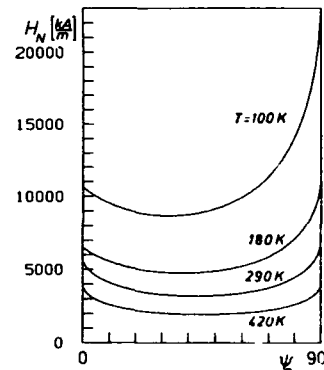


Fig. 6. Angular dependence of the nucleation field for $\text{Fe}_{14}\text{Nd}_2\text{B}$ for different temperatures taking care of K_1 , K_2 and K_3 , $K_d = 0$.

Here it should be noted that eq. (3.8) and (3.9) are approximate expressions which are exact in the case where $K_2 = 0$ (see Stoner and Wohlfarth 1948). An explicit and precise expression for H_N^{min} has been derived by Martinek and Kronmüller (1990). Fig. 6 shows the angular dependence of H_N^1 as determined for $\text{Fe}_{14}\text{N}_{11}\text{B}$ at different temperatures.

2. Inhomogeneous Rotation of the Curling Mode

The curling mode is characterized by vanishing stray fields $H_d = 0$, $H_s = 0$, i.e., volume charges, $\text{div } \underline{M}_s$, as well as surface charges, $\underline{M}_s \cdot \underline{n}$, both vanish. The nucleation field follows from the linearized second order differential equation

$$2A \left[\frac{d^2 \phi}{dr^2} + \frac{1}{r} \frac{d\phi}{dr} - \frac{1}{r^2} \phi \right] - (2K_1 - H_{\text{ext}} M_s) \phi = 0. \quad (3.10)$$

For a cylindrical particle the solution corresponds to the Bessel function of order one, and the nucleation field follows from the boundary condition, $d\phi/dr = 0$, at the particle surface $r = D/2$, which gives (Aharoni 1962)

$$H_N = \frac{2K_1}{M_s} + \frac{2A}{M_s} \left[\frac{3.68}{D} \right]^2. \quad (3.11)$$

3. The buckling mode

The buckling mode combines the homogeneous rotation with curling. This leads to a periodic distribution of alternating surface and volume charges which reduces the stray field in comparison to the homogeneous mode. At small diameters this mode has the same nucleation field as the homogeneous mode and at larger diameters H_N decreases according to a $1/D^{2/3}$ -law, i.e., somewhat slower than for the curling mode which decreases according to a $1/D^2$ -law.

4. SUPERPARAMAGNETIC PARTICLES

In small particles, in the nanometer range, \underline{M}_s fluctuates between the two opposite easy directions due to thermal excitations. The average lifetime, τ , during which \underline{M}_s according to Néel (1949a, 1949b) is oriented in one direction is given by

$$\tau = \tau_0 e^{-K_{\text{eff}} V / kT}, \quad (4.1)$$

where τ_0^{-1} denotes the magnetic resonance frequency, γH_N , (γ = gyromagnetic ratio) of the particle of volume V . The energy barrier, $K_{\text{eff}} V$, to be overcome by thermal excitation corresponds to the maximum anisotropy energy of the heavy direction. For uniaxial material we have

$$K_{\text{eff}} = K_1 + K_2 + K_3 + \frac{1}{2} (N_{\perp} - N_{\parallel}) M_s^2. \quad (4.2)$$

The lifetime τ depends sensitively on the volume and the diameter of the particle. For $K_{\text{eff}} = 10^6 \text{ J/m}^3$, $T = 300 \text{ K}$ we obtain 0.1 sec. for a spherical particle of $D \sim 2 \text{ nm}$, whereas for $D \sim 2.8 \text{ nm}$ τ increases to 10^6 sec . Obviously there exists a very narrow range of diameters where the stability of the particles is lost. In the case of hard magnetic materials with $K_{\text{eff}} > 10^6 \text{ J/m}^3$ τ becomes larger than 10 years for particles with diameters $> 3 \text{ nm}$. This diameter therefore must be considered as the lower size limit for obtaining thermally stable permanent magnets.

Finally, it should be noted that in perturbed regions of lower anisotropies the reversion of \underline{M}_s will be facilitated due to the reduction of the energy barrier.

5. CRITICAL DIAMETER FOR SINGLE DOMAINS

In multidomain particles the magnetization process is governed by domain displacements. If no pinning forces act on the domain walls the saturation field of a particle may be written as

$$H_{\text{sat}} = N_g M_s, \quad (5.1)$$

where N_g corresponds to an effective demagnetization factor describing the total demagnetization field acting on a grain. If each grain of polyhedral shape is ideally surrounded by its neighbouring grains which possess arbitrary easy directions, N_g approximately is given by $4\pi/3$. In the case where the easy directions occupy only angles between 0 and π the inverse Lorentzfield of the polyhedral grain is partially compensated by the demagnetizing field of the neighbouring grains, giving $N_g \sim 2\pi/3$. Accordingly, the technical saturation field is expected to be given by

$$H_{\text{sat}} = \frac{4\pi}{3} \alpha_g M_s \quad (5.2)$$

with $0.5 < \alpha_g < 1$.

The existence of the internal stray fields also has some influence on the critical size, D_{crit} , for the transition between a single and a multidomain state. Comparing the magnetic free energies of a single and a two domain particle the critical diameter is found to be

$$D_{\text{crit}} = \frac{9}{2\pi(2\alpha_g - 1)} \frac{\gamma_B}{M_s^2}, \quad (5.3)$$

where γ_B denotes the specific wall energy, $\gamma_B = 4 \sqrt{AK_1}$, and the effective demagnetization factor of the twodomain particle has been put equal to $2\pi/3$. It is of interest to note that D_{crit} may become rather large if α_g approaches $1/2$. In fact such an increase of D_{crit} has been observed by Grönefeld (1990) in $\text{Fe}_{14}\text{Nd}_2\text{B}$ where we expect $D_{\text{crit}} = 200$ nm for $\alpha_g = 1$. Actually, Grönefeld has determined a critical diameter of ~ 380 nm, i.e., twice as large as expected for free particles. Accordingly, in grains which are embedded within an ensemble of grains D_{crit} is increased which has to be attributed to $\alpha_g = 0.75$, i.e., $N_g = \pi$. Here it should be noted that the formation of the multidomain structure requires that the stray field overcompensates the crystal field (see eq. (2.17)). In hard magnetic materials, however, this situation never holds, and consequently once a grain is saturated the formation of reversed domains should not take place. In contrast to this prediction, however, domain formation is observed even at positive applied magnetic fields. This phenomenon, known as Brown's paradoxon (1945), is due to the existence of magnetically soft regions where the local nucleation field is significantly reduced. The existence of defect structures therefore plays a twofold role: Easy formation of domain patterns and deterioration of hard magnetic properties.

6. NUCLEATION IN INHOMOGENEOUS REGIONS

The strong deviation of the coercive fields of technical permanent magnets from the theoretical nucleation fields is, in general, attributed to microstructural inhomogeneities of the grain surfaces (Durst and Kronmüller 1988, Sagawa and Hirose 1988 and Livingston 1987). Three types of such deteriorating microstructures have been treated so far: Regions of reduced anisotropy, misaligned grains and the effect of enhanced stray fields at sharp edges near nonmagnetic precipitations. For a quantitative treatment of these problems we have to solve the linearized micromagnetic equations with space dependent material parameters and stray fields. The effect of reduced anisotropies in planar regions and of stray fields at edges may be described by the modified nucleation field (Kronmüller et al. 1988a, b; Kronmüller 1987)

$$H_N = \frac{2K_1}{M_s} \alpha_K^{nuc} \alpha_\psi - N_{eff} \cdot M_s, \quad (6.1)$$

where the three microstructural parameters α_K , α_ψ and N_{eff} take into account the anisotropy deficiencies at the surface (α_K) the misalignment of grains (α_ψ) and the enhanced stray fields at edges (N_{eff}). All three parameters have been derived quantitatively for special models.

1. The softening parameter α_K^{nuc} has been derived for a planar inhomogeneity of width r_0 and a vanishing anisotropy in the centre of the inhomogeneity. For narrow perturbed regions, $2\pi r_0 > \delta_B$, the nucleation field is given by (Kronmüller 1987):

$$H_N = \frac{2K_1}{M_s} \frac{\delta_B}{\pi r_0} \alpha_\psi + H_d - 2\pi M_s, \quad (6.2)$$

where δ_B corresponds to the wall width of the perfect material, $\delta_B = \pi \sqrt{A/(K_1 + K_2)} = \pi \delta_0$.

2. The misalignment parameter α_ψ is obtained from (3.8) as the ratio (Kronmüller et al. 1987)

$$\alpha_\psi = \frac{H'_N(\psi)}{H'_N(0)} = \frac{1}{[(\cos \psi)^{2/3} + (\sin \psi)^{2/3}]^{3/2}} \times \left\{ 1 + \frac{2K_2}{K_1 + K_d} \frac{(\tan \psi)^{2/3}}{1 + (\tan \psi)^{2/3}} \right\}. \quad (6.3)$$

The minimum value of α_ψ is obtained for $\psi_0 = \pi/4$

$$\alpha_\psi^{\min} = \frac{1}{2} \frac{K_1 + K_2 + K_d}{K_1 + K_d}. \quad (6.4)$$

Inserting (6.4) into (6.2) gives for the minimum nucleation field with $K_d = 0$

$$H_N^{\min} = \frac{1}{4M_s} \frac{\gamma_B^I}{\delta_0} - N_{eff} M_s, \quad (6.5)$$

Here we have introduced a fictitious wall energy $\gamma_B^I = 4 \sqrt{A(K_1 + K_2)}$, and an effective demagnetization factor $N_{eff} = (2\pi M_s - H_d)/M_s$. Since eq. (6.5) has a similar form as the relations derived for the pinning of domain walls at planar inhomogeneities it has been suggested (Livingston 1987) that (6.5) and the corresponding expression for domain wall pinning have the same origin. Here it should be noted that domain wall pinning always requires the formation of domain walls by a nucleation mechanism. However, it has been shown in detail (Kronmüller et al. 1988) that the pinning coercive field in high quality sintered magnets is always smaller than the nucleation field and consequently the magnetic hardening is governed by the nucleation field.

3. The effective demagnetization factor N_{eff} has been determined for a prisma of quadratic cross-section as a function of the edge length L (Grönefeld and Kronmüller 1989, Schmidts and Kronmüller 1990). At the corners of the prisma the magnetic stray field has a logarithmic singularity inducing an inhomogeneous distribution of M_s . Fig. 7 shows the spin distribution in the

upper right corner of the square for three different states: $H_{\text{ext}} = 0$, the undercritical state just before reversion of \underline{M}_s and the magnetic state just after reversion of \underline{M}_s . It is an important result of these selfconsistent numerical solutions of the micromagnetic equations that the reversion of \underline{M}_s does not take place locally with a successive reversible expansion of the nucleus. In spite of the strongly inhomogeneous magnetic state there seems to exist only one unique nucleation field which is shown in Fig. 8 as a function of the edge length L of the prisma for $\text{Fe}_{14}\text{Nd}_2\text{B}$. The broken line corresponds to the crystal field $2K_1/M_s$ and the full horizontal line to $2K_1/M_s + 2\pi M_s$. Fig. 9 shows the numerically determined $N_{\text{eff}}/4\pi$ which were obtained by comparing the ideal crystal field, $2K_1/M_s$, with the actual nucleation field of Fig. 8 (Schmidts and Kronmüller 1990). In Fig. 8 we have included experimental results showing that the H_c values lie throughout by a factor 2-3 below the theoretical prediction. It is an interesting result of these calculations that in particles with edge lengths < 20 nm the demagnetization field plays a minor role.

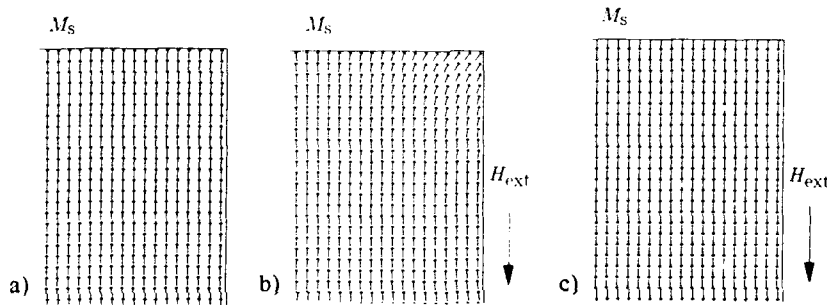


Fig. 7. Distribution of magnetization in the upper right corner of a parallelepiped of quadratic cross-section ($\text{Fe}_{14}\text{Nd}_2\text{B}$), a) $H = 0$, b) Undercritical state, $H = 54.6$ kOe, c) Reversed magnetic state, $H = 54.7$ kOe.

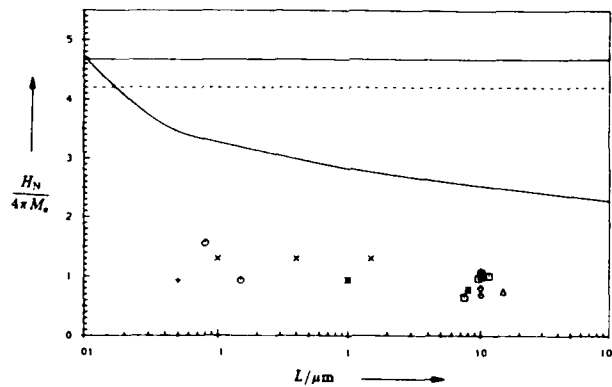


Fig. 8. Nucleation field of parallelepipeds as a function of edge length L (—) $2K_1/M_s$ (---) $2K_1/M_s + 2\pi M_s$ (horizontal line). Experimental results: (+) Croat et al. (1984), (x) Grönefeld and Kronmüller (1988), (O) Hadji-panayis and Kim (1988), (□) Durst and Kronmüller (1987), (Δ) Sagawa et al. (1984), (◇) Martinek (1988).

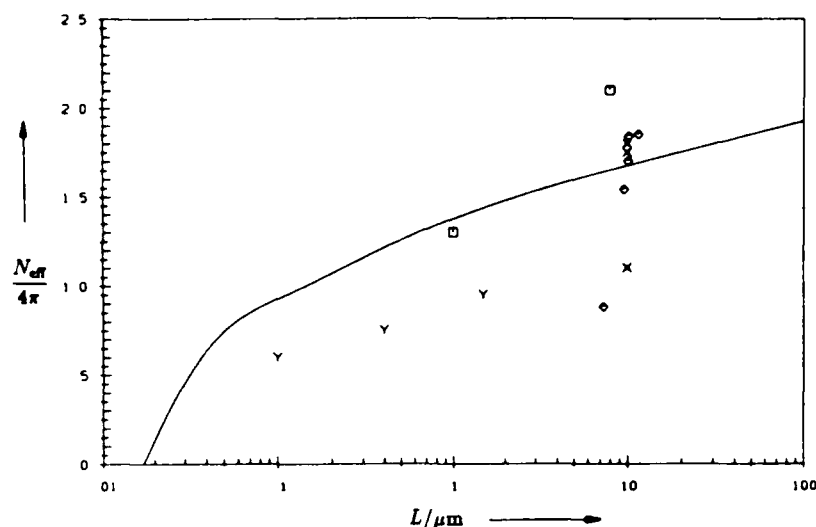


Fig. 9. Effective demagnetization factors of parallelepipeds as a function of edge length L . Experimental results: (Y) Grönefeld and Kronmüller (1988), (x) Martinek (1988), (□) Durst and Kronmüller (1987), (◇) Kiss et al. (1989). $L < 5 \mu\text{m}$ rapidly quenched material, $L > 5 \mu\text{m}$ sintered magnets.

7. DISCUSSION

7.1 Magnetization Processes in Sintered Magnets

Presently, it is generally accepted that in sintered permanent magnets the magnetic hardening is governed by the nucleation mechanism. In particular, this situation holds for Ba-Sr-ferrites, Co_5Sm and $\text{Fe}_{14}\text{Nd}_2\text{B}$, whereas in precipitation hardened $\text{Co}_{17}\text{Sm}_2$ -type magnets the pinning of domain walls at the phase boundaries is predominant. The determination of the dominant hardening mechanism in general is not possible directly because as demonstrated by Fig. 2 the discrepancy between the technically achieved H_c -values and the theoretical values is quite appreciable. Three different experiments can be performed to distinguish between nucleation and pinning hardening:

1. Measurements of the Coercive Field of Minor Hysteresis Loops as a Function of the Maximum Applied Fields

In the nucleation hardened magnets as Co_5Sm and $\text{Fe}_{14}\text{Nd}_2\text{B}$ where the domain walls are not pinned the magnetic field required to saturate the coercive field is a factor of 3-4 smaller than the coercive field itself (Fig. 10). the saturation field for H_c corresponds just to the demagnetizing field of the individual grains, $H_{\text{sat}} = N_g \cdot M_s$. The measured saturation fields of 5000 - 7000 Oe are compatible with $N_g \sim 4\pi/3$ (see chapter 5).

In pinning magnets the magnetic field required to saturate H_c corresponds just to H_c as demonstrated by Fig. 11 for a processed $\text{Sm}(\text{Co}, \text{Cu}, \text{Fe}, \text{Zr})_{7,6}$ magnet (Durst et al. 1988).

2. Temperature Dependence of the Coercive Field

The temperature dependence of H_c is a rather complex property because it is not only determined by the intrinsic material parameters (K_1 , M_s) but also by the microstructural parameters α_K^{nuc} , α_ψ and N_{eff} . The temperature dependence of H_c of several FeNdB-based magnets has been successfully

analysed using eq. (6.1) with $\alpha_\psi = \alpha_\psi^{\min}$ (eq. (6.4)). For determining α_K^{nuc} , α_ψ and N_{eff} the following plot has been applied

$$H_c/M_s \text{ vs } (2K_1/M_s^2) \alpha_\psi^{\min} \alpha_K^{nuc} \quad (7.1)$$

The left hand side presents the experimental result and the right hand side corresponds to the theoretical result containing only r_0 as a fit parameter. From the straight lines obtained for the above plot for optimized r_0 values in addition N_{eff} can be determined. Fig. 12 shows the H_c/M_s plot over a wide temperature range for three types of magnets. In all three cases the width $2r_0$ of the magnetically softened surface region was found to range between 8-30 Å. The numerical values for N_{eff} vary between 5.6π and 7.2π . Comparing these values with our results presented in Fig. 9 for N_{eff} of sharp edges, it is evident that these experimental results are compatible with the model developed in chapter 6.

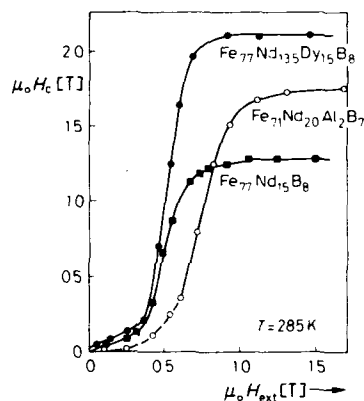


Fig. 10. Field dependence of $H_c(H_{ext}^{max})$ of minor hysteresis loops of nucleation hardened permanent magnets.

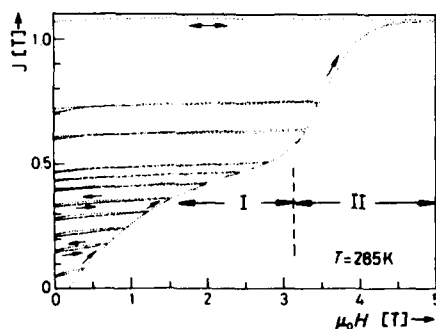


Fig. 11. Minor hysteresis loops of processed $\text{Sm}(\text{Co}, \text{Cu}, \text{Fe}, \text{Zr})_{7.6}$ measured at $T = 285 \text{ K}$ (Durst et al. (1988)).

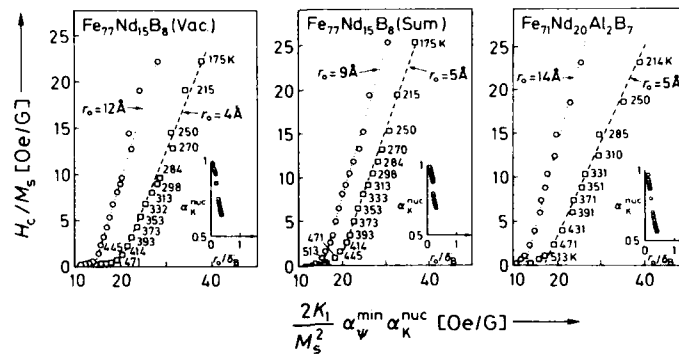


Fig. 12. Test of nucleation mechanism by plotting H_c/M_s vs. $(2K_1/M_s^2)\alpha_K^{\min}\alpha_K^{\text{nuc}}$ for magnets of Vacuumschmelze, Sumitomo and the Max-Planck-Institut.

3. Domain Patterns

Studies of domain patterns by means of the magneto-optical Kerreffect clearly show that in the thermally demagnetized state nearly each grain develops a domain structure (Fig. 13). Applying a magnetic field technical saturation is observed at $H_{\text{sat}} \sim (4\pi/3)M_s$. The demagnetizing behaviour of each grain, however, has been found to depend sensitively on a critical field $H_K < H_{\text{sat}}$. For applied fields $H_{\text{ext}} < H_K$ some small magnetic nuclei remain conserved within edges of grains either by domain wall pinning (Givord et al. 1986) or by strong demagnetizing stray fields. As a consequence, demagnetization of such grains takes place at positive applied fields as demonstrated by Fig. 13c. If the applied field exceeds H_K the grain remains a single domain particle down to the negative nucleation field H_c which is governed by surface deterioration, misalignment and local stray fields. Fig. 14 gives a review over this different behaviour of a grain showing that the critical field H_K in addition to H_c represents a further characteristic magnetic property of the grains.

7.2 Rapidly Quenched Magnets

Since the first discovery of rapidly quenched $\text{Fe}_{14}\text{Nd}_2\text{B}$ magnets (Croat 1984, Lee et al. 1985) it has been a matter of controversy whether the magnetic hardening in these systems occurs by a pinning or a nucleation mechanism (Pinkerton and van Wingerden 1986, Mishra and Lee 1986, Hadjipanayis and Kim 1988, Hadjipanayis and Lawless 1985). The observation of domain patterns in rapidly quenched material by transmission electron microscopy (Mishra 1986) has been taken as a proof that we deal with a domain wall pinning mechanism. On the other hand, Durst and Kronmüller (1987) have shown that the temperature dependence of H_c obeys relation (7.1) as the sintered magnets where the nucleation mechanism holds. Plotting H_c/M_s vs $(2K_1/M_s^2)\alpha_K^{\min}$ leads to a linear relation with the microstructural parameters $\alpha_K \sim 0.8$ and $N_{\text{eff}} \sim 3\pi$ (Grönfeld 1990). This result may be taken as a support of the nucleation model. For a further analysis of the nucleation behaviour of rapidly quenched magnets the initial magnetization curves and hysteresis loops have been studied for different grain sizes. Fig. 15 shows initial magnetization curves of $\text{Fe}_{76}\text{Nd}_{15}\text{B}_9$ -ribbons for different substrate velocities. For the quenching velocities of 5, 14.1 and 21.6 m/s the average grain diameters were 0.1 μm , 400 nm and 100 nm. Therefore, in the low velocity material we are dealing nearly exclusively

with multidomain grains whereas the high velocity material contains mostly single domain particles. Accordingly, the magnetization curves are composed of two regions: A low field region below 400 kA/m where the magnetization occurs by domain wall displacements and a high field region around 2000 kA/m where the magnetization takes place by the reversion of M_s within the grains by a nucleation mechanism.

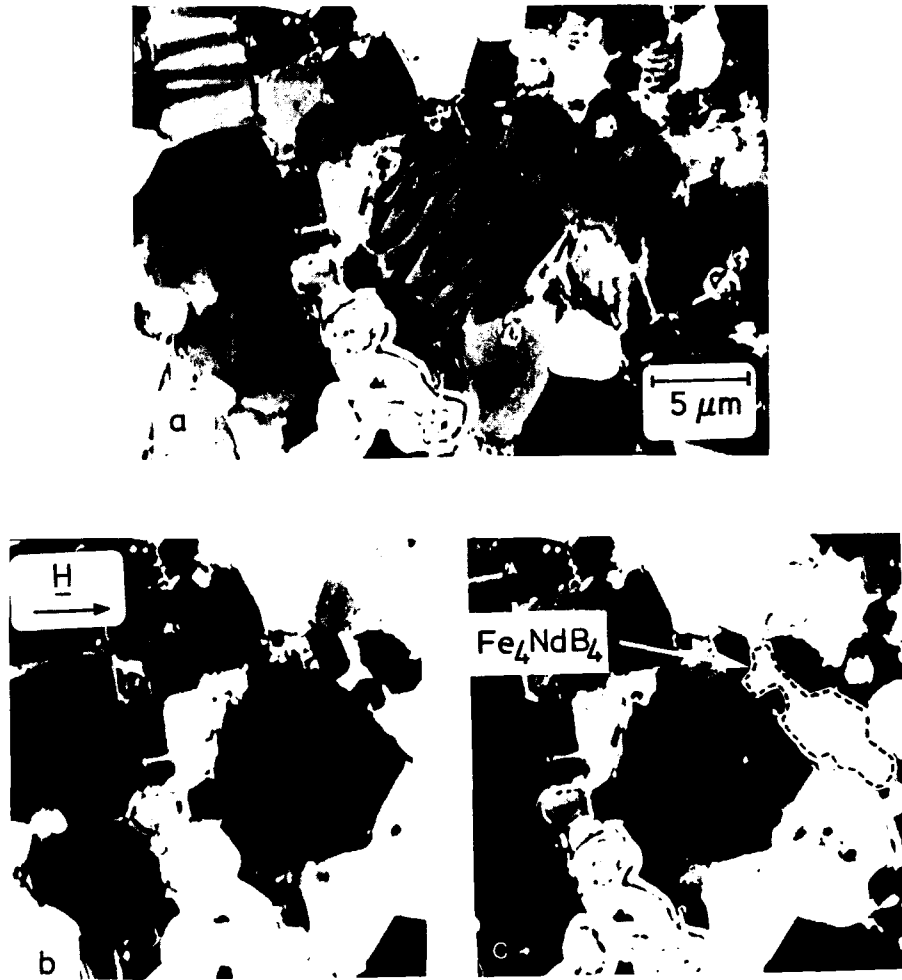


Fig. 13. Sequence of domain patterns in an aligned $\text{Fe}_{77}\text{Nd}_{16}\text{B}_8$ permanent magnet and varying magnetic fields. a) $\mu_0 H_{\text{ext}} = 0$ Tesla (thermally demagnetized state) b) $\mu_0 H_{\text{ext}} = 1.4$ Tesla (technically saturated state), c) $\mu_0 H_{\text{ext}} = 0.4$ Tesla (nucleation of reversed domains).

With decreasing grain diameter the second region of the magnetization curve grows at the expense of the low field region. Once a material is saturated the coercive field turns out to be nearly independent of the distribution function of grain diameters because after magnetic saturation the grains behave as single domain grains and reversion of M_s then requires the nucleation field as demonstrated by Fig. 16. For a further confirmation of the above model a thermo-magnetic experiment has been performed. After thermal demagnetization the specimen was cooled down to 77 K. Due to the increase of the wall energy at lower temperature the critical diameter, D_{crit} , for single domain particles increases (eq. (5.3)) and consequently some of the

grains transform from multidomain into single domain particles. Accordingly, the high field magnetization region grows as shown in Fig. 17 for the so-called MQ III material and the $\text{Fe}_{76}\text{Nd}_{15}\text{B}_9$ -ribbon quenched with $v = 14.1$ m/s. Fig. 18 shows the magnetic polarization as measured at RT at $H = 700$ kA/m for an MQ III magnet after cooling down to a temperature T_0 below RT. It turns out that the main decrease of the magnetic polarization takes place at the so-called spin reorientation temperature, $T_s = 135$ K, i.e., where M_s starts to lie on the easy cone. This leads to a reduction of the magnetic stray fields acting between the grains (decrease of α_g in eq. (5.3)) and therefore to a decrease of the magnetization in the low field region.

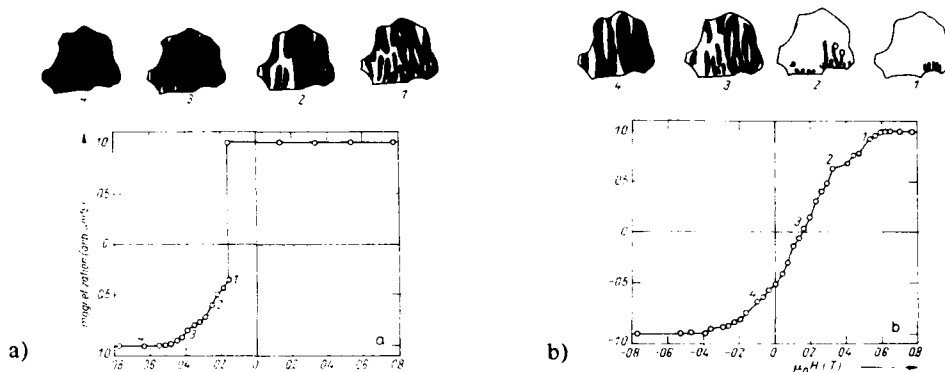


Fig. 14. Demagnetization curves of FeNdB and the development of domain patterns after different applied external fields: a) $H_{\text{ext}} > H_K$, b) $H_{\text{ext}} < H_K$ (Maki et al. (1989)).

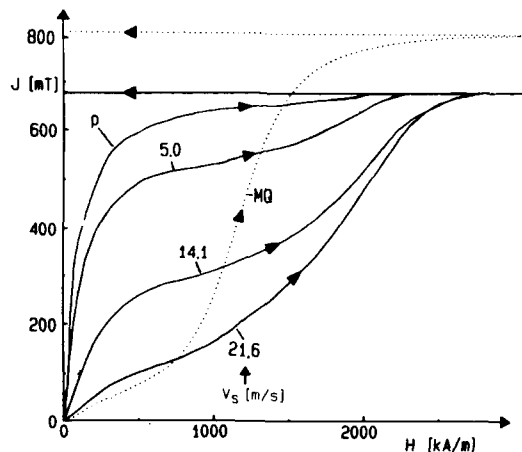


Fig. 15. Initial magnetization curves of $\text{Fe}_{76}\text{Nd}_{15}\text{B}_9$ -ribbons quenched with different substrate velocities (p = ribbon produced with polished wheel side with $v_s = 5$ m/s). The magnetization due to reversible rotations of the recoil curve has been subtracted.

The arguments presented so far clearly show that in rapidly quenched materials the nucleation model gives a far more consistent interpretation of the magnetic properties than the domain wall pinning model. This latter model also runs into principle difficulties to give an explanation for the existence of domain walls running from one grain to the other if these grains are magnetically decoupled by a

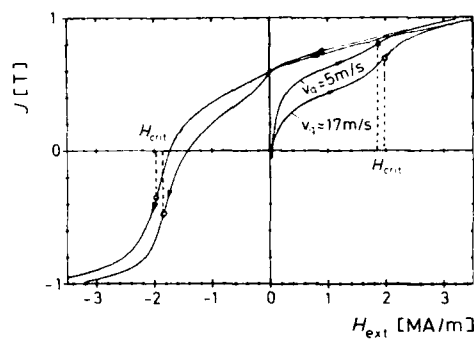


Fig. 16. Hysteresis loops in the first-third quadrant showing that the saturation field is comparable to the coercive field.

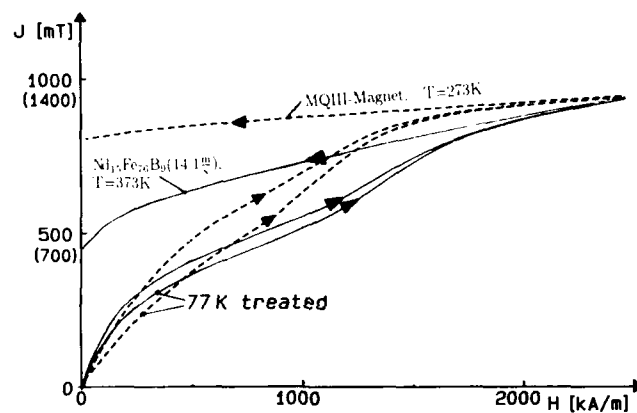


Fig. 17. Initial magnetization curves measured immediately after thermal demagnetization and after cooling the sample to 77 K. Magnetization curves measured at 100°C and for MQIII at 0°C. Scale for MQIII in brackets.

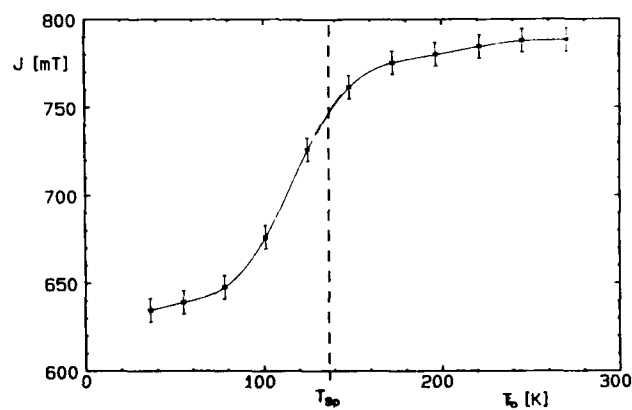


Fig. 18. Magnetic polarisation of an MQIII magnet measured for 273 K at 700 kA/m as a function of cooling temperature T_0 . T_{sp} = spin rotation temperature.

nonmagnetic Nd-rich phase. The existence of "domains" therefore can only be considered as a consequence of the dipolar coupling between the grains which prefer a parallel alignment of the magnetization of neighbouring grains. The macroscopic stray field then is responsible for a domain type long-range arrangement of the single domain particles.

8. ACKNOWLEDGEMENTS

The author acknowledges gratefully many helpful discussions with Drs. A. Forkl, M. Grönefeld, Dipl.-Phys. G. Martinek and H. Schmidts.

9. REFERENCES

- Aharoni, A., 1962, Rev. Mod. Phys., 34:227.
 Brown, W. F. Jr., 1940, Phys. Rev., 58:736, 1941, Phys. Rev., 60:139.
 Brown, W. F. Jr., 1945, Rev. Mod. Phys., 17:15.
 Chikazumi, S., 1964, Physics of Magnetism, John Wiley, New York, p. 260.
 Croat, J. J., Herbst, J. F., Lee, R. W., and Pinkerton, F. E., 1984, J. Appl. Phys., 55:2078.
 Durst, K. D., and Kronmüller, H., 1987, J. Magn. Magn. Mat., 68:63.
 Durst, K. D., Kronmüller, H., and Ervens, W., 1988, phys. stat. sol. (a), 108:403; ibid. 705.
 Givord, D., Tenand, P., and Viadieu, T., 1986, J. Appl. Phys., 60:3263.
 Grönefeld, M., and Kronmüller, H., 1989, J. Magn. Magn. Mat., 80:223.
 Grönefeld, M., and Kronmüller, H., 1990, J. Magn. Magn. Mat., to be published.
 Grönefeld, M., 1990, Dr. rer. nat. Thesis, University Stuttgart.
 Hadjipanayis, G. C., 1982, in: J. Fidler (ed.), Proc. 6th Intern. Workshop on RE-Co Permanent Magnets, Techn. University Vienna, p. 609.
 Hadjipanayis, G. C., Hazelton, R. C., and Lawless, K. R., 1985, Appl. Phys. Lett., 43:797.
 Hadjipanayis, G. C., and Lawless, K. R., 1985, J. Appl. Phys., 57:4097.
 Hadjipanayis, G. C., and Kim, A., 1988, J. Appl. Phys., 63:3310.
 Herzer, G., Fernengel, W., and Adler, E., 1986, J. Magn. Magn. Mat., 58:48.
 Kittel, C., 1949, Rev. Mod. Phys., 21:541.
 Kneller, E., 1962, Ferromagnetismus, Springer-Verlag, Berlin-Göttingen-Heidelberg.
 Kronmüller, H., 1966, "Magnetisierungskurve der Ferromagnetika" in A. Seeger (ed.) Moderne Probleme der Metallphysik, Springer-Verlag, Berlin-Heidelberg-New York, pp. 24-156.
 Kronmüller, H., 1972, Intern. J. of Nondestructive Testing, 3:315.
 Kronmüller, H., 1978, J. Magn. Magn. Mat., 7:341.
 Kronmüller, H., 1985, phys. stat. sol. (b), 130:197; 1987, 144:385.
 Kronmüller, H., Durst, K. D., and Martinek, G., 1987, J. Magn. Magn. Mat., 69:149.
 Kronmüller, H., Durst, K. D., and Sagawa, M., 1988a, J. Magn. Magn. Mat., 74:291.
 Kronmüller, H., Durst, K. D., Hock, S., and Martinek, G., 1988b, J. Physique (Paris), 49:C8-623.
 Landau, L. D. and Lifshitz, E. M., 1935, Physik. Z., Sowjetunion, 8:153.
 Lee, R. W., Brewer, E. G., and Schaffel, N. A., 1985, IEEE Trans. Mag., 21:1958.
 Livingston, J. D., 1987, IEEE Trans. Mag., 23:2109.
 Mishra, R. K., 1986, J. Magn. Magn. Mat., 54-57:450.
 Mishra, R. K., and Lee, R. W., 1986, Appl. Phys. Lett., 48:733.
 Martinek, G., and Kronmüller, H., 1990, J. Magn. Magn. Mat., to be published.
 Néel, L., 1949a, Compt. rend. (Paris), 228:604.
 Néel, L., 1949b, Ann. geophysics, 5:99.
 Néel, L., 1950, J. Phys. Rad., 11:49.
 Maki, K., Forkl, A., Dragon, T., and Kronmüller, H., 1989, phys. stat. sol. (a), 116:803.
 Pinkerton, F. E., and van Wingerden, D. J., 1986, J. Appl. Phys., 60:3685.
 Ray, A. E., 1984, IEEE Trans. Magn., 20:1614; J. Appl. Phys., 55:2094.

- Sagawa, M., Fujijamara, S., Tagawa, M., Yamamoto, H., and Matsuura, Y., J. Appl. Phys., 49:2083.
- Sagawa, M., and Hirose, S., 1988, J. Physique, 49:C8-617.
- Schmidt, H. F., and Kronmüller, H., 1990, J. Magn. Magn. Mat., to be published.
- Stoner, E. C., and Wohlfarth, E. P., 1948, Phil. Trans. Roy. Soc., (London), 240:599.
- Strnat, K. J., 1978, J. Magn. Magn. Mat., 1978, 7:351.

MICROMAGNETIC APPROACH TO MAGNETIC HYSTERESIS

R. H. Victora

Mass Memory - Research Laboratories
Eastman Kodak Company
Rochester, NY 14650-2017

Two types of calculations for hysteretic phenomena are described. The first uses a detailed treatment of the relevant interactions, applied to samples of known microstructure, to predict hysteresis loops in unprecedented agreement with experiment. The second deduces the time dependence of switching fields in the region of weak thermal fluctuations.

I. INTRODUCTION

Hysteresis is one of the primary manifestations of ferromagnetism, and the consequent experimental and theoretical attention has provided considerable qualitative understanding. Nevertheless, many of the proposed explanations are incomplete or contradictory, and it is clear that the development of quantitative theories is of crucial importance for further progress in this field. However, quantitatively accurate predictions from measurable microscopic input are quite difficult for a variety of experimental and theoretical reasons.¹ Accurate characterization of grain boundaries, segregated areas, dislocations, and other irregularities is problematic and the results can vary widely from sample to sample. Many phenomena depend on microscopic nucleation or pinning effects in combination with macroscopic forces. Thermal fluctuations can lead to strong time and temperature dependences. Finally, the magnetostatic interactions and, to a lesser extent, quantum mechanical exchange, make this a many-body problem.

Despite these difficulties, several prominent advances have occurred. In 1948, Stoner and Wohlfarth² introduced a particulate theory that assumed coherent rotation of the particle magnetization and neglected interparticle interactions: The approach provided order-of-magnitude estimates for coercivities and is still frequently used to gain approximate understanding. The problem of incoherent rotations has been subsequently examined in an idealized form by several authors;³ interactions were successfully treated by Hughes⁴ in his calculations for CoP thin films. Thermal fluctuations were examined by Néel⁵ who introduced a simplified model in which the energy barrier is proportional to $(\Delta H)^2$ where ΔH equals the difference of the applied field and the nonthermally assisted switching field. These papers, while not achieving a demonstrated quantitative accuracy, have provided a solid foundation for further theoretical development.

Reported here are two recent calculations that use micromagnetic principles to make quantitative predictions for measurable macroscopic properties. In the first section, hysteresis loops for several thin films are predicted^{6,7}, using only microstructural properties as input, which demonstrate close agreement with experiment. The second section describes the derivation⁸ of a relationship between switching fields and measurement time; exponents are predicted for two phenomena that should be measurable. The paper ends with a short conclusion.

II. HYSTERESIS LOOPS IN WELL CHARACTERIZED THIN FILMS

In this section, attention will be focused on three thin films consisting of long columnar grains separated by substantial grain boundaries. Two of these films are composed of CoNi and possess crystalline anisotropy axes directed along the grain direction. In the third sample, composed of CoPt, the anisotropy axis points at an angle of 28° from the film plane with the in-plane projection randomly distributed from grain-to-grain. A summary of film properties is presented in Table 1; additional information regarding the film microstructures can be obtained in refs. 6, 7, and 9.

For calculational purposes the thin film was divided into cells that contain a number of complete grains. These cells were linked by periodic boundary conditions, and several sizes ranging from 3×3 to 12×10 grains were used. A variety of grain-boundary patterns, including one taken directly from an electron micrograph, were used; results were found to be insensitive to the precise pattern provided that the average grain size, inclination angle, and the proportion of grain boundary were correct. Each grain was then divided along its major axis into segments such that each segment was approximately cubic.

Magnetostatic interactions between all segments are included. For closely neighboring segments, the interaction tensor for each pair of segments is calculated by a finite-element integration.^{6,7} For more distant segments, the interaction is included through a mean field approximation.

The quantum-mechanical exchange parameters of Co and Ni can be calculated⁶ from spin wave dispersion data. Alloy values can be obtained by scaling the bulk results (see Table 1). It is found that the results of the calculations reported here are not overly sensitive to the precise value used. Quantum-mechanical exchange between grains is neglected owing to its expected small value.

The total anisotropy of the thin film may be calculated from torque magnetometry. However, the shape contribution to this due to demagnetization fields may also be calculated for each particular arrangement of grains. The difference is, of course, the crystalline anisotropy, which becomes an effective field in the calculations. The crystalline anisotropy for the CoNi samples is much smaller than the shape anisotropies; the CoPt sample shows the reverse situation (see Table 1).

The Landau-Lifshitz-Gilbert equations are believed to give an adequate description for the time development of the magnetic moment in the case of fixed magnitude.^{10,11} This requirement is fulfilled for the small exchange-coupled segments of the CoNi thin films: it is a useful approximation for the larger CoPt segments. Each segment is assigned a magnetization vector \vec{M} , which moves according to:

$$\frac{d\vec{M}}{dt} = \frac{\gamma}{1+\alpha^2} \vec{M} \times \vec{H} + \frac{\alpha\gamma}{1+\alpha^2} \vec{M} \times (\vec{M} \times \vec{H}) \quad (1)$$

Here, \vec{H} includes the applied magnetic field, the magnetostatic interaction fields, the anisotropy fields, and the exchange field. The gyromagnetic ratio γ is arbitrary for the nearly static phenomena described here. Calculations have been performed using various values of the damping parameter α . It is found that the results for the CoPt sample exhibit some dependence on the value of α : we therefore use the physically realistic value of 0.1. The CoNi samples do not exhibit this dependence; the calculations are therefore executed at the economic value of 1.0, which eliminates much of the precession of the moment. The temporal integration of eqn. 1 is conducted using a fourth-order Runge-Kutta scheme.¹²

Microscopic domain nucleation sites play a major role in magnetization reversal of many materials. Inclusion of these various sites, many of them of unknown nature would be quite difficult in a calculation of this scale. Instead, our treatment is based on the expectation that the nucleated domain can easily grow until it reaches a grain boundary or the magnetostatic shape effects of the sample become large. Thus, to simulate the effects of domain nucleation for the CoNi samples, a single segment within each grain is flipped along the

Table 1. Sample Characteristics

| Sample | I | II | III |
|---|-----------------------------------|-----------------------------------|-----------------------------------|
| Composition | Co ₈₀ Ni ₂₀ | Co ₈₀ Ni ₂₀ | Co ₇₃ Pt ₂₇ |
| Properties of film | | | |
| Saturation magnetization (emu/cm ³) | 660 | 575 | 840 |
| Magnetic fraction | 0.54 | 0.47 | 0.84 |
| Properties of grains | | | |
| Angle relative to normal (°) | 50 | 60 | 0 |
| Saturation magnetization (emu/cm ³) | 1220 | 1220 | 1000 |
| Average radius (Å) | 130 | 100 | 280 |
| Geometrical anisotropy (ergs/cm ³) | 4.7 x 10 ⁶ | 4.7 x 10 ⁶ | 3.1 x 10 ⁶ |
| Crystalline anisotropy (ergs/cm ³) | 0.5 x 10 ⁶ | 0.0 x 10 ⁶ | 4.0 x 10 ⁶ |
| Exchange parameter (ergs/cm ³) | 1.32 x 10 ⁻⁶ | 1.32 x 10 ⁻⁶ | 1.60 x 10 ⁻⁶ |
| Coercivities | | | |
| Experimental perpendicular (Oe) | 2100 | 1710 | 2800 |
| Theoretical perpendicular (Oe) | 2100 | 1700 | 2400 |
| Experimental longitudinal (Oe) | 1350 | 960 | 2200 |
| Theoretical longitudinal (Oe) | 1500 | 1100 | 2400 |

direction of the applied field and this reverse domain is allowed to grow or decay without further intervention. Once equilibrium has been reached and a new external field applied, the process is repeated. No provision for domain nucleation could be made in the CoPt calculations because the grain and segment sizes are too large.

Table 1 shows the theoretical and experimental values of the coercivity for both the longitudinal and perpendicular directions. The worst discrepancy occurs for the CoPt sample with an error of about 15%. The average error is approximately 7%. Calculations performed using the common noninteracting, coherent-rotation model of Stoner and Wohlfarth² produce coercive forces 2-4 times larger than experiment. Clearly, the theoretical approach described in this paper produces coercivities in excellent agreement with experiment for these materials.

This same level of agreement is found for the general hysteresis loop shape; in particular, theory predicts squarenesses, closure points, and energy products that typically match experiment to within 10%. Physically, it is found that CoNi longitudinal loops switch by domain nucleation and propagation and perpendicular loops switch by coherent rotation mechanisms within each grain. CoPt switching mechanisms tend to be more complicated; avalanche switching is common in the longitudinal loops. Complete hysteresis loops and additional details of the switching process may be found in the original references.^{6,7}

III. PREDICTED TIME DEPENDENCE OF THE SWITCHING FIELD

The preceding section demonstrated that rigorous theoretical predictions for hysteresis can be made for a sample that is well-characterized and in which detailed understanding of the thermally activated processes is not necessary. Frequently, the opposite is the case: for these situations, scaling relationships relating two or more physical variables can be very useful. This section will provide a derivation of such a relationship between measurement time and switching field in the case where the height of the energy barrier to thermal fluctuations is much greater than $k_B T$. This corresponds to the physically and technologically interesting case of measurement frequency much less than the attempt frequency and is the situation usually considered. It implies that to a high degree of accuracy, a Maxwell-Boltzmann distribution occurs in the neighborhood of the switching point.¹³ This means⁵ that the probability of switching is given by

$$P = A \exp(-\Delta E/k_B T) \quad (2)$$

Here, τ = measurement time, ΔE = energy barrier, and A is the attempt frequency, which is approximately 10^9 Hz. Actually, A depends on the applied field; however, in the conditions considered here ($\Delta E \gg k_B T$), this contribution to τ is extremely weak in comparison to the ΔE contribution and will be neglected.

We begin the derivation by considering the sample, consisting of numerous small areas of magnetization all interacting with each other both magnetostatically and through quantum-mechanical exchange, to be subject to an applied field H with the nearest high frequency (i.e., without thermal fluctuations) switching field labelled H_0 . We are interested in the limit where thermal fluctuations are weak relative to the magnetostatic effects determining the switching fields. This permits a Taylor expansion about the state at $H = H_0$ the applied field $\Delta H = H_0 - H$ and the numerous variables $\Delta\theta_i = \theta - \theta_0$ representing the magnetization degrees of freedom. The expansion is carried to third order. The first order terms, except for the ΔH dependence, are all equal to zero because the system is in a local minimum. The matrix of second derivatives is diagonalized to obtain the normal modes of the system. Henceforth, the problem shall be addressed in terms of these normal modes:

$$\Delta\beta_i = \sum_j A_{ij} \Delta\theta_j \quad (3)$$

Note that these normal modes do not usually represent the motion of a single grain's magnetization; typically, though, they will be localized.

The second derivative of the energy with respect to the normal mode (or modes) corresponding to $H = H_0$ will be zero. This is a consequence of the definition of a switching point: the point where a neighboring minimum and maximum meet. The assumption will be made that the third derivative with respect to the normal mode does not vanish. There are certain highly symmetric situations where this is not true; for example, the axially symmetric situation examined in the Néel model⁵ exhibits a third derivative equal to zero. However, the usual physical situation is not symmetric and the third derivative does exist. The same physical intuition also prompts us to ignore the possibility of accidental degeneracies and thus simplify the analysis by considering a single switching mode.

The energy expansion may now be written:

$$\begin{aligned} E = E_0 - \frac{\partial E}{\partial H} \Big|_0 \Delta H + \frac{1}{2} \sum_i \frac{\partial^2 E}{\partial \beta_i^2} \Big|_0 (\Delta\beta_i)^2 - \sum_i \frac{\partial^2 E}{\partial \beta_i \partial H} \Big|_0 (\Delta\beta_i)(\Delta H) \\ + \frac{1}{6} \sum_{i,j,k} \frac{\partial^3 E}{\partial \beta_i \partial \beta_j \partial \beta_k} \Big|_0 (\Delta\beta_i)(\Delta\beta_j)(\Delta\beta_k) - \frac{1}{2} \sum_{i,j} \frac{\partial^3 E}{\partial H \partial \beta_i \partial \beta_j} \Big|_0 (\Delta H)(\Delta\beta_i)(\Delta\beta_j) + O(\Delta H)^2 \end{aligned} \quad (4)$$

Here we have anticipated our answer and not listed the higher order contributions $(\Delta H)^2$. Determination of the various modes' contributions to the energy is accomplished by finding the extrema of eqn. 4 and solving for the $\Delta\beta_i$. It is found⁸ that the lowest order contribution is given by the switching mode. The values of this mode at the two neighboring extrema (local minimum and local saddle that the magnetization must cross to switch) is given by:

$$\Delta\beta_s = \pm \sqrt{2\Delta H \frac{\partial^2 E}{\partial \beta_s \partial H} \Big|_0 / \frac{\partial^3 E}{\partial \beta_s^3} \Big|_0} + O(\Delta H) \quad (5)$$

The height of the barrier is given by inserting the values of $\Delta\beta_s$ into eqn. 4 to yield:

$$\Delta E = (\Delta H)^{3/2} \sqrt{32 \left(\frac{\partial^2 E}{\partial \beta_s \partial H} \Big|_0 \right)^3 / \left(9 \frac{\partial^3 E}{\partial \beta_s^3} \Big|_0 \right)} \quad (6)$$

Thus one concludes:

$$k_B T \ln(2A\tau) = C(\Delta H)^{3/2} \quad (7)$$

where C is the scaling constant contained within the square root of eqn. 6.

This result affects the predictions of a number of previous papers which based their analysis upon the $(\Delta H)^2$ dependence described in Néel's simple model. Most obviously, the effect of time in relaxing a system changes from a $(\ln(2A\tau))^{1/2}$ dependence to a $(\ln(2A\tau))^{2/3}$ dependence. Less obviously, the energy barrier preventing fluctuation-induced switching will tend to be larger than the Néel result for a given ΔH . This will lead workers to claim lower effective switching volumes based on their measurements. A particular interesting change will be found in the prediction of Charap¹⁴ for the maximum rate of low temperature magnetization decay normalized to the saturation magnetization. Using Néel's model, he obtained approximately a $T^{1/2}$ variation by assuming a Lorentzian switching field distribution; the new result would be $T^{2/3}$.

Experimental verification of these predictions would obviously be desirable. It is easy to show that the experimental measurements of Oseroff *et al.*¹⁵ for coercivity as a function of time (their Fig. 4) fit a $(\Delta H)^{3/2}$ dependence very well. (The comparison is made for the five swept field points since this avoids their discrepancy as they move to a "jumped" field.) However, a $(\Delta H)^2$ dependence cannot be ruled out. An accurate determination of the exponent by this method may require several measurements at still higher frequency. Alternatively, it may be possible to exploit very low temperature measurements of the maximum magnetization decay rate to test the $T^{2/3}$ dependence discussed in the previous paragraph. Here, special care must be taken that the applied field and temperature are very constant. This measurement was attempted by Tobin *et al.*,¹⁶ unfortunately, their data are too scattered at the lowest temperatures to reliably fit an exponent, and a fit to higher temperatures shows a strong dependence of the exponent on the cutoff temperature.

IV. CONCLUSION

Two theoretical attempts to predict hysteretic phenomena have been described. The first involved a detailed calculation, for three thin film samples, which included incoherent rotation of grain magnetization and complete magnetostatic interactions. Input to these calculations came from a detailed knowledge of the sample microstructure drawn from sources such as electron microscopy. The accuracy of the calculational method and experimental input permitted quantitative predictions for hysteresis in unprecedented agreement with experiment: the longitudinal and perpendicular loops matched experiment to within 15%.

The second calculation featured a derivation of the relationship between measurement time and switching field in the limit of weak thermal fluctuations. The predicted $(\Delta H)^{3/2}$ dependence differs from the commonly used Néel model's $(\Delta H)^2$ dependence: this is because the Néel model is derived for a special case of high symmetry that is usually not applicable. The new relationship implies that the maximum magnetic viscosity at low temperature should exhibit a $T^{2/3}$ dependence and that phenomenologically obtained switching volumes are actually smaller than previously thought. Several of these predictions offer opportunities for experimental testing.

ACKNOWLEDGMENT

I would like to thank A. K. Agarwala, C. F. Brucker, C. Byun, L. S. Meichle, S. B. Oseroff, J. P. Peng, S. Schultz, F. E. Spada, V. M. Tobin, and W. E. Yetter for providing experimental data and/or valuable assistance.

REFERENCES

1. For a more complete description, see W. F. Brown, *Micromagnetics*, Wiley, New York (1963).
2. E. C. Stoner and E. P. Wohlfarth, *Phil. Trans. Roy. Soc. (London)*, A-240:599 (1948).
3. See, for example: E. H. Frei, S. Shtrikman, and D. Treves, *Phys. Rev.* 106:446 (1957); E. Della Torre, *IEEE Trans. Mag.* 21:1423 (1985).
4. G. F. Hughes, *J. Appl. Phys.* 54:5306 (1983).
5. L. Néel, *Ann. Geophys.* 5:99 (1949); *Adv. Phys.* 4:191 (1955).
6. R. H. Victora, *Phys. Rev. Lett.* 58:1788 (1987); *J. Appl. Phys.* 62:4220 (1987).
7. R. H. Victora, C. F. Brucker, and F. E. Spada (in preparation).
8. R. H. Victora, *Phys. Rev. Lett.* 63:457 (1989).
9. J. -S. Gau and W. E. Yetter, *J. Appl. Phys.* 61:3807 (1987).
10. M. Sparks, *Ferromagnetic Relaxation Theory*, McGraw-Hill, New York (1964).
11. A. P. Malozemoff and J. C. Slonczewski, *Magnetic Domain Walls in Bubble Materials*, Academic, New York (1979), p. 30-39.
12. G. F. Simmons, *Differential Equations*, McGraw-Hill, New York (1972).
13. S. Chandrasekhar, *Rev. Mod. Phys.* 15:1 (1943), especially p. 63-68.
14. S. H. Charap, *J. Appl. Phys.* 63:2054 (1988).
15. S. B. Oseroff, D. Franks, V. M. Tobin, and S. Schultz, *IEEE Trans. Mag.* 23:2871(1987).
16. V. M. Tobin, S. Schultz, C. H. Chan, and S. B. Oseroff, *IEEE Trans. Mag.* 24:2880 (1988).

MAGNETIC HYSTERESIS IN DISORDERED MAGNETS

C. M. Soukoulis

Ames Laboratory and Department of Physics
Iowa State University
Ames, Iowa 50011, U.S.A.

By studying the evolution (with field H and temperature T) of the free energy surface, we numerically calculate various history-dependent magnetizations for Ising, and Heisenberg spin glasses as well as for nondisordered ferromagnets. Only the simplest mean-field (MF) approximation to the free energy functional $F[\{m_i\}]$ (where m_i is the thermally averaged spin at the i^{th} site) is studied. We have calculated hysteresis loops which compare favorably with experiment for a variety of situations and make predictions for additional hysteresis effects. The close correspondence between our theory and experiment supports the hypothesis that on intermediate-time scales the behavior of spin glasses is primarily determined by the properties of the free-energy surface: Irreversibility occurs when minima of F are destroyed with changing H or T .

I. INTRODUCTION

In the last few years, theoretical and experimental studies of spin glasses and random fields have been increasingly concerned with nonequilibrium and time-dependent effects. Early theoretical treatments¹ on the spin glass problem were based on the presupposition that a thermodynamic phase transition existed. However, shortly thereafter, experiments^{2,3} provided clear evidence that at low temperatures, the dc magnetization and other properties were time- and history-dependent. Therefore, an equilibrium thermodynamic approach seems to be inappropriate. This failure of equilibrium thermodynamics is presumably connected to the breakdown of ergodicity. The spin glass and the random field do not sample all accessible states in the time of a laboratory experiment.

There have been a number of theoretical approaches aimed at dealing with these nonequilibrium effects. These have built on either dynamical^{4,5} or replica symmetry breaking concept.⁶ Our own work⁷⁻¹¹ has focused on nonergodicity in spin glasses⁷⁻¹⁰ and random fields¹¹ and is based on the assumption that for intermediate time scale experiments the spin glass or random field is contained within a local minimum of the free energy surface. As the magnetic field or temperature changes, this surface evolves; the spin glass or random field follows the evolution of a given minimum as long as it persists and when it disappears, the system hops to a nearby minimum in which it is trapped for some period of time. The results obtained numerically by following the evolution of the free energy surface yield various history-dependent magnetizations, hysteresis loops, and phase diagrams which are in good qualitative agreement with experiment. In this paper, we will review the essential aspects of this work, with emphasis on the effects of different anisotropies on the shape of the magnetic hysteresis loops.

Our techniques are amendable to a treatment of Heisenberg⁸ as well as Ising⁷ spin glasses. For spin glasses, in the Heisenberg case, we have been able to study the effects of

various kinds of anisotropy on the history-dependent magnetization for large-size systems. Within conventional simulation techniques, such studies have not been feasible because of computational limitations.

II. FREE ENERGY SURFACE

In order to study the properties of spin glasses random-field systems, and in general, any disordered system we numerically solved⁷⁻¹¹ the self-consistent equations $\partial F/\partial m_i = 0$ where $F[m_i]$ is the free energy surface and $m_i = \langle S_i \rangle$, where $\langle \rangle$ stands for a thermal average and S_i is the spin at site i .

As in most theoretical descriptions of spin glasses, we consider a Hamiltonian in which spins are located at all sites and the nearest-neighbor exchange interaction J_{ij} is given by a Gaussian probability distribution $P(J_{ij})$ of width J and mean J_0 . In that follows, T , H , J_0 , etc. will be measured in units of J ; we also take the magnetic moment $g\mu_B = 1$. The general energy functional $F[m_i]$ can be written within the mean-field theory as

$$F^{mf}[m_i] = \frac{1}{2} \sum_{ij} J_{ij} m_i m_j - k_B T \sum_i \ln \frac{\sinh(S+1/2)H_i}{\sinh H_i/2}. \quad (1)$$

Here $H_i = \beta \sum_j J_{ij} m_j + \beta H$, $\beta = 1/k_B T$ and $-S < m_i < S$, where S is the magnitude of the spin.

We solve iteratively the self-consistent equations derived from $\partial F^{mf}/\partial m_i = 0$. We consider $[m_i]$ to be converged, when

$$\frac{\sum_i [m_i^n - m_i^{n-1}]^2}{\sum_i (m_i^n)^2} < 10^{-6}, \quad (2)$$

where the superscript n denotes the n^{th} iteration. After a solution is found at a particular H and T , we follow the minimum with H or T , using the previously converged values as the initial guess. It is important to note that iteration generates only minima. We have verified that minima are not lost due to numerical artifacts. We always varied H and T according to the experimental prescription and in this way generated fc and zfc magnetizations as well as hysteresis loops.

In addition to Ising spin systems, it is rather easy to study vector spin models as well as using this method. This case is of considerable interest, since it allows us to study the effect of anisotropy. The anisotropy terms in the Hamiltonian are given by

$$H^A = -\sum_i D(S_i^z)^2 - \sum_{ij} D'_{ij} (S_i \times S_j). \quad (3)$$

Here the first and second terms correspond to uniaxial and Dzyaloshinsky-Moriya¹² (DM) anisotropy, respectively. The limit $D \rightarrow -\infty$ corresponds to the x-y model and $D \rightarrow \infty$, the Ising model. We assume that the coefficients $D'_{ij} = -D'_{ji}$; $P[D'_{ij}] = \delta(D'_{ij} \pm D')$. The parameters D and D' are chosen as variable parameters, in our numerical studies. The generalizations of the mean field equations for the Heisenberg model are straightforward and given in Ref. 8.

We always varied H and T according to the experimental prescription and in this way generated field cooled and zero field cooled magnetizations, hysteresis loops, as well as phase diagrams.

III. SPIN GLASS RESULTS

Based on our numerical work, our most general observation, about the way in which the free energy evolves with H and T , are as follows:

- 1) A free energy minimum never disappears upon cooling.
- 2) Below $T_c(H)$, a minimum will generally disappear upon heating, [unless the minimum was obtained by a cooling procedure].
- 3) For $T < T_c(H)$ minima appears to be continuously created as well as destroyed, upon changing H , by small but finite amounts.

There is thus a directionality associated with the way in which the surface evolves with T . At high T , there is only one minimum in $F[m_i]$, whereas at low T the number of minima is very large. Therefore, it is not surprising that as T increases minima are destroyed.

Zero field cooled states (zfc) were obtained by cooling in zero H from high T to zero temperature. To measure the magnetization, M , a field was applied after cooling to the lowest T . The T dependent magnetizations M^{zfc} are then obtained by warming from low T as in the experimental procedure. The field cooled (fc) magnetization obtained upon cooling at constant field $H \neq 0$. These fc states were always found to have the lowest free energy for a given (H, T) . They were also completely reversible with T . Therefore, our results support the claim that the fc state is the most likely candidate for the true equilibrium state for a spin glass system. We also find that magnetic hysteresis is found when H is changed, in either direction, at constant T . Changing H always leads to magnetic hysteresis below $T_c(H)$. We find that magnetic hysteresis is very sensitive to the parameter J_0 , the center of the Gaussian for the random variables J_{ij} . The larger the tendency towards ferromagnetism, the sharper the magnetization reversals. Our results^{7,8} for $J_0 \neq 0$ are qualitatively similar to the more concentrated $AuFe$ as well as $CuMn$ hysteresis loops which show sharp magnetization reversals. The effect of increasing the spin value S is to narrow the loop slightly and to position it more vertically around the origin.

We have also studied the Heisenberg model^{8,9} with and without anisotropy. The essential difference from the Ising case is that M is now a vector and the mean field equations are slightly more complex, particularly in the presence of uniaxial anisotropy D . A very striking result of our calculations is that in a short-range isotropic Heisenberg spin glass, there is no macroscopic irreversibility. The field cooled magnetization, M^{fc} , and the zero field cooled magnetization M^{zfc} are equal for all T . The introduction of anisotropy produces several interesting effects. Not too surprisingly once anisotropy is introduced, we find that the temperature dependence of M^{fc} and M^{zfc} are qualitatively similar to those found for the Ising model. The fc and zfc magnetizations split at roughly the T at which M^{zfc} has a maximum. We find that both the presence of either Dzyaloshinsky-Moriya or uniaxial anisotropy lead to irreversibility. Hysteresis loops exhibit sharp jumps at constant H , only when the microscopic anisotropy and a ferromagnetic tendency J_0 are present. This produces results for the magnetization which are qualitatively in agreement with the experimental results for $CuMn$. We also observe that displayed loops^{8,9} which are observed in many systems are present only when Dzyaloshinsky-Moriya interactions are present, but not for uniaxial anisotropy. We have also found evidence that the infinite-range¹⁰ Sherrington-Kirkpatrick model for isotropic Heisenberg spin glass is irreversible. For this model, both the number of minima and, more importantly, the size of the barriers between them increase very rapidly with the size of the system. Thus, it becomes more difficult for the system to minima hop and the system shows irreversibility.

IV. RESULTS FOR MAGNETIC HYSTERESIS CURVES

A. Ising Case

There is an abundance of data on magnetic hysteresis effects in spin-glasses.¹³⁻¹⁶ Qualitatively, the results are of two types. The hysteresis loops¹⁶ seen in (dilute) $AuFe$ are smooth and continuous as functions of H . By contrast, more concentrated $AuFe$,¹⁶ as well as $CuMn$ and $AgMn$ alloys show sharp magnetization reversals in magnetic hysteresis.^{13,15} In

Mn-containing spin-glasses, one also sees the so-called "displaced loops" obtained under certain circumstances in field-cooled measurements. Such effects are not seen in *AuFe*. Monte Carlo simulation results are rather scarce. We are only aware of one result by Binder and Kinzel¹⁷ which yielded a characteristic (dilute) *AuFe*-type loop for an Ising 80×80 system. In this section, we discuss hysteresis loops obtained in a variety of different situations. We find the parameter to which the magnetic hysteresis is most sensitive is J_0 , the center of the Gaussian. The larger the tendency toward ferromagnetism is, the sharper are the magnetization reversals. However, for Ising spins, displaced loops are never found to be present. This situation is to be contrasted with that obtained for Heisenberg spin-glasses,⁸ with Dzyaloshinsky-Moriya¹² anisotropy; in this case (as will be discussed in the following chapter) displaced loops will appear under the appropriate circumstances.

It should be emphasized that in our calculations magnetic hysteresis arises directly from the behavior of the free-energy surface. As H changes, a given minimum of the free energy becomes unstable and the system hops to a nearby state. The fact that the new minimum at $H + \Delta H$ has nearly the same magnetization as that at H leads to a very gradual, smooth hysteresis curve. This behavior is characteristic of Ising spin-glasses, with $J_0 = 0$. While we believe the shape of the hysteresis curve reflects primarily the character of the various metastable states in spin-glasses, it is clear that there are also time-dependent or relaxational effects which may play a role. Presumably, these are most clearly evident experimentally when the hysteresis loop is not well closed.

In Fig 1 are plotted two hysteresis loops corresponding to $S = 1/2$ and $5/2$, for an Ising system of $10 \times 10 \times 10$ spins. In these two cases, for convenience, the loops were obtained by slowly decreasing the field from the high-field limit ($H = 2T_C$) to an equally large (in magnitude) negative field and then closing the loop. (Here $T_C = 1.125J$ and $13J$ for $S = 1/2$ and $5/2$, respectively.) At the highest fields, the magnetization assumes a unique value, so that the resulting loop is independent of the way it was generated. This is not the case for smaller field sweeps. As may be seen from Fig. 1, the effect of increasing S is to narrow the loop slightly and to position it more vertically around the origin. In Fig. 2 is plotted an experimentally measured hysteresis loop for *AuFe*. The data, which are taken from Ref. 15, are in qualitative agreement with the Ising model results and with Monte Carlo simulations.¹⁷ The similarity of results obtained in the two different theoretical approaches is not surprising since the calculations were performed at reasonably low T .

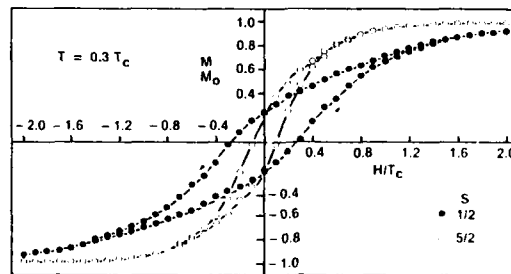


Fig. 1. Magnetic hysteresis curves, M vs. H , for a symmetric field sweep for high maximum H for $T = 0.3T_C$, $N = 10^3$, and $J_0 = 0$ for two values of S .

In more concentrated *AuFe* as well as in *CuMn*, magnetic hysteresis loops are found^{13,15} to exhibit sharp magnetization reversals. To obtain this behavior, we studied the effect of increasing J_0 from 0.0 to 0.25 and finally to 0.50. The three corresponding loops are shown for the cases $S=1$ in Fig. 3. As expected, when J_0 increases, the magnetization exhibits rather sharp jumps, with small changes in the field. This is due to the fact that many spins tend to flip in parallel when J_0 is large. This cooperative behavior is clearly evident from the data¹⁶ shown in Fig. 4 for an *Au88Fe12* spin-glass. This sharp, vertical loop should be contrasted with that observed for the more dilute *AuFe* system shown in Fig. 2. Once J_0 exceeds the critical value for ferromagnetism, the loop becomes almost rectangular

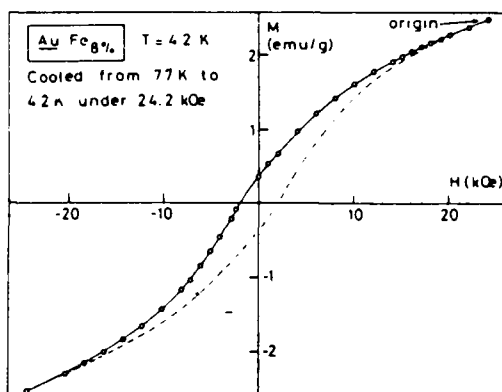


Fig. 2. Experimentally determined hysteresis for 8 at. % AuFe which was field cooled in a field of 24.2 kOe (after Ref. 15).

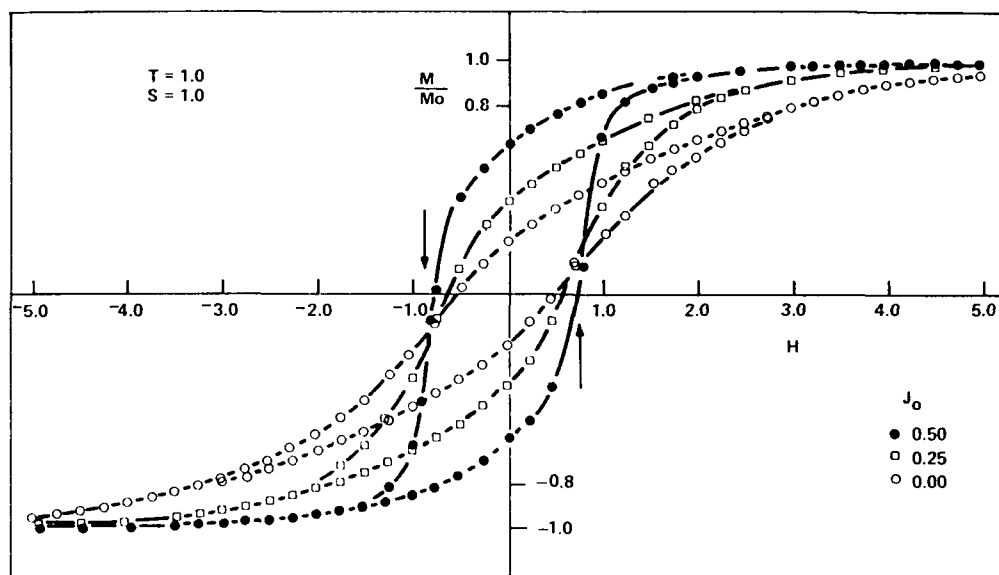


Fig. 3. Magnetic hysteresis curves, M vs. H , for symmetric field sweeps for high maximum H at $T = 1.0$ and $S = 1.0$ for several values of J_0 and $N = 10^3$.

(at low T). In the extreme limit of large J_0 , the system is like an ordered Ising ferromagnet: There are exactly two minima on the free-energy surface, and the sharp reversals represent passing from one minimum to another.

While our numerical results provide insight into what is going on in AuFe spin-glasses, the origin of the sharp magnetization reversals seen in CuMn is less clear. It has been argued^{14,18,19} that dilute CuMn has a tendency towards ferromagnetism; the next-nearest-neighbor Mn-Mn RKKY interactions are believed to be ferromagnetic. Within our theoretical framework, we have found that only the presence of a ferromagnetic tendency can lead to cooperative magnetization reversals such as are found in CuMn. This will be discussed in more detail for anisotropic Heisenberg spin-glasses in the following chapter. However, it is possible that in CuMn there are relaxation effects present (so that the system is not always "quasiequilibrated" at each value of H) and thus our theoretical picture may break down. In summary, the presence of cooperative behavior in a highly disorganized system, such as a spin-glass, appears difficult to understand unless there is a tendency towards ferromagnetism.

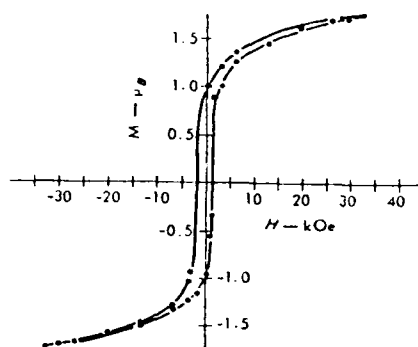


Fig. 4 Experimental hysteresis curve at 4.2 K in 12 at. % AuFe (after Ref. 16).

It has been observed that in *CuMn*, when the field sweep is nonsymmetric, the hysteresis loop is displaced^{13,15} with respect to the $H=0$ axis. Similar results may also be obtained upon field cooling, under the appropriate conditions. Such "displaced" loops have evidently not been seen in *AuFe*.¹⁶ In order to ascertain whether they are present in our theoretical model for Ising spin-glasses, we have generated loops which start at large positive values and reverse direction at much smaller (in magnitude) negative values of the field. We have been no evidence for displaced loops in Ising spin-glasses, with or without a large J_0 .

B. Heisenberg Case

In the Ising case, we saw that magnetic hysteresis occurs because small changes in H destroy minima on the spin-glass free-energy surface; the system must hop to a nearby state (as in a first-order transition). The same processes occur in an isotropic Heisenberg spin-glass. However, these lead to microscopic, but not macroscopic, irreversibility.

In Fig. 5 are plotted the calculated hysteresis curves for an isotropic Heisenberg system of 10^3 spins. Each curve corresponds to a different value of J_0 . For all values of J_0 , including the ferromagnetic case ($J_0 = 1.0$), the M_z vs. H_z curve passes through the origin. There is no macroscopic hysteresis. The temperature T is taken to be 1.0; however, we have verified that the results are qualitatively the same at lower temperatures. When we sweep from negative to positive H , we find that at each value of the field the m_i are different that was found on the sweep from positive to negative H ; however, the states are simply related by a rotation in the x - y plane so that the macroscopic magnetization is unaffected by the history. Furthermore, in a hysteresis calculation each $M_z(H)$ is found to be identical to that obtained by field cooling. This reinforces the observation that because of the rotational degeneracy of the FC state, it is extremely accessible; as a consequence, the spin-glass exhibits no macroscopic irreversibility.

To get additional insight into the behavior of magnetic hysteresis, we have performed hysteresis calculations for *nondisordered* Ising and Heisenberg ferromagnets in mean-field theory. In the Ising case the loop is rectangular, much like that shown in Fig. 6(a) for $J_0 = 1.0$. This loop corresponds to the fact that there are at most two minima on the free-energy surface. In this case, the system stays in the \uparrow minimum, until it becomes unstable with decreasing H . It then jumps discontinuously to the \downarrow state. There is a small range of H over which two minima coexist, so that magnetic hysteresis represents a supercooling, nonequilibrium phenomenon. In the nondisordered isotropic Heisenberg ferromagnet, the magnetization always points along the external field direction (which is the only direction of broken symmetry). As H_z is turned off, there can be no component of \vec{M} along the z direction so that M_z vanishes when $H_z = 0$.⁸ The hysteresis behavior observed for spin-glasses seems to be a direct reflection of these results for nondisordered ferromagnets: The Ising system exhibits macroscopic hysteresis, whereas the Heisenberg case does not. Physically, this corresponds to the fact that vector spins have additional flexibility and can

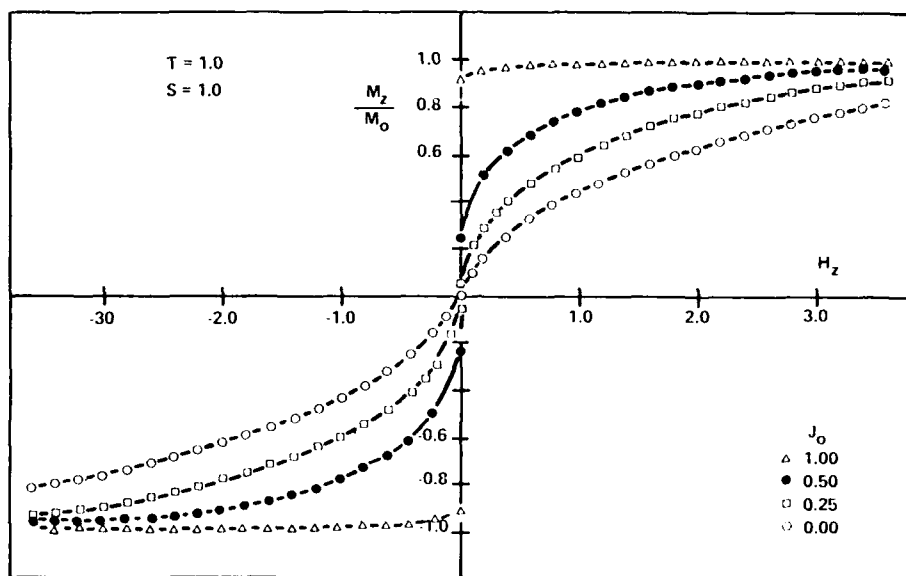


Fig. 5 Magnetization vs. field for various J_0 in isotropic Heisenberg system with $N = 10^3$. Note $J_0 = 1.0$ is ferromagnetic.

"follow" the motion of the external field. They do not get readily trapped into metastable states, as in the Ising case. Thus there is no remanence or macroscopic irreversibility.

In Fig. 6(a) are shown the effects of uniaxial anisotropy on the hysteresis loops for a spin-glass of $N = 6^3$ spins. Here the anisotropy constant was fixed at the value $D = 0.4$ and the loops are plotted for various J_0 . The case $J_0 = 0$ may be contrasted with the results shown by open circles in Fig. 5. The introduction of uniaxial anisotropy opens up the hysteresis loop, in the same way that it splits the FC and ZFC magnetization as a function of temperature.⁸

The effect of increasing J_0 is to make the loops more rectangular. By $J_0 = 1.0$, the spin-glass is ferromagnetically ordered. As noted above, the loop shown in Fig. 6(a) for this case is characteristic of an Ising ferromagnet; in general, the change in shape of the loops with increasing J_0 is similar to that found in the Ising case.

When the same type of calculations are repeated in the presence of DM anisotropy, similar results are obtained. Hysteresis loops for this case are shown in Fig. 6(b) in a $10 \times 10 \times 10$ spin-glass with anisotropy constant $D' = 0.5$ and temperature $T = 0.2$. The values of J_0 are 0.25, 0.50, and 1.00. Only the last case has a nonzero spontaneous magnetization. Comparing Figs. 6(a) and 6(b), it may be seen that in the case of DM anisotropy the loops appear to be narrower and less rectangular, particularly at large J_0 . This last effect is not unexpected since anisotropy of the DM type $[\vec{D}_{ij} \cdot \vec{S}_i \times \vec{S}_j]$ will oppose the tendency for cooperative spin reversal in magnetic hysteresis. Hence the abrupt magnetization reversals seen in the uniaxial case are not as readily obtained. A simultaneous treatment of both uniaxial and DM anisotropy is somewhat difficult, although feasible, to mimic a combined uniaxial DM anisotropy which also includes J_0 effects, we have added a uniaxial component to \vec{J}_{ij} in Eq. (1) called J_0^z . The resulting hysteresis curve for $J_0^z = 0.5$ and all other parameters the same as in Fig. 6(b) is shown in the inset of Fig. 6(b). With the "uniaxial" as well as DM anisotropy present, the loop is broadened and the magnetization reversals are sharper than shown in the main portion of the figure.

It was noted in the Ising case chapter that sharp magnetization reversals are seen^{14,15} in Mn-containing spin-glasses and in concentrated AuFe alloys.¹⁶ All our calculations based on the anisotropic Heisenberg system (of which the Ising model is a special case) suggest that these sharp reversals are only present when J_0 is positive. Only under these

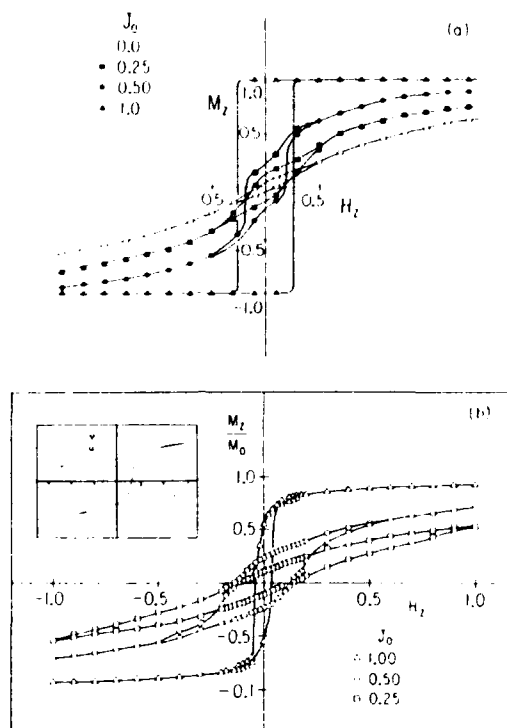


Fig. 6. (a) Magnetic hysteresis curves for case of uniaxial anisotropy with $D = 0.4$ and various J_0 . Here $N = 6^3$. (b) Magnetic hysteresis curves for case of DM anisotropy for $D' = 0.5$ for various J_0 and $N = 10^3$. Inset shows the effect of a type of combined uniaxial DM anisotropy with J_0 also present (see text).

circumstances do the spins flip cooperatively as H is changed. It is clear that such a ferromagnetic tendency is present in $AuFe$ alloys. This was discussed in detail in the Ising case.

As discussed previously, there is experimental evidence which suggests that Mn-containing alloys also have a ferromagnetic tendency. It is important to note that what determine the sharpness of the hysteresis loop is not the magnitude of J_0 alone; it also depends on how much and what kind of anisotropy there is to compete with the cooperative effects induced by the J_0 term. Thus a system with a large degree of DM anisotropy [as, for example, $AuFe^{20}$] may require a larger amount of J_0 to show sharp hysteresis loops. It may be speculated that since $CuMn$ is considerably less anisotropic,²⁰ less of a ferromagnetic tendency is needed to cause the abrupt magnetization reversals seen in hysteresis loops.

The experimentally observed hysteresis loops for Mn-containing alloys are illustrated in Fig. 7. Figure 7(a), which shows the results of a symmetric field sweep, makes it clear that in $CuMn$ the loop is extremely narrow and the field reversal quite dramatic. The closest we have come to reproducing this type of behavior is to add a "uniaxial" J_{ij} component of the Heisenberg Hamiltonian. The resulting loop is shown in Fig. 8 for $J_0' = 0.5$, $T = 0.2$, and $N = 10^3$.

Of equal, if not greater, interest from an experimental viewpoint, is the presence of the so-called "displaced loops."^{14,15} An example of one is shown in Fig. 7(b); although the data¹⁵ is for $AgMn$, the behavior is typical of $CuMn$ spin-glasses as well. These loops are seen when the field sweep is very nonsymmetric or when the spin-glass is field cooled and the loop is generated by reversing the field at sufficiently small (negative) $|H|$ values. A

"memory" effect leads to a displacement of the loop relative to the $H=0$ axis. To search for this behavior, we considered nonsymmetric field sweeps, starting from large positive H values and reversing at small (in magnitude) negative H . For an Ising spin-glass, the loop so obtained is primarily shifted upward. When $J_0 > 0$, the loop is sharp and the asymmetry is only with respect to the $M=0$ axis. We have verified that in the Heisenberg case with uniaxial anisotropy the same qualitative behavior is observed as for Ising spins.

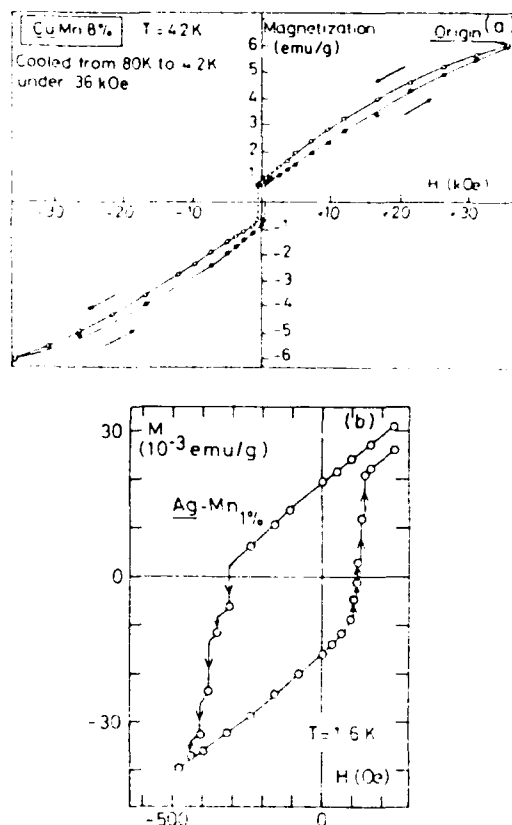


Fig. 7. (a) Measured magnetic hysteresis curve for 8 at. % CuMn for large field sweep (after Ref. 15). (b) Measured displaced magnetic hysteresis loop in 1 at. % AgMn (after Ref. 15).

The introduction of DM anisotropy leads to different behavior, however. In Fig. 9(a) is plotted a hysteresis loop with DM anisotropy constant $D' = 0.5$, $J_0 = 0.5$, and $T = 0.2$ in an 8^3 Heisenberg spin-glass. The loop is obtained by starting at very large H and then reversing the field at around $-H = 0.2$. Only for the case of DM anisotropy have we found that M became positive (as H is increased from negative values) before H changed sign to a positive value. In the uniaxial case, M changes sign after H has become positive. Only in the DM case is there a kind of "memory effect" which directs the system toward positive magnetization. This can be seen more clearly in Fig. 9(b) for $J_0 = 0.75$, which is large enough to make the loop more rectangular. Unfortunately, this value of J_0 is sufficient to cause spontaneous ferromagnetism. Here all other parameters are the same as in Fig. 9(a). For more rectangular hysteresis loops, the effect of DM anisotropy is to displace the loop relative to the $H=0$ axis, in a way which is similar to that observed experimentally. By comparing Figs. 7(b) and 9(b) it may be seen that results for displaced hysteresis loops are in reasonable qualitative agreement.

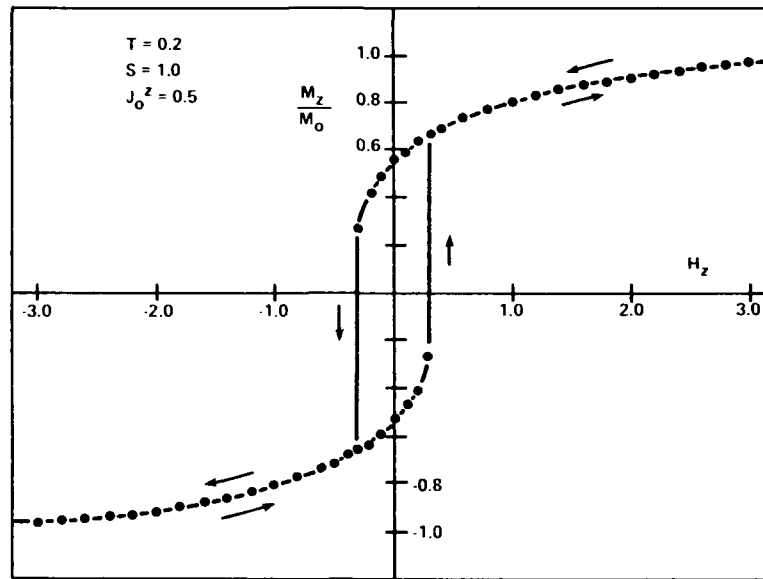


Fig. 8. Magnetic hysteresis loop with a uniaxial anisotropy J_0^z included through the $\{J_{ij}\}$. Note loop tends to have steep reversals as in CuMn. [See Fig. 7(a)].

Fert and Levy²⁰ have argued on the basis of analytical arguments that a unidirectional anisotropy (such as DM) will cause displaced loops. Essential to their derivation is the assumption that the spins all rotate rigidly in response to a rotation of an applied magnetic field. This assumption of rigid rotation can be roughly justified within our framework only when J_0 is sufficiently large. This will be discussed in more detail in the following section. When the spins do not rotate rigidly (i.e., for smaller J_0), then the nature of the "displaced loops" is still characteristically different from that obtained in the uniaxial anisotropy case. Such nonrigid rotations lead to loops like that shown in Fig. 9(a).

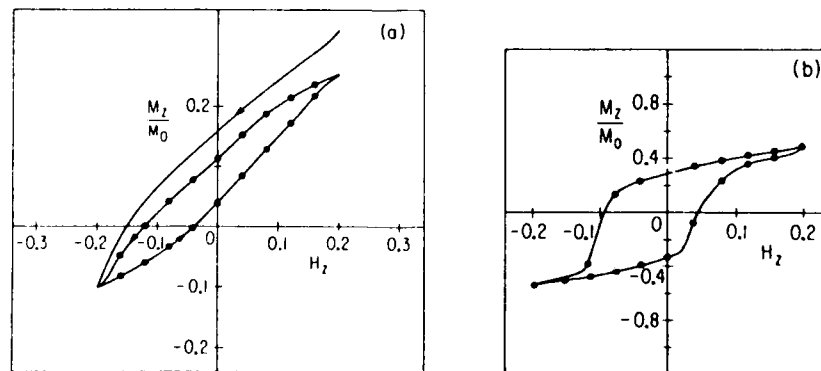


Fig. 9. (a) Magnetic hysteresis loop with DM anisotropy constant $D' = 0.5$ for nonsymmetric field sweep with $J_0 = 0$. (b) Magnetic hysteresis loop with DM anisotropy constant $D' = 0.5$ for nonsymmetric field sweep with $J_0 = 0.75$. This yields a characteristic displaced loop to be compared with Fig. 7(b).

In summary, our numerical results demonstrate that under the assumption of rigid spin rotation (which we find will occur when a ferromagnetic tendency is present) the effect of Dzyaloshinsky-Moriya anisotropy is to yield the so-called displaced hysteresis loops. While it is somewhat disturbing that we need such large values of J_0 to obtain rigid rotations in the DM model, it should be noted that our numerical parameters cannot be quantitatively compared with their experimental counterparts. This is due in part to all the simplifications inherent in our model Hamiltonian, as well as to our (mean-field) approximate solution of this model applied to a finite system.

VI. CONCLUSIONS

The most striking conclusion of our studies is that a variety of experimental measurements can all be reasonably well reproduced by a theoretical model which focuses only on the properties of the free energy surface. Presumably, the reason for the success of this approach is that there are two important time scales in spin glass experiments: "fast times" (which may correspond to $t < 10^{-11}$ sec), during which the system makes small adjustments to find the nearest minimum of the free energy, and "long times," during which the system finds its way over energy barriers to more stable states. These latter processes appear to vary as $\ln t$, suggestive of thermal activation. It is primarily because of these long time processes that our quasistatic or quasiequilibrium viewpoint has some validity. The fast-time "dynamics" are automatically included in our calculations.

Our result for the Heisenberg model show there is no irreversibility in the isotropic, short-range Heisenberg model. This is a consequence of the ready accessibility, due to rotational symmetry, of the field-cooled state. Once microscopic anisotropy is introduced, most history-dependent properties are found to be similar to those we found for the Ising case. As reported elsewhere¹⁰ where we have found evidence that the *infinite*-range Sherrington-Kirkpatrick model for isotropic Heisenberg spin glasses is irreversible. For this model, both the number of minima and, more importantly, the size of the barriers between them increase very rapidly with N . Thus it becomes more difficult for the system to minima hop and the system shows irreversibility.

ACKNOWLEDGMENTS

This work was done in collaboration with G. S. Grest and K. Levin. This work was partially supported by a North Atlantic Treaty Organization Travel Grant No. RG769/87. Ames Laboratory is operated for the U.S. Department of Energy by Iowa State University under Contract No. W-7405-Eng. 82.

REFERENCES

1. K. Fischer, Phys. Status Solidi B 116:357 (1983), and K. Binder and A. P. Young, Rev. Mod. Phys. 58:801 (1986), and references therein.
2. R. V. Chamberlin, J. Appl. Phys. 57:3377, (1985) and references therein.
3. V. Jaccarino and A. R. King, J. de Phys. Coll. (France) 49:C8-1209 (1988); R. A. Cowley, R. J. Birgeneau, G. Shirane and H. Yoshizawa, Physica 140A:285 (1986).
4. J. A. Hertz, J. Appl. Phys. 57:3366 (1985) and references therein.
5. J. Villian, J. Phys. (Paris) 46:1843 (1985); D. S. Fischer, Phys. Rev. Lett. 56:416 (1986); G. Grinstein, Appl. Phys. 55:2371 (1984).
6. G. Parisi, Phys. Rev. Lett. 43:1754 (1980); J. Phys. A 13:1011 (1980); 13:1887 (1980); Phys. Rev. Lett. 50:1946 (1986).
7. C. M. Soukoulis, K. Levin and G. S. Grest, Phys. Rev. Lett. 48:1756 (1982); Phys. Rev. B 28:1495 (1983).
8. C. M. Soukoulis, G. S. Grest and K. Levin, Phys. Rev. Lett. 50:80 (1983); Phys. Rev. B 28:1510 (1983).
9. G. S. Grest, C. M. Soukoulis and K. Levin, J. Appl. Phys. 55:1634 (1984).
10. G. S. Grest and C. M. Soukoulis, Phys. Rev. B 28:2886 (1983); J. Appl. Phys. 55:1661 (1984).

11. C. Ro, G. S. Grest, C. M. Soukoulis and K. Levin, Phys. Rev. B 31:1982 (1985); J. Appl. Phys. 57:3300 (1985); G. S. Grest, C. M. Soukoulis and K. Levin, J. Magn. Magn. Mater. 54-57:51 (1986); Phys. Rev. B 33:7318 (1986).
12. I. E. Dzyaloshinsky, J. Phys. Chem. Solids 4:241 (1958); T. Moriya, Phys. Rev. Lett. 4:5 (1960).
13. R. W. Knitter, J. S. Kouvel and H. Claus, J. Magn. Magn. Mater. 5:356 (1977).
14. J. S. Kouvel, J. Phys. Chem. Solids 21:57 (1961); 26:107 (1960); 24:795 (1963); J. Appl. Phys. 31:1425 (1960).
15. J. J. Prejean, M. J. Jolicearc and P. Monod, J. Phys. (Paris) 41:427 (1980).
16. R. J. Borg and T. A. Kitchens, J. Phys. Chem. Solids 34:1323 (1973).
17. See for example, K. Binder and W. Kinzel, in "Disordered Systems and Localizations," Vol. 149 of Lecture Notes in Physics ed. by C. Castellani et al. (Springer, Berlin 1981) p. 124.
18. J. W. Cable, S. A. Werner, G. P. Felcher and N. Wakabayashi, Phys. Rev. Lett. 49:829 (1982).
19. A. F. Morgownik, J. A. Mydosh and C. van Dijk, J. Magn. Magn. Mater. 31-34:1334 (1983).
20. A. Fert and P. M. Levy, Phys. Rev. Lett. 44:1538 (1980); P. M. Levy and A. Fert, Phys. Rev. B 23:4667 (1981).

COERCIVITY OF NANOSTRUCTURED MATERIALS

Yoshichika Otani

Department of Pure and Applied Physics, Trinity College, Dublin 2, Ireland

1. INTRODUCTION

Nanostructured magnets are generally produced by crystallizing from the amorphous state. Examples of this type of material are crystallized melt-spun ribbons and sputtered thin films of $\text{Sm}(\text{Fe}_{11}\text{Ti})$ and $\text{Nd}_2\text{Fe}_{14}\text{B}$ which are composed of randomly-oriented crystallites with average diameter smaller than or comparable to the critical diameter for single-domain structure[1]. There is no secondary intergranular phase. As reported by Yamamoto et al. [1], the shape of the magnetization curves are quite rectangular and isotropic. These results are far from Stoner-Wohlfarth (S-W) model prediction for non-interacting single domain particles and also the magnitude of the observed coercivity H_c is an order of magnitude less than the S-W model prediction. The S-W model assumes the system adopts a metastable state, so that each monodomain grain exhibits a coercivity equal to the anisotropy field H_a . However such large coercivities are not found in practice. When only the energy minimum state is considered, there is zero coercivity for each monodomain grain, and interactions between the grains then play the decisive role in determining H_c . In other words, the coercivity is a collective property of the system of interacting grains.

We recently considered the analogy between the magnetization of a single-domain grain and a spin in an amorphous material with random axial anisotropy (HPZ model[3]). Transposing the extensive results of computer simulations on the HPZ model, we found that H_c should vary as the interatomic exchange coupling, and increase as the inverse crystallite size in the nanocrystalline case [2]. In order to further investigate the dependence of H_c on exchange and anisotropy, we have now carried out computer simulation on a realistic model of the grain configuration.

2. MODEL AND CALCULATION

2.1 Grain Generation

We used a 343,000 point face-centered cubic array as the basis of the simulation. First, 27 seed points were chosen at random, and the Wigner Seitz cells (grains) were grown around each of them using an algorithm which searches for those lattice points in ever-increasing spheres which are closest to a particular seed point. Periodic boundary conditions are applied. The number of nearest neighbour-pairs crossing the interfaces between grains was evaluated for each one of the grains. It is on average 11 % of the number of nearest neighbour pairs within the grains. Next, an anisotropy direction is randomly assigned to each grain. The arrangement is shown schematically in Fig. 1. Only the small fraction of nearest neighbour exchange bonds that cross an interface (grain boundary) are active in coupling the grains together and there is competition between these exchange interactions and the different anisotropy directions on either side of the interface.

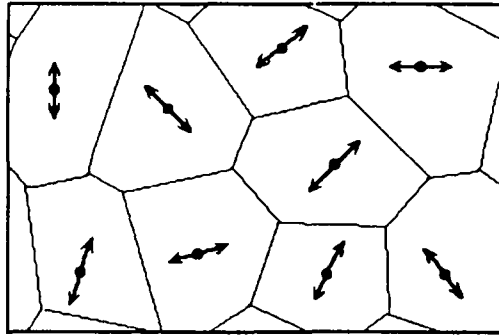


Fig. 1 Schematic representation of the grains used in the simulation. Each grain has a randomly oriented uniaxial anisotropy axis indicated by the double arrow.

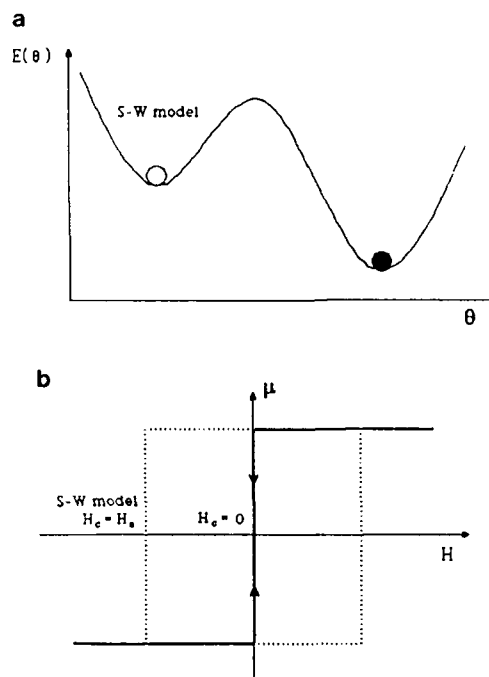


Fig. 2 (a) Free energy E of the single domain grain as a function of the angle θ between the easy axis and the moment. The open circle shows the metastable state used in the S-W model and the solid circle shows the stable state used in our model. (b) The S-W model yields the hysteresis loop with $\mu_0 H_c = \mu_0 H_a$ whereas our model shows no coercivity.

2.2 Coercivity for Strongly Coupled Grains

In our simulation, we abandon the S-W approach entirely; the difference between the S-W model and the present model is illustrated in Fig. 2. Focussing on an isolated single domain grain, the S-W model allows the grain to adopt a metastable energy state which leads to coercivity. However in our model the direction of the grain magnetization, obtained by assuming uniform rotation within the grain, always corresponds to the energy minimum, so the isolated grain has no coercivity.

When the single domain grain is surrounded by neighbours, and the exchange coupling between the grain and the surrounding grains is taken into account, the situation for the grain is changed as illustrated in Fig. 3. Again focussing on a single grain, one now distinguishes two fields which act on it, the external field \mathbf{H}_0 and the exchange field \mathbf{H}_{ex} . The direction of the effective local field \mathbf{H}_{local} , which determines the direction of the moment, is obtained as the sum of these two. Plotting the magnetization of the grain as a function of the external field, the magnetization curve is shifted along the field axis. On calculating the ensemble average for the grains in the system, the coercivity is obtained.

In this calculation, we assume the following free energy for each grain j

$$E^j = E_{ex}^j + E_a^j + E_m^j. \quad (1)$$

The first term is the effective exchange energy between grains assumed to be governed by the interatomic exchange interaction of Fe atoms located at the surface of adjacent grains:

$$E_{ex}^j = -\mu_0 \mathbf{H}_{ex}^j \cdot \boldsymbol{\mu}_j, \quad (2)$$

where

$$\mathbf{H}_{ex}^j = \frac{J_{FeFe}}{12n_j} \sum_{i(nn)} n_{ij}^p \mathbf{S}_i. \quad (3)$$

In Eqs. 2 and 3, \mathbf{H}_{ex}^j is the exchange field, $\boldsymbol{\mu}_j$ is the magnetization of the grain j expressed as $\boldsymbol{\mu}_j = n_j g \mu_B \mathbf{S}_j$, where n_j is the number of the spin within the grain and \mathbf{S} is the classical spin vector, J_{FeFe} is the Fe-Fe interatomic exchange coupling constant, n_{ij}^p is the number of the nearest neighbour pairs located at the interface between the grain j and its nearest neighbour grains and the factor of 12 is the average number of nearest neighbour grains.

The second term is the magnetocrystalline anisotropy energy:

$$E_a^j = n_j D \sin^2 \theta_j, \quad (4)$$

where θ_j is the angle between $\boldsymbol{\mu}_j$ and the anisotropy axis of the grain. D is the anisotropy constant. The third term is the magnetic energy in an external magnetic field \mathbf{H}_0 :

$$E_m^j = -\mu_0 \mathbf{H}_0 \cdot \boldsymbol{\mu}_j. \quad (5)$$

In order to calculate the interesting quantities such as coercivity and hysteresis loops, the energy E^j is first minimized as E_{min}^j and it follows that the total energy for the array of 27 grains is given by

$$E_{tot} = \sum_j (E_{min}^j + \frac{1}{2} \mu_0 \mathbf{H}_{ex}^j \cdot \boldsymbol{\mu}_j), \quad (6)$$

where the second term is included to take account of double counting. For a given external field \mathbf{H}_0 , the magnetic configuration of the array is determined by iteration giving a self-consistent set of $\{\boldsymbol{\mu}\}$.

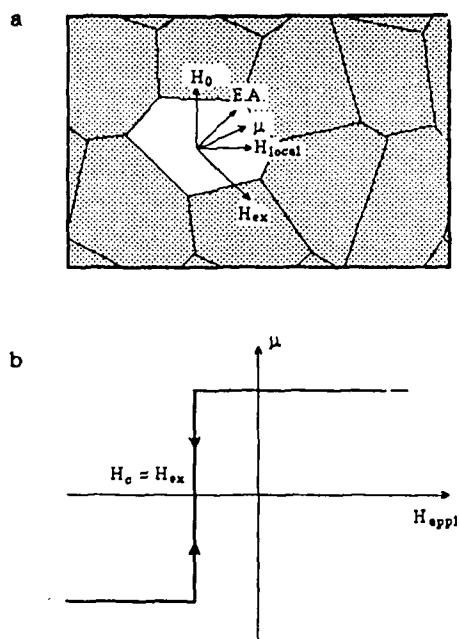


Fig. 3 Schematic illustration of the relation between the applied field H_0 , the exchange field H_{ex} , the local field H_{local} , the easy axis E.A. and the magnetization μ of the grain.

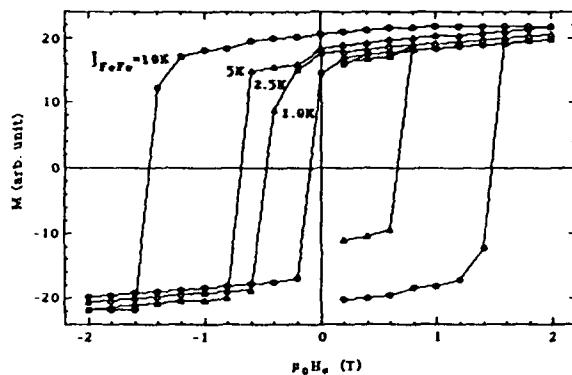


Fig. 4 Calculated hysteresis loops for different exchange constants J_{FeFe} .

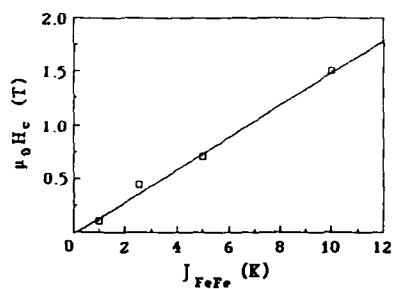


Fig. 5 The relation between the exchange constant J_{FeFe} and the computed coercivity $\mu_0 H_c$, indicating that these quantities are proportional.

3. RESULTS AND DISCUSSION

A series of hysteresis loops calculated, using $D=5$ K and $J_{\text{FeFe}}=1.5, 2.5, 5$ and 10 K is shown in Fig. 4. There is a sharp collective reversal of most of the magnetization at a well defined field H_c , which is proportional to J_{FeFe} (Fig. 5). The most interesting point is that the coercivity is very much less than the anisotropy field ($D=5$ K implies $\mu_0 H_a=10$ T). So the intergranular interactions have the effect of reducing the coercivity below the S-W prediction, $H_c = H_a$. The measured value of J_{FeFe} from Curie temperature for the case of $\text{Sm}(\text{Fe}_{11}\text{Ti})$ is 10 K, which corresponds to a coercivity of 1.5 T. The observed coercivity in nanocrystalline melt-spun $\text{Sm}(\text{Fe}_{11}\text{Ti})$ is 0.6 T at room temperature, and 1.2 T below 50 K which is in good agreement with our (zero temperature) prediction. Our model clearly suggests that the way to improve the coercive field is to increase the effective coupling between the grains which can be achieved in a given material by reducing the grain size.

Acknowledgments

This work forms part of the "Concerted European Action on Magnet", a project supported by the EURAM programme Commission of the European Communities.

REFERENCES

- [1] H. Yamamoto, N. Nagakura, T. Katsuno and T. Yamamoto, IEEE Trans. Magn. (Sept. 1990) to be published.
- [2] H. Sun, Y. Otani and J. M. D. Coey, J. Appl. Phys. **61** (1990) to be published.
- [3] R. Harris, M. Plishke and M. J. Zukermann, Phys. Rev. Lett. **31** 160 (1966).
- [4] J. D. Patterson, G. R. Gruzalski and D. J. Sellmyer, Phys. Rev. **B18** 1377 (1978).

MAGNETIC HYSTERESIS OF CoPt FILMS

A. Tsoukatos, G. C. Hadjipanayis and C. P. Swann

Department of Physics & Astronomy
University of Delaware
Newark, DE 19716

S. Ismat Shah

Central Research & Development Department
E. I. duPont de Nemours & Company
P. O. Box 80356
Wilmington, DE 19880-0356

INTRODUCTION

Co-Pt bulk alloys have been of interest due to their high coercivity and anisotropy.^(1,2) Several uses of these alloys have been suggested in magnetic recording, such as longitudinal recording⁽³⁾ and magnetooptical recording.⁽⁴⁾ Of particular interest are the alloys between 25 and 60 at.% . Within this composition range the alloys undergo an ordering phase transition.^(5,6) Direct evidence of this ordering was first reported by Gebhardt and Koster⁽⁷⁾ who showed that the face centered cubic (fcc) structure of equiatomic alloys transforms into a face centered tetragonal (fct) at temperatures below 835°C. The fct phase is highly anisotropic with $K \simeq 4 \times 10^7 \text{ erg/cc}$.⁽⁸⁾ The coercivity of these films is small for the disordered fcc Co₅₀-Pt₅₀ alloys, but increases with annealing because of the transformation to fct and then decreases in overaged state because of coarsening of the microstructure. Higher Pt content alloys $\sim 75\%$, transform from disordered fcc to ordered fcc. Although there are several reports on the magnetic properties of Co-Pt thin films, most of the work has been on films with high Co concentrations. Yanagisawa et al⁽³⁾ reported a peak in coercivity as high as 1700 Oe for a 350Å thick film with 20% Pt. The coercivity decreased on either side of this composition. Kitada and Shimizu⁽⁹⁾ related this anomaly in coercivity to the microstructure of the films. It was assumed that the increase in coercivity was due to both grain growth and the tendency for the c-axis of α -Co (hcp structure) to collapse into the film surface. Aboaf and co-workers^(10,11) reported the results of annealing in Co₅₀-Pt₅₀ films. The coercivity was reported to increase from 90 Oe for the as-grown films to "very high" values after annealing at 700°C for one hour. They also related this increase in coercivity to the solid state transformation from fcc to ordered fct.

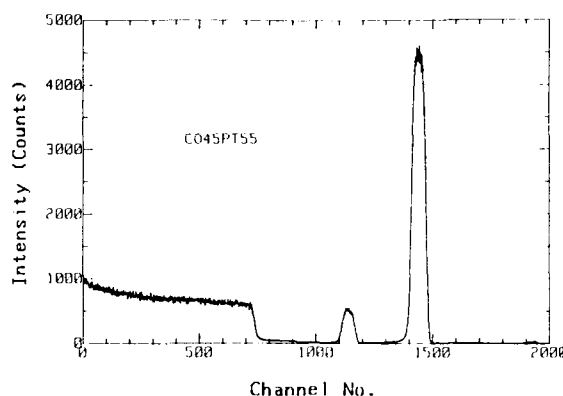


Figure 1. Rutherford Backscattering spectrum for a 120 Å $\text{Co}_{45}\text{Pt}_{55}$ film.

In this paper we study the effect of film thickness on similar observations of the phase transition and its influence on the magnetic properties of Co-Pt alloy thin films prepared by RF sputtering.

EXPERIMENTAL

Co-Pt films were deposited by RF magnetron sputtering using a 5cm magnetron gun. The chamber had a base pressure of 1×10^{-7} Torr. Sputtering was carried out in high purity argon at 3 mTorr pressure. The target was a water cooled target composed of a cobalt disk on which Pt pieces have been placed. The target was pre-sputtered for one half hour prior to the deposition. Films were deposited on various substrates including (100) Si for Rutherford Backscattering (RBS) analysis, graphite coated Cu grids for TEM, Ta foils for annealing and SQUID measurements, and glass coverslip for e-beam microprobe analysis. Microprobe analysis was used for checking the spatial uniformity of the composition. The films were deposited with thicknesses ranging from 100 to 1000 Å.

Annealing was done by encapsulating the films deposited on Ta substrates in evacuated quartz tubes. These sealed ampoules were then annealed at 650°C for one hour. The magnetic measurements were carried out using a SQUID magnetometer.

RESULTS AND DISCUSSION

As-grown films were polycrystalline consisting of fine grains with coercivities ranging between 30 and 300 Oe. Figure 1 is a RBS spectrum obtained from an as-grown film. Since higher atomic number materials give higher backscattering yield, qualitatively, an integrated peak intensity ratio of about 1:8 is expected for a $\text{Co}_{50}\text{Pt}_{50}$ film as $(Z_{\text{Co}}/Z_{\text{Pt}})^2 \approx 1/8.35 \approx 0.12$. This is close to the ratio observed in the RBS spectrum. The average composition of the film calculated from RBS was $\text{Co}_{45}\text{Pt}_{55}$. The variation in the RBS determined compositions is less than 5%. Figure 2a is a bright field micrograph and a diffraction pattern of a $\text{Co}_{45}\text{Pt}_{55}$ as-deposited

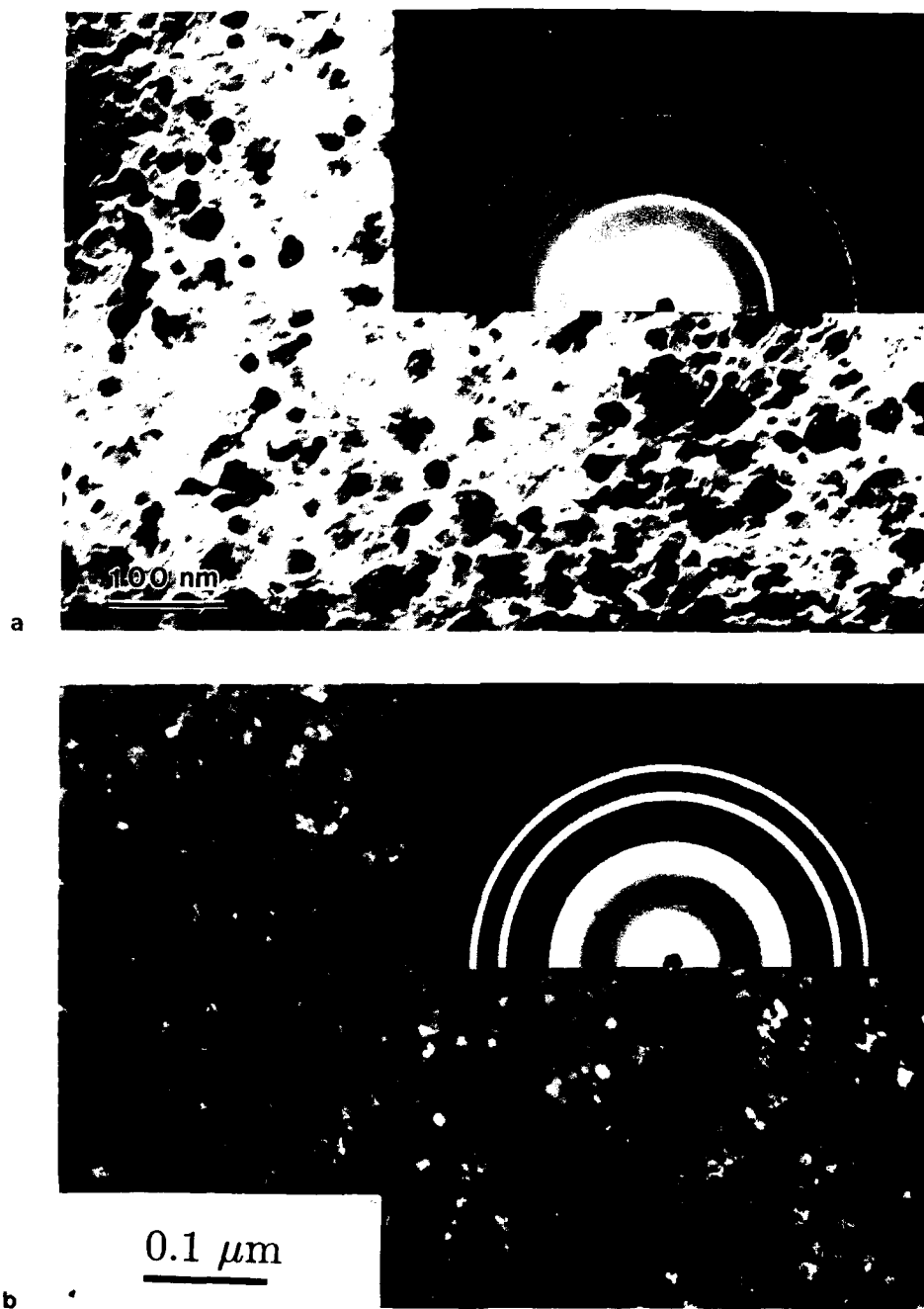


Figure 2. Electron diffraction patterns and bright field micrographs of $\text{Co}_{45}\text{Pt}_{55}$ films. (a) as-deposited, (b) annealed.

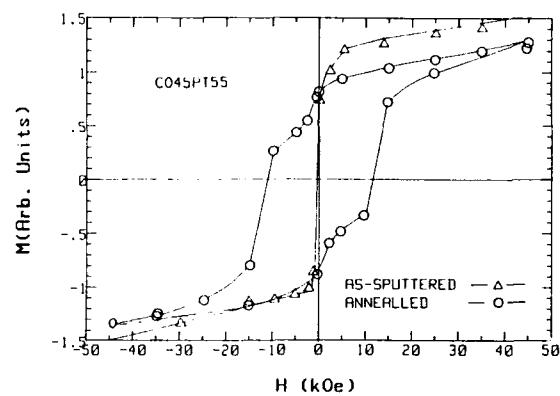


Figure 3. Hysteresis loops of $\text{Co}_{45}\text{Pt}_{55}$ films at $T = 10$ K before and after annealing.

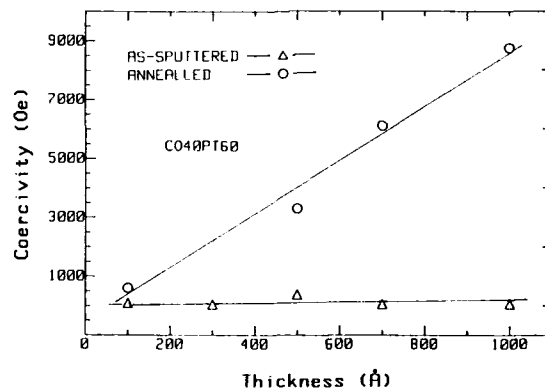


Figure 4. Coercivity as a function of film thickness for $\text{Co}_{40}\text{Pt}_{60}$ films at $T = 10$ K.

film. The film contained very small grains indicated by both the BF micrograph and the diffused diffraction rings. The diffraction pattern is indexed with the fcc disordered structure with $a_0 = 3.85 \text{ \AA}$. Upon annealing at 650°C for 1 hour, the diffraction rings sharpen and additional rings appear (Fig. 2b). Line splitting in the diffraction pattern at 220, 311, and 331 rings indicates the formation of fct phase. Since both the rings for fcc and fct exist, we conclude that the two phases are present simultaneously and the transformation is not complete.

Figure 3 shows the magnetic hysteresis loops of a 1000 \AA thick $\text{Co}_{45}\text{Pt}_{55}$ films before and after annealing. As-grown films had a coercivity of about 60 Oe. This coercivity is associated with the disordered fcc fine grain structure discussed earlier which has a low anisotropy. After annealing, the coercivity increased to about 10 kOe. The high coercivity is due to the formation of the ordered fct phase. The hysteresis loop, however, still shows a shoulder at lower field indicative of the fact that the disordered low coercivity fcc coexists with the high coercivity fct phase. Figure 4 is a summary of the magnetic measurements for as-deposited and annealed $\text{Co}_{40}\text{Pt}_{60}$ films of several thickness. The as-deposited films show very low coercivities (30-300 Oe), irrespective of the thickness of the films. However, the coercivity after annealing was found to be thickness dependent with the thickest film showing the highest increase in coercivity. The grain size and the diffraction patterns of the as-grown films were very similar and therefore the magnetic properties were uniform for different thicknesses. The annealed films, on the other hand, undergo a solid state phase transformation reaction. Hence, the nucleation and growth of the fct phase and the influence of the substrate also become very important. Films with small thicknesses experience the substrate effect to a much larger degree than the thicker films. Fewer and larger grains with c-axis perpendicular to the film plane is typical for thinner films after annealing. We have some preliminary evidence of perpendicular magnetic anisotropy in annealed films with thicknesses lower than 300 \AA . As the film thickness increases, the grain orientation becomes random, and the grain size does not feel any effect from the substrate. A finer grain size is, therefore, obtained. This leads to more nucleation sites during fcc to fct transformation, a larger grain boundary area, and a higher coercivity.

CONCLUSION

$\text{Co}_x\text{Pt}_{100-x}$ films with $x = 45, 40$ were prepared by RF magnetron sputtering in a wide range of thickness. The magnetic and structural properties of these films were studied before and after annealing. The as-sputtered films have a soft magnetic behavior and a disordered fcc structure. After annealing they develop high coercivities which are due to the ordered fct structure which is produced in during the heat treatment. The magnitude of the coercive force in these films is found to be dependent on the sample thickness. That is, the coercivity increases with film thickness in the annealed samples. This is possibly due to surface and substrate effects that tend to be more prominent in the thinner films (i.e. 100 \AA).

REFERENCES

1. A. S. Darling, *Platinum Met. Rev.* 7, 96 (1963).
2. D. J. Craik, *Platinum Met. Rev.* 16, 129 (1972).

3. M. Yanagisawa, N. Yamaguchi, and Y. Suganuma, IEEE Trans. Mag. MAG 19, 1638 (1983).
4. D. Traves, J. T. Jacobs and E. Sawatsky, J. Appl. Phys. 46, 2760 (1975).
5. J. B. Newkirk and R. J. Smoluchowski, Appl. Phys. 22, 290 (1951).
6. Y. A. S. Shur, L. M. Magat, G. G. V. Ivanova, A. I. Mitsek, A. A. S. Yermolenko, and O. A. Ivanova, Fiz. Met. Metalloved. 26, 241 (1968).
7. E. Gebhardt and W. Koster, Z. Metallkunde, 32, 253 (1940).
8. A. S. Darling, Platinum Met. Rev. 7, 82 (1963).
9. M. Kitada and N. Shimizu, J. Appl. Phys. 54, 7089 (1983).
10. J. A. Aboaf, S. R. Herd, and E. Klokholm, IEEE Trans. Mag. MAG 19, 1514 (1983).
11. T. R. McGuire, J. A. Aboaf, and E. Klokholm, J. Appl. Phys. 55, 1951 (1984).

TECHNOLOGY AND APPLICATIONS OF PERMANENT MAGNETS

K.S.V.L. Narasimhan

Hoeganaes Corporation
Riverton, NJ

ABSTRACT

Recently developed high energy permanent magnets SmCo_5 , $\text{Sm}_2\text{Co}_{17}$, $\text{Nd}_2\text{Fe}_{14}\text{B}$ offer an interesting study of magnetic phenomenon. This publication discusses briefly the evolution of these magnets and the origin of the coercive force. Atomized SmCo_5 coarse particles (150 to 300 microns) exhibit unusually large coercive force contrary to the experience in cast alloys.

A brief discussion of utilization of these magnets into devices is also presented.

INTRODUCTION

General definition of a nanostructured material is related to materials with a grain size of less than or equal to 0.1 microns. Most magnetic materials of commercial importance if produced in this size will have significant property advantage. Difficulty of achieving these sizes has been a problem for the past three decades due to pyrophoricity of the materials or due to the crystal damage by excessive deformation in the grinding process. Currently, most magnetic materials are nearly 10 to 40 times the nanostructured definition. However, recently developed neodymium iron boron magnets by rapid solidification process have grain size as small as 0.1 microns.

This article presents an overview of fundamentals of higher energy product magnets and the resultant advantage realized in miniaturization of devices.

Technological Aspects of Permanent Magnets

All matter is either diamagnetic or paramagnetic. Diamagnetism arises from pair of electrons with opposite spin whereas paramagnetism arises from unpaired electrons. Paramagnetism of matter leads to, due to a competition between the exchange interaction and thermal excitations, at a temperature characteristic of the material, ferromagnetism (parallel ordering of spins of adjacent atoms) ferromagnetism (anti-parallel ordering of spins with a resultant net positive magnetic moment) and anti-ferromagnetism (anti-parallel ordering of spin with zero net moment).

Permanent magnets are generally ferro or ferrimagnetic. There are a variety of permanent magnets and a listing and type of magnets are discussed by Narasimhan¹.

The important qualifications that are required for a material to be a permanent magnet are: (1) the Curie temperature of the magnet should be over 300°C - this requirement permits the devices to operate at elevated temperatures and also, in most cases, permits a reasonable temperature coefficient of magnetic induction; (2) reasonable saturation induction, at least over 3,500 Gauss - this will control ultimate volume of the magnetic material used in a device; (3) crystal shape anisotropy - this will permit the realization of coercive force that is required to extract useful flux from the permanent; (4) the processing has to be cost effective - here a compromise is made between performance and cost, the so-called "flux per buck" terminology; (5) the temperature dependence of the magnetic properties should be favorable.

The classification of the alloys useful as permanent magnets can be made by the origin of the coercive force in these materials. There are eight or more different basic mechanisms that can contribute to the coercive force in magnetic materials. These are: (1) mechanical hardening, (2) precipitation hardening, (3) super-structure, (4) shape anisotropy, (5) crystal anisotropy, (6) exchange anisotropy, (7) narrow domain walls, (8) interatomic interactions, and (9) amorphous and microcrystalline alloys.

The technologically important alloys are the shape anisotropy alloys such as alnicos, Fe-Cr-Co, and the crystalline anisotropy materials such as rare earth-Co, rare-earth-iron-boron, ferrites, and MnAlC.

Ferrites and rare-earth cobalt magnets have become the main candidates for applications replacing the alnico magnets which dominated the market place for quite some time. The reason for this changeover is the energy efficiency and critical raw material (cobalt) conservation. Although rare earth-cobalt alloys contain nearly 60% cobalt, as compared to 23% in alnico alloys, the quantity of the alloy required to do the same job as alnico is significantly less, hence the cobalt savings is effected.

An entirely new type of alloy containing neodymium-iron and boron emerged as a result of extensive investigations at various laboratories to conserve cobalt. This new alloy has quite a few other advantages besides having no cobalt. Neodymium is available nearly six to ten times more than samarium which allow the magnet alloy to be utilized in several high volume applications.

The key element in the understanding of permanent magnetism is the concept of domain walls. Nanostructured material may in many cases cannot support a domain wall as they will be single domain as formed.

Table 1 lists the typical size of single domain for some important permanent magnets. A typical processing of alloy into permanent magnet is shown below:

Alloy Composition Selection \Rightarrow Vacuum Melting \Rightarrow Casting to Minimize Segregation \Rightarrow Crush to Nearly Single Domain Particle Size \Rightarrow Orient in a Magnetic Field Inside a Die Cavity \Rightarrow Press to Shape \Rightarrow Sinter \Rightarrow Clean \Rightarrow Ship

There are a variety of intermediate steps that are critical to the final quality of the magnets and these steps are characteristic to each magnet producer. The crushing process to produce nearly single domain particle size is generally believed to be necessary for the achievement of intrinsic coercivity (H_{ci}) force which gives the magnets a measure of resistance to demagnetization. The single domain size also allows the particles to orient in a magnetic field along the crystallographic easy direction of magnetization. This results in high values of remanence (B_r).

Table I. Anisotropy Constants and Saturation Magnetization of SmCo_5 , 2:17 and NdFeB Compounds

| | Single-Domain Particle Size | Exchange Constant | Theoretical $(BH)_{\max}$ | Curie Temperature |
|-----------------|-----------------------------|--------------------------------|---------------------------|------------------------|
| Magnet Type | D_c (μm) | A $\times 10^{-11}$ (J/m) | M G Oe | ($^{\circ}\text{C}$) |
| NdFeB | 0.26 | 1.25 | 65 | 310 |
| SmCo_5 | 1.6 | 3.5 | 29 | 690 |
| 2:17 | 0.66 | -- | 41 | 910 |

| | Saturation Magnetization | Anisotropy Constant | Domain-Wall Energy | Domain-Wall Thickness |
|-----------------|--------------------------|------------------------------|----------------------------|-----------------------|
| Magnet Type | I_s (T) | K_1 (MJ/m^3) | V (mJ/M^2) | δ (nm) |
| NdFeB | 16.1 | 4.5 | 3.0 | 5.2 |
| SmCo_5 | 1.07 | 13.0 | 85.0 | 5.1 |
| 2:17 | 1.28 | 3.3 | 43.0 | 10.0 |

The resistance to demagnetization is dependent on the magnitude of magneto-crystalline anisotropy which locks the magnetic moments preferentially into certain crystallographic direction which normally in permanent magnets the C-axis of the crystal.

The origin and role of crystalline anisotropy in rare earth intermetallics has been discussed extensively in the literature²⁻³. While theoretically the crystalline anisotropy prevents the rotation of the magnetic moments until a certain critical field is exceeded in real materials only 10 to 20% of the critical field is required to reverse the magnetization. Imperfections, chemical in homogenetics, grain boundaries and other defects cause reverse nucleation and growth of reverse domains resulting in demagnetization at lower applied fields than anticipated by the anisotropy field.

Grain Boundaries and Coercive Force

The role of grain boundaries appear to be more pronounced in the case of lower anisotropy magnets (Nd-Fe-B). SmCo_5 magnets have been shown⁴ to have featureless grain boundaries whereas Nd-Fe-B and Nd-Dy-Fe-B magnets have a light phase at the grain boundary. Transmission electron microscopy photographs on sintered Nd-Fe-B magnets is shown in Figures 1 and 2. Reversal or nucleation of domain walls takes place at or near these grain boundaries. This concept of grain boundary pinning or nucleation can explain certain unusual properties of Nd-Fe-B. As cast alloy of Nd-Fe-B with an average grain size exceeding 1000 microns show a coercive force of 6000 Oe but grinding this material results in a lowered coercive force. Powder with average particle size of 3.0 microns will have a coercive force of 1600 Oe. Powder of this average particle size is sintered into a magnet the coercive force will exceed 10,000 Oe. If these sintered magnets are crushed to an average particle size of 30-40 microns intrinsic coercive force is reduced to a few hundred oersted. This lowering of coercive force is observed whether a magnet is mechanically crushed or decrepitated by hydrogen. The coercive force is not increased even after annealing these powders.



Figure 1. Transmission electron micrograph of NdFeB magnet showing the grain boundary phase (216,000X)

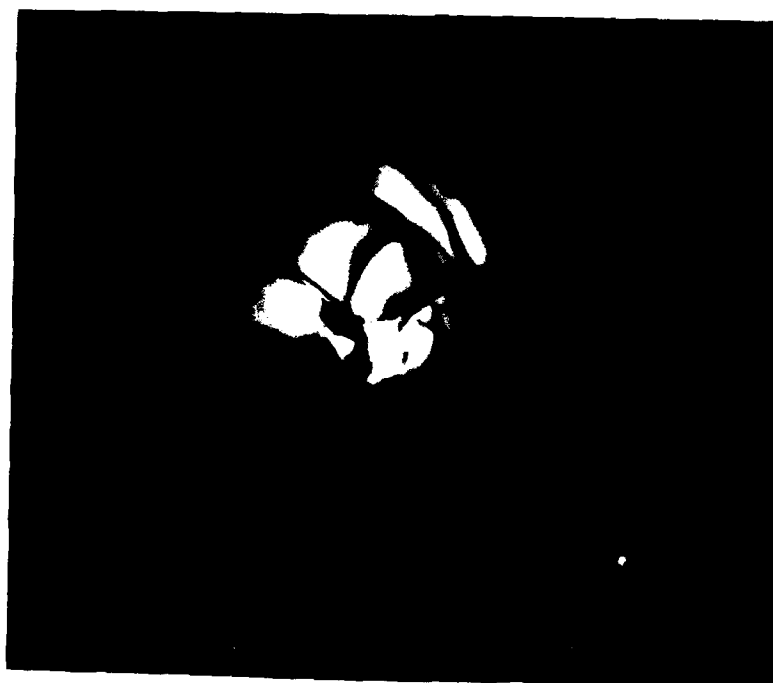


Figure 2. Transmission electron micrograph of NdDyFeB magnet showing the grain boundary phase and dysprosium segregation (80,000X)

These observations are in contrast with what is observed on rapidly solidified powder by melt spinning process⁶⁻⁷. Each of these powder particles have coercive force exceeding 10,000 Oe and have several grains with an average grain size of 0.1 microns, closer to a single domain size. If the grain size is closer to a single domain, the coercive force is not controlled by domain wall since the grain cannot energetically support a wall. The reversal mechanism takes place enmass over a group of grains. Thus, we have two distinct material types from the same alloy compositions. Material that is vacuum melted, cast (slow cooled) to a large grain size (Process A) and a material that is vacuum melted, rapidly cooled to a fine grain size (Process B). The reversal mechanism in Nd-Fe-B produced by Process A is controlled by the grain boundary phase. The uniformity of this phase around the grain boundary appears critical and can be easily damaged by crushing process resulting in lowered coercive force.

SmCo₅ behaves differently to the crushing process. Sintered magnets can be crushed without loss of coercive force. There is no grain boundary phase reported in the sintered magnet. A cast SmCo₅ alloy has a lowered coercive force than a ground alloy. It has been shown⁷ that as a function of milling time coercive force increases until about five microns below which plastic deformation seem to reduce the coercive force. Hence, it has been the standard in the industry to crush SmCo₅ alloy to five microns to achieve coercive force. Examination of the domain wall by magneto-optic kerr effect indicate that the wall in sintered magnet transgress many grain boundaries which would indicate that one should be able to achieve high coercive force in coarser particles as long as the alloy is homogeneous.

SmCo₅ was atomized in an argon gas atmosphere and quenched in liquid argon⁸. The atomized powder was classified into -300 to +150 microns and -150 to +75 micron fractions. These powders were processed into magnets by sintering and heat treatment. Table II lists the coercive force of sintered magnets.

Also listed in the table for comparison is a vacuum melted alloy that was cast, crushed to the particle size shown and sintered.

The coercive forces listed in Table II are much higher than that anticipated from the coarse particles. Atomization process might have produced fine grains that enhanced the coercive force. Further work is necessary to clarify this picture.




Table II. Coercive Force of Sintered SmCo₅ Magnets Made With Coarser Powders

| | Microns | H _{c1} (Oe) |
|---------------------|--------------|----------------------|
| Atomized | -300 to +150 | 22,000 |
| | -150 to +75 | 19,400 |
| Vacuum Melted, Cast | -300 to +150 | 5,000 |
| | -150 to +75 | 9,000 |

Application Aspect of Permanent Magnets

The volume of a magnet required for an optimized device is inversely proportional to BH_{max} , the energy product. Hence for miniaturization of devices higher energy product magnets are desired. Table III lists three types of magnets with different energy products and their effect on miniaturization of devices. Although this example is illustrated for speaker magnets, the same applies to voice coil motors for disc drive application, beam focusing device in travelling wave tubes (TWT), magnetic resonance imaging applications, magnetic separation devices and for a variety of DC motors.

Table III. Comparison of Ferrite, Alnico & Neodymium-Iron As Speaker Magnets

| | Ferrite | Alnico | Neodymium-Iron |
|-----------------------------|---|---|--|
| Br | 3950 | 12,700 | 12,300 |
| Hc | 2400 | 640 | 9250 |
| Hci | 2450 | 645 | 11,000 |
| UNIT | | | |
| PROPERTIES | | | |
| Bd | 2700 | 10,400 | 6,200 |
| Hd | 1150 | 530 | 5,600 |
| BdXHd | 3.60MGoe. | 5.50MGoe. | 35.0MGoe. |
| Density(g/cm ³) | 4.9 | 7.3 | 7.4 |
| Magnet lm | Say 1 | $\frac{1150}{530} = 2.17$ | $\frac{1150}{5600} = .21$ |
| Cross Sectional Area | Say 1 | $\frac{2700}{10,400} = .26$ | $\frac{2700}{6200} = .44$ |
| Vol. | 1X1 : 1 | 44% Less | 91% Less |
| Wt. | 1X4.9 : 4.9 | Same | 86% Less |
| Magnetic Circuit |  |  |  |

Room temperature demagnetization curves are shown in Figure 3. Both induction (B) and coercive force (H_c) are sensitive to temperature to a different degree for each of the permanent magnets. Table IV lists the H_c values at 100°C and -40°C. Device design has to take into consideration these variations and generally magnets are designed to operate above the "knee" in the second quadrant demagnetization curve over the entire range of temperature that a magnet will be exposed to in the device. Permeance coefficient is an important parameter that defines the operation of the magnet. Permeance coefficient (B/H) is related to the magnet geometry and whether or not the magnet is on a steel return path. Permeance coefficient (referred to as load line) is shown in Figure 4 by drawing a line from the origin to the permeance coefficient values. It is possible to determine the flux that can be generated from the magnet from the intersection of permeance line with the B line. If the permeance coefficient line is below the knee of the B Curve then the magnet does not recoil back to original value when the magnet is moved above the knee either by decreasing the temperature or removing the external demagnetizing field. The loss a magnet undergoes when the magnet is taken

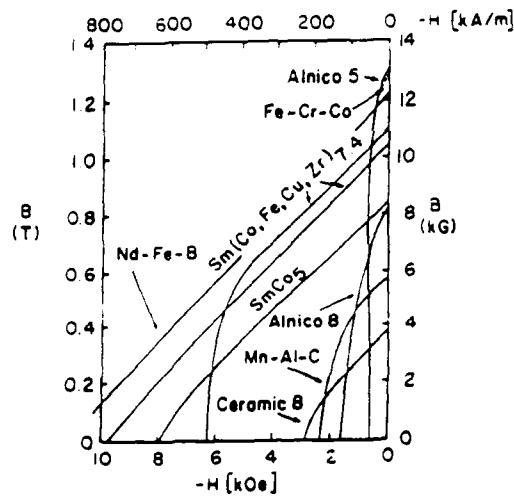


Figure 3. Typical room temperature demagnetization curves for high performance magnets of the most important commercial material families

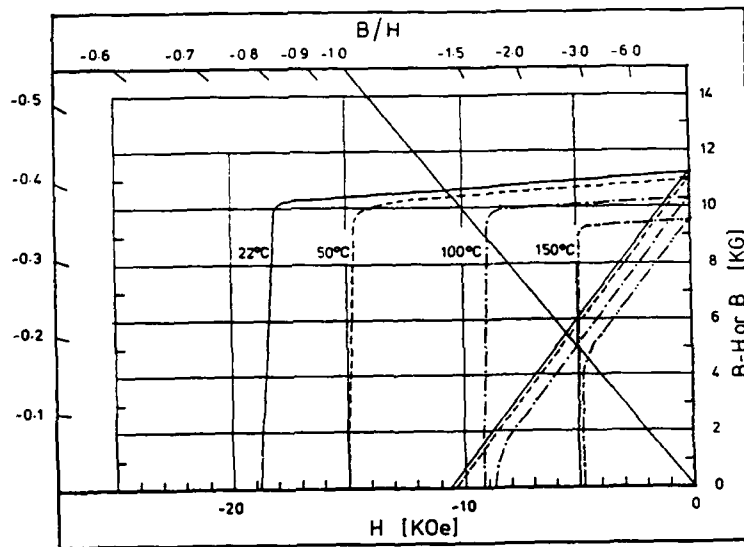


Figure 4. Typical B-H Curve and permeance coefficient (B/H)

below the knee and back above the knee is referred to as the irreversible loss. This loss can only be recovered by remagnetizing the magnet with a magnetizing coil. If a magnet is cycled more than once to the same location below the knee then the losses occur during the first cycling, subsequent cycling produces reversible flux although lowered from the initial values by an amount equal to the irreversible loss. The determination of the location of the knee is difficult because it is not a sharp transition. Hence most design engineers would operate well above the knee. Table V illustrates the location of the knee for the three high energy magnet types.

Table IV. Reversible H_c at Low and High Temperatures

| | Reversible H_c at 100°C | Reversible H_c at -40°C |
|----------------------------------|---------------------------|---------------------------|
| Ferrite | 4,000 Oe | 2,600 Oe |
| Alnico | 500 Oe | 500 Oe |
| SmCo ₅ | 6,000 Oe | 8,000 Oe |
| | 7,000 Oe | 10,000 Oe |
| Sm ₂ Co ₁₇ | 6,000 Oe | 8,000 Oe |
| | 7,000 Oe | 10,000 Oe |
| NdFeB | 4,000 Oe | 10,000 Oe |
| | 7,000 Oe | 11,000 Oe |

Magnets can undergo irreversible losses that are permanent. This type of loss occurs when there is a metallurgical change in the magnet either because of phase separation, severe oxidation, contaminants diffusion or other phase changes. NdFeB magnets lose their utility above 175°C, SmCo₅ above 250°C and '2:17' above 400°C.

Besides these losses that magnets experience, one has to take into consideration reversible losses of magnetization (B_r) with temperature. Table VI lists the reversible losses for the three high energy magnet types.

Table V. Location of the Knee of the Demagnetization Curve (B_k) for the Three Magnet Types

| Magnet Type | Location of the Knee (B_k) | | |
|-------------------|-----------------------------------|------------------------------|------------------------------|
| | -60°C | 100°C | 150°C |
| SmCo ₅ | Third Quadrant | Third Quadrant | Third Quadrant |
| '2:17' | 5000G in the Second Quadrant | 6500G in the Second Quadrant | 6750G in the Second Quadrant |
| NdFeB | Below 8000G in the Third Quadrant | 2500G in the Third Quadrant | 2000G in the Third Quadrant |

Table VI. Reversible Loss of SmCo_5 , '2:17' and NdFeB

| Magnet Type | -50°C to 0°C | 0°C to 100°C | 0 to 150°C |
|-----------------|-----------------|-----------------|---------------|
| SmCo_5 | -0.034 | -0.45 to 0.05 | 0.05 |
| '2:17' | | -0.0 to -0.03 | 0.024 |
| NdFeB | -0.085 to 0.095 | -0.085 to -0.16 | -0.09 to 0.16 |

Nanostructured magnets made from melt spinning process is discussed in detail by Croat⁶. Table VII lists the magnetic properties of resin bonded and hot pressed magnets. Similar principles as mentioned above apply for application of these magnets.

Table VII. Magnetic and Physical Properties of NdFeB Magnets Prepared from Rapidly Solidified Ribbon

| Characteristics | Bonded | Hot Pressed | Hot Formed | CGS Units |
|---|----------|-------------|--------------------------|-------------|
| Maximum Energy Product ($[\text{BH}]_{\text{max}}$) | 8.0 | 13.0 | 32.0 | MGOe |
| Residual Induction (B_r) | 6.3 | 7.9 | 11.75 | kGauss |
| Coercive Force (H_c) | 5.3 | 6.5 | 10.50 | kOersteds |
| Intrinsic Coercive Force (H_{ci}) | 15.0 | 16.0 | 13.0 | kOersteds |
| Saturation Magnetizing Force (99%) | 45.0 | 45.0 | 25.0 | kOersteds |
| Recoil Permeability | 1.15 | 1.15 | 1.05 | G/Oe |
| Density 6.0 | 7.5 | 7.5 | g/cm^3 | |
| Maximum Operating Temperature | 125.0 | 150.0 | 150(B/H-5) 150(B/H-1) | °C |
| Reversible Temperature Coefficient @ a Load Line of 1 | -0.192 | -0.157 | -0.157 | % °C |
| Electrical Resistivity @ 25°C | 18,000.0 | 160.0 | 160.0 | microohm cm |
| Hardness | 36-38 | 60 | 60 | Rockwell-C |

Future Directions

Current concepts of coercivity and processing limit achievement of maximum energy product to far shorter than theoretically achievable in commercial production. In limited production, SmCo_5 has been processed to 28MGOe (theoretical 31MGOe) and NdFeB to 45MGOe¹⁰⁻¹¹ (theoretical 64MGOe). Fine particle technology and theoretical aspects of coercivity has to be further understood to achieve the breakthrough necessary.

REFERENCES

1. K.S.V.L. Narasimhan, ASM Symposium Proceedings, "Soft and Hard Magnetic Materials", Edited by J. Salsgiver et al, p 131-145, (1986).
2. W. E. Wallace and K.S.V.L. Narasimhan, "Science and Technology of Rare Earth Materials", Academic Press, p 393 (1980).
3. W. E. Wallace, "Rare Earth Intermetallics", Academic Press
4. J. Livingston and D. L. Martin, Journal of Applied Physics, 48, p 2608 (1977).
5. G. Hadjipanayis, ASM Symposium Proceedings, "Soft and Hard Magnetic Materials", Edited by J. Salsgiver et al, p 89-104 (1986).
6. J. Croat, Ibid, p 81-88 (1986).
7. K. J. Strnat, Journal of Magnetism and Magnetic Materials, 7, 351 (1978)
8. K.S.V.L. Narasimhan and E. J. Dulis, U.S. Patent 4,585,473 (1986)
9. K.S.V.L. Narasimhan, Eighth International Workshop on Rare Earth-Cobalt Permanent Magnets, Roanoke, VA (1981) Book by University of Dayton, KL-365, Dayton, OH (45469).
10. K.S.V.L. Narasimhan, Journal of Applied Physics, 57, 4085 (1985).
11. M. Sagawa, S. Fujimura, N. Togawa, H. Yamamoto and Y. Matsuura, Journal of Applied Physics, 55, 2083 (1986).

AUTHOR INDEX

- Alexopoulos, P.S., 99, 239
 Amaral, V.S., 393, 399
 Arajs, S., 577
 Arrott, A.S., 15, 77
 Asti, G., 465
 Badia, F., 201
 Barandiarán, J., 387
 Barbara, B., 393, 399
 Beardsley, I.A., 239
 Beatrice, C., 275
 Berker, A.N., 411
 Berkowitz, A.E., 533
 Borchers, J.A., 117
 Broto, J.M., 195
 Buschow, K.H.J., 471
 Celinski, Z., 15, 77
 Celotta, R.J., 335
 Chandhok, V.K., 599
 Chien, C.L., 477
 Christiansen, G., 573
 Cochran, J.F., 15, 77
 Coey, J.M.D., 439
 Colombo, E., 209
 Cullen, J.R., 367
 Daalderop, G.H.O., 185
 de Jonge, W.J.M., 419
 de Miguel, J.J., 37
 Dieny, B., 195
 Donzelli, O., 209
 Du, R., 117
 Dulis, E.J., 599
 Engel, B.N., 67, 137, 181
 England, C.D., 181
 Erwin, R.W., 117
 Fahsold, G., 61
 Falco, C.M., 67, 137, 181
 Fert, A., 221
 Fidler, J., 627
 Filippi, J., 393, 399
 Flevaris, N.K., 177, 191
 Flynn, C.P., 117
 Franse, J.J.M., 459
 Fratucello, G.B., 209
 Freeman, A.J., 1
 Freitas, P.P., 405
 Gambino, R.J., 91, 332
 Gangopadhyay, S., 497
 Garcia, N., 301, 333, 581
 Gavigan, J.P., 81
 Geiss, R.H., 239
 Gibaud, A., 145
 Givord, D., 635
 Hadjipanayis, G.C., 497, 551, 607, 701
 Hammond, M.S., 61
 Hansen, P., 249
 Hathaway, K., 331
 Heinrich, B., 15, 37, 77
 Hendriksen, P.V., 573
 Hernando, A., 387
 Homma, H., 145
 Hui, K., 411
 Humphrey, F.B., 269
 Hurdequint, H., 171
 Jacobs, T.H., 471
 Jacobsen, K.W., 573
 Jakubovics, J.P., 255
 Jansen, A.G.M., 393
 Jansen, H.J.F., 349
 Kearney, P.A., 67
 Kelly, P.J., 185
 Kirschner, J., 25, 37, 61
 Klabunde, K.J., 497
 Klahn, S., 249
 Koch, C.B., 559
 Koon, N.C., 55
 Kostikas, A., 551
 Krishnan, R., 177, 191
 Kronmüller, H., 657
 Leeuwen, R.V., 181
 Li, C., 1
 Li, Y.P., 551
 Linderoth, S., 559, 563
 Liz, L., 567
 Lu, Q., 635
 Majkrzak, C.F., 145
 Martinez, B., 201
 Maurer, M., 195
 Mazzetti, P., 275
 McFadyen, I.R., 99, 239
 Meier, F., 71, 331
 Mergel, D., 249
 Miranda, R., 37
 Moreira, J.M., 393
 Morrish, A.H., 511
 Morup, S., 545, 559, 563, 573
 Myrtle, K., 15, 77
 Nakada, M., 181
 Narasimhan, K.S.V.L., 707
 Nguyen, T.A., 239
 Nogues, J., 339

- O'Handley, R.C., 109
 O'Shea, M.J., 377
 Otani, Y., 695
 Ounadjela, K., 331
 Ousset, J.C., 195
 Papaefthymiou, V., 551
 Piecuch, M., 195
 Pierce, D.T., 335
 Pinkerton, F.E., 591
 Plaskett, T.S., 405
 Porte, M., 177, 191
 Pouloupoulos, P., 177
 Prinz, G.A., 41
 López Quintela, M.A., 567
 Raasch, D., 249
 Radwanski, R.J., 459
 Rao, K.V., 339
 Ravet, M.F., 195
 Rhyne, J.J., 117
 Ribas, R., 201
 Rivas, J., 567
 Rivero, G., 387
 Ronconi, F., 209
 Rossignol, M.F., 635
 Rots, M., 103
 Salamon, M.B., 117
 Sanyal, M.K., 145
 Satija, S.K., 145
 Scheinfein, M., 335
 Schneider, C.M., 37
 Schultz, L., 583
 Schuster, P., 37
 Schuurmans, M.F.H., 185
 Sellmyer, D.J., 151, 215
 Sethi, S.A., 563
 Shah, S.I., 701
 Shan, Z.S., 151, 215
 Simopoulos, A., 551
 Sinha, S.K., 145
 Slaughter, J.M., 67, 137
 Sorensen, C.M., 497
 Soukoulis, C.M., 683
 Sousa, J.B., 393
 Spence, J.C.H., 279
 Stampanoni, M., 71
 Sun, S.W., 109
 Swagten, H.J.M., 419
 Swann, C.P., 701
 Tejada, J., 201
 Tessier, M., 191
 Tsoukatos, A., 701
 Tsui, F., 117
 Unguris, J., 335
 Vaterlaus, A., 71
 Vázquez, M., 387
 Vitoria, R.H., 331, 677
 Vinai, F., 275
 Wang, Z.L., 279
 Wiedmann, M.H., 67
 Winter, I., 567
 Wu, R.Q., 1
 Yiping, L., 497, 551
 Zhou, X.Z., 511

SUBJECT INDEX

- Amorphous magnets
 - α -Dy_xGd_{1-x}Ni, 399
 - Anderson localization, 393
 - law of approach to saturation, 399
 - magnetic hysteresis, 683
 - magnetostriction, 387
 - random magnets, 367
 - Tb-Fe films, 377
 - U_{1-x}Sb_x, 405
- Applications
 - ferromagnetic/semiconductor, 41
 - magneto-optics, 91
 - permanent magnets, 707
- Atomization (see Permanent Magnets), 599
- Band structure, 1
- Bilayers, 15
- Coercivity (see Permanent magnets - Magnetic hysteresis), 607, 635, 657, 677, 683, 695
- Crystal field interactions, 439, 459
- Crystalline structure, 37, 137, 145
- Domain walls (see Magnetic domains), 99, 269, 275
- Electron microscopy, 279, 607, 627
- Electronic structure, 1, 37
- Epitaxial
 - bcc Fe, Co, Ni, 15
 - Co/Pd, 181
 - fcc-Co, 37
 - rare-earths, 117
- Extrusion (see Permanent magnets), 599
- Ferromagnetic resonance, 15, 77, 171
- Fine particles, 477, 497, 511, 533
 - electrical properties, 577
 - Fe-based, 545
 - Fe-Cr-B, 551, 559
 - Fe-Ni-B, 563
 - magnetization reversal, 573
 - Nd-Fe-B, 567
 - spin waves, 581
- Force microscopy, 301
- Granular solids, 477
- Hybrid structures, 41
- Hyperfine interactions (see Mössbauer), 55, 209
- Inelastic electron scattering, 61
- Interfaces, 1, 67, 71
- Intermetallic compounds, 471
- Laser ablation, 81
- Law of approach to saturation, 399
- LEED, 37, 67
- Lorentz microscopy, 279, 607, 627
- Magnetic anisotropy, 349
 - Co_nPd_m multilayers, 185
 - random anisotropy, 367
- Magnetic domains, 99, 269, 275
- Magnetic hysteresis (see Permanent magnets), 607, 635, 657, 677, 683, 695
- Magnetic imaging
 - TEM, 279
 - SEM, 335
- Magnetic moments, 1
- Magnetic semiconductors, 419
- Magnetic transitions, 439, 459
 - FOMP, 465
- Magneto-optics
 - exchanged coupled films, 91
 - Mo-recording, 249
- Magnetoresistance (see Transport properties), 221, 405
- Magnetostriction, 109, 387
- MBE growth, 15, 37, 117, 181
- Melt-spun magnets, 591, 607
- Metastable structures, 15
- Micromagnetics
 - domain structure, 99
 - longitudinal recording media, 239
 - magnetic hysteresis, 677
 - magnetization configurations, 255
 - permanent magnets, 657
- Microstructure, 607
- Monolayers, 15, 37
- Mössbauer
 - Fe/Ag, 55
 - Fe/Ni, 209
 - fine particles, 511, 545, 551
 - surfaces-interfaces, 103

- Multilayers
 - Co_nPd_m, 185
 - Co/Pd, 181
 - Co/Pt, 191
 - Dy/transition metal, 215
 - Fe/Ni, 209
 - Fe/Ru, 195
 - Fe/Si, 201
- Neutron diffraction, 117
- Nucleation field, 657
- Permanent magnets,
 - applications, 707
 - atomization, 599
 - extrusion, 599
 - Lorentz microscopy, 607, 627
 - magnetic hysteresis, 607, 635, 657, 677, 683, 695
 - mechanically alloyed, 583
 - melt-spun, 591
 - microstructure, 607
 - Nd-Fe-B, 599
- Photoemission, 25, 61
- Random magnets (see Amorphous magnets), 367
- Random systems, 411
- REED, 15, 67
- Scanning tunneling microscopy, 301, 331, 339
- Superconductors, 339
- Superlattices, 15, 37, 117, 181
- Surface
 - magnetism, 1, 71
 - magnetostriction, 109
- Thin films
 - amorphous Tb-Fe, 377
 - exchanged coupled films, 15, 91
 - Fe/Ag, 55
 - growth and magnetic properties, 15
 - laser ablation, 81
- Transport properties, 221, 405
- X-ray characterization, 137, 145